

**The influence of multidimensional structures
on the interpretation of LOTEM data
with one-dimensional models
and the application to data from Israel**

Inaugural-Dissertation
zur
Erlangung des Doktorgrades
der Mathematisch-Naturwissenschaftlichen Fakultät
der Universität zu Köln

vorgelegt von
Carsten Scholl
aus Kevelaer

Köln, 2005

Berichterstatter: Prof. Dr. B. Tezkan
Prof. Dr. A. Junge

Tag der letzten mündlichen Prüfung: 11.11.2005

Contents

Abstract	vii
Zusammenfassung	ix
1 Introduction	1
2 Basics of TEM	5
2.1 The SHOTEM modification	6
2.2 The LOTEM modification	7
2.2.1 The system response	8
2.2.2 Data processing	10
2.2.3 Estimation of the measurement errors	10
3 Inversion of geophysical data	13
3.1 Inversion theory	13
3.2 Different strategies of inversion	15
3.2.1 Trial-and-error	15
3.2.2 Inversion through linearisation	16
3.2.3 Monte-Carlo inversion	20
3.2.4 Hybrid Marquardt Monte-Carlo inversion	21
3.3 Joint-inversion	22
3.4 EMUPLUS	22
3.5 Appraisal of resulting models	23

4	Effects of complex geoelectric settings on TEM-data	25
4.1	Effects of different material parameters	25
4.1.1	Non-scalar resistivity	26
4.1.2	Magnetic permeability unequal to vacuum permeability . . .	27
4.1.3	Time depending material parameters	27
4.2	Effects of multidimensional resistivity structures	29
4.2.1	Forward modelling	29
4.2.2	Review of previous studies	31
4.2.3	The calibration factor	40
5	1-D inversion of multidimensional TEM-data	43
5.1	Producing the synthetic data sets	44
5.1.1	Adding artificial noise	45
5.2	Determination of a proper regularisation parameter	48
5.2.1	Choosing a value for λ	50
5.2.2	Restricting the decrease in the value of λ	52
5.2.3	Testing the regularisation schemes with synthetic data	54
5.3	Influence of multidimensional structures on the single 1-D inversion of LOTEM-transients	63
5.3.1	Dipping layers (models B and C)	65
5.3.2	Vanishing layer (models D1 to E3)	65
5.3.3	Small inhomogeneities (models G1 to J2)	71
5.3.4	Faults (models F1 to F3 and K1 to L3)	74
5.3.5	Moderate lateral changes (model M)	78
5.3.6	Summary of the results in this section	78
5.4	The influence of multidimensional structures on joint-inversions . . .	80
5.4.1	Soft Joint-Inversion	84
5.5	Joint-interpretation of LOTEM and SHOTEM data sets	91
5.5.1	Inversions of synthetic SHOTEM-transients	92
5.5.2	Joint-inversions of synthetic LOTEM- and SHOTEM- transients	95
5.5.3	Implications for the joint-interpretation of SHOTEM and LOTEM data sets	100
5.6	Inversion of Tx-distortion parameters	101
5.6.1	Sign of the transients	104

5.6.2	Model N1: Conductive patch	107
5.6.3	Model N2: Resistive patch	114
5.6.4	Results for model N1 and N2	116
5.7	Removing distortions	116
5.7.1	Results of the inversions	118
5.8	An interpretation scheme for the field data sets	125
6	The TEM-measurements in Israel	129
6.1	Geological Background	129
6.1.1	Hydrogeological background	130
6.1.2	Geophysical task	135
6.2	The field campaign	136
6.2.1	LOTEM system response	139
6.2.2	Special problems	141
6.3	Inversions of the field data sets	142
6.3.1	Calibration sites	144
6.3.2	Summary of the results for the calibration sites	162
6.3.3	Sites along the traverse: An example (Sites BSA and BSB)	163
6.4	The results of the field campaign	167
7	Discussion	173
	Bibliography	177
A	Implementation of the Occam's inversion	189
A.1	Transformation of the regularisation parameter λ	189
A.2	High initial misfits	190
A.2.1	Using the second derivative roughness definition R_2	193
B	1-D pseudosections of synthetic 2-D models	195
B.1	Testing the regularisation schemes with a 1-D model (model A)	196
B.2	Pseudo-sections for the models B to M	237
B.2.1	Dipping layers (models B and C)	237
B.2.2	End of a conductive layer (models D1 to D3)	256
B.2.3	End of a resistive layer (models E1 to E3)	284

B.2.4	Extreme case of a fault: Two quarter-spaces (models F1 to F3)	312
B.2.5	Conductive patch at an intermediate depth (models G1 and G2)	340
B.2.6	Resistive patch at an intermediate depth (models H1 and H2)	359
B.2.7	Shallow conductive patch (models I1 and I2)	378
B.2.8	Shallow resistive patch (models J1 and J2)	399
B.2.9	Displacement in a conductive basement (models K1 to K3)	420
B.2.10	Displacement in a conductive basement (models L1 to L3)	448
B.2.11	Model with several lateral changes (model M)	476
B.3	Inversions of synthetic SHOTEM data sets	486
B.3.1	Joint-inversions of synthetic SHOTEM and LOTEM data sets	494
B.4	Shallow patch close to the Tx (models N1 and N2)	510
B.5	Inversions of edited transients of adjacent stations	551
B.5.1	Model F1	552
B.5.2	Model K3	566
B.5.3	Model M	580
C	The field data sets	595
C.1	Coordinates for transmitters and receivers in Israel	595
C.1.1	Tx-coordinates	595
C.1.2	Rx-coordinates	595
C.1.3	Coordinates of the SHOTEM sites	609
C.2	Single inversion results	610
D	Geophysical interpretation of the field data sets	685
D.1	Geophysical interpretation of the Rx-sites	685
D.1.1	Site AFA	685
D.1.2	Sites AUA and AUB	688
D.1.3	Sites BEA and BEB	690
D.1.4	Sites CAA and CAB	694
D.1.5	Sites DVA and DVB	697
D.1.6	Site EMA	702
D.1.7	Site ENA	704
D.1.8	Site GBB	704

D.1.9	Sites HAA and HAB	706
D.1.10	Sites KEA and KEB	711
D.1.11	Sites KKA and KKB	715
D.1.12	Sites KNA and KNB	719
D.1.13	Site PHA	723
D.1.14	Site RAA	723
D.1.15	Sites RZA and RZB	725
D.1.16	Site SAA	728
D.1.17	Site TAA	732
D.1.18	Sites TKA and TKB	734
D.1.19	Sites YAA and YAB	736
D.1.20	Sites YOA and YOB	741
D.2	The statistics for field data set inversions	744
E	On the inversion of geophysical data	779
E.1	Assumptions included in inversions	779
E.2	Linearisation error	781
E.2.1	Few layers with variable thicknesses vs. many layers with fixed thicknesses	781
E.3	Inversion results	784
E.3.1	Model discretisation	784
F	Manual for EMUPLUS	787
F.1	General remarks	787
F.2	The data set concept	788
F.3	The setup	789
F.4	Commands related to earth models	792
F.5	Commands related to the data sets	793
F.6	Plotting, forward calculation and inversion	795
	Acknowledgments	799

Abstract

The influence of multidimensional resistivity structures on inversion results of Transient ElectroMagnetic (TEM) data using one-dimensional (1-D) models is examined. The investigation is focused on the Long-Offset TEM (LOTEM) method. Synthetic data for the electric and magnetic field components typically measured at LOTEM receiver sites are calculated for a wide variety of models. These transients are inverted with a 1-D smooth model inversion algorithm. The inversion results do not exactly reproduce the original model.

An attempt to reduce the model distortions caused by the multidimensional structures with different regularisation schemes fails. Statistically, the new regularisation schemes reduce the roughness of the models slightly, which will suppress artificial structures. In general, however, the geological interpretation will not be changed.

The inversion of synthetic data sets shows that the different LOTEM-components provide different information with respect to the multidimensional structure. The 1-D models resulting from automated inversions thus may be inconsistent for the different components. In most cases meaningful information about the underlying model can be derived from the pseudo-sections of composed 1-D models. However, the inversion results do not only reflect the subsurface close to the receiver (Rx) but also the subsurface close to the transmitter (Tx) and between Rx and Tx. In the best cases, the inversion results thus reflect the gross resistivity structure of the subsurface. Comparing the TEM results to the selective information from a borehole therefore might show some discrepancies.

The LOTEM results will also be different to results for the SHort-Offset TEM (SHOTEM) modification, as the volume of the subsurface contributing to the induction process differs significantly from the one for the LOTEM setup.

The inconsistencies of the models for the different components causes a problem. The various models derived from different TEM-components at one single position have to be merged into one consistent geophysical model. A common approach would be to invert all data sets jointly in one inversion. However, this approach turned out to be dangerous as the so-called joint-inversions of different LOTEM-components tends to produce artifacts instead of suppressing them.

A new joint-inversion approach is presented. Here, variations between the models for the different data sets are allowed to account for inconsistencies in the transients. The regularisation of the inversion favours results, where the variations between the models for the different data sets are small. The resulting pseudo-sections in general show far less spurious structures than for the pseudo-sections derived from the standard joint-inversions. In addition, the different models allow to analyse the inconsistencies and to estimate the reliability of a certain feature.

Further it is shown that the data distortion by certain inhomogeneities close to the Tx can be accounted for by introducing additional parameters to the inversion process. This way pseudo-sections can be derived from the data sets which reproduce the gross resistivity structure very well for almost all data sets.

The new regularisation scheme, the new joint-inversion algorithm and the additional distortion parameters are used to interpret data sets from a field campaign in northern Israel. The objective of the project is to derive the distribution of saline water in the subsurface. This knowledge would help to determine the source of saline water currently flowing into the Sea of Galilee and degrading its water quality.

The new interpretation scheme proves to be very helpful to derive meaningful resistivity models from the measured data sets. The analyses of the data shows that some stations have to be excluded from the interpretation. Nevertheless, a cross-section between the Mediterranean and the Sea of Galilee is derived from the TEM data sets. It supports the hypothesis that saltwater from the Mediterranean plays an active role in the salination of the Sea of Galilee.

Zusammenfassung

In dieser Arbeit werden die Auswirkungen einer mehrdimensionalen Leitfähigkeitsverteilung auf die Inversion von Transient ElektroMagnetischen (TEM) Daten mittels eindimensionaler (1-D) Modelle untersucht. Die Studie konzentriert sich hauptsächlich auf Datensätze der Long-Offset-TEM-Methode (LOTEM). Dazu werden Datensätze der elektrischen und magnetischen Feldkomponenten, die üblicherweise an LOTEM-Empfängern aufgezeichnet werden, für eine große Anzahl synthetischer Modell generiert. Anschließend werden die Datensätze mit einem 1-D Inversionsalgorithmus invertiert. Der Inversionsalgorithmus versucht dabei, über eine zusätzliche Regularisierung ein möglichst glattes Modell zu finden, das die Daten erklärt. Die Modelle, die man aus diesem Inversionsansatz erhält, geben erwartungsgemäß das synthetische Modell nicht exakt wieder.

Der Versuch, die Modellverzerrungen durch eine geeignete Regularisierungsstrategie zu reduzieren, scheitert. Zwar reduzieren einige der neuen Strategien die Rauigkeit der Modelle leicht, wirklich unterdrückt werden die Verzerrungen aber nicht. Die Unterschiede zwischen den Ergebnissen verschiedener Regularisierungsstrategien sind sehr klein. Die Gefahr geologischer Missinterpretation der Ergebnisse wäre identisch.

Die Inversionen der einzelnen LOTEM-Komponenten zeigen, dass diese unterschiedlich von verschiedenen mehrdimensionalen Strukturen beeinflusst werden. Die erhaltenen Modelle weisen unterschiedliche Verzerrungen auf und sind damit inkonsistent. Die Verzerrungen sind allerdings in den meisten Fällen nicht sehr stark. Die Pseudosektionen aus aneinandergfügten 1-D Modellen repräsentieren das wahre Modell meist so gut, dass sinnvolle Informationen über den Untergrund aus ihnen abgeleitet werden können. Die Inversionsergebnisse zeigen, dass die Modelle nicht nur den Untergrund unter dem Empfänger (Rx), sondern auch den unter dem Sender (Tx) und den dazwischen repräsentieren. In den besten Fällen geben die erhaltenen Modelle ein gemittelttes Bild des Untergrunds wieder. Wenn diese Modelle mit den punktuellen Informationen aus einem Bohrloch verglichen werden, sind gewisse Diskrepanzen zu erwarten.

Bei der SHort-Offset-TEM-Methode (SHOTEM) kommen deutlich kleinere Off-

sets als bei LOTEM zum Einsatz. Der Bereich des Untergrunds, der Einfluss auf die Messdaten hat, ist kleiner. Der Einfluss derselben mehrdimensionalen Struktur auf das Inversionsergebnis für einen SHOTEM Datensatz unterscheidet sich daher deutlich von dem auf den an gleicher Stelle aufgezeichneten LOTEM Datensatz.

Die inkonsistenten Modelle für die verschiedenen, am gleichen Ort gemessenen Komponenten stellen ein Problem dar. Für die endgültige Interpretation muss ein einheitliches Leitfähigkeitsmodell aus den unterschiedlichen Modellen erstellt werden. Eine gängige Methode, um ein gemeinsames Modell zu erstellen, wäre eine so genannte "Joint-Inversion". Hier werden die Datensätze gemeinsam in einer Inversion verwendet, um ein einheitliches Modell zu finden, welches alle Datensätze gleichermaßen erklärt. Bei den Modellrechnungen in dieser Arbeit zeigt sich jedoch, dass dieser Ansatz nicht sinnvoll ist, wenn die Daten durch mehrdimensionale Strukturen verzerrt sind. Die Ergebnisse derartiger Joint-Inversionen weisen oft starke Artefakte auf.

Daher wird ein neuer Ansatz zur Joint-Inversion entwickelt. Hierbei wird jeder Datensatz einem eigenen Modell zugeordnet. Über eine geeignete Regularisierungsbedingung wird erreicht, dass sich die Modelle nur unterscheiden soweit dies erforderlich ist. Die daraus abgeleiteten Pseudosektionen weisen weitaus weniger Artefakte auf als für die bisher übliche Joint-Inversion. Zusätzlich kann man über die Betrachtung der Einzelergebnisse die Störungen der Datensätze analysieren und die Verlässlichkeit einzelner Modellmerkmale abschätzen.

Weiterhin wird gezeigt, dass man die Datenverzerrungen, die durch sendernahe Störkörper hervorgerufen werden, durch zwei zusätzliche Modellparameter in der Inversion berücksichtigen kann. Aus den meisten der unter Umständen stark verzerrten Datensätzen kann so die grundsätzliche Leitfähigkeitsverteilung im Untergrund abgeleitet werden.

Die neue Regularisierungsstrategie, die neu entwickelte Joint-Inversion und die Verzerrungsparameter werden verwendet, um die Datensätze einer Messkampagne in Nord-Israel zu interpretieren. Das Ziel des Projekts ist, die Verteilung salinen Wassers im Untergrund festzustellen. Damit möchte man die Frage nach der Quelle des salinen Wassers klären, das sich in den See Genezareth ergießt und die Wasserqualität des Sees deutlich herabsetzt.

Das neue Interpretationsschema stellt sich bei der Bearbeitung der Datensätze als sehr hilfreich heraus. Die Analyse der Datensätze zeigt, dass die Daten einiger Stationen als zu gestört verworfen werden müssen. Dennoch kann ein Leitfähigkeits-Schnittbild vom Mittelmeer zum See Genezareth aus den TEM-Daten abgeleitet werden. Diese unterstützt die Hypothese, dass das Salzwasser aus dem Mittelmeer eine aktive Rolle bei der Versalzung des See Genezareth spielt.

CHAPTER 1

Introduction

ElectroMagnetic (EM) methods in applied geophysics are used to determine the distribution of parameters in the subsurface, which influence the behaviour of electromagnetic fields in the earth. Some of these are especially sensitive to parameters like the relative permittivity ϵ (e.g. Ground Penetrating Radar, GPR, Knödel et al. [1997]) or polarisation effects (e.g. Induced Polarisation, IP, Pelton et al. [1978]). Most methods, however, aim at deriving the distribution of the electrical resistivity $\rho(x, y, z)$ or the magnetic permeability $\mu(x, y, z)$, although changes in the latter are only considered in special cases [Thomas, 1977; Yadav and Lal, 1989; Kriegshäuser, 1991]. In principle, EM methods can be used whenever the target differs from its surrounding in any of these parameters. In this work, mainly changes in the resistivity or its inverse, the conductivity are considered.

EM methods measure the response of the earth to an electromagnetic excitation. Often EM methods are divided into Frequency Domain (FD) and Time Domain methods. FD methods consider earth responses to an electromagnetic signal at discrete frequencies. The sources of the signals can be either natural phenomena (e.g. MagnetoTellurics, MT, Cagniard [1953]) or artificial transmitters (e.g. Controlled Source AudioMagnetoTellurics, CSAMT, Goldstein and Strangway [1975]). TD methods depend on an artificial source. Here, the decaying earth response after shutting off an electromagnetic field produced by a transmitter is measured. Therefore, Time-Domain ElectroMagnetic (TDEM) methods are also called Transient ElectroMagnetic (TEM) methods. With respect to the offset of the transmitter (Tx) to the receiver (Rx), two modifications are in use: SHort-Offset TEM (SHOTEM, sec. 2.1) and Long-Offset TEM (LOTEM, sec. 2.2). The latter has been continuously developed at the Institute of Geophysics and Meteorology of the University of Cologne (IGM). In the LOTEM case, the Rx comprises sensors for the electric and magnetic fields (or their time derivatives) in up to three dimensions.

The standard automated interpretation for TEM methods is still based on the inversion of simple earth models. In most cases, one-dimensional (1-D), layered half-spaces are considered in the inversion [Petry, 1987], where the resistivity ρ changes

only with depth. More complex settings are usually tackled by manual modelling (recent examples are Hördt et al. [2000]; Schaumann [2001]; Kalscheuer [2004]). Although TEM inversion programs for more complex earth structures are beginning to emerge [Mitsuhata et al., 2002; Scholl et al., 2003; Commer, 2003; Newman and Commer, 2005]. At present, however, the multidimensional inversion algorithms are rare and still under development. In addition, they require a vast amount of computer resources. Even more important, a dense grid of TEM-Tx and -Rx is needed to resolve a three-dimensional resistivity structure [Commer, 2003]. However, such a setup will be very expensive unless the area is under investigation is very small. For this reason, 1-D inversion algorithms will still be used in the future.

In the last four years, the IGM participated in a project in Israel (chapter 6). In order to address the (hydro-)geological question of the project, the resistivity structure in the subsurface of a large area in northern Israel had to be investigated. As no rapid lateral variations of the target were expected, it was decided to deploy the TEM equipment pointwise. This means that the distance between different Tx-Rx-setups is significantly larger than the exploration depth. Each station thus has to be considered independent. Still, at each site several data sets for different field components were recorded. It was planned to interpret the data sets by means of 1-D inversions.

The problem with any 1-D interpretation is that even in the best case the subsurface is only “approximately one-dimensional”. Any deviation from this assumed one-dimensionality might change or distort the data sets in a way that an interpretation of these data will lead to a wrong, “distorted” geophysical model. The question which arises is how to detect and maybe reduce the distortion of the resulting model to avoid geological misinterpretations.

This work addresses the problem of how to derive reasonable 1-D resistivity distributions from measured data when only a sparse data set is available, and how to estimate the reliability of the resulting model. The derived interpretation scheme will be applied to the data sets recorded during the Israel campaign.

In chapter 2 the basics of TEM-methods and the equipment used in the field are introduced. Chapter 3 explains the theoretical background of inversions. In chapter 4, the previous studies are reviewed which examine the effects of a parameter distribution more complex than a 1-D resistivity model.

The main parts of the work are presented in the next two chapters. Chapter 5 addresses the question if and how it is possible to derive a meaningful 1-D model from a data set which is measured over a non-1-D subsurface. To answer this question a large number of synthetic data sets for different field components were calculated for several multidimensional resistivity models. The inversion of these data sets give an insight in how the interpretation of different TEM data sets is influenced by multidimensional structures.

Mainly three different approaches are used to derive reasonable 1-D models from these data sets. The first approach is to suppress model-distortions caused by the effect of multidimensional structures by means of a proper regularisation of the inversion. Second, the information from all measured field components are combined in one interpretation scheme. Finally, a certain type of distortions will be parameterised as additional model parameter.

All three approaches are combined for the inversions of the field data sets from Israel (chapter 6). In chapter 7 the results of this work are discussed.

Preliminary notes

This thesis is available in two PDF-versions, a short and a long. The appendices B, C and parts of D are only included in the long version.

For brevity, the term “multidimensional transient” will be used for data sets which are influenced by multidimensional structures. Further, when inversions are referred to as done “with/without (Tx-)distortion” this means that the Tx-distortion parameters (see sec. 5.6) are in- or excluded in the inversion process.

Throughout this thesis, vectors and matrices are represented by bold characters. Lower case characters represent vectors, whereas upper case characters represent matrices.

CHAPTER 2

Basics of TEM

Commonly two types of transmitters are used for Transient ElectroMagnetic (TEM) measurements: either a loop source, forming a vertical magnetic dipole, or a grounded wire, forming a horizontal electric dipole. In the first case the coupling to ground is solely inductive, in the latter it is both inductive and galvanic. In real applications, these dipoles are of finite length (“bipoles”) or area, respectively.

At a certain time, the state of the transmitter current is changed, e.g. the current is switched off or the polarity of current is reversed. The fields caused by this change propagate through the air with an EM-wave almost with the speed of light. However, the propagation through the conducting subsurface is much slower. According to Lenz’ law, currents are induced to counteract the change of the primary magnetic field. The first part of the earth to “notice” the change is the part right below the surface. Here, the induced currents reproduce almost the currents originally flowing through the transmitter cables, thus shielding the deeper parts of the earth from the change of the primary field. Depending on the conductivity of the soil the induced currents decay, exposing the subjacent parts to the change, which then start reproducing the original magnetic field. This way the information about the change in the primary field propagates away from the transmitter.

However, this shielding is never perfect. Also, the collapse of the induced current in a certain volume is not abrupt. Even at early stages of the process currents are induced in remote parts of the earth. Though, the maximum of the induced currents propagate diffusively down- and outwards from the transmitter. The speed of the propagation depends on the conductivity. The induction currents decay faster in resistive environments. Thus, the propagation of the induced current system is faster there [Spies, 1989].

For a loop source, Nabighian [1979] described the induced current system in a homogenous half-space as resembling a “smoke ring” blown by the transmitter, moving downwards with increasing radius and diminishing amplitude. Hoversten and Morrison [1982] and Reid and Macnae [1998] extended the examples for the

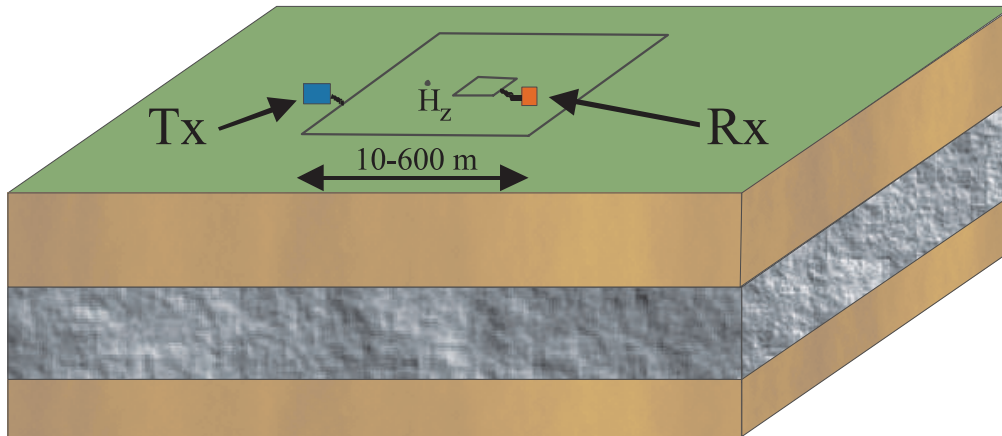


Figure 2.1: Schematic sketch of the field set-up of the SHOTEM modification. Here, a central-loop array is shown. A small receiver loop (Rx) sensing the \dot{H}_z -component is placed in the middle of a large transmitter loop (Tx).

current system in a layered half-space. Wang [2002] presented the current system for anisotropic models. Comparable images for a line source over homogenous medium can be found in Oristaglio [1982]. Gunderson et al. [1986] showed the current system for a bipole source even in inhomogeneous media.

These induced currents also produce EM-fields, which can be recorded with sensors for electric or magnetic fields (or their time derivatives). Unlike, for instance, the DC-geoelectric method the transmitter-receiver-offset does not define the depth of investigation. The induced current system diffuses through the whole subsurface and can be detected and recorded virtually anywhere. The depth from where the signals are originated only depends on the measuring time after the current change in the transmitter.

However, the transmitter type and the offset control whether a signal from the induced currents is still detectable at a certain time t . As the maximum of the induced currents move outwards from the transmitter in time, the signals from these currents at later times are stronger at remote receivers [Petry, 1987]. Depending on the depth to the target, there are two principal modifications of the TEM method. The first is called SHort-Offset TEM (SHOTEM), whereas the second is called Long-Offset TEM (LOTEM).

2.1 The SHOTEM modification

The SHOTEM modification uses transmitter (Tx) - receiver (Rx) separations that could be significantly less than the depth to the target. The Tx consists of a conductor-loop. The so-called primary field produced by this loop is comparable to that of a vertical magnetic dipole. Typically, the Tx cable is a square with side length between 5 and a few hundred meters. The most common array in the SHOTEM modification is the Central Loop (CL) array shown in Figure 2.1. Here, the Rx is set up in the centre of the Tx loop and also consists of a wire loop. Therefore, the voltage induced by the change of the secondary vertical magnetic field $\dot{H}_z(t)$ or short \dot{H}_z is measured. The exploration depth is approximately two to three

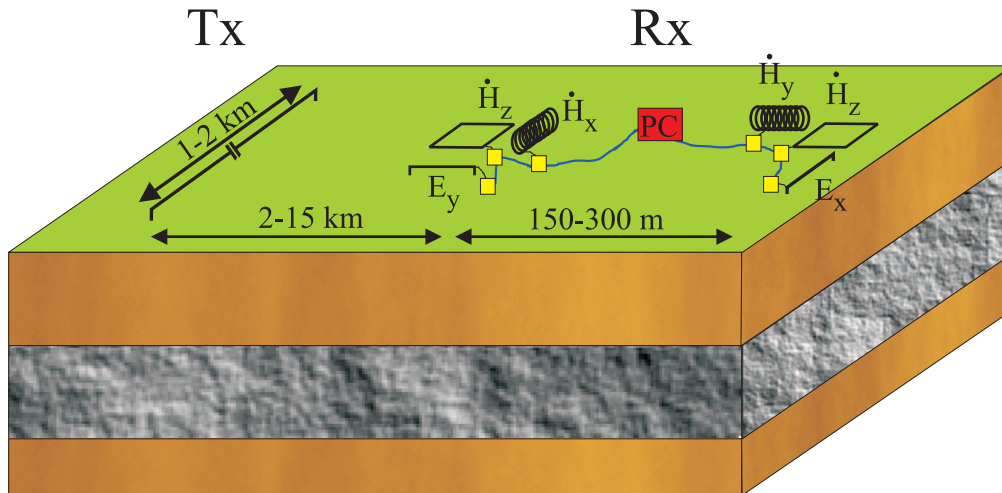


Figure 2.2: Schematical sketch of the field set-up of the LOTEM modification. On the left hand side the grounded dipole is shown (Tx). On the right two receiver stations (Rx) with various sensors are displayed.

times the Tx size and thus bigger than the offset between Tx cable and Rx location [Petry, 1987; Spies, 1989].

Within this project, all SHOTEM measurements were carried out by the Geophysical Institute of Israel (GII), under the supervision of Dr. Mark Goldman. Two different systems were used, the Geonics EM-67 (typical time range between 0.1 ms and 50 ms) and the Russian Cycle-5M (0.1-500 ms).

2.2 The LOTEM modification

The most popular Tx configuration for the LOTEM modification is a grounded dipole [Strack, 1992]. A motor generator produces a current of 5 to 100 Amperes, which is rectified in a so-called switch-box and injected into the ground via a cable of a few kilometres in length. A synchronisation unit (“clock”) toggles the polarity at defined times (e.g. every 2 seconds). The transmitted signal therefore has a rectangular shape.

The Tx-Rx-offset is chosen equal to or bigger than the exploration depth (“Long Offset”). Figure 2.2 shows a schematical field set-up.

Receiver stations (Rx) comprise of sensors for both the electric and magnetic fields. The electric field is sensed with cables grounded with unpolarisable Cu-CuSO₄-electrodes. In our case, coils are used as magnetic field sensors. Therefore, actually the derivatives of the magnetic field are recorded. The electric field components are designated E_x and E_y and the derivatives of the magnetic fields are designated \dot{H}_x , \dot{H}_y and \dot{H}_z . Here, the direction parallel and perpendicular to the Tx are designated x and y respectively. In logistically demanding or topographical complex areas sometimes the sensor cannot be orientated according to the direction of the Tx [Müller, 2000]. These components are designated E_{xy} and \dot{H}_n , respectively [Müller, 2000; Scholl, 2001]. Which components are recorded depends upon the target of the survey and the geometry of the array. For brevity, I will use the

terms “magnetic components” or “magnetic transients” to refer to all \dot{H}_x , \dot{H}_y , \dot{H}_z and \dot{H}_n data sets.

The voltages detected by the sensors are measured and digitised by multi-channel receiver units, either TEAMEX (Transient Electromagnetic Apparatus for Mineral Exploration, Rüter and Strack [1991]) or the newer SUMMIT-TEM. The digital data is sent to a field PC via cable telemetry and saved to a hard disk. The receiver spread often consists of several different Rx, which are spaced by approximately 200 m.

Depending on the strength of the signal and the electromagnetic noise some hundred to thousand switch-over signals are recorded at each Rx to suppress uncorrelated noise (see section 2.2.2).

Results of the measurement after processing the data are voltage curves $d(t)$ of the single components, depending on the time after the switch-over. These curves are called transients. Often the behaviour for $t \rightarrow 0$ s and $t \rightarrow \infty$ is considered. These parts of the transients are called early and late time part respectively (an exact definition is given in Petry [1987]). For early times the \dot{H}_z - and the electric field transients approach a certain asymptote. The horizontal magnetic components show a linear behaviour in log-log diagrams for $t \rightarrow 0$. For late times the $E_{x,y}$ transients approach the DC-value, whereas the $\dot{H}_{x,y,z}$ transients approach zero (see fig. 2.3).

The shape and amplitude of the transients depend greatly on the angle Φ between the Tx-direction and the line between mid-point of the Tx and the Rx-position (lower right panel of fig. 2.3). For simple layered earth cases \dot{H}_x and E_y are $\equiv 0$ for $\Phi = 0^\circ$ and $\Phi = 90^\circ$ for all times¹. For the same cases, \dot{H}_z is $\equiv 0$ for all times for $\Phi = 0^\circ$. The shape of the \dot{H}_z -transient does not depend on Φ , only the amplitude does. \dot{H}_y and E_x do not vanish completely for any Φ [Petry, 1987]. For the geometry used in fig. 2.3 both transients exhibit a sign reversal. For the E_x -component this occurs only for certain geometries.

A comprehensive description of the LOTEM method is given by Strack [1992].

2.2.1 The system response

The sensors and measurement units used at the receiver sites are not “ideal” recording systems. This means an impulse would not be recorded as an impulse. In the best case, an impulse would be reproduced broadened as a “smoothed triangle” of a few ms length. Moreover, the Tx is not capable of transmitting an exactly rectangular signal. Especially shortly after the polarity change the signal often exhibits some wiggles which decay exponentially.

Because of this, the recorded transients are not the earth’s response to a step-like signal. Let $R(t)$ be the step response of the earth, $S_{Rx}(t)$ the impulse response of the receiver system and $S_{Tx}(t)$ the derivative of the real transmitting function. Then, the recorded transient $d(t)$ is:

¹This also holds true, if the resistivity distribution is symmetrical to a line perpendicular to the Tx-direction at the Tx mid-point, i.e. to the y-axis in the lower left panel of fig. 2.3.

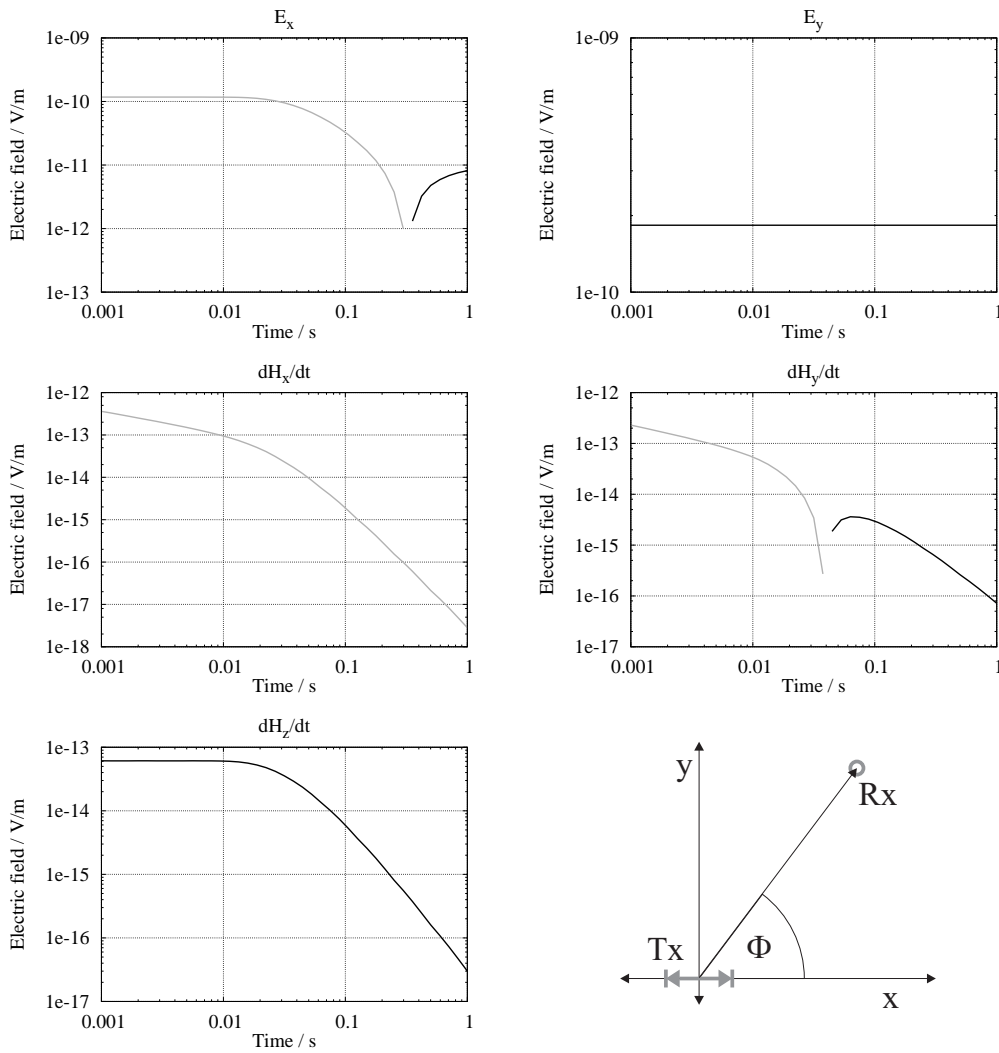


Figure 2.3: Examples of LOTEM-transients for a homogenous half-space of $100 \Omega\text{m}$. Displayed is the electric field (for the E_x - and E_y -component) or the induced voltage (for the magnetic components) for a switch-on signal. Negative values are plotted with a gray line, positive with a black line. The E_x - and H_y -transients show a sign reversal. The data was calculated for a T_x dipole of 1 m length and 1 A transmitting current. The position of the R_x station (gray circle) is $x = 3 \text{ km}$ and $y = 4 \text{ km}$, the T_x is located in the origin. The panels show one LOTEM-component each and a schematical sketch of the setup (lower right).

$$d(t) = R(t) * S_{R_x} * S_{T_x} = R(t) * (S_{R_x} * S_{T_x}) \quad (2.1)$$

The symbol $*$ denotes a convolution. The term $S_{R_x(t)} * S_{T_x(t)}$ describes the influence from the measurement system. It therefore is referred to as “system response” (see sec. 6.2.1 for examples). It causes distortions in the early time of the transients. To interpret the data the system response is measured in the field [Strack, 1992; Scholl, 2001]. To do this a measurement is carried out in the vicinity of the transmitting dipole. In this case $R(t)$ is approximately an impulse [Duncan, 1978]. The measured system responses are accounted for in the interpretation step [Hördt, 1989] according to eqn. 2.1.

2.2.2 Data processing

Because most of the time the electromagnetic noise is much bigger than the signals, the recorded time series have to be processed before interpretation. This processing includes certain steps:

1. First, the data has to be converted to the binary SEG-Y format. The result is a file which contains all recorded time series of one component at one Rx.
2. Each time series is filtered separately to eliminate periodic noise, mostly from the power grid [Hanstein, 1996; Scholl, 2001].
3. All time series are brought to the same DC-value (“levelling”, Scholl [2001]).
4. To reduce aperiodic noise, all time series are selectively stacked [Hanstein et al., 1986; Scholl, 2001].
5. The resulting data is smoothed with a time variable Hanning-window.
6. Again, the time series is levelled.

Depending on the structure of the noise, additional measures have to be taken. A comprehensive description of all processing steps can be found in Scholl [2001].

2.2.3 Estimation of the measurement errors

The error estimates for the transients are calculated in the stacking step of the data processing (cp. 2.2.2). If the mean value \bar{d}_i (the i denotes one discrete time point) of M time series would be calculated from the single measurements d_{ij} , $j \in [1; M]$ after

$$\bar{d}_i = \frac{1}{M} \sum_{j=1}^M d_{ij}, \quad (2.2)$$

a reasonable estimate of the data error is the standard deviation, calculated according to

$$s_i = \sqrt{\sum_{j=1}^M \frac{(\bar{d}_i - d_{ij})^2}{(n-1)}}. \quad (2.3)$$

However, this is only a reasonable error estimate, if all d_{ij} are normally distributed around \bar{d}_i . Tests with real field data showed that most of the time this is not the case [Helwig, 2000; Scholl, 2001]. Hence, it is more reasonable to calculate a selective stack [Hanstein et al., 1986]. First, for each i all d_{ij} are sorted. The biggest and smallest x percent are discarded², the values in between are averaged. This way much better results are achieved in most cases than using eqn. 2.2. In

²Depending on the ambient noise, x is chosen between 5 and 30. In the marginal case of $x = 50$ this would give back the median.

this case an error estimation after eqn. 2.3 is not reasonable. Instead, the errors are estimated according to

$$\tilde{s}_i = \frac{q_{3i} - q_{1i}}{1.35}. \quad (2.4)$$

Here, q_{3i} is the value which is bigger or equal to $\approx 75\%$ of all d_{ij} for a fixed i and q_{1i} the one which is smaller or equal to $\approx 25\%$ of all d_{ij} . The 1.35 in the denominator makes $\tilde{s}_i \approx s_i$ if the d_{ij} are normally distributed.

Unfortunately we found that even calculating the mean with the selective stacking method and an error estimation according to eqn. 2.4 may be flawed [Helwig, 2000; Scholl, 2001]. The reasons for this may be:

- Systematic errors and dependencies between different d_{ij} caused by the recording units or some processing steps, especially when applying the digital filters [Thern et al., 1996; Sylvester, 1997];
- Low frequent noise [Helwig, 2000; Scholl, 2001];
- Systematic errors occurring while generating the system responses;

Up to now, this problem was not yet addressed. We still lack a well-founded, objective procedure for error estimation. A rough appraisal so far is done after following subjective criteria:

- For the derivatives of the magnetic fields $\lim_{t \rightarrow \infty} \dot{H}_{x,y,z}(t) = 0 \text{ V/m}^2$ is true. Therefore, 0 V/m^2 should be in the confidence intervals of the data for sufficiently late times. "Sufficiently late" of course is somewhat subjective.
- It should be possible to fit a "smooth" curve through the confidence intervals of "most" data points. If this is not possible, the intervals are too small. Otherwise, if it is not necessary to use the full size of the intervals they might be too big.

Lacking a better solution, the LOTEM field data in this work are stacked as follows:

- Before stacking the periodic noise is removed. Then, a C_p value is calculated [Scholl, 2001], which describes the variation in different signal periods in a single time series.
- For each individual data set a certain threshold value is determined. Every time series with a higher C_p is discarded. By this step, outlying transients with low frequent noise are removed.
- After this, the data sets are stacked selectively, the error estimates are calculated according to eqn. 2.4.
- For all further processing steps it is assumed that the noise is normally distributed and that the calculated \tilde{s}_i approximate the standard deviation s_i .

Through all post-stack processing steps the error estimates are treated using normal error propagation – except for the smoothing with the time-variable Hanning-window. Here, data points are averaged over an interval of a length increasing with time, weighted by a Hanning-window. Before smoothing, the absolute error estimates normally are more or less constant. As the window is broader for the late times than shortly after the switching signal, the absolute error estimates become smaller according to error propagation. However, experience showed that this results in error estimates which are far too small judged by the criteria described above. Therefore, the \tilde{s}_i are not recalculated during the smoothing step. The absolute error estimates remain constant which seems more realistic, because of the erratic behaviour of the magnetic components at late times (see appendix C).

This subsection hopefully clarifies that the error estimates calculated in the LOTEM data processing are only a rough estimation of the real deviations. This has an impact on the data inversion and interpretation, as shown in chapter 3.

Inversion of geophysical data

The process of “geophysical interpretation” is the search for an earth model which explains the measured data and also fits *a priori* knowledge. This procedure is called “inversion” in contrast to “forward modelling” where a model is assumed and the data one would measure in presence of this model are calculated.

In inversions typically the simplest model is wanted, which means models which can be described by a few parameters such as resistivities and layer thicknesses. The next simple models after the homogenous half-space are layered half-spaces, so-called one-dimensional (1-D) models. “One-dimensional” in this case means that e.g. the resistivity ρ only varies in one-dimension (normally with the depth z). If it is not possible to fit the data satisfactorily the complexity of the model has to be increased, either by introduction of new parameters (e.g. anisotropies, see section 4.1) or by multidimensional structures (see chapter 5).

3.1 Inversion theory

As already mentioned, the intention of the inversion is to find an model which explains the measured data. Let the N observations for a data set be represented by the vector

$$\mathbf{d} = (d_1, \dots, d_N)^T$$

Next, an appropriate parameterisation of the earth is needed, represented by a model parameter vector \mathbf{m} . Assuming an one-dimensional model, the subsurface is normally divided in horizontal layers. Within these layers all electric parameters remain constant. If the variable parameters of the model of K layers are the $K - 1$ layer thicknesses h_k and K layer resistivities ρ_k , those parameters are represented in a model parameter vector

$$\mathbf{m} = (h_1, \dots, h_{K-1}, \rho_1, \dots, \rho_K)^T$$

which, in this case, has $M = 2K - 1$ entries. Another model parameter often used in LOTEM data inversion is the so-called “calibration factor” (CF). I will come back to this parameter in section 4.2.3. The next thing one needs for an inversion, is a so-called forward-code, which is capable of computing the data one would observe, if the assumed model parameterisation describes the real subsurface. In the ideal case, the forward calculation using the model vector \mathbf{m}

$$\mathbf{f}(\mathbf{m}) = (f_1(\mathbf{m}), \dots, f_N(\mathbf{m}))^T$$

equals the measured data \mathbf{d} . However, no model will reproduce real measured, noisy data exactly. Therefore, one has to define a measure for the misfit. In case of uncorrelated, normally distributed noise this leads to a least-squares approach. Here, a model is sought which minimises

$$q = (\mathbf{d} - \mathbf{f}(\mathbf{m}))^T (\mathbf{d} - \mathbf{f}(\mathbf{m})). \quad (3.1)$$

For physical reasons, normally the relative difference between \mathbf{d} and $\mathbf{f}(\mathbf{m})$ are considered instead of the absolute difference [Jupp and Vozoff, 1975]. This may be achieved by weighing observed and calculated data with a weighting matrix

$$\mathbf{W} = \text{diag}(1/d_1, \dots, 1/d_N) \quad (3.2)$$

and thus eqn. 3.1 becomes

$$q = (\mathbf{W}\mathbf{d} - \mathbf{W}\mathbf{f}(\mathbf{m}))^T (\mathbf{W}\mathbf{d} - \mathbf{W}\mathbf{f}(\mathbf{m})) = (\mathbf{d} - \mathbf{f}(\mathbf{m}))^T \mathbf{W}^2 (\mathbf{d} - \mathbf{f}(\mathbf{m})) \quad (3.3)$$

In this case the “root-mean-square” or *RMS*, defined by

$$RMS = \sqrt{q/N} \quad (3.4)$$

is an often used measure of the misfit. If error estimates are available the data are often weighted according to these errors. If one assumes uncorrelated errors for each data point equal to the standard deviation

$$\mathbf{s} = (s_1, \dots, s_N)^T$$

the matrix \mathbf{W} has a diagonal form:

$$\mathbf{W} = \text{diag}(1/s_1, \dots, 1/s_N) \quad (3.5)$$

The result is a different measure of misfit, according to eqn. 3.4 defined as

$$\chi = \sqrt{q/N} \quad (3.6)$$

[Commer et al., 2005]. If the difference between the measured and the calculated data equals the error estimates, χ equals one. Hence, a fit with $\chi = 1.0$ is considered ideal¹. In this work, I will use χ as measure of misfit unless otherwise stated and thus will use both as synonyms.

¹Most authors define a $\chi^2 = q$ (based on terms commonly used in statistics) and thus consider a

3.2 Different strategies of inversion

The problem of minimising eqn. 3.1 with respect to \mathbf{m} is an optimisation problem. Actually, there are three common strategies to invert geophysical data: A manual trial-and-error procedure, automatic inversion by linearising f [Meju, 1994] and automatic inversion using a statistical approach [Mosegaard and Sambridge, 2002].

3.2.1 Trial-and-error

In this simple form of inversion the interpreter constructs an earth model \mathbf{m} and compares the resulting data $f(\mathbf{m})$ with the forward data. If not satisfied the model is changed and the new $f(\mathbf{m})$ is again compared to the measured data. Obviously, there are several drawbacks of this method:

- The interpreter needs to be very experienced. He should know more or less in what way f changes, if \mathbf{m} changes.
- It is very time consuming as it requires a lot of interaction between interpreter and forward code.
- The interpreter needs to have an idea of the subsurface. The solution tends to be biased towards this expectation.

However, there are also some advantages:

- An experienced interpreter will restrict the possible model parameters to reasonable values.
- It is very easy to incorporate additional information from geological or other geophysical methods.
- Although the interpreter may calculate the misfit between observed and calculated data after eqns. 3.6 or 3.4 he is not restricted to judge the fit only by this means. This may seem quite subjective but the least-squares approach actually is only correct, if the distortions of the data are Gaussian, which often is not the case. Therefore, an experienced interpreter may be better in judging the differences between calculated and observed data.

Anyhow, normally the drawbacks outweigh the advantages. However, as automatic inversion algorithms for TEM data and multidimensional model discretisations are just beginning to emerge [Mitsuhata et al., 2002; Scholl et al., 2003; Commer, 2003; Newman and Commer, 2005], this method is still common practice for more complex problems. Recent examples can be found in Hördt et al. [2000], Schaumann [2001] and Kalscheuer [2004].

value of N as ideal. To judge the misfit is only possible knowing N , which I think is intricate. To get a simple measure, I normalised the misfit to N and extracted the square root. The χ defined in eqn. 3.6 might be labelled "weighted *RMS*" by other authors.

3.2.2 Inversion through linearisation

The classical mathematical approach to an optimisation problem would be to find extremal values of $q(\mathbf{m})$ by searching for vectors \mathbf{m} where

$$\frac{\partial q(\mathbf{m})}{\partial \mathbf{m}} = 0. \quad (3.7)$$

This requires the computation of the derivative of $\mathbf{f}(\mathbf{m})$ with respect to \mathbf{m} . Moreover, it has to be possible to solve the resulting equation system analytically. In the TEM case this is not possible.

A common approach to non-linear inversion problems is to start with a so-called initial guess \mathbf{m}_0 . Then, a model update $\hat{\mathbf{m}} = \mathbf{m}_1 - \mathbf{m}_0$ is sought, which minimises q :

$$\frac{\partial q(\mathbf{m}_0 + \hat{\mathbf{m}})}{\partial \hat{\mathbf{m}}} = 0 = \frac{\partial}{\partial \hat{\mathbf{m}}} (\mathbf{W}\mathbf{d} - \mathbf{W}\mathbf{f}(\mathbf{m}_0 + \hat{\mathbf{m}}))^T (\mathbf{W}\mathbf{d} - \mathbf{W}\mathbf{f}(\mathbf{m}_0 + \hat{\mathbf{m}})) \quad (3.8)$$

Next, \mathbf{f} is approximated by a first order Taylor-expansion. For small model perturbations $\hat{\mathbf{m}}$, $\mathbf{f}(\mathbf{m}) = \mathbf{f}(\mathbf{m}_0 + \hat{\mathbf{m}})$ can be expressed as

$$\mathbf{f}(\mathbf{m})|_{\mathbf{m}=\mathbf{m}_0} = \mathbf{f}(\mathbf{m}_0) + \mathbf{J}|_{\mathbf{m}=\mathbf{m}_0} \hat{\mathbf{m}} \quad (3.9)$$

where \mathbf{J} is the Jacobian or sensitivity matrix of partial derivatives

$$J_{ij} = \left. \frac{\partial f_i(\mathbf{m})}{\partial m_j} \right|_{\mathbf{m}=\mathbf{m}_0} \quad \text{for } i = 1, \dots, N \quad \text{and } j = 1, \dots, M \quad (3.10)$$

It describes, how changes in the model parameter m_j affect $f_i(\mathbf{m})$. With this approximation eqn. 3.8 yields

$$0 = \frac{\partial}{\partial \hat{\mathbf{m}}} (\mathbf{W}\mathbf{d} - \mathbf{W}(\mathbf{f}(\mathbf{m}_0) + \mathbf{J}\hat{\mathbf{m}}))^T (\mathbf{W}\mathbf{d} - \mathbf{W}(\mathbf{f}(\mathbf{m}_0) + \mathbf{J}\hat{\mathbf{m}})) \quad (3.11)$$

Substituting $\hat{\mathbf{d}} = \mathbf{d} - \mathbf{f}(\mathbf{m}_0)$ and using $\mathbf{W} = \mathbf{W}^T$ gives

$$\begin{aligned} 0 &= \frac{\partial}{\partial \hat{\mathbf{m}}} (\mathbf{W}\hat{\mathbf{d}} - \mathbf{W}\mathbf{J}\hat{\mathbf{m}})^T (\mathbf{W}\hat{\mathbf{d}} - \mathbf{W}\mathbf{J}\hat{\mathbf{m}}) \\ &= \frac{\partial}{\partial \hat{\mathbf{m}}} (\hat{\mathbf{m}}^T \mathbf{J}^T \mathbf{W}\mathbf{W}\mathbf{J}\hat{\mathbf{m}} - \hat{\mathbf{d}}^T \mathbf{W}\mathbf{W}\mathbf{J}\hat{\mathbf{m}} - \hat{\mathbf{m}}^T \mathbf{J}^T \mathbf{W}\mathbf{W}\hat{\mathbf{d}} + \hat{\mathbf{d}}^T \mathbf{W}\mathbf{W}\hat{\mathbf{d}}) \\ &= 2\mathbf{J}^T \mathbf{W}^2 \hat{\mathbf{d}} - 2\mathbf{J}^T \mathbf{W}^2 \mathbf{J}\hat{\mathbf{m}} \\ &\Leftrightarrow \mathbf{J}^T \mathbf{W}^2 \mathbf{J}\hat{\mathbf{m}} = \mathbf{J}^T \mathbf{W}^2 \hat{\mathbf{d}} \end{aligned} \quad (3.12)$$

The last equation is called the ‘‘normal-equation’’ whose solution for the model update vector $\hat{\mathbf{m}}$ is

$$\hat{\mathbf{m}} = (\mathbf{J}^T \mathbf{W}^2 \mathbf{J})^{-1} \mathbf{J}^T \mathbf{W}^2 \hat{\mathbf{d}} \quad (3.13)$$

which is known as the Gauss-Newton or unconstrained least-squares solution. However, as \mathbf{f} was linearised using the Taylor-expansion dropping higher order terms, so $q(\mathbf{m}_0 + \hat{\mathbf{m}})$ normally will not reach the minimum. Therefore, $\mathbf{m}_1 = \mathbf{m}_0 + \hat{\mathbf{m}}$ will be used as initial guess for the next iteration step and a new model update is calculated. The model update for the n th iteration step will be calculated according to

$$\hat{\mathbf{m}}_n = (\mathbf{J}_{n-1}^T \mathbf{W}^2 \mathbf{J}_{n-1})^{-1} \mathbf{J}_{n-1}^T \mathbf{W}^2 \hat{\mathbf{d}}_{n-1} \quad (3.14)$$

where $\mathbf{J}_{n-1} = \mathbf{J}|_{\mathbf{m}=\mathbf{m}_{n-1}}$ and $\hat{\mathbf{d}}_{n-1} = \mathbf{d} - \mathbf{f}(\mathbf{m}_{n-1})$. This process is repeated until $q(\mathbf{m}_n)$ is sufficiently small or any other stopping criteria are met.

To keep all model parameters positive, the model vector often is transformed logarithmically, e.g. $\mathbf{m} = (\rho_1, \rho_2, h) \rightarrow \tilde{\mathbf{m}} = (\ln \rho_1, \ln \rho_2, \ln h)$. Then, all inversion steps are done using the $\tilde{\mathbf{m}}$ [Jupp and Vozoff, 1975]².

The unconstrained solution may have some undesirable properties. An obvious difficulty occurs when the inverse of $\mathbf{J}^T \mathbf{W}^2 \mathbf{J}$ does not exist, that is, when $\mathbf{J}^T \mathbf{W}^2 \mathbf{J}$ is singular. But even if $(\mathbf{J}^T \mathbf{W}^2 \mathbf{J})^{-1}$ exists, problems arise when $\mathbf{J}^T \mathbf{W}^2 \mathbf{J}$ is nearly singular, especially if noise is present, $\hat{\mathbf{m}}$ may have huge entries. This leads to solutions which are far away from the initial guess where the Taylor-expansion is no longer valid and thus we may be faced with a diverging solution. To circumvent this, constraints are imposed on the normal-equation.

Marquardt inversion

Levenberg [1944] introduced a possibility to prevent divergence of the solution of the normal-equation. He modified eqn. 3.14 to

$$\hat{\mathbf{m}}_n = (\mathbf{J}_{n-1}^T \mathbf{W}^2 \mathbf{J}_{n-1} + \beta \mathbf{I})^{-1} \mathbf{J}_{n-1}^T \mathbf{W}^2 \hat{\mathbf{d}}_{n-1} \quad (3.15)$$

where \mathbf{I} is the identity matrix. The additional term restricts the length of the model update vector to a certain length depending on the choice of the so-called damping factor β . The solution is constructed using mainly eigenvectors of $\mathbf{J}^T \mathbf{W}^2 \mathbf{J}$ with high eigenvalues. For these eigenvectors it is more likely that the Taylor-expansion is valid [Jupp and Vozoff, 1975].

This inversion scheme became very popular after a publication of Marquardt [1963]. It is widely used for inversion problems with only a few model parameters (e.g. 1d-models). For inverting a geophysical data set normally the subsurface is divided into a few layers. Then, the thicknesses of these layers are also subject to the inversion [Jupp and Vozoff, 1975; Lines and Treitel, 1984].

An advantage of this scheme is that it can not diverge. If the algorithm fails to find a better fitting model, one can increase the value of β . With this, the “step-size” (the length of $\hat{\mathbf{m}}$) decreases and finally an update can be found, where the linearisation describes the problem sufficiently. However, the improvement from

²This is also reasonable from a physical point of view. A change of e.g. the resistivity of the first layer ρ_1 from 1 Ωm to 2 Ωm changes $\mathbf{f}(\mathbf{m})$ comparable to a change from 10 to 20 Ωm , not like from 10 to 11 Ωm , which is reflected better by logarithmically transformed parameters.

$$q^* = (\mathbf{d} - \mathbf{f}(\mathbf{m}^*))^T (\mathbf{d} - \mathbf{f}(\mathbf{m}^*)) + \lambda \mathbf{m}^{*T} \mathbf{P}^T \mathbf{P} \mathbf{m}^* \quad (3.21)$$

where $\mathbf{P} = \mathbf{R}$ or $\mathbf{P} = \mathbf{R}^2$ respectively. After substituting $\mathbf{m}^* = \mathbf{m}_{n-1}^* + \hat{\mathbf{m}}_n^*$ and some transformation similar to those shown in section 3.2.2, the equation

$$\hat{\mathbf{m}}_n^* = (\mathbf{J}_{n-1}^T \mathbf{W}^2 \mathbf{J}_{n-1} + \lambda \mathbf{P}^T \mathbf{P})^{-1} (\mathbf{J}_{n-1}^T \mathbf{W}^2 \hat{\mathbf{d}}_{n-1} - \lambda \mathbf{P}^T \mathbf{P} \mathbf{m}_{n-1}^*) \quad (3.22)$$

yields the model update (cp. eqn. 3.14). Normally, a homogenous half-space is chosen as initial model. In this case the inversion algorithm may introduce resistivity changes only if this is necessary to explain the measured data. Ideally, the result is the “smoothest” model, which explains the data.

The variable λ quantifies the trade-off between roughness and data misfit. With decreasing λ the roughness will increase, whereas the misfit will decrease. If λ is big enough, the $\lambda \mathbf{P}^T \mathbf{P}$ term makes sure that $\mathbf{J}^T \mathbf{W}^2 \mathbf{J} + \lambda \mathbf{P}^T \mathbf{P}$ is not singular³.

Typically, the inversion algorithm starts with a large λ , which decreases with each iteration step. However, finding an appropriate strategy to choose values for λ is not trivial. Schemes for choosing λ are presented in sec. 5.2).

Compared to the Marquardt inversion, Occam’s inversion is computationally much more expensive for three reasons:

1. A much bigger amount of layers are used in Occam’s inversion. The computation time for one calculation of $\mathbf{f}(\mathbf{m})$ increases significantly with the numbers of layers (e.g. the calculation for a 25 layer earth model roughly takes six times longer than for a 4 layer case).
2. Normally the number of free parameters is higher. Therefore, the computation of \mathbf{J} needs more calculations of \mathbf{f} .
3. Most strategies to find an appropriate value for λ require many additional calculations of \mathbf{f} (see section 5.2), whereas a suitable value for β is found quickly.

Also, Occam’s inversion approach only is reasonable, if no sharp resistivity contrasts are expected geologically (although EM-methods only resolve subsurface structures somewhat blurred for physical reasons). Thin layers tend to be suppressed. And it is not clear, how to choose λ (which effects the results significantly), whereas the choice of β only influences the convergence.

Another drawback is that the inversion algorithm tends to cease converging at late iteration steps. The reason for this is – roughly speaking – that the algorithm has to construct its search direction as a linear combination of two possibilities. For $\lambda \rightarrow 0$ no constraint will be imposed, the solution therefore most likely will diverge and thus the misfit will not be improved. For $\lambda \rightarrow \infty$ the solution will be a half-space, which also will degrade the fit.

To be able to achieve at least the misfit of the previous model, Constable et al. [1987] suggest to reduce the step-length successively when a model update fails.

³It says, if you can not derive information about one layer from the Jacobian, give it the resistivity from the adjacent layers.

This can be done by using $\tilde{\mathbf{m}}' = \hat{\mathbf{m}}^*/a$ as model update, where a is an arbitrary number. The step-size is reduced further, unless a model update yields a sufficiently low misfit. For $a \rightarrow \infty$ the model update vector has a zero length. The “new” model therefore will be the old model, which of course will achieve the same misfit.

The big advantage of the Occam’s inversion is that the interpreter does not have to worry about an initial model. As mentioned earlier, homogenous half-spaces are used as \mathbf{m}_0 ⁴. The number of layers does not effect the result much, as long as “enough” layers have been chosen⁵. Also the resistivity of the half-space does not change the result (see also appendix A).

Therefore, often both inversion strategies are combined. First, Occam’s inversion is done. This inversion result yields an initial guess about the main subsurface features as number of relevant layers and a (qualitative) resistivity sequence, which is used in a Marquardt inversion.

3.2.3 Monte-Carlo inversion

From a statistical point of view, minimising the misfit between \mathbf{d} and \mathbf{f} can be seen as finding the most probable model giving the measured data. The probability might be modified by *a priori* information. The statistical analogon to the confidence intervals of the resulting model is to know the complete probability distribution, or the likelihood of all models \mathbf{m}_n in the parameter space. This works even for multi-modal distributions.

A so-called “global algorithm” tries to find the global minimum of the misfit or even sample the complete probability distribution (the latter includes the former). The simplest approach would be to test all possible models. This can be approximated by choosing an appropriate model discretisation \mathbf{m} and calculate $\mathbf{f}(\mathbf{m})$ for, say, 20 different discrete values for each parameter. Although possible, this approach becomes unruly if the amount of parameters increases. For 10 parameters and 20 values per parameter this would require $20^{10} \approx 10^{13}$ forward calculations⁶.

To overcome this, random elements are introduced to the search. Methods incorporating random elements are called Monte Carlo methods [Mosegaard and Sambridge, 2002]. Testing random models approximates the probability distribution faster than the “systematic” search described above [Mosegaard and Tarantola, 1995; Mosegaard and Sambridge, 2002]. However, simply testing a number of random models will be computationally to expensive. Huge parts of the model space are seized by models with a very poor fit and thus an extremely low probability. To speed up the search, different techniques have been introduced to narrow the random search to subspaces, where the probability is not that small. A recent overview of the global search algorithms used in geophysical data interpretation is given by Mosegaard and Sambridge [2002].

⁴Meju [1994] shows the effect of choosing \mathbf{m}_0 other than a half-space.

⁵In the LOTEM case 20 to 40 will do, if the depth range is chosen according to the time range of the transient.

⁶Which - in the LOTEM case - would take roughly 35, 000 years on an “Athlon-XP-1800” PC. Also, a sampling of the parameter space with only 20 possible values is quite coarse.

- Metropolis algorithms and simulated annealing algorithms sample the probability distribution by a random walk [Sen and Stoffa, 1991; Mosegaard and Tarantola, 1995; Grandis and M. Menvielle, 1999]. In this cases the probability distribution can be derived from the ensemble of accepted model. The acceptance criterion differs, depending on the implementation.
- The neighbourhood algorithm [Sambridge, 1999] searches the parameter space by continuously densifying the sampling around points, which showed higher probabilities in previous stages.
- Genetic algorithms [Goldberg, 1989; Stoffa and Sen, 1991] apply biologic reproduction and selection rules to the optimisation problem. A “population” of earth models runs through several evolutionary generations, subject to the “survival of the fittest” principle. The “fitness” of an individual model in this case is the reciprocal misfit.

Although there are several example of successful applications of Monte Carlo methods to geophysical inverse problems, I did not yet succeed in applying those to the inversion of TEM data. Mainly there seem to be two main disadvantages of the TEM method which hamper the usefulness of those algorithms:

- Monte Carlo algorithms require a huge amount (some millions) of evaluations of the misfit and thus of $f(\mathbf{m})$. Compared to other methods, computing $f(\mathbf{m})$ even for a simple 1D-case is tedious. Using models with a small number of layers and variable layer thicknesses, decreases the amount of evaluation time. On the other hand, this will increases the number of local minima. Although the above mentioned algorithms are referred to as “global” search procedures, they tend to get stuck in local minima just like the Marquardt inversion if the number of evaluations chosen is small. Increasing this number also is not advisable due to the enormous computational effort.
- Shallow layers influence the trend of the complete TEM-transient. Therefore, an earth model, where every parameter has the “true” value except the resistivity of the first layer, will have a poor fit and thus most likely will be rejected by the algorithm. This degrades the convergence performance of all Monte Carlo methods greatly. This might be avoided by using the apparent resistivity formulation for SHOTEM [Petry, 1987] and a kind of “all time apparent resistivity” [Karlik, 1994] for LOTEM, which again would have some other disadvantages.

The problems get bigger, when the calibration factor (see sec. 4.2.3) is a free parameter. Although the utilisation of pure Monte Carlo algorithms may work in future, there is no solution to these problems yet.

3.2.4 Hybrid Marquardt Monte-Carlo inversion

One approach to combine the good convergence properties of linearised inversions with a global search, is to combine both methods in one algorithm. The easiest way

to do this, is choosing random initial models for a standard linearised inversion [Koch, 2003; Lange, 2003].

At this moment, there are some drawbacks of this method:

- The algorithm is still not very efficient. Most randomly chosen models are bad initial models. Even a Marquardt inversion will fail in say, 90 % of cases to find a sufficiently good model but will spend several tens of forward calculations per trial.
- The algorithm at present needs around a dozen parameters. Extensive tests still have to be carried out in order to find reasonable and effective settings.
- It also is still not well understood, how many of these inversions have to be carried out to keep the result “global”.

The results of Koch [2003] and Lange [2003] thus still are considered to be preliminary. The algorithm is not used for this study because it is computationally expensive and of unestablished relevance.

3.3 Joint-inversion

“Joint-inversion” is a term used for inverting two or more different data sets using the same model [Vozoff and Jupp, 1975]. Basically, the inversion works the same way as described in this chapter. The additional data sets are simply appended to the data vector \mathbf{d} which thus becomes longer. Often the evaluation of the longer $\mathbf{f}(\mathbf{m})$ takes several separate forward modelling runs.

Strictly, all multidimensional inversion algorithms are joint-inversion algorithms. For 1-D inversions often data sets of different geophysical methods are used jointly to combine their resolving capabilities [Jupp and Vozoff, 1977; Hördt, 1989; Commer, 1999].

3.4 EMUPLUS

The 1-D program EMUPLUS allows - besides forward calculations for model studies - the inversion of data sets from different electric and electromagnetic methods. Both Marquardt and Occam’s Inversion is implemented. It is possible to calculate and invert SHOTEM data [Lange, 2003] as well as LOTEM- E_x , $-E_y$, $-\dot{H}_x$, $-\dot{H}_y$ and $-\dot{H}_z$ and even the rotated $-E_{xy}$ and $-\dot{H}_n$.

Additionally, it is possible to invert the frequency domain MT and CSAMT data sets. Further it is possible to do joint-inversions [Vozoff and Jupp, 1975] with up to 30 different data sets [Hördt, 1989; Commer, 1999; Supriadi et al., 2000].

For this work many changes and new features were implemented in the program. See app. F for a description.

3.5 Appraisal of resulting models

After deriving a model which explains the measured data sufficiently well, it is also very important to estimate confidence intervals for each parameter. This is related to the “likelihood” of the model [Mosegaard and Sambridge, 2002]. Statistically, if the model is found which produces the lowest misfit, it is the most likely in the light of the data (and error estimates) measured. However, it doesn’t mean that all other models are completely unlikely. In general, many other models can be found, which produce only slightly higher misfits and are thus only slightly less likely. In the best case, all of these models would result in the same geological interpretation.

Depending on the inversion method an appraisal of the final model can be done in different ways. It is hardest, if the inversion is done by trial-and-error. In this case the interpreter has no additional information, besides the model and the misfit. However, since finding this model involved several tries with different models, he can try to judge which feature of the model was important and which was not well resolved.

Often global search algorithms are used to sample the probability distribution for all models. If this is done, all needed information is available.

In this study only linearised inversions are used. Here, several approaches have been suggested. For smooth model type inversions like Occam’s inversion, different runs with different smoothness constraints can be carried out. Where these models differ, the solution is governed by the smoothness constraint and not by the data. See Oldenburg and Li [1999] for an example in 2D. Although this is a useful tool for estimating the depth of investigation, no real confidence intervals for resolved parameters can be derived with this method. Also, the class of possible solutions is restricted to smooth models. Additionally, the models compared may also differ due to different resulting trade-off parameters λ . Only models producing similar misfits should be compared.

Other approaches use the information contained in the Jacobian. Most authors implement the Marquardt-inversion using a singular value decomposition of \mathbf{J} . The three resulting matrices allow a detailed analysis of the linearised solution. It is possible to derive resolution matrices [Menke, 1984] or parameter error bounds [Jupp and Vozoff, 1975] and to analyse parameter dependencies in the so-called V-matrix [Hördt et al., 1992]. Also very popular is the use of parameter “importances” [Hördt et al., 1992; Lange, 2003]. These approaches have a significant drawback: They rely solely on the linearised and thus localised Jacobian $\mathbf{J}|_{\mathbf{m}=\mathbf{m}_{\text{final}}}$ and its relation to the final damping parameter β . That this may be misleading is shown in Koch [2003].

To circumvent these drawbacks, I choose another approach for model appraisal: The model in question is varied, parameter by parameter, in eight steps from $m_j \cdot 5$ to $m_j/5$ and the number of layers is changed by splitting one layer or combining two layers. Additionally all other parameters are randomly changed within a few percent. With this new initial model a Marquardt-inversion is done. If the inversion reaches a misfit which is only slightly⁷ higher than of the original model, the

⁷As the data errors are known not to be true standard deviations but estimates, “slightly” becomes subjective. For this work I choose 10 %.

new model is saved. After this, the inversion will be finished. If the final model achieves a lower misfit than the original one, the latter is replaced and the process is restarted. The result is an ensemble of models which represents equivalent models. Plotting all models in one figure depict the confidence range for the resistivity at the different depths. Note that these models are still biased towards the original model. This is no global search procedure.

Effects of complex geoelectric settings on TEM-data

As mentioned previously, the interpretation of TEM data sets today is based mainly on 1-D inversions. The assumption of a 1-D distribution of any physical parameter, however, is never fulfilled in nature. A layer uniformly interpreted as e.g. “sand” shows big vertical and lateral changes within a few micrometers when viewed on grain size.

Even if we were able to invert 3-D resistivity distributions on small scales we might end up with unexplainable transients, as TEM fields are also influenced by the magnetic permeability and the dielectric permittivity¹ [Lee, 1981]. Again, also 3-D formulations for resistivity, permeability and permittivity are only approximations: All three may be non-scalar and time/frequency dependent. In the near future models of this complexity will remain untractable.

Nevertheless, simplified models were used successfully in the past to interpret measured TEM data. This means that the assumptions made approximated sufficiently reality meaning that the influence of structures not represented in the simple model were negligible.

In the next section I will briefly review the effects that may appear, when the subsurface cannot be described with a constant scalar resistivity alone.

4.1 Effects of different material parameters

The most often used model in TEM inversions assumes a scalar 1-D resistivity distribution $\rho(z)$ and vacuum permeability $\mu = \mu_0$. In the recent decades many studies were made concerning the effect of more complex settings.

¹The latter actually influences the the wave propagation of the EM field. TEM processes commonly are modelled in the diffusive regime (at “relative” late times) and thus are not affected by the permittivity. However, it influences whether the diffusive approximation is valid or not.

4.1.1 Non-scalar resistivity

A scalar resistivity means that the resistivity is isotropic, i.e. it is uniform in all directions for a certain volume. In general this is not the case. Instead, it can have full matrix form. Anisotropy is a scale issue [Wannamaker, 2004]. Non-scalar resistivity can be simulated by structures with scalar resistivities on a smaller scale. Examples of equivalent scalar models to anisotropic resistivities can be found in Schönfelder [1995]. Anisotropy also exists on the crystal scale, where minerals may have different resistivities along different axes (e.g. [Constable et al., 1992]).

In sedimentary basins the subsurface may consist of finely stratified layers [Christensen, 2000]. If the resistivity of these layers differ, the resistivity parallel and perpendicular the stratification will be different, comparable to a series or parallel connection of varying resistors [Jupp and Vozoff, 1977]. In this case, the medium can be described with an anisotropic bulk resistivity. For a horizontal stratification the layer exhibits a vertical and a horizontal resistivity ρ_v and ρ_h . Jupp and Vozoff [1977] define an anisotropy coefficient as:

$$\gamma = \sqrt{\rho_v/\rho_h} \quad (4.1)$$

Jupp and Vozoff [1977] use the MT and DC methods to discriminate between the two different resistivities. MT is influenced only by ρ_h , whereas $\rho_{DC} = \sqrt{\rho_v\rho_h}$. Thus, using both methods in a joint-inversion allows one to determine the anisotropy coefficient. A similar approach, using SHOTEM and DC, is presented by Eckard [1993] and Christensen [2000]. The SHOTEM-component here is only sensitive to ρ_h . Hördt [1992] combines electric and magnetic LOTEM-components in an inversion. Here, the electric components are influenced by both ρ_v and ρ_h , whereas all magnetic TEM-components are only affected by ρ_h .

The effect of this type of anisotropy would be that inversions of electric LOTEM- and magnetic TEM-components would give different resistivities at a given depth. The resistivity derived by inverting the electric components roughly would be higher compared to the one derived from the magnetic components. However, inverting single data sets, the inversion algorithm should find a model which explains the measured data well. Thus an interpretation of the single inversion results will still fit the geological facts fairly in most cases.

Different bulk resistivities in x- and y-direction are far more complex for TEM, due to complicated geometry of the source. Schönfelder [1995] made some calculations for LOTEM on an arbitrarily anisotropic half-space. He found that the effect of anisotropy can be as complex as 3-D structures, which is not surprising, as anisotropy can be simulated by small scale 3-D structures. He was able to reproduce sign reversals in \dot{H}_z , which are commonly interpreted as effects of multi-dimensionality. The same can be expected for the SHOTEM method.

Inversions of models with arbitrary anisotropy or even forward calculations for a complex anisotropic layering have not yet been done for TEM. For the MT-case, where the source is a plane wave, this has been considered for 2-D cases [Pek, 1994; Schmucker, 1994; Li, 2000].

4.1.2 Magnetic permeability unequal to vacuum permeability

The magnetic permeability is the product of the vacuum permeability $\mu_0 = 1.257 \times 10^{-6}$ Vs/Am and the relative permeability μ_r . For most rocks, the relative permeability is around 1.0 [Telford et al., 1990]. Sediments may show values of 1.001, whereas igneous rocks like basalts may have up to $\mu_r \approx 1.2$.

Considering models with $\mu_r \neq 1.0$ in MT increases the number of equivalent models significantly, because data produced over a earth with $\mu_r \neq 1.0$ can be explained by a model with $\mu_r = 1.0$ everywhere but different resistivities [Yadav and Lal, 1989]. This is not the case for LOTEM [Hanstein, 2001], where a non-unity relative permeability also distorts the layer thicknesses [Kriegshäuser, 1991]. Hanstein [2001] stated that models with $\mu_r > 4.0$ will produce transients, which can not be explained by a pure 1-D resistivity distribution. However, in real geology μ_r is near unity. Thus, the distortions normally produced are not severe.

4.1.3 Time depending material parameters

The bulk resistivity ρ and magnetic permeability μ of any volume may be frequency dependent ($\rho(\omega)$ and $\mu(\omega)$). Of course, these parameters may be transformed to time domain, leading to $\rho(t)$ and $\mu(t)$ respectively, where t is the time after shut-off of the primary field [Hönig, 2002].

Frequency dependent resistivity is measured with the so-called Induced Polarisation (IP) method [Pelton et al., 1978]. The change of magnetisation with time is referred to as magnetic viscosity. For material showing magnetic viscosity on a short time scale (order of milliseconds, comparable to typical TEM time scales) the term super-paramagnetism is used [Buselli, 1982]. Both effects are resulting from structures on grain- and mineral scale.

For TEM both effects normally are not considered. Any such effect could lead to distorted transients and thus may cause misinterpretations. Weidelt [1982] argued that the frequency dependence of resistivity and permeability may cause noticeable distortions of TEM data.

Induced Polarisation

If a part of the subsurface consists of polarisable material, the primary field stores energy in polarisation, mostly in chemical form. This can be a result of variations in the mobility of ions in fluids throughout the rock structure. The other cause can be variations between ionic and electronic conductivity where metallic minerals are present [Telford et al., 1990]. The first, known as membrane effect is most pronounced in the presence of clay minerals. The second, known as electrode polarisation effect is strongest in rocks containing disseminated minerals that are electronic conductors like sulfides, some oxides and graphite. This energy build-up and release is very slow and will look similar to a transient response, but normally is considered to be far weaker than the actual transient.

Although IP is an useful method for exploring minerals responsible for the electrode polarisation effect or ground-water studies, the IP-effect is normally ne-

glected for TEM measurements.

Smith and West tried to explain sign reversals in coincident-loop TEM measurements [Smith and West, 1988; 1989] with polarisable bodies. Similar calculations are presented by Flis et al. [1989] (see also Flis and Newman [1989]). They point out that the effect can be observed mainly after the normal induced current system had decayed away. The effect thus not big, if the subsurface is conductive. The response of a polarisable 3-D body increases with decreasing distance from the setup.

The results can be applied to SHOTEM as well, although in this configuration sign reversals can be produced also by small-scale inhomogeneities close to the Rx Hohmann and Newman [1990].

Schaumann [2001] explained late time sign reversals in SHOTEM data with polarisable 1D-models. The transients were recored above a waste known to exhibit polarisable zones. She did not succeed to explain these sign reversals by a multidimensional resistivity structure. 1-D-models with polarisable layers reproduced the measured features well.

Hoheisel [2000] investigated the influence of IP-effects on the LOTEM method. He found that the effect of a polarisable subsurface is quite complex. It greatly depends on the Tx-Rx-geometry and the position of the polarisable volume. The measured voltages may be in- or decreased. Even sign reversals can be produced. However, for reasonable polarisabilities the effect can only be seen if the induced fields decayed away.

The results of these studies can be summarised with the following points:

- The strength of the polarisation effect depends on the strength of the primary field. Thus, the effect is strongest near the transmitter. Therefore, a big impact of a near surface polarisable layer can be expected when measuring the system response.
- The resistivity distribution in the subsurface affects the IP-effect in two ways: First, it influences the strength of the primary field in the subsurface. Second, it controls the diffusion process of the transient field. If the induced field decays faster than the IP-effect, the latter prevails at late times.
- The effect obviously is stronger, if the polarisability of the body is bigger. Moderate polarisabilities need certain Tx-Rx-body geometries to have an effect [Smith and West, 1988; 1989].
- The IP-effect influences electric fields stronger than the magnetic field derivatives [Hoheisel, 2000].

Super-paramagnetic effect

Material may show a magnetic viscous behaviour, if it contains magnetisable material of different grain sizes. The smaller the grains, the smaller the affected time scale. The effect is strongly temperature dependent [Buselli, 1982]. The effect of super-paramagnetic soil was first considered for coincident loop measurements.

Buselli [1982] explained anomalies in field data recorded on lateritic soil in Australia with the super-paramagnetic effects.

If a strong super-paramagnetic effect is visible, at late times the measured \dot{H}_z -transients decay $\sim t^{-1}$ instead of $\sim t^{-\frac{5}{2}}$ like undistorted curves [Lee, 1984]. If one tries to interpret these distorted transients this would lead to models, where the resistivity decreases with depth [Lee, 1984].

Lee [1984] showed that the strength of the effect decreases when the Tx-Rx-offset increases. In fact, the strength of the distortion depends on the mutual inductance of Tx and Rx, which decreases with increasing offset [Hanstein et al., 2005; Neumann, 2005 in preparation]. Thus, the influence of super-paramagnetic material on SHOTEM or especially on LOTEM measurements should be small. Nevertheless, Gaidetzka [2002] found indications for a super-paramagnetic effect in central-loop measurements above a waste site.

4.2 Effects of multidimensional resistivity structures

In nature one will not find a real “layered earth” case. Sedimentary basins may be close, but the general geology consists of faults, graben and horst structures, isolated bodies and so on. Often, the aim of a geophysical survey is to find and describe any distortion in the otherwise more or less 1-D earth, like ore bodies or oil traps.

This work deals mainly with multidimensional effects on TEM data. Therefore, I would like to describe the background of multidimensional modelling in this section in more detail. However, for a comprehensive description - particularly of multidimensional EM forward calculations - please consult the given references. I also restricted the references to work related to at least active methods. For a more general review of 3-D EM modelling, refer to Avdeev [2004].

4.2.1 Forward modelling

For any study of multidimensional effects, of course, an appropriate forward-code for modelling is needed. For EM-methods the code should solve the Maxwell's equations in their quasi-static approximation

$$\nabla \times \mathbf{e} = -\dot{\mathbf{b}} \quad (4.2)$$

$$\nabla \times \mathbf{b} = \mu(\sigma \mathbf{e} + \mathbf{j}_e) \quad (4.3)$$

or after elimination of \mathbf{b}

$$\nabla \times \nabla \times \mathbf{e} + \mu\sigma\dot{\mathbf{e}} = -\mu\dot{\mathbf{j}}_e \quad (4.4)$$

\mathbf{e} and \mathbf{b} are the vectors of the electric and magnetic field, \mathbf{j}_e is the source current density, μ the magnetic permeability and σ the electric conductivity.

TEM methods use an artificial source, which excites EM fields at a certain time $t = 0$ s. A common modelling approach is to calculate the static fields \mathbf{e} and \mathbf{b} for $t < 0$ s and then to obtain solutions for later times. This way the external source current density \mathbf{j}_e equals zero for $t > 0$ s. The electric and magnetic fields then are sampled on a Yee-cell [Yee, 1966] applying a Finite Difference Method (FDM). Alternatively, using a Finite Element Method (FEM) a variational formulation of the problem is needed, which is sampled using some basic (edge or nodal) functions [Goldman et al., 1986; Unsworth et al., 1993; Mitsuhata, 2000]. The FDM approach is widely used in EM methods due to the apparent simplicity of its numerical implementation. The main attraction of the FEM approach is that it is believed to be better able to accurately account for subsurface geometry.

The continuation of the initial field in both formulations can be done either explicit by a time stepping scheme [Goldman and Stoyer, 1983; Goldman et al., 1986; Wang and Hohmann, 1993; Commer and Newman, 2004] or implicit by solving a linear equation for all desired $t > 0$ s [Haber et al., 2004]. A different approach is proposed by Druskin and Knizhnerman [1988]. They developed an implicit FDM scheme based on a spectral Lanczos decomposition (SLDM). Here, the initial values are approximated by a system of orthogonal decay modes. The solution then is constructed from a subspace of the original system matrix formed by these decay modes. The key of this method is the subspace approximation by the Lanczos method [Druskin and Knizhnerman, 1994; Arnason, 1999; Druskin et al., 1999; Davdycheva et al., 2003].

Instead of a FDM or a FEM formulation, the Integral Equation (IE) approach uses an integral formulation for Maxwell's equations, e.g.

$$\mathbf{e}(\mathbf{r}) = \mathbf{e}_0(\mathbf{r}) + \int_V \mathbf{G}_0(\mathbf{r}, \mathbf{r}')(\sigma - \sigma_0)\mathbf{e}(\mathbf{r}')d\mathbf{r}' \quad (4.5)$$

with respect to the electric field [Weidelt, 1975; Hohmann, 1975; SanFilippo and Hohmann, 1985]. Here, \mathbf{e}_0 is the known background field, \mathbf{G}_0 is the Green's function of the 1-D reference medium and V is the volume where σ differs from the background σ_0 . The integral equation is discretised on V , provided that σ and \mathbf{e} is constant within each cell. The IE approach is often used, when only few multi-dimensional bodies are introduced in an otherwise layered subsurface [Hohmann, 1975; Vasseur and Weidelt, 1977; Newman et al., 1986; Gunderson et al., 1986; Xiong et al., 1986]. Although very feasible when only a small part of the earth is heterogeneous, accurate computation using the IE approach becomes very tedious for complex problems. Therefore, nowadays most EM software developers refrain from implementation of the IE scheme [Avdeev, 2004].

In the 80s it was still computationally too expensive to simulate general cases. Early model studies thus were made using codes which could deal with restricted model or source geometries only, e.g.:

- Codes calculating the response of perfectly conducting but infinitesimal thin plate, embedded in a layered half-space with an IE approach [Vasseur and Weidelt, 1977].
- Goldman and Stoyer [1983] propose an explicit FDM code to calculate the transient fields of an axially symmetric earth below a loop source. In Gold-

man et al. [1994b] a similar approach for a grounded dipole source was presented.

- With the time stepping FEM code by Goldman et al. [1986] it is possible to calculate EM-fields for an arbitrary 2-D resistivity distribution. However, also the grounded dipole source has to be 2-D, which means it is of infinite length.
- Newman et al. [1986] developed an IE code, which could compute TEM responses of arbitrarily shaped 3-D bodies within a layered earth.

Often, a frequency domain formulation of the Maxwell's equations are used for modelling codes. To obtain the time domain responses, tedious forward modelling has to be done for several frequencies over many decades. The results then are transformed to time domain (e.g. Newman et al. [1986] and Gunderson et al. [1986] for an IE example, Rätz [1999; 2000]; Mitsuhata [2000] for a FEM solution).

Weidelt [2000] compared three different modelling approaches for time domain data. First, he ruled out the frequency domain approach followed by a transformation to time domain, due to its ineffectiveness. Instead, he favoured either the explicit time-stepping scheme (presented by Wang and Hohmann [1993] for a loop source or Commer and Newman [2004] for a grounded dipole transmitter) or the SLDM approach by Druskin and Knizhnerman [1988]. Weidelt found that both approaches are acceptable, whereas the latter is more efficient for modelling transient fields. Other comparisons of different TEM modelling programs can be found in Hördt et al. [1992], Hördt [1992], Helwig [1994], Mitsuhata [2000] and Commer [2003].

Although the focus of the reviewed modelling codes is to calculate the responses of a multidimensional resistivity distribution, some of those codes can even model multidimensional distributions of other material parameters. The codes of Druskin and Knizhnerman [1994] and Commer and Newman [2004] can also deal with arbitrary magnetic permeability distributions. Wang and Fang [2001], Weiss and Newman [2002] and Davydycheva et al. [2003] presented FD algorithms which can handle 3-D anisotropic earth models for logging applications.

All 3-D modelling for this work was done using the SLDM code by Druskin and Knizhnerman [1988], which is called SLDMEM3T.

4.2.2 **Review of previous studies**

The effects of multidimensional subsurface structures on TEM data have been subject of many studies. Most of the studies address only the \dot{H}_z -component, as it is the classical receiver component used in TEM surveys.

Most of the studies work with an anomalous region embedded in an otherwise homogenous or layered earth. Obviously, the strength of the effect is bigger if the anomalous volume is larger and if the conductivity deviates more from the background conductivity [Kriegshäuser, 1991]. The volume of the anomaly has to be viewed relative to the total induction space.

TEM data is affected mainly by the subsurface below and between the Tx and the Rx [Hördt, 1998; Martin and Hördt, 2001; Martin, 2003]. At early times transients

are affected mainly by shallow structures in the vicinity of transmitter or receiver.

Since the induced current system maximum starts close to the transmitter (chapter 2), the latter may seem counter-intuitive. Thus, the induced currents close to the Rx at early times are very small. However, the receiver is more sensitive to current filaments in its vicinity. Therefore, the small currents induced below the Rx have about the same effect as the large but remote currents below the Tx. In fact, if e.g. an electric dipole Tx and an electric dipole Rx are used, reciprocity says that the sensitivities below Tx and Rx in a layered earth are identical [Hördt, 1998].

At later times, when the induced currents propagated downwards and outwards, the transient shape is affected by the parameters of a larger volume of the subsurface. Although the maximum of the induced currents now is in deeper parts of the subsurface, the actual current system still depends on the current system at earlier stages of the diffusion process. This way, the absolute values of the transients at late stages may still depend on the shallow resistivity distribution [Hördt, 1998; Martin and Hördt, 2001; Martin, 2003].

The lateral extension of a LOTEM field setup is - by definition - larger than of a SHOTEM setup. This means that the induction space is bigger in the LOTEM case. Small inhomogeneities may distort SHOTEM data more, for the anomalous volume is bigger compared to the induction space [Goldman et al., 1994b]. On the one hand, for LOTEM a bigger part of the subsurface has to be approximately 1-D, if a 1-D interpretation should be applied.

Inhomogeneities may be seen as 1-D structures in SHOTEM, but as distortions in LOTEM, if their size is much bigger than the SHOTEM Tx-loop-size but smaller than the LOTEM offset. Further, if lateral changes along a LOTEM profile are present, one encounters the problem of where to assign the resulting 1-D models.

Previous studies on multidimensional effects on TEM data followed different approaches:

- Newman et al. [1986] modelled the central-loop response of conductive horst- and graben structures in depth. They found that the distortion is time limited in the transients. This means that only intermediate times of the transients are distorted, whereas early and late times remain undistorted. They also succeeded in inverting the data using 1-D models. However, the inversions gave kind of a blurred image of the real subsurface underestimating the vertical extension of the anomaly.
- Gunderson et al. [1986] used a similar approach to model data for a LOTEM field setup using \dot{H}_z -receivers. They show transients for a buried conductive prism and a conductive horst structure. The grounded bipole transmitter is located 1.4 and 2.2 km respectively away from the middle of the structure. Interestingly, in both cases the \dot{H}_z -transients closest to the Tx (and thus away from the anomalies) showed the biggest distortions, exhibiting sign reversals. The least distortions are displayed with the \dot{H}_z simulated atop the prisms. Stations directly in front of and behind the structures are moderate distorted. They did not try any inversion but assumed that the resulting model will have fictitious features. They concluded also that the distortions for the horst model are band limited. 1-D inversions thus would yield the correct upper-layer and basement resistivity but the depths would be misleading.

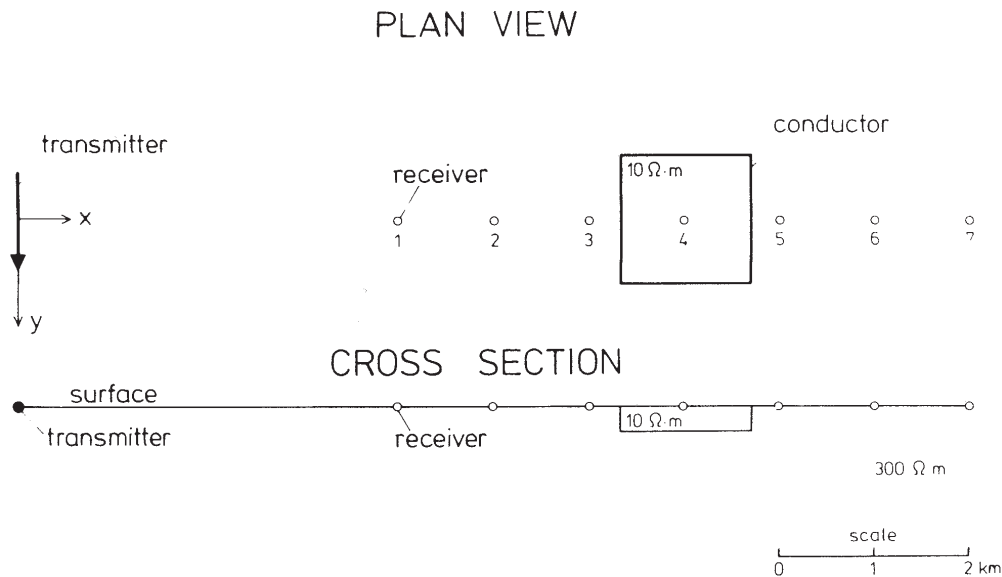


Figure 4.1: Rx-Tx-setup and earth model used by Newman [1989] for the transients displayed in fig. 4.2 [Newman, 1989];

- Sternberg et al. [1988] found that central-loop TEM measurements were not effected at late times by a surface inhomogeneity. The authors claim that this behaviour could be expected, since the central-loop TEM method uses magnetic fields as Tx and Rx and is not effected by the buildup of charge at the inhomogeneities surface.
- Newman [1989] presented the influence of near surface conductors on the LOTEM- \dot{H}_z -component. He presented two cases: One, where the conductive patch is at least partly below the Tx and one where it is located within a broadside receiver spread.

Body below Tx: If the conductive body is below the grounded dipole Tx, the \dot{H}_z -transients are distorted at early times and shifted at late times. Newman compared this effect to static shifts in MT [Jones, 1988], where the whole apparent resistivity curve is shifted. Newman found shifts up to one order of magnitude in- or decreasing the 1-D response.

Body within Rx-spread: Newman considered a broadside LOTEM spread with a Rx-station spacing of 1 km starting with an offset of 4 km (fig. 4.1). The conductor is placed at a distance of 7 km below the fourth Rx-station. Fig. 4.2 shows the \dot{H}_z -transients calculated at the Rx-positions. The response of the body is not observed at Rx-stations 1 and 2. It increased the voltage at early times measured at station 3 and decreased the voltage at early times for all later stations, producing a sign reversal at station 5 beyond the patch. In any case the response of the near-surface 3-D conductor is not observed after early times ($\approx 10^{-2}$ s).

He concluded that as shape of the transients is changed only at early times, it may be interpreted with 1-D models if the early time data points are removed prior to inversion. If a conductor is present near to the Tx, the curves are shifted at late times. He proposed to include a "calibration factor" in the inversion process to account for these shifts (see sec. 4.2.3). With this technique

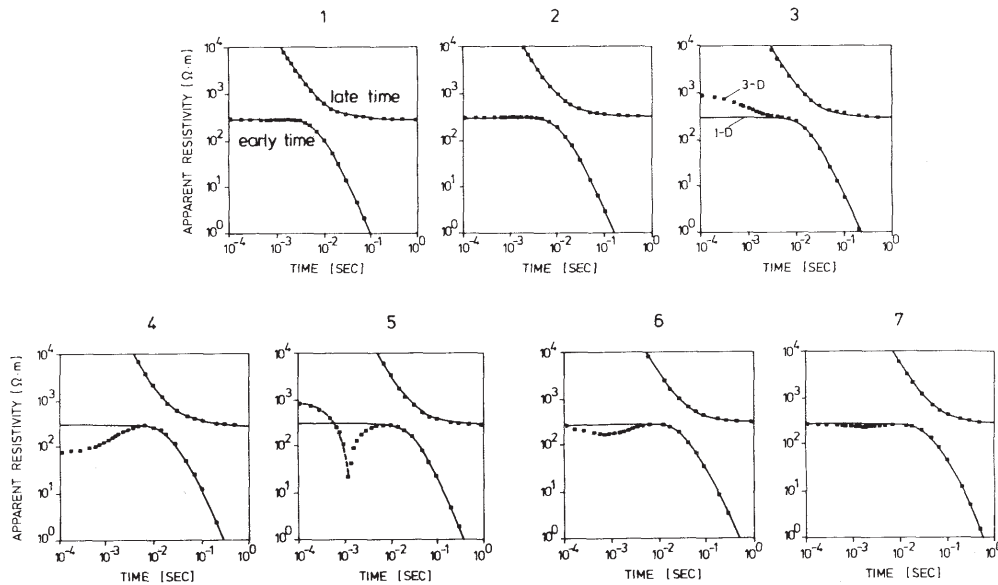


Figure 4.2: \dot{H}_z -transients calculated for the model shown in fig. 4.1 [Newman, 1989]; the points denote the transients for the 3-D model, the solid lines the transients for the model without conductive patch.

he succeeded inverting distorted transients. Deeper parts of the original layered model were reproduced, although fictitious shallow layers showed up (he did not delete early time data points).

- In the thesis of Kriegshäuser [1991] 1-D inversions of synthetic data simulated for 3-D models can be found. The data were calculated for the LOTEM-component \dot{H}_z . For some models also E_x -data were calculated, although the shown E_x -transients seem to be shut-off responses.

Resistive dike: Here a spread of E_x - and \dot{H}_z -receivers is placed atop and around a resistive dike structure running N-S. The inversion showed that the effects of the dike are not very large on the \dot{H}_z -component. Inversions of the east-west profile transients reproduced the regional 1-D model. Biggest effects on the magnetic component were found for stations where the dam was between Rx and Tx. Kriegshäuser states that the effects on the E_x -component are much bigger and biggest atop of the dam. Joint-inversions of E_x and \dot{H}_z again suppressed the structure. Unfortunately, results of the inversions using also the E_x -components are not shown.

Thin conductive sheet: A thin shallow conductive sheet is embedded in three layer model. Only \dot{H}_z -transients are simulated. The geometry is similar to the one used by Newman [1989], as are the transients. The data simulated for stations close to the sheet show distortions. The biggest distortions up to sign reversals are found, if the sheet is between Rx and Tx. As one would expect, the effects increase with the conductance of the sheet. Kriegshäuser [1991] inverted the transients with an Occam's inversion after deleting the sign reversals. For lower conductances, the earth model below the Rx-stations are reproduced well. For higher conductances especially the results for stations behind the sheet are severely

distorted in the upper part. Similar results were found for a shallow conductor with a vertical extension of 250 m. Kriegshäuser concluded that even in presence of a 3-D inhomogeneity qualitative information of the subsurface can be derived from the data using 1-D inversions.

Buried conductive body: In this case, a conductive body with an extension of $1200 \times 1200 \times 500$ m was embedded in a homogenous half-space of $30 \Omega\text{m}$. The depth of the top of the body was 500 m, its resistivity was $1 \Omega\text{m}$. The effect on the simulated \dot{H}_z -transients is similar to the one for a surficial body. Again the transients show a voltage increase for stations close to the Tx and a depression for stations behind the body. The difference to a shallow patch is that the effects show up at intermediate times and are less pronounced. The 1-D Occam's inversions show a distorted picture of the subsurface, especially for stations behind the inhomogeneity. A similar result was achieved for a conductive horst structure.

Conductive patch close to Tx: The results here are similar to the ones of Newman [1989]. Additionally, Kriegshäuser simulated the E_x -component. He also succeeded inverting the 3-D transients with a 1-D model introducing a "calibration factor" to the inversion process. The resulting models reproduced the layering fairly, although the shallow parts were slightly distorted.

- A large number of case and feasibility studies for LOTEM is shown in Strack [1992]. For spreads where the changes in the \dot{H}_z -transients due to geologic variations are not strong, Strack simply generates 1-D pseudo-sections by displaying the 1-D inversion results below the Rx position, which is a common strategy for TEM data (e.g. Müller [2000]). He also promotes profile inversions, where either the results of the first station are used as a starting model for the next station or the inversion is forced to keep the result close to a background model. If the resulting model for one station of the profile looks much different from the two neighbouring models, the transient was removed from the data set.

More severe \dot{H}_z -transient distortions are classified, with a special focus on sign reversals produced by conductive anomalies. He also shows examples for 3-D modelling of distorted measured data sets.

In the feasibility study section inversions of synthetic data sets from 2-D models are shown. Here, \dot{H}_z - and E_x -transients are used in single and joint-inversions. The models are layered cases, where in one certain layer the resistivity increases gradually along the profile. This should simulate a porous medium, which is filled with either water (conductive) or oil (resistive). The 1-D Marquardt inversion show that the E_x - and the \dot{H}_z -component provide complementary information. Strack states that the resulting models are still too distorted. The use of *a priori* knowledge about the structures (simulating additional information from e.g. seismics) enhances the results. This additional information is included in the inversion process by keeping the layer thicknesses fixed and inverting only the resistivities. The resulting models reproduce the original model well.

- Goldman et al. [1994b] modelled and 1-D-inverted transients for both central-loop and LOTEM measurements over multidimensional bodies. In both cases

\dot{H}_z -receivers where used. The models are basically two-layered models with circular horst or graben structures with both conductive and resistive basements. The SHOTEM data was modelled in CL-configuration for a profile across the structure. In the LOTEM case, the Rx-spread is running across the structure with a Tx at some offset from the profile line. The inversions were done with a 1-D Marquardt-type inversion algorithm (see section 3.2.2). The number of layers was selected as a minimum number for which a reasonable fit was achieved.

Central-Loop, resistive graben in conductive basement: The transients are not severely distorted. Near the vertical boundaries an additional layer with a resistivity far less than the resistivity of the upper layer appears. The authors suggest to combine both layers into a single layer. Doing this, the depression can be retrieved, although the depth of the graben is underestimated.

Central-Loop, conductive graben in resistive basement: Here, the late time branches of the transients are distorted for stations over the structure. Although the graben structure is reproduced, a fictitious, highly conductive basement is introduced below the depression. As the resistivity of this half-space usually is much lower than the resistivity of any known lithology, excluding the layer from the interpretation is easy.

Central-Loop, horst structures: In the cases shown by the authors, the data was best fit using four layer models close to the structures. The thickness and resistivity of the overburden and the resistivity of the basement was reproduced fairly well. However, fictitious layers of medium resistivities showed up in intermediate depths. The authors suggest taking the results along a profile into account: A sharp increase in layers needed to explain the data, may indicate a vertical boundary.

LOTEM: For the LOTEM setup the transients are nearly undistorted by the structures, for the bodies are small compared to the whole induction space. The biggest effects are found at stations behind the structure. Here, the structures can be recovered, although their vertical extension is greatly underestimated.

- A first study about the resolution capabilities of the horizontal magnetic field components \dot{H}_x and \dot{H}_y for LOTEM was done by Donat [1996]. In particular, he presented synthetic data examples for two 2-D cases. The regional 1-D model is in both cases the same, a six layer case. The author is mainly interested in a 1 Ωm layer at a depth of 915 m with a thickness of 55 m, which should simulate a water-filled reservoir rock. In this layer a small inhomogeneity consisting of three blocks of 10, 3 and 2 Ωm representing hydrocarbons is embedded. He found that the biggest deviation from the 1-D transients for \dot{H}_x and \dot{H}_z is found around the borders of the anomaly, whereas the distortion in the \dot{H}_y is biggest for stations above the anomaly.

He also did 1-D Marquardt inversions with the 2-D data. In any case the distortions due to the 2-D model were small enough to fit the data sets with 1-D models. As expected, the earth model was changed most at Rx-stations, where significant distortions in the transients occurred. The resulting models for the \dot{H}_y component thus differed most from the starting model for stations

atop the anomaly, whereas the other two components varied their models at the borders of the anomalous region.

Donat [1996] also simulated data, where an additional surficial conductor representing a metal pipeline is included in the 2-D model. The result was that all components were heavily distorted. However, \dot{H}_y was distorted differently to the other two components. Here again, the biggest effects were found above the pipe, whereas \dot{H}_z and \dot{H}_x were distorted mostly around the pipe. Also the distortion itself was different. The \dot{H}_y -transient seemed to be shifted over the whole time range, whereas the distortions in \dot{H}_z and \dot{H}_x changed sign in the observed time range. Donat [1996] did not invert this data set.

- Caldwell and Bibby [1998] presented a scheme to visualise distortions in the electric components of LOTEM. They needed two perpendicular transmitters and both E_x - and E_y -component to construct time dependent apparent resistivity tensors which allow the location of subsurface inhomogeneities. Applications of this technique can be found in Blaschek and Hördt [2001] and Blaschek [2002].
- Hördt and Müller [2000] modelled the effects of mountains on LOTEM- \dot{H}_z -components. They found that a mountain in general acts as near surface conductor. The transients were distorted as expected from a near surface conductive patch, mostly in the early part. This results in a depression or even sign reversal for a Rx-station behind the mountain and an increased voltage for transients in front of the mountain. However, the late times were also distorted slightly, which gave slightly distorted 1-D inversion results. Least distorted were the data on top of the mountain. These results fit those of Gundersen et al. [1986], although Hördt and Müller [2000] did not conclude that the distortion vanishes completely at late times.
- Toft [2001] shows Occam's inversion results of multidimensional models for different SHOTEM configurations. The investigated structures are comprised of sloping models and representations of shallow resistivity variations: A small resistive/conductive block and a random distribution of surficial blocks. He found that the central-loop configuration in general is only slightly distorted. Distortions are stronger, when the out-loop setup is used, where the Rx-loop is set up outside the Tx-loop.

Regarding the sloping models, the author found that slopes of up to 11.25 degrees could be considered in 1-D, if the basement is conductive. The distortions increase with steeper slopes or if the basement is resistive. The distortions result in fictitious layers on both sides of the slopes. The depth to these artifacts increases outwards.

- Several studies were made to explain a specific data set. Often they focus on explaining sign reversals in the LOTEM- \dot{H}_z -component, which cannot be explained using 1-D models (see also section 4.1). Examples can be found in Hördt [1992], Hördt et al. [2000], Müller [2000], Klitzsch [2000] and Kalscheuer [2004]. However, only few can be derived from these studies in terms of a more general insight. The main result is that single or double sign reversals in the LOTEM- \dot{H}_z -component can be produced by relative small shallow conductors [Hördt, 1992; Hördt et al., 2000; Müller, 2000]. Helwig

[1994] could explain steep SHOTEM-transients by horst, graben and fault structures. Schaumann [2001] modelled SHOTEM-transient to explain data sets measured above two waste sites. The modelling done by Hördt et al. [2000] and Klitzsch [2000] includes also LOTEM- E_x -components.

- The first work to describe multidimensional distortions on LOTEM data with a theoretical approach was presented by Hördt and Scholl [2004]. They calculated the response of LOTEM-components in presence of a small conductive body close to the Tx- or Rx-position similar to an approach for FD by Qian and Pedersen [1992]. Their solution is valid for sufficiently late times, after the inductive currents in the body decayed away. They found that the resulting transients are mainly linear combinations of the fields that would be measured in absence of the body. They call these field “primary fields”. Unfortunately, they can be confused with the source field of the Tx, which in general are also referred to as “primary fields”. In the following, I instead will call the fields which would be measured in absence of the inhomogeneity “undisturbed fields”.

Body in vicinity of Tx: In this case, the resulting transients for any receiver component $V(t)$ are linear combinations of the undisturbed fields produced by the actual Tx $V_{px}(t)$ and a perpendicular Tx $V_{py}(t)$:

$$V(t) = T_x V_{px}(t) + T_y V_{py}(t) \quad (4.6)$$

Thus, the distortion is static if $V_{py}(t) \equiv 0$ (e.g. for the E_x - or \dot{H}_y -component in exact in-line or broadside setups in 1-D or special 2-D cases) or if the shape of the transient does not depend on the angle between the Tx-direction and the Rx-position. The latter is only the case for the \dot{H}_z -component. In any other case the distortion is time dependent, unless $T_y \equiv 0$.

Body in vicinity of electric Rx: In this case, the resulting electric fields measured are linear combinations of the undisturbed fields for the actual component and the one perpendicular to it:

$$E_x(t) = D_{xx}^E E_{px}(t) + D_{xy}^E E_{py}(t) \quad (4.7)$$

$$E_y(t) = D_{yx}^E E_{px}(t) + D_{yy}^E E_{py}(t) \quad (4.8)$$

Here, the distortion can only be static in the E_x -component. namely for in-line and broadside configurations in 1-D and special 2-D cases, when $E_{py}(t) \equiv 0$.

Body in vicinity of magnetic Rx: This is the most complicated case. Here the calculations yield

$$\dot{H}_x(t) = \dot{H}_{px} + D_{xx}^H \dot{E}_{px}(t) + D_{xy}^H \dot{E}_{py}(t) \quad (4.9)$$

$$\dot{H}_y(t) = \dot{H}_{py} + D_{yx}^H \dot{E}_{px}(t) + D_{yy}^H \dot{E}_{py}(t) \quad (4.10)$$

$$\dot{H}_z(t) = \dot{H}_{pz} + D_{zx}^H \dot{E}_{px}(t) + D_{zy}^H \dot{E}_{py}(t). \quad (4.11)$$

As $\dot{E}_{px}(t)$ never is $\equiv 0$ the distortion in the magnetic field components is limited to early times and does not become static in general cases.

With this study Hördt and Scholl [2004] for the first time could explain the findings of Newman [1989] theoretically. They agree with Newman's calculations, who found a static shift in the \dot{H}_z -component for conductive patches below the Tx. They also showed that even for shallow conductive patches below the Tx the distortion is not static for all geometries. Also, the eqns. 4.9 to 4.11 show, that the distortions in the magnetic components are not static and may not be neglected at late time. However, model calculations and a study by Qian [1994] suggest that the distortions for these components are not that big, which would mean that D^H is small.

Hördt and Scholl [2004] found also examples of these distortions in field data. Further, they showed that it is possible to invert distorted electric field components by also including the distortion factors as unknowns in the inversion process (see also section 5.6).

Summary of the review

- Typically, the results of 1-D inversions for different Rx-stations are plotted in a pseudo-section below the station's position [Strack, 1992; Müller, 2000]. Of course this is reasonable as changes in the structure of the transients along a profile have to be related to sub-surficial changes in the vicinity of the Rx. However, in a multidimensional case it is not clear in what way the subsurface below the Tx contributes to the transients. This practice is also problematic if different Tx are used. E.g. Klitzsch [2000] relates her results simply to an arbitrary Tx number and references the models not geographically.
- The different LOTEM-components provide different information [Strack, 1992; Donat, 1996; Commer, 1999]. However, it is not clear in what way they vary with respect to multidimensional structures.
- If the signal for one component is small in a certain Tx-Rx-geometry, the component is easily dominated by distortions due to inhomogeneities [Hördt and Scholl, 2004]. In the typical in-line or broadside configurations this is the case for the E_y - and \dot{H}_x -transients.
- Small inhomogeneities can produce shifts in the data at late times in certain geometries [Newman, 1989; Hördt and Scholl, 2004]. Early times are distorted unpredictably due to induction in the body.
- Inhomogeneities produce distortions only after certain times related to their depth. Deeper inhomogeneities distort the transients after later times [Gunderson et al., 1986; Goldman and Neubauer, 1994; Kriegshäuser, 1991; Donat, 1996]. From this time point on, the transients have to be considered as distorted. However, it is questionable whether or not the distortions at very late times are negligible [Gunderson et al., 1986; Sternberg et al., 1988; Newman, 1989; Hördt and Scholl, 2004].
- The distortions on the \dot{H}_z -component is biggest, if the \dot{H}_z -sensor is placed on the lateral borders of the inhomogeneity [Newman, 1989; Goldman et al., 1994b; Donat, 1996].

- All authors think that it is possible to derive information about the subsurface from the distorted data, at least in some cases. However, they suggest different procedures to do so: inverting additional calibration or distortion factors [Newman, 1989; Hördt and Scholl, 2004], deleting distorted data points [Kriegshäuser, 1991; Müller, 2000], editing the resulting earth model [Goldman and Neubauer, 1994] or constructing certain tensors [Caldwell and Bibby, 1998];

4.2.3 The calibration factor

The “calibration factor” or “scaling factor” is an arbitrary factor applied to the synthetic forward curve to fit the measured transients. Originally the factor was introduced to correct errors due to incorrect transmitting current or receiver area estimations.

However, since Newman [1989] published his results the calibration factor (CF) has been commonly used (see previous section). It should account for the so-called “transmitter overprint” [Strack, 1992], the shift introduced at intermediate to late times to the \dot{H}_z -component in presence of a surficial conductor below the Tx. The shift Newman [1989] found in his calculations were up to one order of magnitude.

Since then it has been also used for the other TEM-components, although the results of Hördt and Scholl [2004] makes its use questionable, as distortions in general are only static in special cases.

Inversion of the calibration factor

The CF is introduced to the inversion as additional model parameter. This allows one to fit shifted transients. The starting value for the CF is 1.0, which means the data is not shifted. If wanted by the user, the CF can be changed during the inversion process.

It is desirable that the CF stays close to 1.0. As the model parameters are transformed logarithmically for the inversion (see section 3.2.2), the desired value is 0.0 as $\ln 1.0 = 0.0$. Setting the starting \ln CF as 0.0 biases the Marquardt inversion implemented in EMUPLUS to this value. Nevertheless, the final values are not restricted in any form.

For Occam’s inversion biasing the resulting CF towards 1.0 is achieved using the smoothness constraint [Commer, 1999; Hördt and Scholl, 2004]. The entries in the smoothness matrix \mathbf{R} corresponding to the CFs consist of ones on the main diagonal². Thus, an ideally smooth model has to have a $\ln m_{CF} = 0.0$ [Commer, 1999; Hördt and Scholl, 2004] and the regularisation forces the CF to be close to 1.0.

In the 1-D case, the area below the magnetic transients, $\int_0^\infty \dot{H}(t) dt$ does not depend on the resistivity distribution [Hördt, 1989; Donat, 1996]. The shift of the curve is unambiguous and can be calculated by comparing the measured transients

²The value for the entries on the main diagonal is arbitrary. Any other value might be as reasonable. It controls the ratio between the smoothness of the rest of the model and the CF’s deviation from 1.0. Other entries thus will produce varying results. However, lacking a possibility to determine an “ideal” value, ones were chosen for the sake of simplicity.

to synthetic curves. In sec. 5.7 this is used to convert the transients to reasonable apparent resistivity curves. As real transients only are measured in a limited time band, the (hopefully small) parts of the area at very early and very late times are unknown and little ambiguity is introduced by allowing the CF to vary.

As $\int_0^\infty E(t)dt$ depends on the earth model this is not the case for the components of the electric fields. Keeping the CF as a free parameter in inversion greatly increases ambiguity for those components (see sec. 5.3.3).

1-D inversion of multidimensional TEM-data

This chapter provides an insight into what happens if TEM (mainly LOTEM) data sets measured over a multidimensional resistivity distribution are inverted with a 1-D code. In the best case, the obtained 1-D model should reflect the gross resistivity structure in the subsurface. Deviations from the model below the position of the Rx are defined as model distortions. However, even distorted models can be used to derive meaningful geological information when the distortions are not big and still resemble the true resistivity structure. Any feature which can not be correlated to the true resistivity structure and thus will lead to misinterpretations is an artifact.

Small subsurficial features may be interesting for certain surveys. In these cases, methods which are most sensitive to small features will be most pertinent. In a 1-D survey one is more interested in the gross structure, as the result will be extrapolated over a larger area. Therefore, I will consider any structure with a scale length significantly smaller than the Tx-Rx-offset as not pertinent. These features do not have to be resolved by the 1-D inversion.

Often, 1-D pseudo-sections are plotted where the individual 1-D models are displayed below the Rx-site. This is a simplification, as the whole subsurface between and around Tx and Rx will influence the electromagnetic fields. It is not clear, how well these pseudo-sections represent the subsurface, i.e. how structures with a scale length comparable to the Tx-Rx-setup will be reflected in the 1-D pseudo-sections.

The aim of this chapter is to understand how certain multidimensional structures are reflected in the inversion results. This is done by 1-D-inversions of synthetic data sets calculated for various models. Sec. 5.1 describes how the synthetic data sets are produced. At best, artificial features are suppressed completely. If this is not possible it is necessary to recognise the artificial structures. This means to estimate the reliability of certain features of the inversion result.

Different approaches are tested with respect to the question if they help to suppress or detect artifacts in the 1-D models.

The first attempt is to suppress artificial structures by a proper regularisation scheme (sec. 5.2). This includes the presentation of several regularisation schemes. A first test with a 1-D model is done to see whether all schemes are capable of finding models with a sufficiently low misfit in an easy case. Thereafter some results for multidimensional models are presented.

In the recent LOTEM surveys, generally more than one field component is recorded at each Rx-site. In the second part (sec. 5.3) I will present the results of the inversions of the multidimensional transients for the different LOTEM-components.

In general, different measured data sets will yield different models after 1-D inversions. For the interpretation this is impracticable as only a single, consistent geophysical model can be used for the geological interpretation. Up to now, varying inversion results of individual LOTEM-components have been explained mostly by their different resolving capabilities, which may be combined in a joint-inversion. Only a few authors addressed the question if the model differences are generated by multidimensional structures (see sec. 4.2.2). Probably, joint-inversions can be used to suppress artificial structures. This is tested in sec. 5.4.

Sec. 5.5 will present the results for inversions of simulated SHOTEM data sets. In this section the joint-interpretation of SHOTEM and LOTEM data sets will be discussed. In sec. 5.6 a different approach is tested. The section will describe how it is possible to parameterise the data distortions produced by certain small inhomogeneities. Sec. 5.7 examines the possibilities opened by the use of data sets from two adjacent stations.

The results of this chapter will be combined to one interpretation scheme in sec. 5.8. This scheme will be used to interpret the field data sets in chap. 6. Therefore, the derivation of an interpretation strategy for the field data sets from Israel takes into account that generally only two Rx-sites are deployed on each side of the Tx with an offset of ≈ 3 km. Approaches involving correlations of data sets of more than two adjacent stations are thus not studied. For the final discussion of the techniques presented in this chapter see chap. 7.

5.1 Producing the synthetic data sets

The models used for the simulations exhibit only moderate resistivity contrasts. The results shown here can thus be considered as a lower limit for effects which can be expected when measuring in real field cases. The simulated spreads are motivated by the field measurements made in Israel (chap. 6), so the broadside configuration is modelled.

The Tx-Rx-geometry used (unless otherwise stated) is displayed in fig. 5.1. At each receiver point transients for the E_x -, \dot{H}_y - and \dot{H}_z -components are calculated in a time range from 1 to 750 ms. For the chosen model- and Tx-Rx-geometry, E_y and \dot{H}_x are $\equiv 0$.

The synthetic transients were calculated using SLDMEM3T. The grids were evaluated by comparing SLDMEM3T (sec. 4.2.1) results for 1-D models with EMUPLUS-transients (sec. 3.4). Although some transients – especially \dot{H}_z – show

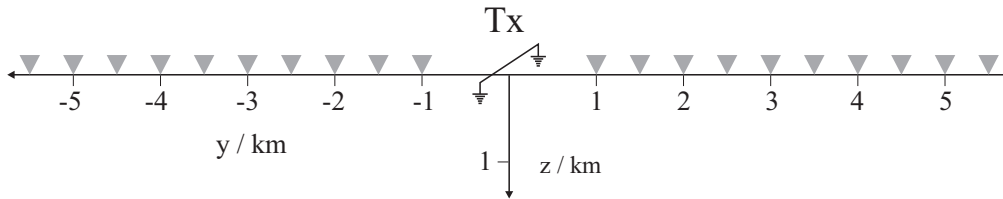


Figure 5.1: Tx-Rx-setup used for the 2-D calculations; the triangles mark the positions of the Rx-stations. At every station E_x -, \dot{H}_y - and \dot{H}_z -transients are calculated. All Rx and the midpoint of the Tx is at $x = 0$ m. The length of the transmitter dipole is ≈ 73 m.

an inevitable shift at early times, the overall agreement is good. The average deviations are within 3 % of each datum.

The effect of the modelling errors on the inversions can be checked with the results for the 1-D models in sec. 5.2.3. The final models from inverting the transients produced with SLDMEM3T with EMUPLUS are close to the original 1-D model (see figs. 5.8-5.10).

Figs. 5.2 to 5.4 show all multidimensional models used. The resistivity structure in these cases is 2-D (all blocks are of infinite length in x-direction), except for the models G1 to J2. These models contain a small inhomogeneity with the dimensions $600 \times 600 \times 300$ m³. The x-coordinate of the midpoint is at $x = 0$ m. Examples where the inhomogeneity is not located on the y-axis are shown in sec. 5.6.

5.1.1 Adding artificial noise

Prior to the inversion, artificial noise was added to the data sets. The noise consists of Gaussian random numbers. As the noise has to be added to a large number of data sets, an automatic procedure had to be found to determine reasonable values for the standard deviation s_i for each datum d_i . The typical choice would be to assume a standard deviation of some percent of each datum. However, this would lead to an unrealistic noise pattern, as real field data sets show larger relative standard deviations for data points with small voltages.

The problem is the dynamic range of the data sets. The electric fields vary roughly over two orders of magnitude. The magnetic field on the other hand show large variations around six orders of magnitude for small offsets and around three orders for large offsets. The absolute values for the first data points decrease significantly with the offset.

Simply assuming a fixed noise floor for all data sets thus provides either almost undistorted transients at small offsets and unusable noisy transients at large offsets. The inversion results thus would mainly show the loss of resolution with offset, which is of no interest for this study. Instead, all transients should be only slightly distorted, resembling a transient with fair data quality.

First tests were made with an individual noise floor proportional to $\exp \frac{1}{5} \sum_{j=N-4}^N \ln |d_j|$ if N is the number of data points for each single transient. This accounts for the decreasing signal strength with offset. However, it still provided unrealistic noise patterns, because of the different dynamic ranges for the magnetic fields. Magnetic transients at small offsets showed distorted late times

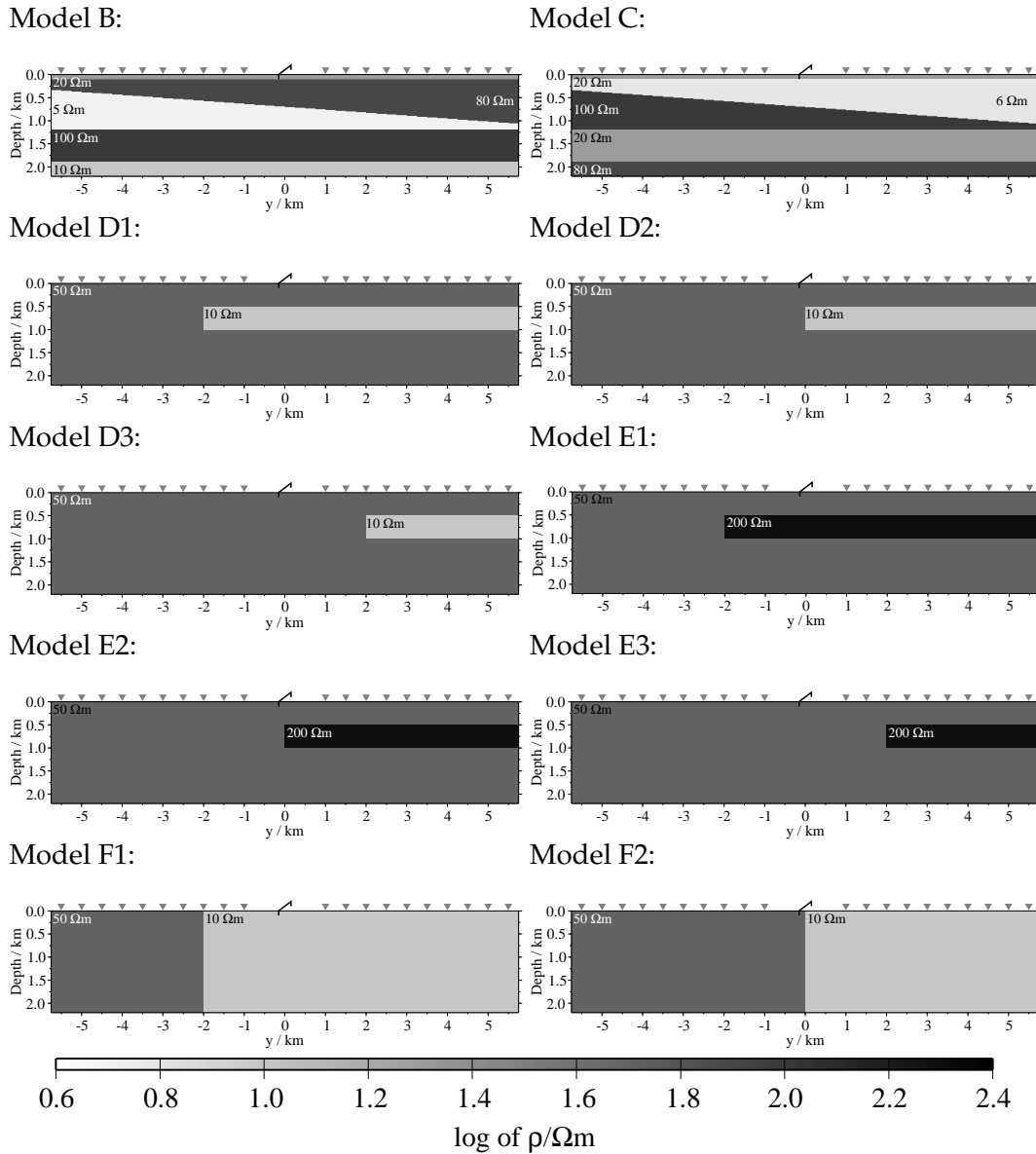


Figure 5.2: List of models used for the synthetic data sets (I); the titles denote the names which will be used in the text to refer to a model. More details are given in the text.

but very small error estimates for intermediate to early times. On the other hand, magnetic fields at large offset and electric fields showed medium sized error estimates throughout the whole time range.

This is considered not optimal. More desirable would be to construct data sets with similar error estimates at intermediate times. This way, the early times are less and the late times are more distorted for a magnetic field close to the Tx, compared to one calculated at large offsets. Using directly the data points at intermediate times does not provide satisfying results, as most of the H_y -transients exhibit a sign reversal there. Thus, in some cases several data points with extremely small voltages would be included in the calculation, which would lead to erratic noise floors. Instead an additional factor, based on the dynamic of the signal is included in the formula. Instead of the smallest absolute value of the transients, which again

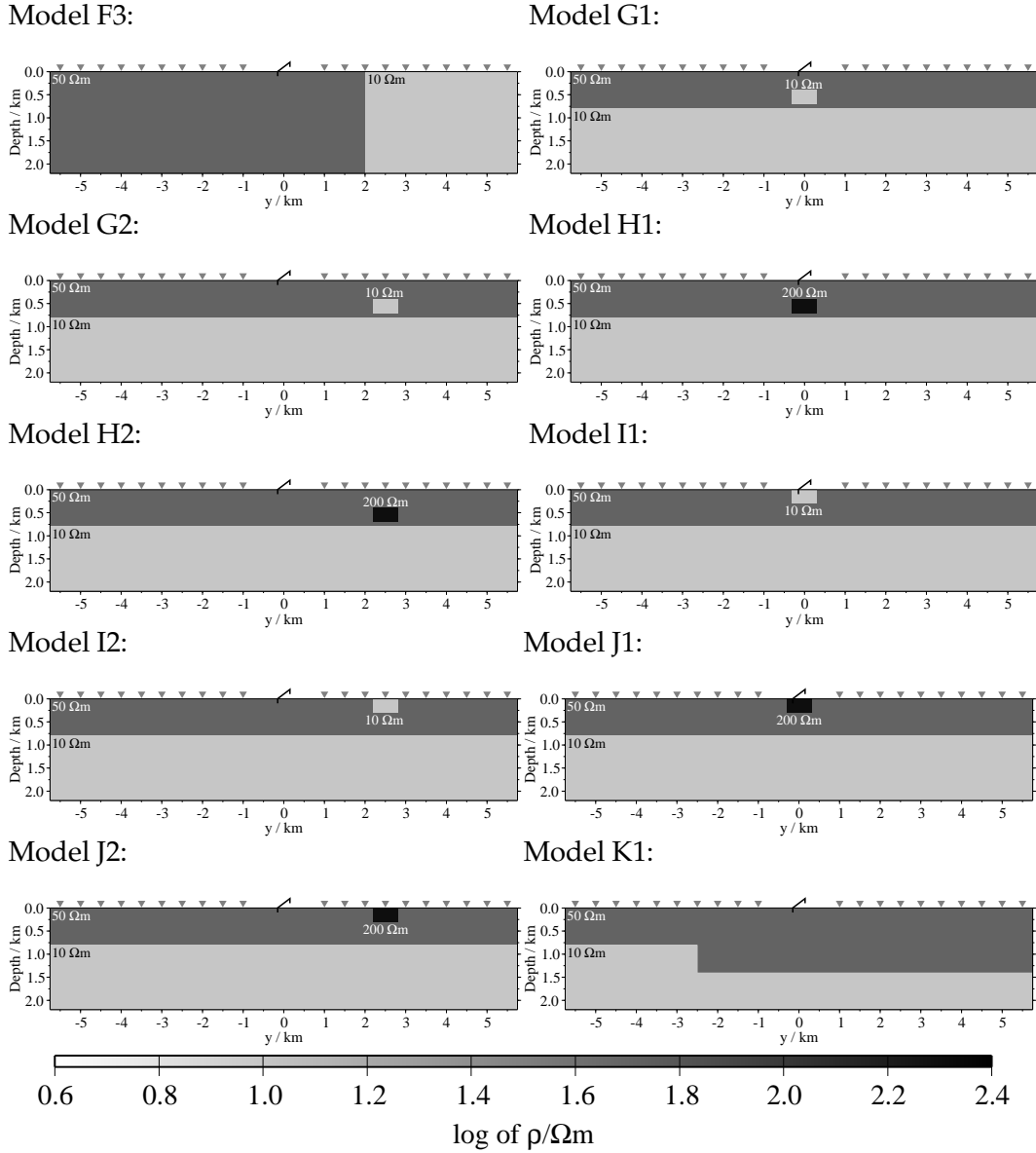


Figure 5.3: List of models used to calculate the synthetic data sets (II); the titles denote the names which will be used in the text to refer to a model. More details are given in the text.

might be one around a sign reversal, the absolute value of the last datum $|d_N|$ is used for the estimation of the signal dynamic. If d_{MAX} is the maximum absolute value, $|d_{\text{MAX}}|/|d_N|$ is multiplied to the sum given above.

Finally, the standard deviation should not drop below 1 % of each datum, as this would be not realistic because of the data processing steps (sec. 2.2.2) prior to inversion. Including an empirical factor of $1/100 \exp(4)$, the final standard deviation of each datum d_i is set to

$$s_i = \max \left(0.01|d_i|, \frac{1}{100 \exp(4)} \frac{|d_{\text{MAX}}|}{|d_N|} \exp \frac{1}{5} \sum_{j=N-4}^N \ln |d_j| \right). \quad (5.1)$$

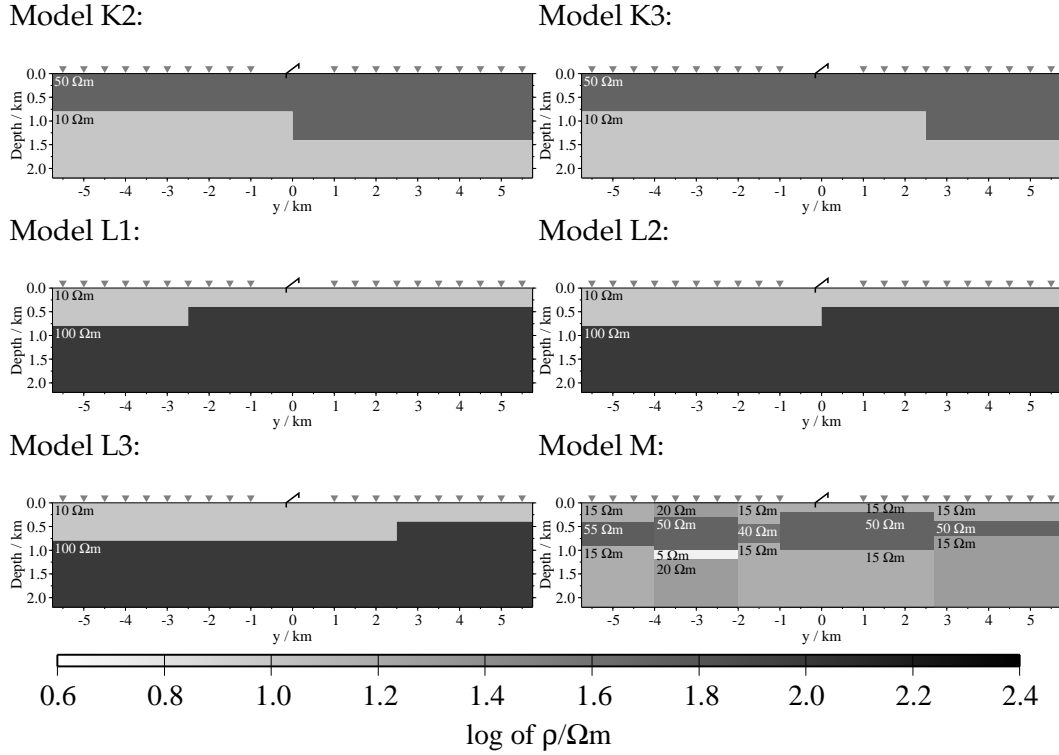


Figure 5.4: List of models used to calculate the synthetic data sets (III); the titles denote the names which will be used in the text to refer to a model. More details are given in the text.

In few cases the last data point of a \dot{H}_y -transient is the one around the sign reversal. In this case the transient will be very noisy. This occurred only a few times. Therefore, no additional measures were taken.

In several cases, the models obtained at positions close to the Tx showed distortions at depth. Possibly, this is a result of modelling errors due to the large dynamic range at small offsets. For the offsets ± 1.0 , 1.5 and 2.0 km, 9, 6 and 3 data points were removed from the end of each transient, respectively. In general, all CFs are treated as free model parameters in the inversions.

5.2 Determination of a proper regularisation parameter

In section 3.2.2 model update formulas for two different inversion schemes based on a linearisation were derived. For a Marquardt inversion the resulting model update $\hat{\mathbf{m}}$ is obtained by

$$\hat{\mathbf{m}}_n = (\mathbf{J}_{n-1}^T \mathbf{W}^2 \mathbf{J}_{n-1} + \beta \mathbf{I})^{-1} \mathbf{J}_{n-1}^T \mathbf{W}^2 \hat{\mathbf{d}}_{n-1} \quad (5.2)$$

The associated equation for an Occam's inversion model update $\hat{\mathbf{m}}^*$ at iteration n is

$$\hat{\mathbf{m}}_n^* = (\mathbf{J}_{n-1}^T \mathbf{W}^2 \mathbf{J}_{n-1} + \lambda \mathbf{P}^T \mathbf{P})^{-1} (\mathbf{J}_{n-1}^T \mathbf{W}^2 \hat{\mathbf{d}}_{n-1} - \lambda \mathbf{P}^T \mathbf{P} \mathbf{m}_{n-1}^*) \quad (5.3)$$

The choice of the two damping or regularisation parameters β and λ is crucial for the convergence of the inversion algorithms. However, in the Marquardt case the choice of β is not critical as it will not affect the inversion result greatly. At each iteration step simply the β is chosen, which minimises the misfit. The model itself is not constrained by β .

In an Occam's inversion the function of λ is two-fold. First, it should keep the model as smooth as possible. Second, it should damp the solution in order to achieve a better misfit. The value of λ in the Occam's inversion thus will affect the resulting earth model as it controls how much roughness may be introduced in the model.

The Occam's inversion algorithm starts with an arbitrary high value for λ . At every iteration the inversion routine searches for a value for λ which minimises the misfit [Constable et al., 1987]. At an early stage of inversion – when the misfit is still large – a large damping is required. At later iterations the linearisation of $f(\mathbf{m})$ becomes more accurate and less damping and thus less smoothing is needed [Jupp and Vozoff, 1975; Constable et al., 1987]. Typically, the value of λ decreases throughout the inversion. This correlates to an increasing roughness of the model, although this correlation is not mandatory. In this way, the choice of a value for λ and the amount of roughness are related to when the inversion process stops. Stopping early will result in a smooth model with a poor misfit.

Criteria to stop the inversion may be:

1. The misfit is lower than a certain threshold, i.e.

$$\chi_n \leq \tau_1. \quad (5.4)$$

This means a target misfit should be achieved [Constable et al., 1987]. In the case of well-selected error estimates $\chi = 1.0$ should be achieved. If a $\chi < 1.0$ is found, the regularisation should be increased to find a smoother model with $\chi = 1.0$. This allows the removal of unnecessary structure, which was introduced at early iteration stages.

In most field cases the error estimates are made under the assumption of uncorrelated, normally distributed noise of known deviation, which unfortunately is not realistic (see sec. 2.2.3). Thus, for real applications a target misfit only can be guessed. The choice of the target misfit has a great impact on the smoothness. All in all, this method is not suitable for field data. Many regularisation schemes rely on the estimation of a target misfit [Constable et al., 1987; Farquharson and Oldenburg, 1993]. These schemes are therefore also not applicable.

2. The model update is small [Gill et al., 1981], i.e.

$$\|\hat{\mathbf{m}}_n^*\| < \tau_2 \|\mathbf{m}_n^*\|. \quad (5.5)$$

If the norm of the model update vector is very small compared to the model vector the inversion has converged. In our case, the model vector is comprised of the logarithms of the resistivities. Thus, $\hat{\mathbf{m}}_n^*$ already describes the relative changes, which leads to:

$$\|\hat{\mathbf{m}}_n^*\| < \tau_2 \quad (5.6)$$

3. The relative misfit decrease is small [Constable et al., 1987], e.g.

$$\chi_{n-1} - \chi_n < \tau_3 \chi_n. \quad (5.7)$$

This again is a necessary criterion for convergence. However, even if the relative misfit decrease is small at iteration n , it does not have to be small at step $n + 1$. Instead of the χ the RMS could be used in eqn. 5.7.

4. Similar to the previous criterion, the relative decrease of the cost function q^* (see eqn. 3.21) could be regarded [Gill et al., 1981]. The cost function is not directly comparable to the one from the previous iteration if the value for λ was changed. Instead, $q_{n-1}^*(\lambda_n)$ is calculated. This yields

$$q_{n-1}^*(\lambda_n) - q_n^*(\lambda_n) < \tau_3 q_n^*(\lambda_n). \quad (5.8)$$

5. A maximum number of iterations is reached. This is the least problem oriented criterion. However, as most geophysical inversions are tedious, it might be useful on occasion to make sure the inversion process ends sometime to avoid further waste of computation time [Gill et al., 1981]. Results obtained by ending the inversion process this way should be inspected carefully. The maximum number of iteration steps should be high enough that inversions are not ended regularly by this criterion.

Criteria 3 and 4 concern the acceptability of an update. If criterion 3 is used, the model update is only accepted if it provides at least the same misfit as the previous one. If criterion 4 is used, the model update is accepted if a decrease in the cost function according to eqn. 5.8 is reached. This means the misfit is allowed to increase a few percent if the model gets smoother.

Up to now, EMUPLUS used the criteria 1, 3 and 5. If any of these criteria was met, the inversion stopped. However, for reasons given above, criterion 1 is not reasonable for field data and criterion 5 is not desirable. I implemented criterion 2 and changed the code in such a way that both criterion 2 and 3 have to be met to stop the inversion. This would mean that the process converged [Gill et al., 1981]. It is unlikely that the next iteration will provide a lower misfit, if both the relative decrease in misfit and the change of the model for the actual iteration is low. To keep the number of parameters set by the user low, Gill et al. [1981] proposed to use $\tau_2 = \sqrt{\tau_3}$. Tests showed that a $\tau_3 = 0.01$ works well.

To allow the algorithm to reduce the roughness at later stages if the misfit is increased moderately, I implemented also criterion 4. A comparison of using criterion 2 and 3 or 2 and 4 is shown in the next section.

5.2.1 Choosing a value for λ

Farquharson and Oldenburg [2004] proposed to suppress multidimensional distortions in EM data by choosing an appropriate value for λ . They tested their algorithms with airborne FD-EM data for the horizontal coplanar Tx-Rx combination. Their idea is that distorted data sets should produce rough models (for TEM e.g. to fit over-steep transients [Goldman and Neubauer, 1994]). Restricting the roughness to a "reasonable" value should thus suppress mainly structures introduced by distortions of the data sets.

They tested three approaches:

- The “discrepancy principle” proposed by Constable et al. [1987], which means simply to choose the value of λ which minimises the misfit. An univariate search algorithm is used to find the minimum of $\chi(\lambda)$, starting at the value of λ of the previous iteration. Constable et al. [1987] promote the use of the golden section search [Gill et al., 1981].
- The L-curve criterion; if for several values of λ the misfit norm $\sqrt{q(\lambda)} = \chi(\lambda)\sqrt{N}$ (eqn. 3.6) is plotted versus the model roughness norm $\|\mathbf{P}\mathbf{m}^*(\lambda)\|$ using log-log axes, the graph tends to have a characteristic “L” shape [Hansen, 1997]. The branch for values of λ smaller than the corner of the L-curve represents the part where the roughness has to be increased greatly to get a better misfit. On the other branch small decreases in roughness will degrade the misfit seriously. Thus, the value of λ at the corner of the L-curve is the most reasonable choice. The corner commonly is found by searching for the point of maximum curvature [Hansen, 1997].
- The “Generalised Cross-Validation” (GCV) criterion uses a cross-validation function to determine an optimal value for λ . As Farquharson and Oldenburg [2004] found that this approach gave about the same results as the L-curve criterion, I did not consider it further. For additional information please refer to Farquharson and Oldenburg [2004].

For all criteria many additional evaluations of $\mathbf{f}(\mathbf{m}^*)$ are needed to calculate $\chi(\lambda)$, especially for the latter two. As these evaluations in general are computationally expensive, often the linearised approximation is used (e.g. Smith and Booker [1988]):

$$q(\lambda) = (\mathbf{d} - \mathbf{f}(\mathbf{m}^*(\lambda)))^T \mathbf{W}^2 (\mathbf{d} - \mathbf{f}(\mathbf{m}^*(\lambda))) \quad (5.9)$$

$$\approx (\mathbf{d} - \mathbf{f}(\mathbf{m}_{n-1}^*) - \mathbf{J}_{n-1} \hat{\mathbf{m}}_n^*(\lambda))^T \mathbf{W}^2 (\mathbf{d} - \mathbf{f}(\mathbf{m}_{n-1}^*) - \mathbf{J}_{n-1} \hat{\mathbf{m}}_n^*(\lambda)) \quad (5.10)$$

Similar to Mitsuhashi et al. [2002] I found that for TEM the linearisation errors are too big. As an example, fig. 5.5 shows L-curves for both approaches for an Occam’s inversion of a synthetic \dot{H}_z -transient at the first (left panel) and fifth (right panel) iteration step. In the linear case the value of λ decreases with increasing roughness. The curves for the linearised solution and exact solution for $q(\lambda)$ show huge differences. Only the curves for the linearised solution show the distinct L-shape (left panel, for $20 < \sqrt{q(\lambda)} < 50$).

The graphs for the exact evaluation show a minimum of $\sqrt{q(\lambda)}$ (gray circle in the left panel of fig. 5.5). If the value of λ is further decreased, both $q(\lambda)$ and the roughness increase. This means that the matrix inversion in eqn. 5.3 is damped too little and the $\hat{\mathbf{m}}^*(\lambda)$ departs from the interval where the linearisation of $\mathbf{f}(\mathbf{m})$ yields a reasonable approximation. If the “optimal” value for λ would be determined from the linearised curve, $\sqrt{q(\lambda)}$ in fact would be close to the maximal value.

After some iterations the situation is even worse (fig. 5.5, right). The minimum for $\sqrt{q(\lambda)}$ in the exact solution (gray circle) is very narrow. The point of maximum

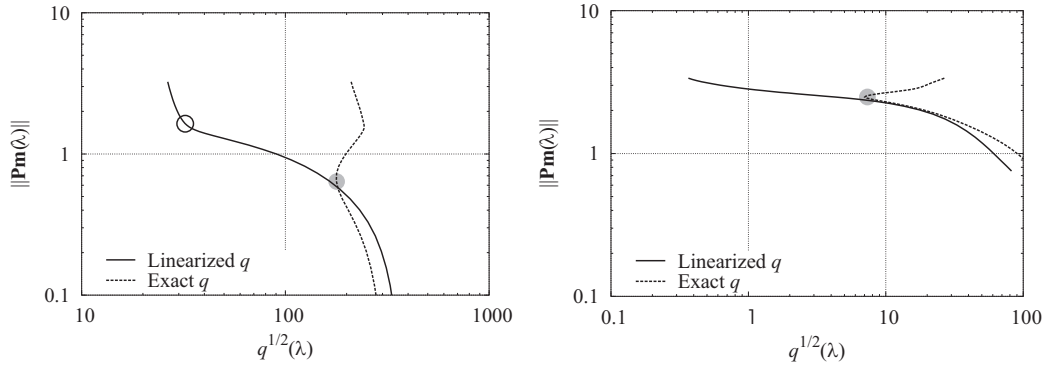


Figure 5.5: L-curves for the inversion of a LOTEM- \dot{H}_z -transient; in both plots the L-curves for using the linearised solution for $q(\lambda)$ after eqn. 5.10 and an exact $q(\lambda)$ by evaluating $\mathbf{f}(\mathbf{m})$ is shown. The points of maximum curvature are marked with an open circle (linearised q) and a gray circle (exact q), respectively. Left: L-curves for the first iteration. Right: L-curves for the fifth iteration. The point of maximum curvature for the linearised solution is not within the used λ -range.

curvature in the linearised case is not within the range of values of λ used to produce the plot. The narrow minimum of $\sqrt{q(\lambda)}$ also prohibits the use of a fixed value for λ throughout the inversion process.

The use of the linearised L-curve thus is prohibitive. This is in agreement to the results of Mitsuhashi et al. [2002]. Nevertheless, the L-curve criterion in principle could also be applied using the exact solution. However, the points of maximum curvature are located at the minimum of $q(\lambda)$ (fig. 5.5). Applying the L-curve criterion, one thus obtains the same results as using the discrepancy principle.

5.2.2 Restricting the decrease in the value of λ

Occam's inversion tends to introduce additional structure to models like e.g. overshoots at resistivity changes [Farquharson and Oldenburg, 1993; Hördt and Scholl, 2004; Farquharson and Oldenburg, 2004]. This happens mainly at early iteration steps. At later inversion stages the inversion should reduce this unnecessary structure. In any case it is better prevent the build up of structure at early stages.

Similar to an idea in Farquharson and Oldenburg [1993], where the misfit decrease from one iteration to the next is limited, Farquharson and Oldenburg [2004] propose to limit the decrease in the value of λ . They chose

$$\lambda_n = \max(c\lambda_{n-1}, \lambda^*) \quad (5.11)$$

where $0.01 \leq c \leq 0.5$ and λ^* is the regularisation parameter which minimises $\chi(\lambda)$. This restriction rule was implemented to EMUPLUS. First test, however, showed that the algorithm in some cases failed to converge at low misfit levels. Most likely, this is caused by the narrow minima of $q(\lambda)$ (see sec. 5.2.1). To prevent the inversion from converging too early, the strategy was changed slightly. If λ_n was set to $c\lambda_{n-1}$ and the resulting model would meet the chosen convergence criteria, c is divided by two for this iteration. The full scheme for the inversion algorithm is displayed in fig. 5.6.

Unfortunately, restricting the decrease in the value of λ makes the inversion result

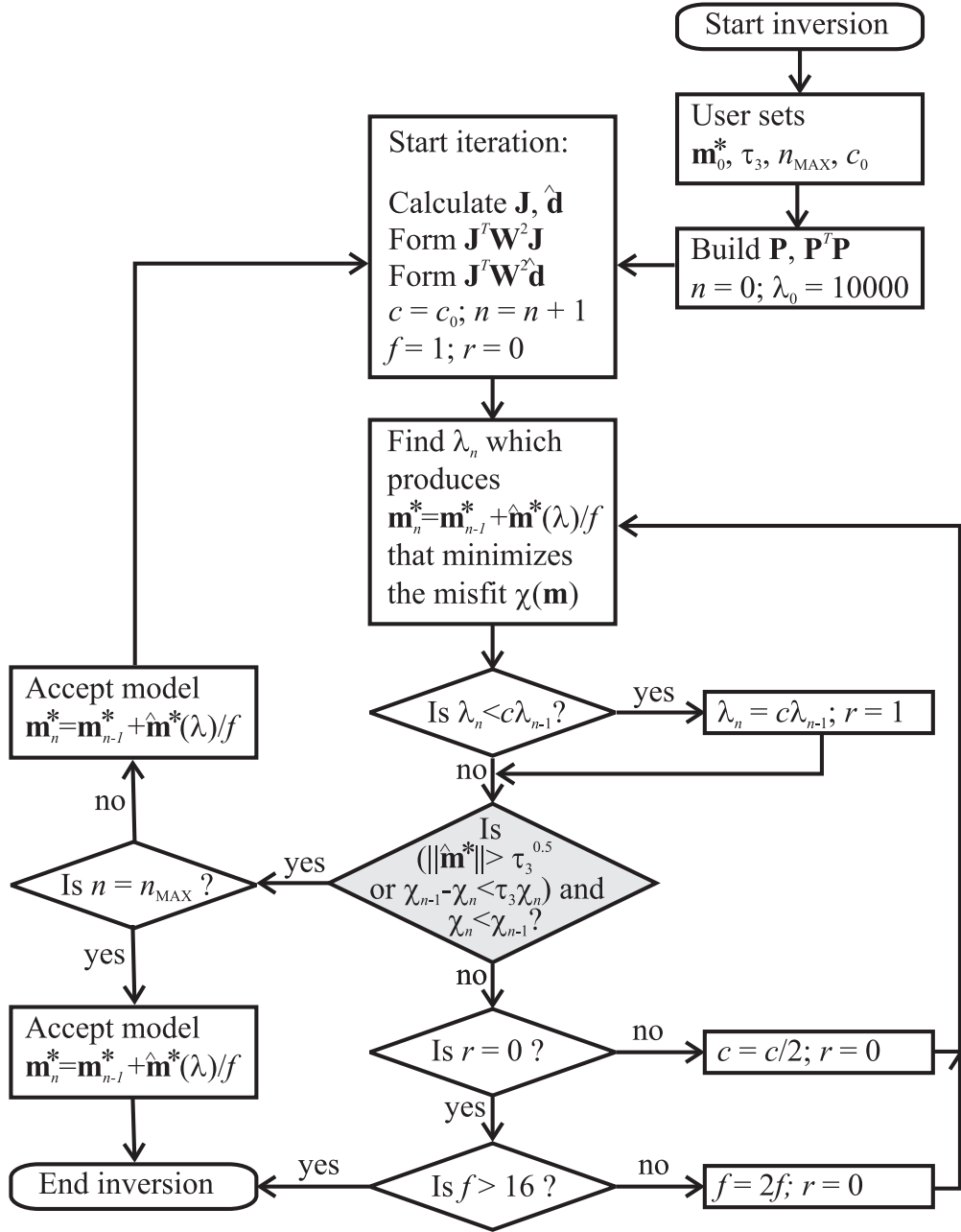


Figure 5.6: Flow chart for the Occam's inversion implemented in EMUPLUS, if convergence criteria after eqns. 5.6 and 5.7 are used. Additionally, a maximum number of iteration n_{MAX} is set. If the convergence should be based on the cost-function instead of the misfit (eqn. 5.8), the condition in the gray rhombus changes to "Is $(\|\hat{\mathbf{m}}_n^*\| > \sqrt{\tau_3}$ or $q_{n-1}^*(\lambda_n) - q_n^*(\lambda_n) < \tau_3 q_n^*(\lambda_n)$ and $q_n^*(\lambda_n) < q_{n-1}^*(\lambda_n)$?". f is the inverse step-size. r logs, if the value of λ was set to $c\lambda_{n-1}$. All other variable meanings are identical to the ones found in the text and section 3.2.2.

depending on the initial value of λ ($:= \lambda_0$). For all inversions shown in this work, λ_0 is set to 10,000.

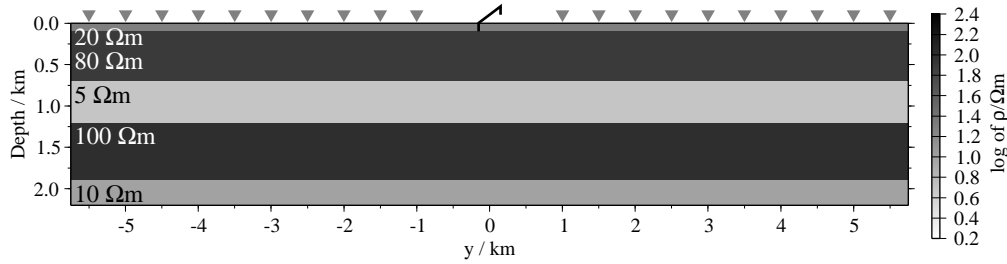


Figure 5.7: Model used for the model-calculations in this section; in the text this model is referred to as “model A”.

5.2.3 Testing the regularisation schemes with synthetic data

In this section I will test if different regularisation schemes are suited to suppress artifacts which are produced by multidimensional structures. This is done by using four different regularisation schemes in the inversion of several synthetic data sets.

The inversions are stopped after 50 iteration steps, or if convergence is reached either in χ_n or q_n^* with $\tau_3 = 1.0\%$ (see fig. 5.6). Further, the allowed decrease of $\lambda_n - c$ was set to 0.0 (infinite decrease allowed) or 0.5 ($\lambda_n \geq \lambda_{n-1}/2$). Table 5.1 shows the designations of all parameter combinations used in this section.

Designation	C1	C2	C3	C4
Convergence controlled by	χ_n	q_n^*	χ_n	q_n^*
Maximum decrease factor c	0.0	0.0	0.5	0.5

Table 5.1: Designations and parameters for the four regularisation schemes tested in this section;

The initial model for the inversion is discretised in 25 layers. The thicknesses of layers are increased logarithmically starting with a thickness of 30 m up to a depth of 2000 m. The initial resistivity is optimised by the algorithm prior to inversion to achieve a low starting misfit (see app. A).

For a first test, a synthetic data set calculated for a 1-D model is used (model A, fig. 5.7). The model is not intended to have any geological meaning. As it was also used for the grid test (cp. sec. 5.1) it simply should comprise of layers with the typical resistivities used in the other synthetic models of this chapter.

The test with a 1-D model allows to compare the final misfit with the expected misfit of $\chi = 1.0$. Regularisation schemes which produced a significant lower misfit thus tend to fit the noise by introducing artificial structure in the model. There is no target roughness, i.e. no expected value for the roughness. It simply should be as small as possible. The calibration factors should be close to 1.0 and the number of iterations should be small. Ideally, all inversion results should not change strongly from one station to the next, although different noise realisations are imposed¹.

From theory I expected that the strategies using q_n^* (C2 and C4) produce smoother models, because here models are also accepted which degrade the misfit slightly if the roughness is reduced. Farquharson and Oldenburg [2004] further claim that

¹For all transients eqn. 5.1 was used. However, the pseudo random number sequence calculated by the computer are different for each station.

Str.	Comp.	$\bar{\chi}$	Roughn.	# of It.	CF
C1	E_x	0.81 ± 0.19	5.92 ± 1.56	15.5 ± 4.2	0.92 ± 0.21
C1	\dot{H}_y	0.87 ± 0.21	5.90 ± 1.67	13.5 ± 3.9	1.02 ± 0.23
C1	\dot{H}_z	0.88 ± 0.21	6.30 ± 1.64	11.7 ± 3.3	1.01 ± 0.23
Avg. C1:		0.85 ± 0.20	6.04 ± 1.62	13.6 ± 3.8	0.98 ± 0.22
C2	E_x	0.81 ± 0.19	5.39 ± 1.38	14.8 ± 4.0	0.92 ± 0.22
C2	\dot{H}_y	0.87 ± 0.21	5.83 ± 1.62	16.8 ± 4.7	1.02 ± 0.24
C2	\dot{H}_z	0.88 ± 0.21	6.40 ± 1.67	15.1 ± 4.2	1.01 ± 0.23
Avg. C2:		0.85 ± 0.20	5.87 ± 1.56	15.6 ± 4.3	0.98 ± 0.23
C3	E_x	0.81 ± 0.19	5.89 ± 1.55	23.2 ± 5.8	0.92 ± 0.21
C3	\dot{H}_y	0.87 ± 0.21	5.97 ± 1.72	24.0 ± 6.3	1.02 ± 0.23
C3	\dot{H}_z	0.88 ± 0.21	6.66 ± 1.84	21.6 ± 5.6	1.01 ± 0.23
Avg. C3:		0.85 ± 0.20	6.17 ± 1.70	22.9 ± 5.9	0.98 ± 0.22
C4	E_x	0.80 ± 0.19	5.55 ± 1.51	24.2 ± 6.1	0.87 ± 0.21
C4	\dot{H}_y	0.86 ± 0.21	5.04 ± 1.31	23.1 ± 6.1	1.03 ± 0.24
C4	\dot{H}_z	0.88 ± 0.21	6.18 ± 1.63	23.1 ± 6.2	1.01 ± 0.23
Avg. C4:		0.85 ± 0.20	5.59 ± 1.48	23.5 ± 6.1	0.97 ± 0.23

Table 5.2: Mean values and standard deviations for misfit $\bar{\chi}$, roughness (“Roughn.”), the number of iterations and the calibration factors \overline{CF} for all single component 1-D inversion of synthetic data sets with the four regularisation schemes (“Str.”) C1 to C4; the column “Comp.” defines the component used. For more information see the text.

limiting the decrease in the value of λ would reduce the roughness (C3 and C4). I could observe this for extreme cases, when the initial misfit was very high and dominated by a few data points. In these cases eventually the algorithm finds a minimal misfit for a very low value of λ introducing significant structure to the models. If these low values are accepted, the algorithm fails to converge at low misfit levels at later inversion steps. An example is shown in appendix A. However, as this occurred only rarely and the problem could be circumvented by finding individual initial half-spaces, the question remains if limiting the decrease helps to find smoother models in ordinary cases.

The tabs. 5.2 and 5.3 show the results for the inversions of single and joint-inversions, respectively. Listed are the values for misfit, roughness, the number of iterations and the calibration factors averaged over all 20 Rx-sites along the profile. Standard deviations are given to show the variance of the inversions². The individual values and resulting pseudo-sections can be found in app. B.

The differences between the strategies are small. The misfit and the calibration factors are similar. The models are slightly rougher for C1 and C3. Minimising q_n^* instead of χ (C3 and C4) only seems to increase the number of iterations needed. No significant difference in roughness could be observed there. Examining individual cases, one can find data sets where even C1 gave the smoothest results (app. B).

The resulting roughnesses and misfits for C4 and C2 are almost similar, although the average results in the joint-inversions for C4 are slightly better (misfit closer to

²Calculating the standard deviation for these values is inaccurate in a strict sense, as none of these quantities is normally distributed. It would be more accurate to consider their logarithms. As this would be less intuitive, I will ignore this for the sake of simplicity.

Str.	Comp.	$\bar{\chi}$	Roughn.	# of It.	CF
C1	$E_x, \dot{H}_y \& \dot{H}_z$	0.95 ± 0.22	11.86 ± 2.93	18.9 ± 5.0	1.00 ± 0.13
C1	$E_x \& \dot{H}_y$	0.91 ± 0.21	8.07 ± 2.26	16.1 ± 4.3	1.00 ± 0.16
C1	$E_x \& \dot{H}_z$	0.91 ± 0.21	11.06 ± 2.73	16.1 ± 4.3	1.00 ± 0.16
C1	$\dot{H}_y \& \dot{H}_z$	0.95 ± 0.22	6.81 ± 1.79	12.8 ± 3.6	1.00 ± 0.16
Avg. C1:		0.93 ± 0.22	9.45 ± 2.43	16.0 ± 4.3	1.00 ± 0.15
C2	$E_x, \dot{H}_y \& \dot{H}_z$	0.95 ± 0.22	11.26 ± 2.82	17.1 ± 4.4	1.00 ± 0.13
C2	$E_x \& \dot{H}_y$	0.90 ± 0.21	9.18 ± 2.47	15.3 ± 4.0	0.99 ± 0.16
C2	$E_x \& \dot{H}_z$	0.91 ± 0.21	10.44 ± 2.69	16.3 ± 4.3	1.00 ± 0.16
C2	$\dot{H}_y \& \dot{H}_z$	0.82 ± 0.19	6.22 ± 1.75	11.8 ± 3.1	1.01 ± 0.16
Avg. C2:		0.90 ± 0.21	9.28 ± 2.43	15.1 ± 4.0	1.00 ± 0.15
C3	$E_x, \dot{H}_y \& \dot{H}_z$	0.95 ± 0.22	11.96 ± 2.96	24.4 ± 6.0	1.00 ± 0.13
C3	$E_x \& \dot{H}_y$	0.90 ± 0.21	10.23 ± 2.66	24.2 ± 5.8	0.99 ± 0.16
C3	$E_x \& \dot{H}_z$	0.91 ± 0.21	10.42 ± 2.73	23.4 ± 5.8	1.00 ± 0.16
C3	$\dot{H}_y \& \dot{H}_z$	0.96 ± 0.22	6.01 ± 1.50	19.3 ± 4.6	1.01 ± 0.16
Avg. C3:		0.93 ± 0.22	9.66 ± 2.46	22.8 ± 5.6	1.00 ± 0.15
C4	$E_x, \dot{H}_y \& \dot{H}_z$	0.95 ± 0.22	11.22 ± 2.90	24.9 ± 6.2	1.00 ± 0.13
C4	$E_x \& \dot{H}_y$	0.91 ± 0.21	7.38 ± 2.12	21.1 ± 5.2	1.00 ± 0.16
C4	$E_x \& \dot{H}_z$	0.90 ± 0.21	10.71 ± 2.66	24.0 ± 5.8	1.00 ± 0.16
C4	$\dot{H}_y \& \dot{H}_z$	0.96 ± 0.23	5.55 ± 1.41	17.6 ± 4.2	1.00 ± 0.16
Avg. C4:		0.93 ± 0.22	8.72 ± 2.27	21.9 ± 5.4	1.00 ± 0.15

Table 5.3: Mean values and standard deviations for misfit $\bar{\chi}$, roughness (“Roughn.”), the number of iterations and the calibration factors \overline{CF} for all 1-D joint-inversion of synthetic data sets with the four regularisation schemes (“Str.”) C1 to C4; the column “Comp.” defines the component used. For more information see the text.

1.0, roughness smaller, see tab. 5.3). Also the resulting roughnesses and misfits for C3 and C1 are similar. Therefore, I will use only C4 and C1 later in this study.

Figs. 5.8 and 5.9 show the results for the inversions of all three components for both schemes. The results of the inversions of the different components are displayed as section, plotting the resulting 1-D models below the respective Rx-position. These sections of composed 1-D models are called “pseudo-sections” throughout this study. In the pseudo-sections, the model for each station is placed below the Rx-site. The sites are marked with gray triangles. The Tx is located at $y = 0$ km and pointing in x-direction. The model boundaries are marked with black lines in the pseudo-section. Below the Tx the original model is plotted. Lines in the sections mark the layer boundaries. The gray-scale which is coding the resistivities is displayed at least once in each figure. Values exceeding the scale slightly are either displayed as white (too small) or black (too big). Areas where very unrealistic values are obtained ($< 0.2 \Omega\text{m}$ or $> 20 \text{ k}\Omega\text{m}$, only found in few pseudo-sections) are marked with diagonal lines. Above every pseudo-section, the misfit (χ), the model roughness and the CF for each inversion result are displayed³.

³In every pseudo-section-plot the displayed range of values for these parameters is limited to [0.1 : 50]. If one of the symbols does not show up, it should be obvious if the parameter has a higher (> 50) or lower (< 0.1) value. If the model is very smooth, the roughness can be < 0.1 , whereas the χ might be > 50 . If the model shows significant structure, the roughness may exceed 50.0. If this happens along large parts of the profile, often the roughness/10 is displayed instead.

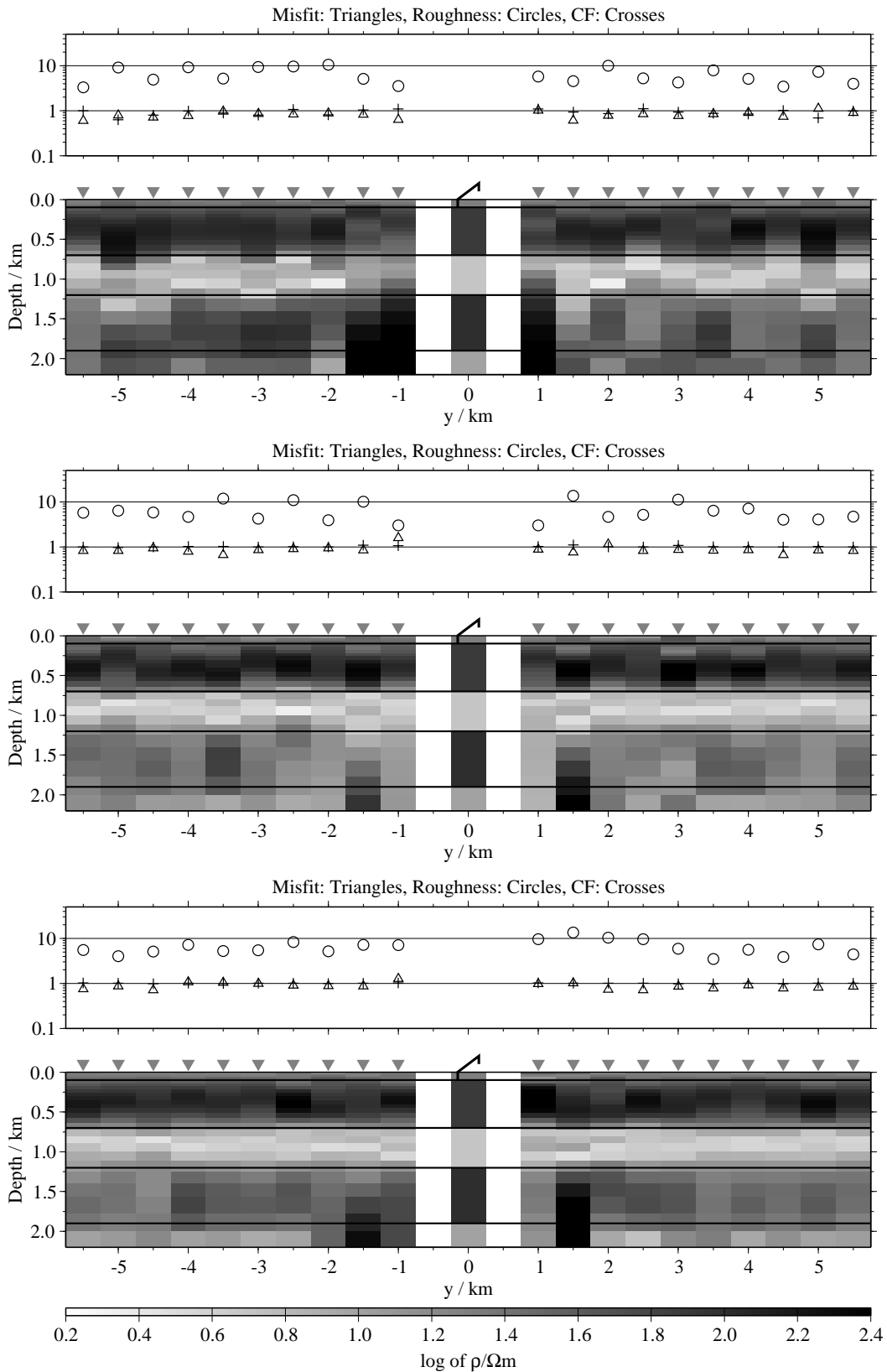


Figure 5.8: The single component inversion results for strategy C1; from top to bottom: Results for the component E_x , \dot{H}_y and \dot{H}_z . Above every pseudo-section the final misfit, roughness and calibration factor is plotted. Further explanations are given in the text.

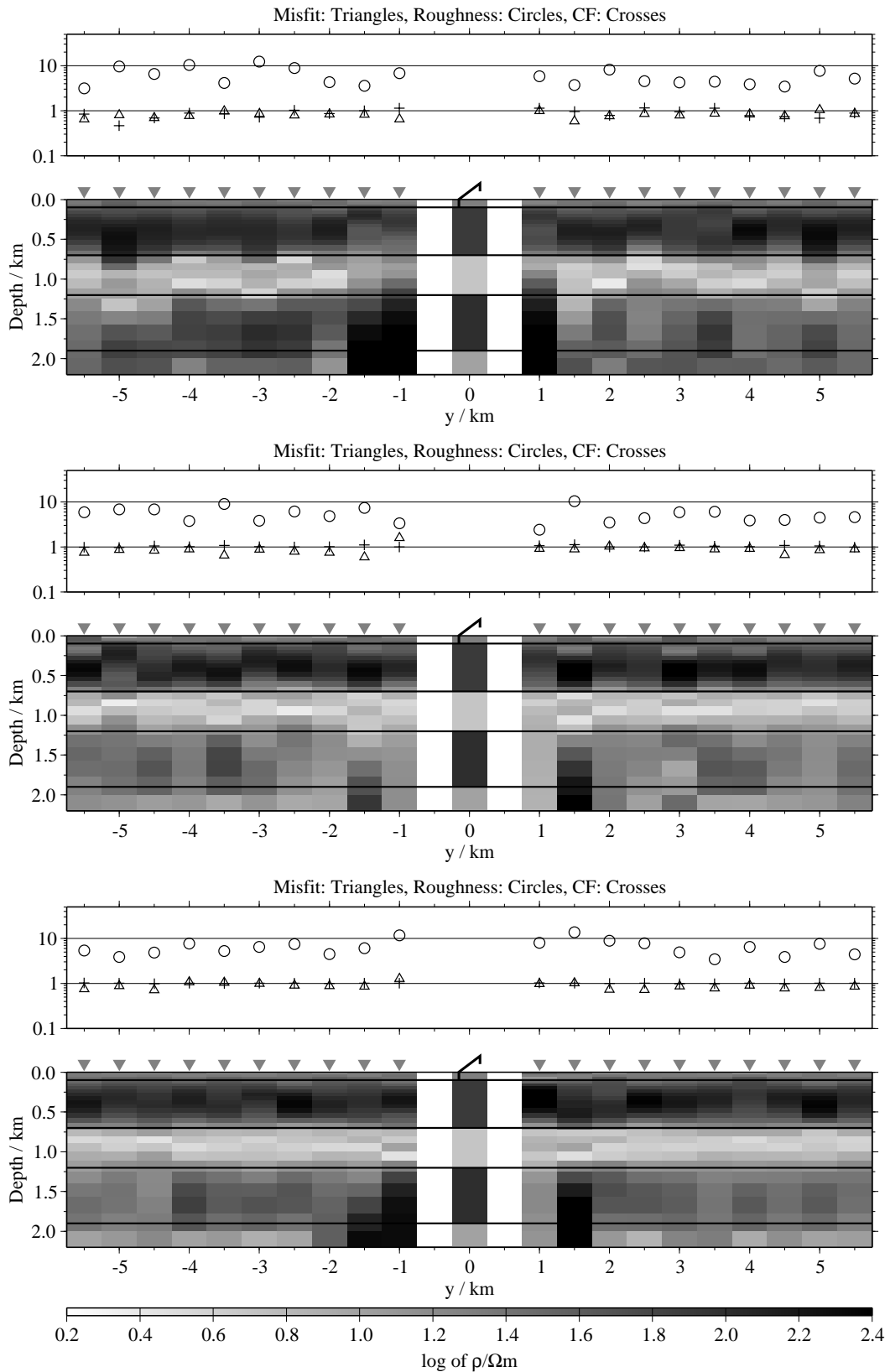


Figure 5.9: The single component inversion results for strategy C4; from top to bottom: Results for the component E_x , \dot{H}_y and \dot{H}_z . Above every pseudo-section the final misfit, roughness and calibration factor is plotted. Further explanations are given in the text.

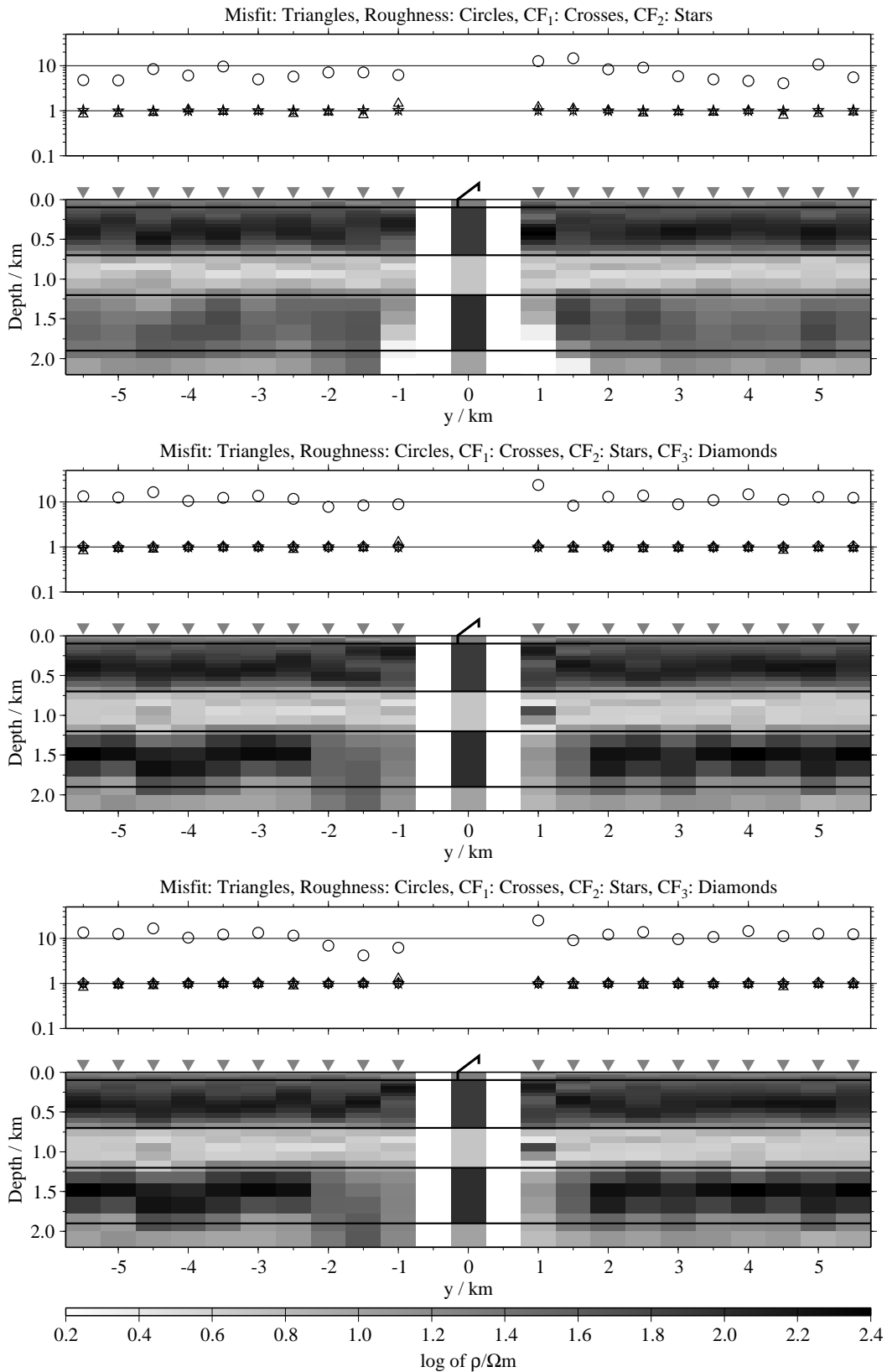


Figure 5.10: Pseudo-sections for joint-inversions; from top to bottom: Joint-inversions of the two magnetic components with regularisation scheme C1, joint-inversions of all three components with regularisation scheme C1, joint-inversions of all three components with regularisation scheme C4. Further explanations are given in the text.

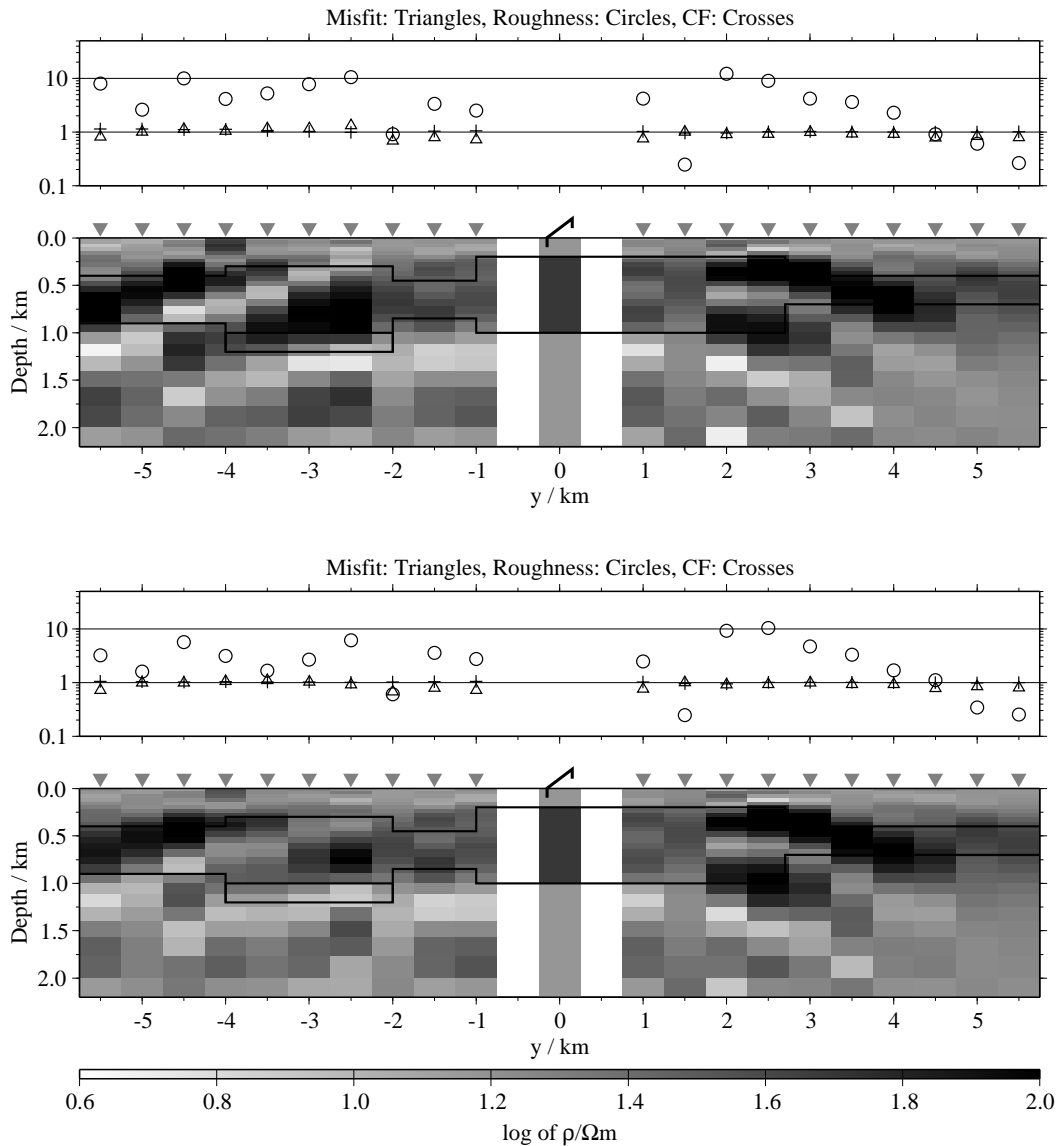


Figure 5.11: 1-D pseudo-section for the inversions of the \dot{H}_z -transients calculated for model M; the upper panels show the results for regularisation scheme C1, the lower panels the results for regularisation scheme C4.

Fig. 5.10 shows the pseudo-sections for three different sets of joint-inversions. For the uppermost section only the magnetic field transients \dot{H}_y and \dot{H}_z are used. The other two panels show the results of joint-inversions of all three components for the two different regularisation schemes C1 and C4. In plots showing joint-inversion results, the CFs of the different components in the upper parts are coded by different symbols.

In general, the main features of the model are found in all inversions. Comparing the pseudo-section for the regularisation scheme C1 (fig. 5.8) and C4 (fig. 5.9) no significant differences are found. This is also observed comparing the joint-inversion results in the lower panels of fig. 5.10. This fits the statistics in tabs. 5.2 and 5.3 as they show only minor differences.

There are some features in these pseudo-sections which show up systematically also in pseudo-sections shown later in this chapter:

- In general, small scale fluctuations in models of adjacent stations can be observed. That (and the average χ of 0.85 for model A) indicates that the algorithm for both regularisation schemes fits some of the noise. This effect is significantly reduced in the joint-inversions, as their pseudo-sections are laterally smoother. Unlike the single inversions, the final χ for the joint-inversions is close to 1.0 for model A (0.92 on average). This is an expression of the fact that the noise in the three data sets is not correlated.
- The models for the \dot{H}_y -transients are slightly rougher and show more lateral fluctuations, especially compared to the \dot{H}_z -results. This is caused by the fact that often the overall SNR is slightly higher for the \dot{H}_y -transients compared to the other components due to the sign reversal in the \dot{H}_y s.
- Including the CF in the inversion process introduces ambiguities in the interpretation, especially for the E_x -transients. Often, the single inversions of the electric fields fit the original model only qualitatively, although joint-inversion with other components reveal consistent pseudo-sections.
- The results for the stations with an offset of 1 and 1.5 km differ from the other results. As this is often observed, this might be caused by inaccuracies in the model calculations for these transients, which exhibit a high dynamic range.
- In the pseudo-section for the E_x -transients the resistors seem to be better resolved. Especially the resistivity of the second resistive layer is closer to the true resistivity for large parts of the profile (figs. 5.8 and 5.9). This is obvious, comparing the uppermost panel from fig. 5.10 (joint-inversion excluding the electric field data sets) to the lower two panels of the same figure, where all components are used in a joint-inversion. The conductive features in the single inversion pseudo-sections, however, looks less erratic for the magnetic components, especially for the \dot{H}_z -transients.
- In some cases the single inversion the model for a certain station is different to those of the adjacent two. In most cases, the structure of the model is similar, but is more pronounced at this certain station, i.e. the model is rougher. In other cases, the calibration factor at this certain station is different. This effect is produced by the different noise realisations and their unforeseeable effects during the inversion. Like the other lateral fluctuations caused by the added noise, this effect is significantly reduced in joint-inversions.

Using multidimensional synthetic models, the inversion results for the regularisation schemes are still very similar. In fig. 5.11 the results for the \dot{H}_z -transients calculated for model M are shown. Here, the models at sites with $y < 0$ km are significantly smoother using C4 instead of C1. Nevertheless, the structures are similar in both cases.

Fig. 5.12 shows a more typical example for the few pseudo-sections where the C4 scheme produces a smoother picture of the subsurface. Again, the biggest differences can be observed for $y < 0$ km. The main structures are similar in both results.

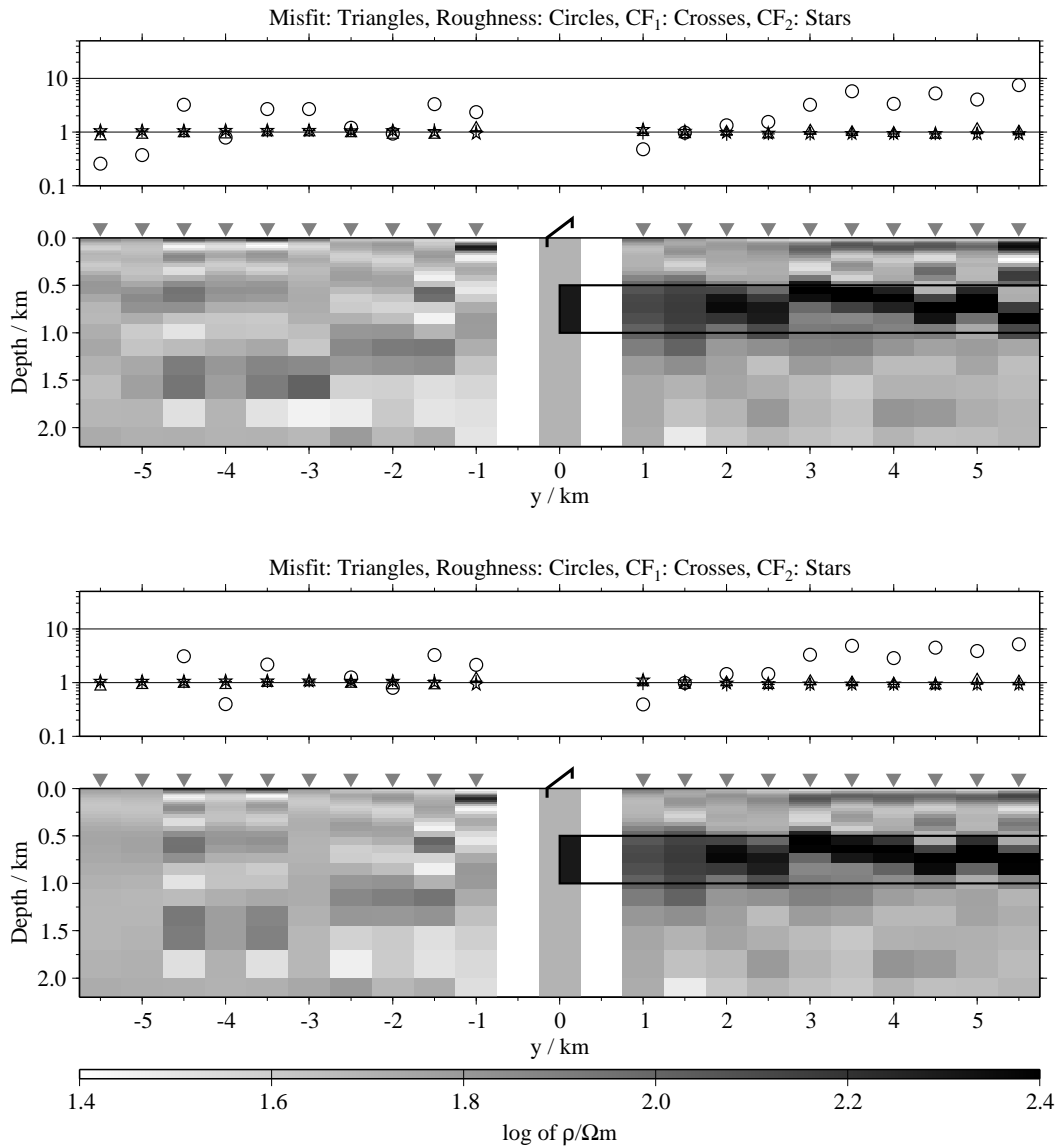


Figure 5.12: 1-D pseudo-section for the joint-inversions of the E_x - and \dot{H}_y -transients calculated for model E2; the upper panels show the results for regularisation scheme C1, the lower panels the results for regularisation scheme C4.

The Artifacts produced by the multidimensional model are not significantly suppressed.

In most cases no difference can be observed in the results for the two strategies. Fig. 5.13 shows a typical example derived from the E_x -transients calculated for model K3. Hence, the choice between the four regularisation schemes seems to have only a minor effect on the inversion results. In the best cases, the models are slightly smoother. Artifacts are not suppressed effectively. In the following thus only results for regularisation scheme C4 are presented.

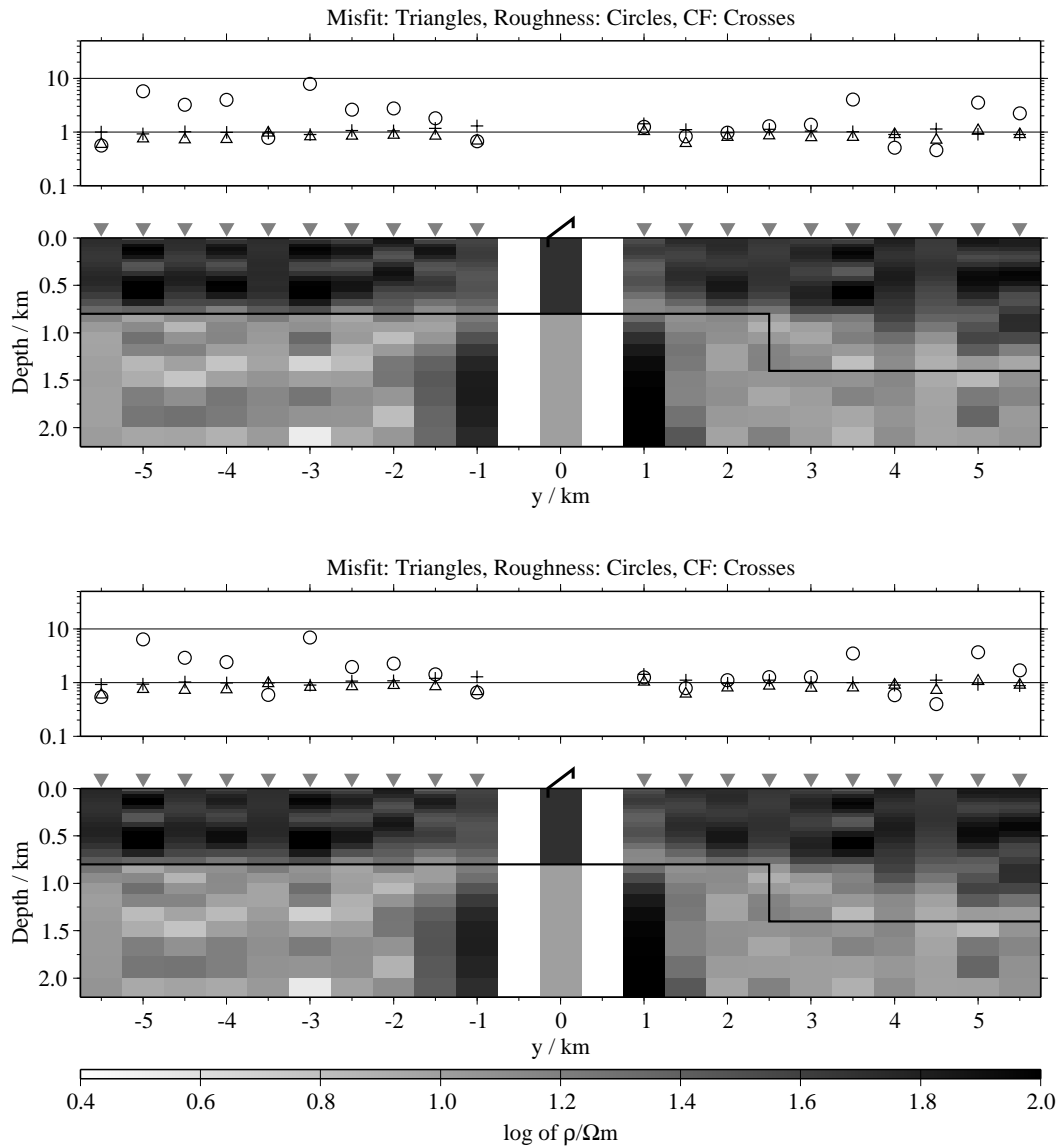


Figure 5.13: 1-D pseudo-section for the inversions of the E_x -transients calculated for model K3; the upper panels show the results for regularisation scheme C1, the lower panels the results for regularisation scheme C4.

5.3 Influence of multidimensional structures on the single 1-D inversion of LOTEM-transients

In this section the behaviour of the three LOTEM-components E_x , \dot{H}_y and \dot{H}_z in presence of multidimensional structures is examined. It would be most desirable if the pseudo-section reconstructs the original synthetic model perfectly. However, this is not expected to happen often.

The pseudo-section is considered to be usable, when the danger of misinterpretation is small, i.e. when

- the pseudo-section resembles the gross resistivity structure, i.e. only small

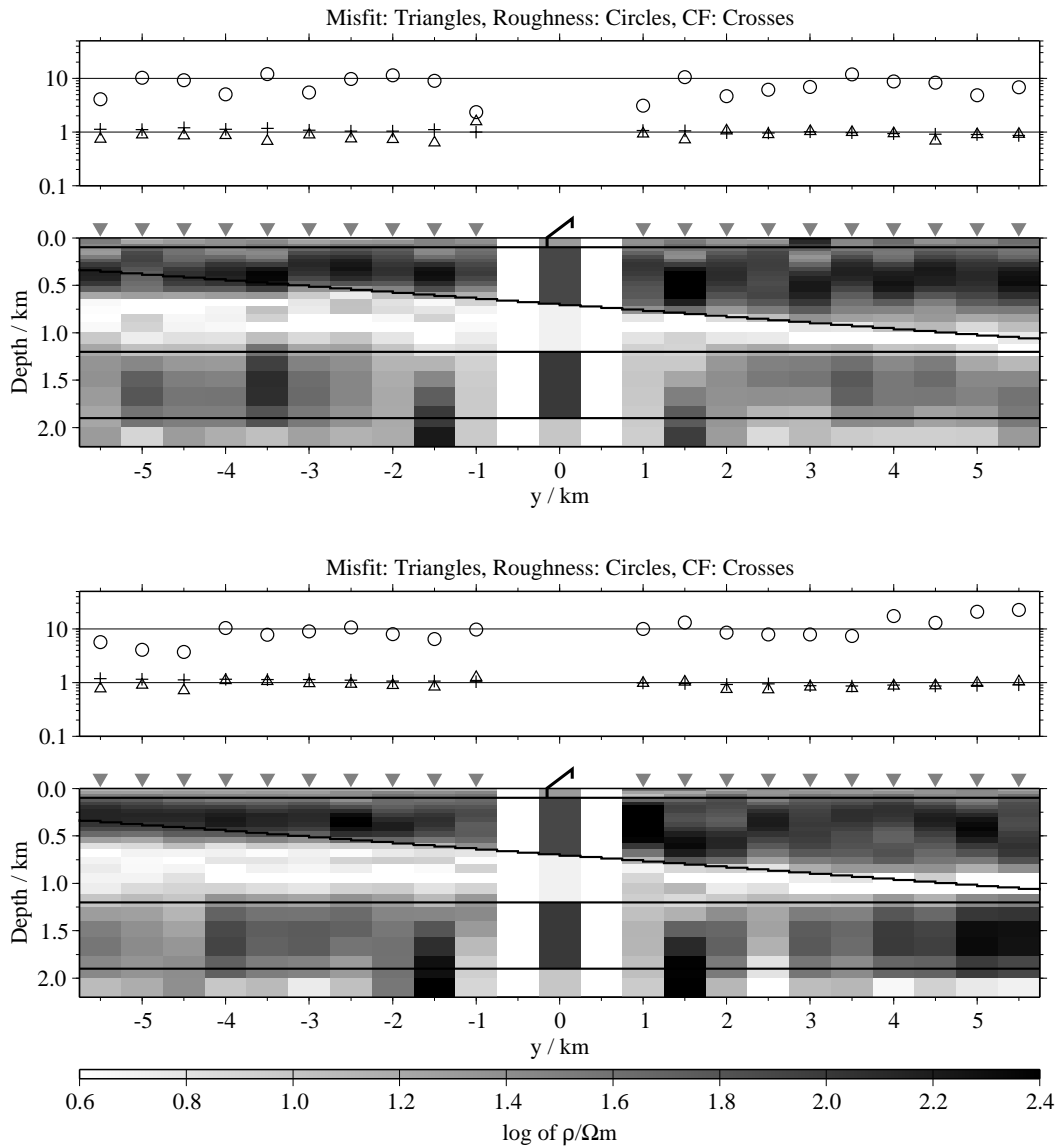


Figure 5.14: Pseudo-sections of single 1-D inversions, model B, regularisation scheme C4; displayed are the results for the \dot{H}_y - (top) and the \dot{H}_z -transients (bottom).

inhomogeneities might be suppressed.

- the pseudo-section shows artifacts only for unresolved, i.e. very shallow or very deep parts, respectively. For the time range and offsets used here, the part between ≈ 200 and 1500 m depth should not exhibit spurious features.
- the artifacts are not correlated for two adjacent stations. In this case a misinterpretation is unlikely, as features which change or disappear from one station to the next should be rejected as unreliable.
- distortions are so big that unreasonable values (striped areas) show up. In this case again the model should be rejected. However, if lower resistivity contrasts are chosen in the synthetic model, the distortions may be smaller and the models thus might not be considered as “unreasonable”.

Pseudo-sections showing strong artifacts which are consistent along parts of the spread are most dangerous, as they might lead to a wrong geophysical and thus geological interpretations.

The complete results of all inversions can be found in app. B.

5.3.1 Dipping layers (models B and C)

The models B and C are five layer cases, where the depth to the boundary between the second and the third layer increases with y . The dipping angle is $\approx 3.66^\circ$. Similar to the 1-D model the electric field pseudo-section is more noisy due to the ambiguity introduced with the CF.

In general, model B is well reproduced (fig. 5.14). The dip, however, is underestimated. The best results are achieved using the \dot{H}_z -transients. Here the obtained thicknesses of the layers at each station are closer to the actual thicknesses at the Rx-site. For the \dot{H}_y -transients the thickness of the upper layers is similar for all sites with $y < 0$ km. In the \dot{H}_z -section the resistivity of the fourth layer seems to compensate for the over- or underestimated thickness of the conductive third layer. For $y = -5.5$ km, where the third layer is too thin, the resistivity of the underlying fourth is decreased, compared to the true resistivity. At $y = 5.5$ km, where the conductive layer is too thick, the resistivity of the fourth is increased. The result for the E_x -transient is similar, but too noisy for closer analyses.

The pseudo-sections for model C show artificial structure below the second, conductive layer (fig. 5.15). The increase in resistivity below the conductor is found, but the resistivity of the underlying layer is not well constrained. The fourth layer is almost never resolved, although the pseudo-section for the E_x -component show a conductive feature at depth.

5.3.2 Vanishing layer (models D1 to E3)

In these models a layer is embedded in an otherwise homogenous half-space with $50 \Omega\text{m}$. The layer is either conductive ($10 \Omega\text{m}$) or resistive ($200 \Omega\text{m}$) compared to the half-space and ends at $y = -2$, $y = 0$ or $y = 2$ km.

In all cases, the results are best for the electric field component. The pseudo-sections are resembling the original synthetic models, although the lateral changes are suppressed. For models where the layer ends at $y = -2$ km (D1 and E1), the layer fades out slowly (upper panel of fig. 5.16). When the layer starts at $y = 2$ km (models D3 and E3) it is almost completely suppressed, probably up to large offsets. For the other two models D2 and E2, where the layer starts below the Tx, the pseudo-sections reveal the original model (middle panel of fig. 5.16). However, the pseudo-sections show slightly more artifacts, when the layer is resistive.

The situation is more complicated for the magnetic components. They show stronger artifacts for models including the conductive layer. Still, the distortions of the models are moderate. For model D1, the conductive layer ending at $y = -2$ km seems to dip instead of end in the pseudo-section (lower panel of fig. 5.16).

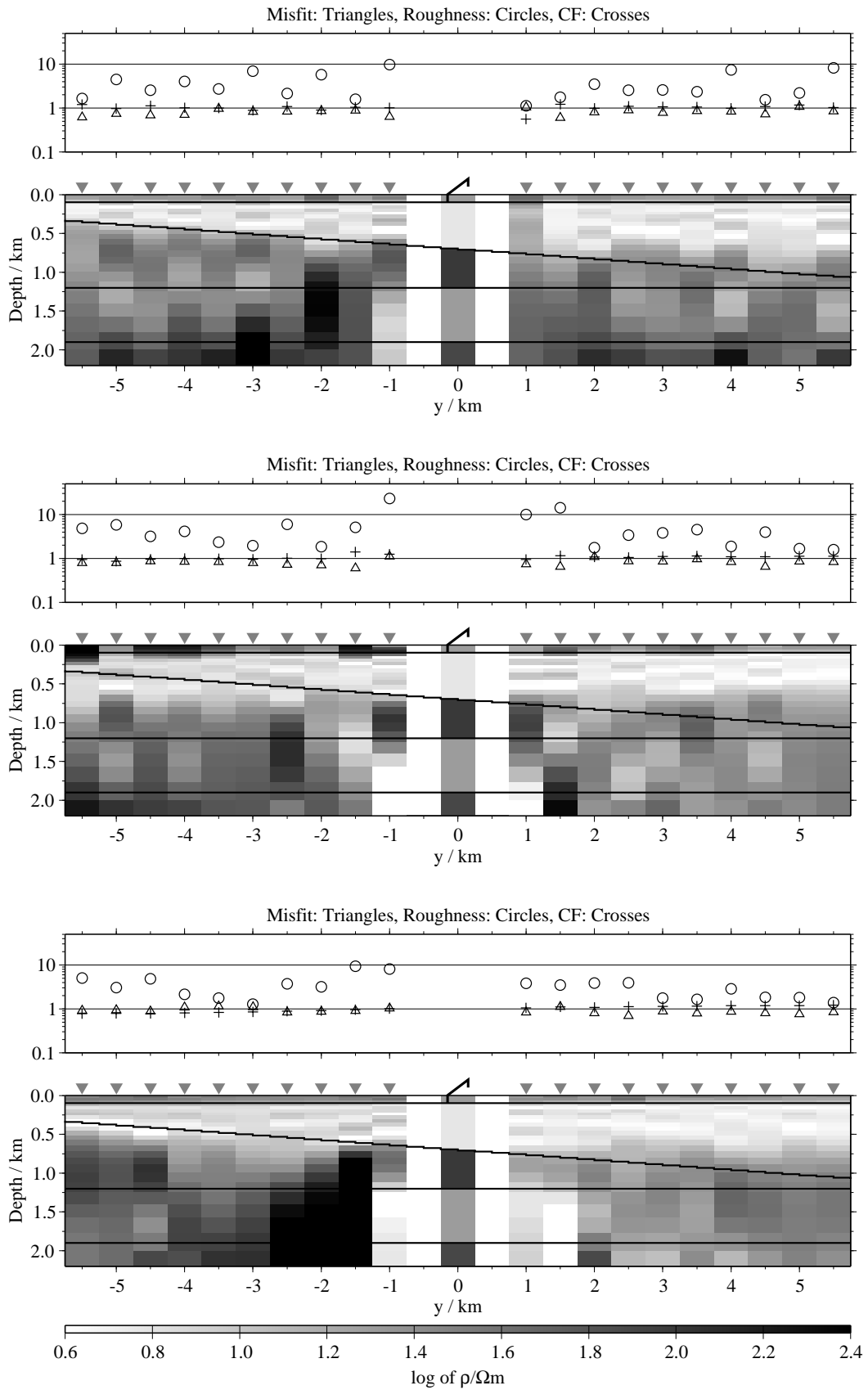


Figure 5.15: Pseudo-sections of single 1-D inversions for model C, regularisation scheme C4; from top to bottom: Results for the E_x -, \dot{H}_y - and \dot{H}_z -transients;

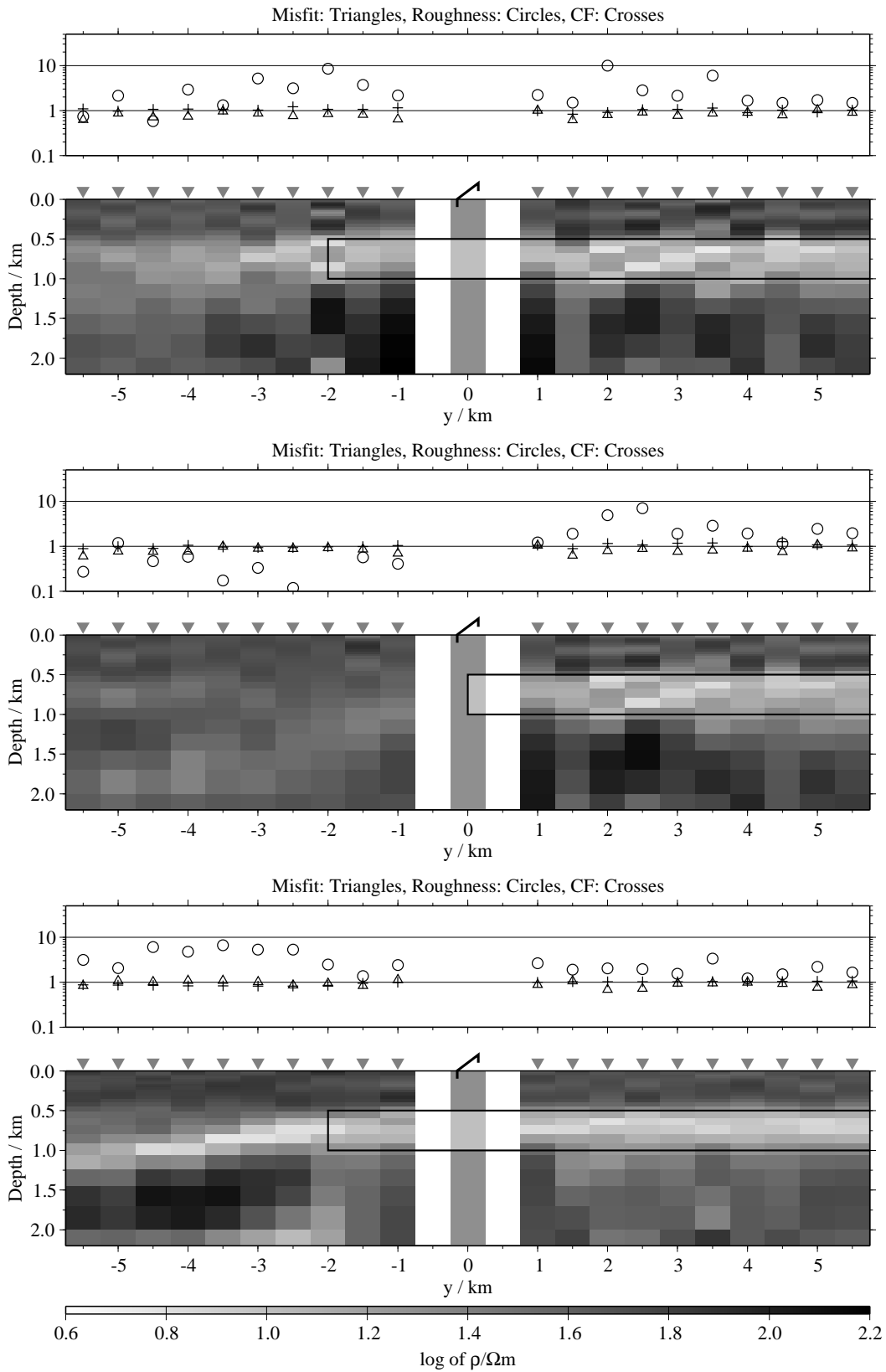


Figure 5.16: Pseudo-sections of single 1-D inversions, regularisation scheme C4; top: Results for the E_x -transients, model D1; middle: Results for the E_x -transients, model D2; bottom: Results for the H_z -transients, model D1;

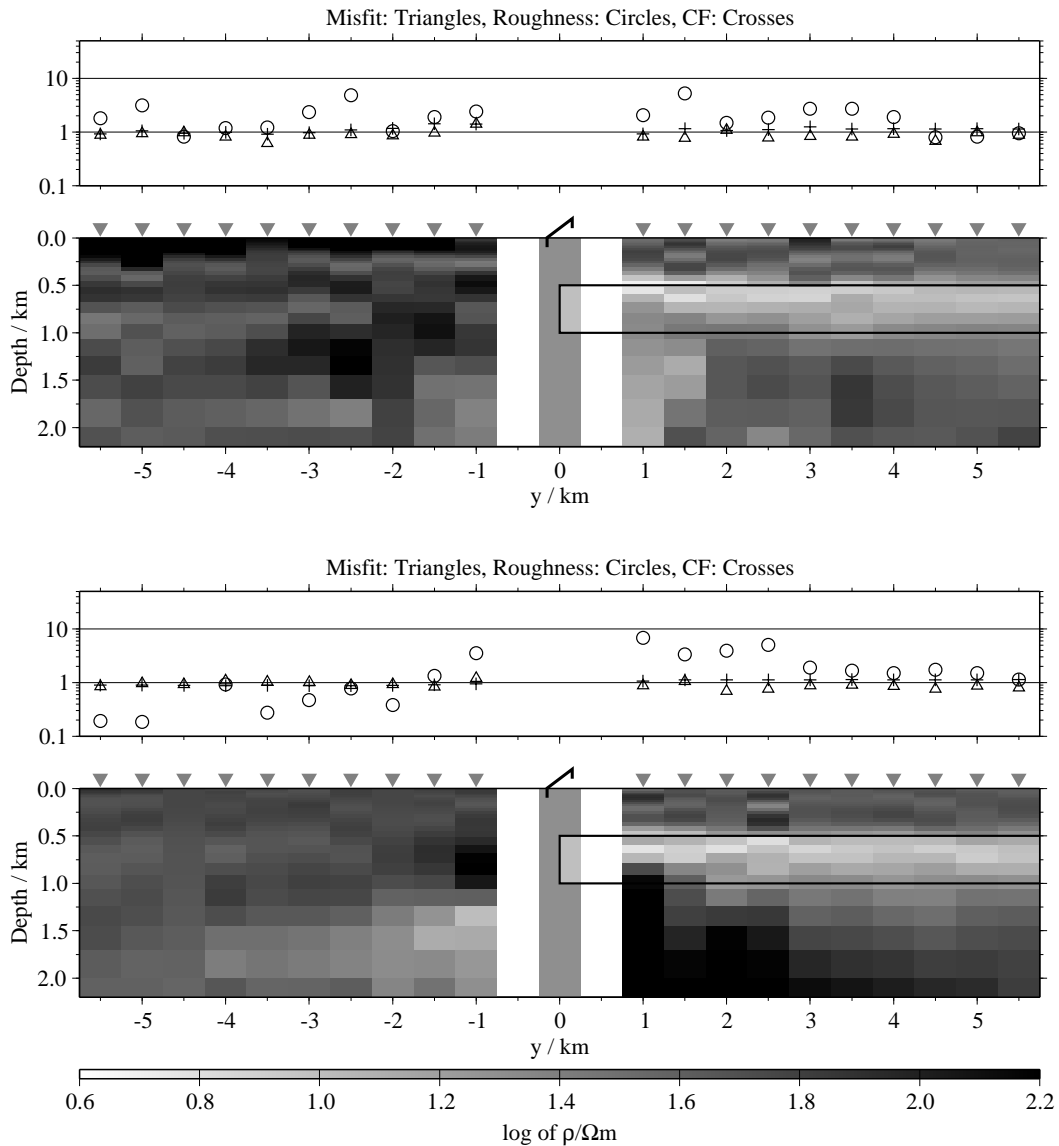


Figure 5.17: Pseudo-sections of single 1-D inversions for model D2, regularisation scheme C4; top: Results for the \dot{H}_y -transients; bottom: Results for the \dot{H}_z -transients;

In general, the models for the \dot{H}_z -transients are most distorted at sites close to the lateral change, i.e. the start of the layer. Here, the models are least undistorted up to the depth of the layer. With increasing distance from the end of the layer, the distortions are found to be deeper (fig. 5.17, bottom). In the pseudo-section for the \dot{H}_y -transients, distortions can be found in greater distance from the end of the layer. The inversion tends to introduce shallow resistive artifacts (fig. 5.17, top). This is also found for other synthetic models.

The results for the resistive layer are slightly different (see fig. 5.18). Here, the \dot{H}_z -transient reconstructs the model even better than the electric field component. The pseudo-section for the \dot{H}_y s proposes an extension of the layer for $y < -2$ km.

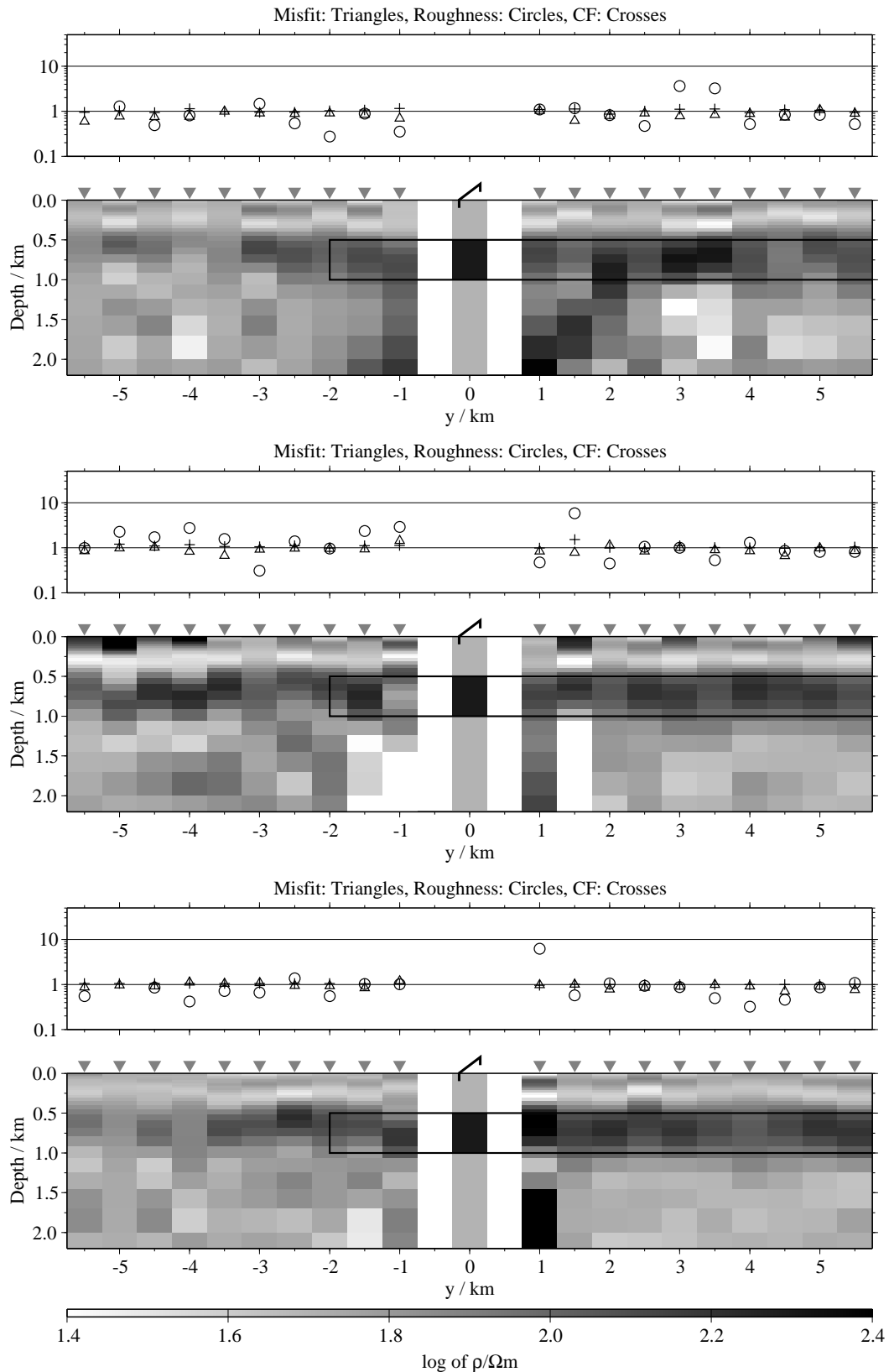


Figure 5.18: Pseudo-sections of single 1-D inversions for model E1, regularisation scheme C4; from top to bottom: Results for the E_x -, \dot{H}_y - and \dot{H}_z -transients;

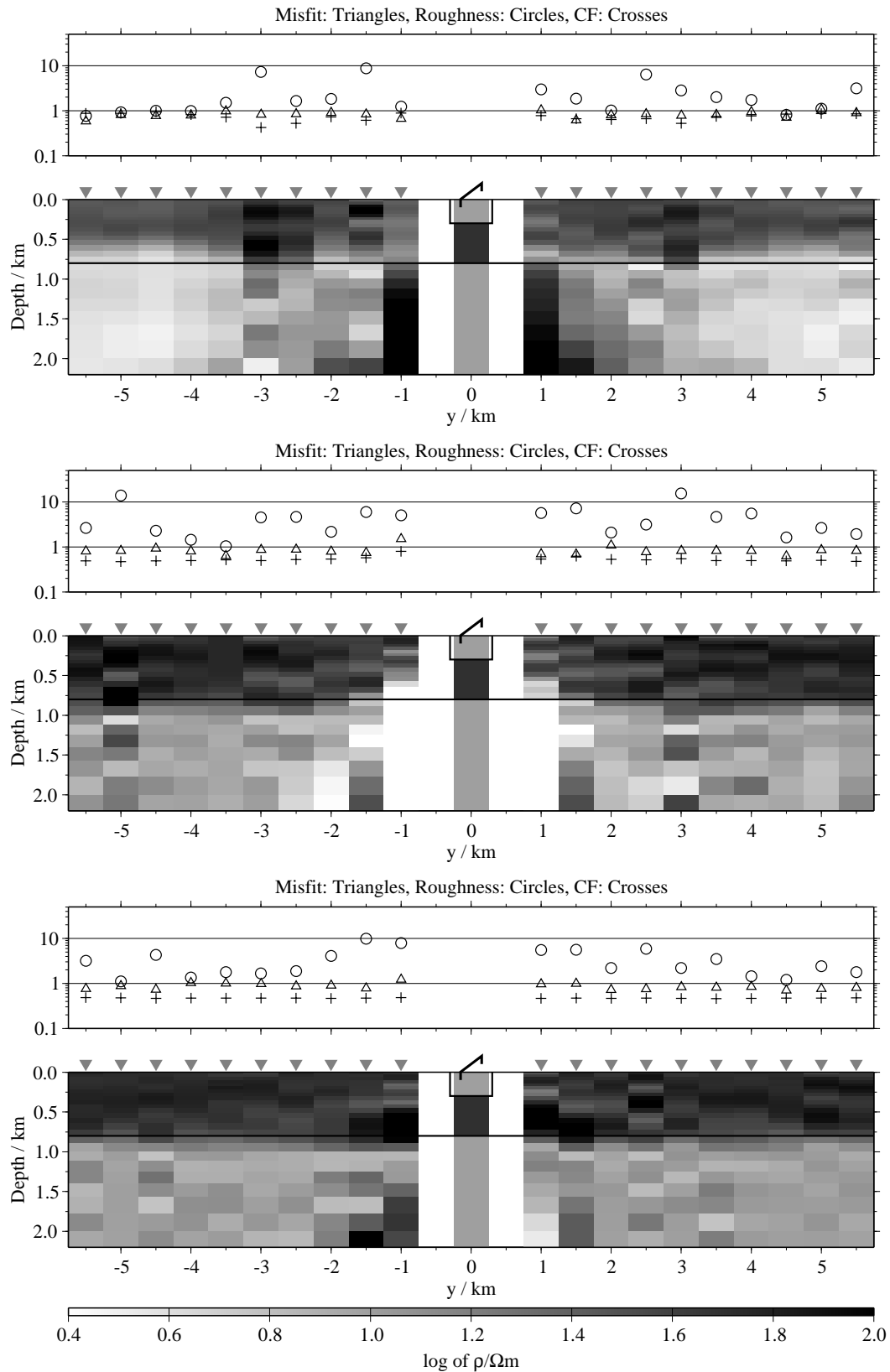


Figure 5.19: Pseudo-sections of single 1-D inversions, model I1, regularisation scheme C4; from top to bottom E_x -, H_y - and H_z -component;

5.3.3 Small inhomogeneities (models G1 to J2)

Data sets for four different models with small scale 3-D bodies are simulated. The blocks have a size of $600 \times 600 \times 300 \text{ m}^3$. Their midpoint is located on the y -axis at either $y = 0 \text{ km}$ or $y = 2.5 \text{ km}$. The underlying model is a two layer case with a $10 \text{ } \Omega\text{m}$ half-space below a 800 m thick $50 \text{ } \Omega\text{m}$ layer. The blocks have a resistivity of either 10 or $200 \text{ } \Omega\text{m}$. The top of the block is at the surface in the models I1, I2, J1 and J2, whereas in the other four models the midpoint is at $z = 550 \text{ m}$.

Some of the pseudo-sections for the \dot{H}_y -components show distorted models for $y = \pm 5 \text{ km}$. These distortions are not produced by the inhomogeneities, but by the noise added. The underlying 1-D model produces \dot{H}_y -responses where the last data point is at the sign reversal at these offsets. In this case the noise algorithm after eqn. 5.1 produces very noisy data.

In general, the distortions produced by the resistive block are smaller than the ones produced by the conductive block. In no case the block itself is resolved. At best it is simply suppressed and produces no artificial structures. If distortions show up they have only a poor lateral correlation. Therefore, they will not be mistaken as geological features.

Shallow block (models I1 to J2)

If the block is placed below the Tx, the effect on the data is a shift in the transients, which can be counteracted by the CF. The CFs are ≈ 1.3 for the resistive body and ≈ 0.5 for the conductive body. This agrees well with the results of Newman [1989].

Fig. 5.19 shows the pseudo-sections for model I1 with regularisation scheme C4 as an example. Only the transients from stations very close to the Tx produce distorted models. For the conductive block, the inversions of the E_x -transients converged at an equivalent model with a CF of around 0.85 and a more conductive basement.

If the block is located within the spread at $y = 2.5 \text{ km}$, only minor distortions are found. The E_x -component is least distorted followed by the \dot{H}_y -transients, where distortions are found at the sites at $y = 2.5$ and $y = 3.0 \text{ km}$. The \dot{H}_z s are distorted most. Here, the models for all three stations close to the body show distortions.

The introduction of the CF to the inversion process increases the ambiguity, especially for the electric components. Fig. 5.20 (top) shows the results for the \dot{H}_y -components without inverting the CF. The models show very large distortions along the whole profile. Thus, inverting the CF is necessary to derive only slightly distorted models from the transients. Strack [1992] states that this effect is frequently observed in field situations. Therefore, including the CF to the inversion of field data sets is almost inevitable, although the CF seems to introduce undesirable ambiguity to the interpretation⁴.

⁴Sec. 5.7 shows a possibility to remove the shift prior to the inversion. However, the method shown there is only an approximation.

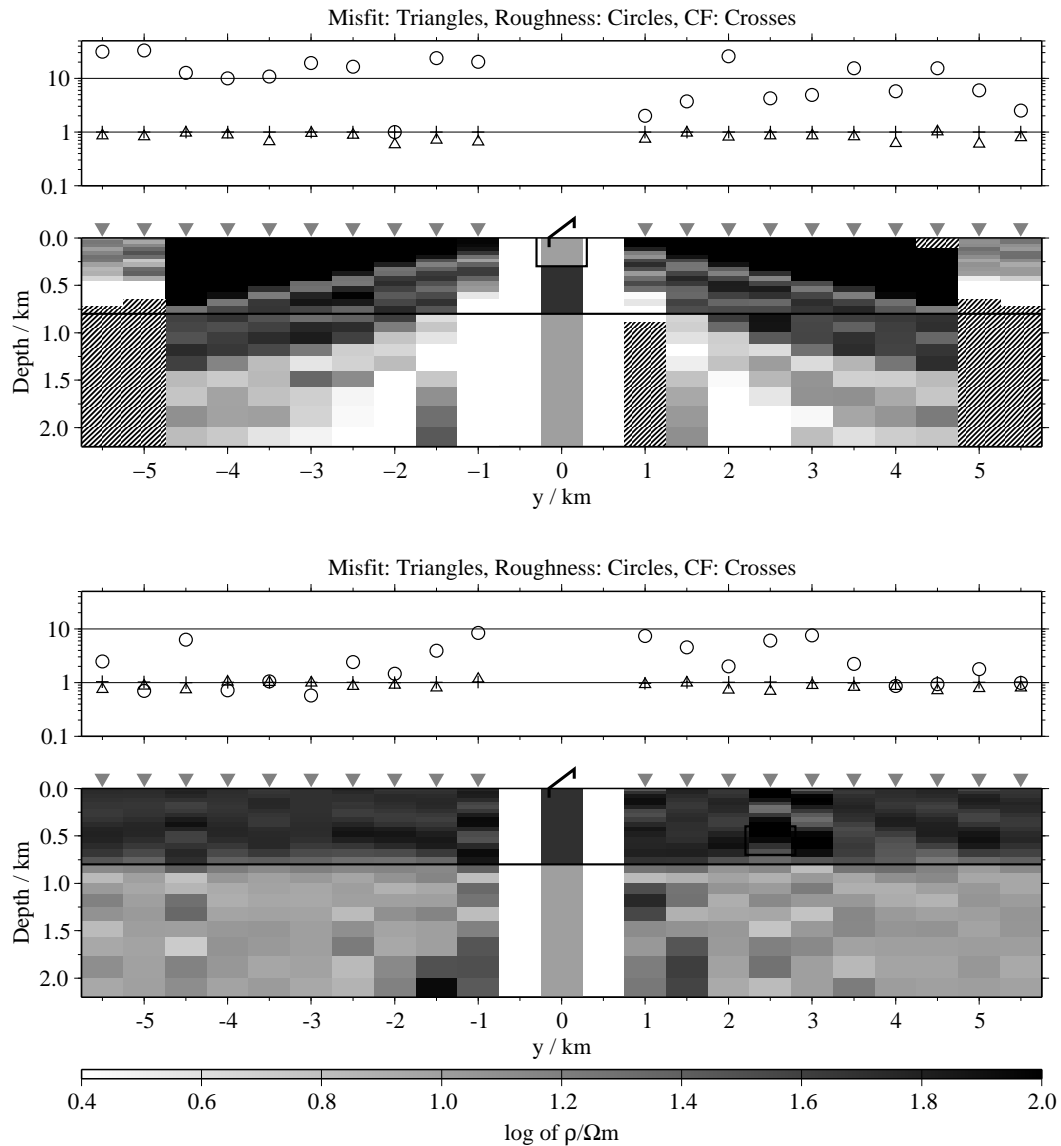


Figure 5.20: Pseudo-section of single 1-D inversions, regularisation scheme C4; top: \dot{H}_y -component, model I1; in the inversions the CF was fixed. bottom: \dot{H}_z -component, model G2;

Block at intermediate depth (models G1 to H2)

The influence of the deeper block is much smaller than that of the shallow block. If the block is placed beneath the Tx, only the models at $y = \pm 1.0$ km show stronger distortions. If the body is situated within the spread at $y = 2.5$ km, no distortions are visible in the E_x - and \dot{H}_y -pseudo-sections. The \dot{H}_z -transients are only slightly distorted and produce weak artifacts at $y = 2.5$ and $y = 3.0$ km (fig. 5.20, bottom).

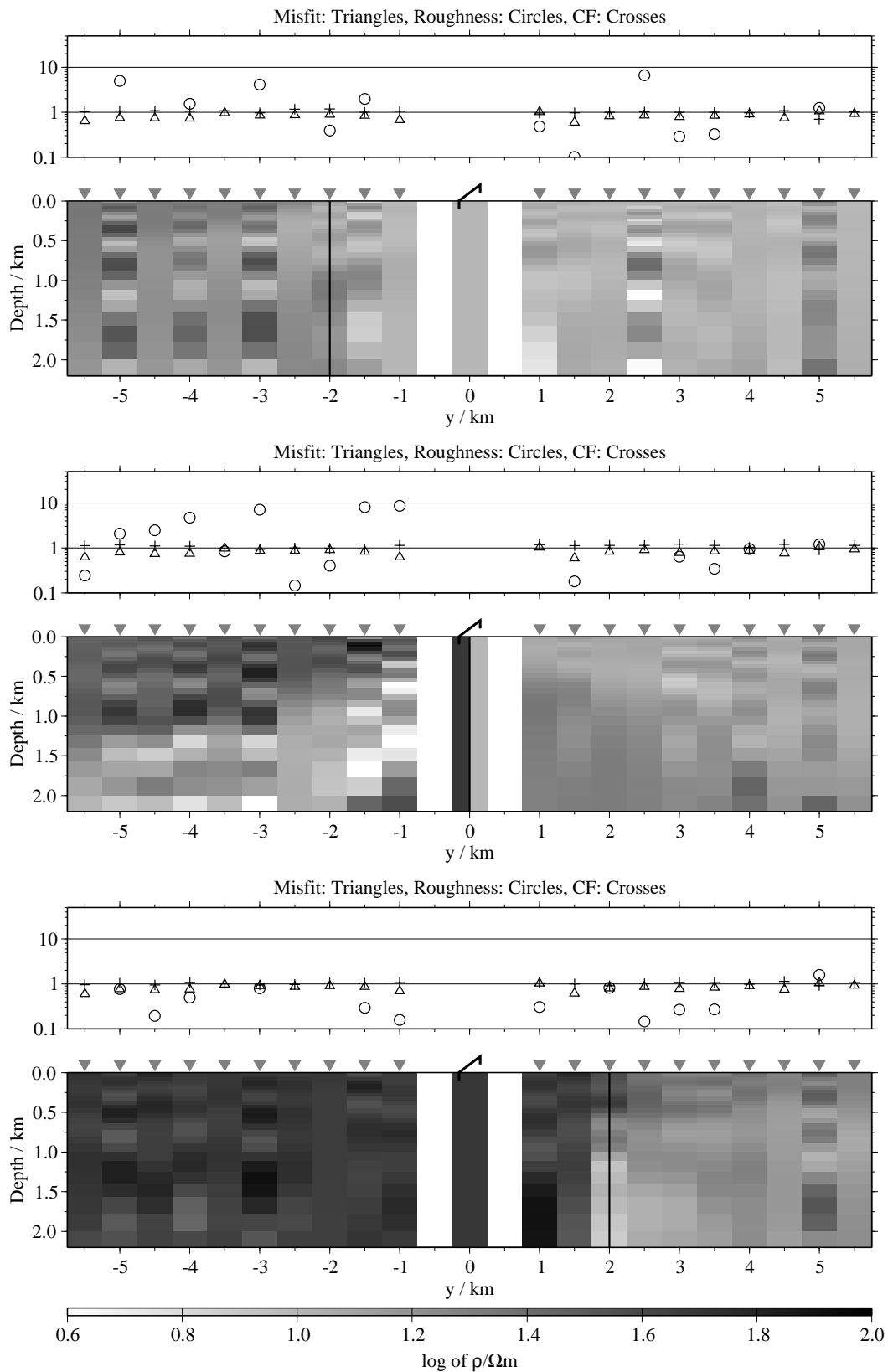


Figure 5.21: Pseudo-sections of single 1-D inversion for the E_x -component, regularisation scheme C4, model F1 (top), F2 (middle) and F3 (bottom);

5.3.4 Faults (models F1 to F3 and K1 to L3)

Two different types of fault models are investigated. The first type is comprised of two quarter-spaces (models F1 to F3). This type thus displays a worst case. The models K1 to L3 are constructed out of two two-layer cases with a displacement of 600 (models K1 to K3, conductive basement) or 400 m (models L1 to L3, resistive basement), respectively. For both types, models with different offsets between the fault line and Tx are simulated.

Two quarter-spaces (model F1 to F3)

The models F1 to F3 are comprised of two quarter-spaces with 50 and 10 Ωm , respectively. The fault line dividing both is at $y = -2$, $y = 0$ or $y = 2$ km. In general, the pseudo-sections for the E_x -component showed the best agreement to the synthetic models. If the Tx is positioned on the conductive quarter-space (model F1), the resistivity of the other quarter-space is underestimated. However, the transition from lower to higher resistivities for $y < -1.5$ km is visible (fig. 5.21, top). If the Tx is located on the resistive quarter-space (model F3), the pseudo-section for the E_x -component resembles the original model very well. Only the station atop the fault line shows artifacts (fig. 5.21, bottom). If the fault line is below the Tx (model F2), the results for the E_x -component are more complicated. The conductive part of the model is reconstructed well, but in the resistive part the models indicate a spurious conductive basement, which gets deeper with increasing offsets (fig. 5.21, middle).

The pseudo-sections for the \dot{H}_y -transients show a complex behaviour. If the Tx is located on the conductive quarter-space, the models show no obvious transition to higher resistivities across the fault. Instead, both quarter-spaces show a complex pattern of diagonal stripes (fig. 5.22, top). Even the conductive quarter-space is reconstructed only for big offsets ($y \geq 5$ km). A similar pattern is found in the pseudo-section in the conductive part of model F2. In the resistive part, the inversions introduce a shallow resistive artifact, which thickness increases with the offset. However, at depth the resistivity is well resolved at site with $y \leq -3.5$ km (fig. 5.22, middle). A similar behaviour is found for model F3. Here, the pseudo-section shows a shallow resistive artifact at site close the fault line at $y = 2$ km. All models at stations with $-3.5 \leq y \leq 4.5$ km show artificial structures at depth (fig. 5.22, bottom).

The distortions found in the pseudo-sections for the \dot{H}_z -transients are easier to describe. For all three synthetic models, the model obtained at the position of the fault line is most distorted. Here, the transients exhibit sign reversals, which can not be fitted by any 1-D model. The corresponding misfit thus is very high. With increasing distance from the fault line, the artifacts are weaker and appear at greater depths. Fig. 5.23 shows two examples.

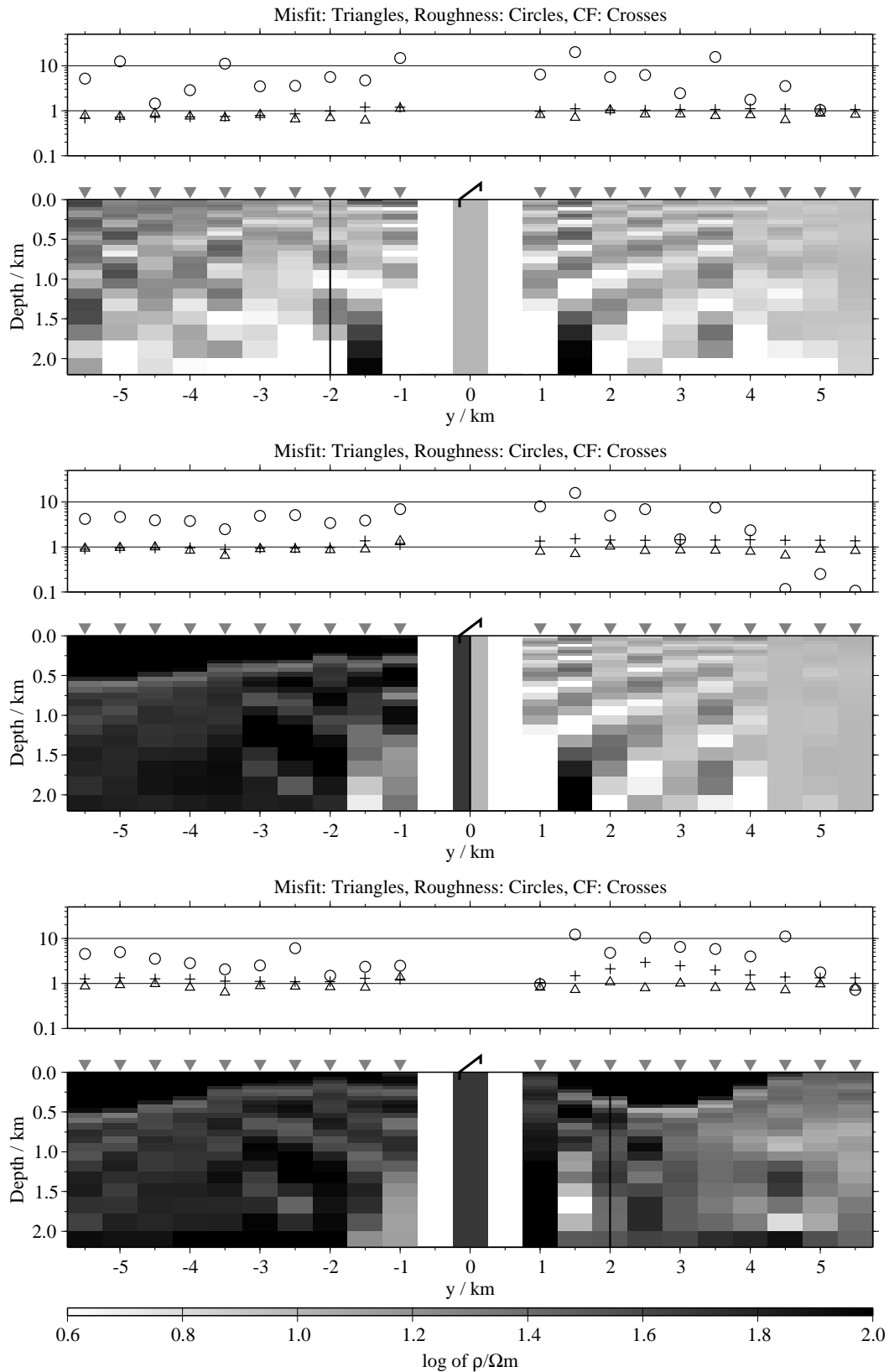


Figure 5.22: Pseudo-sections of single 1-D inversion for the \hat{H}_y -component, regularisation scheme C4, model F1 (top), F2 (middle) and F3 (bottom);

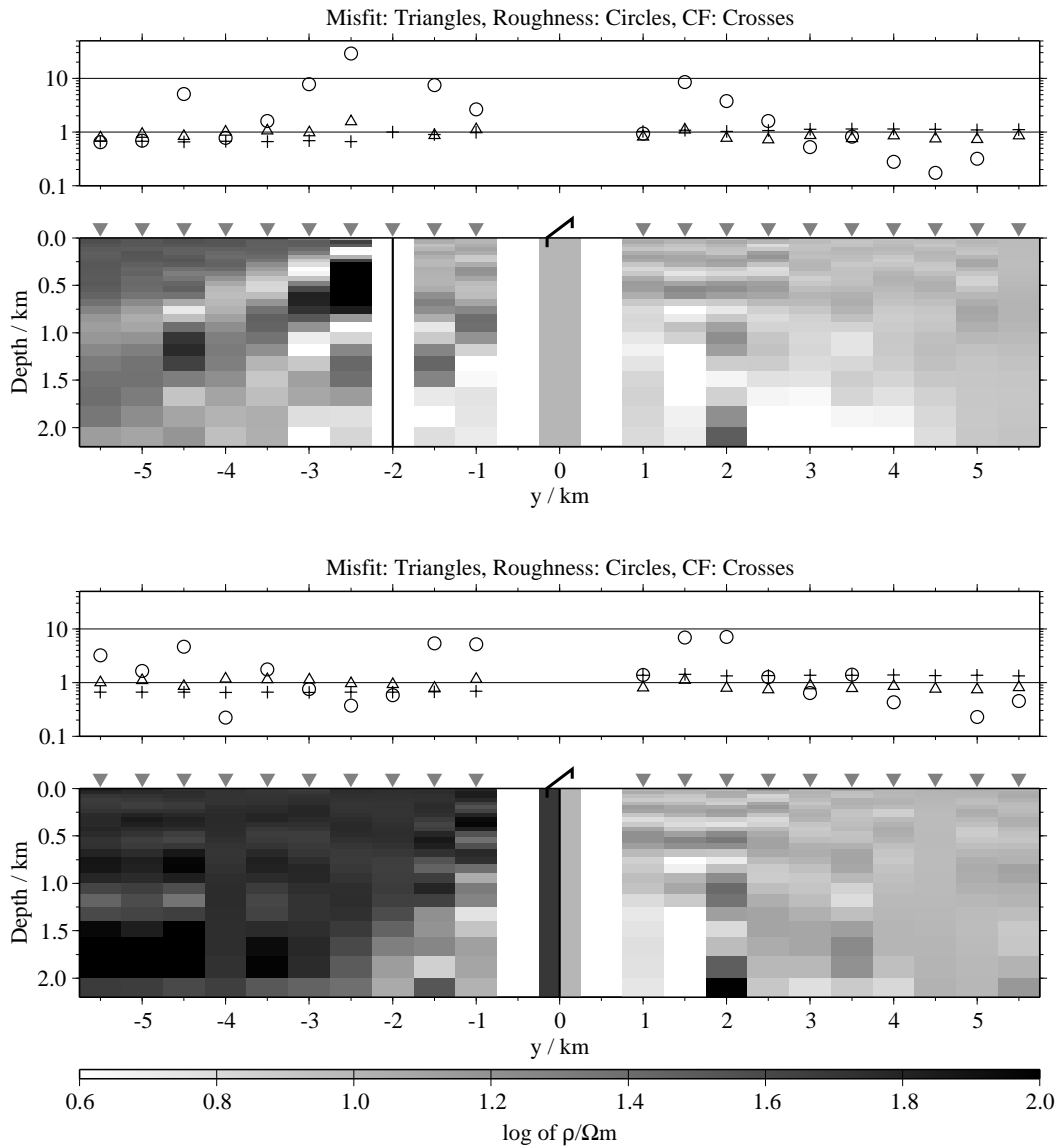


Figure 5.23: Pseudo-sections of single 1-D inversion for the \dot{H}_z -component, regularisation scheme C4, model F1 (top) and model F2 (bottom);

Displacement (models K1 to L3)

The fault line in the models K1 to L3 are at $y = -2.5$, $y = 0$ and $y = 2.5$ km. In general, the pseudo-sections for these models show only slight distortions. In any case the fault line is smoothed out, i.e. the model below the Tx is extended over the fault line. For the larger offsets the 1-D models resemble the situation behind the fault line (as seen from the Tx). The pseudo-sections for the \dot{H}_z -transients reproduce the synthetic model best, followed by the E_x , although the differences are not big (fig. 5.24).

The results are better for the conductive basement (models K1 to K3). In the pseudo-sections for the resistive basement, the resistivity of the second layer is not well resolved, especially in the magnetic field inversions. Even spurious layers are

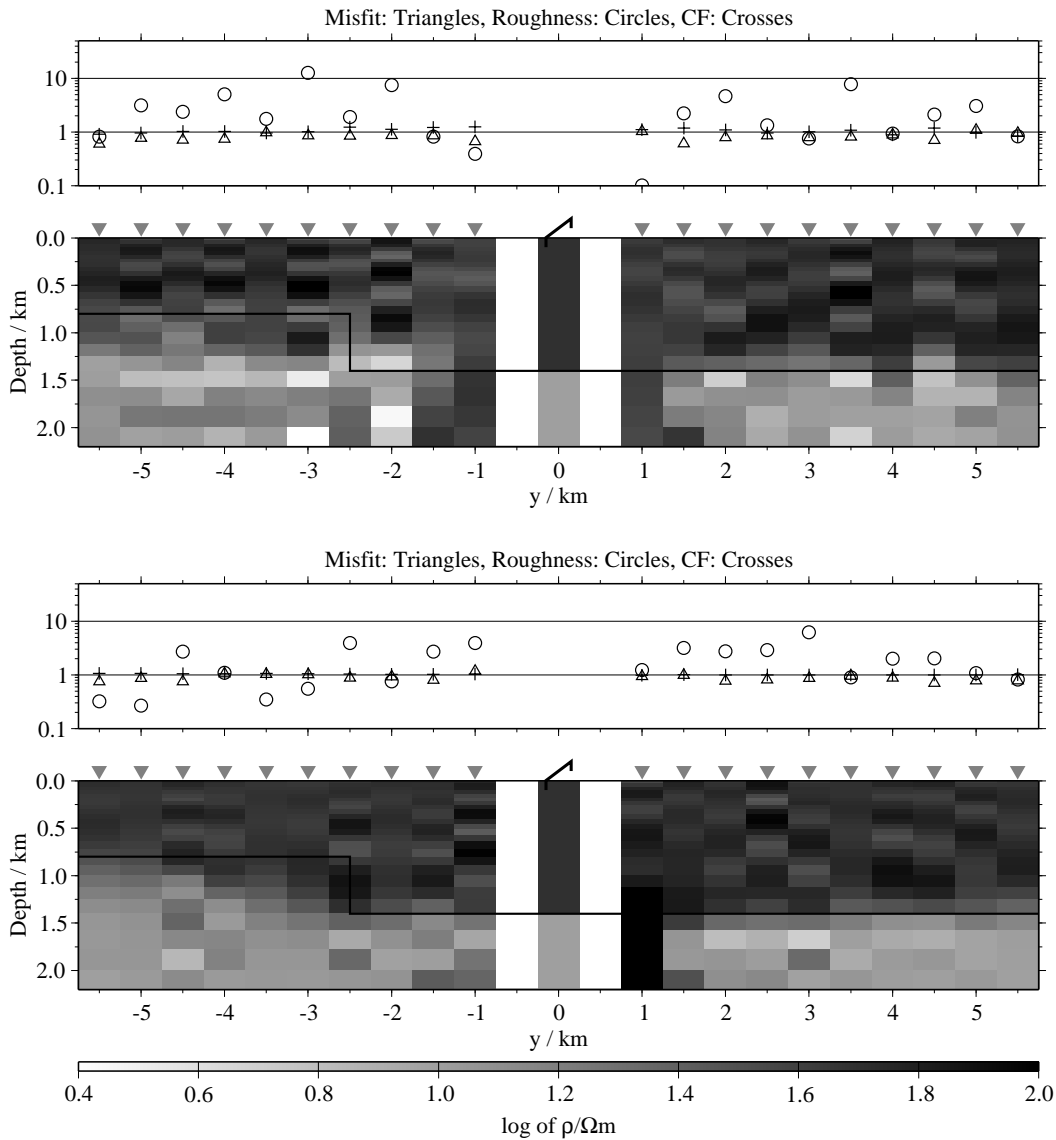


Figure 5.24: Pseudo-sections of single 1-D inversion, model K1, regularisation scheme C4; Upper panels: E_x -component; lower panels: \dot{H}_z -component; the missing conductive basement for some of the sites close to the Tx can be explained by the low depth resolution at these offsets.

introduced here. However, as the joint-inversions in sec. 5.4 will show, these layers are not necessary to explain the data.

If the fault line is below the Tx, the pseudo-sections reproduce the synthetic models very well (except for one case, see below). Deviations are only observed for the smallest offsets.

However, the \dot{H}_y -pseudo-sections for the resistive basement models show severe artifacts. First, a shallow resistor is introduced throughout large parts of the pseudo-section. If the fault is at $y = -2.0$ km, an additional resistive zone is introduced for stations behind the fault (fig. 5.25).

The pseudo-section for the \dot{H}_z -transient and model L3 also shows artifacts at depth for stations around the fault line.

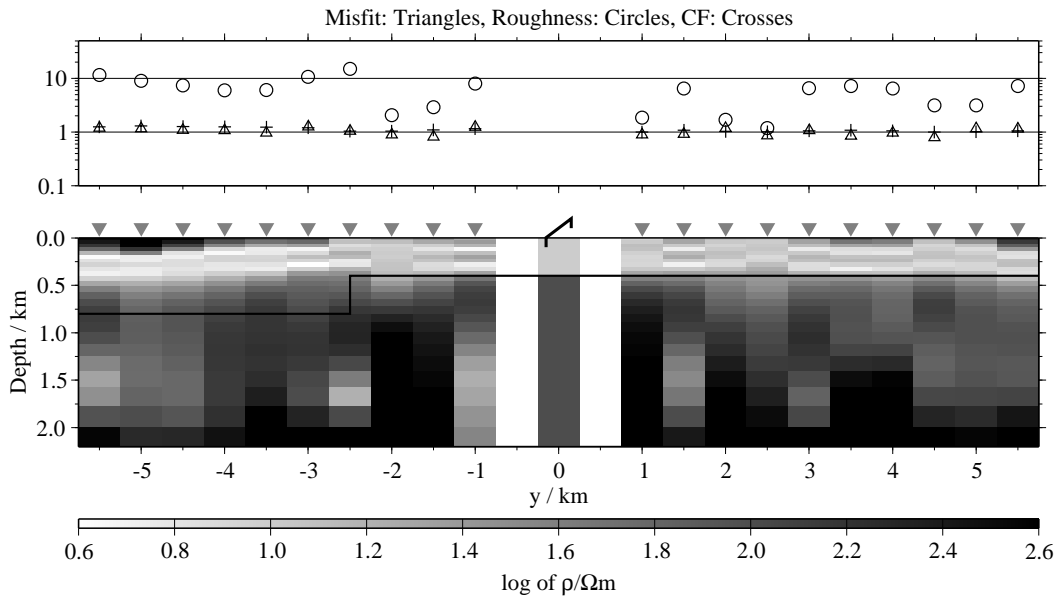


Figure 5.25: Pseudo-section for the \dot{H}_y -component, model L1, regularisation scheme C4;

5.3.5 Moderate lateral changes (model M)

This model represents a more realistic model of the subsurface. It consists mainly of a resistive layer between more conductive media. The thicknesses and resistivities of the layers, however, change slightly throughout the profile. Between $y = -4$ km and $y = -2$ km an additional very conductive layer is overlying the basement.

At first, the pseudo-sections for this model look very chaotic (fig. 5.26). The right part of the model is fairly reconstructed by the E_x - and \dot{H}_y -pseudo-sections. However, the information that the resistive layer is thinner for $y > 2.7$ km is suppressed. The shallow part of the model for $y < 0$ km is fairly resolved for the E_x -component.

The left part of the \dot{H}_y -pseudo-section as well as the complete \dot{H}_z -pseudo-section shows artificial diagonal structures, which can not be correlated to any feature of the synthetic model. The conductive feature at $-4 \leq y \leq -2$ km is only weakly indicated in the pseudo-sections of the magnetic components.

All in all, the results for this model – especially the part left of the Tx – are discouraging, even though the resistivity contrasts are not very high. In particular the conductive, diagonal artifact found in the left part of the pseudo-sections derived from the magnetic components is problematic. It seems to be caused by displacement of the bottom of the first, conductive layer at $y = -2$ km.

5.3.6 Summary of the results in this section

In all cases differences between the pseudo-sections for the individual LOTEM-components are observed. Nevertheless, for several models the distortions are not severe. A geological interpretation would lead to the same result, regardless of which component is chosen. At locations where the results for all three models agree well, the model resembles the situation in subsurface fairly.

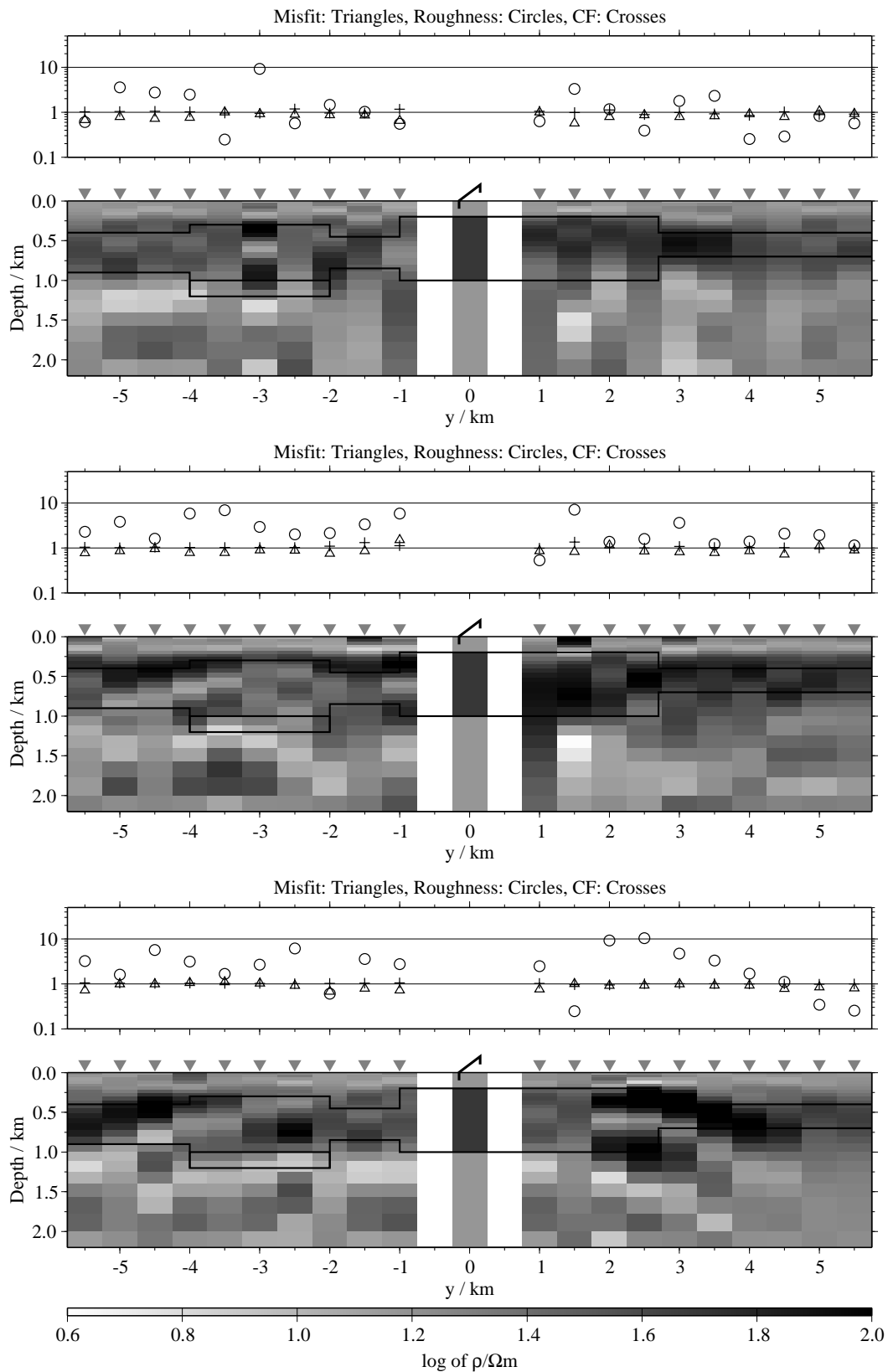


Figure 5.26: Pseudo-sections of single 1-D inversion, model M, regularisation scheme C4; from top to bottom E_x -, \dot{H}_y - and \dot{H}_z -component;

However, even in the best cases one can not expect that the TEM result at a certain Rx-site will match the information from a borehole drilled at the same location. The resistivity structure below the Tx influences the resulting models up to large offsets. Lateral changes thus are suppressed. As expected, the distortions in most cases are strongest at stations close to the lateral change. Interestingly, when a lateral change happens below the Tx, it is possible to derive undistorted models already at short offsets. In some cases distortions are found even when no lateral changes occur between Tx and Rx but on the other side the Tx.

The strength of the distortions in the pseudo-sections depends not only on the model geometry, but also on the resistivity sequence. The pseudo-sections seem to be more distorted, when the top of a resistive unit in the synthetic model is not horizontal (models C, L1 to L3 and M). This is good agreement to the results of Toft [2001] for the SHOTEM modification. The reason for this might be that the induction currents in the resistor are far smaller. The induced current system diffusing downward is first distorted by the non-1-D structure of the bottom of the upper conductive layer. It penetrates the resistive layer, but the induced currents here are small compared to the decaying distorted fields from the conductive layer. The resulting models are thus more influenced by the distorted remnants of the conductor than by the resistor (at a certain depth range). This hypothesis is supported by the fact that for these models the E_x -pseudo-sections are less distorted, as the influence of resistive structures is stronger on E_x -transients.

No component was found to be the least distorted in all cases. The E_x -transients often showed fewer artifacts, but also the largest ambiguity problem. Additionally, it is less trivial to measure electric components in the field (see sec. 6.2.1). The \dot{H}_z -transient seems to be most distorted by near surface inhomogeneities at their lateral boundaries. This is agreement to the results of Donat [1996].

The influence on the \dot{H}_y -transients is not easy to describe. In some cases the \dot{H}_y -pseudo-sections seem to ignore any lateral changes and reproduce the resistivity structure below the Tx even in a considerable distance across the multidimensional structure. In other cases slight artifacts – mostly shallow resistors – are found in \dot{H}_y -pseudo-sections even at sites far away from the lateral boundary.

5.4 The influence of multidimensional structures on joint-inversions

Joint-inversions often are proposed to combine resolving capabilities of different geophysical methods, e.g. DC-geoelectric and MT [Vozoff and Jupp, 1975] or electric and magnetic LOTEM-components [Hördt, 1992; Commer, 1999]. This works well in a true 1-D surrounding as demonstrated in fig. 5.10. Another important task for a joint-inversion is to provide one model for the geological interpretation which is consistent with most of the geophysical data sets. Otherwise the interpreter would have to choose between several single inversion results.

The model calculations in the previous sections showed that the different TEM-components are affected differently by several subsurface structures, i.e. the multidimensional distortions of the transients produce different artificial structures in the pseudo-sections. In a joint-inversion process this might not be the case, as one

single model has to explain all data sets. Contrary artificial structures might be cancelled out, revealing a better picture of the subsurface.

Goldman et al. [1993] encountered problems while joint-inverting simulated TEM and AMT data over a graben structure. The single inversions for both data sets gave slightly distorted models, which still can be geologically interpreted after obvious model distortions are removed [Goldman et al., 1993]. In joint-inversions however, the algorithm fails to find a model, which describes both data sets well. This results in a misfit which is significantly higher than for the single inversions. Due to this high misfit, the authors rejected the corresponding models.

If it would be clear that the joint-inversions reveal a better picture of the subsurface, i.e. if they might produce less artifacts compared with the single inversions, it might be reasonable to accept the models despite of the higher misfits.

To test the effects of multidimensional resistivity distributions, joint-inversions for the models shown in figs. 5.2 to 5.4 were carried out. All four possible combinations of components are used ($E_x\text{-}\dot{H}_y$, $E_x\text{-}\dot{H}_z$, $\dot{H}_y\text{-}\dot{H}_z$, $E_x\text{-}\dot{H}_y\text{-}\dot{H}_z$). The complete results of the inversions are found in app. B. The pseudo-sections are judged with respect to the likeliness of a misinterpretation (see sec. 5.3).

In general, the pseudo-sections of joint-inversion results show less lateral fluctuations as observed comparing figs. 5.9 and 5.10. The Gaussian noise added to the data sets is effectively suppressed.

In a few cases, the pseudo-section derived from joint-inversions show better results than the single inversion pseudo-sections. As an example, the upper panels of fig. 5.27 show the results for three component joint-inversions for model L1. As expected from the single inversion results, the displacement is suppressed. The pseudo-section shows only slight artifacts and resembles the synthetic model better than the single inversion results (cp. fig. 5.25).

The lower panels of fig. 5.27 show the results of joint-inversions of the components E_x and \dot{H}_z . The pseudo-section almost perfectly reconstructs the synthetic model. The results are worse when the \dot{H}_y -transients are included in the inversions.

Joint-inversions in some case are useful to determine, whether the transients for one component are distorted or the single inversions only found equivalent models. E.g. inverting the data from model I1 (conductive patch below the Tx), the E_x -pseudo-section shows a basement with lower resistivities than the original model (fig. 5.19). Joint-inversions of all three components demonstrate that this is case of equivalence, as models are found which are not distorted for offsets larger than 2.5 km and exhibit low misfit and the right conductivity (fig. 5.28, top). Nevertheless, even at short offsets where the models show huge artifacts, the misfits low.

However, in most cases the joint-inversion approach introduces additional artifacts to the pseudo-section. What is even worse is that these spurious features are consistent over a larger part of the profile and thus are likely to be falsely interpreted as geological features. Fig. 5.28 (bottom) shows an example for model F1 consisting of two quarter-spaces. On both sides of the fault line appear fictitious resistive layers, even for stations which are 6 km away from the resistive half-space. The resulting pseudo-section differs completely from the synthetic model.

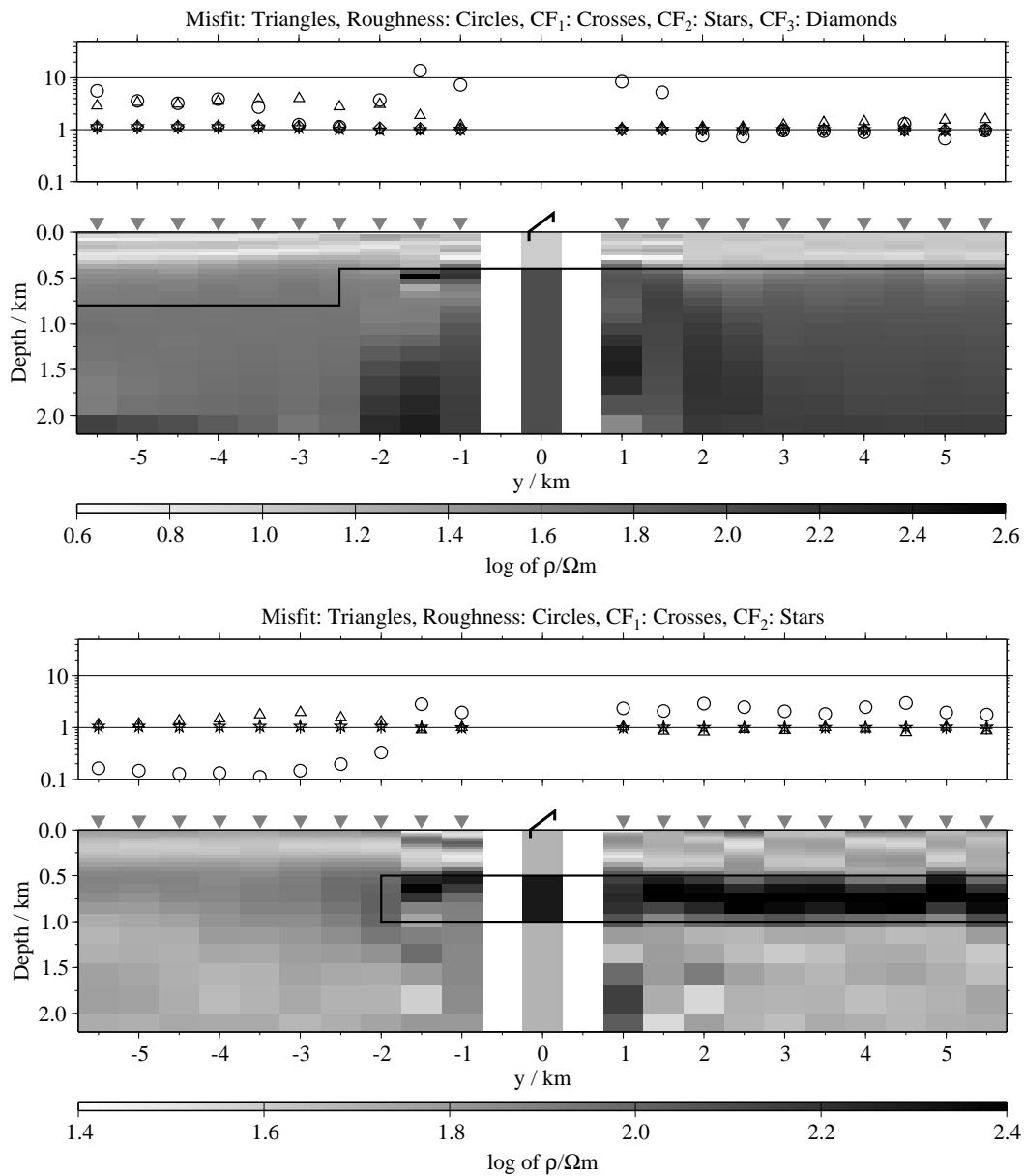


Figure 5.27: Pseudo-section of 1-D joint-inversions; upper panel: All three components are used in the inversion. Model L1, regularisation scheme C4; lower panel: The E_x - and \dot{H}_z -component are used in the inversions. Model E1, regularisation scheme C4;

Considering the misfit is also not very helpful in this case. The inversions for the stations on the resistive quarter-space yield high misfits, but the inversions for $y > 0$ km, which show the artificial resistive layer result in a χ around 1.0.

High misfits do not mean necessarily that the models are distorted. Fig. 5.29 (top) shows the joint-inversion results of the \dot{H}_y - and \dot{H}_z -transients calculated for model B. Although the pseudo-section reconstructs the original model well, the misfits are significantly higher than 1.0 for the sites at $y < -4$ km.

Other frequently observed features are models with shallow resistive artifacts, which fit the synthetic model reasonable at depth. As an example, fig. 5.29 (bottom)

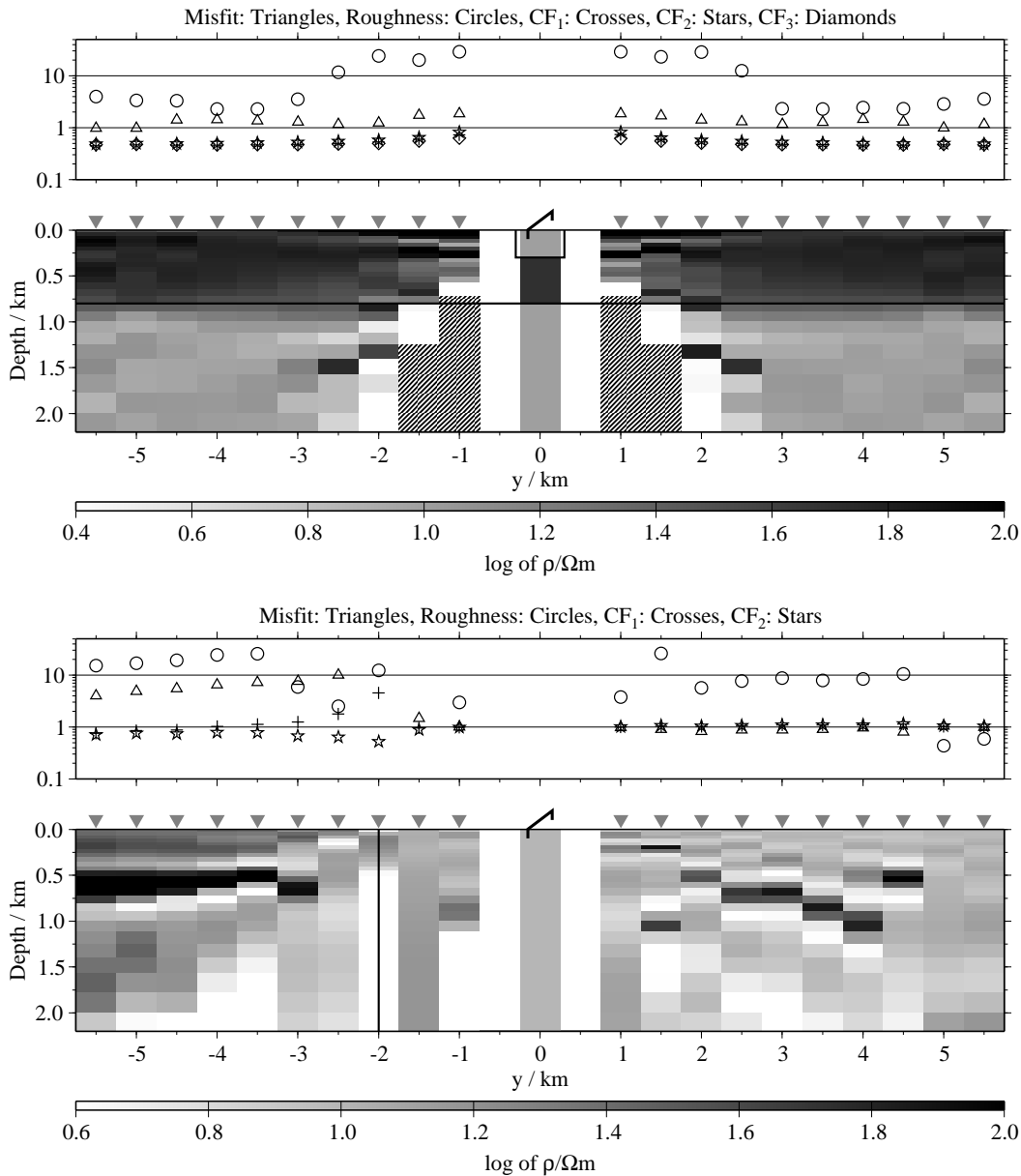


Figure 5.28: Top: Pseudo-section of 1-D joint-inversions of all three components, model I1, regularisation scheme C4; bottom: Pseudo-section of 1-D joint-inversion results of the E_x - and \dot{H}_z -components, model F1, regularisation scheme C4; including the \dot{H}_y -component results in even stronger artifacts.

shows the pseudo-section of the joint-inversion results for all three components calculated for model K3. Deeper, conductive artifacts can be observed for the sites $1 \leq y \leq 2.5$ km. For bigger offsets, however, the models are acceptable, besides that the displacement of the basement is suppressed. The shallow region of these models show a consistent resistive layer.

The results for the synthetic data sets show that the joint-inversion in general is no tool suited to reduce multidimensional distortions. In most cases the opposite is true. In presence of multidimensional structures joint-inversions tend to create artificial structures. Most of the pseudo-sections are more misleading than the single

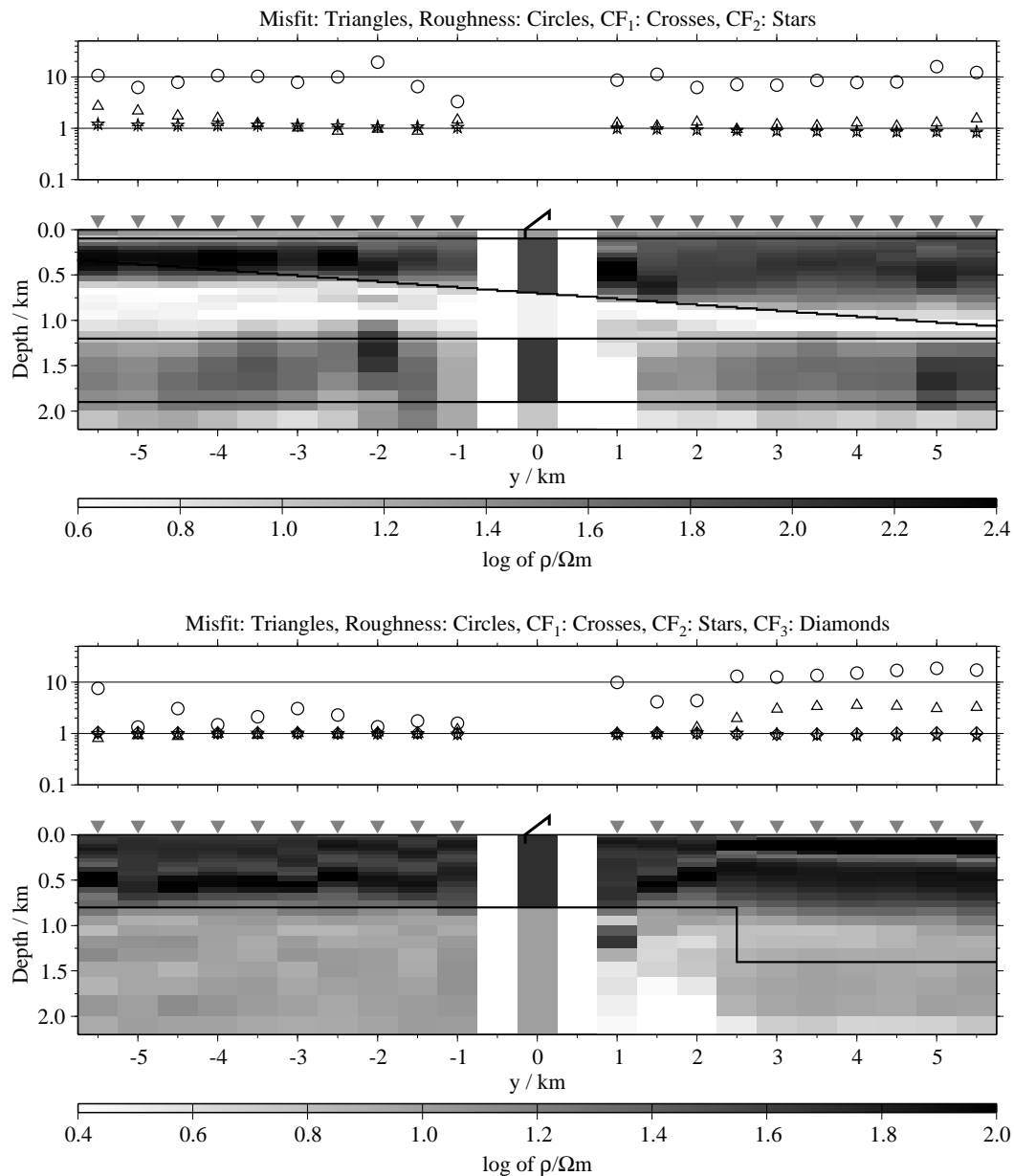


Figure 5.29: Top: Pseudo-section of 1-D joint-inversion results of the \dot{H}_y - and \dot{H}_z -components, model B, regularisation scheme C4; bottom: Pseudo-section of 1-D joint-inversion results of all three components, model K3, regularisation scheme C4;

inversion results. This is in agreement to the results of Goldman et al. [1993] for the joint-inversion of SHOTEM and AMT data sets. Features which are only resolved in joint-inversions therefore should be excluded from the interpretation.

5.4.1 Soft Joint-Inversion

As shown in the previous section, the joint-inversion of different LOTEM-transients does not help to suppress or avoid distorted models. In most cases, the joint-inversions even produced artifacts, which are not observed in the single inver-

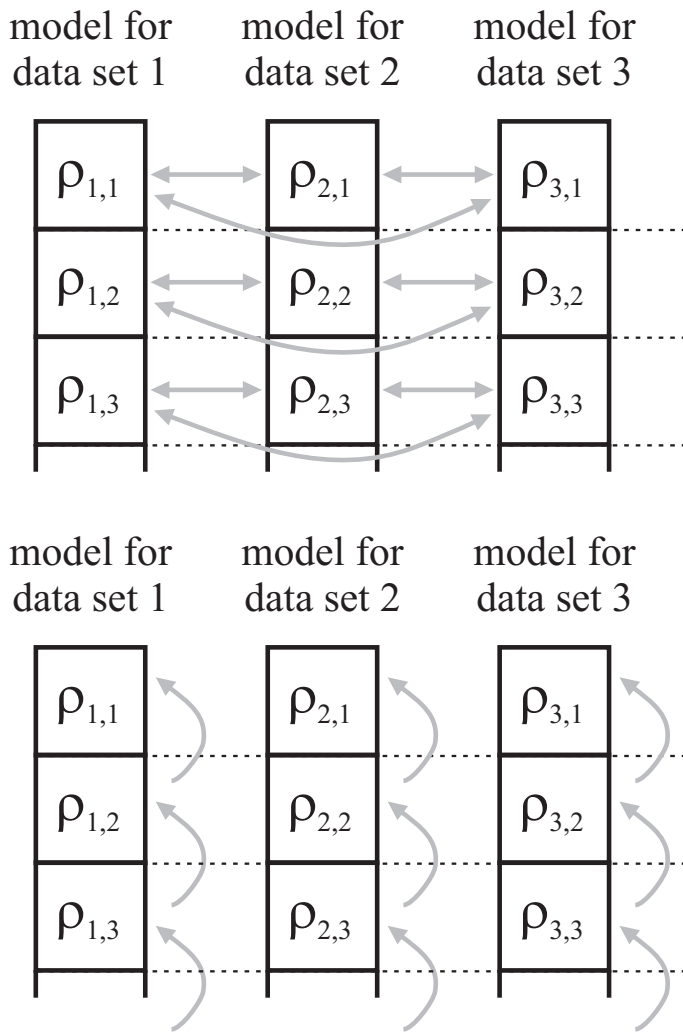


Figure 5.30: This figure illustrates the two constraints used in the SJI approach. The example shows the case of a SJI using three different components. The upper three layers of the models for data set 1, 2 and 3 are displayed. The thicknesses of the layers are the same for all models and will not be changed by the inversion algorithm. The upper panel illustrates the constraint defined by the matrix \mathbf{P}_D (eqn. 5.13). This constraint penalises differences in the resistivities of the three models for each layer. The lower panel illustrates the smoothness matrix \mathbf{P} as defined in eqn. 3.18. Both constraints are used simultaneously.

sions. On the other hand, when inverting the transients with single inversions, the improved resolving capabilities of joint-inverted data sets are lost. Especially the E_x -component seems to be more ambiguous, when inverted using the CF as free parameter. Additionally, the interpreter has the undesirable choice between several models for one location.

Auken et al. [2001] proposed to invert an DC-goelectric and central-loop data set with distinct models. An additional constraint keeps both models closely related. This Mutually Constrained Inversion (MCI) method allows one to combine the different resolving capabilities. They showed, that even if the goelectric data set is shifted, the data could be fitted with two models which differ slightly. The only difference is that the resistivity of a shallow conductive layer is a few percent higher for the model corresponding to the goelectric data set. The geological interpretation for both models would be the same. Both models are far closer to the original, synthetic model as the resulting model from a standard joint-inversion.

Unlike Auken et al. [2001], I will introduce the additional constraint to the Occam's inversion. Each data set in the joint-inversion will be connected to an individual resistivity model. In this case the number of entries in the data vector \mathbf{m}^* is increased. The regularisation should keep the differences between the resistivi-

ties of the separate models smallest possible (fig. 5.30). The trade-off between the model regularisation and the misfit will be controlled by the same regularisation parameter λ . This means that the algorithm can reduce the model regularisation, if this is necessary to achieve an appropriate misfit. From here on, this type of joint-inversion will be called Soft Joint-Inversion (SJI). The standard type of joint-inversion, where the same model is used for all components, will be called Fixed Joint-Inversion or FJI.

If X data sets (each with a CF) are inverted allowing Y different models with Z layers, \mathbf{m}^* has $W = X + Y \cdot Z$ entries. Extending eqn. 3.21 we obtain

$$q^* = (\mathbf{d} - \mathbf{f}(\mathbf{m}^*))^T (\mathbf{d} - \mathbf{f}(\mathbf{m}^*)) + \lambda \left(\mathbf{m}^{*T} \mathbf{P}^T \mathbf{P} \mathbf{m}^* + \nu \mathbf{m}^{*T} \mathbf{P}_D^T \mathbf{P}_D \mathbf{m}^* \right). \quad (5.12)$$

The matrix \mathbf{P}_D penalises differences between the separate models. It is a $W \times W$ matrix with

$$\mathbf{P}_D = \begin{pmatrix} (Y-1)\mathbf{I} & -\mathbf{I} & \dots & \dots & -\mathbf{I} & \tilde{\mathbf{0}}_{Z,X} \\ -\mathbf{I} & (Y-1)\mathbf{I} & -\mathbf{I} & \dots & -\mathbf{I} & \vdots \\ \vdots & -\mathbf{I} & \ddots & \ddots & \vdots & \vdots \\ \vdots & \vdots & \ddots & (Y-1)\mathbf{I} & -\mathbf{I} & \vdots \\ -\mathbf{I} & -\mathbf{I} & \dots & -\mathbf{I} & (Y-1)\mathbf{I} & \tilde{\mathbf{0}}_{Z,X} \\ \tilde{\mathbf{0}}_{X,Z} & \dots & \dots & \dots & \tilde{\mathbf{0}}_{X,Z} & \tilde{\mathbf{0}}_{X,X} \end{pmatrix}, \quad (5.13)$$

where \mathbf{I} is a $Z \times Z$ identity matrix and $\tilde{\mathbf{0}}_{x,z}$ is a $x \times z$ matrix of zeros. The scalar ν controls the relation between smoothing and reducing the differences between the models. After some steps similar to the ones shown in section 3.2.2, this approach yields the model update formula

$$\hat{\mathbf{m}}_n^* = \left(\mathbf{J}_{n-1}^T \mathbf{W}^2 \mathbf{J}_{n-1} + \lambda (\mathbf{P}^T \mathbf{P} + \nu \mathbf{P}_D^T \mathbf{P}_D) \right)^{-1} \left(\mathbf{J}_{n-1}^T \mathbf{W}^2 \hat{\mathbf{d}}_{n-1} + \lambda (\mathbf{P}^T \mathbf{P} + \nu \mathbf{P}_D^T \mathbf{P}_D) \mathbf{m}_{n-1}^* \right). \quad (5.14)$$

SJIs were carried out for the four possible combinations of data sets for the models shown in figs. 5.2 to 5.4. The results for all models can be found in app. B. In all of this inversion the scalar ν was set to unity. This is as justified as all other possible values for ν . As it seemed to work well, no other settings were tested.

The top panel of fig. 5.31 shows the results of the SJIs using all three components for model A. The model section displays the averages of the three models. The average was calculated according to

$$\rho_{\text{AVG}} = \exp \left(\frac{1}{3} \sum_{i=1}^3 \ln \rho_i \right). \quad (5.15)$$

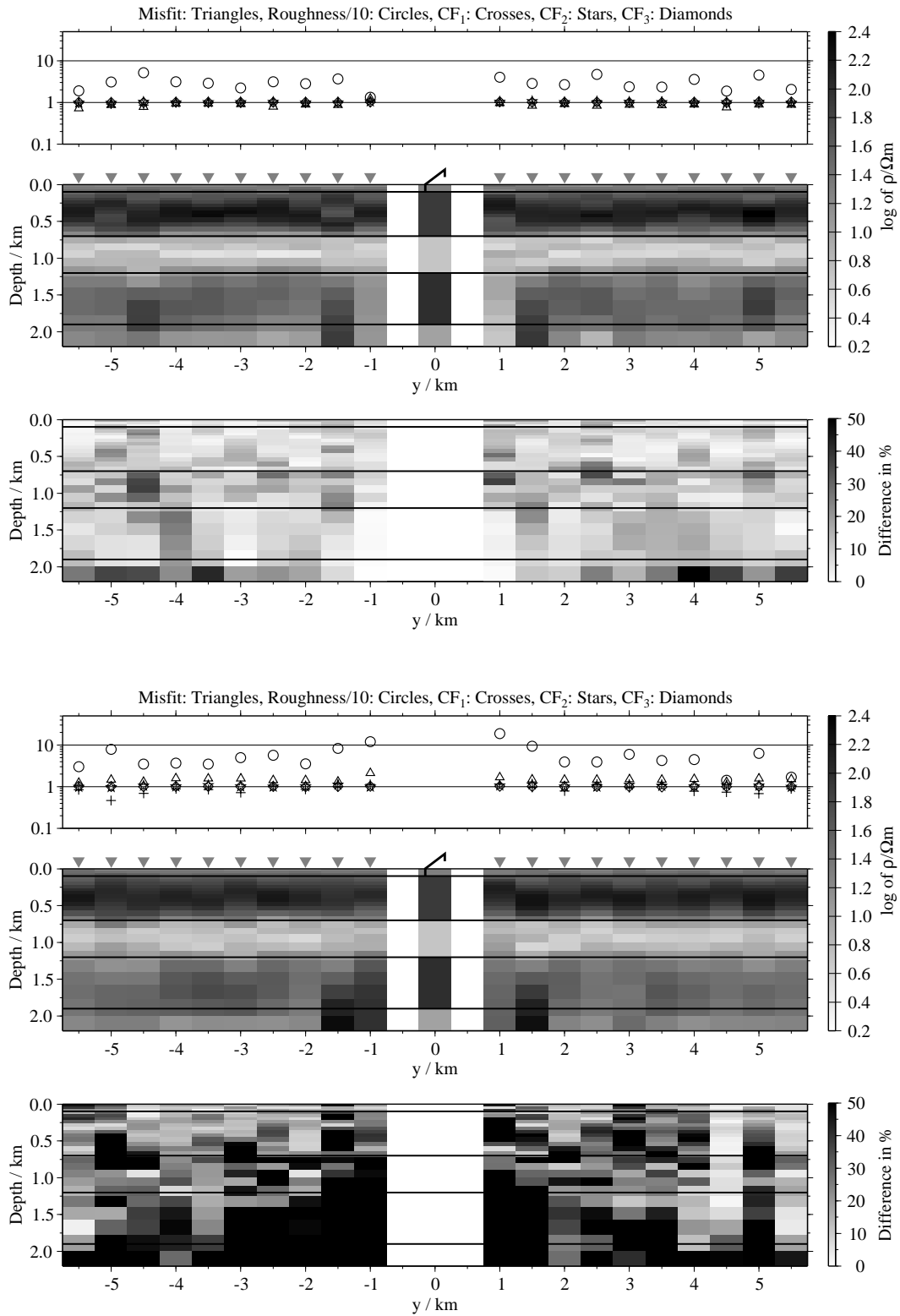


Figure 5.31: Pseudo-sections of 1-D inversions using all three components with regularisation scheme C4, model A (displayed below Tx); Top panels: Average inversion results using the soft joint-inversion approach and relative differences of the models; bottom: Average inversion results using the single 1-D inversions and relative differences of the models (see text);

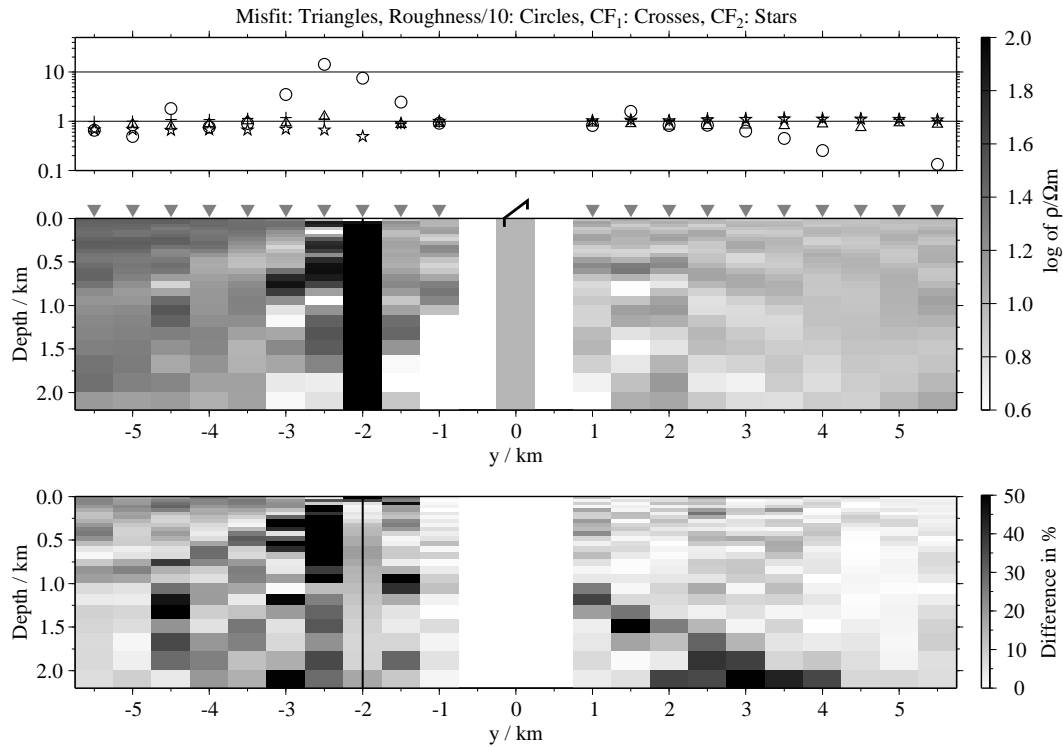


Figure 5.32: Pseudo-section of SJI-results of the E_x - and H_z -components, model F1, regularisation scheme C4;

Below the model section, a section of the relative differences between the three models is displayed. Black boxes indicate that the 1-D models at this place on average differ at least 50 % from ρ_{AVG} . The roughness plotted in the section atop of the model section includes also the variations between the three models. For comparison, the lower panels show the results if the components are inverted separately and averaged afterwards using eqn. 5.15. The overall results are similar, but in detail the SJI shows an improved resolution, as can be observed at the deeper resistive layer. Also, the differences between the individual models are significantly smaller using the SJI approach.

To understand where differences in the models will occur, it is important to keep in mind that eqn. 5.14 includes a similarity *and* a smoothness constraint. This means that features, which are only resolved by data set A will not be similar in the model for data set B. Instead, the second model will show a smoothed representation of the feature. Differences in the models thus do not necessarily mean that the used transients are inconsistent. This is only the case for equally rough but different features, e.g. a resistive zone starting at a different depth or models showing an opposite behaviour at a certain depth range.

Comparing the pseudo-section with the single inversion (fig. 5.9) or FJI results (fig. 5.9) shows that the SJI-results are in between. The layers are better constrained than using only the single inversions. Also, the lateral fluctuations are suppressed. The resolution and suppression of the added noise is better in the pseudo-section derived from the FJIs. However, in almost all cases the artifacts are significantly reduced in the SJI pseudo-sections.

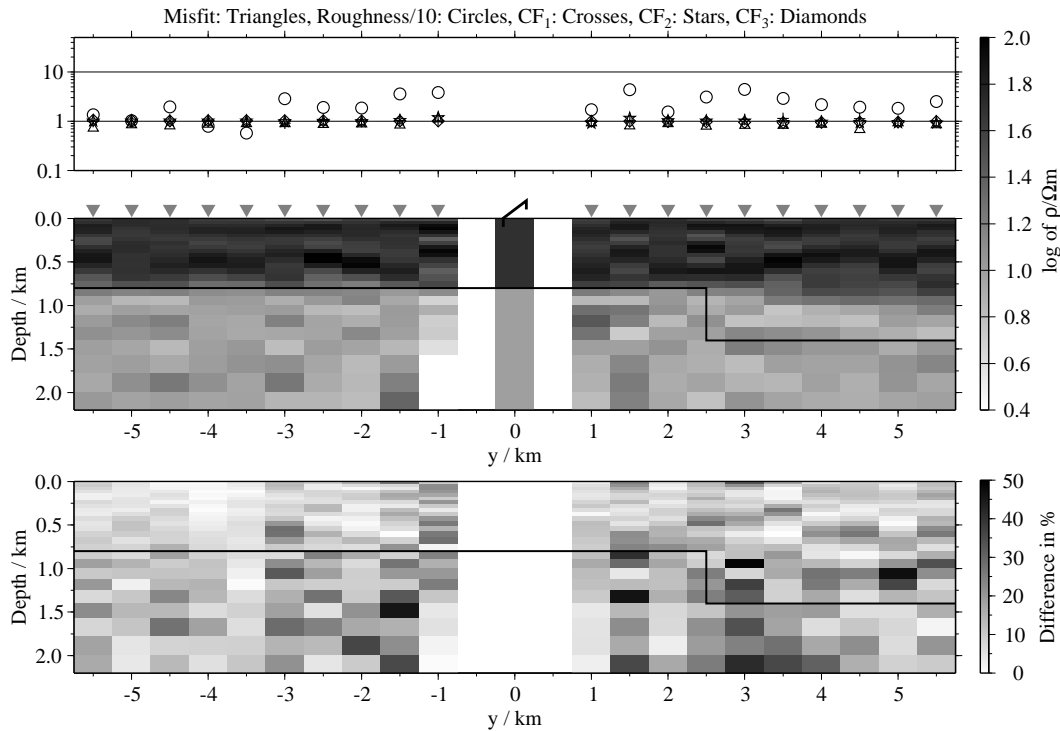


Figure 5.33: Pseudo-section of SJI-results for all three components, model K3, scheme C4;

Fig. 5.32 shows the SJI-results for the E_x - and \dot{H}_z -transients calculated for model F1. The corresponding pseudo-section for the FJIs of these components showed strong artifacts, which are consistent along large parts of the profile (cp. fig. 5.28, bottom). As can be seen, the SJIs produce far less artifacts. Strong distortions are only visible around the fault line. As these distortions are not consistent for both components and the two adjacent stations, it is not likely that the artifacts are interpreted geologically.

Fig. 5.33 shows the results for the SJIs of all three components calculated for model K3. The pseudo-section shows almost no artificial structures, besides a smeared out transition across the displacement. The results of the FJIs are displayed in fig. 5.29 (bottom).

Fig. 5.34 shows the results for model M using all three components. Here, the results for both strategies, C1 and C4, are displayed, as this is one of the rare cases, where inversion with strategy C4 gave noticeably smoother results. Nevertheless, the models for sites with $-4.5 \leq y \leq -3$ km still show a spurious diagonal feature within the second, resistive layer. Additionally, the basement shows some artificial structures in most parts of the profile. I will come back to point in sec. 5.7. Still, the SJI results are far less distorted by multidimensional structures than the FJI results.

In very few case the SJIs produced pseudo-sections which are more distorted than the FJI results. This happens, when the FJI results are better than the single inversion results. The best example is model L1 (fig. 5.35, the FJI results is shown in fig. 5.27, top). Here a spurious conductive layer appears at depth for $y < 0$ km which is consistent over the whole spread. This feature is produced by the \dot{H}_z -transients, as it does not show up in any inversion without this component.

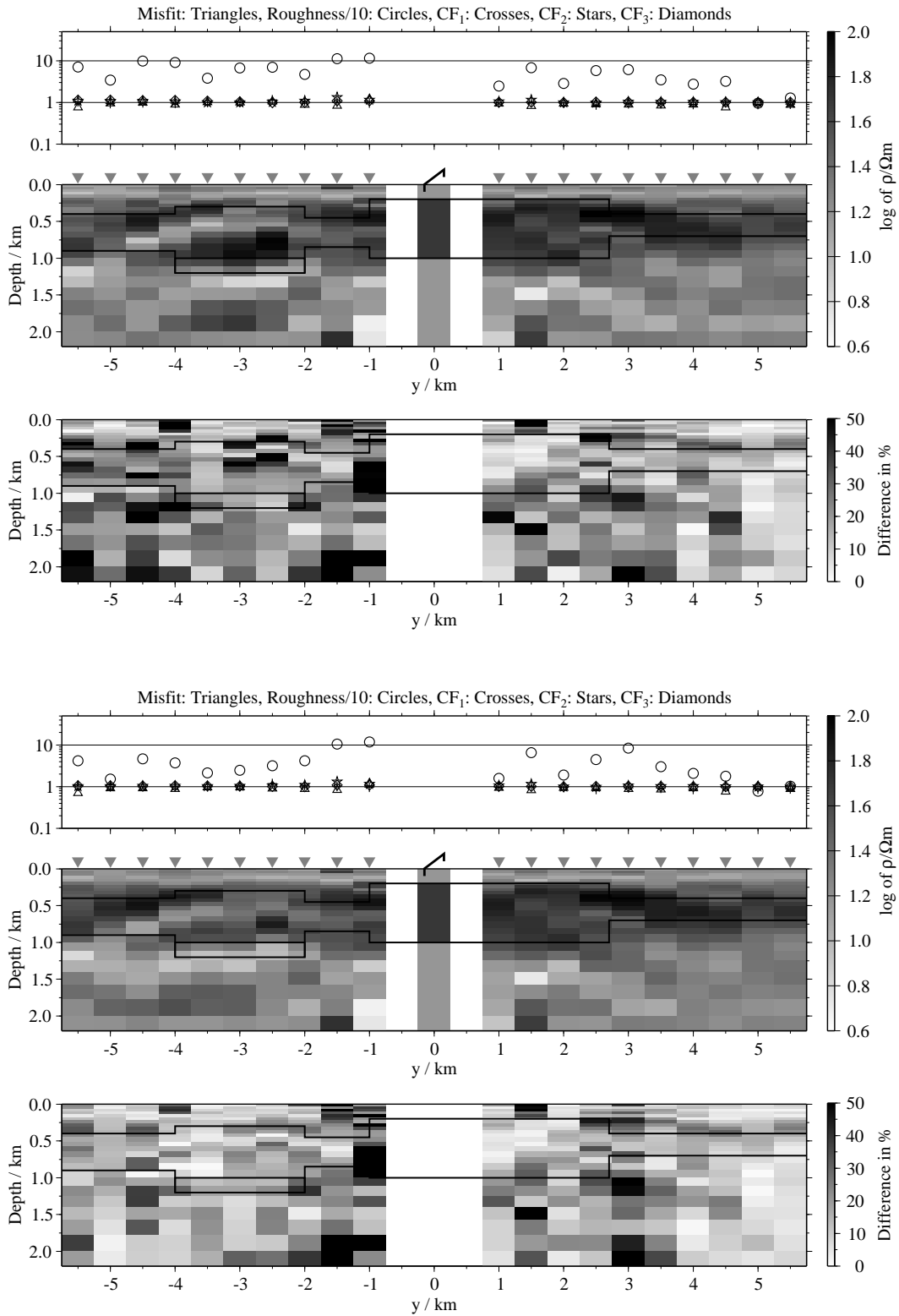


Figure 5.34: Pseudo-sections of 1-D soft joint-inversions using all three components, model M; Top panels: Average inversion results and relative differences (regularisation scheme C1); bottom: Average inversion results and relative differences (regularisation scheme C4);

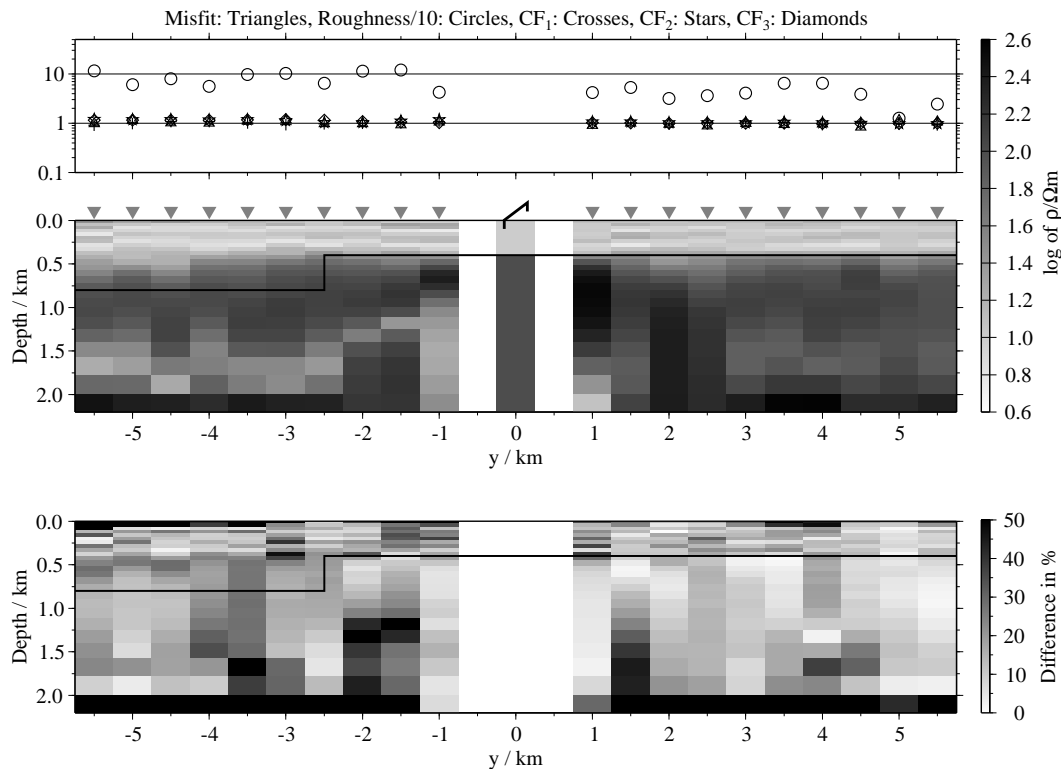


Figure 5.35: Pseudo-section of SJI-results of all three components, model L1, regularisation scheme C4;

5.5 Joint-interpretation of LOTEM and SHOTEM data sets

In this section I want to examine if and how the results for SHOTEM- and LOTEM-transients can be interpretations jointly.

The ambiguity of TEM data can be reduced by increasing the length of the transients. Goldman et al. [1994a] found that extending the transients to early times can even reduce the ambiguity for deeper structures. Lange [2003] demonstrated with synthetic data sets calculated for layered models that joint-inversions of LOTEM and SHOTEM data sets can greatly improve the resolution in all depth intervals.

For the field campaign in Israel it thus was planned to carry out SHOTEM measurements on the positions of LOTEM-Rx-sites. Both data sets should be interpreted jointly.

Although SHOTEM is “only” another modification of the TEM method, the transients provide different information to typical LOTEM data sets. First, the transients are measured earlier times than typical LOTEM-transients. More important, the offset between Tx and Rx is much smaller. Both TEM-transients are influenced at least by the subsurface around and between Tx and Rx. However, in the SHOTEM case the offset between Tx and Rx is very small, compared to the LOTEM setup.

In a 1-D environment the difference is not important. This changes if multidimensional structures are present. In this case, the SHOTEM-transient will reflect

only the subsurface close to the LOTEM-Rx, whereas the LOTEM-transient might be influenced by structures which are located some kilometres away, closer to the Tx. This will lead to inconsistencies in the interpretation.

In sec. 5.3 the difference between multidimensional structure and a small inhomogeneity was defined by a comparison between the feature's scale length and the offset. The smaller bodies (models G1 to J2) were not resolved in the LOTEM sections. At best, they did not influence the transients significantly. However, these bodies are bigger than a typical SHOTEM offset. For SHOTEM, they are thus to be considered as a structure which should be resolved.

The same effect was observed by Goldman et al. [1994b], who simulated SHOTEM and LOTEM data over a layered model including a horst or graben structure. For both setups the size of the structure was the same. However, the effect on the SHOTEM-transients was far stronger than for the LOTEM setup, where almost no distortion was observed.

5.5.1 Inversions of synthetic SHOTEM-transients

Similar to the LOTEM data sets, the SHOTEM-transients were calculated with SLD-MEM3T. The designation of the synthetic models is the same as in figs. 5.2 to 5.4. SHOTEM-transients were calculated for all LOTEM-Rx-positions. The time range of the transients is 0.1 to 40 ms. The Tx consists of a 260×260 m² square loop.

A different noise strategy was used for the SHOTEM-transients. Here, 1 % Gaussian noise was added to the data points. This was done, because the SHOTEM-transients from the field campaign in Israel were not provided with error estimates (sec. 6.3). This means that all data points have to have equal weights in the inversion. This is done by assuming a fix relative noise level.

In general, the pseudo-sections derived from the simulated SHOTEM-transients reproduce the original models very well. However, all models show artificial oscillations in the upper 200 m (e.g. fig. 5.37). They are produced by inaccuracies in the forward modelling for the first data points. However, the deeper parts of the pseudo-sections seem to be unaffected. These oscillations are stable and consistent for all models. I will treat them like true model features. This way I can use them in the next sections to see whether the SHOTEM-transients contribute to the resolution of the shallow parts of the models.

Often the deep structure of the models is not resolved due to the short transients. In some of these cases, the inversions introduce spurious structures at depth. This happens in particular, when the shallow part of the model exhibits low resistivities, which decreases the maximum depth of resolution [Spies, 1989].

Fig. 5.36 shows the pseudo-section for model M. Both effects can be observed very well. The shallow oscillations in the resistivity are very strong for the stations at $-4 \leq y \leq -2.5$. Unfortunately, it is not clear whether the strong artifacts here are produced by the multidimensional structures or simply by the modelling. The latter is more likely, as the subsurface exhibits no lateral changes for $-4 \leq y \leq -2$ km.

The synthetic model is very well reproduced. Unlike the LOTEM pseudo-

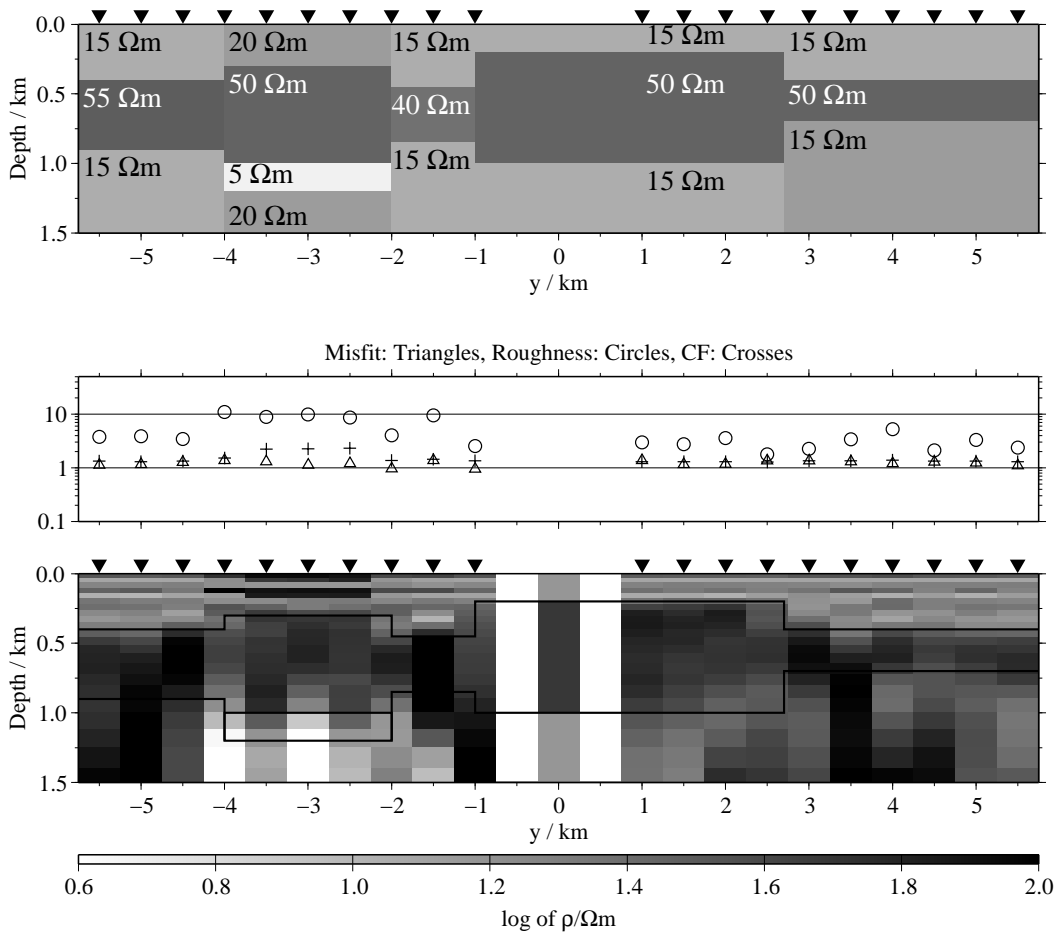


Figure 5.36: Pseudo-sections of 1-D inversions of SHOTEM-transients simulated for model M; top: Original model; bottom: Results using regularisation scheme C4; note the different depth scale compared to the LOTEM pseudo-sections.

sections, even the conductive feature at $-4 \leq y \leq -2$ is resolved. The conductivity of the basement, however, varies strongly due to the short transients. In some cases even spurious structure is included.

Fig. 5.37 shows the results for model K1. For $y > -2$ km, the basement is not resolved. In the critical region around $y = -2.5$ km, the models are not strongly distorted. The misfit for the transient calculated directly over the displacement is slightly higher. In the corresponding model, only a slight decrease of the resistivity is observed. In the model at $y = -2$ km next to the displacement, the transition to the conductive basement is observed too shallow. However, as the subsurface is 1-D in the vicinity of most stations, the synthetic model is better resolved than in the LOTEM sections.

The 3-D prisms at intermediate depths are not resolved (models G2 and H2). Especially for the case of a resistive block no obvious influence is observed. This is different for the shallow prisms. As an example, fig. 5.38 shows the results for model I2. At the station above the prism, the misfit is very high. The model shows a conductive zone which can be correlated to the block. Below the block however, the resistivities are too large. In addition, the thickness of the block is significantly

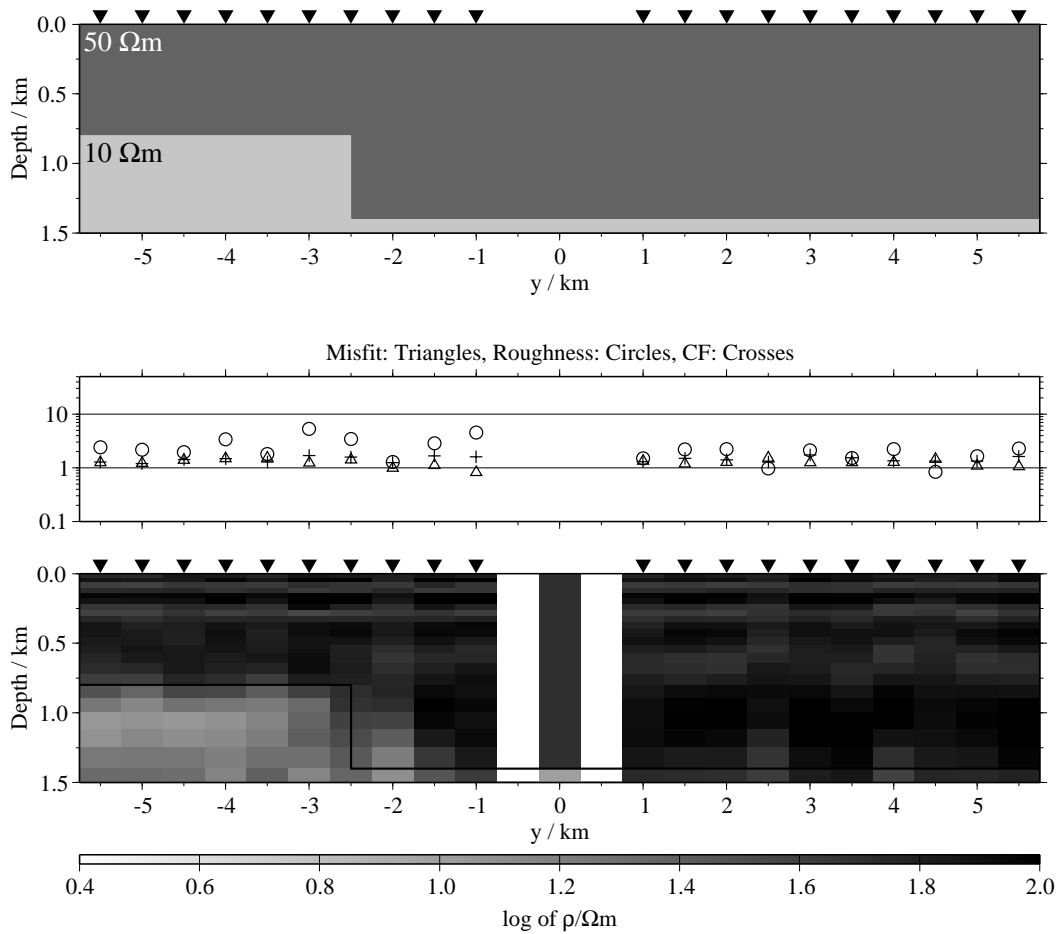


Figure 5.37: Pseudo-sections of 1-D inversions of SHOTEM-transients simulated for model K1; top: Original model; bottom: Results using regularisation scheme C4; note the different depth scale compared to the LOTEM pseudo-sections.

underestimated. Right above the basement an artificial conductor is introduced.

Artificial structures can be observed even at stations close to the block, although neither the Tx-loop nor the Rx is located on the block. The artifacts are conductive zones located at the depth of the base of the block. The pseudo-section for model J2 (resistive block) shows no obvious distortions at depth. The shallow artifacts at the stations next to the block are similar, but resistive.

This behaviour can easily be understood, recalling the smoke ring analogy. At very early times, the current systems are confined to the subsurface close to the Tx, which is 1-D in this case. With increasing time, the current system diffuses not only down- but also outwards. At stations close to a lateral change, the induced current start to diffuse into the block. The models resulting from inversions of such transients thus also reflect the nearby structure at certain times.

The inversions of the synthetic SHOTEM-transients showed that the SHOTEM modification reproduces far less artifacts than the LOTEM setup. The main reason is the small Rx-Tx-offset. In addition, the structures under investigation have scales comparable to the LOTEM setup. Artifacts show up when the induced current sys-

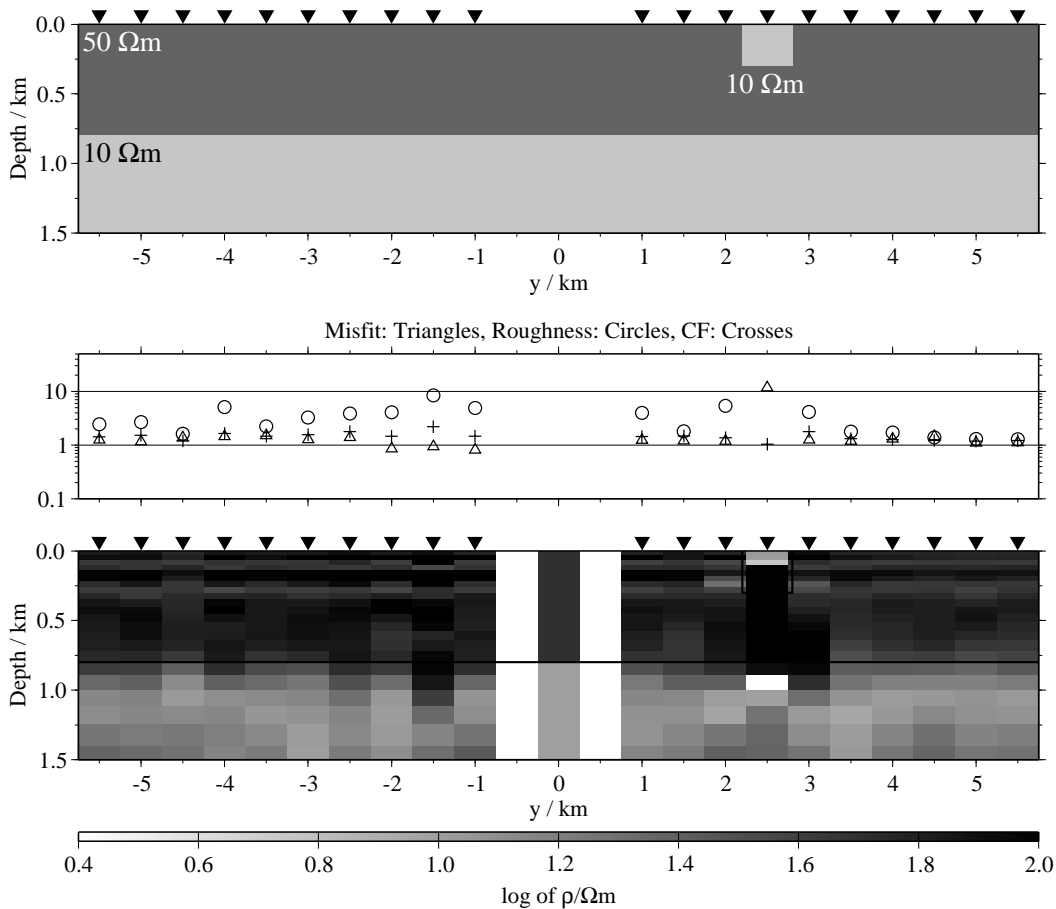


Figure 5.38: Pseudo-sections of 1-D inversions of SHOTEM-transients simulated for model I2; top: Original model; bottom: Results using regularisation scheme C4; note the different depth scale compared to the LOTEM pseudo-sections.

tem crosses lateral borders, which is the case only for a few stations. For large parts of the profiles, the relevant subsurface is 1-D. Stronger distortions can be expected when the size of the inhomogeneities is reduced [Toft, 2001].

5.5.2 Joint-inversions of synthetic LOTEM- and SHOTEM- transients

As shown in the previous sections, the synthetic models are resolved in a different way using the SHOTEM- instead of the LOTEM-transient. Unless the models are completely distorted, the bigger offsets of the LOTEM modification result in models which represent larger parts of the subsurface. For a joint-inversion this means that in a non 1-D environment SHOTEM and LOTEM data sets might provide inconsistent information. The results of joint-inversions thus might be inferior to single inversion results.

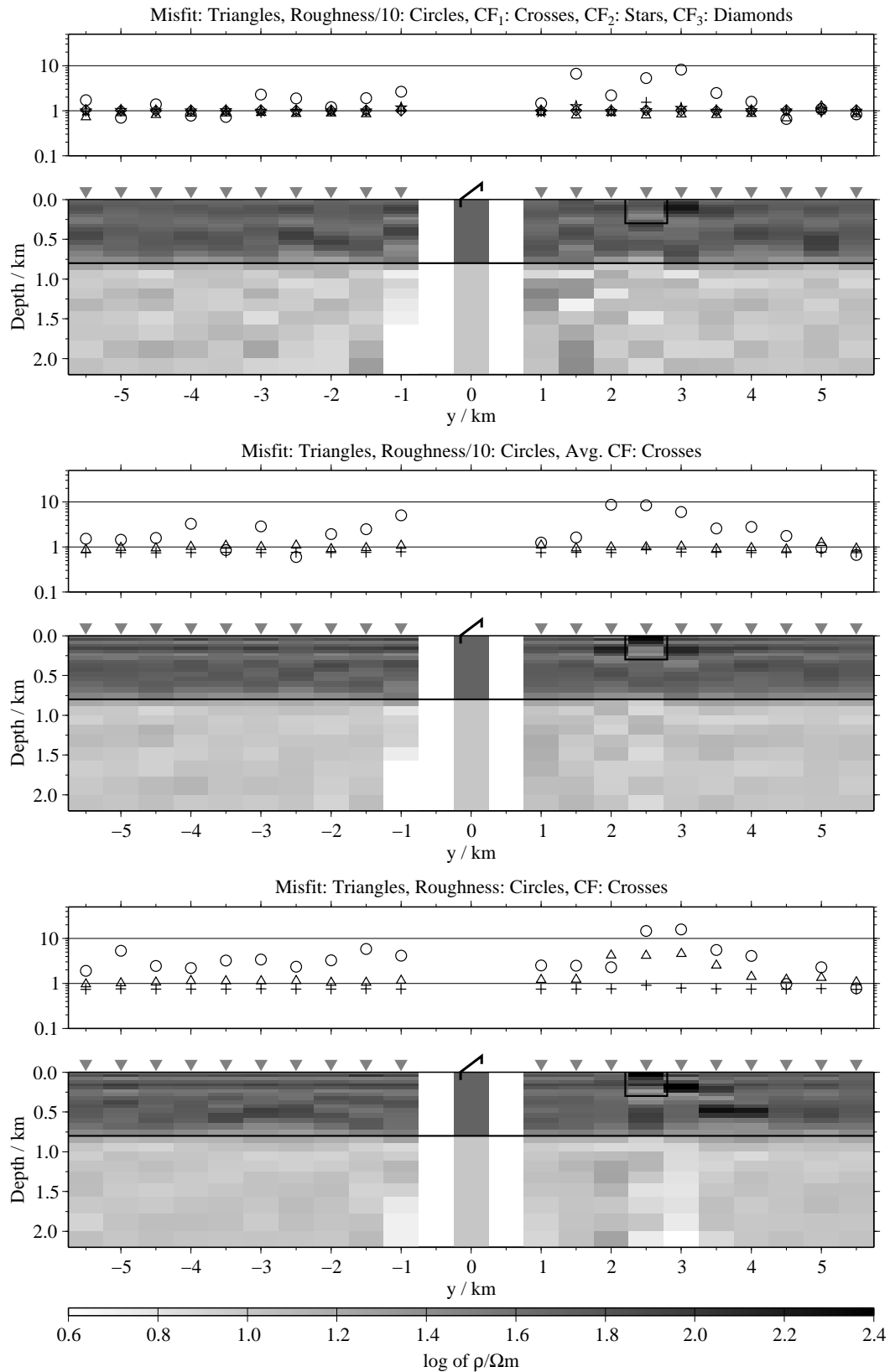


Figure 5.39: Pseudo-sections for model J2, regularisation scheme C4; from top to bottom: SJIs of the three LOTEM-components only, SJIs of the SHOTEM- and all three LOTEM-components, FJIs of the SHOTEM- and all three LOTEM-components.

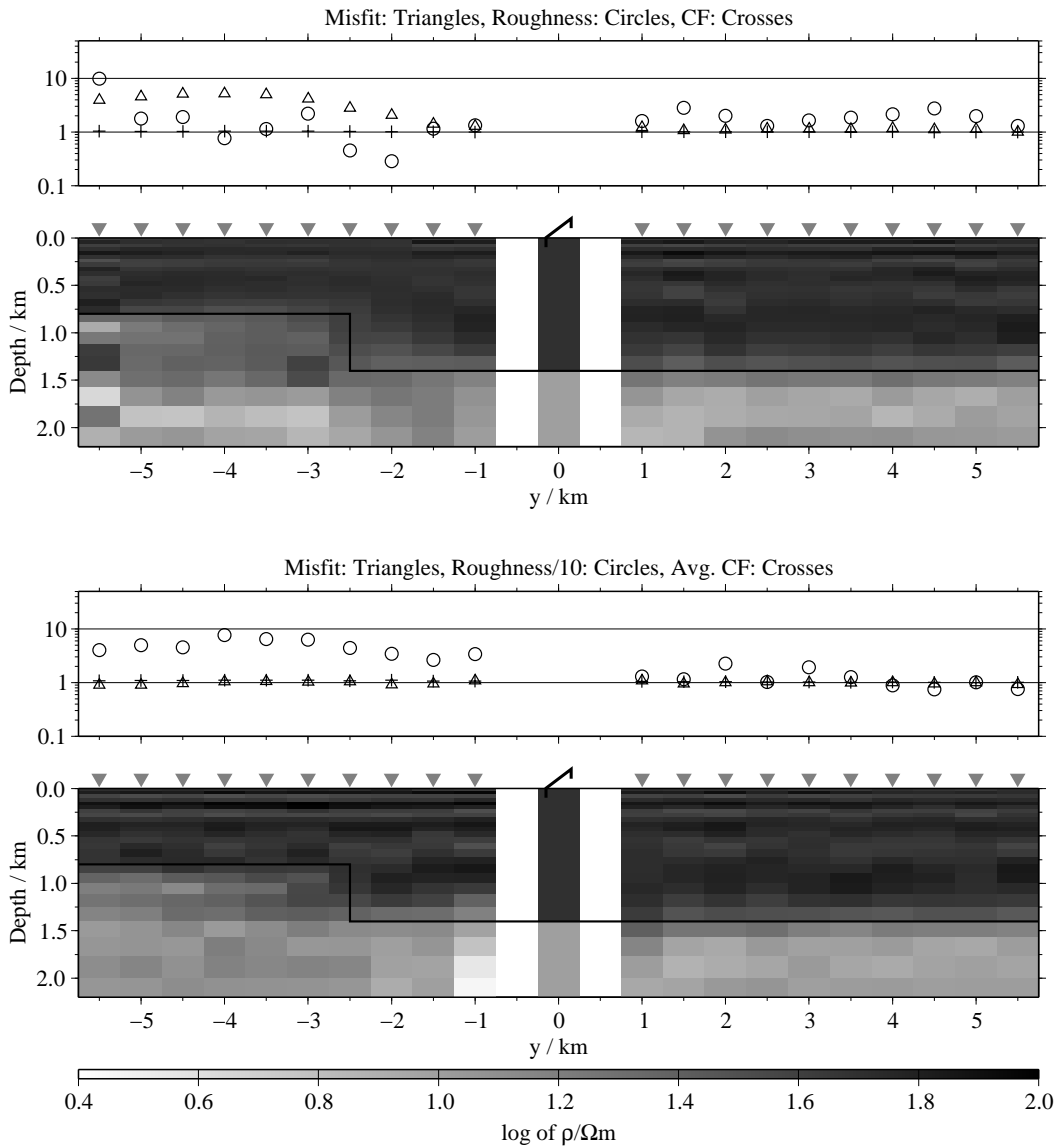


Figure 5.40: Pseudo-sections of joint-inversion for the SHOTEM-transients and all three LOTEM data sets for regularisation scheme C4 and model K1; top panel: Results for the FJIs; bottom panels: Results for the SJIs;

No problems occur when both methods do not resolve a certain structure (models with prisms at intermediate depths G1-H2). For the shallow block model I2 and J2, the results are similar to the LOTEM results. The SHOTEM-transients mainly introduce the shallow oscillations in resistivity observed also in the SHOTEM pseudo-section (sec. 5.5.1). These oscillations occur due to modelling inaccuracies. Nevertheless, they show that the SHOTEM-transients provide additional “information” about the shallow structure.

Around the prisms the structure of the artifacts is very similar to the artifacts found in the LOTEM pseudo-sections. The blocks are not well resolved. Fig. 5.39 shows a comparison of pseudo-sections for the SJIs using the LOTEM-transient only (top) or – in addition – the SHOTEM-transient (middle). The inversions have

been carried out with data simulated for model J2. The resistive patch is almost perfectly suppressed using the LOTEM-transients only. Using also the SHOTEM-transients, the resistive body is indicated by a shallow structure. These are similar to those found in the pseudo-sections for the SHOTEM-transients.

In the fig. 5.39 (bottom) a pseudo-section of FJI-results is displayed. The body itself is resolved better, but at intermediate depths and for bigger offsets the models show spurious resistive features. The misfit at these stations is high.

The models including a displacement again give results similar to the results for the LOTEM-components only. For model K1, the LOTEM data sets help to constrain the resistivity of the basement (fig. 5.40) which was not resolved by the SHOTEM-transients (fig. 5.37). The SHOTEM-transient on the other hand improves the resolution in the shallow parts (thin, shallow artifacts). Also, the transition to the shallower basement is better resolved when the SHOTEM-transient is included. The FJI result is inferior. Here, the shallow "structure" is not resolved for $-5 \leq y \leq -2$ km. Probably the FJIs converged to early because of inconsistent data sets at a model with high misfits and low roughnesses.

Like the LOTEM-only case, the FJIs produce better results when the basement is resistive. Here, an artificial conductive layer is introduced at depth. Similar results are obtained for model F3.

The results for model M are more interesting. Fig. 5.41 shows a comparison of the results without (top) and with SHOTEM data sets (bottom). The models for $y > 0$ km match the synthetic model slightly better, when the SHOTEM-transient is included. However, the uppermost layer shows the oscillations introduced by the SHOTEM data set.

For $y < 0$ km, the averaged models are similar to the SJIs of the LOTEM-transients only. Again, an artificial diagonal conductive layer is embedded in the second, resistive layer. Unlike the results for the LOTEM-components, this layer is not a feature consistent with all data sets. The panels showing the relative differences, indicate inconsistencies at the depths of the artificial structures.

To examine this closer, fig. 5.42 (left) shows the resulting models for all components at the position $y = -3.5$ km. All LOTEM-components show a similar behaviour. The shallow oscillations are mainly observed in the model corresponding to the SHOTEM-transient. The top of the resistor is obtained at about 200 m which is about 100 m too shallow. At the depth of the spurious conductor, the models differ significantly. This is an indication that this feature is artificial. The deep conductive feature is comparatively well resolved. The information about the resistive basement is provided by the LOTEM-transients, as the single SHOTEM inversions do not resolve the bottom of the deep conductor (fig. 5.42, right).

The model derived by the FJI does not resolve the model that well. The upper part is similar to the SJI results. However, the resistivity of the resistor is overestimated. At 500 m the model shows an artificial drop in resistivity. At greater depths, the model shows only slight variations. The conductive feature is not well resolved, although indications for a conductor can be found.

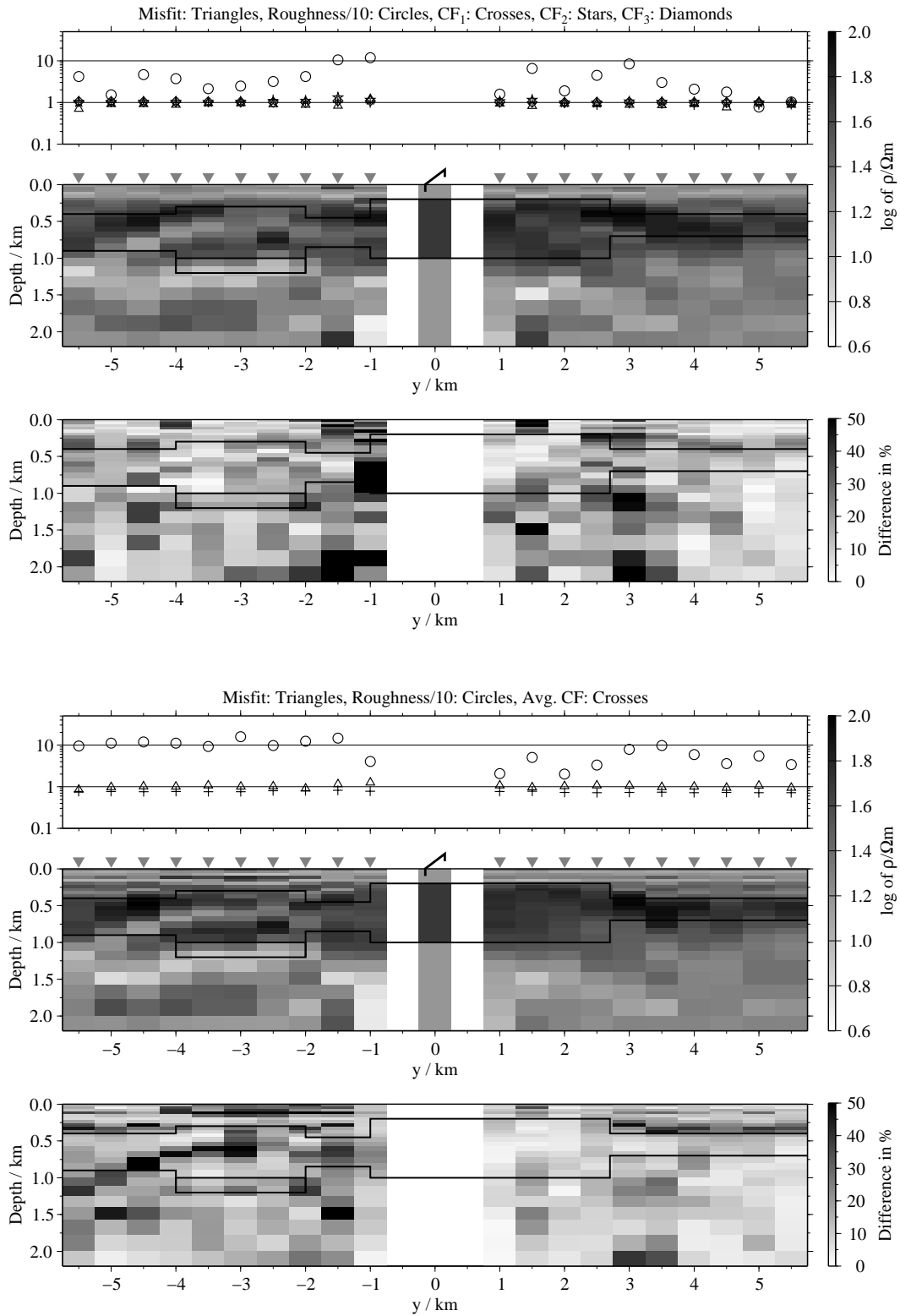


Figure 5.41: Pseudo-sections of SJs for regularisation scheme C4 and model M; top panel: Results for the LOTEM-components only; bottom panels: Results using all LOTEM-transients and the SHOTEM data set;

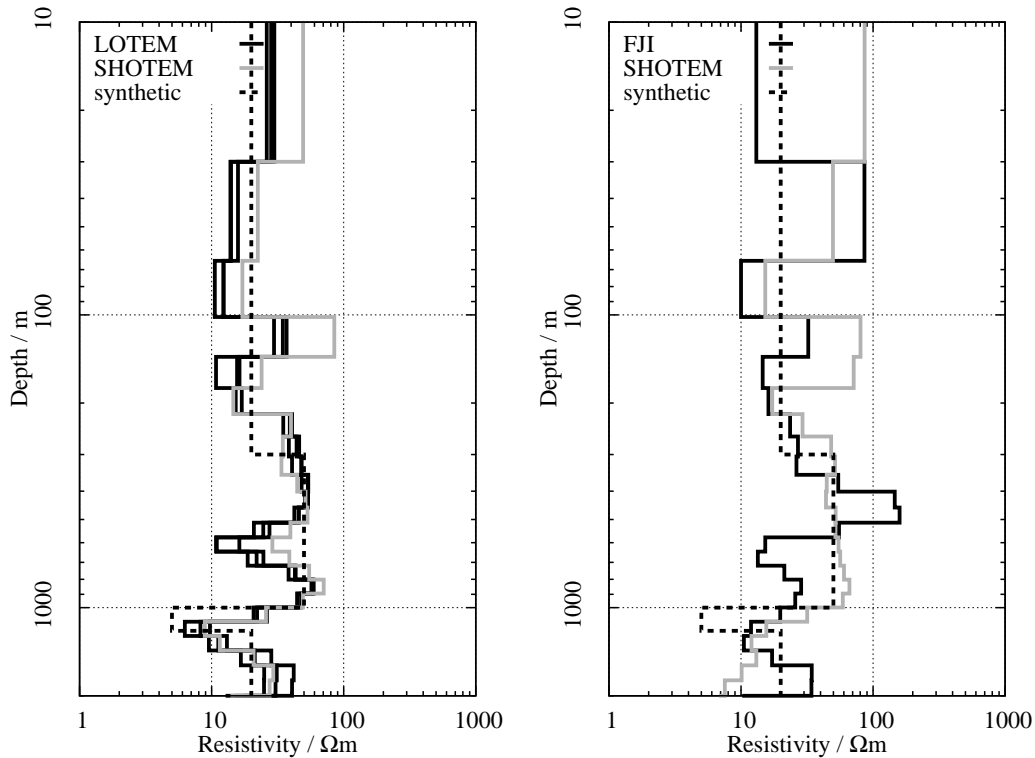


Figure 5.42: Joint-inversion results using all four TEM-components for model M, regularisation scheme C4; plotted are the models obtained at $y = -3.5$ km. The synthetic model at this position is plotted with a dashed black line in both figures. Left: SJI-results; the models obtained are plotted either with solid black lines (all LOTEM-components) or a gray line (SHOTEM). Right: Comparison of the synthetic model, the result of the FJI and the model obtained by the SHOTEM single inversion;

5.5.3 Implications for the joint-interpretation of SHOTEM and LOTEM data sets

SHOTEM and LOTEM data sets contain complementary information. The influence of a multidimensional structure on SHOTEM data sets is restricted to the vicinity of this structure. On the other hand the LOTEM data sets are reflecting a much larger part of the subsurface. At best, multidimensional structures appear smoothed in the pseudo-sections.

When the subsurface is approximately 1-D, the resolving capabilities of both modifications can be combined (see the $y > 0$ km part of the pseudo-sections in fig. 5.40). In reality however, this will not be the case very often. Even in presence of slight inconsistencies (see the $y < 0$ km part of the pseudo-sections in fig. 5.40) the FJI tends to introduce artificial structures. In the shown examples this is connected to high misfits. This problem was also observed by Lange [2003] who found that FJIs of LOTEM and SHOTEM field data sets failed in almost all cases.

The SJI approach again showed better results than the FJIs. Adding the SHOTEM-transient e.g. sharpens the transition in model K1 instead of introducing new artifacts. In the results for model M, the SHOTEM data set in the SJI indicates that the diagonal feature found in the pseudo-section for $y < -2$ km is spurious. Also, the conductive feature at depth was slightly better resolved than using the FJIs.

At sites where an inconsistent artificial structure was found, it would be better to construct a combined model instead of using a joint-inversion result. This means to combine the shallow part of a SHOTEM model and the deep part of the LOTEM model. The problem for real data sets would be to derive a proper transition depth. An adequate choice would be a deep, consistent feature. In the example shown in fig. 5.42 this would be the deep conductive feature.

However, this approach includes the assumption that the SHOTEM result is undistorted. With measured data sets this is not easy. For instance, Goldman et al. [1994b] uses the appearance of layers with unreasonable low resistivities as indicator for distortions. The model calculation in sec. 5.5.1 showed that at least the inversions of transients simulated atop of inhomogeneities resulted in high misfits. In this case the models should be rejected. However, both criteria are not sufficient. The SHOTEM pseudo-sections for model I2 showed artificial structures at stations close to the inhomogeneity, although neither the resulting resistivities nor the misfit indicate any distortions.

Inconsistencies can also be interpreted as lateral changes due to the different lateral resolutions. For instance, the smoothed displacement in fig. 5.40 and the resulting inconsistencies for the SJI models at $-5 \leq y \leq -2$ can be resolved by assigning the SHOTEM result to the Rx-position and the LOTEM result half-way between the Rx- and the Tx-position. This makes it as reasonable to joint-interpret a single LOTEM data set with a SHOTEM-transient recorded at the Tx-position.

However, if LOTEM-transients are recorded along a profile, one would be interested in lateral changes. Relating all LOTEM-inversions to the SHOTEM measurement at the Tx-position therefore seems not expedient. Unfortunately, I did not test this approach with synthetic data sets. The statement therefore is only an educated guess.

5.6 Inversion of Tx-distortion parameters

In this section I will test if a certain type of multidimensional structures can be accounted for by two scalar parameters which are added to the inversion procedure as additional model parameters.

As described in sec. 4.2.2, Hördt and Scholl [2004] were able to quantify the distortions of LOTEM-transients for inhomogeneities close to the Tx or the Rx. For distorting bodies close the Rx, the distortion of the electric field components can be described by

$$E_x(t) = D_{xx}^E E_{px}(t) + D_{xy}^E E_{py}(t) \quad (5.16)$$

$$E_y(t) = D_{yx}^E E_{px}(t) + D_{yy}^E E_{py}(t), \quad (5.17)$$

where the D s denote arbitrary distortion parameters and $E_{px}(t)$ and $E_{py}(t)$ are the undistorted electric fields, which would be measured in absence of this body in the x and y directions, respectively. No assumptions are made whatsoever regarding the origin of the undistorted fields. The undistorted fields are skewed by the

body. In their paper they also showed that it is possible to include the distortion parameters in the inversion algorithm for electric fields.

With respect to the magnetic components, the equations are a little more complicated. In this case the derivatives of the electric fields are multiplied by distortion parameters and added to the magnetic components (cp. eqns. 4.9 to 4.11).

The value of the distortion parameters depends on the geometry between distorting body and Rx-site. They will be the same when two different Tx are used, but different varying Rx locations. To reduce the ambiguity which will be increased by introducing the distortion parameters to the inversion process, Hördt and Scholl [2004] thus propose to use data sets for two different Tx-sites and one Rx-location.

In the field campaign in Israel, each Rx-site was used with only one Tx-position (see sec. 6.2), but in most cases at least two Rx-sites were used. With this setup inhomogeneities close to the Rx-site are not well constrained. One would end up with several different parameters for the individual components measured at the two stations.

For a data set like this it is more convenient consider inhomogeneities close to the Tx. According to Hördt and Scholl [2004], the resulting transient $V(t)$ for each component can be calculated as

$$V(t) = T_x V_{px}(t) + T_y V_{py}(t) \quad (5.18)$$

for sufficiently late times. Here, T_x and T_y are arbitrary distortion parameters, $V_{px}(t)$ the transient which would be measured in absence of the inhomogeneity and $V_{py}(t)$ the transient measured by the same sensor but with a perpendicular Tx. Similar to eqn. 5.16, the electric field produced by the electric dipole is skewed.

Although eqn. 5.18 is the same for all components, the distortion parameters T_x and T_y do not have to be the same for the individual transients at first. However, no assumptions are made in eqn. 5.16 (inhomogeneity close to E_x -sensor) regarding the nature of the undistorted fields. The distortion parameters still will be the same, regardless what resistivity structure or Tx produced the undistorted fields. Using the reciprocity theorem, which states that Rx and Tx are interchangeable, this means that the distortion parameters are also the same, when one electric dipole Tx close to a distorting body is used with different Rx-sensors. This fits both the observations made by Kriegshäuser [1991] and the results of the inversions of the synthetic data sets for the models L1, L2, M1 and M2 in the previous sections.

I included the Tx-distortion parameters in the 1-D inversion algorithm similar to the approach by Hördt and Scholl [2004] for the Rx-distortion parameters. The two distortion parameters T_x and T_y are appended to the model vector \mathbf{m} . The forward calculation is modified to compute the superposition of two perpendicular transmitters with respect to the two distortion parameters (eqn. 5.18).

In the undistorted case T_x equals 1.0 and T_y equals 0.0. If distortions are present T_y can be negative. For the inversion, T_x is transformed logarithmically similar to the other entries of \mathbf{m} (especially the CF, see sec. 4.2.3). T_y is not transformed. In the undistorted case, the value for the entries in \mathbf{m} related to the two parameters thus is 0.0.

A common approach would be to prefer undistorted models. For the Occam's inversion this is achieved by putting ones in the corresponding entries of the main diagonal of the smoothing matrix⁵. If e.g. the R_1 roughness is chosen, and two data sets including two calibration factors and the distortion parameters are inverted in a FJI, the regularisation matrix is

$$\mathbf{P} = \begin{pmatrix} 0 & 0 & & \dots & & & & 0 \\ -1 & 1 & 0 & & & & & \\ 0 & -1 & 1 & 0 & & & & \\ & \ddots & \ddots & \ddots & \ddots & & & \\ \vdots & & & 0 & -1 & 1 & 0 & \vdots \\ & & & & 0 & 0 & 1 & 0 \\ & & & & & 0 & 0 & 1 & 0 \\ & & & & & & 0 & 0 & 1 & 0 \\ 0 & & & \dots & & & 0 & 0 & 1 \end{pmatrix}. \quad (5.19)$$

Initially, the calibration factors should account for the phenomenon now described with the distortion parameters (cp. the inversion results for the models L1, L2, M1 and M2). They thus might be considered obsolete. Strictly speaking, only two of the three parameters T_x , CF_1 and CF_2 assumed in the above example are linearly independent. However, they still might account for several other effects related to one specific data set (e.g. inaccurate dipole lengths). Inverting the field data sets (chap. 6) using the CFs proved to be convenient. Another possibility would be to fix T_x if the CFs from all data sets used in the inversion are allowed to be free parameters. For the sake of simplicity I rejected this approach, although it is worthwhile to keep this in mind as an option for further studies.

To test the inversion including the Tx-distortion, new synthetic data sets were calculated. Similar to the models I1, I2, J1 and J2 shown in the previous sections, a conductive or resistive patch are included in an otherwise layered model. To produce a non-static distortion, $T_y V_{py}(t)$ has to be $\neq 0.0$. In order to get a nonzero T_y , the midpoint of the distorting patch is moved away from the $x = 0$ km line. For broadside- and in-line-configuration $V_{py}(t)$ will be $\equiv 0.0$ for any layered half-space. Thus, the whole Rx-spread is moved to $x = 2$ km. The horizontal configuration is shown in fig. 5.43.

The synthetic data were calculated for two models, one with a conductive, the other with a resistive patch with $\rho_A = 10$ and $\rho_A = 400 \Omega\text{m}$, respectively. The general model is a three layer case with a resistive layer in otherwise conductive material (fig. 5.44). The patches have a size of $500 \times 500 \times 200 \text{ m}^3$.

Again, ten Rx-sites on both sides of the Tx are simulated, each consisting of one E_x -, \dot{H}_y - and \dot{H}_z -sensor. The complete set of single inversions, FJIs and SJIs are carried out with these transients.

⁵I included the distortion parameter also in the Marquardt inversions algorithm of EMUPLUS. Here, the distortion parameters are not regularised. Nevertheless, as the inversion commonly begins with the undistorted case, the results will be biased towards undistorted models. Examples can be found in chap. 6 and app. D.

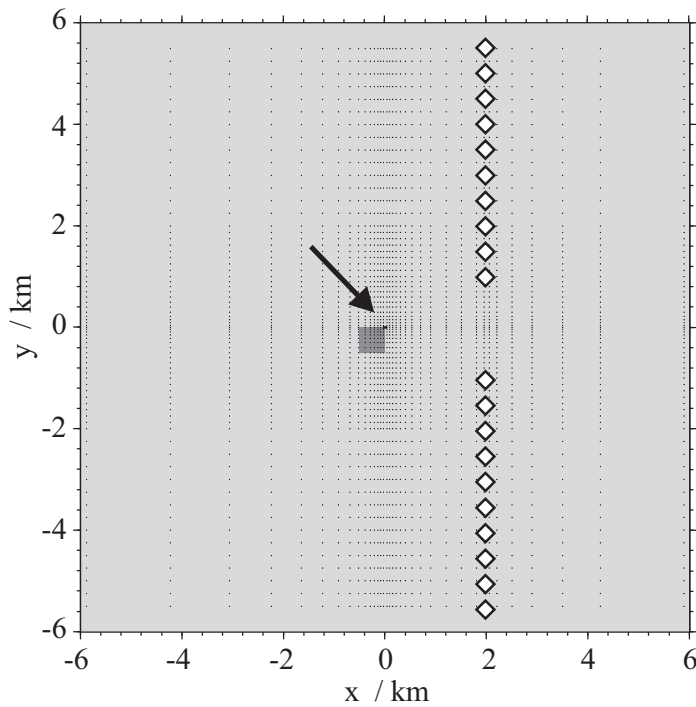


Figure 5.43: Tx-Rx-geometry used in the model studies with inhomogeneities close to the Tx; the white squares denote the position of the Rx-sites. The midpoint of the Tx is at $x = 0$ km, $y = 0$ km (arrow). In this scale, Tx appears as a dipole. It is pointing in x-direction with a length of ≈ 72 m. The dark gray square displays the position of the resistive or conductive patch. Its size is $500 \times 500 \times 200$ m³. The dots denote the inner part of the grid used for the calculation of the E_x -transients. At each Rx-site each one E_x -, \dot{H}_y - and \dot{H}_z -transient is modelled.

Model N1:

Model N2:

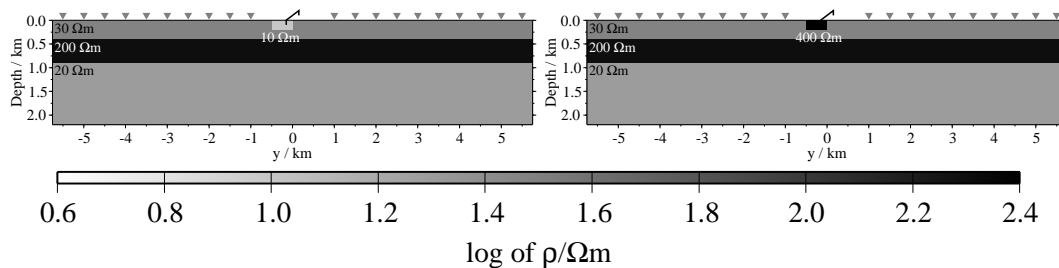


Figure 5.44: Sections of the two models used for the simulation of a sub-surficial distortion close to the Tx; the horizontal geometry is displayed in fig. 5.43.

5.6.1 Sign of the transients

The first problem which is encountered inverting these data sets is to determine the signs of the transients. The polarity of the transient is a question of definition. It is set by defining the direction of a positive current flow⁶. In field measurements also the polarity of the sensors is not clear and may change from one point to the next unless strict conventions are used with respect to setting up the Rx-sites.

In 1-D environments this is not critical, as the polarity of the measured transient can be compared to a synthetic one. In presence of multidimensional structures which can introduce or delay sign reversals this is not trivial. The interpreter has to decide whether the sign at late times or the early times has to fit the one from the 1-D curve.

⁶E.g. these definitions are different for EMUPLUS and SLDMEM3T. In EMUPLUS any spread is rotated such that the Tx points eastward. "Positive currents" are currents flowing east- or northward. In SLDMEM3T the definition is fixed to the calculating grid, i.e. a positive current is flowing in positive x- and y-directions, regardless of the orientation of the Tx.

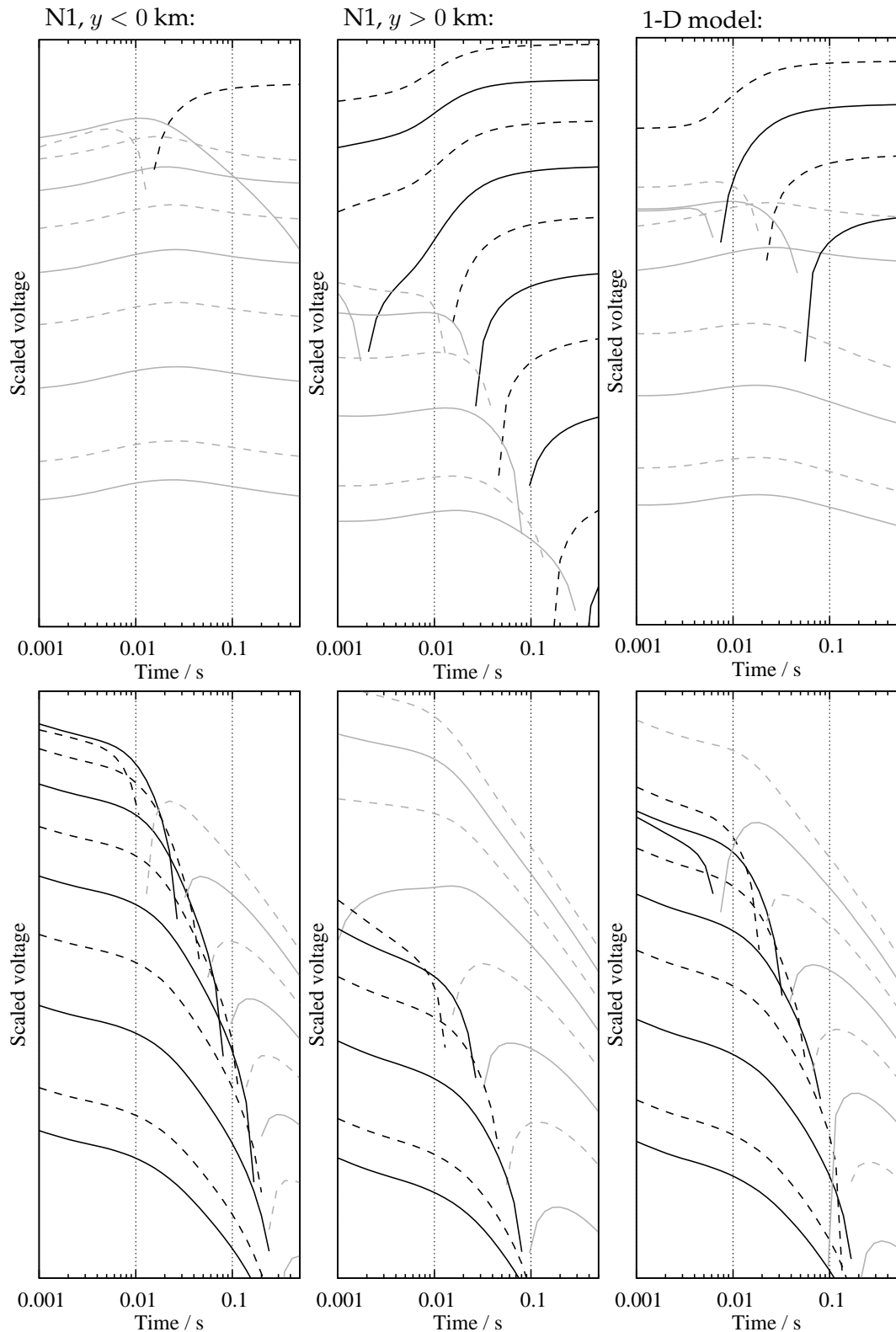


Figure 5.45: From left to right: Transients for model N1, $y < 0$ km, transients for model N1 $y > 0$ km, transients for the 1-D model (without the patch, the transients for $y < 0$ and $y > 0$ km do not differ here); the upper row shows the E_x^- , the lower the H_y^- -transients. The transients are scaled for clearness. In each row the transients are scaled with the same factors. The lowermost curves are the ones for the Rx-sites with the largest offsets. The transients at $y = \pm 1, \pm 2, \pm 3, \pm 4, \pm 5$ km are displayed with dashed and the others with solid lines. Gray lines denote negative and black lines positive values.

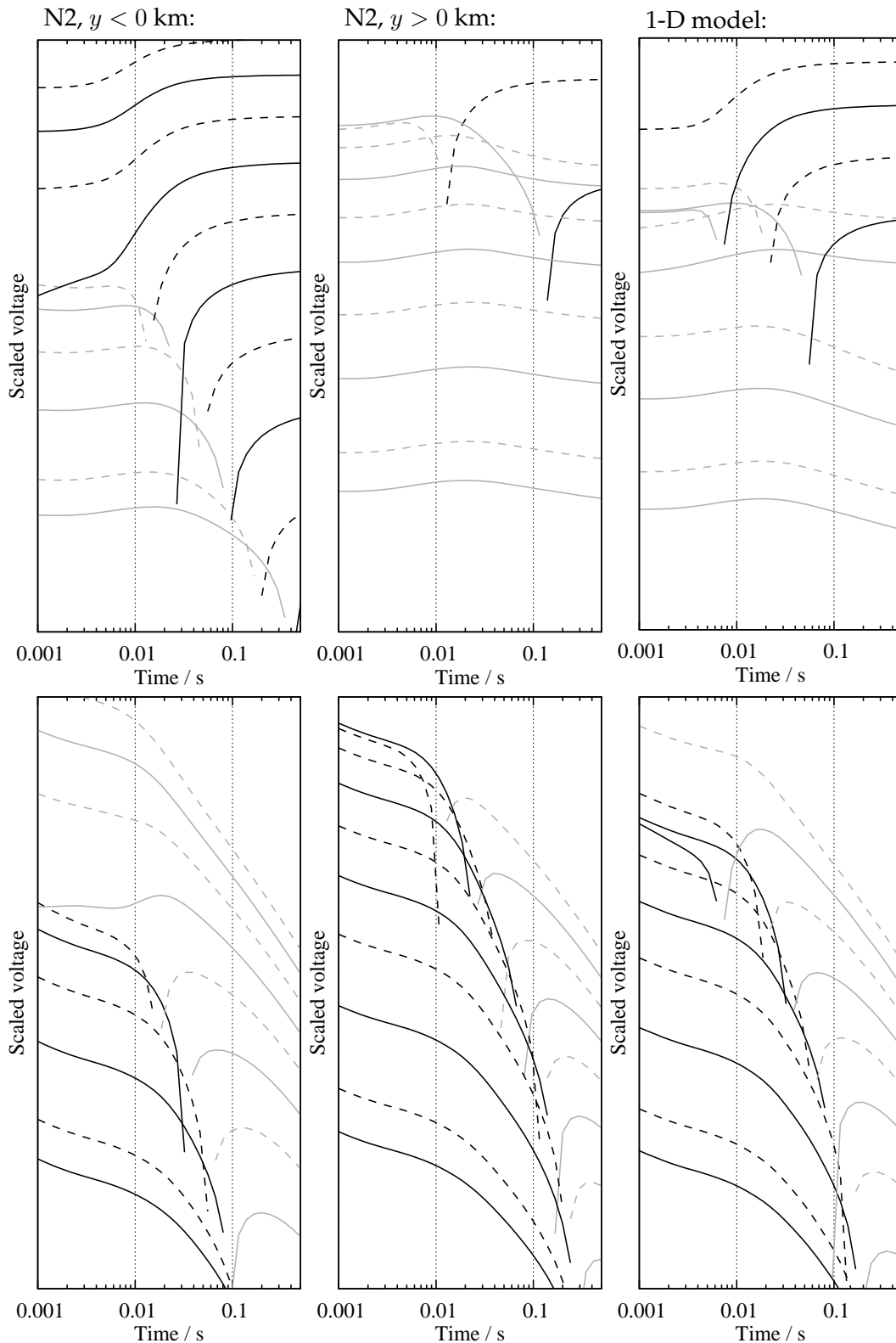


Figure 5.46: From left to right: Transients for model N2, $y < 0$ km, transients for model N2 $y > 0$ km, transients for the 1-D model (without the patch, the transients for $y < 0$ and $y > 0$ km do not differ here); the upper row shows the E_x -, the lower the H_y -transients. The transients are scaled for clearness. In each row the transients are scaled with the same factors. The lowermost curves are the ones for the Rx-sites with the largest offsets. The transients at $y = \pm 1, \pm 2, \pm 3, \pm 4, \pm 5$ km are displayed with dashed and the others with solid lines. Gray lines denote negative and black lines positive values.

Figs. 5.45 and 5.46 show a comparison of the distorted transients for the horizontal components with the undistorted ones for the underlying 1-D model. The 1-D responses are displayed in the left panels. The other two panels show the distorted transients for $y < 0$ km (left) and $y > 0$ km (right). The upper panels show all E_x -transients, the lower all \dot{H}_y -transients. The voltages are scaled for clarity. The smallest voltages correspond to the outermost Rx-sites at $y = -5.5$ and $y = 5.5$ km. In addition, the transients for $y = \pm 1, \pm 2, \pm 3, \pm 4, \pm 5$ km are displayed with dashed lines.

The figs. show that the distortions for the stations with large offsets (the lower curves in each plot) are less severe than for the others. They exhibit only a static shift. This is reasonable, as at these sites the signals from the virtual perpendicular Tx are much smaller than the ones from the (undistorted) Tx. Still, the outermost E_x -transients on one side of the Tx exhibit a sign reversal, which is not observed in the 1-D data (upper middle panel in fig. 5.45, upper left panel in fig. 5.46).

The biggest problems determining the “true” sign will be encountered for the stations closer to the Tx. For instance, for both models the E_x -transients of the third Rx-site have a polarity different to the one with the same offset on the other side of the Tx, whereas the undistorted transients show a sign reversal. If no other data sets along a profile are available, it will be not possible to derive the right sign from this single curve.

Nevertheless, this is only a minor problem if the geometry of the Tx is close to a in-line- or broadside-setup, as in these cases again $V_{py}(t)$ will be small compared to $V_{px}(t)$ for E_x and \dot{H}_y .

Comparing the transients for the models N1 (fig. 5.45) and N2 (fig. 5.46), the curves for stations of the opposite side are quite similar. This means, that a conductive patch on one side of the Tx has an effect similar to a resistive patch on the other side. In general, the transients on the more “conductive side” ($y < 0$ km for N1, $y > 0$ km for N2) seem to be less distorted. This is also observed for the \dot{H}_z -transients. Fig. 5.47 shows the \dot{H}_z -curves for N1. A plot for N2 will look similar, except the left and middle panel have to be interchanged, together with their polarity.

The electric fields are most distorted, as many of the distorted transients show sign reversals whereas the corresponding undistorted ones do not and vice versa. The \dot{H}_z -transients on the other hand seem to be the least distorted. Only the two curves simulated at $y = 1$ and $y = 1.5$ km show a significant distortion. This could be expected, as the shapes of $V_{px}(t)$ and $V_{py}(t)$ are similar.

5.6.2 Model N1: Conductive patch

In general, inverting the data sets with the procedure used in the previous sections produces extremely distorted models for the two horizontal components (fig. 5.48). The results are in accordance with what could be expected from the discussion of the shape of the transient in the previous section.

The electric fields yield acceptable models only for $y \leq -4.5$ (fig. 5.48, top). The inversion algorithm converges also at low misfit levels at sites with smaller offsets, although these models are very distorted and show unreasonable resistivities.

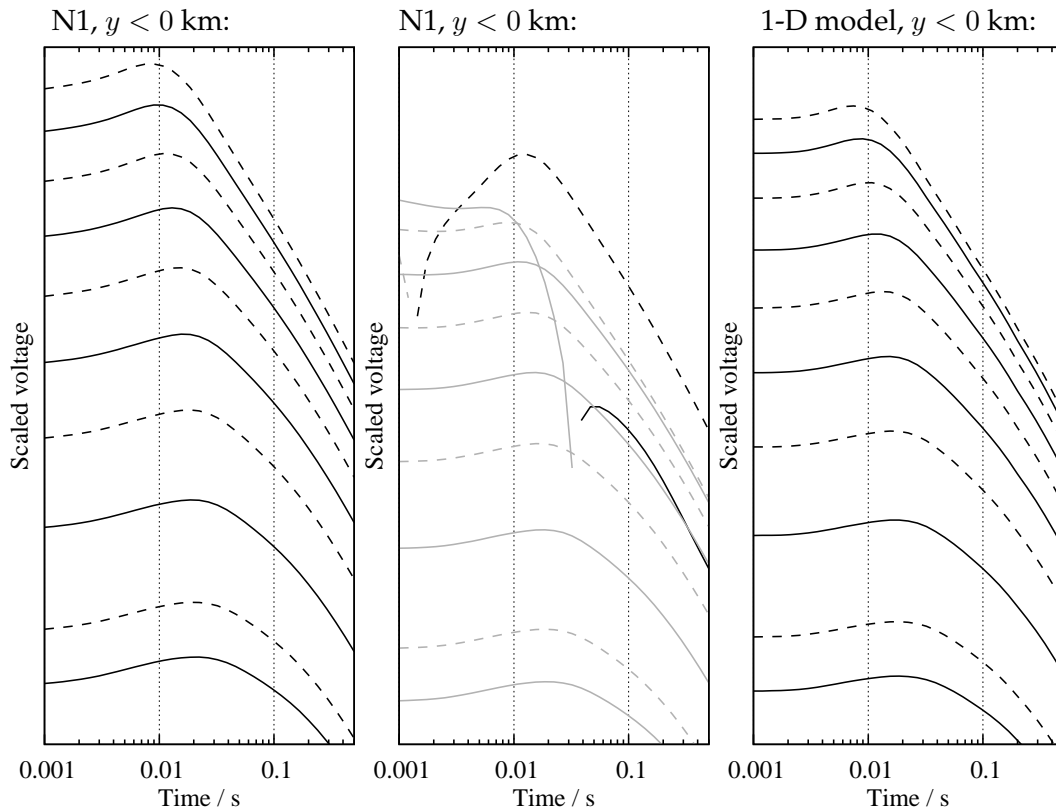


Figure 5.47: From left to right: \dot{H}_z -transients for model N1, $y < 0$ km; \dot{H}_z -transients for model N1, $y > 0$ km; \dot{H}_z -transients for the 1-D model, $y < 0$ km (the transients for $y > 0$ km have identical shapes but a different sign); the curves are scaled for clearness. In each plot the transients are scaled with the same factors. The lowermost curves are the ones for the Rx-sites with the largest offsets. The transients at $y = \pm 1, \pm 2, \pm 3, \pm 4, \pm 5$ km are displayed with dashed and the others with solid lines. Gray lines denote negative and black lines positive values.

The inversion results for the \dot{H}_y -component (fig. 5.48, middle) show only moderate distortions for $y \leq -3$ km, although severe distortions show up at depth. For $y > 0$ km the inversions succeed in finding models with acceptable misfits, although the models show no similarity to the original 1-D model.

As expected, inversions for the \dot{H}_z -transients fail only at site with $y = 1$ and $y = 1.5$ km (fig. 5.48, bottom). In the other cases, the distortion can be compensated by the CF. Interestingly, the CFs are smaller than 1.0 for $y < 0$ km and bigger than 1.0 for the other stations.

The joint-inversions of two or three components give similar results. As at least one of the two horizontal components is included, their pseudo-sections are similar to the two upper panels of fig. 5.48. Fig. 5.49 shows a comparison of the FJIs and SJIs of all three components. Similar to the findings of sec. 5.4, the results of the SJIs is slightly better than those of the FJIs. In the FJIs' results distinct artifacts are found below the second layer even for sites with $y \leq -4.5$ km, although the misfit is in an acceptable range. Compared to the single inversion results from fig. 5.48, the FJI at least shows the advantage that the completely distorted models for $y > -4.5$ km produce unreasonable misfits. The SJIs produce reasonable models for sites with $y \leq -3.5$ km.

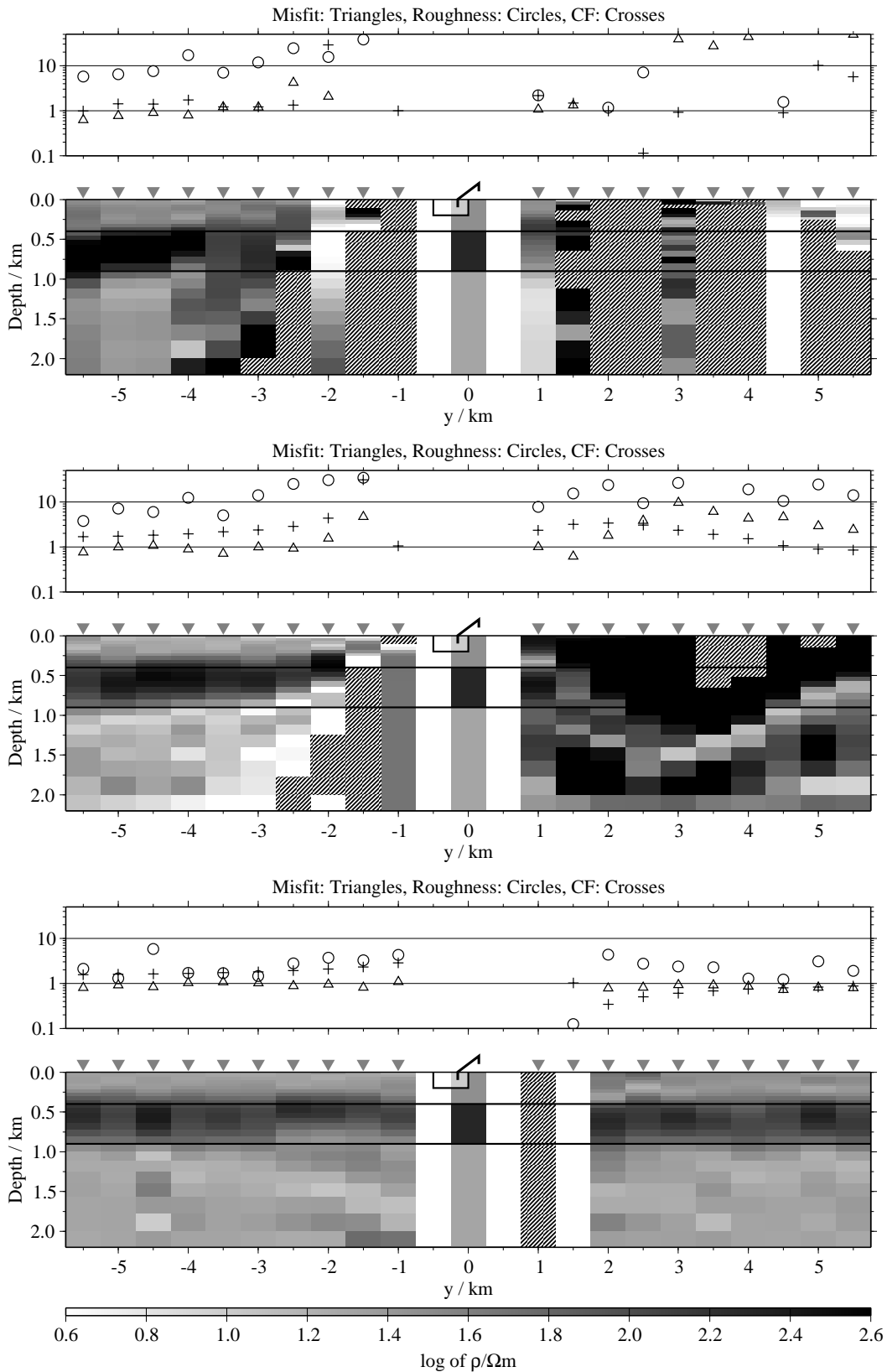


Figure 5.48: The single component inversion results for model N1, regularisation scheme C4; the inversions are done excluding the Tx-distortion parameters. From top to bottom: Results for the component E_x , \dot{H}_y and \dot{H}_z ;

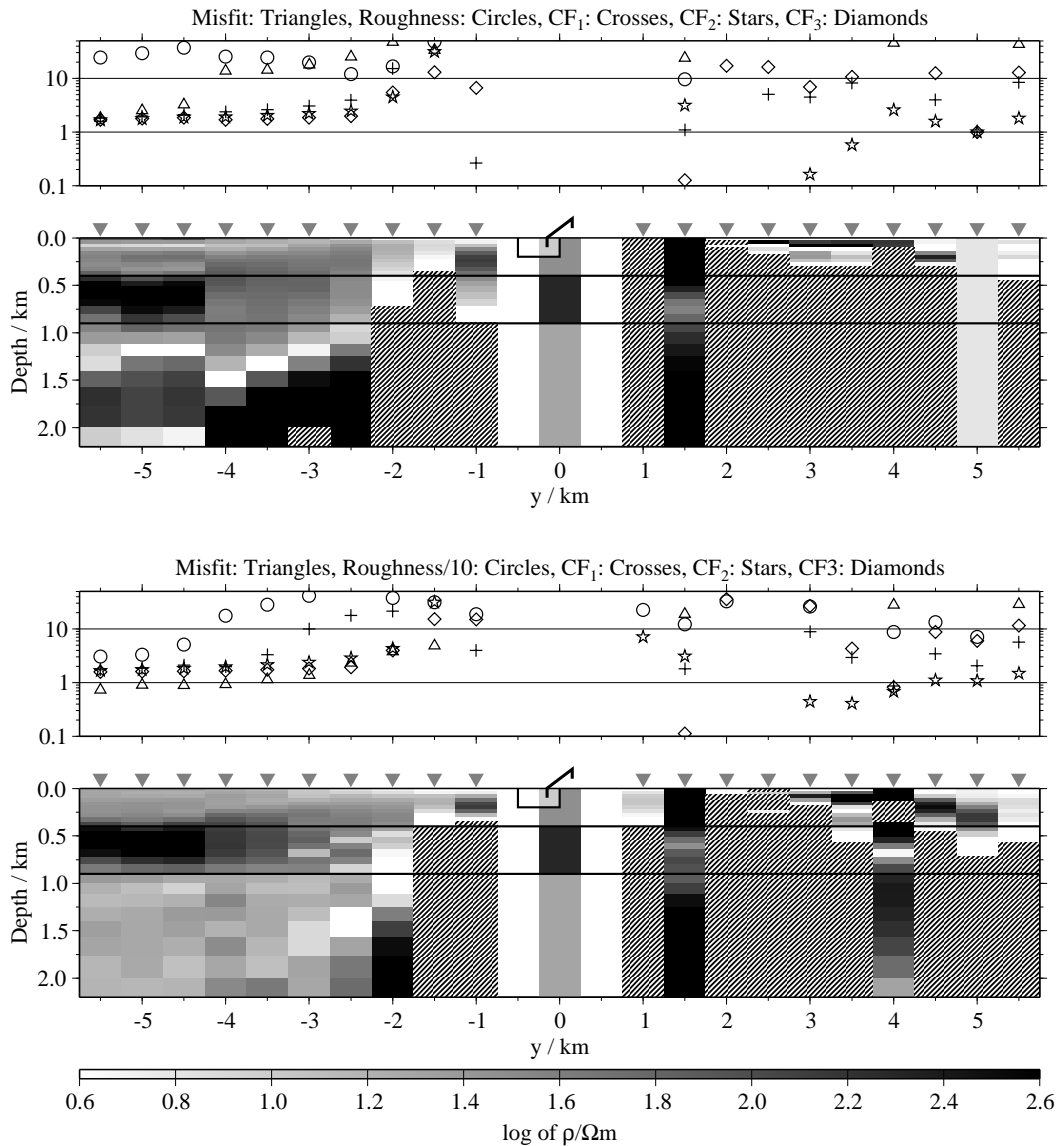


Figure 5.49: Results of the joint-inversions for all three components for model N1, regularisation scheme C4; the inversions are done excluding the T_x -distortion parameters. Top: FJIs; bottom: Averaged models from the SJs;

At first, the results for inversions including the distortion parameters are disappointing. The pseudo-section for the \dot{H}_z -transients is similar to the one shown in fig. 5.48. Fig. 5.50 shows the results for the two horizontal components. Very smooth models yielding high misfits are obtained for E_x and \dot{H}_y , since the inversion process broke down after a few iterations. At least the \dot{H}_y -results for sites with $y \leq 2.0$ km show a blurred picture of the true model. The bad convergence properties are most likely caused by the linear dependency of T_x , T_y and the CF. It seems that the damping of the matrix inversion in eqn. 5.3 is more complicated. The inversion fails to find an appropriate model update.

If two or more data sets are used in joint-inversions, the results are much better. The best results are obtained using only the magnetic components. Fig. 5.51 shows

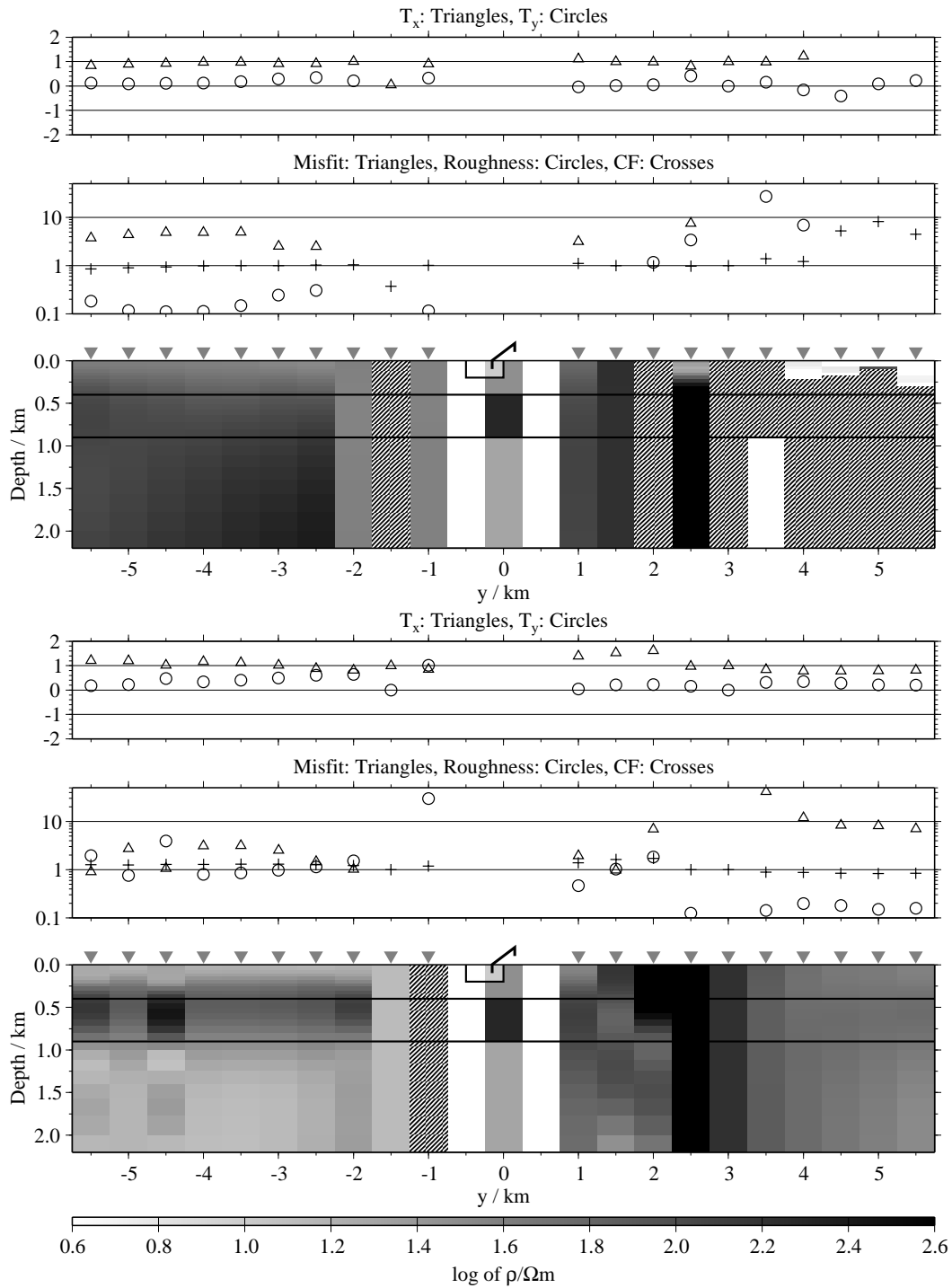


Figure 5.50: The single component inversion results for model N1, regularisation scheme C4; the inversions are done including the T_x -distortion parameters, which are displayed in the uppermost subpanels. Top: Results for the component E_x ; bottom: Results for the component H_y ;

a comparison of the results for FJIs and SJIs. Results for the SJIs are slightly better, since the 1-D model is reconstructed for all but the sites with $-1.0 \leq y \leq 2.5$ km. The FJIs introduce a minor shallow, resistive artifact, but still resolve the 1-D structure well for all but the stations at $1.0 \leq y \leq 3.5$.

If the E_x -transients are included the results are not that good, but still better than

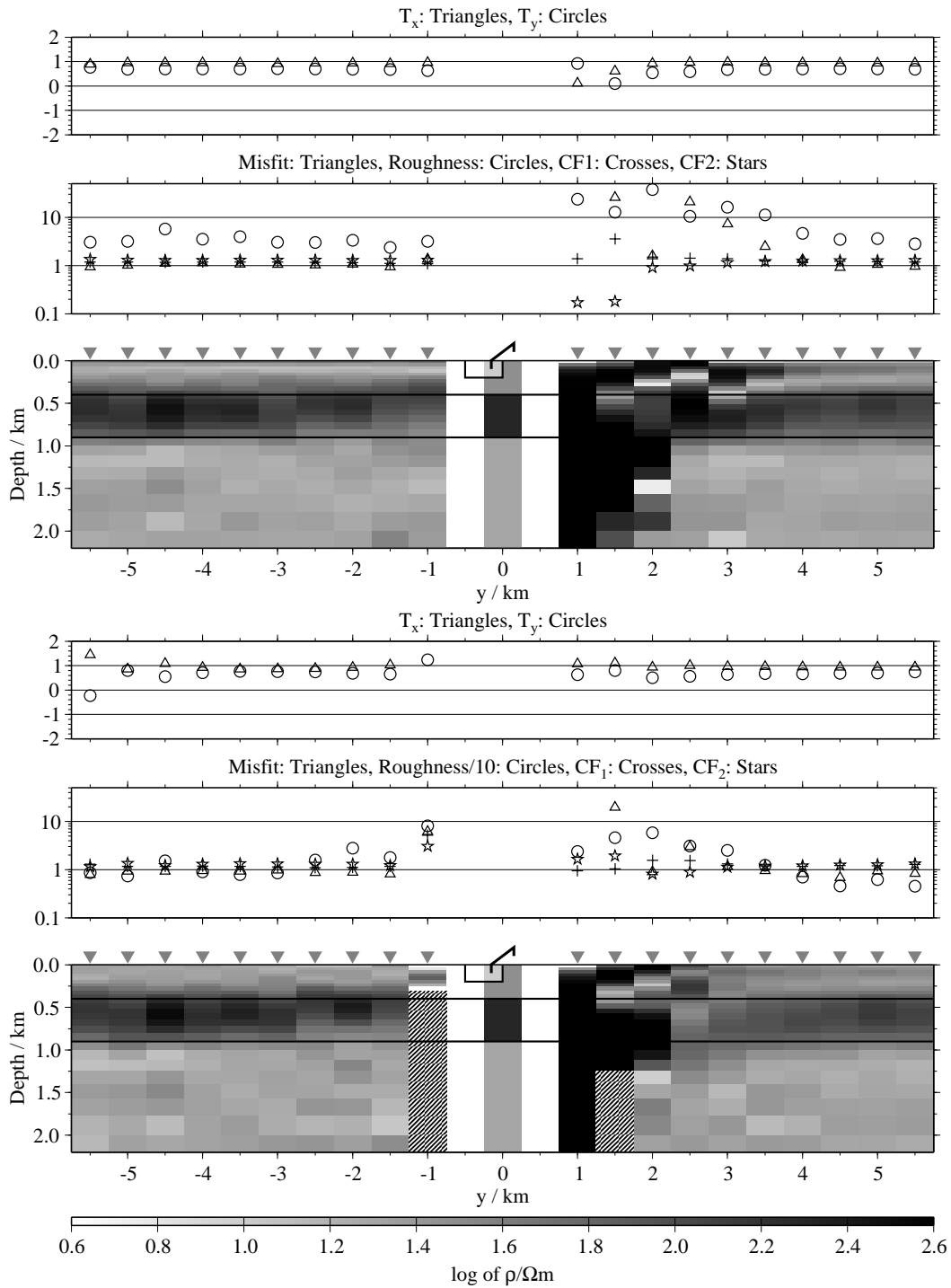


Figure 5.51: Results of the joint-inversions for the \dot{H}_y - and \dot{H}_z -components for model N1, regularisation scheme C4; the inversions are done including the T_x -distortion parameters, which are displayed in the uppermost subpanels. Top: FJIs; bottom: Averaged models from the SJIs;

for the standard inversions from figs. 5.48 and 5.49. Fig. 5.52 shows the results for the FJIs (upper panel) and the SJIs (lower panel) of all three components. The pseudo-sections are similar to the ones from fig. 5.51. The results for the FJIs in this case are slightly better, as the 1-D model is recovered at more stations, although again an artificial shallow resistor is introduced. The additional information from

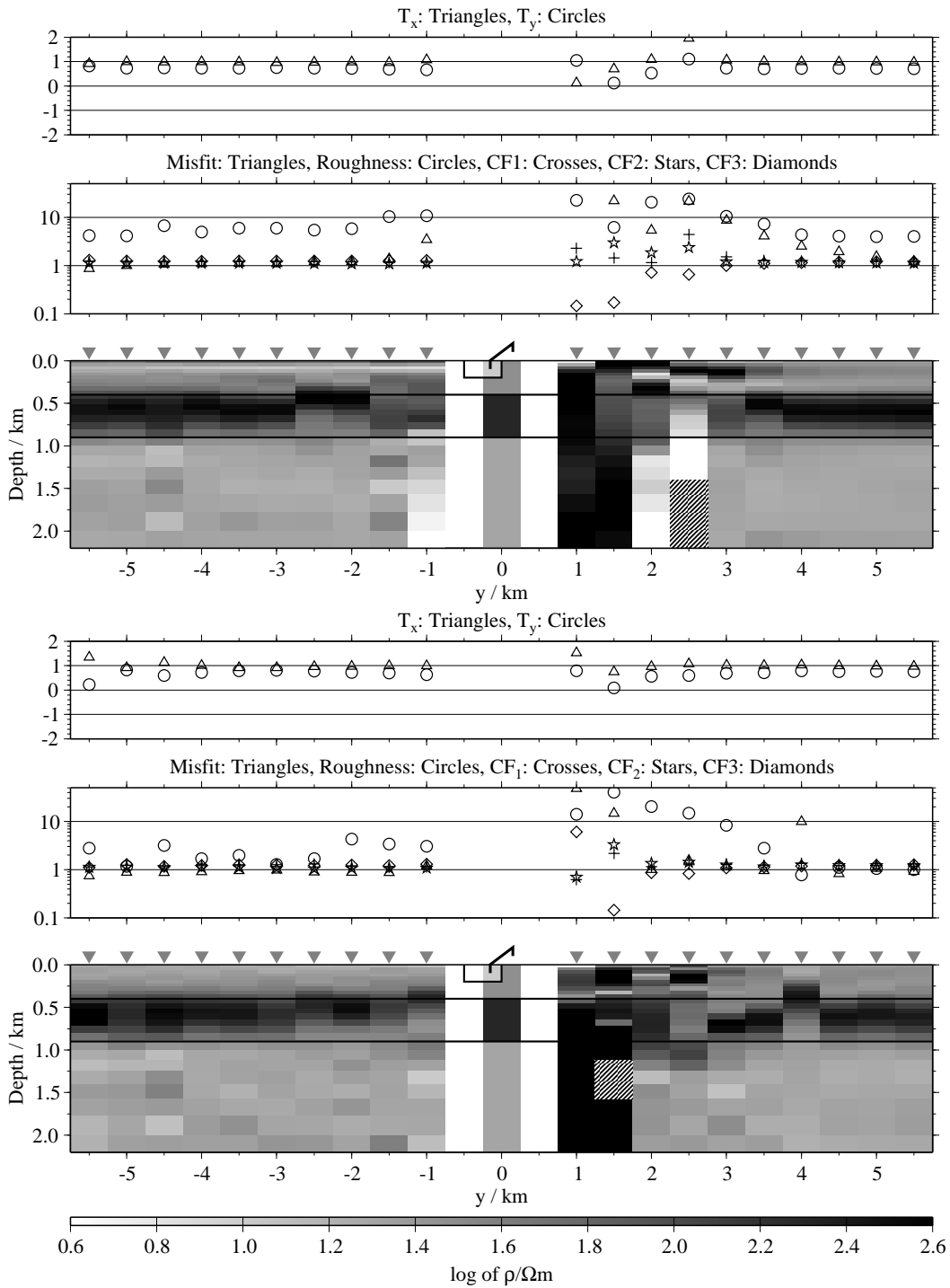


Figure 5.52: Results of the joint-inversions for all three components for model N1, regularisation scheme C4; the inversions are done including the T_x -distortion parameters, which are displayed in the uppermost subpanels. Top: FJIs; bottom: Averaged models from the SJIs;

the electric fields helps slightly to constrain the resistivity of the second layer. All models yielding a sufficiently low misfit had $T_x \approx 0.99$ and $T_y \approx 0.73$, respectively.

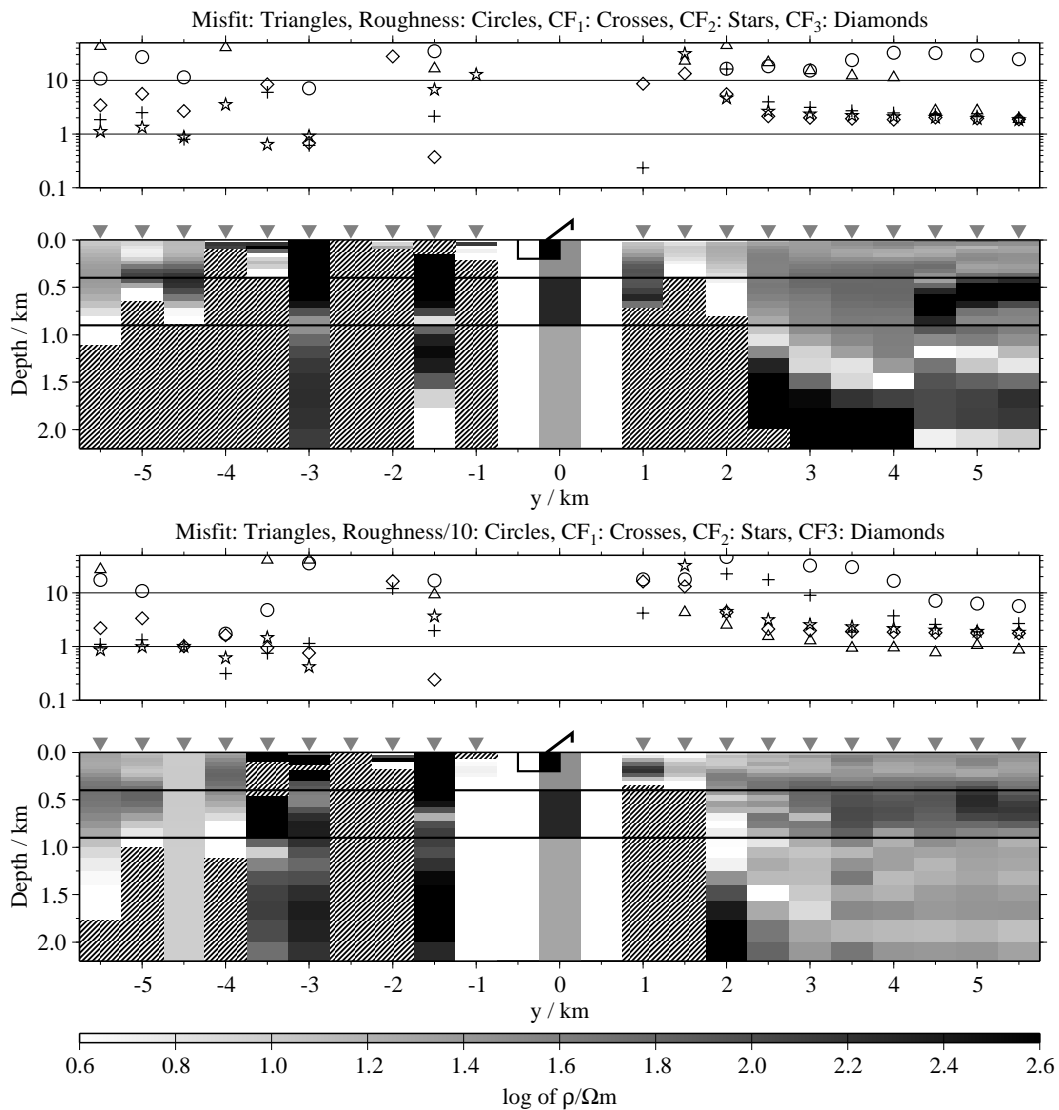


Figure 5.53: Results of the joint-inversions for all three components for model N2, regularisation scheme C4; top: FJIs, bottom: Averaged models from the SJIs; the inversions are done excluding the Tx-distortion parameters.

5.6.3 Model N2: Resistive patch

The transients for model N2 show a similar shape as the transients for model N1, simulated at the Rx-location with the same offset but on the other side of the Tx (cp. figs. 5.45 and 5.46). The results of the inversions are also similar.

Again, the standard inversions excluding the distortion parameters fail for the horizontal components. The results for the joint-inversions (fig. 5.53) are very similar to the ones for model N1 (cp. fig. 5.49).

The results can be improved by including the Tx-distortion parameters (fig. 5.54). The pseudo-sections are slightly less distorted than the ones in fig. 5.52, although the relative difference between ρ_1 and the resistivity of the patch ρ_A is higher. The results of the FJIs are slightly better than for the SJIs, as the resistive layer is better resolved. At $y = -3.5$ km the SJI failed to find a reasonable model. Different to

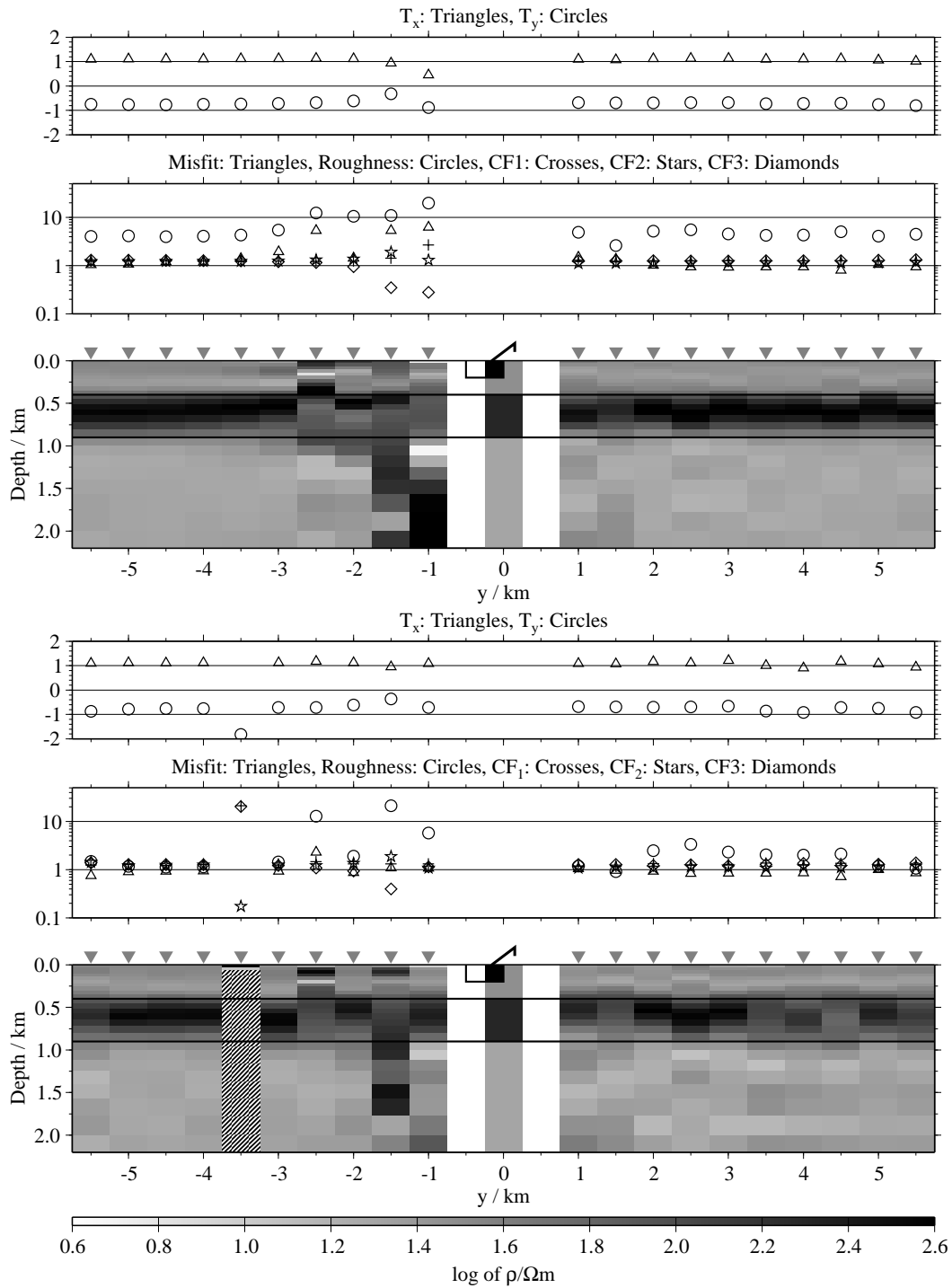


Figure 5.54: Results of the joint-inversions for all three components for model N2, regularisation scheme C4; top: FJIs, bottom: Averaged models from the SJIs; the inversions are done excluding the T_x -distortion parameters.

the FJIs for model N1, no artificial resistor is introduced to the pseudo-section. All models yielding a sufficiently low misfit had $T_x \approx 1.07$ and $T_y \approx -0.74$.

5.6.4 Results for model N1 and N2

The distortions produced by the blocks near the Tx are strong. Except for sites at small offsets they are described well with the equations derived by Hördt and Scholl [2004]. The conductive patch on one side of the Tx has a similar effect on the data sets than a resistive patch on the other side. As already mentioned, the transients on the more “conductive side” ($y < 0$ km for N1, $y > 0$ km for N2) are less distorted.

If the Tx-distortion parameters are not included in the inversion, the resulting pseudo-sections for the horizontal components shows huge artifacts. These artifacts are stronger for the E_x -component than for the \dot{H}_y -component. The pseudo-sections for the \dot{H}_z -component are only slightly distorted, because the \dot{H}_z -transients are mainly shifted [Newman, 1989]. Thus, the CF is sufficient to describe the distortion in the data sets.

For the horizontal components, the Tx-distortion parameter has to be included in the inversions. The resulting pseudo-sections are only distorted at few stations. However, in several cases the algorithm failed to converge at low misfit levels. The results are far better when more than one component is used in a joint-inversion.

5.7 Removing distortions

Until now, the complete transients calculated for the synthetic models were used in the inversions. Some of the transients, however, can not be explained by any 1-D model. For a true 1-D model, the \dot{H}_z -transient never exhibits sign reversals. Other transients show over-steep parts which can not be fitted.

If these transients are used for inversion, they result often in models showing unreasonable high or low resistivities and high misfits. It seems logical to remove clearly distorted parts of the transients prior to inversion. As Newman [1989] suggests, the rest of the transients might be shifted but otherwise undistorted in some cases. Inverting the remaining data points can still reveal useful information about the subsurface.

The problem is to detect distorted parts of a transient. A distortion which shows up as sign reversal in a \dot{H}_z data set at one position might just appear as a depression or even an increase in the induced voltage at another Rx-site [Strack, 1992]. In the last two cases, the data distortion might not be noticeable. But even when a distinct sign reversal is observed, it is still questionable how many data points have to be removed.

Fortunately, the previous studies as well as the results from sec. 5.3 show that the distortion of the transients depends on the distance from the distorting structure. Thus, it is reasonable to compare the transients for adjacent stations, as they might be at different offsets from the distorting structure. However, the different offset from the Tx will change the shape and the amplitude of the transients. To reduce the geometric effect, all magnetic transients are converted in apparent resistivity curves. Before doing this, shifts in the transients are removed. This is possible, because for a 1-D subsurface the integral $\int_{t=0}^{\infty} V(t)$ does not depend on the parameters

of the layered model for any magnetic component.

Donat [1996] derived equations for the correction factors for all three magnetic components. For \dot{H}_y and \dot{H}_z the correction factors c_y and c_z are

$$c_y = -\frac{\mu_0 A D_0}{4\pi R^2 \int_0^\infty V_y(t) dt} (1 - 2 \sin^2 \Phi) \quad (5.20)$$

and

$$c_z = \frac{\mu_0 A D_0}{4\pi R^2 \int_0^\infty V_z(t) dt} \sin \Phi, \quad (5.21)$$

where t is the time after e.g. a polarity change at the Tx, Φ is the angle between the Tx-direction and the line between mid-point of the Tx and the Rx-position (fig. 2.3), R is the distance of the Rx-site to the mid-point of the Tx, D_0 is the dipole moment of the Tx, A the effective area of the Rx-coil and $V(t)$ the measured induced voltage in y- and z-direction. For real data sets this is only an approximation, as the induced voltage is neither measured for $t \rightarrow 0$ s nor for $t \rightarrow \infty$ s. Nevertheless, for comparing the data sets this approximation is sufficient.

The early time ("et") and late time ("lt") apparent resistivities for both components can be calculated according to

$$\rho_y^{\text{et}} = \frac{R^6 \pi^3 (c_y V_y(t))^2}{(1 - 1.5 \cos^2 \Phi)^2 A^2 D_0^2 \mu_0} t, \quad (5.22)$$

$$\rho_y^{\text{lt}} = -\frac{A D_0 \mu^2}{64\pi c_y V_y(t) t^2}, \quad (5.23)$$

$$\rho_z^{\text{et}} = -\frac{2\pi R^4 c_y V_y(t)}{3A D_0 \sin \Phi} \quad (5.24)$$

and

$$\rho_z^{\text{lt}} = -\left(\frac{A D_0 R \sin \Phi}{40\pi \sqrt{\pi} c_y V_y(t)} \right)^{\frac{2}{3}} \left(\frac{\mu_0}{t} \right)^{\frac{5}{3}} \quad (5.25)$$

[Petry, 1987; Donat, 1996].

The apparent resistivity curves for the magnetic fields of two adjacent stations are compared. The data points are determined, for which the early and late time curves for the two transients differ. These are removed prior to inversion. As neither the early time nor the late time approximation is valid at intermediate times, the transients can not be compared here. The problem is imminent for the stations at $y = \pm 1$ km, as the early time approximation is never valid. If distortions are found over the complete early and late time range, one should consider to reject both transients.

An all-time apparent resistivity definition would be helpful. Although some authors addressed this subject, no practical and stable solution was found for LOTEM. For the electric fields, apparent resistivity conversion is not feasible. Both issues are discussed by Karlik [1994]. Instead of comparing the E_x -transients of adjacent stations, the first 4 data points are removed from all electric field data sets. The reason for this is that field data sets of these components are often found to be distorted at early times for technical reasons (see secs. 6.2.1 and 6.3).

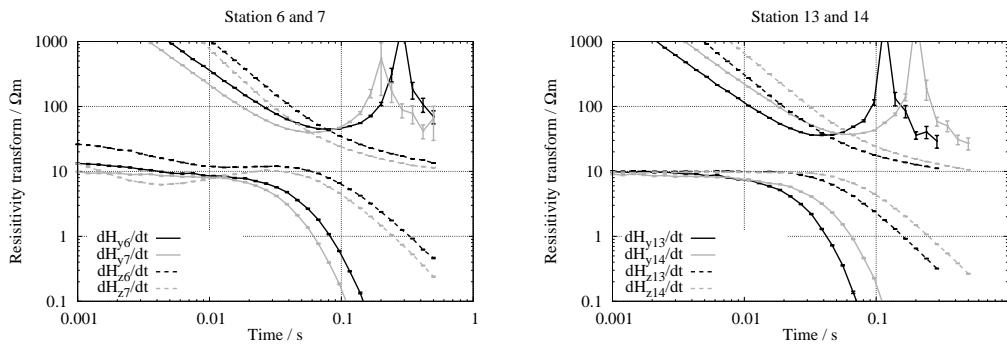


Figure 5.55: Comparison of the apparent resistivity curves for the magnetic transients calculated for two adjacent stations for model F1; for \dot{H}_y the apparent resistivity curves (solid lines) exhibit sign reversals. Left: Comparison of the magnetic components for the stations at $y = -3$ km and $y = -2.5$ km; right: Comparison of the magnetic components for the stations at $y = 2$ km and $y = 2.5$ km;

Fig. 5.55 shows an example for the model F1. Here, the apparent resistivities for the magnetic components of two adjacent stations are compared. The left panel shows a comparison for the stations at $y = -3$ km and $y = -2.5$ km. The first 10 data points were removed from the \dot{H}_y -transients. The mutual deviations in the \dot{H}_z s are visible even at later times. The first 18 data points were removed here. The right panel of fig. 5.55 shows a comparison for the stations at $y = 2$ km and $y = 2.5$ km. Here, no significant deviations are observed in the \dot{H}_z -transients. No data points were removed. 11 data points were removed from the \dot{H}_y -transients, although the differences here are not big.

A comparison for all stations and the three models used (F1, K3 and M) can be found in app. B. There are also the numbers of data points listed which are removed for each pair of Rx-stations. Data points from the end of the transient had never to be removed. No obvious differences in the apparent resistivity curves are found for model K3. Here, unedited transients were used in the inversions.

The models F1 and M were chosen because of the significant distortions found in their pseudo-sections in the previous sections. K3 is an example of a well-resolved model. The shortened transients of both stations are used in FJIs and SJIs. In the pseudo-sections, the results for the data sets of two stations are displayed between the Rx-sites. The complete set of pseudo-sections can be found in app. B.

5.7.1 Results of the inversions

The results for the joint-inversions of transients calculated at adjacent stations do not differ much from the results presented in the other sections of this chapter. One difference is that it is possible to check the consistency within one component by inverting e.g. two E_x -transients simulated at adjacent positions.

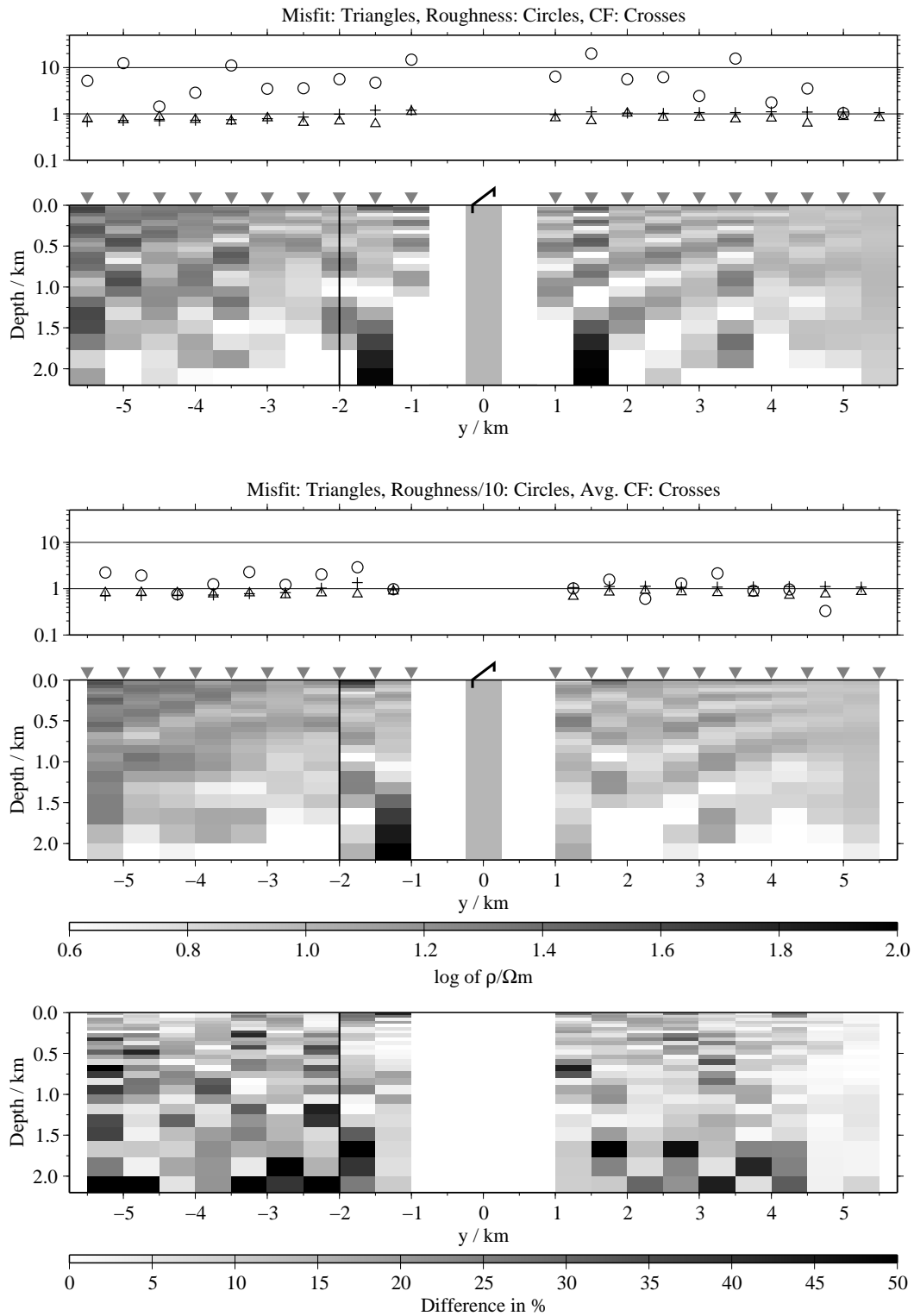


Figure 5.56: Pseudo-sections for the \dot{H}_y -component, regularisation scheme C4, model F1; top: Results of single inversions; bottom: Results of the SJIs of the shortened \dot{H}_y -transients of two adjacent stations; note that the roughness is divided by ten in the panel for the SJIs.

Fig. 5.56 shows a comparison of the single inversion results of the \dot{H}_y -transients (top) and the SJI results of the shortened \dot{H}_y -transients of two adjacent stations.

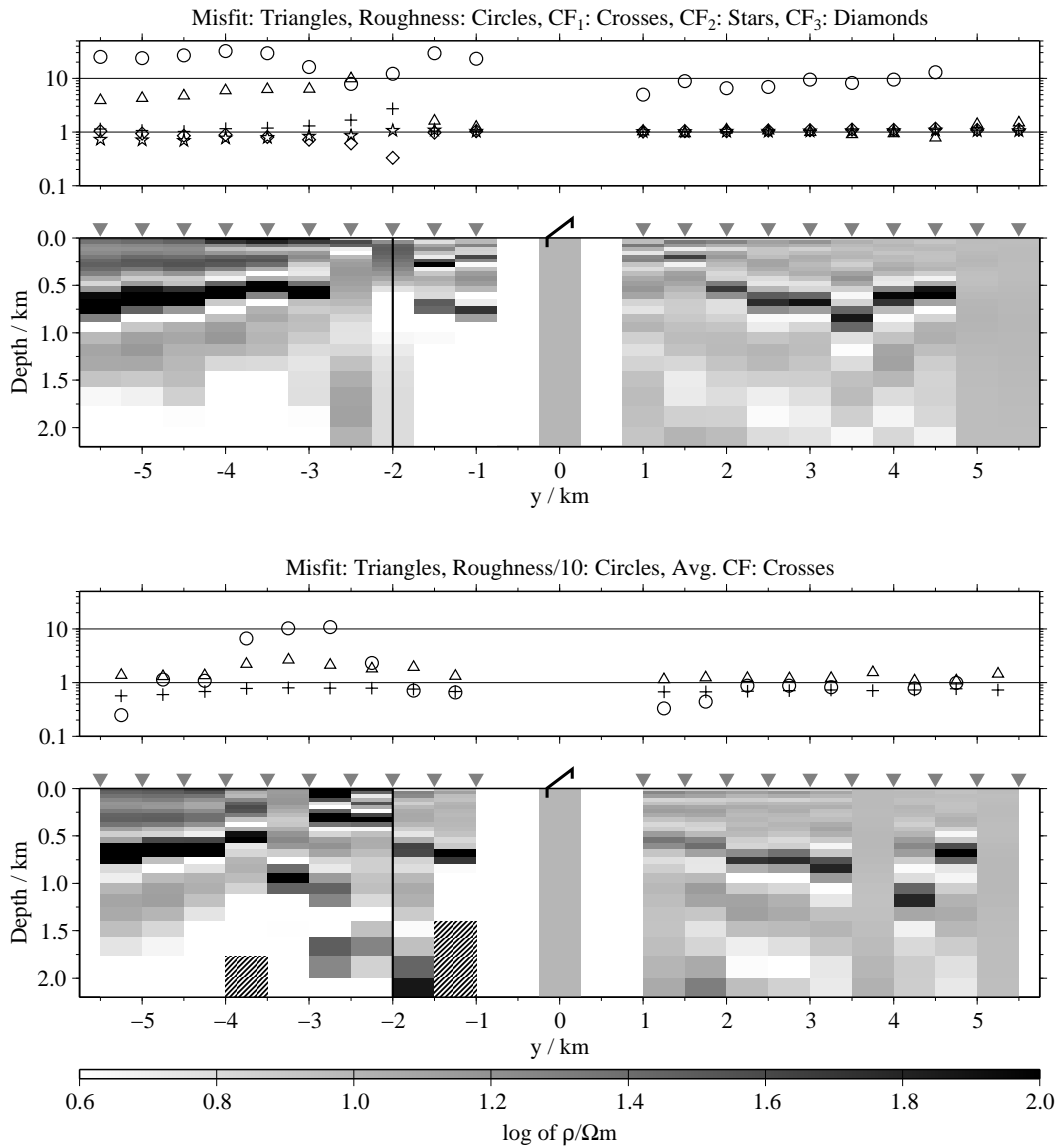


Figure 5.57: Pseudo-sections for the all three LOTEM components, regularisation scheme C4, model F1; top: Results of FJIs of data sets of one station each; bottom: Results of the FJIs of the shortened transients of two adjacent stations; note that the roughness is divided by ten in the panel for the SJIs.

The pseudo-section for the SJIs exhibits far less lateral fluctuations. The laterally correlated artificial structures are suppressed only slightly. Both effects were expected. After removing inconsistent data points, only correlated structures remain in the transients. This means that correlated artifacts in the models are persistent, whereas uncorrelated features are suppressed.

Like in the previous sections, the pseudo-sections of FJI results exhibit more artificial structures than their SJI counterparts. In fact, the FJI results are quite similar to the FJI results using data sets from only one station.

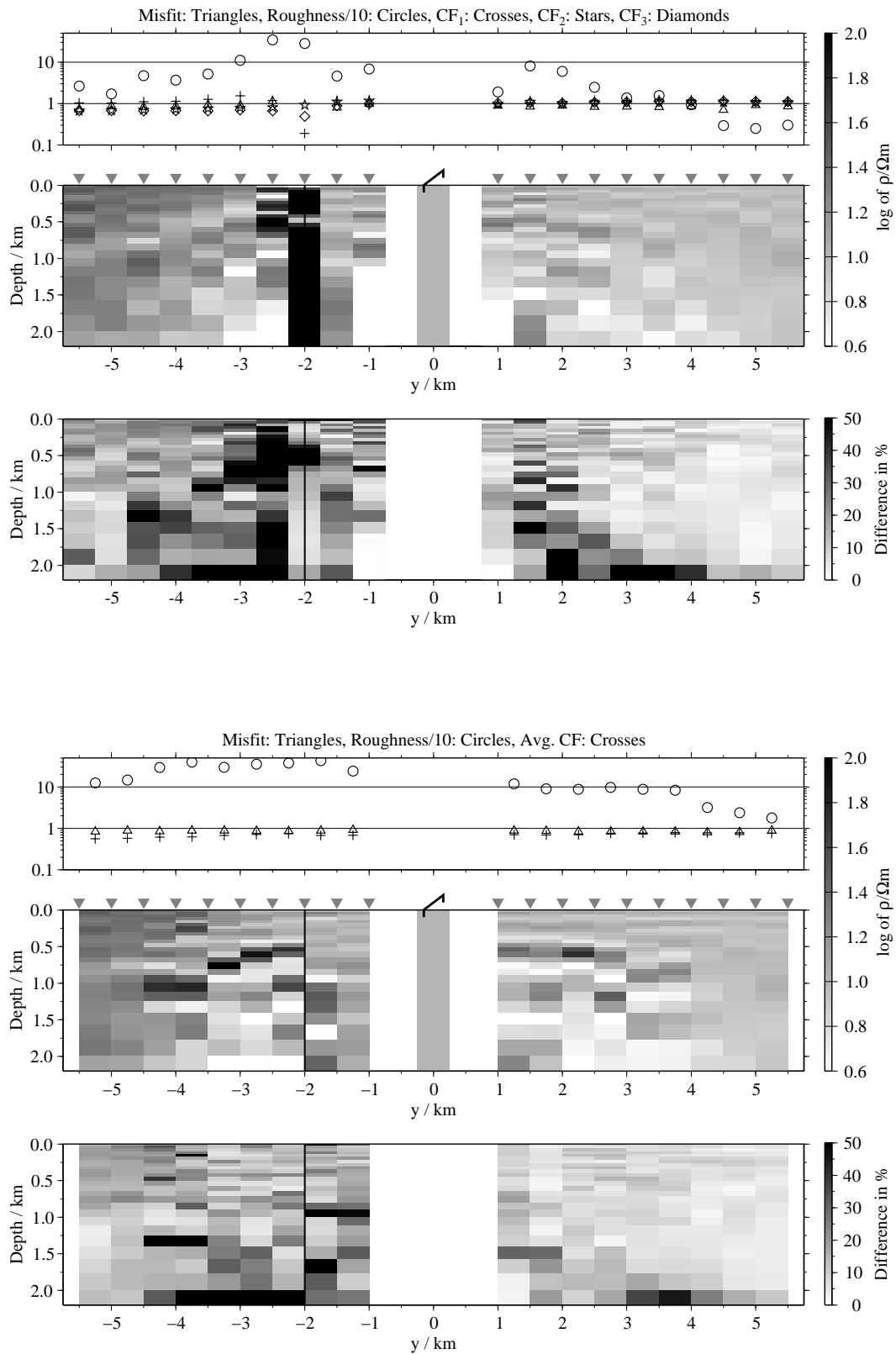


Figure 5.58: Pseudo-sections for all three LOTEM components, regularisation scheme C4, model F1; top: Results of SJI of data sets of one station each; bottom: Results of the SJI of the shortened transients of two adjacent stations;

Fig. 5.57 shows a comparison between pseudo-section derived from FJIs using all three components. The upper panel shows the result using only the data sets from one station. The lower panel shows the results using the shortened transient from two adjacent stations. The pattern of the artifacts is similar. The main difference is that the FJIs of the original transients fail to converge at a low misfit level for all stations at $y \leq 2$ km.

Unfortunately, the SJIs using more than two data sets of adjacent stations also introduce more correlated artifacts to the pseudo-sections than the SJIs of single stations. Fig. 5.58 shows a comparison between the SJIs of all three components. The upper panels show the results using the data sets from only one station. The lower panels present the results using the six shortened data sets from two adjacent stations. The pseudo-section here exhibit far more spurious structures. These are not reflected in the panels showing the differences. However, the results are still better than for the FJIs (fig. 5.58). The removal of distorted data points from the magnetic transients reduces also the artifacts close to the fault line.

The results for model K3 are similar. Again, lateral fluctuations are suppressed but laterally correlated artifacts are more obvious. Fig. 5.59 shows a comparison between the pseudo-sections derived from all three components for the two approaches. The shallow resistive artifact is slightly more pronounced in the lower pseudo-section presenting the results for the SJIs using the transient from adjacent stations. Nevertheless, the pseudo-section is laterally smoother than the one derived using only the data sets from one station (upper panel, fig. 5.59). The stabilising effect can also be observed in the panels showing the relative differences between the three or six models, respectively. For the six components case the relative differences are less erratic distributed than for the three components case.

The pseudo-sections for model M show similar results. The biggest difference to the results from the previous sections can be found in the joint-inversion results for one individual component simulated for adjacent stations. Fig. 5.60 shows a comparison for the E_x -components. The single inversion pseudo-section (upper panel) shows an erratic behaviour, in particular for $y < 0$ km. The FJIs for two E_x -transients of adjacent stations (middle panel) result in a far more consistent pseudo-section. Shallow resistive artifacts are found in the models at $-4 < y < 2$ km. The deep confined conductor is better resolved than in most other pseudo-sections. Similar results are obtained using the SJI approach (lower panel of fig. 5.60). The pseudo-section shows some spurious structures for model at $-2 < y < -1$ km. Also, the deep conductive features show slightly higher resistivities. The shallow artifacts are suppressed. The confined conductor at depth ($-4 \leq y \leq -2$ km) is slightly better resolved. For both – FJIs and SJIs – this conductor is still visible for sites with $y < -4$ km.

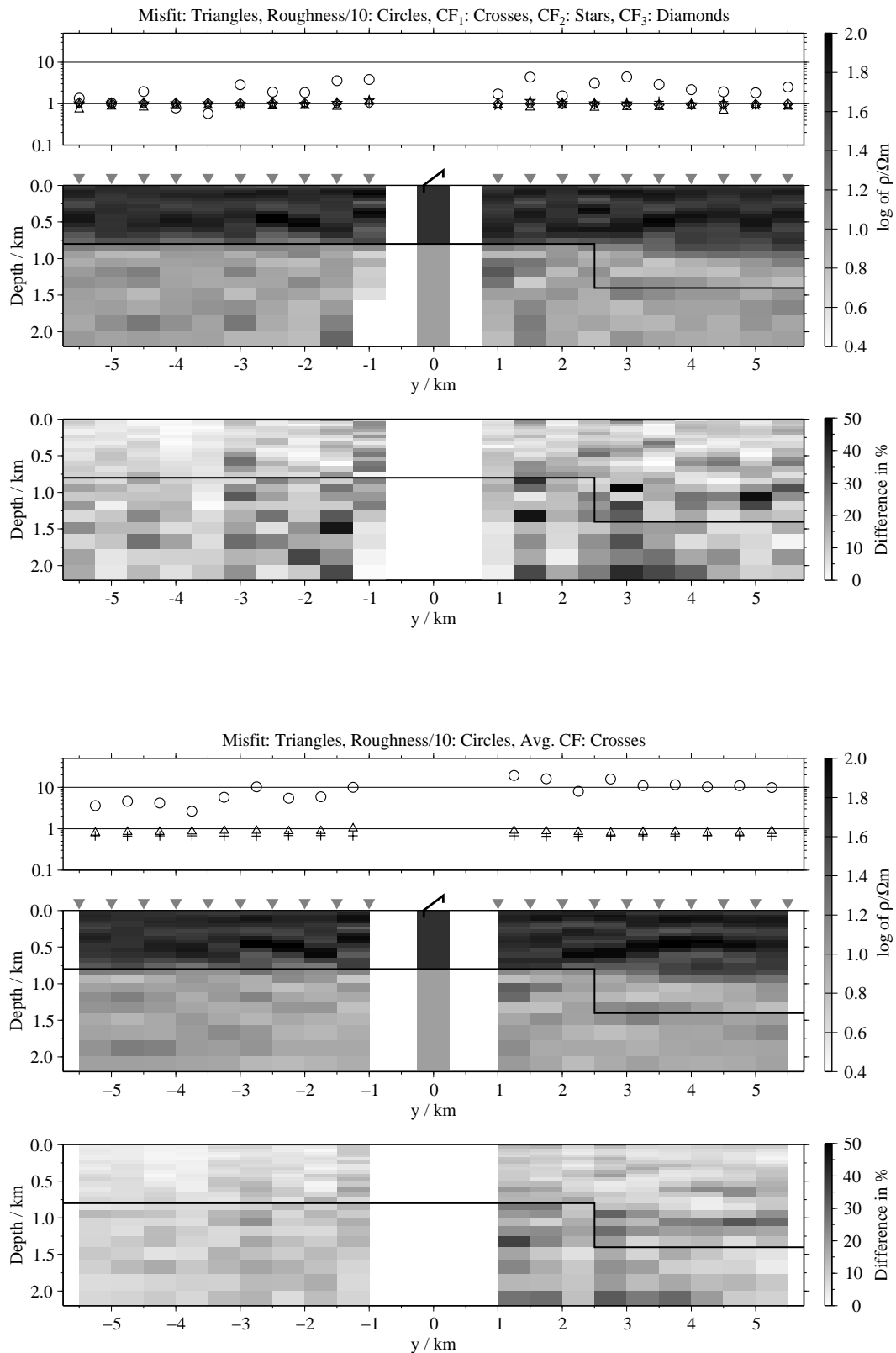


Figure 5.59: Pseudo-sections for all three LOTEM components, regularisation scheme C4, model K3; top: Results of SJIs using data sets of one station each; bottom: Results of the SJIs using the transients of two adjacent stations;

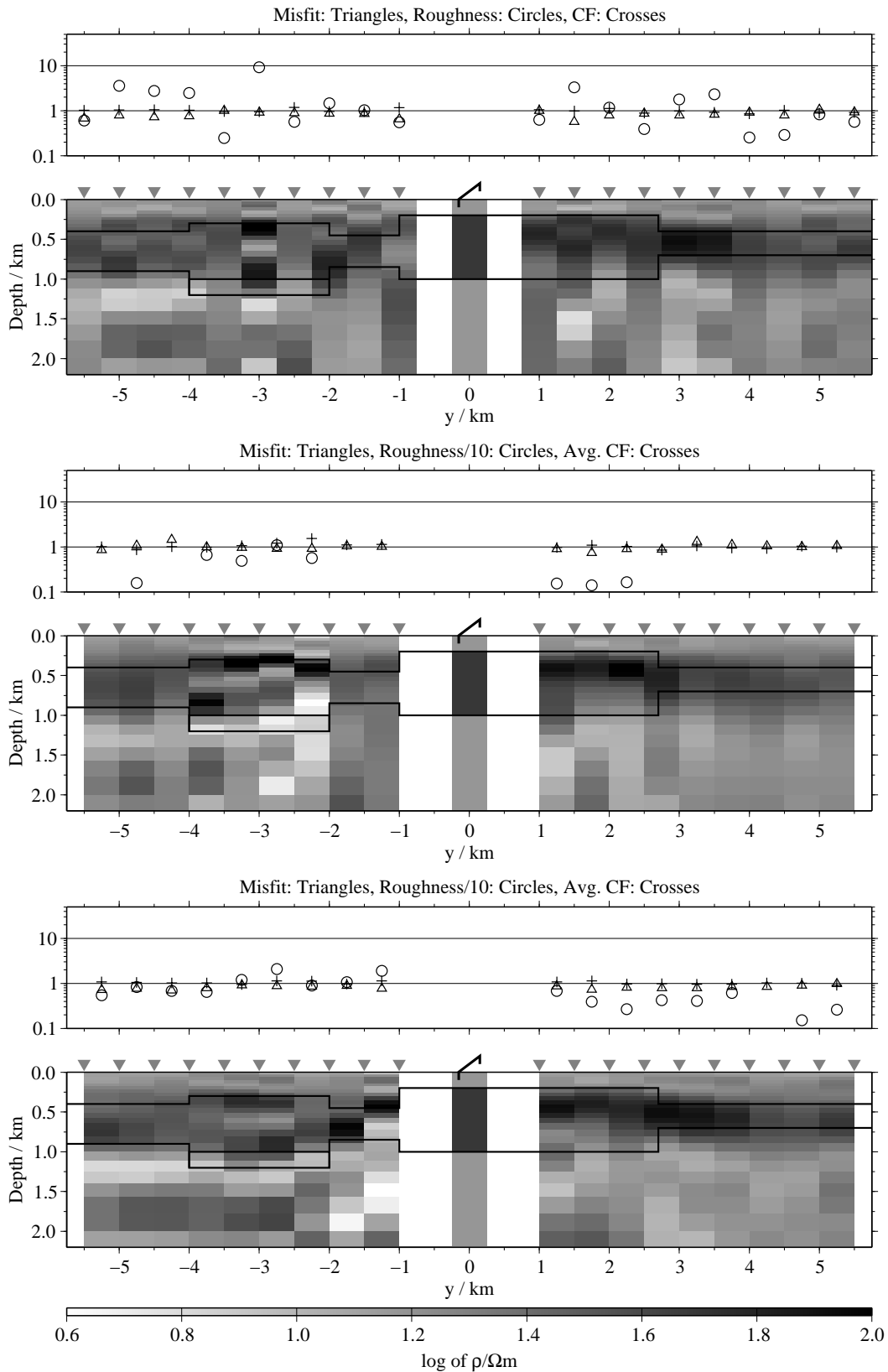


Figure 5.60: Pseudo-sections for the E_x -components, regularisation scheme C4, model M; from top to bottom: Results of the single inversions, results of the FJIs using the transients of two adjacent stations, results of the SJIs using the transients of two adjacent stations;

5.8 An interpretation scheme for the field data sets

The simulations in this chapter showed that in many cases it is possible to derive useful models from 1-D inversions in presence of multidimensional structures. Of course one can not expect that the 1-D pseudo-sections reproduce the multidimensional resistivity distribution perfectly. Nevertheless, the final models often resemble the gross resistivity structure in the area.

In general, the single inversions of the measured data sets will result in different models. In some cases the differences are not significant and will lead to similar geological interpretations, i.e. a certain feature appears at slightly different depths or with slightly varying resistivities. In other cases the models will exhibit completely different features. These differences can be caused by different resolving capabilities, noise levels or distortions of the transients. The question is which feature represents the geology and which is artificial.

None of the three components examined in this work is less distorted than the others in all cases. Unless the distorting structure is known, it will not be possible to decide which model resembles the true situation best. This means that no component can be excluded from the start.

Unfortunately, the FJI approach is not suitable, as it tends to introduce artificial structures in models. Artificial structures are significantly reduced using SJIs instead. Still, in some cases artificial structures are observed. The artificial structures seem to change for inversions of different components or subsets of components. Therefore, the best way is to carry out SJIs of different sets of components and to interpret only features which are stable in a variety of inversions. Structures which are only found using joint-inversions should be considered unreliable.

The model calculations showed that models can be distorted in shallow parts and still reconstruct deeper structures well. This means that even if a shallow feature is considered spurious, deeper structures can be accepted.

The misfit is no help in judging the reliability of the final models. In some cases even distorted models produce low misfits. In other cases the misfit was higher, but the synthetic model was reasonably reconstructed. Joint-inversion results will produce higher misfits even if the underlying model is 1-D simply because of varying noise on the different data sets (see examples for model A in sec. 5.2.3). For real data sets the inherent inconsistencies will be higher because of slight inaccuracies with respect to the system response or the measurement geometry. This means that joint-inversion results have to be accepted although their misfit is higher than for the single inversion results. The question would be how much higher the misfit may be before rejecting the model. SJIs in general showed far smaller misfits, as individual features of the data set can be accounted for in the models.

For the interpretation of the field data set, I will mainly judge the similarity to other inversion results, unless the misfit of one model is much higher (say a few hundred percent). Nevertheless, I will consider models with lower misfits more reliable.

In most cases, the joint-inversions with the SHOTEM-transients resulted in a better model resolution. However, the SHOTEM-transient will resolve a different part of the subsurface. Thus, inconsistencies between SHOTEM and LOTEM data sets

thus can be expected and joint-inversion might fail. As the model calculations showed, this does not necessarily mean that the deeper part of the earth model which is resolved by the LOTEM transients is completely distorted.

The removal of distorted data points by comparing the transients from adjacent stations and jointly inverting these data sets mainly reduced lateral fluctuations in the models. Although this is useful, bigger artifacts are not reduced much. Still, this step will be useful to check the consistency within one component (e.g. if the sensors worked well).

The different regularisation schemes had no obvious effect. The resulting pseudo-sections are similar. The models derived by strategy C4 resulted in slightly smoother models. No artifact was significantly suppressed. I will choose this regularisation scheme for the field data sets because of the smoother results.

The introduction of the Tx-distortion parameters can help to derive consistent results, at least when inhomogeneities are expected close to the Tx. According to Strack [1992] this is frequently the case in field situations. However, these parameters will introduce additional ambiguity in the inversion process. The use of the distortion parameters will only effect inversions including horizontal field components. In the best case it will be possible to find more consistent models in joint-inversions between \dot{H}_z data sets and horizontal field components.

In the field measurements presented in the next chapter, the Tx-Rx-geometry is chosen close to a broadside configuration. This means that the undistorted fields in a 1-D case produced by the virtual perpendicular Tx are close to zero. The influence of the Tx-distortion parameters is thus not expected to be very big for \dot{H}_y and E_x . The undistorted fields produced by the actual Tx for \dot{H}_x and E_y , however, will also be close to zero. Therefore, transients will likely be dominated by distortions and consequently are excluded from the interpretation.

This leads to the following interpretation scheme:

1. \dot{H}_x - and E_y -transients are discarded. Data set from the other components are edited in order to remove inconsistent features within one component.
2. SJIs using different data sets at one site (which in most cases will consist of two stations) are carried out. The SHOTEM-transients will be included if available. The SJIs are made in- and excluding the Tx-distortion parameters.
3. The models are compared. The reliability of the features are judged based on
 - (a) how consistent they are in each SJI.
 - (b) how consistent they appear in the different SJIs.
 - (c) the number of components resolving the feature consistently.
 - (d) the misfits of the resulting models.
 - (e) the value of the calibration factors and the Tx-distortion parameters. They should not be too extreme, i.e. between 0.1 and 10, although T_y can also be negative.

If no consistent features are found, the site is discarded.

Unfortunately, the model appraisal scheme described in sec. 3.5 which will be used to check for equivalent models works with a standard Marquardt inversion. This means that a set of components has to be derived, which produces the same features considered reliable in a FJI. This set of transients (if one can be found) will then be used for the final equivalence check.

The TEM-measurements in Israel

Two of the main water resources of Israel, namely the Sea of Galilee (also known as Lake Kinneret or Lake Tiberias) and the Yarkon-Taninim Cretaceous aquifer are threatened by salinisation. However, the sources and mechanism of salination are still subject to on-going scientific debates. Regarding the saline sources, which constitute the saline end members, these are attributed either to dissolution of salt deposits, trapped brines or seawater or to current intrusion of seawater. Regarding the driving mechanism it is debatable whether the saline end member has its own pressure or is being driven by the head of the fresh groundwater system. These conditions dictate different water resource utilisation policies for sustainable water management.

The debate has arisen mainly due to the absence or scarcity of borehole data. Aquifers filled with saline water should exhibit noticeably lower resistivities than aquifers filled with fresh water. Within this project we therefore applied TEM techniques to determine the existence and distribution of deep seated saline sources in the northern coastal plain and along a traverse across northern Israel between the Mediterranean and the Jordan Rift valley.

6.1 Geological Background

A NNE-SSW-trending mountain backbone of Israel forms a divide between the Mediterranean Sea in the West and the Dead Sea Rift Valley (fig. 6.1). The valley is the deepest terrestrial location on earth. The saline Dead Sea is located in the deepest part with a surface water elevation of about -400 m B.S.L. [Gvirtzman et al., 1997]. The Sea of Galilee is situated some 100 km north of the Dead Sea along the Rift Valley. It is the lowest fresh water lake on Earth, with an average water level of about 210 m B.S.L. [Simon and Mero, 1992].

The mountain range, namely the Judea, Samaria and Galilee mountains, consist

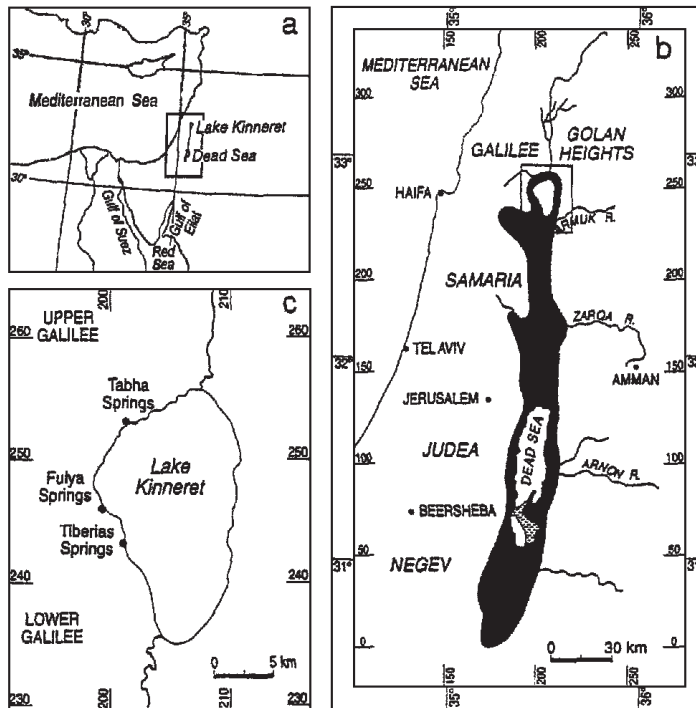


Figure 6.1: Map showing the Dead Sea Rift Valley; The rectangular in a is enlarged in b, and that in b is enlarged in c. The black area in b is the region below sea level. In c the locations of some on-shore saline springs are shown (after Gvirtzman et al. [1997]).

mainly of Cretaceous carbonate formations exposing the upper part of the Judea Group of late Albian–Turonian age. Westward, beneath the coastal plain, it is overlain by Senonian chalks of the Mt. Scopus Group, impervious clays of the Neogene Saqiye Group and Quarternary formations (fig. 6.2, Weinberger et al. [1994]).

The Galilee Mountains and the Samaria Mountains are separated by the NW–SE trending Yizre’el, Harod and Bet Shean morpho-tectonic internal valleys, which branch out of the Rift Valley (fig. 6.3). The young Tivon High and the Mount Carmel tilted block separate these valleys from the Zevulun and the Coastal Plains. The subsurface of the valleys consists of Neogene to Quarternary graben fill, composed of clastic, lagoonal and volcanic formations which unconformably overlie the Judea Group or younger formations (Kafri and Arad [1979], see also fig. 6.8 in the next section).

6.1.1 Hydrogeological background

The Sea of Galilee provides about 25% of the water consumed annually in Israel. Although the main water source of the lake, the Jordan River, has a low salinity ($\approx 20 \text{ mg/l Cl}^-$), the lake’s water salinity is higher by one order magnitude ($\approx 215\text{--}230 \text{ mg/l Cl}^-$). This is due to sometimes thermal, saline springs and seepages that discharge into the lake (fig. 6.1) with salinities up to, but never exceeding that of Mediterranean seawater ($\approx 22,000 \text{ mg/l Cl}^-$) [Kafri and Arad, 1979; Simon and Mero, 1992; Bergelson et al., 1999]. As these saline sources deteriorate the lake’s water quality significantly, it is most desirable to keep the salt output as low as possible by an appropriate water management. To do this, it is necessary to understand the salinisation mechanism, namely the driving force of the saline end member from the deep aquifers to the surface [Mazor and Mero, 1969; Simon and Mero, 1992; Gvirtzman et al., 1997].

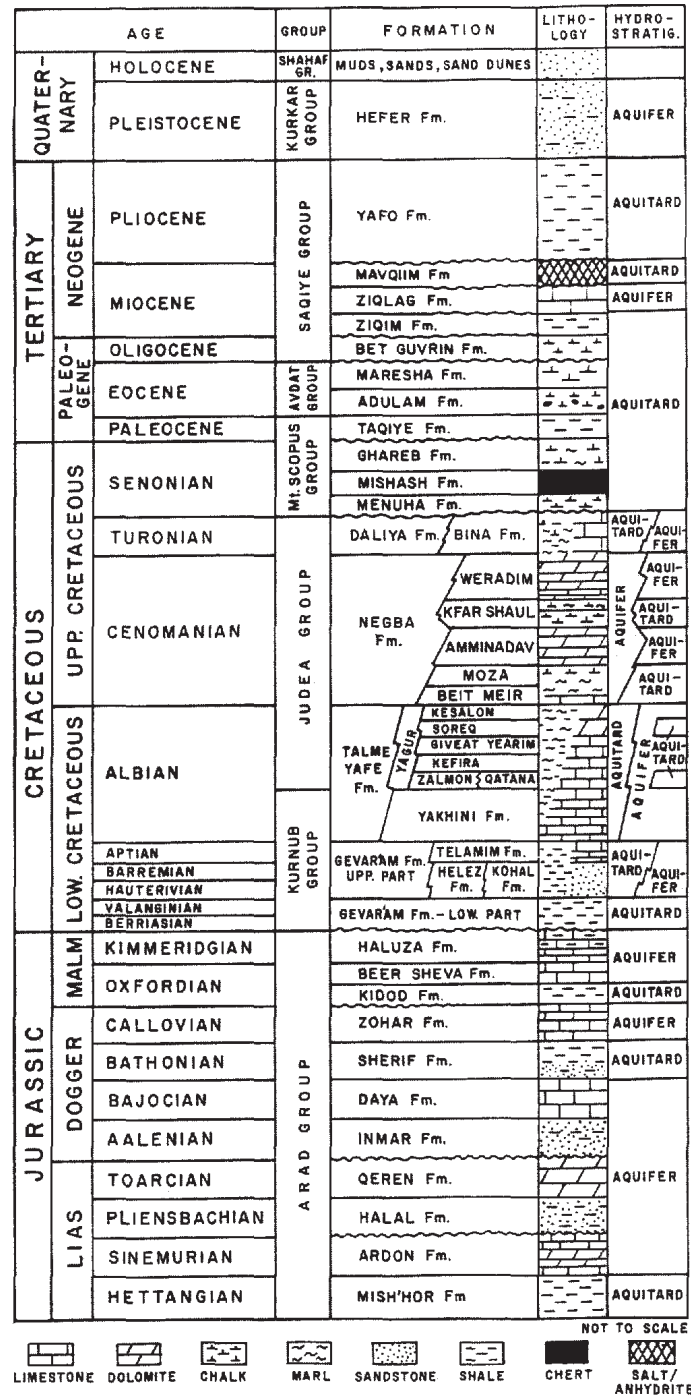


Figure 6.2: Stratigraphic column of the coastal plain after Weinberger et al. [1994]; For the internal valleys (fig. 6.3) the Neogene and Quaternary part differs.

In principle, most researchers agree that the water from the saline springs is a mixture of hot brines and fresh meteoric water derived from different aquifers. However, there is disagreement about the origin of the saline end member, the mixing mechanism and the driving force [Mazor and Mero, 1969; Simon and Mero, 1992; Gvirtzman et al., 1997].

During the Pliocene, the old "Mediterranean" invaded the Rift Valley through

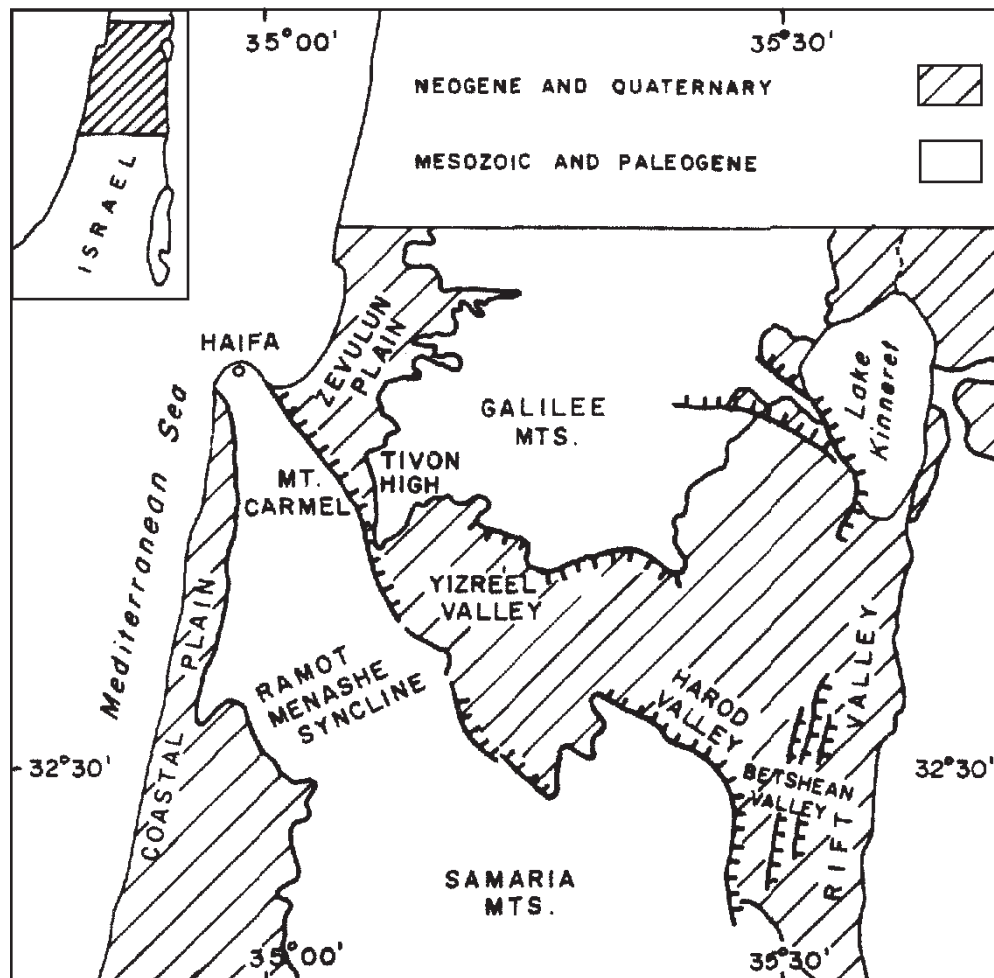
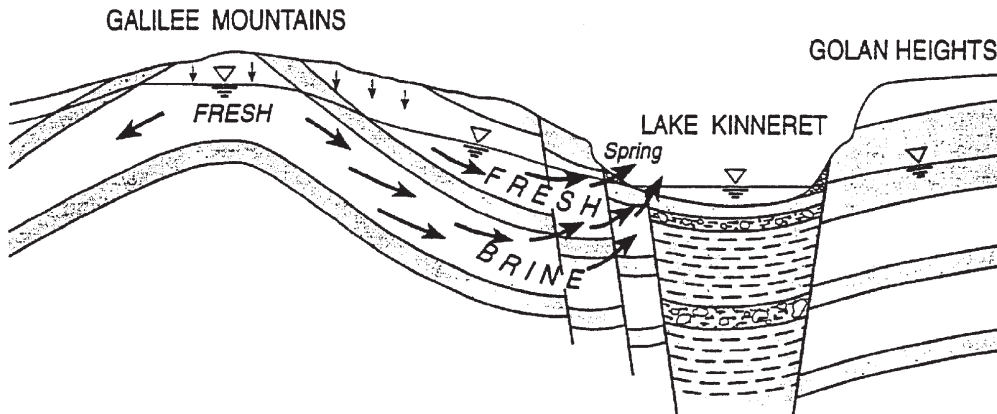


Figure 6.3: Generalised geological and location map of the study area (from Kafri and Arad [1979]);

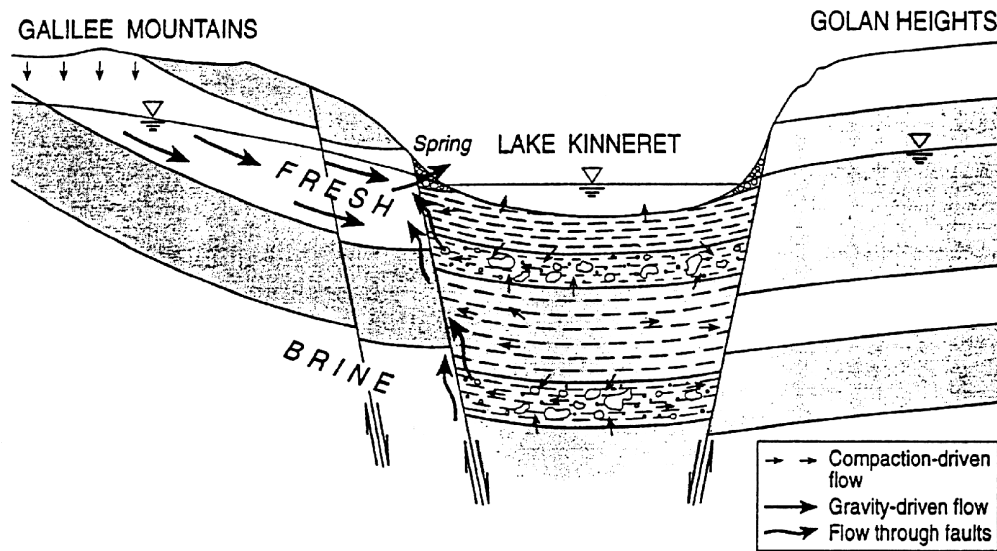
the Yizre'el, Harod and Bet Shean valleys. These waters became trapped after the disconnection of the ocean from the Rift Valley [Mazor and Mero, 1969; Kafri and Arad, 1979]. Following Goldshmidt et al. [1967] this trapped water changed from seawater to highly concentrated brine by evaporation and penetrated deep geologic formations. According to their model, the upward movement of these brines is governed by meteoric water, recharged in the eastern Galilee. The hydraulic head of the shallower fresh water aquifers drives the brines from deeper horizons (fig. 6.4a). According to Mazor and Mero [1969], the trapped water was only slightly evaporated, before entering the aquifers. It is presently squeezed out by tectonic pressure (fig. 6.4b) and mixes with meteoric fresh water. Kafri and Arad [1979] proposed as an additional saline source the recent intrusion of Mediterranean seawater. The topographical difference of 210 m between the Mediterranean and the Sea of Galilee base levels drives the water towards the Rift Valley (fig. 6.4c). Flexer et al. [2000] on the other hand suggested a halite dissolution mechanism. The hypotheses are reviewed e.g. by Mazor and Mero [1969], Simon and Mero [1992] and Bergelson et al. [1999].

The other important source of fresh groundwater is the Yarkon–Taninim aquifer, which is formed by the western part of the Judea Group aquifer (formations 3-5

a: Model by Goldshmidt et al. [1967]



b: Model by Mazor and Mero [1969]



c: Model by Kafri and Arad [1979]

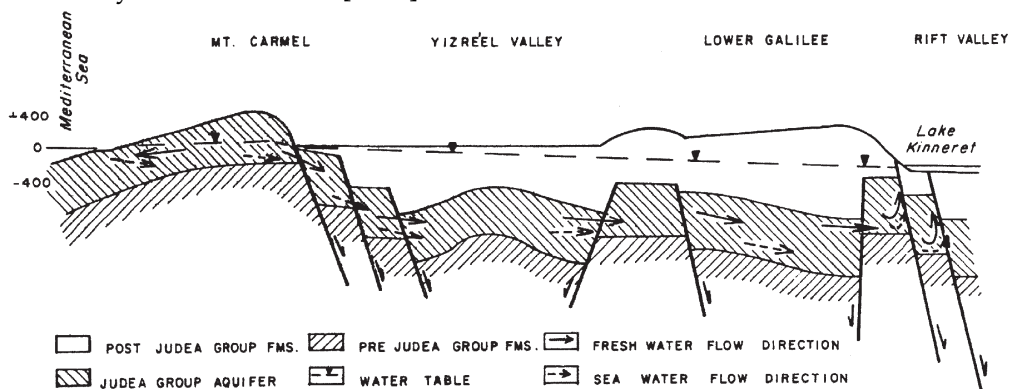


Figure 6.4: Schematic E–W cross sections illustrating the models suggested for the emergence of the saline water through springs at the Sea of Galilee (Lake Kinneret): Panel a shows the model by Goldshmidt et al. [1967], where deep seated brines are pushed by meteoric groundwater (from Gvirtzman et al. [1997]). Panel b sketches the model by Mazor and Mero [1969], according to which the brines are overpressured due to tectonic movements (from Gvirtzman et al. [1997]). Panel c shows the “seawater intrusion” model, where water from the Mediterranean is driven gravitational to the Rift Valley (from Kafri and Arad [1979]).

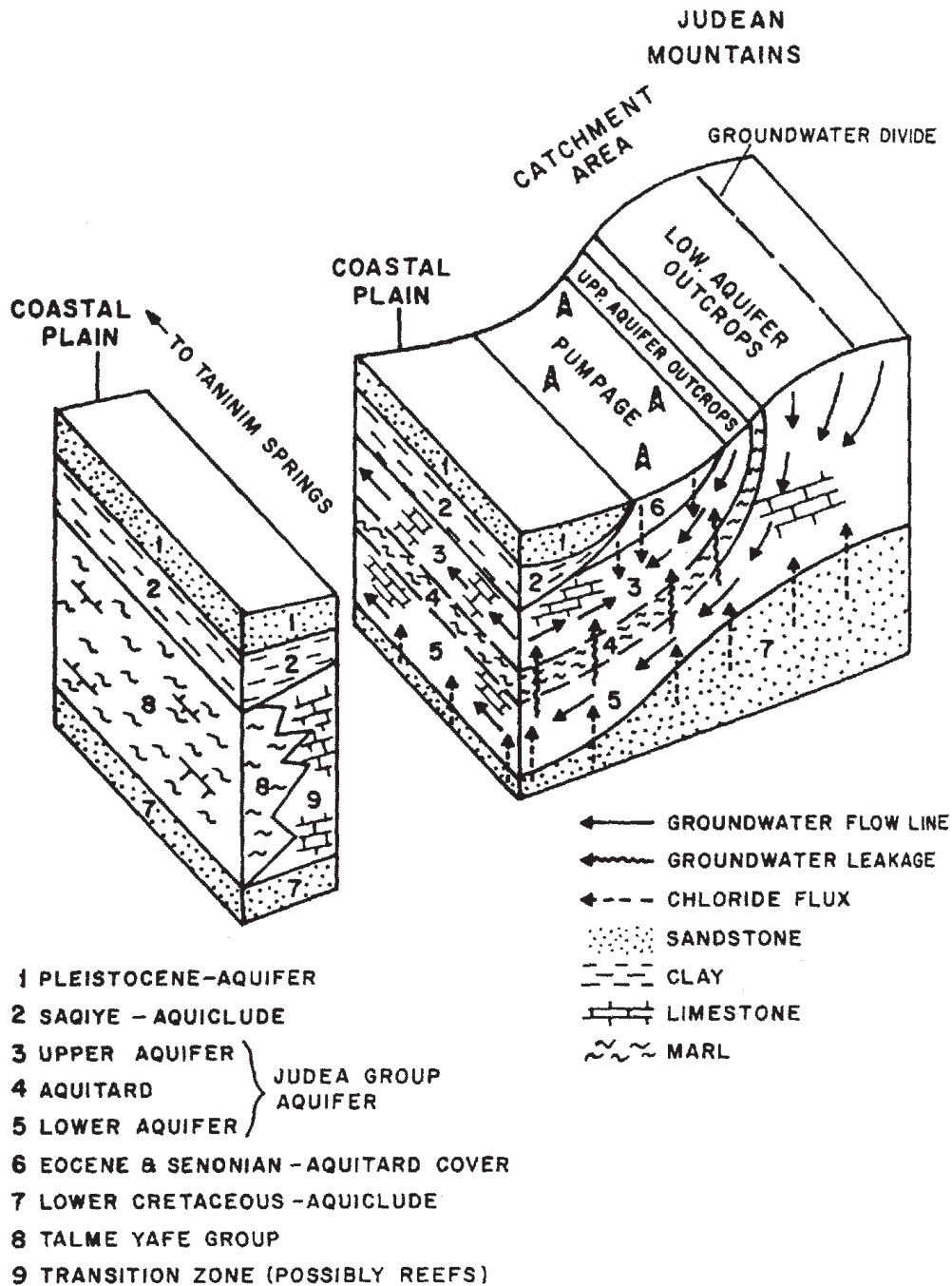


Figure 6.5: The hydrological setting of the Yarkon-Taninim aquifer (after Weinberger et al. [1994]); rainfall replenishes the aquifer in the catchment area.

in fig. 6.5). It is exposed along the Judea, Samaria and Carmel mountain backbone and extends westward in the subsurface of the foothills and the coastal plain [Weinberger et al., 1994]. It is naturally replenished by rainfall in the mountains (fig. 6.5). The western boundary of the aquifer is presumably a facies change to the marly Talme Yafe aquiclude (formations 8-9 in fig. 6.5). Therefore, a direct connection between the aquifer and the Sea was previously rejected.

The, possibly ongoing, salinisation process of this aquifer was also in discussion.

The saline sources were interpreted as (among other theories) current seawater intrusion into the northern and, possibly, southern border [Kafri, 1967; Kafri and Arad, 1979] or deep seated brines in the underlying Lower Cretaceous formations diffusing upwards (see fig. 6.5 and Weinberger et al. [1994]). For an explicit discussion see Weinberger et al. [1994].

Since 2002, several deep monitoring wells were drilled in the coastal plain (see fig. 6.7). As seawater was found in all of these wells at depths around 1 km, the seawater intrusion model is now widely accepted for this aquifer [U. Kafri, pers. comm.].

6.1.2 Geophysical task

Knowing the distribution of saline water in the subsurface of the area would greatly improve the understanding of sources and mechanisms of the salinisation. Saline water can be distinguished from fresh water mainly by the electric resistivity which decreases with salinity. EM-Methods thus are suited to map the interface between fresh and saline water [Fitterman and Stewart, 1986; Goldman et al., 1991].

Because most rocks are poor conductors, their resistivity – if porous – is governed by their pore fluid. According to Archie's empirical formula (e.g. Telford et al. [1990])¹, the resistivity can be described as

$$\rho = a\Phi^{-m}S_W^{-n}\rho_W, \quad (6.1)$$

where Φ is the porosity, S_W is the fraction of pores containing water, ρ_W is the resistivity of the water, $n \approx 2$ and a and m are constants with $0.5 \leq a \leq 2.5$ and $1.3 \leq m \leq 2.5$ depending on the formation. With seawater ($\rho_W \approx 0.2$) the effective resistivity ρ could easily be lower than most other lithologies (depending on the porosity).

Goldman et al. [1991] mapped the seawater intrusion in the shallow coastal aquifer of Israel with a TEM system. He concluded:

- Geoelectric and lithological boundaries do not coincide necessarily. The main factor affecting resistivity is the groundwater salinity.
- The resistivity of a seawater bearing clastic aquifer is below 2.9 Ωm .

Highly evaporated brines as those suggested by Goldshmidt et al. [1967] should produce even lower resistivities, whereas brackish waters account for higher values. However, the latter may produce resistivities which can be explained by other lithological units. The geological interpretation thus might be non-unique. Still, the possible lithologies in the area has to be known. Clay layers like the above mentioned Neogene Saqiye Group, exhibit similar resistivity values to the seawater filled aquifers. Additionally, if the porosity of the host rocks is significantly lower, the resistivities of the seawater filled aquifer will be higher.

¹Archie's formula can not be applied to carbonatic formations like the Judea Group aquifer. Nevertheless, eqn. 6.1 should give an impression what influences the bulk resistivity of an aquiferous formation.

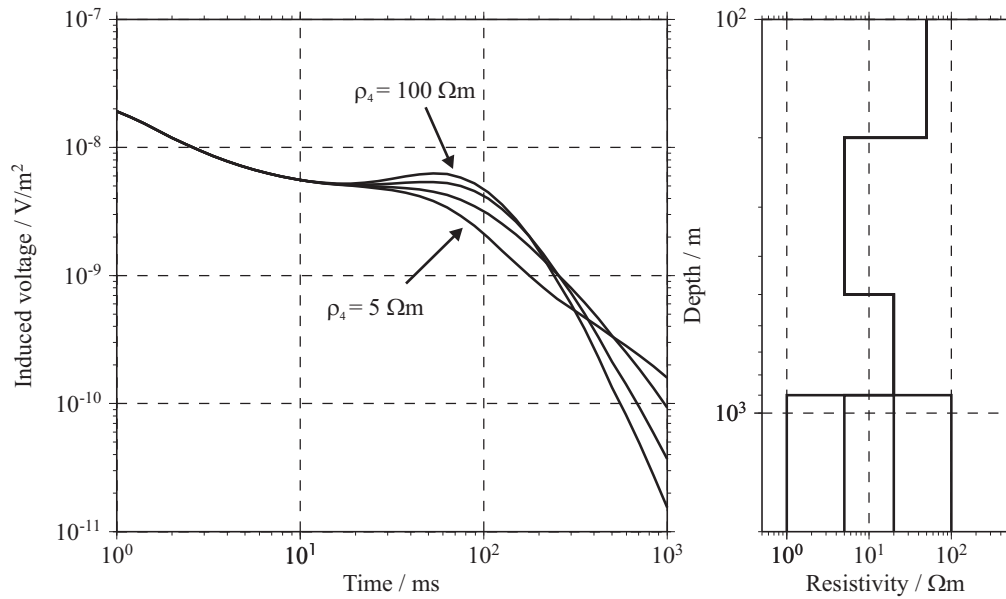


Figure 6.6: LOTEM-calculations for the expected earth model; the target is the fourth layer of the model displayed in the left panel. The right panel shows the induced voltages in a \dot{H}_z -sensor with an area of 1 m^2 and an offset of 3 km from a dipole Tx with a dipole-moment of 10,000 Am (broadside configuration) for four different resistivity for the fourth layer (1, 5, 20 and $100 \Omega\text{m}$).

The aim of the project is to determine the depth of a fresh to saline water interface in the Judea Group aquifer. This means to derive the resistivity at a depth of approximately 800–1200 m, which is deeper than the expected exploration depth for the Geonics SHOTEM equipment used by our Israeli partners but a proper target for a LOTEM survey. SHOTEM data can be used to constrain the shallow part of the subsurface.

Model calculations carried out previous to the campaign based on the expected parameters provided by our Israeli partners suggested an Tx-Rx-offset of about 3 km would be optimal. With this setup, the target should be visible in the transient after ≈ 50 ms (fig. 6.6).

6.2 The field campaign

The LOTEM measurements were carried out in two stages. The first stations were recorded in spring of 2002 and all others in December of 2003. The SHOTEM measurement where made between summer 2001 and spring 2005 (except for the stations BSH7, BSH19, BSH20 and BSH21 in the SE, where the transients from a different campaign were used).

To cover an area this large, we chose to set up selected Tx-Rx-spreads consisting of one Tx and two Rx-sites in broadside configuration on either side of the transmitting dipole. The data would be interpreted geophysically using 1-D inversions. In most cases a switching time of 1 s was used [Scholl, 2001]. The transmitters are designated by two characters.

To analyse distortions, it was planned that each Rx-site consisted of at least two

Rx-stations which are spaced around 200 m from each other. In total 21 LOTEM-Tx were set up, recording multicomponent data sets for 74 Rx-stations. The different LOTEM-Rx-sites are designated by an additional character. The stations of one site are enumerated. Thus, "GBA1" is the first station of the A site used with the Tx GB. The Rx-site names are shown in the upper panel of fig. 6.7. The Tx-designations can be found in fig. 6.8. In most cases it is not necessary to discriminate the different stations of one site, as all transients recorded at one site are interpreted jointly. Their coordinates can be found in app. C, together with all other information regarding the field setup.

As the target is conductive, mainly magnetic sensors were deployed. For broad-side configurations and a 1-D layered earth, \dot{H}_x - and E_y -component should be identically zero. Therefore only a few \dot{H}_x - and E_y -transients were recorded within this campaign.

The upper panel of fig. 6.7 shows the locations of all sites in the northern area. An additional Tx was set up close to the coast ≈ 30 km south of the map, close to Ra'annana (Tx-designation RA). The sites can be divided into two groups: The coastal sites (GA, GB, EN, PH, RA, TA) close to recent boreholes and the traverse (all other stations) covering the area between the Mediterranean and the Rift valley. As the boreholes drilled close to the coastal stations provided useful lithological and salinity information, these sites are used for calibration. The resistivities derived from the geophysical interpretation were compared with the borehole information. Also, the geophysical interpretation strategy developed in chapter 5 should be tested.

The SHOTEM data set consists of 43 transients recorded close to the LOTEM-Rx- and -Tx-positions (see lower panel of fig. 6.7). For logistical reasons at most places only data could be recorded using the Geonics Protem equipment. These almost never reached the target and could only provide additional information about the shallow parts of the subsurface. At twelve places additional SHOTEM-transients were recorded using the bigger and more powerful Cycle-5M equipment. These data sets provide roughly the same exploration depth as the LOTEM data. If Cycle-5M data was available at a certain site, it was preferred for the combined interpretation.

Along the traverse some stations were also placed near boreholes. Originally, they were planned as calibration sites because the coastal wells didn't exist when the project commenced. Later it turned out that there is little usable information from these boreholes. Moreover, as they are mainly oil exploration wells, they are made in tectonical structures which could serve as oil traps. The assumption of one-dimensionality thus is not fulfilled and the data in most cases turned out to be distorted.

For several reasons, the surveyed area is very challenging for geophysical and especially EM-methods. The area is intensively used for agricultural and industrial purposes. This limits the possible measurement sites. Often fields used for a SHOTEM measurement could not be used for a LOTEM-Rx some months later because of crops growing there. Most acres are irrigated and a dense network of water pipelines is found almost anywhere. Those metal pipelines may act as near surface conductors and can distort any measurements of EM-fields. Also widespread power-lines produce high EM noise levels. This justifies the use of an active EM-

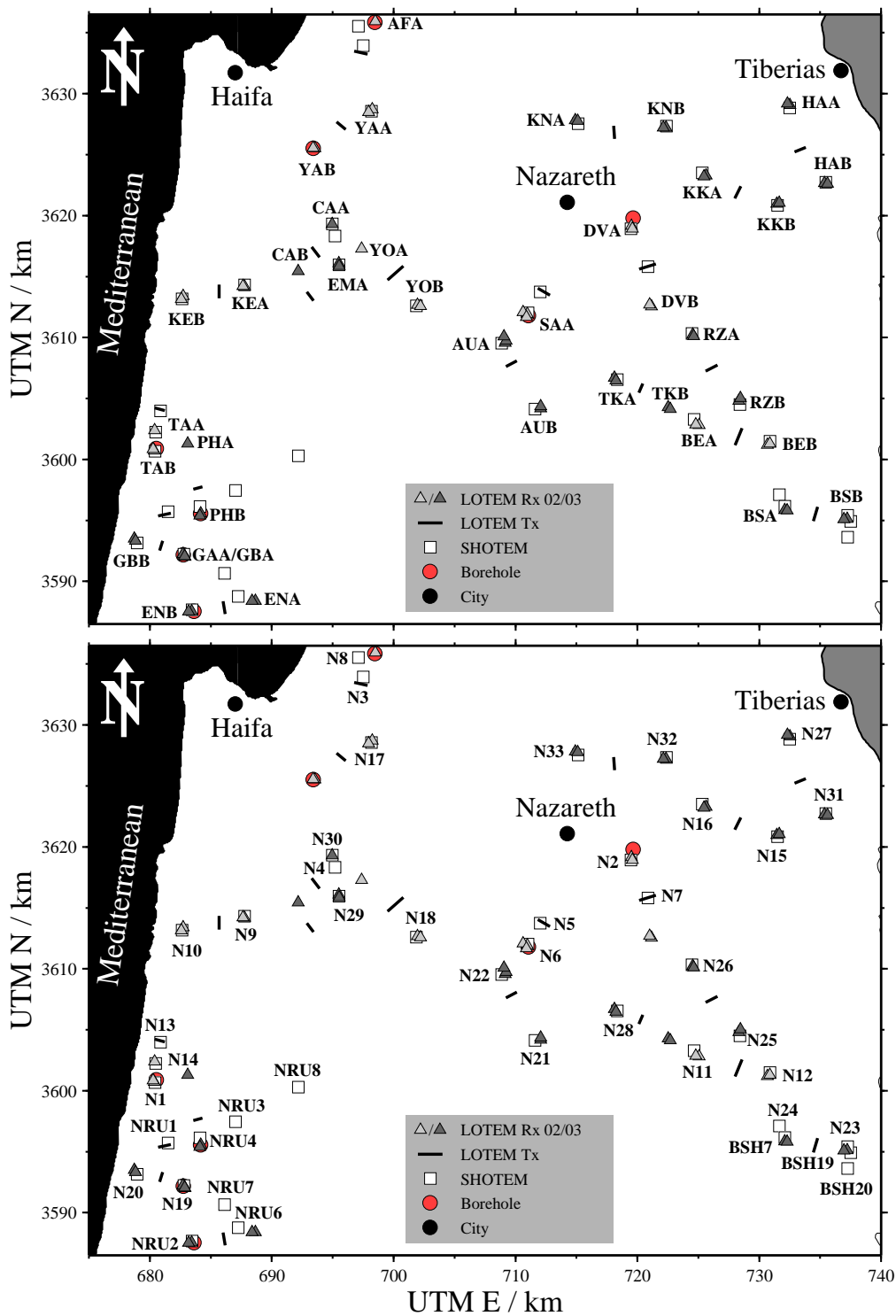


Figure 6.7: Maps of the northern Rx-stations; There is an additional LOTEM-Tx ≈ 30 km south of the map in the coastal area with the two stations RAA and RAB in addition to a SHOTEM site (NRU5). See also the left panel of fig. 6.21. Top: Designations for all LOTEM Rx-sites. The first two letters of the Rx-site's name denotes the name of the Tx with which the Rx was used (see fig. 6.8). The different Rx-positions within one Tx-site are not labelled here, as they are not discriminated in the inversions. See app. C for the exact coordinates. Bottom: Designations for the SHOTEM stations. At all SHOTEM sites data sets were recorded with the Geonics equipment. Additionally, at N1-N4 and all NRU sites the Cycle-5M system was used.

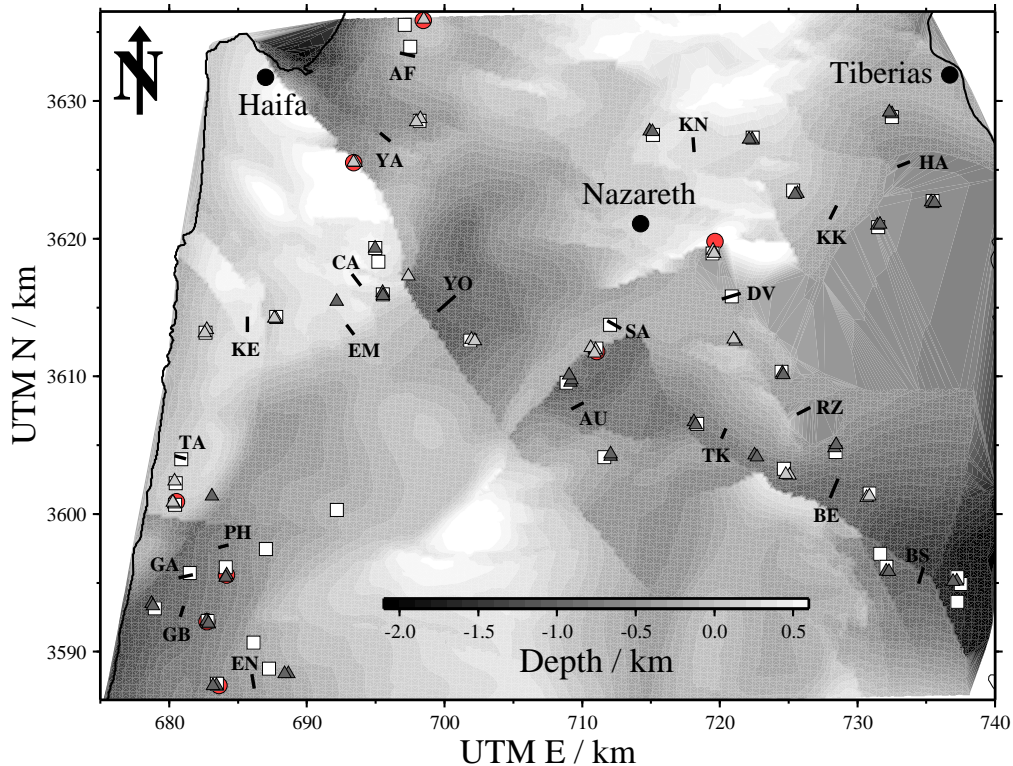


Figure 6.8: This map shows the elevation of the top of the Judea Group and the designations of the LOTEM-Rx. The elevation information was provided by the GII.

method.

The area still is tectonically very active with a lot of faults cutting through the entire region. Fig. 6.8 shows the topography of the Judea Group as compiled from seismic measurements by the GII (e.g. Rotstein et al.). It is clear that the 1-D-assumption is valid only for small parts of the area. Unfortunately, this information was not available in the planning phase of the first LOTEM measurement in 2001. For the second measurement the LOTEM sites were planned according to this map to at least minimise the multidimensional effects. However, this was not possible in all cases because some positions were fixed to borehole locations or simply restricted by logistical issues.

6.2.1 LOTEM system response

Unlike any other campaign, each day a new Tx was set up and used. Fortunately, in most cases the top soil consisted of a clayey material. It was possible to get low contact resistivities with little effort, resulting in relatively high transmitting currents. These provided a reasonable SNR in most places, although the EM-noise was high. The shallow part of the subsurface was not considered to be interesting for the LOTEM part, as the SHOTEM transients should provide information about these upper layers. Low sampling rates were therefore selected.

The system response was only measured twice. In 2002 a Tx close to the SA-Tx was set up especially for this purpose. In 2003 the Tx at Ramat-Zevi (RZ) was used. Individual transmitting current functions could thus not be considered. In 2003 the

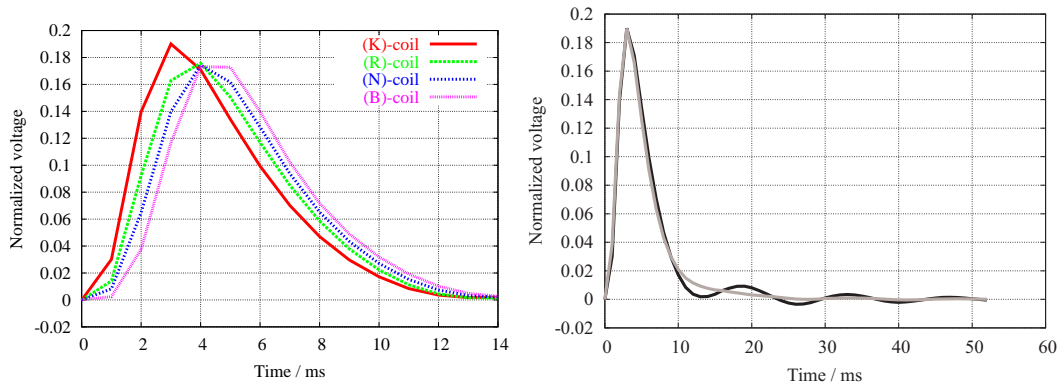


Figure 6.9: Processed system responses from the field campaign for the TEAMEX units with a 100 Hz high cut filter; left: Early time part of the system responses for four different magnetic sensors (explained in the text); right: Full system response for the (K)-coil; the black line shows the original system responses exhibiting strong oscillations. The gray line shows the same system response after removal of the oscillations.

current function was measured by an experimental device. Unfortunately, those data were not usable due to technical problems.

In total, five different magnetic sensors were used (for the system responses see the left panel of fig. 6.9):

- The standard Cologne LOTEM air coil, custom built out of a seismic cable with 108 leads; here, 54 leads are connected to form the coil and 54 are bypassed. Laid down a square of $40 \times 40 \text{ m}^2$ this results in an effective area of $86,400 \text{ m}^2$ (designation "(N)" in tables).
- A TEM-3 induction coil, manufactured by Zonge Engineering; this coil was mainly used for the horizontal magnetic fields. Including an amplifier, the coil has an effective area of $10,000 \text{ m}^2$ with a shorter system response than the air coil [Donat, 1996; Stahl, 1999] (designation "(K)").
- The coil from the Cycle-5M SHOTEM system; this small coil (only $4 \times 4 \text{ m}^2$) also comes with an amplifier, resulting in an effective area of $250,000 \text{ m}^2$. The system response is comparable to the one of the Longe TEM-3 coils (designation "(R)").
- A standard Cologne air coil, but with all 108 leads connected to form a coil with an effective area of $172,800 \text{ m}^2$; the system response is comparatively long (designation "(B)").
- An old version of the standard cologne air coil; this coil was shipped as backup coil. It was used only on the last day of the 2003 measurements. No special system response was recorded in Israel, thus a (N) system response was used (designation "(O)").

Like in previous field campaigns, measuring a system response for the electric components failed for as yet unknown reasons. As Müller [2000] suggests, I chose to use a \dot{H}_z -(N)-system response for the electric fields instead. During a LOTEM field campaign in Jordan in 2002 [Koch et al., 2004] we found that the system

response for the electric fields depends on the contact resistivity of the receiver dipole. If the contact resistivity is higher than a few $k\Omega$, the system response gets considerably longer. This effect is more pronounced for the SUMMIT-TEM system but also visible on the TEAMEX units. During the 2003 measurements the contact resistivity of all electric fields was logged. Still, the early times of the electric fields – especially for the 2002 data – are not considered to be very reliable.

From both system response measurements a set of system responses for the different sensor/recording units is produced. The system response recorded showed strong oscillations (black line in the right panel of fig. 6.9). This was also observed in the field by the Tx-operator using an oscilloscope.

The oscillations can be described well with $\exp(At)(B \sin Dt + C \cos Dt)$. To get an oscillation-free system response, this function is fitted to the part of the system response, where the influence of the receiver unit and sensor is negligible (say, $t > 15$ ms). The parameters A to D are adjusted with a Marquardt inversion. Then, the function is subtracted from the system response. The gray line in the right panel of fig. 6.9 show the same system response with the oscillations removed.

Some of the measured transients show these oscillations and some do not (cp. app. C). The strength of those oscillations seem to depend on the Tx used. Some earth responses also can reduce the oscillations. If the early time part of the earth response is an asymptote of the length of one period of the oscillation, the latter will be suppressed. For the interpretation, an inversion with the oscillating responses was first made. If the forward curve of the resulting model showed more oscillations than the measured transient, the inversion was repeated with the non-oscillating system response.

6.2.2 Special problems

The Tx position was fixed on the morning of each day of measurement. The orientation of the x-direction – needed to set up the horizontal electric and magnetic sensors – was calculated in the field from standard GPS measurements. The measurement of the Tx-electrodes' positions were repeated later with differential GPS measurements, which are more accurate. The orientation derived from the differential GPS measurements in general differed by a few degrees from the previously measured orientation, which was used to set up the Rx-sites. Most horizontal components thus are actually not measured exactly in the x- and y-direction, respectively. Therefore, the horizontal components were interpreted as rotated fields E_{xy} and \dot{H}_n [Müller, 2000]. On two days the Tx-orientation was miscalculated in the field (Tx SA and GA). Here, the deviation is significantly higher.

Another problem occurred regarding the (R) and (B) magnetic field sensors. As mentioned, the (R)-coil uses an active amplifier to increase its effective area. This amplifier is powered by a pack of chargeable batteries. Instead of a display showing the charge of the batteries, there is only a flashing LED. Unfortunately, even with nearly empty batteries, the LED flashes for a few minutes. On the last days of the second measurements, they were mistaken for fully charged batteries. Thus, the amplifier did not work on the last days of the second measurement. Fortunately, the transients still are usable, although their amplitude does not fit the effective area of the (R)-sensor. The calibration factors used here to interpret the transients

thus are very small.

The (B)-sensor uses a multi-pin jack to connect all leads to one multi-turn coil. When dismantling the ENA-Rx-site, two pins were found bent. The transient showed clear distortions in the late times. These were also found in the data sets recorded with this sensor on the previous two days (BSA and HAB). These transients were not used for interpretation.

6.3 Inversions of the field data sets

In this section I will present the geophysical interpretation step for the measured data sets. The final results for the relevant sites along the traverse are presented and discussed in sec. 6.4. The strategy for the interpretation follows the one developed in the previous chapter (sec. 5.8):

1. Removal of time points at early and late times, for which the apparent resistivities of two adjacent stations differ; E_y - and \dot{H}_x -transients in general are discarded as they are most affected by distortions.
2. Because of the problems with the system response, the error estimates for early time points of the LOTEM transients are artificially increased. This way they have less influence on the inversion process. Early times of the electric field transients (especially from the 2002 measurement) are removed if a late polarity change indicates a high contact resistivity.
3. The different TEM data sets are joint-inverted with SJIIs with fixed and freed Tx-distortion parameters.
4. Common, stable features are sought in the inversion results. This is the most important step of the interpretation as it includes the estimation of the reliability of certain model features. In general, a feature is considered more reliable, when it is supported by a bigger number of components. Therefore, the biggest number of components is sought, which still gives consistent models. Every component, which has to be excluded is considered distorted. This does not decrease the reliability of this site's results significantly, when this distortion can be explained by e.g. problems during the measurement or the distorting geological structure is known. In the latter, only the components are used which are known to be least affected by the structure (sec. 5.3). Electric field transients are considered less reliable by default (sec. 6.2.1). In addition, inconsistent SHOTEM-transients reduce the reliability not much (sec. 5.5.3). If no consistent, stable features are found, the site is not further used in the interpretation.
5. A combination of components is derived, which reproduces the features found in the previous step in a FJI. The combination involving the most TEM data sets is preferred, as long as it reproduces the desired structures. Again the site no further interpretation steps are done, if no such combination is found.
6. The components identified in the previous step are used for Marquardt joint-inversions. The starting model is derived from the smooth model inversions.

Equivalences are checked using the approach described in sec. 3.5. The equivalence analyses are done with fix and free Tx-distortion parameters. The results of both analysis-runs are combined into one data set.

As the measured transients are earth responses convolved with the system response, the illustrated apparent resistivities are in fact “resistivity transforms” [Strack, 1992]. Sign reversals found in the LOTEM- \dot{H}_y s or distorted \dot{H}_z -transients are not marked. However, they should be obvious by their notch shape in the curves. Sign reversals in the \dot{H}_z s are indicated in the text.

The comparison of the resistivity transforms for the measured transients is less straight forward as in sec. 5.7. First, the early times might differ because of different system responses. Additionally, only one \dot{H}_z or \dot{H}_y might be available. In these cases, the single resistivity transform has to be compared to the ones from the other component.

Fig. 6.8 is used to check for geological features which may distort the transients. As pipes etc. can be found almost everywhere in the area, the assumption of the presence of near-surface distortions is prudent in general.

In all inversions, the single data points are weighted according to their error estimate. The minimal assumed error is 1 % of the data value. For the SHOTEM-measurements no error estimates exist. They are assumed to be undistorted by noise. Noisy data points, especially at the late stage, were removed prior to inversion [M. Goldman, pers. comm.]. However, for joint-inversions it is important to assume a noise level relative to the LOTEM-transients. Lange [2003] advocates a normalised weighting scheme, where every data set is as important as all others. In this study, many – mostly LOTEM data sets – were inverted jointly. Normalising all weights as proposed by [Lange, 2003] would mean to ignore different SNR of the transients. As I want to preserve the relation between the SNR of the different data sets and components, I prefer to keep the weights without normalisation. Instead, I assume an error of 1 % for the SHOTEM data sets.

This might lead to models dominated by the SHOTEM-transients. To prevent misinterpretation due to faulty SHOTEM data, the same inversions are done without the SHOTEM data set. The joint-inversion result with the SHOTEM data will only be accepted, if the model does not change significantly at depth, which should not be resolved by the short Geonics-transients.

At the SHOTEM-NRU-sites on the coastal plain, the GII provided unedited Cycle-5M data sets [M. Goldman, pers. comm.]. These may include distorted data points in the late stage, which are not obvious as no error estimates are provided (see also Lange [2003]). Inverting these sets with a fixed error estimate of 1 % would lead to results where the deeper parts are governed by inaccurate data. Of course, edited data sets would be available, but these points are used mainly for calibration and almost no Cycle-5M data sets were available along the traverse. Therefore, I chose to use these questionable data sets to see, how the outlined inversion scheme works in the case of possibly distorted SHOTEM-transients. This is discussed in sec. 6.3.1 for site ENB.

In most plots showing comparisons of different SJIs, only one resulting model is displayed. This model is considered to be representative for this SJI. The other component’s models will show a similar behaviour. The complete statistics of all

single- and joint-inversions can be found in appendix C. In all figures showing the final result including the equivalent models, the best model is plotted with a solid black line, the Occam's inversion result for the same components with a dashed black line and all models found with a misfit $\leq 110\%$ of the best fitting model in solid gray lines. In general, the equivalence analyses were done both with and without free Tx-distortion. The results are combined in one picture. However, if Tx-distortion plays an important role for fitting the data sets, it is likely that none of the models without Tx-distortion is within the 110% of the best model.

6.3.1 Calibration sites

All calibration sites are located in the coastal plain SW of the Yizre'el valley. Unfortunately, the Judea Group is overlain by a thick Saqiye Group clay layer at sites ENB, GBA, PHB and RAB. These clays exhibit very low resistivities of a few Ωm , shielding the deeper Judea Group.

Site ENB

There are no obvious geological distortions visible in fig. 6.8. However, the surface of the Judea Group is more shallow below the Tx than below the Rx. Fig. 6.10 shows the resistivity transform curves for the magnetic fields recorded at site ENB close to the borehole Beit-Eliezer. Additionally, one E_x -component was recorded. The SHOTEM data set NRU2 was recorded at the Rx-site, using the Cycle-5M equipment. It provides a transient with a length of 400 ms.

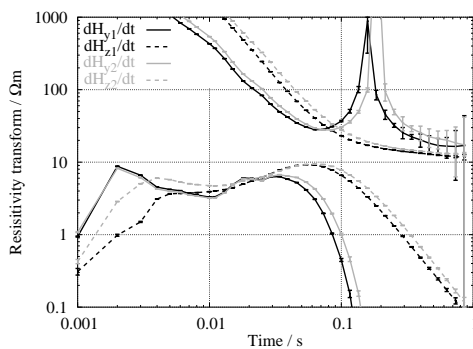


Figure 6.10: Resistivity transform curves for the Rx-site ENB;

More interestingly, the conductor in the SHOTEM model appears at depths greater than 1500 m.

Adding the electric field data, the resistivity of the resistor above 1000 m depth increases (fig. 6.11b). Additionally, a shallow conductive feature is introduced, which is also visible – although it appears thicker – in the SHOTEM inversion result.

If the SHOTEM-transient is inverted jointly with the LOTEM data sets, the fit is degraded. The long Cycle-5M transient dominates the inversion results. All SJI-results incorporating the SHOTEM data set are similar to its single inversion result. As an example, fig. 6.11c shows the models resulting from a SJI of all six TEM-components. Again, the conductive feature is much deeper than suggested by the LOTEM inversions (fig. 6.11d).

Both \dot{H}_z -transients differ up to 20 ms. Therefore, the first 9 data points were removed prior to inversion. The SJIs of the magnetic components found similar models, all showing a distinct conductor in a depth of around 1000 m (fig. 6.11a). Below, all models show an increase in resistivity, which is unrealistically high for the \dot{H}_y -components if no Tx-distortion is allowed (dashed line). The SHOTEM-transient shows more structure in the upper part. More interestingly, the conductor in the SHOTEM

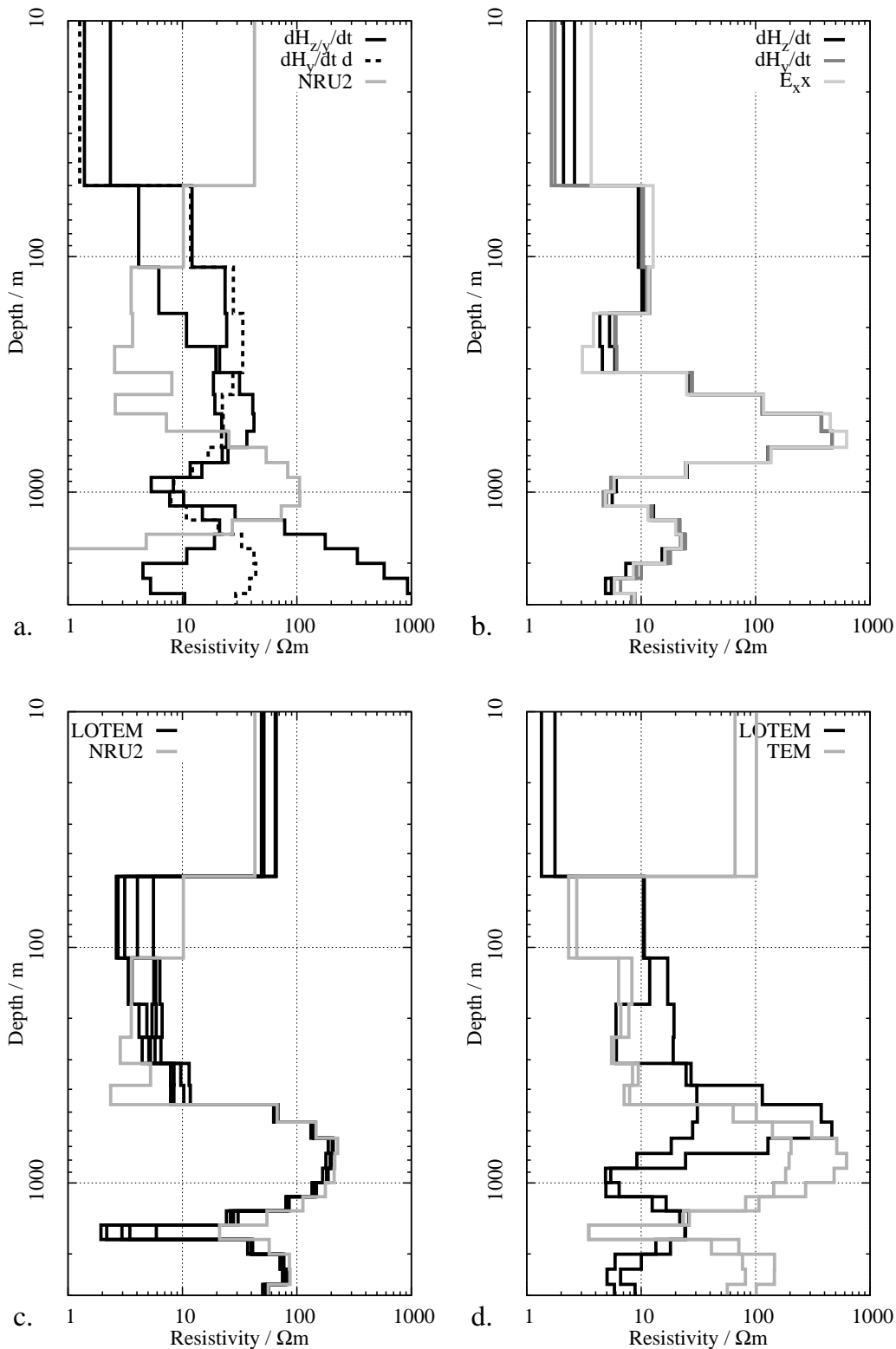


Figure 6.11: Soft-Joint-Inversion results for the transients recorded at ENB; a: Comparison between typical models from the SJI of LOTEM- \dot{H}_z and $-\dot{H}_y$ without Tx-distortion, solid black lines), LOTEM- \dot{H}_y with Tx-distortion (dashed black line) and the SHOTEM-transient NRU2; b: Resulting models for the SJI of all LOTEM-components with free Tx-distortion; c: Resulting models for the SJI of all TEM-components with free Tx-distortion; d: Comparison of the model for the ENB1- \dot{H}_y -transient after the SJIs with LOTEM-components only and, additionally, with the SHOTEM-transient.

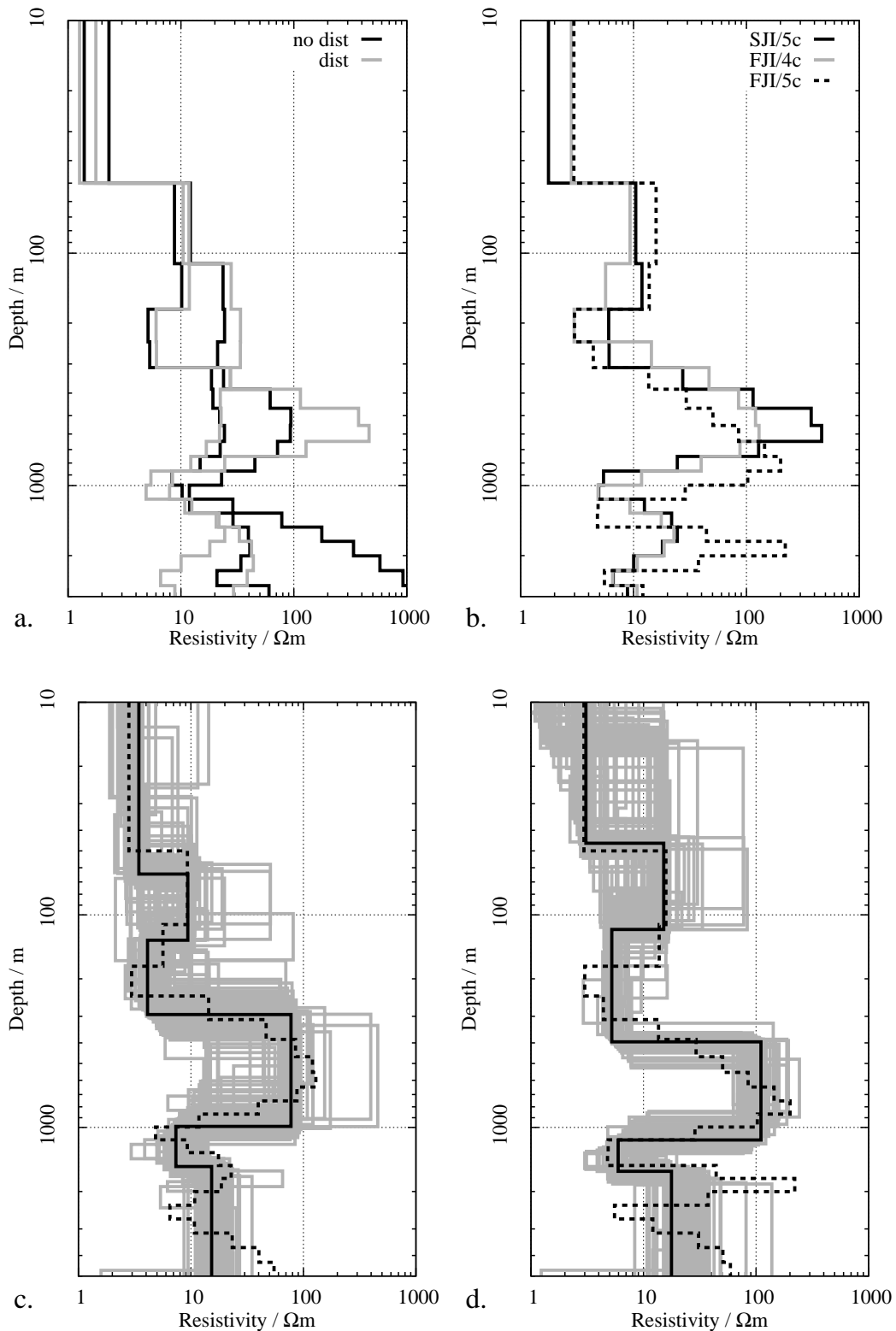


Figure 6.12: Joint-Inversion results for site ENB; a: Comparison of SJIs with and without fixed Tx-distortion; b: Comparison of on SJI and two fixed joint-inversions; all inversion are made with free Tx-distortion. For the "5c" inversion all LOTEM-components, whereas in for the "4c"-inversion only \dot{H}_z/\dot{H}_y were used. c: FJI-results for four magnetic components; d: FJI-results for all LOTEM-components;

In this case, all LOTEM-components are mutually consistent. The models derived using the SHOTEM-transients, however, are different. The SHOTEM data are inconsistent with the LOTEM data. If the deep SHOTEM-transient would have reliable late times, the derived model would reflect the earth below the Rx-site (sec. 5.5). The LOTEM model instead reflects also the subsurface between Tx and Rx (chapter 5). Here, the deviation is most likely caused by noise on the late times of the transient, as the unedited transient was used.

Fig. 6.12a shows models for the \dot{H}_y -component of ENB1 resulting from SJIs with and without free Tx-distortion parameters (both with and without the E_x -transient). In all cases the conductive feature is located in similar depths. The biggest differences are found at depth. However, the resistivity range is more reasonable and the misfit is smaller with freed distortion parameters.

Fig. 6.12b shows a comparison of FJIs, with and without the E_x -transient, with one model from the five component SJI (all with freed Tx-distortion). The models look similar. However, the conductive feature seem to start a little bit deeper than in the SJIs.

Marquardt inversions are done for all LOTEM- \dot{H} s and all LOTEM-components including the E_x (fig. 6.12c and d). Although the Occam's-inversion results for these two combinations differed regarding the depth of the deeper conductor, the results show that in both cases the transition from the resistive to the conductive layer is in the same depth range. However, if the E_x -transient is included, the result is far better constrained. Therefore, this model was used for the final interpretation.

Fig. 6.13 compares the TEM-results to the information from the nearby borehole Beit-Eliezer. The conductive Saqiye Group up to a depth of 351 clearly shows up in the TEM models. All models show a drop in resistivity between ≈ 800 and ≈ 1400 m, which corresponds with the appearance of very saline water at 1180 m. The resolution of the position of the saline water table and the resistivity of the aquifer filled with saline water is poor. All models within the equivalence range, however, show a conductive zone at least between 1000 and 1350 m depth with a resistivity $< 11.5 \Omega\text{m}$. The depth of the interface seems to increase with the conductivity of the aquifer. This behaviour is found at nearly all sites.

The models derived including the unedited SHOTEM-transient contradict the information from the borehole. The inversion made by the GII with the edited transient do not show any features below the increase in resistivity around 450 m [M. Goldman, pers. comm.]. However, the test showed that if changes at depth occur when a SHOTEM data set is included, these transients should be rejected for the interpretation of deeper structures. Still, a combined interpretation taking shallow features from the SHOTEM models and deeper structures from LOTEM-components is reasonable (sec. 5.5).

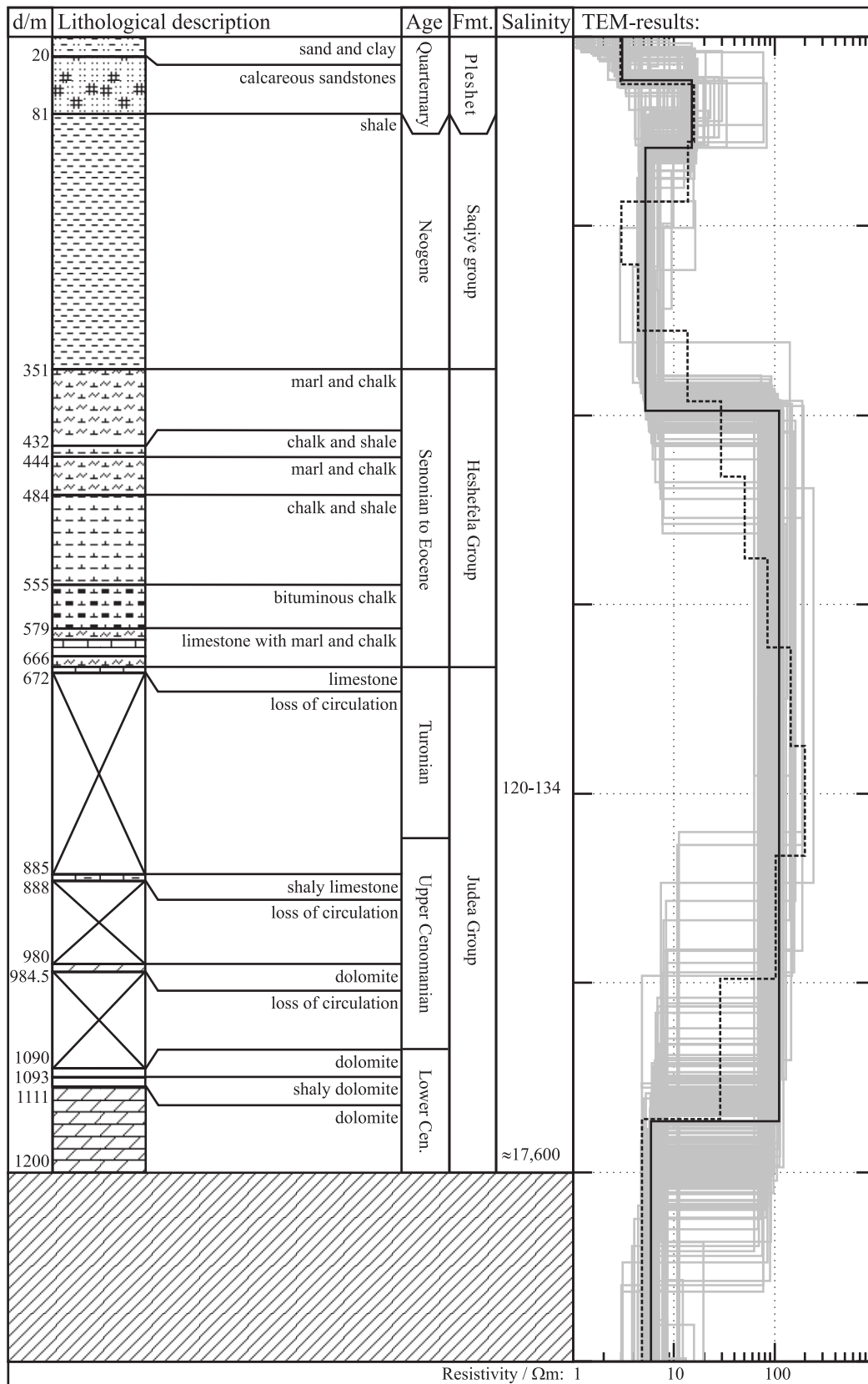


Figure 6.13: Information from the borehole "Beit-Eliezer" and results from the nearby Rx-site ENB; The TEM results were derived using all LOTEM-components. The black lines shows the best model ($\chi = 1.55$), the dashed line the Occam's-inversion result ($\chi = 1.45$) and the gray lines models with $\chi < 1.70$.

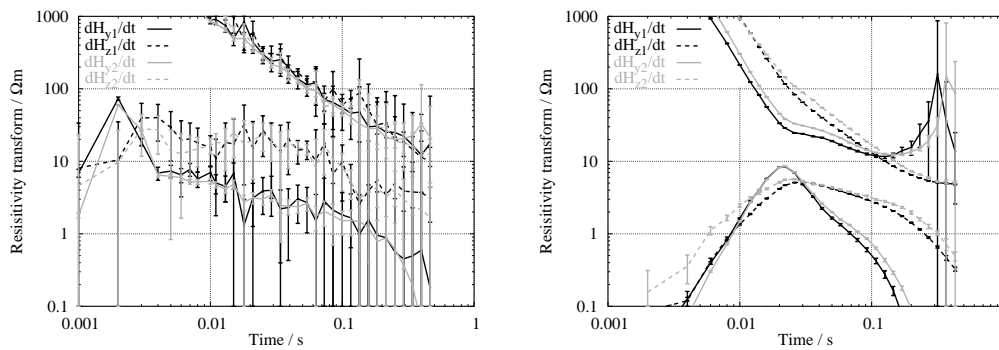


Figure 6.14: Resistivity transform curves for the Rx-sites GAA (left) and GBA (right), both located close to the same borehole;

Site GBA and GAA

The noise in this area is very high: A power plant is located in the coastal area near Rx-site GBB. Several high-voltage power lines are found in the vicinity of the borehole. It was thus decided that a short signal period should be used to be able to record and stack many transients. However, the first attempt in 2002 failed. The data is still too noisy (fig. 6.14 left) due to a comparably low transmitting current. Finally, in 2003 a new Tx-position allowed far higher currents. Additionally, the analog 50 Hz notch filter on the TEAMEX units were used. This way, short but usable transients were recorded (fig. 6.14 right). The notch filter produces very long system responses, which is clearly visible in the right panel of 6.14. The \dot{H}_z s differ until very late times. Thus, the first eleven data points of these transients were removed prior to interpretation.

The SJIs of single components of both stations show medium consistent models. Fig. 6.15a shows a comparison of the SJIs for the individual components and the inversion result from the SHOTEM data set. The main features are a drop in resistivity at around 100 m depth and a resistivity increase at a depth of ≈ 650 m. The results from the \dot{H}_y -inversions show an additional feature, a moderately resistive zone between 250-500 m. Tx-distortion is not important at this site.

The SJIs of different components are moderately successful. In general, the inversions reached a low misfit. The main features of the resulting models are similar, but depths and resistivities sometimes deviate from one component to the other. Fig. 6.15 shows examples for the SJIs of the LOTEM- \dot{H}_y - and $-\dot{H}_z$ -transients (fig. 6.15b) and of all seven TEM-components (fig. 6.15c). In inversions without the electric fields an additional conductive feature shows up at around 1000 m depth (fig. 6.15b). This feature is not visible when the E_x -components are used (fig. 6.15c).

FJI of the different components again are moderately consistent. They show the same structure in the upper 1000 m, but differ for greater depths. The conductive feature found in the SJI of the magnetic components only, could not be reproduced in the fixed joint-inversions. Fig 6.15d shows the results of the equivalence analysis for all four LOTEM- \dot{H} -components. Again the deep conductive feature is not found. Also, the resistivities of the resistive feature in medium depths and the basement are not well defined. The very conductive material at 100-800 depth in combination with the comparably short transients reduce the resolution at depth.

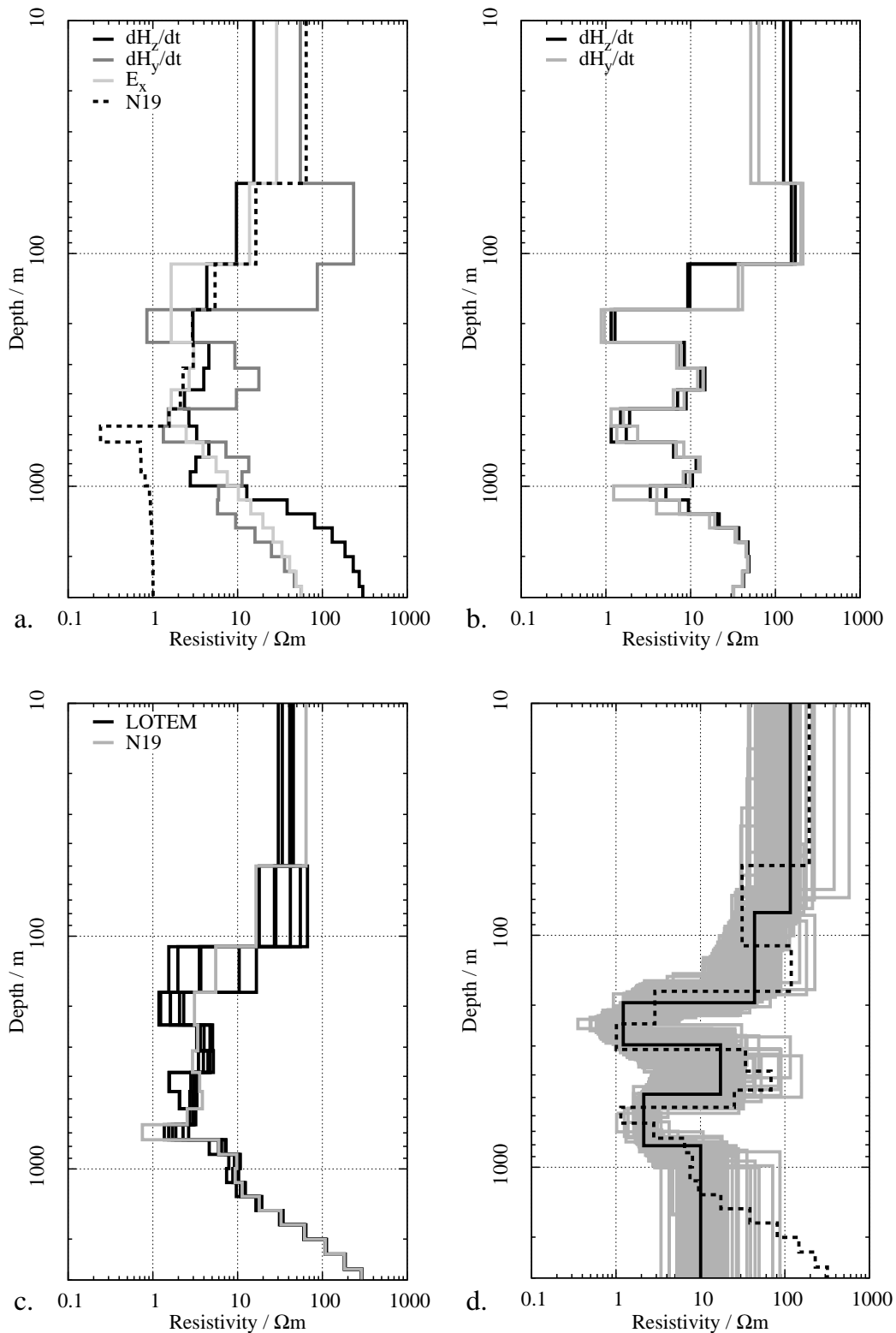


Figure 6.15: Joint-inversion results for the transients recorded at GBA; all SJI inversions shown here are done without Tx-distortion. *a:* Comparison of the individual SJI results for the different components and the single inversion of the SHOTEM-transient; *b:* SJI results for the LOTEM- \dot{H}_y - and $-\dot{H}_z$ -component; note the conductive feature at around 1000 m depth. *c:* SJI results for all TEM-components. *d:* Equivalence analysis for the four LOTEM- \dot{H} -components; The black lines shows the best model ($\chi = 1.08$), the dashed line the Occam's-inversion result ($\chi = 1.06$) and the gray lines models with $\chi < 1.18$.

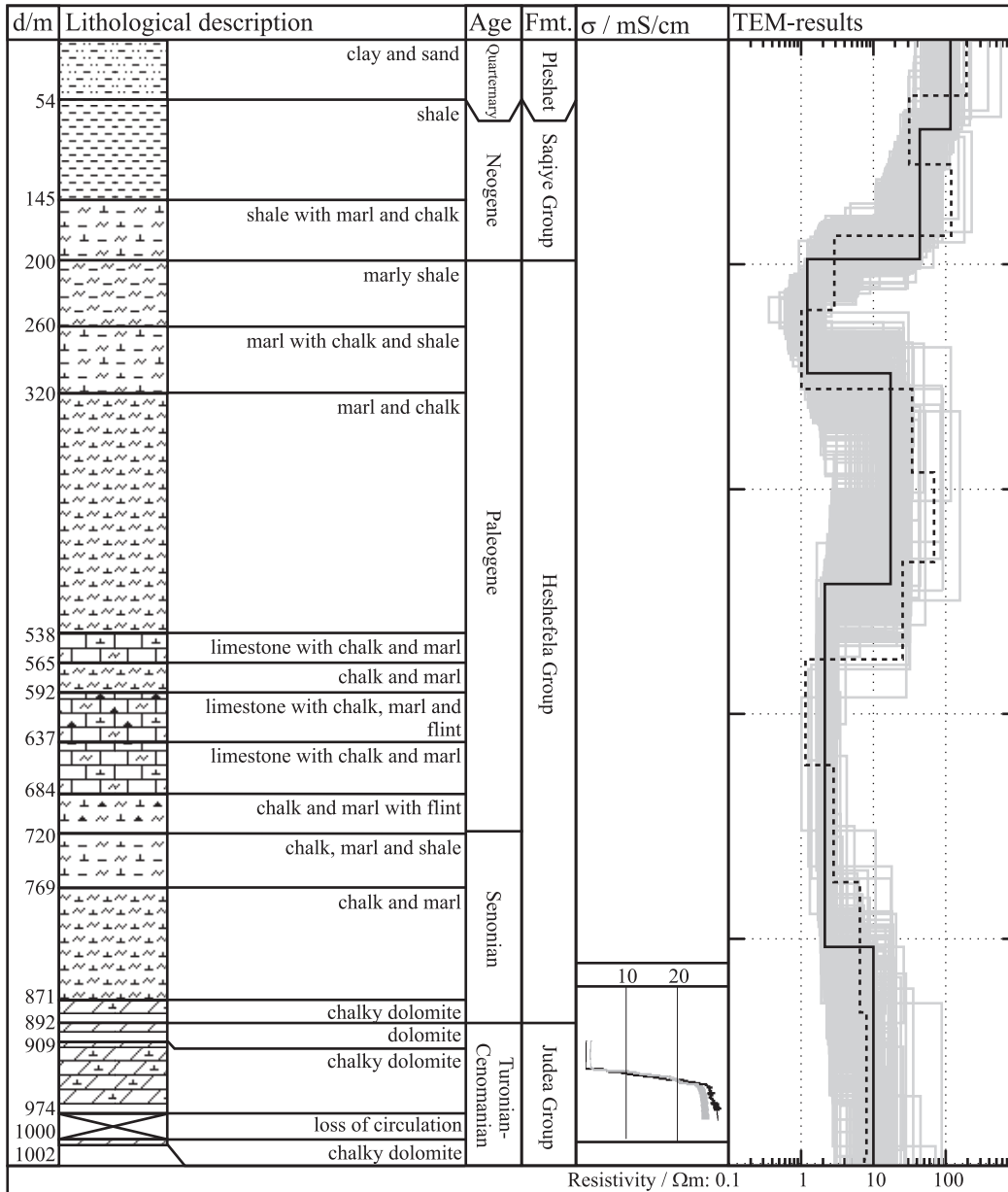


Figure 6.16: Borehole information and TEM results for site GBA; the measurement of the water conductivity in the borehole were done at the 21.03.2002 (gray) and the 28.05.2002 (black). At 920 m depth a water salinity of 584 mg Cl^-/l was found which changes to 15,800 mg Cl^-/l in 980 m. The TEM measurements were done on the 17th of December 2003. The TEM results were derived using all magnetic LOTEM-components (fig. 6.15).

Fig. 6.16 shows the information from the borehole in comparison to the TEM results. The upper conductive feature is likely to be related to the not well resolved Saqiye Group, although its depth differs. However, the same structure including the underlying resistor and the very conductive feature within the Heshefela Group is also found at PHB, even in the SHOTEM results. Therefore, it is likely caused by the lithology. The reasons for these high conductivities is unknown. Possibly, the Palaeogene-Senonian formations retain very saline formation water [U. Kafri, pers. comm.].

The main target, the saline water interface at a depth of around 960 m can not be resolved by the transients due to several problems. First, the data quality is only mediocre since the transients are short. Second, the overlying formations are very conductive. This does mean that, on the one hand, the underlying structures are masked, while on the other hand, the contrast with the target is very small.

The SJIs of some components showed indications for a conductive feature which could be related to the target. This effect that the SJIs seem to have a higher resolution compared to the FJIs is not observed in the model calculations. This might be an interesting subject for future research.

Site PHB

At PHB five LOTEM-components were recorded: two \dot{H}_z s, two \dot{H}_y s and one E_x . For logistical reasons the SHOTEM measurement site NRU4 is located some hundred meters closer to the LOTEM-Tx. The SHOTEM-transient was recorded with the Cycle-5M equipment. There are no obvious geological distortions in the area. However, similar to the nearby GA and GB sites, several power-lines cross the spread.

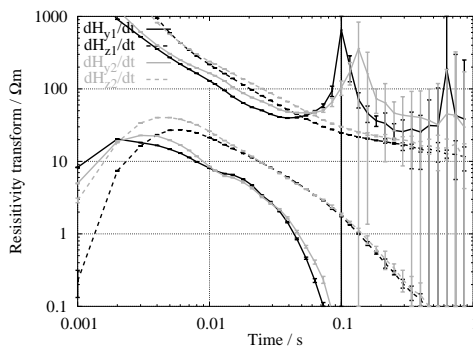


Figure 6.17: Resistivity transform curves for the Rx-site PHB;

also compared to the SHOTEM result (fig. 6.18, right). The models from SJIs of all LOTEM- \dot{H} -components differ significantly in the upper part. Similar is the conductive feature in a depth of around 700 m (fig. 6.19 a)). Including the E_x , the conductive feature is shifted to ≈ 400 m (fig. 6.19 b)). If Tx-distortion is introduced to the inversion, the SJI of all five LOTEM-components reaches a slightly better misfit ($\chi = 0.54$ instead of $\chi = 0.61$). The conductor is shifted back to its depth of around 700 m (fig. 6.19c)). This model agrees grossly with the model found using also the SHOTEM-transient.

If further the SHOTEM-transient is included in the inversion, the long Cycle-5M transient dominates the inversion. The LOTEM data constrain the model mainly at depth. Additionally, the resistive feature in 300 – 550 m becomes even more resistive due to the additional information from the LOTEM- E_x . The models for the LOTEM-components differ mainly in the shallow conductive part (100-300 m depth, fig. 6.19d).

Unfortunately, the fixed joint-inversions fail. Their misfit is three times higher

This results in rather noisy late times (fig. 6.17). The resistivity transform curves for all magnetic field components deviate in the early times from one station to the other. Especially both \dot{H}_y s seem to differ slightly over the whole time range. SJIs of either \dot{H}_y - or \dot{H}_z -transients show slightly different models for both stations. Fig. 6.18 (left) shows an example for the SJI of both \dot{H}_y -components without Tx-distortion.

The separate SJI-results for the magnetic field components are inconsistent,

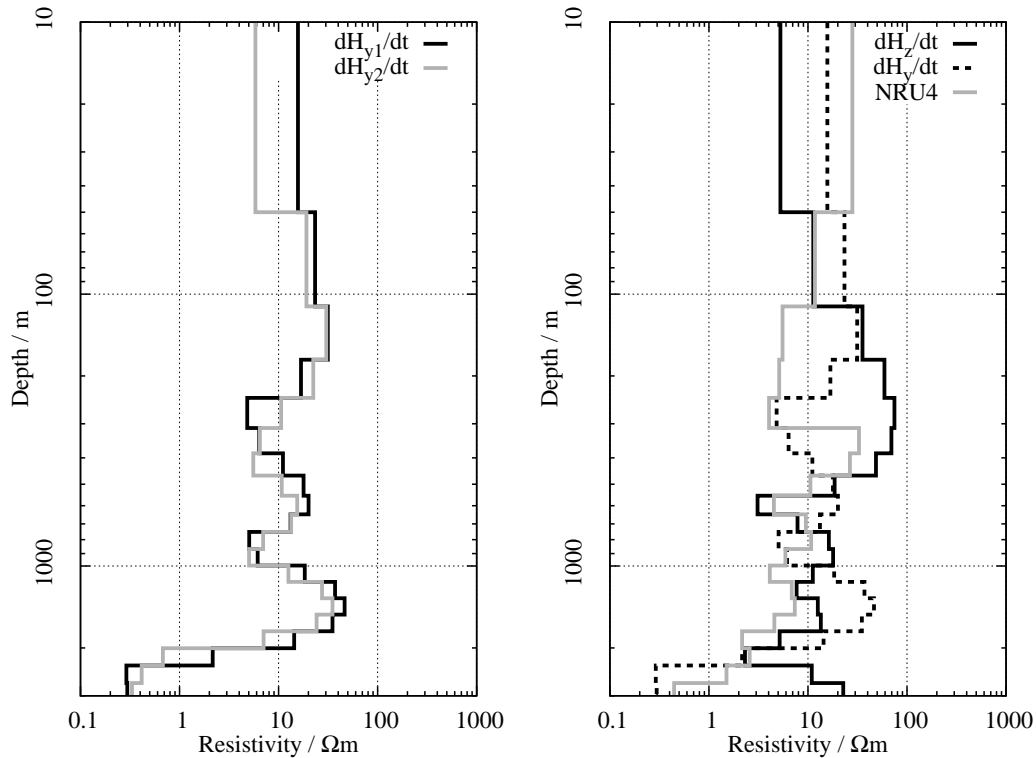


Figure 6.18: Inversion results for the transients recorded at PHB; left: SJI-result for the \dot{H}_y -transients; right: Comparison of the SJI-results for \dot{H}_z and \dot{H}_y and the single inversion of the SHOTEM-transient NRU4;

than the corresponding SJIs and the models for different data set combinations show an erratic behaviour at depth. Thus, Marquardt joint-inversions could not be made.

Fig. 6.20 shows the information from the nearby borehole in comparison with the results of the six-component SJI including distortion parameters. The shallow conductor, which is mainly constrained by the SHOTEM-transient, correlates with the clays of the Saqiye Group. The target in this case is the rise in conductivity of the well's water in a depth of ≈ 930 m. This coincides with the slight drop in resistivity in the Occam's inversion result (see also lower right panel of fig. 6.19). However, the ambiguous results in the previous inversions in this depth show that the TEM results are not reliable below ≈ 800 m depth. Without *a priori* knowledge, this feature would be discarded for the geological interpretation.

Due to the length of the Cycle-5M transient (631 ms), the LOTEM-transients which are of similar length could not provide additional information, except for the resistivity of the zone between 400 and 550 m depth. Anyway, using all four magnetic components or better yet, all LOTEM-components, the SJIs would yield a realistic picture of the deeper part of the subsurface (300 to 800 m depth).

The results here are very similar to the ones at GBA. Again, the SJIs showed a better picture of the subsurface than the FJIs which in this case failed completely. Also, the model is very similar, showing a conductive upper part which correlates to the Saqiye Group, followed by a resistor in intermediate depths and a conductive feature already above the saline water interface.

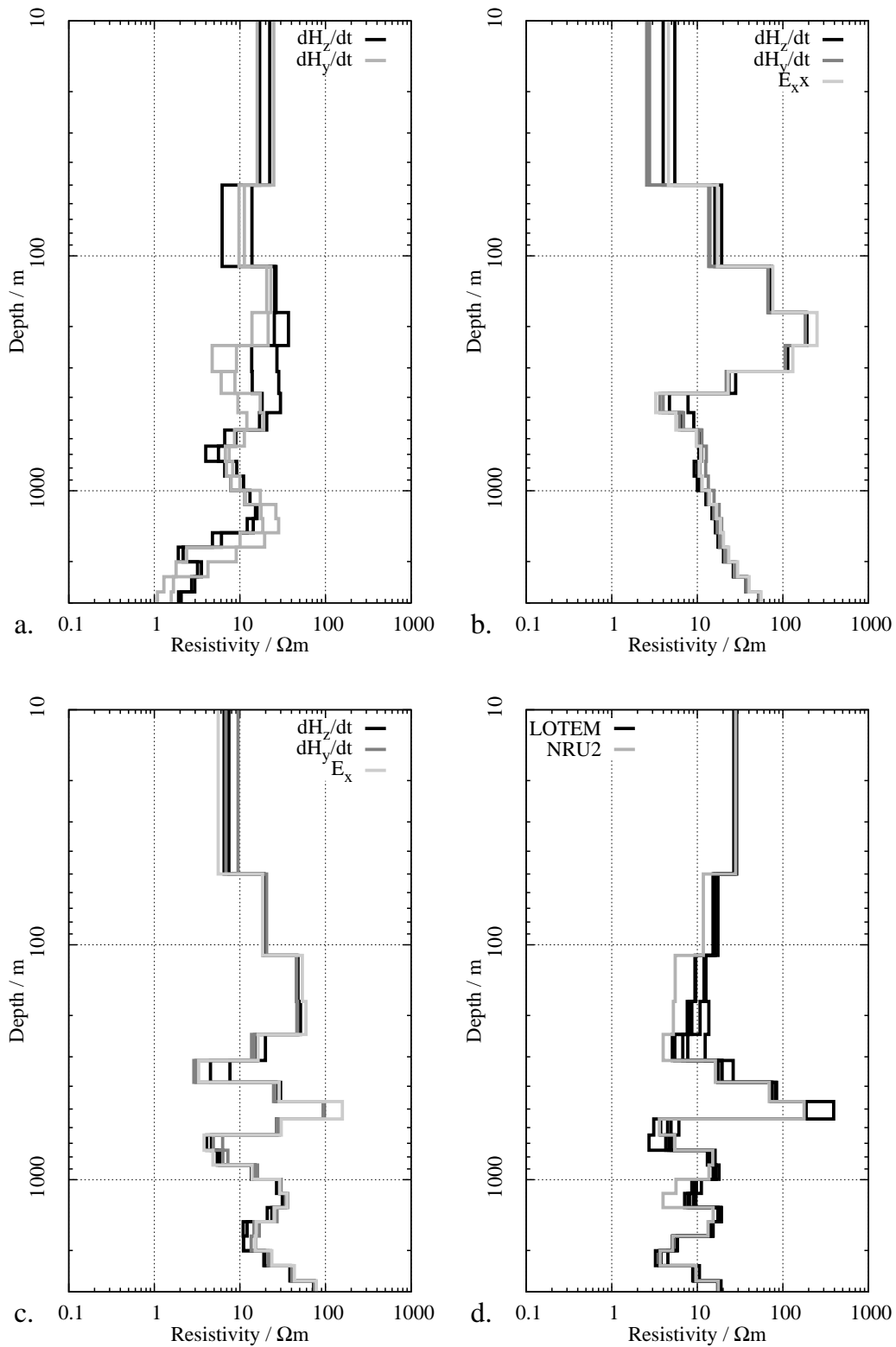


Figure 6.19: Soft-Joint-Inversion results for the LOTEM-transients recorded at PHB; a: SJI of all magnetic LOTEM-components without Tx-distortion; b: SJI of all five LOTEM-components without Tx-distortion; c: SJI of all magnetic LOTEM-components with Tx-distortion; d: SJI of all six TEM-components with Tx-distortion;

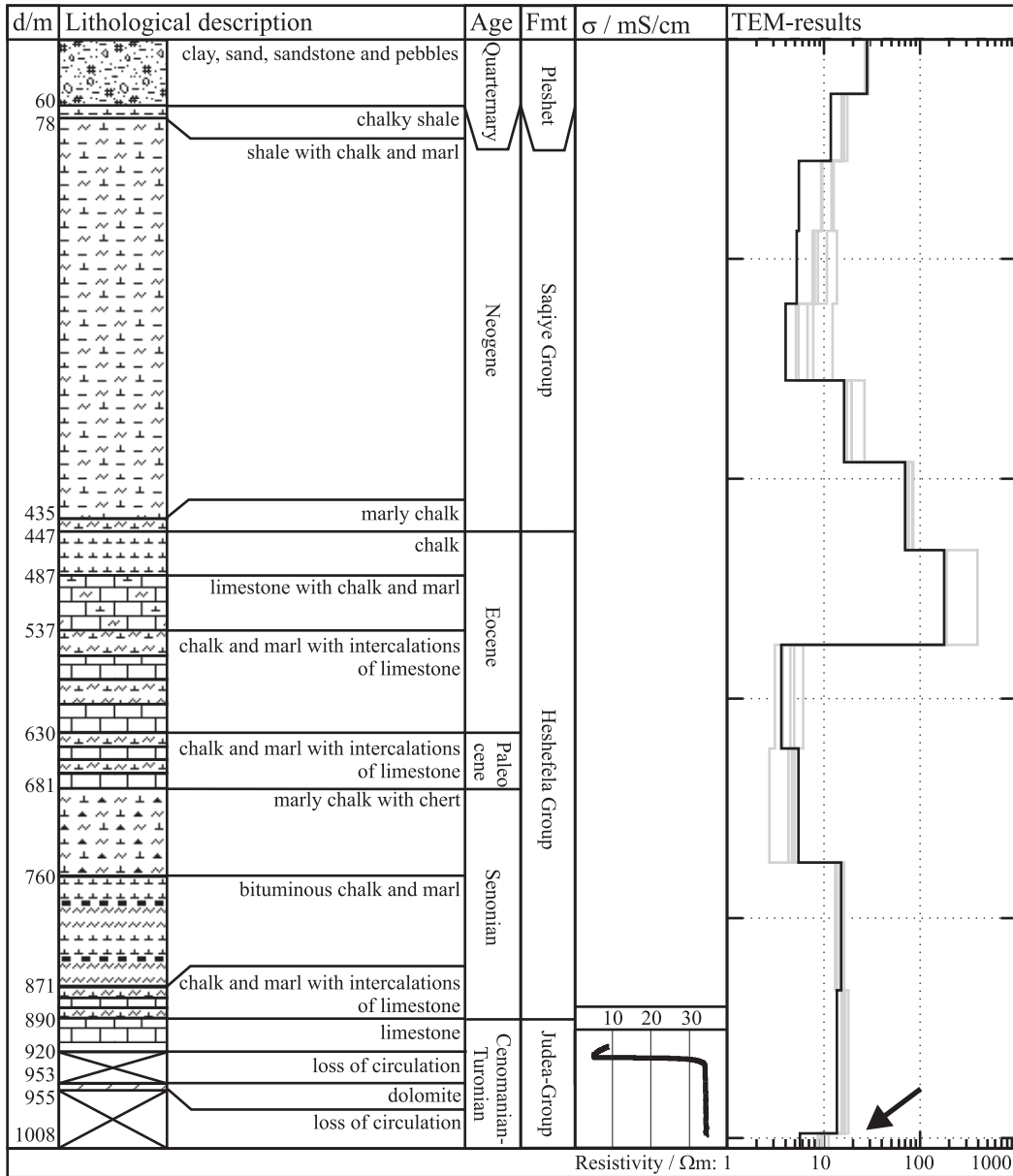


Figure 6.20: Borehole information from the borehole "Pardes Hanna" and TEM results for site PHB; In 918 m depth a water salinity of 2, 260 mg Cl^-/l was found which changes to 17, 576 mg Cl^-/l in 960 m. The TEM results are the different smooth models from a SJI of all six TEM-components. The black line denotes the model corresponding to the SHOTEM-transient. The models for the LOTEM-components are drawn with gray lines. These are the same results as shown in the lower right panel of 6.19. The arrow points towards the drop in resistivity, which corresponds with the increasing conductivity in the well's water.

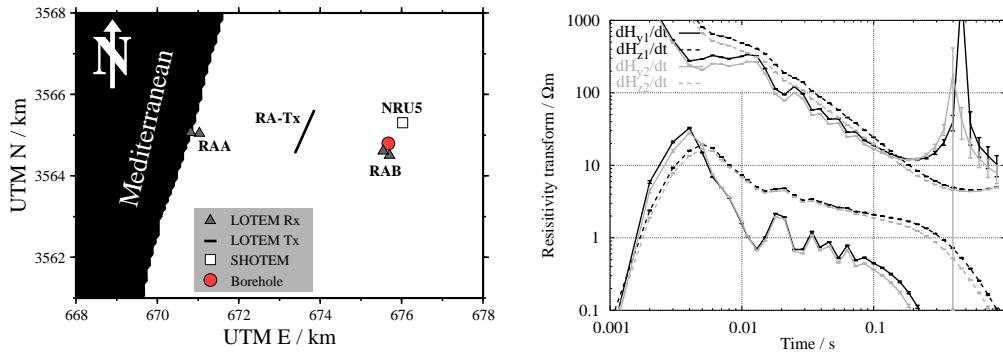


Figure 6.21: Left: Map for the RA-spread; the spread is located ≈ 10 km north of Tel-Aviv; right: Resistivity transform curves for the Rx-site RAB;

Site RAB

The Tx RA is located in the coastal plain approximately 30 km south of the area shown in fig. 6.7 (fig. 6.21, left). All data sets recorded with this Tx show strong oscillations (figs. 6.21 and D.37, right). These are fitted very well at the RAA stations using the oscillating system responses. At the RAB stations, an additional delay can be found. The transients seem to start a few milliseconds later than $t = 0$ s logged by the SUMMIT-TEM units. This is a unique feature, which could be explained by synchronisation problems. For inversion, the transients were shifted back 3 ms. After this procedure, the oscillations of the system response are in phase with the ones from the recorded transients. Additionally, the error estimates for the early time data points are increased more. Close to the site the SHOTEM data set NRU5 was recorded using the Cycle-5M equipment.

The differences between the transients of the adjacent stations are small. SJIs for the three components showed a good agreement between the models for the two stations' data sets. Qualitatively, all models are similar, including the one for the SHOTEM-transient. They show a conductive zone ($< 10 \Omega\text{m}$) at depths between 100 and 600 m. The E_x s and \dot{H}_y s show an additional conductive feature around 1000 m (fig. 6.22a). Even with the inclusion of Tx-distortion the misfit stays virtually the same. The models change mainly at depth. With the distortion, the geologically unrealistic high resistivities at depths greater than 2000 are reduced (fig. 6.22b).

SJIs of different components show the same structures down to a depth of ≈ 1100 m. Below, the models differ. The same resistivity structure can be obtained by FJIs. Fig. 6.22c shows a comparison of three different joint-inversion results. The final equivalence analysis was done using all six LOTEM-components (fig. 6.22d). The most prominent feature is the thick conductive layer with $\approx 2 \Omega\text{m}$. Comparing the results to the nearby borehole (fig. 6.23) shows that this conductor correlates well with the Saqiye Group shales. However, the interface of the saline water could not be detected due to the high conductance of the upper layers.

The conductive zones at depths of around 1 km, found in the E_x - and \dot{H}_y -SJIs seem to represent the deep aquifer with saline water. This layer is also found with SJIs of E_x s and \dot{H}_y s combined (fig. 6.24, left). Like at GBA and PHB, it vanishes when these components are used in a FJI (fig. 6.24, right).

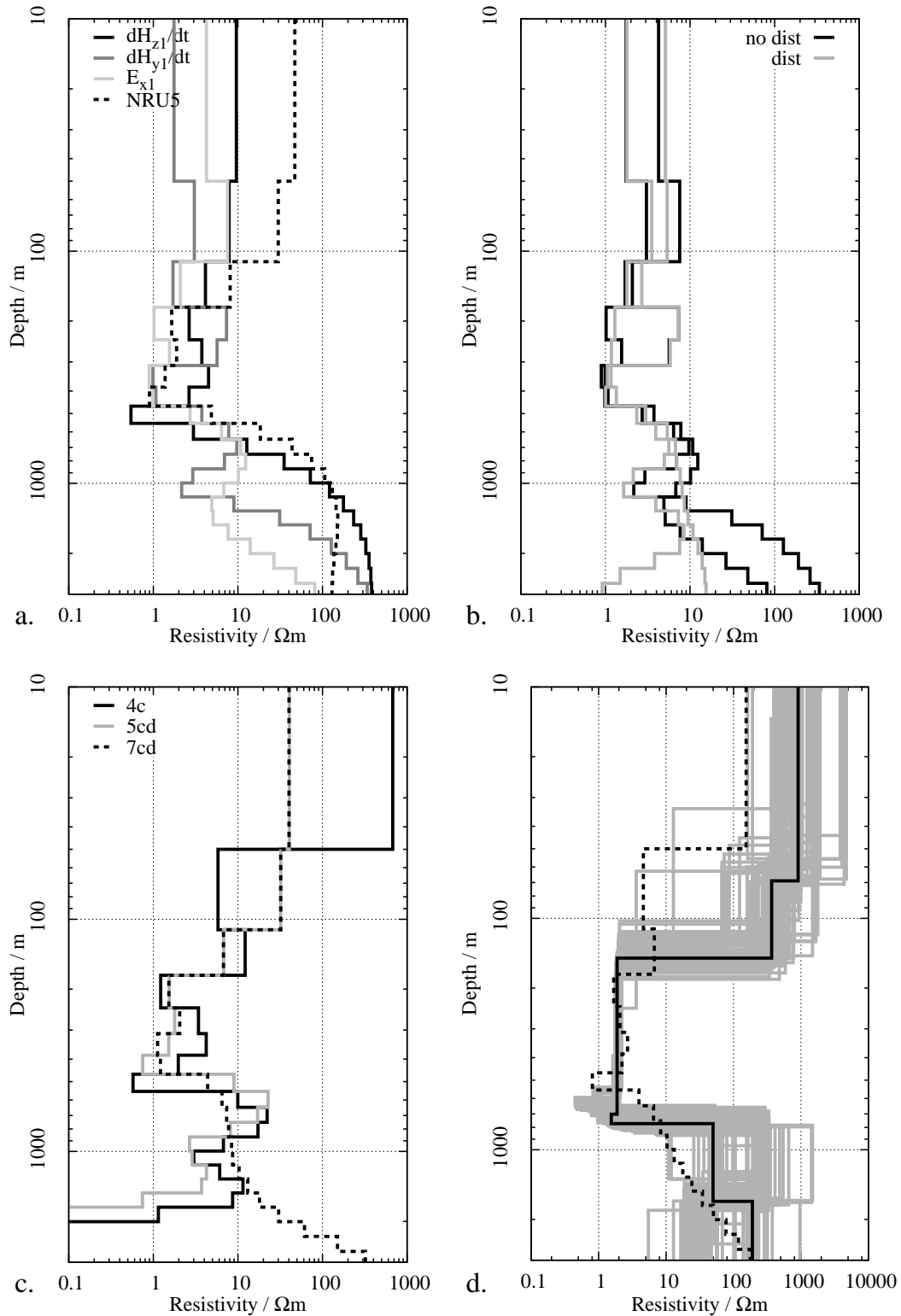


Figure 6.22: Inversion results for the transients recorded at RAB; a: Comparison of the SJI-results for E_{x1} , H_{y1} and H_{z1} and the single inversion of the SHOTEM-transient NRU5; b: Comparison of the results of SJI of the horizontal LOTEM-components E_x and H_y with and without Tx-distortion; c: FJIs of different components using only the LOTEM- H_s ("4c"), the same also with Tx-distortion and the SHOTEM-transient ("5cd") and of all TEM-components with free distortion ("7cd"); d: Equivalence analysis using all LOTEM-components; the black lines show the best model ($\chi = 1.54$), the dashed line the Occam's-inversion result ($\chi = 1.56$) and the gray lines models with $\chi < 1.70$.

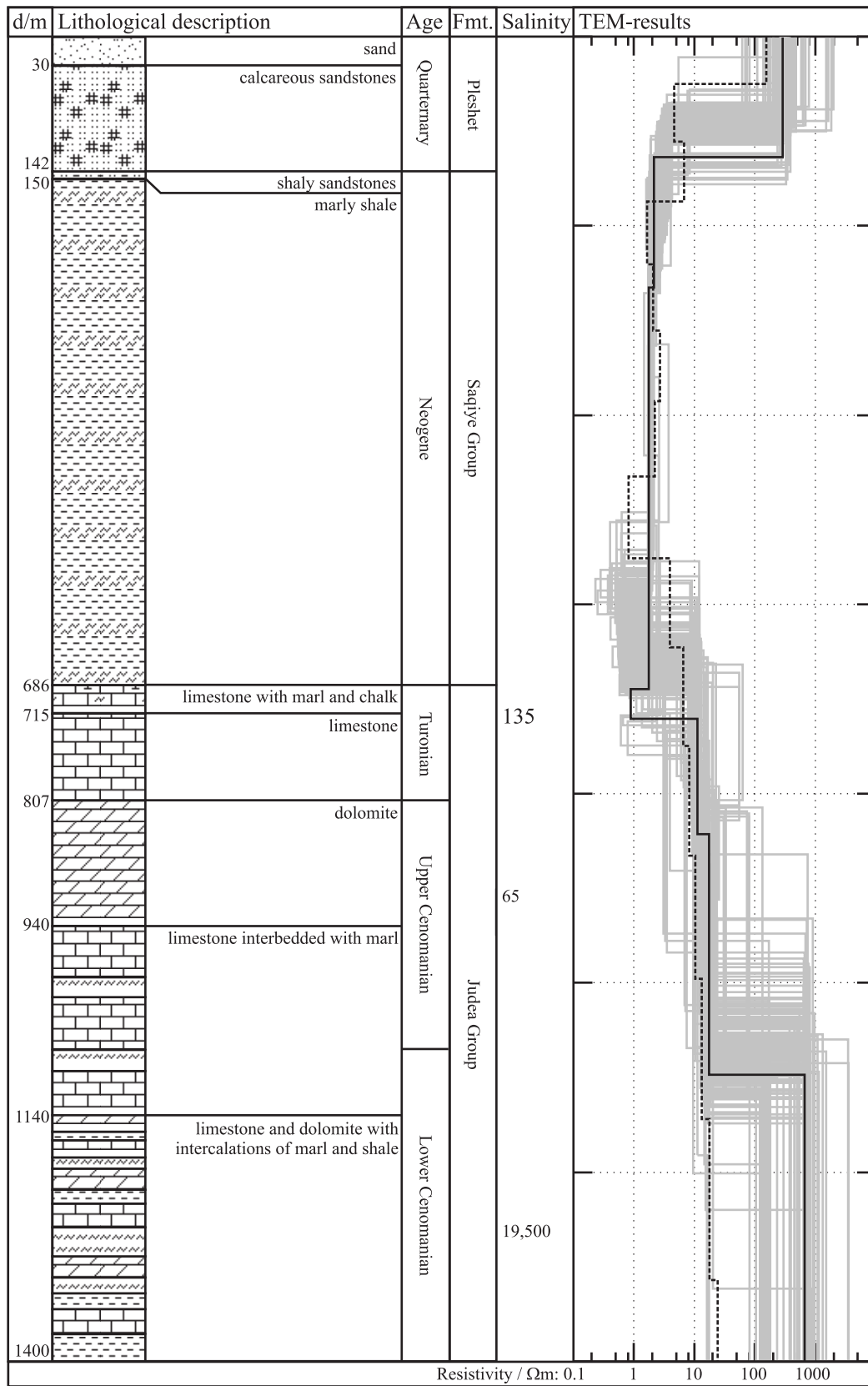


Figure 6.23: Borehole information from the borehole "Ra'annana" and TEM results for site RAB; The TEM result were derived using all LOTEM-components.

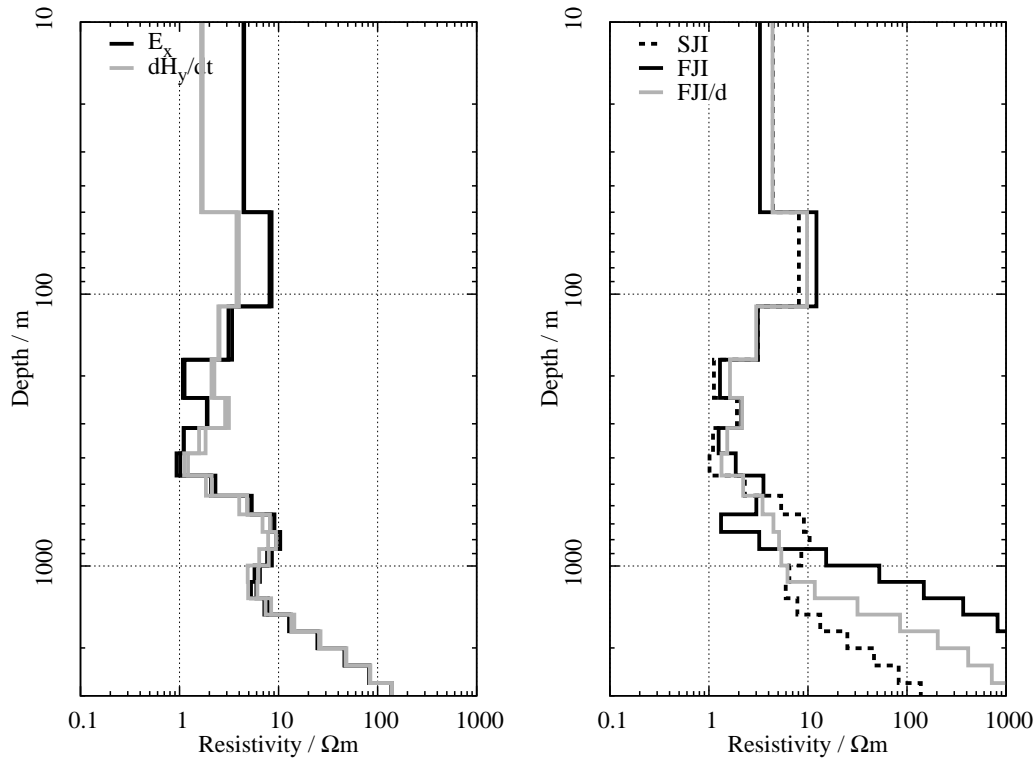


Figure 6.24: Joint-inversion results for the E_x - and \dot{H}_y -transients recorded at RAB; left: Resulting models for the SJI with free Tx-distortion; right: Comparison between one representative model from the SJI and the FJI with and without Tx-distortion.

Site TAB

TAB is located north of the previous four sites, close to the borehole “Tananim Deep”. Unlike to the other boreholes no Saqiye Group is expected here. A fault is running E-W south of the Rx-site (fig. 6.8). Two stations with in total two \dot{H}_z -, two \dot{H}_y - and one E_x -sensors were set up here. Additional information is provided by the Cycle-5M data set N1.

The resistivity transform curves for the \dot{H}_z -components show signs of early time distortions. The \dot{H}_z -transient of TAB1 exhibits a sign reversal between 2 and 3 ms. The E_x -transient shows a slow increase at early times. The data set was recorded during the first survey in 2002 with the SUMMIT-TEM system. The top-soil was relatively sandy in the area. Most likely the slow increase for the electric field transient is caused by a long system response produced by a high contact resistivity. The first 10 data points thus were removed from the E_x and \dot{H}_z data sets prior to inversion.

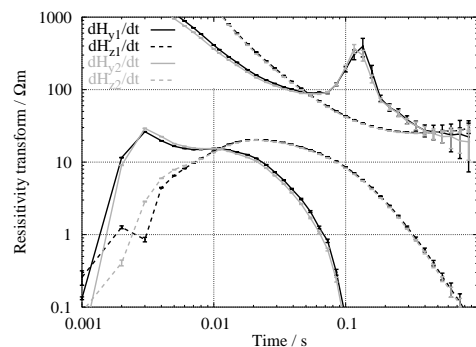


Figure 6.25: Resistivity transform curves for the Rx-site TAB;

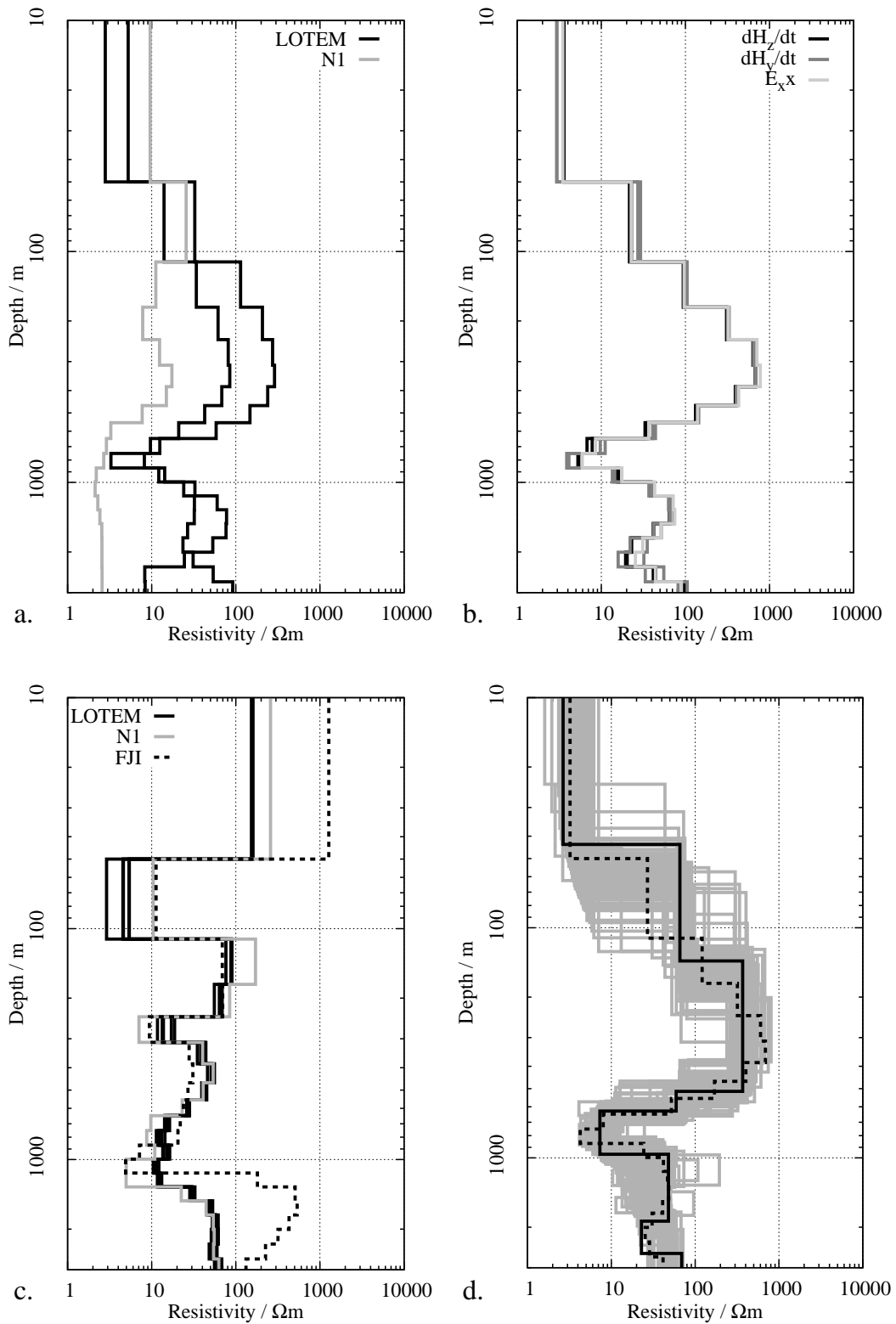


Figure 6.26: Inversion results for the transients recorded at TAB; all inversions involving horizontal components were done including the T_x -distortions. a: Comparison of the SJI-results for \dot{H}_z s and \dot{H}_y s and the single inversion of the SHOTEM-transient N1; b: SJI and FJI results for all five LOTEM-components; c: SJI results for all TEM-components; d: Results of the equivalence analysis using all five LOTEM-components;

Individual SJIs for both magnetic LOTEM-components result in very similar models for both stations. Also, the difference between the different components is small (fig. 6.26a). All inversions produced a conductive feature at 600-1000 m depth.

The result for the SHOTEM data set shows increases and decreases of the resistivity in similar depths, but the resistivities in general are smaller in intermediate depths. Also, an additional conductive feature around 200 m appears.

SJI using different subsets of the LOTEM data show very stable results (fig. 6.26b). The models exhibit the afore-mentioned conductor at intermediate depths and a deep conductive feature around 2000 m. The results do not change with or without the addition of Tx-distortion. The fit, however, is far better if inversion of the distortion parameters is enabled (e.g. $\chi = 1.00$ with distortion to $\chi = 1.60$ without distortion for the inversion of all five components).

Inversions including the SHOTEM data degrades the misfit of the LOTEM data sets by $\approx 20\%$. The model changes mainly in the upper part, which is only constrained by the SHOTEM-transient (fig. 6.26c). Also, the intermediate conductor reaches greater depths.

FJIs of different components give virtually the same models as the SJIs. Here, including Tx-distortion parameters improves the misfit even more. It has approximately only half of the misfit for models without free distortion parameters, depending on the components used. However, even without free distortion, the main features of the model remain. Fig. 6.26d shows the equivalence analysis using the five LOTEM-components. The results looks very similar, if the SHOTEM data set is also used. The main differences appear in the shallow part, which then shows more structure.

Fig. 6.27 shows a comparison of the borehole information with the TEM results. Two salinity measurements were made. In shallow depths (200 m) brackish water with a salinity of 1,475 mg Cl^- /l was found, whereas the second sample at 600 m showed a salinity close to that of seawater (17,000 mg Cl^- /l). The conductive zone thus can be interpreted as aquifer filled with seawater. The depth of the fresh to saline interface from the LOTEM data fits this information, although the interface is not well restrained. Also, the resistivity is not well constrained. All models have a zone with resistivities $< 14.1 \Omega\text{m}$, at least in the depth range between 550 and 720 m depth.

Using the SHOTEM transient (which is edited in this case) in a single inversion, the saline water interface is found at ≈ 600 m depth (cp. fig. 6.26a). The aquifer then has a resistivity of around $6.0 \Omega\text{m}$ [Goldman and Kafri, 2002]. It is very interesting, that similar results could be obtained by both methods, although joint-inversions failed. This is in accordance to the results from sec. 5.5.

The increase in resistivity at depths greater than 1 km is visible in many of the inversions, although the equivalence analysis shows that it is not well resolved. This phenomenon, however, occurs at several other sites along the traverse. From a hydrogeological point, this increase at first seems to be unreasonable, as the water salinity is not supposed to decrease with depth. However, at site AFA (sec. D.1.1) strong evidence is found that this feature is no geophysical artifact but caused by the geology.

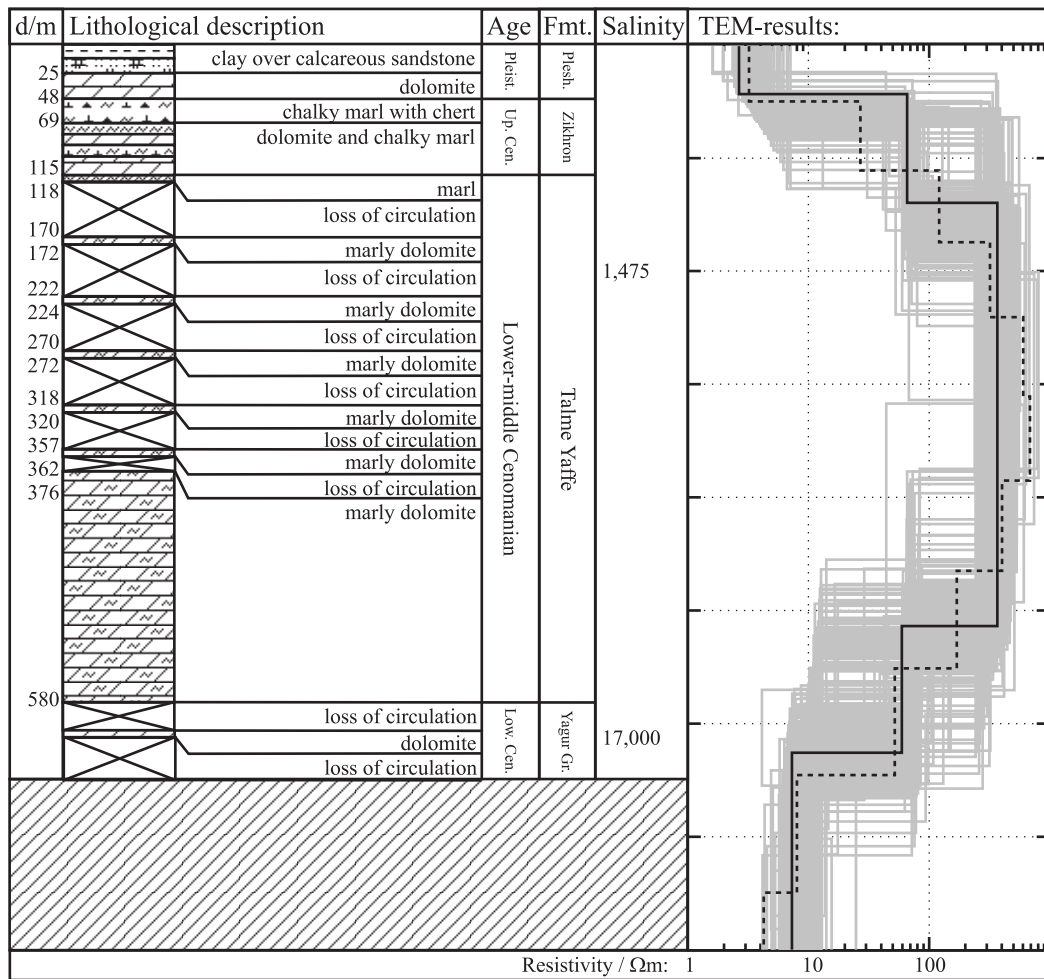


Figure 6.27: Information from the borehole "Tananim-Deep" and TEM results for site TAB; Salinity is given in $\text{mg Cl}^-/\text{l}$. The TEM result were derived using all LOTEM-components. The black lines shows the best model ($\chi = 1.28$), the dashed line the Occam's-inversion result ($\chi = 1.24$) and the gray lines models with $\chi < 1.41$.

6.3.2 Summary of the results for the calibration sites

In general, the results from the calibration sites show a good agreement to the borehole information. Unfortunately, the very conductive Saqiye Group inhibits the resolution of the deeper target at many stations.

At ENB and RAB the agreement to the lithological borehole information is striking. A confined conductor is found at depths of the Saqiye Group clays. At TAB the correlation to the borehole information is good, although the resistivity model is only moderately constrained. At PHB the correlation between a very conductive layer to the Saqiye Group is very good. At greater depths the resistivity models show a second highly conductive structure within the Heshefela Group formations. The existence of this low resistivity seems to be certain, as it was found by LOTEM and by SHOTEM as well as at site GBA which is close to PHB. The origin of the low resistivity, however, is not clear. They might be related to saline formation water [U. Kafri, pers. comm.].

At PHB and RAB the SJI's also show indications for a conductive feature at depth,

which most likely is produced by an aquifer bearing saline water. However, the feature is not very stable and vanishes in FJIs. A comparable effect was found in the model calculation for model M in sec. 5.5.2. The resolution of the conductor is not very good. Without any additional information (on the traverse) I would consider this feature very unreliable.

The target is resolved at ENB and TAB. In both cases the depth to the target is only resolved within an accuracy of 10 %. The resistivity of the targets as determined from the LOTEM measurements is between 3 and 15 Ωm . Using the TAB SHOTEM data set only, Goldman and Kafri [2002] derived a resistivity of around 6 Ωm . This means that the resistivity of a carbonatic aquifer bearing saline water is higher than for clastic aquifers, where Goldman et al. [1991] found values $< 2.9 \Omega\text{m}$. The higher values will introduce some ambiguity in the geological interpretation.

At GBA the quality of the data sets and the low resistivities of the shallow formations makes it impossible to resolve the target.

At ENB and TAB it was possible to use all five LOTEM components for the final interpretation. The ambiguity in particular could be reduced by including the E_x -transient. At PHB, all FJIs failed, although the SJIs gave reasonable results, which also fitted the SHOTEM inversion result.

FJIs including the SHOTEM data sets failed, although in some cases SJIs worked. At all stations the long Cycle-5M data sets were available. This means that the overlap between the SHOTEM- and LOTEM-transients is large. For a FJI the data sets have to be very consistent over almost the whole time range. This can not be expected (sec. 5.5).

At ENB the unedited SHOTEM transient hampered any joint-inversion approach. The model for the edited data set fits the LOTEM data (and thus the borehole information) very well although the deep conductor is not resolved [M. Goldman, pers. comm.]. If a SHOTEM data set changes the resulting model at depth, it thus should be ignored for the interpretation of deeper structures.

6.3.3 Sites along the traverse: An example (Sites BSA and BSB)

In this section I will present the results for the sites BSA (inconsistent data) and BSB (consistent data) as an example. In sec. 6.4 the final results for the other sites along the traverse are listed in tabular form. Sec. D.1 discusses the results for each site measured during the campaign (also for the sites on the coastal plain).

The spread BS was placed in the Beit-Shean Valley, near the Rift Valley. Unfortunately, there are faults below the Tx position (see fig. 6.8). Because of the dense infrastructure (the city of Beit-Shean is located north of the spread) it was not possible to choose a different location.

Previous to the LOTEM measurement, the two SHOTEM-transients were recorded at the sites N24 (N of BSA) and N23 (SE of BSB). The interpretation of N24 showed that the transient is distorted by an unknown multidimensional structure [M. Goldman, pers. comm.]. The GII recorded SHOTEM-transients previously in this area. The data set BSH7, recorded a few kilometres south of N24 showed no signs of distortion. It was thus decided to move the site BSA to this location.

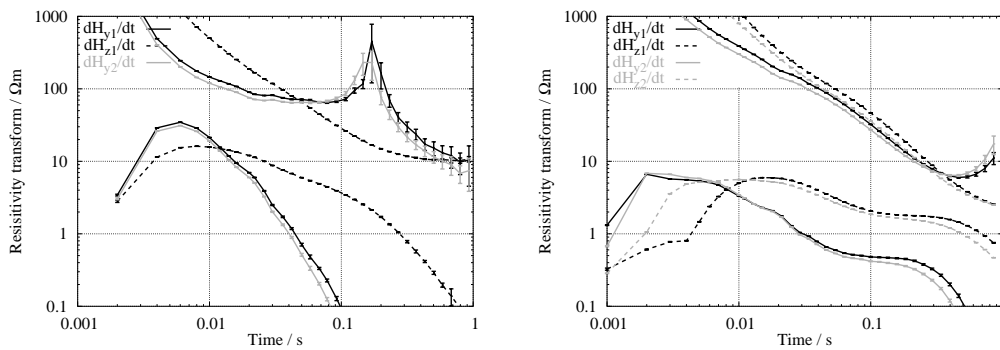


Figure 6.28: Resistivity transform curves for the Rx-sites BSA (left) and BSB (right);

From the same campaign data sets also existed close to the Rx-site BSB (BSH19 and BSH20). These were also included in the inversion.

That day the damaged (B)-coil was used at the western site BSA, which produced distorted transients (sec. 6.2.2). This data set was discarded, thus only one \dot{H}_z -transient remained for inversion. The resistivity transform curves for site BSB show a completely different behaviour than the ones for site BSA, indicating an extremely conductive subsurface. The \dot{H}_z -transients at BSB show inconsistencies up to 20 ms. These data points were removed prior to the inversions. Only one E_x -transient was recorded at this position.

The SJI worked well with \dot{H}_y which was the only component measured at two positions. The main feature is a drop in resistivity to a minimum between a depth of 700 and 1000 m. The SHOTEM data set shows some conductive layers in the upper part but can not resolve deeper structures (fig. 6.29a). SJIs with other components give inconsistent models (fig. 6.29b). The main feature, the deep conductive zone, is only qualitatively similar. FJIs of different components show an erratic behaviour (fig. 6.29c), although again a conductive zone above 1000 depth is observed.

As no stable combination of components can be found, no additional steps were taken at BSA. There are indications for a conductive zone $< 10 \Omega\text{m}$ between 700 and 1000 m, but the results are very unreliable.

At BSB, two E_x , \dot{H}_y and \dot{H}_z were recorded. Additionally, three SHOTEM data sets were recorded in the vicinity, where BSH19 is closest to the receiver followed by N23 and BSH20. The inversions of the SHOTEM-transients result in similar models, all showing a conductive zone at $\approx 100\text{-}200$ m depth. However, SJIs of all SHOTEM-transients show slight differences regarding the exact depth extent of the conductor (fig. 6.30a).

The LOTEM-components give consistent results in their SJIs. All SJIs for the two transients of one field component produce essentially the same model (fig. 6.30b). Including the Tx-distortion parameters does not change the inversion output significantly. The same model is reproduced for various combinations of components, even for FJIs. As BSH19 is closest to the Rx-site, this SHOTEM data set was chosen for the joint-inversions with the LOTEM-transients. Fig. 6.30c shows the results for a SJI of all six LOTEM-components and the BSH19-transient. The deeper structure, especially the conductive zone around a depth of 400 m is resolved by the LOTEM data sets, whereas the upper 200 m are constrained by the BSH19-transient.

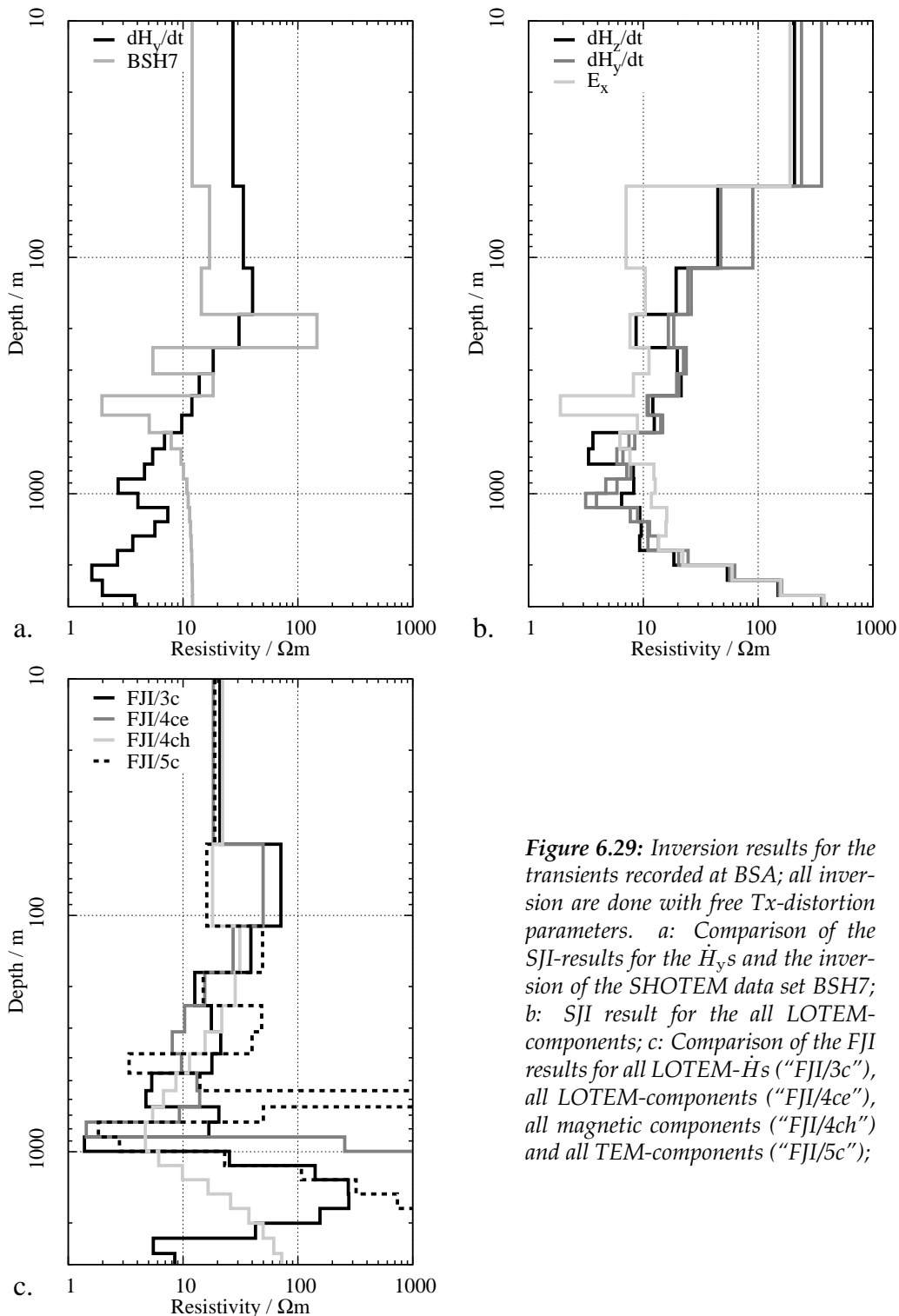


Figure 6.29: Inversion results for the transients recorded at BSA; all inversion are done with free Tx-distortion parameters. a: Comparison of the SJI-results for the \dot{H}_y s and the inversion of the SHOTEM data set BSH7; b: SJI result for the all LOTEM-components; c: Comparison of the FJI results for all LOTEM- \dot{H}_s ("FJI/3c"), all LOTEM-components ("FJI/4ce"), all magnetic components ("FJI/4ch") and all TEM-components ("FJI/5c");

The result of the equivalence analysis for these seven components shows that the conductive feature is well resolved. Its resistivity is around $1 \Omega\text{m}$ at a depth of ≈ 300 to ≈ 700 m. From hydrogeology it is known that the graben fill, which is underneath BSB is filled with various mixtures of brines and fresh water. The extremely conductive subsurface obtained by the inversions thus is expected and can be related to high salinity waters. The result at BSB differs from all other results.

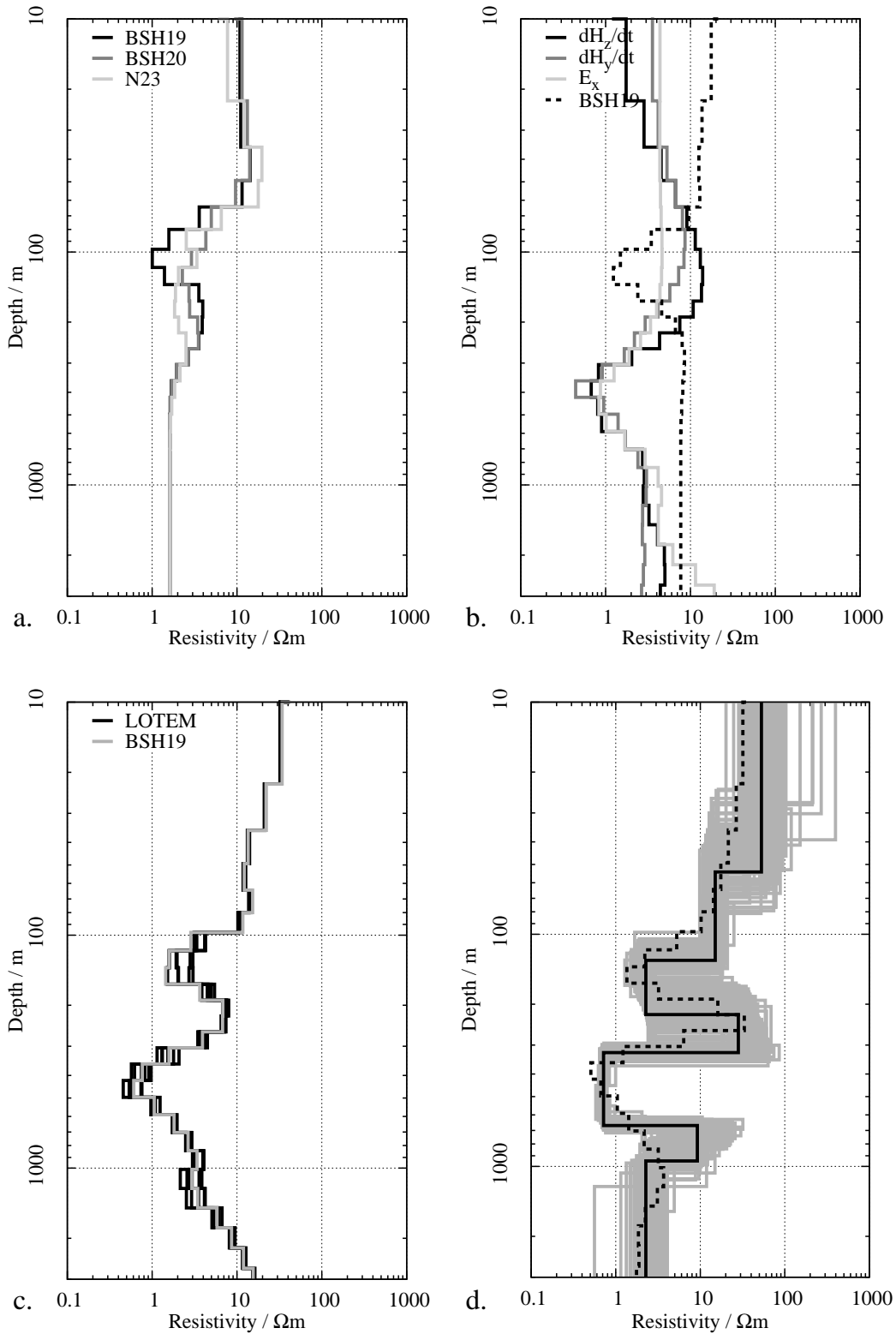


Figure 6.30: Inversion results for the transients recorded at BSB; all SJIs shown are done without Tx-distortion. *a:* SJI results for the three SHOTEM-transients; *b:* Comparison of SJIs results for the individual LOTEM-components and the SHOTEM data set BSH19; *c:* SJI results for seven TEM-components (“LOTEM+BSH19”); *d:* Equivalence analysis for seven TEM data sets (“LOTEM+BSH19”); the black lines shows the best model ($\chi = 2.64$), the dashed line the Occam’s-inversion result ($\chi = 3.00$) and the gray lines models with $\chi < 2.90$.

6.4 The results of the field campaign

Resistivity information can be derived at a considerable number of sites. In practice the SJI approach proved to be very useful. It was very easy to find out which of the components does not fit the informational content of the others by just checking the resulting models. Using only the FJI approach, this could only be achieved by comparing the separate misfits for the individual components in different FJI runs. Using SJIs it was also possible to find some data sets, where the sensor were faulty or wrongly deployed. These transients were excluded from the interpretation.

In several cases the electric fields can only be included to joint-inversions when the Tx-distortion parameters are used (e.g. site TKA). At EMA, for instance, the \dot{H}_y -SJI results resemble the \dot{H}_z -results only after introducing the additional parameters to the inversion. In the most cases however, only the misfit decreases using the distortion parameters but the resistivity structure does not change significantly.

Often the Occam's inversions fail to converge at a low misfit level when the Tx-distortion parameters are included. This fits the observations made in sec. 5.6. Nevertheless, in some cases inversions failed to converge at lower misfit levels when the parameters are *not* included. In most cases, the best models found in the equivalence analyses were obtained by using the Tx-distortion parameters as free parameters.

The results from the electric fields often show ambiguous results if inverted on their own. In cases where it is possible to invert them jointly with magnetic field components, they significantly reduce the ambiguity. At KEB and TKA it was possible to resolve a thin resistor at depth using the E_x -transients. These resistors can not be resolved using only the magnetic field components. Although these structures are not pertinent to the project, this shows the potential of combining several field components in one interpretation.

Some of the stations had to be rejected because no stable, consistent or meaningful model could be derived (AUA, AUB, BSA, EMA, KNA, KNB, SAA, TKB, YAA, YAB). In all other cases a conductive feature was found at depth. Tab. 6.1 lists the results for all stations along the traverse. As the LOTEM results reflects the subsurface in the vicinity of the whole spread (and not only at the Rx-site) I will assign the models to a point half-way between the Tx and the Rx. h in tab. 6.1 denotes roughly the elevation above sea level of this point. The next column "Rel.", gives a rating of the reliability of the results in five grades:

- ++: The data sets are very consistent. All SJIs and FJIs result in similar models.
- +: The data sets are consistent. The resulting models show inconsistencies which are not severe.
- 0: Some transients had to be discarded. However, the reason for the distortion is known and the effect can be estimated. At some sites only few data sets are available. These sites are also rated "0".
- : Some models can be derived, but the results are inconsistent in the relevant depth range.

- -: Each inversion resulted in a different resistivity structure or the data sets are too noisy.

The rating however, only refers to the reliability of the resolved features. It does not describe how well the conductive feature is resolved. For this information please refer to the row "Remarks" or the site's description in sec. D.1.

The results for two sites are not easy to compare. The number and type of the measured components as well as the SNR and the structure of the data sets differ from one site to the next. Therefore I did not derive a quantity describing the reliability. This classification has to stay somewhat subjective. See sec. D.1 for more details.

If a model was obtained, d_C and ρ_C are the depth (below sea level) to the top of the conductor and its resistivity, respectively. All analyses show one type of equivalence. In general, the conductor may be deeper and thinner when the resistivity is decreased at the same time. On the other hand, the top of the conductor can be placed shallower, when the resistivity is increased. The values given in tab. 6.1 are medium values. As a rough estimate, the depth is fixed within ± 100 m. The resistivity in general ranges from 4 to 15 Ωm . For more individual estimates again please refer to D.1.

The row "SHOTEM" denotes, whether a SHOTEM data set is used to derive the final model ("+") or not ("-"). If no SHOTEM data set is available, the row contains a "N.A.". In half of the cases the SHOTEM-transient is consistent to the LOTEM-transients and could be used in a joint-inversion. At KEB the target is very shallow. It is resolved mainly by the SHOTEM data set.

In some cases (e.g. DVA) the model was better constrained at depth when the SHOTEM-transient was used in the joint-inversions. However, according to the findings at ENB I considered changes at depth as not reliable when they are introduced by a SHOTEM data set. To avoid misinterpretations, I accepted a lower model resolution.

Fig. 6.31 displays the spatial distribution of the results in tab. 6.1 over the survey area. The numbers denote the depth to the conductor. Only the results for stations with at least a medium reliability are used (++, + or 0 in the Rel.-row). The numbers are displayed roughly at a position half-way between the Rx-sites and their corresponding Tx. A general trend can be observed. The depth in general increases from east to west along the paths from A or B to E or F.

The results are displayed in a cross-section along the line \overline{ACDF} in fig. 6.32. The positions of the sites in the vicinity of this line are projected perpendicular on the line. For the sake of simplicity the lower boundary of the conductor which is resolved at several stations is not displayed. The east-west dip of the conductor is obvious, with exception of the sites in the Carmel (CAA and CAB) and the Jordan Rift Valley (BSB).

The most important question is, if the conductive feature represents saline water or a certain lithological unit. This is not clear *a priori*, as the obtained resistivity values can be explained also by other geological formations. The dashed line in fig. 6.32 marks roughly the top of the Judea Group. This formation is exposed at the sites CAA, CAB, KEB and KEA. If the conductor would represent a lithological fea-

Site	h / m	Rel.	d_C / m	ρ_C / Ωm	SHOTEM	Remarks
AFA	20	0	580	10	+	only one station
AUA	60	-	260	3	+	see sec. D.1.2
AUB	60	--	-	-	-	too noisy
BEA	-80	0	1280	18	+	see sec. D.1.3
BEB	-90	0	1470	5	+	see sec. D.1.3
BSA	-110	-	810	< 10	-	inconsistent, FJIs failed
BSB	-170	++	470	< 1	+	low ρ below ≈ 200 m
CAA	450	0	710	6	+	only one station
CAB	350	0	710	4	N.A.	only one transient
DVA	130	0	770	9	-	
DVB	180	++	860	7	N.A.	
EMA	260	-	-	-	-	
HAA	-20	0	1300	10	-	not well resolved
HAB	-70	+	910	7	-	
KEA	90	0	310	9	+	not well resolved
KEB	50	0	180	6	+	resolved by SHOTEM
KKA	190	++	880	6	+	
KKB	220	+	860	13	+	
KNA	220	-	640	2	+	
KNB	190	--	-	-	N.A.	too inconsistent
RZA	60	-	760	10	+	not well resolved
RZB	-10	+	1090	8	-	
SAA	70	-	-	-	-	see sec. D.1.16
TKA	10	+	1000	4	+	not well resolved
TKB	-20	--	-	-	N.A.	too inconsistent
YAA	10	-	-	-	+	FJIs fail
YAB	10	-	-	-	N.A.	too ambiguous
YOA	60	0	580	4	N.A.	not well resolved
YOB	40	+	540	4	+	

Table 6.1: Results for all LOTEM-sites along the traverse; for more details, refer to the text.

ture, one would expect a correlation to the Judea Group topography. This correlation is not observed. At YOA and YOB, the conductor is found even shallower than the Judea group. The feature thus seems to cross lithological boundaries, which indicates that it represents saline water.

The top of the conductor at the sites CAA and CAB is deeper than at the sites YOA and YOB. This corroborates the hypothesis that the top of the conductor reflects the fresh to saline water interface. The groundwater table in the Carmel is elevated because of the topography [Kafri and Arad, 1979]. The higher column of the fresh water increases the pressure on the saline water. The interface thus is expected a greater depths. As long as the groundwater table is higher than sea level, this is described by the Ghyben-Herzberg formula [Kafri and Arad, 1979]. Further eastward the groundwater table drops which results in a shallower fresh to saline water interface.

At the easternmost station BSB, the conductor rises again. In addition, the resulting model exhibits extremely low resistivities $\leq 1 \Omega\text{m}$. This is also in accordance

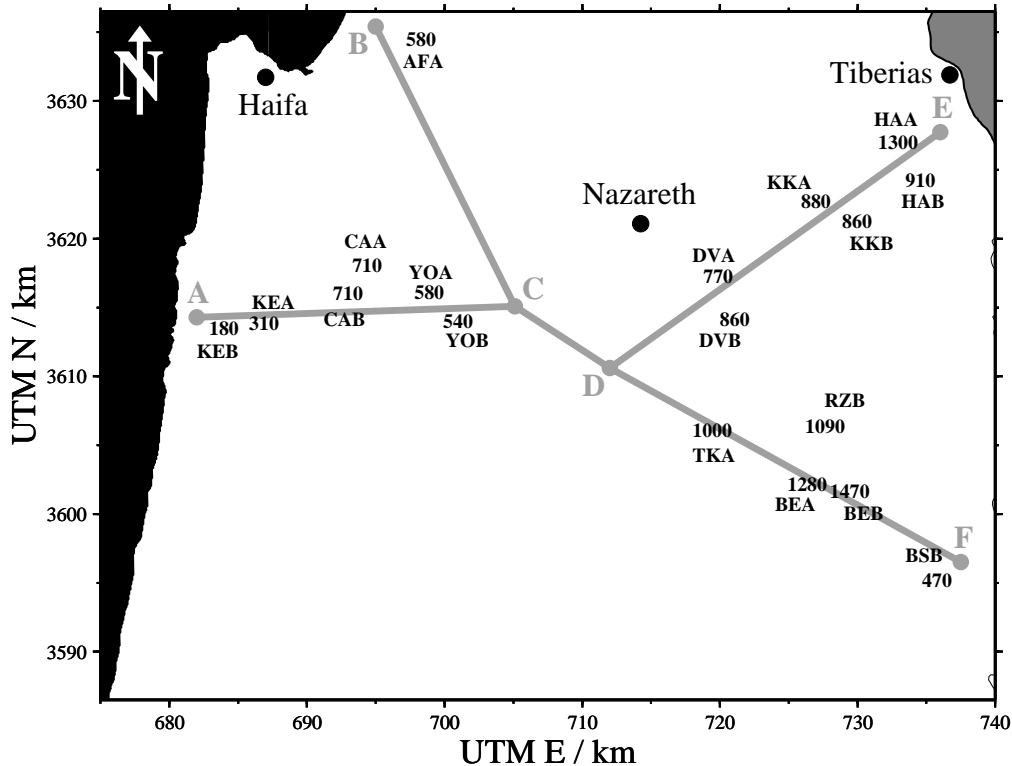


Figure 6.31: Results of all sites along the traverse, which are rated as medium reliable or better (at least a "0" in tab. 6.1); the numbers indicate the depth to the conductor described in tab. 6.1. The gray lines denote the flow path of sea-water from the Mediterranean as suggested by Kafri and Arad [1979].

to the hydrogeological observations, as upwelling saline water and deeper seated brines were found along the Rift Valley [U. Kafri, pers. comm.]. The transition from the deep conductor at BEB and the shallower feature at BSB is not resolved. Unfortunately, the data sets recorded at BSA (the site between BEB and BSB) is too inconsistent. Probably, the inconsistency is caused by the strong lateral changes which have to exist if the conductive zones at BEB and BSB are connected.

In the north it was not possible to set up a site in the Rift Valley, similar to BSB in the south. The topography in this area is very steep and strong data distortions were expected for sites close to the Sea of Galilee. A direct connection between the deep conductor and the saline springs close to the shore of the lake could thus not be detected.

With only 13 measurement sites for a traverse of almost 60 km length, the area seems to be greatly undersampled. However, unlike borehole measurement the models derived from the sites' data sets represent a larger part of the subsurface.

Although the results are satisfying, some problems remain. As the measurements at YAA and YAB failed, no real connection can be made between the Zevulun plain (AFA) in the NW and the internal valleys. This is also a flow path for the water from the Mediterranean suggested by Kafri and Arad [1979]. The sparse results along \overline{BC} can not clarify this question.

In the middle of the traverse – between the points C and D in fig. 6.31 – the geophysical interpretations of all three sites (SAA, AUA and AUB) fail, leaving a gap

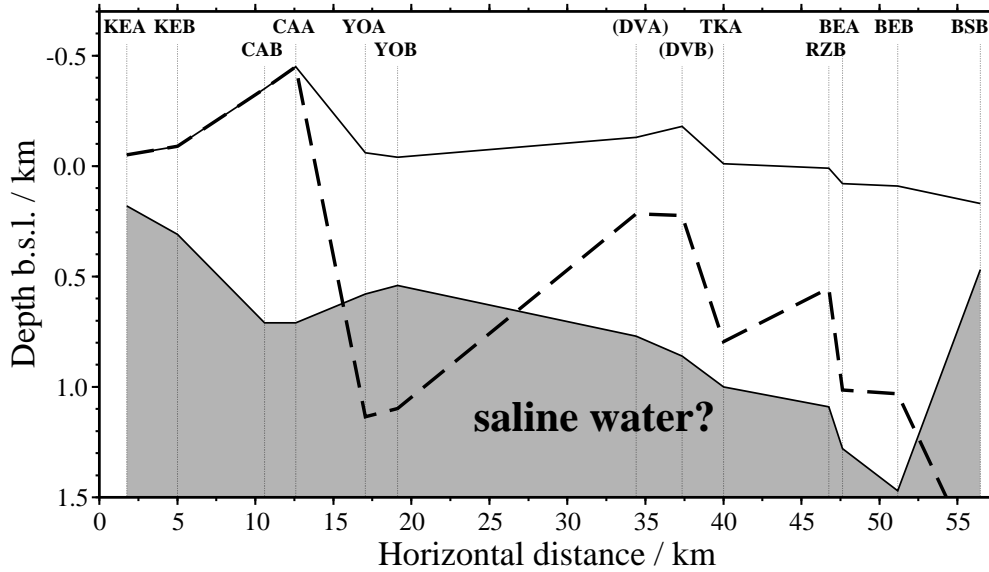


Figure 6.32: Section along \overline{ACDF} (fig. 6.31); the sites are projected perpendicular on the line \overline{ACDF} . The uppermost line displays roughly topography (i.e. the elevations of the sites from tab. 6.1). The dashed line denotes roughly the elevation of the top of the Judea Group (cp. fig. 6.8). The gray shape marks the top of the conductor found at each site. At several sites also the lower boundary of the conductor is resolved which is not displayed here. Note that the sites DVA and DVB are located several kilometres north of the line \overline{DF} .

between the Carmel and the Rift Valley. Resistivity models for these points would be very important. The conclusion that the conductor does not reflect any lithological formation is based mainly on the missing correlation between the Judea Group topography and the top of the conductor. The lack of correlation is most evident at YOA and YOB as these are the only places where the top of the conductor is shallower than the top of the Judea Group. It would be very pertinent to trace the conductor from the YOB site either to DVA or to TKA.

Nevertheless, the results so far indicate that saline water from Mediterranean intrudes the internal valleys and flows to the Rift Valley. Here it will act as a source of salinity.

CHAPTER 7

Discussion

The number of multidimensional models is infinite. Although the number of models used in chap. 5 is large, it is far from comprehensive. Generalising the obtained results therefore is dangerous. The models used in this study exhibited only moderate resistivity contrasts. The effects are expected to be far stronger when higher contrasts are involved. In addition, the results are equivocal even for the limited number of models examined. All conclusions trying to derive general statements should be treated with care. Nevertheless, the model calculations provide valuable precedences for several questions.

Most important, the single inversions in sec. 5.3 show that it is possible to derive meaningful models from 1-D inversions even in presence of multidimensional structures. If the Tx is placed on a lateral boundary it is possible to obtain the true resistivity structure on both sides of the Tx, when the Rx-sites are setup at some distance of the Tx. In some cases the true resistivity structure at greater depths can be resolved, although the shallow part of the model shows distortions.

The pseudo-sections derived from the data sets in general gave a blurred picture of the true model. In a way, the better inversion results represented a resistivity distribution averaged over the subsurface between the Rx and Tx. Small features are suppressed. Lateral changes show up as slow transitions instead of abrupt changes. In some cases however, the 1-D inversions resulted in models with strong artifacts which will lead to wrong geological interpretations. The strength of the distortions depends not only on the geometry (i.e. the position and shape of model boundaries), but also on the resistivity distribution. For instance, stronger distortions are observed when the lower boundary of a conductor shows some structure. In the models comprising of two quarter-spaces the distortions are stronger when the Tx is placed on the more conductive part.

The distortion effect of the multidimensional structures is different for the three components under investigation (see sec. 5.3.6). In several cases the electric fields are least distorted. On the other hand, the electric fields were most problematic

in the inversions of the field data sets. The reason for this might be fundamental technical problems in measuring the electric fields [S. L. Helwig, pers. comm.]. In addition, it can not be ruled out that some of the layers in the survey area show anisotropic properties (sec. 4.1.1), which will cause inconsistencies between the magnetic and the electric components.

One fundamental difference between the electric fields and the magnetic components is that the latter measure the time derivative of the magnetic fields, whereas the electric transients reflect the actual electric field. This difference is important for an inversion. The DC-value reached by the electric field for $t \rightarrow \infty$ will be changed by any inhomogeneity in the subsurface. Depending on the length of the data set, this structure manifests itself in several data points at the end of the transient. The effect of off-spread structures on the DC-value and thus on the inversion result can be large. This can be observed in the results for the models N1 and N2 in sec. 5.6, where the pseudo-sections derived without the Tx-distortion parameters show stronger distortions for the E_x - than for the \dot{H}_y -transients. Probably, the inversions of the electric fields would be more stable, if the the time derivative of the electric fields would be inverted.

The influence on the \dot{H}_y -component is not easy to understand. In some cases the pseudo-sections simply seem to ignore lateral changes. In other cases the final models showed shallow artifacts at stations which are at some distance from the distorting structure. However, the shape of the distortion differed depending on the model. The \dot{H}_z -transients seem to most distorted close to a lateral boundaries¹.

The influence on the SHOTEM-modification is completely different, mainly because of the different offsets used. The interpretation of LOTEM and SHOTEM data sets recorded at similar positions often will exhibit inconsistent structures, especially in the shallow part. This is caused by the fact that the LOTEM data sets also reflect the subsurface below the Tx. Still, it was possible to include the measured SHOTEM-transients in a joint-inversion scheme.

The main issue in this work is how to derive a model from the measured data sets which can be used for the geological interpretation. Further it is important to assess the reliability of the model. The main approach is based on the varying influence of the multidimensional structures on the three LOTEM components. At first, the various results obtained by the single inversions of the components cause a problem as the geophysical interpretation has to yield one model. The common approach to combine the informations of several data sets is the joint-inversion.

However, if distorted data sets are included in a standard joint-inversion (FJI), the resulting models often exhibit distortions. In a real field situation this approach thus is not suitable. Far better results are obtained by using the SJI approach (sec. 5.4.1). Inverting the field data sets, often the models obtained by one SJI showed only slight inconsistencies in the shallow parts but are consistent in the deeper regions. When the same data sets are used in a FJI, the slight inconsistencies prevent the algorithm from converging on a low misfit level. Moreover, often the FJI results

¹Discussing the effects on different components one should keep in mind that in real measured data sets not all components will be available with similar SNRs. Their signal quality depends on the underlying resistivity structure as well as on the noise situation in the area. For instance, at the southern flank of Merapi volcano, Indonesia the \dot{H}_y -transients were available with a higher quality than the \dot{H}_z s [Kalscheuer, 2004]. The quality of \dot{H}_y s measured in Jordan was significantly worse than the one of the \dot{H}_z s [Scholl et al., 2003].

obtained by using different components of one site showed an erratic behaviour, whereas the various SJIs gave consistent results. In fact, the SJI approach was very helpful during the field data inversion stage. It was easy to find out which data set was inconsistent to the other data sets. Both in the SJIs of the synthetic and the field data sets indications were found that the SJIs provide even better resolution capabilities than the FJIs at some sites.

It would have been very helpful to have a Marquardt joint-inversion algorithm at hand, which allows slight differences in the models for the respective components. This way, the FJIs could have been avoided completely. Although in most cases it was possible to find a set of components which reproduced the SJI results in FJIs, it is not clear what the subsequent equivalence analyses of these subsets actually reflect. The (indicated) improved resolution capabilities of the SJIs remain unused. A Marquardt approach is presented by Auken et al. [2001].

Assessing the reliability is not easy, because the choice of a reliability criteria is subjective. The danger of misinterpretation can not be ruled out completely unless all results are rejected. Increasing the number of accepted models will also increase the number of misinterpretations [Beck-Bornholdt et al., 2001].

As discussed in sec. 5.8 the misfit is not very helpful. In some cases distorted models are found which produced low misfits. In other cases the model was a reasonable representation of the subsurface but the misfit was quite high.

If data sets are available along a profile, the chances of detecting artifacts are much better. However, the pseudo-sections for the synthetic data sets showed several examples where laterally consistent artifacts appeared, in particular when FJIs have been used. This means that even lateral consistency is no proof that a certain feature is not artificial. The model calculations indicate that the use of a second transmitter on the same profile might be helpful, as the spurious structures depend on the position of the structure relative to the Tx-Rx-geometry.

I chose to judge the reliability according to the consistency of SJI results of different sets of components as criterion. This means that a e.g. conductive feature in one model has to appear at a similar depth in the other models. Inconsistencies of single components are allowed, when the distortion of the data set can be explained by additional informations about e.g. the subsurface. Reasons for the inconsistency of the SHOTEM- or LOTEM- E_x -transients can be found easily as discussed above.

The regularisation scheme is still an open question. The results for the synthetic data sets show that the tested regularisation schemes still tend to fit noise. The differences between the four schemes are small. The main difference is that if the minimisation of q_n^* is controlled (C2 and C4) the inversion needs more iteration steps. Limiting the decrease of λ (C3 and C4) leads to statistically slightly smoother models. However, for individual cases the results for C1 or C2 can be smoother. In some cases inversions using C2 and C4 failed to find a model producing low misfits (see app. A). Probably, an upper limit for λ would help (e.g. $\lambda_n \leq \lambda_{n-1}$). The best choice of the regularisation schemes so far seems to be C3. None of the four tested schemes prevented the build up of artificial structures.

Besides some convergence problems, the inversions including the Tx-distortion parameters worked well. For the field data sets they helped to find consistent models at some sites (e.g. DVA, EMA, HAB). The E_x -transients seem to profit most

from introducing the Tx-distortion parameters. However, in most cases only the misfit was improved. This can be expected as the Tx-Rx-geometry was close to a broadside configuration. In this case, the CF should be sufficient to describe the “distortions” produced by inhomogeneities close to the Tx.

Although the Tx-distortion parameters were derived by Hördt and Scholl [2004] to describe features close to the Tx, it is very likely that during the inversion of field data sets the additional parameters are used to fit distortions produced by other structures².

The interpretation scheme proved to be useful at the calibration sites. The correlation between the resistivity models and the borehole information is stronger when the data sets are mutually more consistent. In general, the results agree very well with the borehole information. The derived resistivity model from the other stations can be explained well by one of the three proposed hydrogeological models.

²If data sets from more than one station are involved in the inversion, the structure is supposed to be located in some distance from the Rx-sites as otherwise the necessary parameters should be different for both stations.

Bibliography

- Arnason, K., 1999, Consistent discretization of electromagnetic fields and transient modelling *in* Oristaglio, M., and Spies, B., Eds., Three-Dimensional Electromagnetics:: Soc. Expl. Geophys.
- Auken, E., Sørensen, K. I., Danielsen, J. E., and Pellerin, L., 2001, Mutually constrained inversion (MCI) of electrical and electromagnetic data from Skaro, Denmark.; EEGS Birmingham 2001 Proceedings.
- Avdeev, D. B., 2004, Three-Dimensional Electromagnetic Modelling and Inversion from Theory to Application:, 17th International Workshop on Electromagnetic Induction in the Earth, Hyderabad 2004, Abstracts, 193–213.
- Beck-Bornholdt, H.-P., Dubben, H.-H., and Beck-Bornholdt, H.-P., 2001, Der Hund, der Eier legt: Rowohlt TB, second Edition.
- Bergelson, G., Nativ, R., and Bein, A., 1999, Salinization and dilution history of ground water discharging into the Sea of Galilee, the Dead Sea Transform, Israel: Applied Geochemistry, **14**, 91–118.
- Blaschek, R., and Hördt, A., 2001, Der scheinbare Widerstandstensor in der LOTEM-Auswertung, Dt. Geophys. Gesellschaft, Protokoll über das 19. Kolloquium Elektromagnetische Tiefenforschung, 212–219.
- Blaschek, R., 2002, Der zeitabhängige scheinbare Widerstandstensor und sein Einsatz bei der Analyse von Long-Offset Transient Elektromagnetic Daten: Master's thesis, University of Cologne, Institute for Geophysics and Meteorology.
- Buselli, G., 1982, The effect of near-surface superparamagnetic material on electromagnetic measurements: Geophysics, **47**, no. 9, 1315–1324.
- Cagniard, L., 1953, Basic theory of the Magneto-Telluric Method of geophysical prospecting: Geophysics, **18**, 605–635.
- Caldwell, T. G., and Bibby, H. M., 1998, The instantaneous apparent resistivity tensor: a visualization scheme for LOTEM electric field measurements: Geophys. J. Int., **135**, 817–834.

- Christensen, N. B., 2000, Difficulties in determining electrical anisotropy in subsurface investigations: *Geophys. Prospect.*, **48**, 1–19.
- Commer, M., and Newman, G. A., 2004, A parallel finite-difference approach for 3D transient electromagnetic modeling with galvanic sources: *Geophysics*, **69**, no. 5, 1192–1202.
- Commer, M., Helwig, S. L., Hördt, A., and Tezkan, B., 2005, Interpretation of long-offset transient electromagnetic data from Mount Merapi, Indonesia, using a three-dimensional optimization approach: *J. Geophys. Res.*, **110**.
- Commer, M., 1999, Ein spezielles Verfahren der eindimensionalen kombinierten Inversion von Long-Offset Transient Electromagnetic (LOTEM)- und Magnetotellurik (MT)-Daten: Master's thesis, University of Cologne, Institute for Geophysics and Meteorology.
- Commer, M., 2003, Three-dimensional inversion of transient electromagnetic data: A comparative study: Ph.D. thesis, University of Cologne, Institute for Geophysics and Meteorology.
- Constable, S. C., Parker, R. L., and Constable, C. G., 1987, Occam's inversion: A practical algorithm for generating smooth models from electromagnetic sounding data: *Geophysics*, **52**, 289–300.
- Constable, S., Shankland, T. J., and Duba, A., 1992, The Electrical Conductivity of an Isotropic Olivine Mantle: *J. Geophys. Res.*, **97**, no. B3, 3397–3404.
- Davydycheva, S., Druskin, V., and Habashy, T., 2003, An efficient finite-difference scheme for electromagnetic logging in 3D anisotropic inhomogeneous media: *Geophysics*, **68**, no. 5, 1525–1536.
- Donat, A., 1996, Untersuchung der magnetischen Horizontalkomponenten bei long-offset transient electromagnetics (LOTEM): Master's thesis, University of Cologne, Institute for Geophysics and Meteorology.
- Druskin, V. L., and Knizhnerman, L. A., 1988, A spectral semi-discrete method for the numerical solution of 3D-nonstationary problems in electrical prospecting: *Physics of the solid Earth*, **24**, 641–648.
- Druskin, V., and Knizhnerman, L., 1994, Spectral approach to solving three-dimensional Maxwell's diffusion equations in the time and frequency domains: *Radio Science*, **29**, no. 4, 937–953.
- Druskin, V. L., Knizhnerman, L. A., and Lee, P., 1999, New spectral Lanczos decomposition method for induction modeling in arbitrary 3-D geometry: *Geophysics*, **64**, no. 3, 701–706.
- Duncan, P. M., 1978, Electromagnetic deep crustal sounding with a controlled, pseudo-noise source: Ph.D. thesis, University of Toronto.
- Eckard, M., 1993, Joint Inversion von Gleichstromgeoelektrik und Transientenelektromagnetik: Master's thesis, Institut für Geophysik und Meteorologie an der Universität zu Köln.

- Farquharson, C. G., and Oldenburg, D. W., 1993, Inversion of time-domain electromagnetic data for a horizontally layered Earth: *Geophys. J. Int.*, **114**, no. 3, 433–442.
- Farquharson, C. G., and Oldenburg, D. W., 2004, A comparison of automatic techniques for estimating the regularization parameter in non-linear inverse problems: *Geophys. J. Int.*, **156**, no. 3, 411–425.
- Fitterman, D. V., and Stewart, M. T., 1986, Transient electromagnetic sounding for groundwater: *Geophysics*, **51**, no. 4, 995–1005.
- Flexer, A., Yellin-Dror, A., Kronfeld, J., Rosenthal, E., Ben-Avraham, Z., Artsztein, P., and Davidson, L., 2000, A Neogene salt body as the primary source of the salinity in Lake Kinneret: *Arch. Hydrobiol. Spec. Issues Advanc. Limnol.*, **55**, 69–85.
- Flis, M. F., and Newman, G. A., 1989, Reply by the authors to R. S. Smith: *Geophysics*, **54**, no. 12, 1655–1660.
- Flis, M. F., Newman, G. A., and Hohmann, G. W., 1989, Induced-polarization effects in time-domain electromagnetic measurements: *Geophysics*, **54**, no. 4, 514–523.
- Gaidetzka, A., 2002, Erste Erfahrungen mit der NanoTEM-Apparatur: Master's thesis, University of Cologne, Institute for Geophysics and Meteorology.
- Gill, P. E., Murray, W., and Wright, M. H., 1981, *Practical optimization*: Academic Press, London.
- Goldberg, D. E., 1989, *Genetic Algorithms in Search, Optimization and Machine Learning*: Addison Wesley Publishing, first Edition.
- Goldman, M., and Kafri, U., 2002, Integrated electromagnetic geophysical technology applied to the detection of deep/saline groundwater interfaces in northern Israel., Geophysical Institute of Israel, Report prepared for: Ministry of National Infrastructures, Earth Science Administration, Report No. 911/188/01.
- Goldman, M., and Neubauer, F. M., 1994, Groundwater exploration using integrated geophysical techniques: *Surveys in Geophysics*, **15**, 331–361.
- Goldman, M., and Stoyer, C. H., 1983, Finite-difference calculations of the transient field of an axially symmetric earth for vertical magnetic dipole excitation: *Geophysics*, **48**, no. 7, 953–963.
- Goldman, Y., Hubans, C., Nicoletis, S., and Spitz, S., 1986, A finite-element solution for the transient electromagnetic response of an arbitrary two-dimensional resistivity distribution: *Geophysics*, **51**, 1450–1461.
- Goldman, M., Gilad, D., Ronen, A., and Melloul, A., 1991, Mapping of seawater intrusion into the coastal aquifer of Israel by the time domain electromagnetic method: *Geoexploration*, **28**, 153–174.
- Goldman, M., Eckard, M., Rabinovich, M., and Zacher, G., 1993, One-dimensional Joint Inversion of 3D Transient Electromagnetic (TEM) and Audiomagnetotelluric (AMT) Data., EAEG, 55th Conference and Technical Exhibition, Stavanger 1993, D018.

- Goldman, M., du Plooy, A., and Eckard, M., 1994a, On reducing the ambiguity in the interpretation of transient electromagnetic sounding data: *Geophys. Prospect.*, **42**, 3–25.
- 1994b, On the influence of 3-D structures in the interpretation of transient electromagnetic sounding data: *Geophysics*, **59**, no. 6, 889–901.
- Goldshmidt, M. J., Arad, A., and Neev, D., 1967, The mechanism of the saline springs in the Lake Tiberias depression: *Geol. Surv. Israel Bull.*, **45**, 1–19.
- Goldstein, M. A., and Strangway, D. W., 1975, Audio frequency magnetotellurics with a grounded electric dipole source: *Geophysics*, **40**, no. 4, 669–683.
- Grandis, H., and M. Menvielle, M. R., 1999, Bayesian inversion with Markov chains - I. The magnetotelluric one-dimensional case: *Geophys. J. Int.*, **138**, 757–768.
- Gunderson, B. M., Newman, G. A., and Hohmann, G. W., 1986, Three dimensional transient electromagnetic response for a grounded source: *Geophysics*, **51**, no. 11, 2117–2130.
- Gvirtzman, H., Garven, G., and Gvirtzman, G., 1997, Hydrogeological modeling of the saline hot springs at the Sea of Galilee, Israel: *Water Resources Research*, **33**, no. 5, 913–926.
- Haber, E., Ascher, U. M., and Oldenburg, D. W., 2004, Inversion of 3D electromagnetic data in frequency and time domain using an inexact all-at-once approach: *Geophysics*, **69**, no. 5, 1216–1228.
- Hansen, P. C., 1997, Rank-deficient and discrete ill-posed problems: numerical aspects of linear inversion: SIAM, Philadelphia.
- Hanstein, T., Eilenz, H. N., and Strack, K. M., 1986, Einige Aspekte der Aufbereitung von LOTEM Daten, Dt. Geophys. Gesellschaft, Protokoll über das 11. Kolloquium Elektromagnetische Tiefenforschung, 319–328.
- Hanstein, T., Lange, J., and Helwig, S. L., 2005, Der Einfluss (viskoser) magnetischer Böden auf Metalldetektoren., Dt. Geophys. Gesellschaft, 65. Jahrestagung der DGG, Graz 2005, Abstracts, 93.
- Hanstein, T., 1996, Digitale Optimalfilter für LOTEM Daten, Dt. Geophys. Gesellschaft, Protokoll über das 16. Kolloquium Elektromagnetische Tiefenforschung.
- Hanstein, T., 2001, Der Einfluss der magnetischen Permeabilität auf elektromagnetische Felder., DGG 61st annual Meeting, Frankfurt 2001, Abstracts.
- Helwig, S. L., 1994, Auswertung transient elektromagnetischer Meßdaten aus dem Makhtesh Ramon, Israel unter Benutzung rotationssymmetrischer Modelle: Master's thesis, University of Cologne, Institute for Geophysics and Meteorology.
- Helwig, S. L., 2000, VIBROTEM: Ph.D. thesis, University of Cologne, Institute for Geophysics and Meteorology.

- Hoheisel, A., 2000, Untersuchung des Einflusses von Induzierter Polarisation (IP) auf "Long-Offset Transient Electromagnetics" (LOTEM): Master's thesis, University of Cologne, Institute for Geophysics and Meteorology.
- Hohmann, G. W., and Newman, G. A., 1990, Transient electromagnetic responses of surficial, polarizable patches: *Geophysics*, **55**, no. 8, 1098–1100.
- Hohmann, G. W., 1975, Three-dimensional induced polarization and electromagnetic modeling: *Geophysics*, **40**, 309–324.
- Hönig, M., 2002, Entwicklung und Anwendung von Auswerteargorithmen für die Induzierte Polarisation im Zeitbereich in bis zu drei Dimensionen: Ph.D. thesis, University of Cologne, Institute for Geophysics and Meteorology.
- Hördt, A., and Müller, M., 2000, Understanding lotem data from mountainous terrain: *Geophysics*, **65**, no. 4, 1113–1123.
- Hördt, A., and Scholl, C., 2004, The effect of local distortions on time-domain electromagnetic measurements: *Geophysics*, **69**, no. 1, 87–96.
- Hördt, A., Druskin, V. L., and Knishnerman, L. A., 1992, Interpretation of 3-D effects on long-offset transient electromagnetic (LOTEM) soundings in the Münsterland area/Germany: *Geophysics*, **57**, 1127–1137.
- Hördt, A., Dautel, S., Tezkan, B., and Thern, H., 2000, Interpretation of long-offset transient electromagnetic data from the Odenwald area, Germany, using two-dimensional modelling: *Geophys. J. Int.*, **140**, 577–586.
- Hördt, A., 1989, Ein Verfahren zur 'Joint Inversion' angewandt auf 'Long Offset Electromagnetics' (LOTEM) und Magnetotellurik (MT): Master's thesis, University of Cologne, Institute for Geophysics and Meteorology.
- Hördt, A., 1992, Interpretation transient elektromagnetischer Tiefensondierungen für anisotrop horizontal geschichtete und für dreidimensionale Leitfähigkeitsstrukturen: Ph.D. thesis, University of Cologne, Institute for Geophysics and Meteorology.
- Hördt, A., 1998, Calculation of electromagnetic sensitivities in the time domain: *Geophys. J. Int.*, **133**, 713–720.
- Hoversten, G. M., and Morrison, H. F., 1982, Transient fields of a current loop source above a layered earth: *Geophysics*, **47**, no. 7, 1068–1077.
- Jones, A. G., 1988, Static shift of magnetotelluric data and its removal in a sedimentary basin environment: *Geophysics*, **53**, no. 7, 967–978.
- Jupp, D. L. B., and Vozoff, K., 1975, Stable iterative methods for the inversion of geophysical data: *Geophys. J. R. astr. Soc.*, **42**, 957–976.
- Jupp, D. L. B., and Vozoff, K., 1977, Resolving anisotropy in layered media by joint inversion: *Geophys. Prospect.*, **25**, no. 25, 460–470.
- Kafri, U., and Arad, A., 1979, Current Subsurface Intrusion of Mediterranean Seawater – a possible Source of Groundwater Salinity in the Rift Valley System, Israel: *J. Hydrol.*, **44**, 267–287.

- Kafri, U., 1967, Facies changes in the southwestern Carmel (Israel) and their influence on groundwater regime: *Isr. J. Earth-Sci.*, **16**, 206–214.
- Kalscheuer, T., 2004, Die Auswertung der LOTEM-Daten vom Südhang des Merapi: Master's thesis, University of Cologne, Institute for Geophysics and Meteorology.
- Karlik, G., 1994, Eine schnelle und direkte Interpretationsmethode für transient elektromagnetische Daten: Ph.D. thesis, University of Cologne, Institute for Geophysics and Meteorology.
- Klitzsch, C., 2000, Interpretation von "long offset transient electromagnetics" (LOTEM) Daten zur Erkundung der Struktur eines Erdgasreservoirs: Master's thesis, University of Cologne, Institute for Geophysics and Meteorology.
- Knödel, K., Krummel, H., and Lange, G., 1997, Handbuch zur Erkundung des Untergrundes von Deponien und Altlasten - Geophysik:, Vol 3 Springer-Verlag, Berlin.
- Koch, O., Scholl, C., Helwig, S. L., Martin, R., Meqbel, N., and the DESERT Group, 2004, LOTEM and SHOTEM measurements at the Dead-Sea-Transform within the DESERT-project:, *Eos Trans. AGU, Fall Meet. Suppl.*, San Francisco 2004, Abstract, GP14AA-07.
- Koch, O., 2003, Transient-elektromagnetische Messungen zur Erkundung einer Leitfähigkeitsanomalie am Vulkan Merapi in Indonesien: Master's thesis, University of Cologne, Institute for Geophysics and Meteorology.
- Kriegshäuser, B., 1991, Einige Aspekte der 3D Interpretation von LOTEM Daten: Master's thesis, University of Cologne, Institute for Geophysics and Meteorology.
- Lange, J., 2003, Joint Inversion von Central-Loop-TEM und Long-Offset-TEM Transienten am Beispiel von Messdaten aus Israel 2002: Master's thesis, University of Cologne, Institute for Geophysics and Meteorology.
- Lee, T., 1981, The effect of displacement currents on time domain electromagnetic fields: *Bull., Austral. Soc. Explor. Geophys.*, **12**, 34–36.
- Lee, T., 1984, The effect of a superparamagnetic layer on the transient electromagnetic response of a ground: *Geophys. Prospect.*, **32**, 480–496.
- Levenberg, K., 1944, A method for the solution of certain nonlinear Problems in least squares: *Quarterly of Applied Mathematics*, **2**, 164–168.
- Li, Y., 2000, Finite element modelling of magnetotelluric fields in 2-D structures with arbitrary anisotropy, *Dt. Geophys. Gesellschaft, Protokoll über das 18. Kolloquium Elektromagnetische Tiefenforschung*, 200–208.
- Lines, L. R., and Treitel, S., 1984, Tutorial: A review of least-squares inversion and its application to geophysical problems: *Geophys. Prospect.*, **32**, 159–186.
- Marquardt, D. W., 1963, An algorithm for least-squares estimation of non-linear parameters: *SIAM J. Sci. Stat. Comput.*, **11**, 431–441.

- Martin, R., and Hördt, A., 2001, Approximierte Sensitivitäten für TEM, Dt. Geophys. Gesellschaft, Protokoll über das 19. Kolloquium Elektromagnetische Tiefenforschung, 194–203.
- Martin, R., 2003, Realisierung von laufzeitoptimierten Methoden zur Bestimmung der 3D-TEM-Jacobimatrix: Master's thesis, University of Cologne, Institute for Geophysics and Meteorology.
- Mazor, E., and Mero, F., 1969, The origin of the Tiberias-Noit Mineral Water association in the Tiberias-Dead Sea Rift Valley, Israel: *J. Hydrol*, **7**, 318–333.
- Meju, M. A., 1994, Geophysical data analysis: Understanding inverse problem theory and practice: Society of Exploration Geophysics, Tulsa.
- Menke, W., 1984, Geophysical data analysis: Discrete inversion theory: Academic Press, Inc., Orlando, Florida.
- Mitsuhata, Y., Uchida, T., and Amano, H., 2002, 2.5-D inversion of frequency-domain electromagnetic data generated by a grounded-wire source: *Geophysics*, **67**, no. 6, 1753–1768.
- Mitsuhata, Y., 2000, 2-D electromagnetic modeling by finite element method with a dipole source and topography: *Geophysics*, **65**, no. 2, 465–475.
- Mosegaard, K., and Sambridge, M., 2002, Monte Carlo analysis of inverse problems: *Inverse Problems*, **18**, R29–R54.
- Mosegaard, K., and Tarantola, A., 1995, Monte Carlo sampling of solutions to inverse problems: *J. Geophys. Res.*, **100**, no. B7, 12,431–12,447.
- Müller, M., 2000, Elektromagnetik an Vulkanen: Ph.D. thesis, University of Cologne, Institute for Geophysics and Meteorology.
- Nabighian, M. N., 1979, Quasi-static transient response of a conducting half-space — an approximate representation: *Geophysics*, **44**, no. 10, 1700–1705.
- Neumann, J., 2005 (in preparation), TEM-responses of a waste site in Cologne: Master's thesis, University of Cologne, Institute for Geophysics and Meteorology.
- Newman, G. A., and Commer, M., 2005, New advances in three dimensional transient electromagnetic inversion: *Geophys. J. Int.*, **160**, 5–32.
- Newman, G. A., Hohmann, G. W., and Anderson, W. L., 1986, Transient electromagnetic response of a three-dimensional body in a layered earth: *Geophysics*, **51**, no. 8, 1608–1627.
- Newman, G. A., 1989, Deep transient electromagnetic soundings with a grounded source over near-surface conductors: *Geophys. J.*, **98**, 587–601.
- Oldenburg, D. W., and Li, Y., 1999, Estimating depth of investigation in dc resistivity and IP surveys: *Geophysics*, **64**, no. 2, 403–416.
- Oristaglio, M. L., 1982, Diffusion of electromagnetic fields into the earth from a line source of current: *Geophysics*, **47**, no. 11, 1585–1592.

- Pek, J., 1994, 2-D numerical models of magnetotelluric fields in anisotropic structures — an FD algorithm.; *Elektromagnetische Tiefenforschung* — 15. Kolloquium Höchst im Odenwald.
- Pelton, W. H., Ward, S. H., Hallof, P. G., Sill, W. R., and Nelson, P. H., 1978, Mineral discrimination and removal of inductive coupling with multifrequency IP: *Geophysics*, **43**, no. 3, 588–609.
- Petry, H., 1987, Transient elektromagnetische Tiefensondierungen — Modellrechnungen und Inversion: Master's thesis, University of Cologne, Institute for Geophysics and Meteorology.
- Qian, W., and Pedersen, L. B., 1992, Near-surface distortion effects on controlled source magnetotelluric transfer functions: *Geophys. J. Int.*, **108**, 833–847.
- Qian, W., 1994, On small-scale near-surface distortions in controlled-source tensor electromagnetics: *Geophysics*, **42**, 501–520.
- Raimundo, C., 2005, Transient Electromagnetic Measurements on a Waste Site in Düren and Their Interpretation: Master's thesis, University of Cologne, Institute for Geophysics and Meteorology.
- Rätz, S., 1999, A 3D Finite Element Code for Modeling of Electromagnetic responses.; University of Utah, Second International Symposium on Three-Dimensional Electromagnetics.
- Rätz, S., 2000, Ein dreidimensionales Finite Elemente Programm zur Simulation elektromagnetischer Oberflächen- und Bohrlochverfahren: Ph.D. thesis, University of Cologne, Institute for Geophysics and Meteorology.
- Reid, J. E., and Macnae, J. C., 1998, Short Note: Comments on the electromagnetic „smoke ring“ concept: *Geophysics*, **63**, no. 6, 1908–1913.
- Rotstein, Y., Bruner, I., and Kafri, U., 1993, High-resolution seismic imaging of the C-armel fault and its implications for the structure of Mt. Carmel: *Isr. J. Earth Sci.*, pages 55–69.
- Rüter, H., and Strack, K.-M., 1991, Bedrock exploration system using transient electromagnetic measurements: Patent PCT/DE91/00238.
- Sambridge, M., 1999, Geophysical inversion with a neighbourhood algorithm - I. Searching a parameter space: *Geophys. J. Int.*, **138**, 479–494.
- SanFilipo, W. A., and Hohmann, G. W., 1985, Integral equation solution for the transient electromagnetic response of a three-dimensional body in a conductive half-space: *Geophysics*, **50**, no. 5, 798–809.
- Schaumann, G., 2001, Transientelektromagnetische Messungen auf Mülldeponien – Untersuchung des Einflusses von 3D-Leitfähigkeitsvariationen und 1D-frequenzabhängiger Polarisierbarkeit: Ph.D. thesis, Technical University of Brunswick.
- Schmucker, U., 1994, 2-D Modellrechnungen zur Induktion in inhomogenen dünnen Deckschichten über anisotropen geschichteten Halbräumen.; *Elektromagnetische Tiefenforschung* — 15. Kolloquium Höchst im Odenwald.

- Scholl, C., Martin, R., Commer, C., Helwig, S. L., and Tezkan, B., 2003, 2D-Inversion von LOTEM-Daten, Dt. Geophys. Gesellschaft, Protokoll über das 20. Kolloquium Elektromagnetische Tiefenforschung, 230–239.
- Scholl, C., 2001, Die Periodizität von Sendesignalen bei Long-Offset Transient Electromagnetics: Master's thesis, University of Cologne, Institute for Geophysics and Meteorology.
- Schönfelder, T., 1995, Interpretation von LOTEM-Daten bei anisotroper Leitfähigkeitsverteilung: Master's thesis, University of Cologne, Institute for Geophysics and Meteorology.
- Sen, M. K., and Stoffa, P. L., 1991, Nonlinear one-dimensional seismic waveform inversion using simulated annealing: *Geophysics*, **56**, no. 10, 1624–1638.
- Simon, E., and Mero, F., 1992, The salinization mechanism of Lake Kinneret: *J. Hydrology*, **138**, 327–343.
- Smith, R. S., and Booker, J. R., 1988, Magnetotelluric Inversion for minimum structure: *Geophysics*, **53**, no. 12, 1565–1576.
- Smith, R. S., and West, G. F., 1988, Inductive interaction between polarizable conductors: An explanation of a negative coincident-loop transient electromagnetic response: *Geophysics*, **53**, no. 5, 677–690.
- Smith, R. S., and West, G. F., 1989, Field examples of negative coincident-loop transient electromagnetic responses modeled with polarizable half-planes: *Geophysics*, **54**, no. 11, 1491–1498.
- Spies, B. R., 1989, Depth of investigation in electromagnetic sounding methods: *Geophysics*, **54**, 872–888.
- Stahl, U., 1999, Horizontale Magnetfeldkomponenten und Magnetfeldsensoren der long-offset transient electromagnetic (LOTEM)-Methode: Master's thesis, University of Cologne, Institute for Geophysics and Meteorology.
- Sternberg, B. K., Washburne, J. C., and Pellerin, L., 1988, Correction for the static shift in magnetotellurics using transient electromagnetic soundings: *Geophysics*, **53**, no. 11, 1459–1468.
- Stoffa, P. L., and Sen, M. K., 1991, Nonlinear multiparameter optimization using genetic algorithms: Inversion of plane-wave seismograms: *Geophysics*, **56**, no. 11, 1794–1810.
- Strack, K. M., 1992, Exploration with deep transient electromagnetic, *Methods in Geochemistry and Geophysics*, Bd. 30 Elsevier, Amsterdam.
- Supriadi, Hördt, A., Müller, M., and Hanstein, T., 2000, Joint Inversion of CSAMT-Lotem Data from Merapi, Dt. Geophys. Gesellschaft, Protokoll über das 18. Kolloquium Elektromagnetische Tiefenforschung, 99–106.
- Sylvester, D., 1997, Bearbeitung und Interpretation von Daten transient-elektromagnetischer Tiefensondierungen im Umfeld der Kontinentalen Tiefbohrung (KTB) unter Berücksichtigung von Anisotropie: Master's thesis, University of Cologne, Institute for Geophysics and Meteorology.

- Telford, W. M., Geldart, L. P., and Sheriff, R. E., 1990, *Applied geophysics*: Cambridge University Press, 2. Edition.
- Thern, H., Hanstein, T., and Hördt, A., 1996, LOTEM im Odenwald — Ein Krustenleiter auch dort?, Dt. Geophys. Gesellschaft, Protokoll über das 16. Kolloquium Elektromagnetische Tiefenforschung.
- Thomas, L., 1977, Electromagnetic sounding with susceptibility among the model parameters: *Geophysics*, **42**, no. 1, 92–96.
- Toft, M., 2001, Three-dimensional TEM-modelling of near-surface resistivity variations: Master's thesis, University of Aarhus, Denmark.
- Unsworth, M. J., Travis, B. J., and Chave, A. D., 1993, Electromagnetic induction by a finite electric dipole source over a 2-D earth: *Geophysics*, **58**, 198–214.
- Vasseur, G., and Weidelt, P., 1977, Bimodal electromagnetic induction in non-uniform thin sheets with an application to the northern Pyrenean induction anomaly: *Geophys. J. R. astr. Soc.*, **51**, 669–690.
- Vozoff, K., and Jupp, D. L. B., 1975, Joint Inversion of Geophysical Data: *Geophys. J. R. astr. Soc.*, **42**, 977–991.
- Wang, T., and Fang, S., 2001, 3-D electromagnetic anisotropy modeling using finite differences: *Geophysics*, **66**, no. 5, 1386–1398.
- Wang, T., and Hohmann, G. W., 1993, A finite-difference, time-domain solution for three-dimensional electromagnetic modeling: *Geophysics*, **58**, no. 6, 797–809.
- Wang, T., 2002, The electromagnetic smoke ring in a transversely isotropic medium: *Geophysics*, **67**, no. 6, 1779–1789.
- Wannamaker, P. E., 2004, Anisotropy versus Heterogeneity in Continental Soil Earth Electromagnetic Studies: Fundamental Response Characteristics and Implications for Physicochemical State., 17th International Workshop on Electromagnetic Induction in the Earth, Hyderabad 2004, Abstracts, 237–260.
- Weidelt, P., 1975, Electromagnetic Induction in Three-Dimensional Structures: *J. Geophys.*, **41**, 85–109.
- Weidelt, P., 1982, Response characteristics of coincident loop transient electromagnetic systems: *Geophysics*, **47**, no. 9, 1325–1330.
- Weidelt, P., 2000, Numerical modelling of transient-electromagnetic fields in three-dimensional conductors: A comparative study, Dt. Geophys. Gesellschaft, Protokoll über das 18. Kolloquium Elektromagnetische Tiefenforschung, 200–208.
- Weinberger, G., Rosenthal, E., Ben-Zvi, A., and Zeitoun, D. G., 1994, The Yarkon-Taninim groundwater basin, Israel hydrogeology: case study and critical review: *J. Hydrol.*, **161**, 227–255.
- Weiss, C. J., and Newman, G. A., 2002, Electromagnetic induction in a fully 3-D anisotropic earth: *Geophysics*, **67**, no. 4, 1104–1114.

- Xiong, Z., Luo, Y., Wang, S., and Wu, G., 1986, Induced-polarization and electromagnetic modeling of a three-dimensional body buried in a two-layer anisotropic earth: *Geophysics*, **51**, no. 12, 2235–2246.
- Yadav, G. S., and Lal, T., 1989, Analysis of the Effect of Magnetic Permeability Variation on Magnetotelluric (MT) Response in relation to Delineation of Deccan Traps, India: *Jour. Assoc. Expl. Geophys.*, **10**, no. 3, 135–145.
- Yee, K. S., 1966, Numerical solution of initial boundary value problems involving Maxwell's equations in isotropic media: *IEEE Trans. Antenn. Propagat.*, **AP-14**, 302–307.

APPENDIX A

Implementation of the Occam's inversion

This appendix should give more detailed information about the implementation of the Occam's inversion algorithm. It is an extension especially to chapter 5. Reading chapter 5 will thus be necessary to understand this appendix.

The general work flow of the inversion algorithm is shown in the flow chart in fig. 5.6. However, in some special cases the inversion will fail to find a minimum of the misfit.

For this work, some 10,000 inversions are made. Although it still remains necessary to check the inversion results, it is desirable to make the inversion scheme as stable as possible. This means that with a standard set of parameters, the inversion should work in most cases (i.e. find a model with a reasonable misfit).

For the most of the problems addressed in this section I can not present a general solution. Probably there is no such solution which works with every TEM data set. The main objectives of this appendix is to describe, which measures I used for the 1-D inversions shown in this work and to alert the reader for these problems.

A.1 Transformation of the regularisation parameter λ

In all cases, after calculating the Jacobian, the algorithm searches for a value for λ which minimises the misfit. As proposed by Constable et al. [1987], this is done by a golden section search [Gill et al., 1981]. This is a two step process. First, the algorithm tries to find an interval, which brackets the minimum. As a starting interval for the iteration $n + 1$, $[\lambda_n \cdot 0.9, \lambda_n]$ is used. After bracketing the minimum, the position of the actual minimum is determined.

For the stability of the matrix inversion involved in solving the normal equation (e.g. eqn. 3.22) and of the model update, the ratio between the eigenvalues of \mathbf{J} and $\lambda \mathbf{P}^T \mathbf{P}$ is important. This is controlled by choosing an appropriate value for λ . This

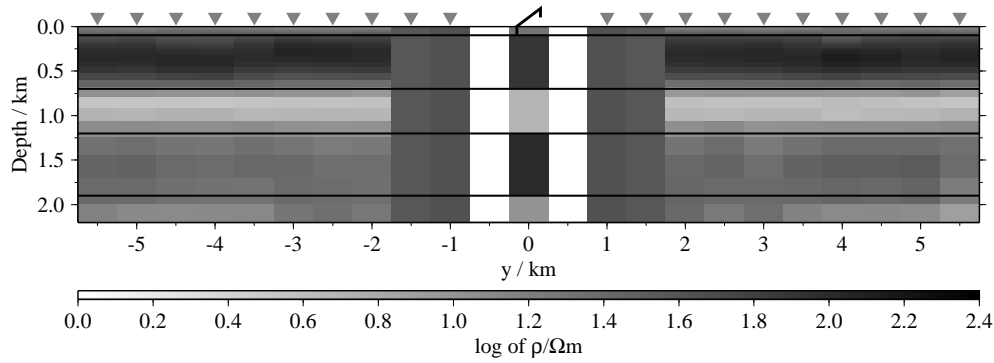


Figure A.1: 1-D pseudo-section of the synthetic data produced for the five layer case displayed below the Tx (at $x = 0$ m). In this case the \dot{H}_y -transients were inverted, with parameter set C4. The triangles mark the positions of the Rx-stations. The black lines mark the layer boundaries.

means, the difference between $\lambda = 0.1$ and $\lambda = 1$ should be as important as the difference between e.g. $\lambda = 100$ and $\lambda = 1000$. This is accounted for by internally transforming λ logarithmically. In fact, the golden section search tries to find a λ' which minimises $\chi(\exp(\lambda'))$. By doing so, the amount of forward calculations needed to find an appropriate value for λ is reduced. Further, this prevents any value for $\lambda < 0$ from being tested, which in most cases would make the matrix inversion via Cholesky decomposition impossible.

A.2 High initial misfits

The pseudo-sections and the field data inversions shown in this work are results of a long process. Fig. A.1 shows a first pseudo-section for single inversions of \dot{H}_y -transients using the parameter set C4 (see chapter 5)¹. Here, a typical problem shows up. Although most of the section is smooth and reproduces the model well, the models at the Rx-positions with offsets ≤ 1.0 km look different. They more or less are homogenous half-spaces, producing very high ($\chi > 50$) misfits.

This is caused by the huge dynamic range of the \dot{H}_y -transient at small offsets. The left part of fig. A.2 shows the transient at $x = -1.0$ km and the forward curve for the starting model. Especially shortly before the sign reversal the difference between both transients is around one order of magnitude, although the error bars are small. This results in a huge initial misfit of $\chi \approx 190$.

As can be seen in the right part of fig. A.2, $\chi(\lambda)$ shows a distinct maximum for $\lambda \approx 5000$, if $f = 1.0$. This is a result of the high misfit, because then the norm of the model update vector is likely to be very high and the linearisation error large. For $\lambda \gg 5000$ the solution of the normal equation is damped enough to achieve a better misfit. For $\lambda \ll 5000$ the norm of the model update vector is large and the behaviour of $\chi(\lambda)$ is erratic, showing two sharp minima and a sharp maximum.

The result of the one-dimensional search routine used to find a minimum of $\chi(\lambda)$

¹The discretisation of the initial homogenous half-space is chosen differently from the examples in chapter 5. Here, the first layer has a thickness of 10 m, whereas the deepest starts at a depth of 2000 m. It is divided into 30 layers instead of the 25. The discretisation was changed later to speed up the inversions.

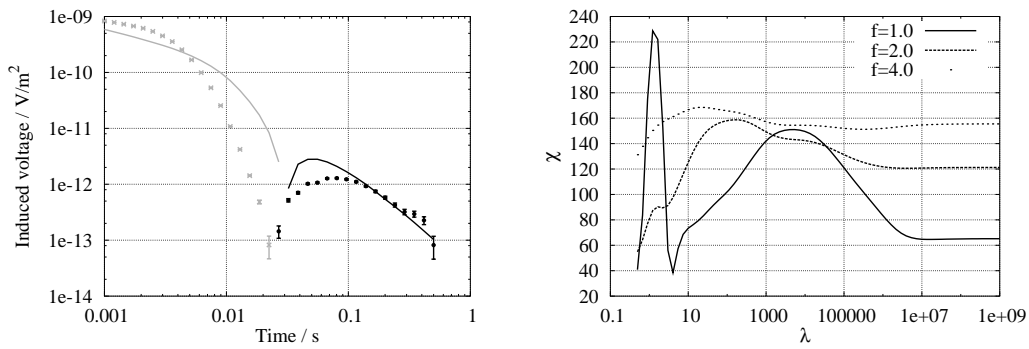


Figure A.2: Left: \dot{H}_y -transient at $x = -1.0 \text{ km}$; the simulated transient with noise added is shown with error bars, the line is the forward curve for the starting model ($20 \Omega\text{m}$ half space). The shade denotes the sign of the transients (gray = negative, black = positive). Right: $\chi(\lambda)$ for the transients shown in the left part of this figure at the first iteration; the graphs are plotted for three different inverse step-lengths f .

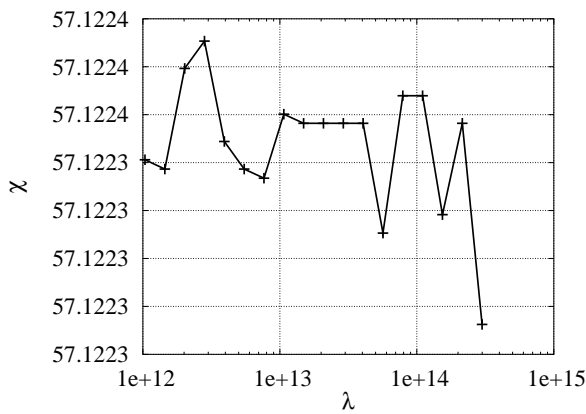


Figure A.3: $\chi(\lambda)$ for $10^{12} < \lambda < 3 \cdot 10^{14}$ for the inversion described in the text in the second iteration; the values for χ differ mainly only in the 5th decimal place, which is not displayed here. the erratic behaviour is caused by numerical rounding errors but are interpreted as real minima and maxima by the golden section search.

will depends strongly on the initial value of λ . For $\lambda_0 = 10,000$ the minimum in the left branch is found and thus $\lambda_1 \approx 4 \cdot 10^{16}$ in this case.

This value of λ defines the initial interval for the search routine in the next iteration. Although here $\chi(\lambda)$ has only one minimum, starting with huge values for λ impedes the univariate search because numerical rounding errors mimic local minima (fig. A.3). Thus, λ_2 again is $\approx 2 \cdot 10^{16}$. In the third iteration the algorithm is not able to find any better model and stops with a bad misfit and an over-smooth model, regardless of what regularisation scheme is used (C1-C4, see section 5.2.3).

Using a more global approach than the localised golden section search does not solve the problem in all cases. fig. A.4 shows the inversion progress if prior to the bracketing routine the minimum is approximated by scanning $\chi(\lambda)$ for $0.4 < \lambda < 1.2 \cdot 10^9$ with 8 nodes per decade. Here, the minima for small λ s are found (fig. A.2, left) and used for the first iteration, unless the decrease in the regularisation is limited (C3 and C4, see tab. 5.1). The low regularisation combined with the high starting misfit results in very rough models (A.4, right). This unnecessary roughness introduced at early inversion stages obviously prevents the algorithm from finally converging at low misfit levels. The inversions with a restricted regularisation decrease succeed, which shows the superiority of this strategy in these cases.

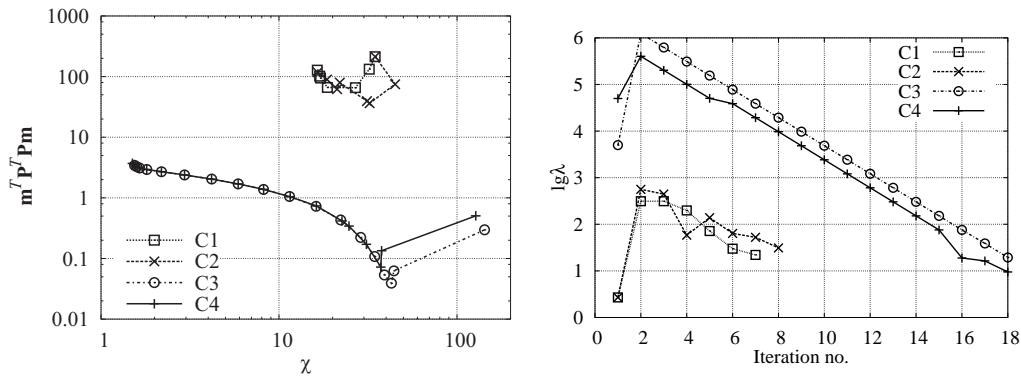


Figure A.4: Inversion progress if a global search for the minimum of $\chi(\lambda)$ is done prior to the golden section; Left: χ_n against $\mathbf{m}_n^T \mathbf{P}^T \mathbf{P} \mathbf{m}_n$ for the iteration steps using the different regularisation schemes (see tab. 5.1). Right: $\lg \lambda_n$ used in the inversions.

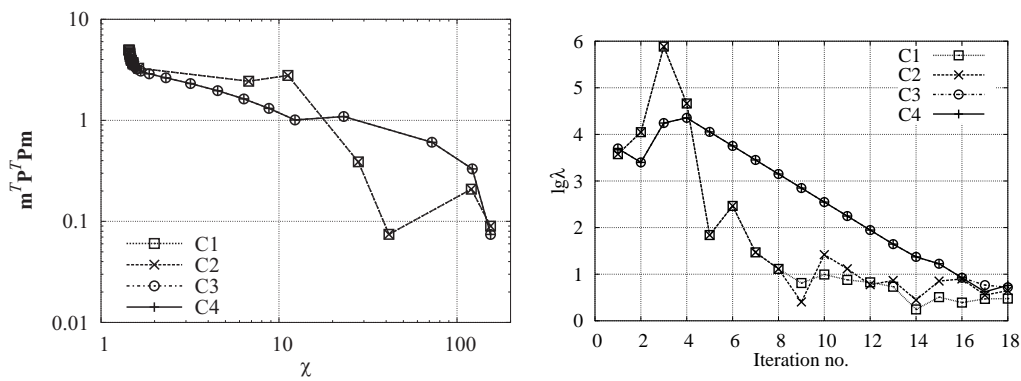


Figure A.5: Inversion progress, when the increase in the value of λ is restricted as described in the text; Left: χ_n against $\mathbf{m}_n^T \mathbf{P}^T \mathbf{P} \mathbf{m}_n$ for the iteration steps using the different regularisation schemes (see tab. 5.1). Right: $\lg \lambda_n$ used in the inversions.

Another idea is to try to damp the increase in the values of λ . After the golden section search, the algorithm checks, whether $\lambda_{n+1} > \min(100\lambda_n, 10^9)$ and the inverse step-length is $f \leq 16$. If this is the case, f is doubled and the search is repeated with a starting interval of $[\lambda_n \cdot 0.9/f, \lambda_n/f]$. fig. A.2, right suggests that increasing f moves the minimum of $\chi(\lambda)$ to smaller regularisations. fig. A.5 shows the course of inversion using the explained damping of the value of λ .

Although this strategy works in this case, it might fail in general. As can be seen in the left part of fig. A.2, the initial value of λ greatly affects which minimum of $\chi(\lambda)$ the golden section search will find. If 1,000 instead of 10,000 had been used, the inversion progress would be the same as shown in fig. A.4. This supports the use of high starting regularisations, which on the other hand hamper the inversions with limited decreases in the value of λ .

Both the high regularisations used in the original inversion (fig. A.2) and the unnecessary high roughnesses appearing in fig. A.4 are caused by the very high initial misfit. The simplest and yet most effective countermeasure thus is reducing the starting misfit. This can be done by finding a resistivity for the starting half-space which minimises the misfit prior to inversion²

²This contradicts the statement made in section 3.2.2 that the resistivity used for the initial homogenous half-space does not effect the result of the inversion. However, in most cases this is true.

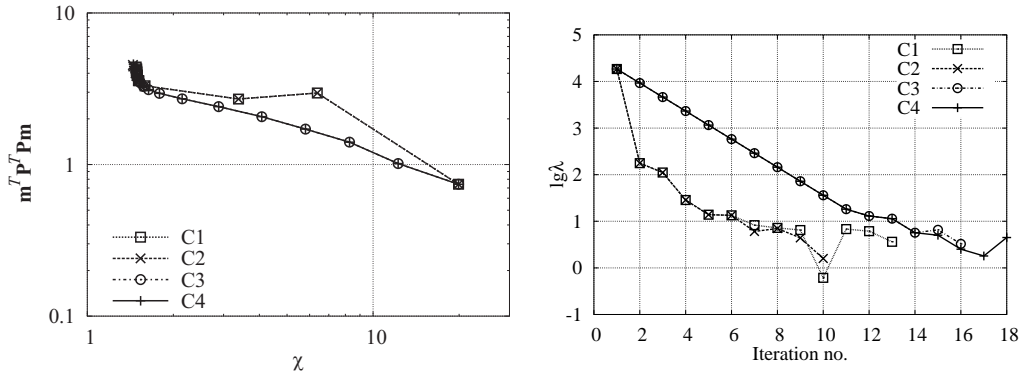


Figure A.6: Inversion progress, when the resistivity of the half-space is optimised prior to inversion; Left: χ_n against $m_n^T P^T P m_n$ for the iteration steps using the different regularisation schemes (see tab. 5.1). Right: $\lg \lambda_n$ used in the inversions.

Starting with $\rho = 30 \Omega\text{m}$, a golden section search is again applied. The resistivity of the starting half-space is set to this optimal value, unless it is smaller than $1 \Omega\text{m}$ or higher than $10,000 \Omega\text{m}$. In this case, the resistivity is set to $1 \Omega\text{m}$ or $10,000 \Omega\text{m}$, respectively.

For this data set the starting resistivity of the half-space was changed from the original $20 \Omega\text{m}$ to $\approx 39 \Omega\text{m}$. With this model the initial misfit has decreased from ≈ 190 to ≈ 57 . As can be seen in fig. A.6 this also leads to a stable inversion.

If all else fails, the last possibility to reduce the starting misfit is to remove the data points producing with the biggest deviation.

A.2.1 Using the second derivative roughness definition R_2

The problem with respect to high initial misfits is even more severe using the second derivative roughness definition R_2 from eqns. 3.17 and 3.20. Again, the inversion might be tempted to use very high values for λ at early iteration steps. Using R_2 an additional problem might occur, because the matrix $P^T P$ itself is singular³. At least ONE information has to be provided by the data, either which resistivity (R_1) or which resistivity gradient (R_2) should be applied to all layers.

High values for λ thus lead to a model with a arbitrary but homogenous resistivity for the first derivate roughness definition. For R_2 , high values for λ may result in models, where an initial resistivity gradient is extended to depth, producing layers with unreasonable resistivities⁴. Inverting field data sets with the standard inversion scheme from fig. 5.6, occasional models with resistivities lower than 10^{-40} or higher than 10^{40} appeared. These extreme resistivity values make the evaluation of

Typically the algorithm changes more or less only the half-space resistivity in the first iteration /em without choosing extreme values for λ . The problems seem to occur – as in this case – mainly, when few data points dominate the misfit. Optimising the resistivity of the half-space has the same effect as doing one iteration and resetting the regularisation parameter, but is computationally cheaper.

³“Smooth” models in a R_1 - or R_2 -sense are ambiguous. For R_1 , a model is smooth if all layers have the same resistivity, regardless of which one. For R_2 , the change in resistivity between any adjacent layers have to be the same, regardless of how big this change is.

⁴Unless plasma, ideal vacuum or supra-conducting material is concerned, the resistivity ranges between 10^{-8} (metals) and 10^8 (air).

$\mathbf{f}(\mathbf{m})$ unstable. Thus, the entries in the model vector used for the model response calculation have to be limited to values between 10^{-10} and 10^{10} .

The problem described in this section for a synthetic data set was also encountered several times inverting field data sets. As a result, for all inversion shown in this work, the resistivity of the starting model was optimised prior to inversion as described. As an additional fall-back, the regularisation was damped as in fig. A.5.

Inverting field data another problem showed up. Sometimes the inversion algorithm decreased the misfit in early iterations but afterwards failed to decrease the misfit further. Depending on the starting point for the search routine for λ the algorithm again chose very high regularisations, degrading the misfit to its initial value. This happens because for $\lambda \rightarrow \infty$ the misfit is much smaller than $\lambda \mathbf{m}_n^T \mathbf{P}^T \mathbf{P} \mathbf{m}_n$. The cost function thus is dominated by the roughness, and the algorithm will return to the homogenous half-space. In the future it might be useful to restrict the λ_i to values $\leq \lambda_{i-1}$. Probably, a search algorithm other than the golden section search can solve this problem.

To circumvent these problems, I switched back to the standard discrepancy principle in cases where the algorithm failed to converge at a reasonable level of misfit.

1-D pseudosections of synthetic 2-D models

In this appendix the results of 1-D inversions of synthetic data sets are shown. All transients are calculated with the 3-D forward algorithm SLDMEM3T. More information on how the data are produced and modified prior to inversion can be found in chapter 5. Here, also the regularisation schemes are described.

The general regularisation scheme used for the following pseudo section is one of these four:

Designation	C1	C2	C3	C4
Convergence controlled by	χ_n	q_n^*	χ_n	q_n^*
Maximum decrease factor c	0.0	0.0	0.5	0.5

The designation can be found in the caption of the different figures of this appendix.

The results of the inversions of the different components are displayed as 1-D pseudo-section, plotting the resulting models below the respective Rx-position. The gray-scale coding the resistivities is displayed at least once in each figure. Values exceeding the scale are either displayed as white (too small) or black (too big). Areas where very unrealistic values are obtained (< 0.2 or > 20 k Ω m) are marked with diagonal lines. The pseudo-sections for the SJIs show averaged values.

The Rx-sites are marked with gray triangles. The Tx is located at $y = 0$ km and pointing in x-direction. The model boundaries are marked with black lines in the pseudo-section. At $y = 0$ km, the synthetic model at the location of the Tx is shown for comparison. Above every pseudo-section the misfit (χ), the model roughness and the CF for each inversion result is displayed.

The order of components used is E_x , \dot{H}_y and \dot{H}_z , e.g. in a joint-inversion of E_x and \dot{H}_y the first CF will be the one for the E_x , the second the one for the \dot{H}_y . The order of two component combinations is E_x - \dot{H}_y , E_x - \dot{H}_z and \dot{H}_y - \dot{H}_z .

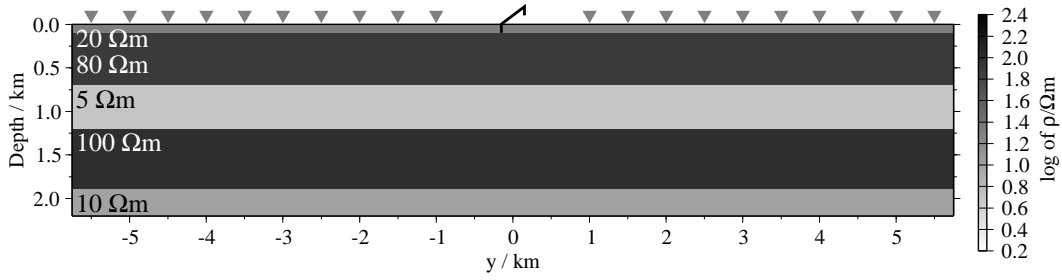


Figure B.1: Model A used for the model calculations of this section;

B.1 Testing the regularisation schemes with a 1-D model (model A)

In this section the results of the inversions of the synthetic data sets for model A (see fig. B.1) for the four different regularization schemes are presented. First, the inversion statistics are shown in several tables, followed by the pseudo-sections.

x/km	χ	Roughn.	# of It.	CF
-5.5	0.60	3.31	6	1.00
-5.0	0.79	9.10	24	0.63
-4.5	0.71	4.88	16	0.80
-4.0	0.77	9.18	21	0.99
-3.5	0.97	5.18	13	0.89
-3.0	0.86	9.34	15	0.80
-2.5	0.84	9.65	30	1.07
-2.0	0.88	10.53	25	0.81
-1.5	0.82	5.09	23	1.04
-1.0	0.64	3.53	10	1.10
1.0	1.02	5.72	25	1.09
1.5	0.61	4.55	13	0.94
2.0	0.78	10.01	23	0.87
2.5	0.85	5.21	25	1.11
3.0	0.78	4.26	9	0.94
3.5	0.85	7.88	17	0.88
4.0	0.90	5.11	13	0.84
4.5	0.74	3.44	6	1.01
5.0	1.11	7.30	20	0.69
5.5	0.91	3.96	9	0.99
Avg.	0.81	5.92	15.5	0.92
Std. dev.	0.19	1.56	4.2	0.21

Table B.1: Statistics of the inversion of E_x -transients calculated for the 1-D model with the parameter set C1; The columns give the position (x) of the Rx-station and the misfit χ and roughness of the resulting models. The last two columns state the number of iterations needed and the resulting calibration factor (CF). In the last two lines the average and standard deviation for all stations are given.

x/km	χ	Roughn.	# of It.	CF
-5.5	0.82	5.78	11	1.00
-5.0	0.83	6.35	12	0.97
-4.5	0.93	5.79	11	1.00
-4.0	0.79	4.67	23	1.02
-3.5	0.67	11.87	17	1.03
-3.0	0.86	4.26	7	1.00
-2.5	0.90	10.94	24	1.01
-2.0	0.93	3.93	12	1.00
-1.5	0.84	10.09	28	1.10
-1.0	1.60	3.02	6	1.07
1.0	0.88	3.00	9	1.03
1.5	0.76	13.74	29	1.11
2.0	1.15	4.68	13	1.00
2.5	0.83	5.17	13	1.00
3.0	0.86	11.20	29	1.09
3.5	0.83	6.39	11	1.02
4.0	0.86	7.14	13	1.02
4.5	0.67	4.05	8	1.00
5.0	0.84	4.10	8	1.03
5.5	0.83	4.73	19	0.99
Avg.	0.87	5.90	13.5	1.02
Std. dev.	0.21	1.67	3.9	0.23

Table B.2: Statistics of the inversion of \dot{H}_y -transients calculated for the 1-D model with the parameter set C1; The columns give the position (x) of the Rx-station and the misfit χ and roughness of the resulting models. The last two columns state the number of iterations needed and the resulting calibration factor (CF). In the last two lines the averages and standard deviations are given.

x/km	χ	Roughn.	# of It.	CF
-5.5	0.76	5.55	15	1.03
-5.0	0.87	4.02	7	1.01
-4.5	0.71	5.07	16	0.99
-4.0	1.07	7.18	10	1.01
-3.5	1.05	5.26	7	1.01
-3.0	1.00	5.46	12	1.01
-2.5	0.90	8.26	19	1.01
-2.0	0.88	5.20	16	1.00
-1.5	0.87	7.15	11	1.01
-1.0	1.27	7.07	13	1.02
1.0	0.97	9.61	32	1.02
1.5	1.02	13.59	24	1.01
2.0	0.73	10.45	15	1.01
2.5	0.71	9.63	9	1.02
3.0	0.86	5.87	10	0.99
3.5	0.78	3.48	6	0.99
4.0	0.91	5.59	8	1.01
4.5	0.78	3.88	6	0.99
5.0	0.81	7.37	15	1.02
5.5	0.86	4.41	8	1.01
Avg.	0.88	6.30	11.7	1.01
Std. dev.	0.21	1.64	3.3	0.23

Table B.3: Statistics of the inversion of \dot{H}_z -transients calculated for the 1-D model with the parameter set C1; The columns give the position (x) of the Rx-station and the misfit χ and roughness of the resulting models. The last two columns state the number of iterations needed and the resulting calibration factor (CF). In the last two lines the averages and standard deviations are given.

x/km	χ	Roughn.	# of It.	CF
-5.5	0.60	3.30	6	1.00
-5.0	0.80	7.74	23	0.64
-4.5	0.72	4.39	14	0.79
-4.0	0.78	7.53	18	0.97
-3.5	0.97	5.12	13	0.89
-3.0	0.85	10.81	26	0.80
-2.5	0.84	8.06	29	1.07
-2.0	0.88	7.97	21	0.88
-1.5	0.83	4.33	14	1.09
-1.0	0.64	3.48	10	1.10
1.0	1.02	5.18	19	1.09
1.5	0.61	4.71	15	0.94
2.0	0.79	7.47	20	0.87
2.5	0.85	5.08	25	1.09
3.0	0.78	4.21	9	0.94
3.5	0.85	7.08	15	0.88
4.0	0.91	4.53	14	0.84
4.5	0.74	3.44	6	1.01
5.0	1.12	5.72	17	0.70
5.5	0.91	3.93	9	0.99
Avg.	0.81	5.39	14.8	0.92
Std. dev.	0.19	1.38	4.0	0.22

Table B.4: Statistics of the inversion of E_x -transients calculated for the 1-D model with the parameter set C2; The columns give the position (x) of the Rx-station and the misfit χ and roughness of the resulting models. The last two columns state the number of iterations needed and the resulting calibration factor (CF). In the last two lines the averages and standard deviations are given.

x/km	χ	Roughn.	# of It.	CF
-5.5	0.81	6.42	29	1.01
-5.0	0.81	9.63	38	0.97
-4.5	0.93	5.57	11	1.00
-4.0	0.79	5.14	25	1.03
-3.5	0.67	10.77	15	1.03
-3.0	0.86	4.49	20	1.00
-2.5	0.90	9.61	20	1.01
-2.0	0.94	3.80	11	1.00
-1.5	0.86	6.63	12	1.08
-1.0	1.58	2.86	6	1.07
1.0	0.88	2.68	10	1.03
1.5	0.75	14.28	32	1.11
2.0	1.14	5.28	18	1.00
2.5	0.82	4.78	13	1.00
3.0	0.86	9.92	29	1.09
3.5	0.83	6.60	20	1.02
4.0	0.85	7.44	24	1.02
4.5	0.66	3.98	14	1.00
5.0	0.84	4.06	8	1.03
5.5	0.83	4.53	18	0.99
Avg.	0.87	5.83	16.8	1.02
Std. dev.	0.21	1.62	4.7	0.24

Table B.5: Statistics of the inversion of H_y -transients calculated for the 1-D model with the parameter set C2; The columns give the position (x) of the Rx-station and the misfit χ and roughness of the resulting models. The last two columns state the number of iterations needed and the resulting calibration factor (CF). In the last two lines the averages and standard deviations are given.

x/km	χ	Roughn.	# of It.	CF
-5.5	0.76	4.83	11	1.02
-5.0	0.87	4.03	12	1.01
-4.5	0.72	4.36	9	0.99
-4.0	1.06	9.08	19	1.01
-3.5	1.05	5.13	9	1.00
-3.0	0.99	6.60	21	1.01
-2.5	0.90	7.52	12	1.01
-2.0	0.88	5.05	13	1.00
-1.5	0.86	6.95	35	1.01
-1.0	1.27	7.58	15	1.02
1.0	0.98	8.35	24	1.02
1.5	1.02	11.72	25	1.01
2.0	0.73	10.73	24	1.01
2.5	0.75	12.00	24	1.00
3.0	0.88	9.41	22	1.00
3.5	0.84	3.68	6	0.99
4.0	0.88	4.90	18	1.00
4.5	0.73	5.22	11	1.01
5.0	0.88	4.64	9	1.00
5.5	0.86	4.85	13	1.02
Avg.	0.88	6.40	15.1	1.01
Std. dev.	0.21	1.67	4.2	0.23

Table B.6: Statistics of the inversion of \dot{H}_z -transients calculated for the 1-D model with the parameter set C2; The columns give the position (x) of the Rx-station and the misfit χ and roughness of the resulting models. The last two columns state the number of iterations needed and the resulting calibration factor (CF). In the last two lines the averages and standard deviations are given.

x/km	χ	Roughn.	# of It.	CF
-5.5	0.62	3.07	12	0.87
-5.0	0.79	9.34	28	0.64
-4.5	0.72	4.61	18	0.79
-4.0	0.78	8.97	25	0.98
-3.5	0.97	5.55	22	0.88
-3.0	0.85	10.14	20	0.80
-2.5	0.84	7.67	32	1.07
-2.0	0.88	8.64	27	0.88
-1.5	0.83	4.23	18	1.10
-1.0	0.63	5.57	39	1.20
1.0	1.02	5.07	28	1.09
1.5	0.61	4.73	23	0.94
2.0	0.79	6.15	20	0.87
2.5	0.85	5.17	31	1.13
3.0	0.77	4.83	22	0.98
3.5	0.84	11.51	34	0.90
4.0	0.90	5.66	26	0.84
4.5	0.75	3.31	14	0.94
5.0	1.11	8.39	28	0.72
5.5	0.92	3.68	17	0.91
Avg.	0.81	5.89	23.2	0.92
Std. dev.	0.19	1.55	5.8	0.21

Table B.7: Statistics of the inversion of E_x -transients calculated for the 1-D model with the parameter set C3; The columns give the position (x) of the Rx-station and the misfit χ and roughness of the resulting models. The last two columns state the number of iterations needed and the resulting calibration factor (CF). In the last two lines the averages and standard deviations are given.

x/km	χ	Roughn.	# of It.	CF
-5.5	0.82	5.60	24	1.00
-5.0	0.81	10.06	45	0.97
-4.5	0.93	8.87	31	1.00
-4.0	0.80	4.32	21	1.02
-3.5	0.67	12.03	36	1.03
-3.0	0.86	4.84	18	1.00
-2.5	0.91	7.65	20	1.01
-2.0	0.94	3.66	15	1.00
-1.5	0.86	7.05	25	1.08
-1.0	1.58	2.82	16	1.06
1.0	0.88	2.82	18	1.02
1.5	0.76	12.81	36	1.11
2.0	1.14	4.56	21	0.99
2.5	0.82	5.44	23	1.00
3.0	0.85	14.48	50	1.08
3.5	0.83	7.09	36	1.02
4.0	0.85	7.69	28	1.02
4.5	0.67	3.85	14	1.00
5.0	0.84	4.13	19	1.03
5.5	0.83	4.14	18	0.99
Avg.	0.87	5.97	24.0	1.02
Std. dev.	0.21	1.72	6.3	0.23

Table B.8: Statistics of the inversion of \dot{H}_y -transients calculated for the 1-D model with the parameter set C3; The columns give the position (x) of the Rx-station and the misfit χ and roughness of the resulting models. The last two columns state the number of iterations needed and the resulting calibration factor (CF). In the last two lines the averages and standard deviations are given.

x/km	χ	Roughn.	# of It.	CF
-5.5	0.76	5.13	16	1.03
-5.0	0.87	4.07	14	1.01
-4.5	0.71	5.00	19	0.99
-4.0	1.07	7.34	19	1.01
-3.5	1.05	5.07	16	1.01
-3.0	1.00	4.98	17	1.01
-2.5	0.90	8.00	25	1.01
-2.0	0.88	5.34	20	1.00
-1.5	0.86	6.82	26	1.01
-1.0	1.27	9.95	39	1.02
1.0	0.97	9.65	39	1.03
1.5	1.02	14.24	34	1.01
2.0	0.73	9.78	25	1.01
2.5	0.74	16.34	40	1.00
3.0	0.88	9.90	24	1.00
3.5	0.85	3.62	13	0.99
4.0	0.88	4.93	19	1.00
4.5	0.72	5.50	24	1.01
5.0	0.88	4.89	14	1.00
5.5	0.85	5.00	17	1.03
Avg.	0.88	6.66	21.6	1.01
Std. dev.	0.21	1.84	5.6	0.23

Table B.9: Statistics of the inversion of \dot{H}_z -transients calculated for the 1-D model with the parameter set C3; The columns give the position (x) of the Rx-station and the misfit χ and roughness of the resulting models. The last two columns state the number of iterations needed and the resulting calibration factor (CF). In the last two lines the averages and standard deviations are given.

x/km	χ	Roughn.	# of It.	CF
-5.5	0.65	3.12	12	0.84
-5.0	0.81	9.56	35	0.46
-4.5	0.70	6.55	27	0.69
-4.0	0.77	10.38	27	0.88
-3.5	0.98	4.11	21	0.85
-3.0	0.85	12.30	45	0.72
-2.5	0.79	8.92	29	1.03
-2.0	0.84	4.31	17	0.87
-1.5	0.82	3.59	17	0.99
-1.0	0.65	6.86	35	1.13
1.0	0.99	5.83	33	1.13
1.5	0.59	3.73	20	0.96
2.0	0.77	8.18	25	0.79
2.5	0.86	4.53	34	1.15
3.0	0.79	4.23	18	0.95
3.5	0.87	4.43	23	1.14
4.0	0.84	3.88	20	0.78
4.5	0.76	3.46	19	0.74
5.0	1.04	7.64	27	0.68
5.5	0.86	5.14	23	0.89
Avg.	0.80	5.55	24.2	0.87
Std. dev.	0.19	1.51	6.1	0.21

Table B.10: Statistics of the inversion of E_x -transients calculated for the 1-D model with the parameter set C4; The columns give the position (x) of the Rx-station and the misfit χ and roughness of the resulting models. The last two columns state the number of iterations needed and the resulting calibration factor (CF). In the last two lines the averages and standard deviations are given.

x/km	χ	Roughn.	# of It.	CF
-5.5	0.75	5.90	31	0.99
-5.0	0.86	6.81	22	0.97
-4.5	0.84	6.82	23	1.05
-4.0	0.89	3.80	21	1.02
-3.5	0.65	8.96	44	1.09
-3.0	0.89	3.80	17	1.01
-2.5	0.79	6.18	20	1.00
-2.0	0.75	4.82	19	1.01
-1.5	0.60	7.42	30	1.11
-1.0	1.59	3.34	19	1.00
1.0	0.91	2.42	19	1.06
1.5	0.89	10.34	45	1.13
2.0	1.03	3.47	15	0.99
2.5	0.94	4.35	15	1.00
3.0	0.95	5.89	50	1.10
3.5	0.89	6.08	22	1.04
4.0	0.91	3.89	15	1.01
4.5	0.67	4.00	21	1.09
5.0	0.85	4.47	23	1.05
5.5	0.89	4.59	22	0.99
Avg.	0.86	5.04	23.1	1.03
Std. dev.	0.21	1.31	6.1	0.24

Table B.11: Statistics of the inversion of \dot{H}_y -transients calculated for the 1-D model with the parameter set C4; The columns give the position (x) of the Rx-station and the misfit χ and roughness of the resulting models. The last two columns state the number of iterations needed and the resulting calibration factor (CF). In the last two lines the averages and standard deviations are given.

x/km	χ	Roughn.	# of It.	CF
-5.5	0.75	5.40	25	1.03
-5.0	0.88	3.86	12	1.01
-4.5	0.71	4.84	21	0.99
-4.0	1.07	7.64	19	1.01
-3.5	1.05	5.27	23	1.00
-3.0	0.99	6.44	44	1.01
-2.5	0.90	7.49	27	1.01
-2.0	0.88	4.50	18	1.00
-1.5	0.86	6.05	40	1.01
-1.0	1.27	11.69	32	1.02
1.0	0.98	8.02	50	1.02
1.5	1.02	13.72	35	1.01
2.0	0.73	8.83	21	1.00
2.5	0.73	7.82	22	1.01
3.0	0.87	4.89	19	0.99
3.5	0.78	3.44	14	0.99
4.0	0.90	6.44	27	1.02
4.5	0.78	3.87	15	0.99
5.0	0.80	7.56	19	1.02
5.5	0.86	4.42	15	1.01
Avg.	0.88	6.18	23.1	1.01
Std. dev.	0.21	1.63	6.2	0.23

Table B.12: Statistics of the inversion of \dot{H}_z -transients calculated for the 1-D model with the parameter set C4; The columns give the position (x) of the Rx-station and the misfit χ and roughness of the resulting models. The last two columns state the number of iterations needed and the resulting calibration factor (CF). In the last two lines the averages and standard deviations are given.

x/km	χ	Roughn.	# of It.	$\overline{\text{CF}}$
-5.5	0.73	5.96	23	0.95
-5.0	0.95	6.40	21	0.93
-4.5	0.85	12.36	24	0.98
-4.0	0.90	12.06	17	0.98
-3.5	0.85	14.23	15	1.00
-3.0	0.90	12.21	24	1.00
-2.5	0.89	10.08	12	0.99
-2.0	0.85	12.60	27	0.98
-1.5	0.77	6.02	18	0.99
-1.0	1.22	6.67	13	1.01
1.0	1.04	6.56	23	1.00
1.5	0.82	6.05	16	0.99
2.0	0.94	7.34	9	0.98
2.5	0.94	17.74	22	1.00
3.0	0.96	6.97	13	0.99
3.5	0.95	8.78	17	1.00
4.0	0.99	3.64	6	0.97
4.5	0.79	3.75	10	1.05
5.0	0.98	15.83	33	1.09
5.5	0.93	3.95	8	0.95
Avg.	0.91	8.07	16.1	1.00
Std. dev.	0.21	2.26	4.3	0.16

Table B.13: Statistics of joint-inversions of E_x - and \dot{H}_y -transients calculated for the 1-D model with the parameter set C1; The columns give the position (x) of the Rx-station and the misfit χ and roughness of the resulting models. The last two columns state the number of iterations needed and the average of the resulting calibration factors ($\overline{\text{CF}}$). In the last two lines the average and standard deviation for all stations are given.

x/km	χ	Roughn.	# of It.	$\overline{\text{CF}}$
-5.5	0.79	13.01	17	0.96
-5.0	0.88	11.75	18	0.97
-4.5	0.80	15.58	34	0.98
-4.0	0.95	10.36	12	0.99
-3.5	1.07	11.10	12	1.00
-3.0	0.96	13.99	16	1.01
-2.5	0.83	11.68	13	0.99
-2.0	0.92	5.55	13	0.99
-1.5	0.93	4.03	5	0.99
-1.0	1.02	14.96	26	0.99
1.0	1.05	12.69	30	0.98
1.5	0.86	12.41	13	1.00
2.0	0.80	9.35	18	0.98
2.5	0.86	13.86	17	1.01
3.0	0.87	9.22	12	0.99
3.5	0.93	10.95	16	0.98
4.0	0.90	15.81	28	1.02
4.5	0.85	11.21	17	0.97
5.0	0.99	11.34	14	0.99
5.5	0.94	12.05	18	0.97
Avg.	0.91	11.06	16.1	1.00
Std. dev.	0.21	2.73	4.3	0.16

Table B.14: Statistics of joint-inversions of E_x - and \dot{H}_z -transients calculated for the 1-D model with the parameter set C1; The columns give the position (x) of the Rx-station and the misfit χ and roughness of the resulting models. The last two columns state the number of iterations needed and the average of the resulting calibration factors ($\overline{\text{CF}}$). In the last two lines the average and standard deviation for all stations are given.

x/km	χ	Roughn.	# of It.	$\overline{\text{CF}}$
-5.5	0.83	4.79	11	0.98
-5.0	0.85	4.73	12	0.98
-4.5	0.90	8.46	19	0.99
-4.0	1.08	6.09	11	1.00
-3.5	0.95	9.64	21	1.00
-3.0	0.97	4.95	12	1.01
-2.5	0.86	5.74	9	1.01
-2.0	0.93	7.13	16	1.00
-1.5	0.80	7.09	15	1.01
-1.0	1.46	6.23	11	1.02
1.0	1.21	12.69	35	1.01
1.5	1.13	14.68	8	1.00
2.0	1.03	8.26	11	1.01
2.5	0.87	9.16	12	1.01
3.0	0.95	5.82	11	1.01
3.5	0.91	4.99	14	1.00
4.0	1.00	4.63	8	1.00
4.5	0.78	4.09	8	0.99
5.0	0.85	10.67	27	1.00
5.5	0.93	5.50	9	0.99
Avg.	0.95	6.81	12.8	1.00
Std. dev.	0.22	1.79	3.6	0.16

Table B.15: Statistics of joint-inversions of \dot{H}_y - and \dot{H}_z -transients calculated for the 1-D model with the parameter set C1; The columns give the position (x) of the Rx-station and the misfit χ and roughness of the resulting models. The last two columns state the number of iterations needed and the average of the resulting calibration factors ($\overline{\text{CF}}$). In the last two lines the average and standard deviation for all stations are given.

x/km	χ	Roughn.	# of It.	$\overline{\text{CF}}$
-5.5	0.72	11.11	27	0.96
-5.0	0.88	4.00	10	0.93
-4.5	0.86	13.24	14	0.98
-4.0	0.84	12.84	17	0.99
-3.5	0.85	13.43	15	0.99
-3.0	0.91	10.76	13	1.00
-2.5	0.96	8.89	8	0.99
-2.0	0.93	10.81	17	0.98
-1.5	0.95	6.07	19	0.99
-1.0	1.24	5.06	15	1.00
1.0	1.00	5.63	12	1.00
1.5	0.74	5.80	17	1.00
2.0	1.01	6.44	9	0.98
2.5	0.88	14.85	19	1.00
3.0	0.93	15.97	27	0.99
3.5	0.89	11.28	11	1.00
4.0	0.90	15.10	17	0.99
4.5	0.78	13.28	21	0.98
5.0	1.00	12.33	31	1.05
5.5	0.90	4.02	9	0.95
Avg.	0.90	9.18	15.3	0.99
Std. dev.	0.21	2.47	4.0	0.16

Table B.16: Statistics of joint-inversions of E_x - and \dot{H}_y -transients calculated for the 1-D model with the parameter set C2; The columns give the position (x) of the Rx-station and the misfit χ and roughness of the resulting models. The last two columns state the number of iterations needed and the average of the resulting calibration factors ($\overline{\text{CF}}$). In the last two lines the average and standard deviation for all stations are given.

x/km	χ	Roughn.	# of It.	$\overline{\text{CF}}$
-5.5	0.74	14.80	28	0.98
-5.0	0.87	11.77	20	1.00
-4.5	0.78	18.61	27	0.97
-4.0	0.95	10.33	11	0.99
-3.5	1.03	11.44	17	1.00
-3.0	0.97	15.26	21	1.02
-2.5	0.92	10.66	13	0.99
-2.0	0.92	5.38	12	0.99
-1.5	0.93	3.90	5	0.99
-1.0	1.03	8.31	18	0.99
1.0	1.04	14.36	33	0.98
1.5	0.86	13.09	16	1.00
2.0	0.79	10.70	20	0.98
2.5	0.98	3.90	8	0.98
3.0	0.87	12.50	19	0.99
3.5	0.92	11.82	14	0.99
4.0	0.93	12.04	21	1.00
4.5	0.81	11.65	14	1.00
5.0	1.00	11.33	16	0.99
5.5	0.92	11.93	19	0.99
Avg.	0.91	10.44	16.3	1.00
Std. dev.	0.21	2.69	4.3	0.16

Table B.17: Statistics of joint-inversions of E_x - and \dot{H}_z -transients calculated for the 1-D model with the parameter set C2; The columns give the position (x) of the Rx-station and the misfit χ and roughness of the resulting models. The last two columns state the number of iterations needed and the average of the resulting calibration factors ($\overline{\text{CF}}$). In the last two lines the average and standard deviation for all stations are given.

x/km	χ	Roughn.	# of It.	$\overline{\text{CF}}$
-5.5	0.75	9.26	13	0.99
-5.0	0.75	6.46	11	0.99
-4.5	0.78	6.72	10	1.00
-4.0	0.73	9.29	13	1.00
-3.5	0.72	11.19	12	1.00
-3.0	0.72	12.23	18	1.01
-2.5	0.77	7.37	12	1.01
-2.0	0.85	4.47	11	1.00
-1.5	0.82	3.77	12	1.01
-1.0	0.97	3.26	10	1.02
1.0	1.13	6.22	28	1.01
1.5	0.93	17.28	22	1.00
2.0	0.84	6.14	12	1.00
2.5	0.82	4.07	5	1.01
3.0	0.80	4.36	7	1.01
3.5	0.79	5.02	12	1.01
4.0	0.78	4.91	6	1.01
4.5	0.81	4.79	12	1.00
5.0	0.81	4.70	12	1.00
5.5	0.84	5.69	16	0.99
Avg.	0.82	6.22	11.8	1.01
Std. dev.	0.19	1.75	3.1	0.16

Table B.18: Statistics of joint-inversions of \dot{H}_y - and \dot{H}_z -transients calculated for the 1-D model with the parameter set C2; The columns give the position (x) of the Rx-station and the misfit χ and roughness of the resulting models. The last two columns state the number of iterations needed and the average of the resulting calibration factors ($\overline{\text{CF}}$). In the last two lines the average and standard deviation for all stations are given.

x/km	χ	Roughn.	# of It.	$\overline{\text{CF}}$
-5.5	0.72	10.71	28	0.96
-5.0	0.88	4.64	19	0.93
-4.5	0.86	13.14	20	0.98
-4.0	0.84	12.85	21	0.99
-3.5	0.85	14.08	22	0.99
-3.0	0.91	10.79	18	1.00
-2.5	0.95	11.99	21	0.99
-2.0	0.93	11.73	24	0.98
-1.5	0.94	6.72	31	1.00
-1.0	1.24	5.58	26	1.00
1.0	0.99	6.50	25	1.00
1.5	0.74	6.71	25	0.99
2.0	1.01	6.48	17	0.98
2.5	0.88	17.33	30	1.00
3.0	0.93	18.11	41	0.99
3.5	0.89	11.58	18	1.00
4.0	0.90	15.26	24	0.99
4.5	0.78	13.24	29	0.98
5.0	1.00	12.37	27	1.05
5.5	0.88	9.13	31	0.96
Avg.	0.90	10.23	24.2	0.99
Std. dev.	0.21	2.66	5.8	0.16

Table B.19: Statistics of joint-inversions of E_x - and \dot{H}_y -transients calculated for the 1-D model with the parameter set C3; The columns give the position (x) of the Rx-station and the misfit χ and roughness of the resulting models. The last two columns state the number of iterations needed and the average of the resulting calibration factors ($\overline{\text{CF}}$). In the last two lines the average and standard deviation for all stations are given.

x/km	χ	Roughn.	# of It.	$\overline{\text{CF}}$
-5.5	0.75	14.62	29	0.98
-5.0	0.87	11.79	21	0.99
-4.5	0.78	18.27	36	0.97
-4.0	0.94	10.60	18	0.99
-3.5	1.03	11.46	22	1.00
-3.0	0.97	16.81	30	1.03
-2.5	0.91	11.48	20	0.99
-2.0	0.92	6.17	21	0.99
-1.5	0.93	3.98	17	0.99
-1.0	1.03	7.05	24	0.99
1.0	1.04	16.37	47	0.98
1.5	0.86	13.26	23	1.00
2.0	0.80	6.31	19	0.98
2.5	0.97	4.16	16	0.98
3.0	0.87	13.63	28	0.99
3.5	0.92	12.07	21	0.99
4.0	0.93	12.08	24	0.99
4.5	0.81	11.60	19	1.00
5.0	1.00	11.32	25	0.98
5.5	0.92	11.96	24	0.99
Avg.	0.91	10.42	23.4	1.00
Std. dev.	0.21	2.73	5.8	0.16

Table B.20: Statistics of joint-inversions of E_x - and \dot{H}_z -transients calculated for the 1-D model with the parameter set C3; The columns give the position (x) of the Rx-station and the misfit χ and roughness of the resulting models. The last two columns state the number of iterations needed and the average of the resulting calibration factors ($\overline{\text{CF}}$). In the last two lines the average and standard deviation for all stations are given.

x/km	χ	Roughn.	# of It.	$\overline{\text{CF}}$
-5.5	0.85	5.47	20	0.99
-5.0	0.88	4.17	15	0.99
-4.5	0.91	6.36	22	0.99
-4.0	1.03	6.00	21	1.00
-3.5	0.91	9.89	26	1.00
-3.0	1.00	5.10	18	1.01
-2.5	0.99	7.58	23	1.01
-2.0	0.98	7.16	19	1.00
-1.5	0.94	6.18	24	1.02
-1.0	1.51	2.99	15	1.03
1.0	1.15	5.17	19	1.02
1.5	0.99	11.48	20	1.01
2.0	1.06	7.09	17	1.01
2.5	0.89	7.25	23	1.01
3.0	0.94	7.11	25	1.01
3.5	0.88	5.43	17	1.00
4.0	0.95	4.68	14	1.00
4.5	0.72	4.40	17	1.00
5.0	0.88	5.88	17	0.99
5.5	0.90	5.98	19	0.99
Avg.	0.96	6.01	19.3	1.01
Std. dev.	0.22	1.50	4.6	0.16

Table B.21: Statistics of joint-inversions of \dot{H}_y - and \dot{H}_z -transients calculated for the 1-D model with the parameter set C3; The columns give the position (x) of the Rx-station and the misfit χ and roughness of the resulting models. The last two columns state the number of iterations needed and the average of the resulting calibration factors ($\overline{\text{CF}}$). In the last two lines the average and standard deviation for all stations are given.

x/km	χ	Roughn.	# of It.	$\overline{\text{CF}}$
-5.5	0.73	5.00	20	0.95
-5.0	0.95	4.61	21	0.93
-4.5	0.85	13.80	36	0.99
-4.0	0.90	12.19	22	0.98
-3.5	0.85	12.98	22	1.00
-3.0	0.90	11.86	30	1.00
-2.5	0.88	9.96	21	0.99
-2.0	0.85	10.36	25	0.98
-1.5	0.77	5.59	24	0.99
-1.0	1.23	5.76	20	1.01
1.0	1.05	6.29	25	1.00
1.5	0.82	5.36	19	0.99
2.0	0.93	6.97	19	0.98
2.5	0.93	17.47	27	1.00
3.0	0.97	5.42	16	0.99
3.5	0.94	8.56	23	1.00
4.0	0.99	3.54	11	0.97
4.5	0.79	3.66	16	1.06
5.0	0.98	13.43	31	1.08
5.5	0.93	3.54	11	0.95
Avg.	0.91	7.38	21.1	1.00
Std. dev.	0.21	2.12	5.2	0.16

Table B.22: Statistics of joint-inversions of E_x - and \dot{H}_y -transients calculated for the 1-D model with the parameter set C4; The columns give the position (x) of the Rx-station and the misfit χ and roughness of the resulting models. The last two columns state the number of iterations needed and the average of the resulting calibration factors ($\overline{\text{CF}}$). In the last two lines the average and standard deviation for all stations are given.

x/km	χ	Roughn.	# of It.	$\overline{\text{CF}}$
-5.5	0.79	13.13	25	0.96
-5.0	0.89	11.66	22	0.97
-4.5	0.80	14.84	39	0.98
-4.0	0.95	10.06	20	0.99
-3.5	1.07	11.02	19	1.00
-3.0	0.95	13.95	22	1.01
-2.5	0.83	11.25	21	0.99
-2.0	0.92	5.66	20	0.99
-1.5	0.93	4.14	19	0.99
-1.0	1.03	6.70	22	0.99
1.0	1.05	11.18	33	0.98
1.5	0.86	13.03	23	1.00
2.0	0.79	10.00	25	0.98
2.5	0.85	14.40	25	1.01
3.0	0.86	10.46	24	0.99
3.5	0.93	11.30	20	0.98
4.0	0.89	17.29	40	1.02
4.5	0.85	10.95	21	0.97
5.0	0.99	11.17	23	0.99
5.5	0.93	12.12	28	0.97
Avg.	0.90	10.71	24.0	1.00
Std. dev.	0.21	2.66	5.8	0.16

Table B.23: Statistics of joint-inversions of E_x - and \dot{H}_z -transients calculated for the 1-D model with the parameter set C4; The columns give the position (x) of the Rx-station and the misfit χ and roughness of the resulting models. The last two columns state the number of iterations needed and the average of the resulting calibration factors ($\overline{\text{CF}}$). In the last two lines the average and standard deviation for all stations are given.

x/km	χ	Roughn.	# of It.	$\overline{\text{CF}}$
-5.5	0.84	4.62	17	0.98
-5.0	0.86	4.33	17	0.98
-4.5	0.91	7.68	20	0.99
-4.0	1.08	5.65	16	1.00
-3.5	0.95	7.47	19	1.00
-3.0	0.97	4.59	15	1.01
-2.5	0.86	5.80	23	1.01
-2.0	0.99	5.23	15	1.00
-1.5	0.94	5.00	19	1.02
-1.0	1.51	2.95	14	1.03
1.0	1.15	4.65	16	1.02
1.5	0.99	9.51	20	1.01
2.0	1.06	7.41	19	1.01
2.5	0.87	8.84	19	1.01
3.0	0.95	5.48	20	1.01
3.5	0.92	4.07	13	1.00
4.0	1.00	4.25	14	1.00
4.5	0.78	4.09	16	0.99
5.0	0.85	10.19	33	1.00
5.5	0.93	4.96	15	0.98
Avg.	0.96	5.55	17.6	1.00
Std. dev.	0.23	1.41	4.2	0.16

Table B.24: Statistics of joint-inversions of \dot{H}_y - and \dot{H}_z -transients calculated for the 1-D model with the parameter set C4; The columns give the position (x) of the Rx-station and the misfit χ and roughness of the resulting models. The last two columns state the number of iterations needed and the average of the resulting calibration factors ($\overline{\text{CF}}$). In the last two lines the average and standard deviation for all stations are given.

x/km	χ	Roughn.	# of It.	$\overline{\text{CF}}$
-5.5	0.82	13.43	22	0.97
-5.0	0.92	12.50	18	0.96
-4.5	0.88	16.40	34	0.98
-4.0	1.00	10.52	12	0.99
-3.5	0.97	12.30	17	1.00
-3.0	0.98	13.62	15	1.01
-2.5	0.87	11.64	12	0.99
-2.0	0.99	7.81	21	0.99
-1.5	0.96	8.46	39	0.99
-1.0	1.29	8.93	26	0.99
1.0	1.11	23.82	38	0.99
1.5	0.90	8.28	19	0.99
2.0	0.99	13.06	16	0.99
2.5	0.91	13.81	18	1.00
3.0	0.94	8.86	10	0.99
3.5	0.96	10.93	13	0.99
4.0	0.97	14.82	25	0.99
4.5	0.83	11.31	15	0.98
5.0	0.96	12.87	18	1.00
5.5	0.94	12.25	17	0.98
Avg.	0.95	11.86	18.9	1.00
Std. dev.	0.22	2.93	5.0	0.13

Table B.25: Statistics of the joint-inversion of all three components calculated for the 1-D model with the parameter set C1; The columns give the position (x) of the Rx-station and the misfit χ and roughness of the resulting models. The last two columns state the number of iterations needed and the average of the resulting calibration factors ($\overline{\text{CF}}$). In the last two lines the averages and standard deviations are given.

x/km	χ	Roughn.	# of It.	$\overline{\text{CF}}$
-5.5	0.80	14.35	21	0.97
-5.0	0.90	12.36	20	0.98
-4.5	0.87	15.45	20	0.98
-4.0	0.97	11.09	11	0.99
-3.5	0.95	13.94	20	0.99
-3.0	1.01	12.89	13	1.01
-2.5	0.98	10.61	10	0.99
-2.0	1.00	6.69	16	0.99
-1.5	0.98	4.64	13	0.99
-1.0	1.29	6.42	30	0.99
1.0	1.11	21.13	38	0.99
1.5	0.89	9.20	22	0.99
2.0	0.99	12.46	16	0.99
2.5	0.91	12.08	15	1.00
3.0	0.93	11.67	16	0.99
3.5	0.92	11.58	15	1.00
4.0	0.95	13.99	18	0.99
4.5	0.80	12.39	16	0.99
5.0	0.97	11.67	15	0.99
5.5	0.93	11.74	14	0.98
Avg.	0.95	11.26	17.1	1.00
Std. dev.	0.22	2.82	4.4	0.13

Table B.26: Statistics of the joint-inversion of all three components calculated for the 1-D model with the parameter set C2; The columns give the position (x) of the Rx-station and the misfit χ and roughness of the resulting models. The last two columns state the number of iterations needed and the average of the resulting calibration factors ($\overline{\text{CF}}$). In the last two lines the averages and standard deviations are given.

x/km	χ	Roughn.	# of It.	$\overline{\text{CF}}$
-5.5	0.80	14.66	29	0.98
-5.0	0.90	12.58	26	0.99
-4.5	0.88	15.02	23	0.98
-4.0	0.97	11.11	17	0.99
-3.5	0.95	13.40	23	0.99
-3.0	1.01	13.22	20	1.01
-2.5	0.97	11.12	19	0.99
-2.0	0.99	7.79	23	0.99
-1.5	0.96	7.19	38	0.99
-1.0	1.29	8.87	36	0.99
1.0	1.11	25.47	42	0.99
1.5	0.89	8.93	28	0.99
2.0	0.99	11.33	18	0.98
2.5	0.91	11.94	20	1.00
3.0	0.93	12.44	25	0.99
3.5	0.92	11.63	18	1.00
4.0	0.95	14.43	20	0.99
4.5	0.79	12.72	28	0.99
5.0	0.97	11.94	24	0.99
5.5	0.92	12.10	27	0.98
Avg.	0.95	11.96	24.4	1.00
Std. dev.	0.22	2.96	6.0	0.13

Table B.27: Statistics of the joint-inversion of all three components calculated for the 1-D model with the parameter set C3; The columns give the position (x) of the Rx-station and the misfit χ and roughness of the resulting models. The last two columns state the number of iterations needed and the average of the resulting calibration factors ($\overline{\text{CF}}$). In the last two lines the averages and standard deviations are given.

x/km	χ	Roughn.	# of It.	$\overline{\text{CF}}$
-5.5	0.82	13.46	29	0.97
-5.0	0.91	12.55	30	0.96
-4.5	0.88	16.72	39	0.98
-4.0	1.00	10.42	17	0.99
-3.5	0.97	12.16	25	1.00
-3.0	0.98	13.41	21	1.01
-2.5	0.87	11.51	21	0.99
-2.0	0.99	6.90	21	0.99
-1.5	0.99	4.17	16	0.99
-1.0	1.29	6.24	34	0.99
1.0	1.10	25.00	49	0.99
1.5	0.89	9.14	31	0.99
2.0	0.99	12.21	22	0.99
2.5	0.90	13.83	24	1.00
3.0	0.94	9.55	19	0.99
3.5	0.96	10.80	18	0.99
4.0	0.96	14.54	32	0.99
4.5	0.83	11.19	24	0.98
5.0	0.96	12.60	22	1.01
5.5	0.94	12.27	25	0.98
Avg.	0.95	11.22	24.9	1.00
Std. dev.	0.22	2.90	6.2	0.13

Table B.28: Statistics of the joint-inversion of all three components calculated for the 1-D model with the parameter set C4; The columns give the position (x) of the Rx-station and the misfit χ and roughness of the resulting models. The last two columns state the number of iterations needed and the average of the resulting calibration factors ($\overline{\text{CF}}$). In the last two lines the averages and standard deviations are given.

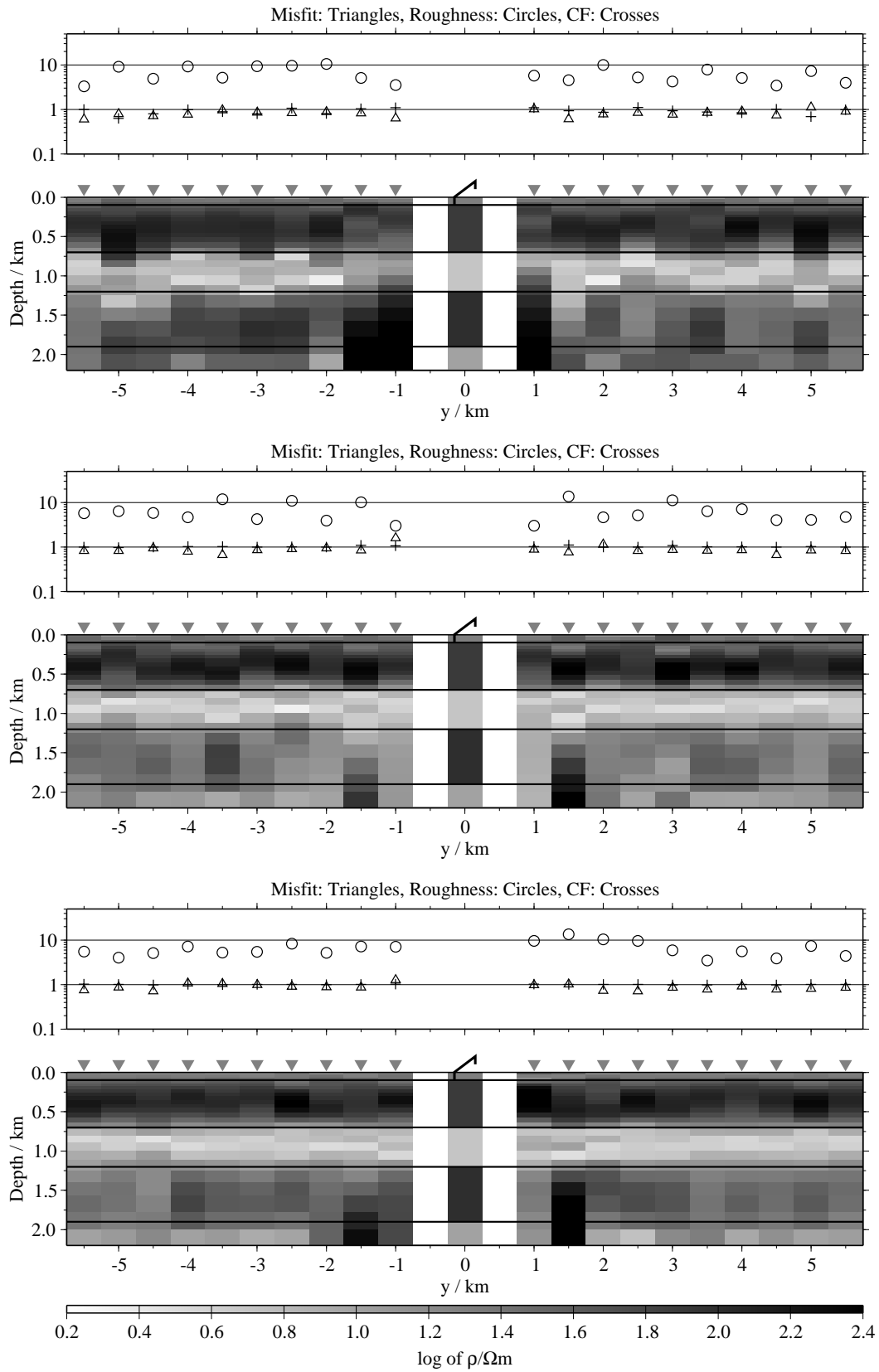


Figure B.2: Pseudo-sections of single 1-D inversion, model A (displayed below T_x), regularisation scheme C1; from top to bottom E_x -, \dot{H}_y - and \dot{H}_z -component;

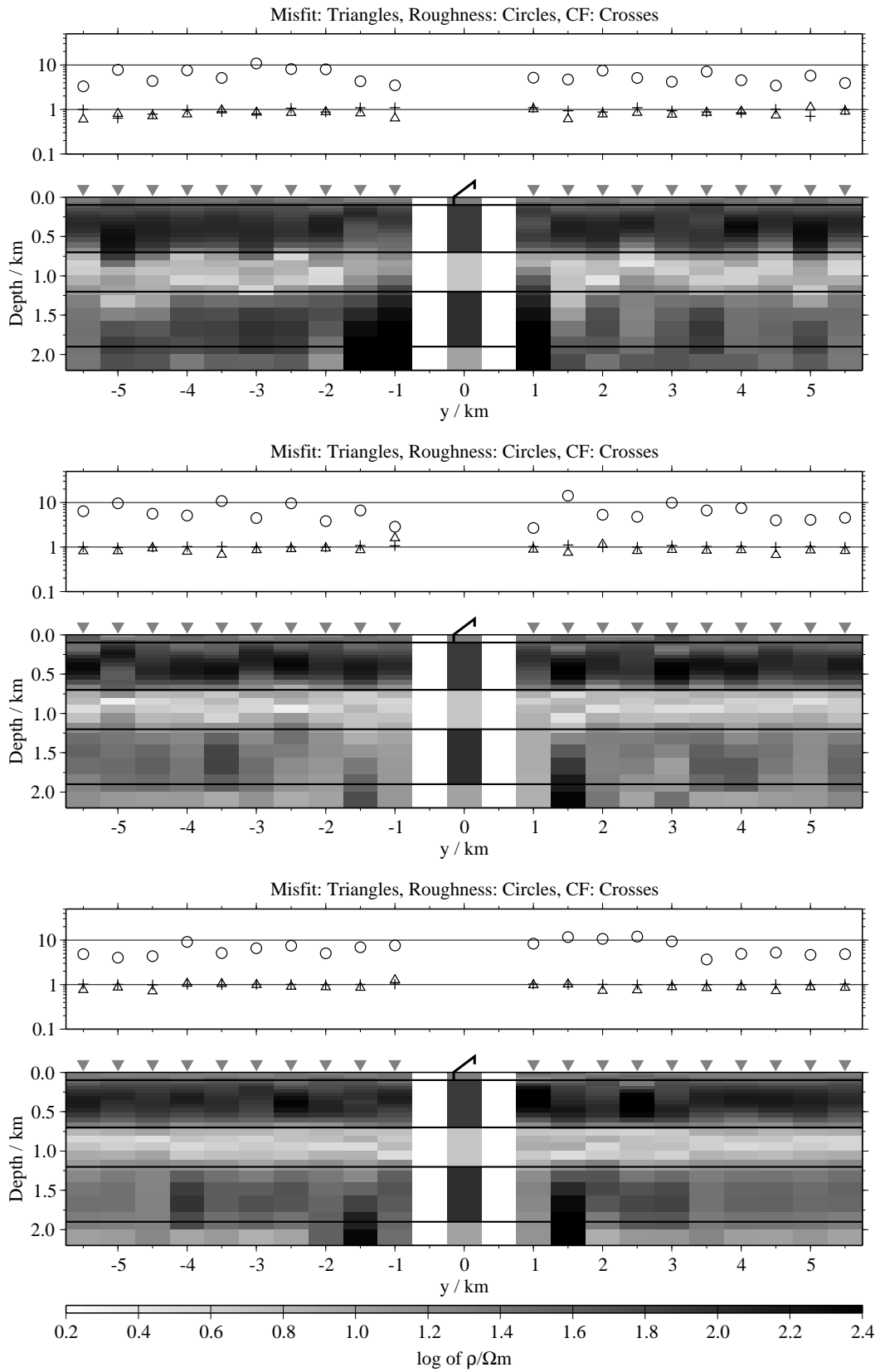


Figure B.3: Pseudo-sections of single 1-D inversion, model A (displayed below T_x), regularisation scheme C2; from top to bottom E_x -, H_y - and H_z -component;

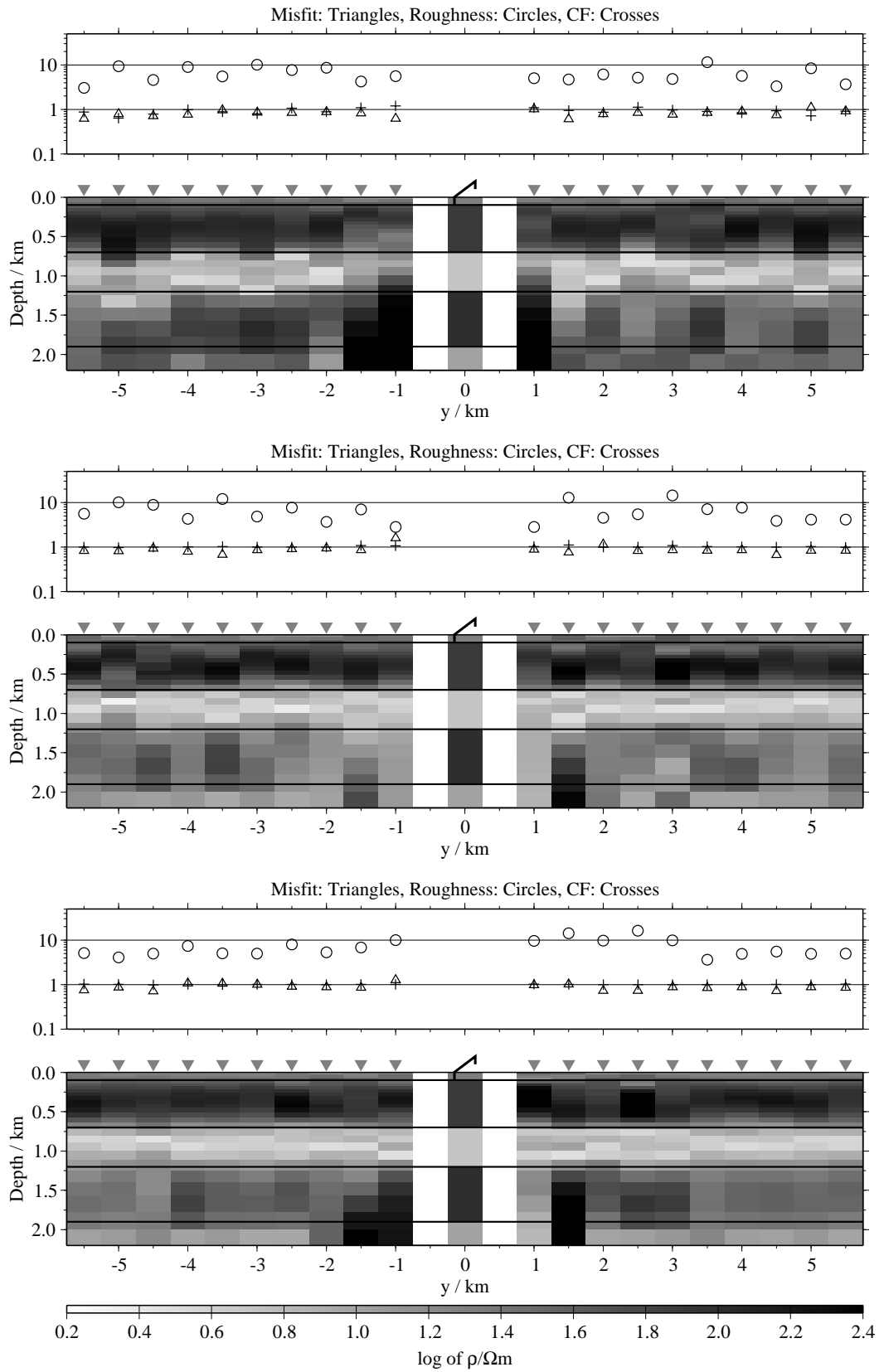


Figure B.4: Pseudo-sections of single 1-D inversion, model A (displayed below T_x), regularisation scheme C3; from top to bottom E_x -, \dot{H}_y - and \dot{H}_z -component;

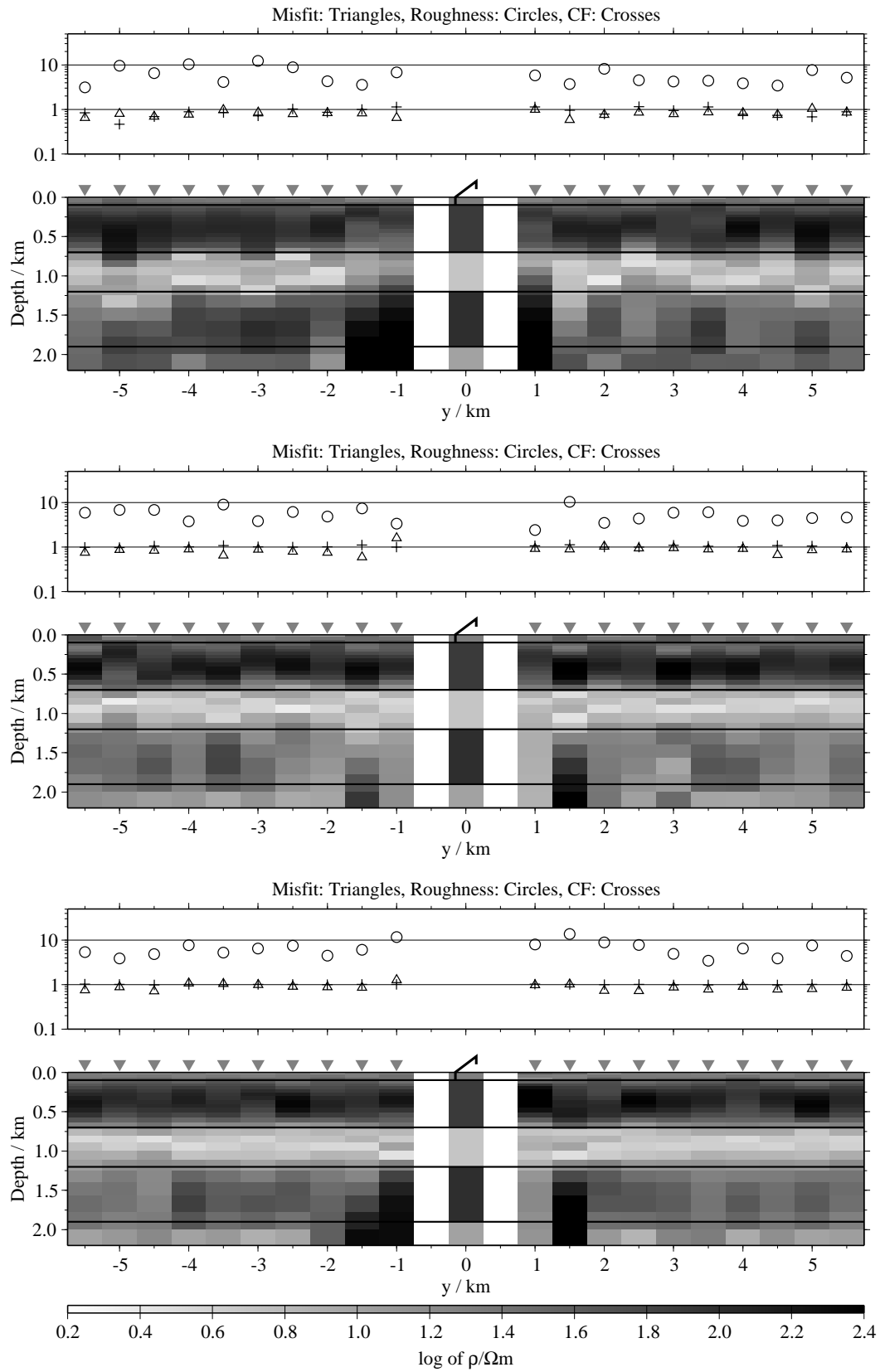


Figure B.5: Pseudo-sections of single 1-D inversion, model A (displayed below T_x), regularisation scheme C4; from top to bottom E_x , \dot{H}_y and \dot{H}_z component;

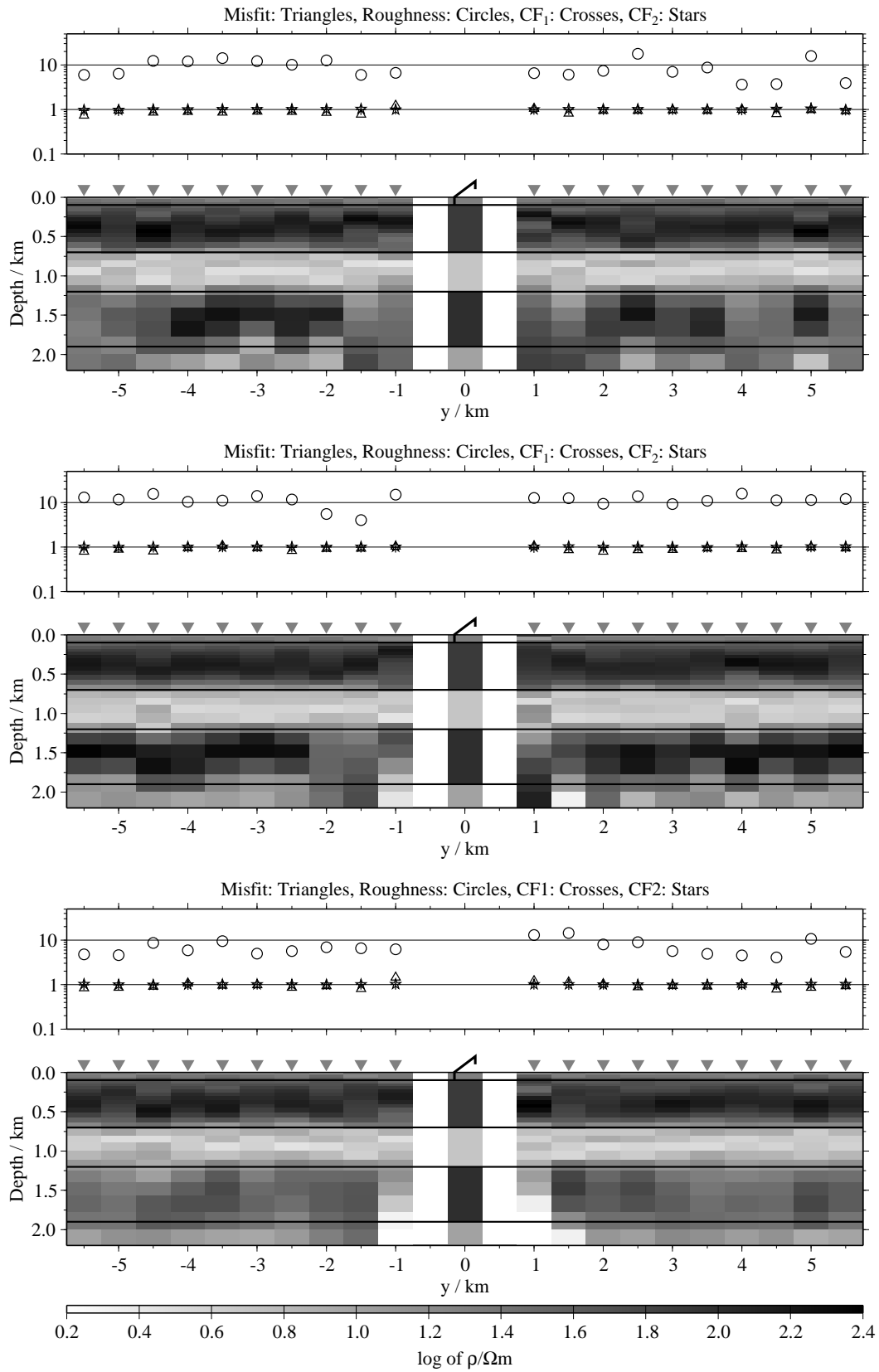


Figure B.6: Pseudo-sections of two component 1-D joint-inversions, model A (displayed below T_x), regularisation scheme C1; from top to bottom $E_x-\dot{H}_y$, $E_x-\dot{H}_z$ and $\dot{H}_y-\dot{H}_z$;

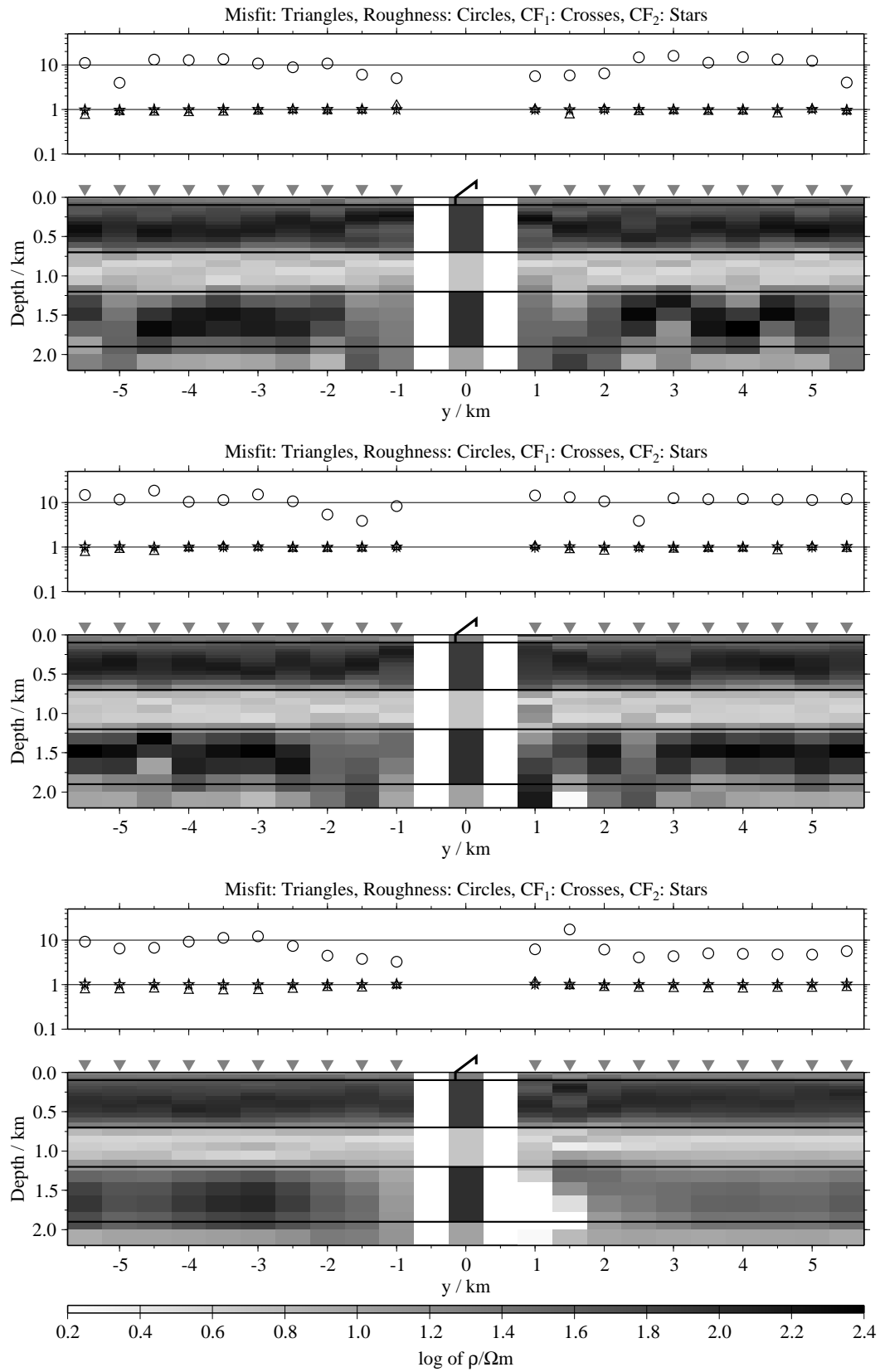


Figure B.7: Pseudo-sections of two component 1-D joint-inversions, model A (displayed below T_x), regularisation scheme C2; from top to bottom $E_x\text{-}\dot{H}_y$, $E_x\text{-}\dot{H}_z$ and $\dot{H}_y\text{-}\dot{H}_z$;

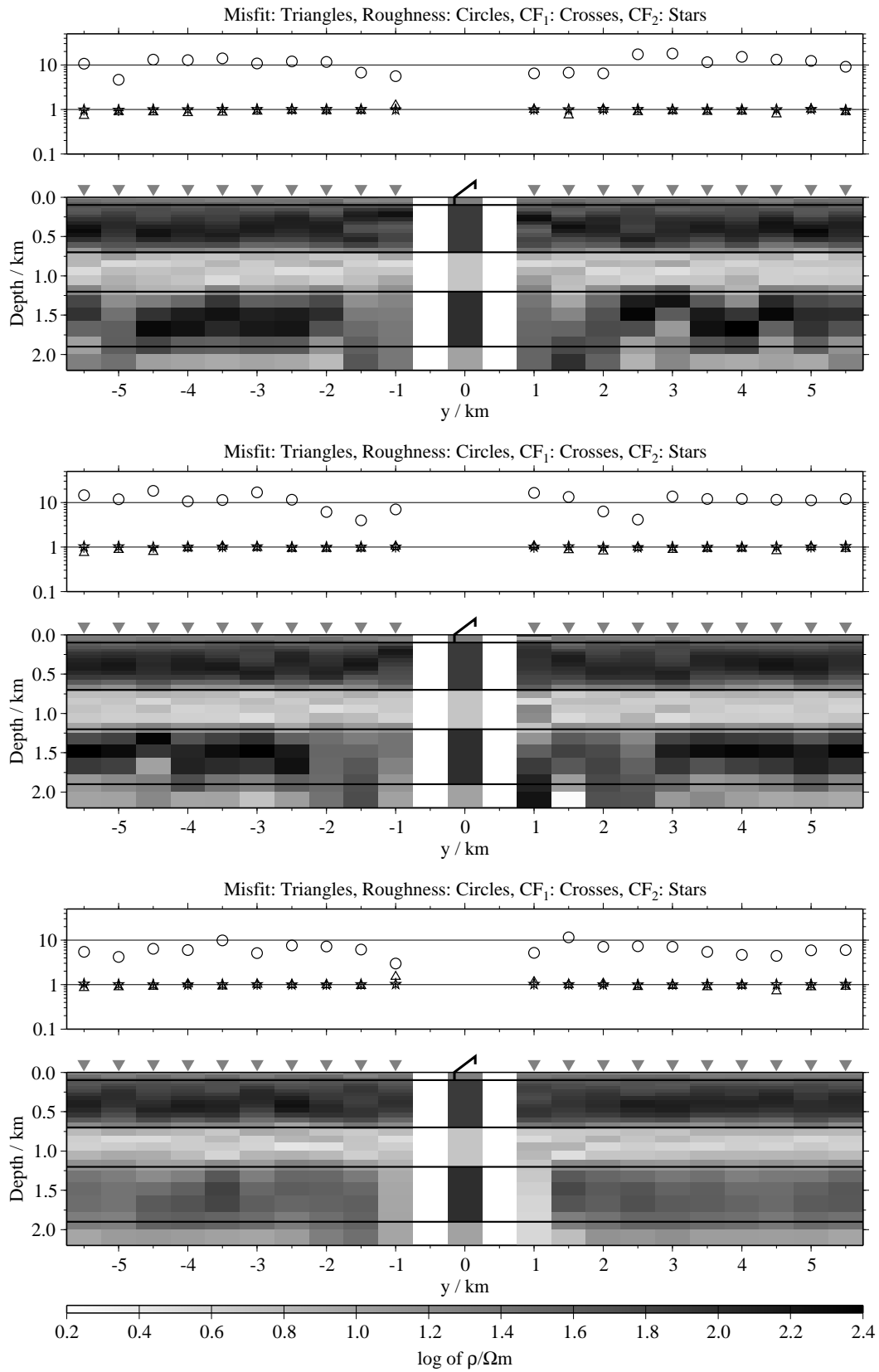


Figure B.8: Pseudo-sections of two component 1-D joint-inversions, model A (displayed below Tx), regularisation scheme C3; from top to bottom $E_x-\dot{H}_y$, $E_x-\dot{H}_z$ and $\dot{H}_y-\dot{H}_z$;

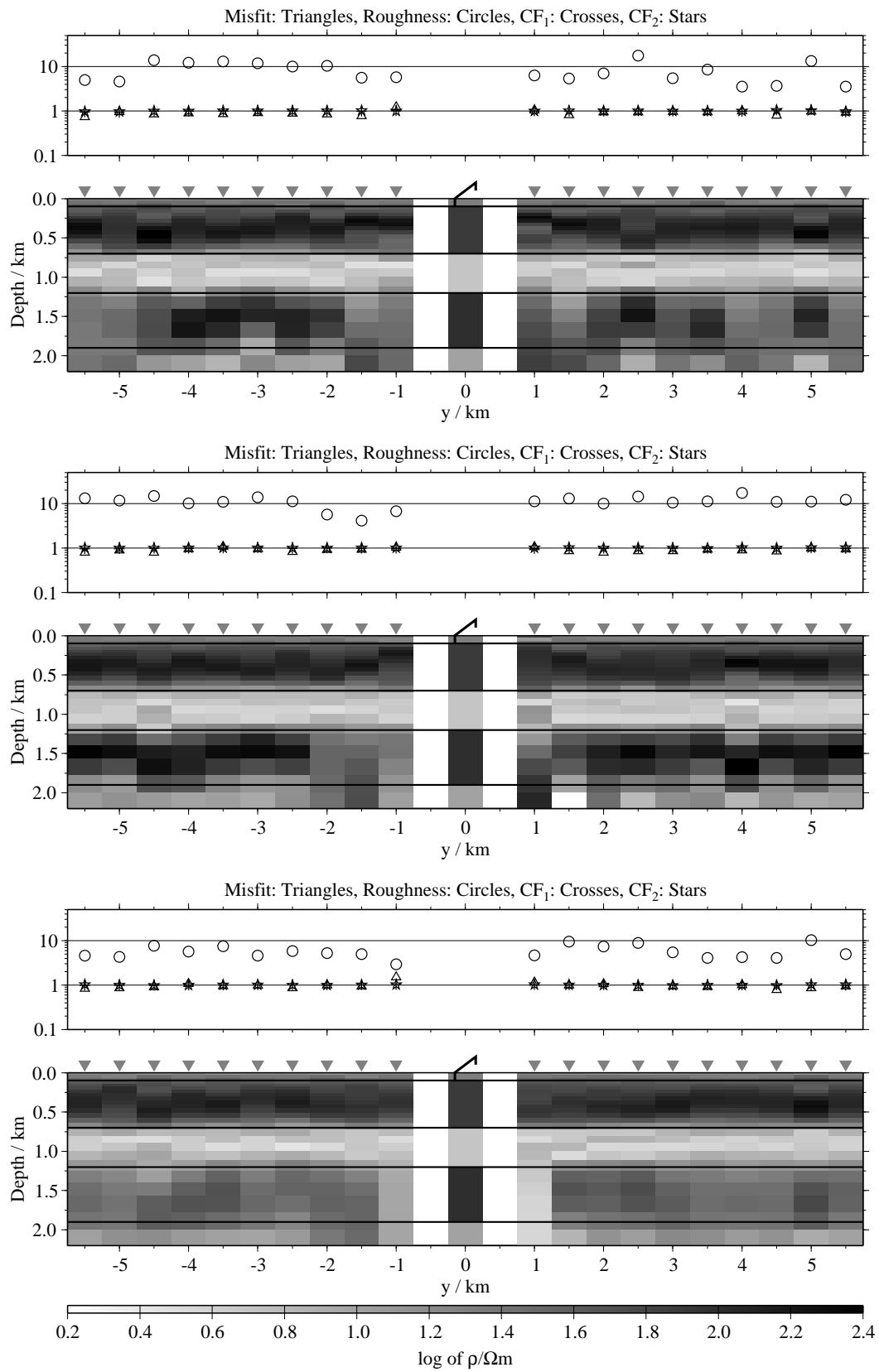


Figure B.9: Pseudo-sections of two component 1-D joint-inversions, model A (displayed below T_x), regularisation scheme C4; from top to bottom E_x - \dot{H}_y , E_x - \dot{H}_z and \dot{H}_y - \dot{H}_z ;

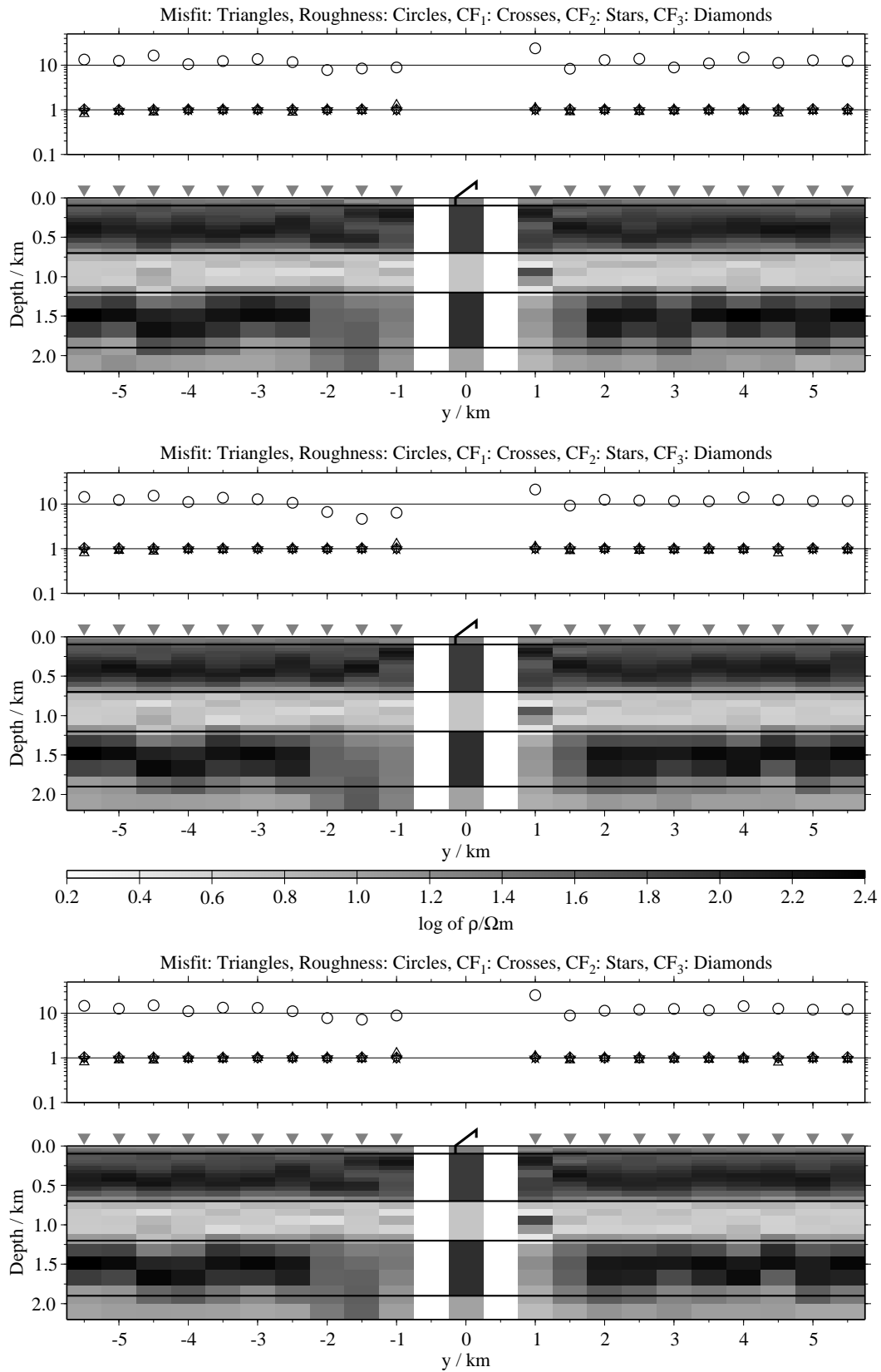


Figure B.10: Pseudo-sections of three component 1-D joint-inversions, model A (displayed below Tx); from top to bottom: C1, C2 and C3 strategy;

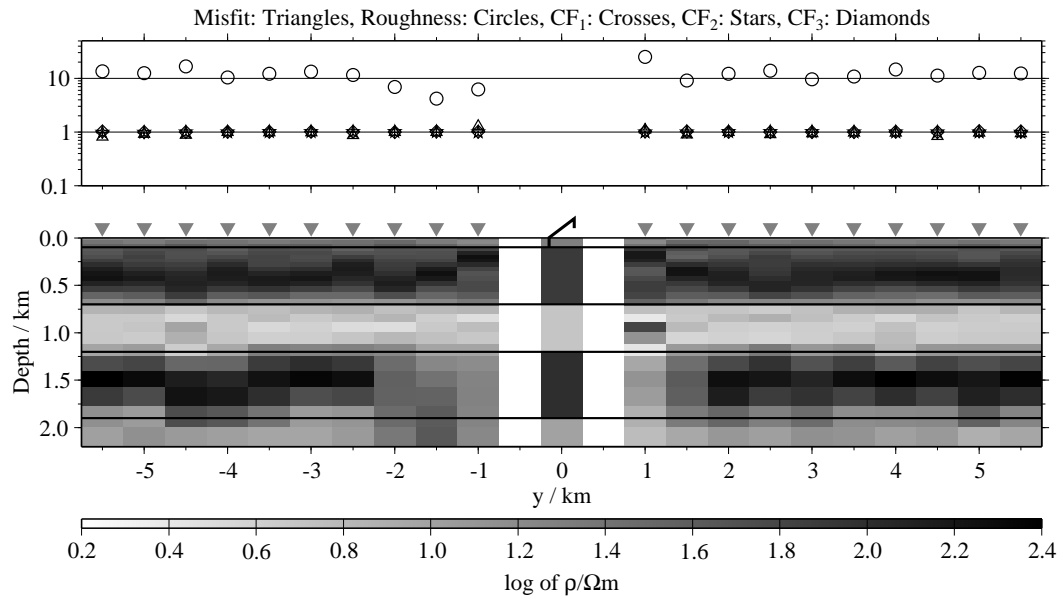


Figure B.11: Pseudo-section of three component 1-D joint-inversions, model A (displayed below Tx) with the C4 strategy;

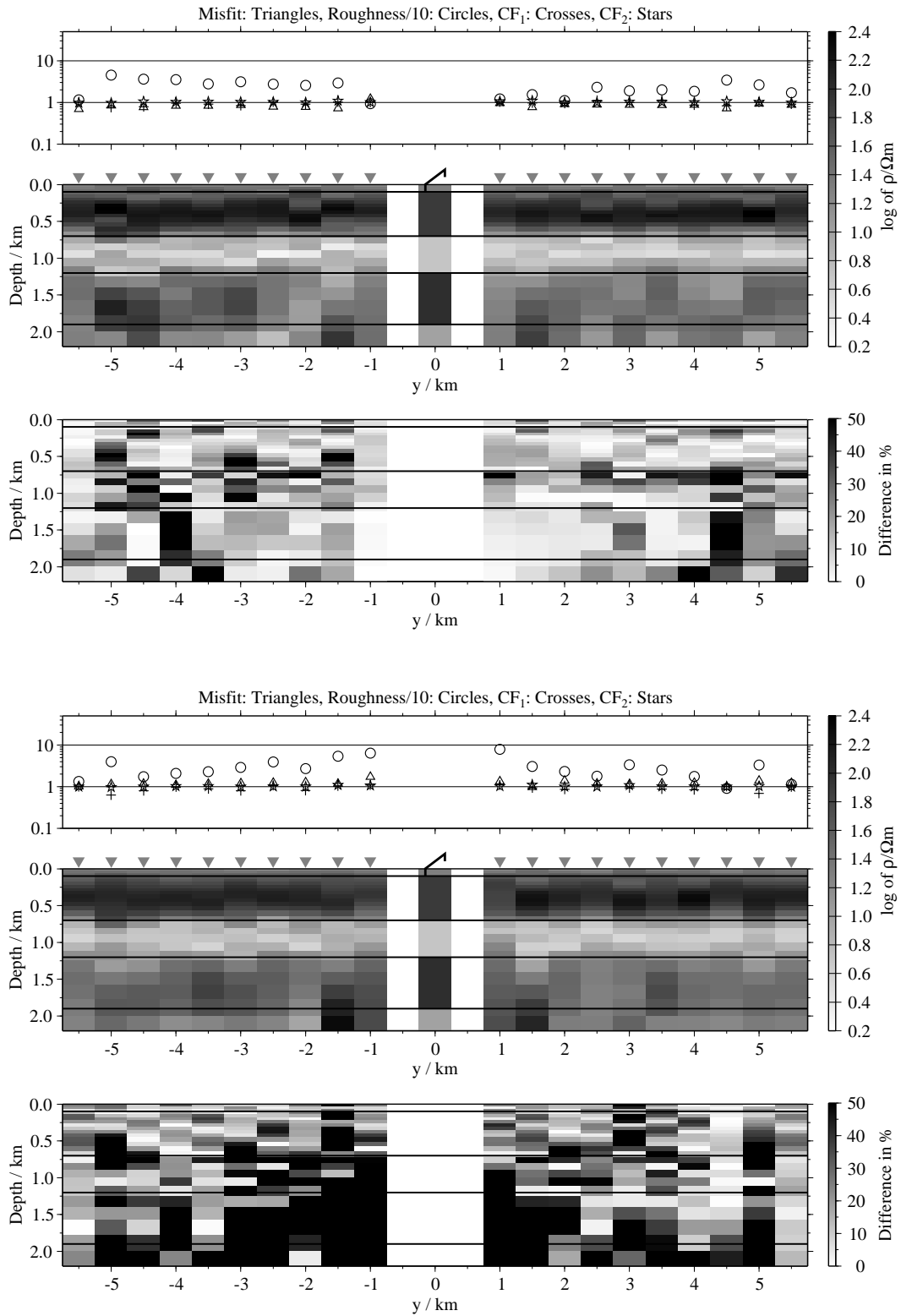


Figure B.12: Pseudo-sections of 1-D inversions using the components E_x and \dot{H}_y with regularisation scheme C1, model A (displayed below Tx); Top panels: Average inversion results using the soft joint-inversion approach and relative differences; bottom: Average inversion results using the single 1-D inversions and relative differences;

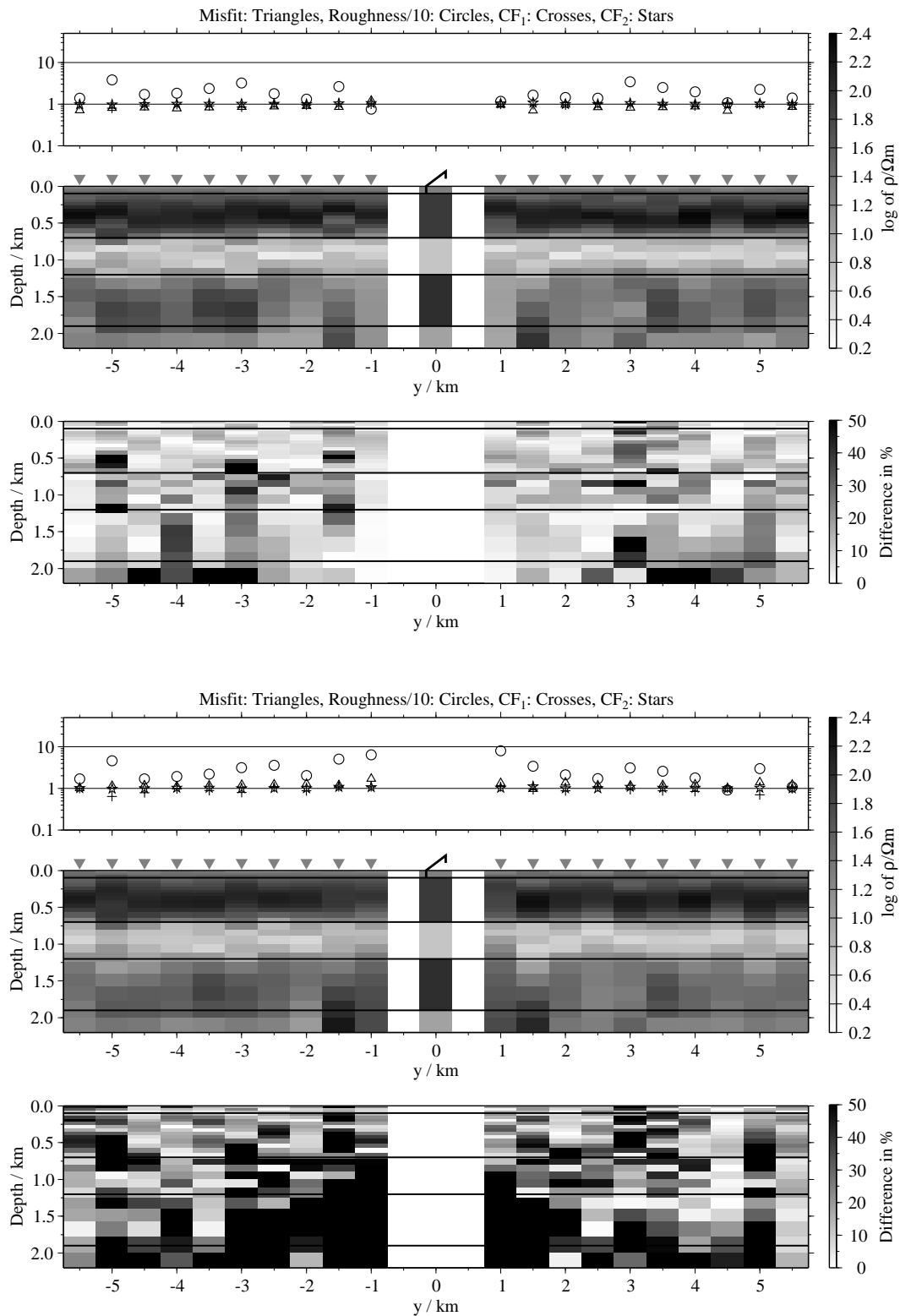


Figure B.13: Pseudo-sections of 1-D inversions using the components E_x and \dot{H}_y with regularisation scheme C2, model A (displayed below Tx); Top panels: Average inversion results using the soft joint-inversion approach and relative differences; bottom: Average inversion results using the single 1-D inversions and relative differences;

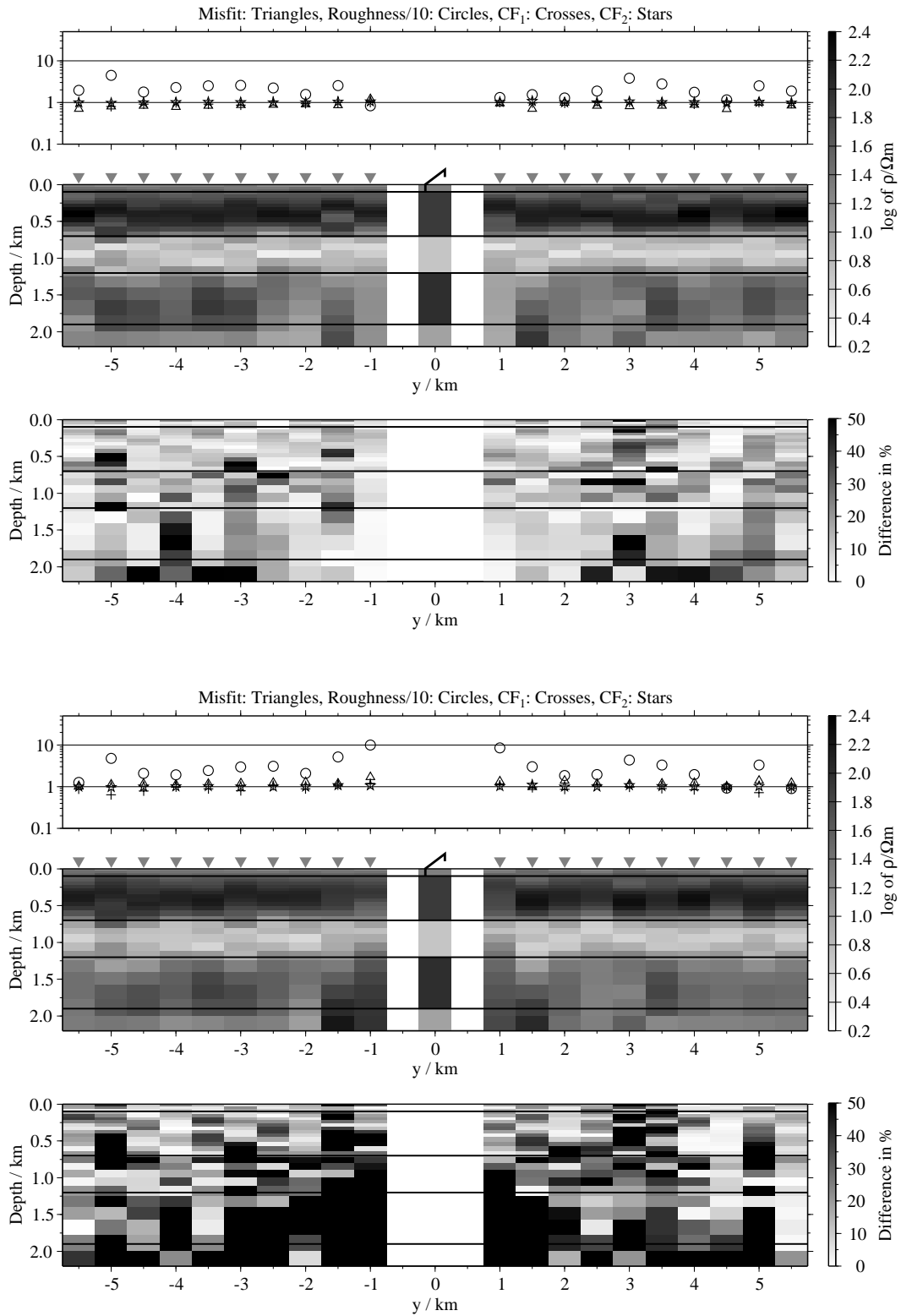


Figure B.14: Pseudo-sections of 1-D inversions using the components E_x and \dot{H}_y with regularisation scheme C3, model A (displayed below Tx); Top panels: Average inversion results using the soft joint-inversion approach and relative differences; bottom: Average inversion results using the single 1-D inversions and relative differences;

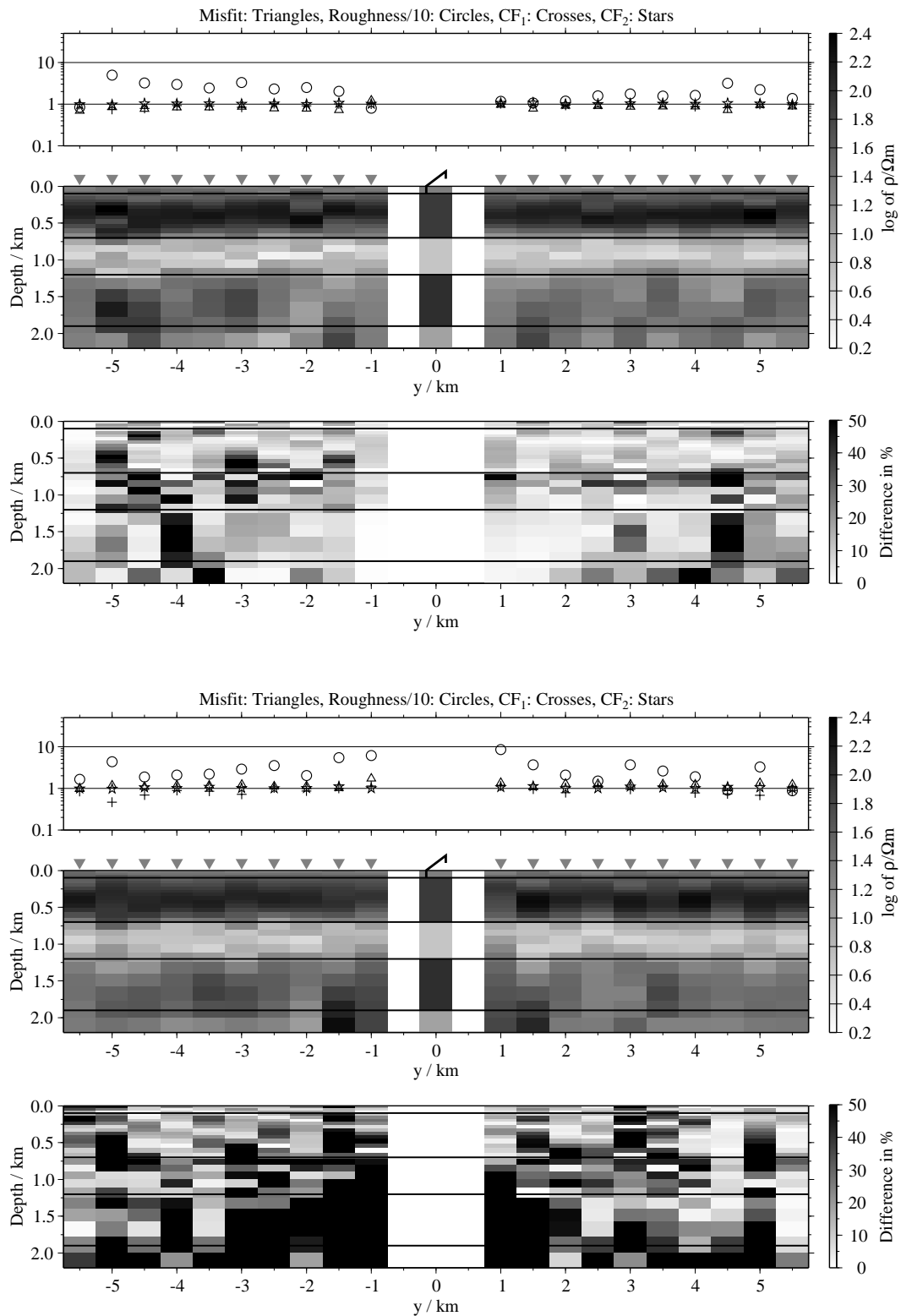


Figure B.15: Pseudo-sections of 1-D inversions using the components E_x and \dot{H}_y with regularisation scheme C4, model A (displayed below Tx); Top panels: Average inversion results using the soft joint-inversion approach and relative differences; bottom: Average inversion results using the single 1-D inversions and relative differences;

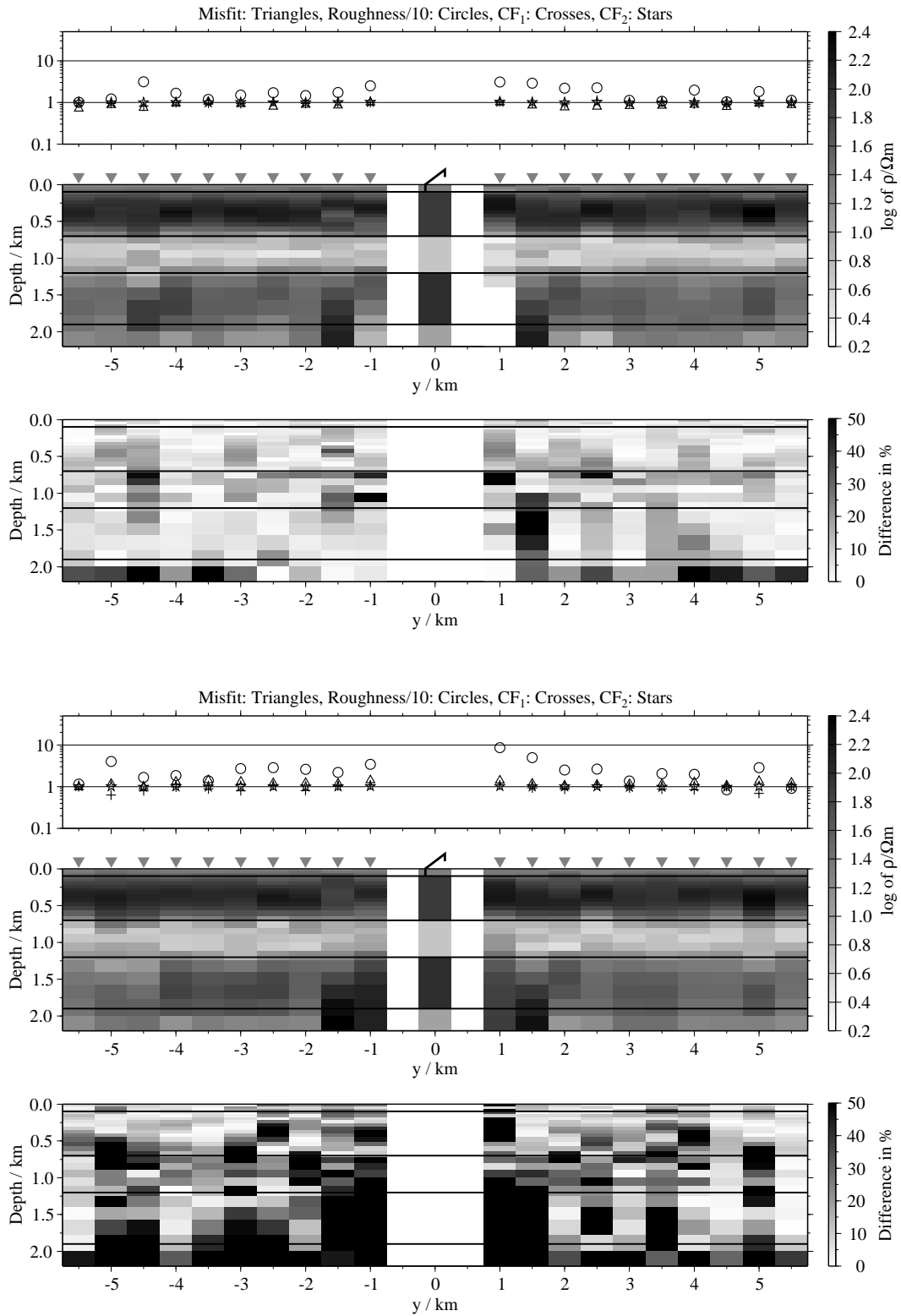


Figure B.16: Pseudo-sections of 1-D inversions using the components E_x and \dot{H}_z with regularisation scheme C1, model A (displayed below Tx); Top panels: Average inversion results using the soft joint-inversion approach and relative differences; bottom: Average inversion results using the single 1-D inversions and relative differences;

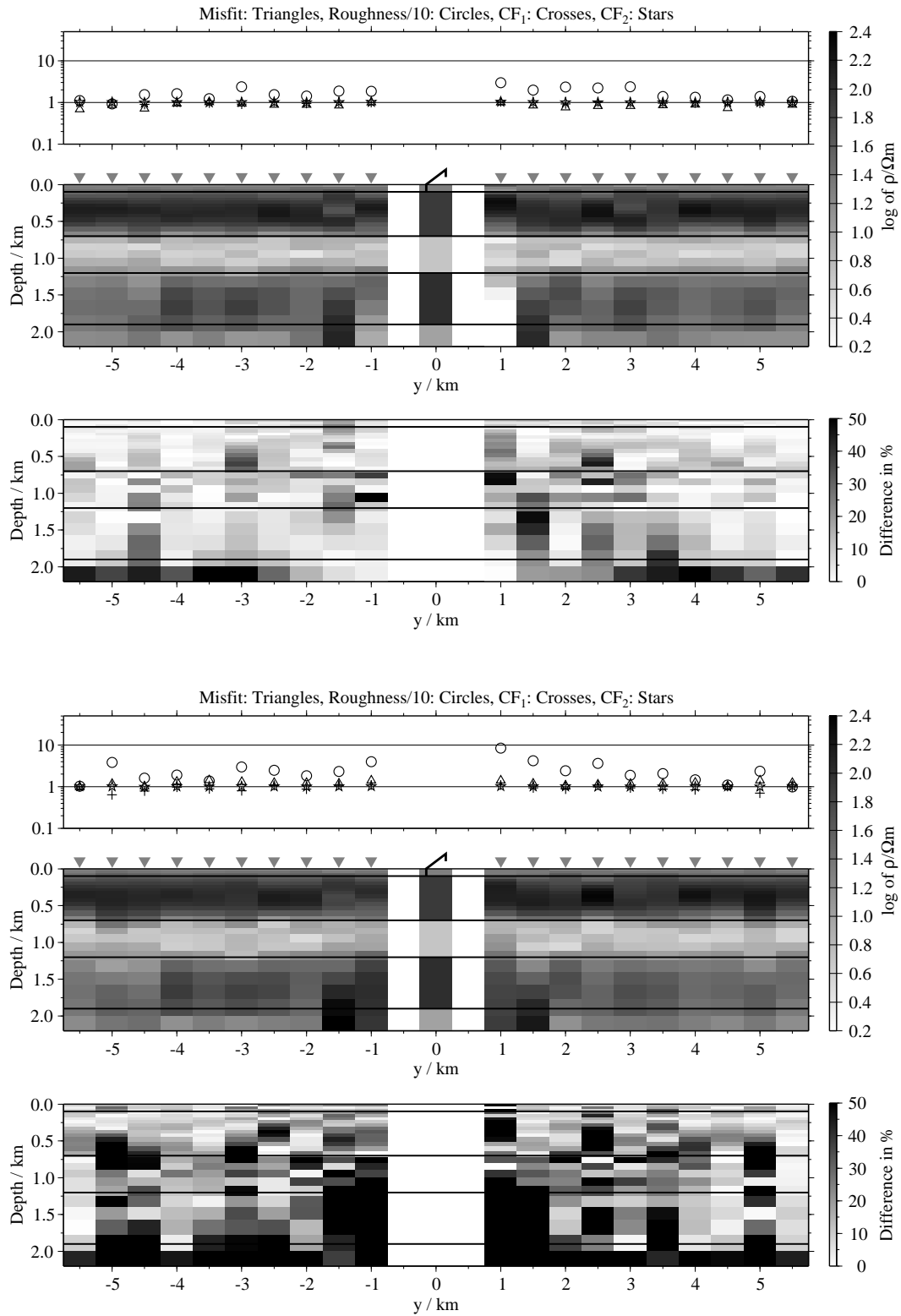


Figure B.17: Pseudo-sections of 1-D inversions using the components E_x and \dot{H}_z with regularisation scheme C2, model A (displayed below Tx); Top panels: Average inversion results using the soft joint-inversion approach and relative differences; bottom: Average inversion results using the single 1-D inversions and relative differences;

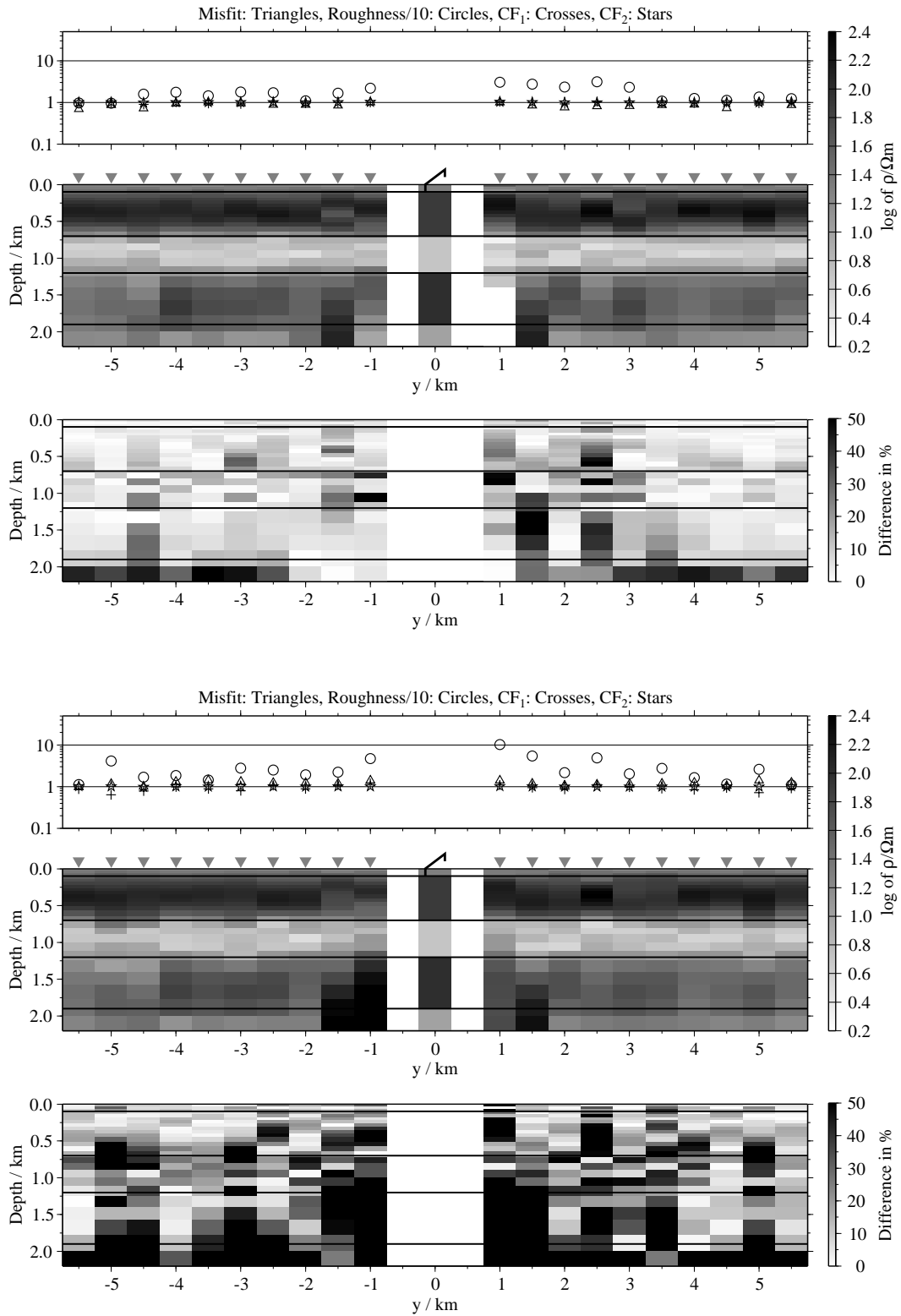


Figure B.18: Pseudo-sections of 1-D inversions using the components E_x and \dot{H}_z with regularisation scheme C3, model A (displayed below Tx); Top panels: Average inversion results using the soft joint-inversion approach and relative differences; bottom: Average inversion results using the single 1-D inversions and relative differences;

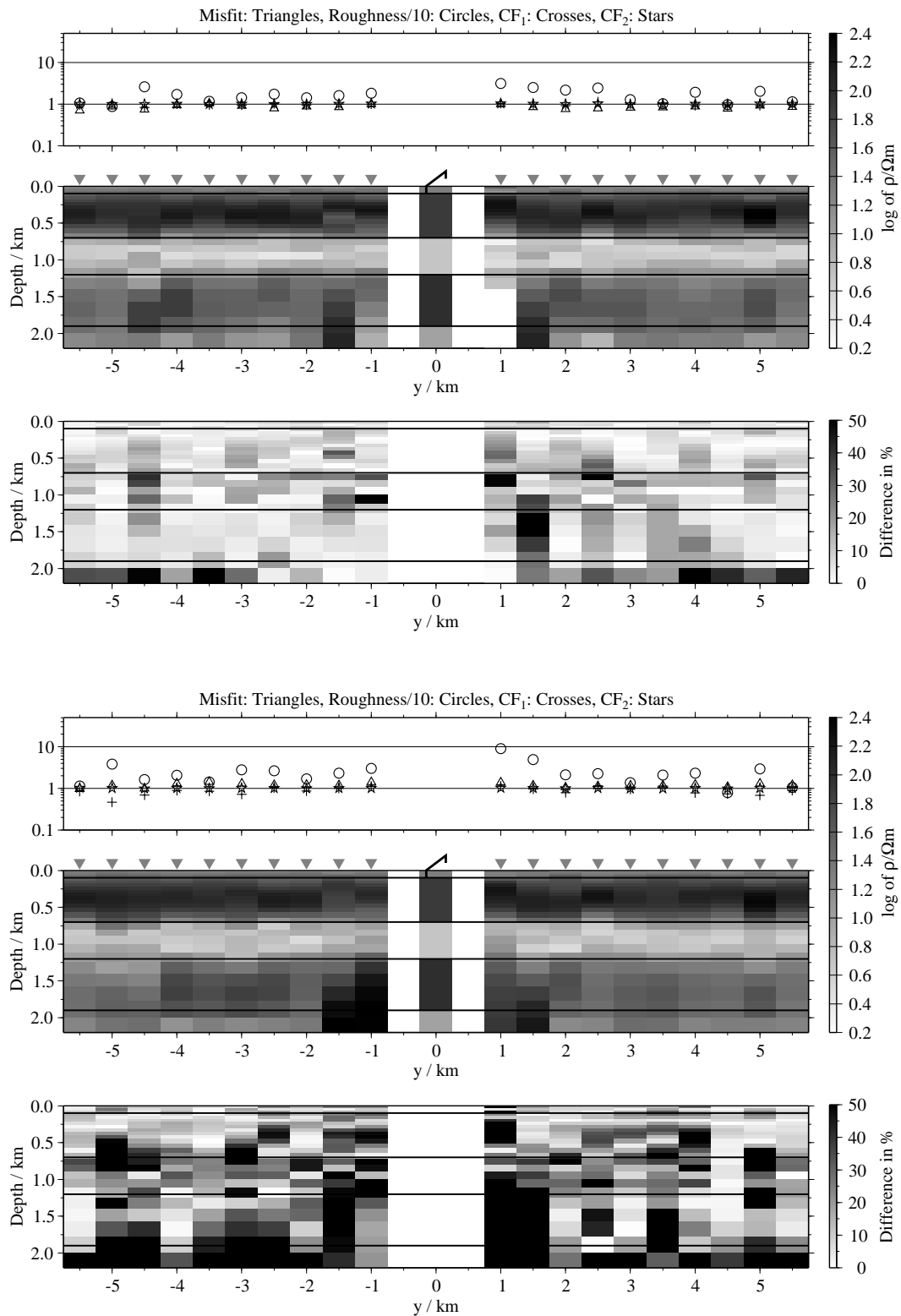


Figure B.19: Pseudo-sections of 1-D inversions using the components E_x and \dot{H}_z with regularisation scheme C4, model A (displayed below Tx); Top panels: Average inversion results using the soft joint-inversion approach and relative differences; bottom: Average inversion results using the single 1-D inversions and relative differences;

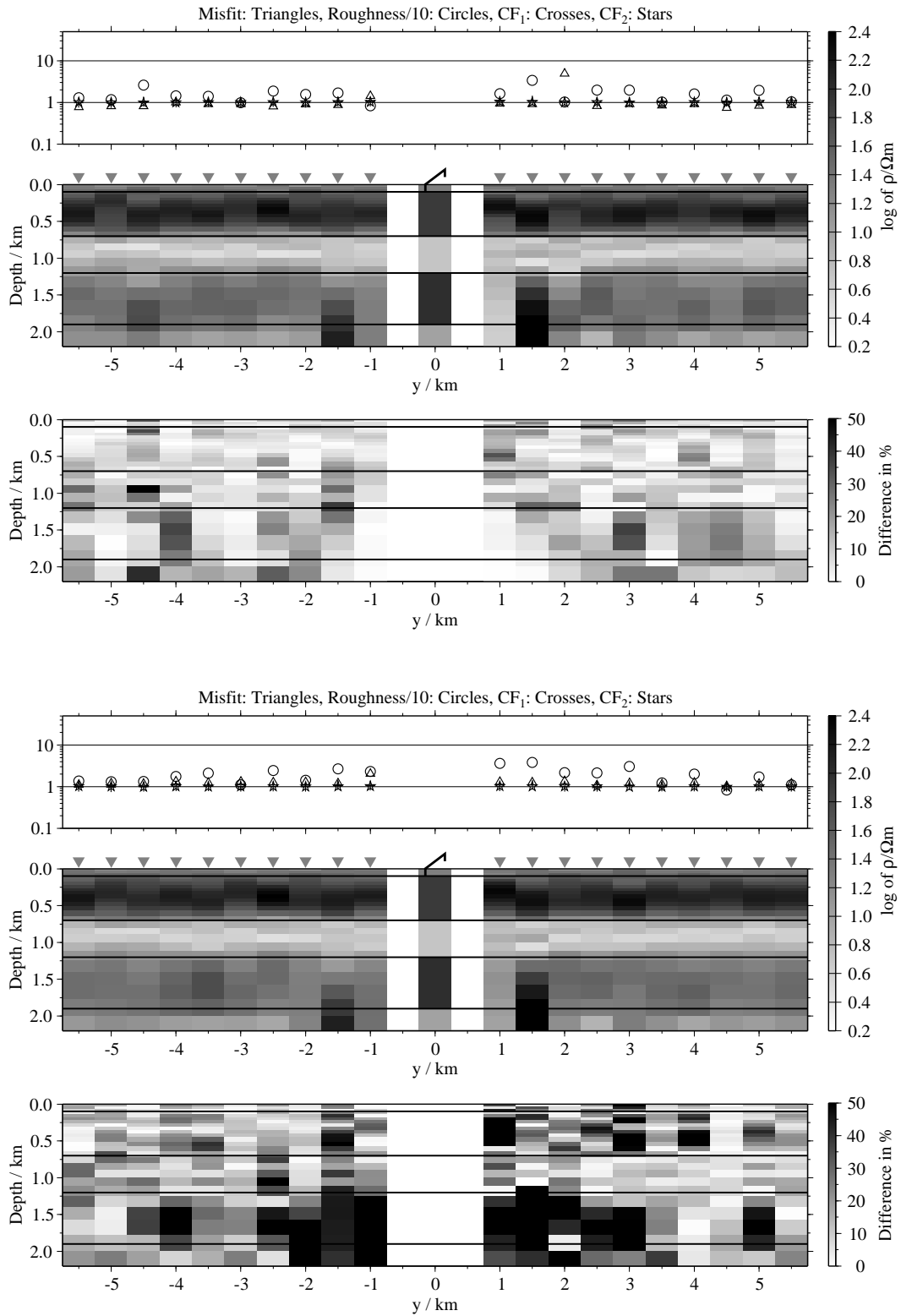


Figure B.20: Pseudo-sections of 1-D inversions using the components \dot{H}_y and \dot{H}_z with regularisation scheme C1, model A (displayed below Tx); Top panels: Average inversion results using the soft joint-inversion approach and relative differences; bottom: Average inversion results using the single 1-D inversions and relative differences;

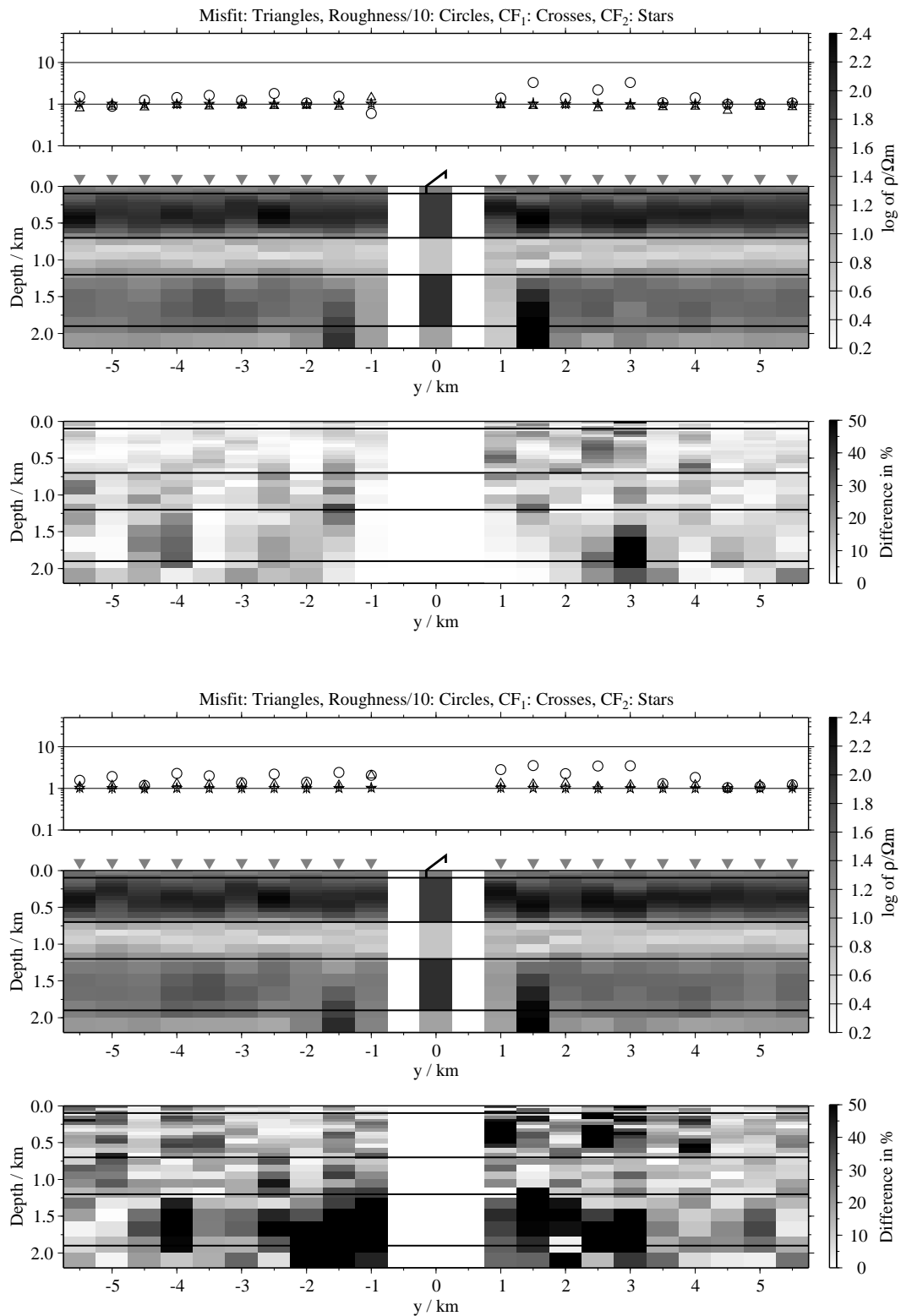


Figure B.21: Pseudo-sections of 1-D inversions using the components \dot{H}_y and \dot{H}_z with regularisation scheme C2, model A (displayed below Tx); Top panels: Average inversion results using the soft joint-inversion approach and relative differences; bottom: Average inversion results using the single 1-D inversions and relative differences;

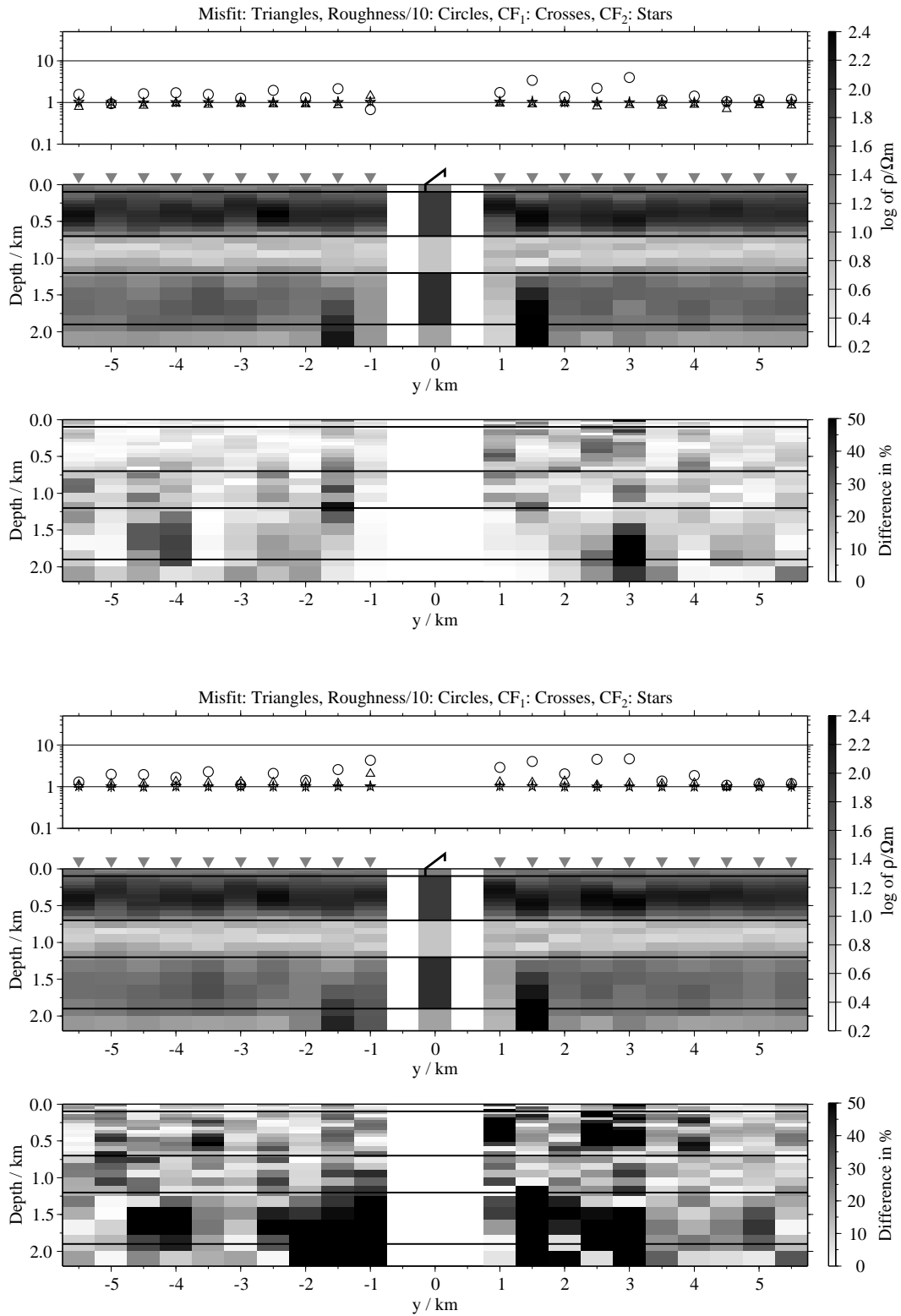


Figure B.22: Pseudo-sections of 1-D inversions using the components \dot{H}_y and \dot{H}_z with regularisation scheme C3, model A (displayed below Tx); Top panels: Average inversion results using the soft joint-inversion approach and relative differences; bottom: Average inversion results using the single 1-D inversions and relative differences;

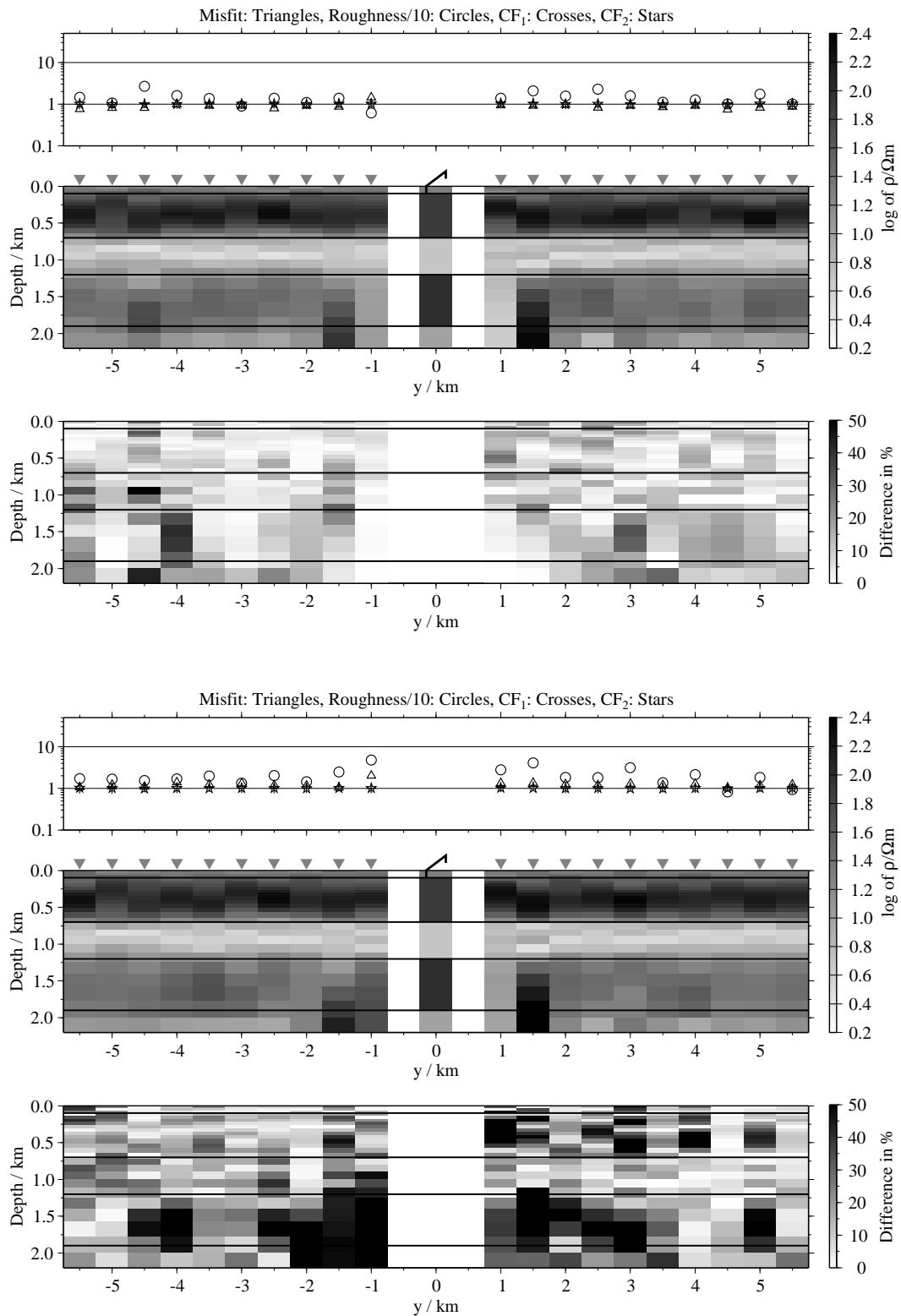


Figure B.23: Pseudo-sections of 1-D inversions using the components \dot{H}_y and \dot{H}_z with regularisation scheme C4, model A (displayed below Tx); Top panels: Average inversion results using the soft joint-inversion approach and relative differences; bottom: Average inversion results using the single 1-D inversions and relative differences;

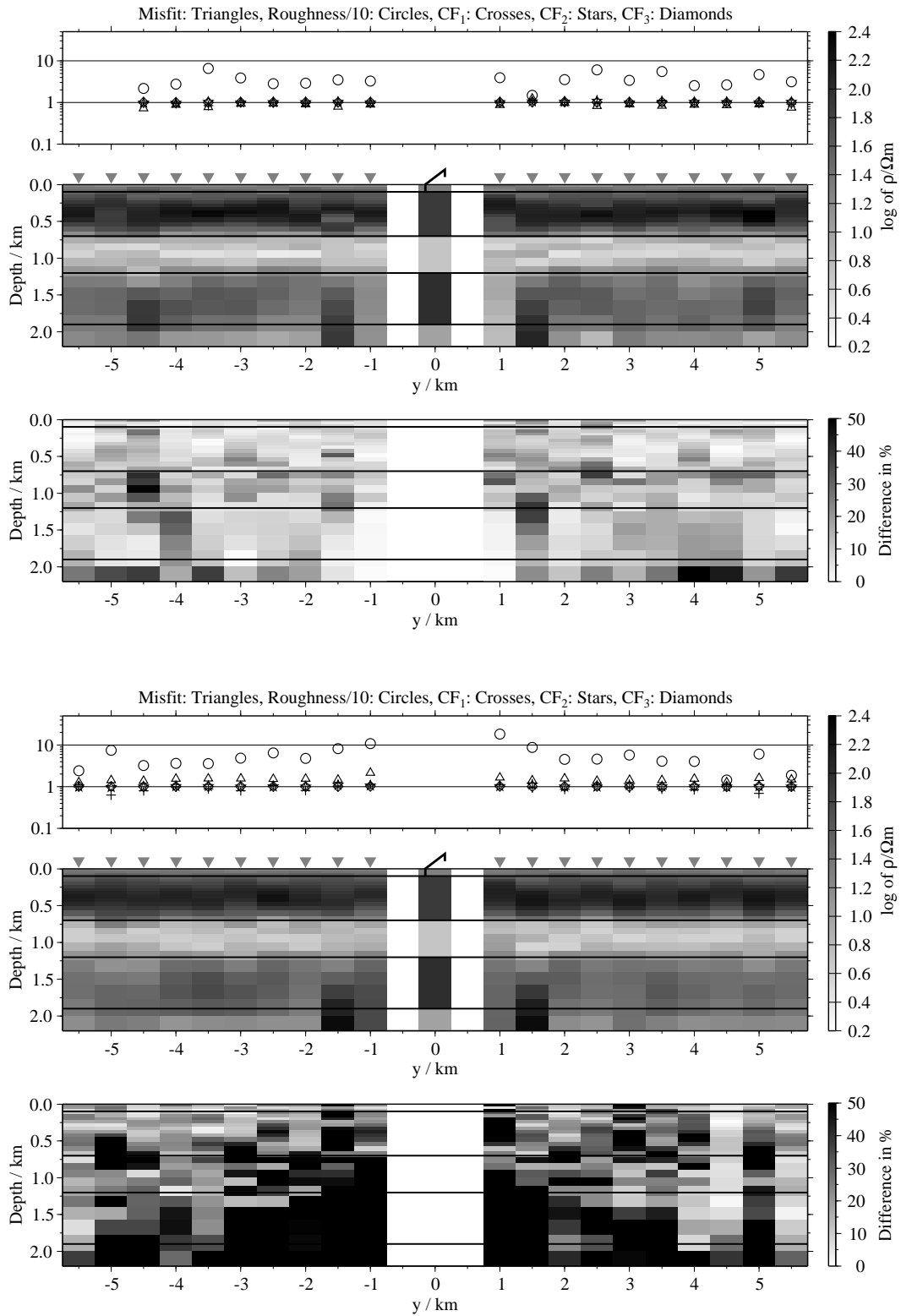


Figure B.24: Pseudo-sections of 1-D inversions using all three components with regularisation scheme C1, model A (displayed below Tx); Top panels: Average inversion results using the soft joint-inversion approach and relative differences; bottom: Average inversion results using the single 1-D inversions and relative differences;

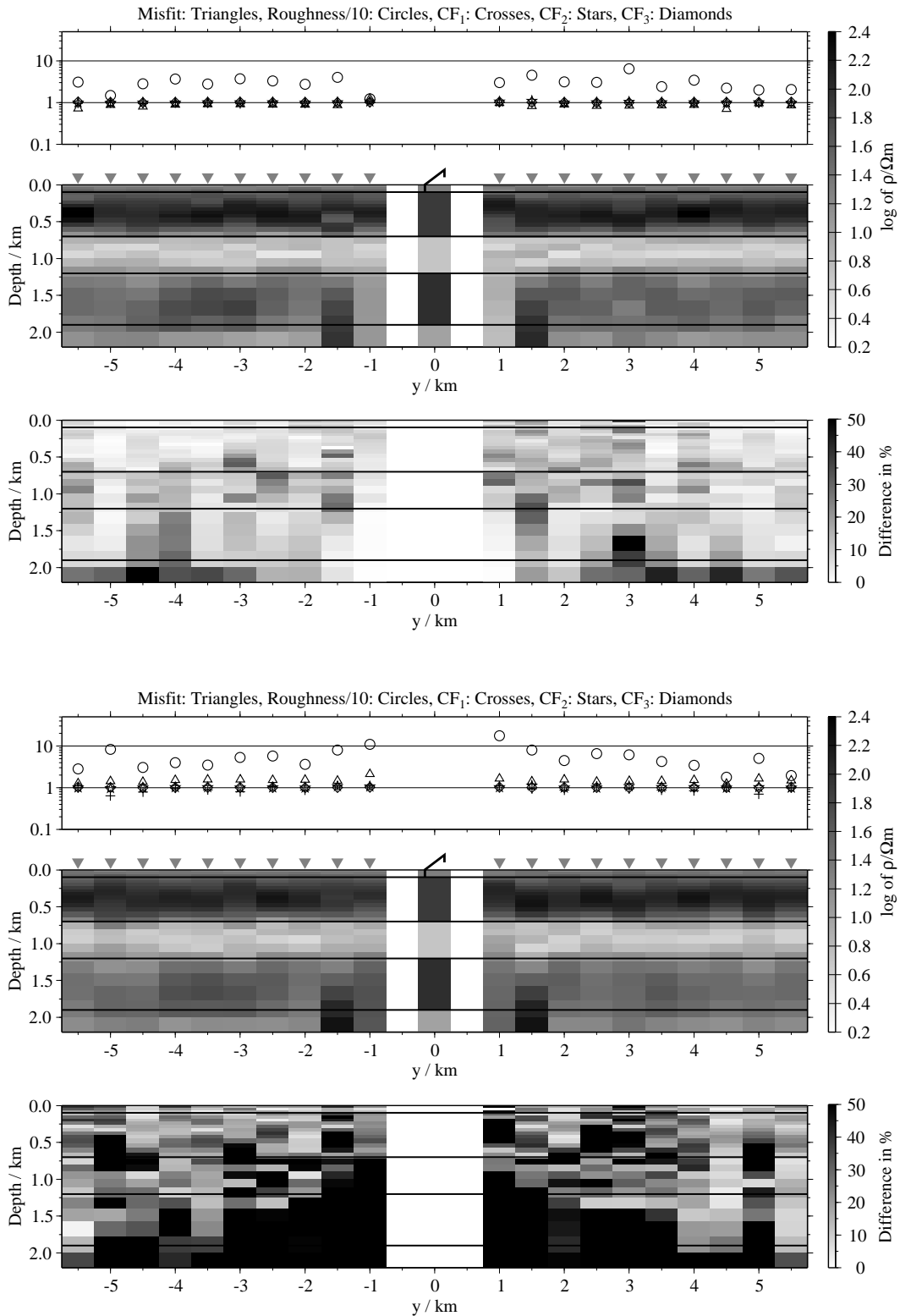


Figure B.25: Pseudo-sections of 1-D inversions using all three components with regularisation scheme C2, model A (displayed below Tx); Top panels: Average inversion results using the soft joint-inversion approach and relative differences; bottom: Average inversion results using the single 1-D inversions and relative differences;

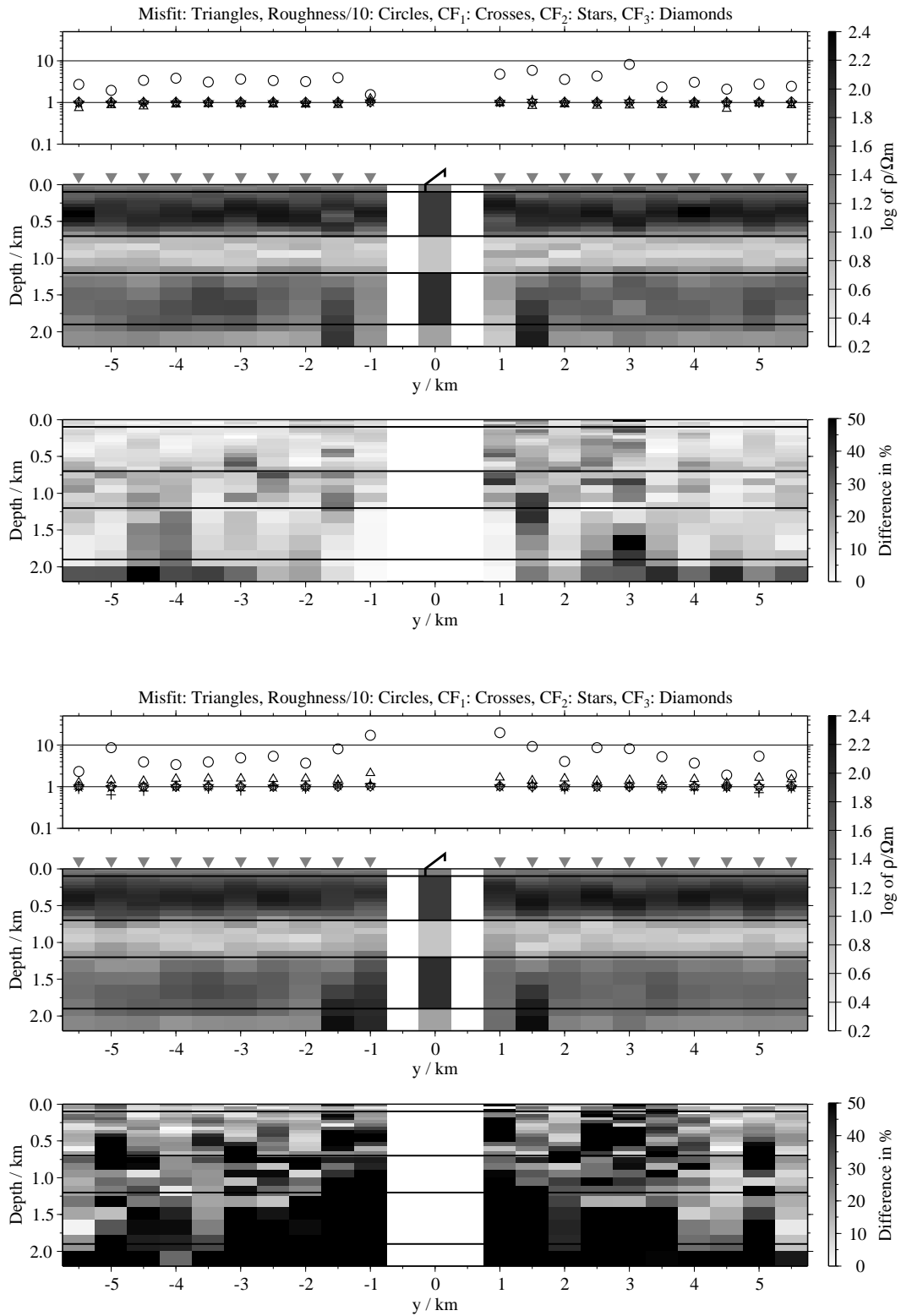


Figure B.26: Pseudo-sections of 1-D inversions using all three components with regularisation scheme C3, model A (displayed below Tx); Top panels: Average inversion results using the soft joint-inversion approach and relative differences; bottom: Average inversion results using the single 1-D inversions and relative differences;

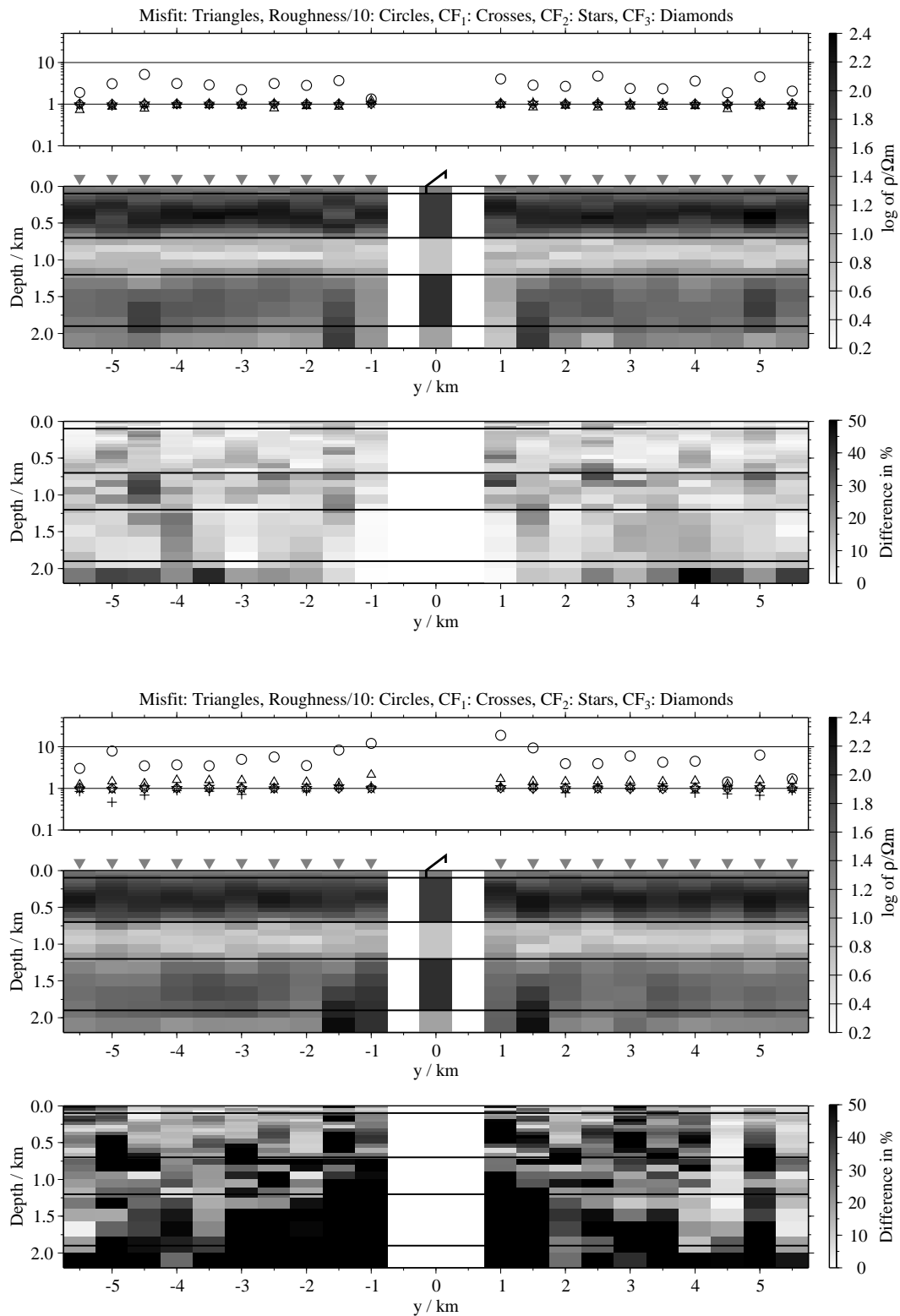
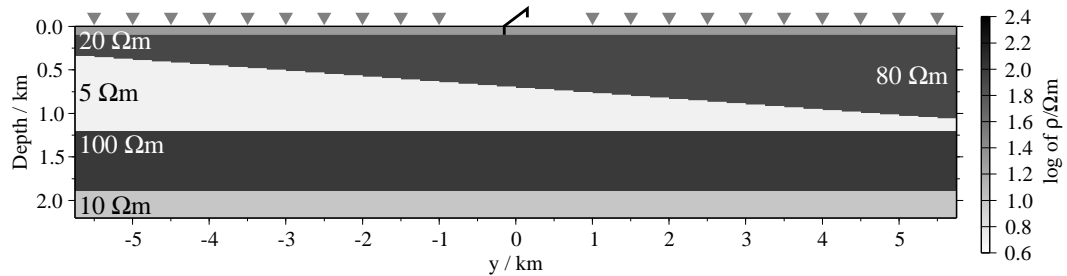


Figure B.27: Pseudo-sections of 1-D inversions using all three components with regularisation scheme C4, model A (displayed below Tx); Top panels: Average inversion results using the soft joint-inversion approach and relative differences; bottom: Average inversion results using the single 1-D inversions and relative differences;

B.2 Pseudo-sections for the models B to M

B.2.1 Dipping layers (models B and C)

Model B:



Model C:

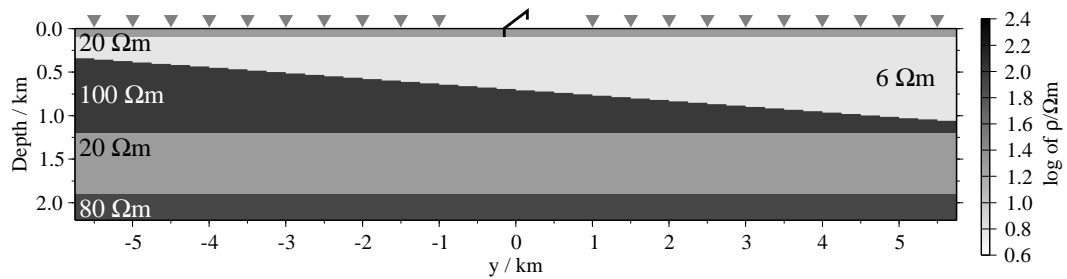


Figure B.28: The dipping layer models B and C used in this section;

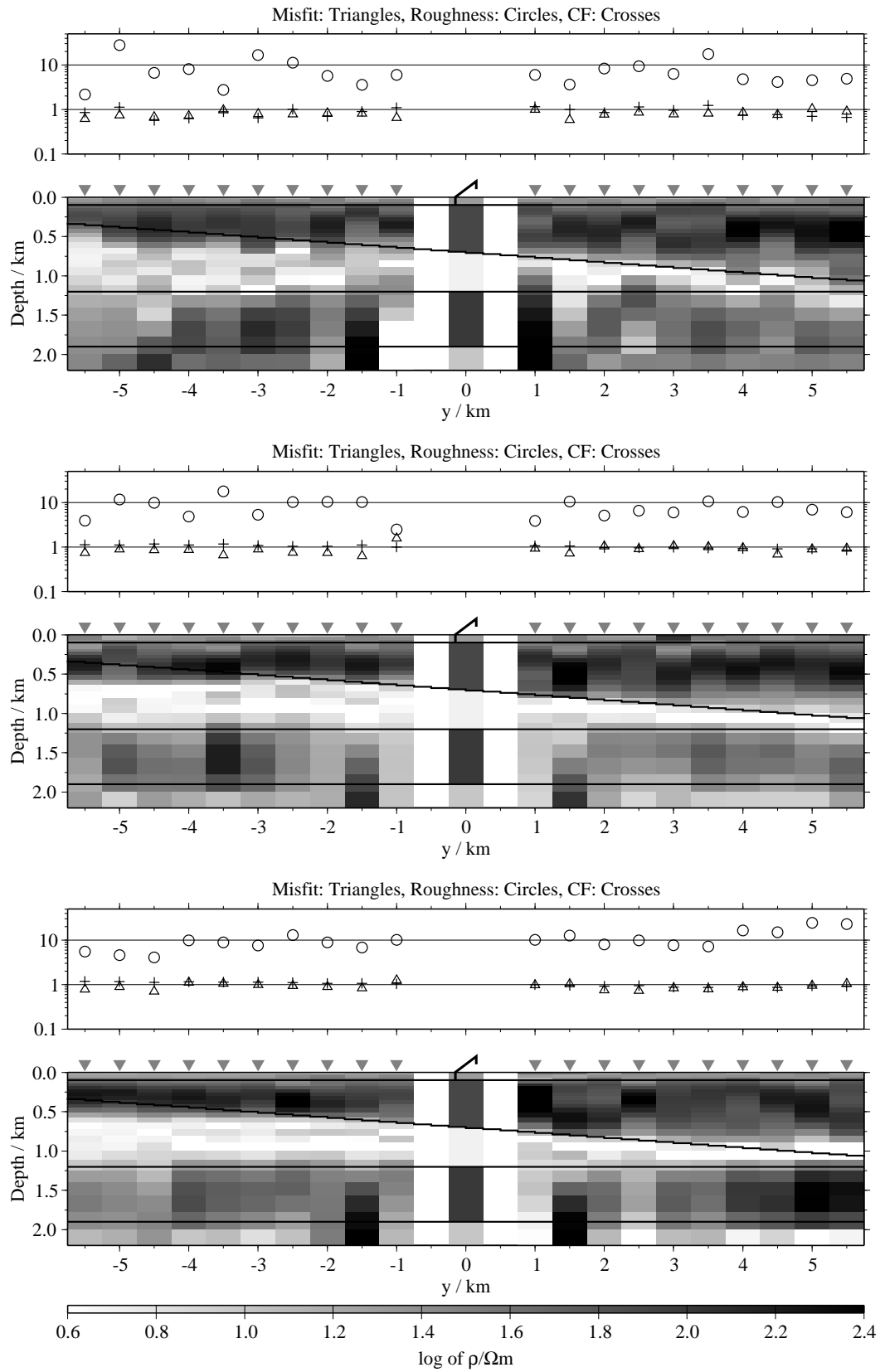


Figure B.29: Pseudo-sections of single 1-D inversion, model B, regularisation scheme C1; from top to bottom E_x -, H_y - and H_z -component;

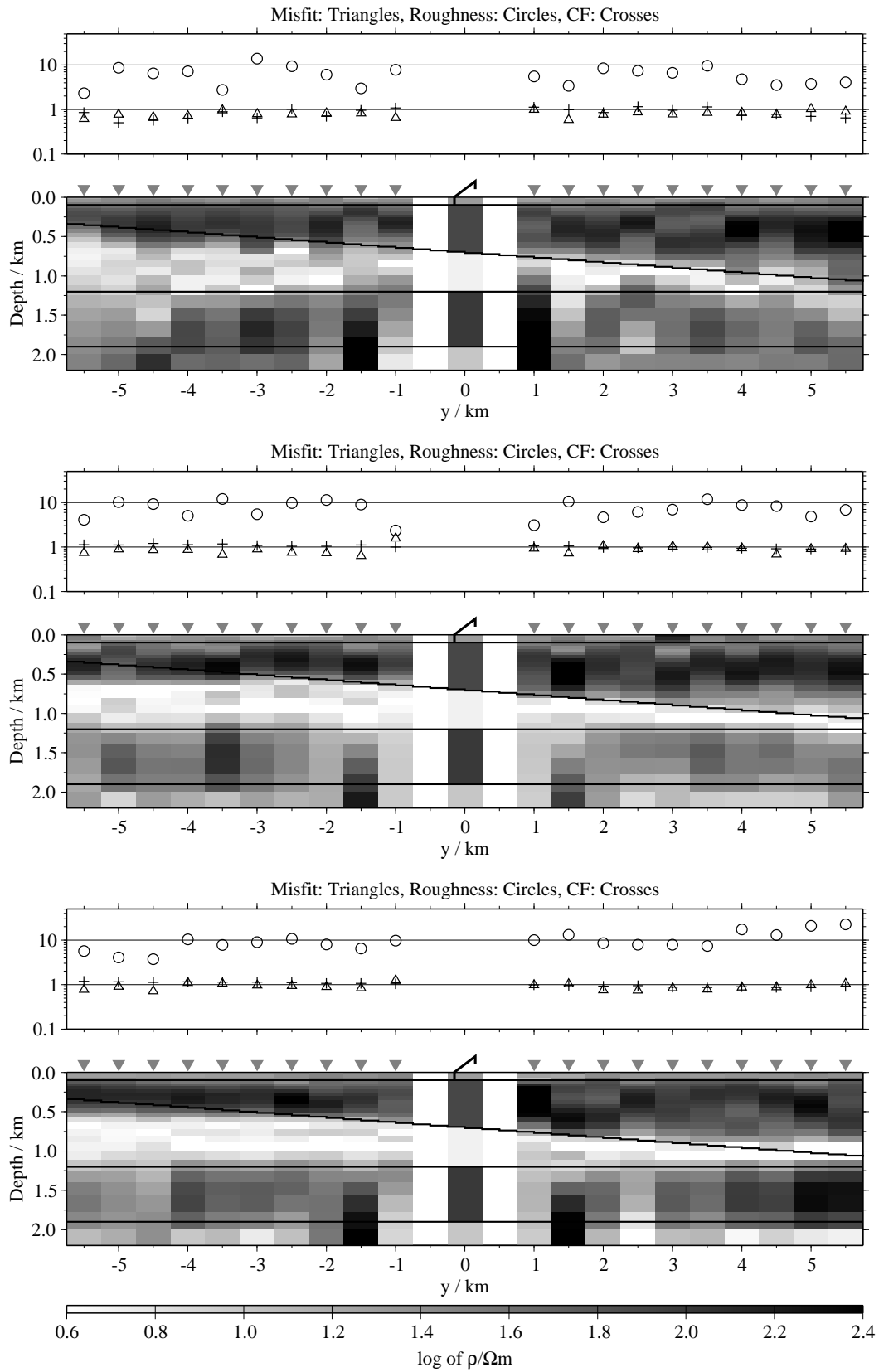


Figure B.30: Pseudo-sections of single 1-D inversion, model B, regularisation scheme C4; from top to bottom E_x -, \dot{H}_y - and \dot{H}_z -component;

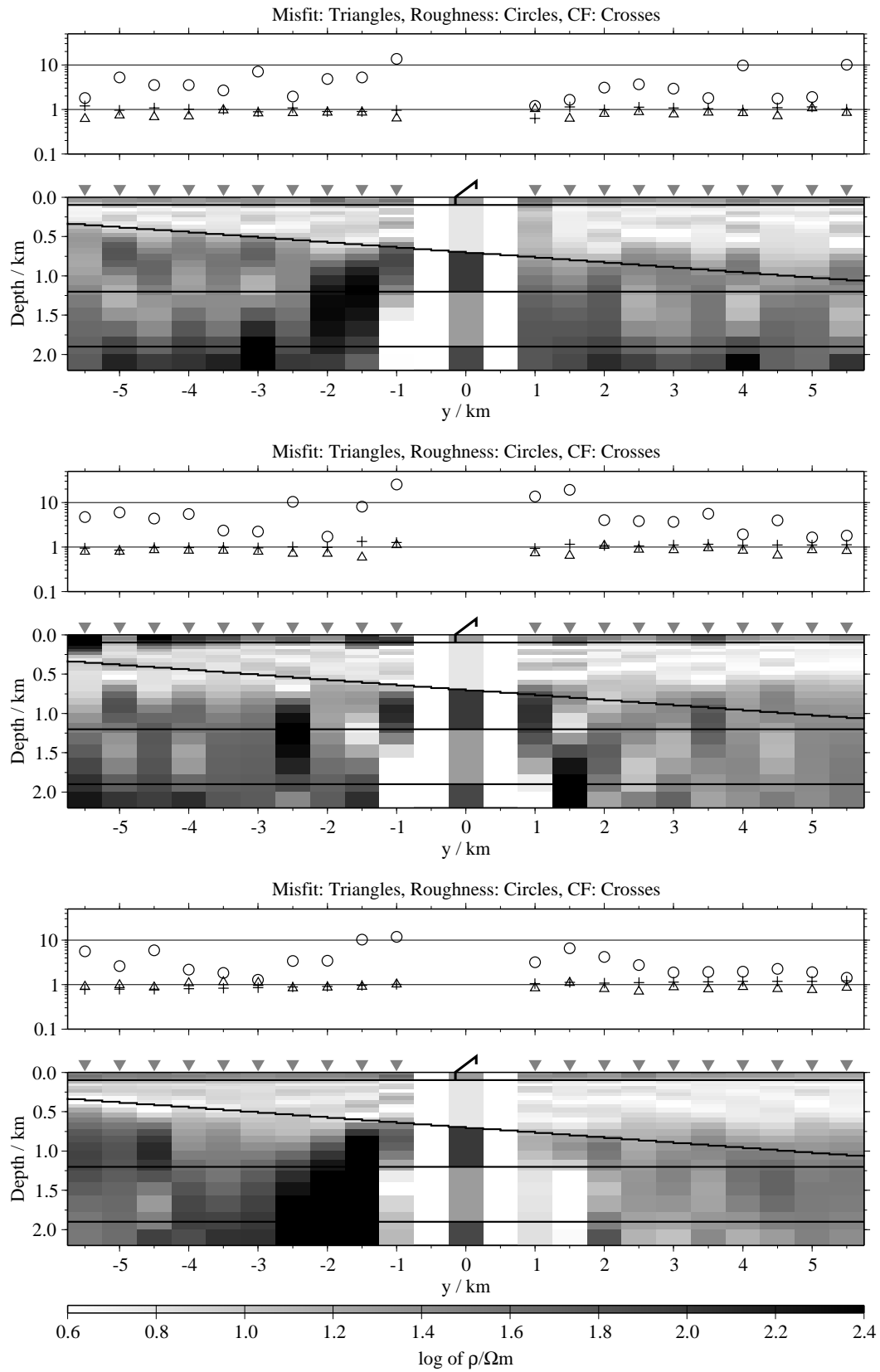


Figure B.31: Pseudo-sections of single 1-D inversion, model C, regularisation scheme C1; from top to bottom E_x -, H_y - and H_z -component;

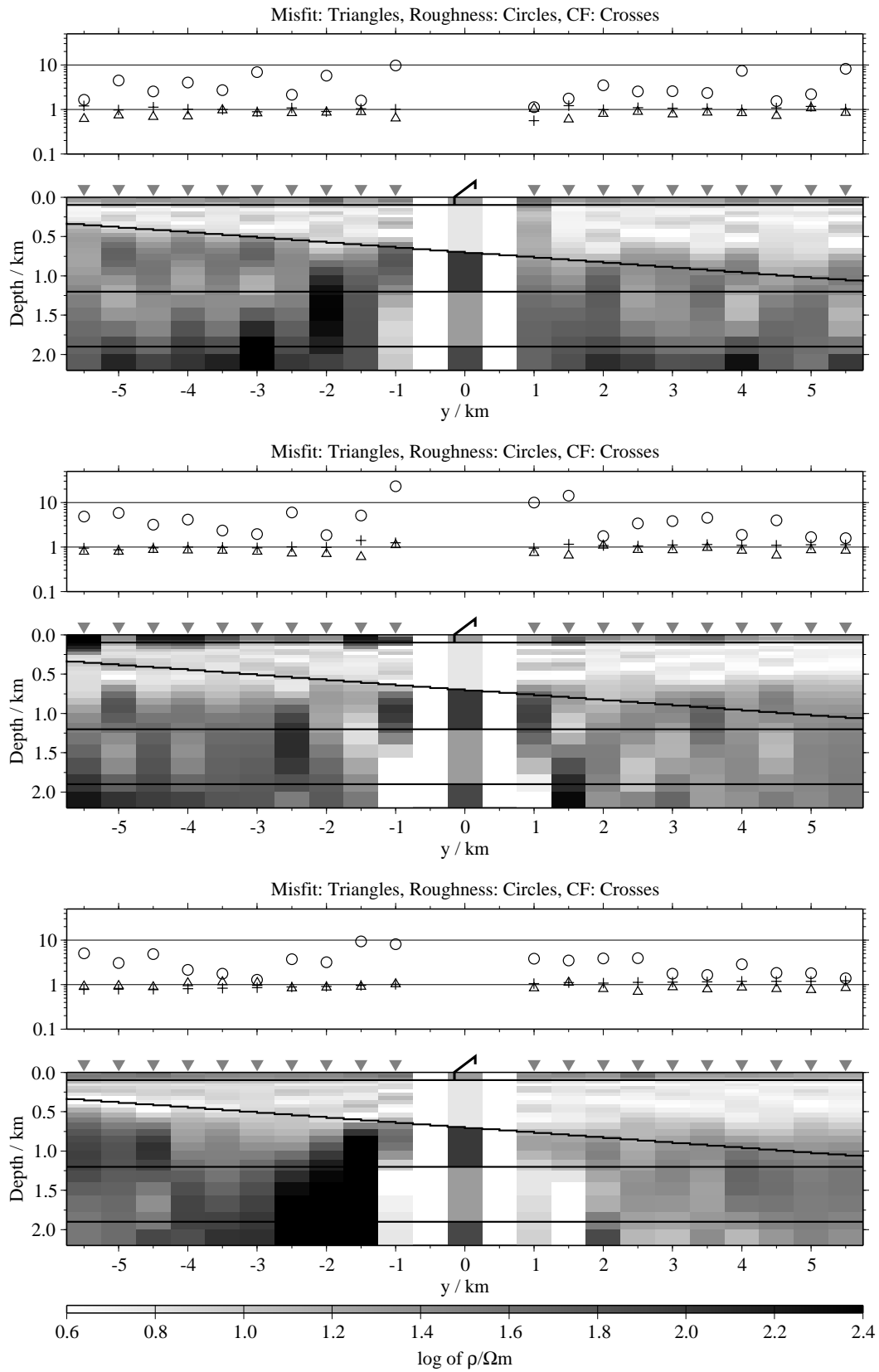


Figure B.32: Pseudo-sections of single 1-D inversion, model C, regularisation scheme C4; from top to bottom E_x -, H_y - and H_z -component;

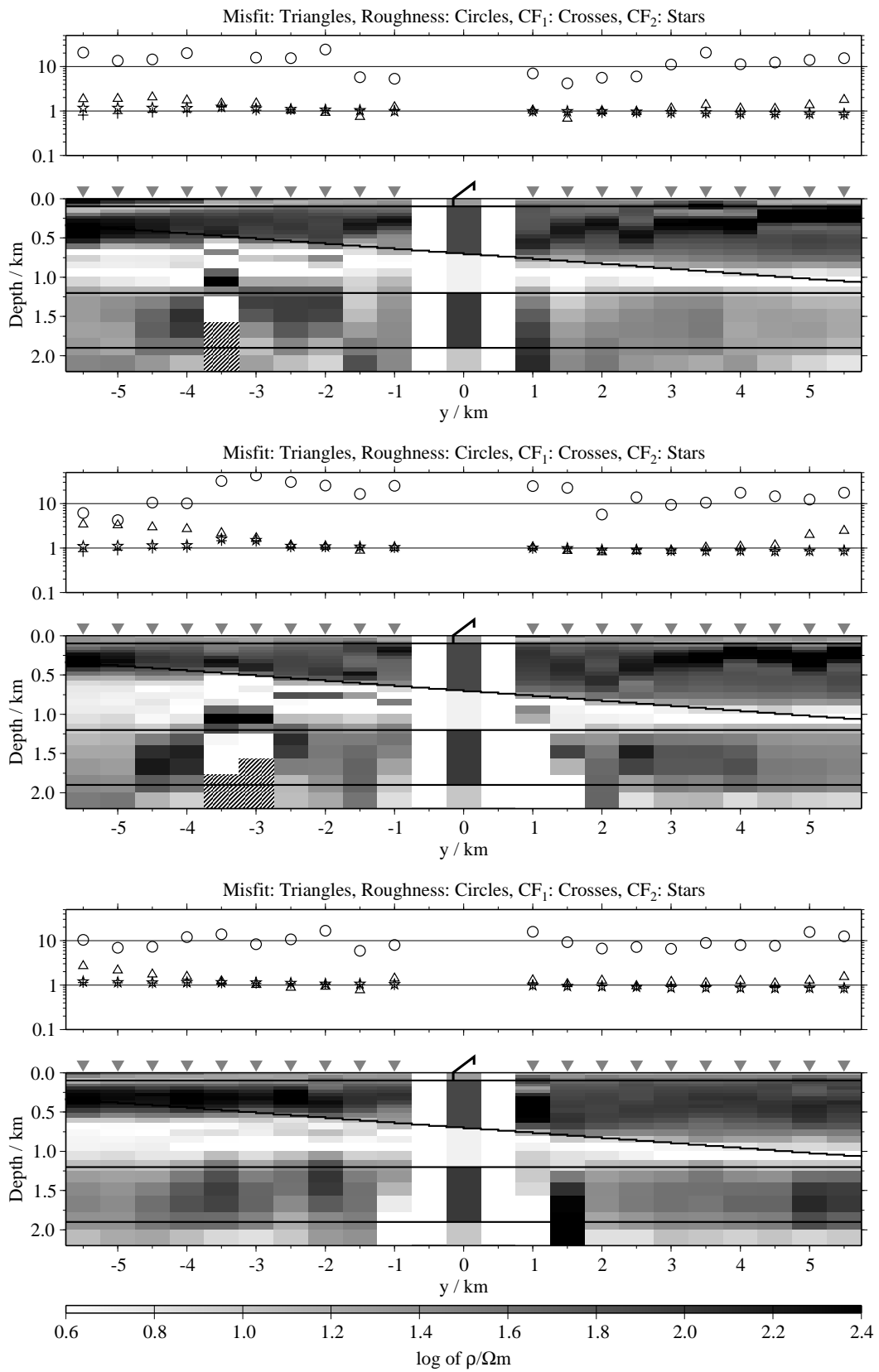


Figure B.33: Pseudo-sections of two component 1-D joint-inversions, model B, regularisation scheme C1; from top to bottom $E_x-\dot{H}_y$, $E_x-\dot{H}_z$ and $\dot{H}_y-\dot{H}_z$;

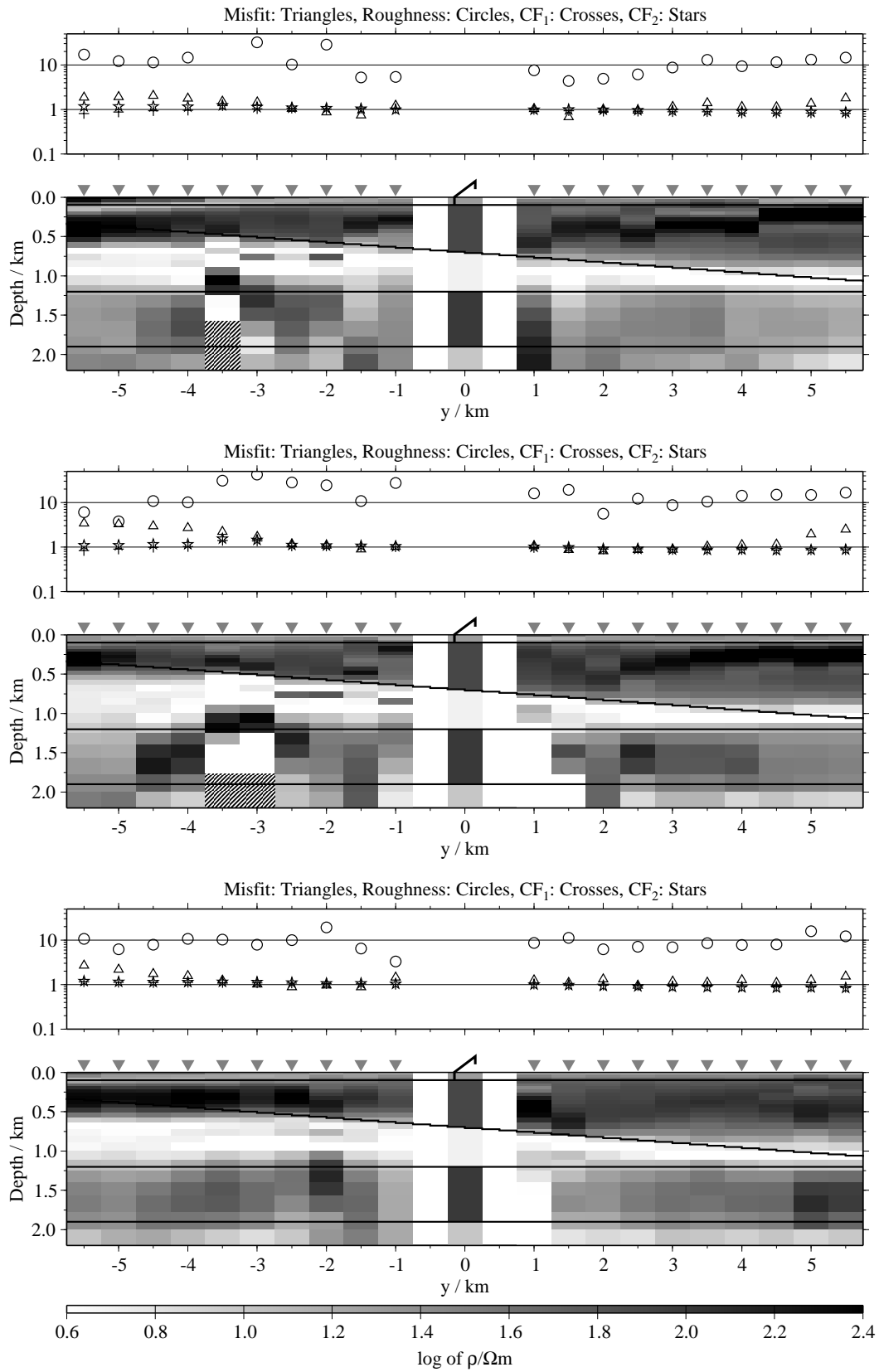


Figure B.34: Pseudo-sections of two component 1-D joint-inversions, model B, regularisation scheme C4; from top to bottom $E_x-\dot{H}_y$, $E_x-\dot{H}_z$ and $\dot{H}_y-\dot{H}_z$;

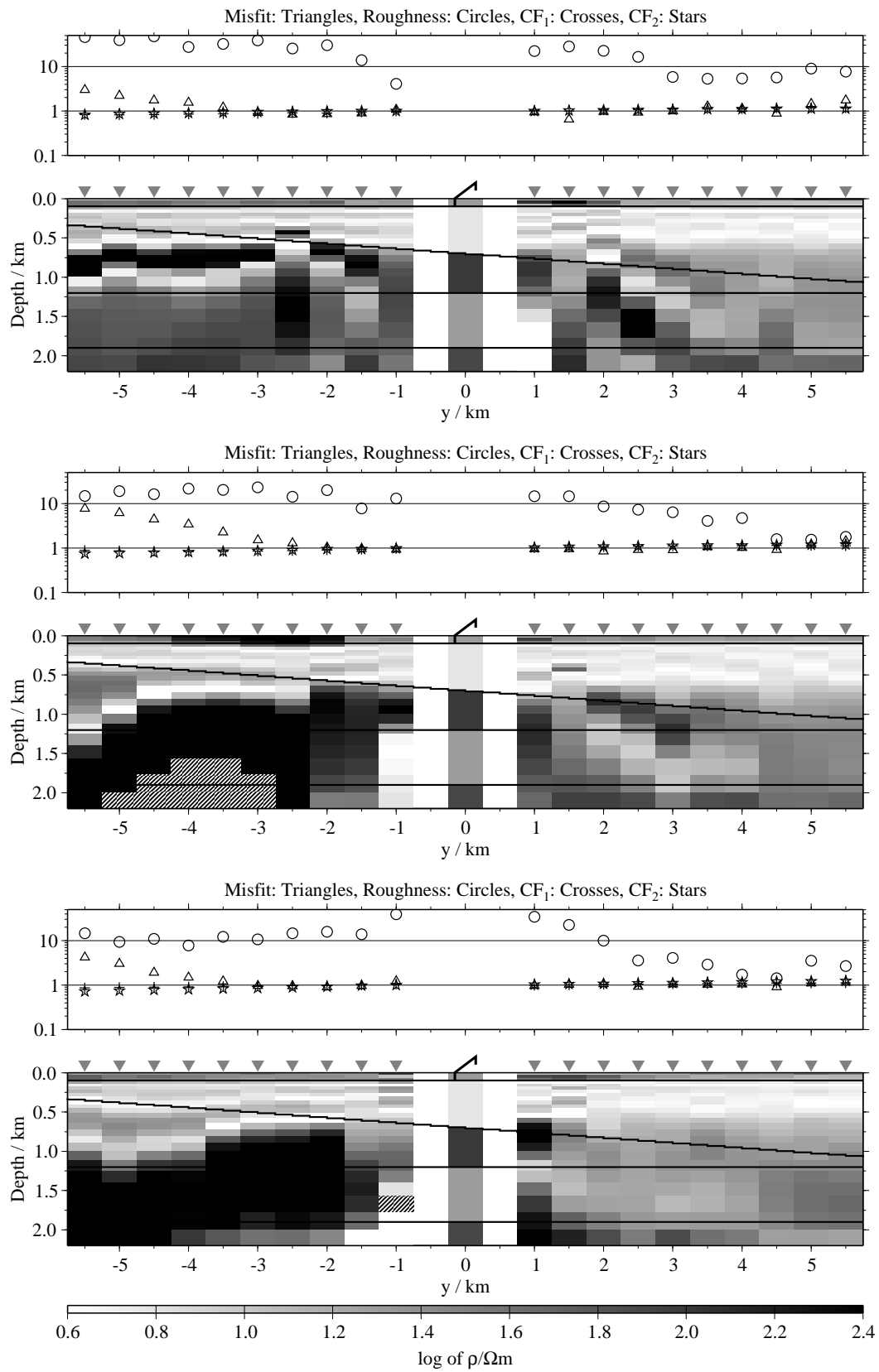


Figure B.35: Pseudo-sections of two component 1-D joint-inversions, model C, regularisation scheme C1; from top to bottom $E_x-\dot{H}_y$, $E_x-\dot{H}_z$ and $\dot{H}_y-\dot{H}_z$;

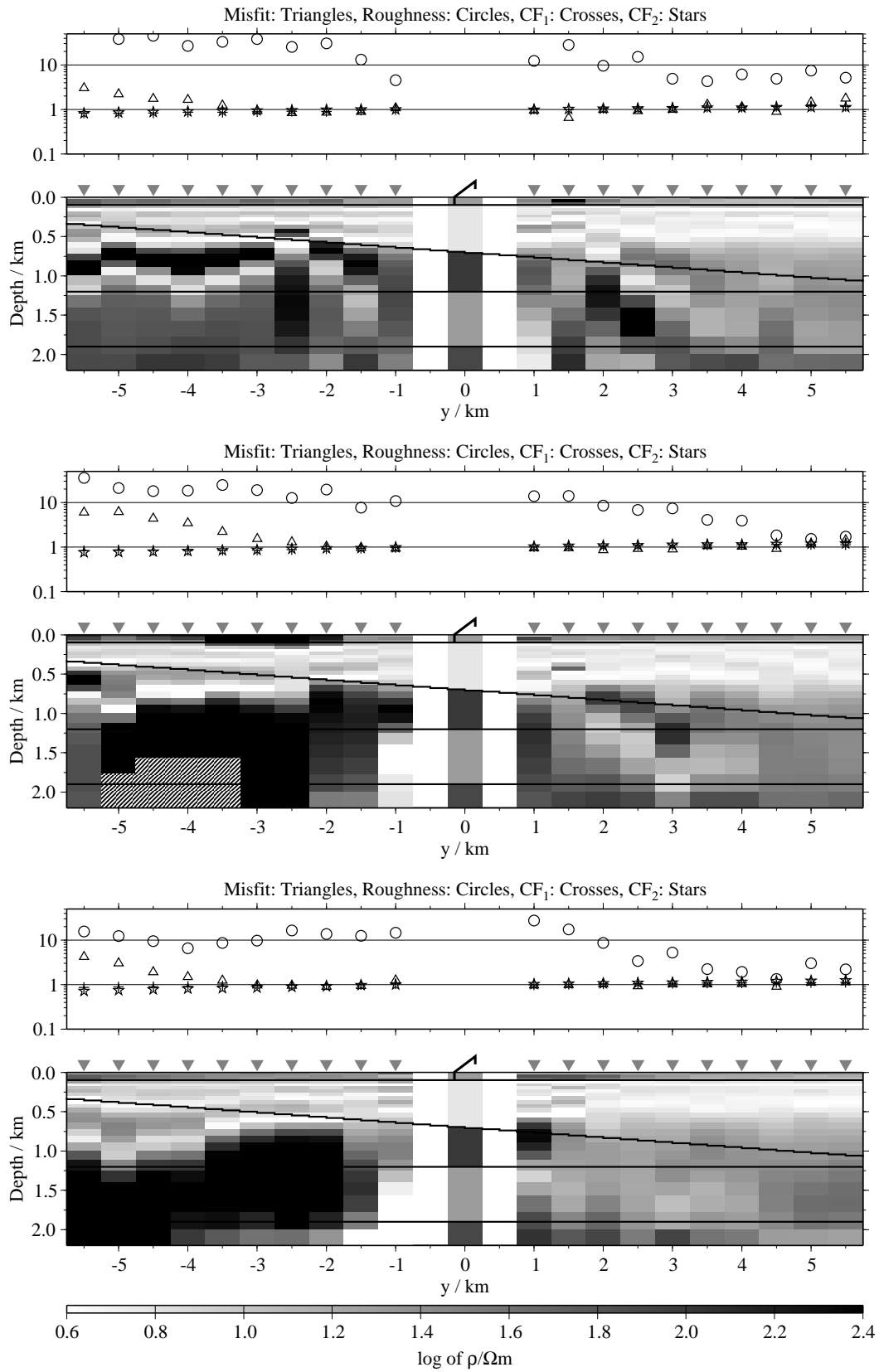


Figure B.36: Pseudo-sections of two component 1-D joint-inversions, model C, regularisation scheme C4; from top to bottom $E_x-\dot{H}_y$, $E_x-\dot{H}_z$ and $\dot{H}_y-\dot{H}_z$;

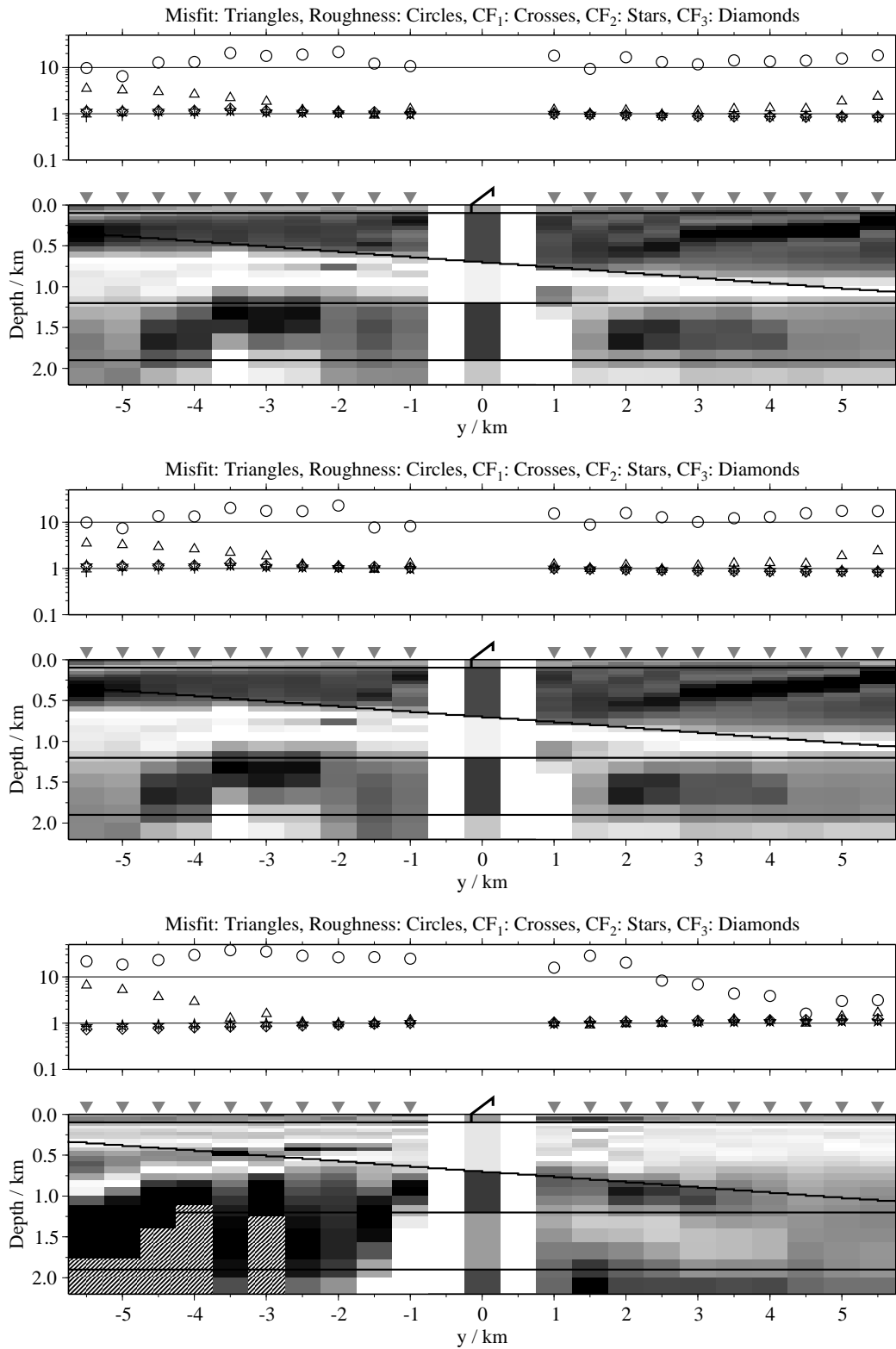


Figure B.37: Pseudo-sections of 1-D joint-inversions using all three components; from top to bottom: Regularisation scheme C1 / model B, regularisation scheme C4 / model B, regularisation scheme C1 / model C;

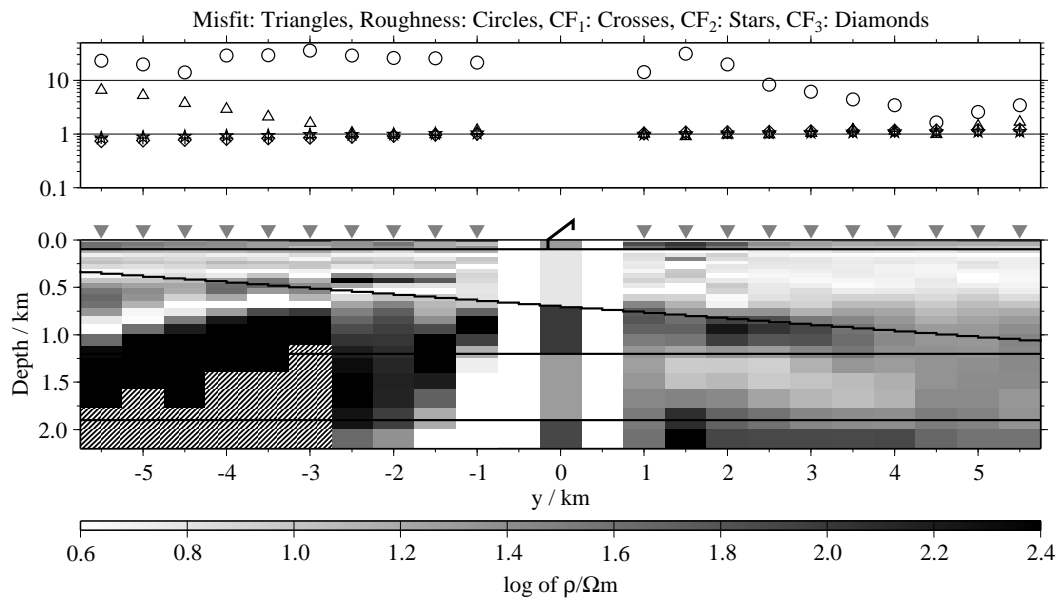


Figure B.38: Pseudo-sections of 1-D joint-inversions using all three components, model C, regularisation scheme C4;

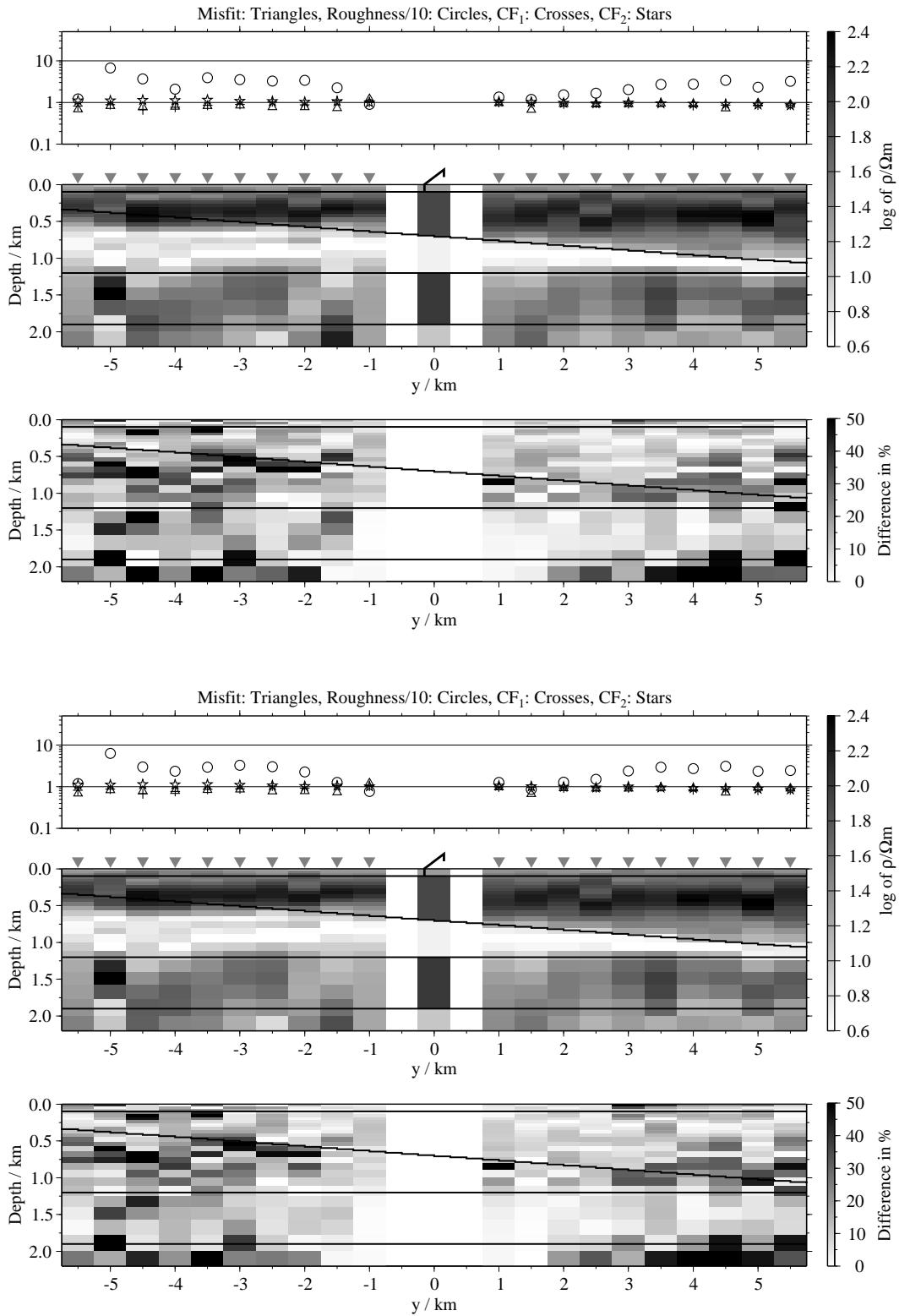


Figure B.39: Pseudo-sections of 1-D soft joint-inversions using the components E_x and H_y , model B; Top panels: Average inversion results and relative differences (regularisation scheme C1); bottom: Average inversion results and relative differences (regularisation scheme C4);

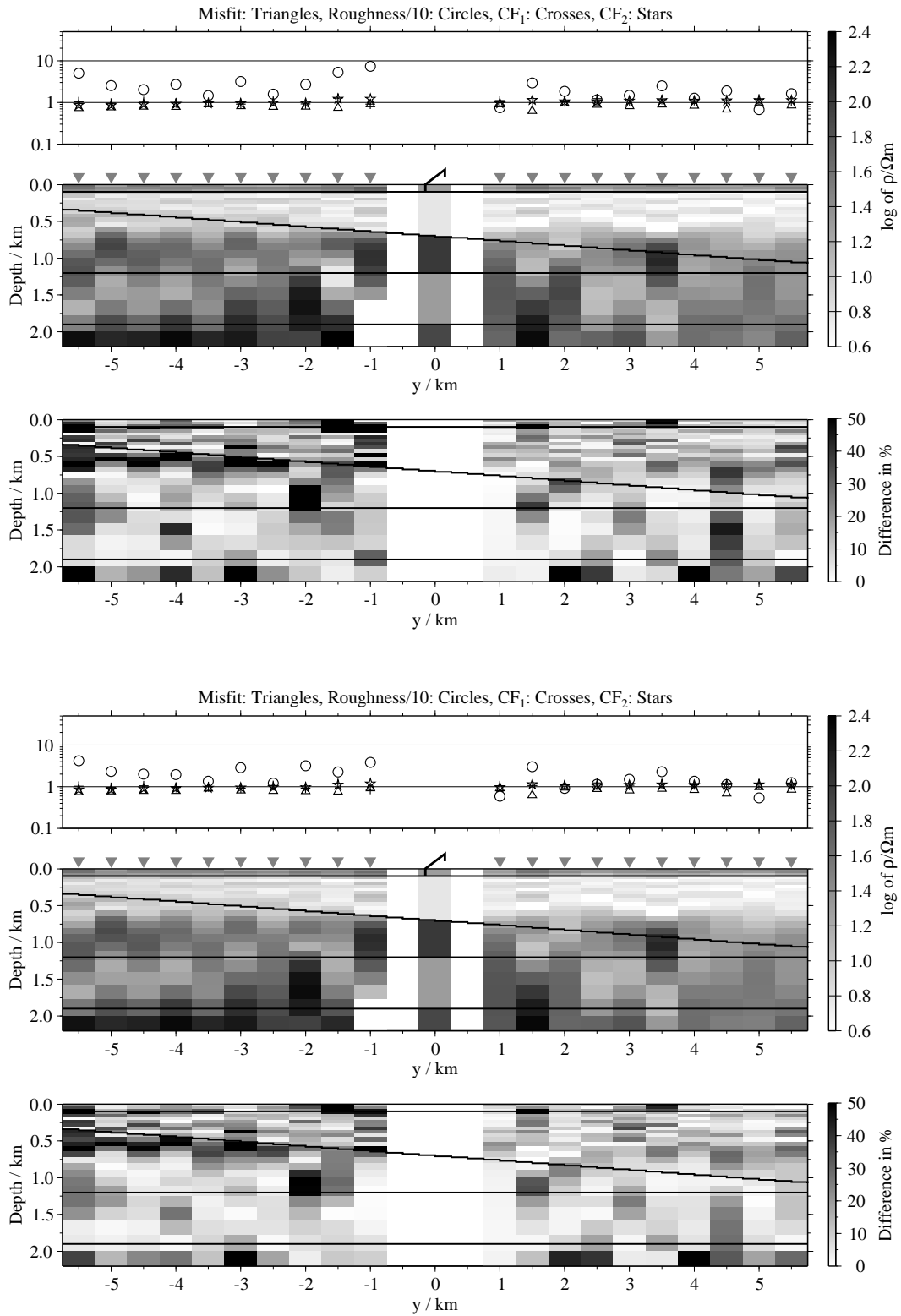


Figure B.40: Pseudo-sections of 1-D soft joint-inversions using the components E_x and \dot{H}_y , model C; Top panels: Average inversion results and relative differences (regularisation scheme C1); bottom: Average inversion results and relative differences (regularisation scheme C4);

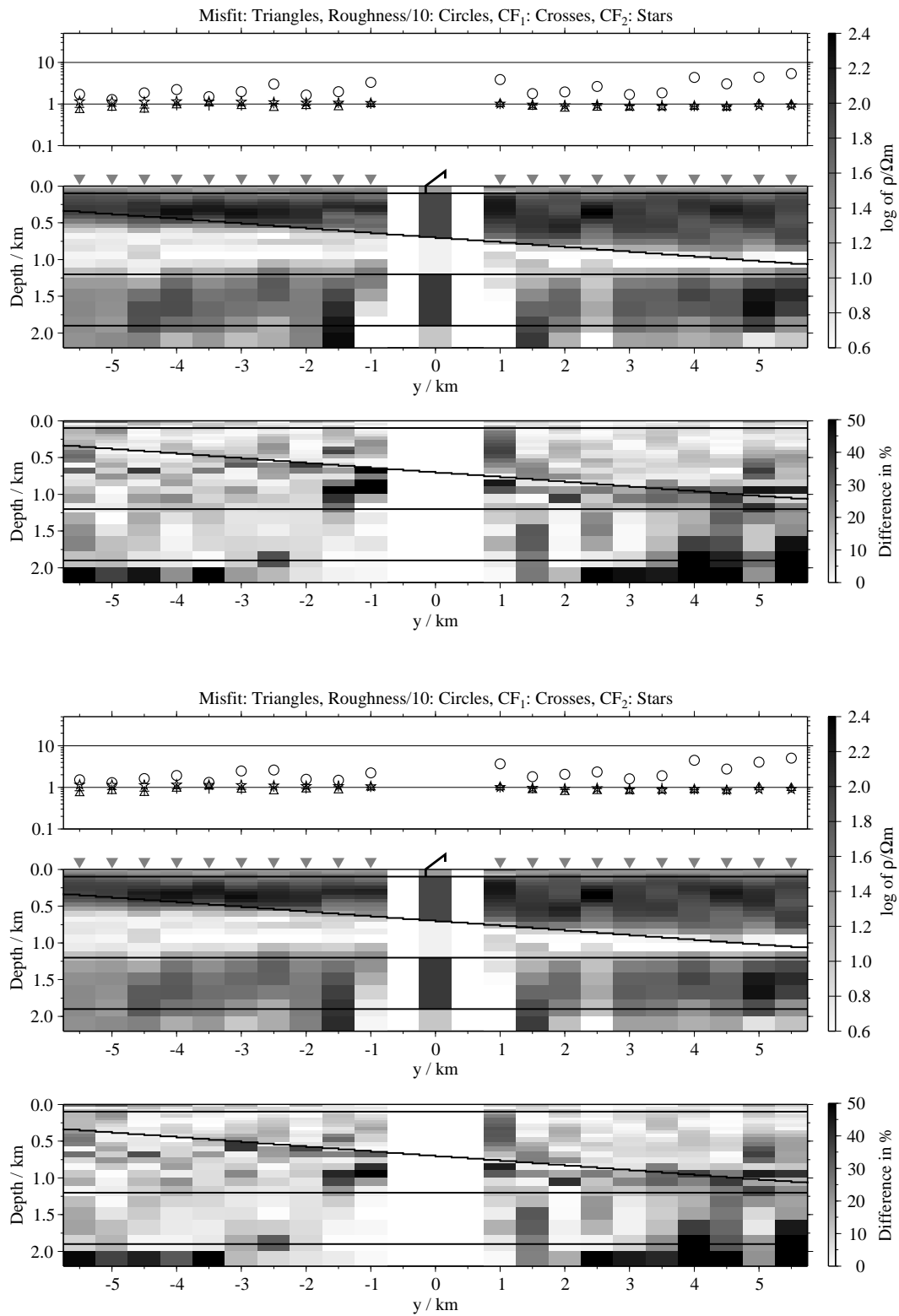


Figure B.41: Pseudo-sections 1-D of soft joint-inversions using the components E_x and \dot{H}_{zi} , model B; Top panels: Average inversion results and relative differences (regularisation scheme C1); bottom: Average inversion results and relative differences (regularisation scheme C4);

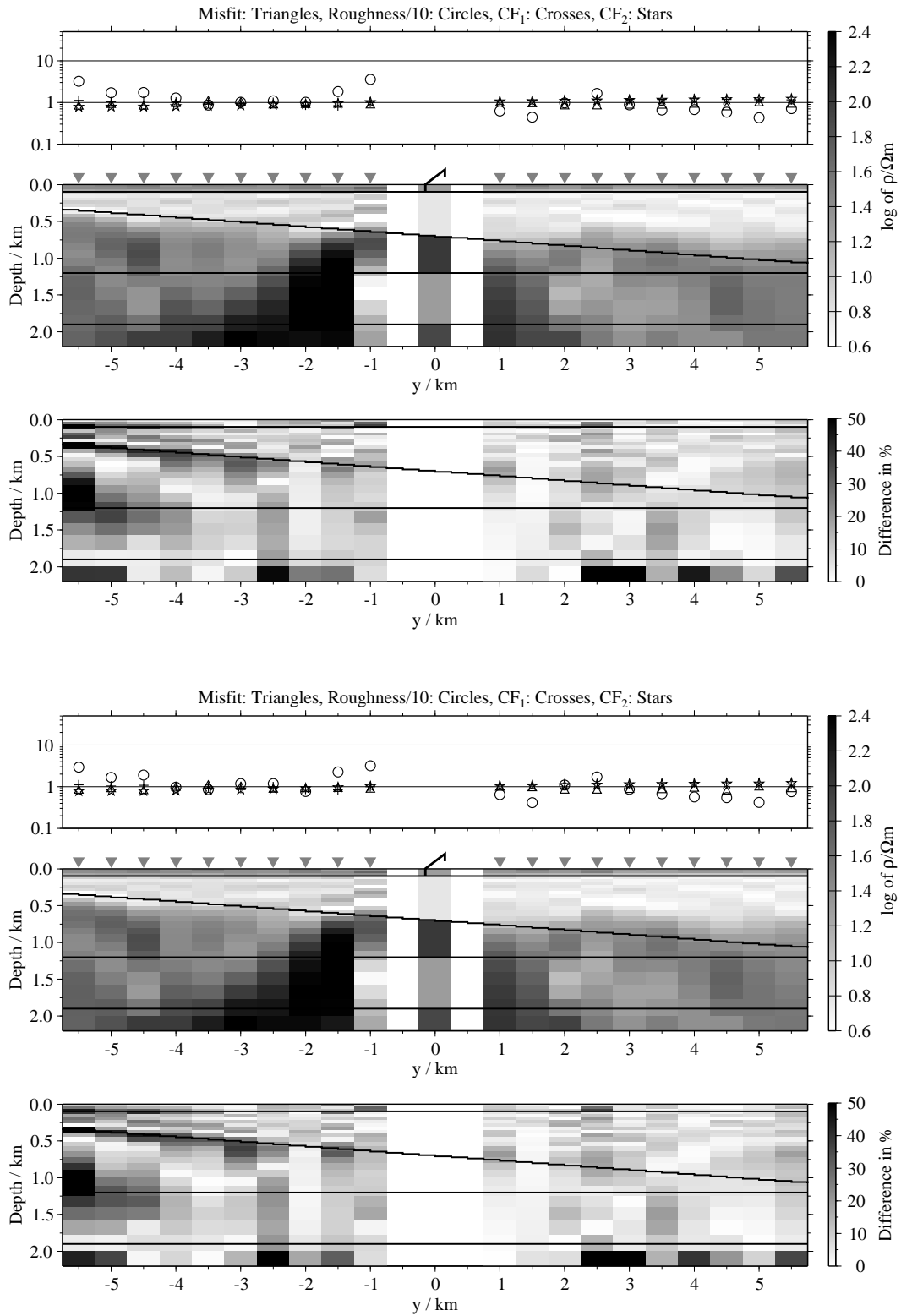


Figure B.42: Pseudo-sections of 1-D soft joint-inversions using the components E_x and H_z , model C; Top panels: Average inversion results and relative differences (regularisation scheme C1); bottom: Average inversion results and relative differences (regularisation scheme C4);

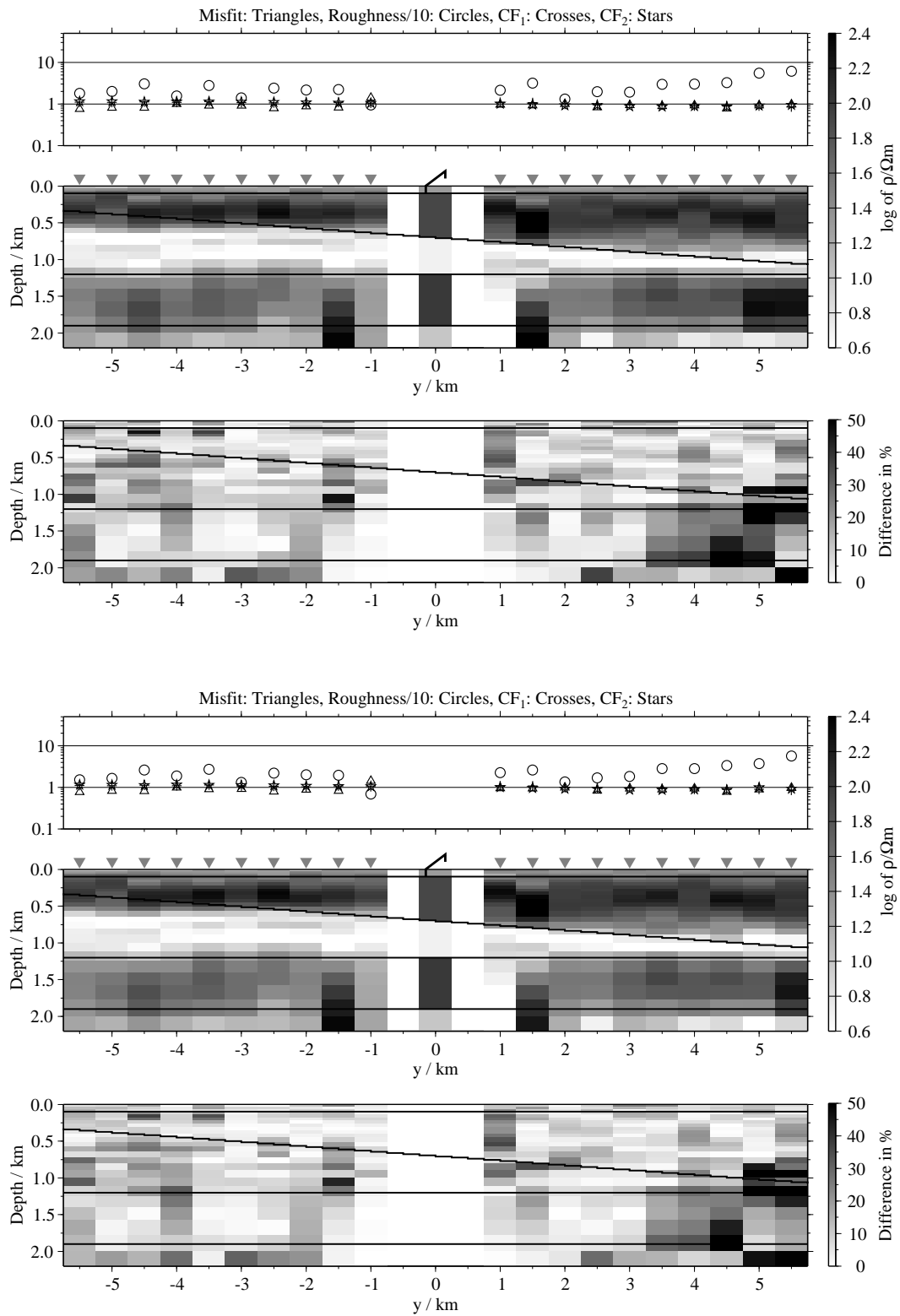


Figure B.43: Pseudo-sections of 1-D soft joint-inversions using the components \hat{H}_y and \hat{H}_{z_i} , model B; Top panels: Average inversion results and relative differences (regularisation scheme C1); bottom: Average inversion results and relative differences (regularisation scheme C4);

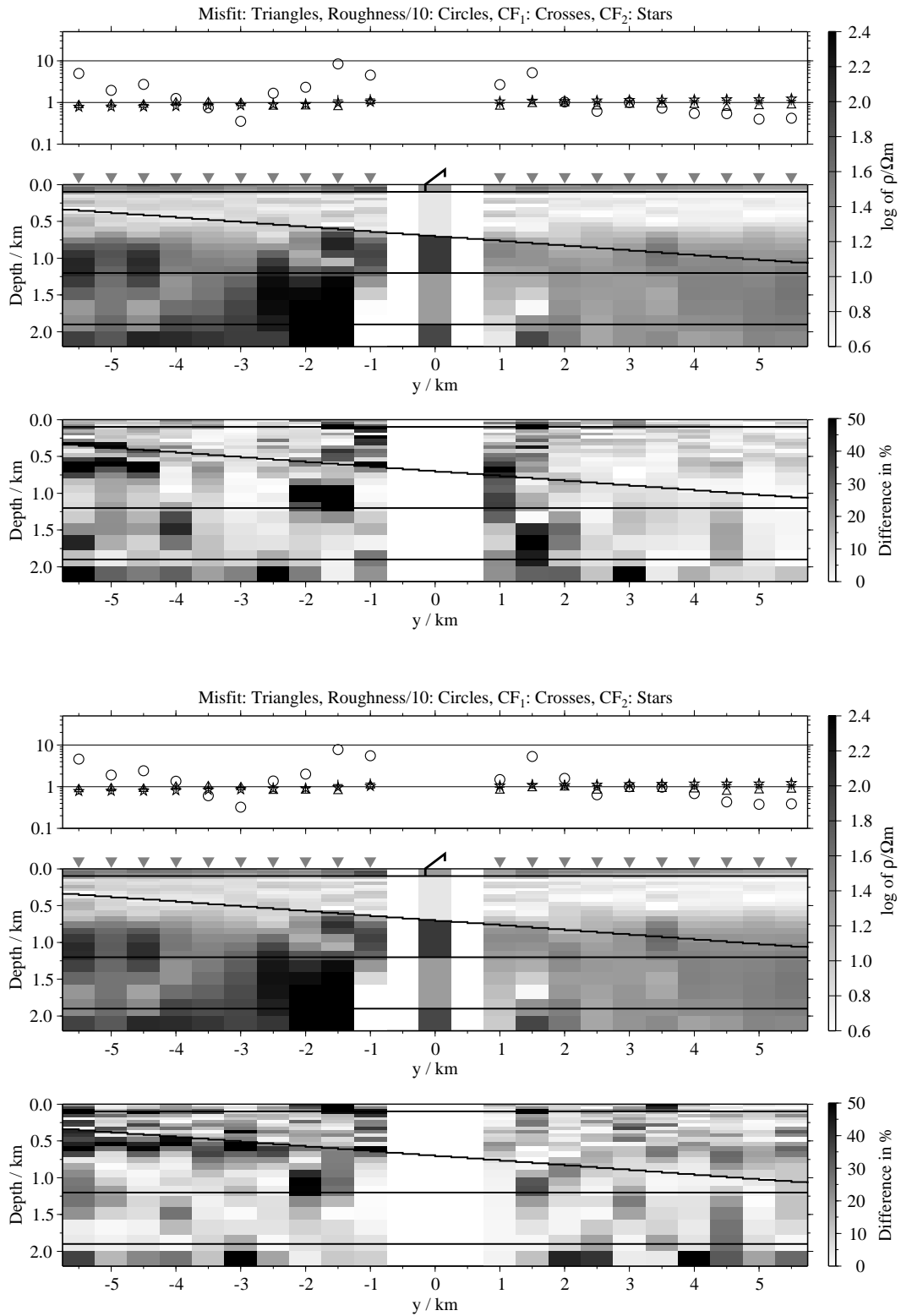


Figure B.44: Pseudo-sections of 1-D soft joint-inversions using the components \dot{H}_y and \dot{H}_z , model C; Top panels: Average inversion results and relative differences (regularisation scheme C1); bottom: Average inversion results and relative differences (regularisation scheme C4);

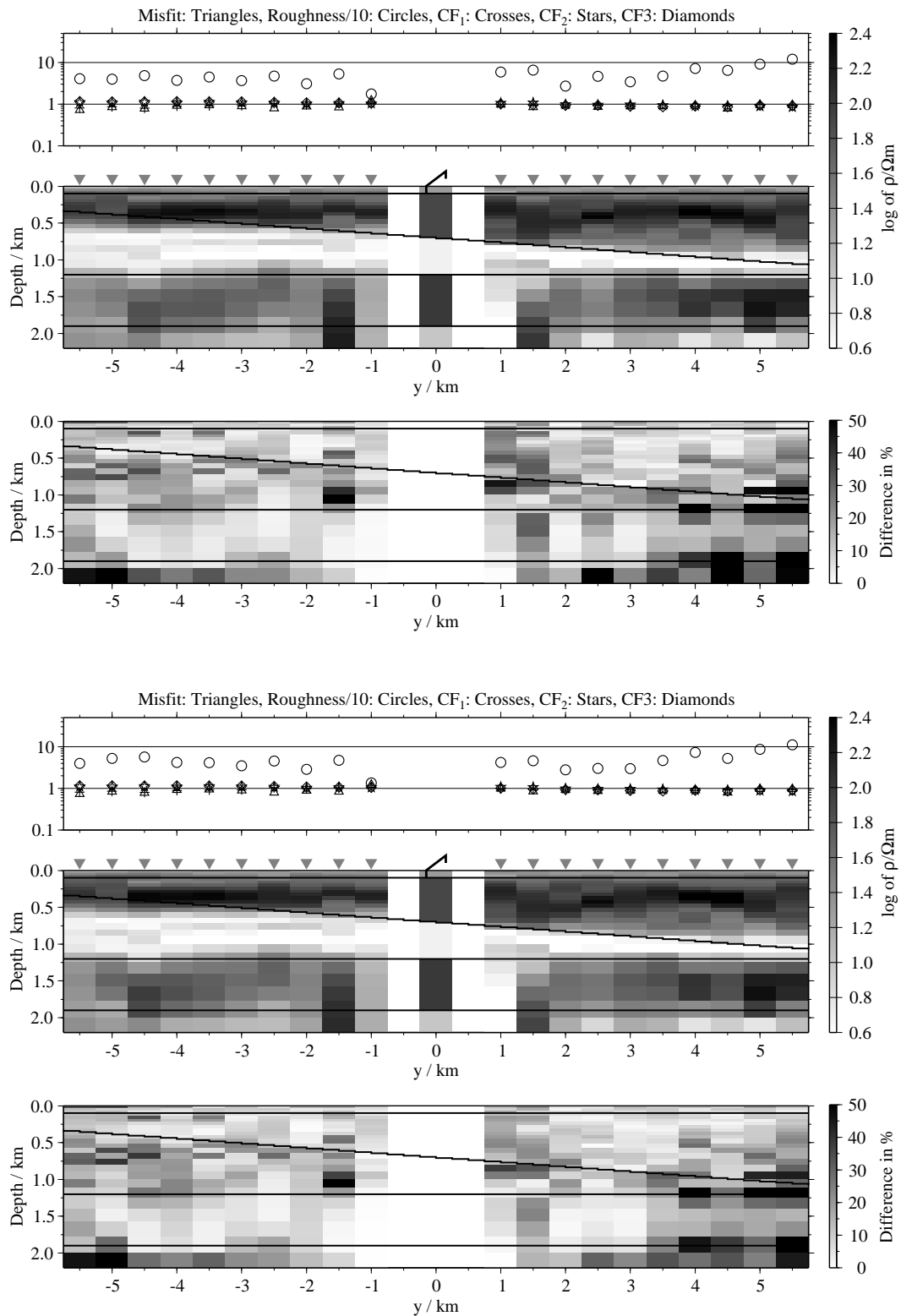


Figure B.45: Pseudo-sections of 1-D soft joint-inversions using all three components, model B; Top panels: Average inversion results and relative differences (regularisation scheme C1); bottom: Average inversion results and relative differences (regularisation scheme C4);

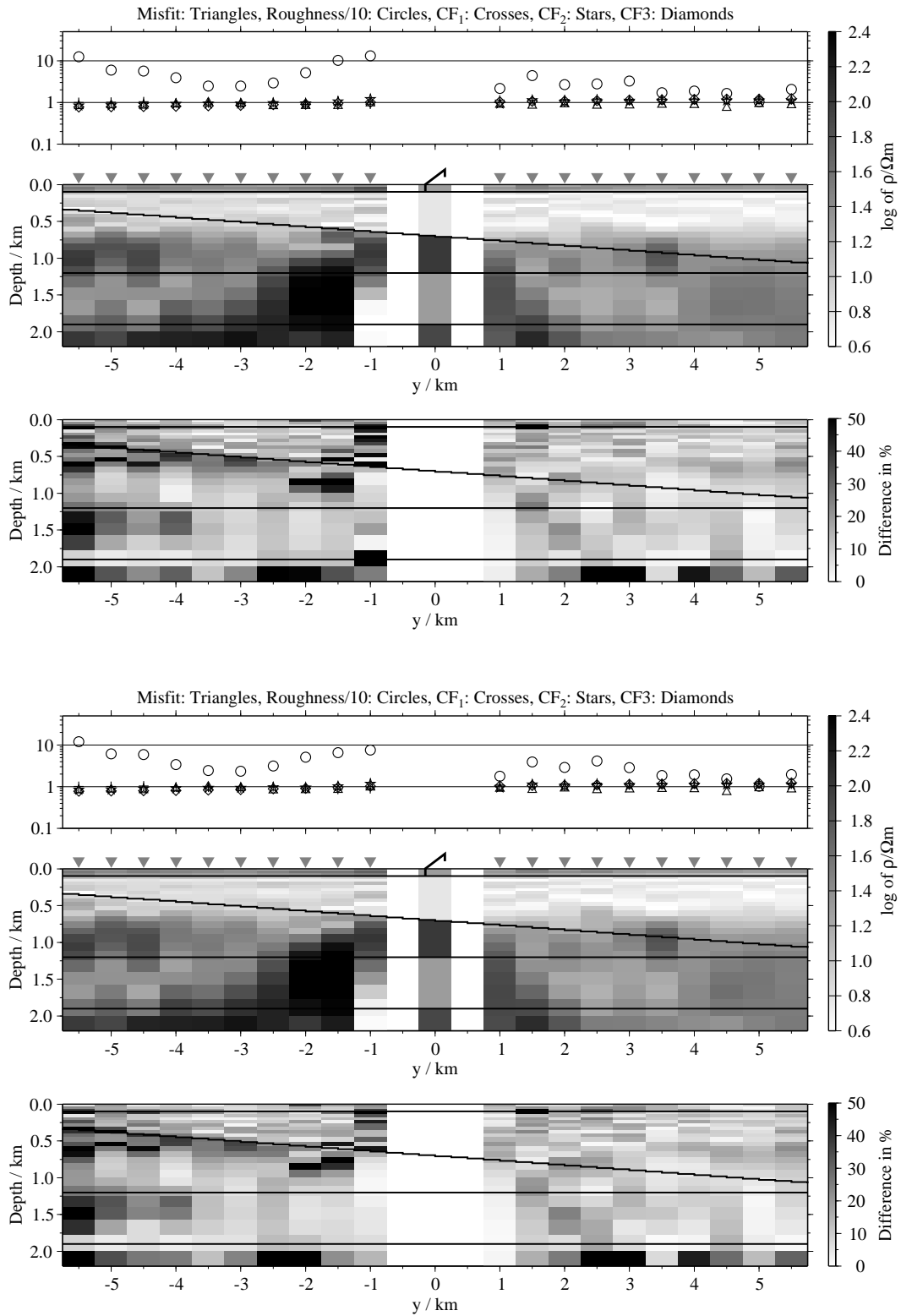
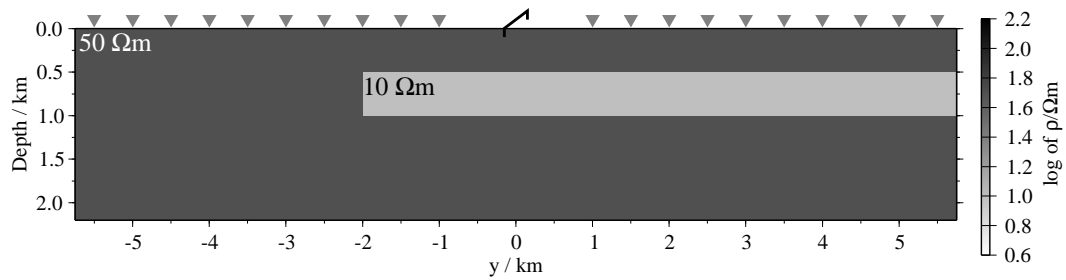


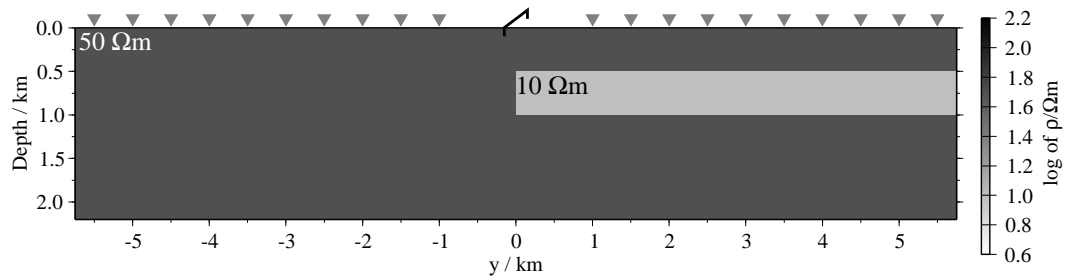
Figure B.46: Pseudo-sections of 1-D soft joint-inversions using all three components, model C; Top panels: Average inversion results and relative differences (regularisation scheme C1); bottom: Average inversion results and relative differences (regularisation scheme C4);

B.2.2 End of a conductive layer (models D1 to D3)

Model D1:



Model D2:



Model D3:

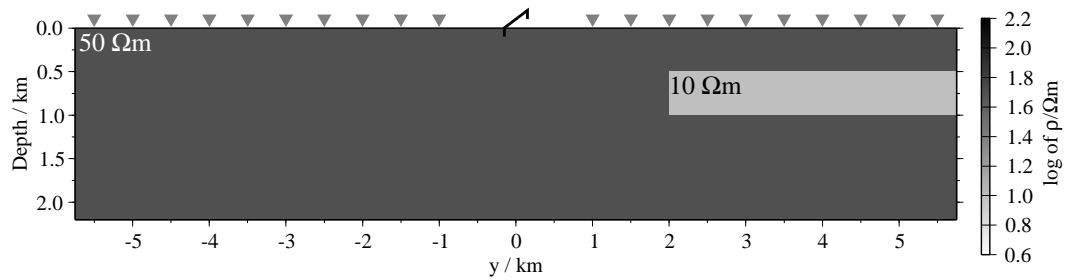


Figure B.47: Model, where a conductive layer ends at $y = -2$ km (model D1), $y = 0$ km (model D2) and $y = 2$ km (model D3);

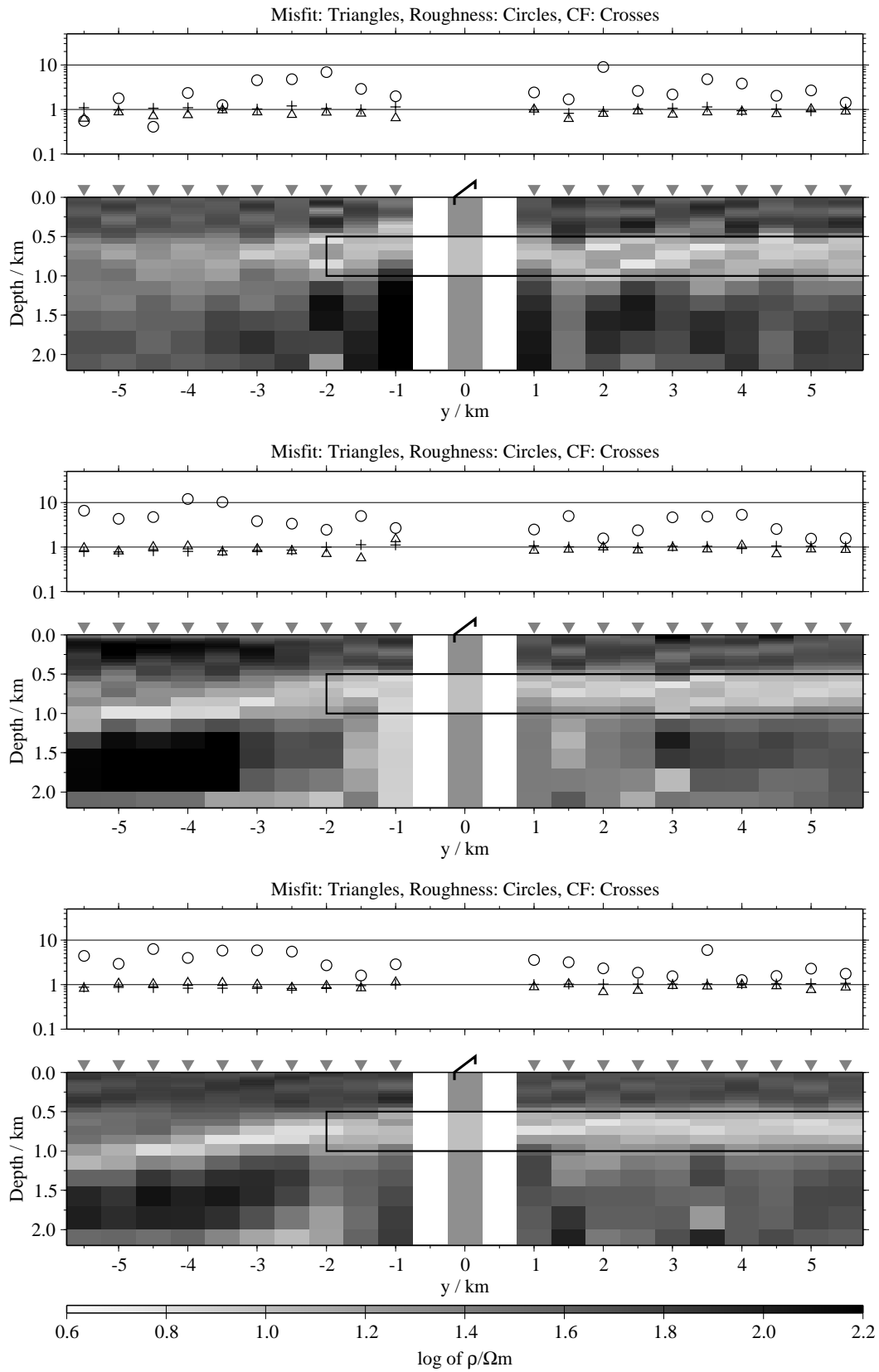


Figure B.48: Pseudo-sections of single 1-D inversion, model D1, regularisation scheme C1; from top to bottom E_x -, H_y - and H_z -component;

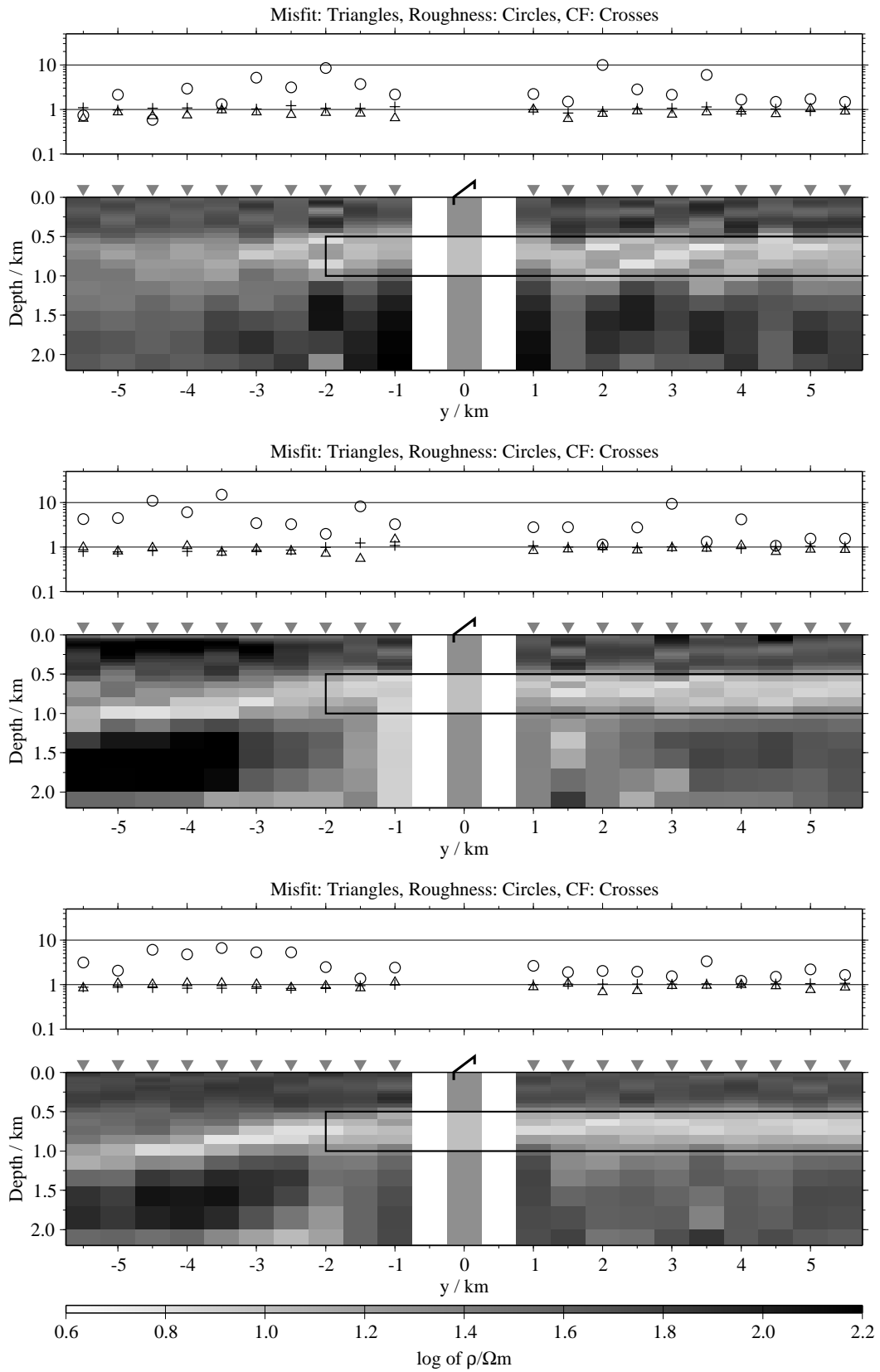


Figure B.49: Pseudo-sections of single 1-D inversion, model D1, regularisation scheme C4; from top to bottom E_x -, \dot{H}_y - and \dot{H}_z -component;

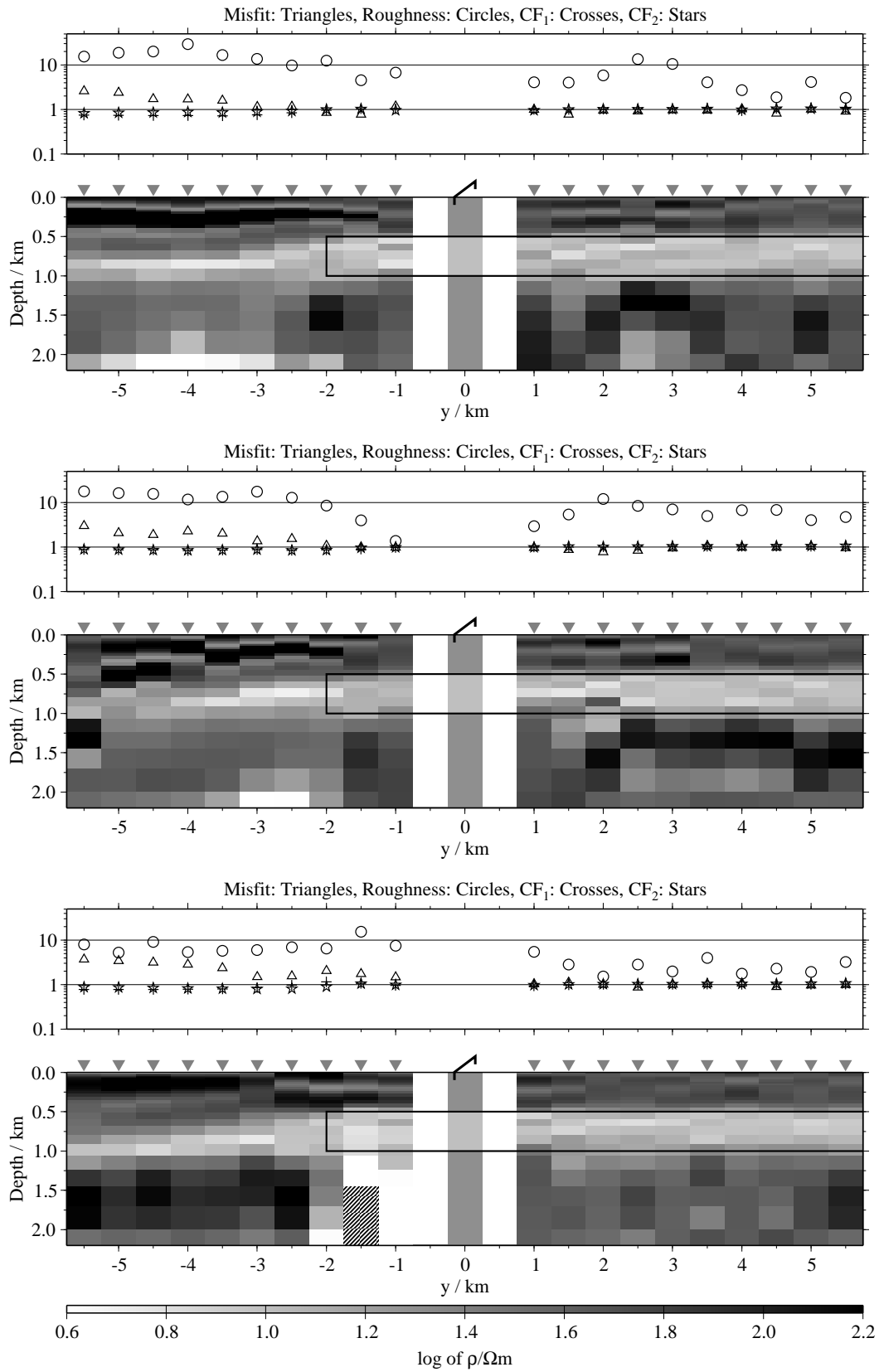


Figure B.50: Pseudo-sections of two component 1-D joint-inversions, model D1, regularisation scheme C1; from top to bottom $E_x-\dot{H}_y$, $E_x-\dot{H}_z$ and $\dot{H}_y-\dot{H}_z$;

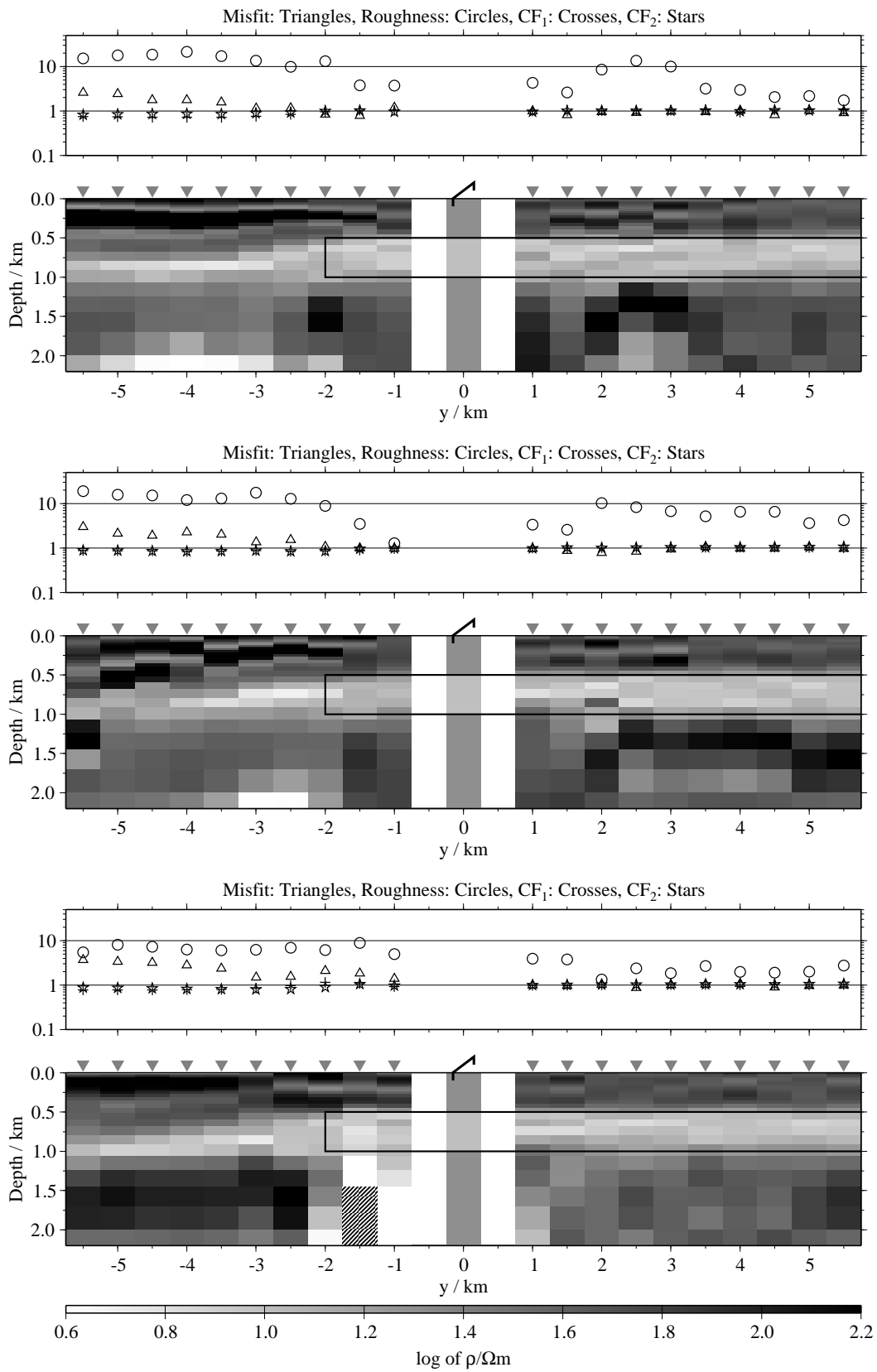


Figure B.51: Pseudo-sections of two component 1-D joint-inversions, model D1, regularisation scheme C4; from top to bottom $E_x-\dot{H}_y$, $E_x-\dot{H}_z$ and $\dot{H}_y-\dot{H}_z$;

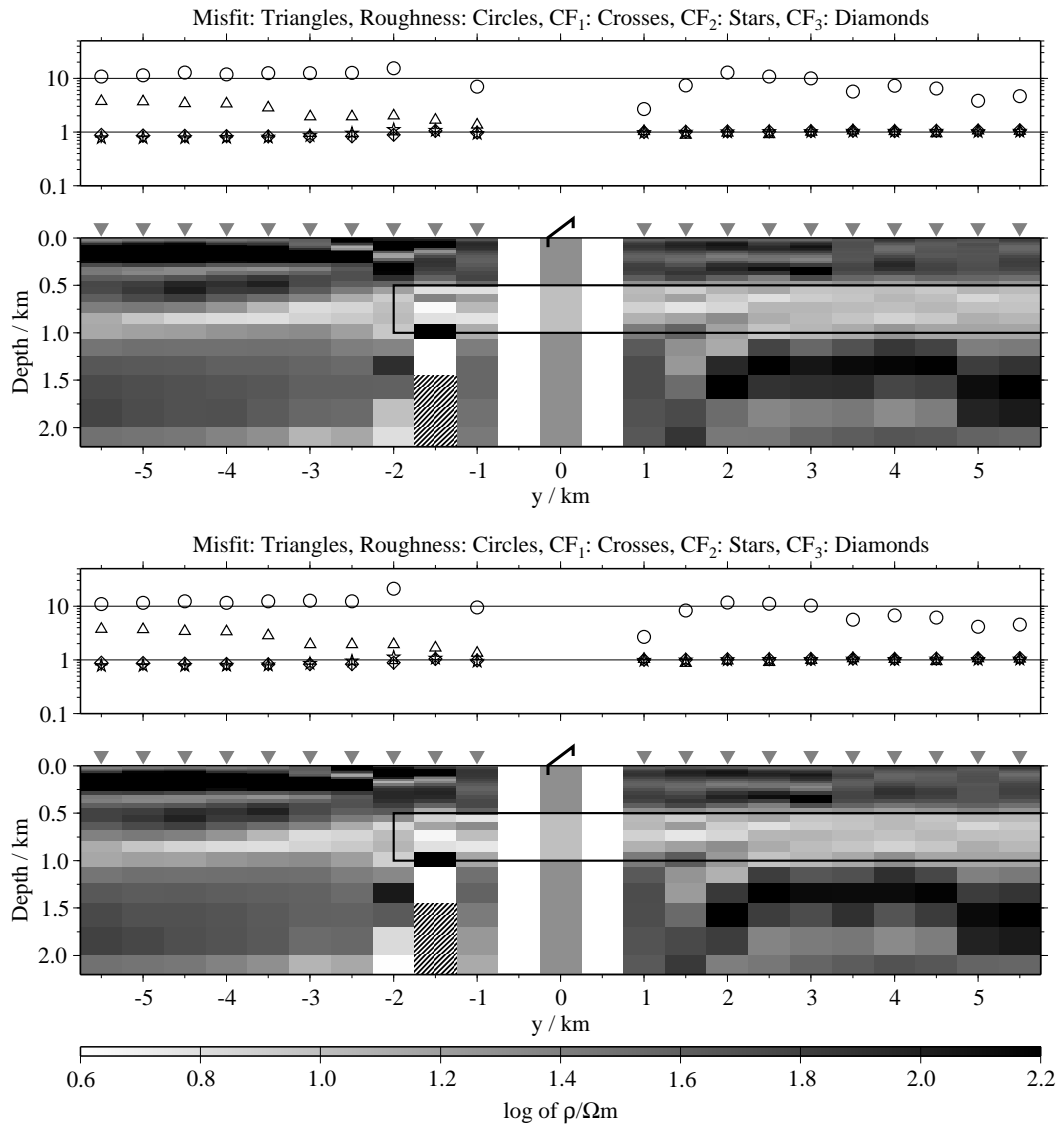


Figure B.52: Pseudo-sections of 1-D joint-inversions using all three components, model D1; top: Regularisation scheme C1; bottom: Regularisation scheme C4;

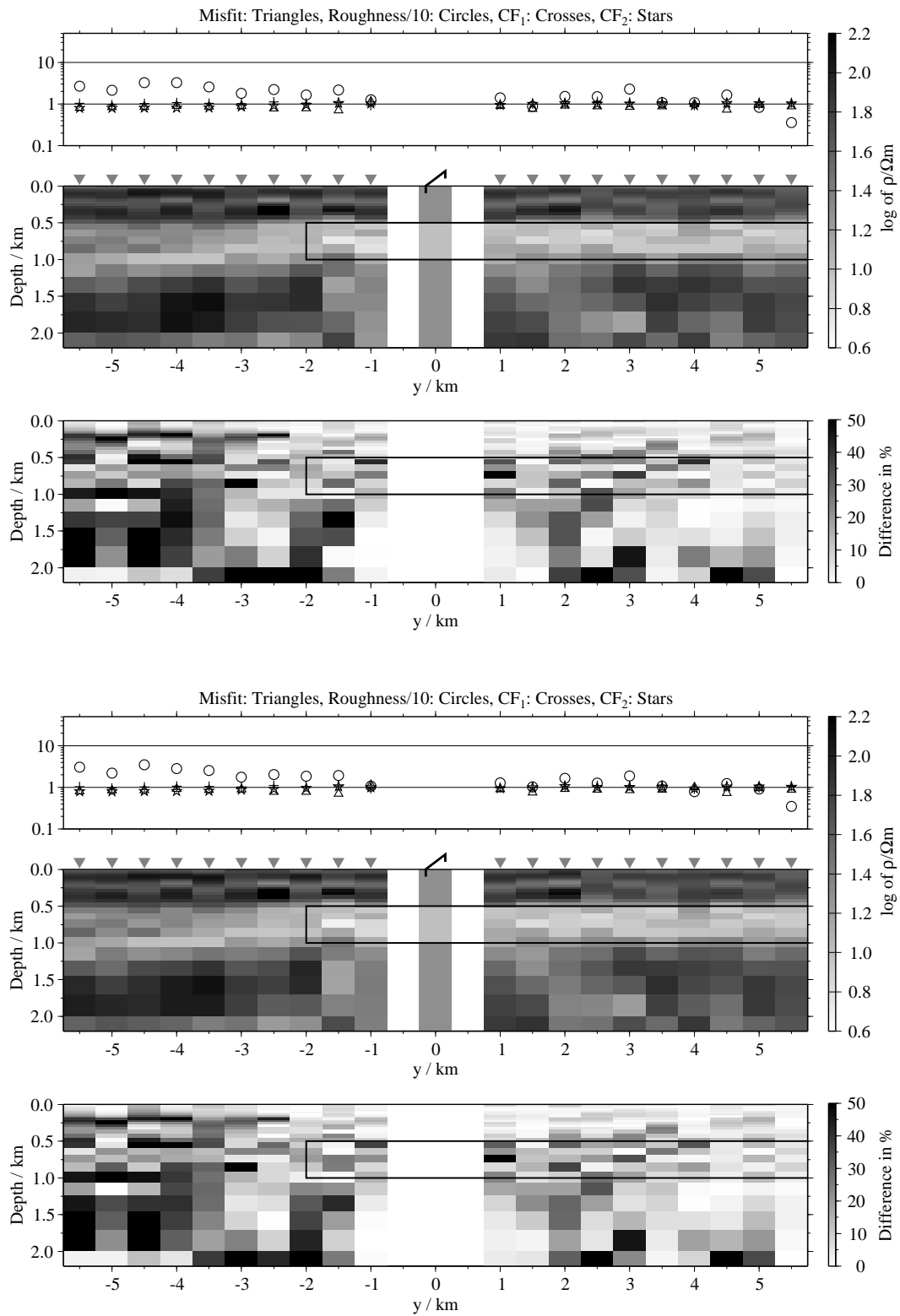


Figure B.53: Pseudo-sections of 1-D soft joint-inversions using the components E_x and H_y , model D1; Top panels: Average inversion results and relative differences (regularisation scheme C1); bottom: Average inversion results and relative differences (regularisation scheme C4);

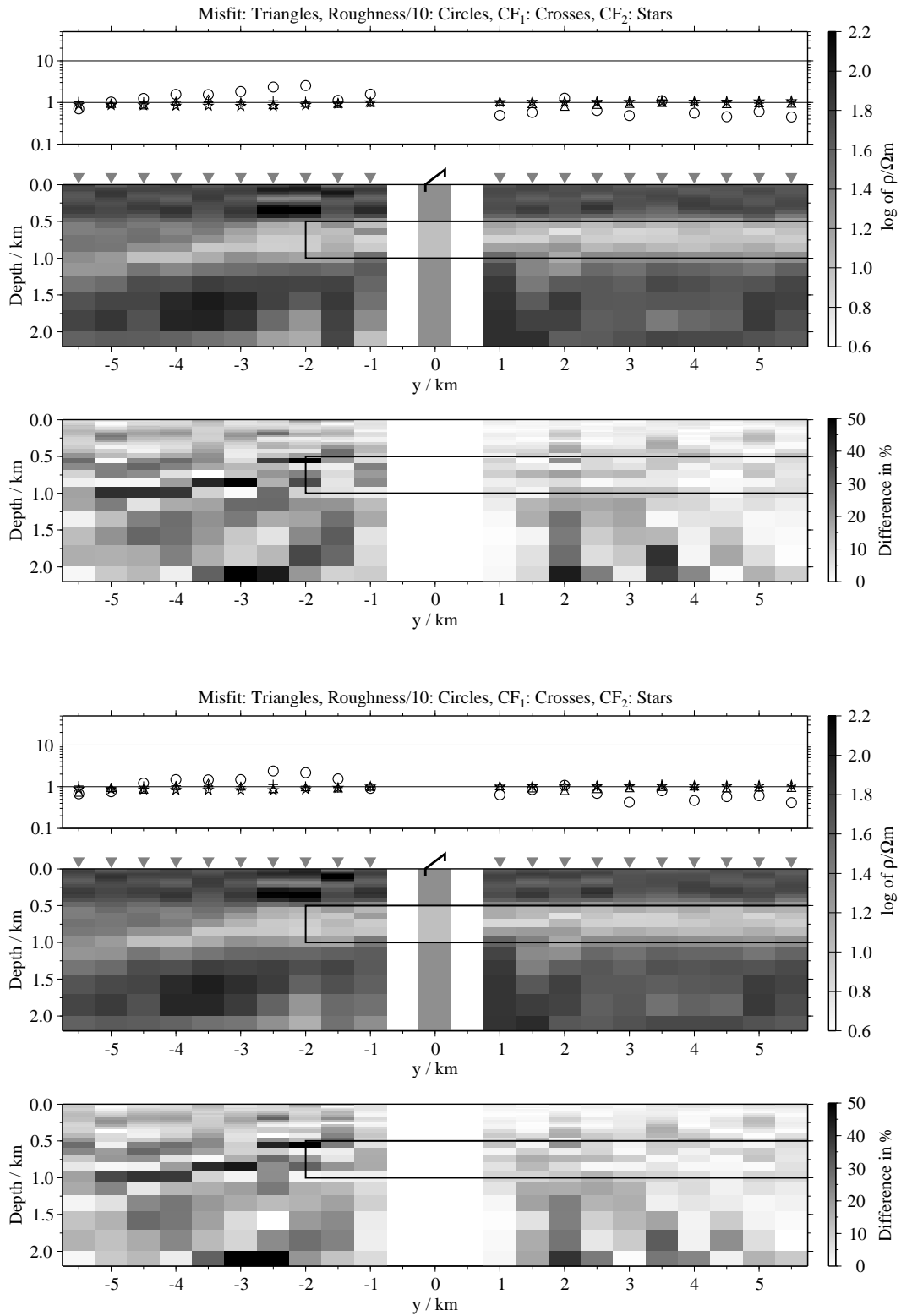


Figure B.54: Pseudo-sections 1-D of soft joint-inversions using the components E_x and H_z , model D1; Top panels: Average inversion results and relative differences (regularisation scheme C1); bottom: Average inversion results and relative differences (regularisation scheme C4);

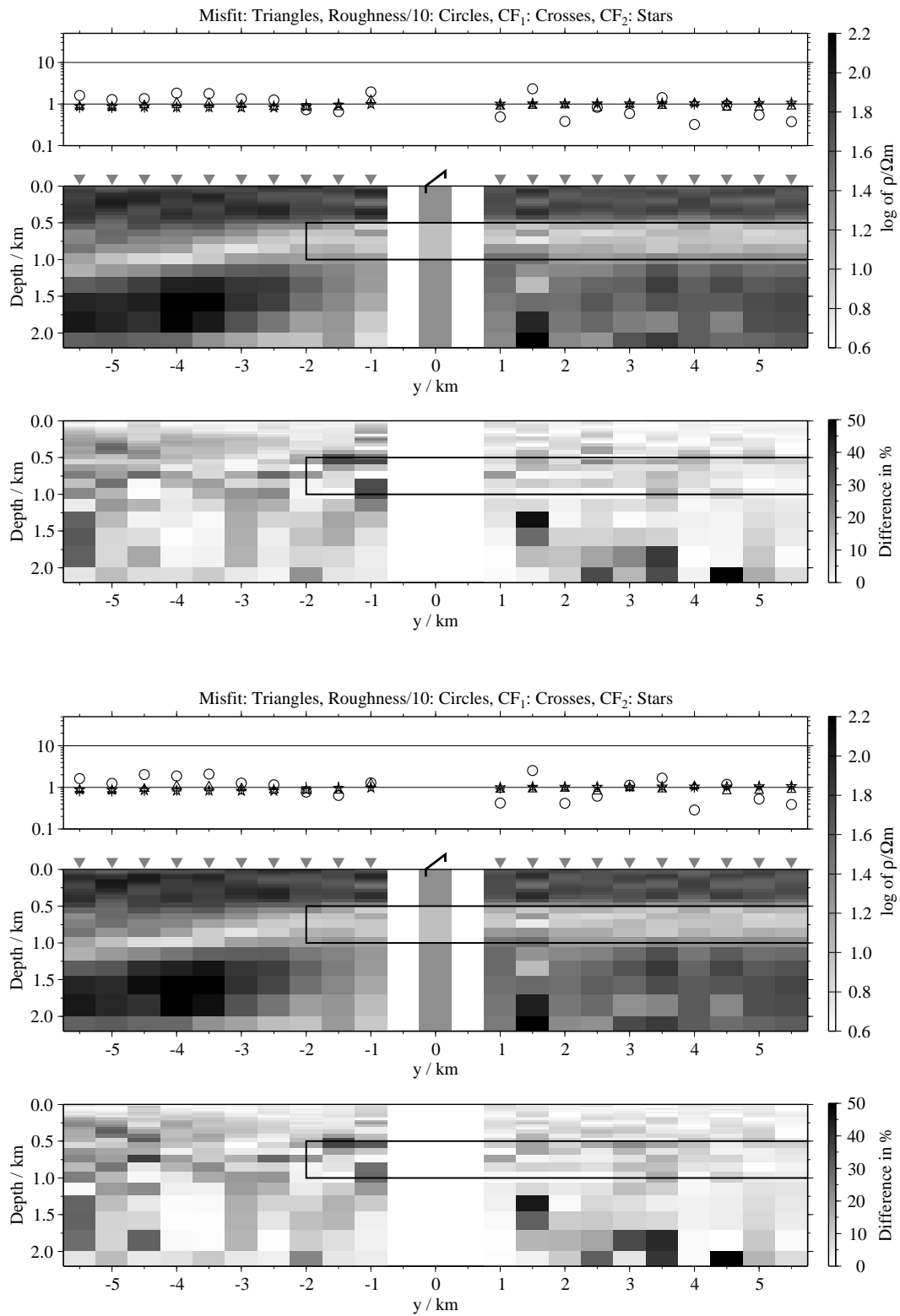


Figure B.55: Pseudo-sections of 1-D soft joint-inversions using the components \hat{H}_y and \hat{H}_{zi} , model D1; Top panels: Average inversion results and relative differences (regularisation scheme C1); bottom: Average inversion results and relative differences (regularisation scheme C4);

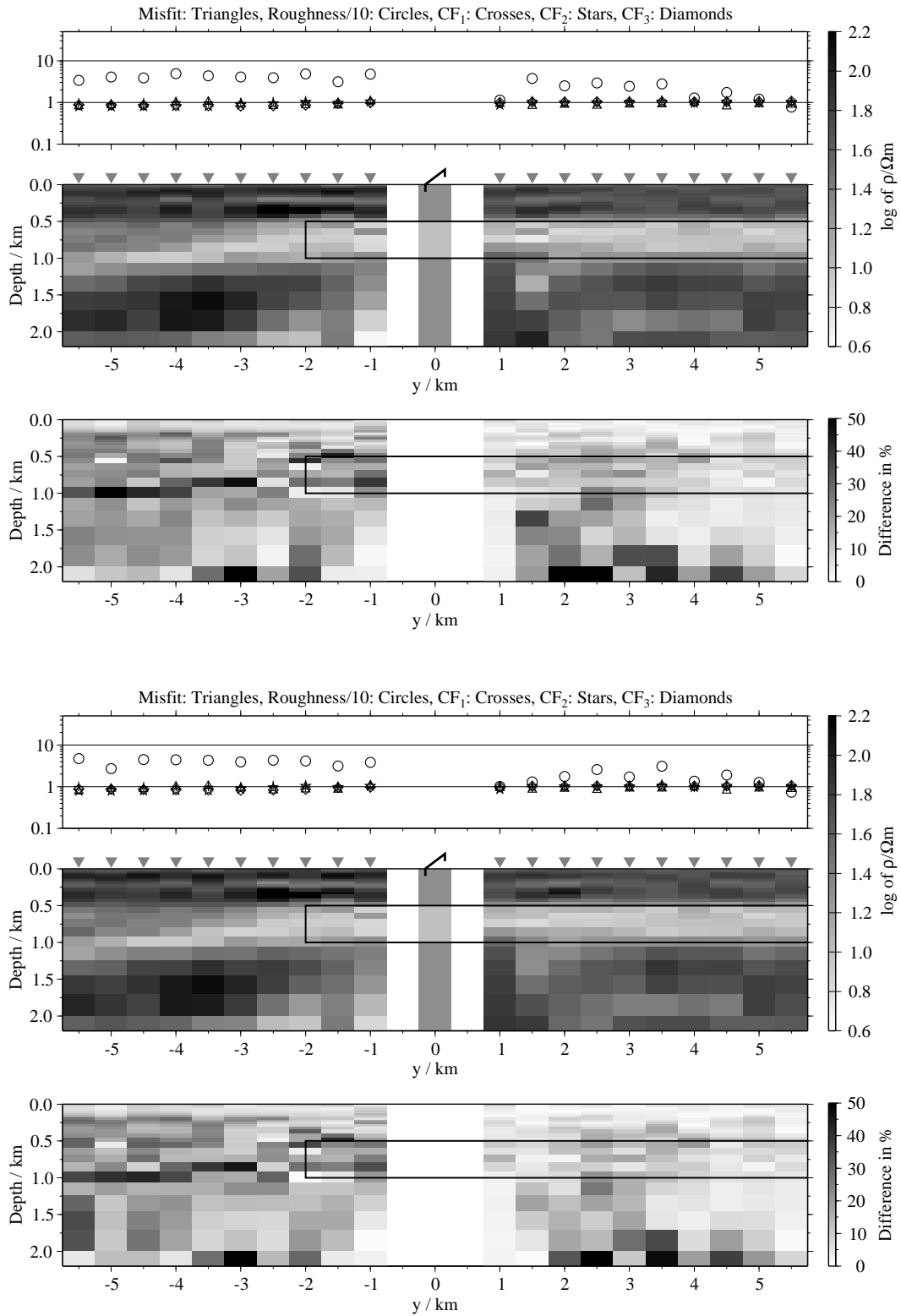


Figure B.56: Pseudo-sections of 1-D soft joint-inversions using all three components, model D1; Top panels: Average inversion results and relative differences (regularisation scheme C1); bottom: Average inversion results and relative differences (regularisation scheme C4);

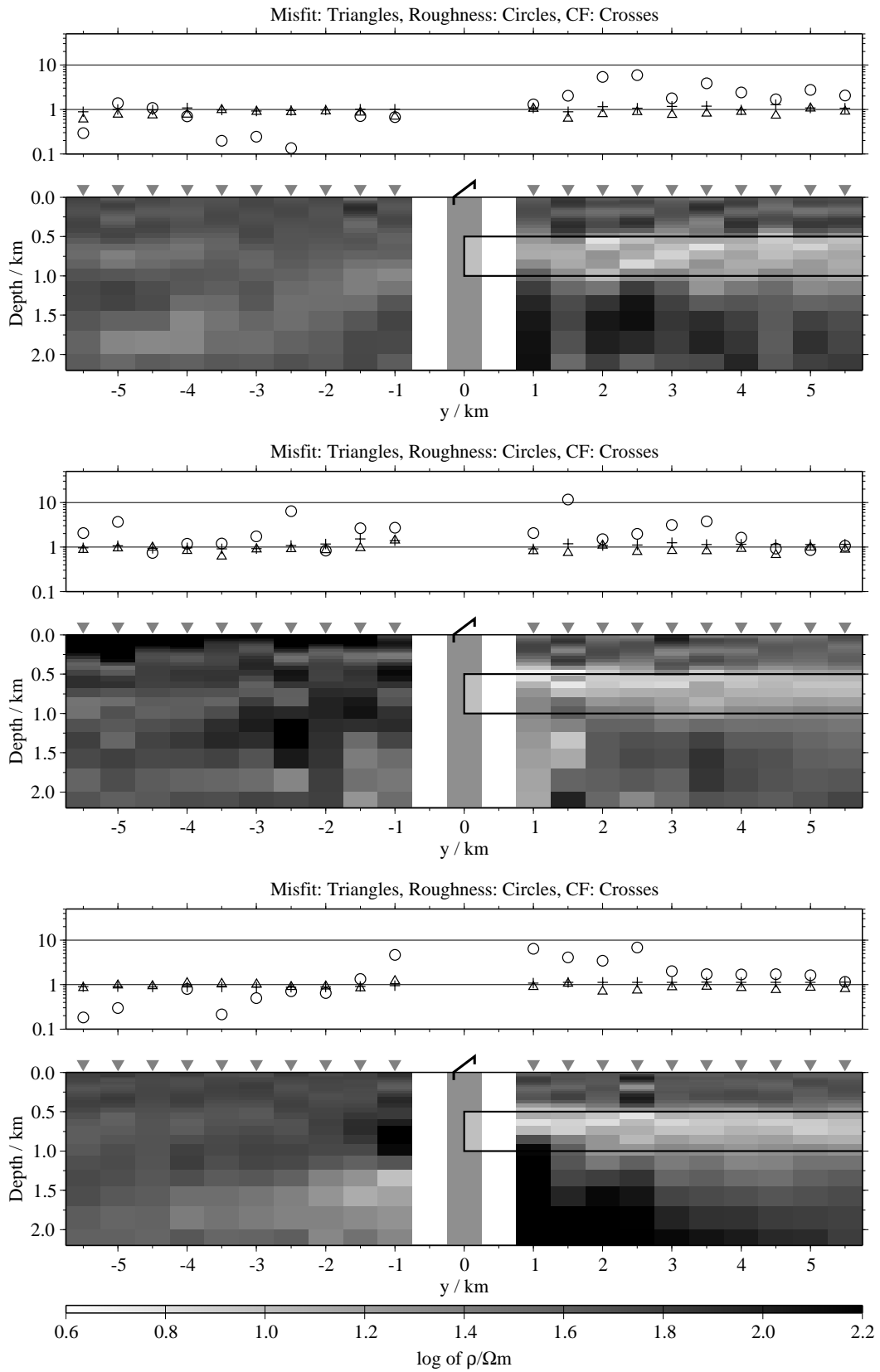


Figure B.57: Pseudo-sections of single 1-D inversion, model D2, regularisation scheme C1; from top to bottom E_x -, \dot{H}_y - and \dot{H}_z -component;

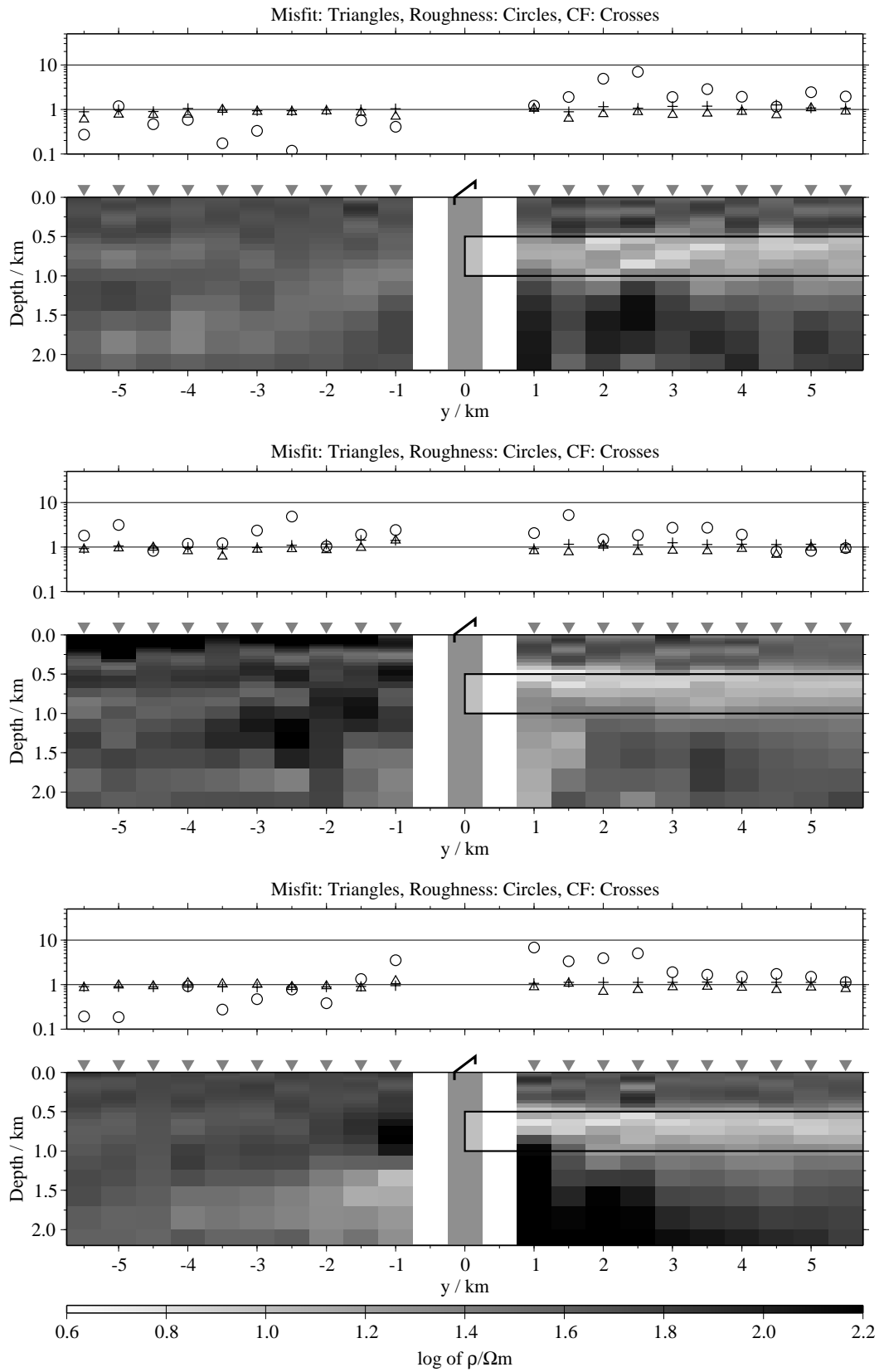


Figure B.58: Pseudo-sections of single 1-D inversion, model D2, regularisation scheme C4; from top to bottom E_x -, H_y - and H_z -component;

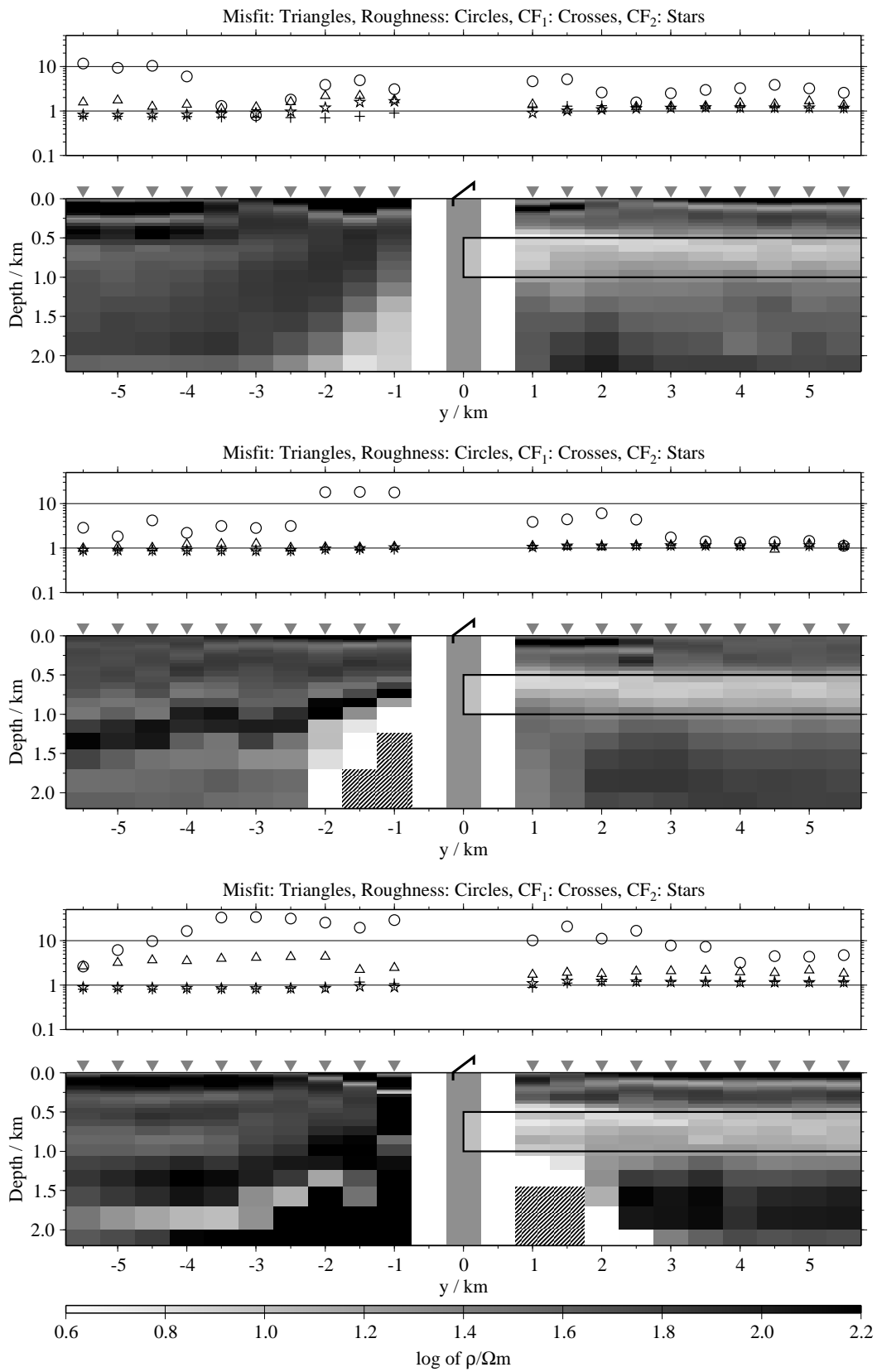


Figure B.59: Pseudo-sections of two component 1-D joint-inversions, model D2, regularisation scheme C1; from top to bottom $E_x-\dot{H}_y$, $E_x-\dot{H}_z$ and $\dot{H}_y-\dot{H}_z$;

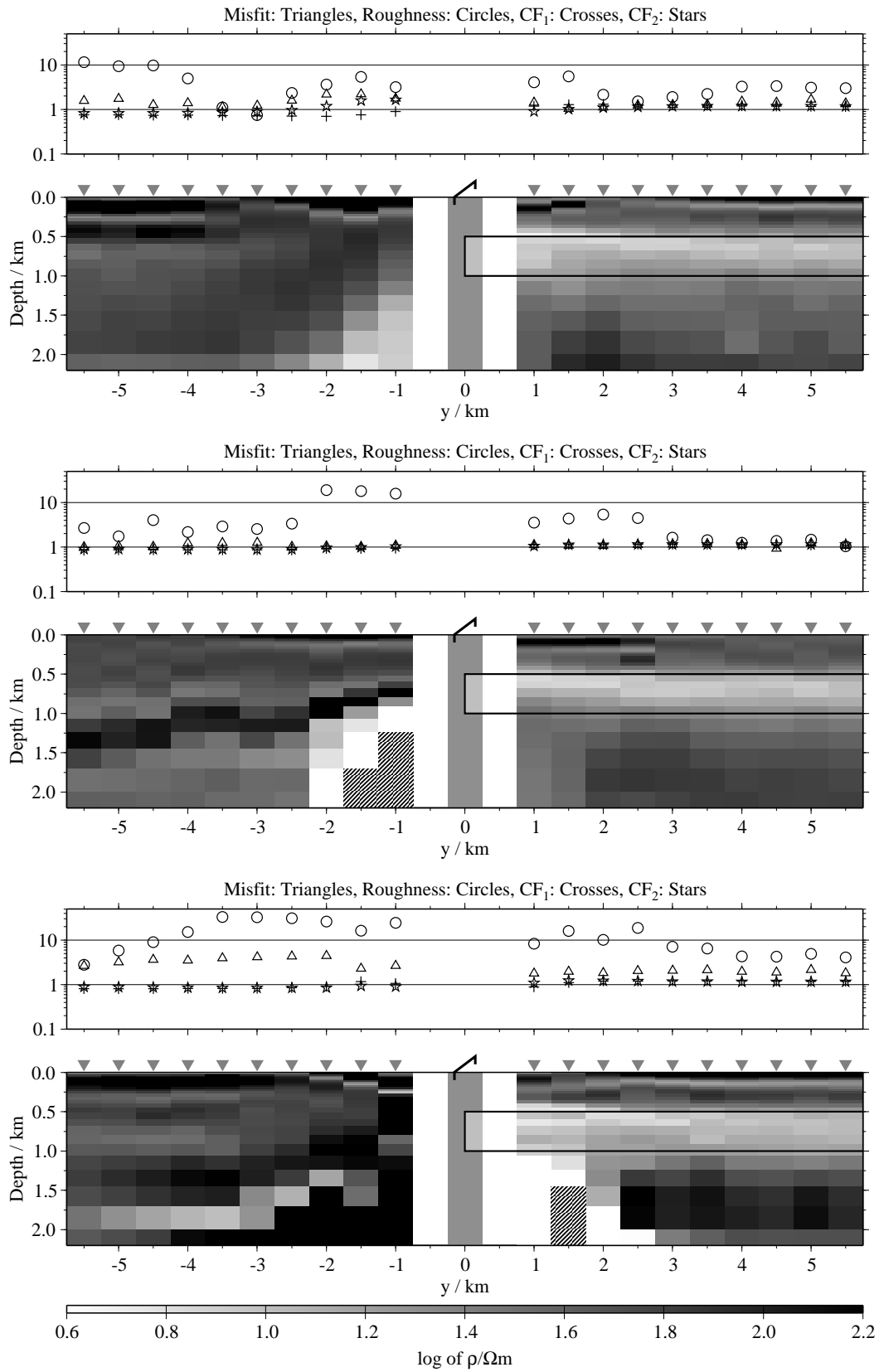


Figure B.60: Pseudo-sections of two component 1-D joint-inversions, model D2, regularisation scheme C4; from top to bottom E_x-H_y , E_x-H_z and H_y-H_z ;

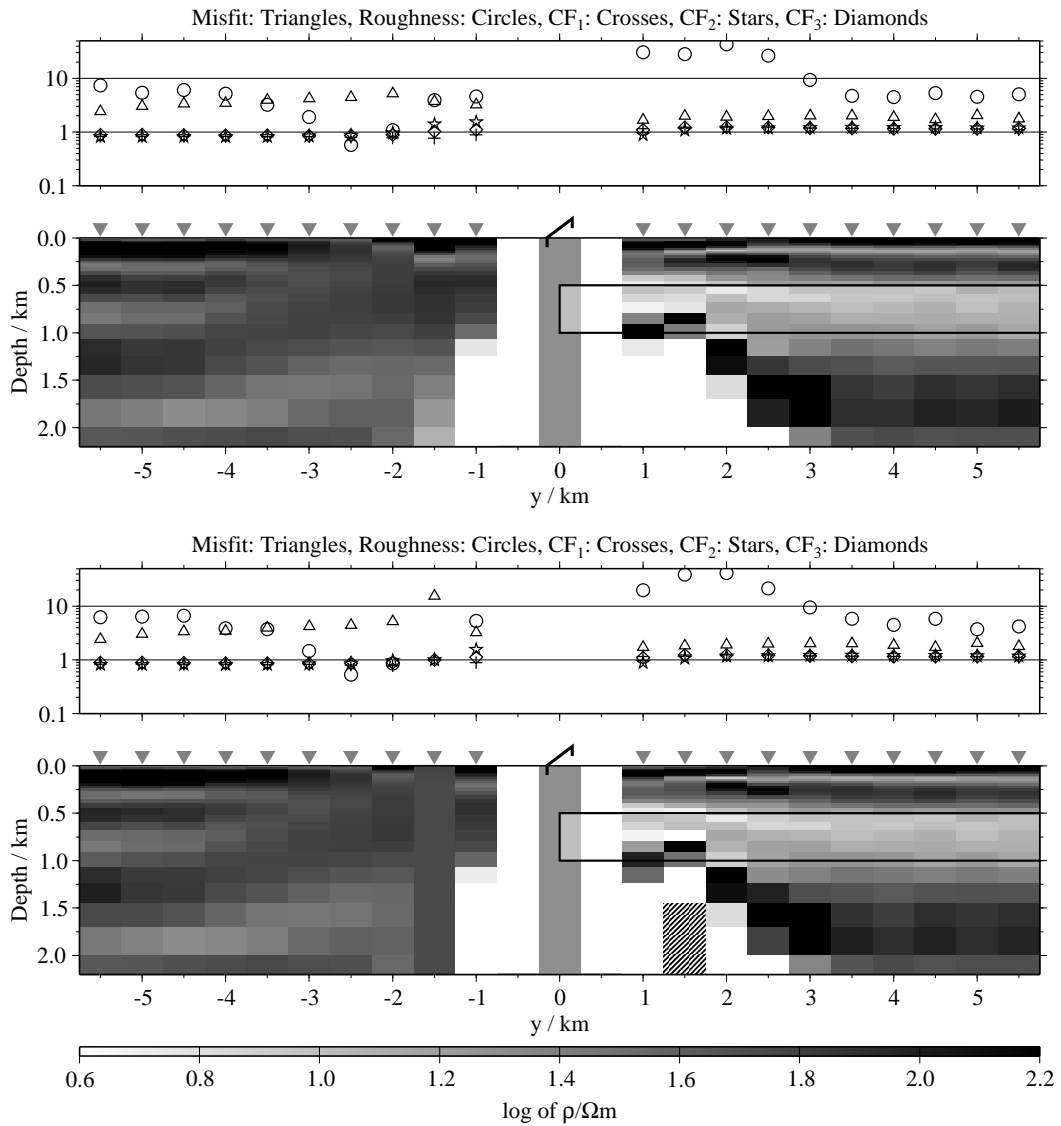


Figure B.61: Pseudo-sections of 1-D joint-inversions using all three components, model D2; top: Regularisation scheme C1; bottom: Regularisation scheme C4;

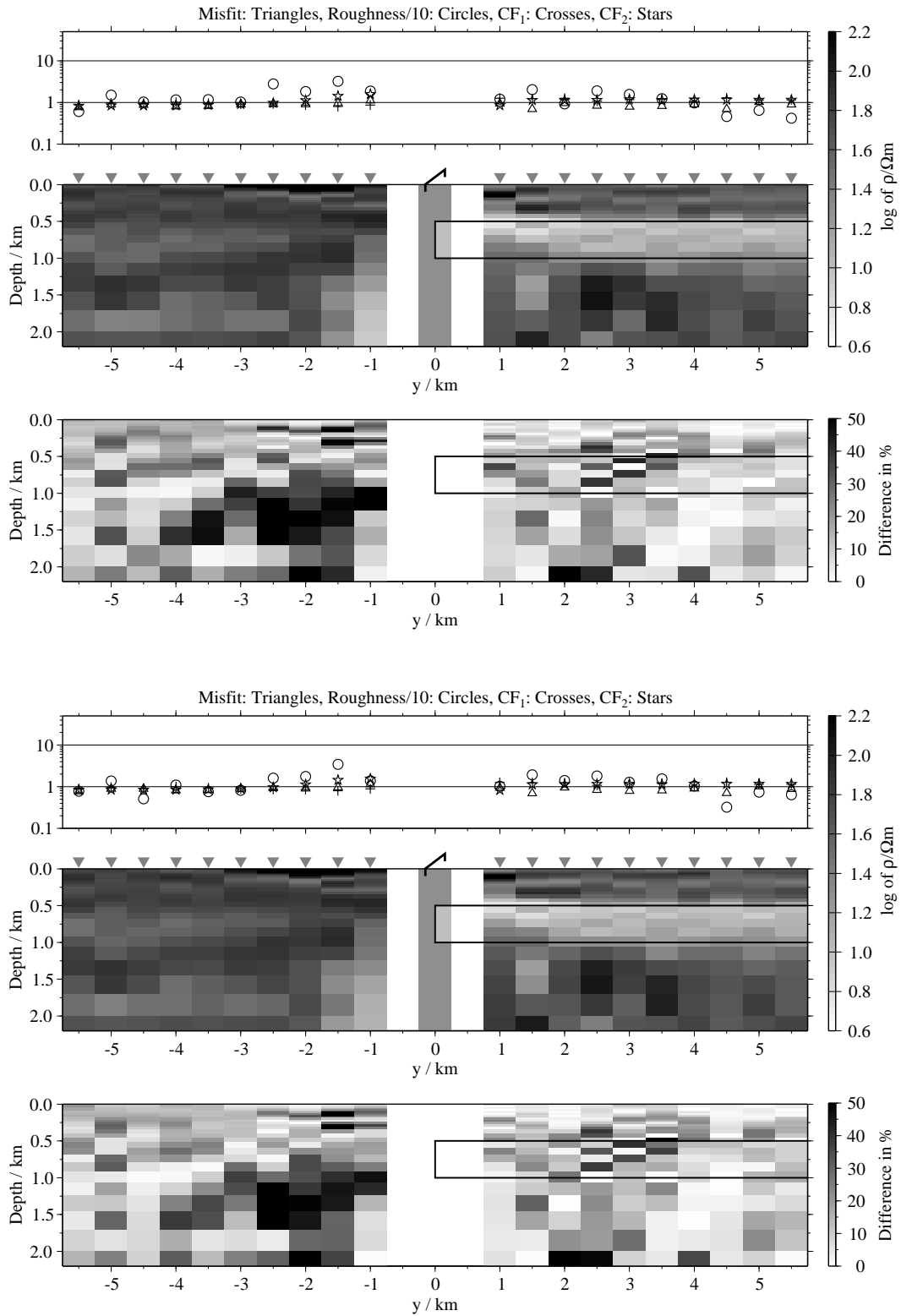


Figure B.62: Pseudo-sections of 1-D soft joint-inversions using the components E_x and H_y , model D2; Top panels: Average inversion results and relative differences (regularisation scheme C1); bottom: Average inversion results and relative differences (regularisation scheme C4);

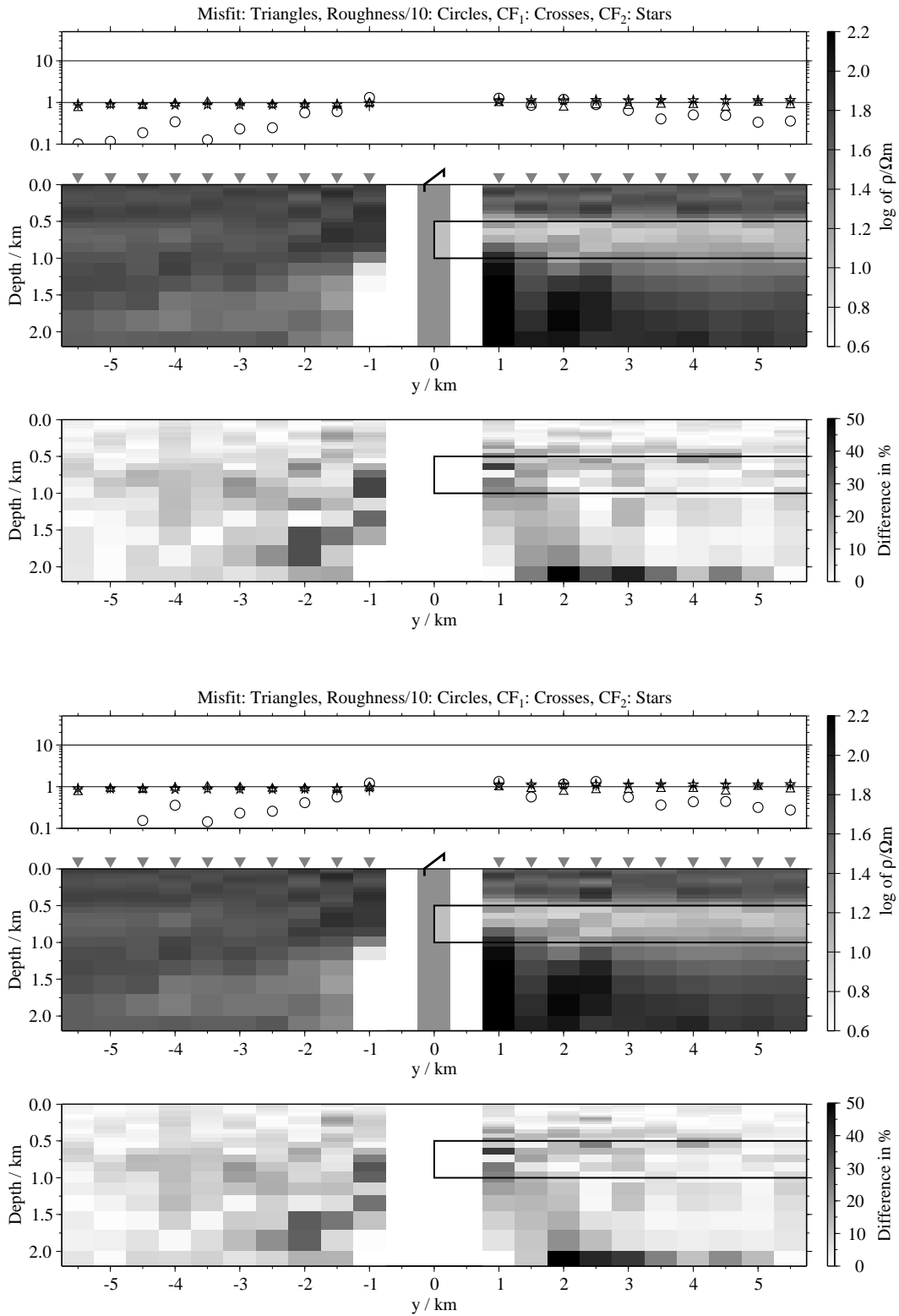


Figure B.63: Pseudo-sections 1-D of soft joint-inversions using the components E_x and H_{zi} , model D2; Top panels: Average inversion results and relative differences (regularisation scheme C1); bottom: Average inversion results and relative differences (regularisation scheme C4);

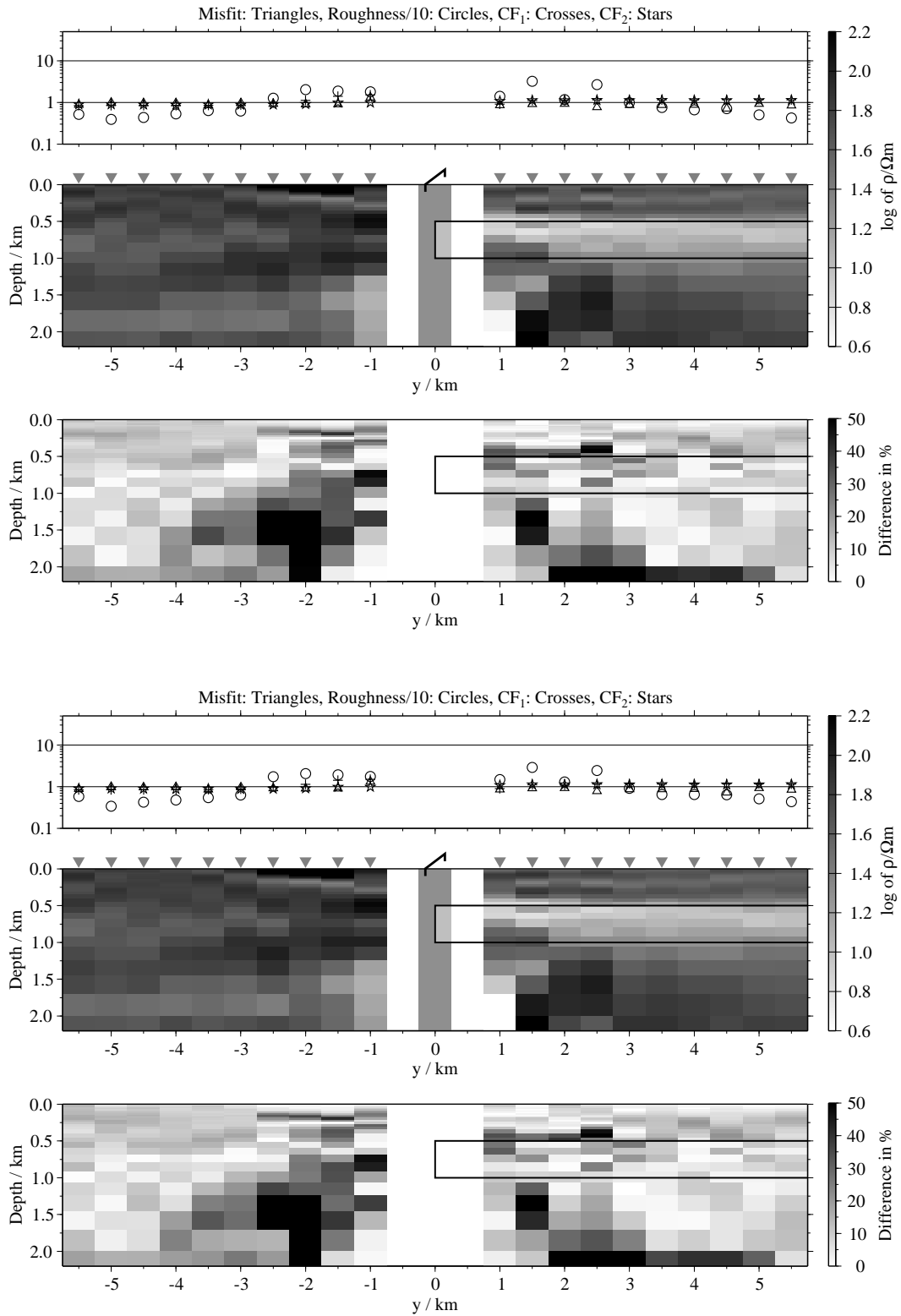


Figure B.64: Pseudo-sections of 1-D soft joint-inversions using the components \dot{H}_y and \dot{H}_z , model D2; Top panels: Average inversion results and relative differences (regularisation scheme C1); bottom: Average inversion results and relative differences (regularisation scheme C4);

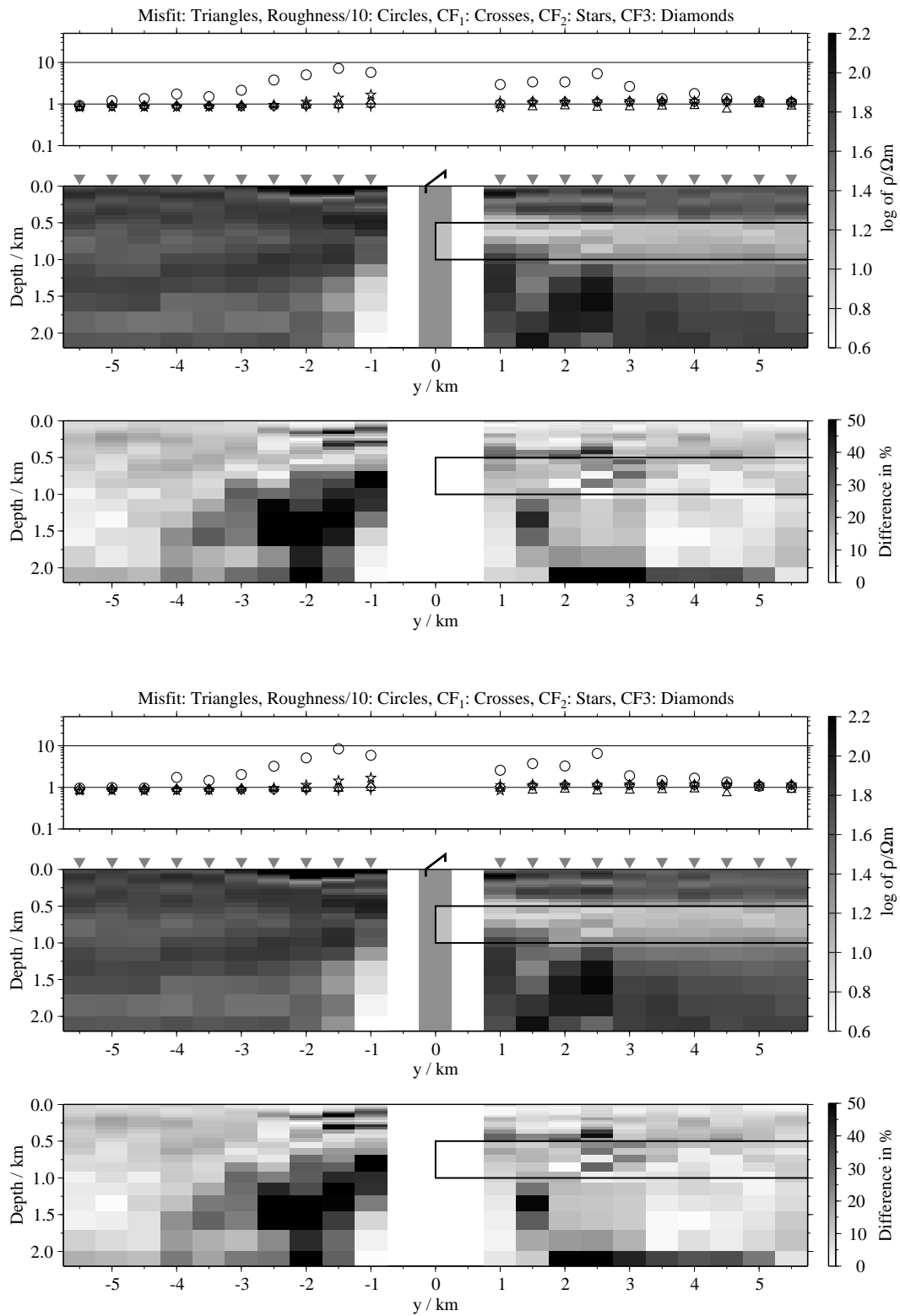


Figure B.65: Pseudo-sections of 1-D soft joint-inversions using all three components, model D2; Top panels: Average inversion results and relative differences (regularisation scheme C1); bottom: Average inversion results and relative differences (regularisation scheme C4);

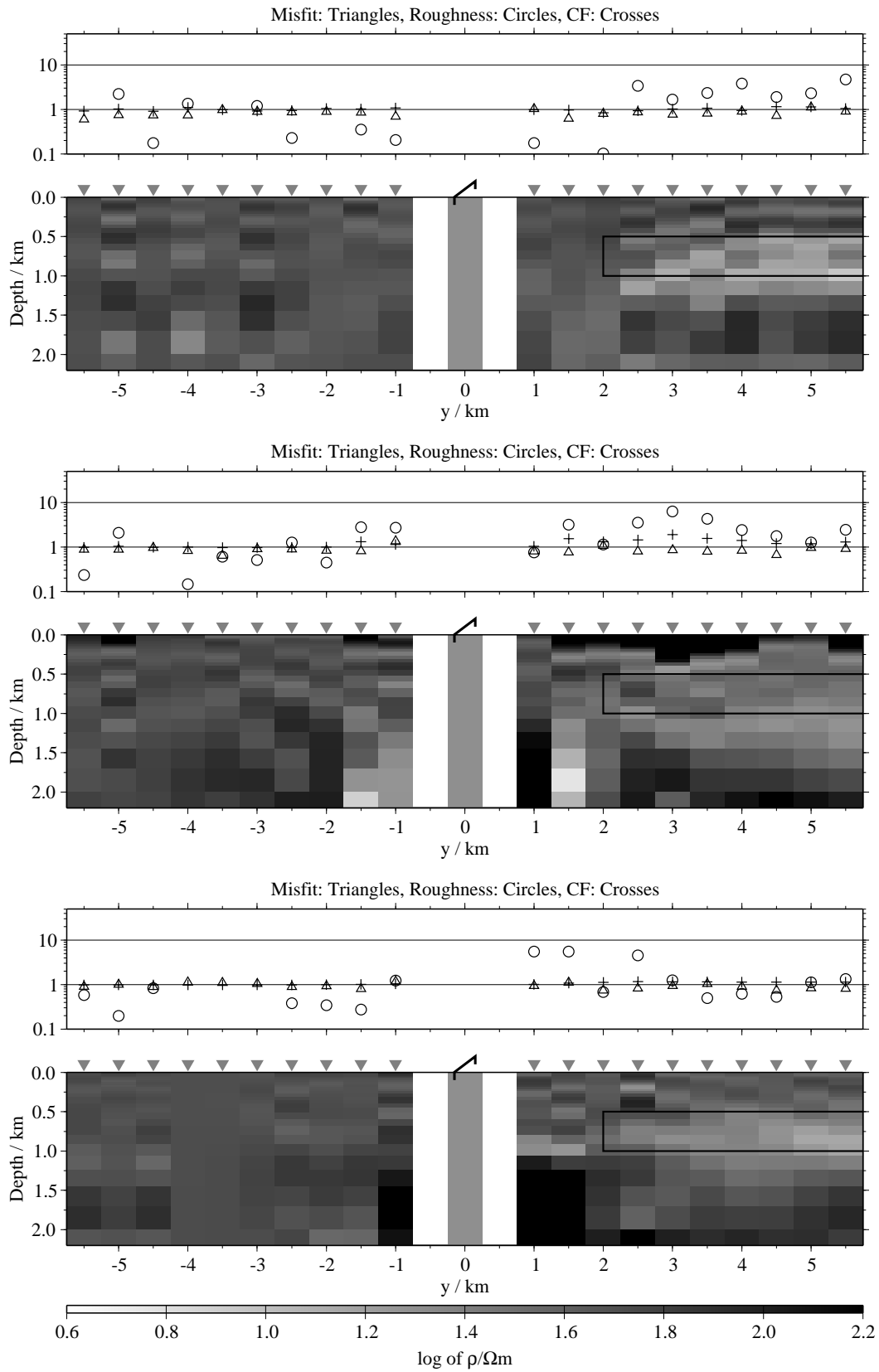


Figure B.66: Pseudo-sections of single 1-D inversion, model D3, regularisation scheme C1; from top to bottom E_x -, H_y - and H_z -component;

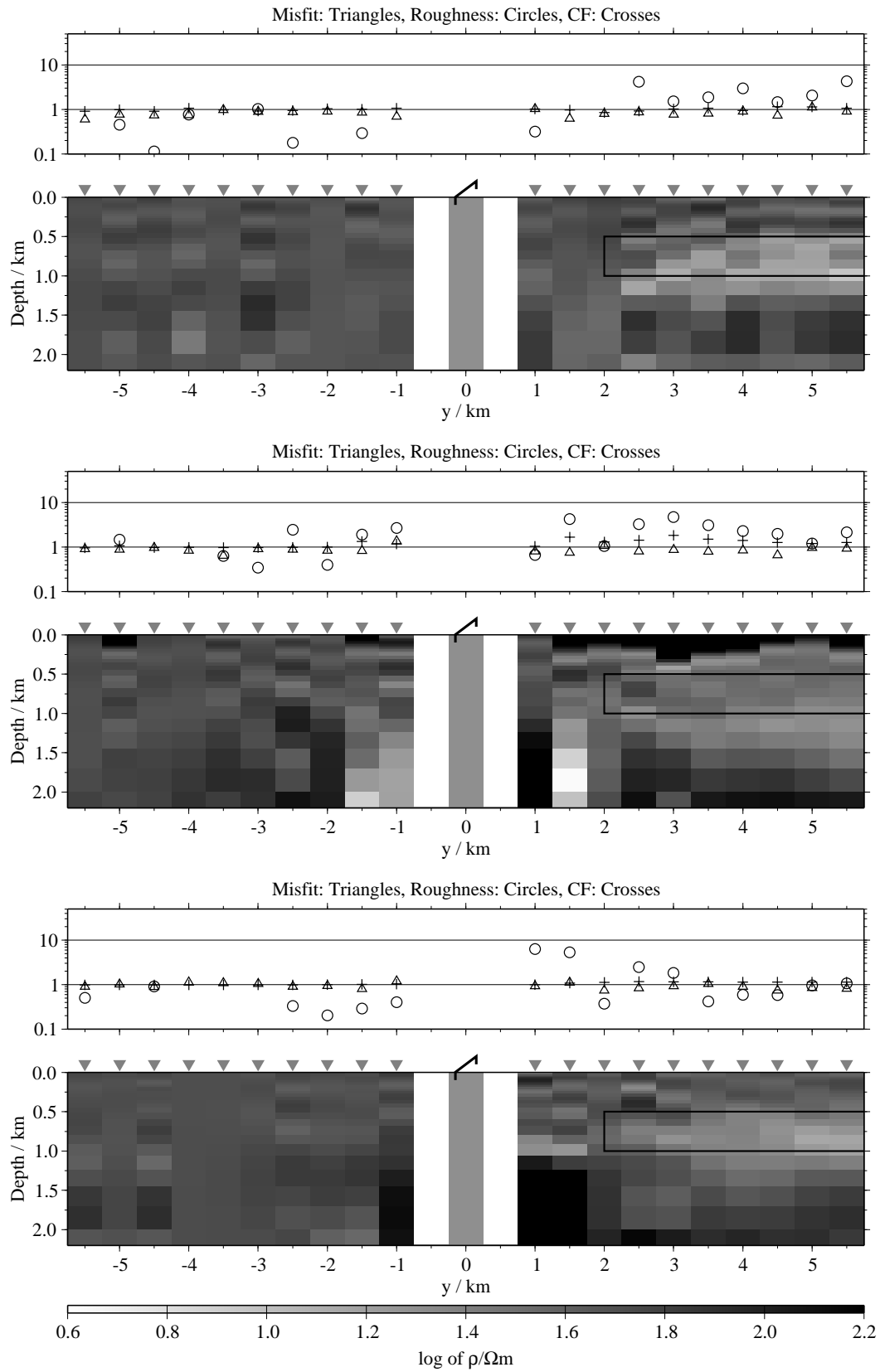


Figure B.67: Pseudo-sections of single 1-D inversion, model D3, regularisation scheme C4; from top to bottom E_x -, H_y - and H_z -component;

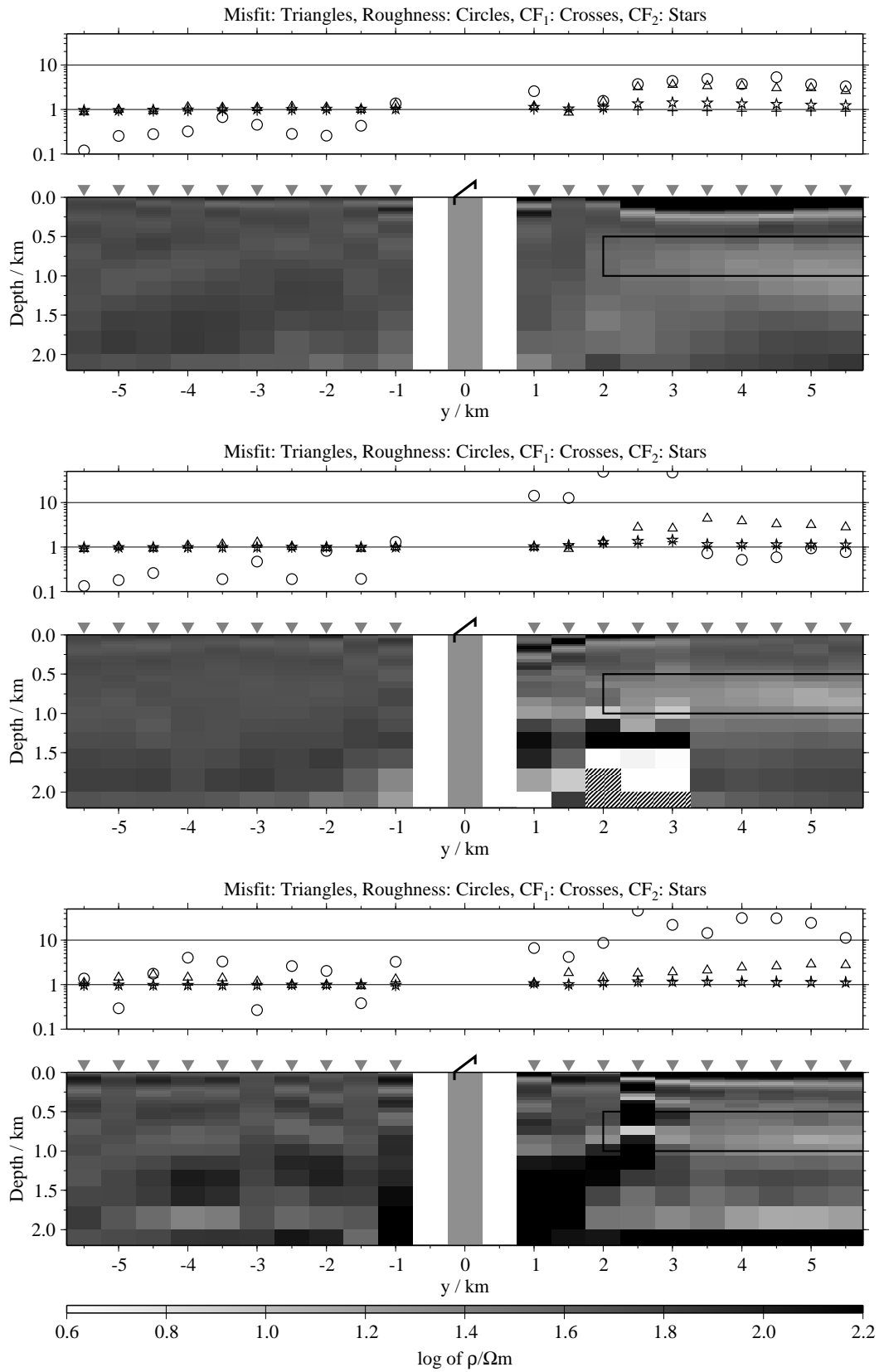


Figure B.68: Pseudo-sections of two component 1-D joint-inversions, model D3, regularisation scheme C1; from top to bottom $E_x - \dot{H}_y$, $E_x - \dot{H}_z$ and $\dot{H}_y - \dot{H}_z$;

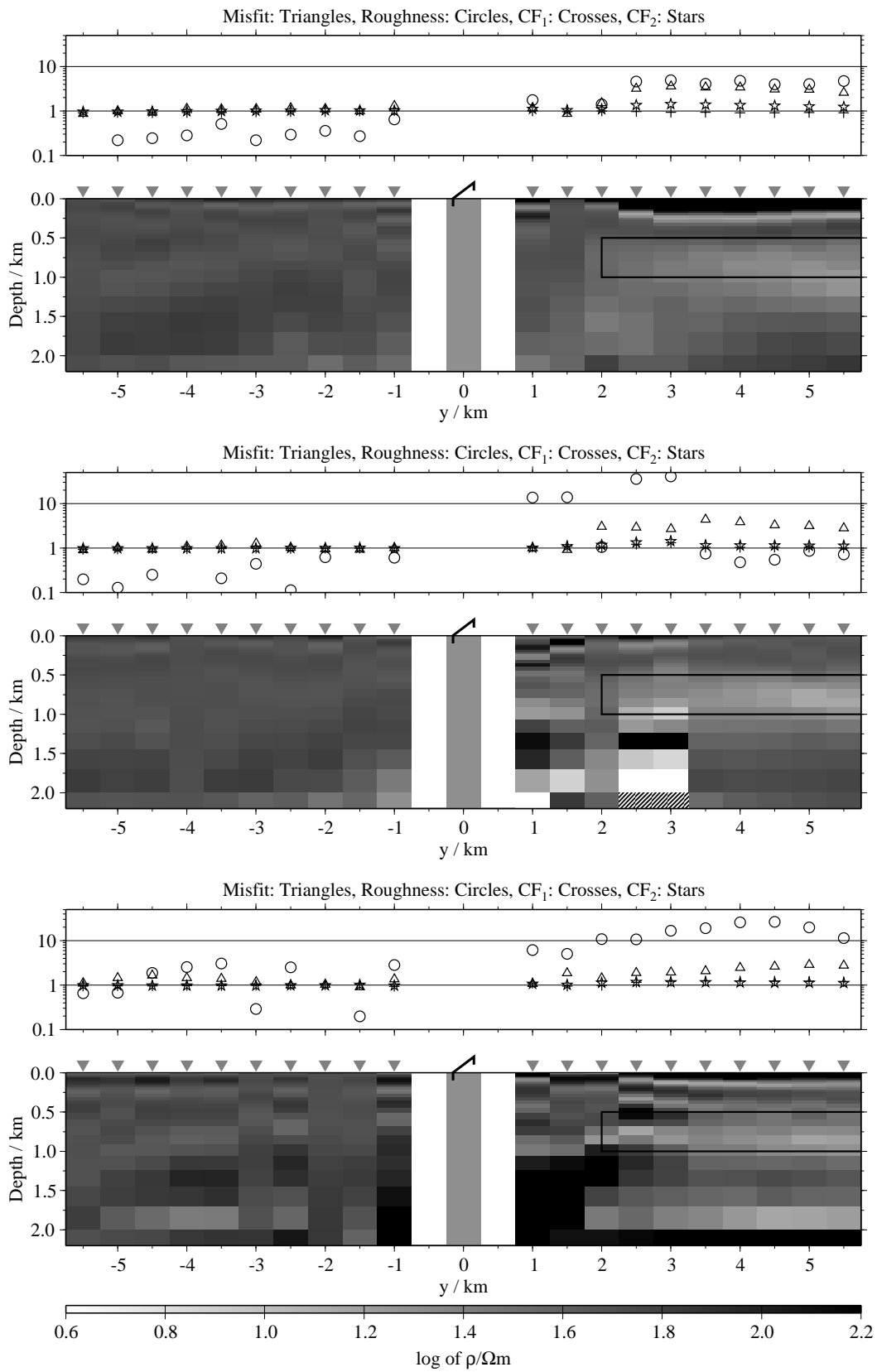


Figure B.69: Pseudo-sections of two component 1-D joint-inversions, model D3, regularisation scheme C4; from top to bottom $E_x - \dot{H}_y$, $E_x - \dot{H}_z$ and $\dot{H}_y - \dot{H}_z$;

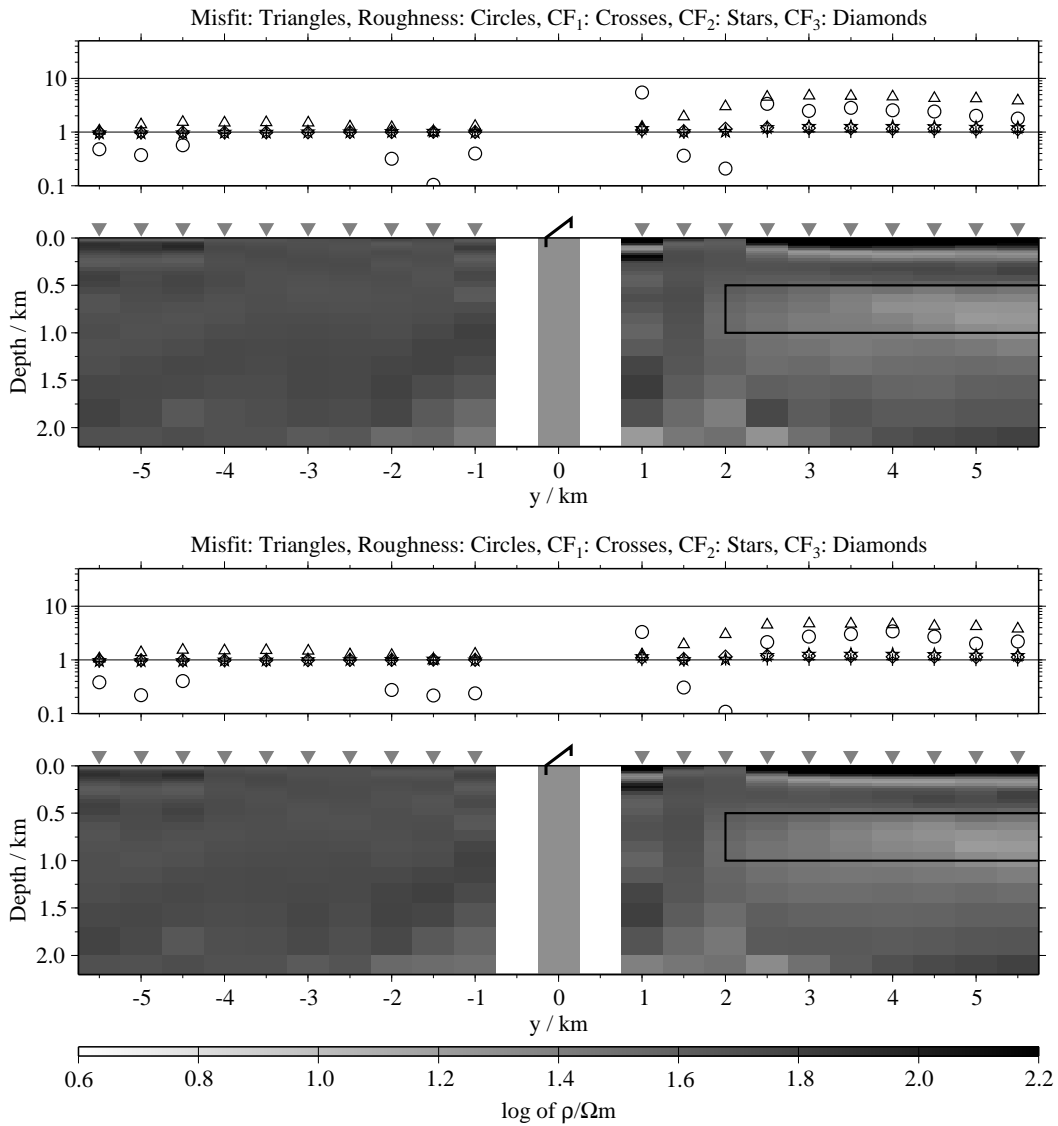


Figure B.70: Pseudo-sections of 1-D joint-inversions using all three components, model D3; top: Regularisation scheme C1; bottom: Regularisation scheme C4;

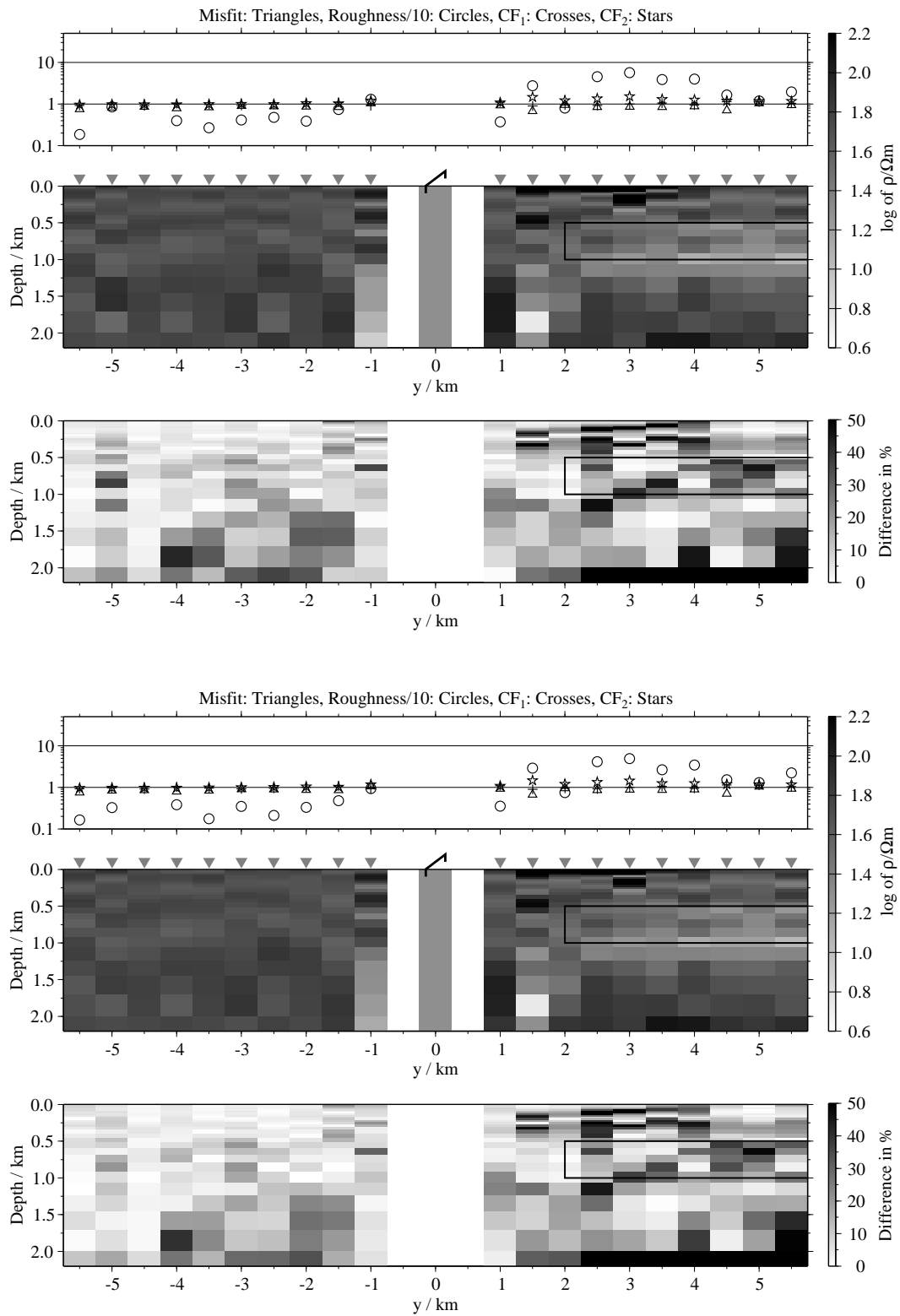


Figure B.71: Pseudo-sections of 1-D soft joint-inversions using the components E_x and H_y , model D3; Top panels: Average inversion results and relative differences (regularisation scheme C1); bottom: Average inversion results and relative differences (regularisation scheme C4);

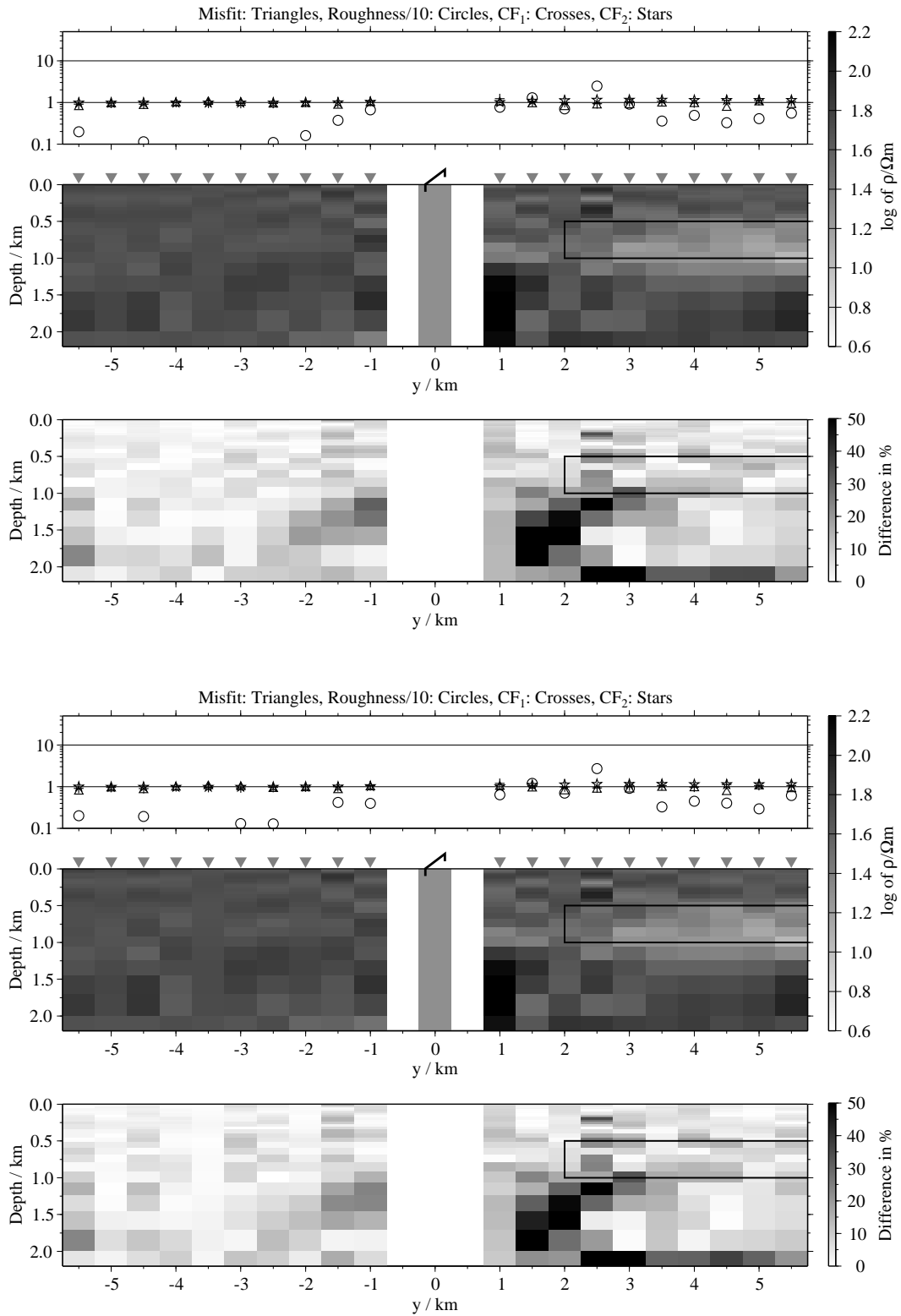


Figure B.72: Pseudo-sections 1-D of soft joint-inversions using the components E_x and H_z , model D3; Top panels: Average inversion results and relative differences (regularisation scheme C1); bottom: Average inversion results and relative differences (regularisation scheme C4);

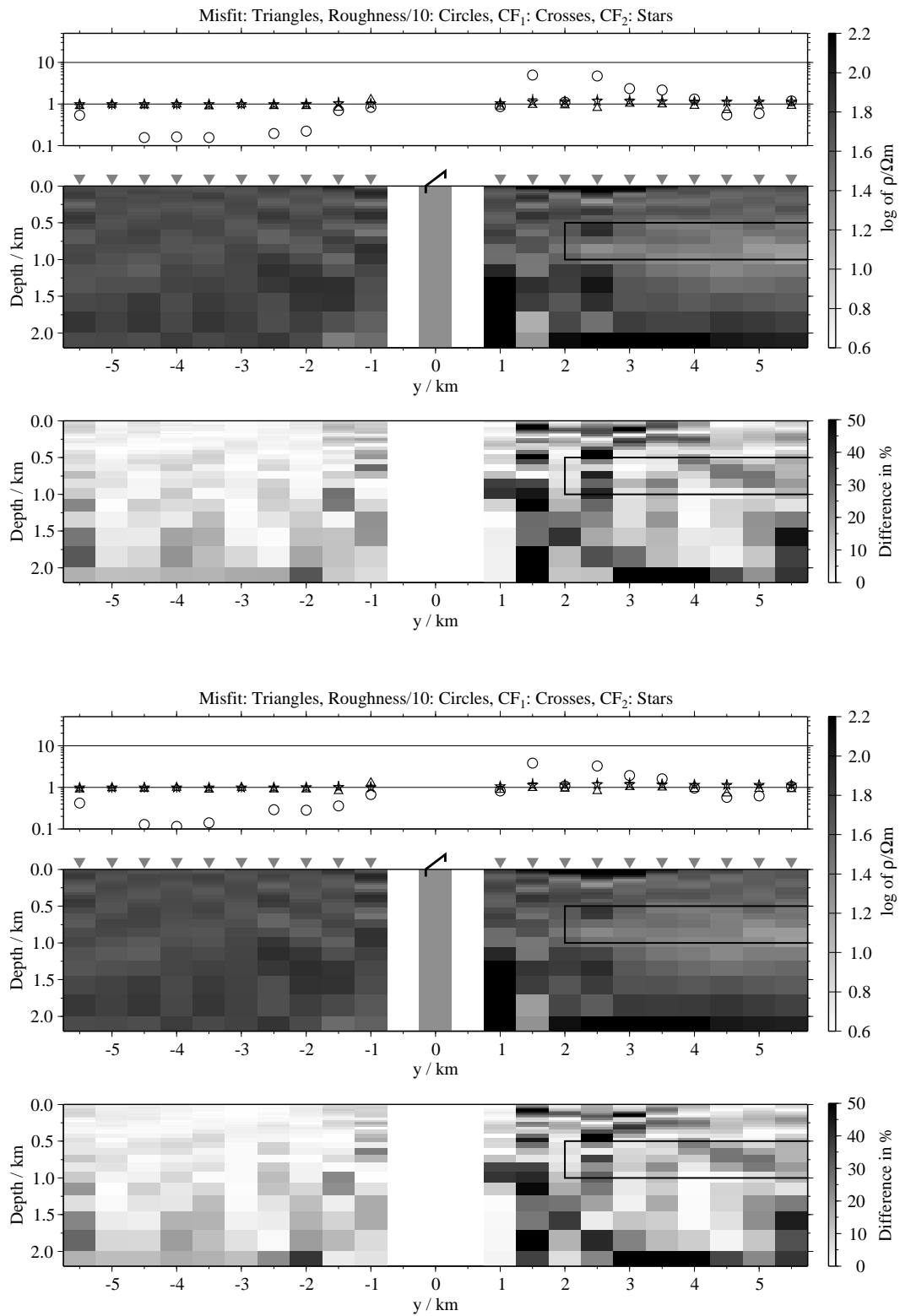


Figure B.73: Pseudo-sections of 1-D soft joint-inversions using the components \hat{H}_y and \hat{H}_{z_i} , model D3; Top panels: Average inversion results and relative differences (regularisation scheme C1); bottom: Average inversion results and relative differences (regularisation scheme C4);

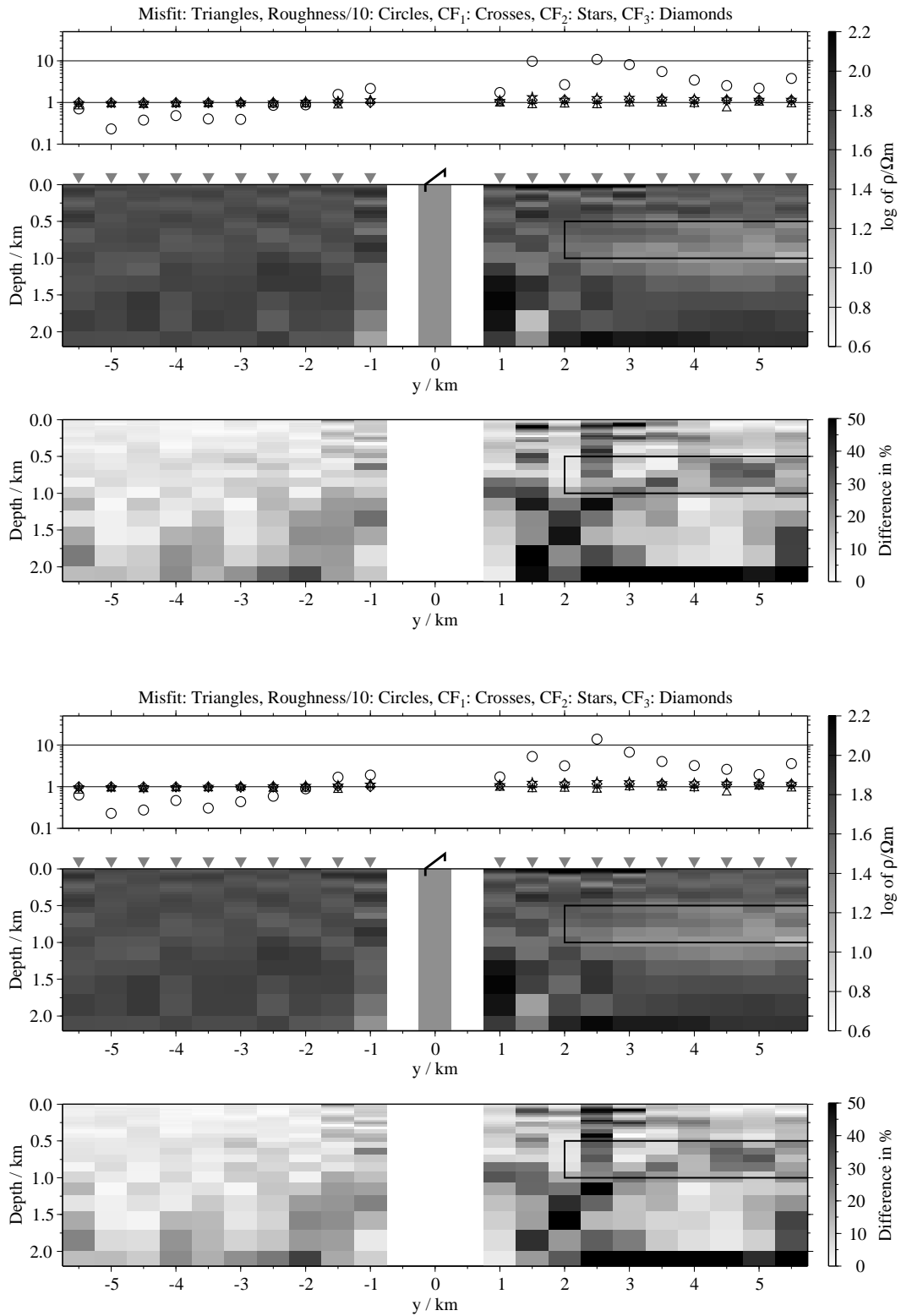
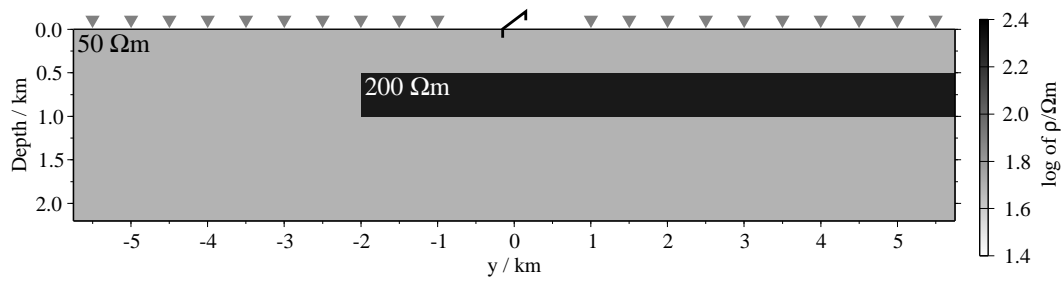


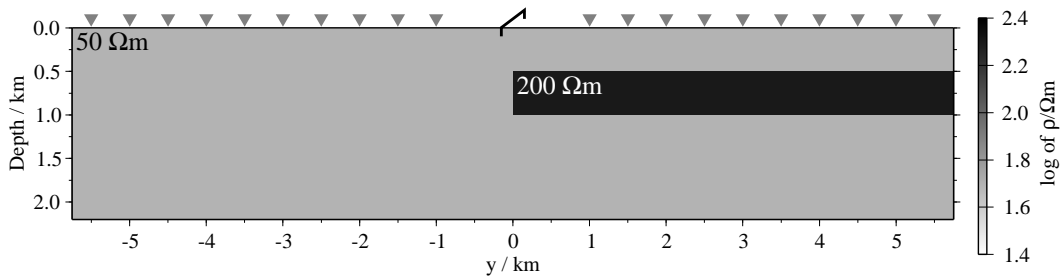
Figure B.74: Pseudo-sections of 1-D soft joint-inversions using all three components, model D3; Top panels: Average inversion results and relative differences (regularisation scheme C1); bottom: Average inversion results and relative differences (regularisation scheme C4);

B.2.3 End of a resistive layer (models E1 to E3)

Model E1:



Model E2:



Model E3:

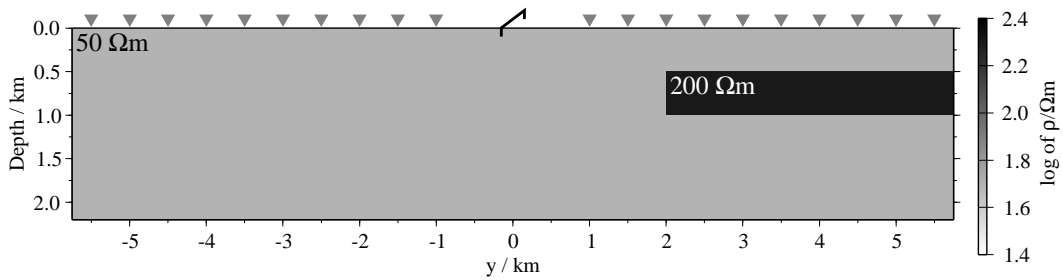


Figure B.75: Model, where a resistive layer ends at $y = -2$ km (model E1), $y = 0$ km (model E2) and $y = 2$ km (model E3);

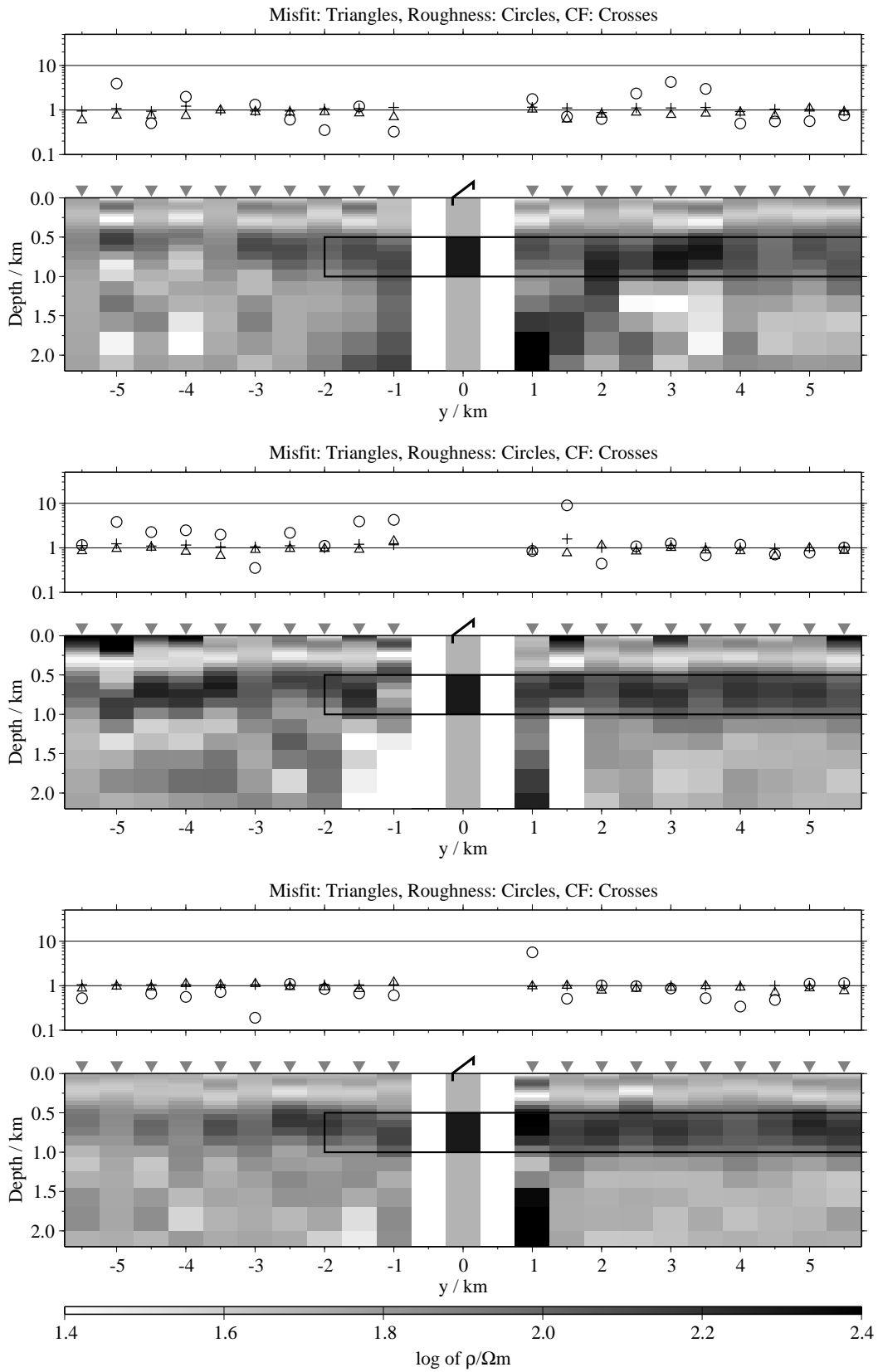


Figure B.76: Pseudo-sections of single 1-D inversion, model E1, regularisation scheme C1; from top to bottom E_x -, \dot{H}_y - and \dot{H}_z -component;

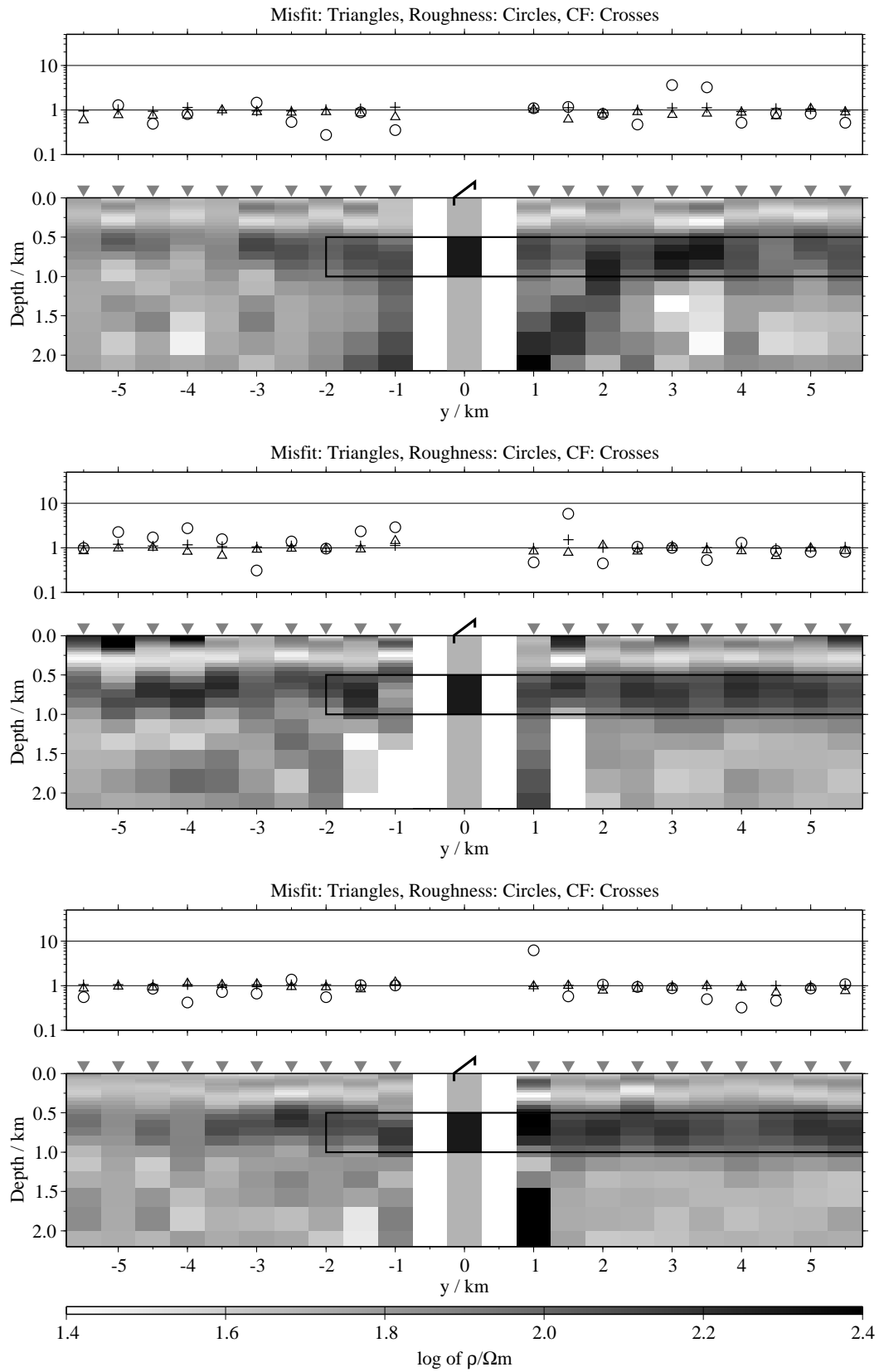


Figure B.77: Pseudo-sections of single 1-D inversion, model E1, regularisation scheme C4; from top to bottom E_x -, H_y - and H_z -component;

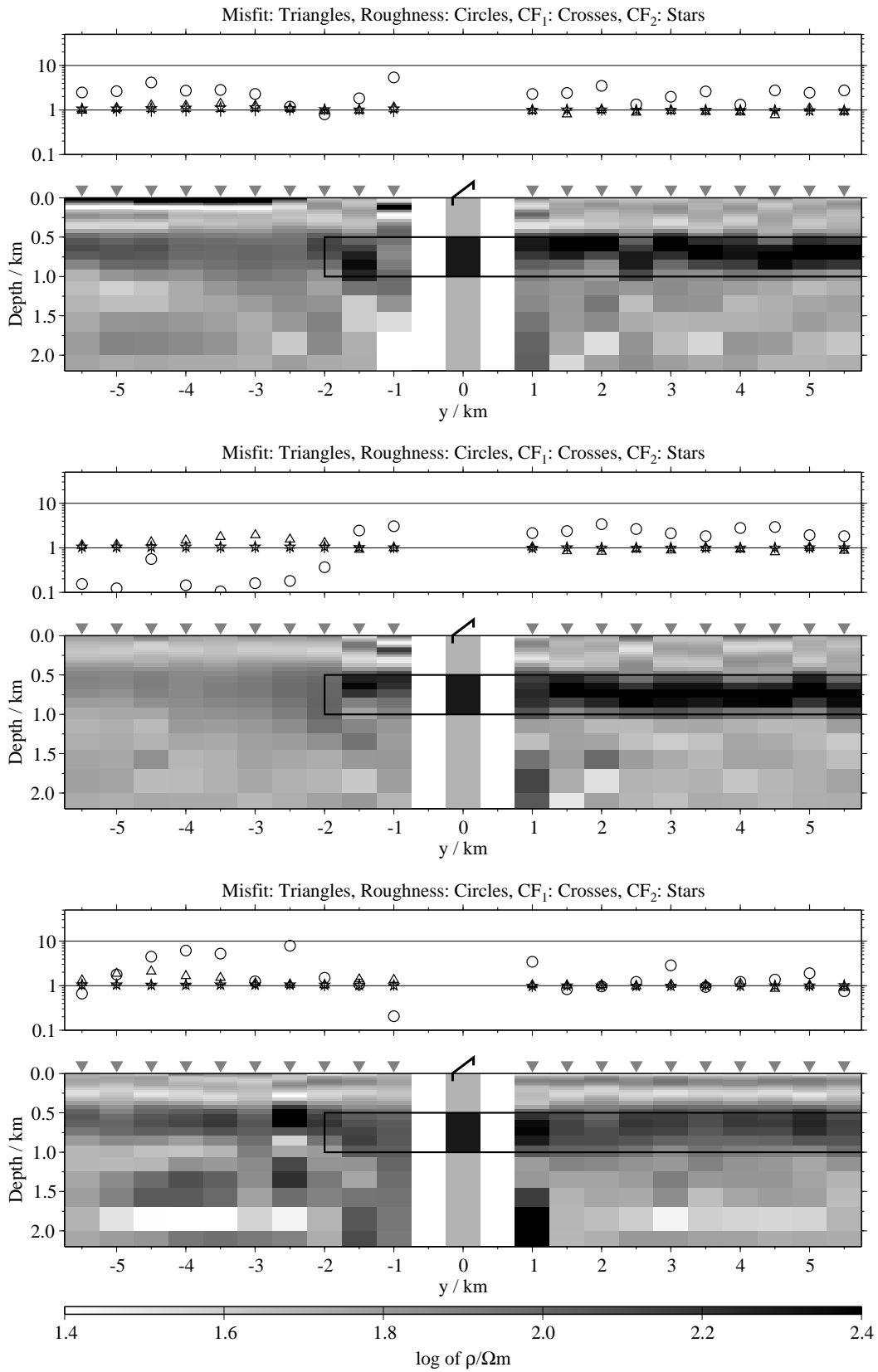


Figure B.78: Pseudo-sections of two component 1-D joint-inversions, model E1, regularisation scheme C1; from top to bottom $E_x-\dot{H}_y$, $E_x-\dot{H}_z$ and $\dot{H}_y-\dot{H}_z$;

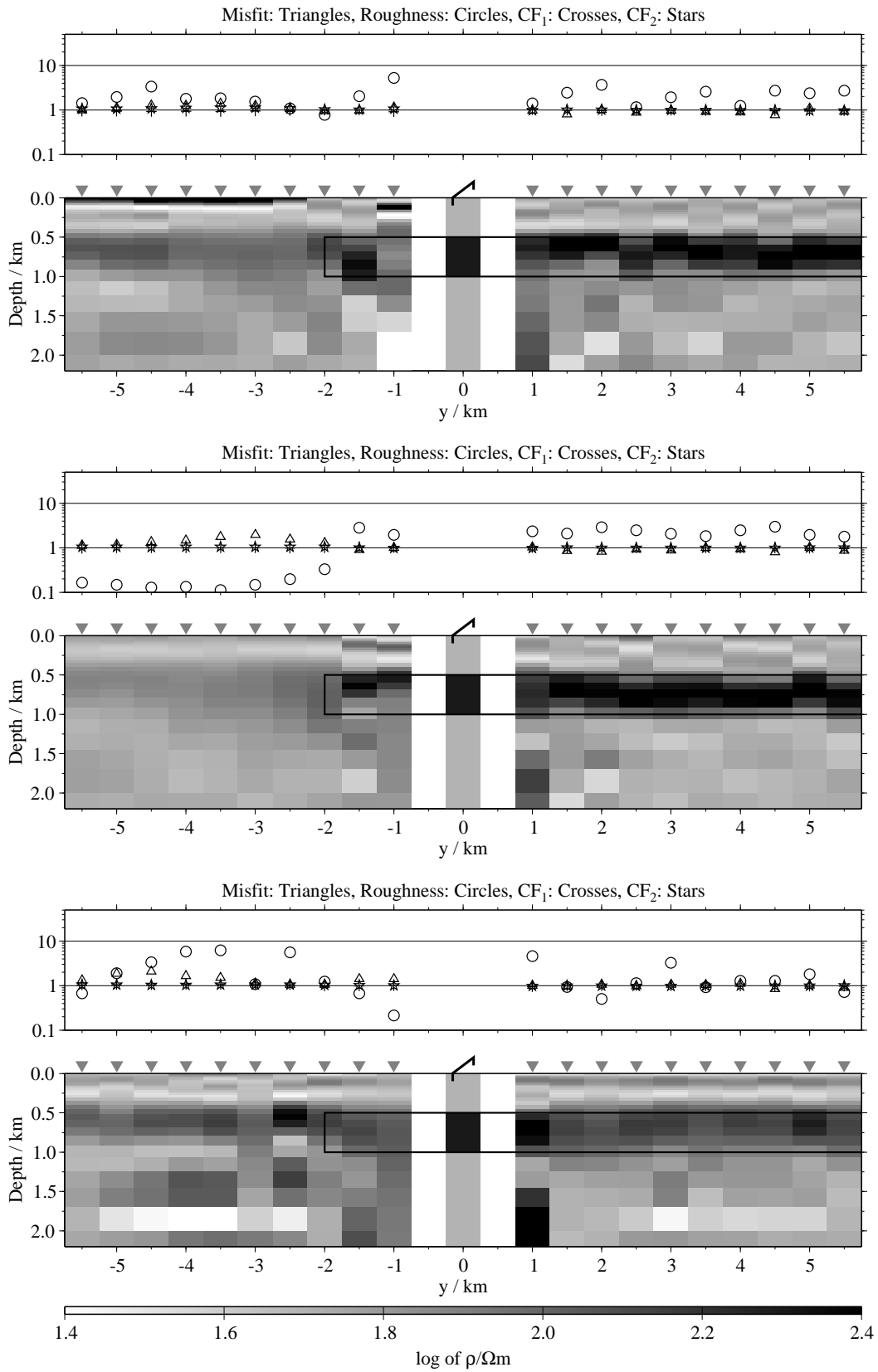


Figure B.79: Pseudo-sections of two component 1-D joint-inversions, model E1, regularisation scheme C4; from top to bottom $E_x-\dot{H}_y$, $E_x-\dot{H}_z$ and $\dot{H}_y-\dot{H}_z$;

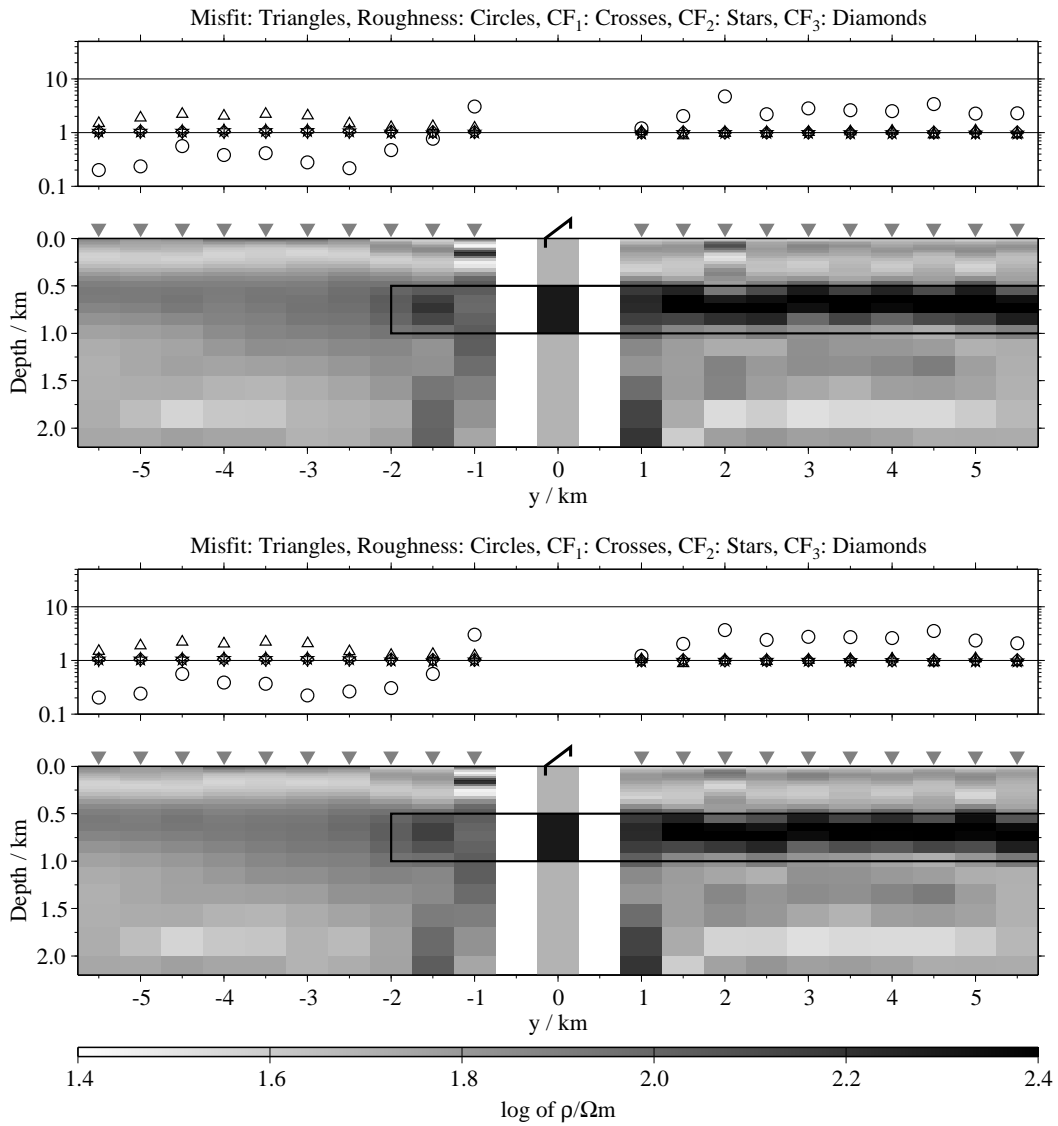


Figure B.80: Pseudo-sections of 1-D joint-inversions using all three components, model E1; top: Regularisation scheme C1; bottom: Regularisation scheme C4;

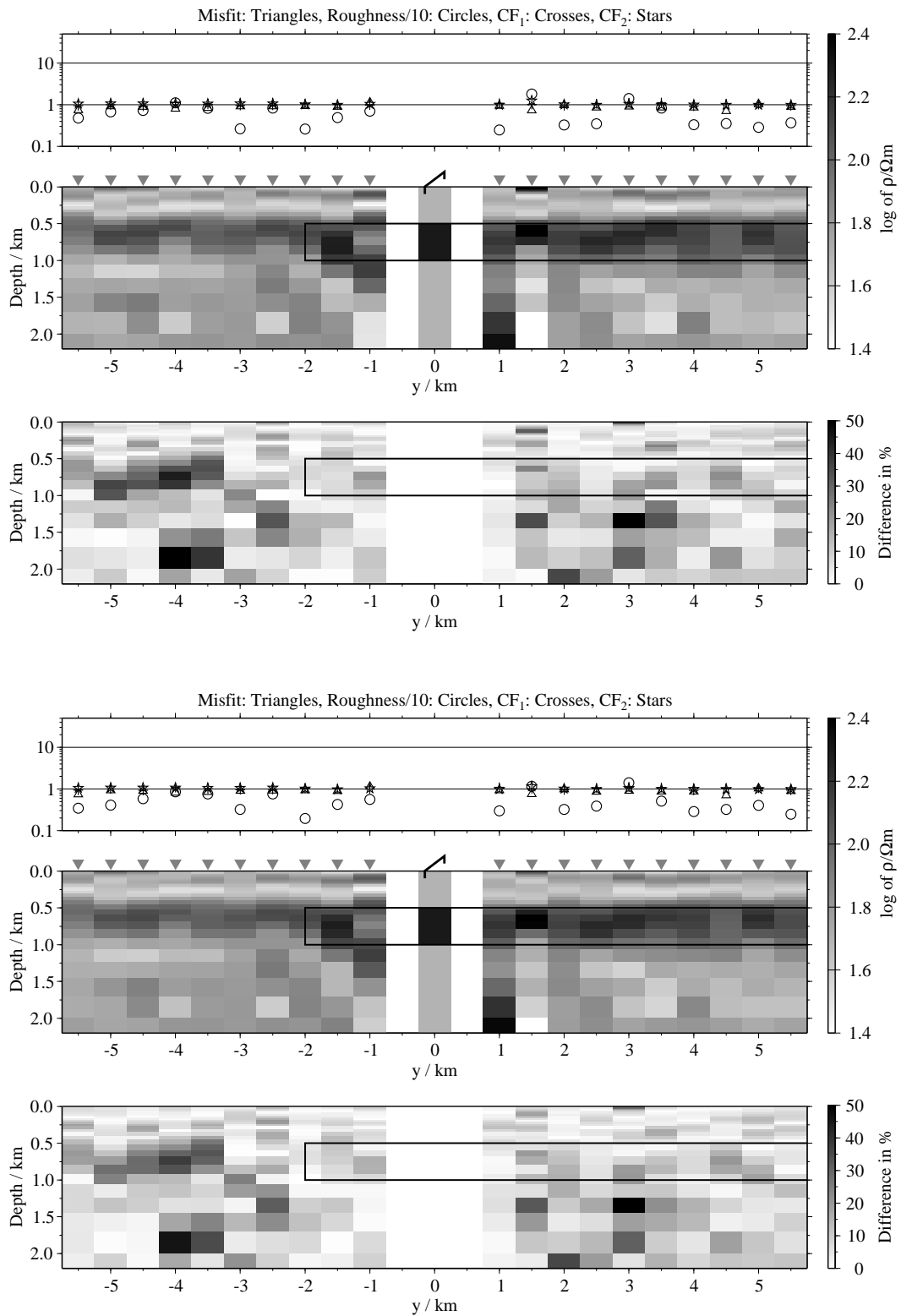


Figure B.81: Pseudo-sections of 1-D soft joint-inversions using the components E_x and H_y , model E1; Top panels: Average inversion results and relative differences (regularisation scheme C1); bottom: Average inversion results and relative differences (regularisation scheme C4);

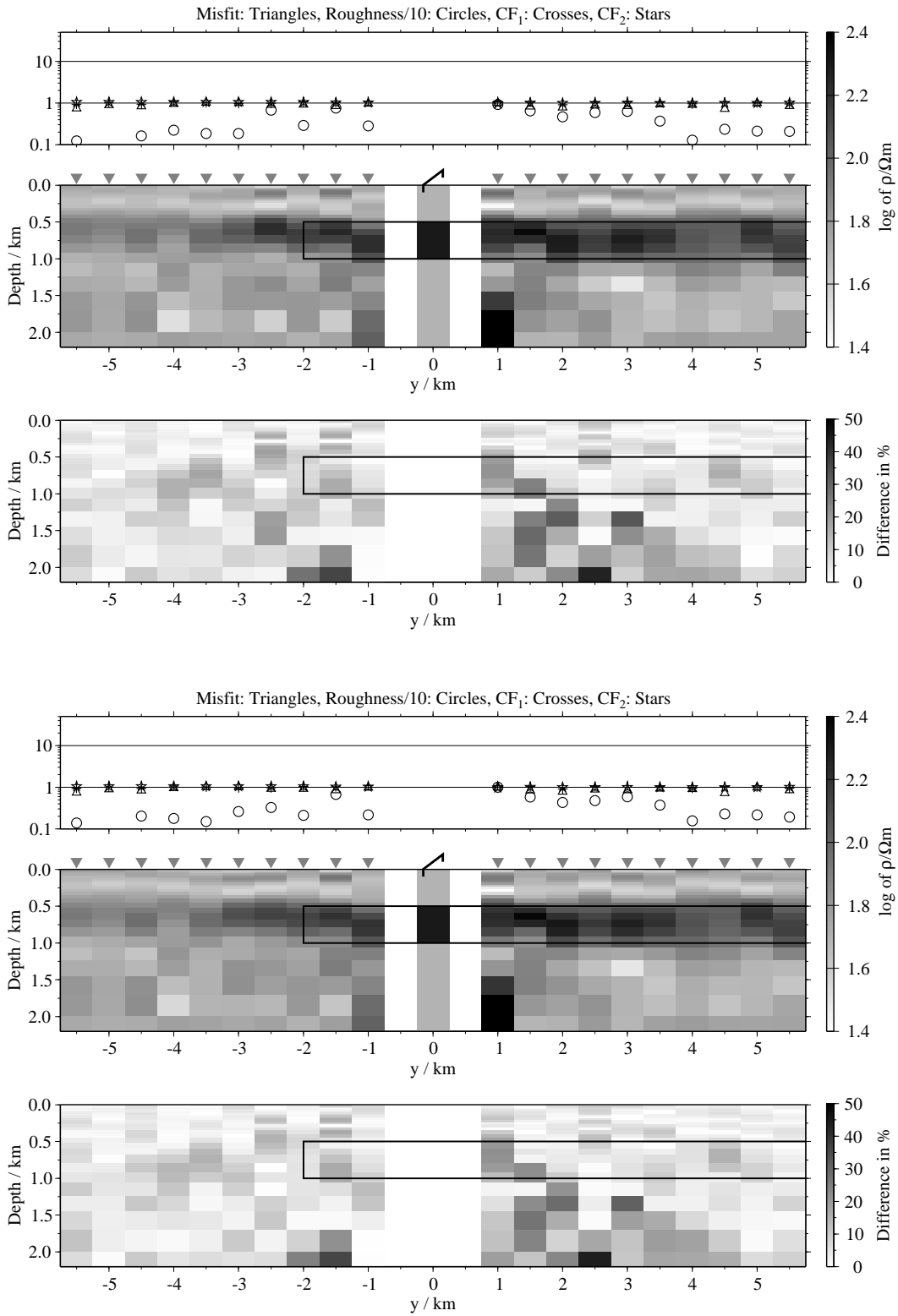


Figure B.82: Pseudo-sections 1-D of soft joint-inversions using the components E_x and \dot{H}_z , model E1 (displayed below Tx); Top panels: Average inversion results and relative differences (regularisation scheme C1); bottom: Average inversion results and relative differences (regularisation scheme C4);

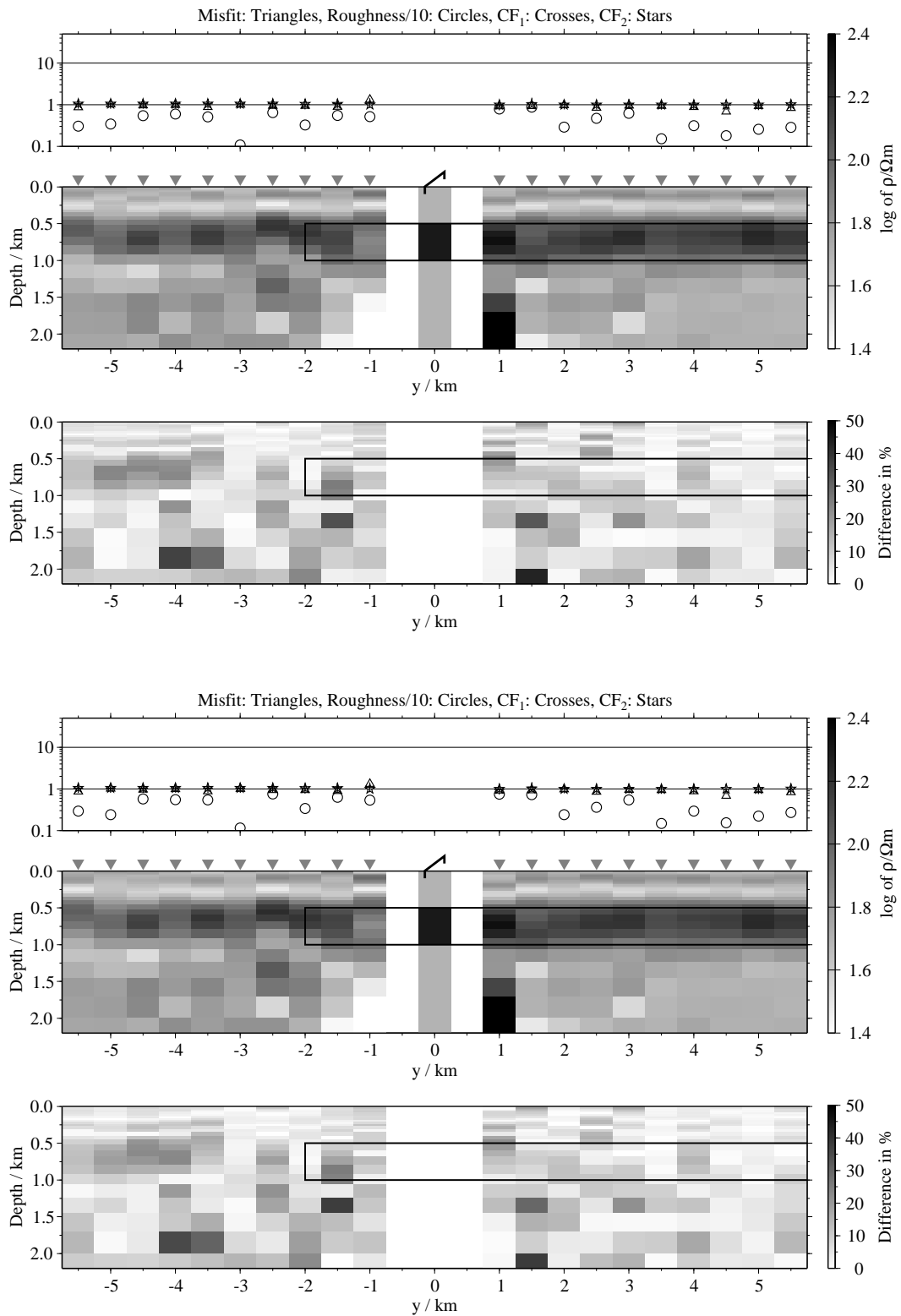


Figure B.83: Pseudo-sections of 1-D soft joint-inversions using the components \hat{H}_y and \hat{H}_{z_i} , model E1; Top panels: Average inversion results and relative differences (regularisation scheme C1); bottom: Average inversion results and relative differences (regularisation scheme C4);

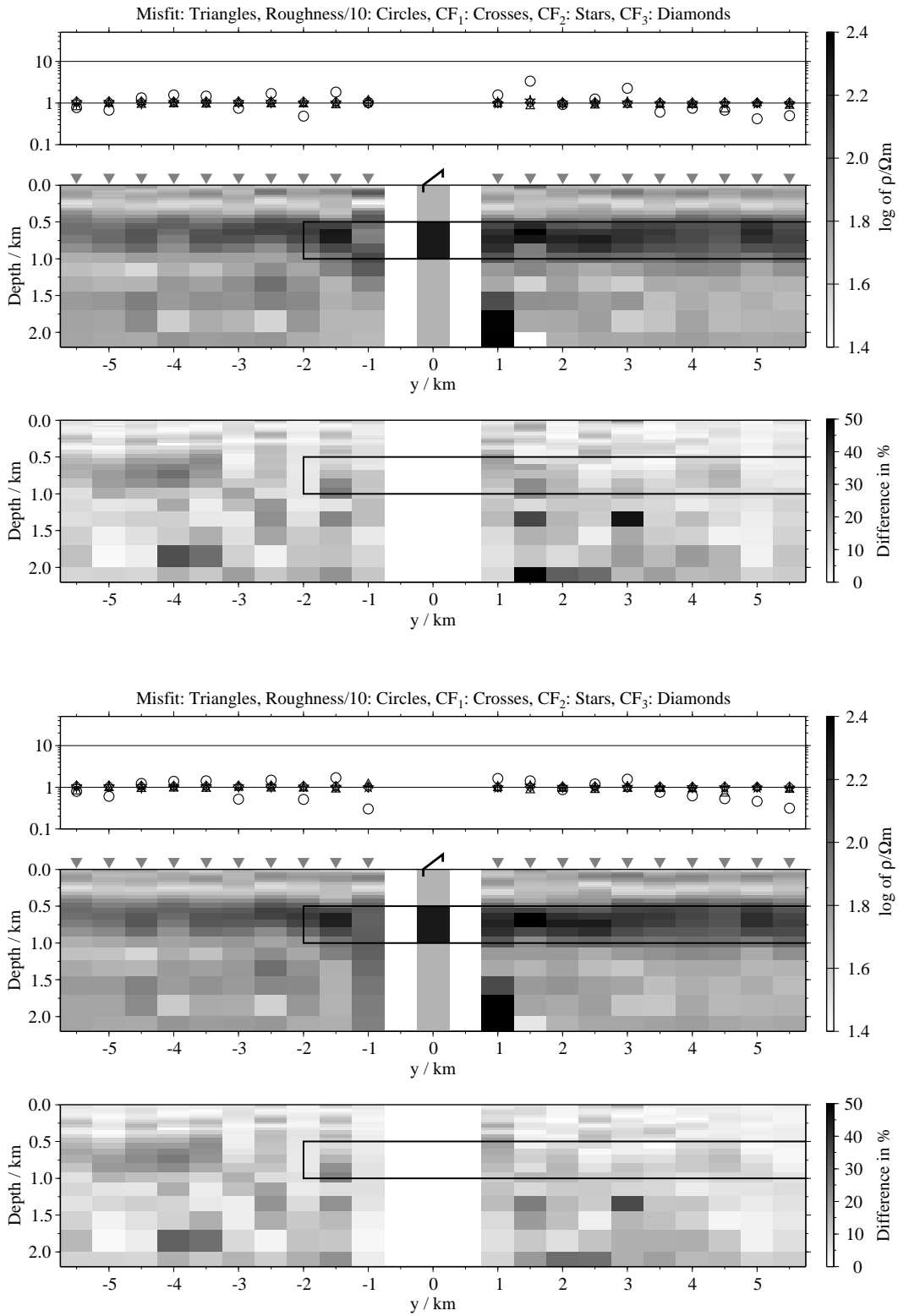


Figure B.84: Pseudo-sections of 1-D soft joint-inversions using all three components, model E1; Top panels: Average inversion results and relative differences (regularisation scheme C1); bottom: Average inversion results and relative differences (regularisation scheme C4);

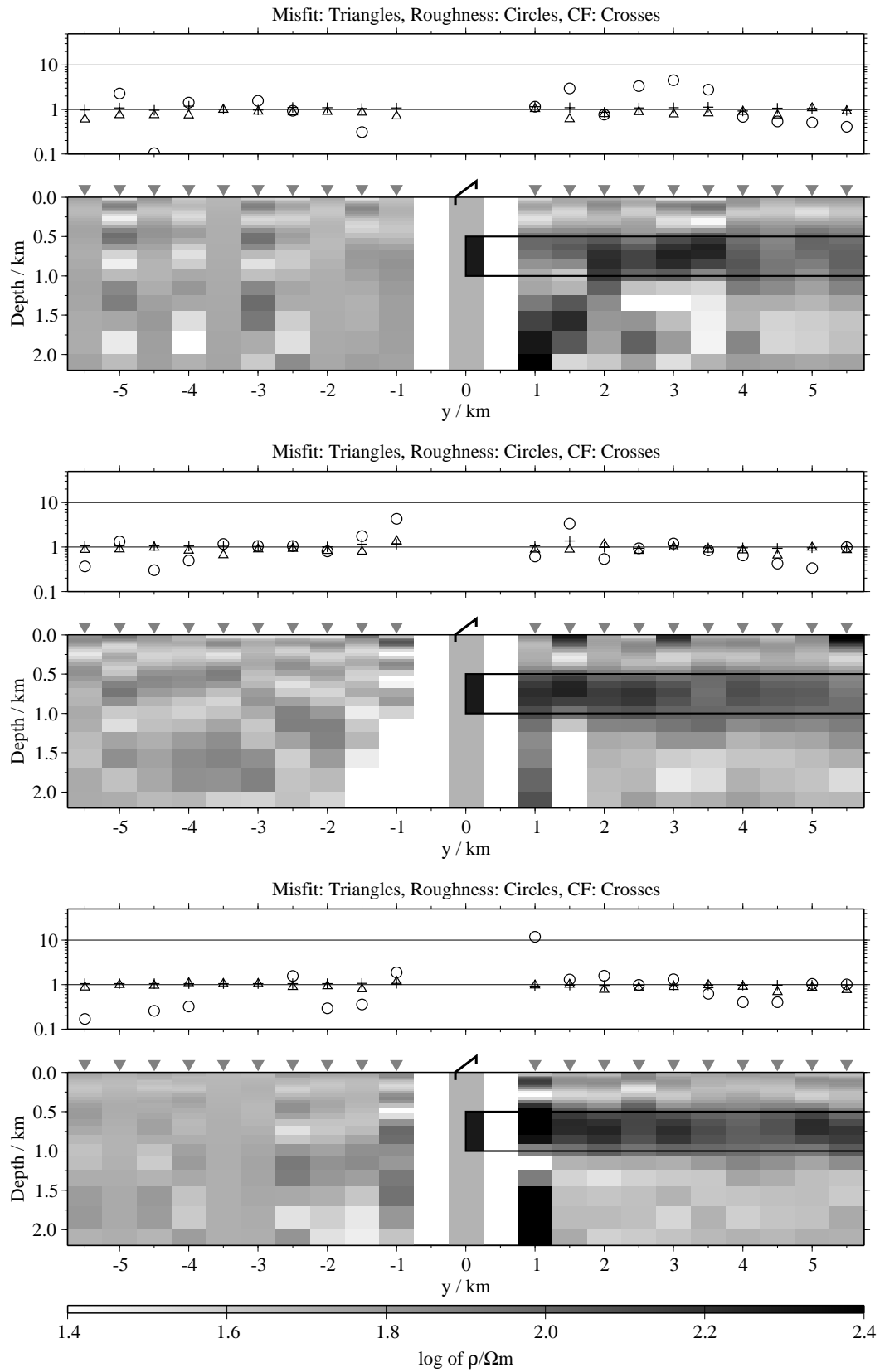


Figure B.85: Pseudo-sections of single 1-D inversion, model E2, regularisation scheme C1; from top to bottom E_x -, \dot{H}_y - and \dot{H}_z -component;

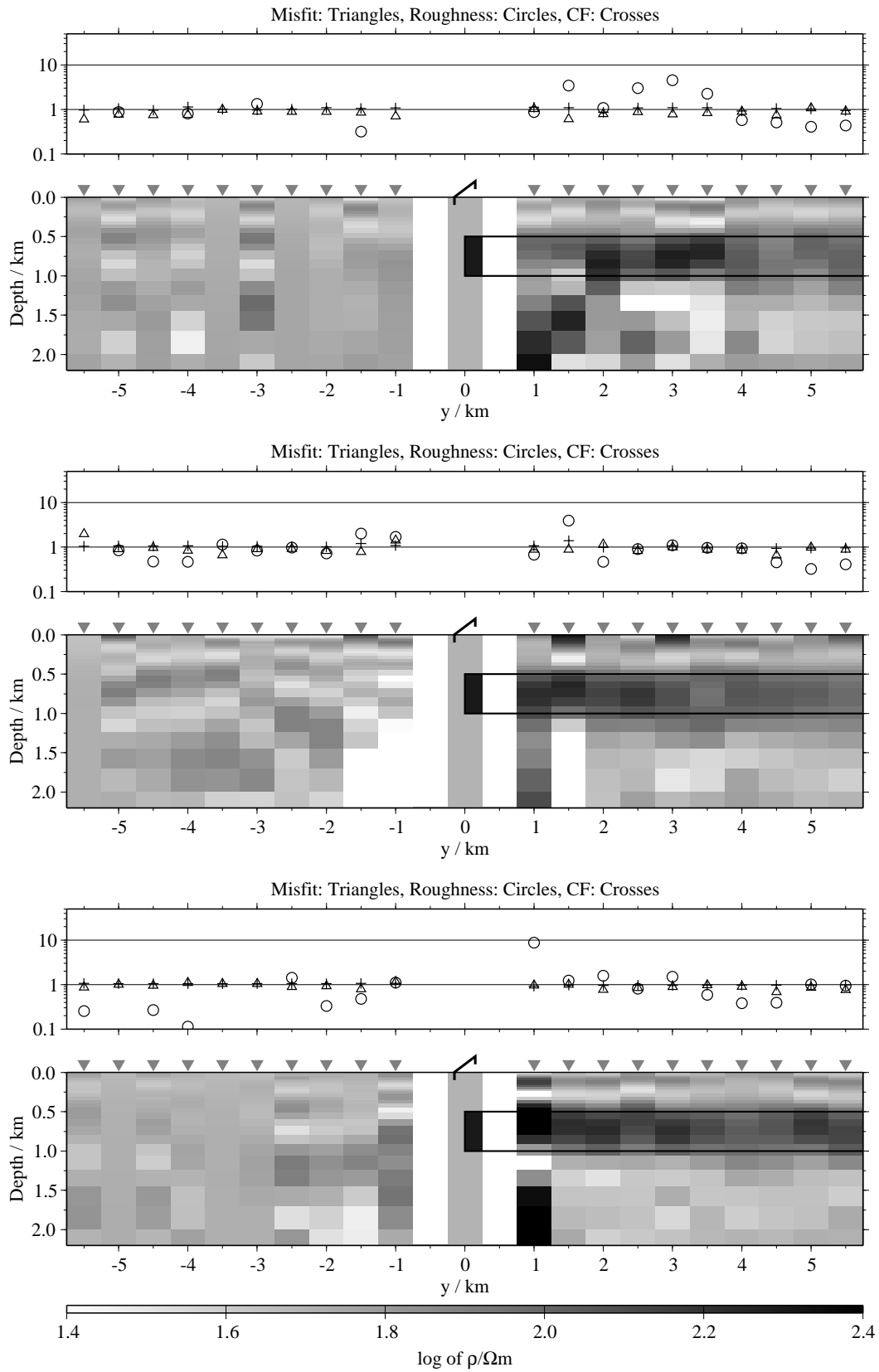


Figure B.86: Pseudo-sections of single 1-D inversion, model E2, regularisation scheme C4; from top to bottom E_x -, \dot{H}_y - and \dot{H}_z -component;

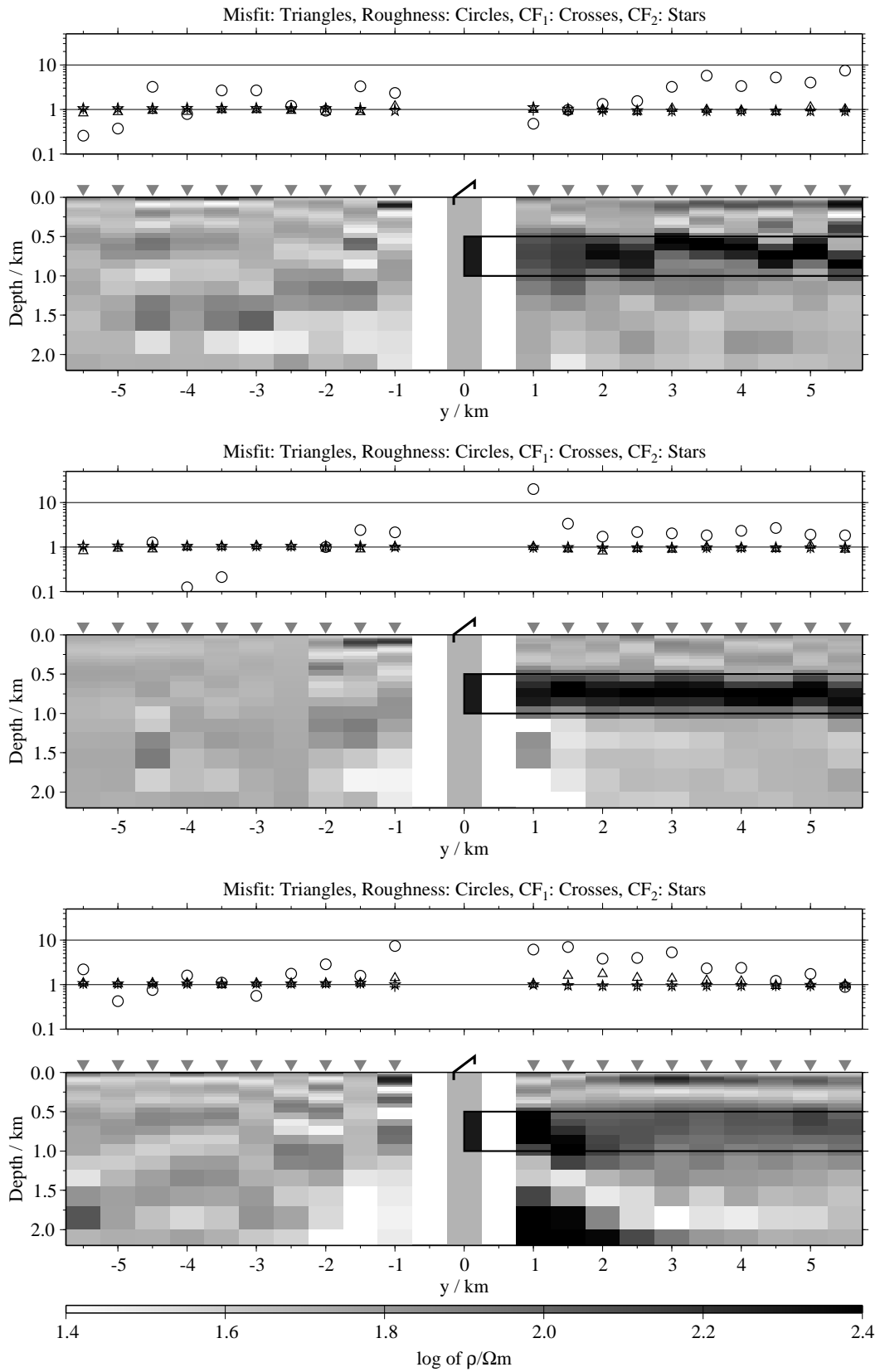


Figure B.87: Pseudo-sections of two component 1-D joint-inversions, model E2, regularisation scheme C1; from top to bottom $E_x-\dot{H}_y$, $E_x-\dot{H}_z$ and $\dot{H}_y-\dot{H}_z$;

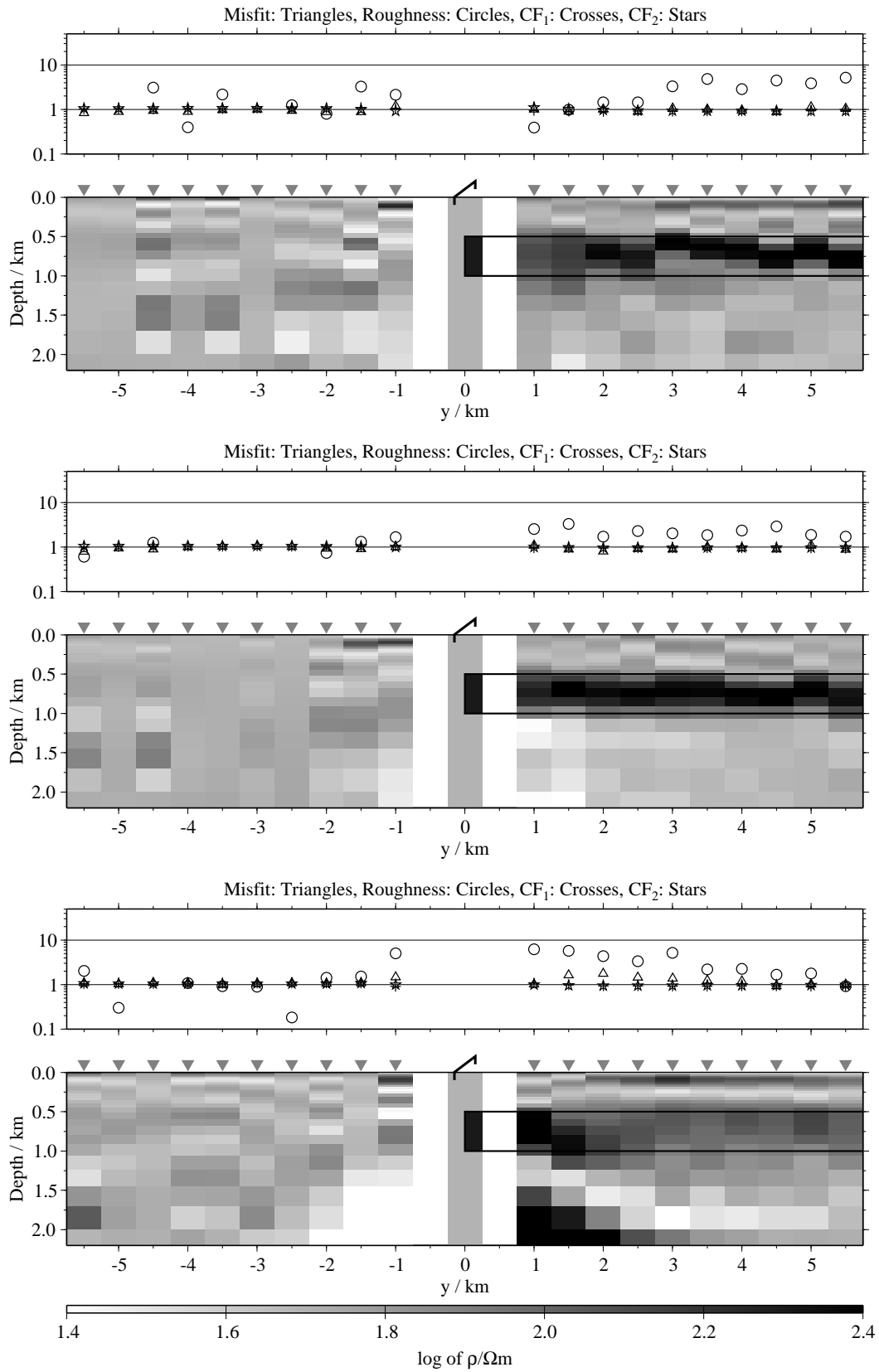


Figure B.88: Pseudo-sections of two component 1-D joint-inversions, model E2, regularisation scheme C4; from top to bottom $E_x - \dot{H}_y$, $E_x - \dot{H}_z$ and $\dot{H}_y - \dot{H}_z$;

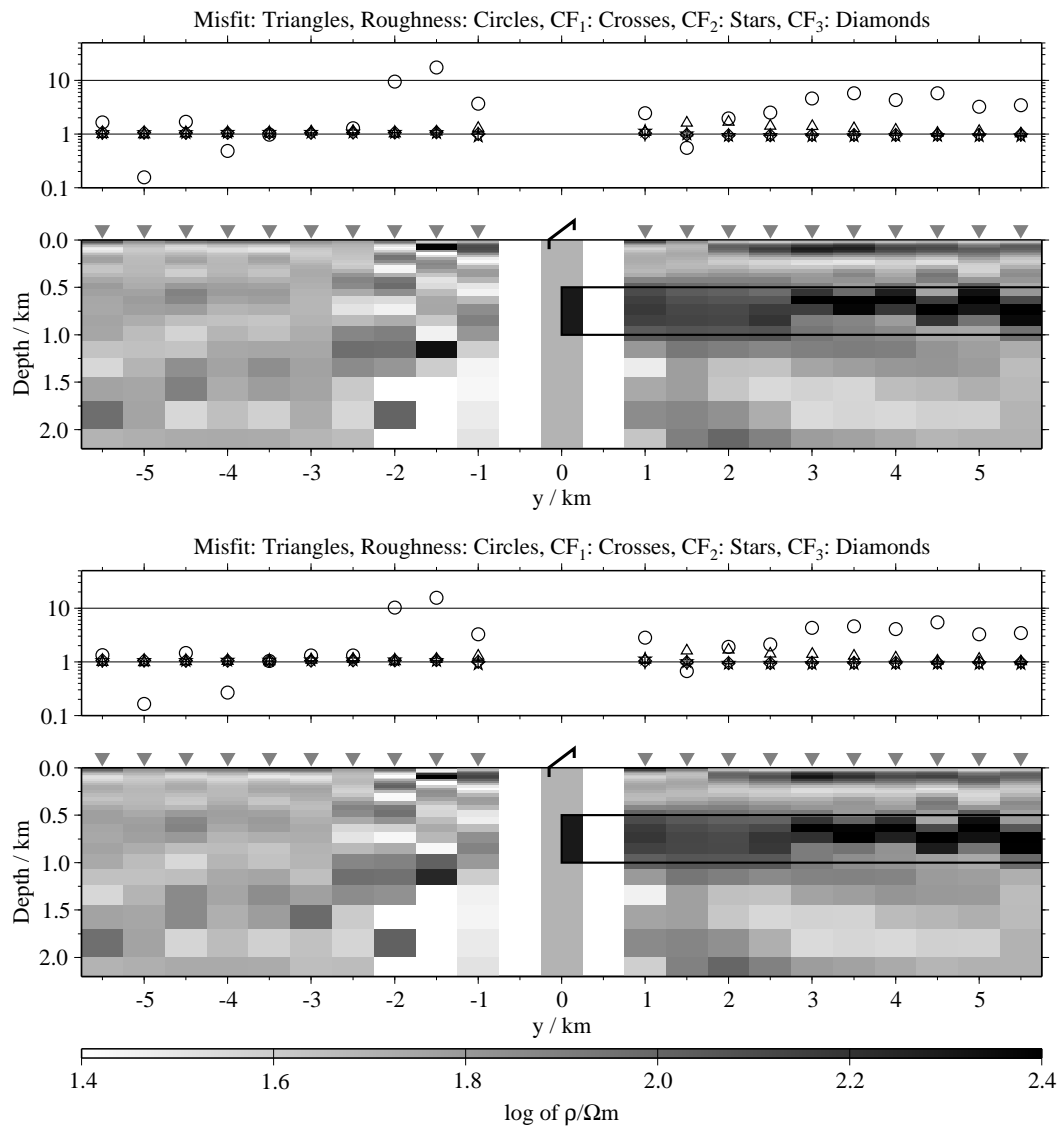


Figure B.89: Pseudo-sections of 1-D joint-inversions using all three components, model E2; top: Regularisation scheme C1; bottom: Regularisation scheme C4;

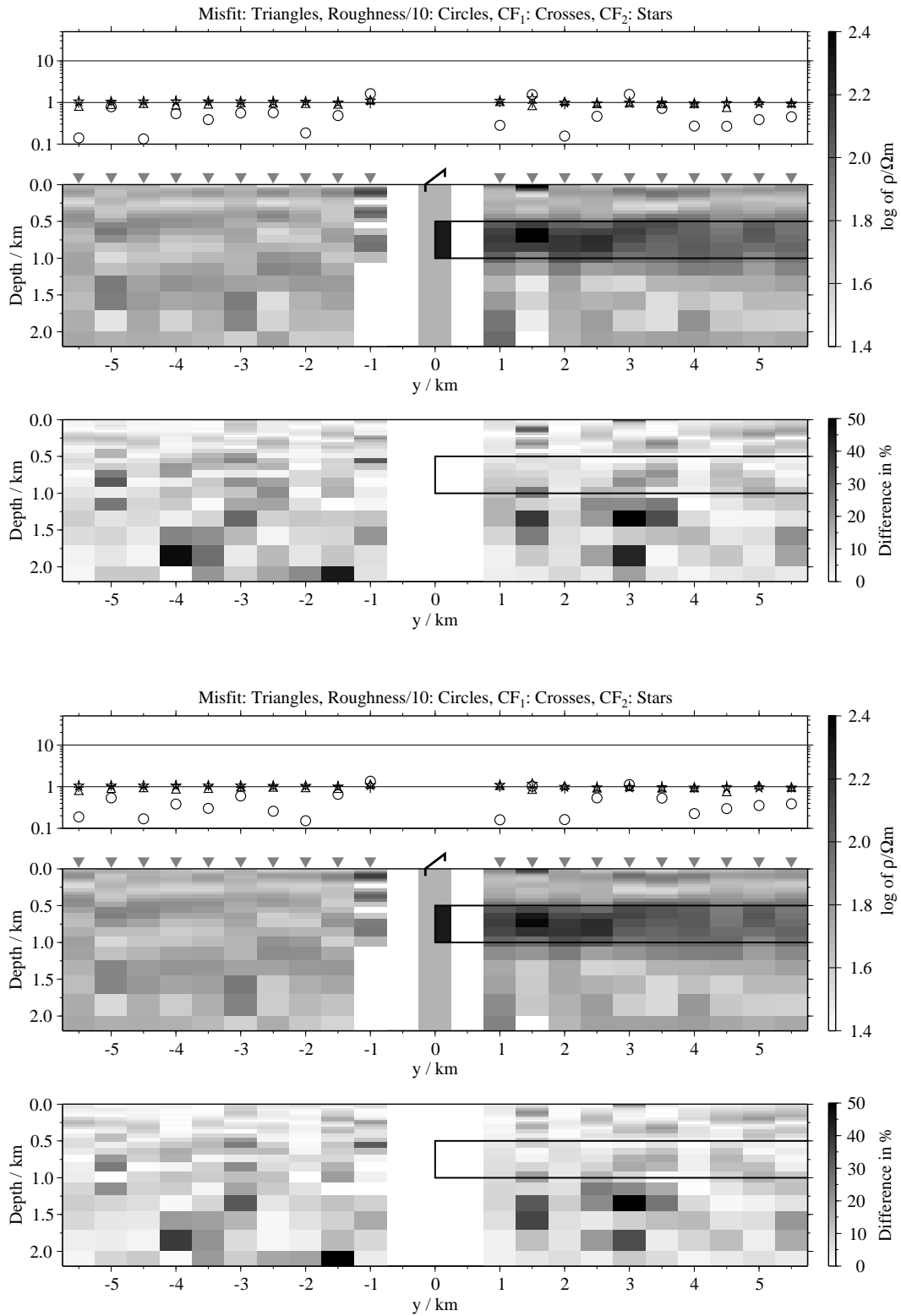


Figure B.90: Pseudo-sections of 1-D soft joint-inversions using the components E_x and H_y , model E2; Top panels: Average inversion results and relative differences (regularisation scheme C1); bottom: Average inversion results and relative differences (regularisation scheme C4);

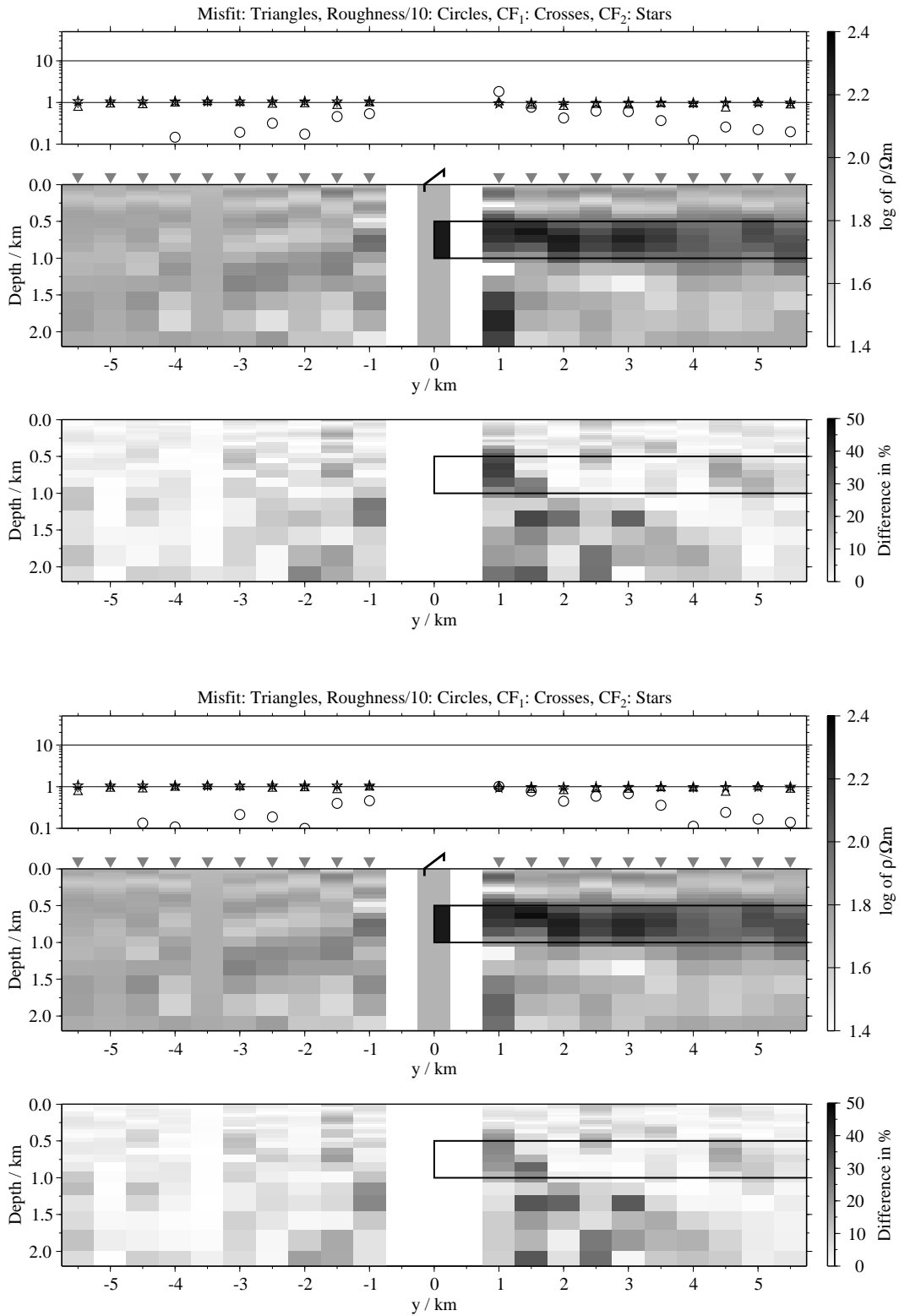


Figure B.91: Pseudo-sections 1-D of soft joint-inversions using the components E_x and H_{zi} , model E2; Top panels: Average inversion results and relative differences (regularisation scheme C1); bottom: Average inversion results and relative differences (regularisation scheme C4);

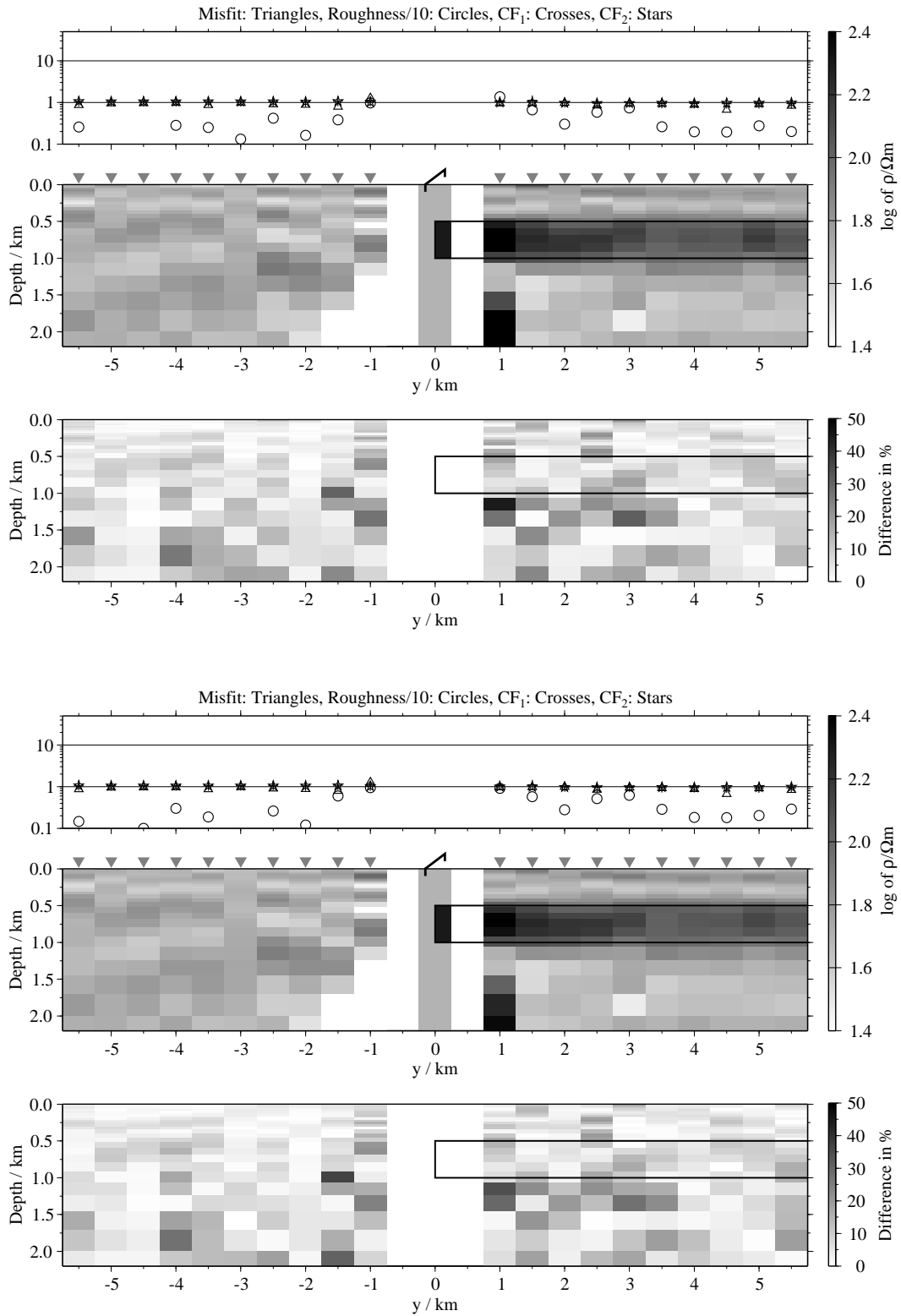


Figure B.92: Pseudo-sections of 1-D soft joint-inversions using the components \dot{H}_y and \dot{H}_z , model E2; Top panels: Average inversion results and relative differences (regularisation scheme C1); bottom: Average inversion results and relative differences (regularisation scheme C4);

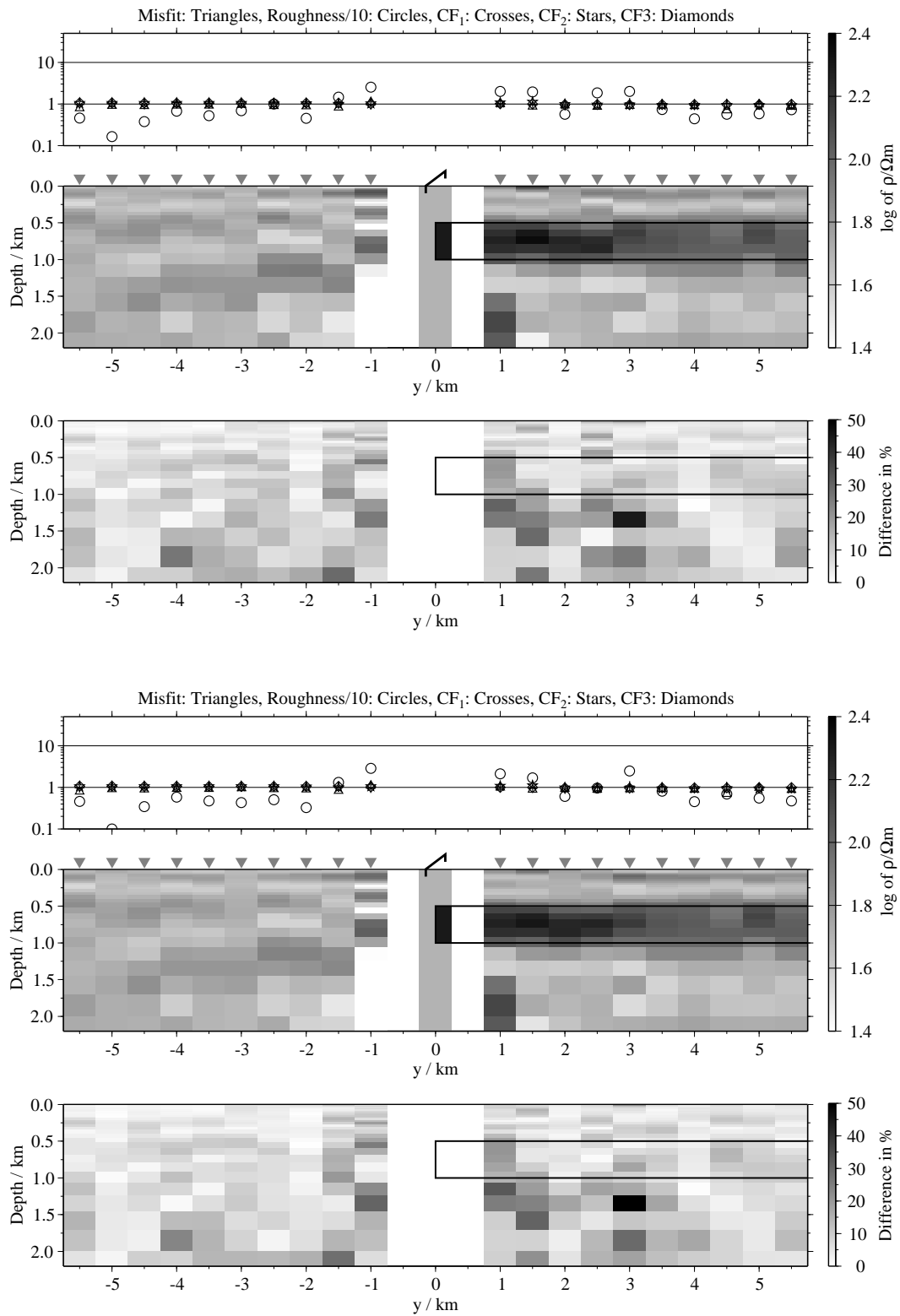


Figure B.93: Pseudo-sections of 1-D soft joint-inversions using all three components, model E2; Top panels: Average inversion results and relative differences (regularisation scheme C1); bottom: Average inversion results and relative differences (regularisation scheme C4);

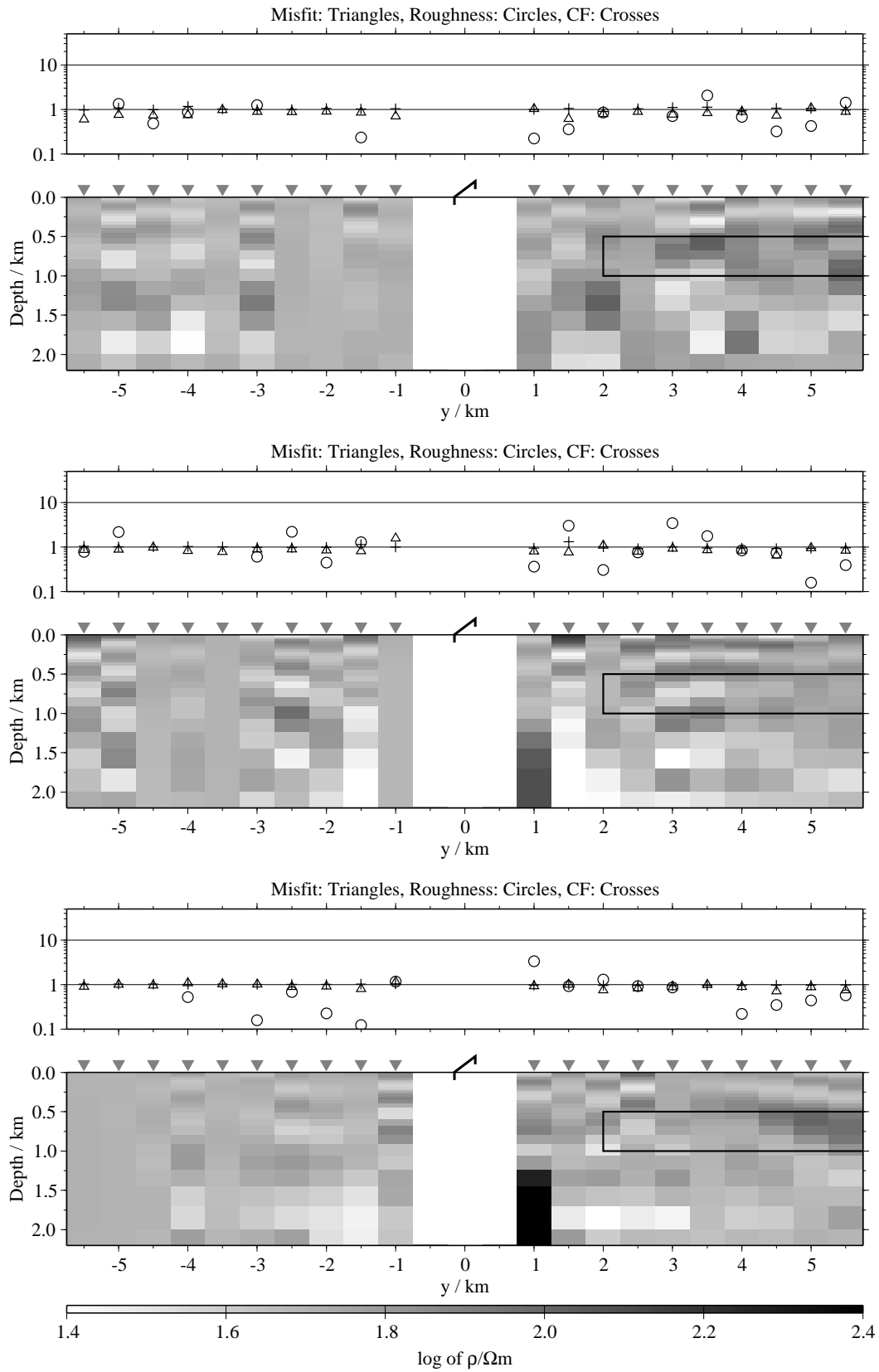


Figure B.94: Pseudo-sections of single 1-D inversion, model E3, regularisation scheme C1; from top to bottom E_{x^-} , \dot{H}_y^- and \dot{H}_z^- -component;

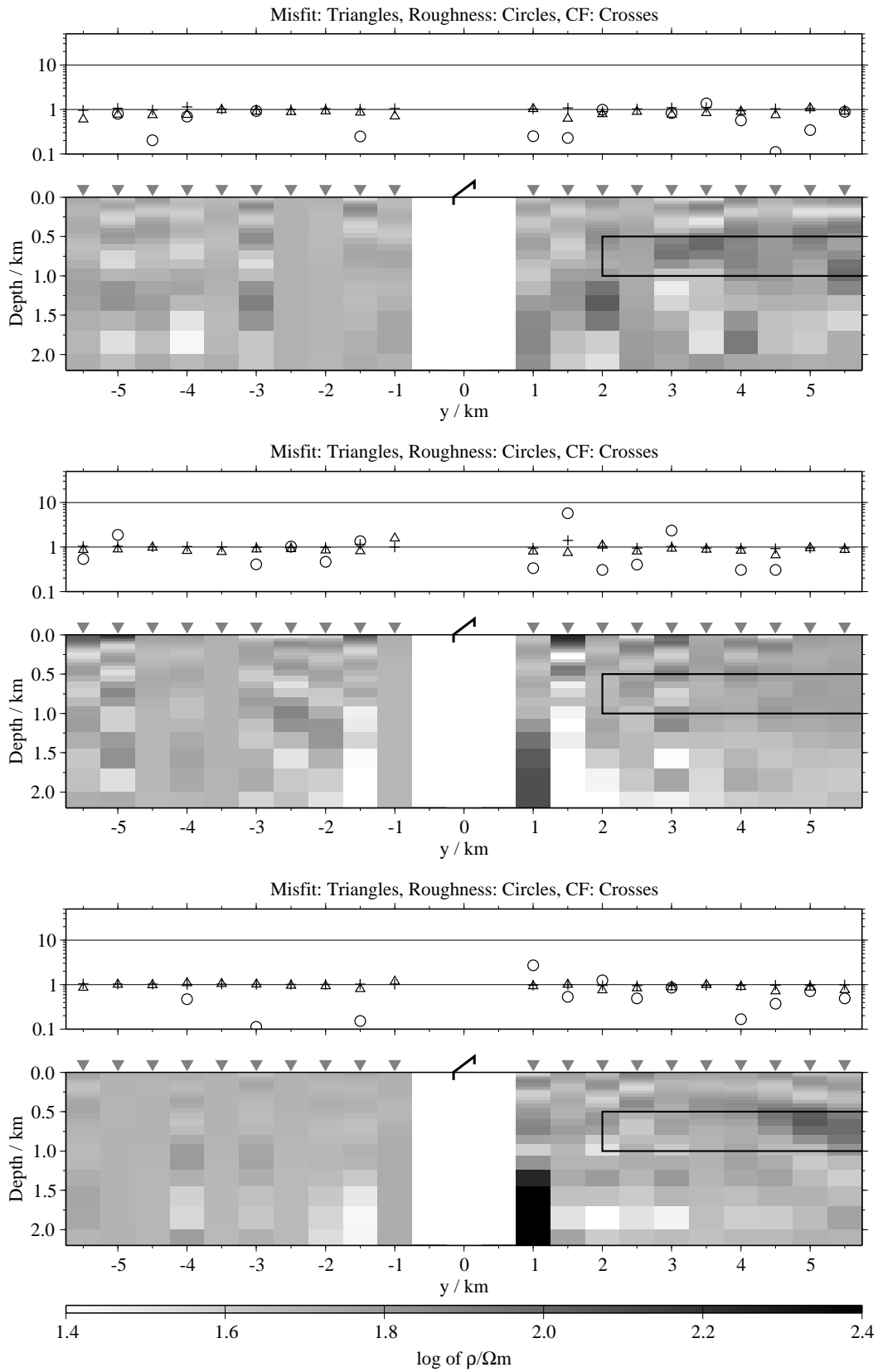


Figure B.95: Pseudo-sections of single 1-D inversion, model E3, regularisation scheme C4; from top to bottom E_x -, H_y - and H_z -component;

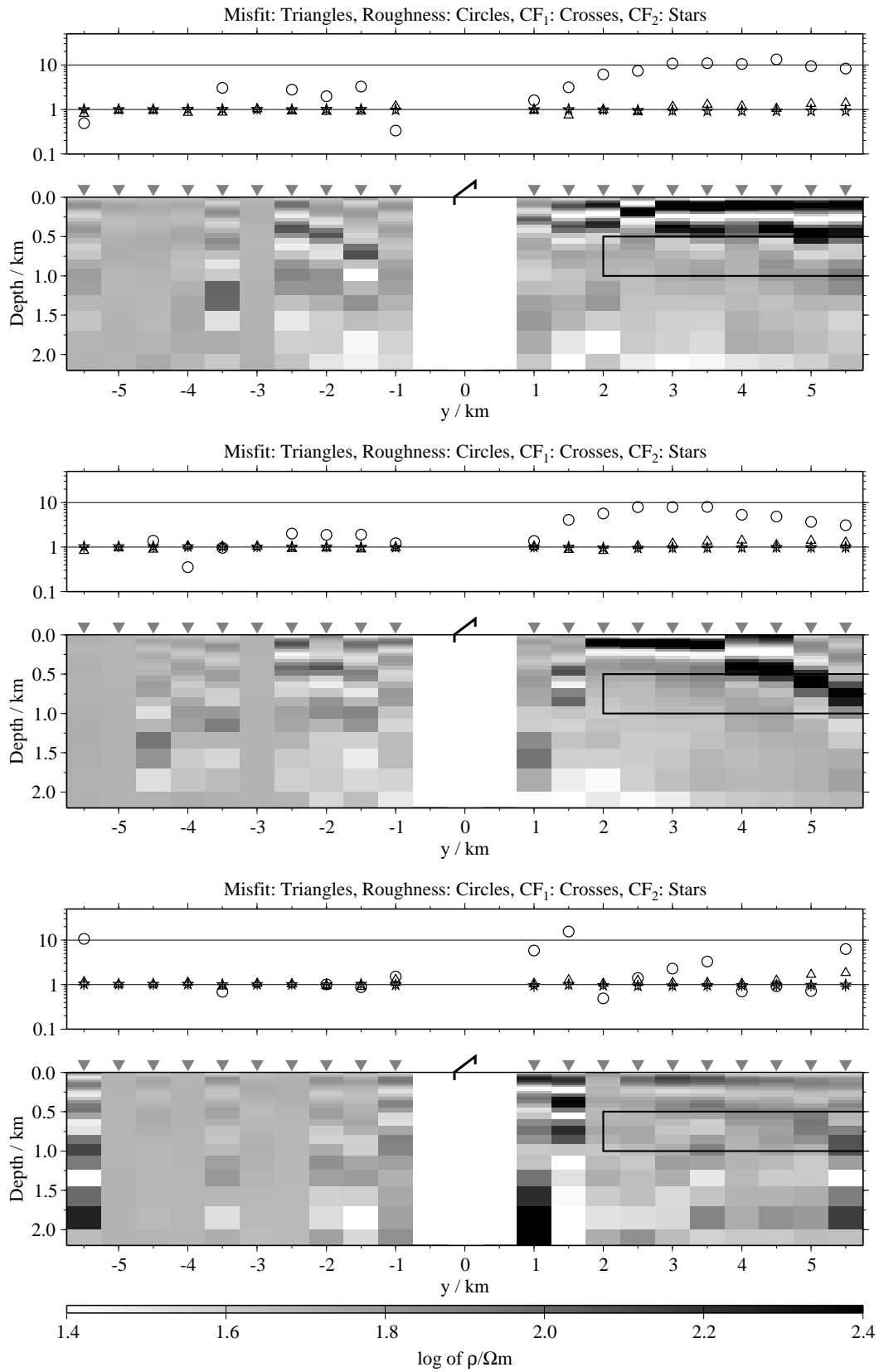


Figure B.96: Pseudo-sections of two component 1-D joint-inversions, model E3, regularisation scheme C1; from top to bottom $E_x-\dot{H}_y$, $E_x-\dot{H}_z$ and $\dot{H}_y-\dot{H}_z$;

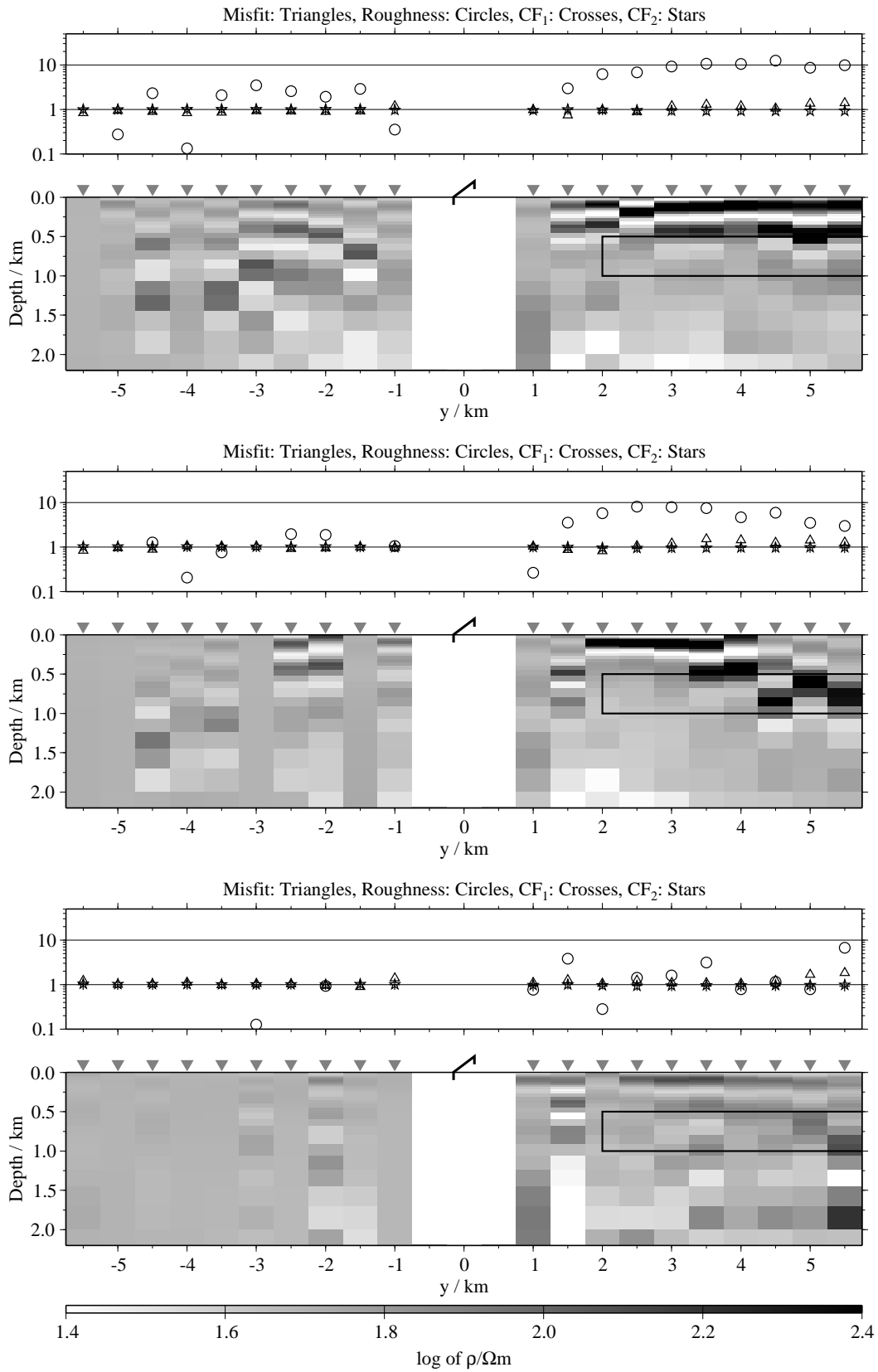


Figure B.97: Pseudo-sections of two component 1-D joint-inversions, model E3, regularisation scheme C4; from top to bottom $E_x\text{-}\dot{H}_y$, $E_x\text{-}\dot{H}_z$ and $\dot{H}_y\text{-}\dot{H}_z$;

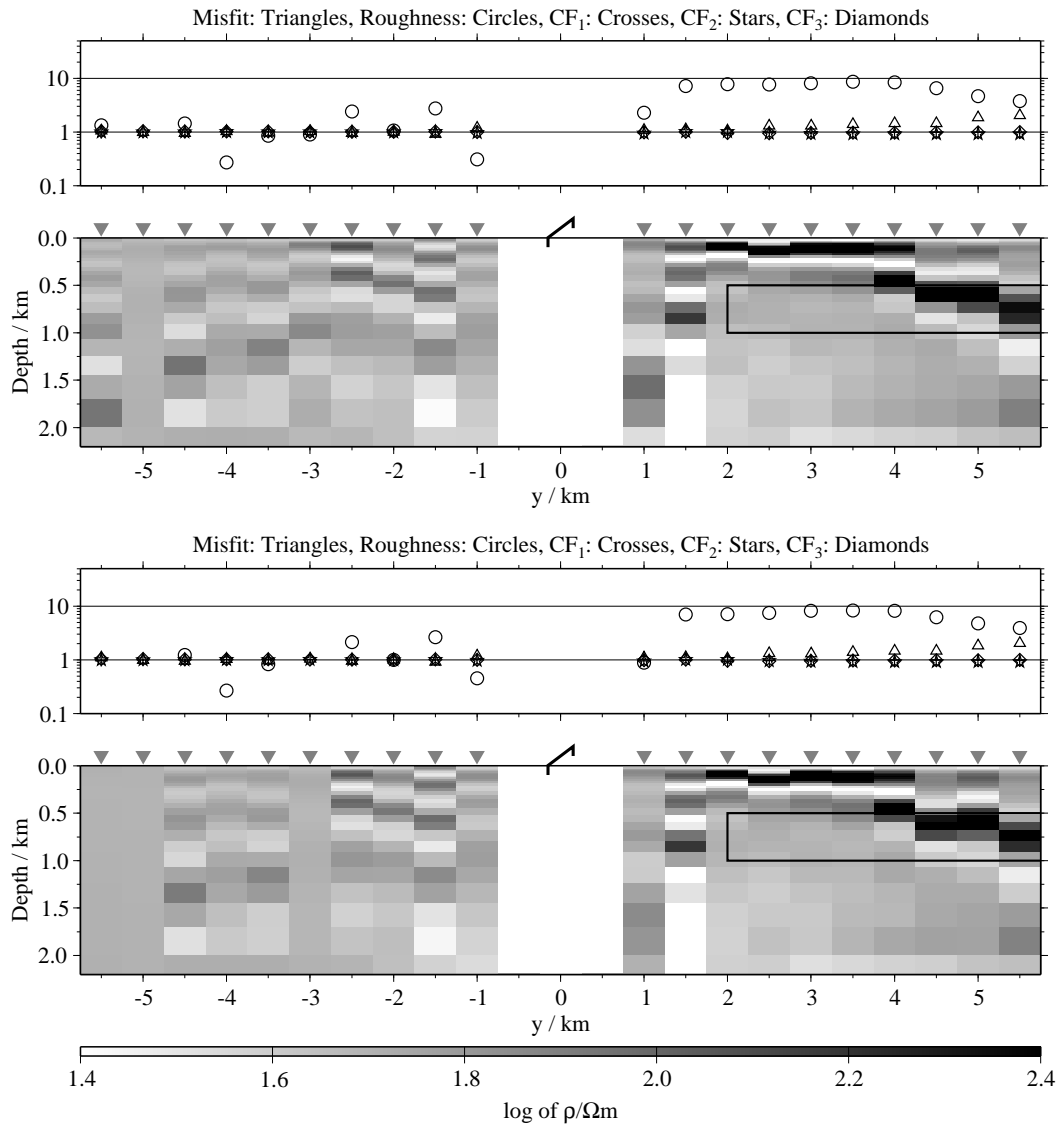


Figure B.98: Pseudo-sections of 1-D joint-inversions using all three components, model E3; top: Regularisation scheme C1; bottom: Regularisation scheme C4;

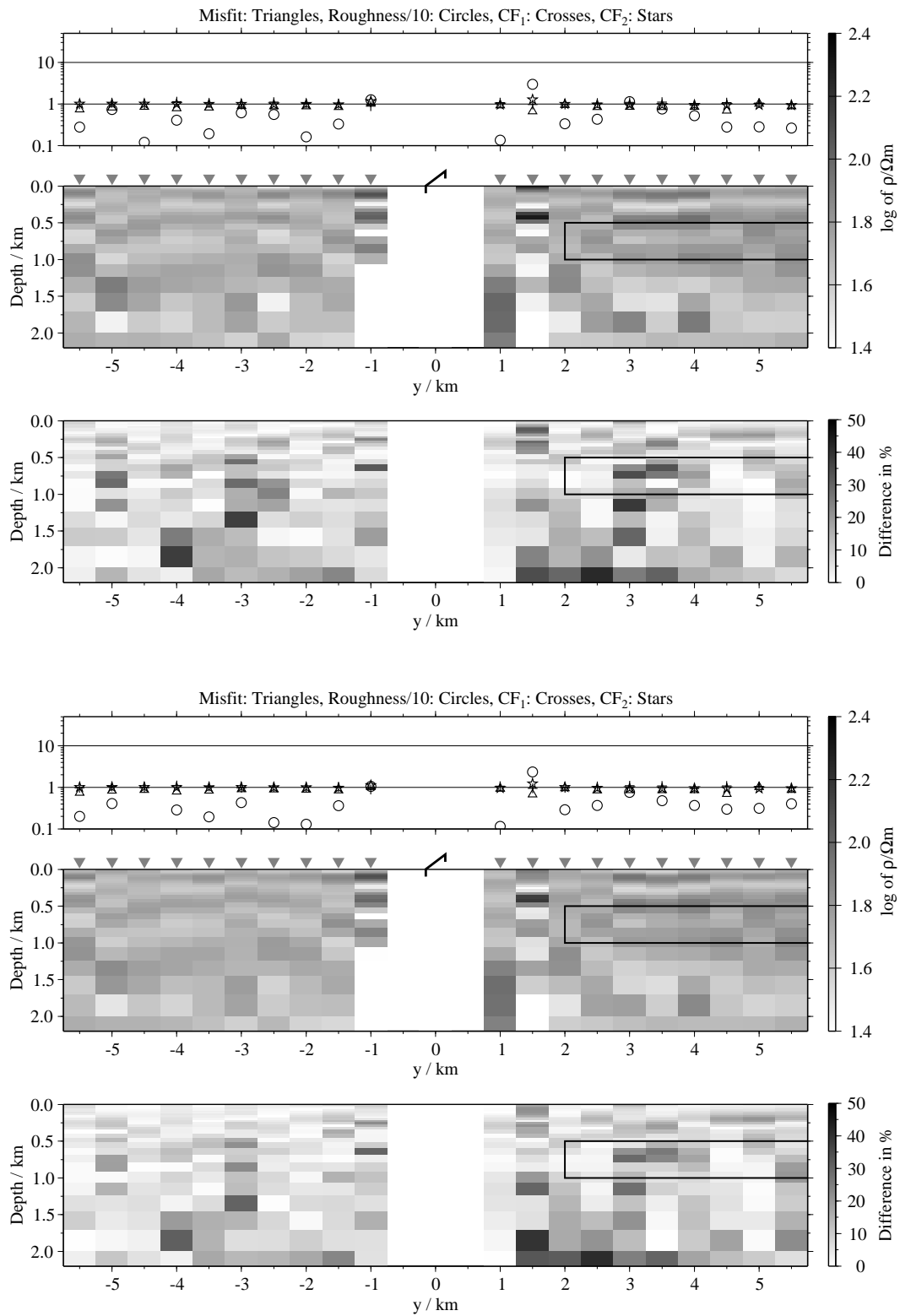


Figure B.99: Pseudo-sections of 1-D soft joint-inversions using the components E_x and H_y , model E3; Top panels: Average inversion results and relative differences (regularisation scheme C1); bottom: Average inversion results and relative differences (regularisation scheme C4);

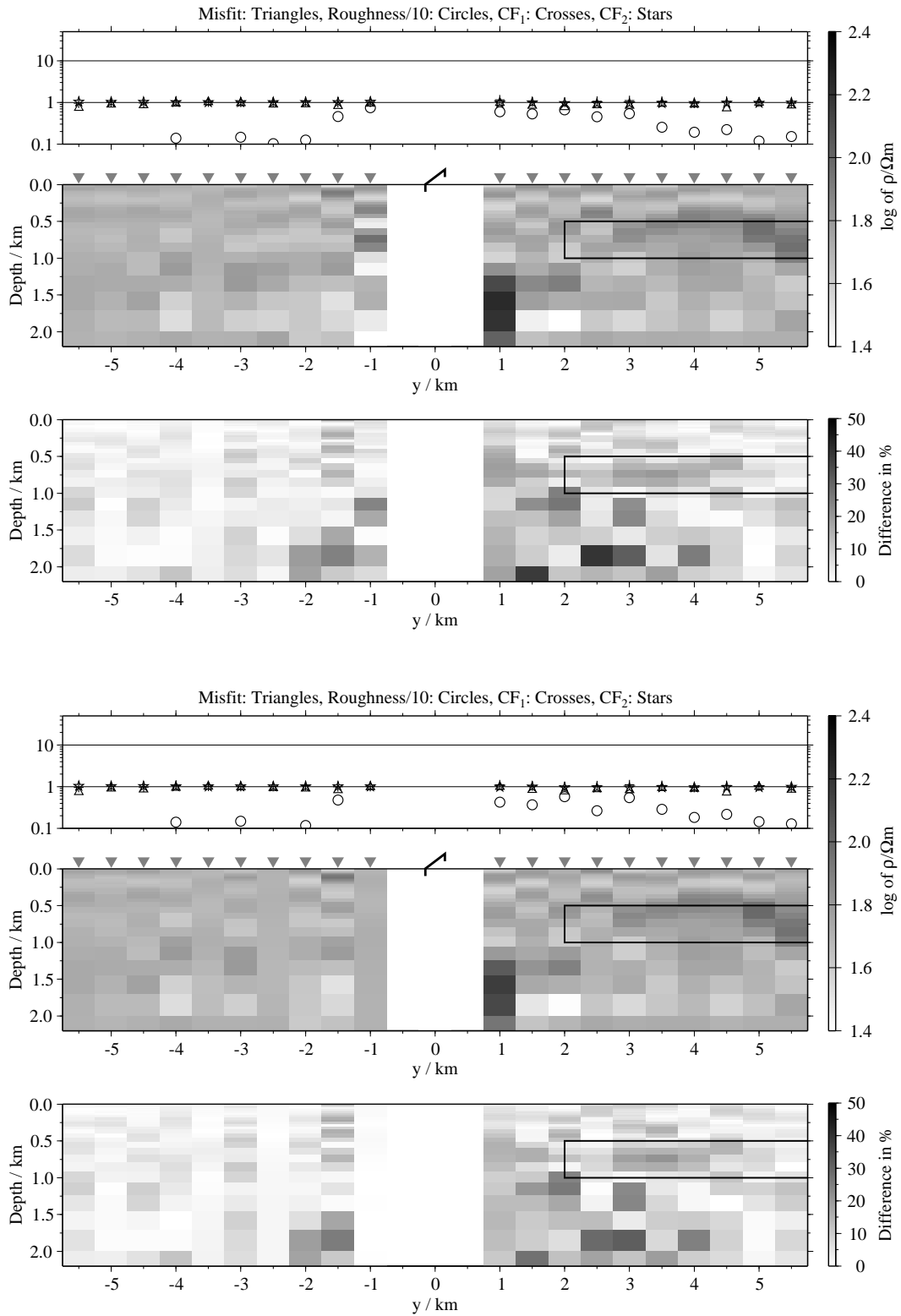


Figure B.100: Pseudo-sections 1-D of soft joint-inversions using the components E_x and H_z , model E3; Top panels: Average inversion results and relative differences (regularisation scheme C1); bottom: Average inversion results and relative differences (regularisation scheme C4);

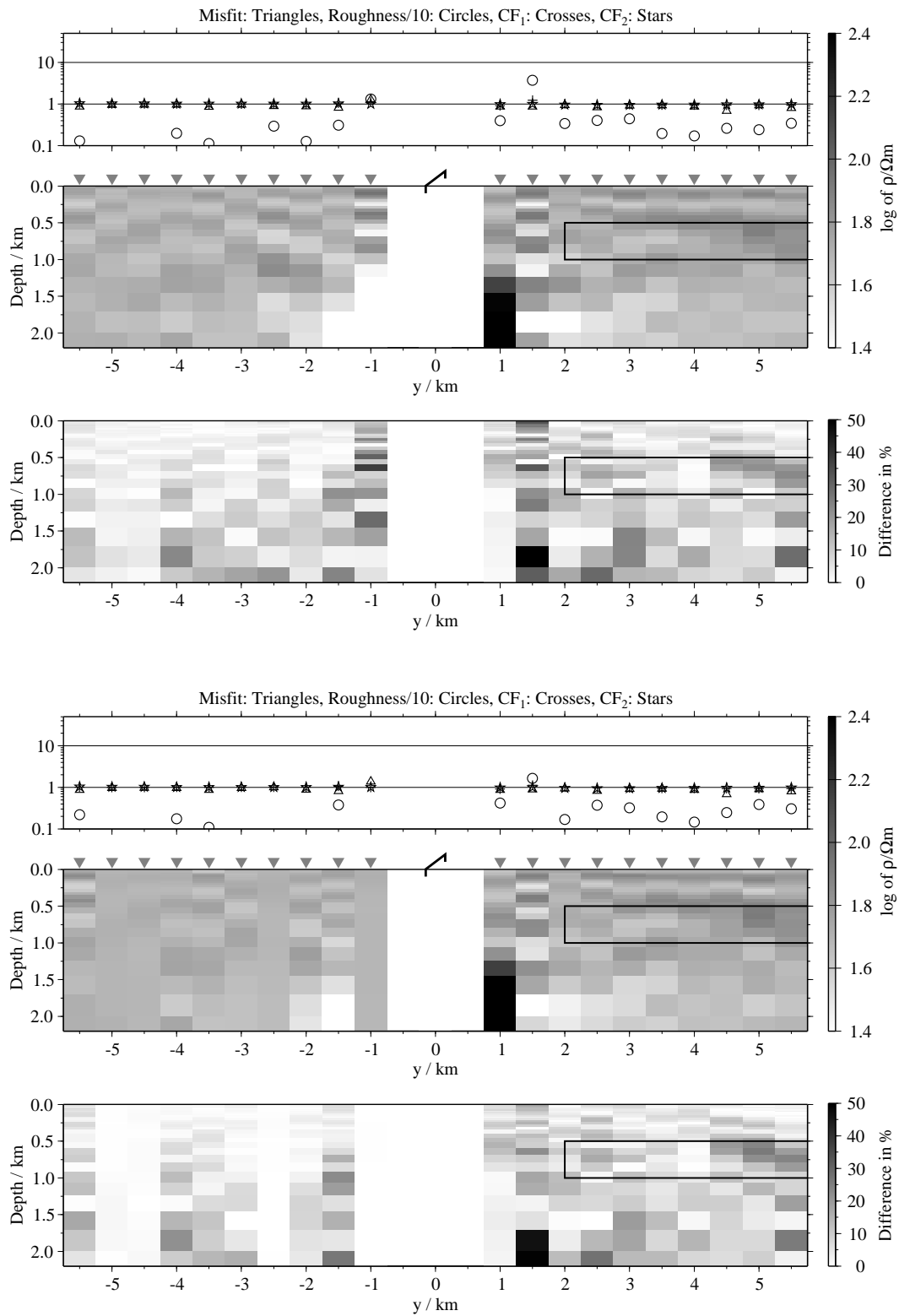


Figure B.101: Pseudo-sections of 1-D soft joint-inversions using the components \dot{H}_y and \dot{H}_{zi} , model E3; Top panels: Average inversion results and relative differences (regularisation scheme C1); bottom: Average inversion results and relative differences (regularisation scheme C4);

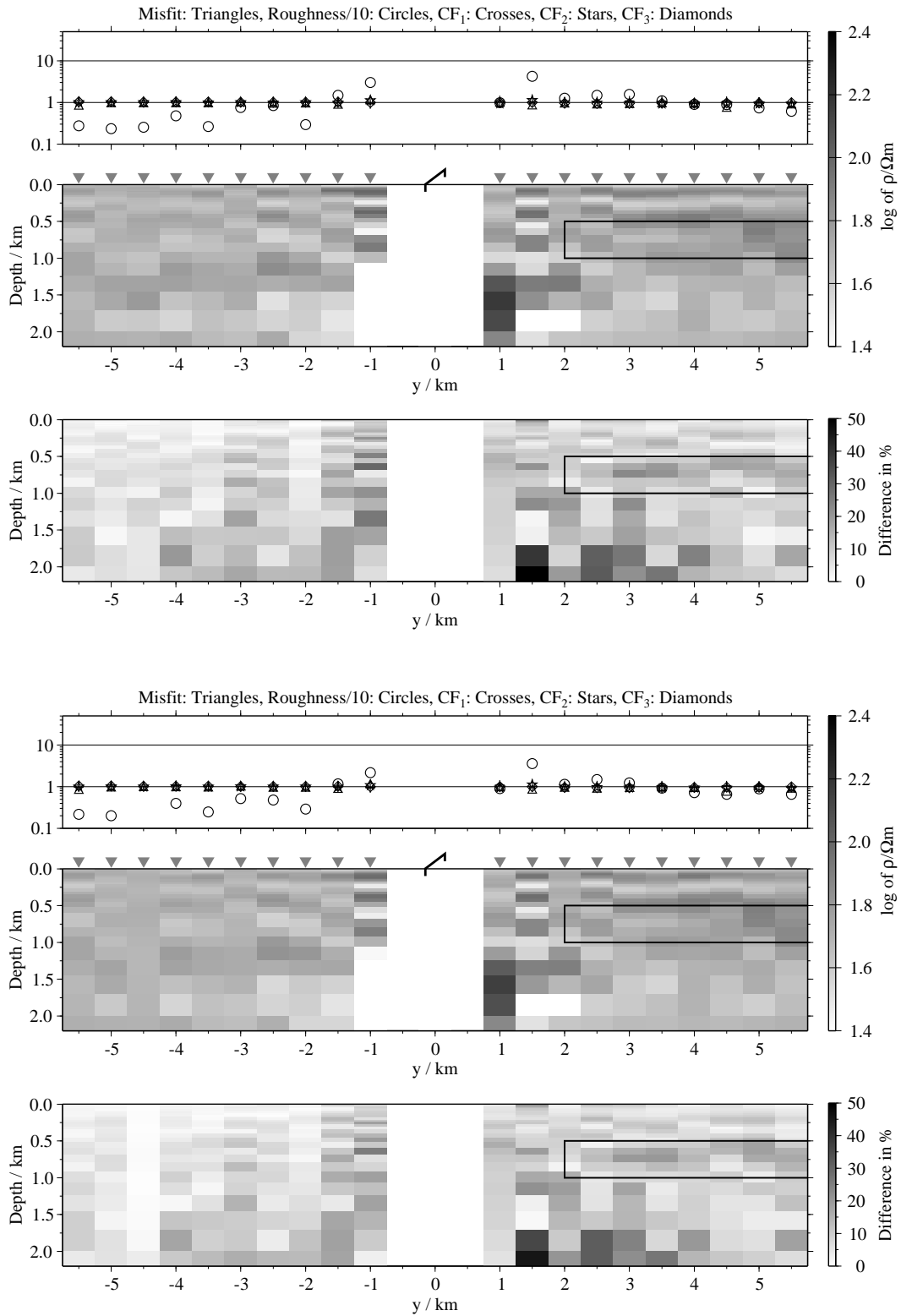
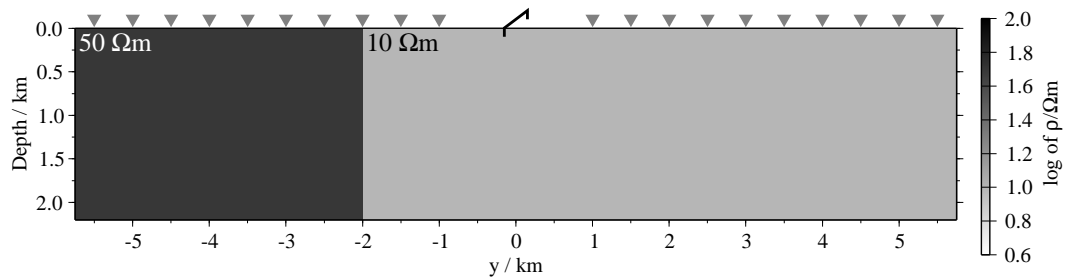


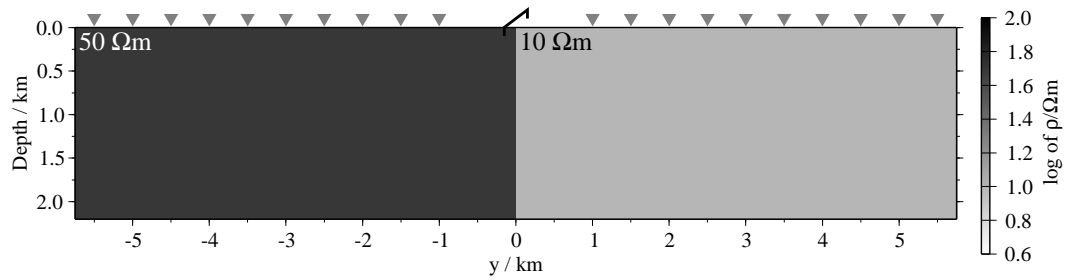
Figure B.102: Pseudo-sections of 1-D soft joint-inversions using all three components, model E3; Top panels: Average inversion results and relative differences (regularisation scheme C1); bottom: Average inversion results and relative differences (regularisation scheme C4);

B.2.4 Extreme case of a fault: Two quarter-spaces (models F1 to F3)

Model F1:



Model F2:



Model F3:

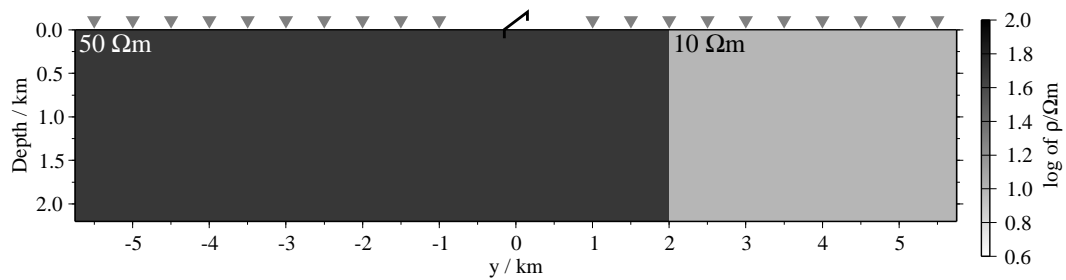


Figure B.103: Model consisting of two quarter-spaces; the fault-line is at $y = -2$ km (model F1), $y = 0$ km (model F2) and $y = 2$ km (model F3).

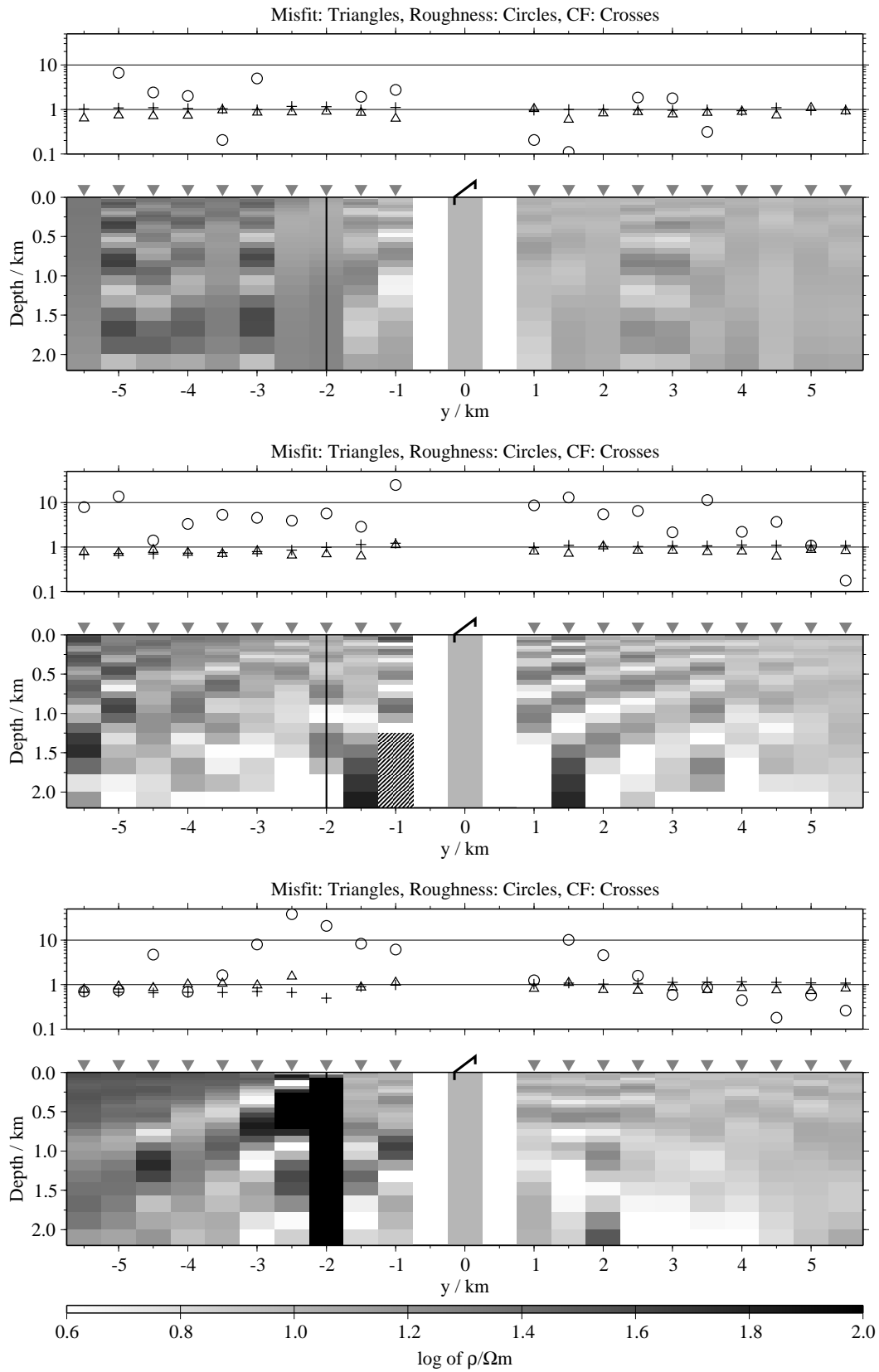


Figure B.104: Pseudo-sections of single 1-D inversion, model F1, regularisation scheme C1; from top to bottom E_x -, H_y - and H_z -component;

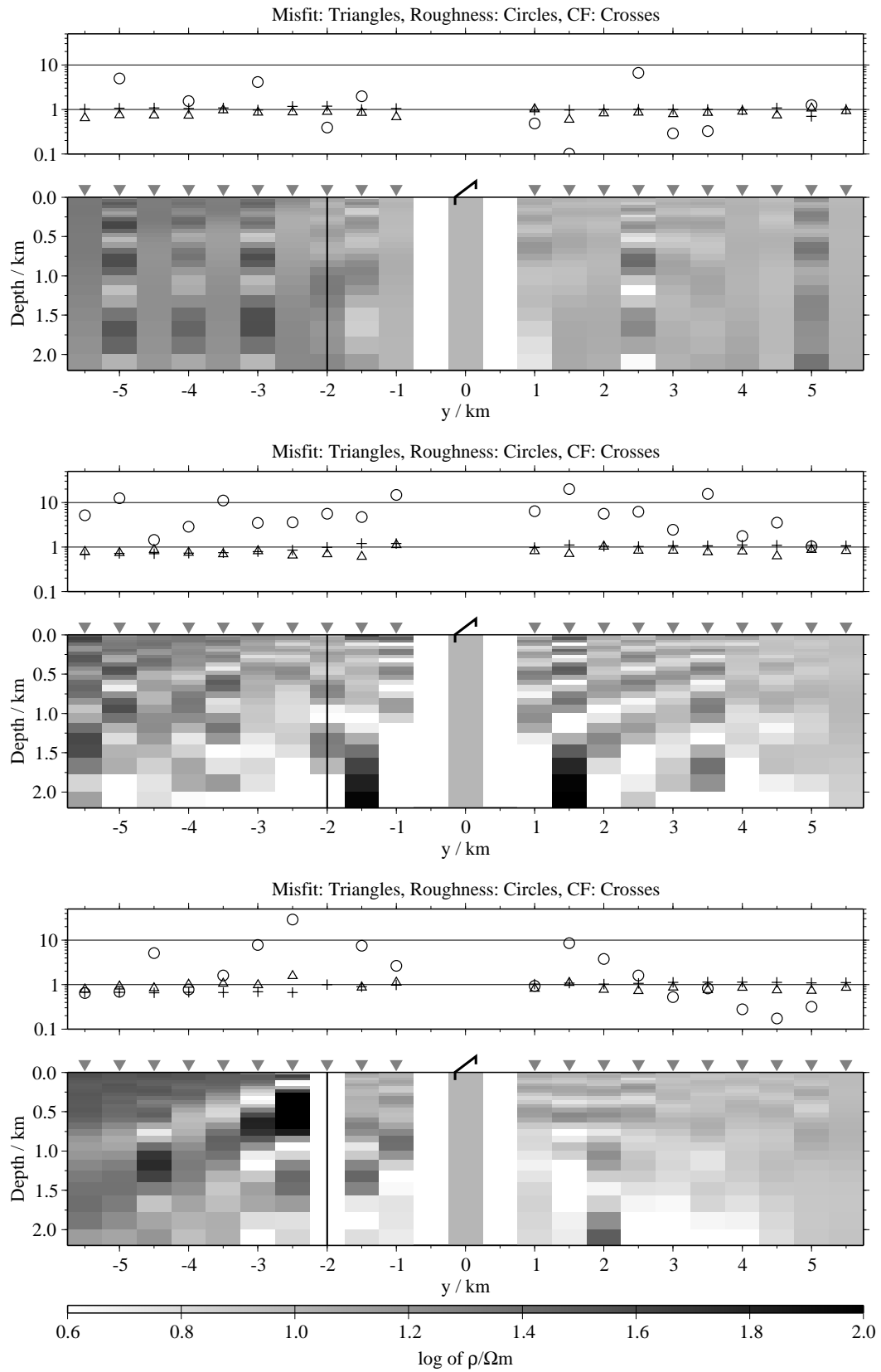


Figure B.105: Pseudo-sections of single 1-D inversion, model F1, regularisation scheme C4; from top to bottom E_x -, H_y - and H_z -component;

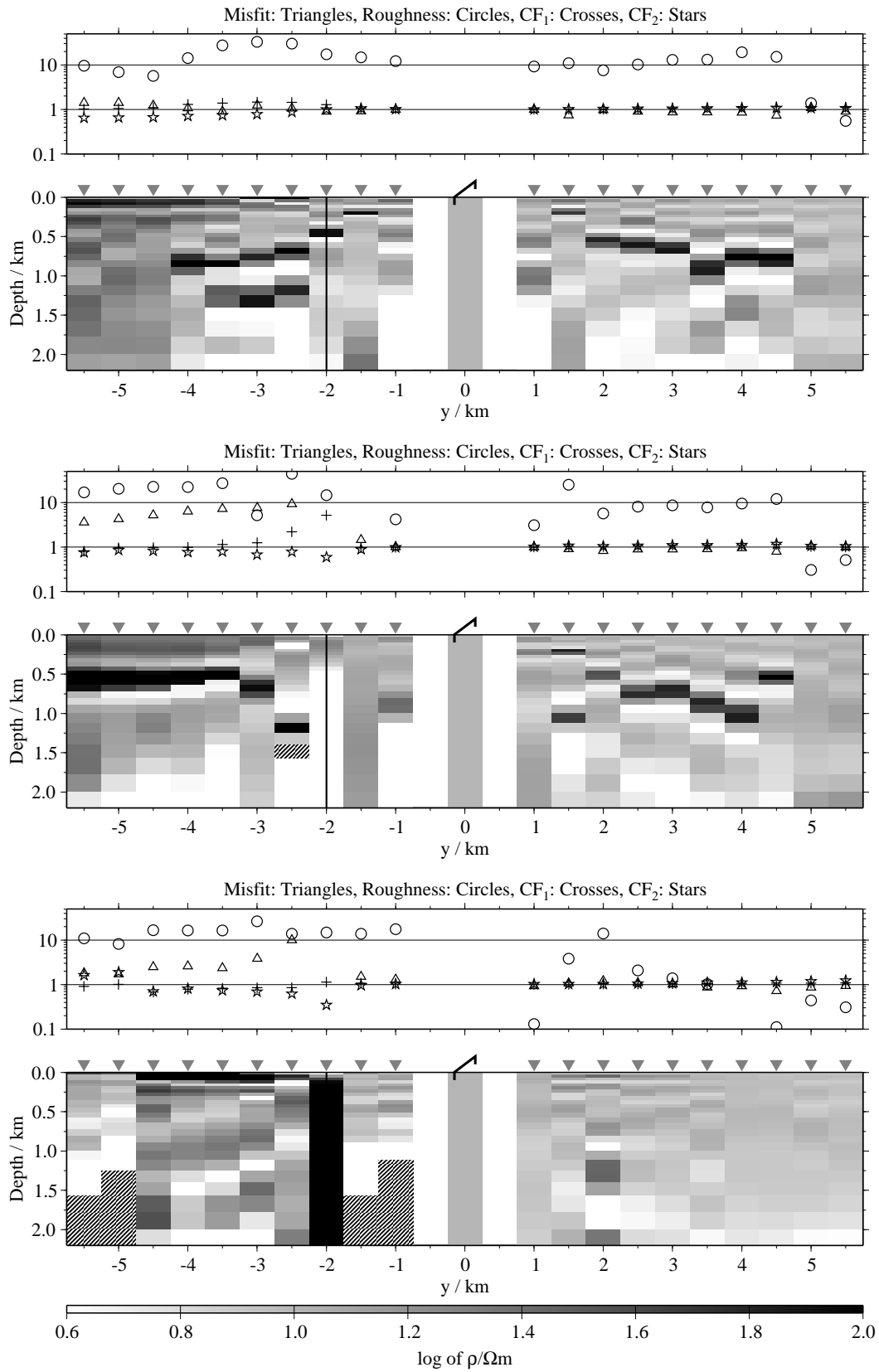


Figure B.106: Pseudo-sections of two component 1-D joint-inversions, model F1, regularisation scheme C1; from top to bottom $E_x-\dot{H}_y$, $E_x-\dot{H}_z$ and $\dot{H}_y-\dot{H}_z$;

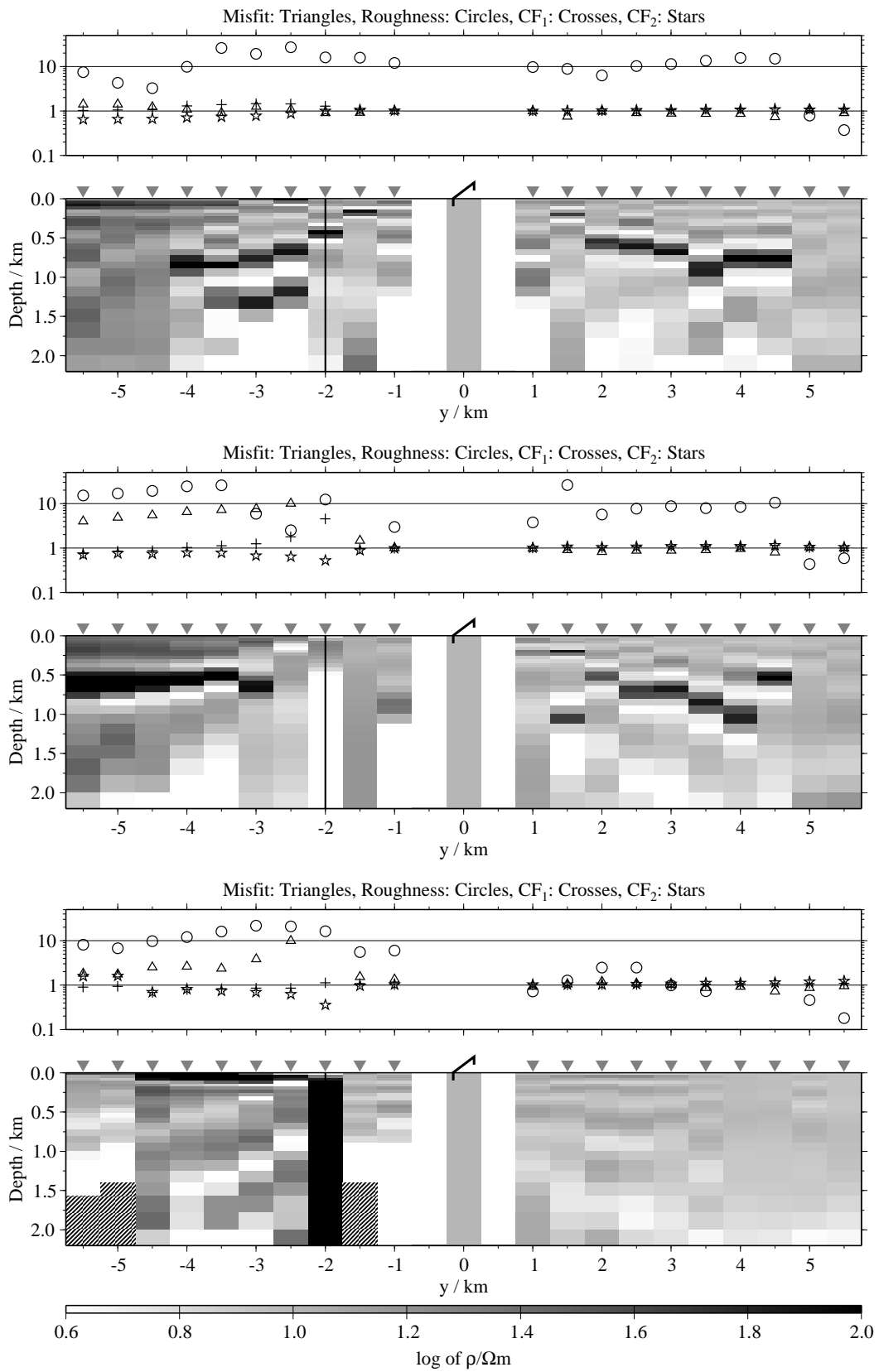


Figure B.107: Pseudo-sections of two component 1-D joint-inversions, model F1, regularisation scheme C4; from top to bottom $E_x\text{-}\dot{H}_y$, $E_x\text{-}\dot{H}_z$ and $\dot{H}_y\text{-}\dot{H}_z$;

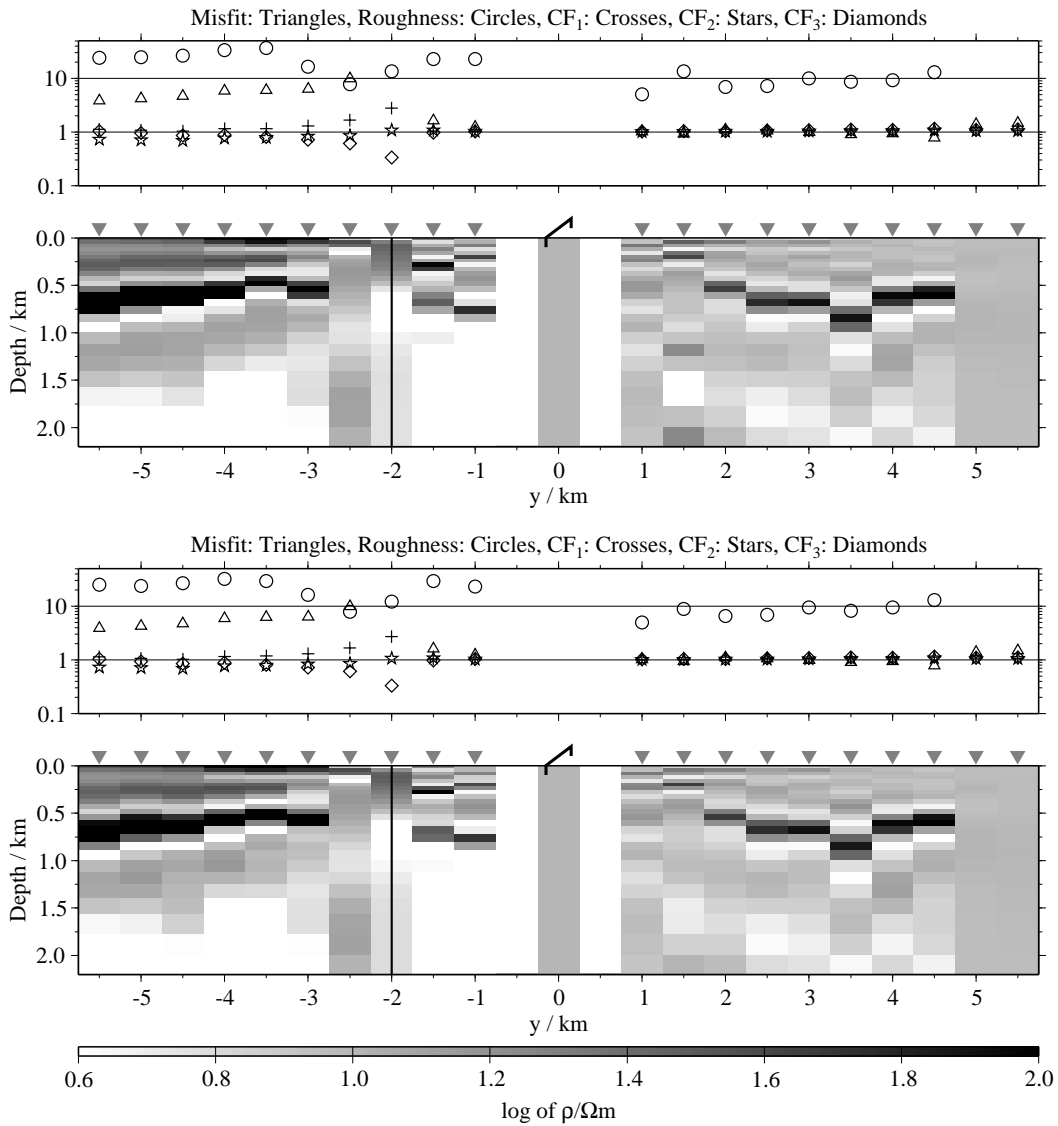


Figure B.108: Pseudo-sections of 1-D joint-inversions using all three components, model F1; top: Regularisation scheme C1; bottom: Regularisation scheme C4;

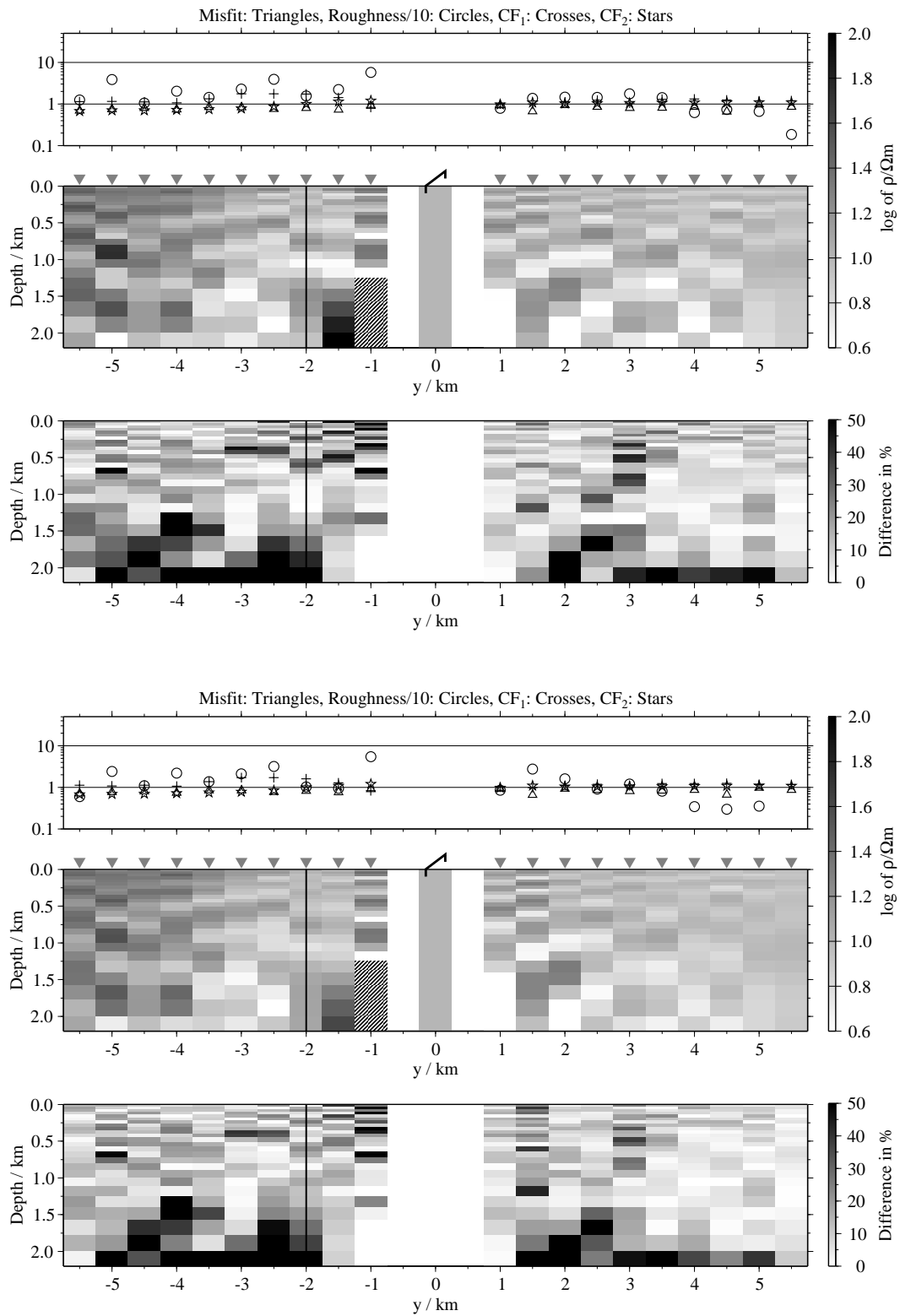


Figure B.109: Pseudo-sections of 1-D soft joint-inversions using the components E_x and H_y , model F1; Top panels: Average inversion results and relative differences (regularisation scheme C1); bottom: Average inversion results and relative differences (regularisation scheme C4);

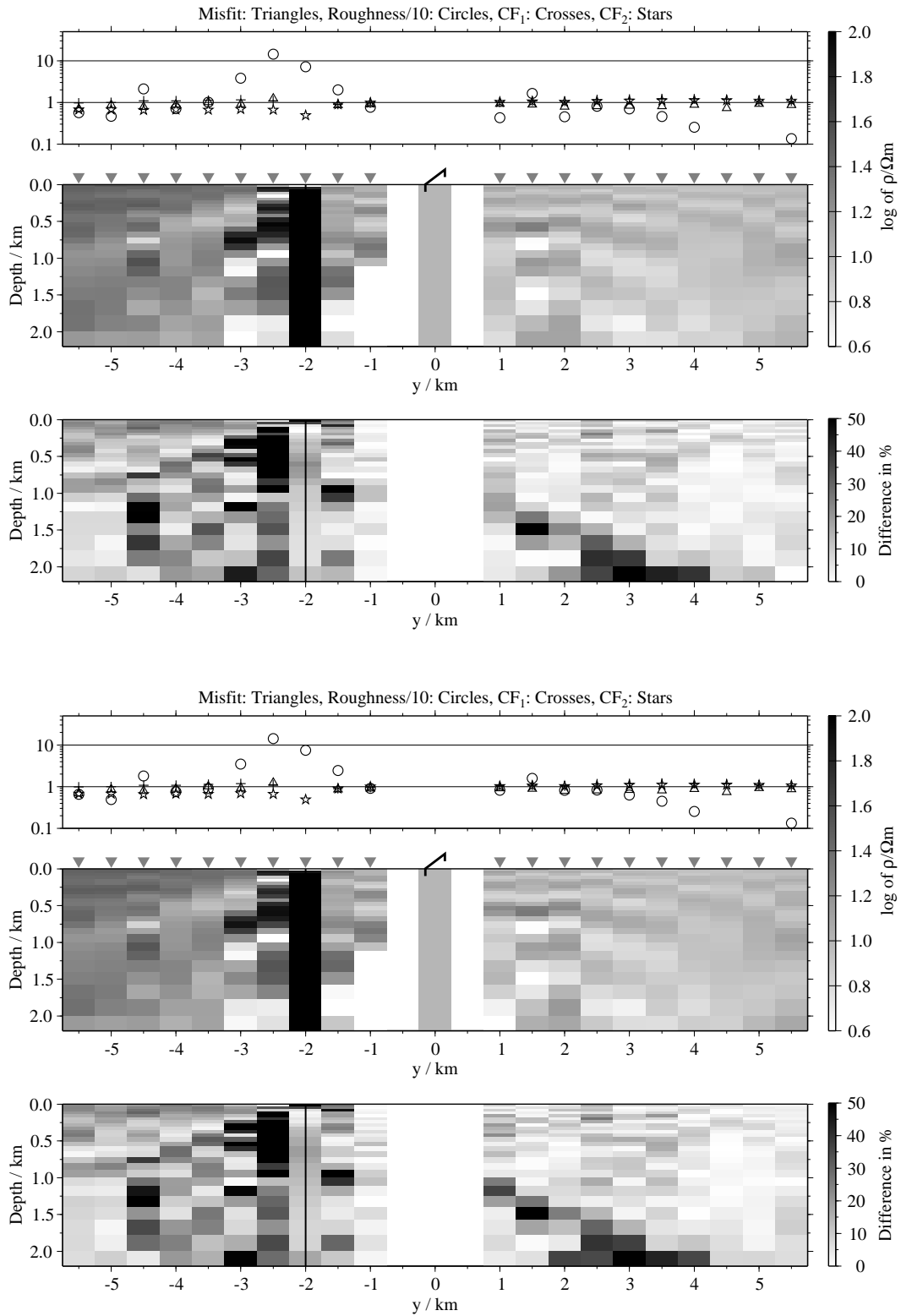


Figure B.110: Pseudo-sections 1-D of soft joint-inversions using the components E_x and H_z , model F1; Top panels: Average inversion results and relative differences (regularisation scheme C1); bottom: Average inversion results and relative differences (regularisation scheme C4);

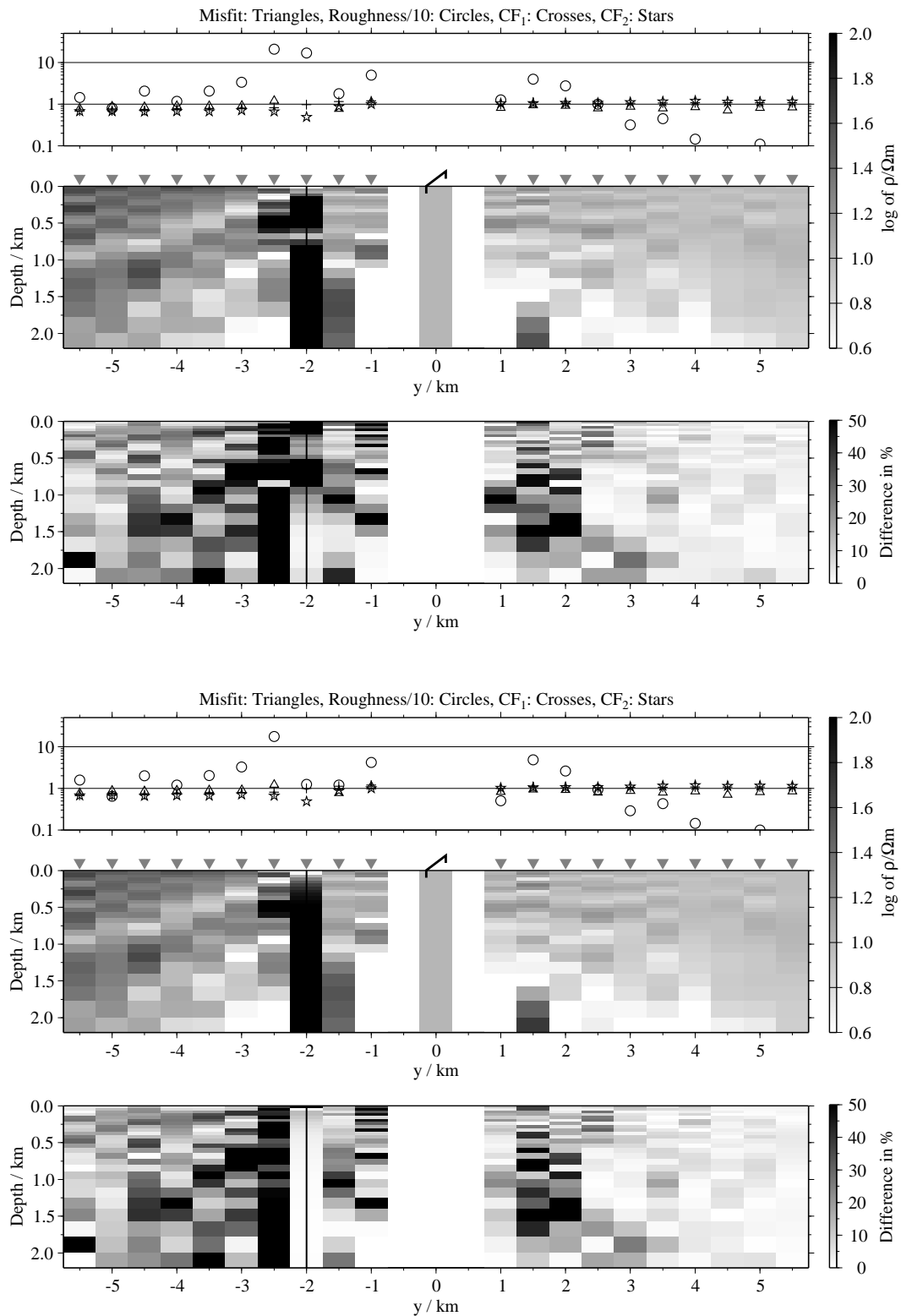


Figure B.111: Pseudo-sections of 1-D soft joint-inversions using the components \dot{H}_y and \dot{H}_{zi} , model F1; Top panels: Average inversion results and relative differences (regularisation scheme C1); bottom: Average inversion results and relative differences (regularisation scheme C4);

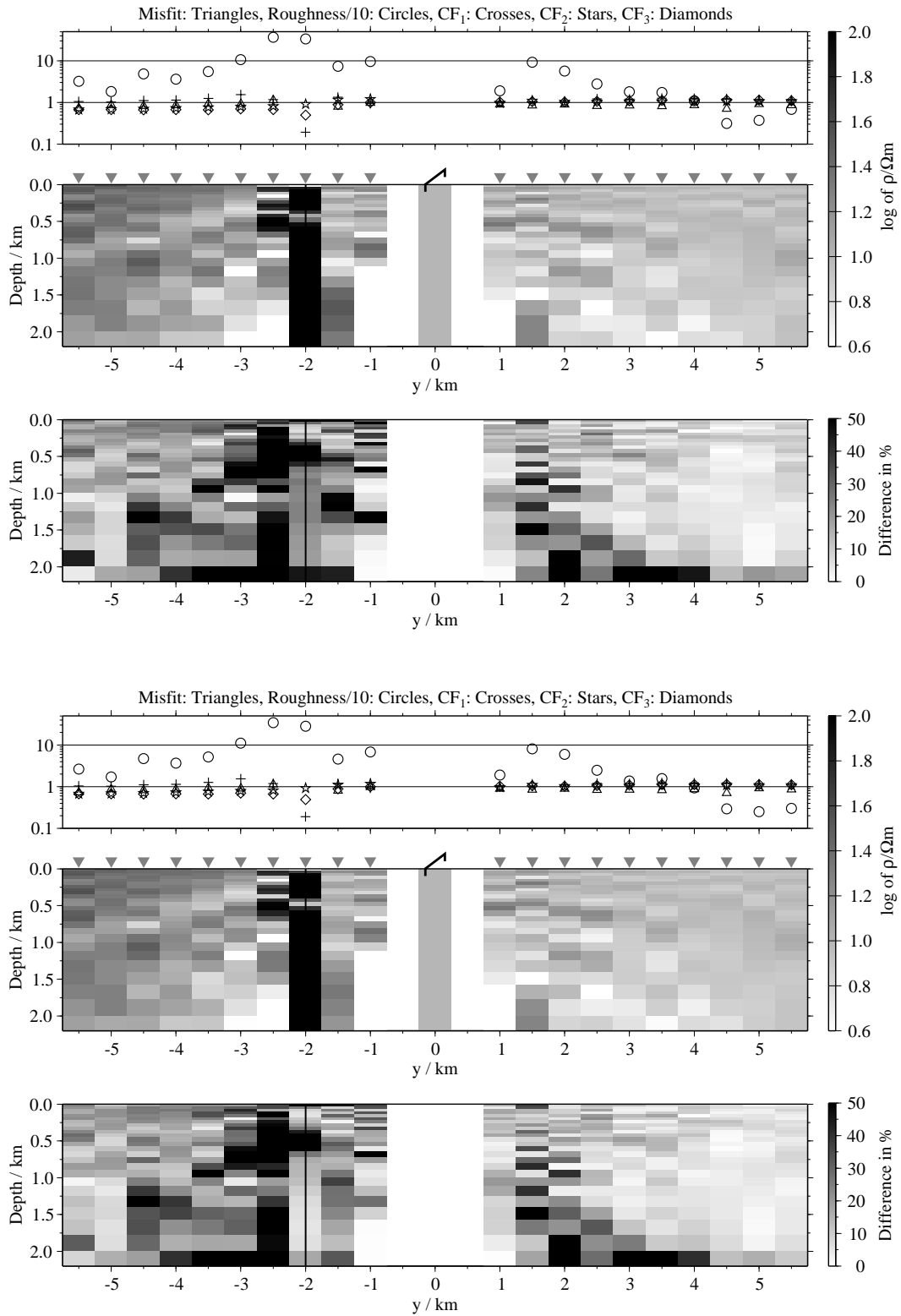


Figure B.112: Pseudo-sections of 1-D soft joint-inversions using all three components, model F1; Top panels: Average inversion results and relative differences (regularisation scheme C1); bottom: Average inversion results and relative differences (regularisation scheme C4);

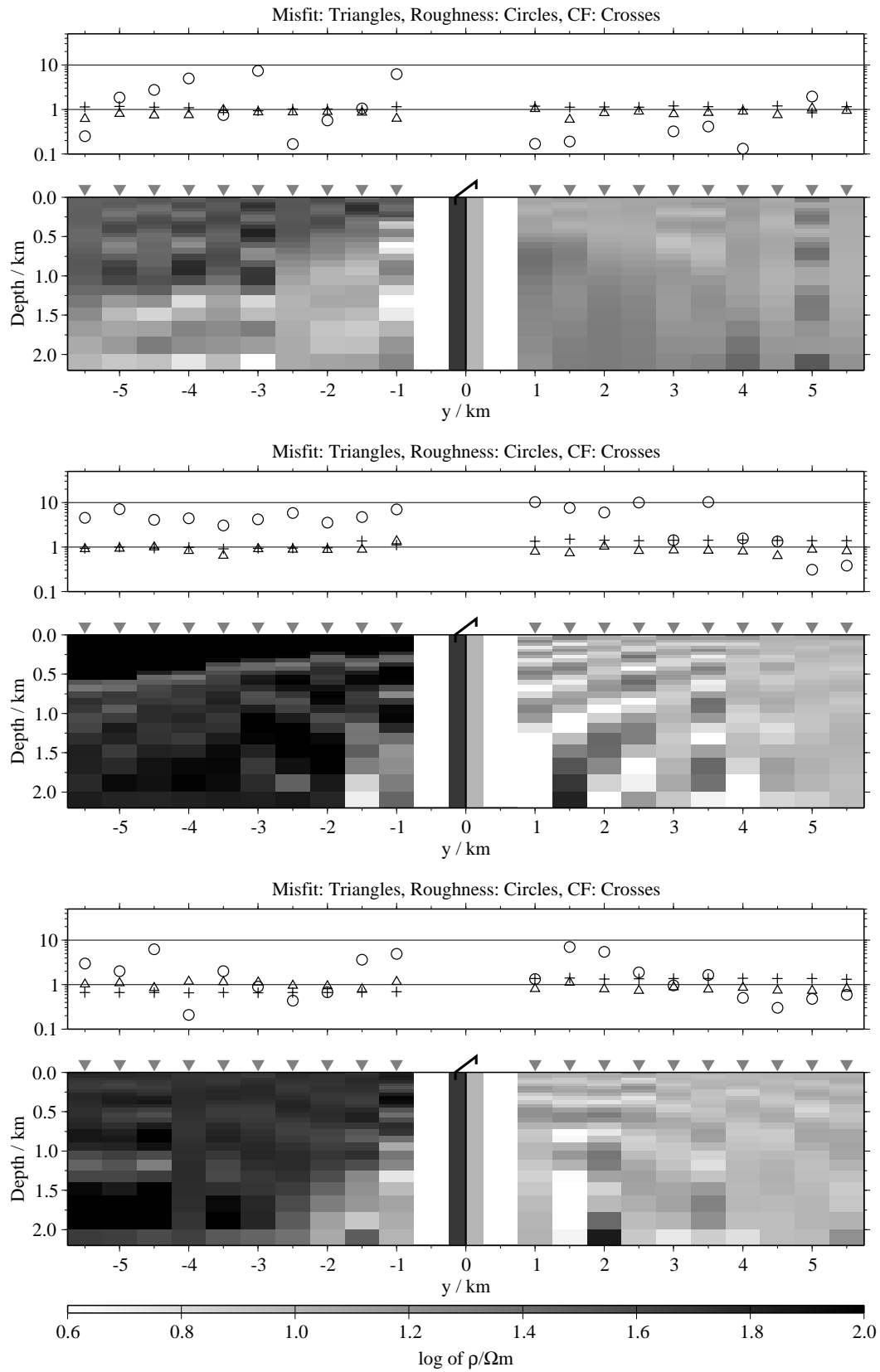


Figure B.113: Pseudo-sections of single 1-D inversion, model F2, regularisation scheme C1; from top to bottom E_x -, H_y - and H_z -component;

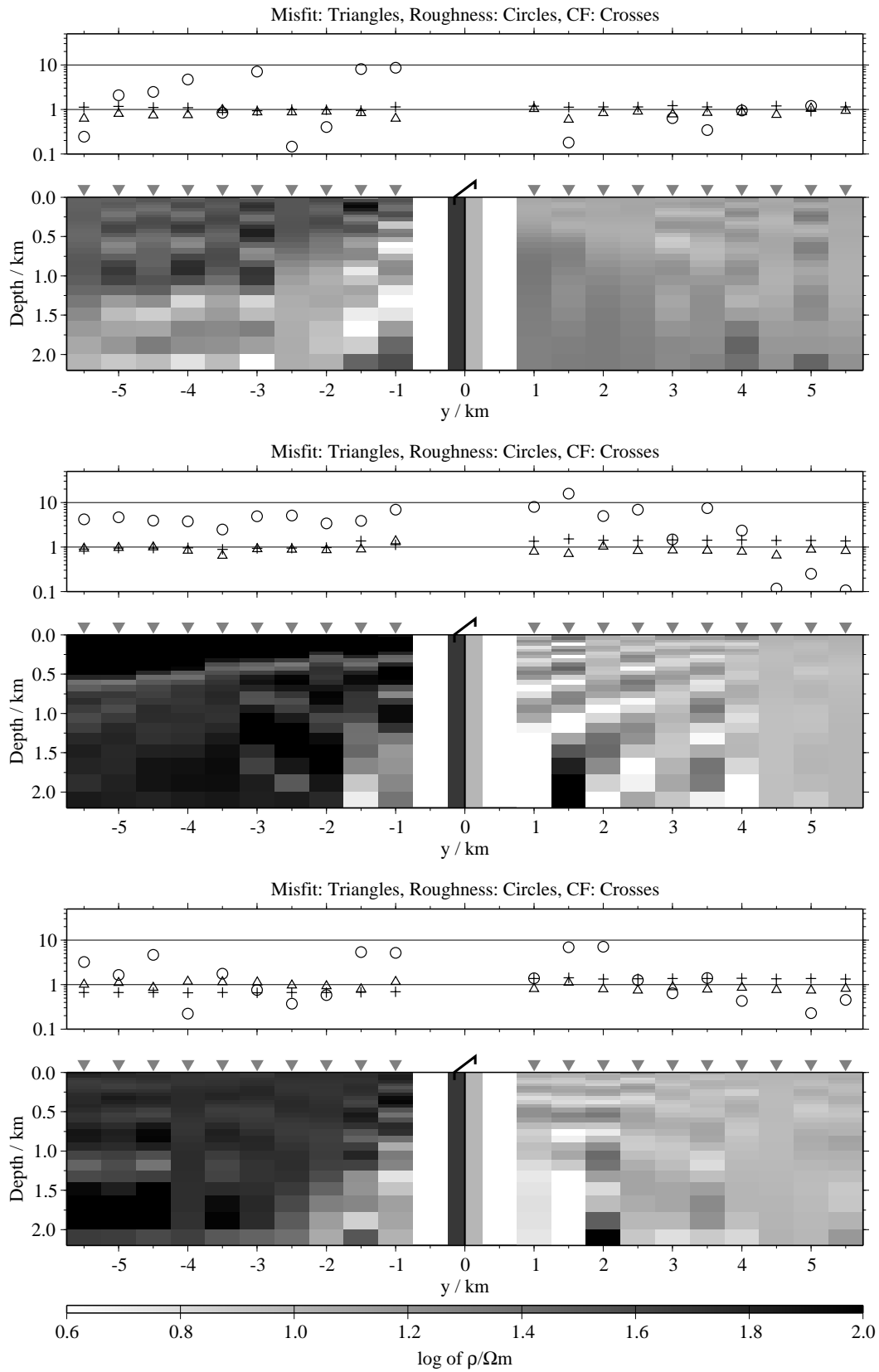


Figure B.114: Pseudo-sections of single 1-D inversion, model F2, regularisation scheme C4; from top to bottom E_x -, \dot{H}_y - and \dot{H}_z -component;

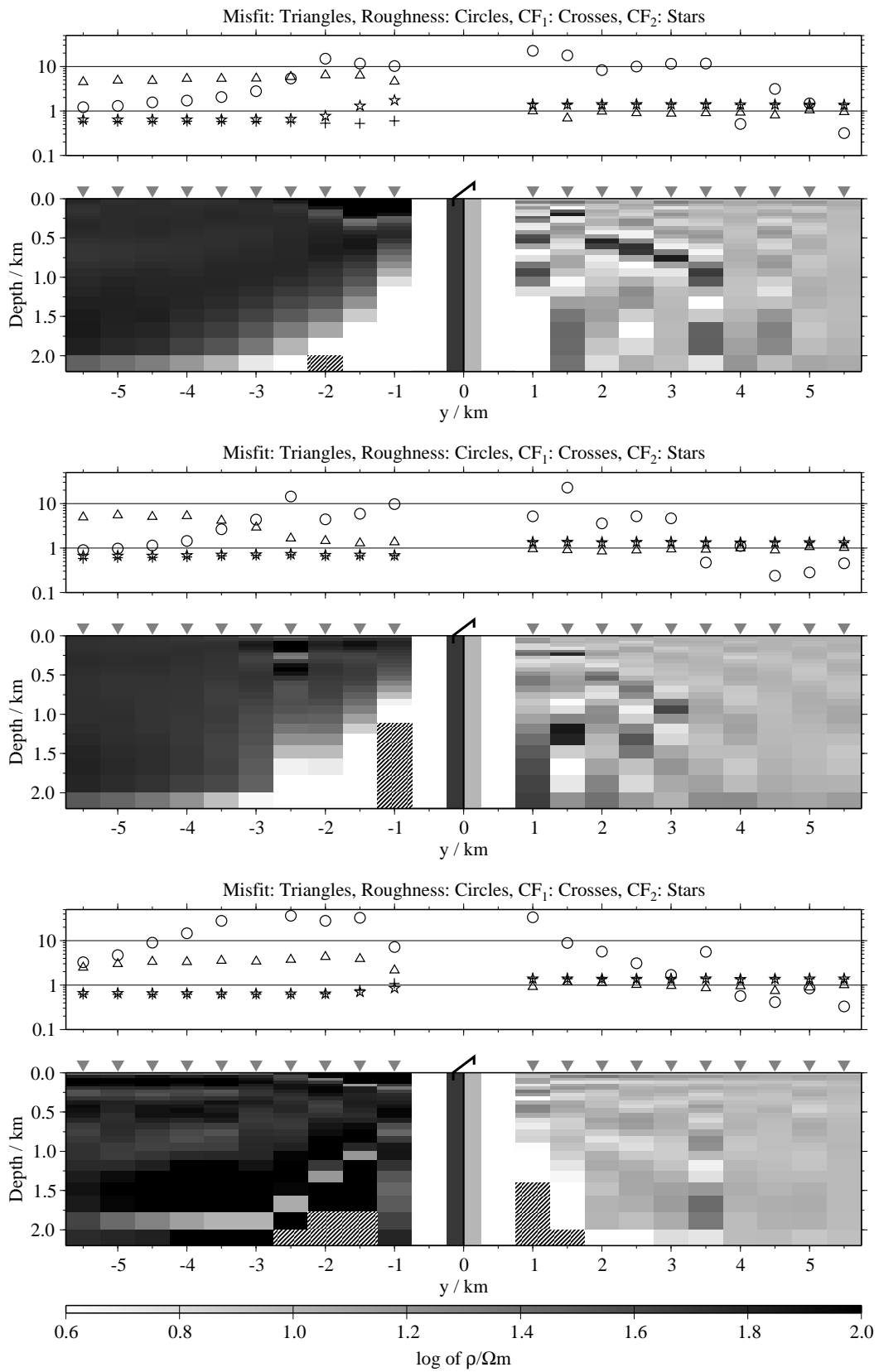


Figure B.115: Pseudo-sections of two component 1-D joint-inversions, model F2, regularisation scheme C1; from top to bottom $E_x-\dot{H}_y$, $E_x-\dot{H}_z$ and $\dot{H}_y-\dot{H}_z$;

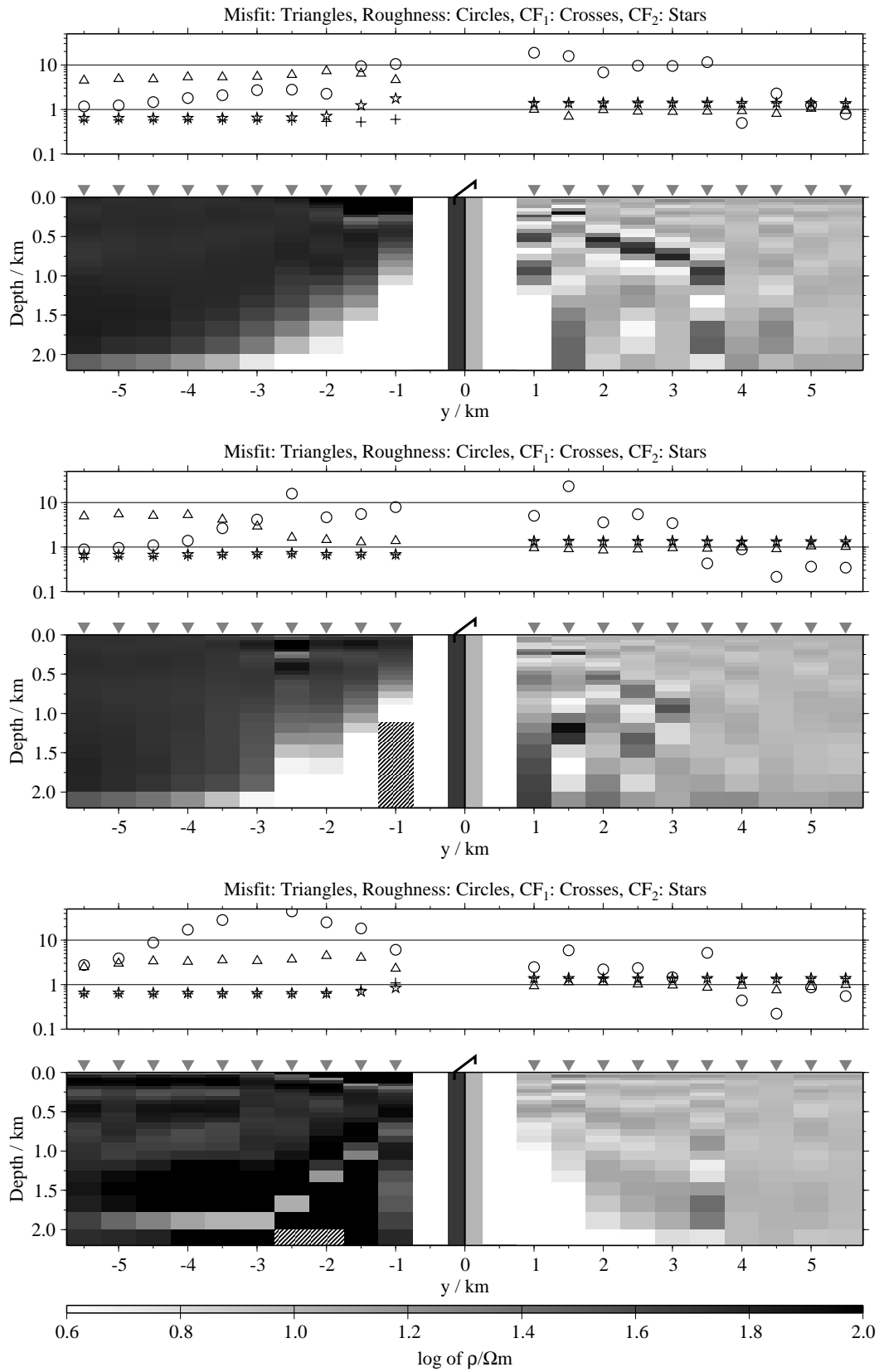


Figure B.116: Pseudo-sections of two component 1-D joint-inversions, model F2, regularisation scheme C4; from top to bottom $E_x-\dot{H}_y$, $E_x-\dot{H}_z$ and $\dot{H}_y-\dot{H}_z$;

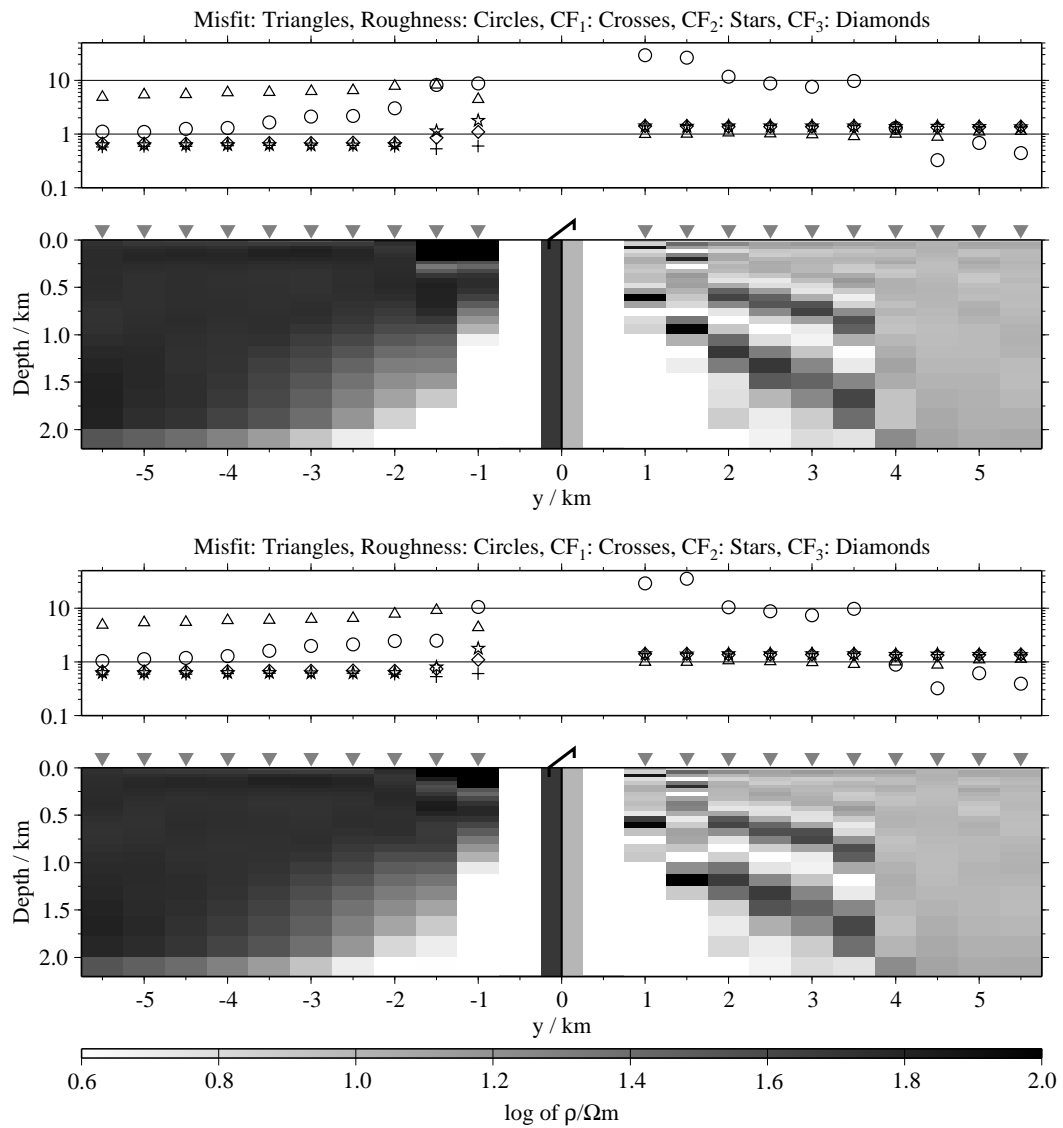


Figure B.117: Pseudo-sections of 1-D joint-inversions using all three components, model F2; top: Regularisation scheme C1; bottom: Regularisation scheme C4;

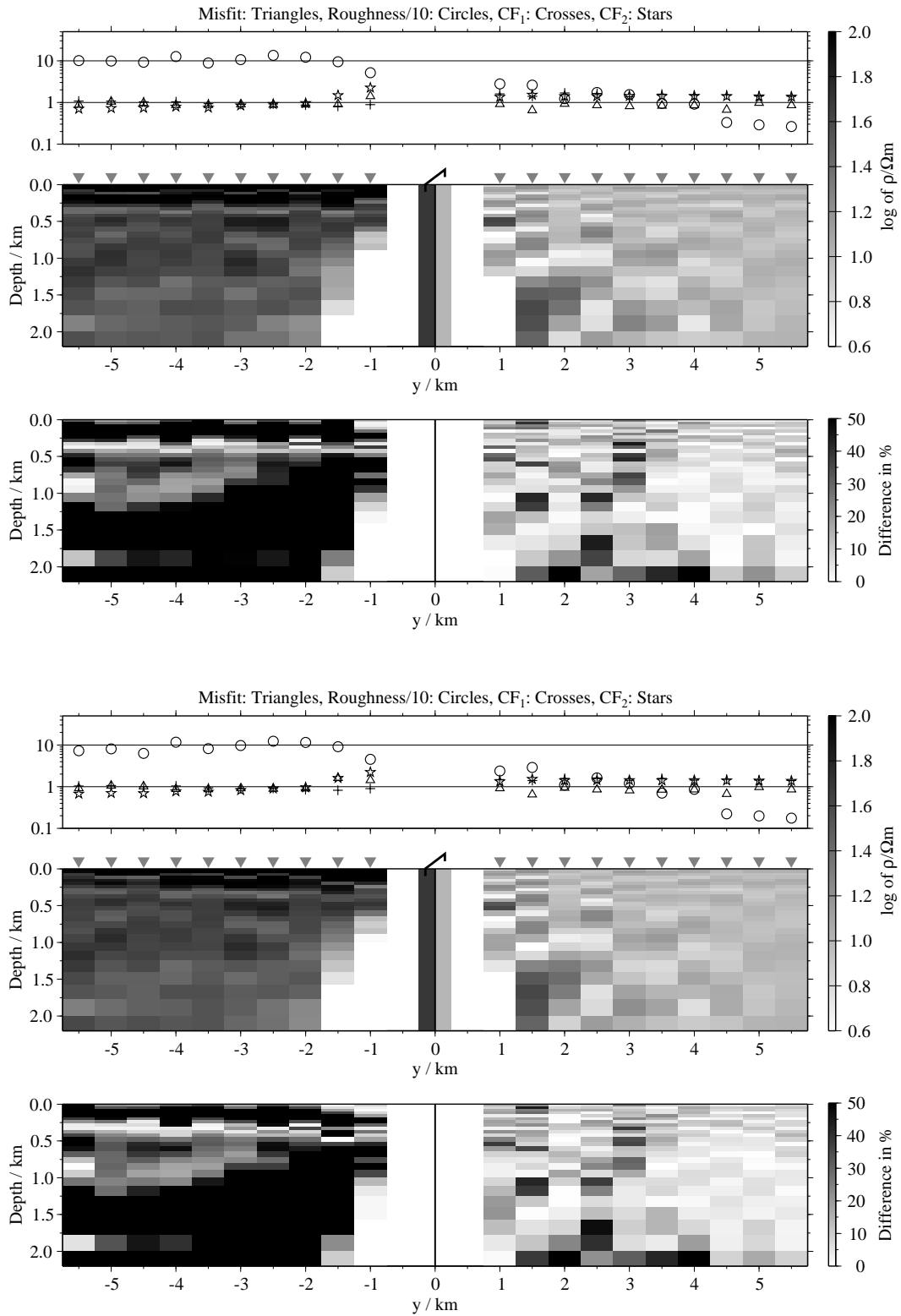


Figure B.118: Pseudo-sections of 1-D soft joint-inversions using the components E_x and H_y , model F2; Top panels: Average inversion results and relative differences (regularisation scheme C1); bottom: Average inversion results and relative differences (regularisation scheme C4);

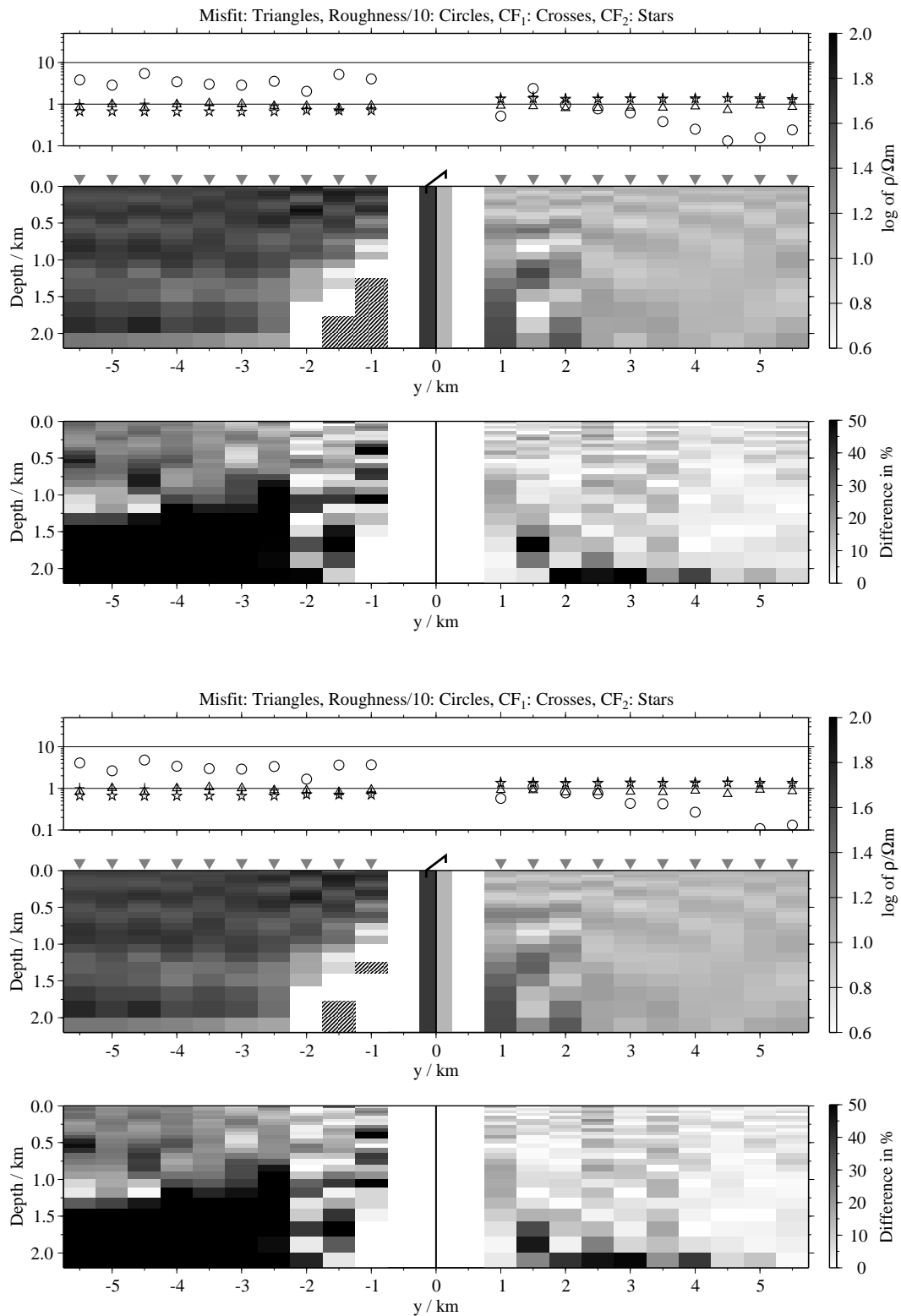


Figure B.119: Pseudo-sections 1-D of soft joint-inversions using the components E_x and \dot{H}_z , model F2; Top panels: Average inversion results and relative differences (regularisation scheme C1); bottom: Average inversion results and relative differences (regularisation scheme C4);

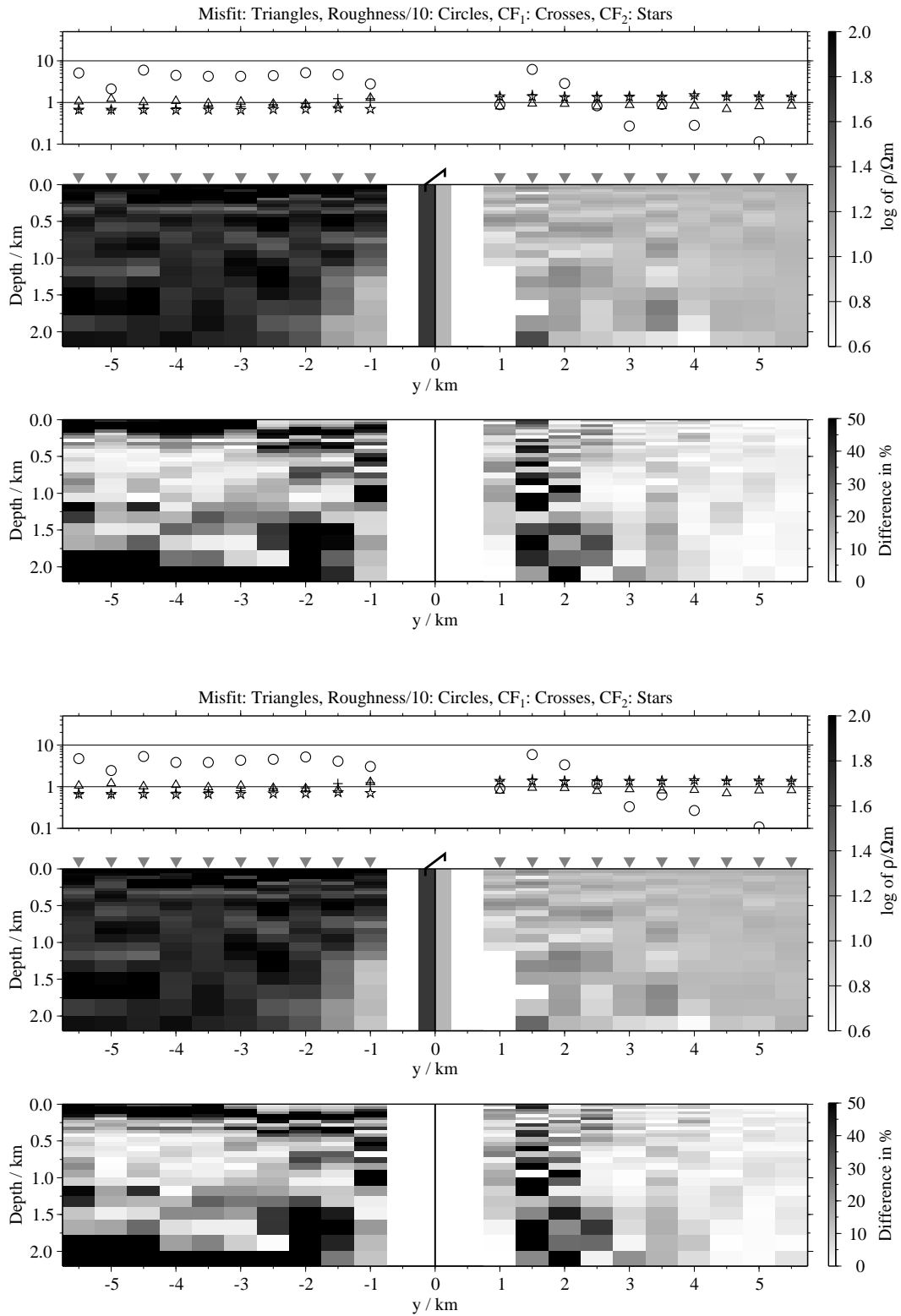


Figure B.120: Pseudo-sections of 1-D soft joint-inversions using the components \dot{H}_y and \dot{H}_z , model F2; Top panels: Average inversion results and relative differences (regularisation scheme C1); bottom: Average inversion results and relative differences (regularisation scheme C4);

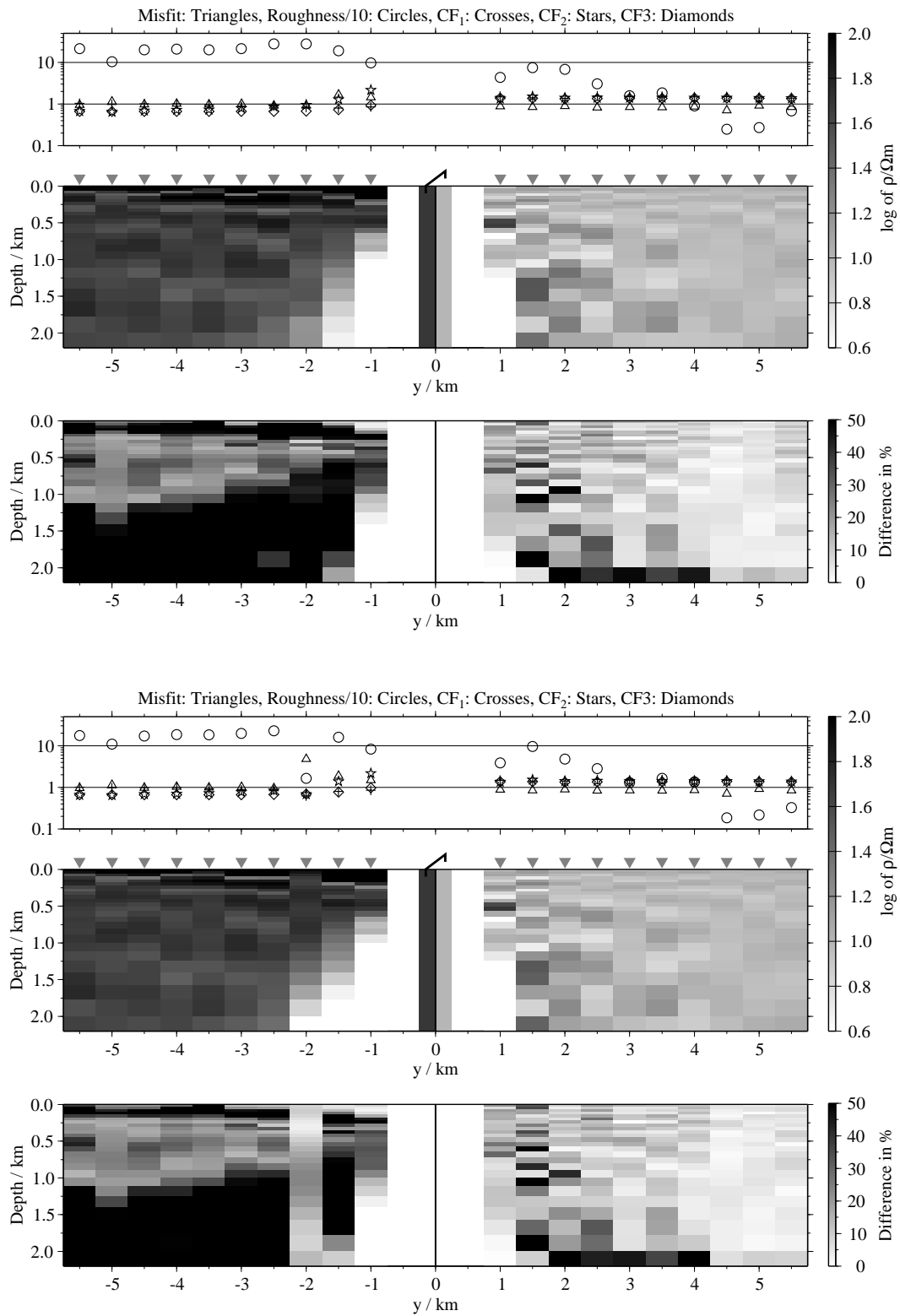


Figure B.121: Pseudo-sections of 1-D soft joint-inversions using all three components, model F2; Top panels: Average inversion results and relative differences (regularisation scheme C1); bottom: Average inversion results and relative differences (regularisation scheme C4);

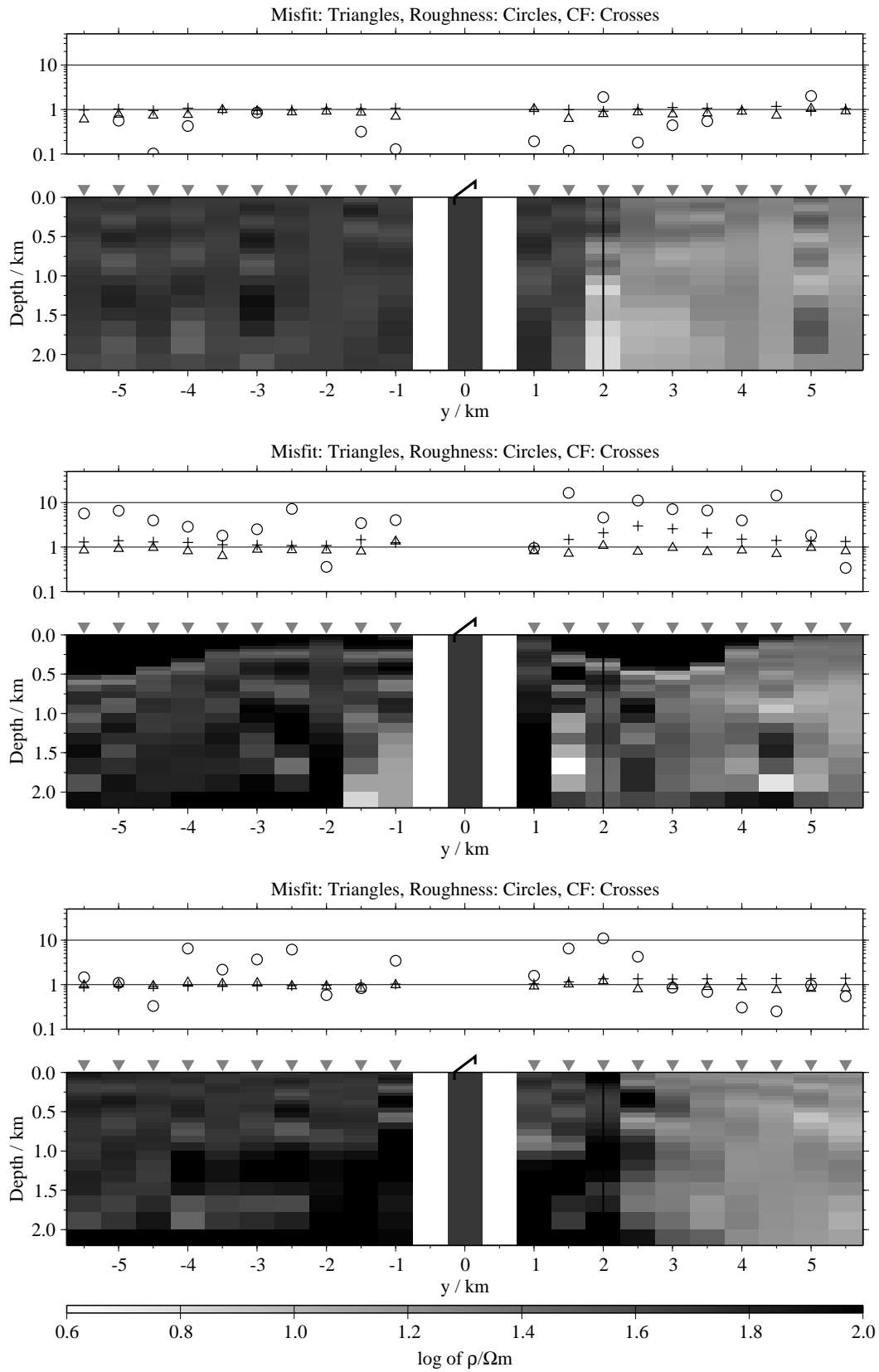


Figure B.122: Pseudo-sections of single 1-D inversion, model F3, regularisation scheme C1; from top to bottom E_x -, \dot{H}_y - and \dot{H}_z -component;

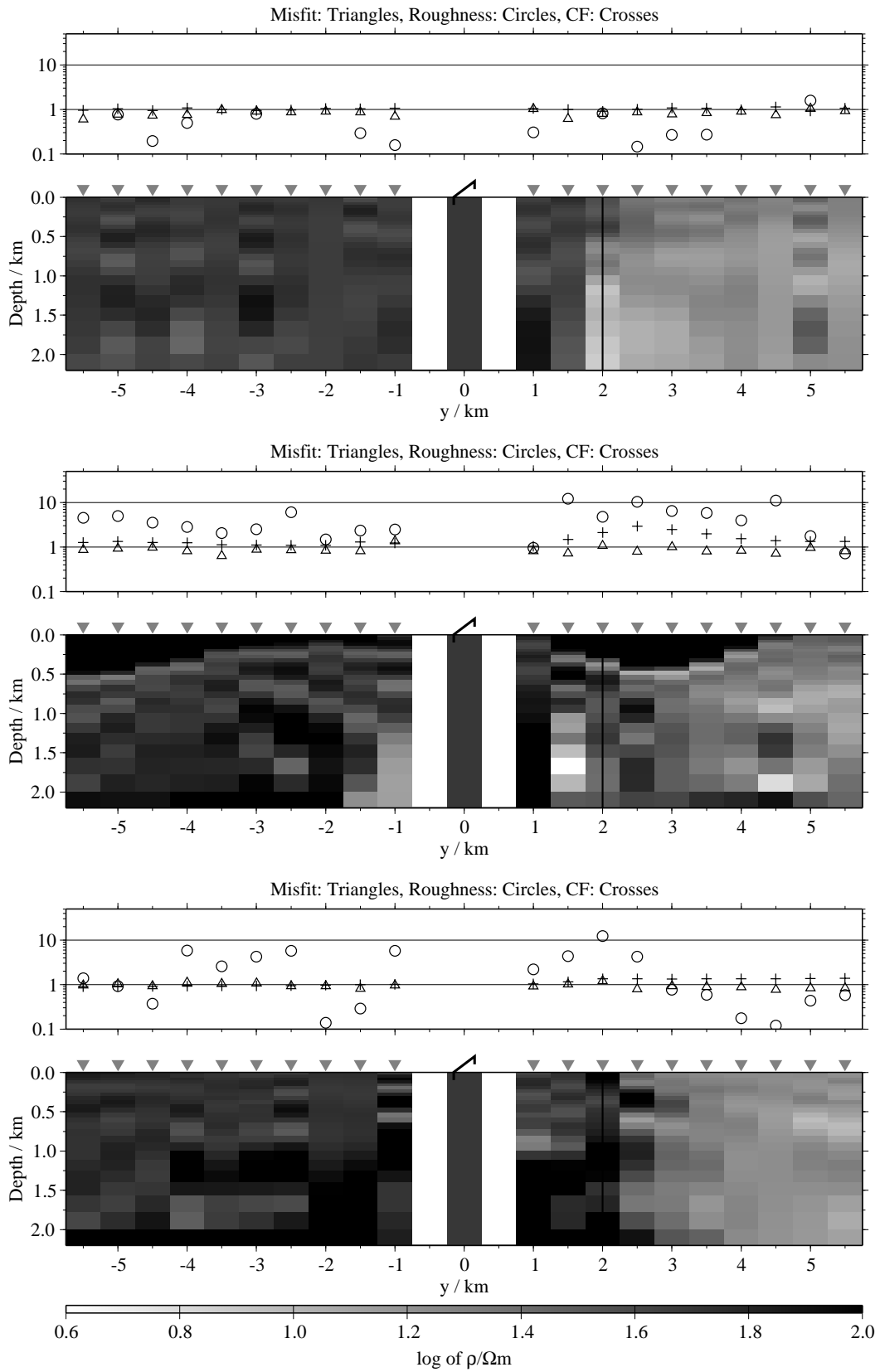


Figure B.123: Pseudo-sections of single 1-D inversion, model F3, regularisation scheme C4; from top to bottom E_x -, H_y - and H_z -component;

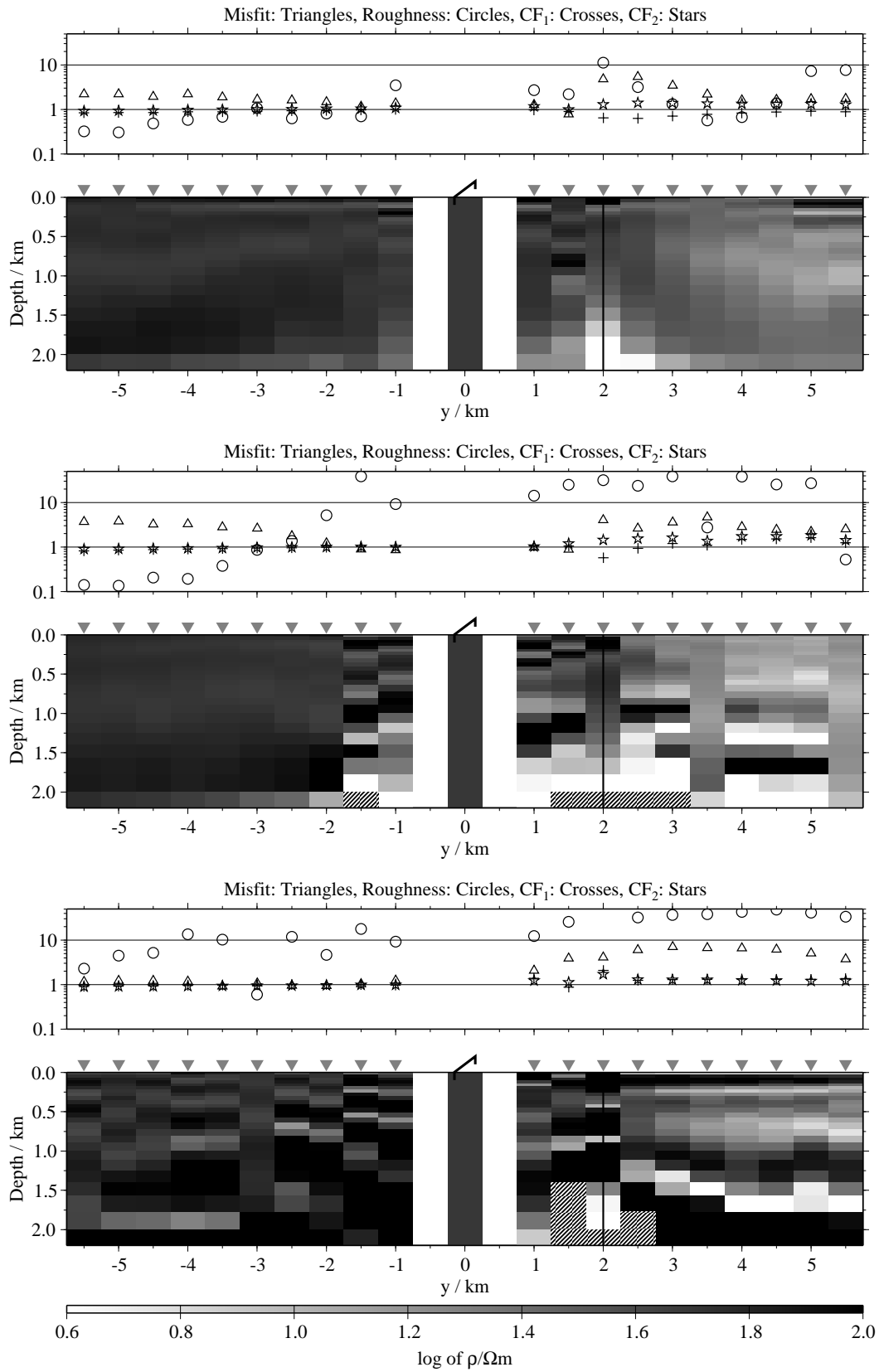


Figure B.124: Pseudo-sections of two component 1-D joint-inversions, model F3, regularisation scheme C1; from top to bottom $E_x - \dot{H}_y$, $E_x - \dot{H}_z$ and $\dot{H}_y - \dot{H}_z$;

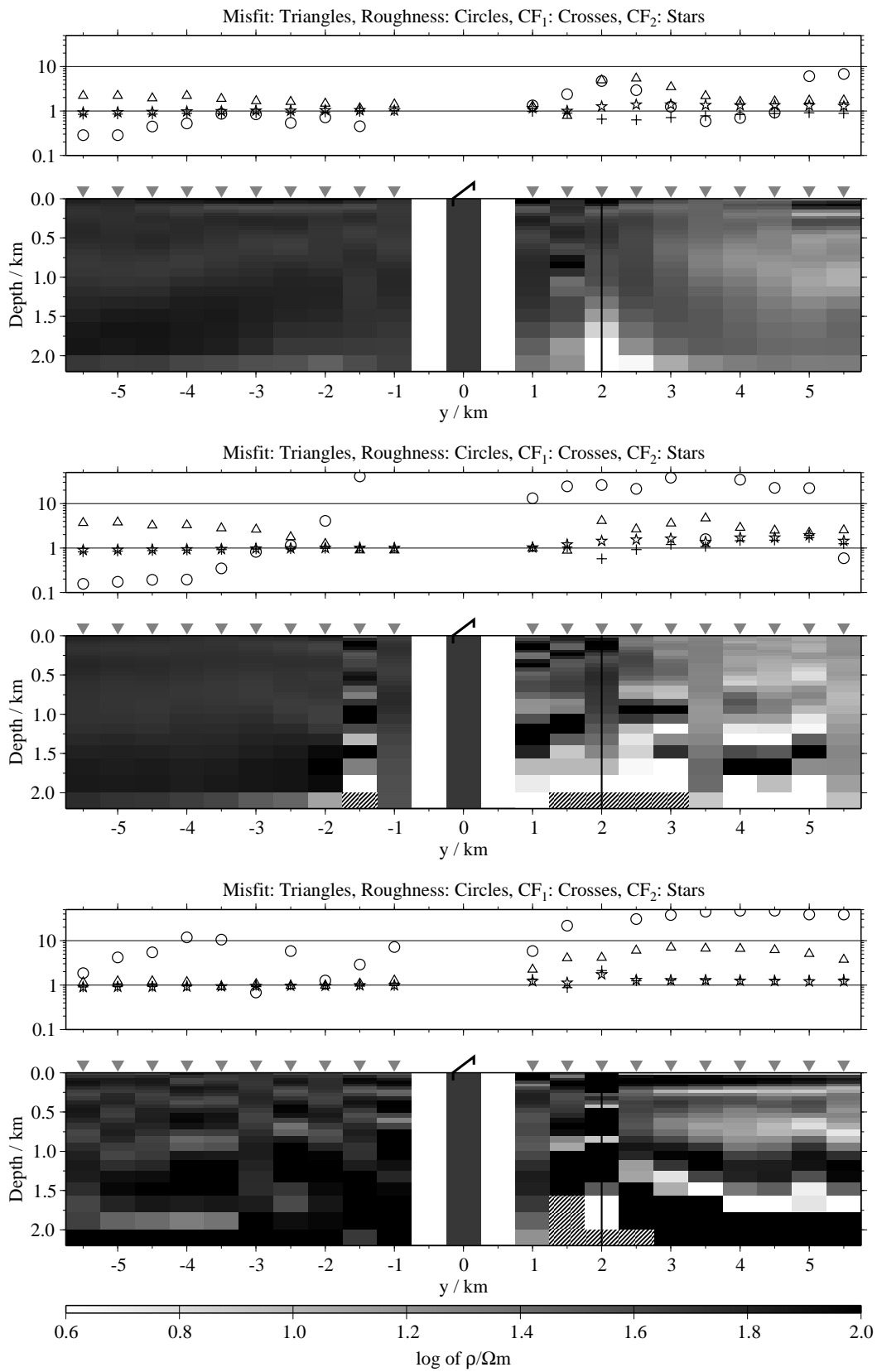


Figure B.125: Pseudo-sections of two component 1-D joint-inversions, model F3, regularisation scheme C4; from top to bottom $E_x\text{-}\dot{H}_y$, $E_x\text{-}\dot{H}_z$ and $\dot{H}_y\text{-}\dot{H}_z$;

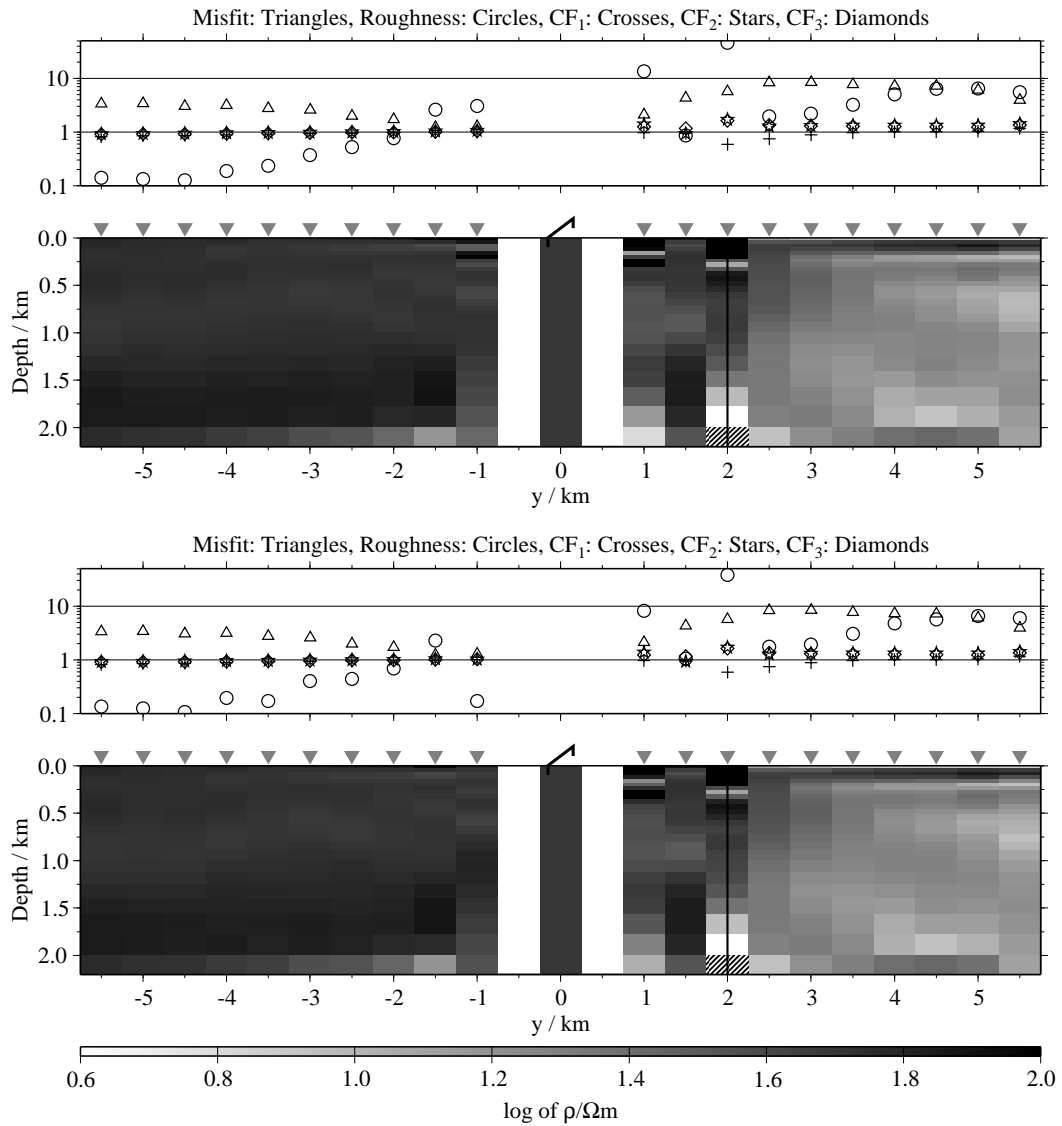


Figure B.126: Pseudo-sections of 1-D joint-inversions using all three components, model F3; top: Regularisation scheme C1; bottom: Regularisation scheme C4;

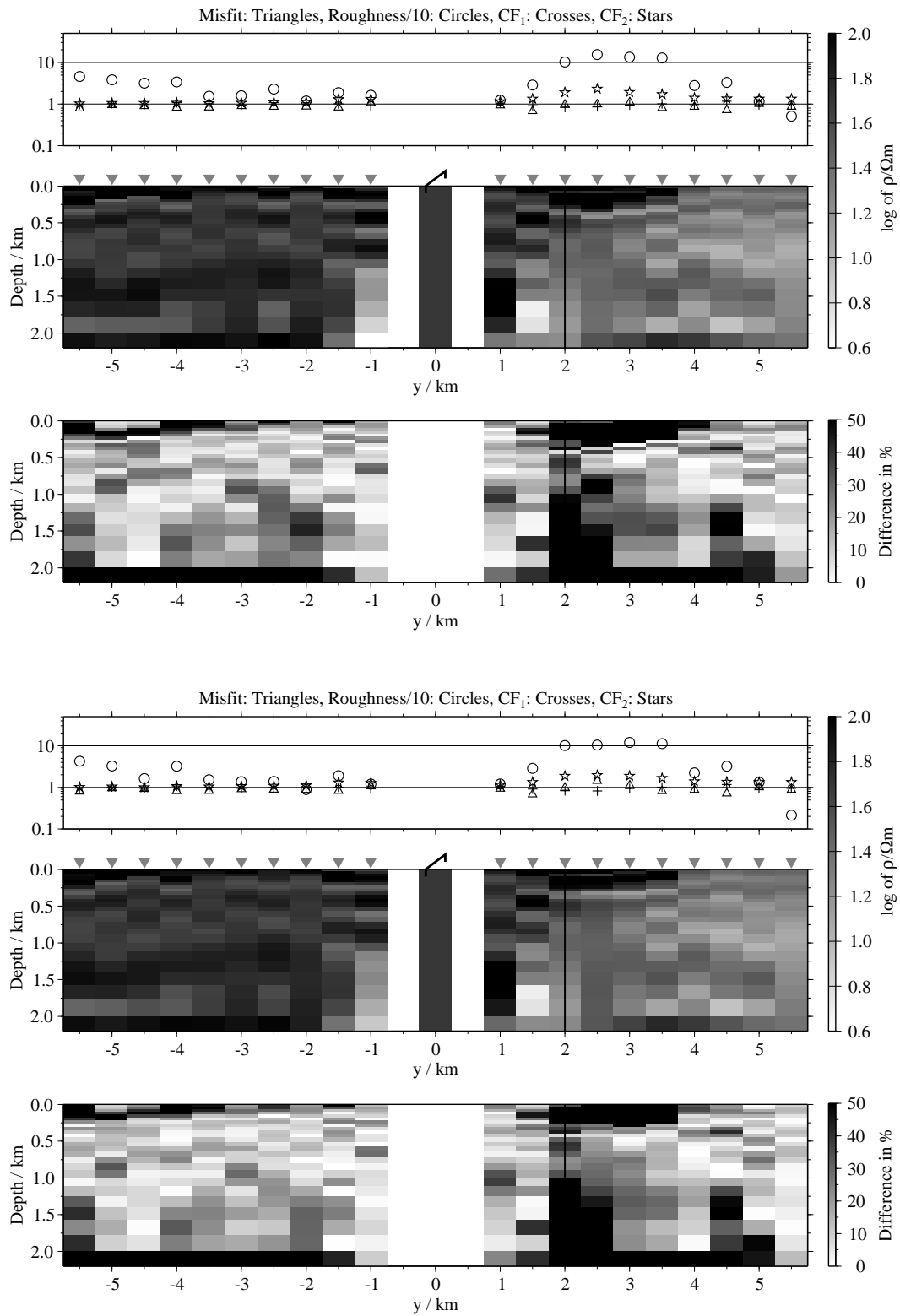


Figure B.127: Pseudo-sections of 1-D soft joint-inversions using the components E_x and H_y , model F3; Top panels: Average inversion results and relative differences (regularisation scheme C1); bottom: Average inversion results and relative differences (regularisation scheme C4);

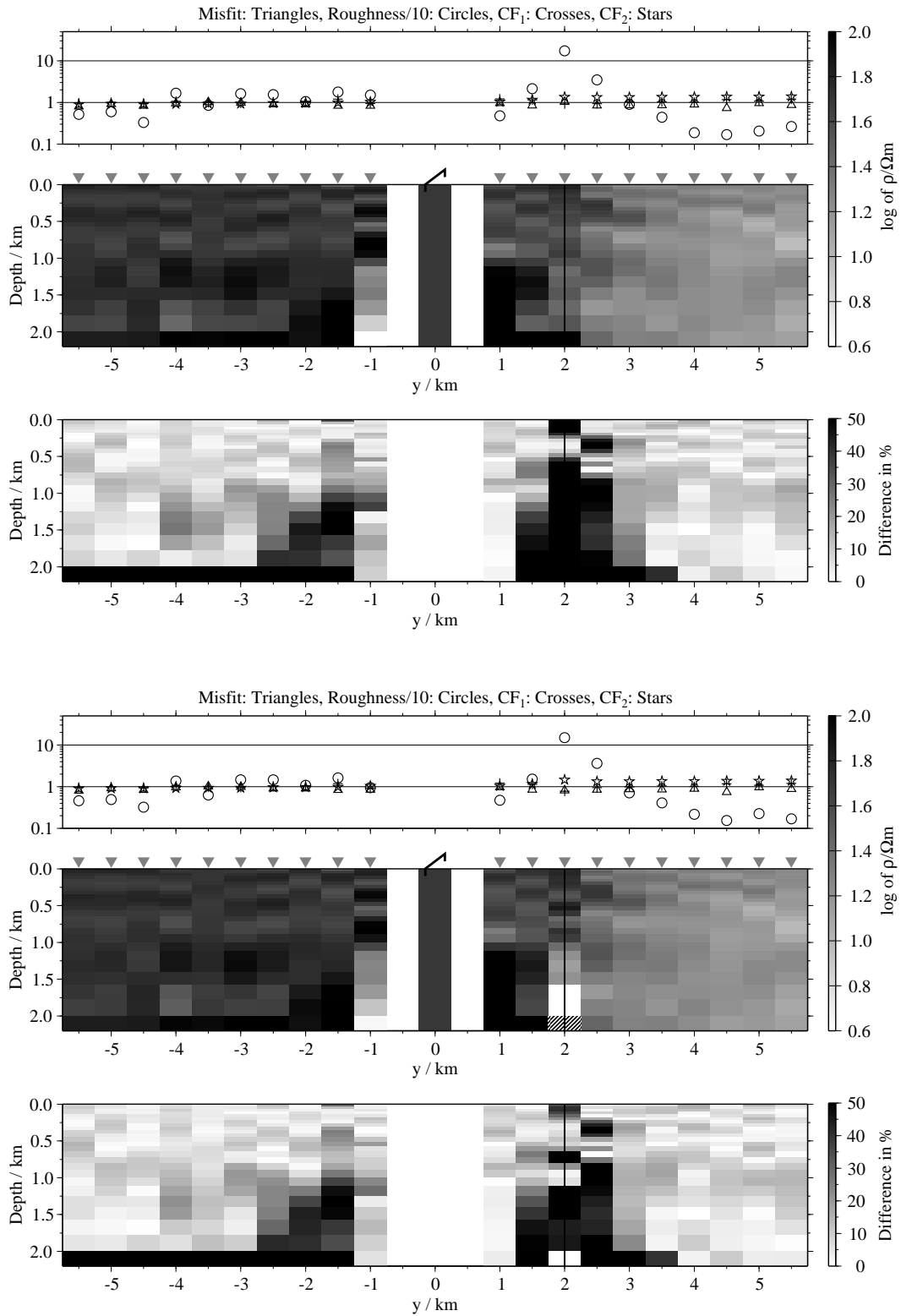


Figure B.128: Pseudo-sections 1-D of soft joint-inversions using the components E_x and H_z , model F3; Top panels: Average inversion results and relative differences (regularisation scheme C1); bottom: Average inversion results and relative differences (regularisation scheme C4);

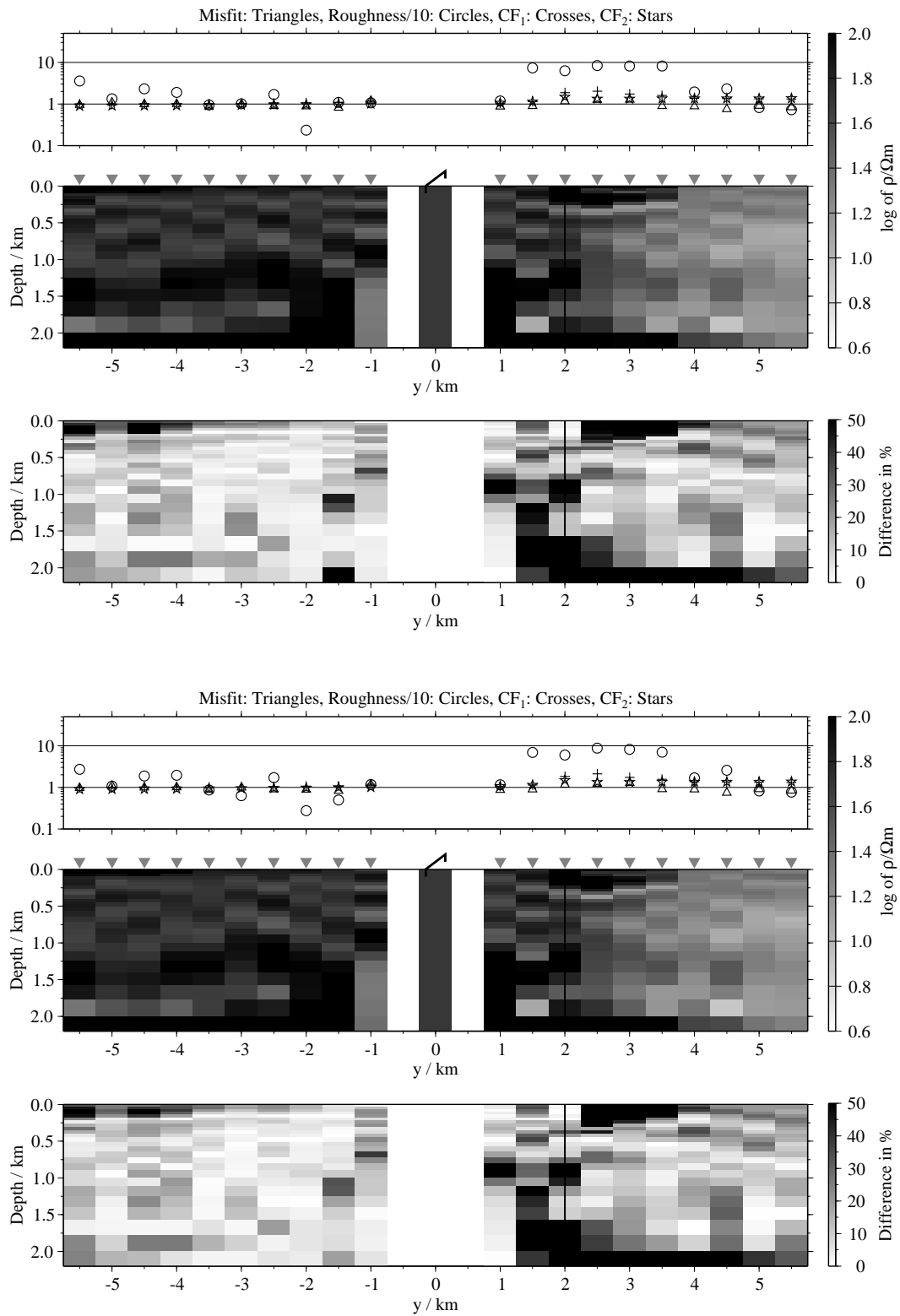


Figure B.129: Pseudo-sections of 1-D soft joint-inversions using the components \dot{H}_y and \dot{H}_{zi} , model F3; Top panels: Average inversion results and relative differences (regularisation scheme C1); bottom: Average inversion results and relative differences (regularisation scheme C4);

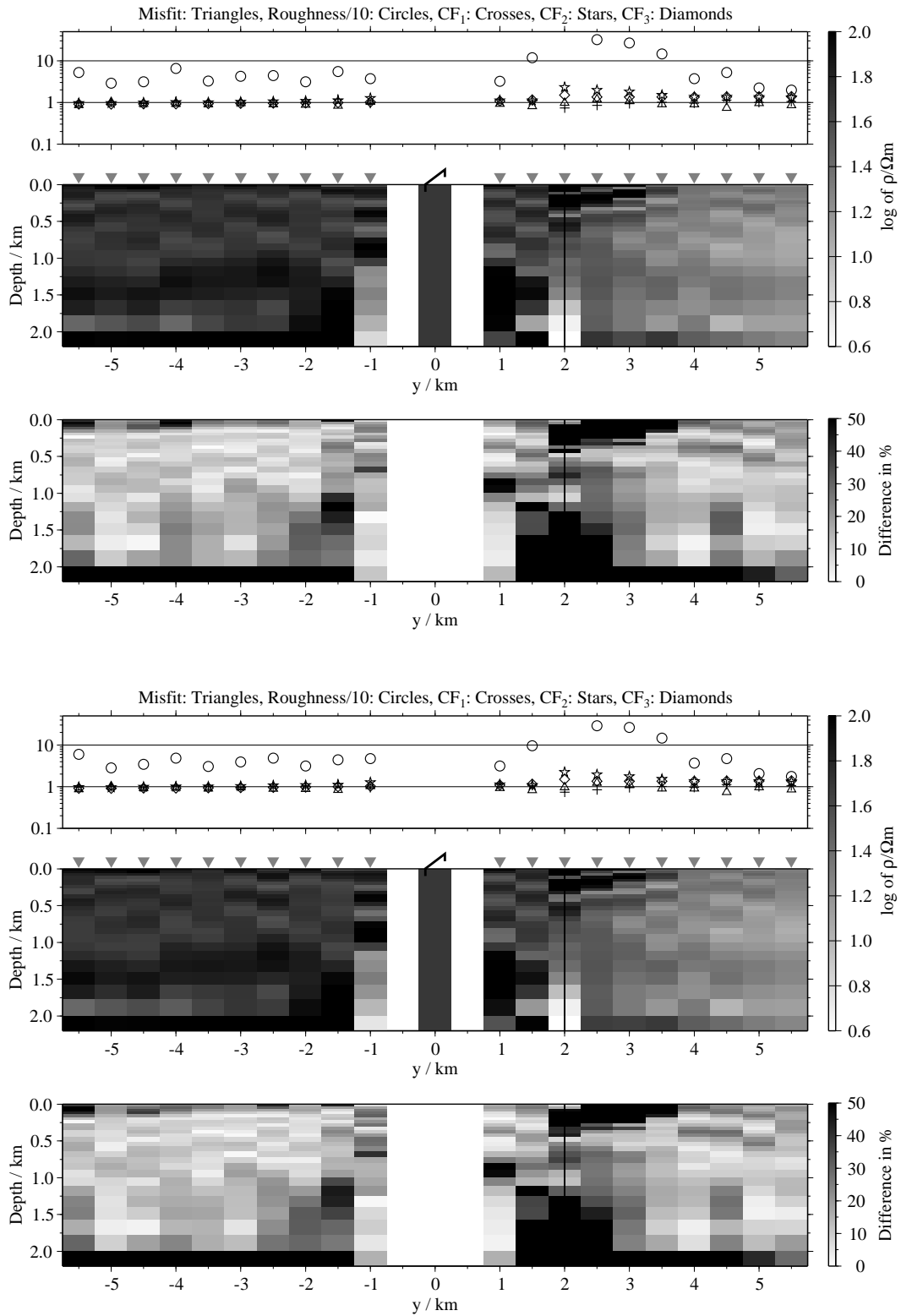
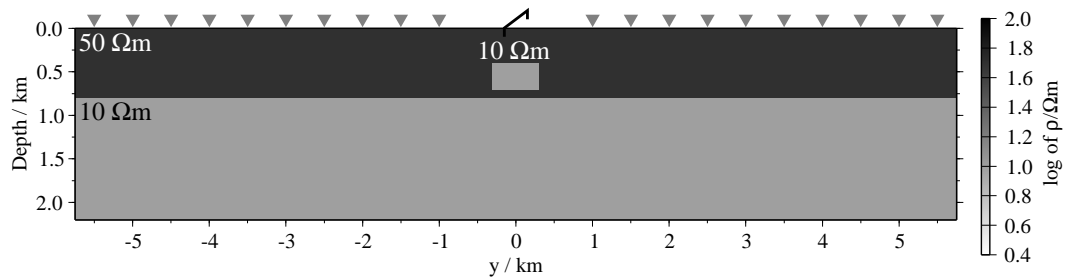


Figure B.130: Pseudo-sections of 1-D soft joint-inversions using all three components, model F3; Top panels: Average inversion results and relative differences (regularisation scheme C1); bottom: Average inversion results and relative differences (regularisation scheme C4);

B.2.5 Conductive patch at an intermediate depth (models G1 and G2)

Model G1:



Model G2:

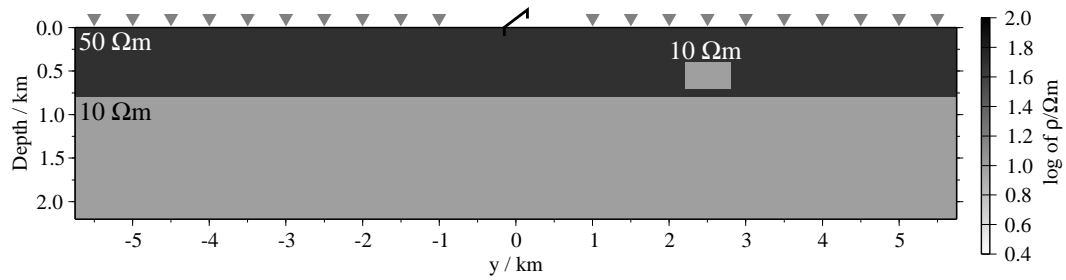


Figure B.131: Model with a conductive patch in an intermediate depth; the mid-point of the patch is in both cases at $x = 0$ km and $y = 0$ km (model G1) and $y = 2.5$ km (model G2), respectively. The patch has the size $600 \times 600 \times 300$ m³.

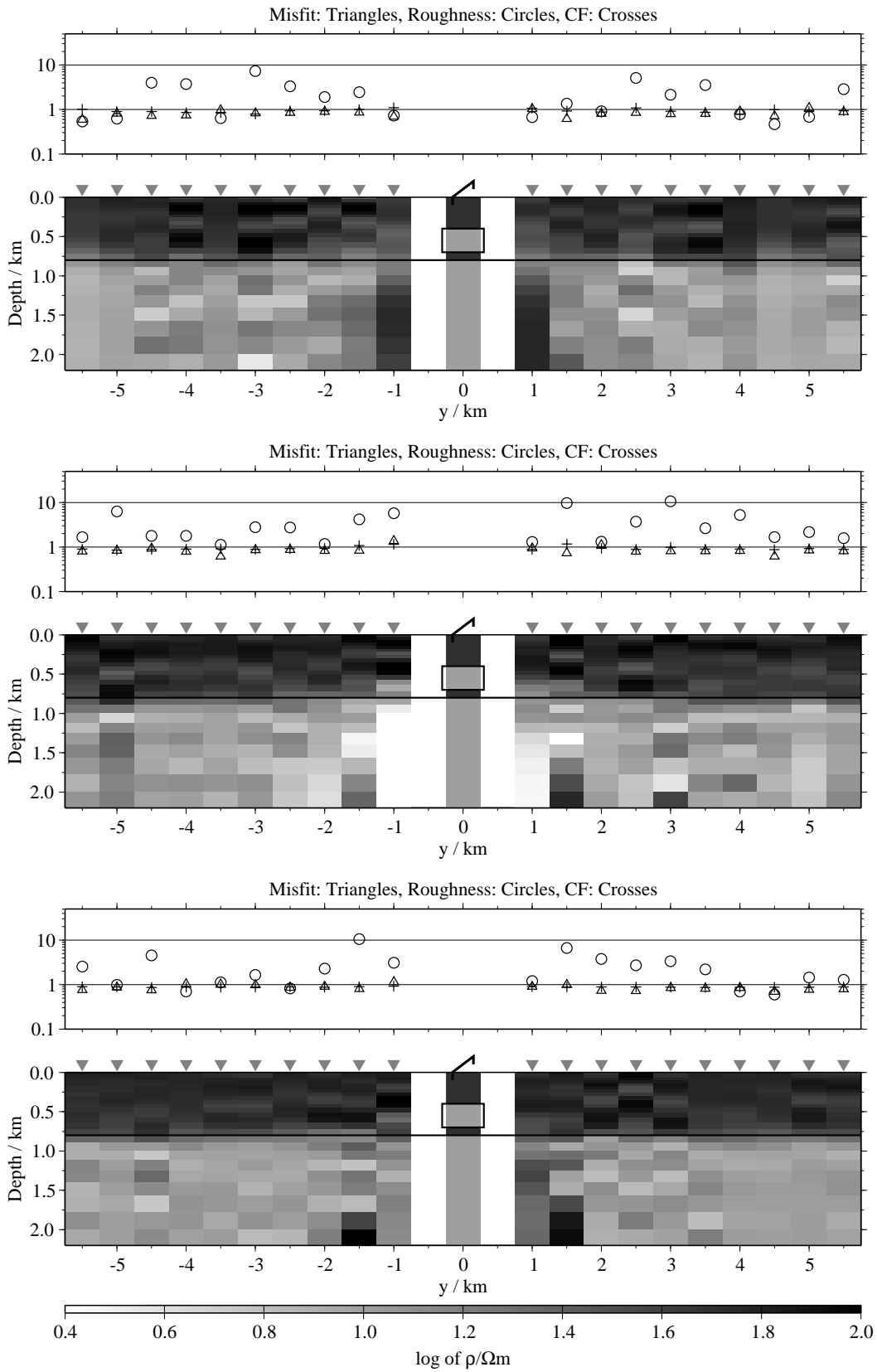


Figure B.132: Pseudo-sections of single 1-D inversion, model G1, regularisation scheme C1; from top to bottom E_x -, \dot{H}_y - and \dot{H}_z -component;

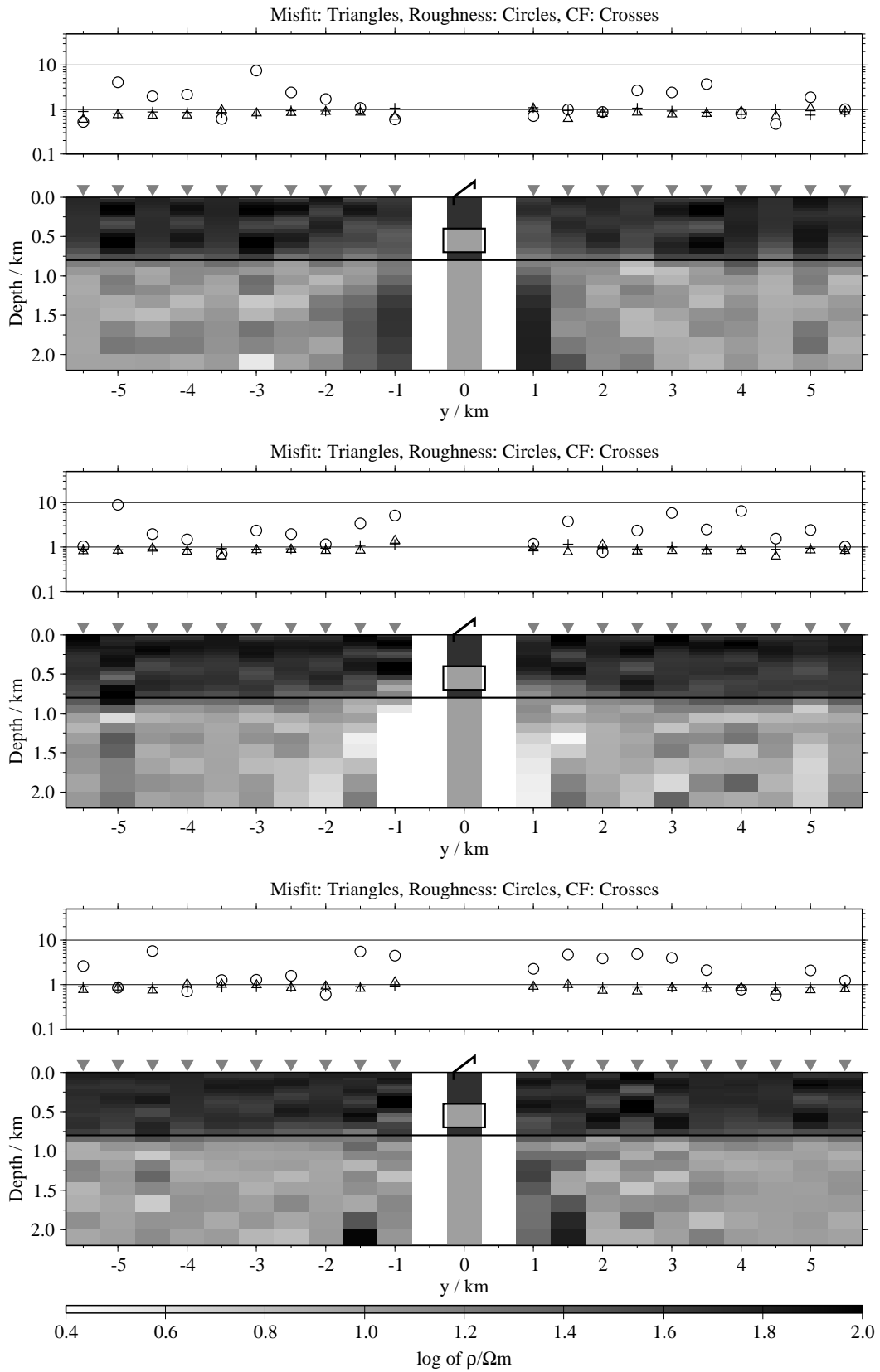


Figure B.133: Pseudo-sections of single 1-D inversion, model G1, regularisation scheme C4; from top to bottom E_x -, H_y - and H_z -component;

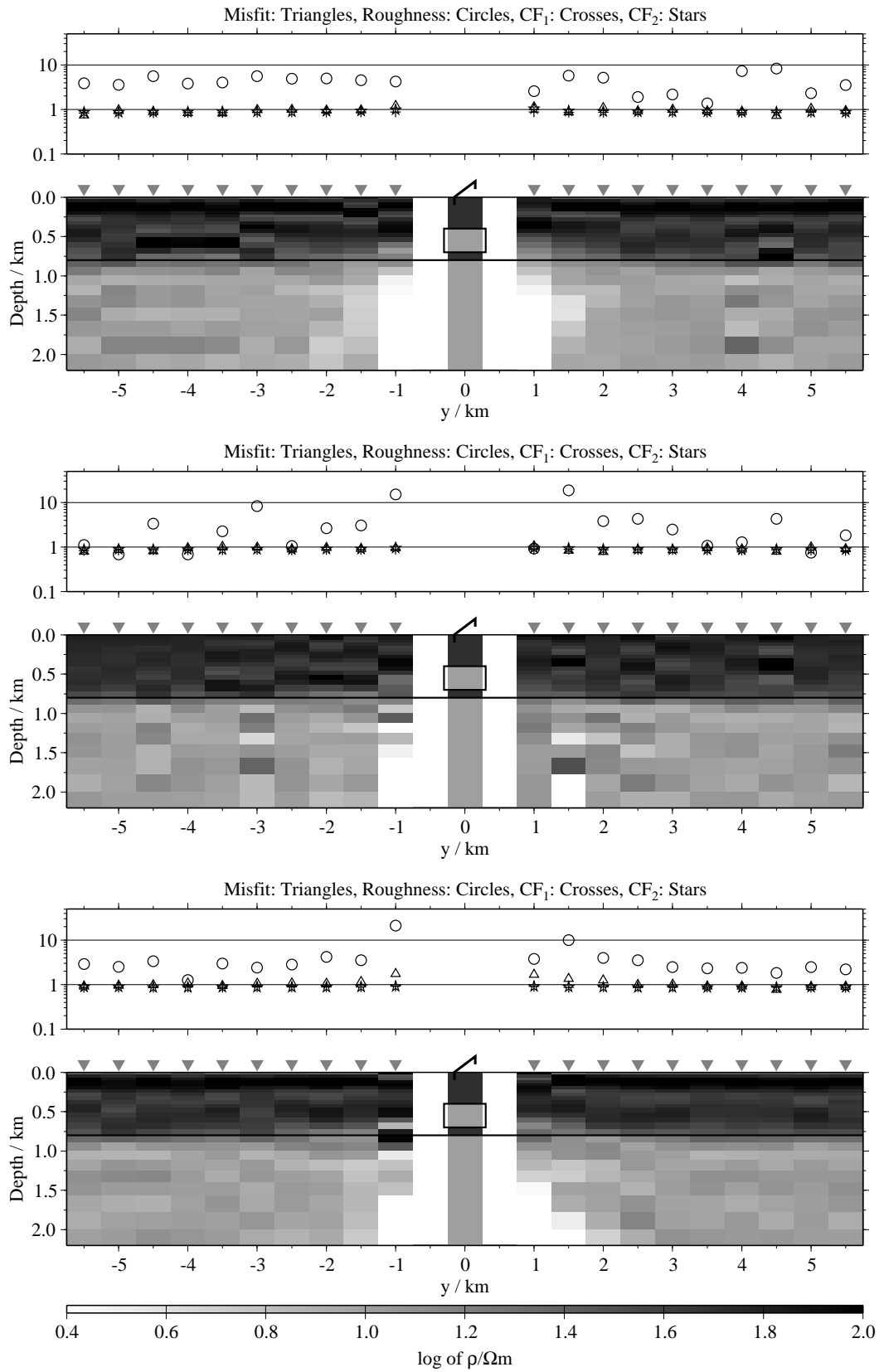


Figure B.134: Pseudo-sections of two component 1-D joint-inversions, model G1, regularisation scheme C1; from top to bottom $E_x-\dot{H}_y$, $E_x-\dot{H}_z$ and $\dot{H}_y-\dot{H}_z$;

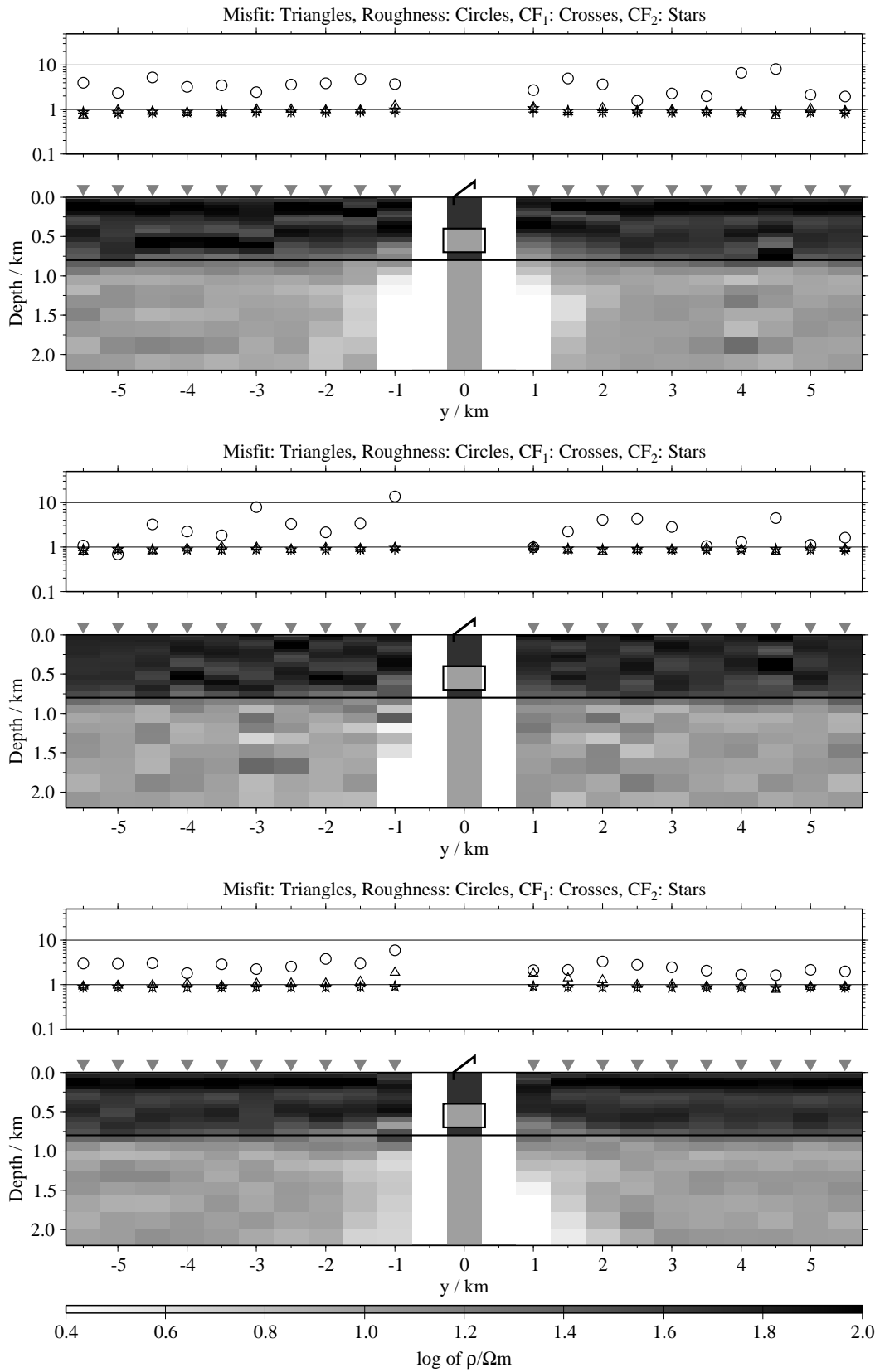


Figure B.135: Pseudo-sections of two component 1-D joint-inversions, model G1, regularisation scheme C4; from top to bottom $E_x\text{-}\dot{H}_y$, $E_x\text{-}\dot{H}_z$ and $\dot{H}_y\text{-}\dot{H}_z$;

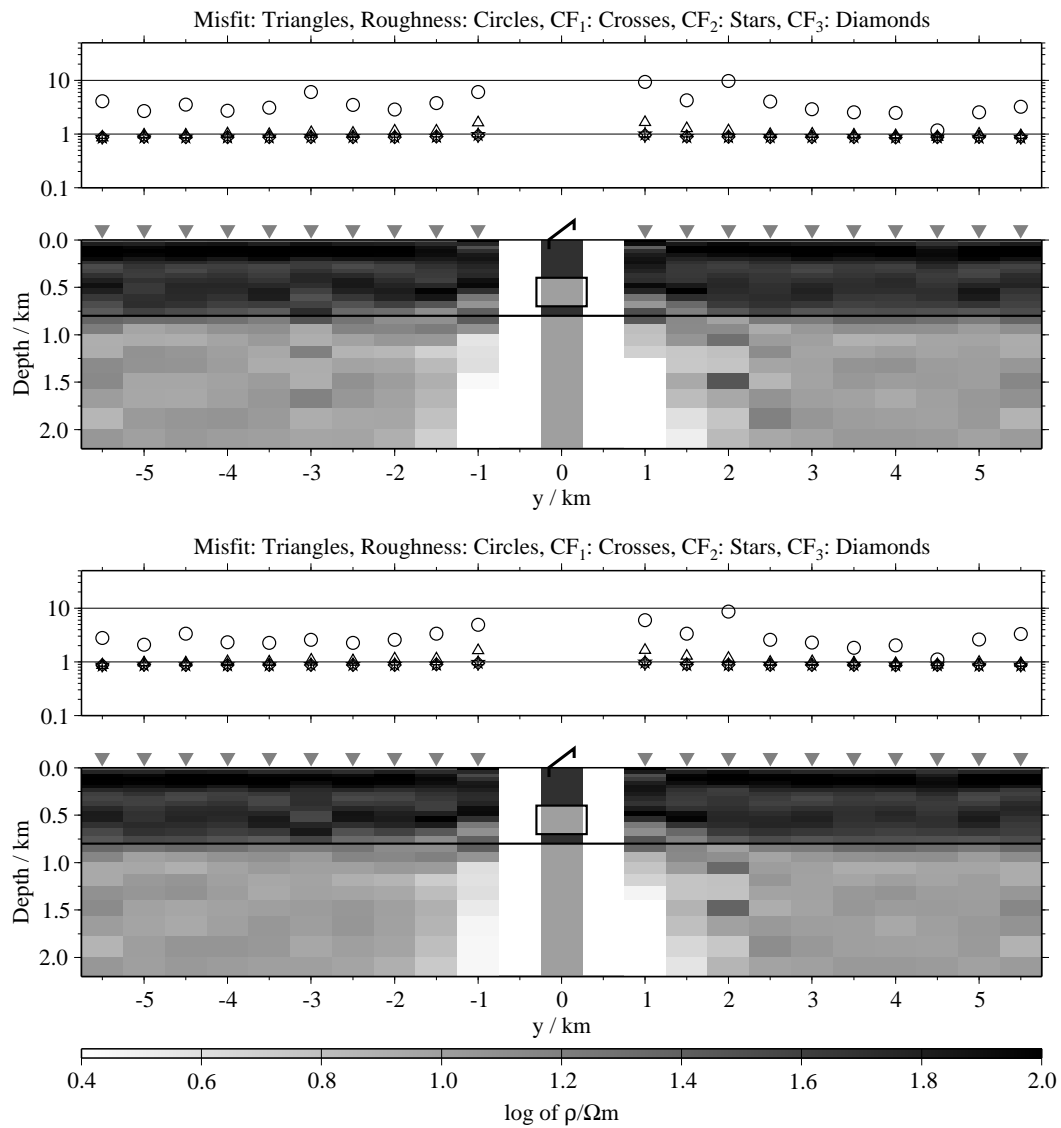


Figure B.136: Pseudo-sections of 1-D joint-inversions using all three components, model G1; top: Regularisation scheme C1; bottom: Regularisation scheme C4;

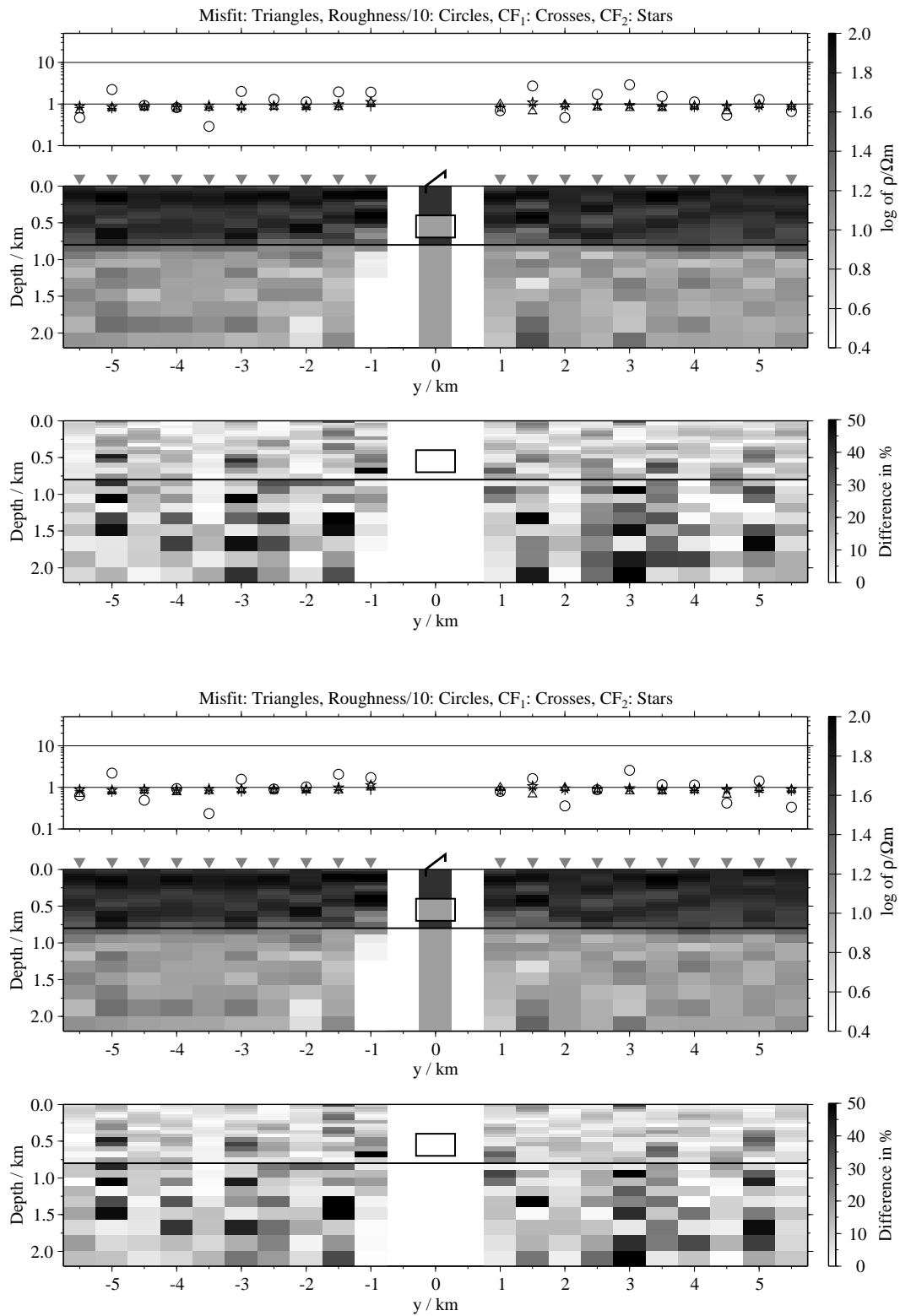


Figure B.137: Pseudo-sections of 1-D soft joint-inversions using the components E_x and H_y , model G1; Top panels: Average inversion results and relative differences (regularisation scheme C1); bottom: Average inversion results and relative differences (regularisation scheme C4);

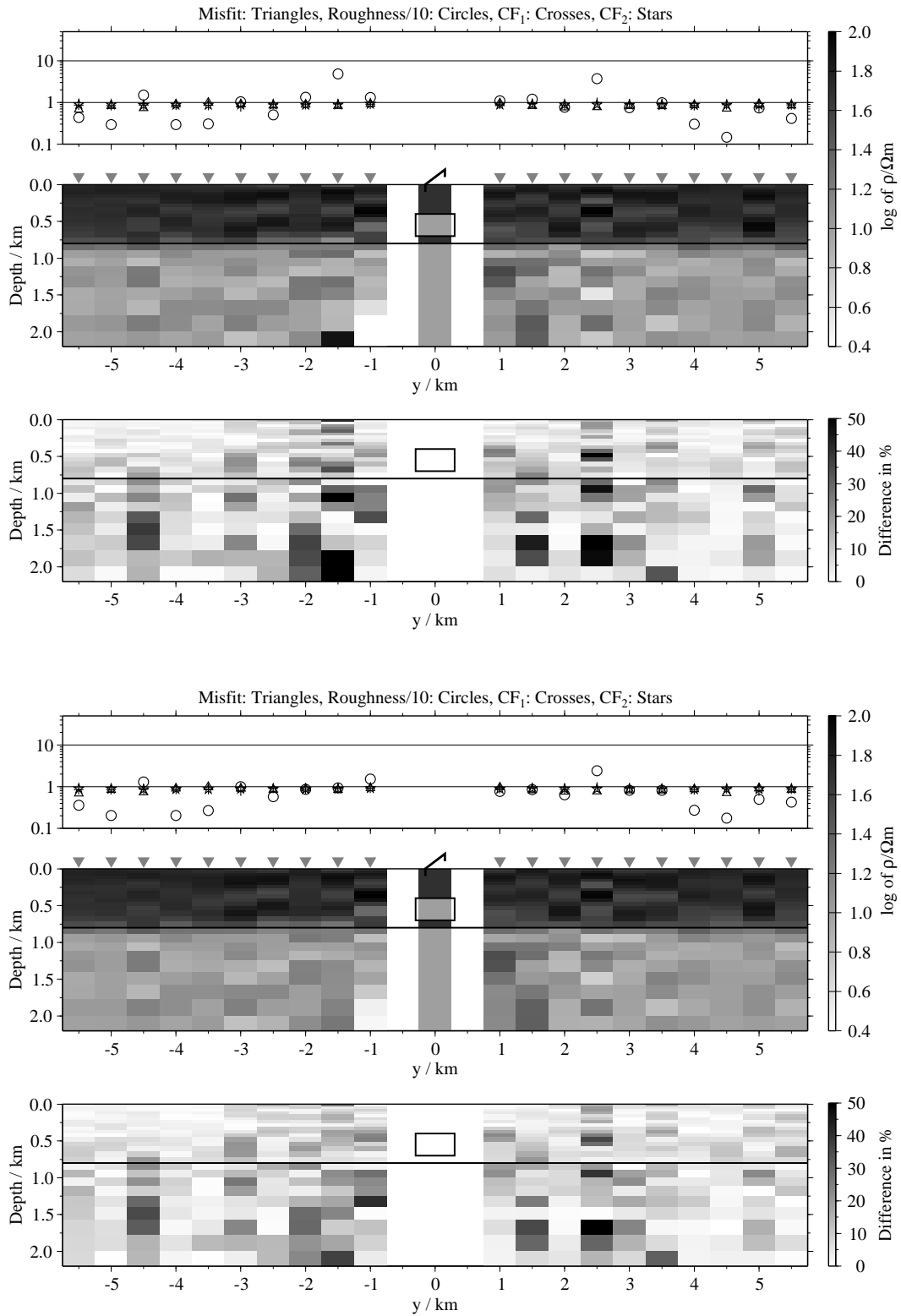


Figure B.138: Pseudo-sections 1-D of soft joint-inversions using the components E_x and H_z , model G1; Top panels: Average inversion results and relative differences (regularisation scheme C1); bottom: Average inversion results and relative differences (regularisation scheme C4);

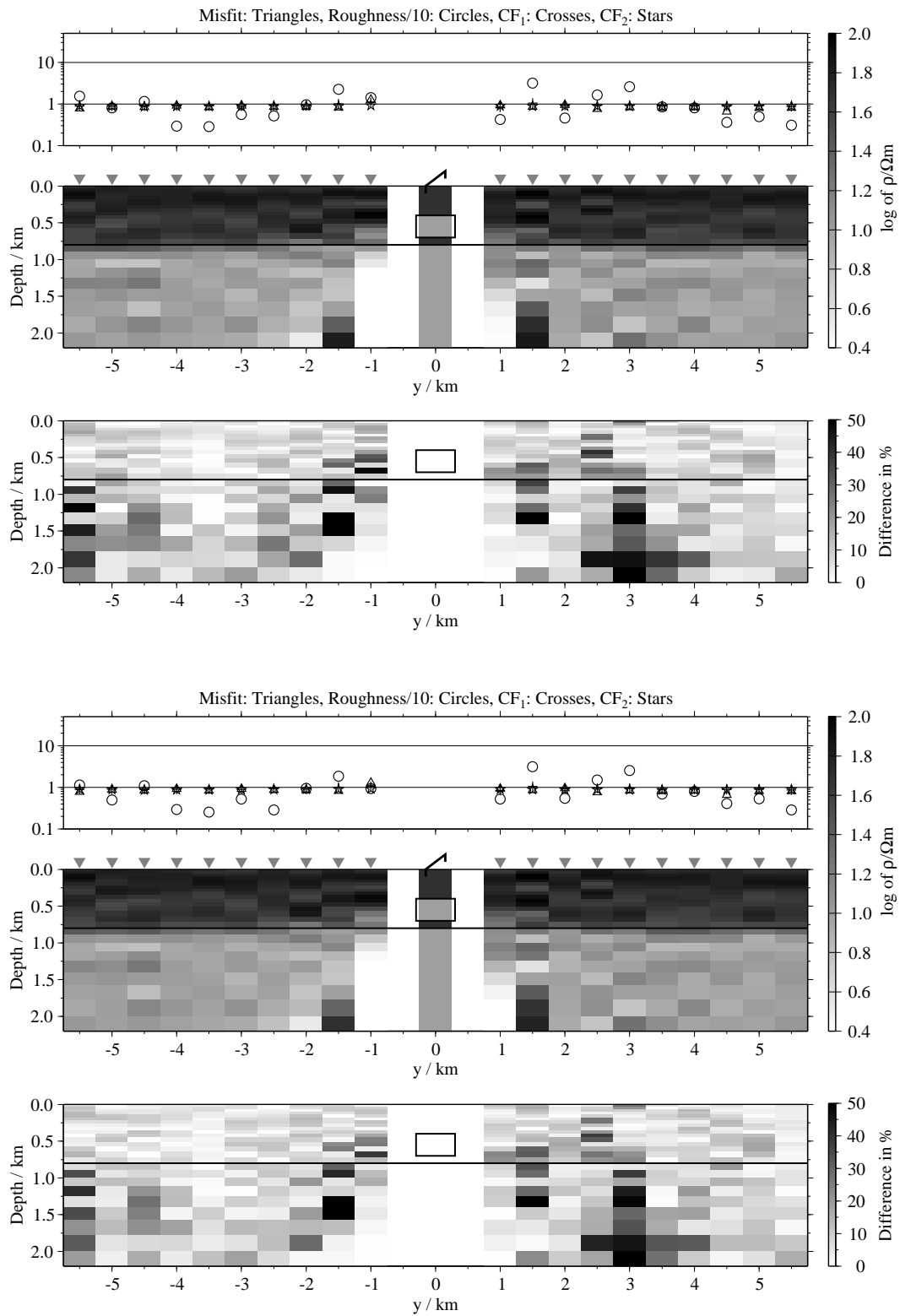


Figure B.139: Pseudo-sections of 1-D soft joint-inversions using the components \dot{H}_y and \dot{H}_{zi} , model G1; Top panels: Average inversion results and relative differences (regularisation scheme C1); bottom: Average inversion results and relative differences (regularisation scheme C4);

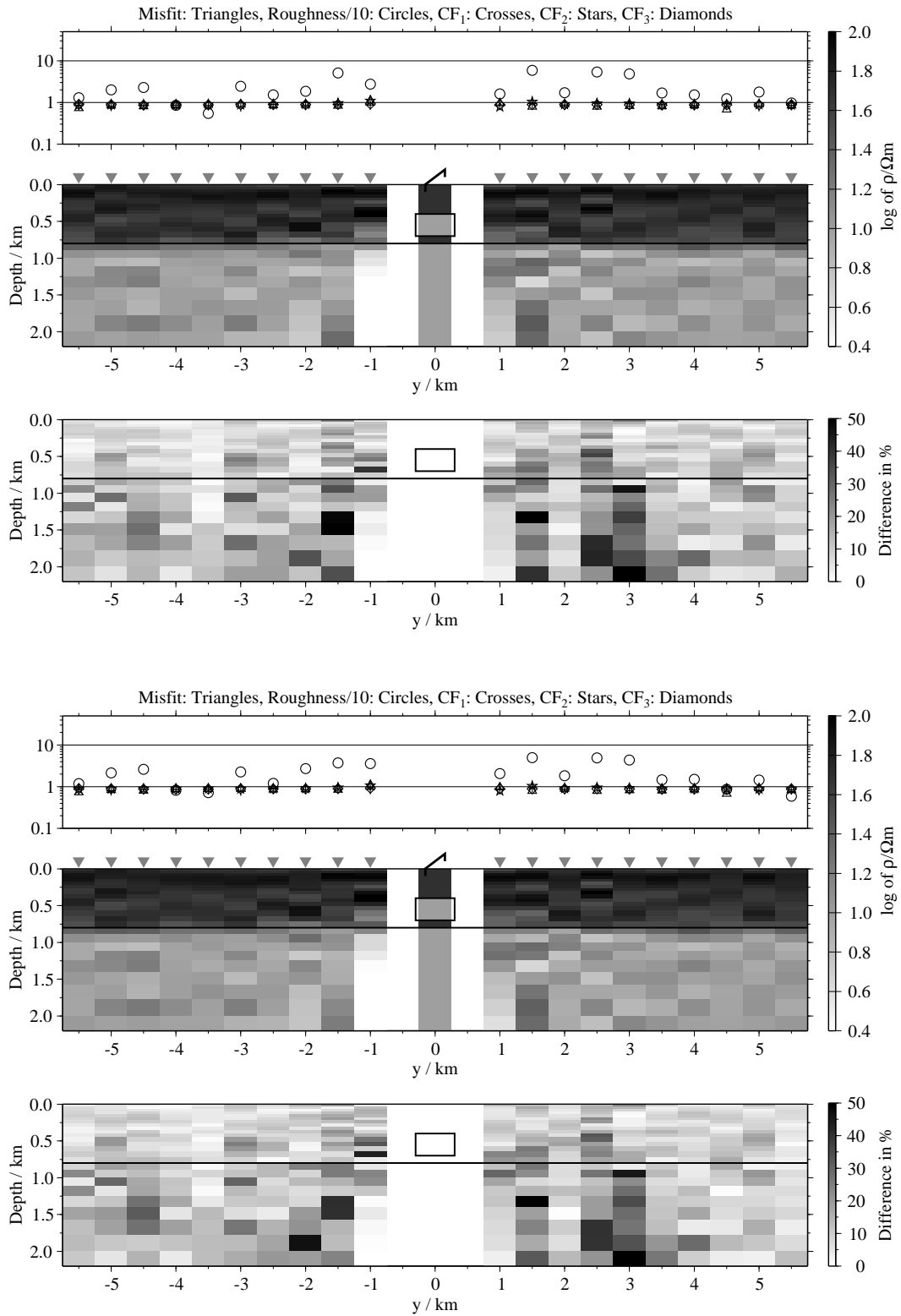


Figure B.140: Pseudo-sections of 1-D soft joint-inversions using all three components, model G1; Top panels: Average inversion results and relative differences (regularisation scheme C1); bottom: Average inversion results and relative differences (regularisation scheme C4);

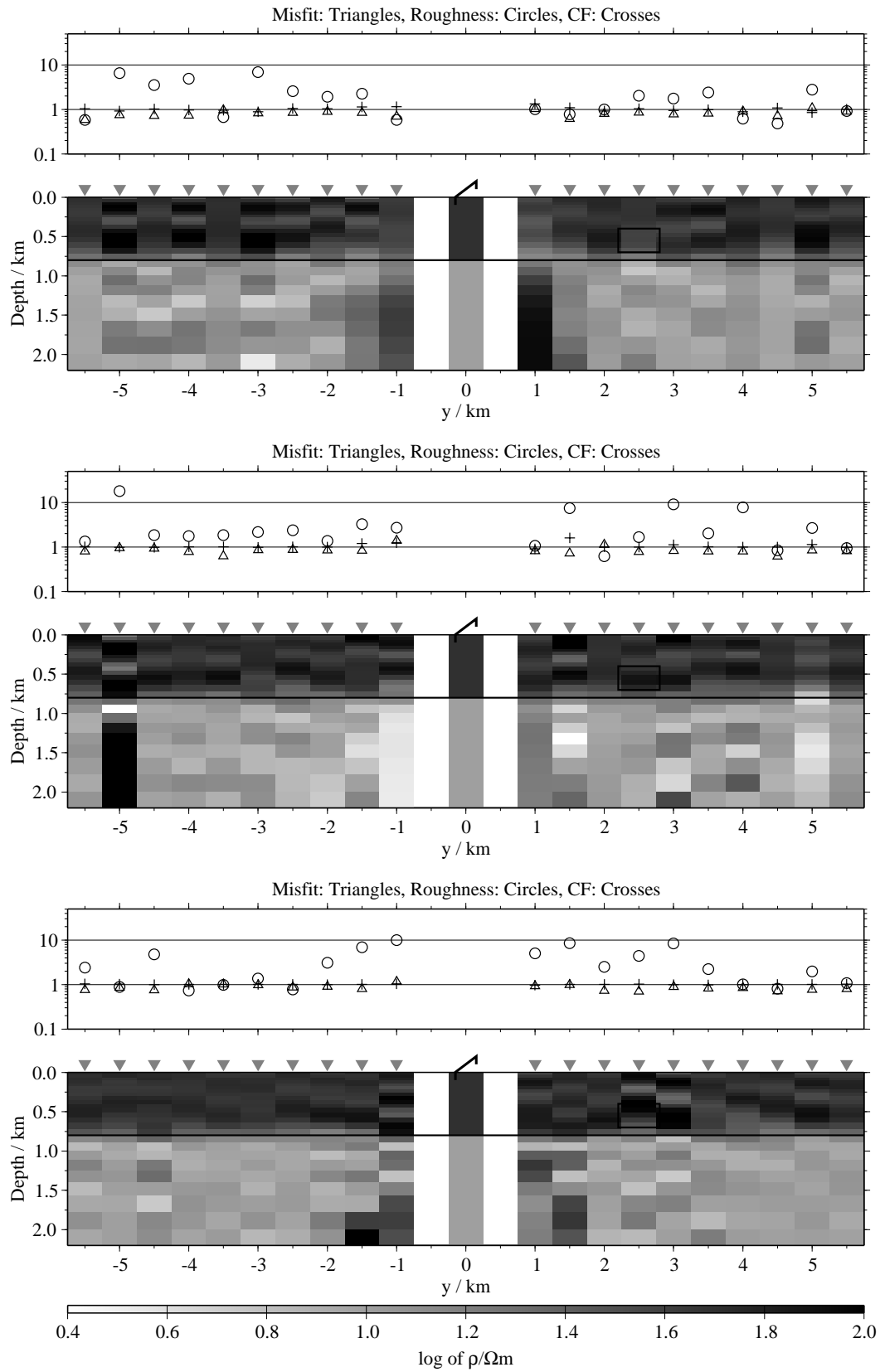


Figure B.141: Pseudo-sections of single 1-D inversion, model G2, regularisation scheme C1; from top to bottom E_x -, H_y - and H_z -component;

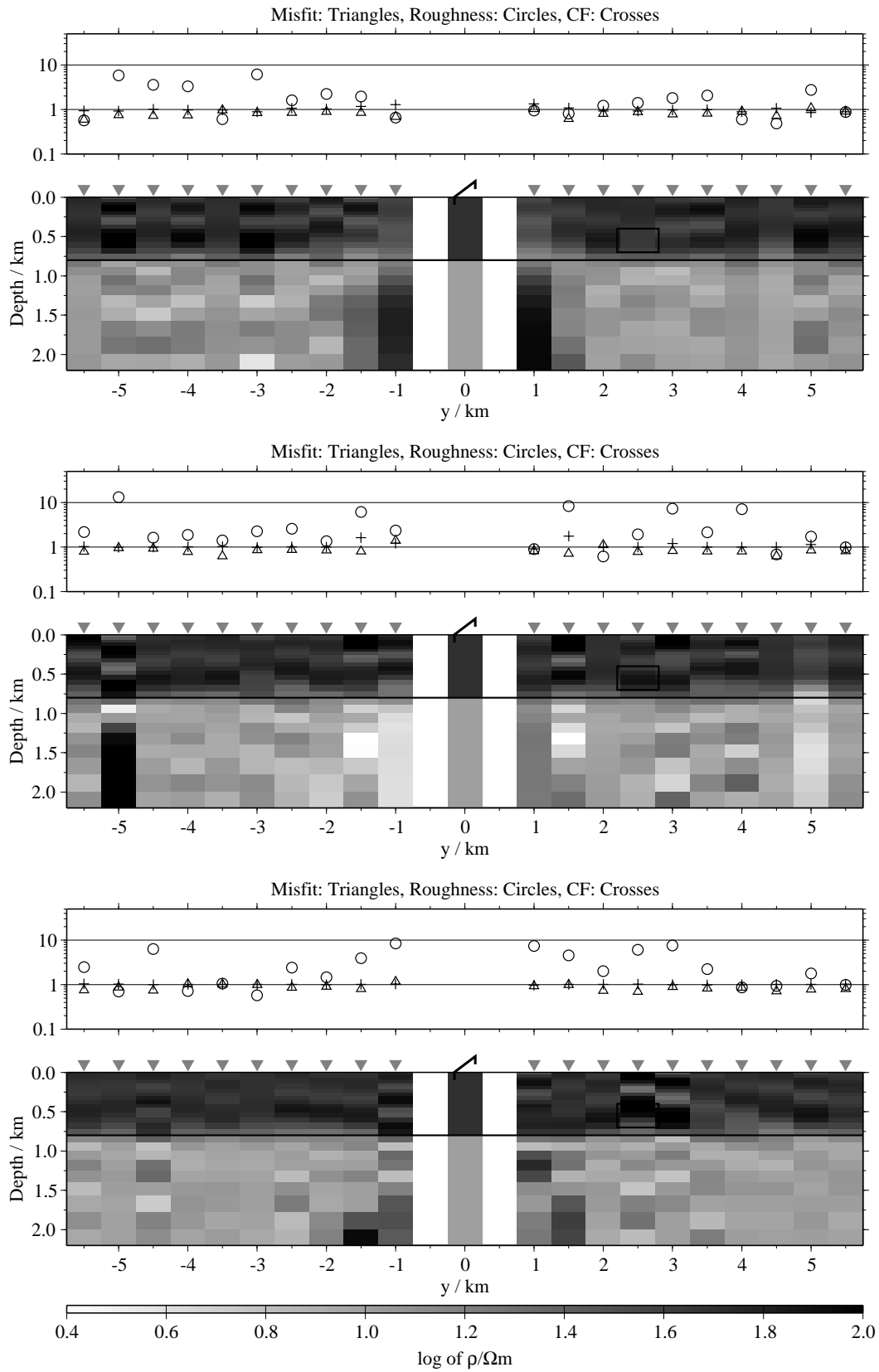


Figure B.142: Pseudo-sections of single 1-D inversion, model G2, regularisation scheme C4; from top to bottom E_x -, H_y - and H_z -component;

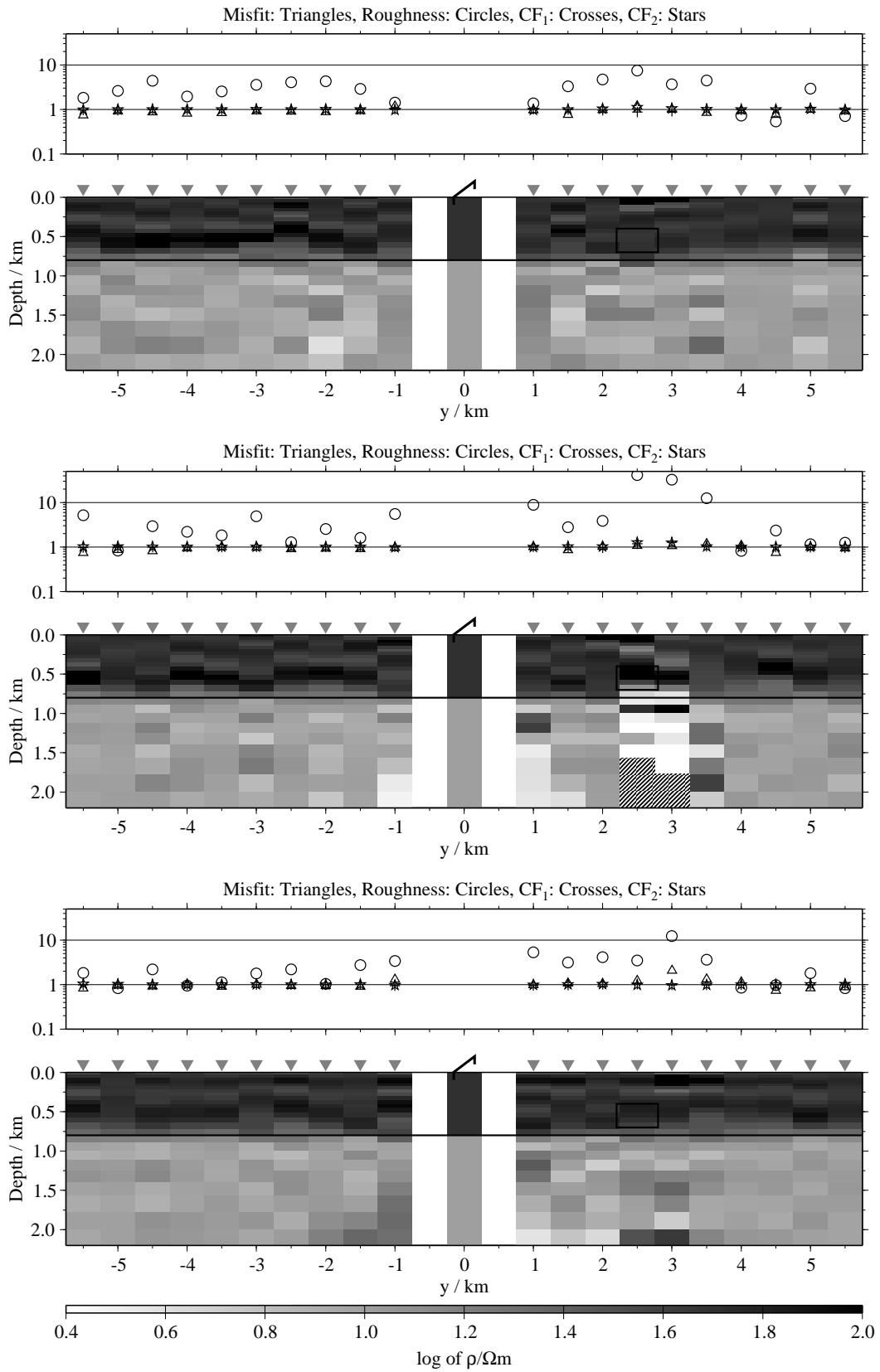


Figure B.143: Pseudo-sections of two component 1-D joint-inversions, model G2, regularisation scheme C1; from top to bottom $E_x - \dot{H}_y$, $E_x - \dot{H}_z$ and $\dot{H}_y - \dot{H}_z$;

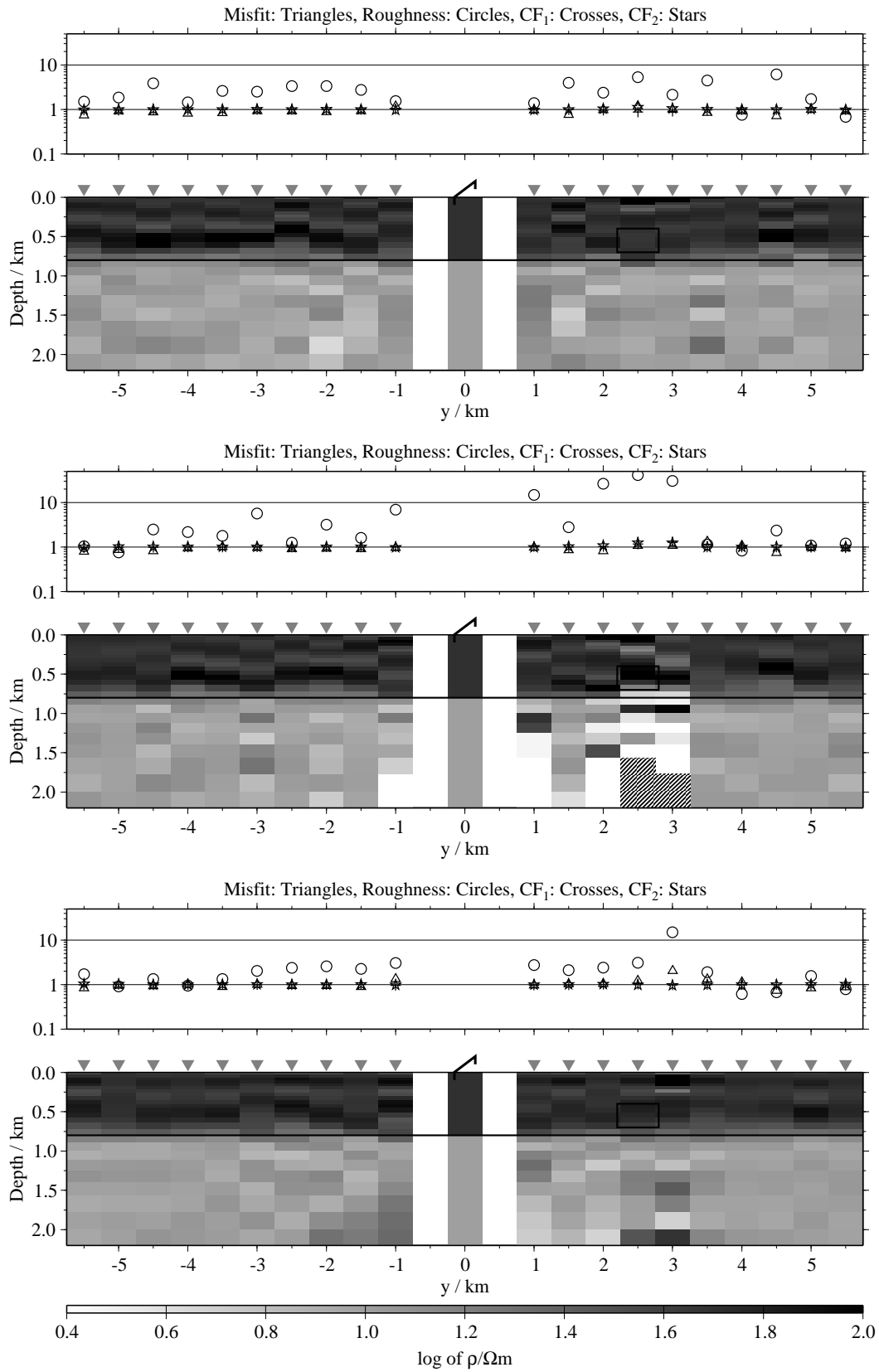


Figure B.144: Pseudo-sections of two component 1-D joint-inversions, model G2, regularisation scheme C4; from top to bottom $E_x\text{-}\dot{H}_y$, $E_x\text{-}\dot{H}_z$ and $\dot{H}_y\text{-}\dot{H}_z$;

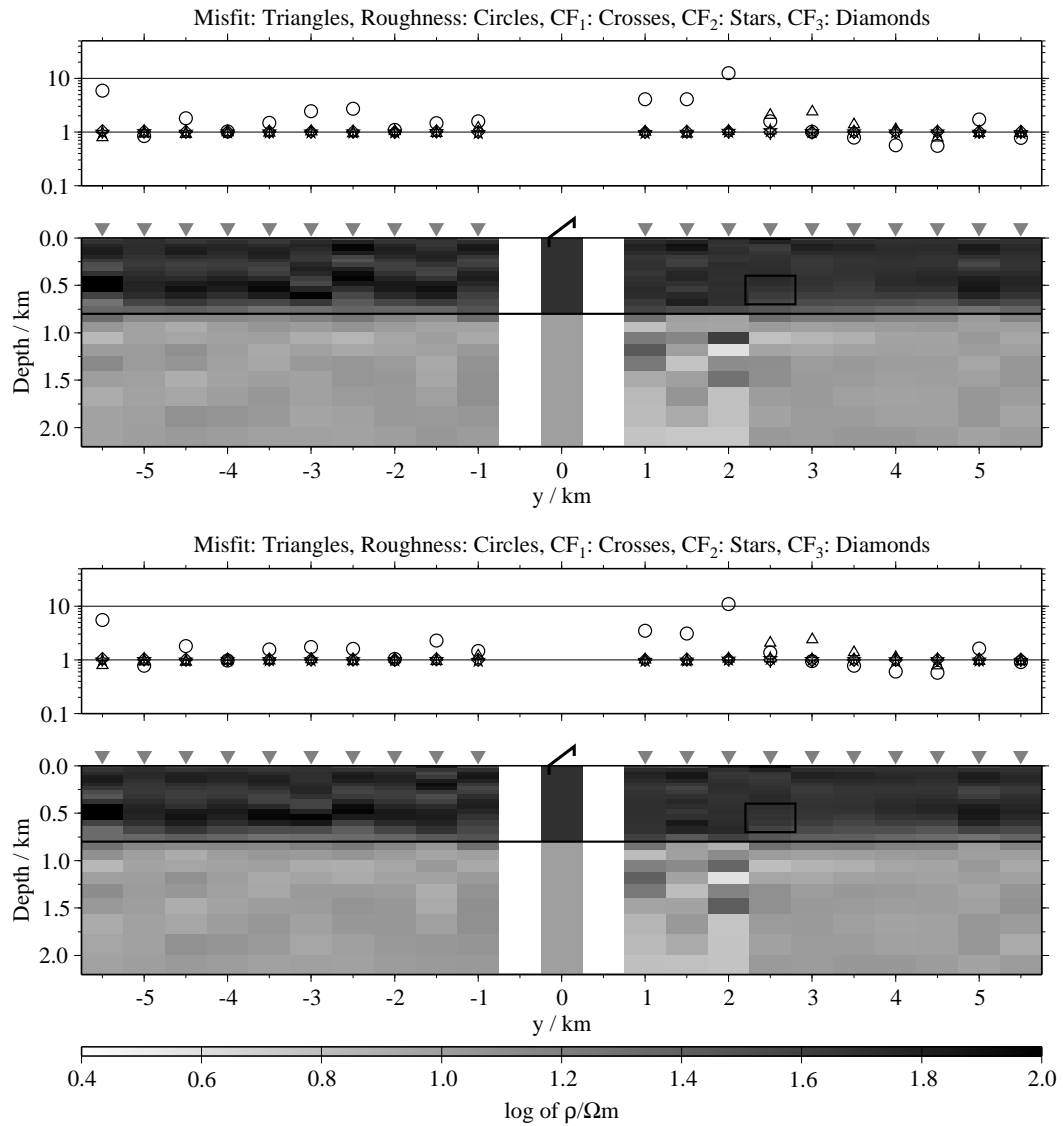


Figure B.145: Pseudo-sections of 1-D joint-inversions using all three components, model G2; top: Regularisation scheme C1; bottom: Regularisation scheme C4;

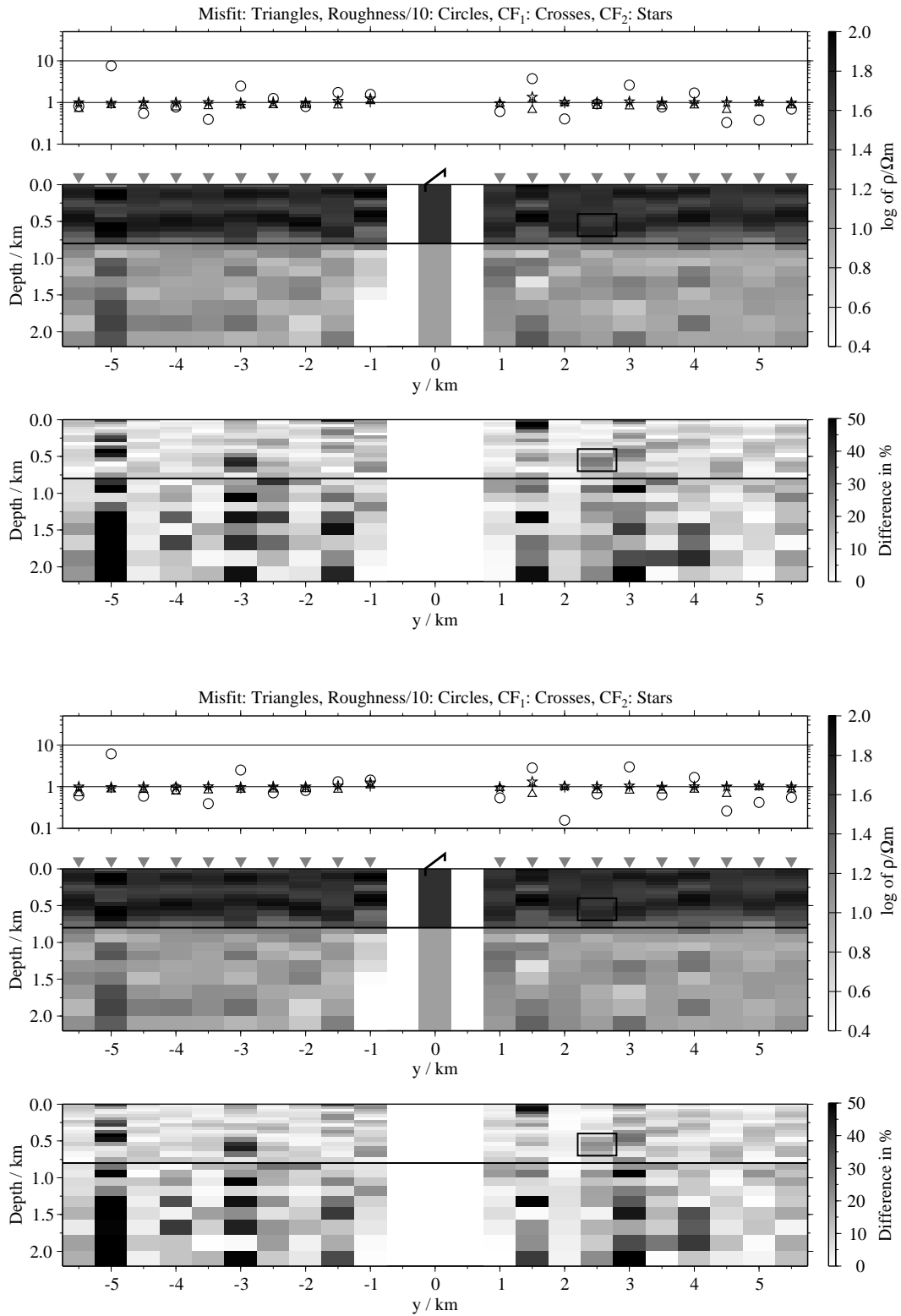


Figure B.146: Pseudo-sections of 1-D soft joint-inversions using the components E_x and H_y , model G2; Top panels: Average inversion results and relative differences (regularisation scheme C1); bottom: Average inversion results and relative differences (regularisation scheme C4);

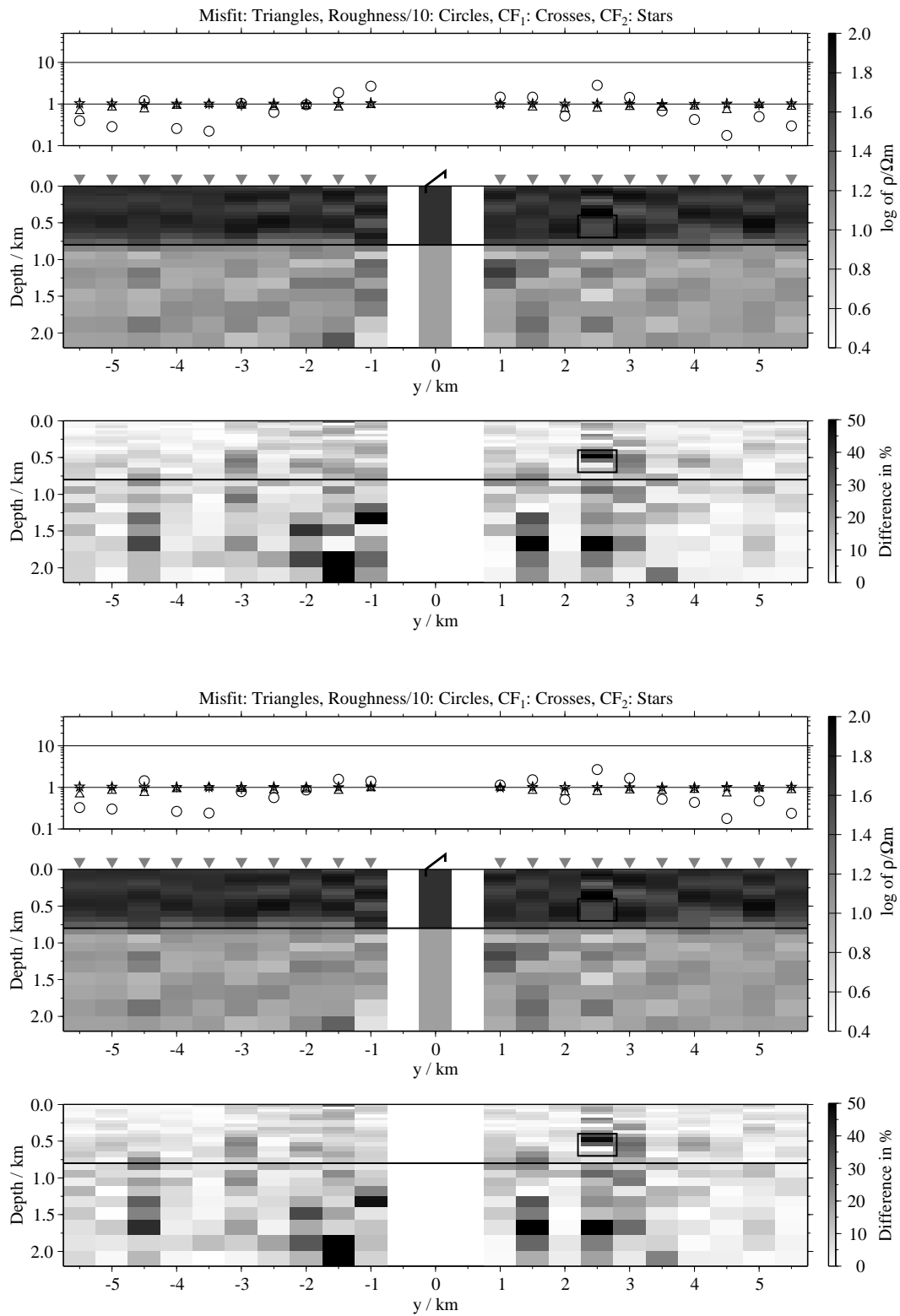


Figure B.147: Pseudo-sections 1-D of soft joint-inversions using the components E_x and \dot{H}_{zi} , model G2; Top panels: Average inversion results and relative differences (regularisation scheme C1); bottom: Average inversion results and relative differences (regularisation scheme C4);

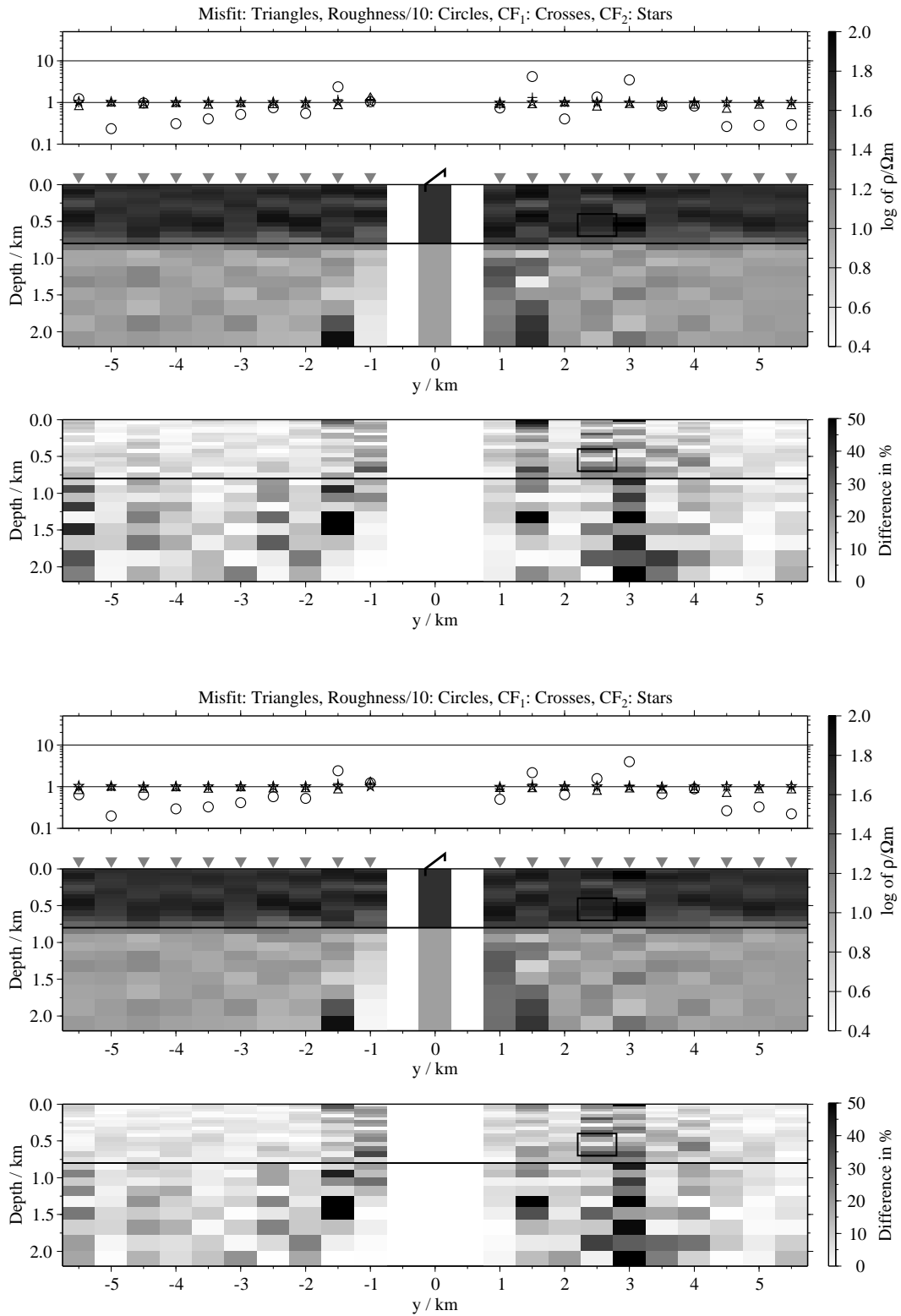


Figure B.148: Pseudo-sections of 1-D soft joint-inversions using the components \dot{H}_y and \dot{H}_z , model G2; Top panels: Average inversion results and relative differences (regularisation scheme C1); bottom: Average inversion results and relative differences (regularisation scheme C4);

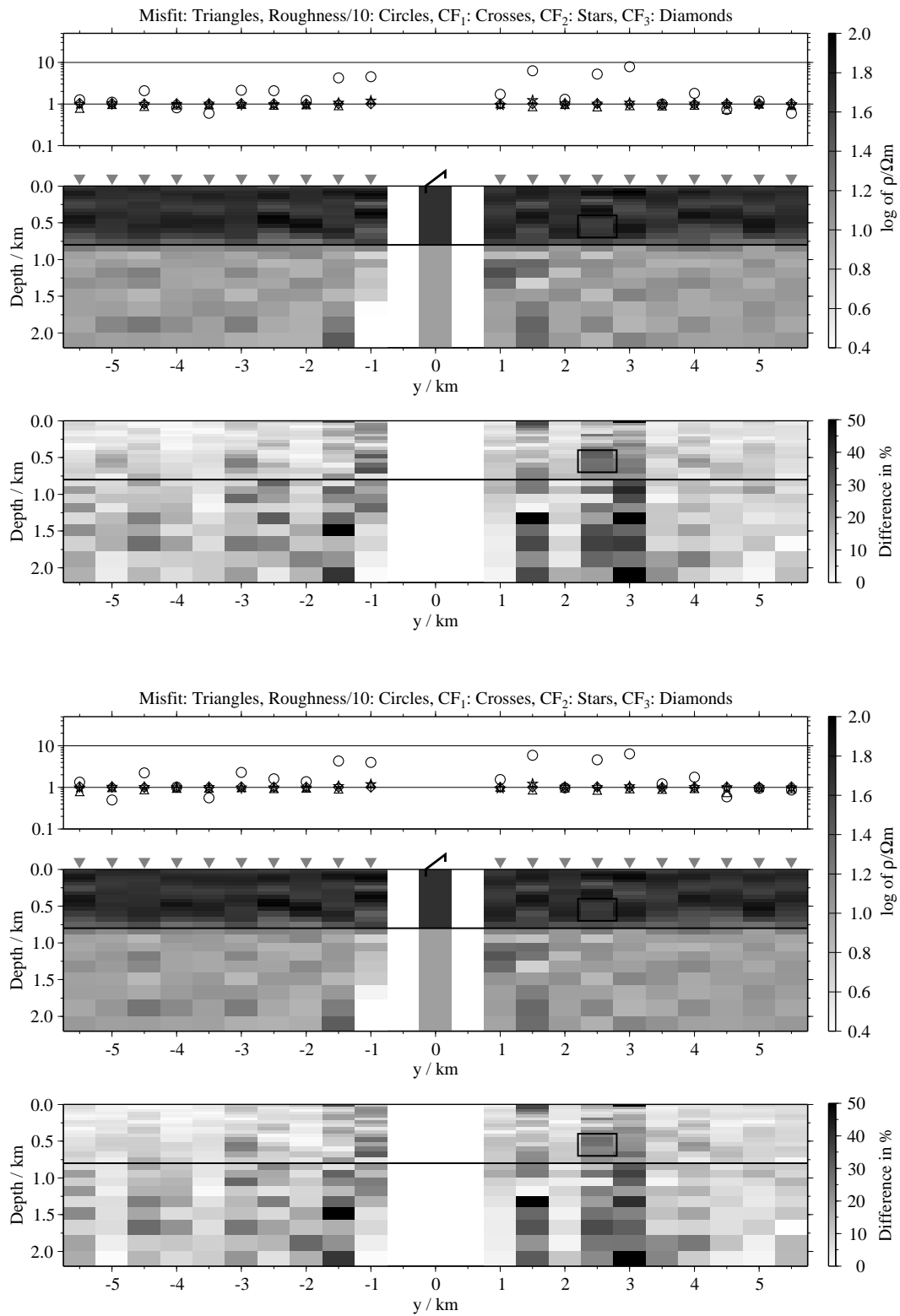
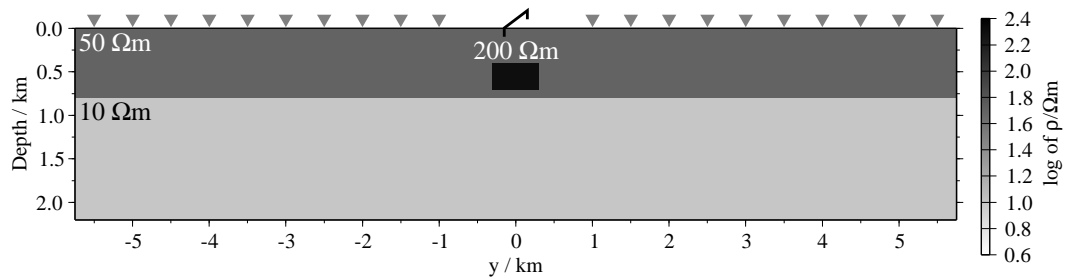


Figure B.149: Pseudo-sections of 1-D soft joint-inversions using all three components, model G2; Top panels: Average inversion results and relative differences (regularisation scheme C1); bottom: Average inversion results and relative differences (regularisation scheme C4);

B.2.6 Resistive patch at an intermediate depth (models H1 and H2)

Model H1:



Model H2:

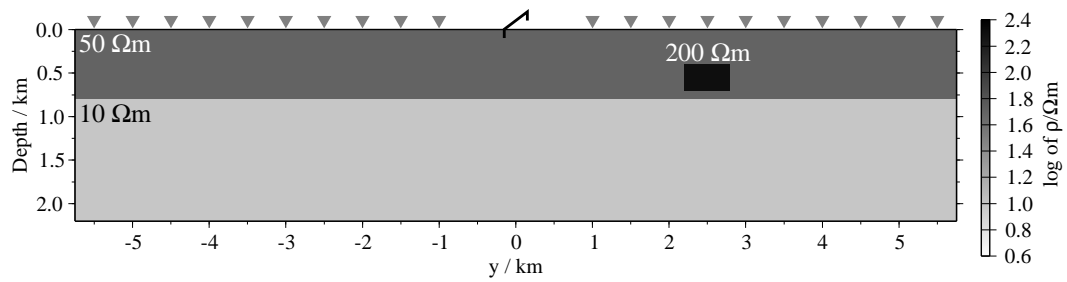


Figure B.150: Model with a resistive patch in an intermediate depth; the mid-point of the patch is in both cases at $x = 0$ km and $y = 0$ km (model H1) and $y = 2.5$ km (model H2), respectively. The patch has the size $600 \times 600 \times 300 \text{ m}^3$.

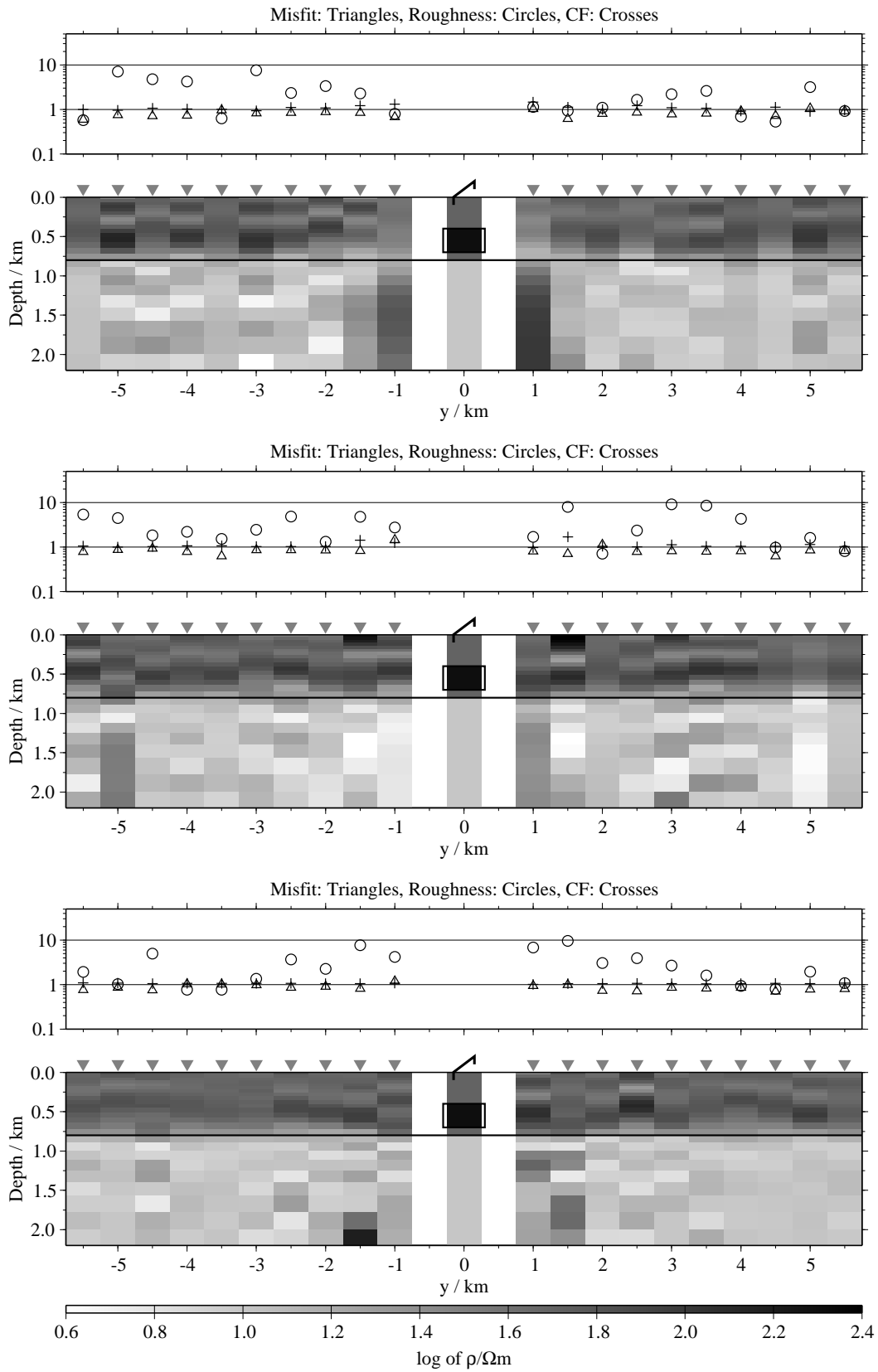


Figure B.151: Pseudo-sections of single 1-D inversion, model H1, regularisation scheme C1; from top to bottom E_{x^-} , \dot{H}_y - and \dot{H}_z -component;

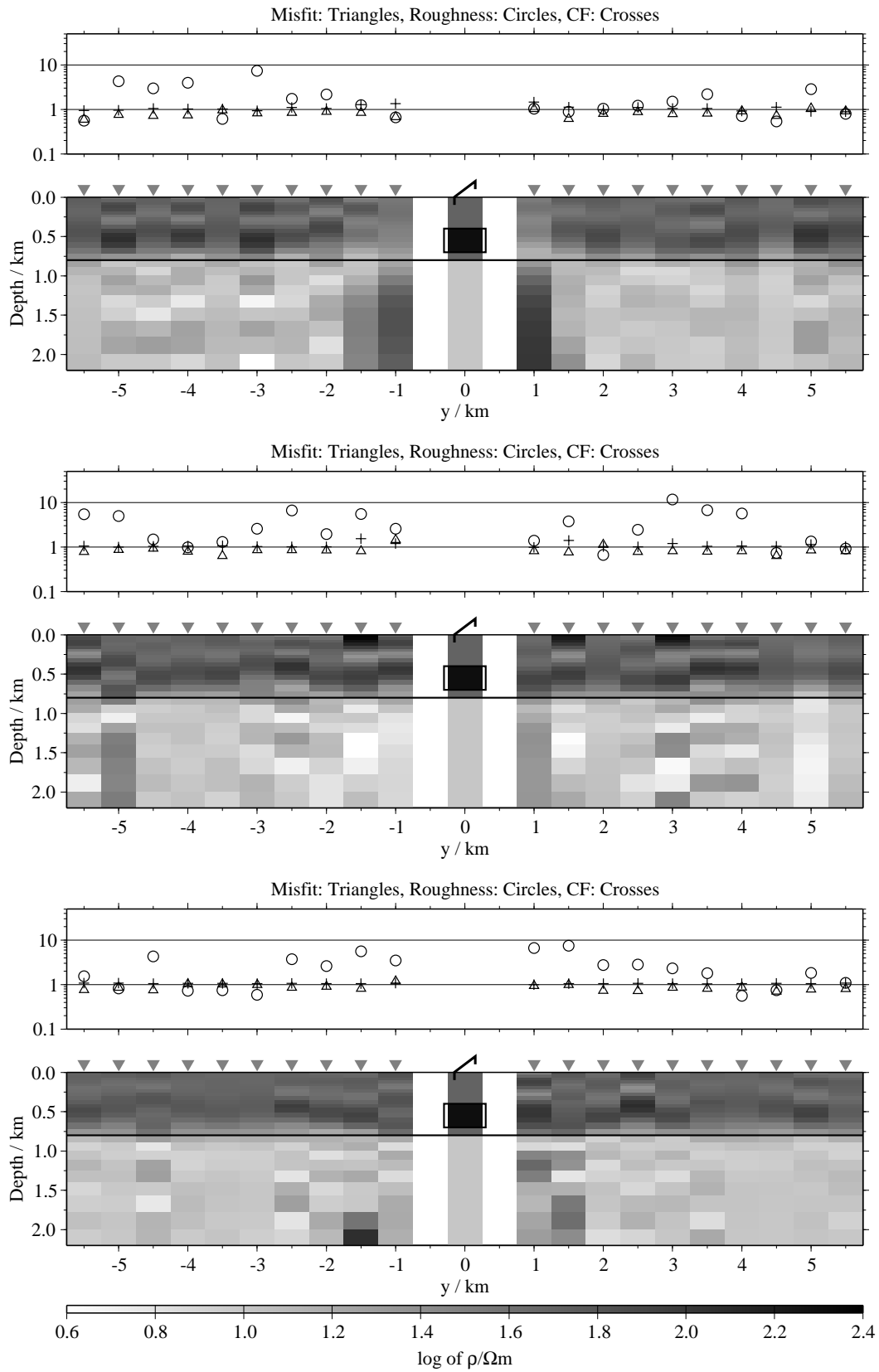


Figure B.152: Pseudo-sections of single 1-D inversion, model H1, regularisation scheme C4; from top to bottom E_x -, H_y - and H_z -component;

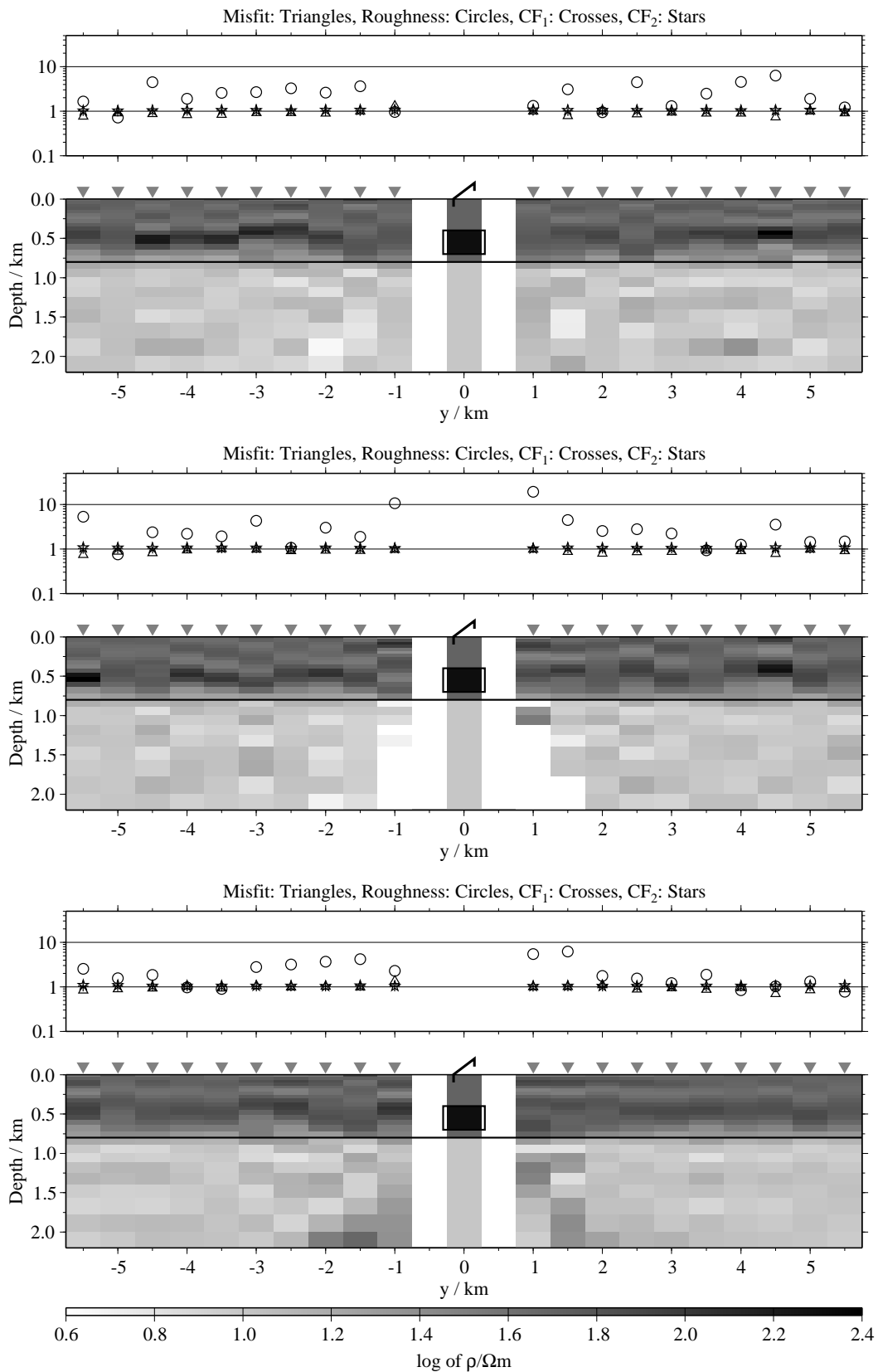


Figure B.153: Pseudo-sections of two component 1-D joint-inversions, model H1, regularisation scheme C1; from top to bottom $E_x-\dot{H}_y$, $E_x-\dot{H}_z$ and $\dot{H}_y-\dot{H}_z$;

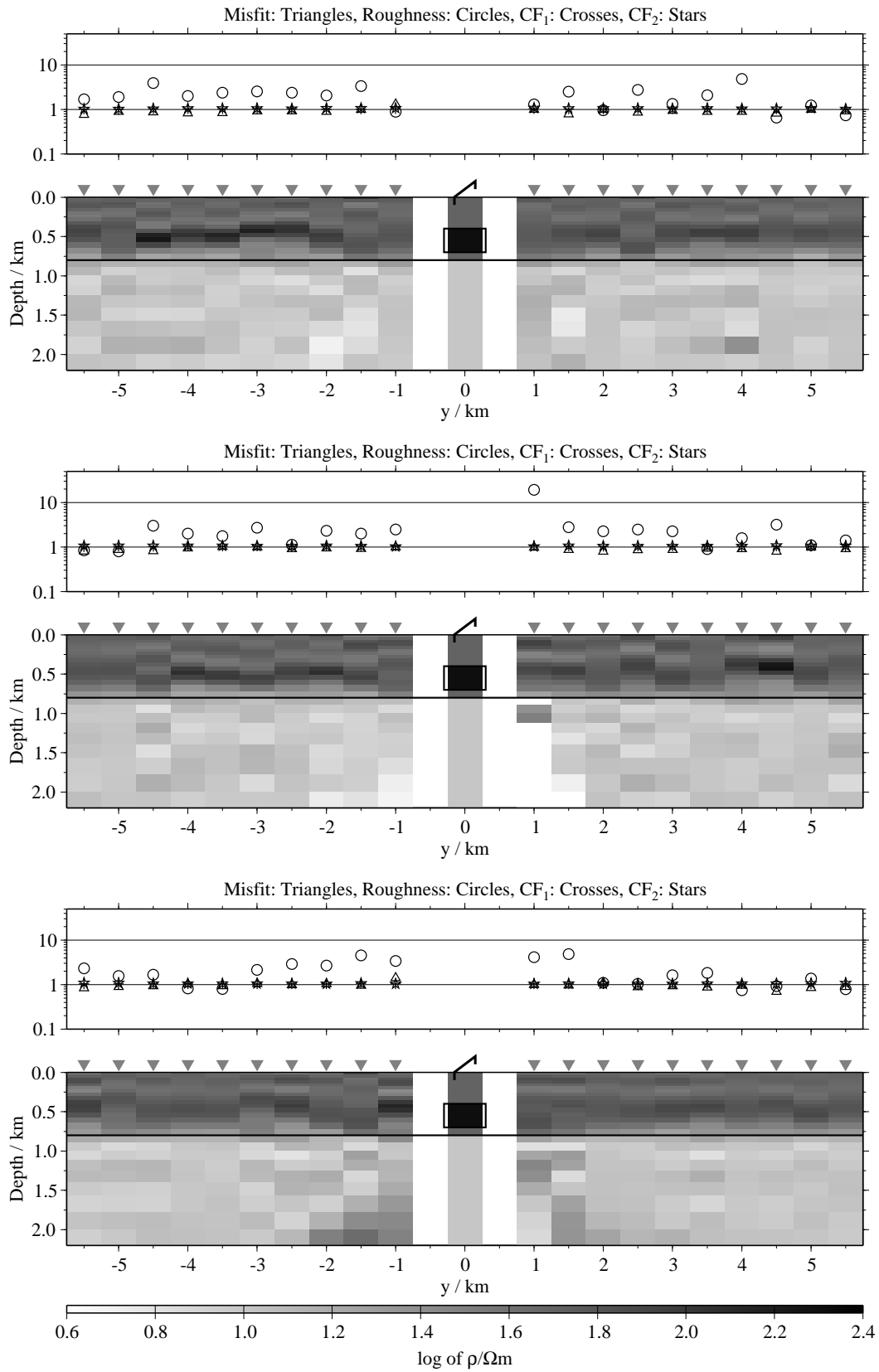


Figure B.154: Pseudo-sections of two component 1-D joint-inversions, model H1, regularisation scheme C4; from top to bottom $E_x-\dot{H}_y$, $E_x-\dot{H}_z$ and $\dot{H}_y-\dot{H}_z$;

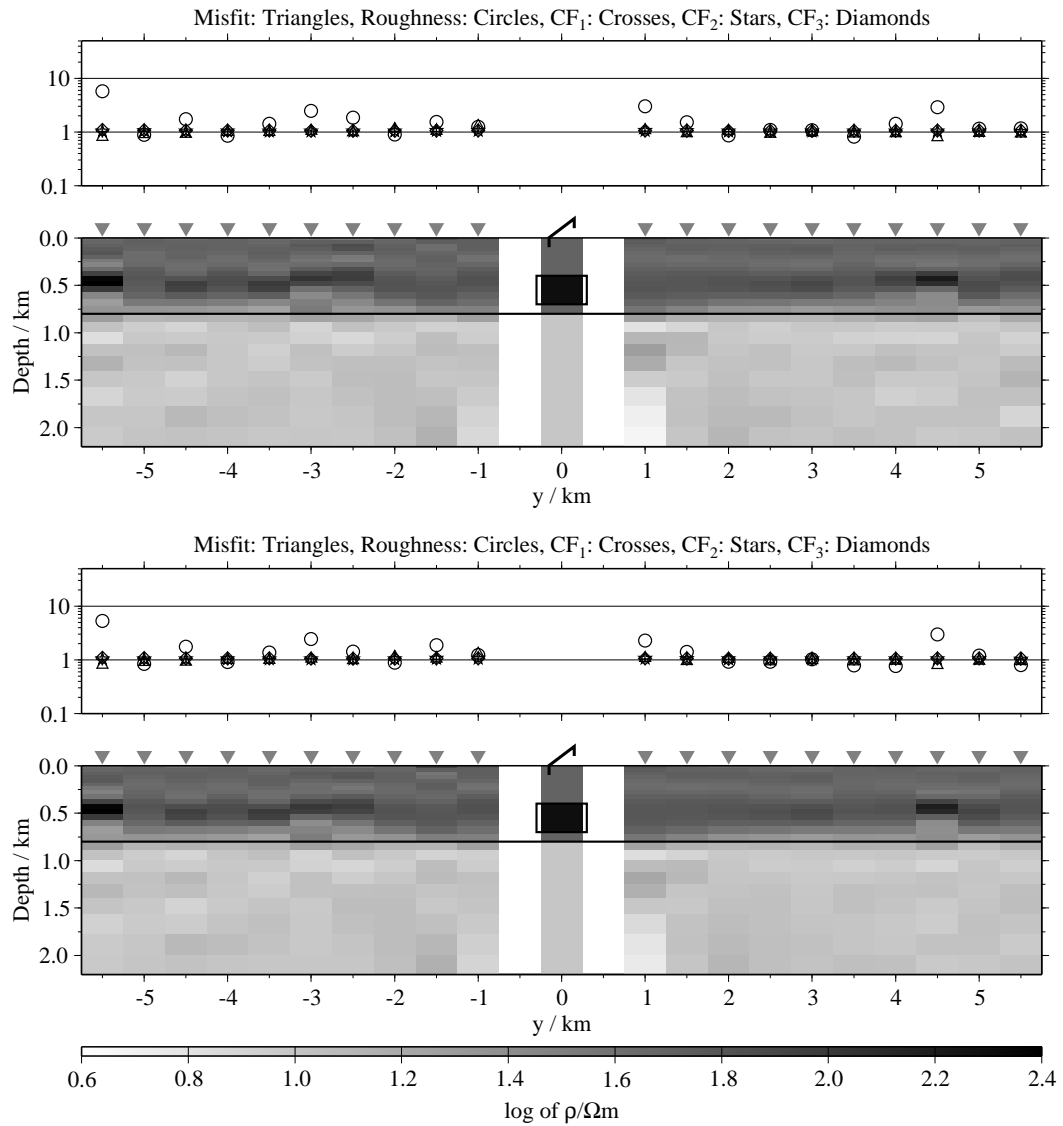


Figure B.155: Pseudo-sections of 1-D joint-inversions using all three components, model H1; top: Regularisation scheme C1; bottom: Regularisation scheme C4;

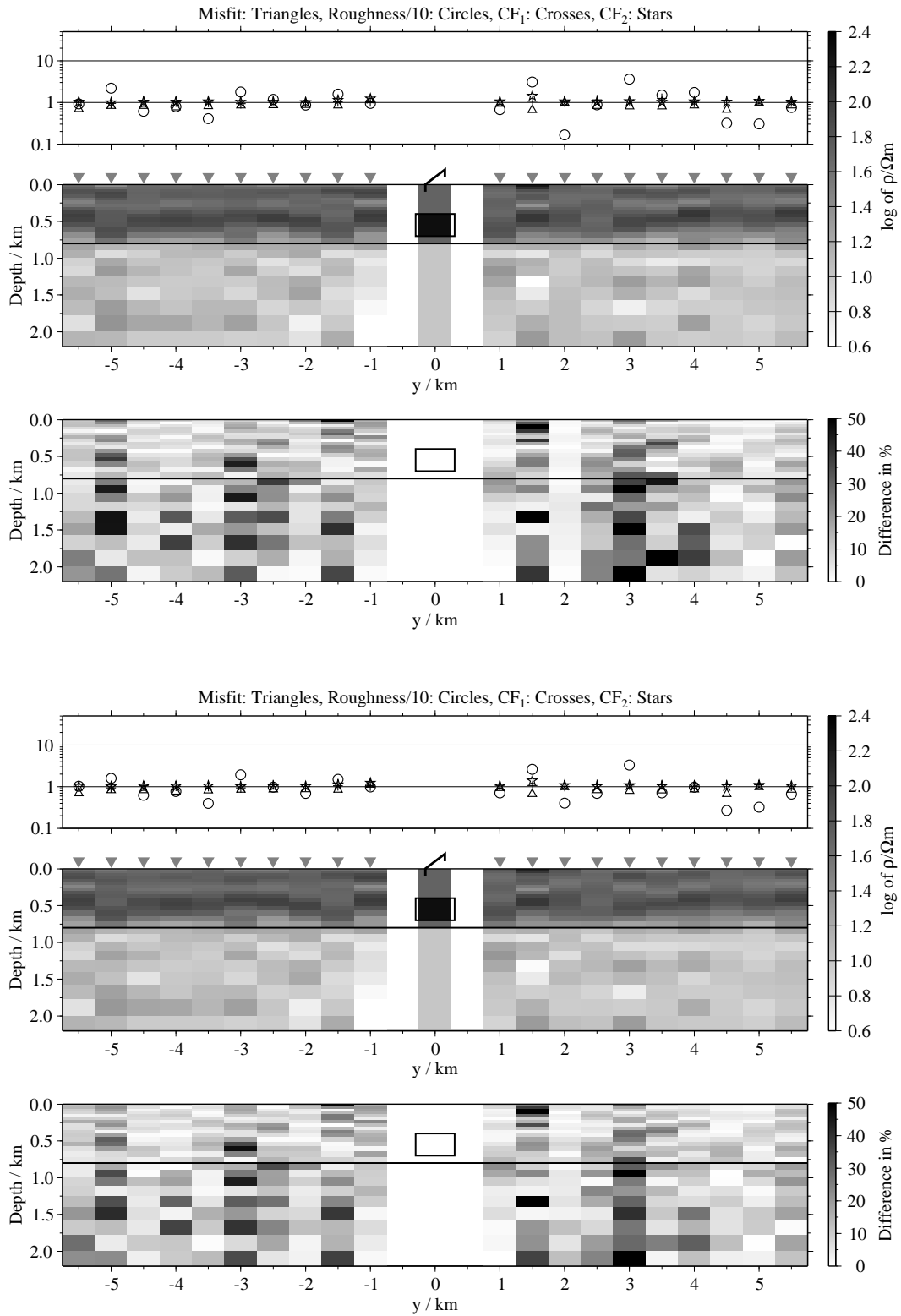


Figure B.156: Pseudo-sections of 1-D soft joint-inversions using the components E_x and H_y , model H1; Top panels: Average inversion results and relative differences (regularisation scheme C1); bottom: Average inversion results and relative differences (regularisation scheme C4);

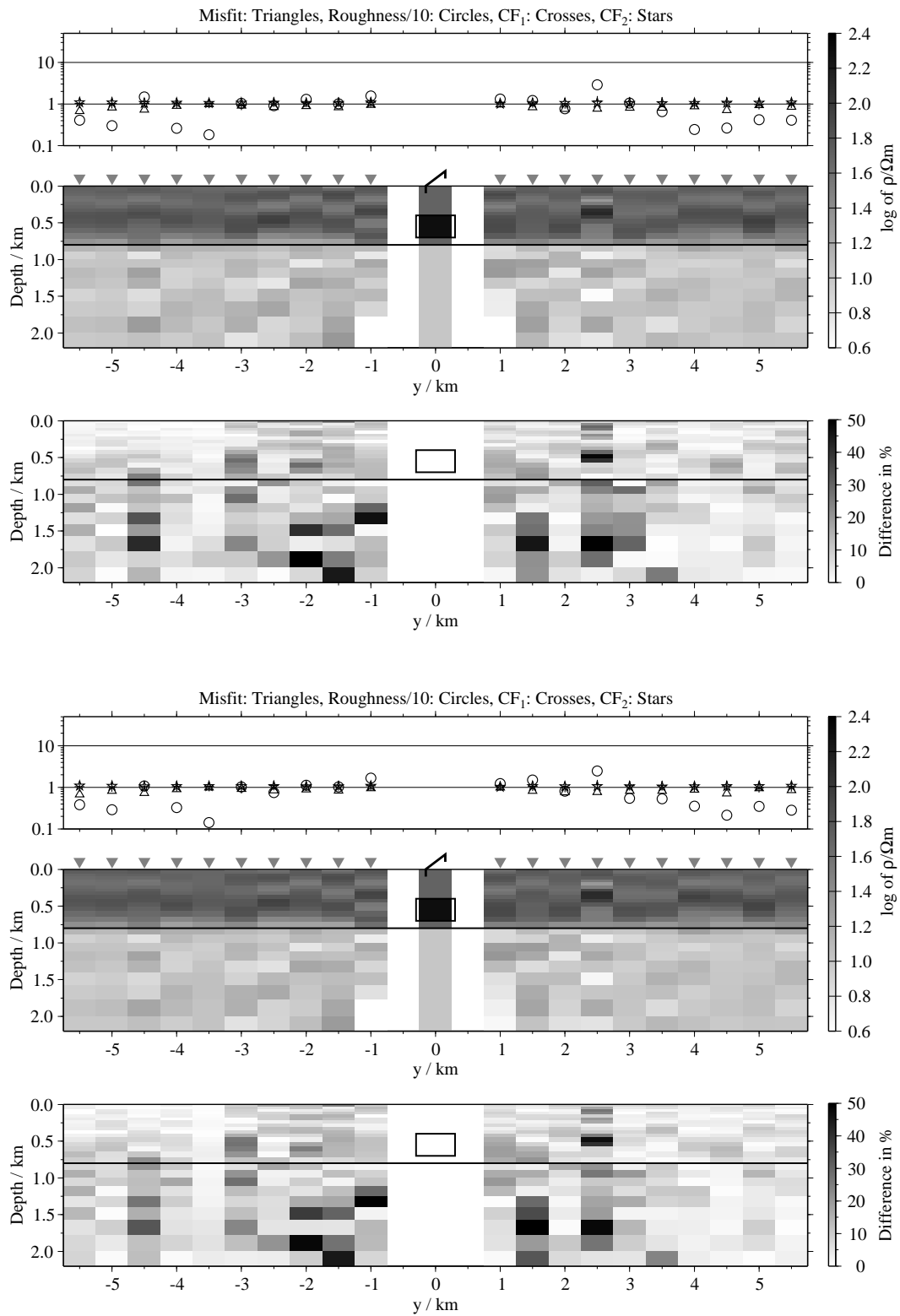


Figure B.157: Pseudo-sections 1-D of soft joint-inversions using the components E_x and H_z , model H1; Top panels: Average inversion results and relative differences (regularisation scheme C1); bottom: Average inversion results and relative differences (regularisation scheme C4);

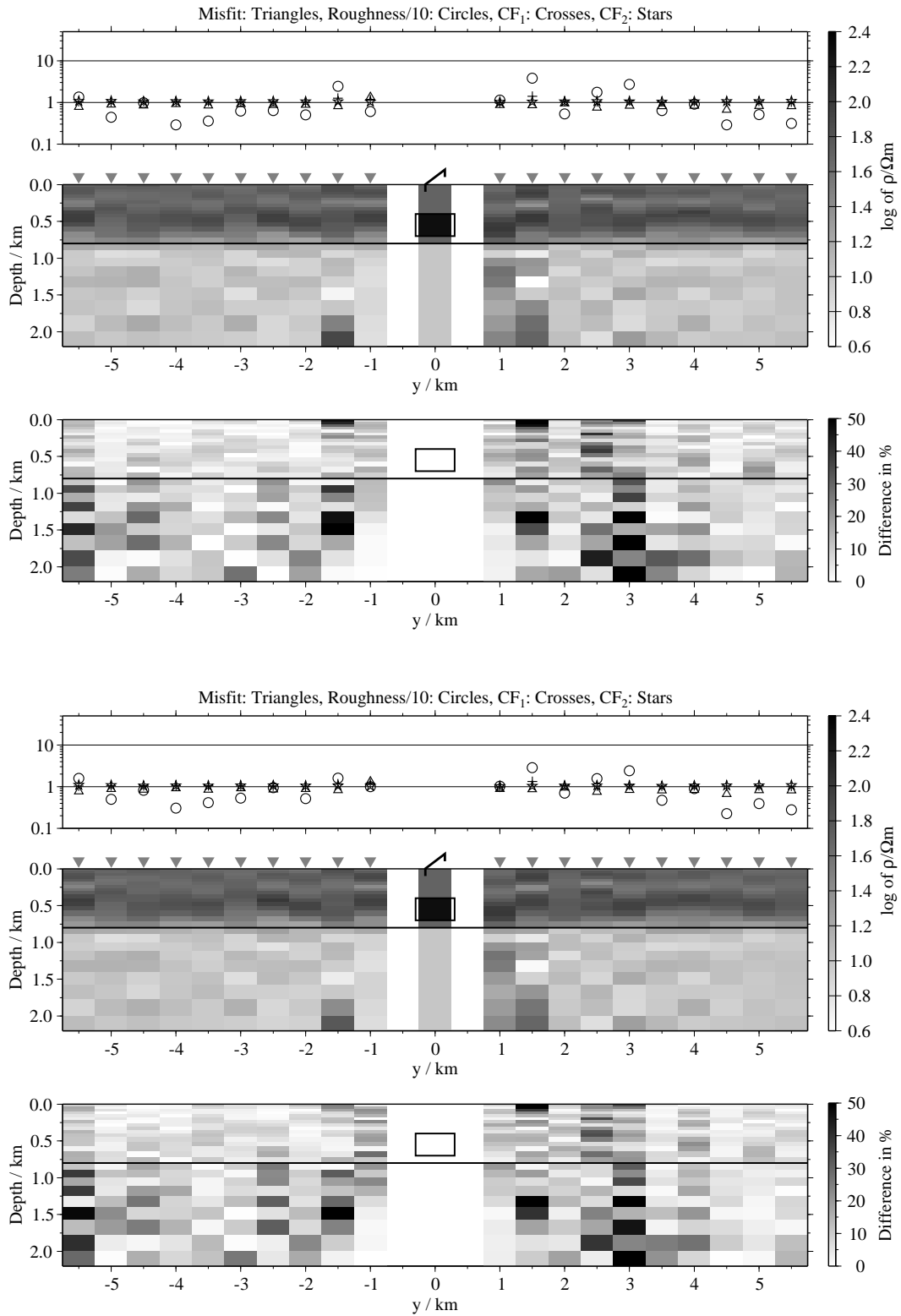


Figure B.158: Pseudo-sections of 1-D soft joint-inversions using the components \dot{H}_y and \dot{H}_z , model H1; Top panels: Average inversion results and relative differences (regularisation scheme C1); bottom: Average inversion results and relative differences (regularisation scheme C4);

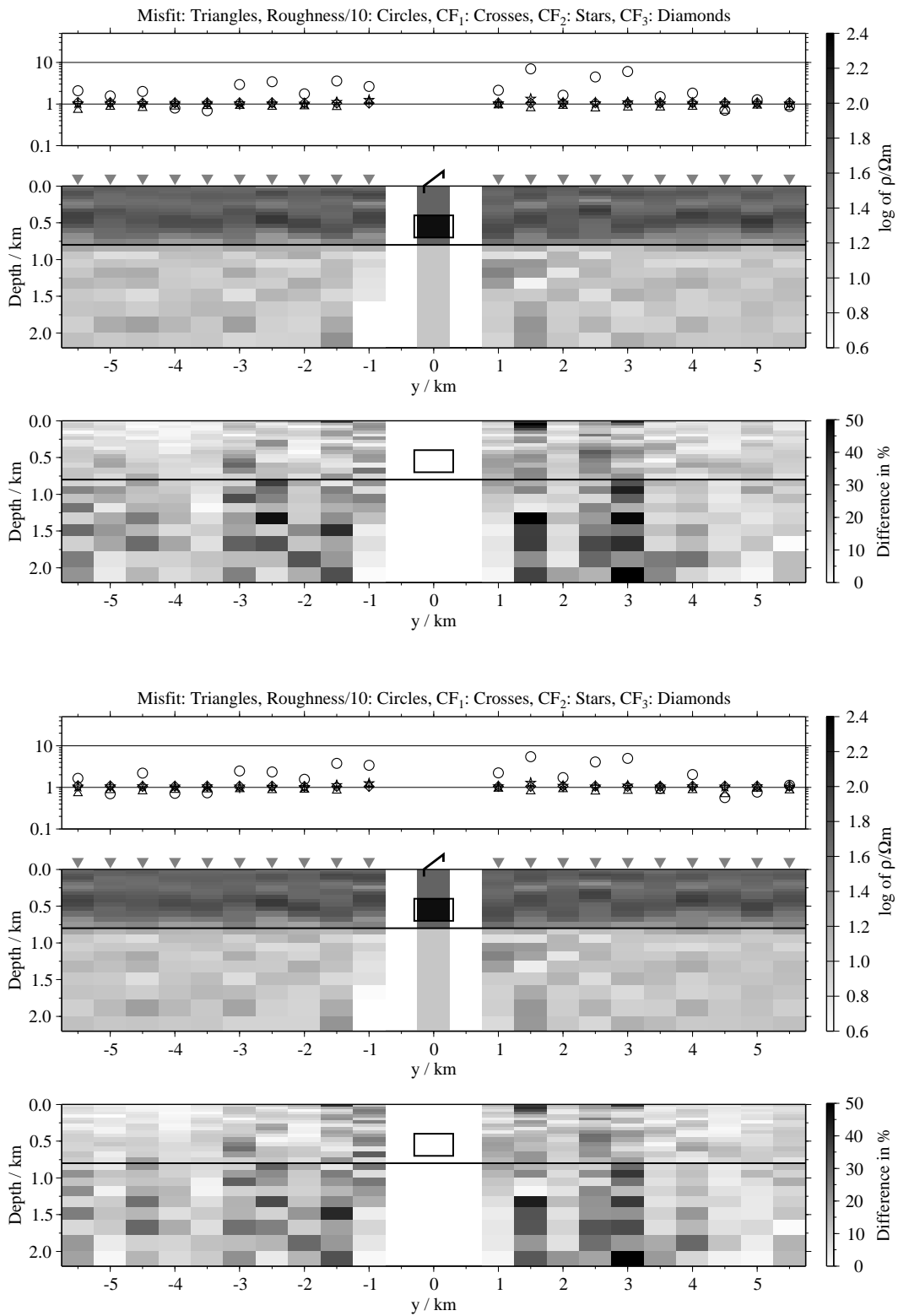


Figure B.159: Pseudo-sections of 1-D soft joint-inversions using all three components, model H1; Top panels: Average inversion results and relative differences (regularisation scheme C1); bottom: Average inversion results and relative differences (regularisation scheme C4);

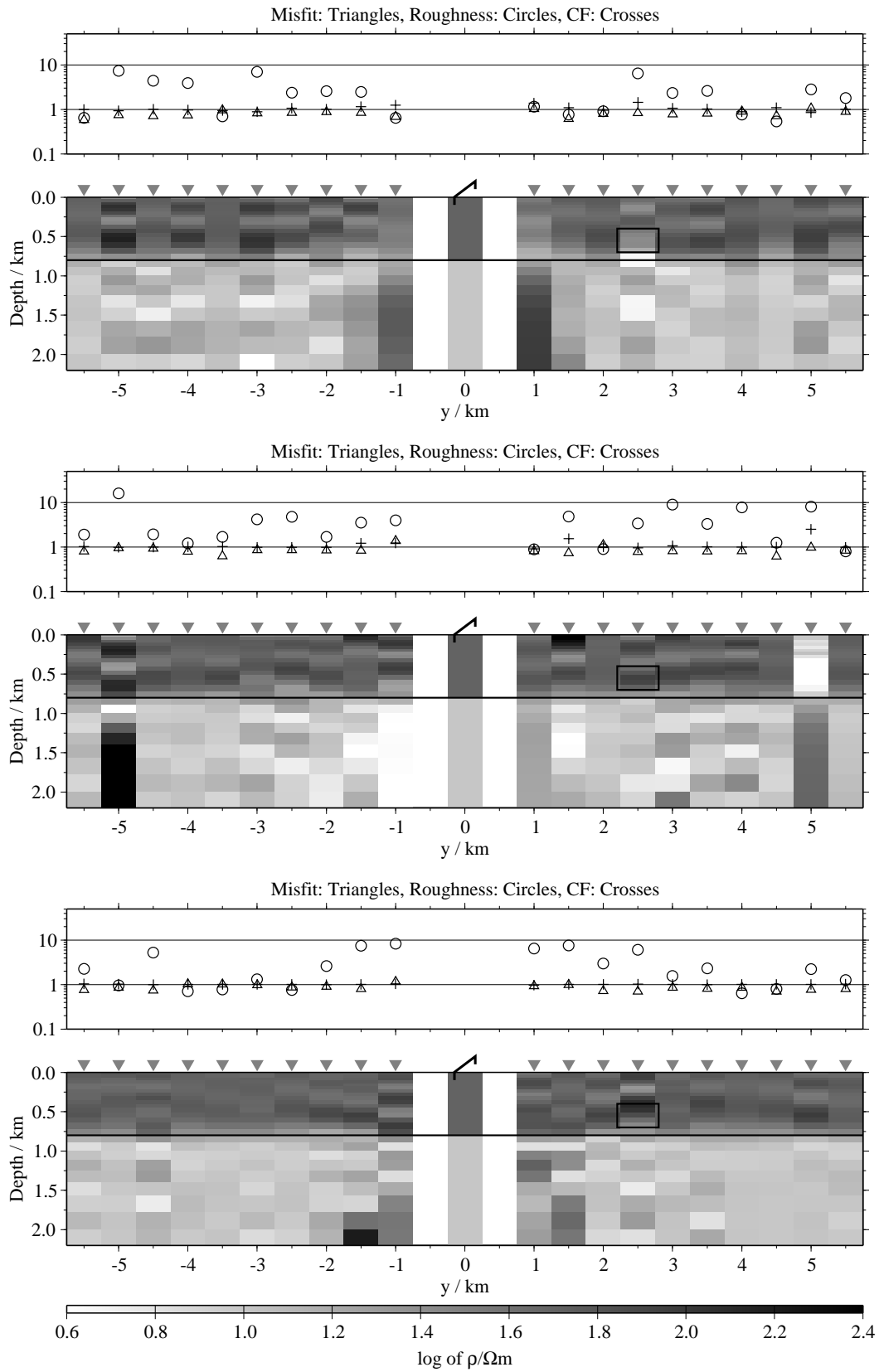


Figure B.160: Pseudo-sections of single 1-D inversion, model H2, regularisation scheme C1; from top to bottom E_x -, \dot{H}_y - and \dot{H}_z -component;

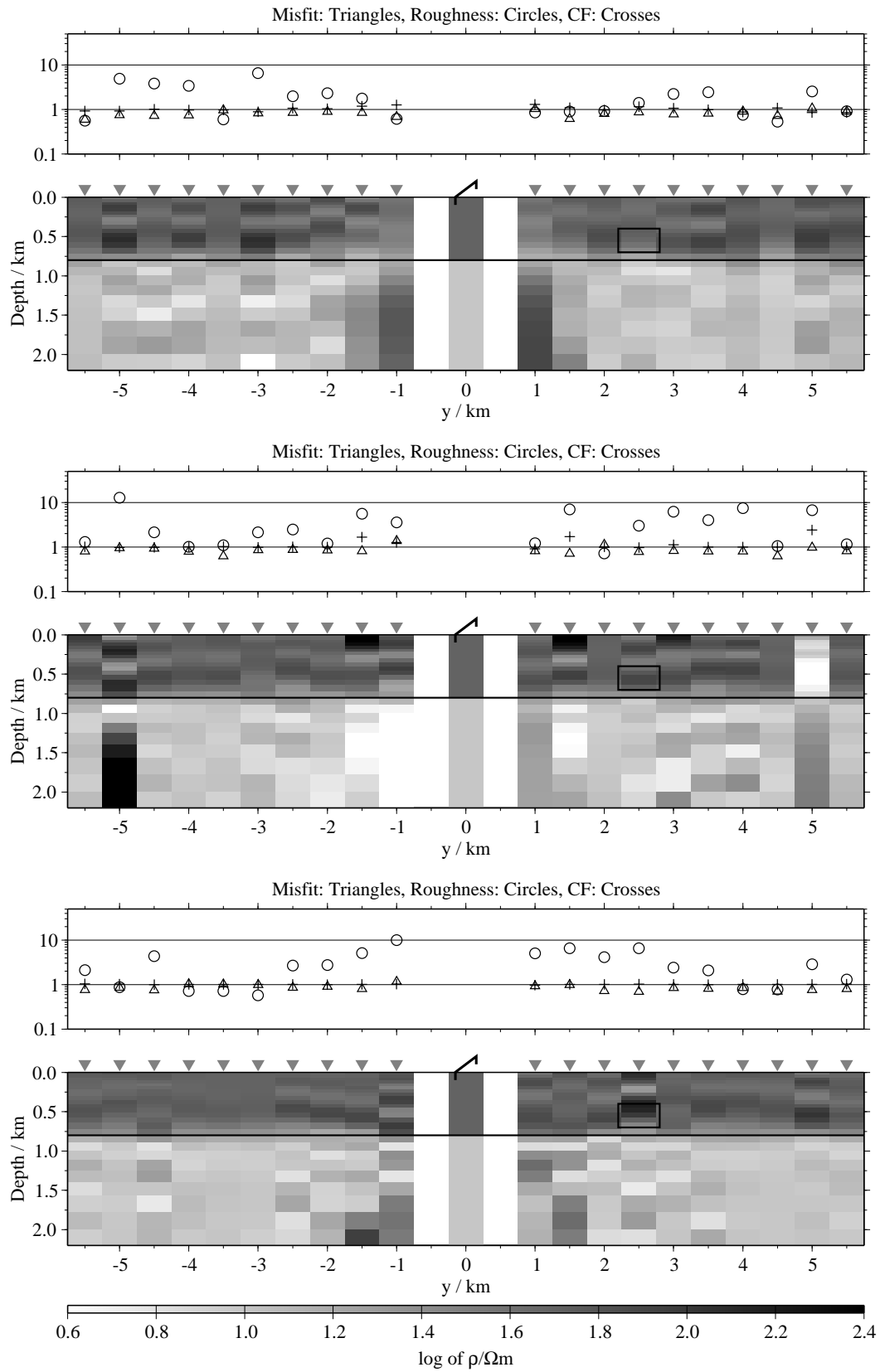


Figure B.161: Pseudo-sections of single 1-D inversion, model H2, regularisation scheme C4; from top to bottom E_x -, \dot{H}_y - and \dot{H}_z -component;

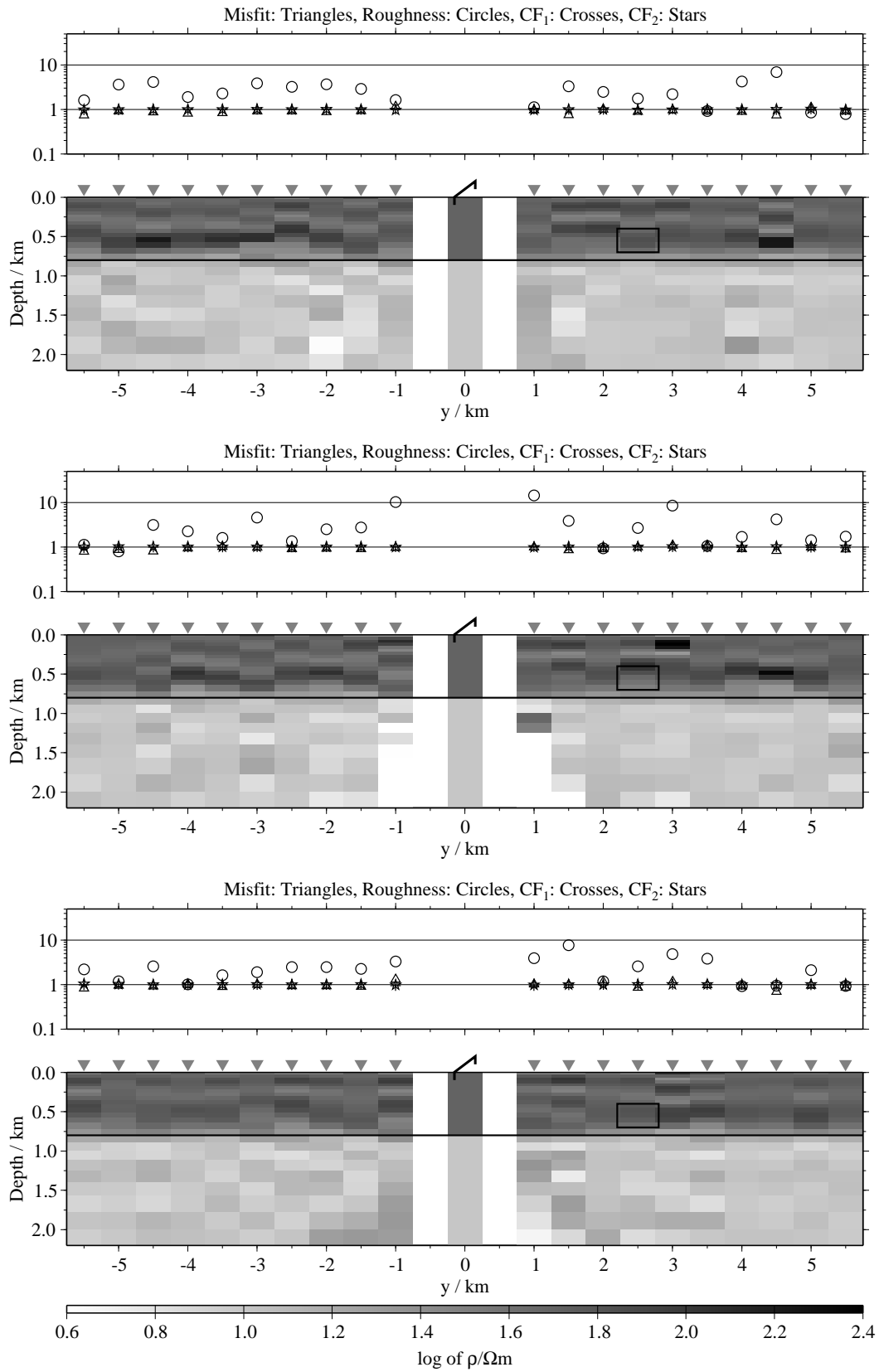


Figure B.162: Pseudo-sections of two component 1-D joint-inversions, model H2, regularisation scheme C1; from top to bottom $E_x-\dot{H}_y$, $E_x-\dot{H}_z$ and $\dot{H}_y-\dot{H}_z$;

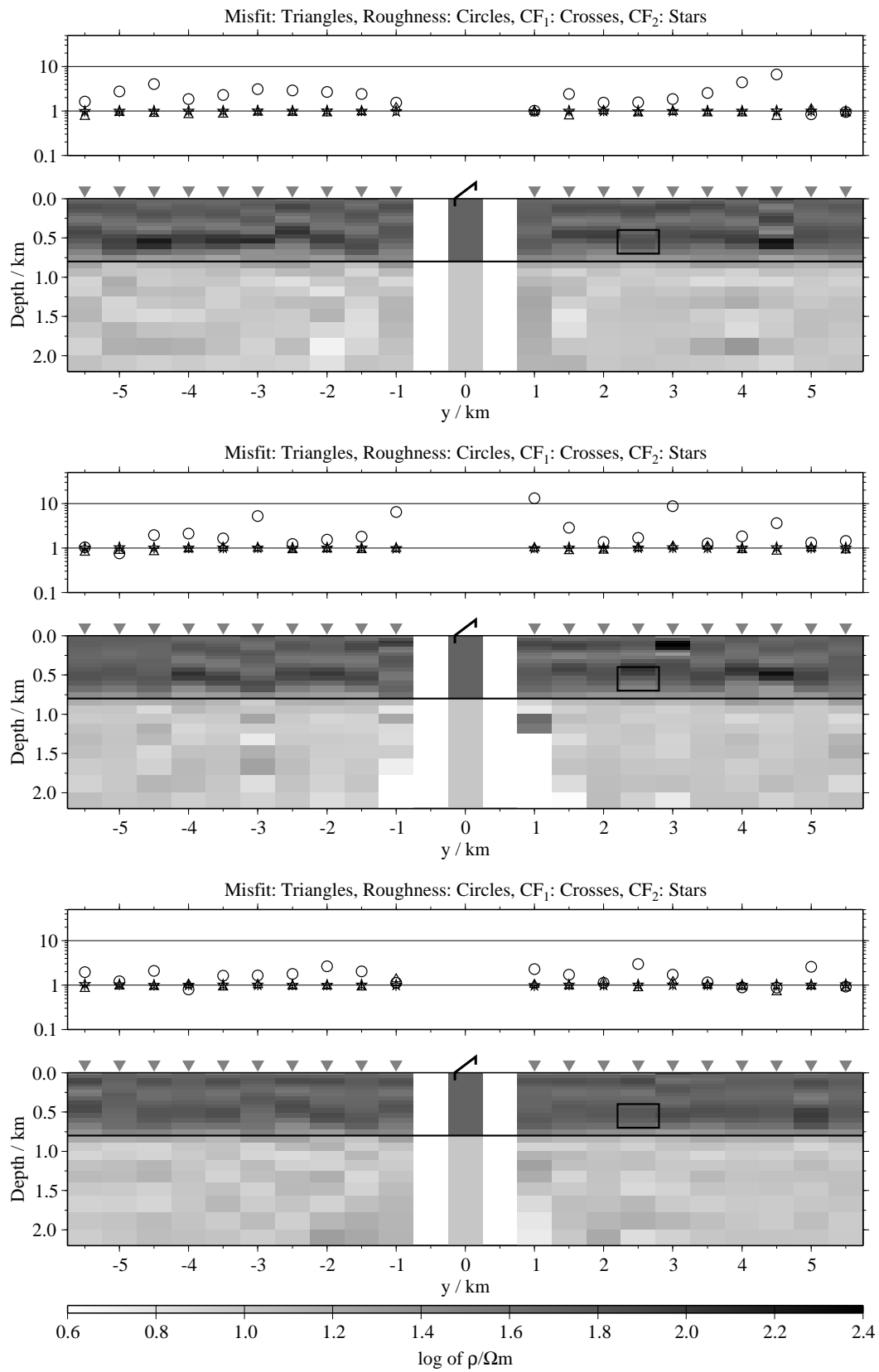


Figure B.163: Pseudo-sections of two component 1-D joint-inversions, model H2, regularisation scheme C4; from top to bottom $E_x\text{-}\dot{H}_y$, $E_x\text{-}\dot{H}_z$ and $\dot{H}_y\text{-}\dot{H}_z$;

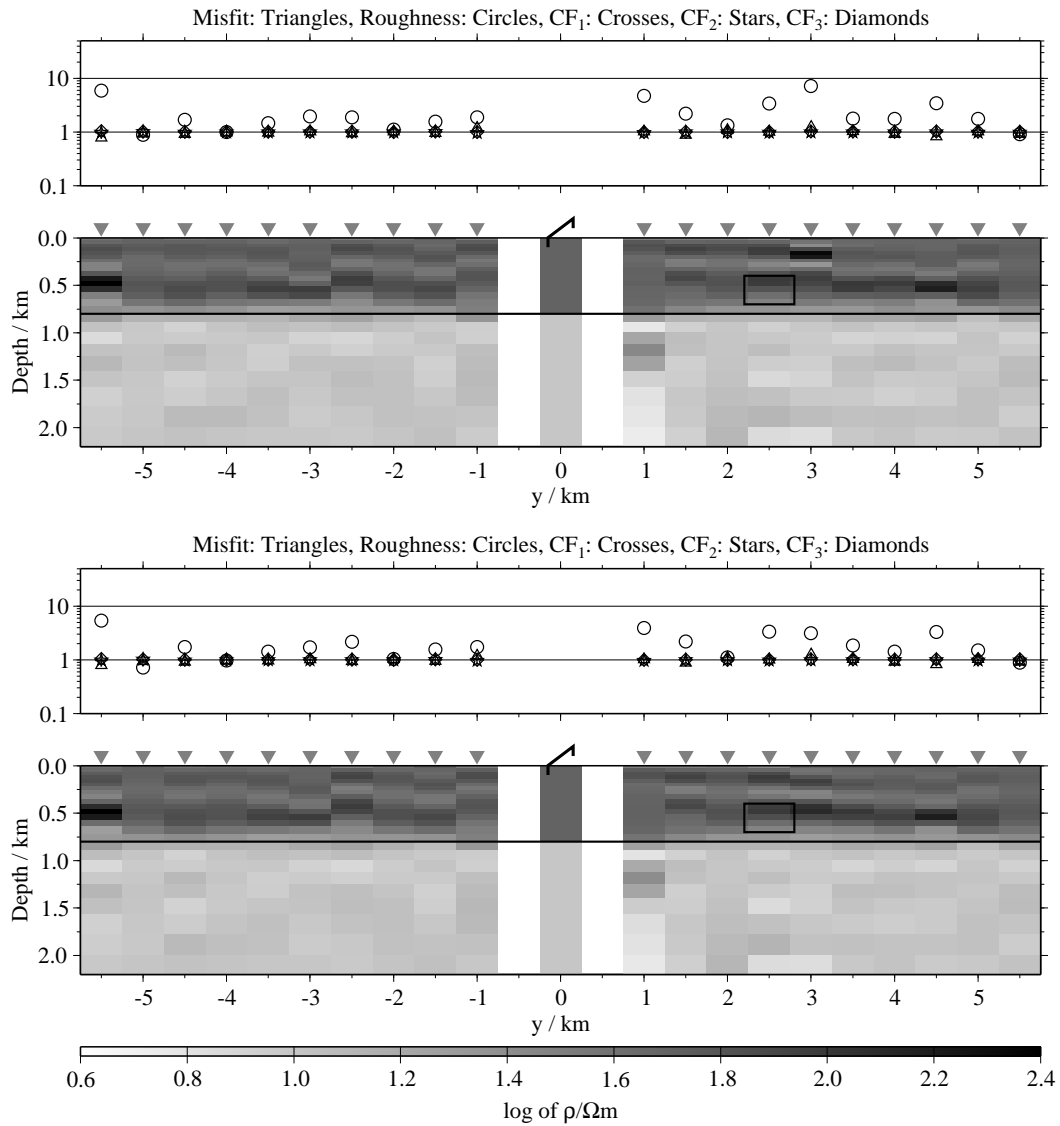


Figure B.164: Pseudo-sections of 1-D joint-inversions using all three components, model H2; top: Regularisation scheme C1; bottom: Regularisation scheme C4;

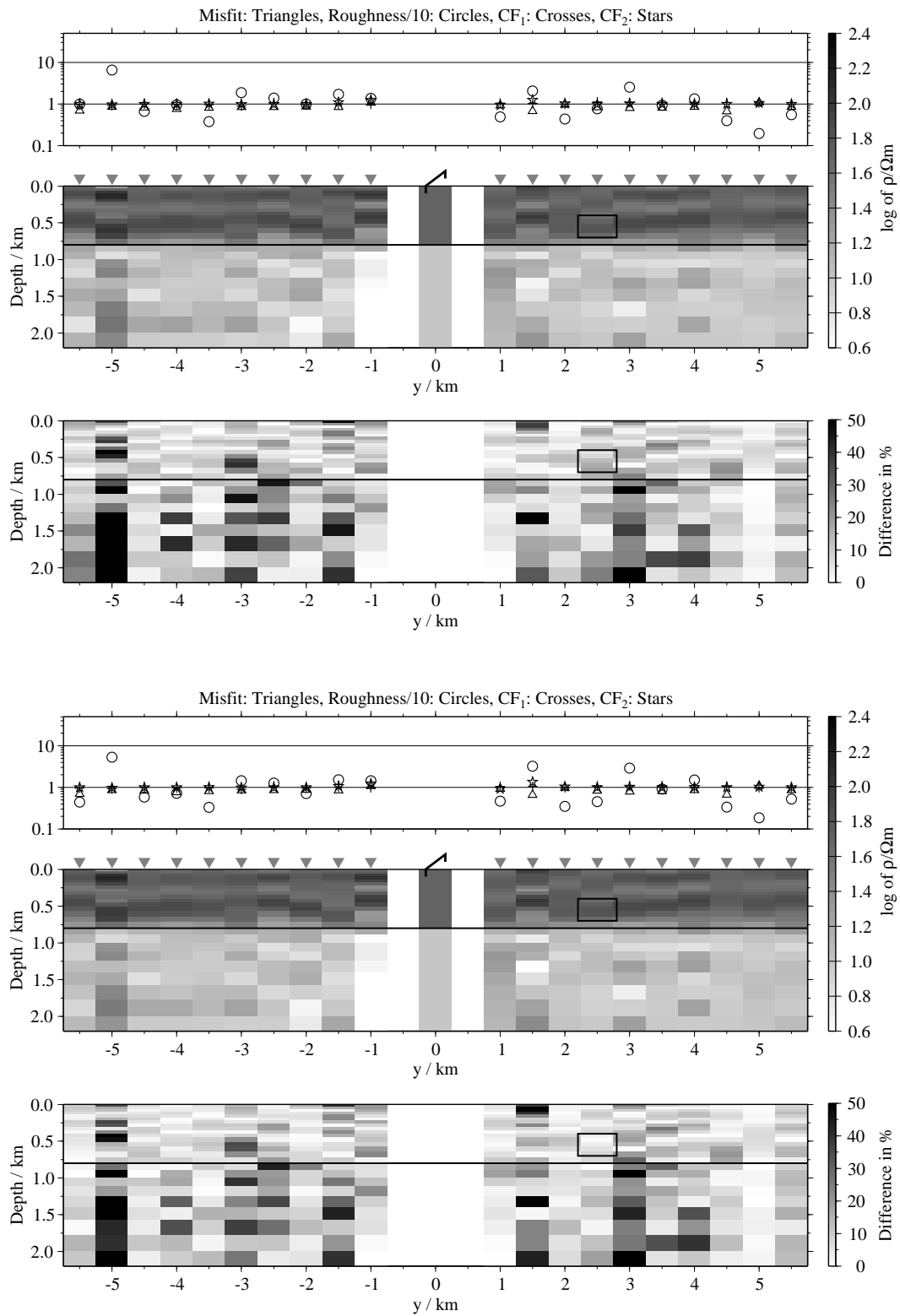


Figure B.165: Pseudo-sections of 1-D soft joint-inversions using the components E_x and H_y , model H2; Top panels: Average inversion results and relative differences (regularisation scheme C1); bottom: Average inversion results and relative differences (regularisation scheme C4);

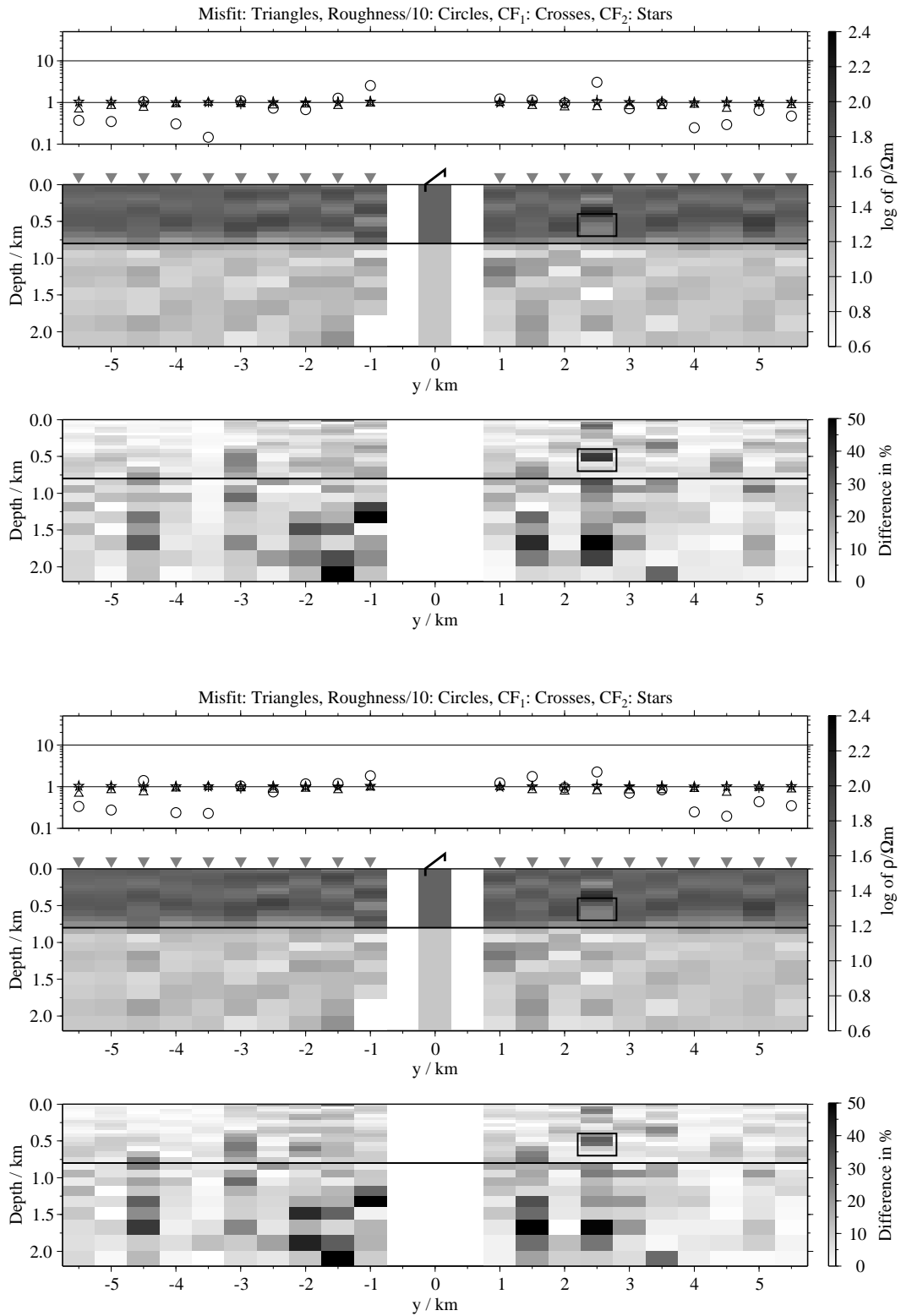


Figure B.166: Pseudo-sections 1-D of soft joint-inversions using the components E_x and H_z , model H2; Top panels: Average inversion results and relative differences (regularisation scheme C1); bottom: Average inversion results and relative differences (regularisation scheme C4);

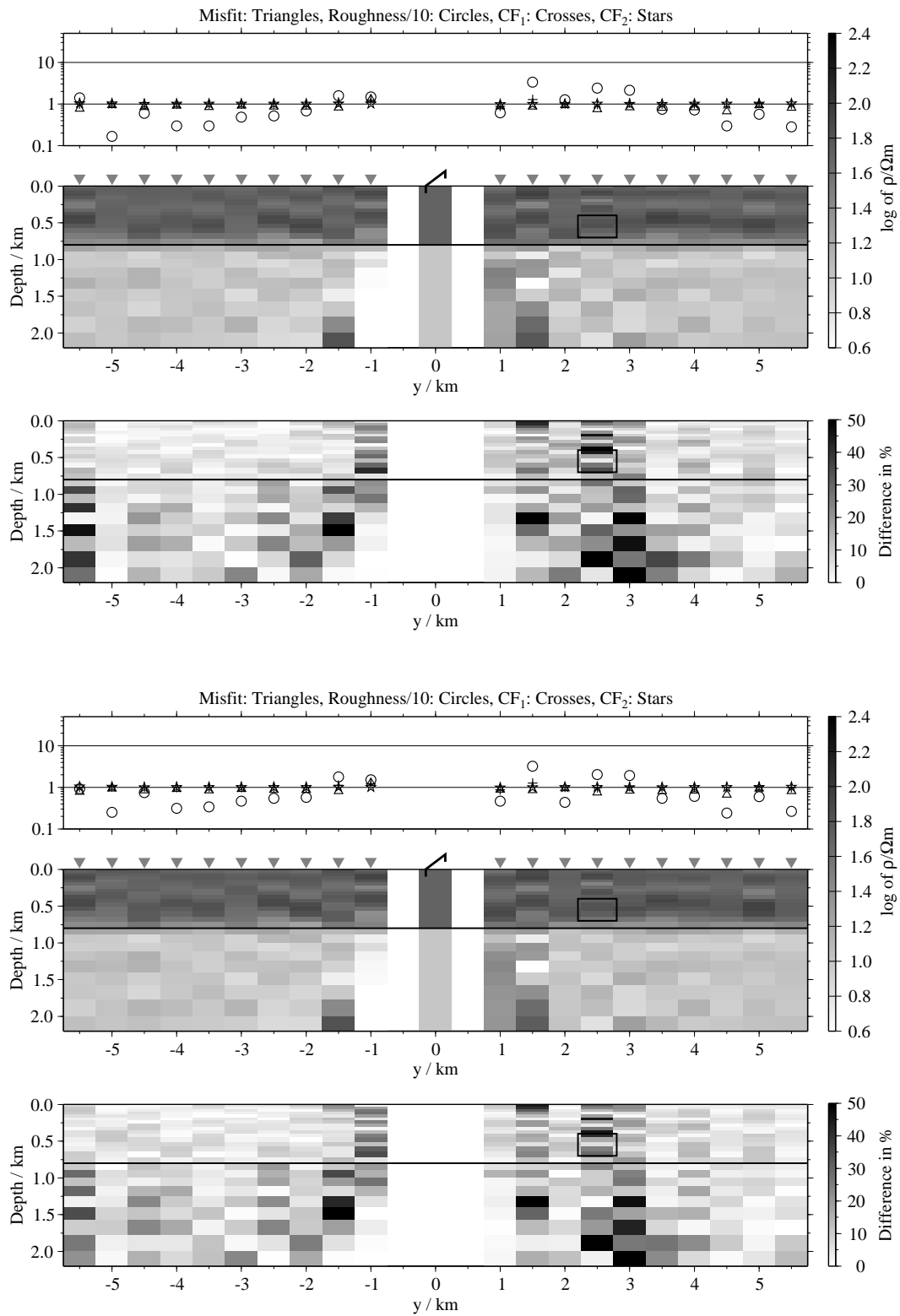


Figure B.167: Pseudo-sections of 1-D soft joint-inversions using the components \dot{H}_y and \dot{H}_z , model H2; Top panels: Average inversion results and relative differences (regularisation scheme C1); bottom: Average inversion results and relative differences (regularisation scheme C4);

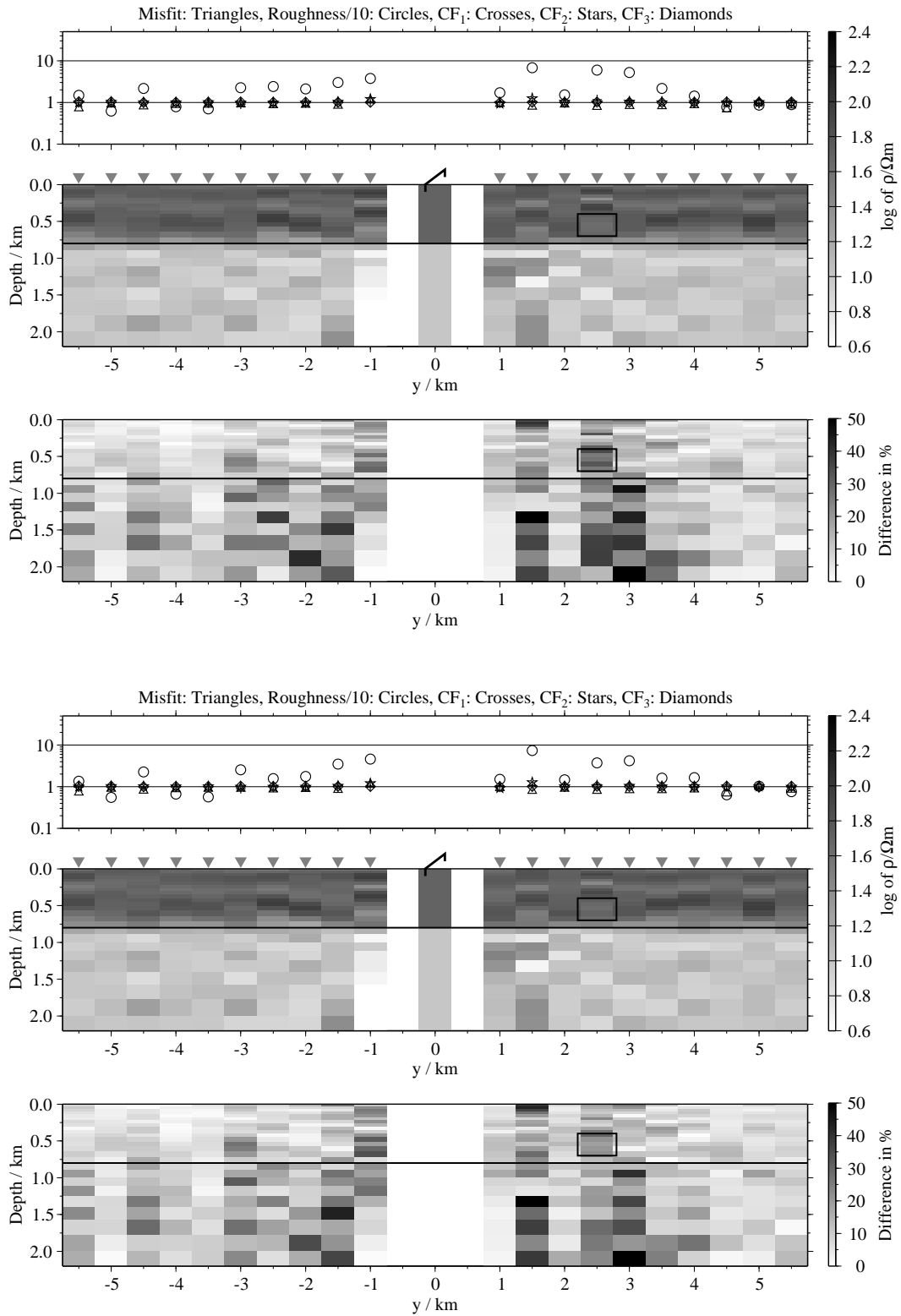
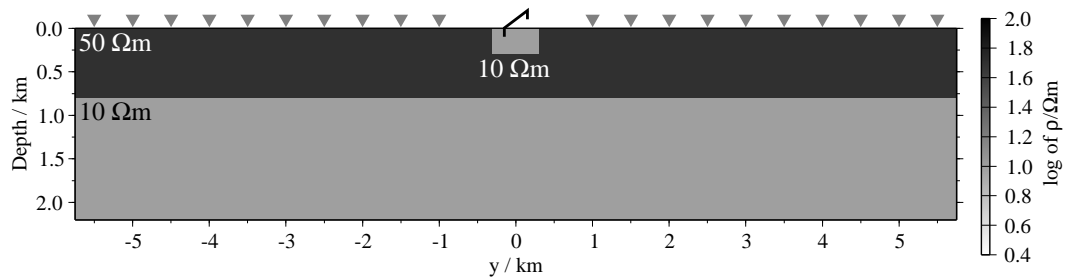


Figure B.168: Pseudo-sections of 1-D soft joint-inversions using all three components, model H2; Top panels: Average inversion results and relative differences (regularisation scheme C1); bottom: Average inversion results and relative differences (regularisation scheme C4);

B.2.7 Shallow conductive patch (models I1 and I2)

Model I1:



Model I2:

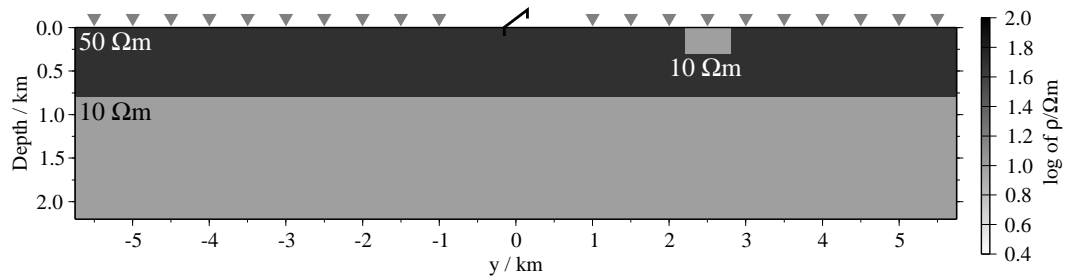


Figure B.169: Model with a shallow resistive patch; the mid-point of the patch is in both cases at $x = 0$ km and $y = 0$ km (model I1) and $y = 2.5$ km (model I2), respectively. The patch has the size $600 \times 600 \times 300$ m³.

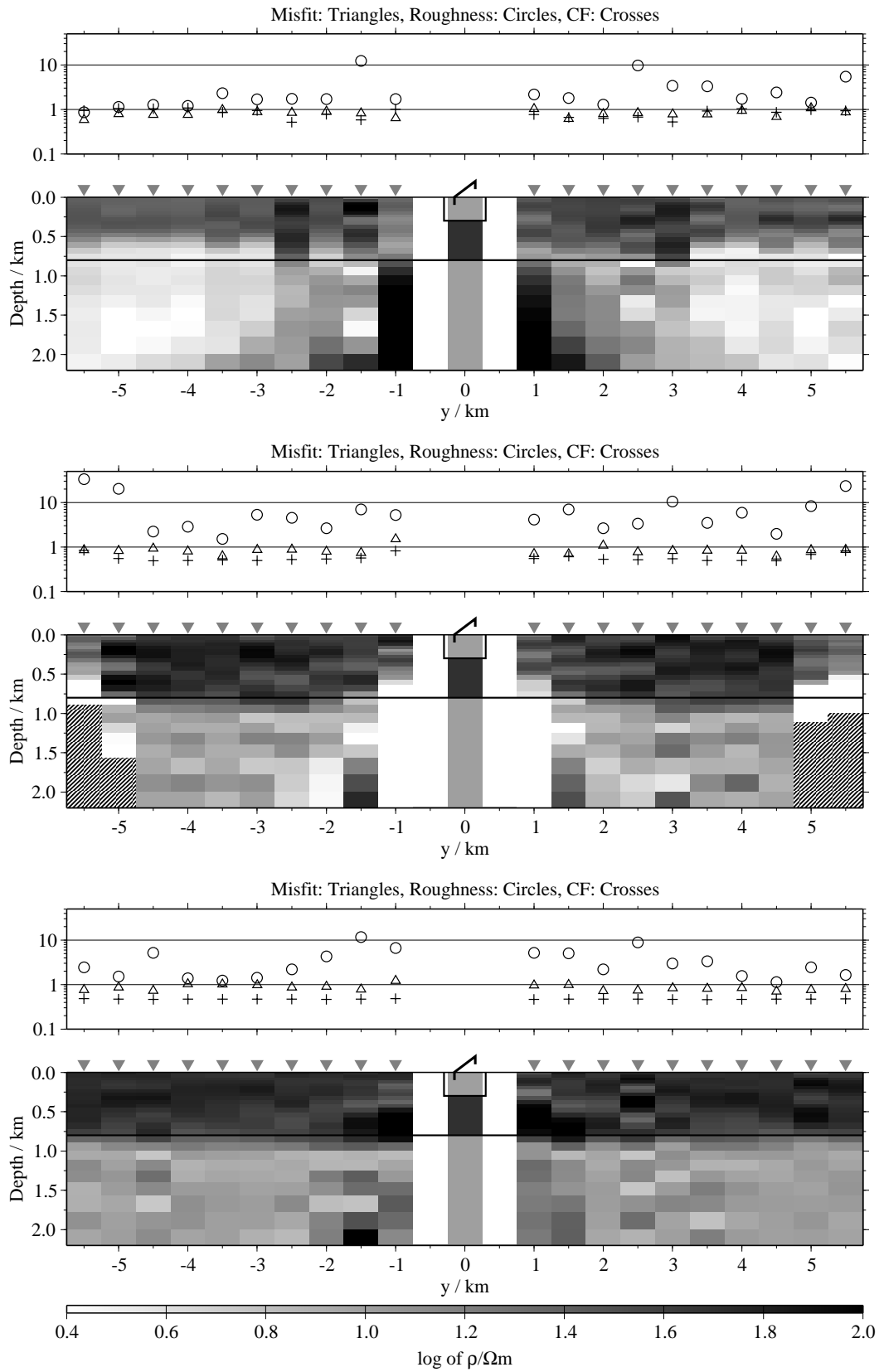


Figure B.170: Pseudo-sections of single 1-D inversion, model I1, regularisation scheme C1; from top to bottom E_x -, H_y - and H_z -component;

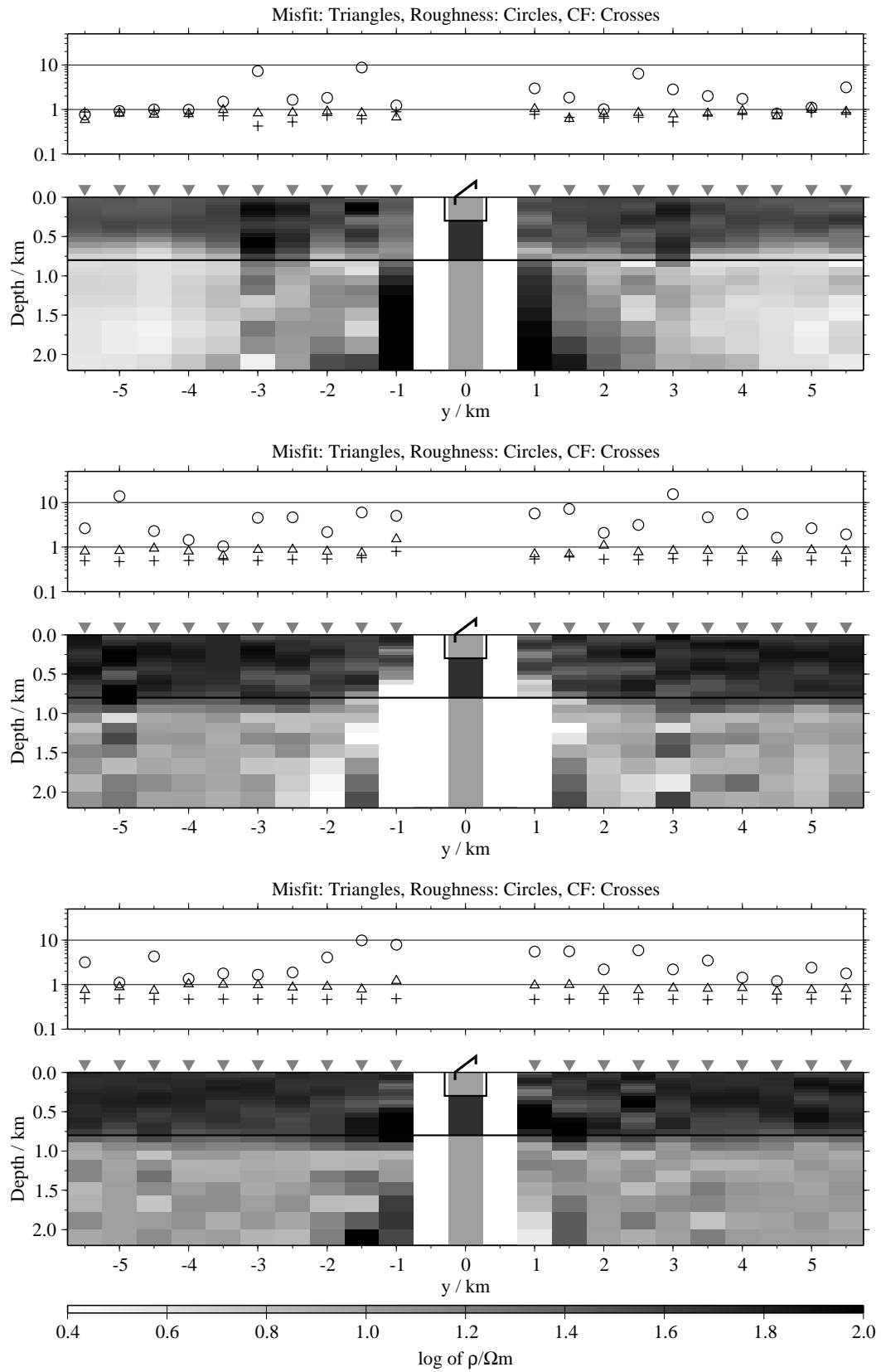


Figure B.171: Pseudo-sections of single 1-D inversion, model I1, regularisation scheme C4; from top to bottom E_x -, H_y - and H_z -component;

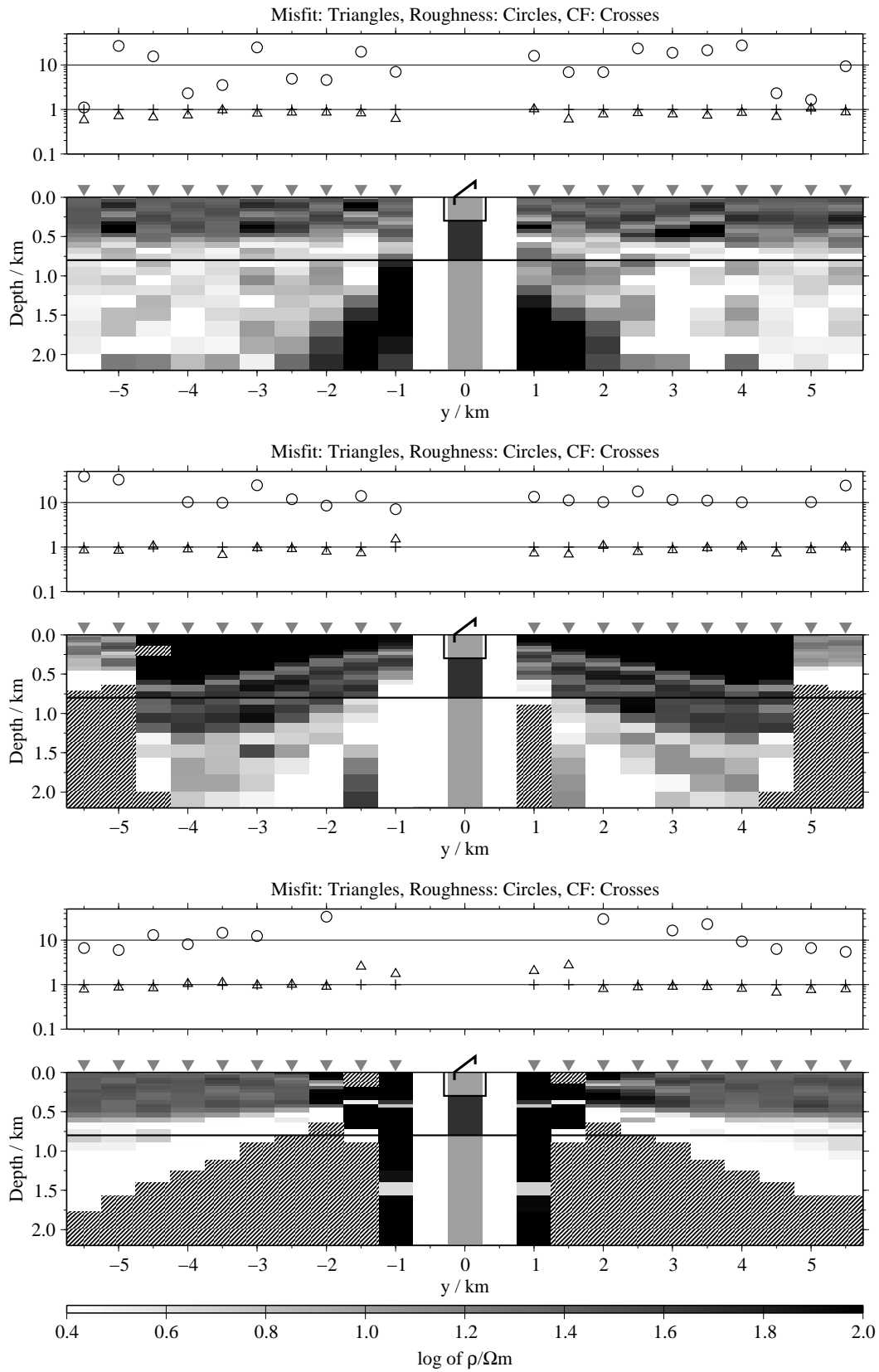


Figure B.172: Pseudo-sections of single 1-D inversion, model I1, regularisation scheme C1; from top to bottom E_x -, H_y - and H_z -component; the CF was fixed in the inversions.

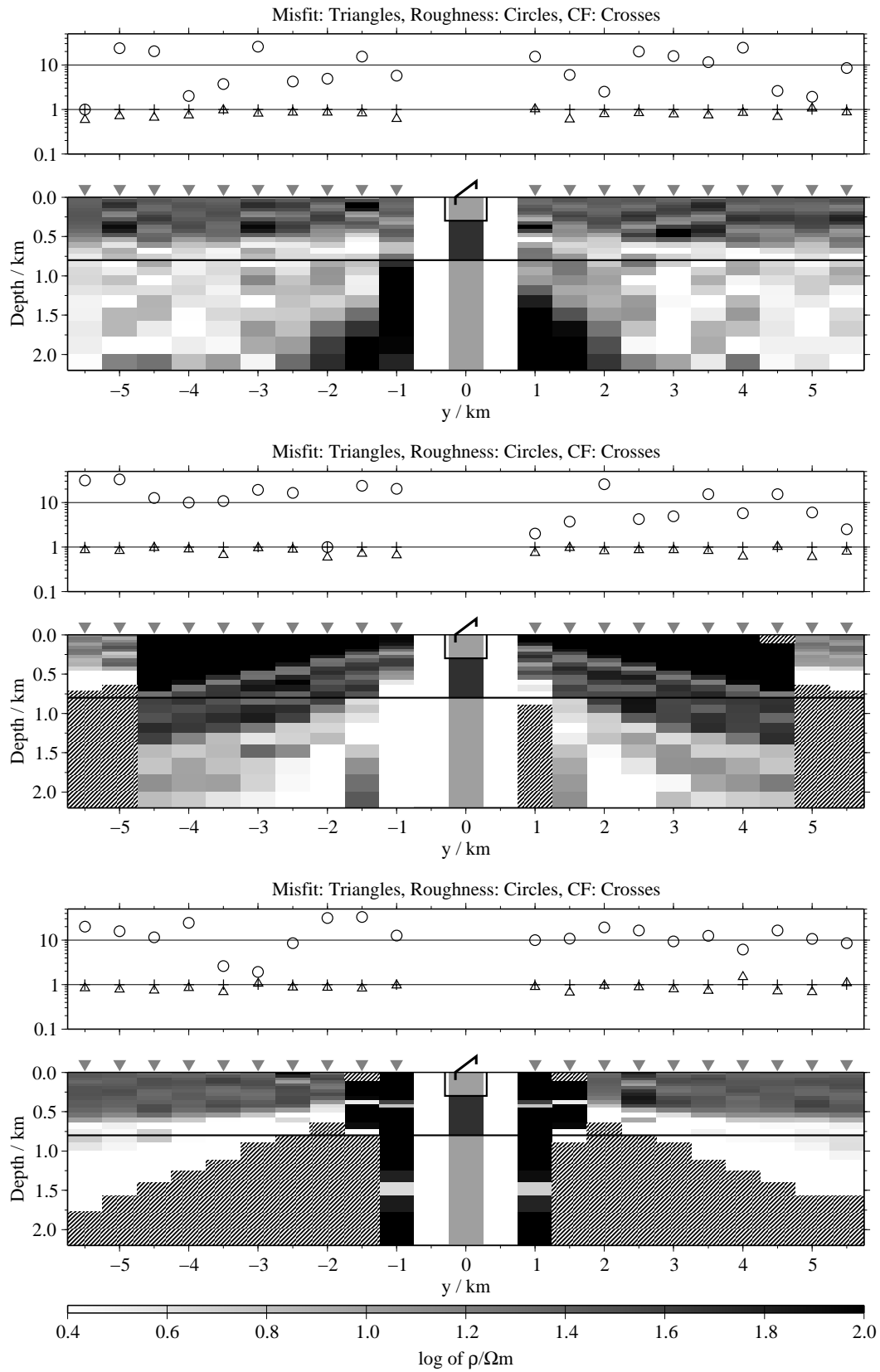


Figure B.173: Pseudo-sections of single 1-D inversion, model I1, regularisation scheme C4; from top to bottom E_x^- , \dot{H}_y^- and \dot{H}_z^- -component; the CF was fixed in the inversions.

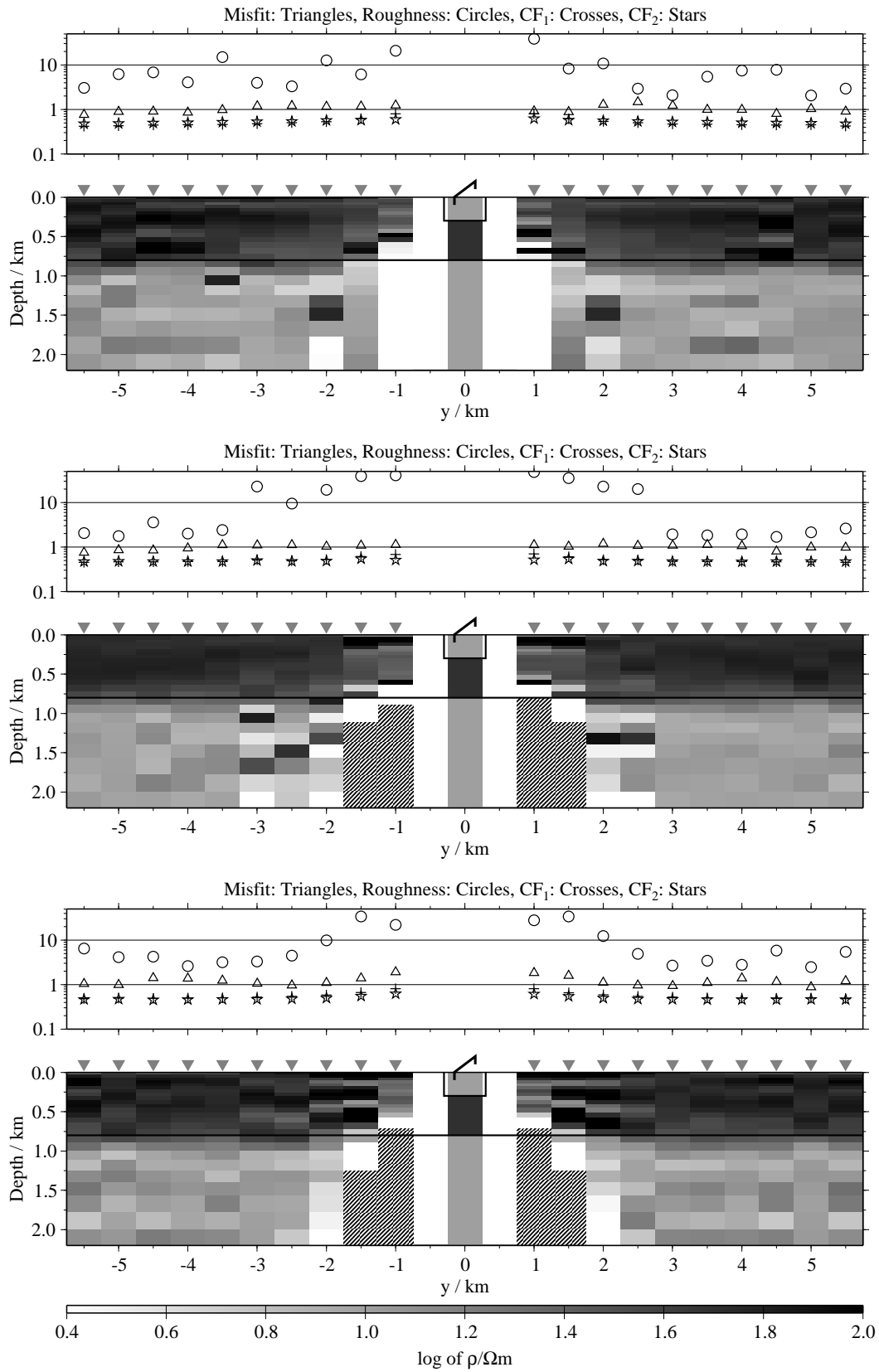


Figure B.174: Pseudo-sections of two component 1-D joint-inversions, model I1, regularisation scheme C1; from top to bottom $E_x-\dot{H}_y$, $E_x-\dot{H}_z$ and $\dot{H}_y-\dot{H}_z$;

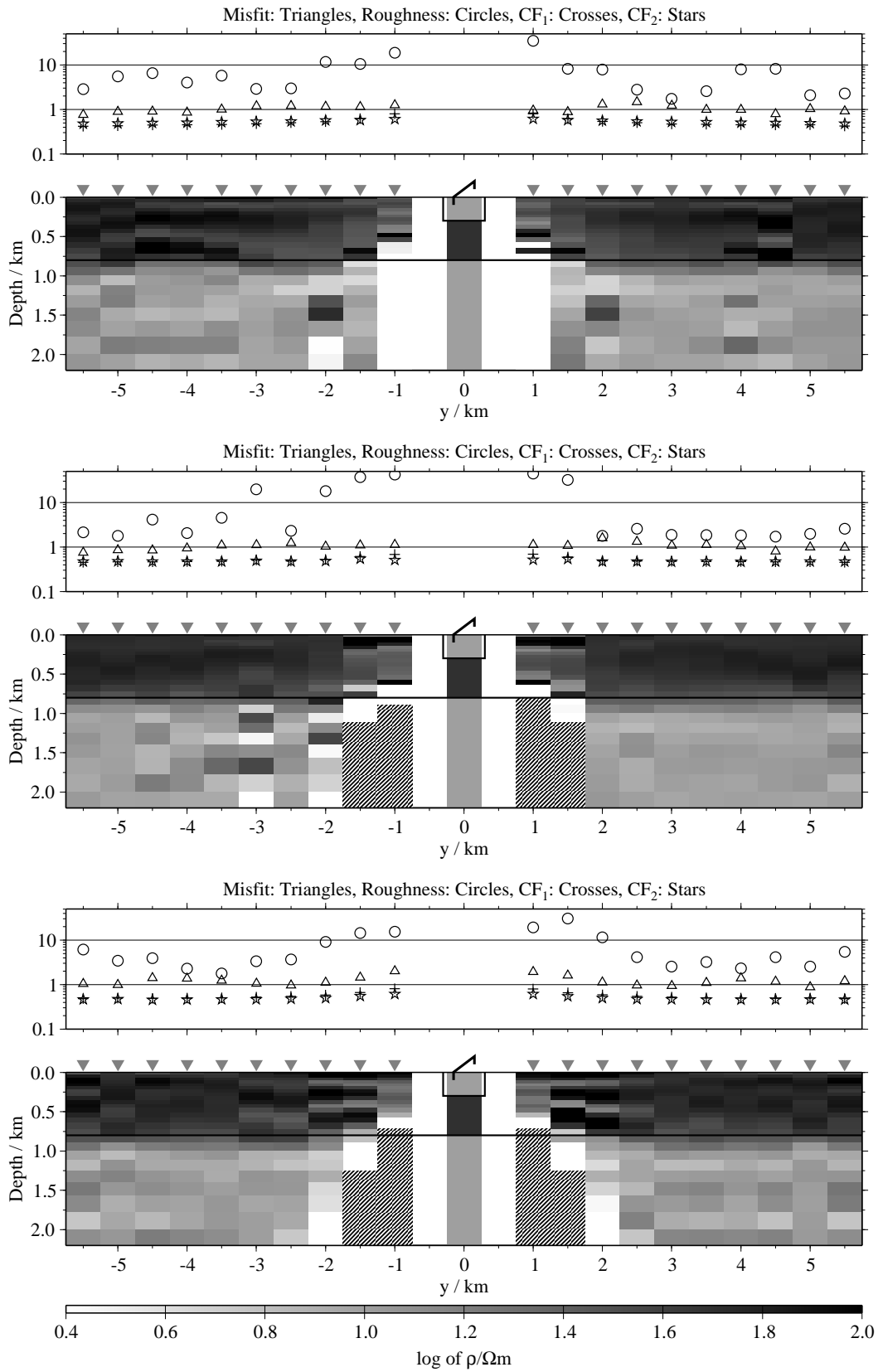


Figure B.175: Pseudo-sections of two component 1-D joint-inversions, model I1, regularisation scheme C4; from top to bottom $E_x-\dot{H}_y$, $E_x-\dot{H}_z$ and $\dot{H}_y-\dot{H}_z$;

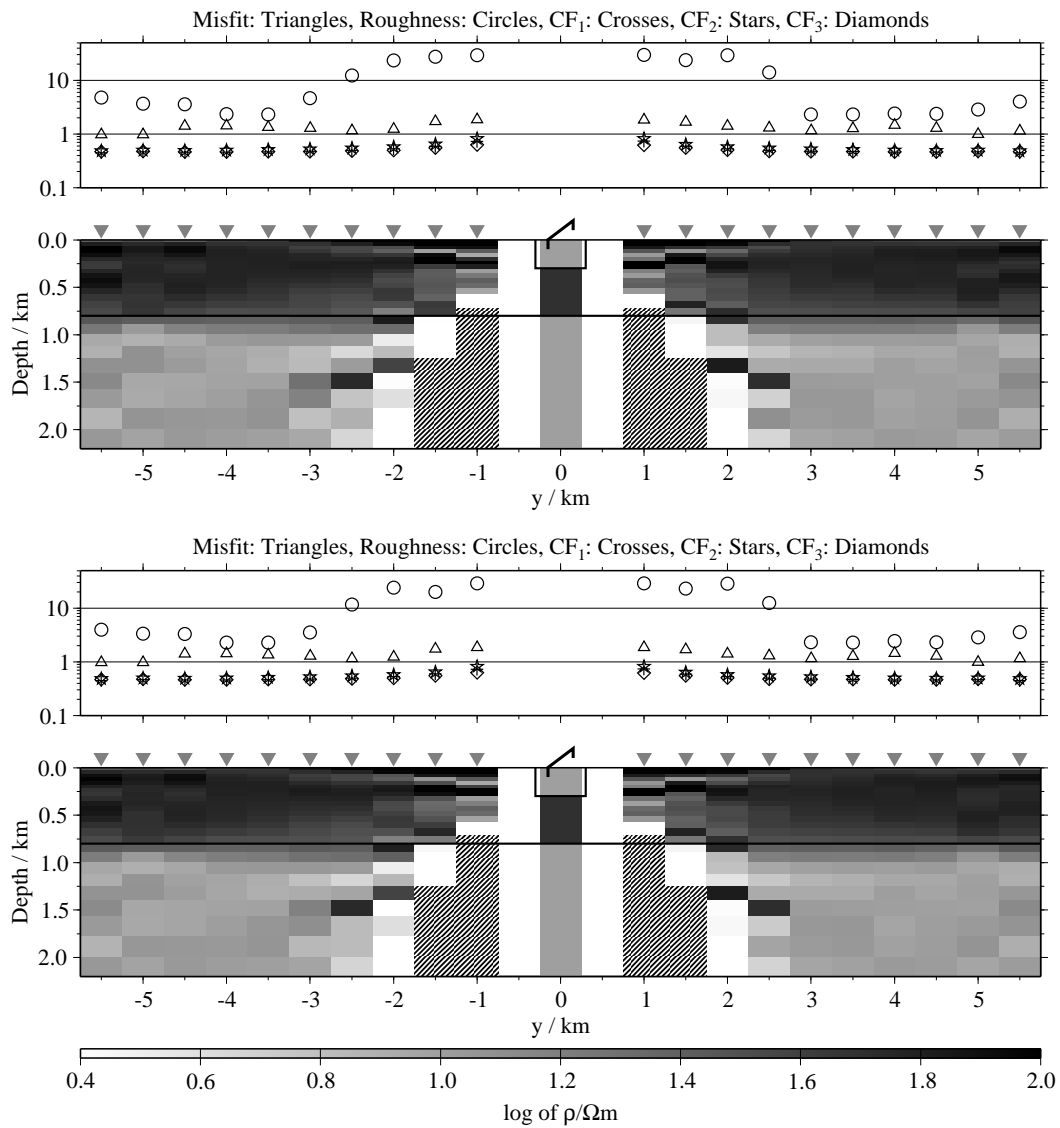


Figure B.176: Pseudo-sections of 1-D joint-inversions using all three components, model I1; top: Regularisation scheme C1; bottom: Regularisation scheme C4;

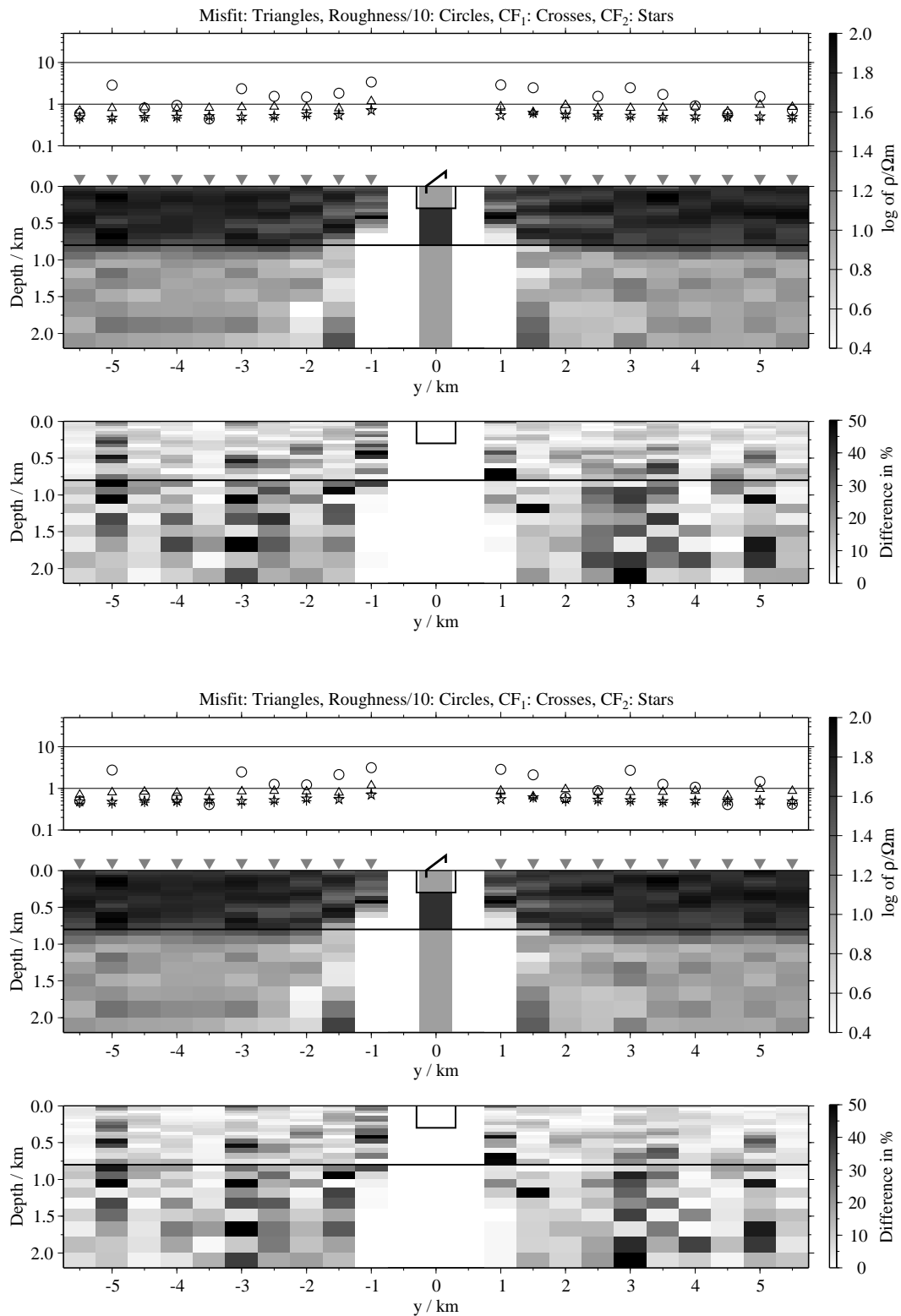


Figure B.177: Pseudo-sections of 1-D soft joint-inversions using the components E_x and H_y , model I1; Top panels: Average inversion results and relative differences (regularisation scheme C1); bottom: Average inversion results and relative differences (regularisation scheme C4);

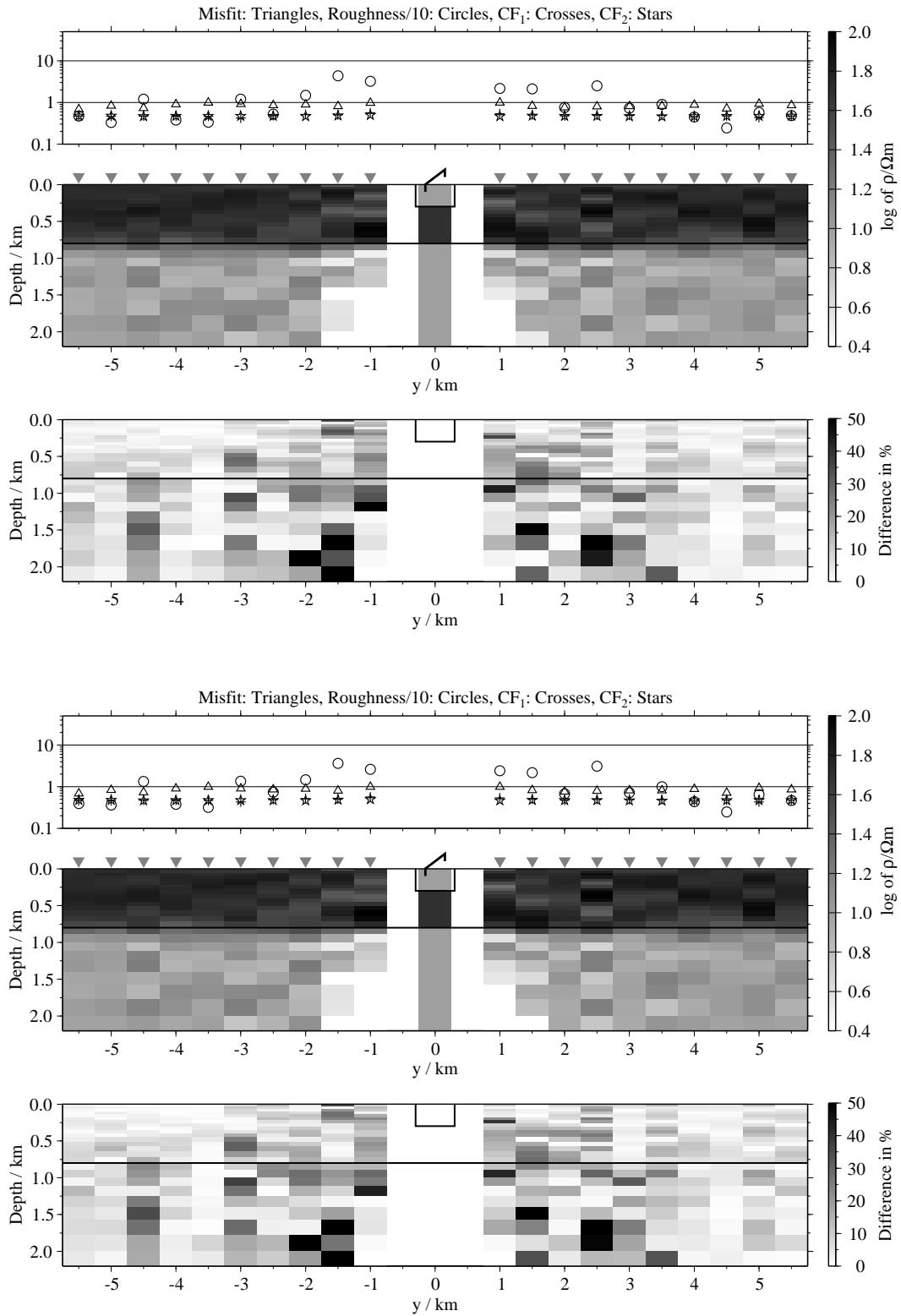


Figure B.178: Pseudo-sections 1-D of soft joint-inversions using the components E_x and H_z , model I1; Top panels: Average inversion results and relative differences (regularisation scheme C1); bottom: Average inversion results and relative differences (regularisation scheme C4);

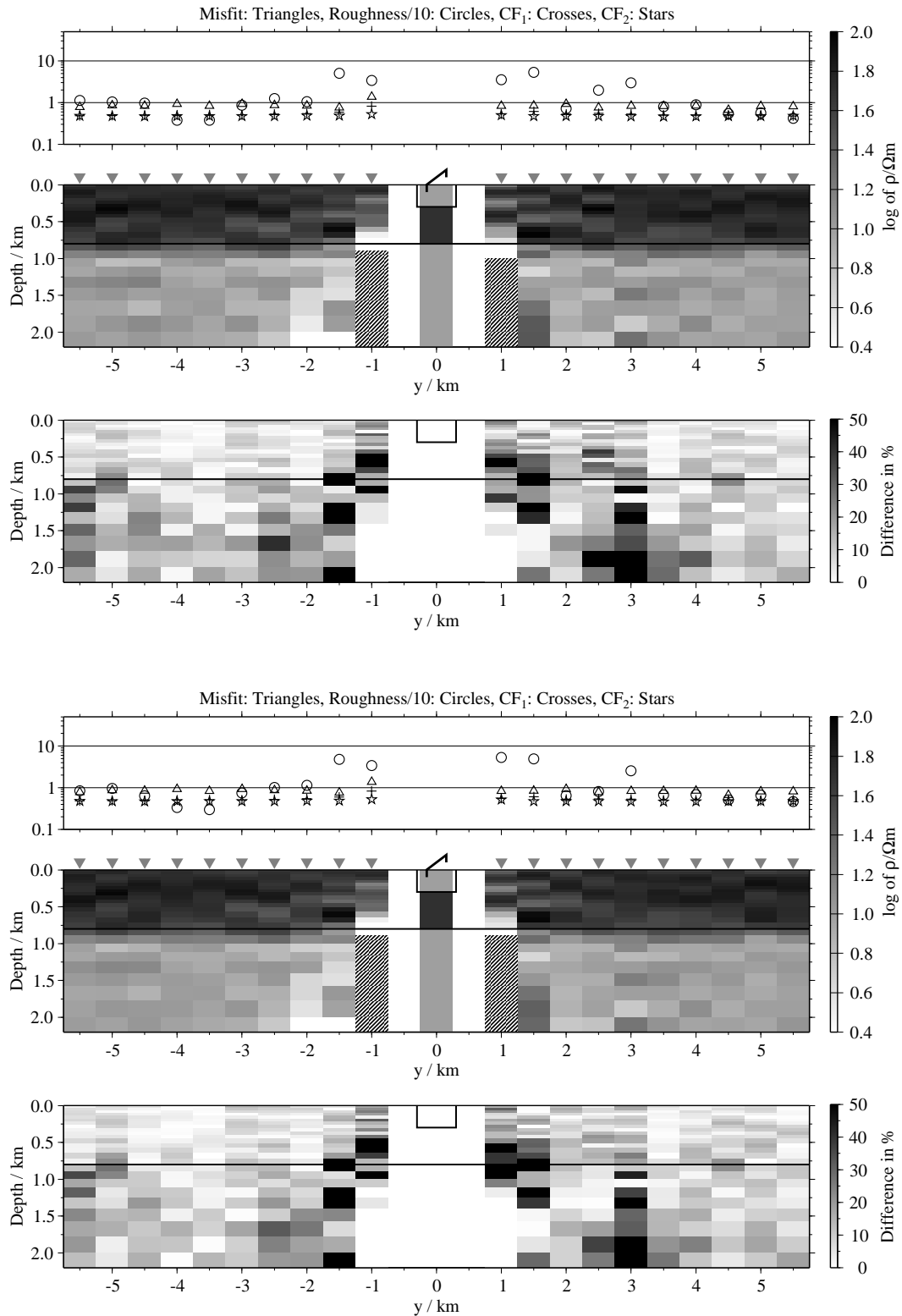


Figure B.179: Pseudo-sections of 1-D soft joint-inversions using the components \dot{H}_y and \dot{H}_z , model I1; Top panels: Average inversion results and relative differences (regularisation scheme C1); bottom: Average inversion results and relative differences (regularisation scheme C4);

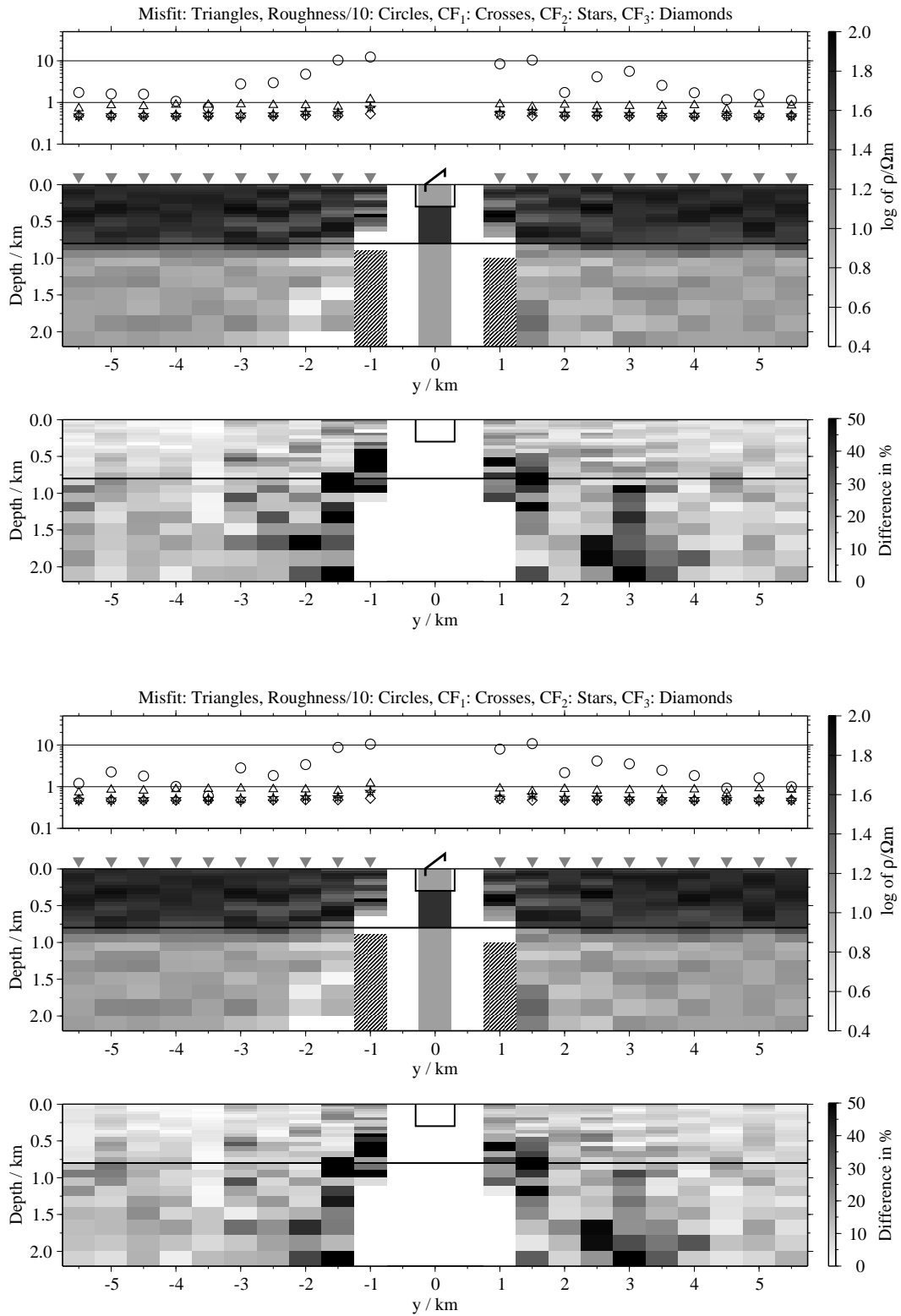


Figure B.180: Pseudo-sections of 1-D soft joint-inversions using all three components, model I1; Top panels: Average inversion results and relative differences (regularisation scheme C1); bottom: Average inversion results and relative differences (regularisation scheme C4);

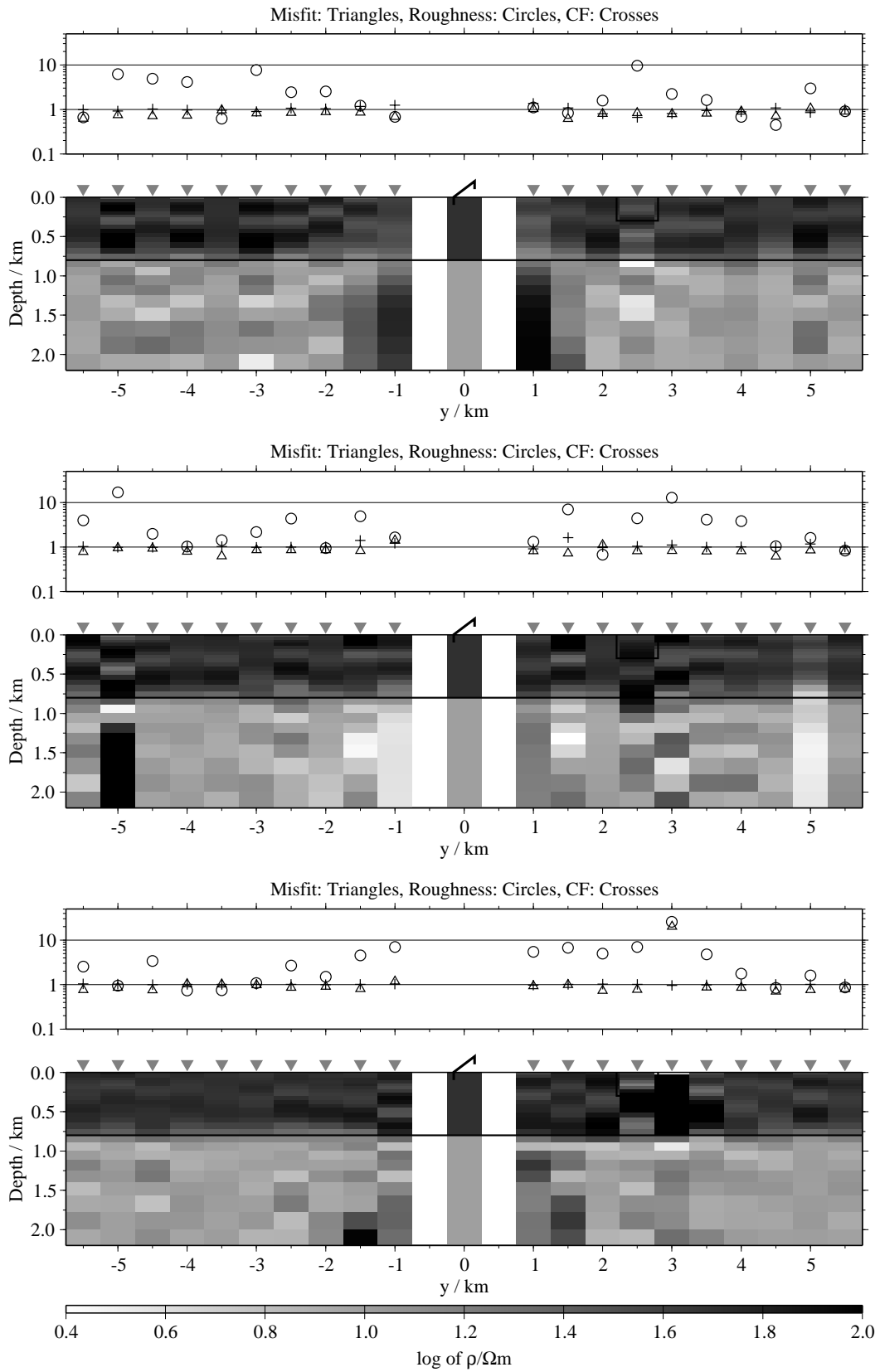


Figure B.181: Pseudo-sections of single 1-D inversion, model I2, regularisation scheme C1; from top to bottom E_x -, H_y - and H_z -component;

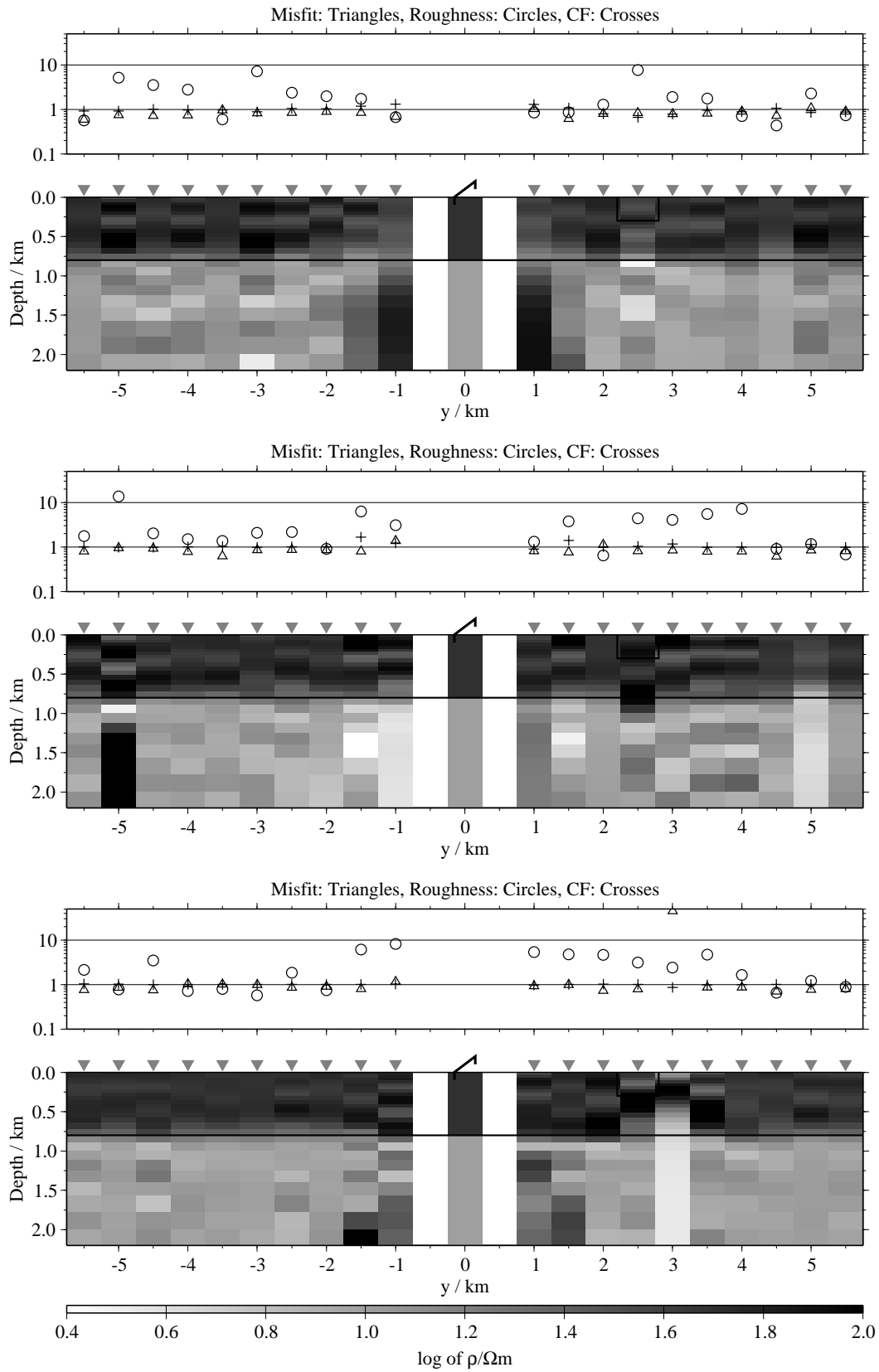


Figure B.182: Pseudo-sections of single 1-D inversion, model I2, regularisation scheme C4; from top to bottom E_x -, \dot{H}_y - and \dot{H}_z -component;

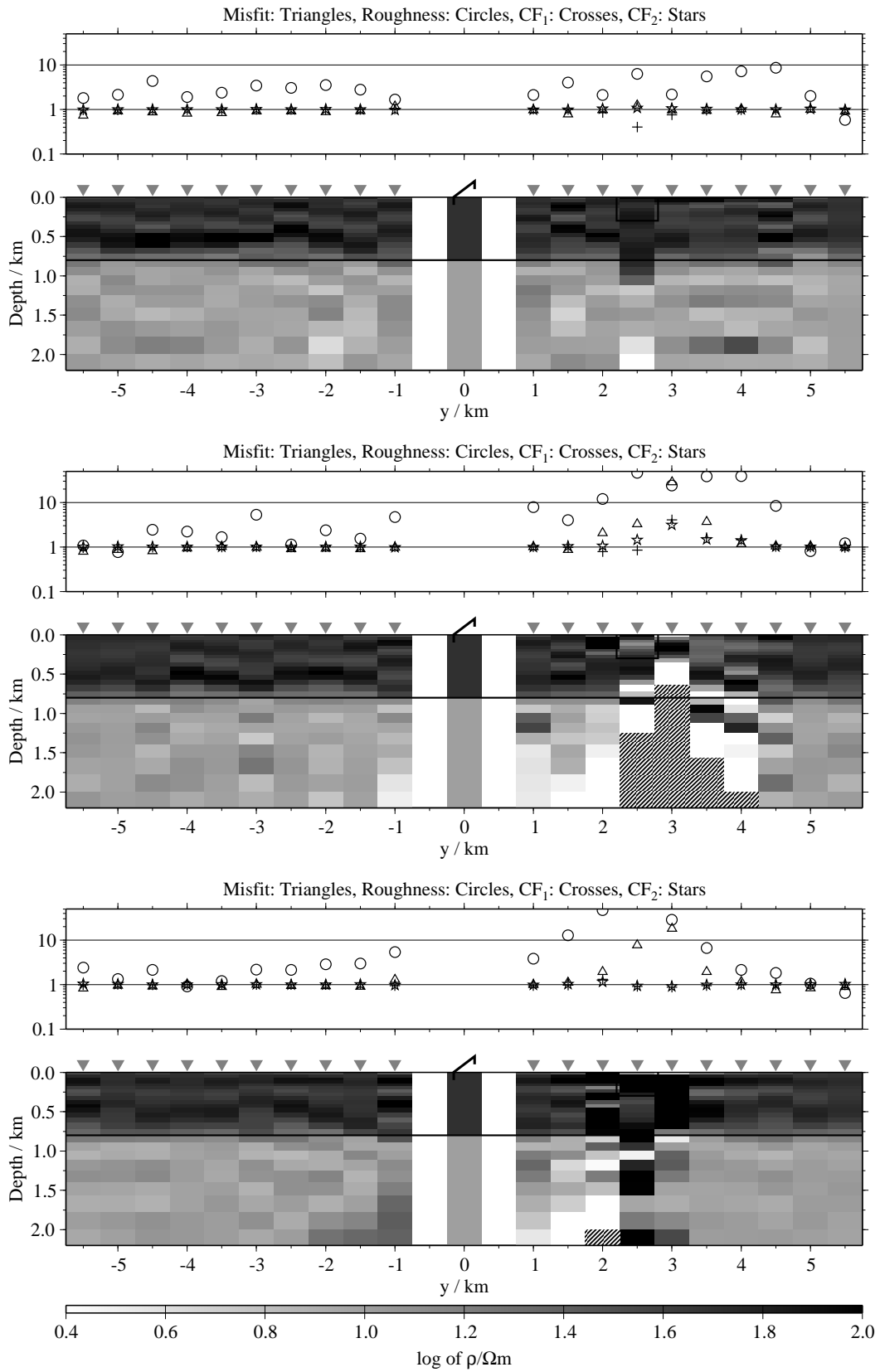


Figure B.183: Pseudo-sections of two component 1-D joint-inversions, model 12, regularisation scheme C1; from top to bottom $E_x\text{-}\dot{H}_y$, $E_x\text{-}\dot{H}_z$ and $\dot{H}_y\text{-}\dot{H}_z$;

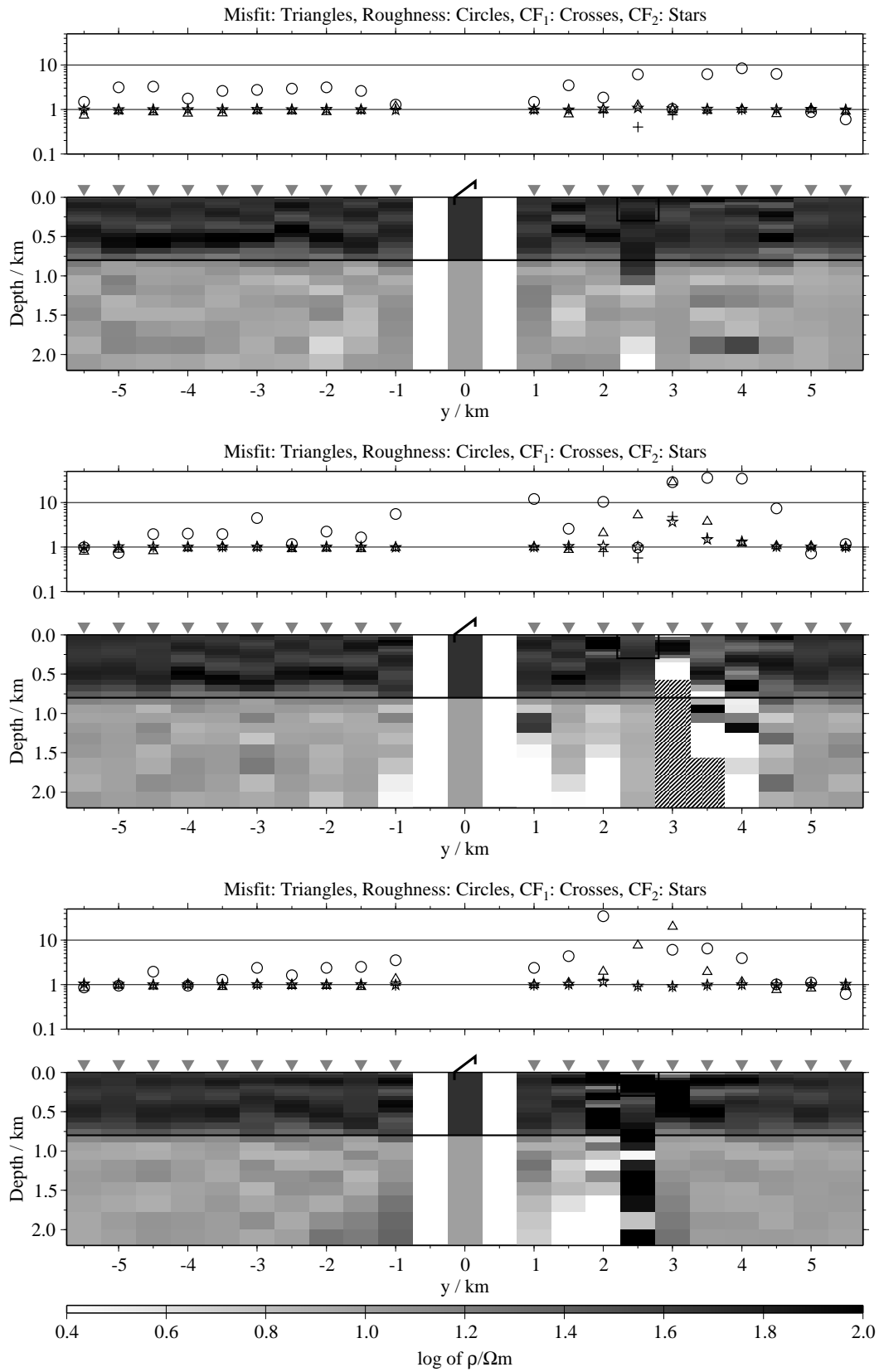


Figure B.184: Pseudo-sections of two component 1-D joint-inversions, model I2, regularisation scheme C4; from top to bottom $E_x - \dot{H}_y$, $E_x - \dot{H}_z$ and $\dot{H}_y - \dot{H}_z$;

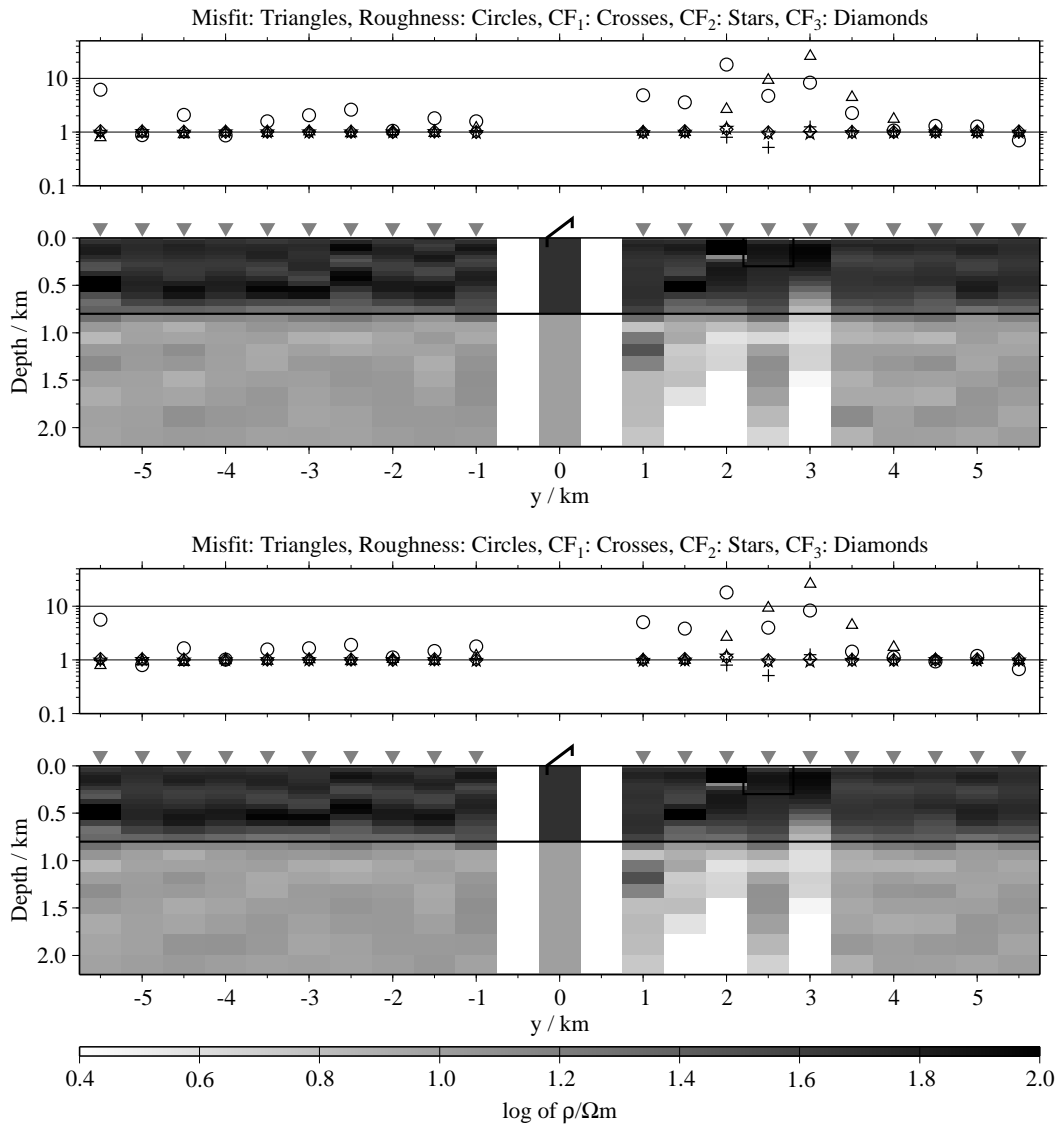


Figure B.185: Pseudo-sections of 1-D joint-inversions using all three components, model I2; top: Regularisation scheme C1; bottom: Regularisation scheme C4;

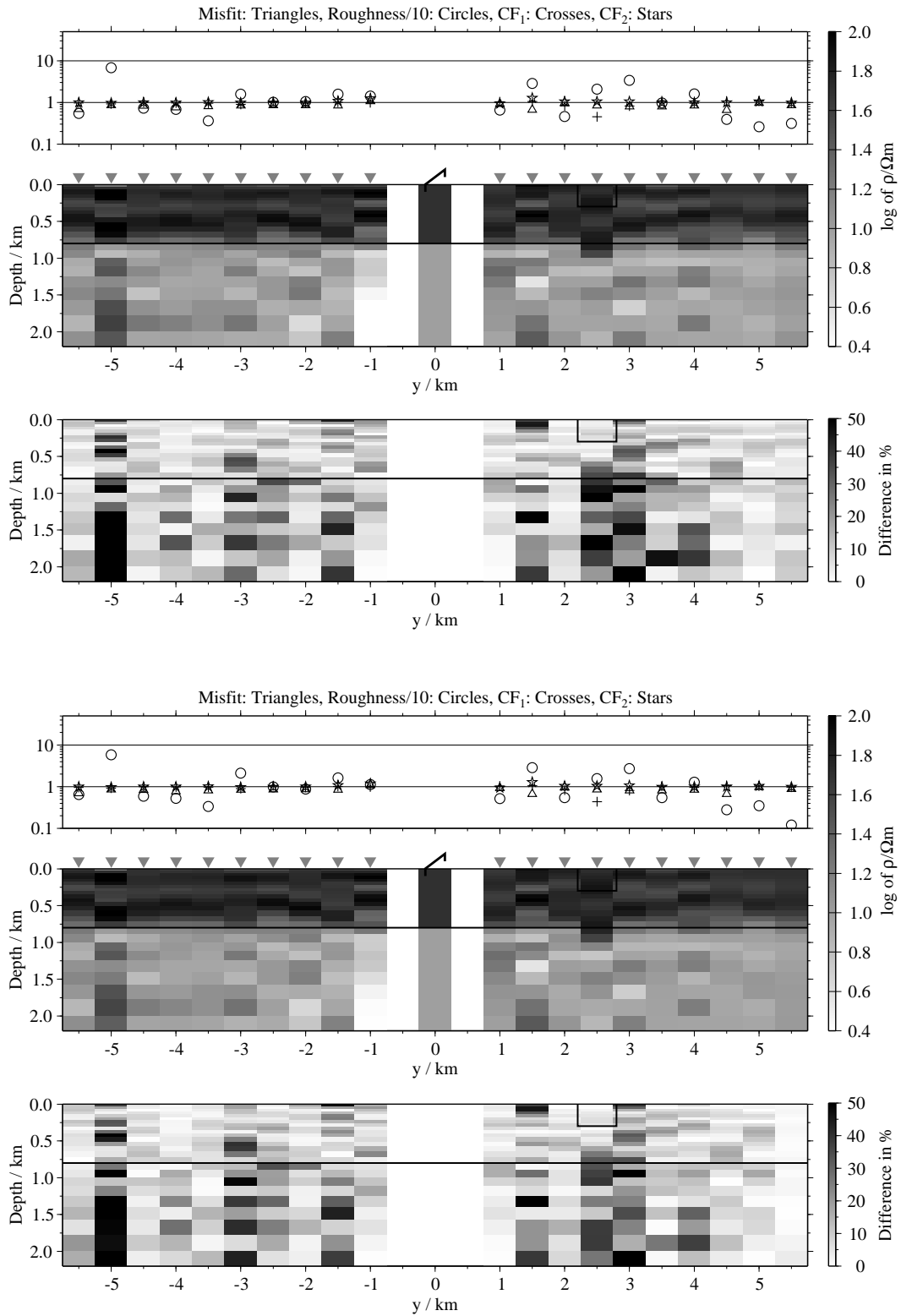


Figure B.186: Pseudo-sections of 1-D soft joint-inversions using the components E_x and H_y , model I2; Top panels: Average inversion results and relative differences (regularisation scheme C1); bottom: Average inversion results and relative differences (regularisation scheme C4);

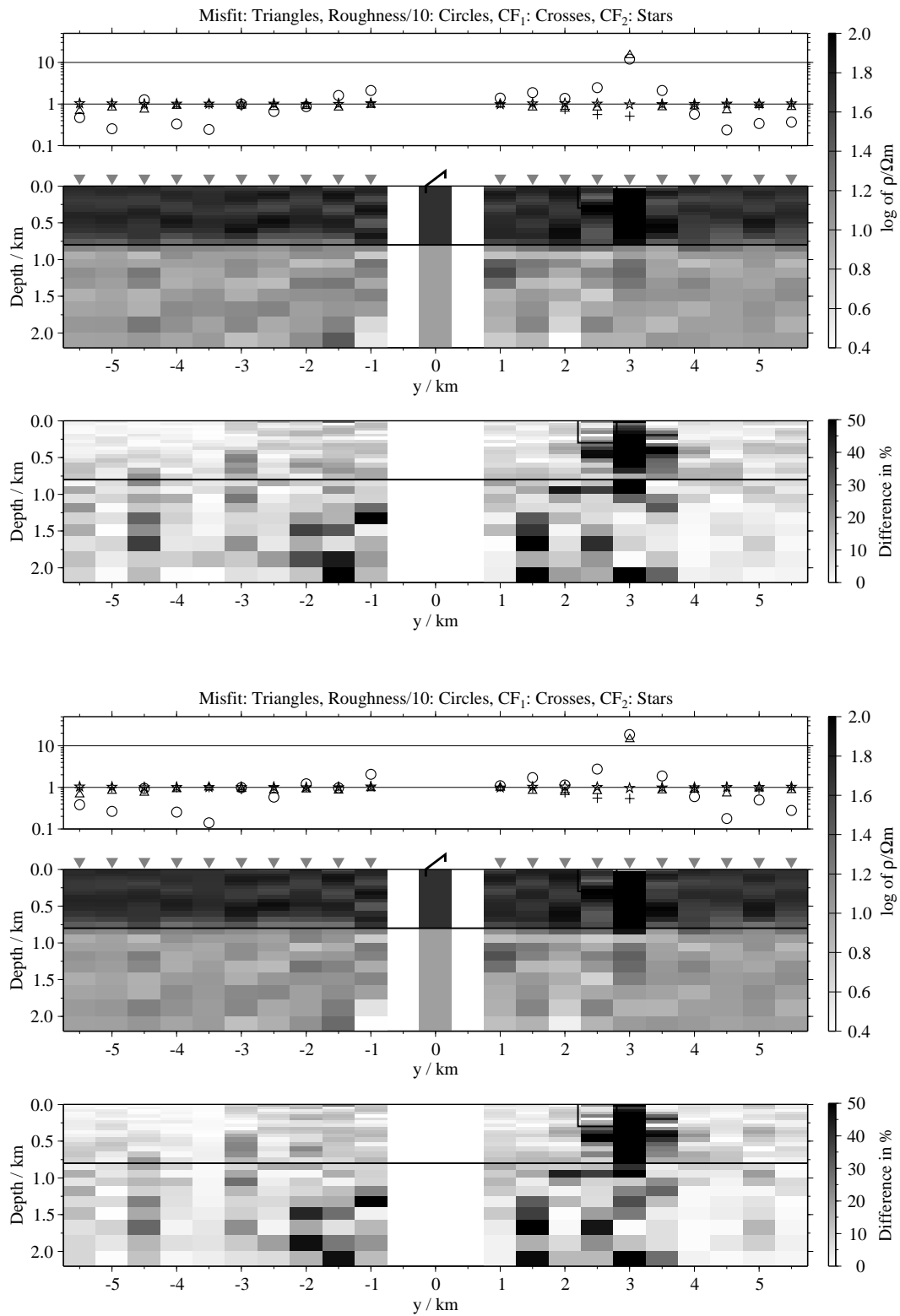


Figure B.187: Pseudo-sections 1-D of soft joint-inversions using the components E_x and H_{zi} , model I2; Top panels: Average inversion results and relative differences (regularisation scheme C1); bottom: Average inversion results and relative differences (regularisation scheme C4);

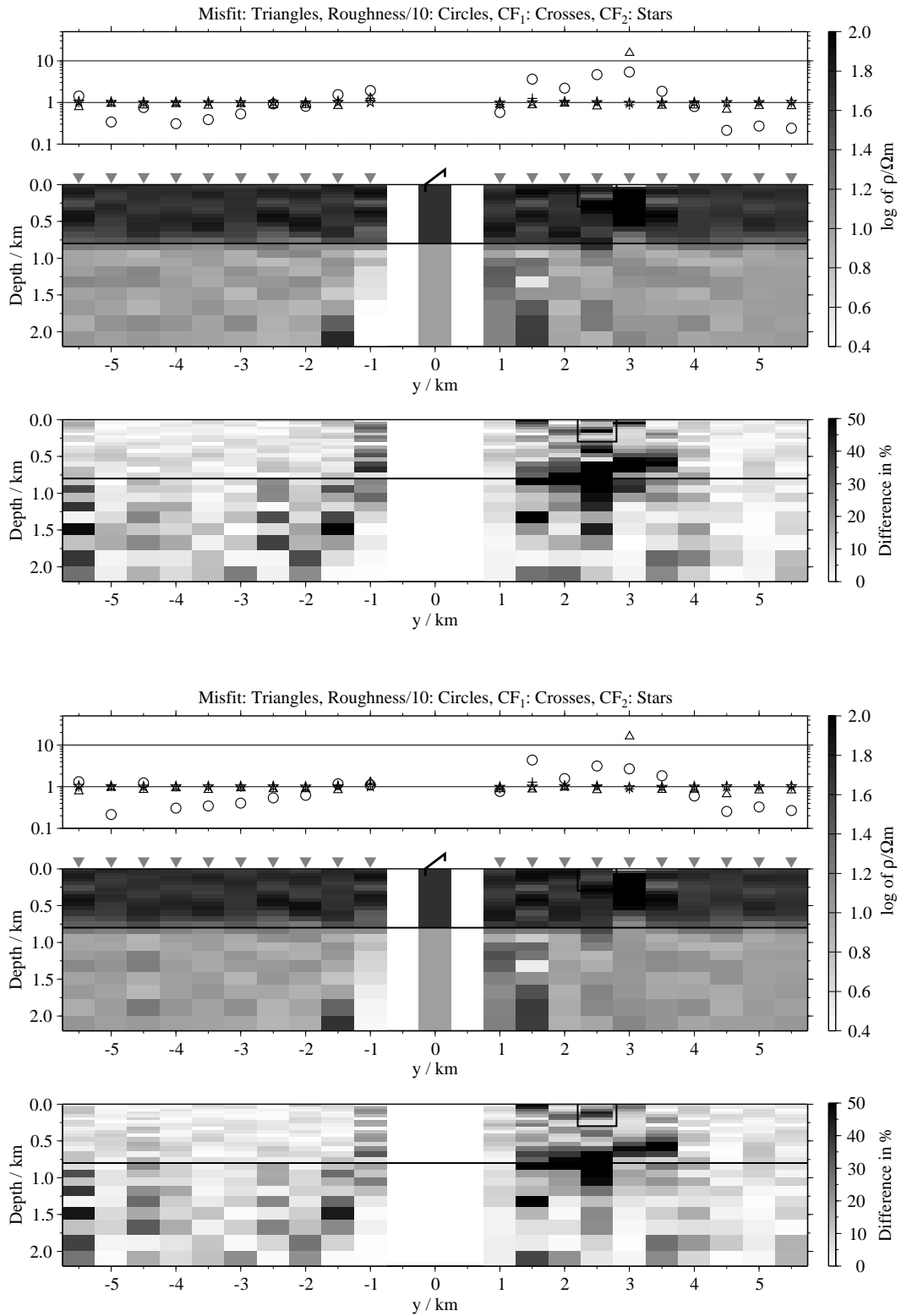


Figure B.188: Pseudo-sections of 1-D soft joint-inversions using the components \dot{H}_y and \dot{H}_z , model I2; Top panels: Average inversion results and relative differences (regularisation scheme C1); bottom: Average inversion results and relative differences (regularisation scheme C4);

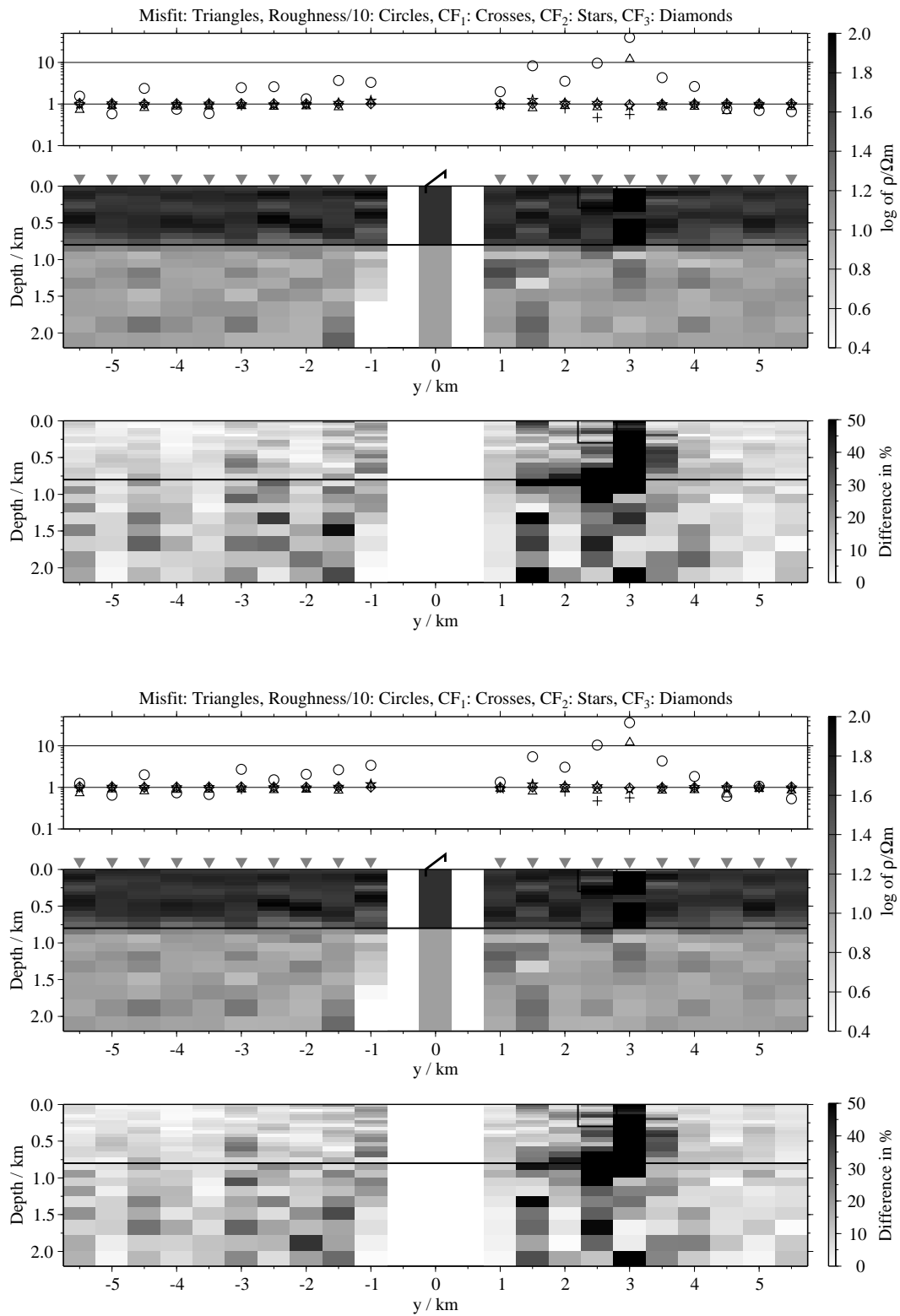
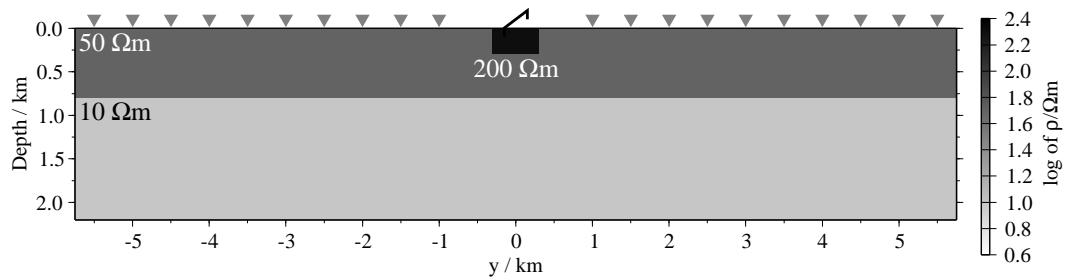


Figure B.189: Pseudo-sections of 1-D soft joint-inversions using all three components, model I2; Top panels: Average inversion results and relative differences (regularisation scheme C1); bottom: Average inversion results and relative differences (regularisation scheme C4);

B.2.8 Shallow resistive patch (models J1 and J2)

Model J1:



Model J2:

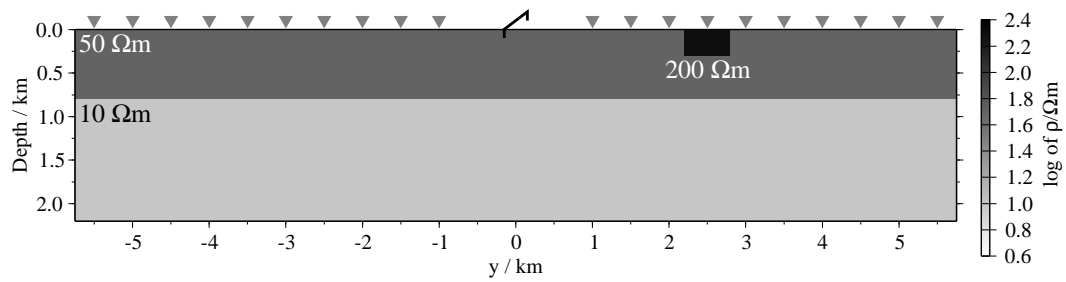


Figure B.190: Model with a shallow resistive patch; the mid-point of the patch is in both cases at $x = 0$ km and $y = 0$ km (model J1) and $y = 2.5$ km (model J2), respectively. The patch has the size $600 \times 600 \times 300 \text{ m}^3$.

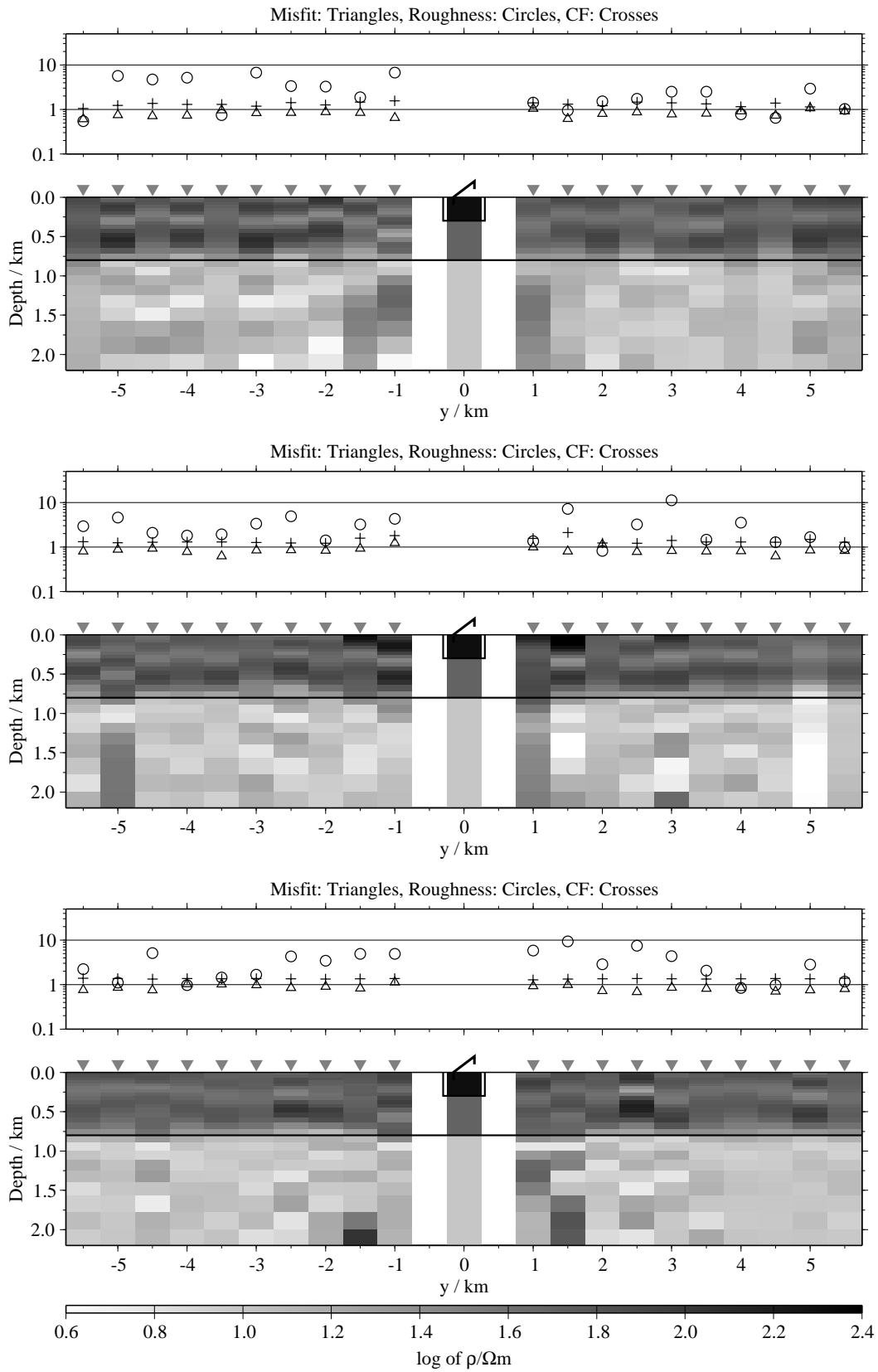


Figure B.191: Pseudo-sections of single 1-D inversion, model J1, regularisation scheme C1; from top to bottom E_x -, \dot{H}_y - and \dot{H}_z -component;

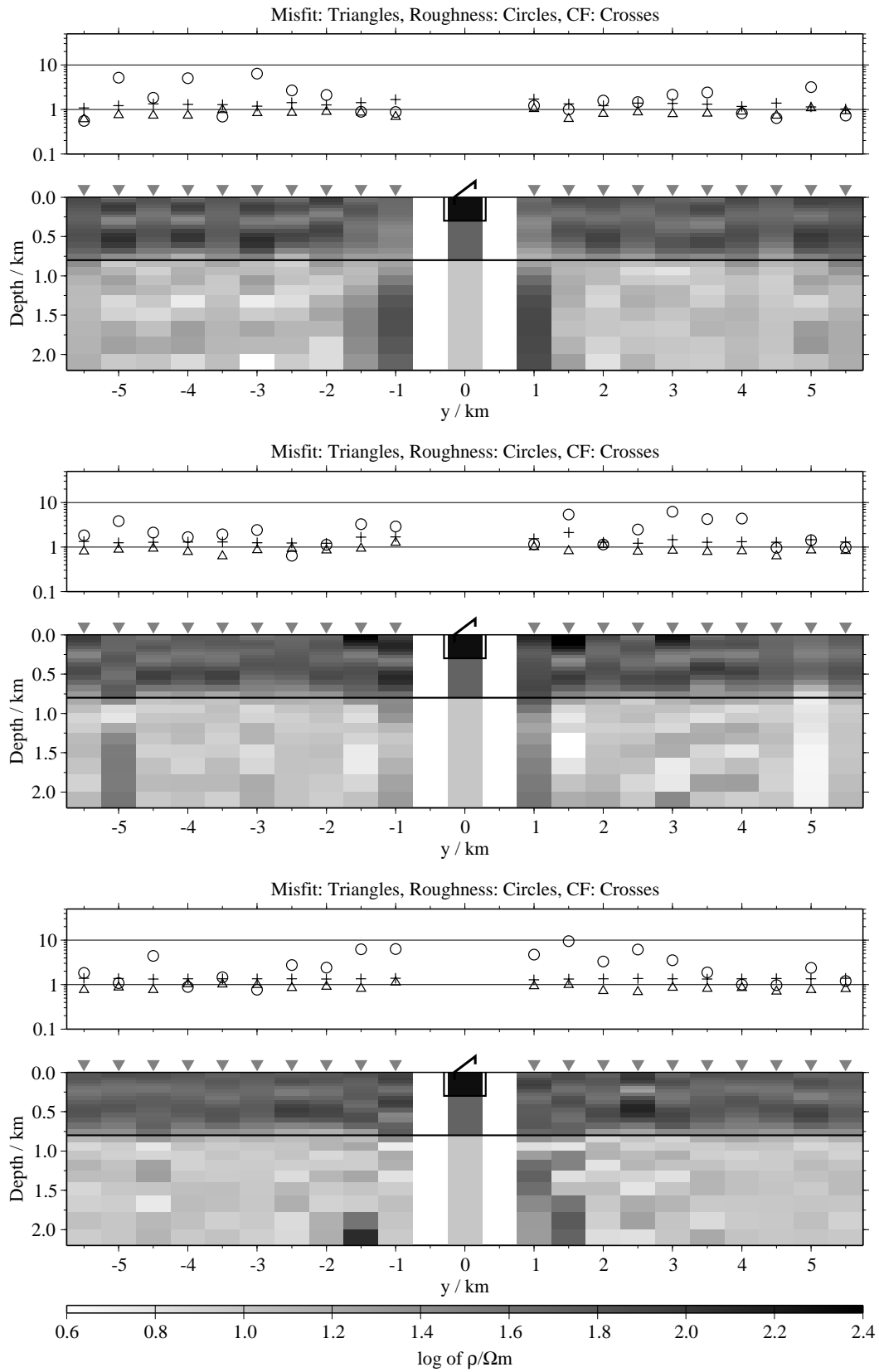


Figure B.192: Pseudo-sections of single 1-D inversion, model J1, regularisation scheme C4; from top to bottom E_x -, \dot{H}_y - and \dot{H}_z -component;

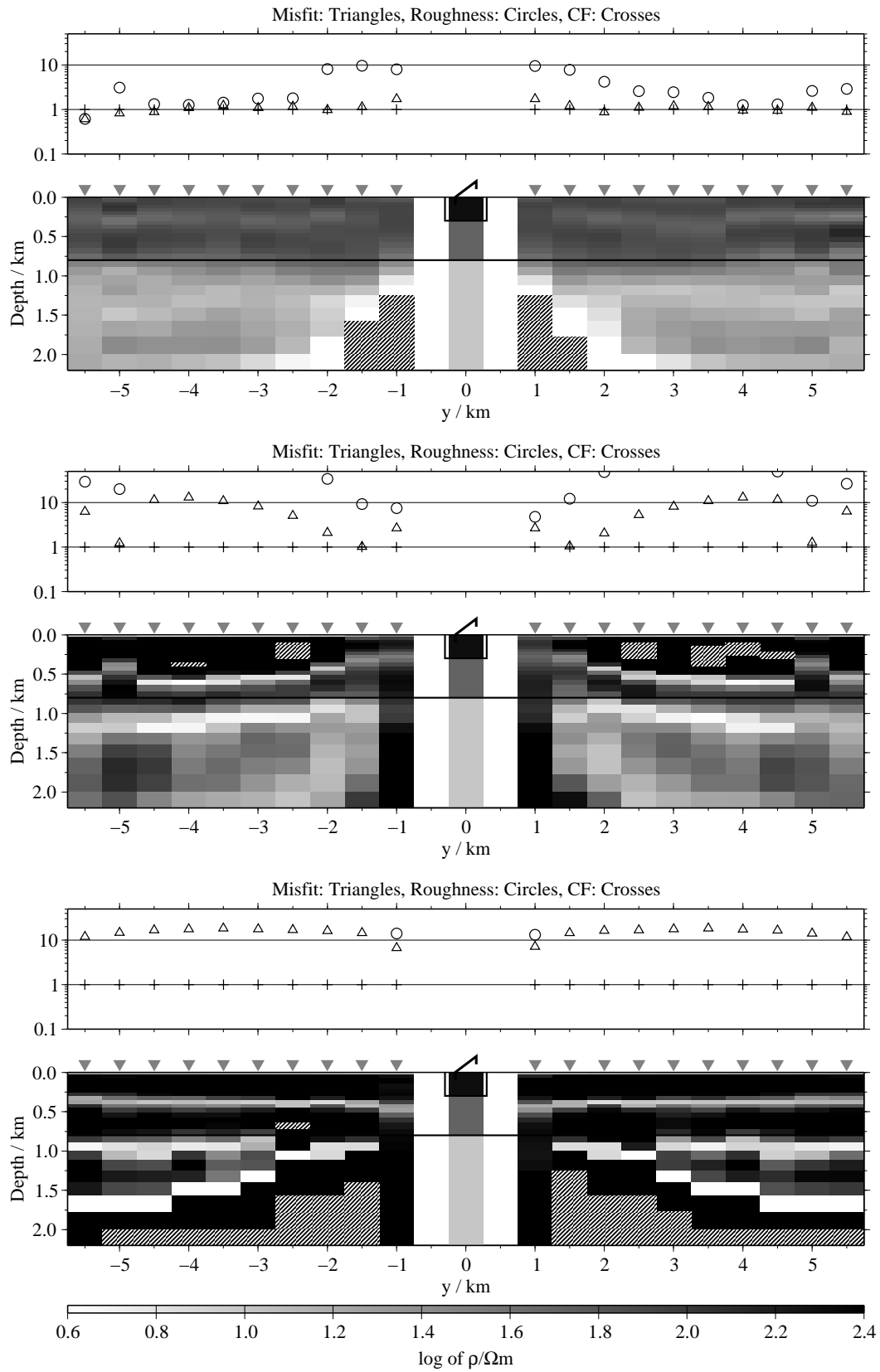


Figure B.193: Pseudo-sections of single 1-D inversion, model J1, regularisation scheme C1; from top to bottom E_x -, H_y - and H_z -component; the CF was fixed in the inversions.

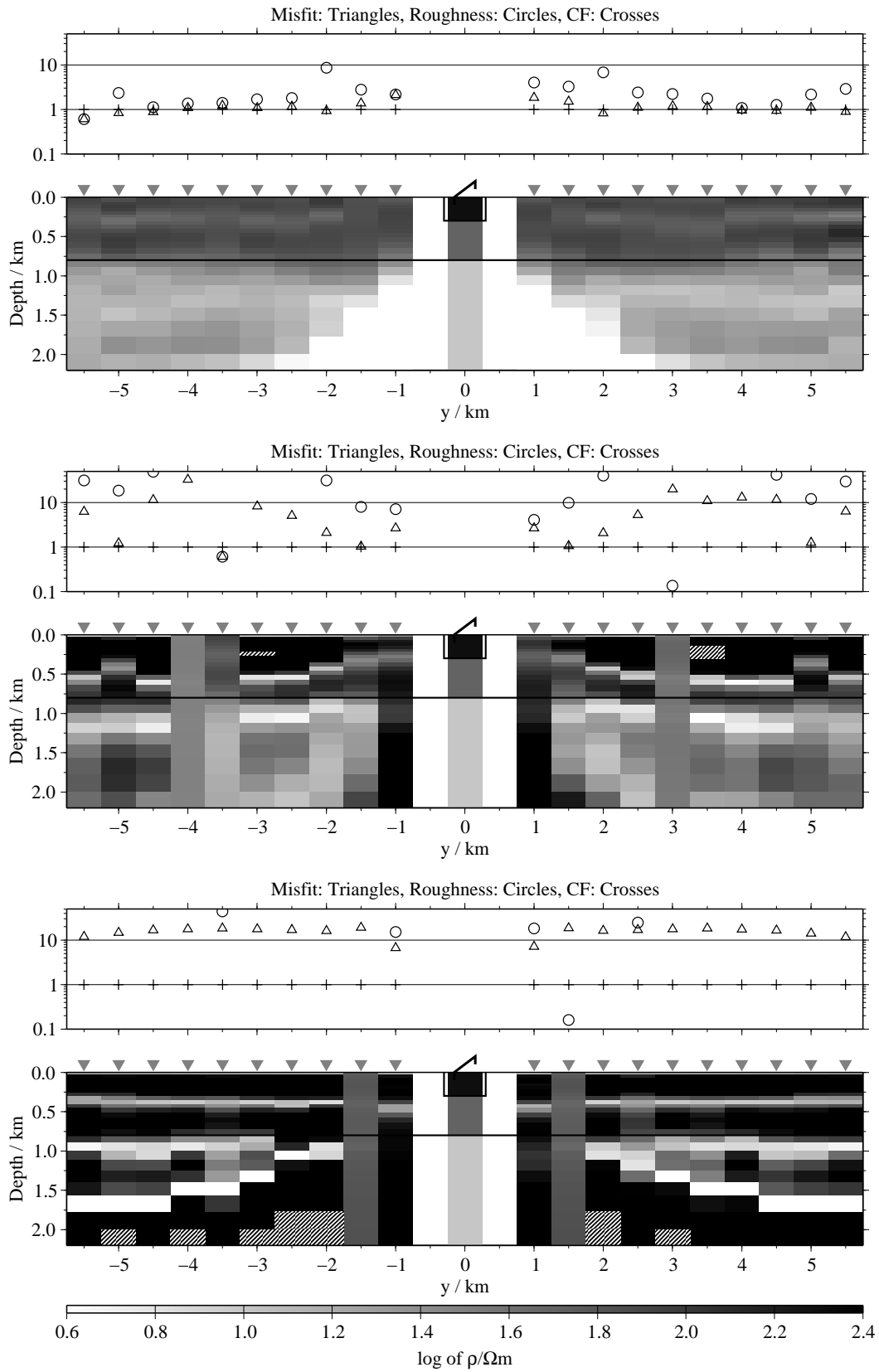


Figure B.194: Pseudo-sections of single 1-D inversion, model J1, regularisation scheme C4; from top to bottom E_x -, H_y - and H_z -component; the CF was fixed in the inversions.

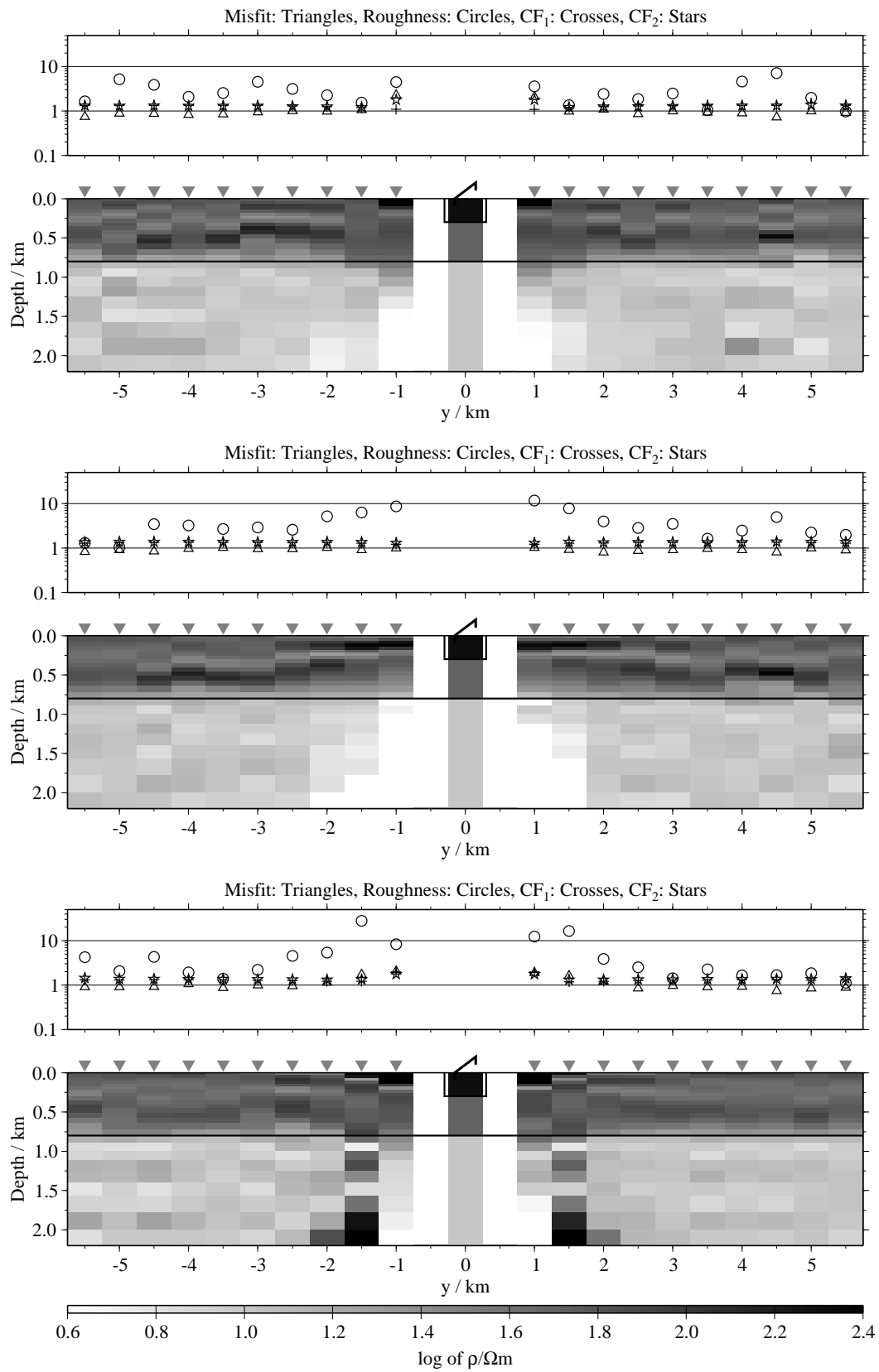


Figure B.195: Pseudo-sections of two component 1-D joint-inversions, model J1, regularisation scheme C1; from top to bottom $E_x-\dot{H}_y$, $E_x-\dot{H}_z$ and $\dot{H}_y-\dot{H}_z$;

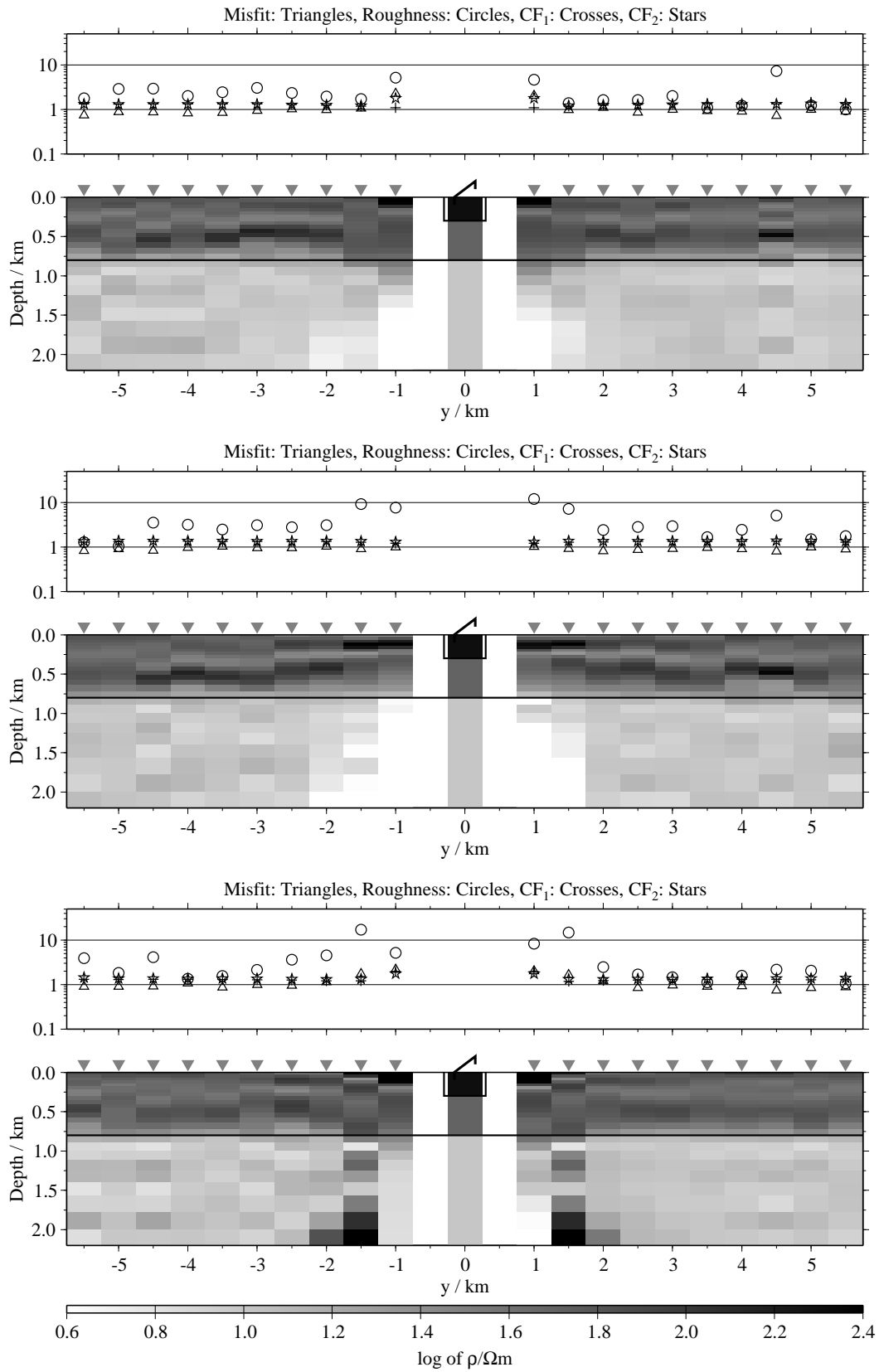


Figure B.196: Pseudo-sections of two component 1-D joint-inversions, model J1, regularisation scheme C4; from top to bottom $E_x-\dot{H}_y$, $E_x-\dot{H}_z$ and $\dot{H}_y-\dot{H}_z$;

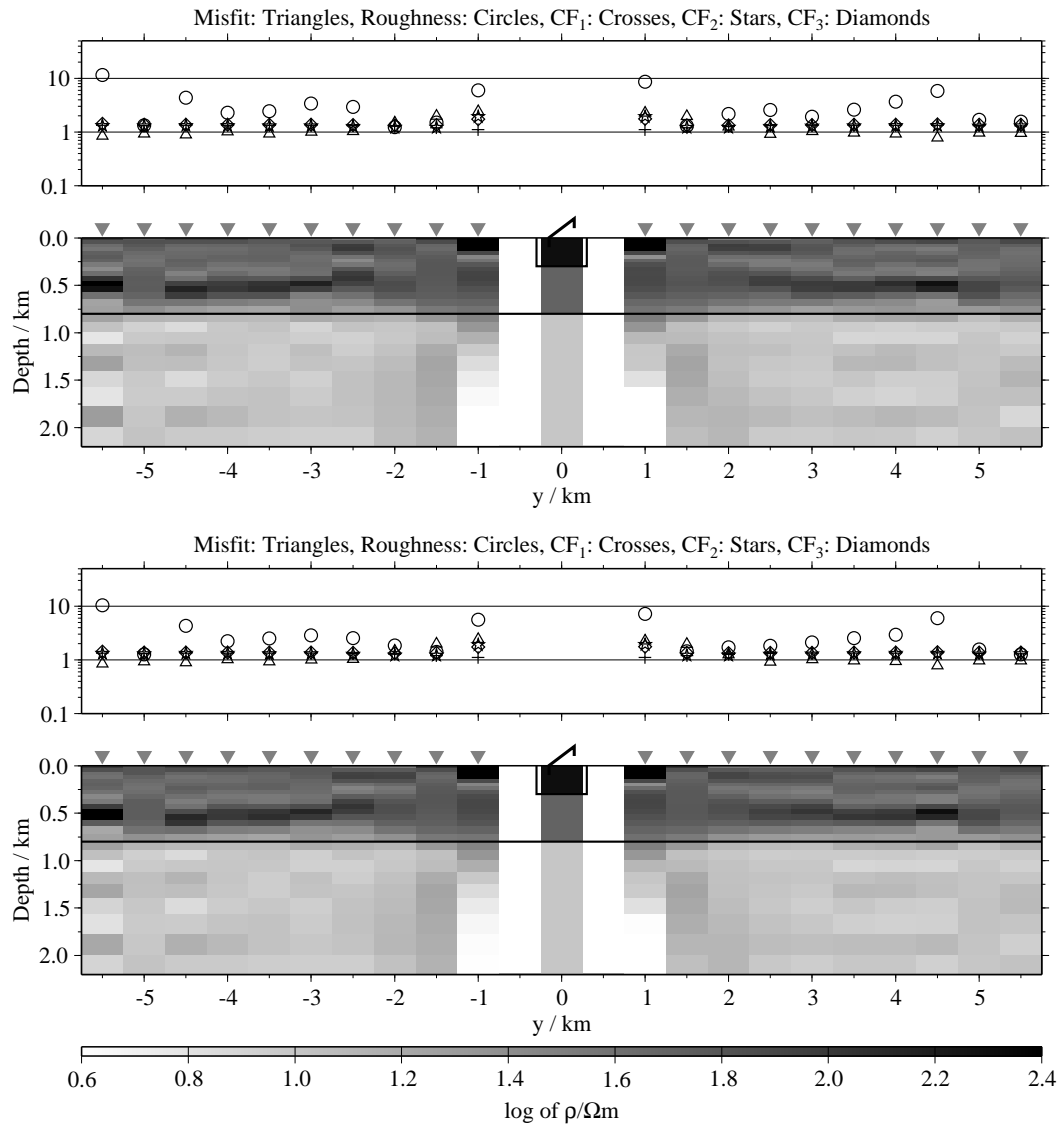


Figure B.197: Pseudo-sections of 1-D joint-inversions using all three components, model J1; top: Regularisation scheme C1; bottom: Regularisation scheme C4;

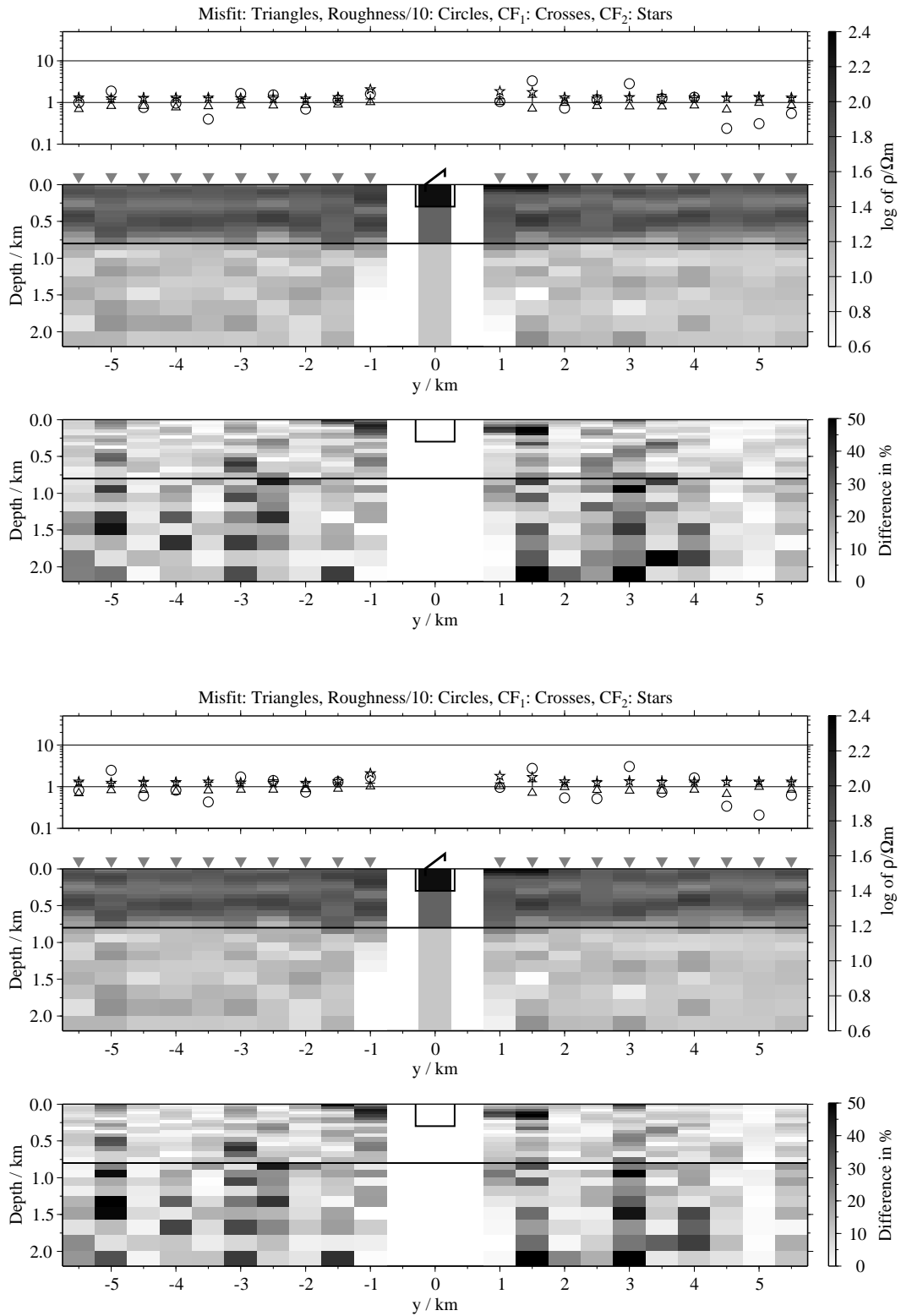


Figure B.198: Pseudo-sections of 1-D soft joint-inversions using the components E_x and H_y , model J1; Top panels: Average inversion results and relative differences (regularisation scheme C1); bottom: Average inversion results and relative differences (regularisation scheme C4);

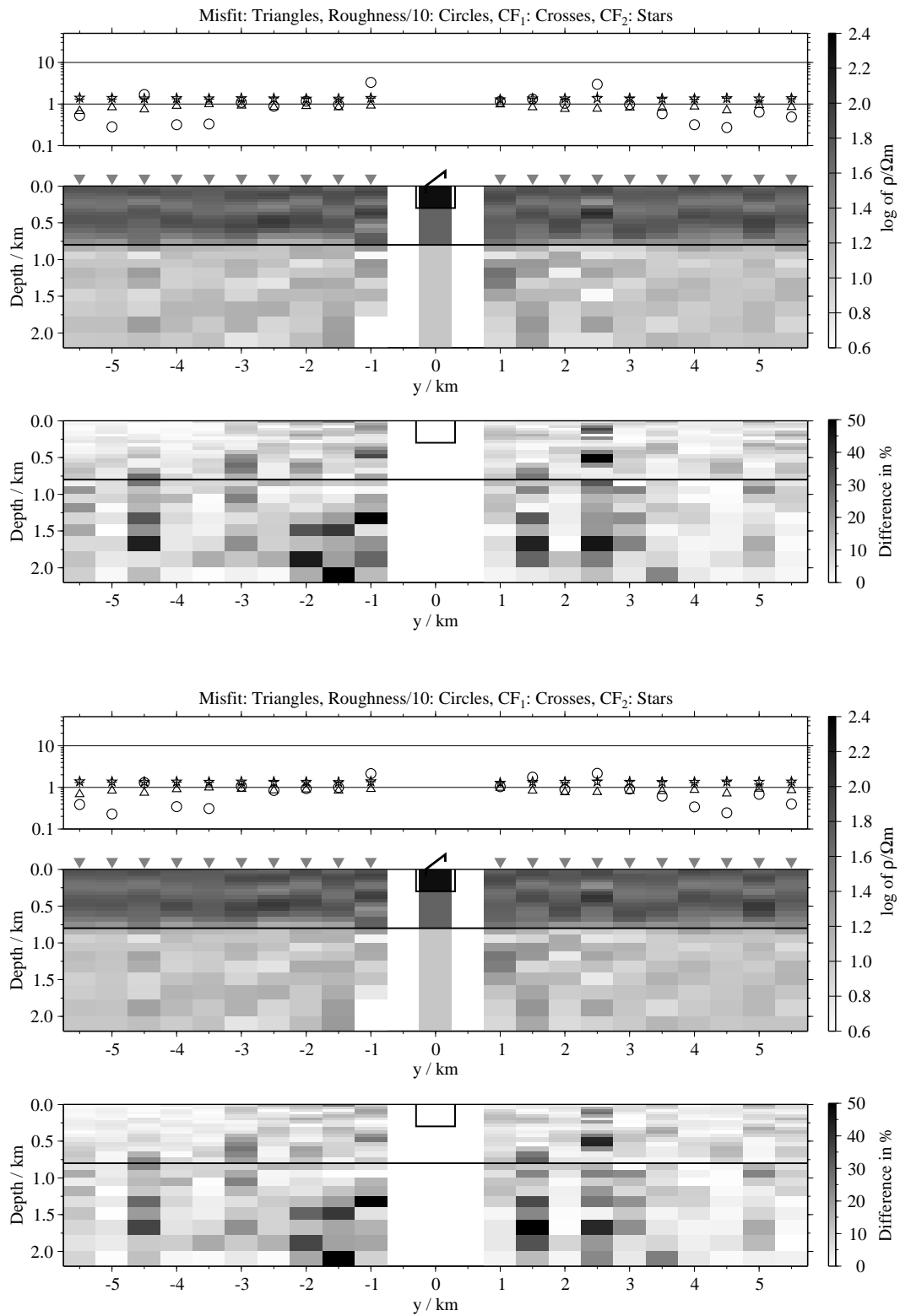


Figure B.199: Pseudo-sections 1-D of soft joint-inversions using the components E_x and H_z , model J1; Top panels: Average inversion results and relative differences (regularisation scheme C1); bottom: Average inversion results and relative differences (regularisation scheme C4);

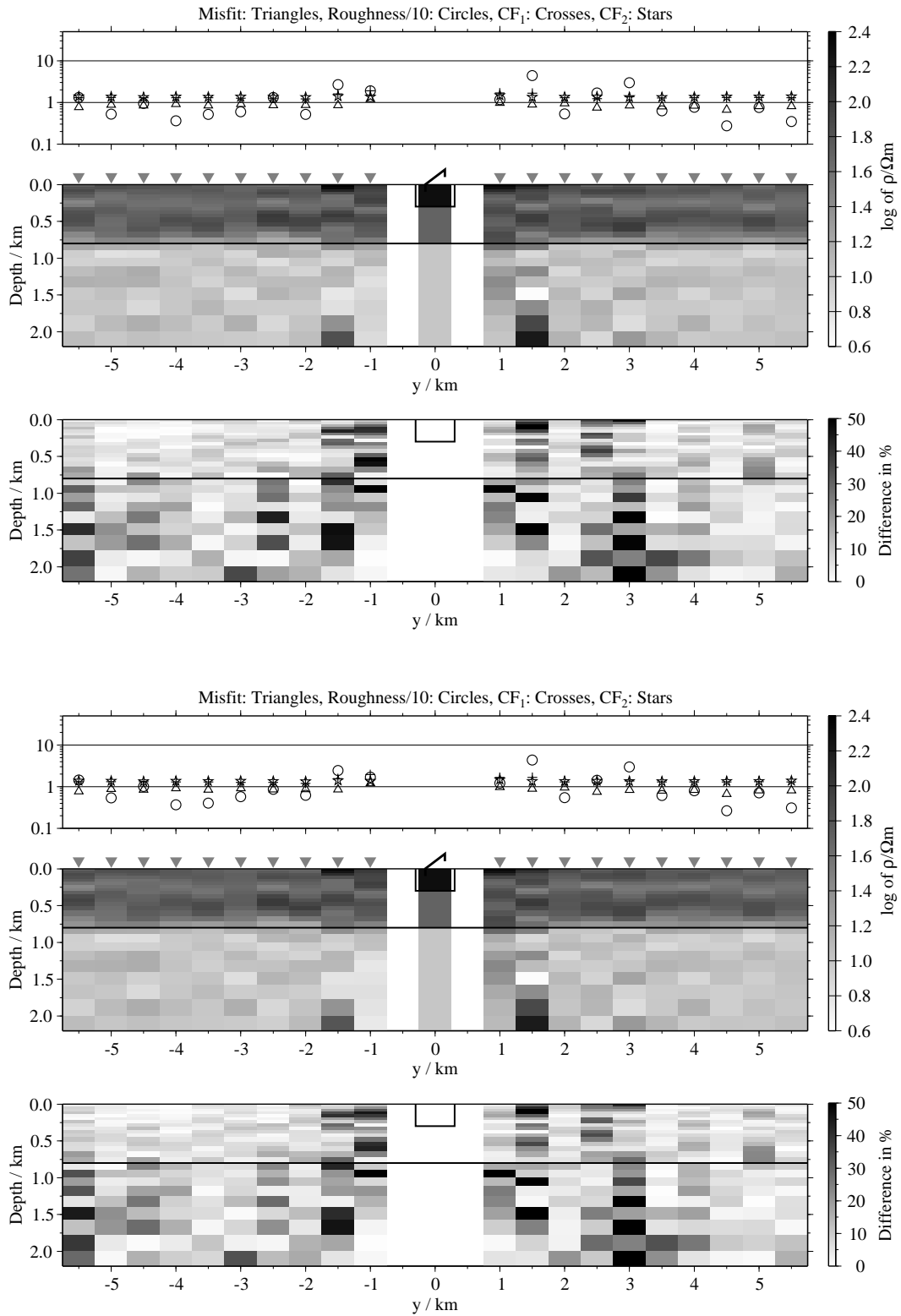


Figure B.200: Pseudo-sections of 1-D soft joint-inversions using the components \dot{H}_y and \dot{H}_z , model J1; Top panels: Average inversion results and relative differences (regularisation scheme C1); bottom: Average inversion results and relative differences (regularisation scheme C4);

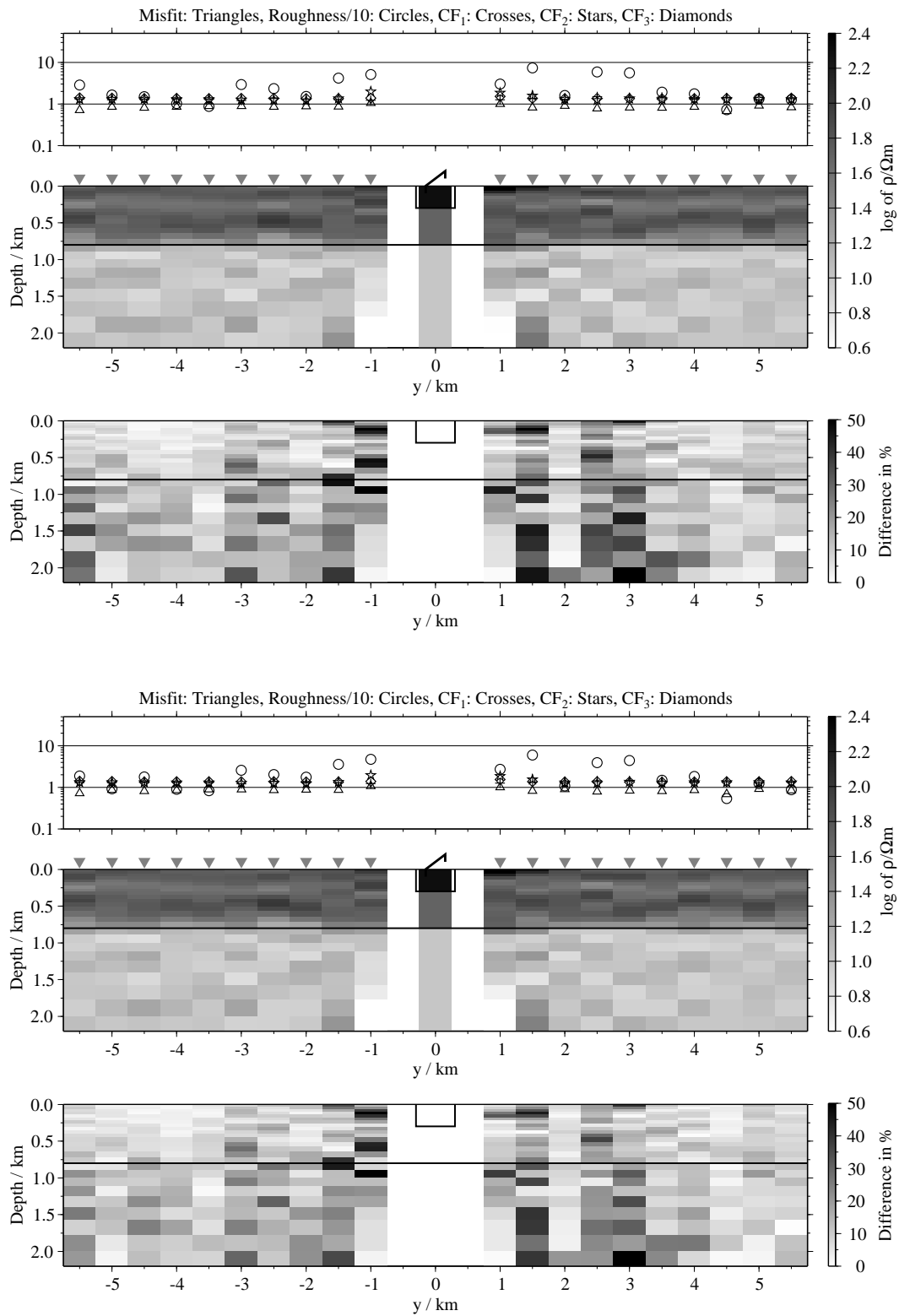


Figure B.201: Pseudo-sections of 1-D soft joint-inversions using all three components, model J1; Top panels: Average inversion results and relative differences (regularisation scheme C1); bottom: Average inversion results and relative differences (regularisation scheme C4);

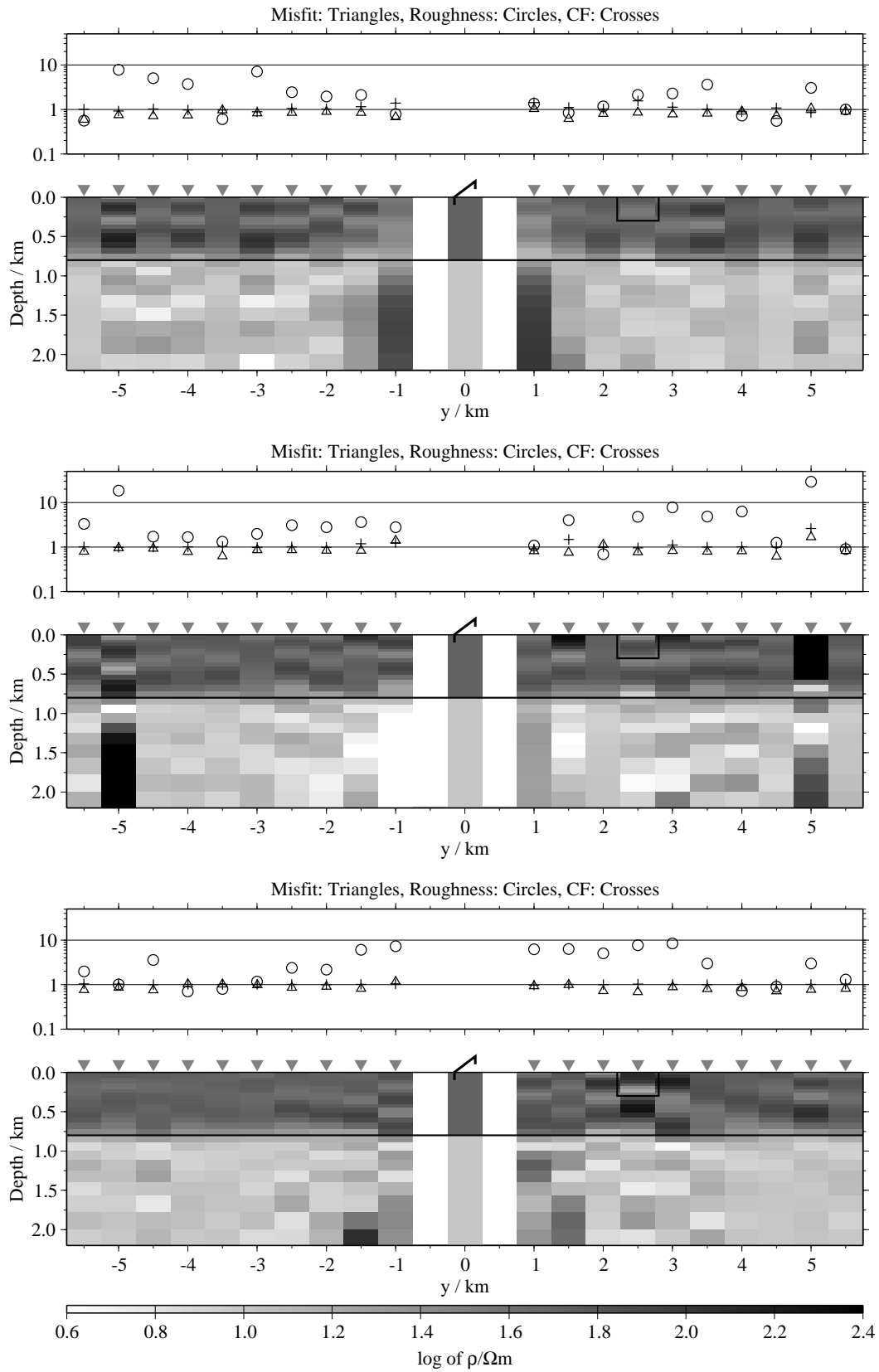


Figure B.202: Pseudo-sections of single 1-D inversion, model J2, regularisation scheme C1; from top to bottom E_x -, \dot{H}_y - and \dot{H}_z -component;

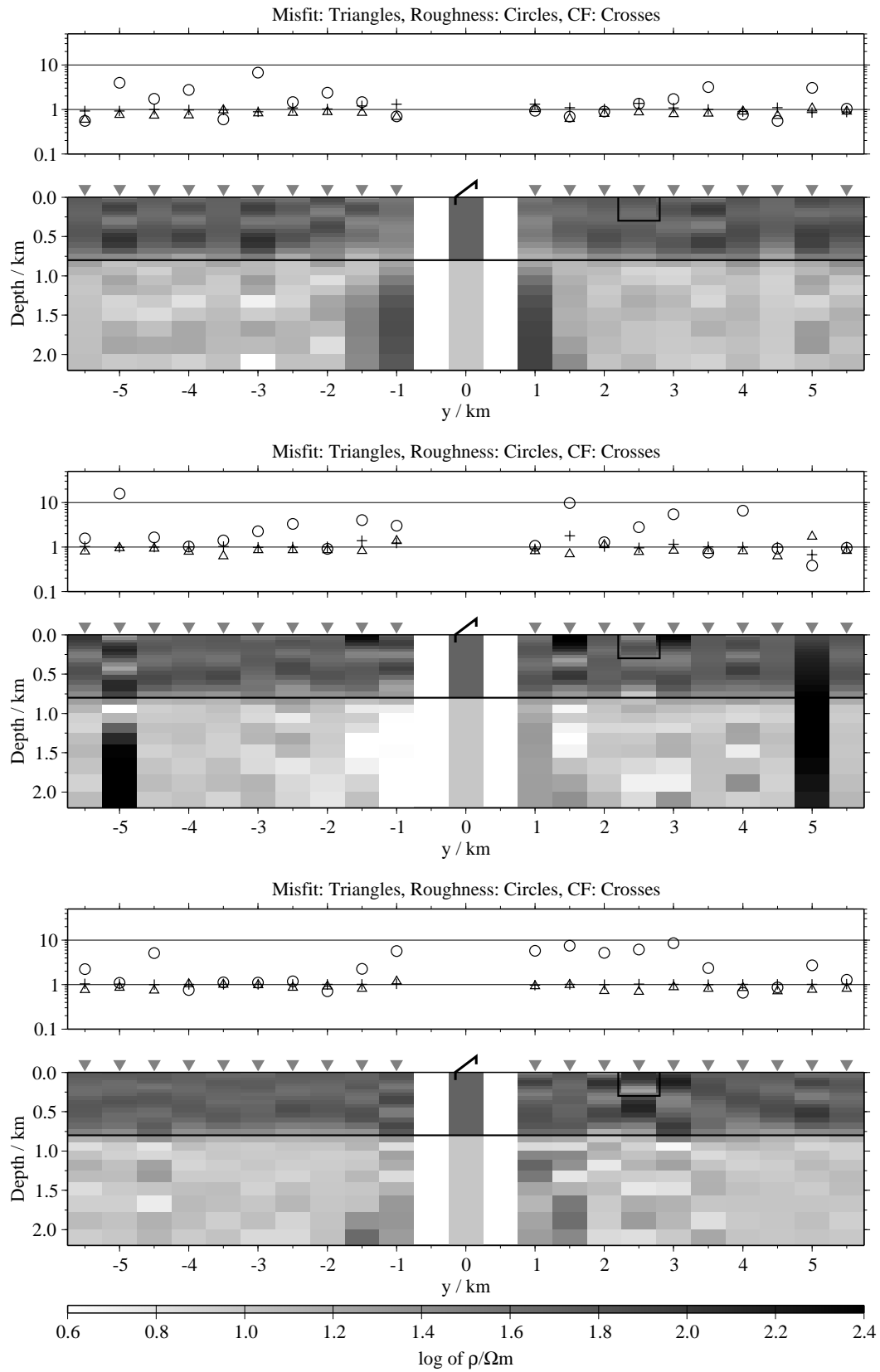


Figure B.203: Pseudo-sections of single 1-D inversion, model J2, regularisation scheme C4; from top to bottom E_x -, H_y - and H_z -component;

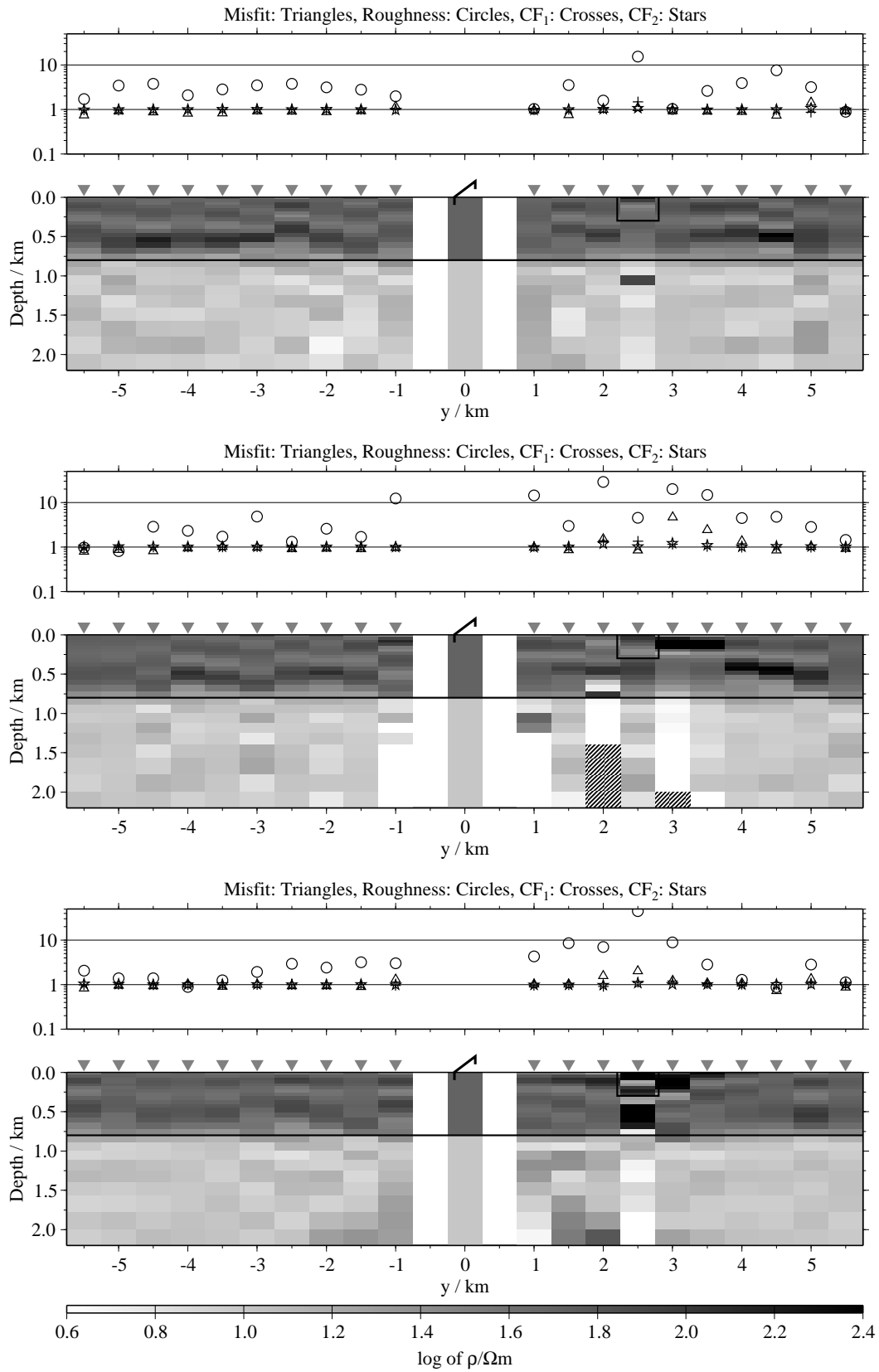


Figure B.204: Pseudo-sections of two component 1-D joint-inversions, model J2, regularisation scheme C1; from top to bottom E_x-H_y , E_x-H_z and H_y-H_z ;

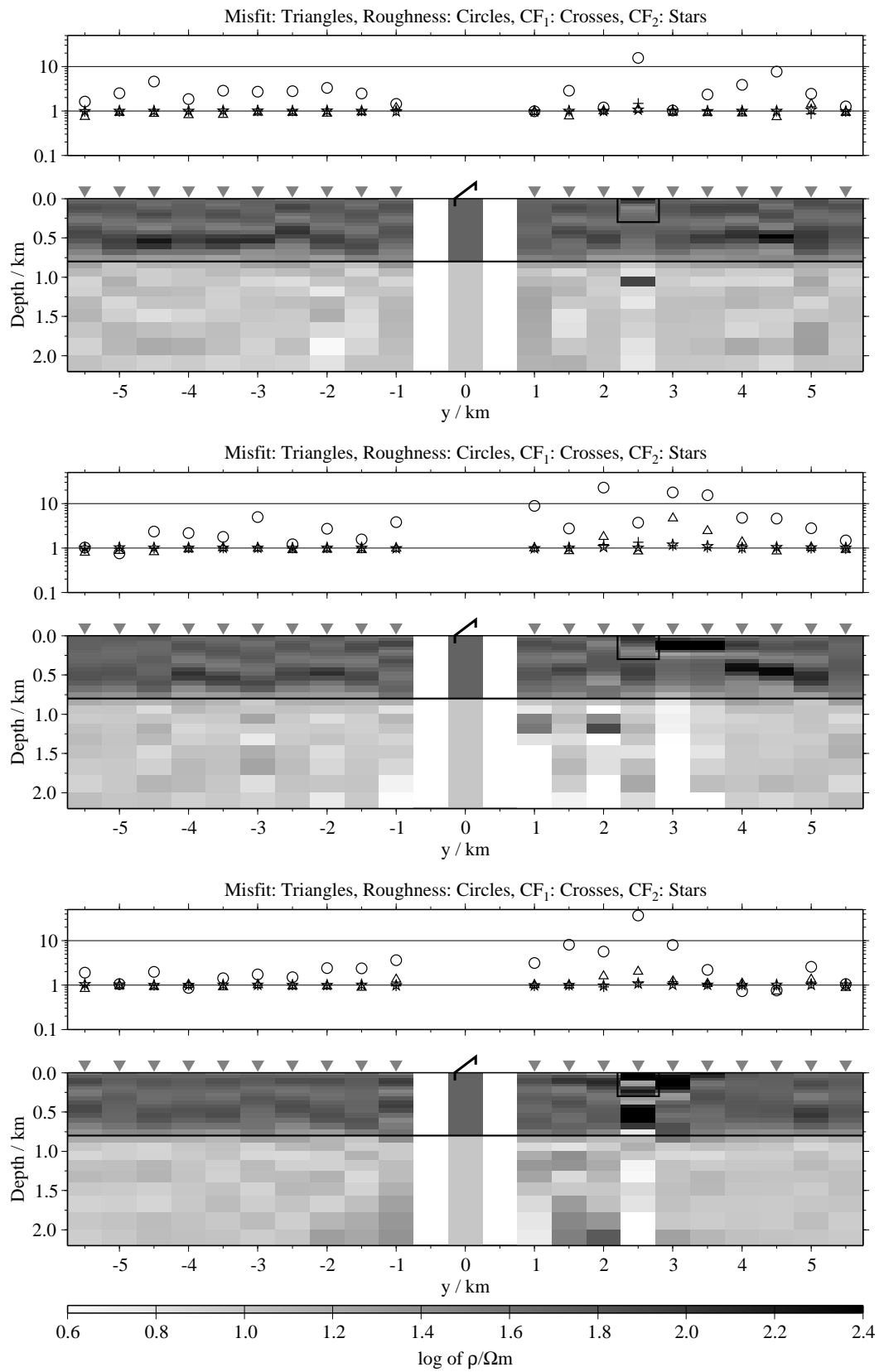


Figure B.205: Pseudo-sections of two component 1-D joint-inversions, model J2, regularisation scheme C4; from top to bottom $E_x\text{-}\dot{H}_y$, $E_x\text{-}\dot{H}_z$ and $\dot{H}_y\text{-}\dot{H}_z$;

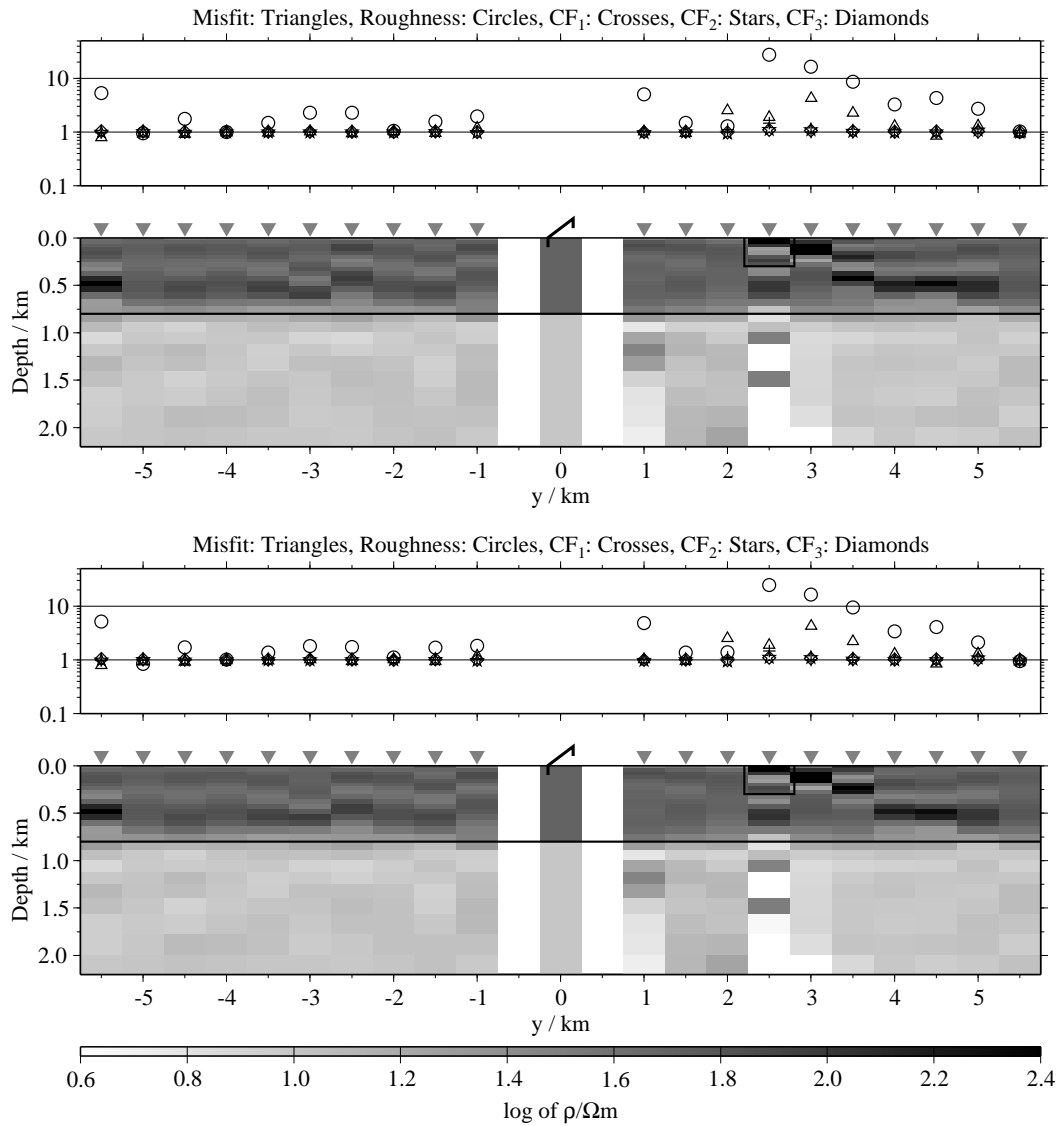


Figure B.206: Pseudo-sections of 1-D joint-inversions using all three components, model J2; top: Regularisation scheme C1; bottom: Regularisation scheme C4;

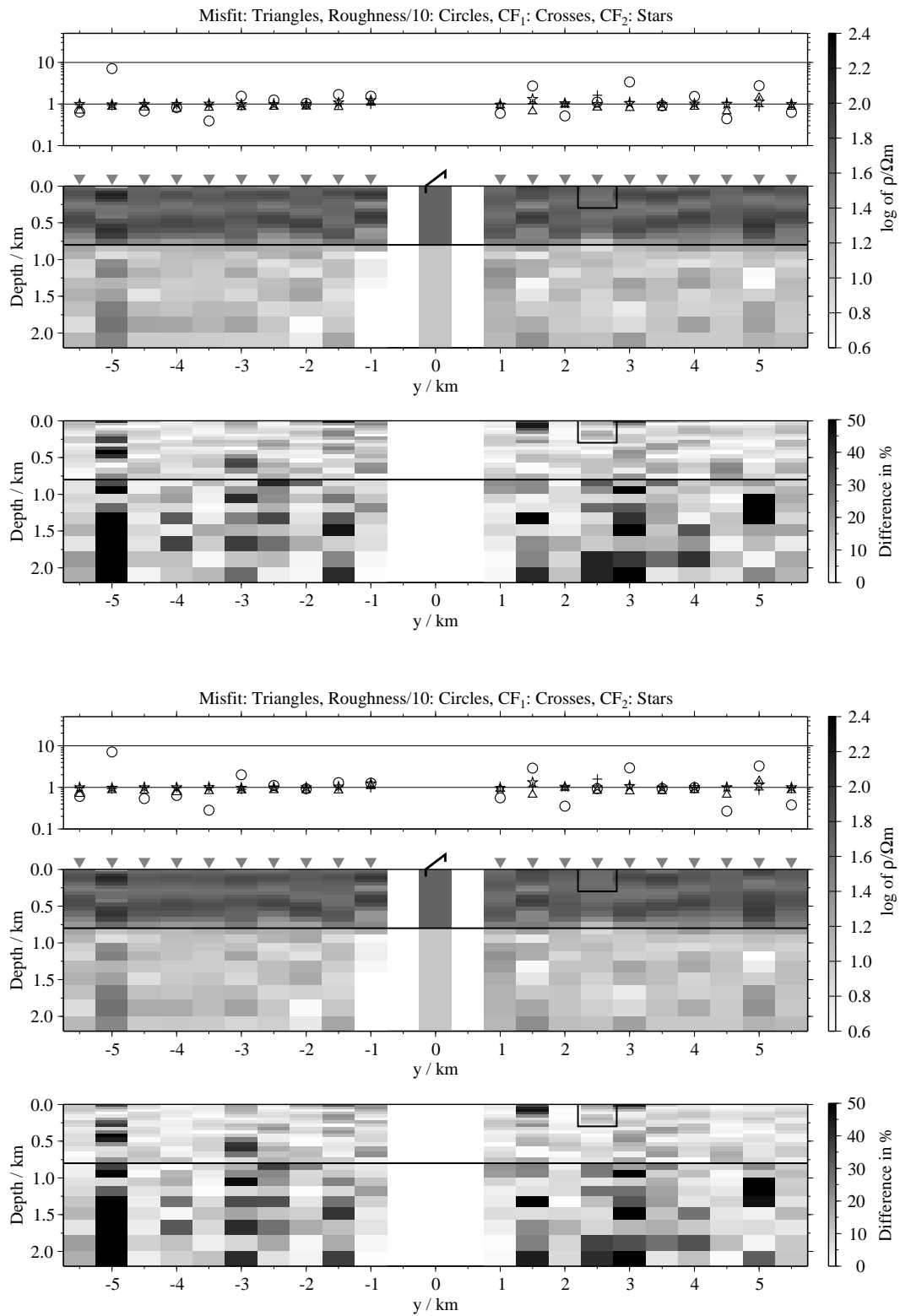


Figure B.207: Pseudo-sections of 1-D soft joint-inversions using the components E_x and H_y , model J2; Top panels: Average inversion results and relative differences (regularisation scheme C1); bottom: Average inversion results and relative differences (regularisation scheme C4);

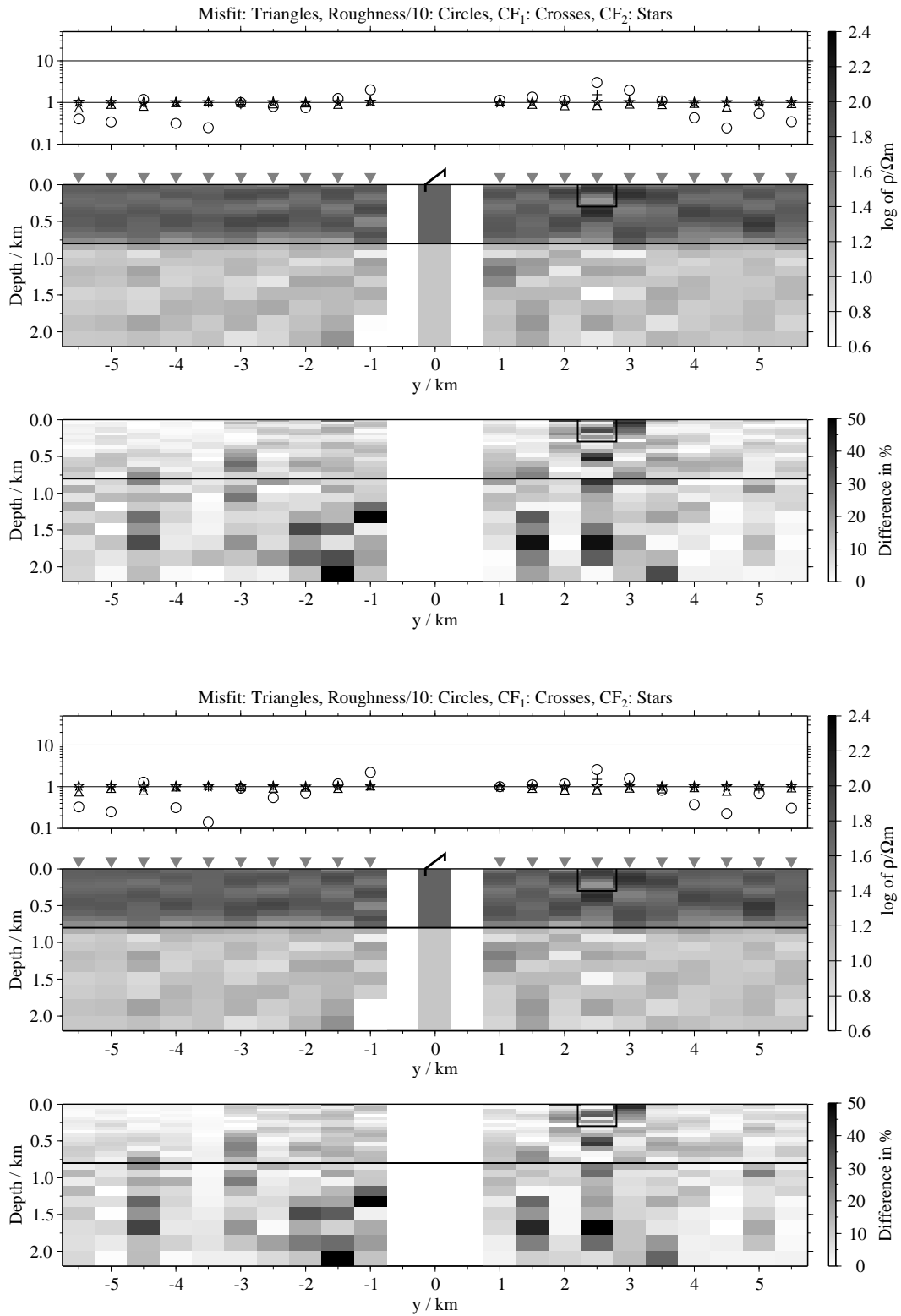


Figure B.208: Pseudo-sections 1-D of soft joint-inversions using the components E_x and \dot{H}_z , model J2; Top panels: Average inversion results and relative differences (regularisation scheme C1); bottom: Average inversion results and relative differences (regularisation scheme C4);

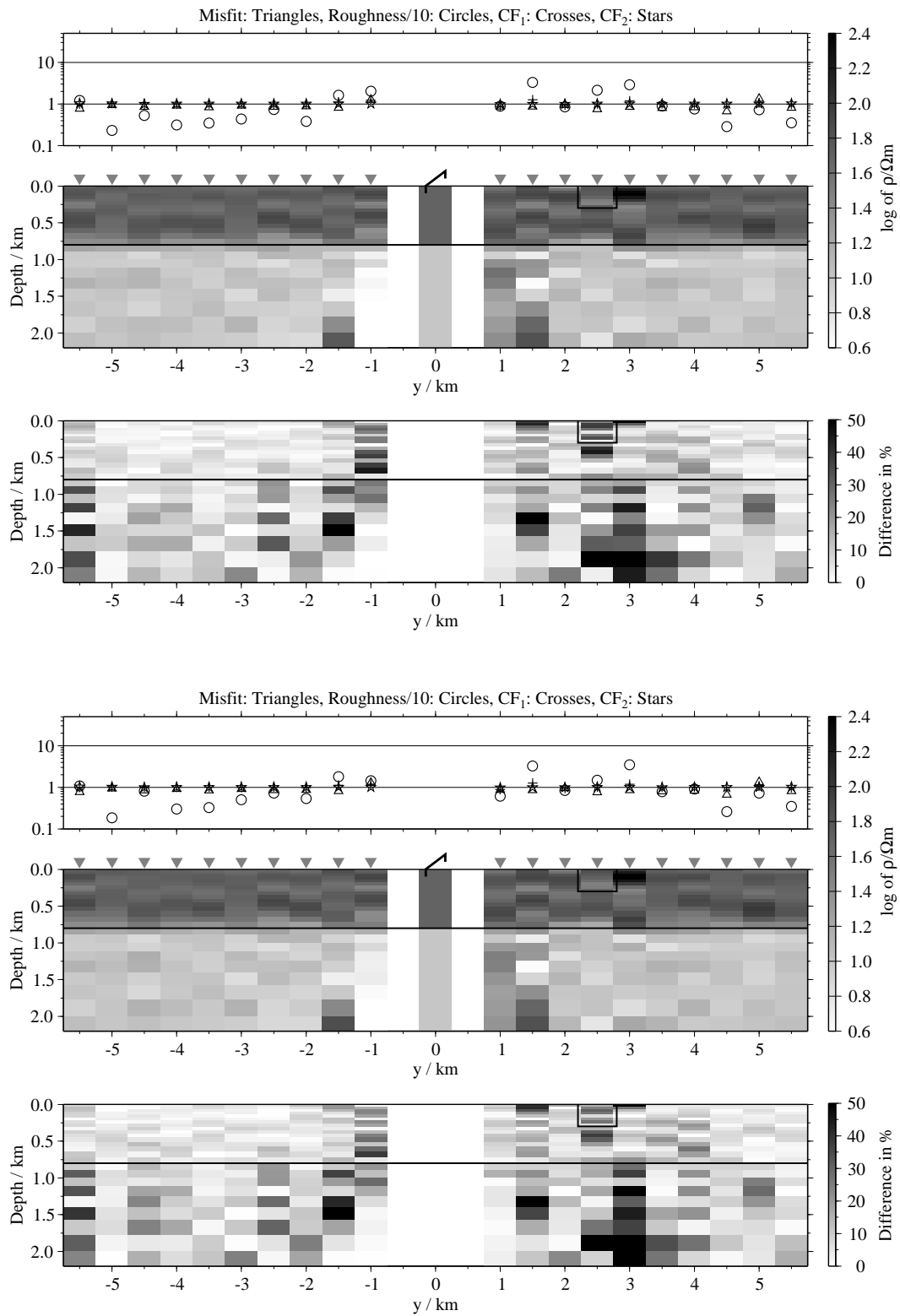


Figure B.209: Pseudo-sections of 1-D soft joint-inversions using the components \dot{H}_y and \dot{H}_z , model J2; Top panels: Average inversion results and relative differences (regularisation scheme C1); bottom: Average inversion results and relative differences (regularisation scheme C4);

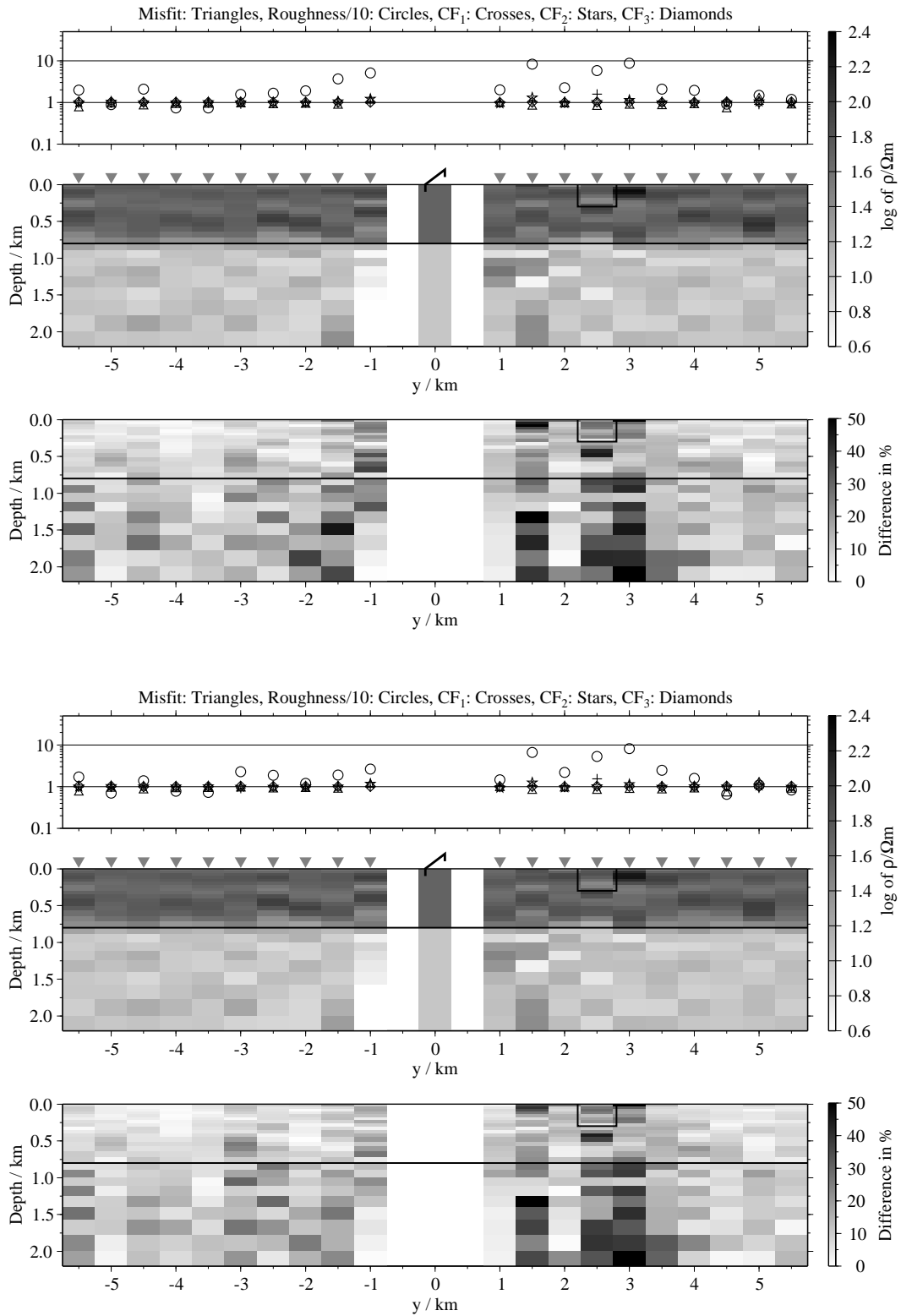
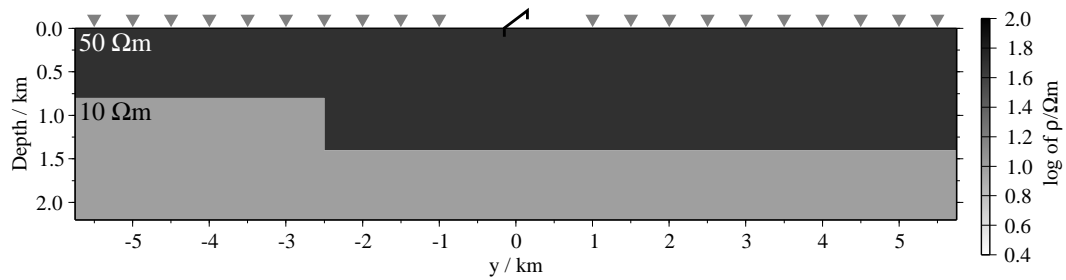


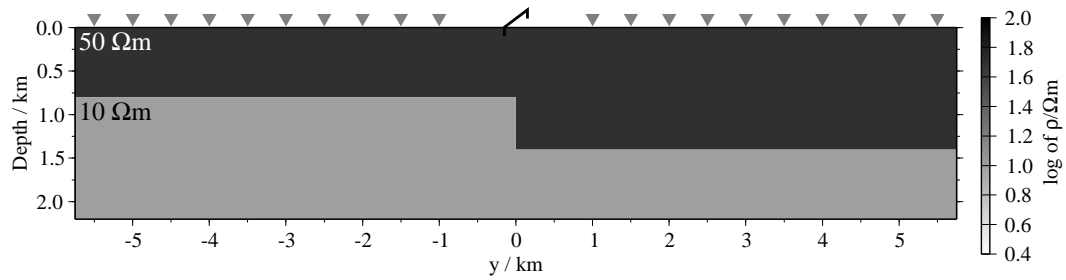
Figure B.210: Pseudo-sections of 1-D soft joint-inversions using all three components, model J2; Top panels: Average inversion results and relative differences (regularisation scheme C1); bottom: Average inversion results and relative differences (regularisation scheme C4);

B.2.9 Displacement in a conductive basement (models K1 to K3)

Model K1:



Model K2:



Model K3:

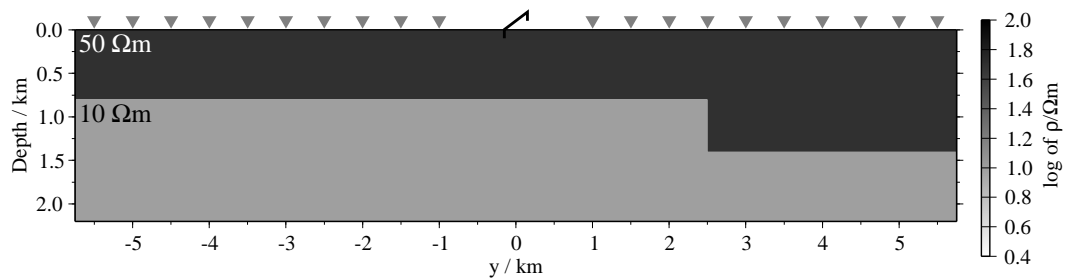


Figure B.211: Model for a fault with a conductive basement; the fault-line is at $y = -2.5$ km (model K1), $y = 0$ km (model K2) and $y = 2.5$ km (model K3).

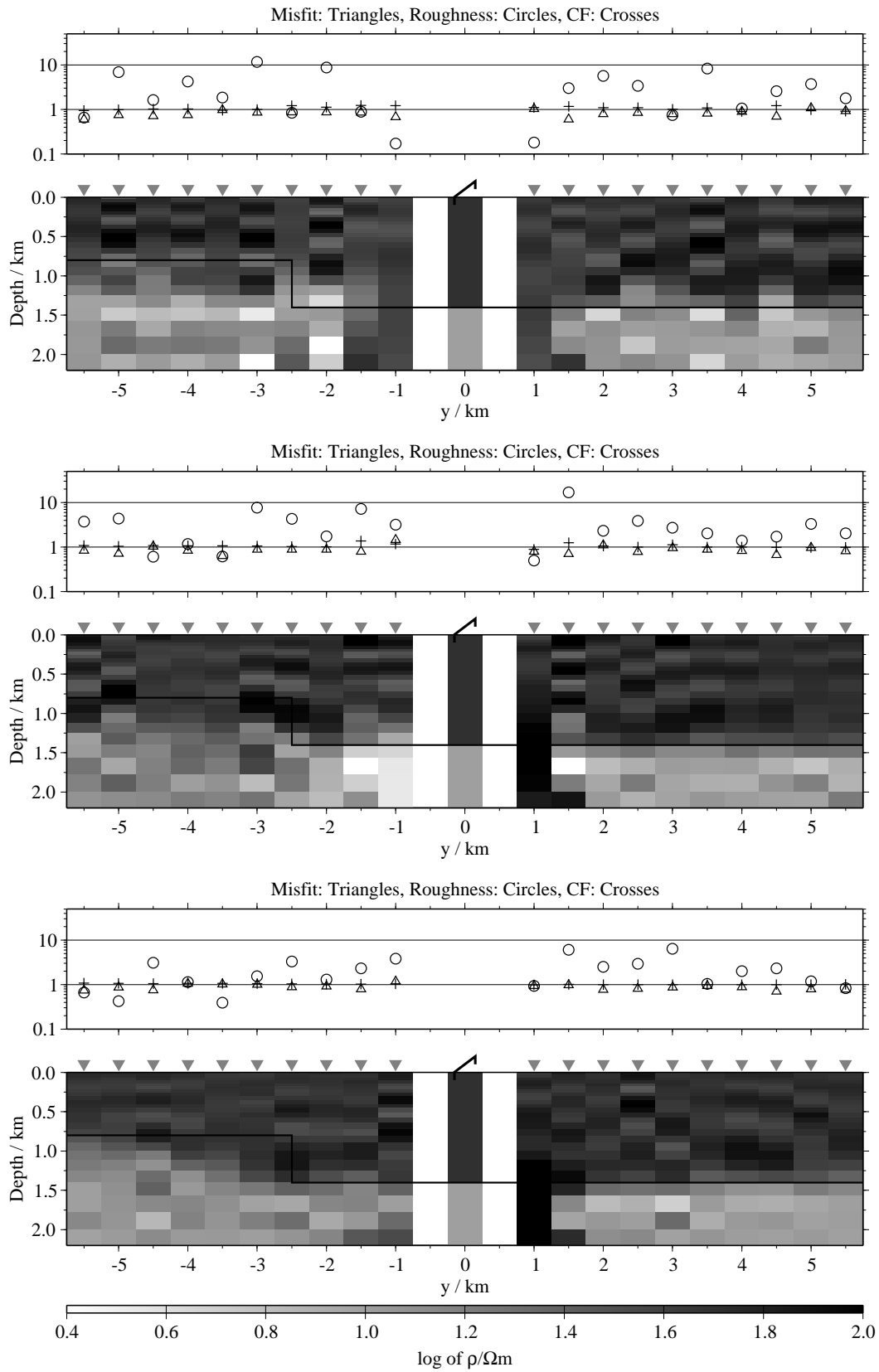


Figure B.212: Pseudo-sections of single 1-D inversion, model K1, regularisation scheme C1; from top to bottom E_x -, \dot{H}_y - and \dot{H}_z -component;

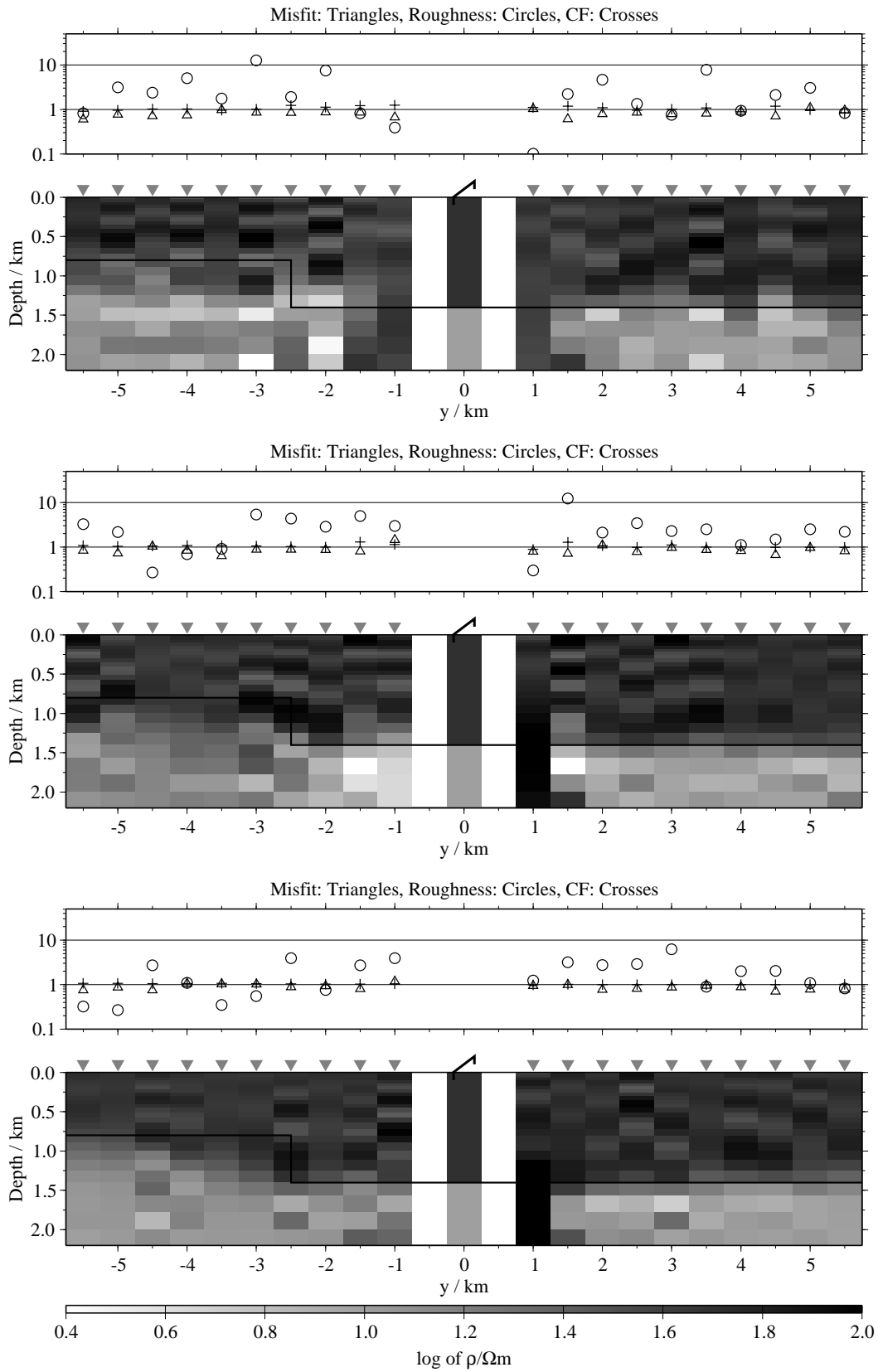


Figure B.213: Pseudo-sections of single 1-D inversion, model K1, regularisation scheme C4; from top to bottom E_{x-} , \dot{H}_y - and \dot{H}_z -component;

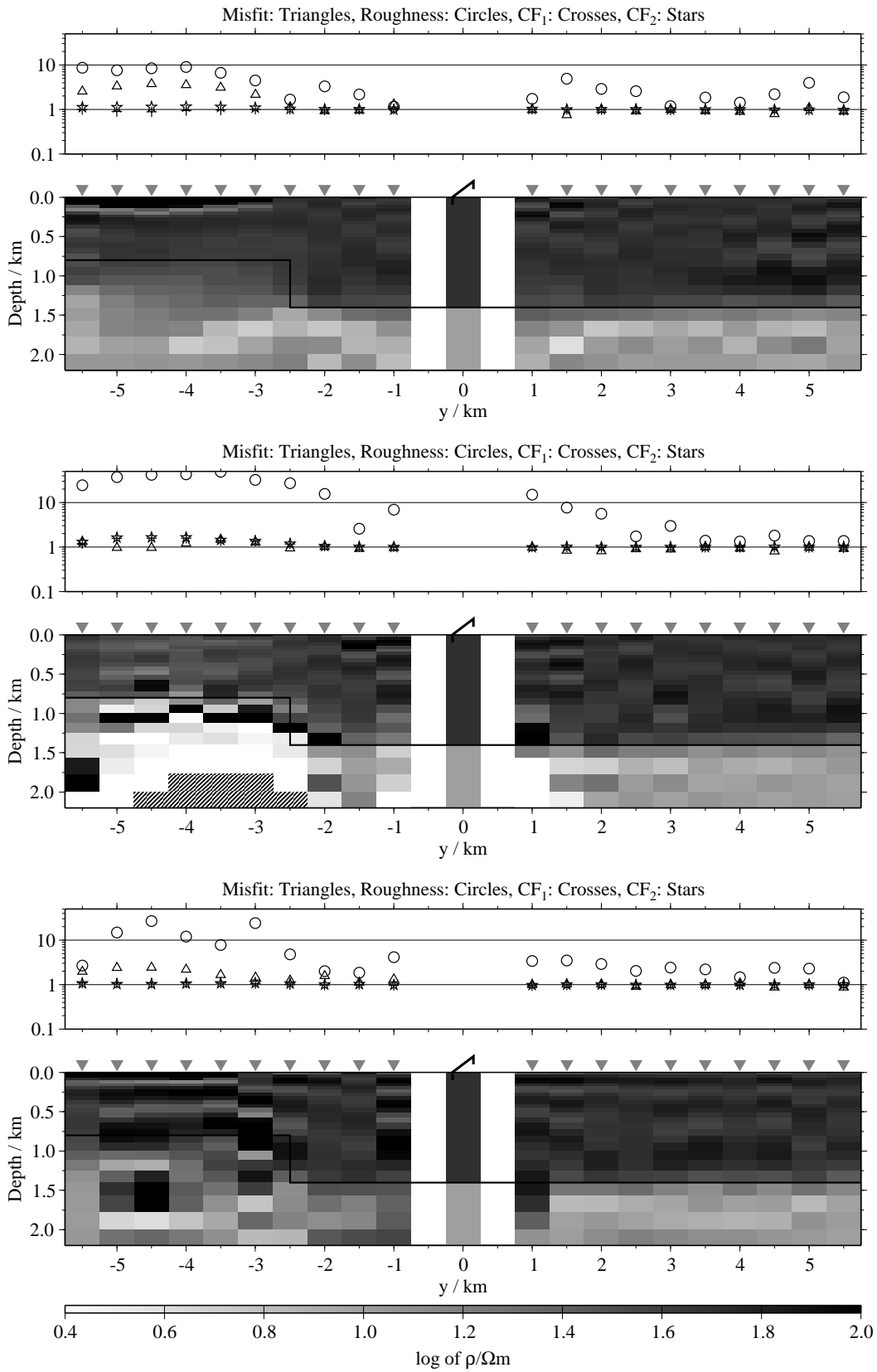


Figure B.214: Pseudo-sections of two component 1-D joint-inversions, model K1, regularisation scheme C1; from top to bottom $E_x - \dot{H}_y$, $E_x - \dot{H}_z$ and $\dot{H}_y - \dot{H}_z$;

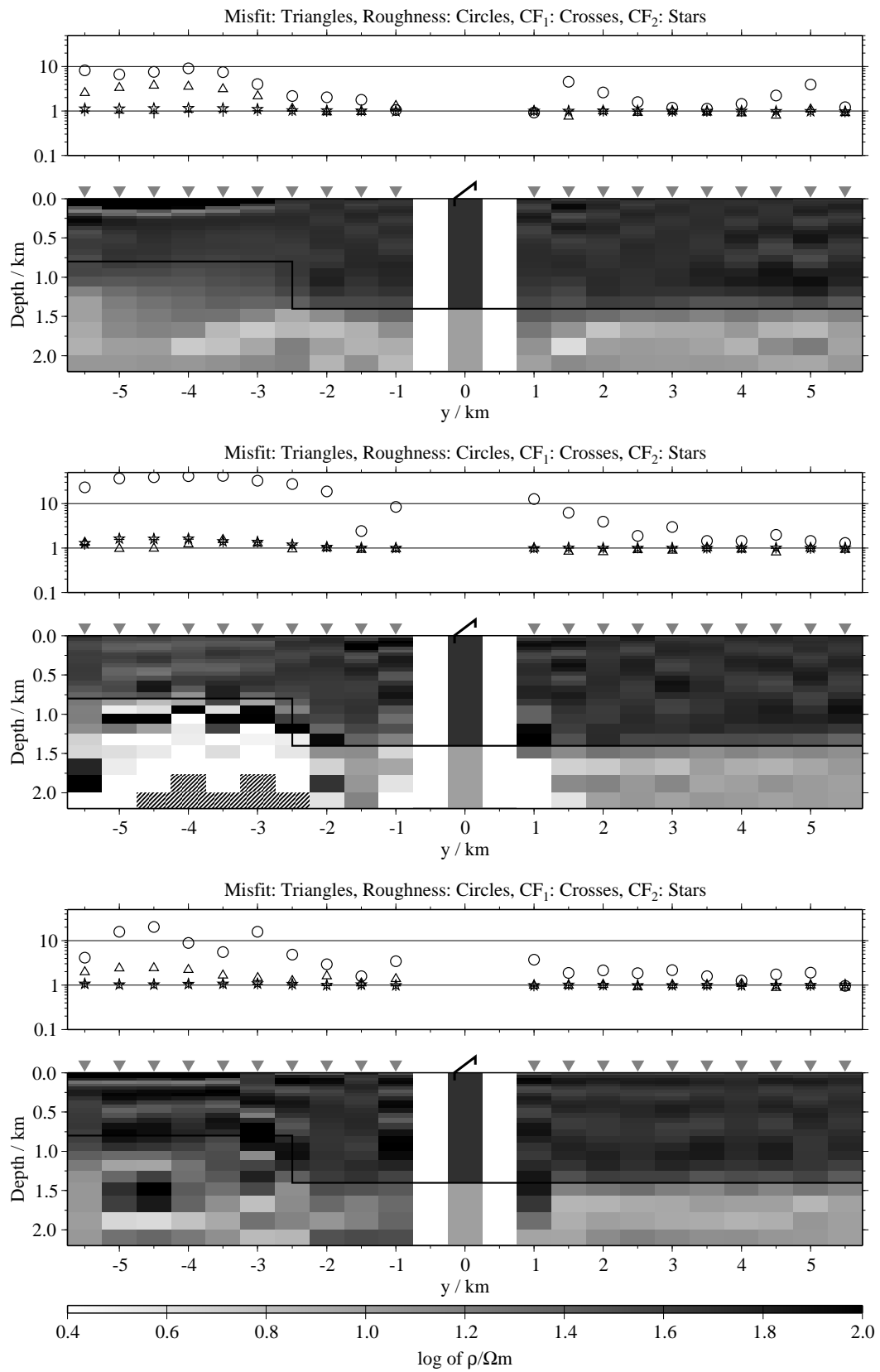


Figure B.215: Pseudo-sections of two component 1-D joint-inversions, model K1, regularisation scheme C4; from top to bottom $E_x - \dot{H}_y$, $E_x - \dot{H}_z$ and $\dot{H}_y - \dot{H}_z$;

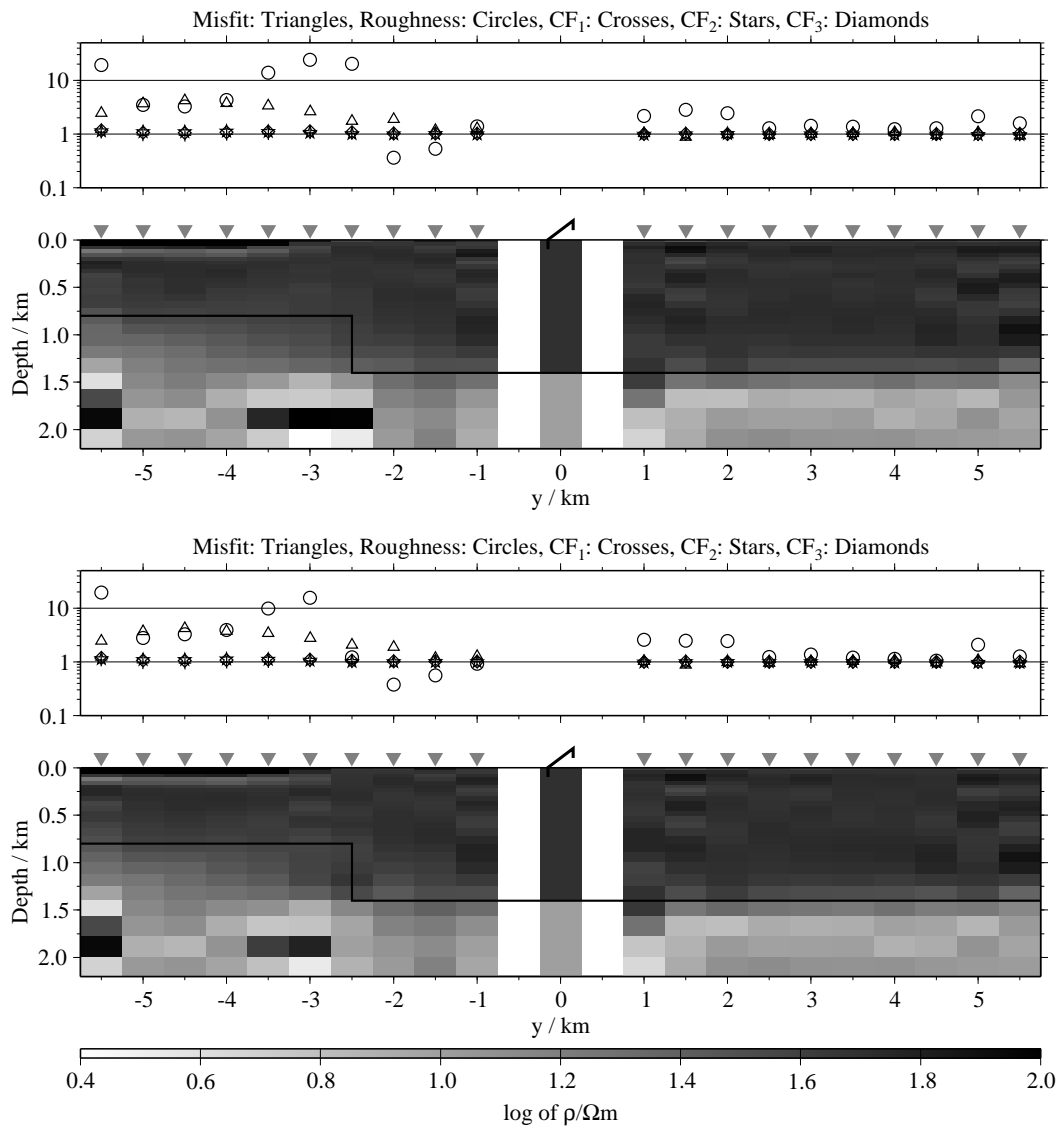


Figure B.216: Pseudo-sections of 1-D joint-inversions using all three components, model K1; top: Regularisation scheme C1; bottom: Regularisation scheme C4;

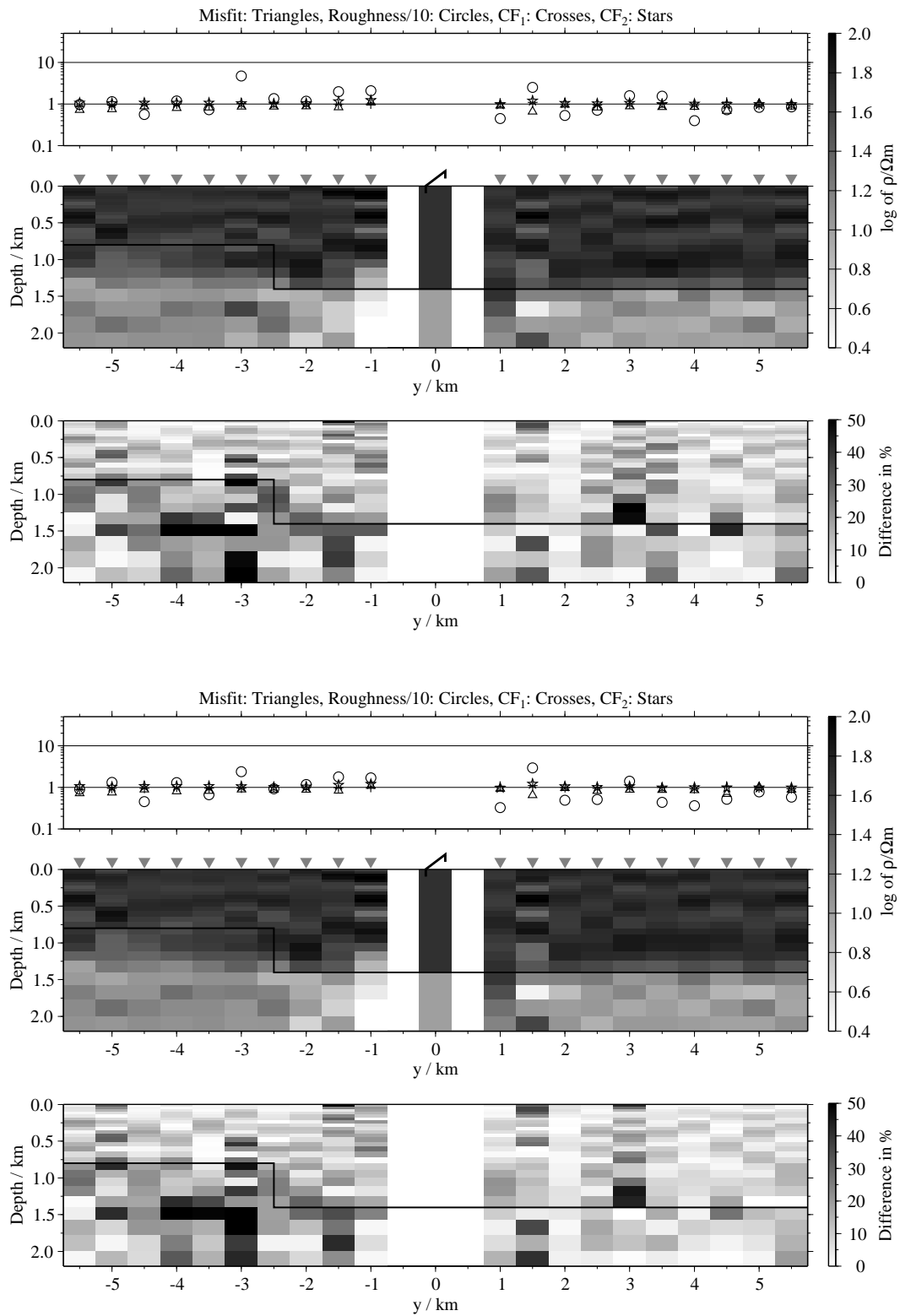


Figure B.217: Pseudo-sections of 1-D soft joint-inversions using the components E_x and H_y , model K1; Top panels: Average inversion results and relative differences (regularisation scheme C1); bottom: Average inversion results and relative differences (regularisation scheme C4);

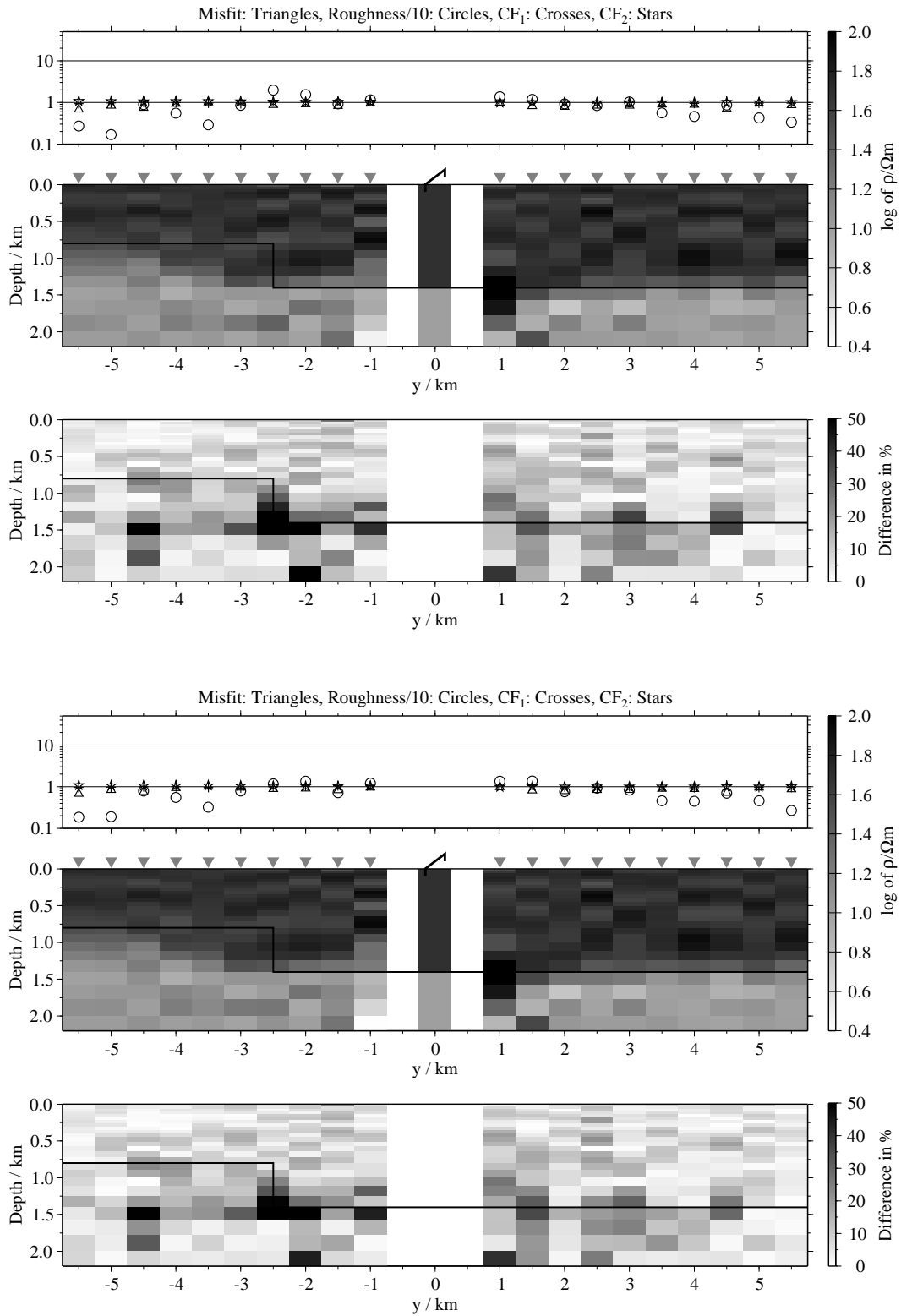


Figure B.218: Pseudo-sections 1-D of soft joint-inversions using the components E_x and H_z , model K1; Top panels: Average inversion results and relative differences (regularisation scheme C1); bottom: Average inversion results and relative differences (regularisation scheme C4);

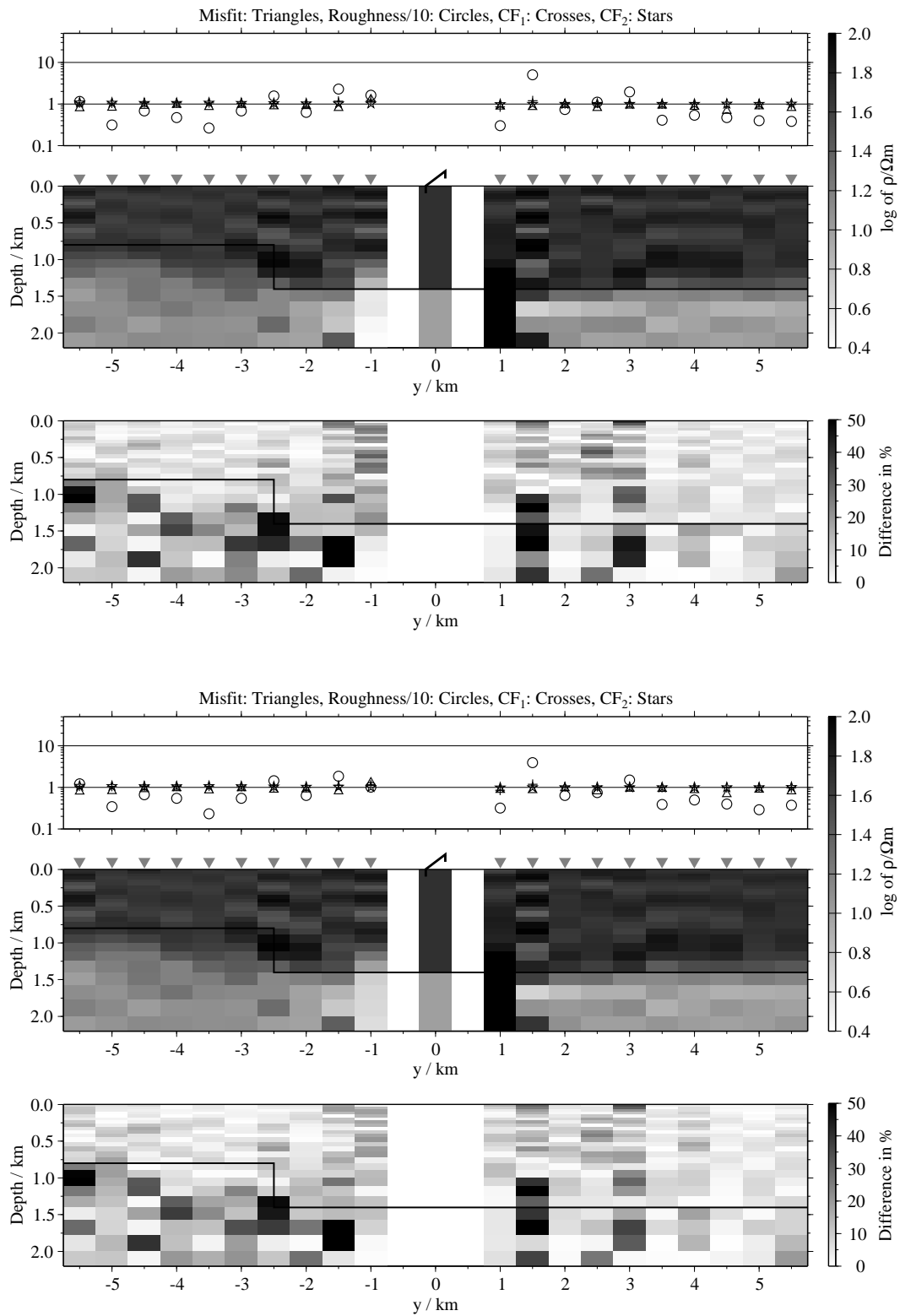


Figure B.219: Pseudo-sections of 1-D soft joint-inversions using the components \dot{H}_y and \dot{H}_{zi} , model K1; Top panels: Average inversion results and relative differences (regularisation scheme C1); bottom: Average inversion results and relative differences (regularisation scheme C4);

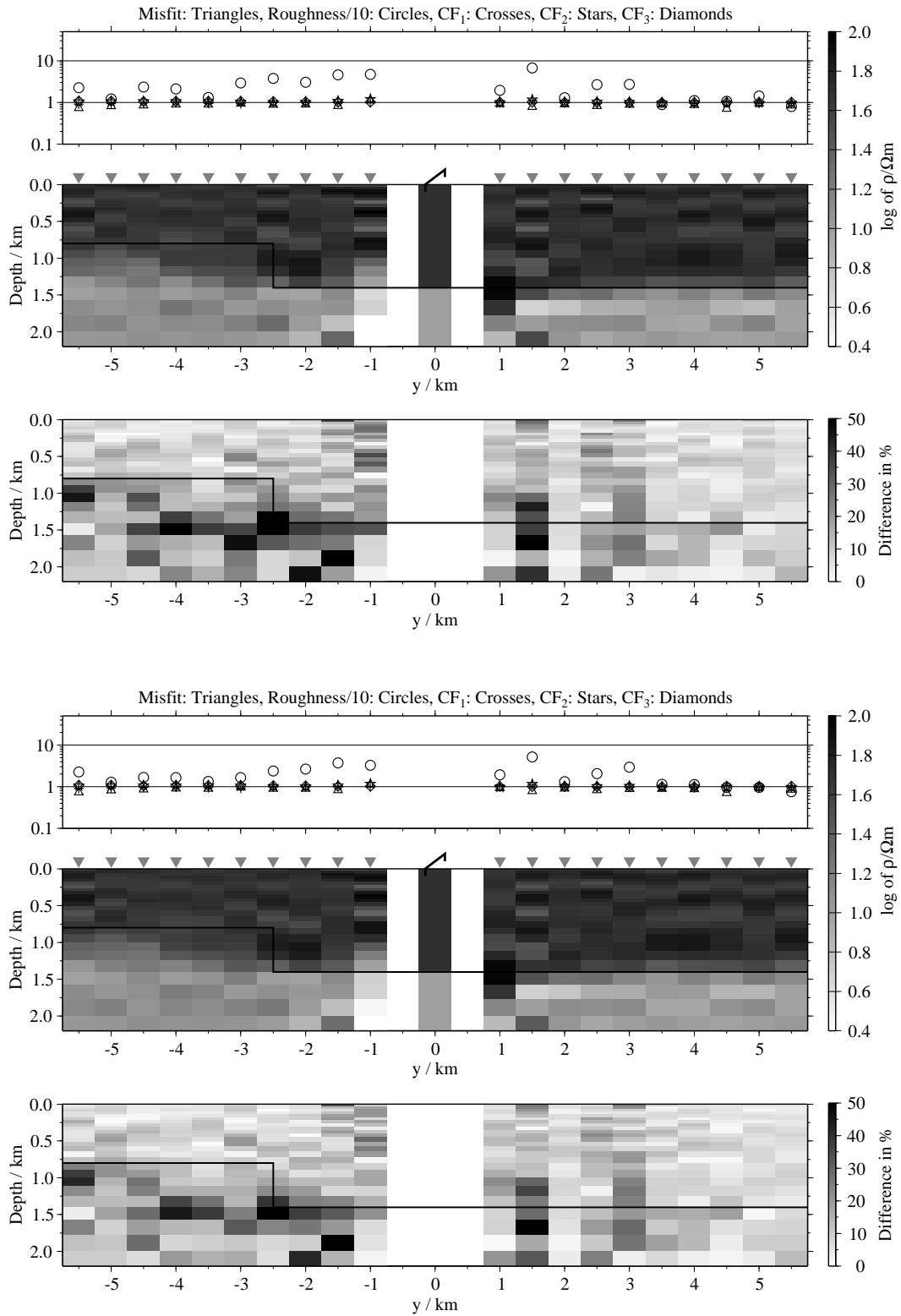


Figure B.220: Pseudo-sections of 1-D soft joint-inversions using all three components, model K1; Top panels: Average inversion results and relative differences (regularisation scheme C1); bottom: Average inversion results and relative differences (regularisation scheme C4);

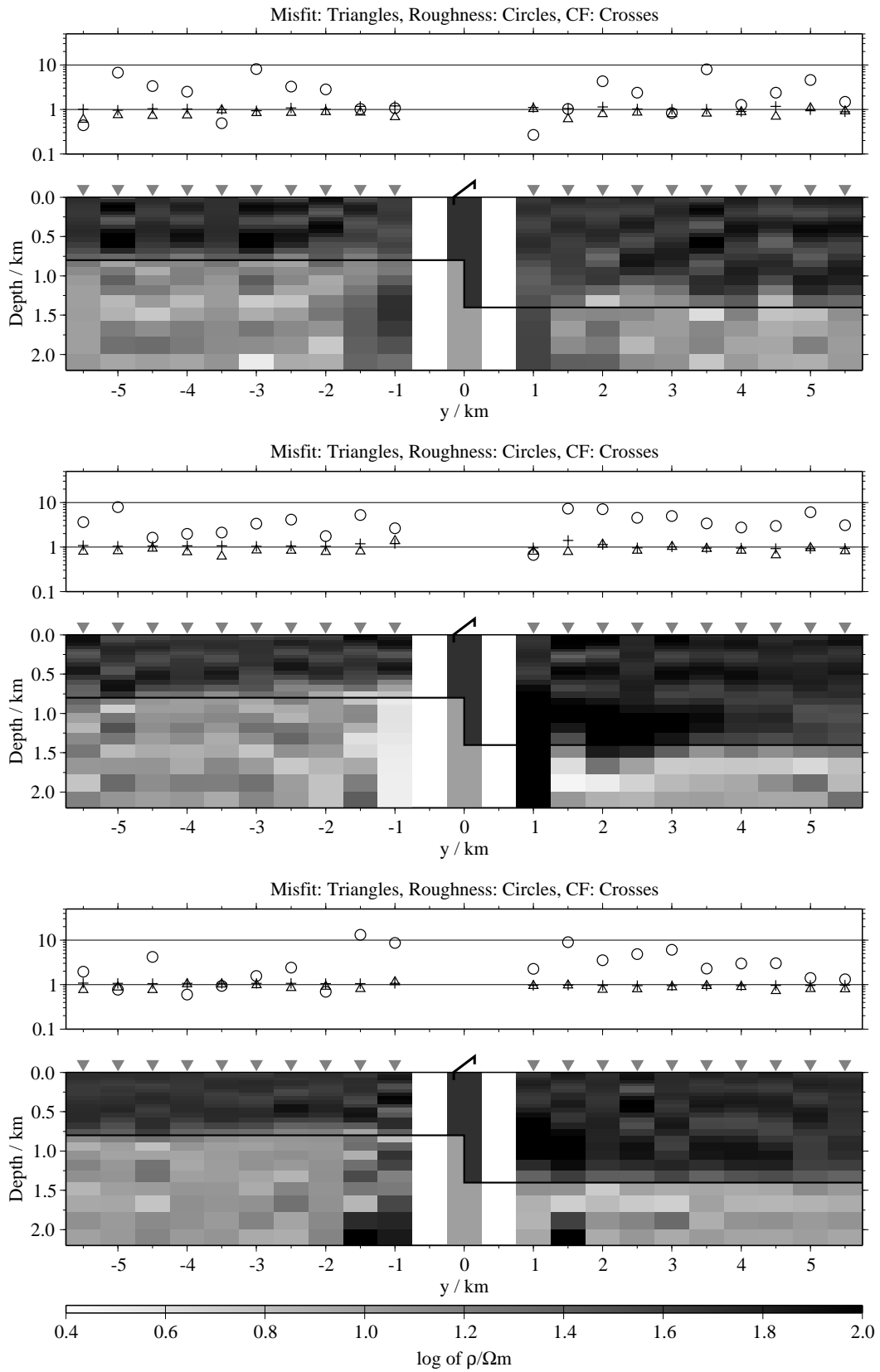


Figure B.221: Pseudo-sections of single 1-D inversion, model K2, regularisation scheme C1; from top to bottom E_x -, \dot{H}_y - and \dot{H}_z -component;

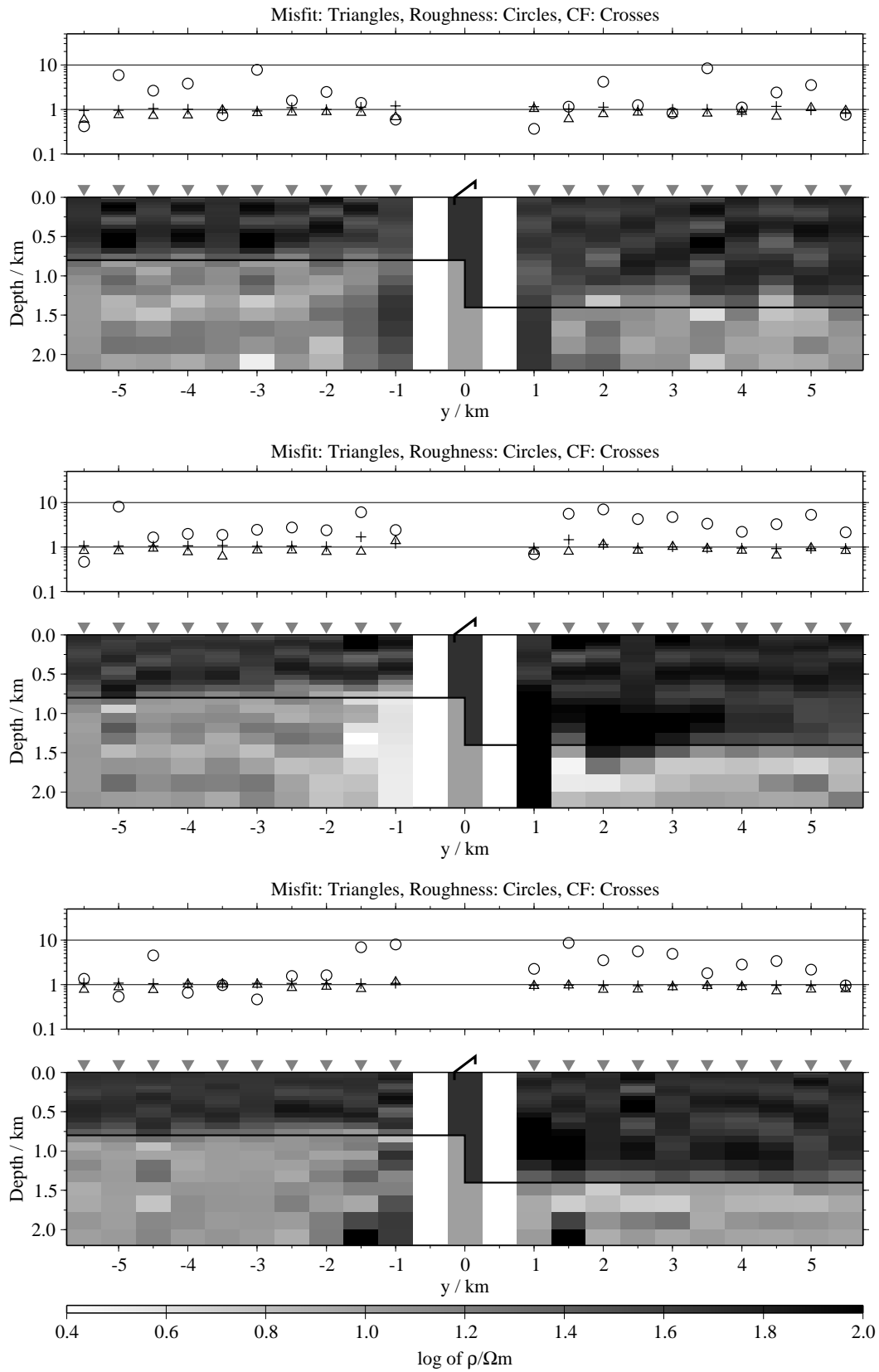


Figure B.222: Pseudo-sections of single 1-D inversion, model K2, regularisation scheme C4; from top to bottom E_x -, \dot{H}_y - and \dot{H}_z -component;

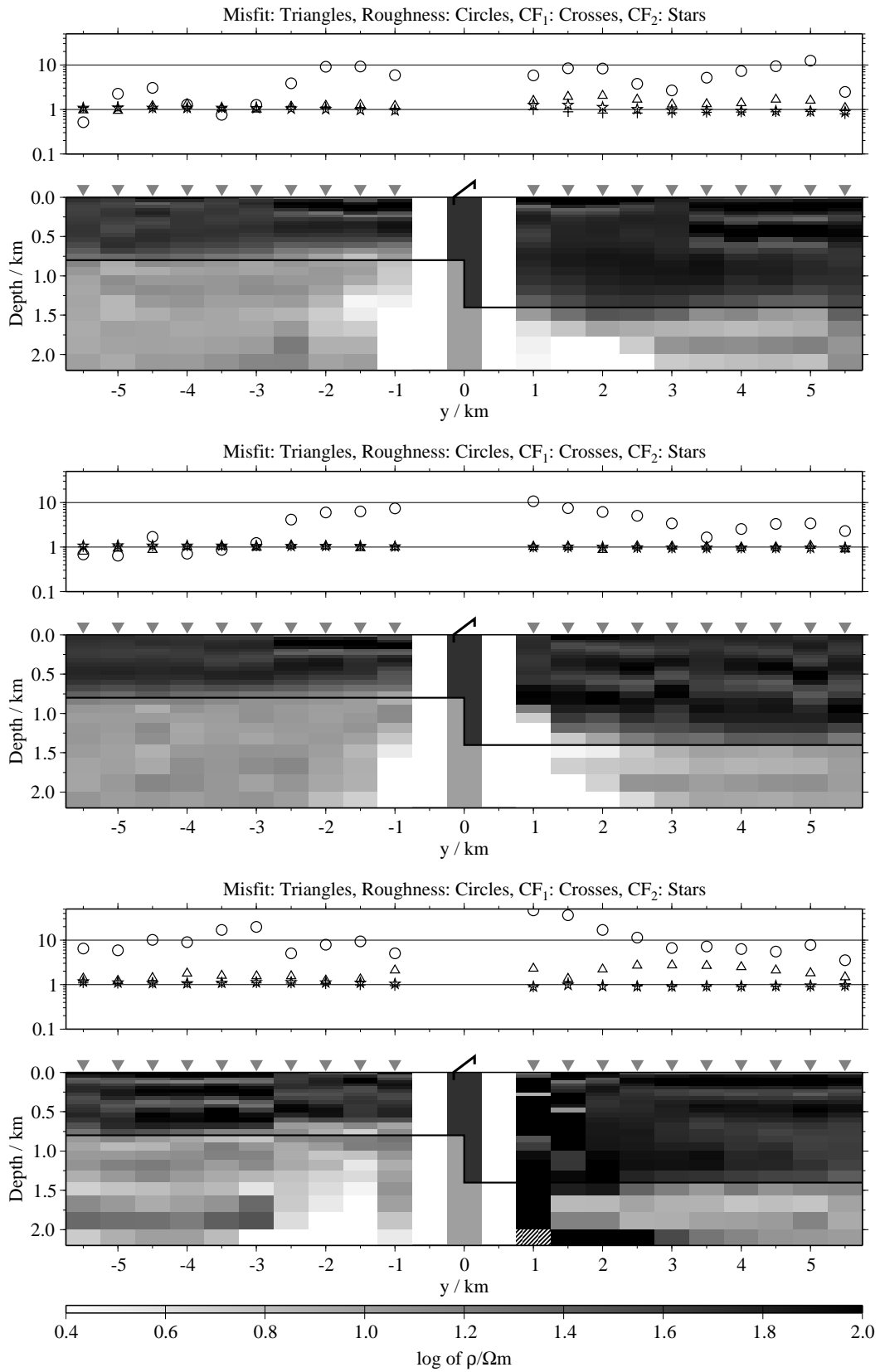


Figure B.223: Pseudo-sections of two component 1-D joint-inversions, model K2, regularisation scheme C1; from top to bottom $E_x-\dot{H}_y$, $E_x-\dot{H}_z$ and $\dot{H}_y-\dot{H}_z$;

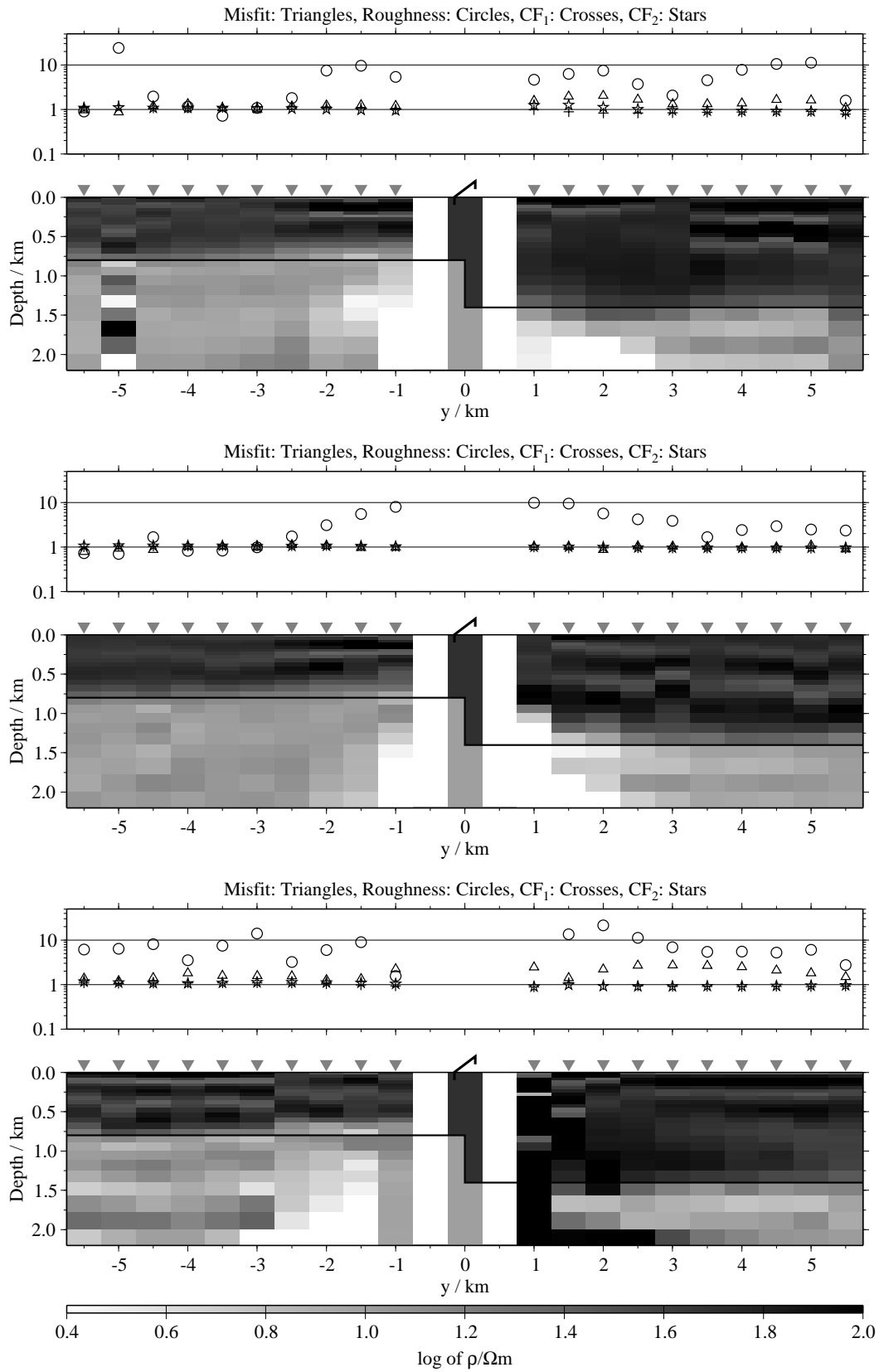


Figure B.224: Pseudo-sections of two component 1-D joint-inversions, model K2, regularisation scheme C4; from top to bottom E_x-H_y , E_x-H_z and H_y-H_z ;

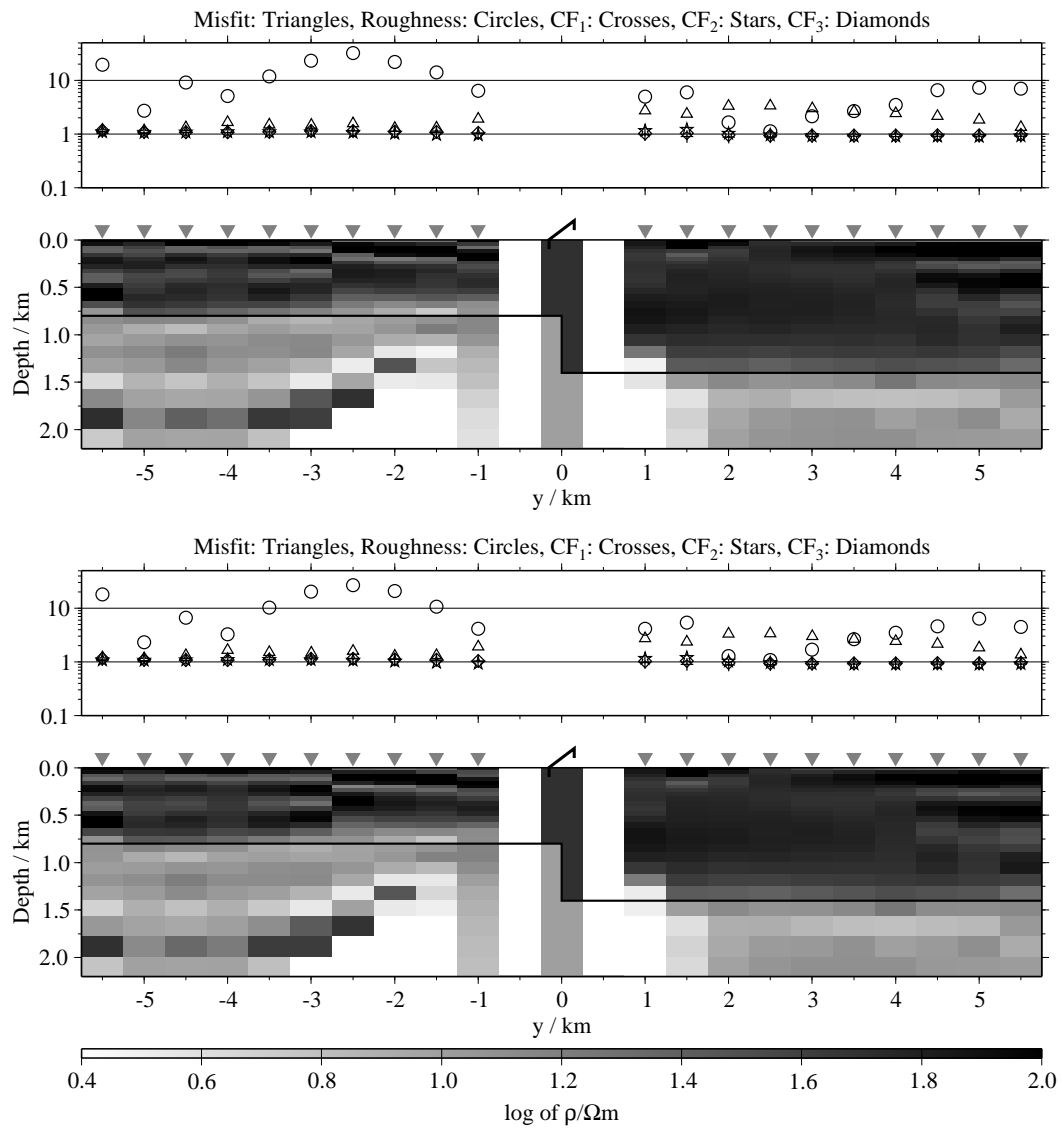


Figure B.225: Pseudo-sections of 1-D joint-inversions using all three components, model K2; top: Regularisation scheme C1; bottom: Regularisation scheme C4;

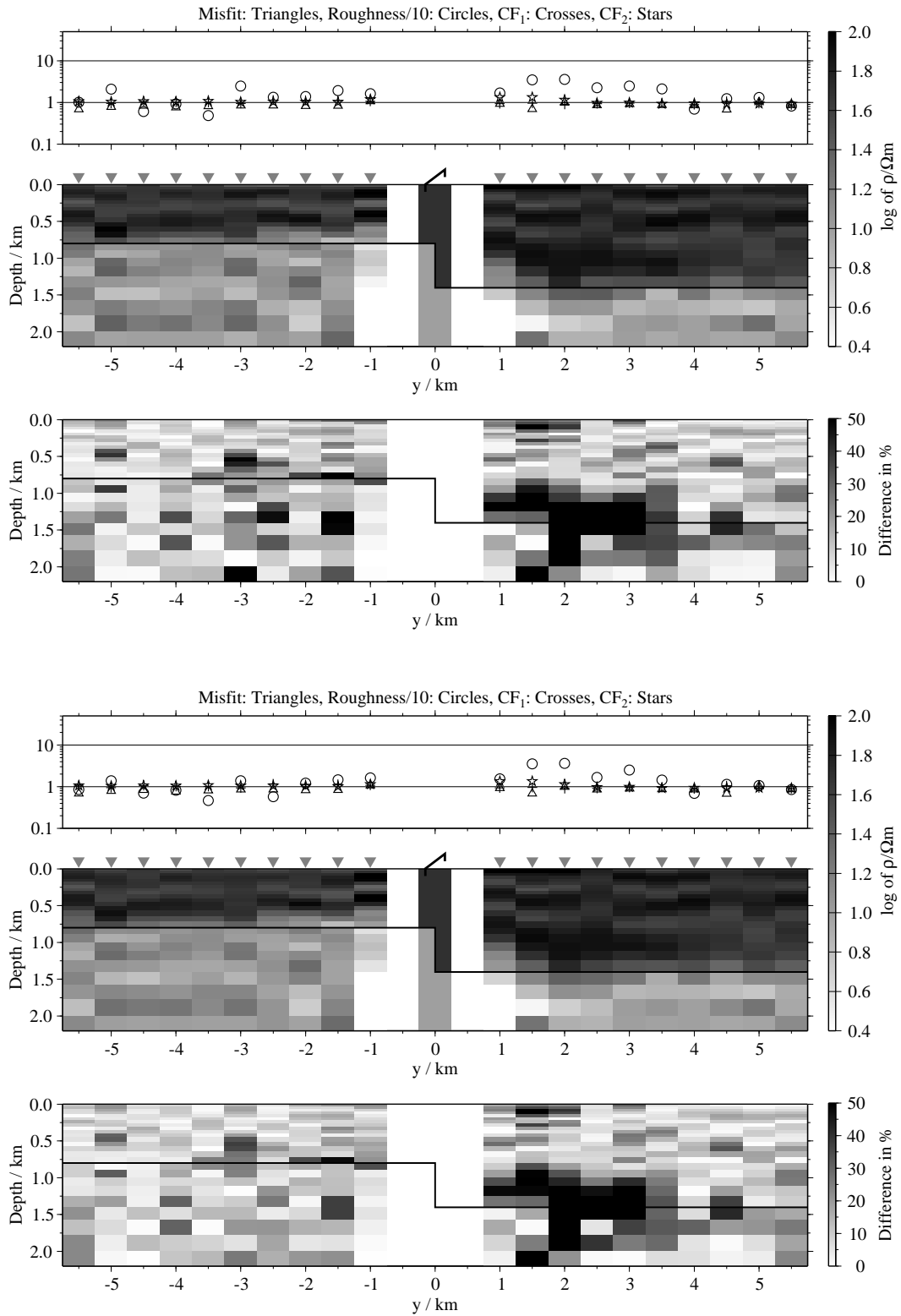


Figure B.226: Pseudo-sections of 1-D soft joint-inversions using the components E_x and H_y , model K2; Top panels: Average inversion results and relative differences (regularisation scheme C1); bottom: Average inversion results and relative differences (regularisation scheme C4);

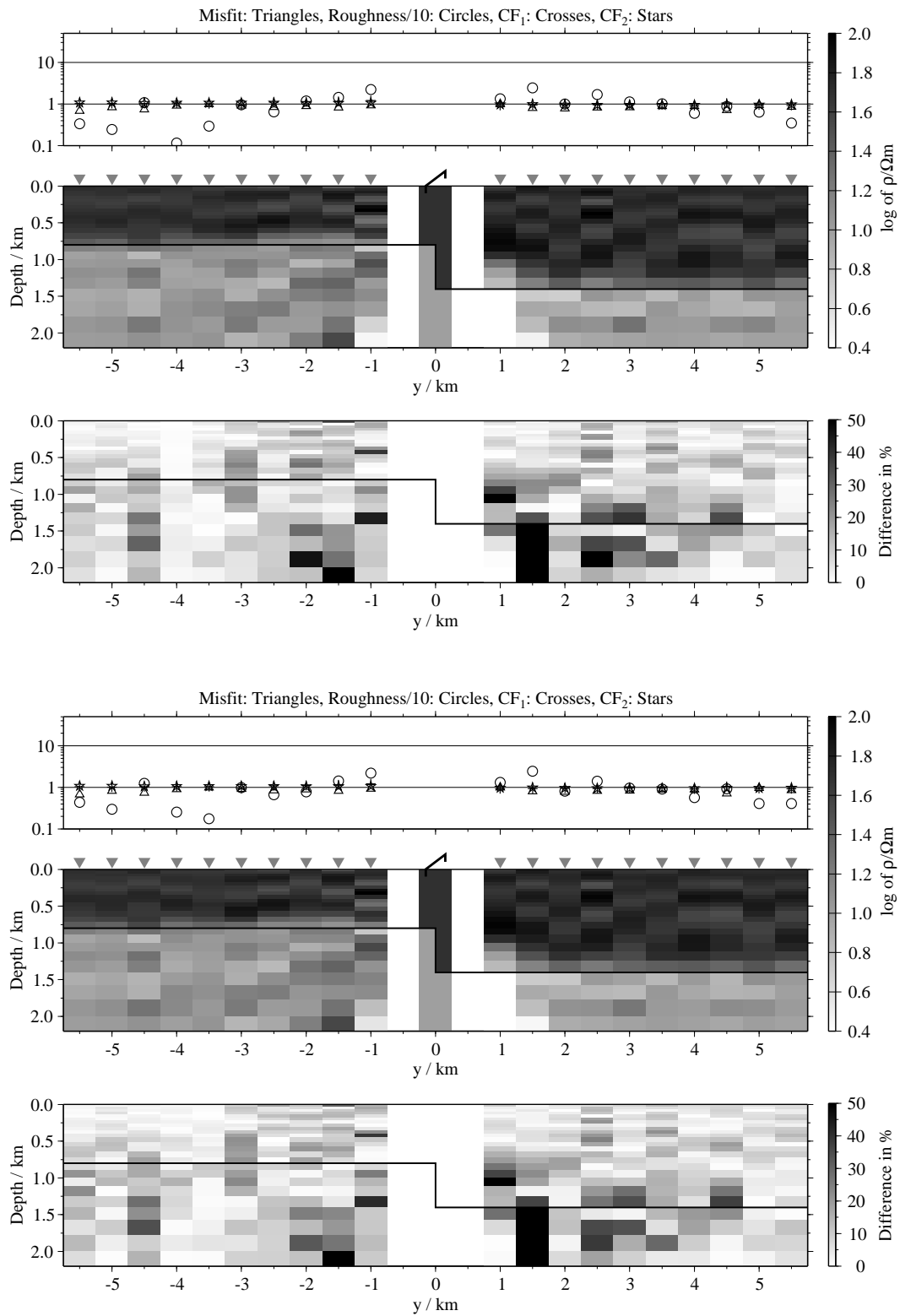


Figure B.227: Pseudo-sections 1-D of soft joint-inversions using the components E_x and \dot{H}_z , model K2; Top panels: Average inversion results and relative differences (regularisation scheme C1); bottom: Average inversion results and relative differences (regularisation scheme C4);

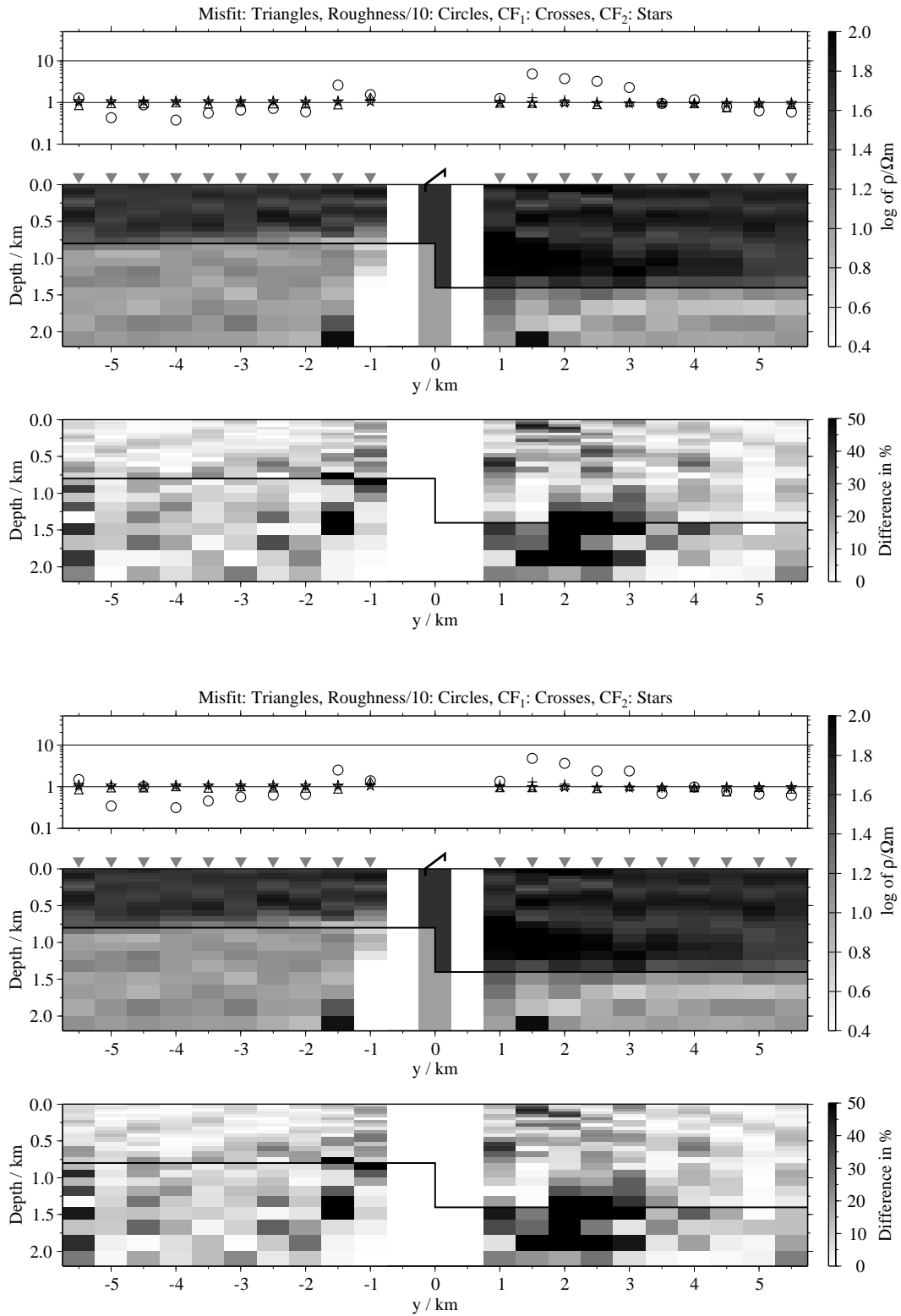


Figure B.228: Pseudo-sections of 1-D soft joint-inversions using the components \dot{H}_y and \dot{H}_z , model K2; Top panels: Average inversion results and relative differences (regularisation scheme C1); bottom: Average inversion results and relative differences (regularisation scheme C4);

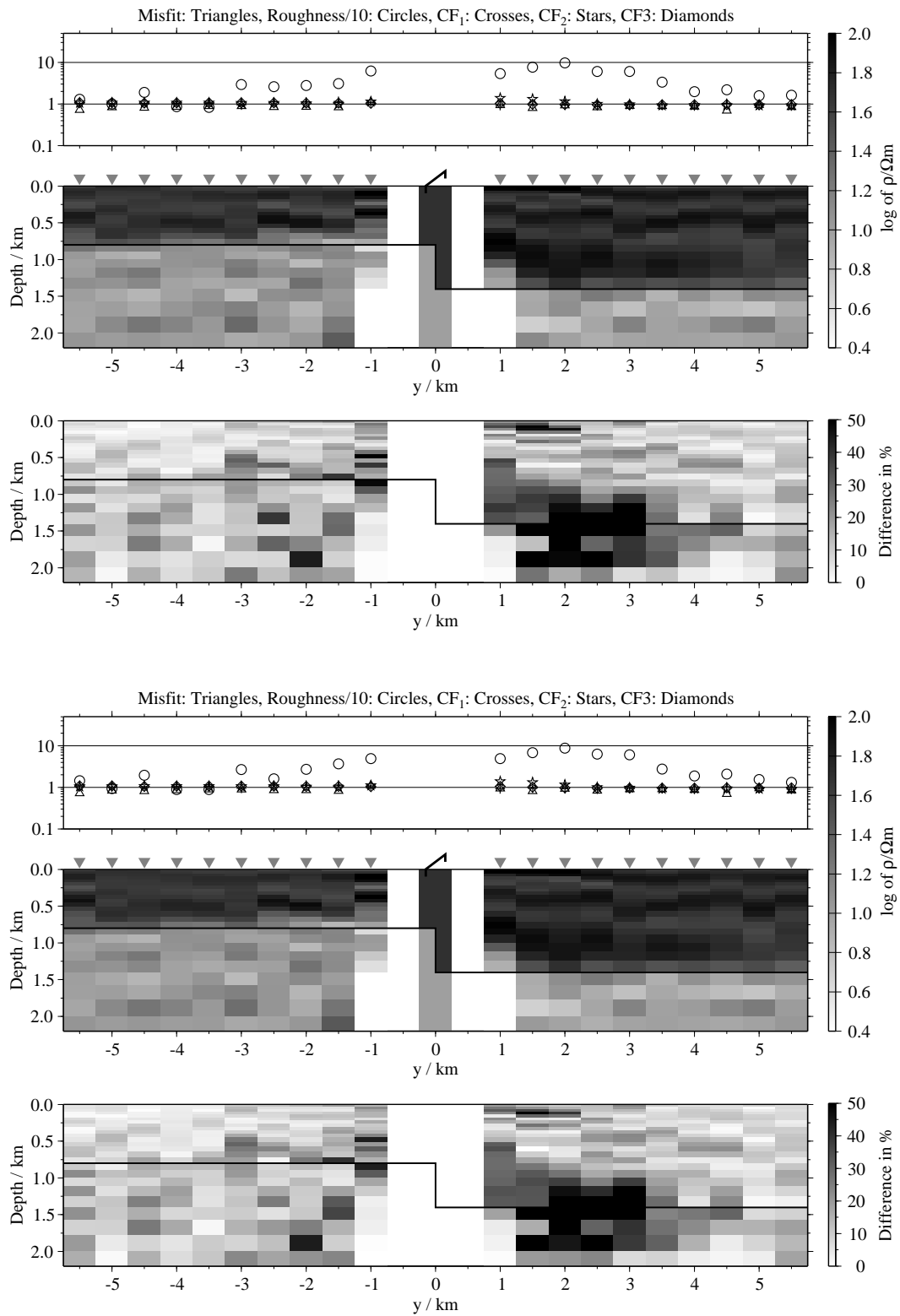


Figure B.229: Pseudo-sections of 1-D soft joint-inversions using all three components, model K2; Top panels: Average inversion results and relative differences (regularisation scheme C1); bottom: Average inversion results and relative differences (regularisation scheme C4);

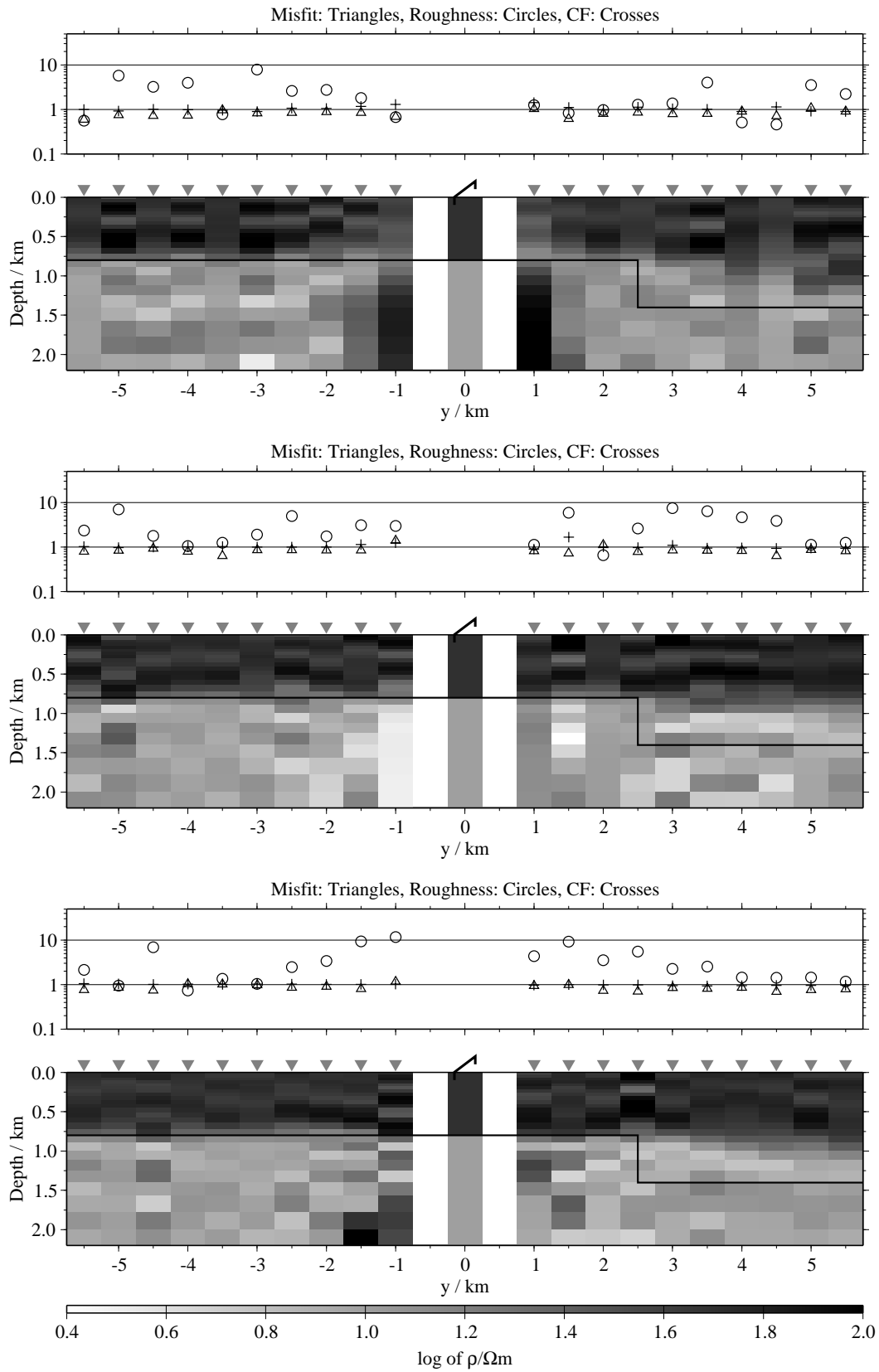


Figure B.230: Pseudo-sections of single 1-D inversion, model K3, regularisation scheme C1; from top to bottom E_x -, H_y - and H_z -component;

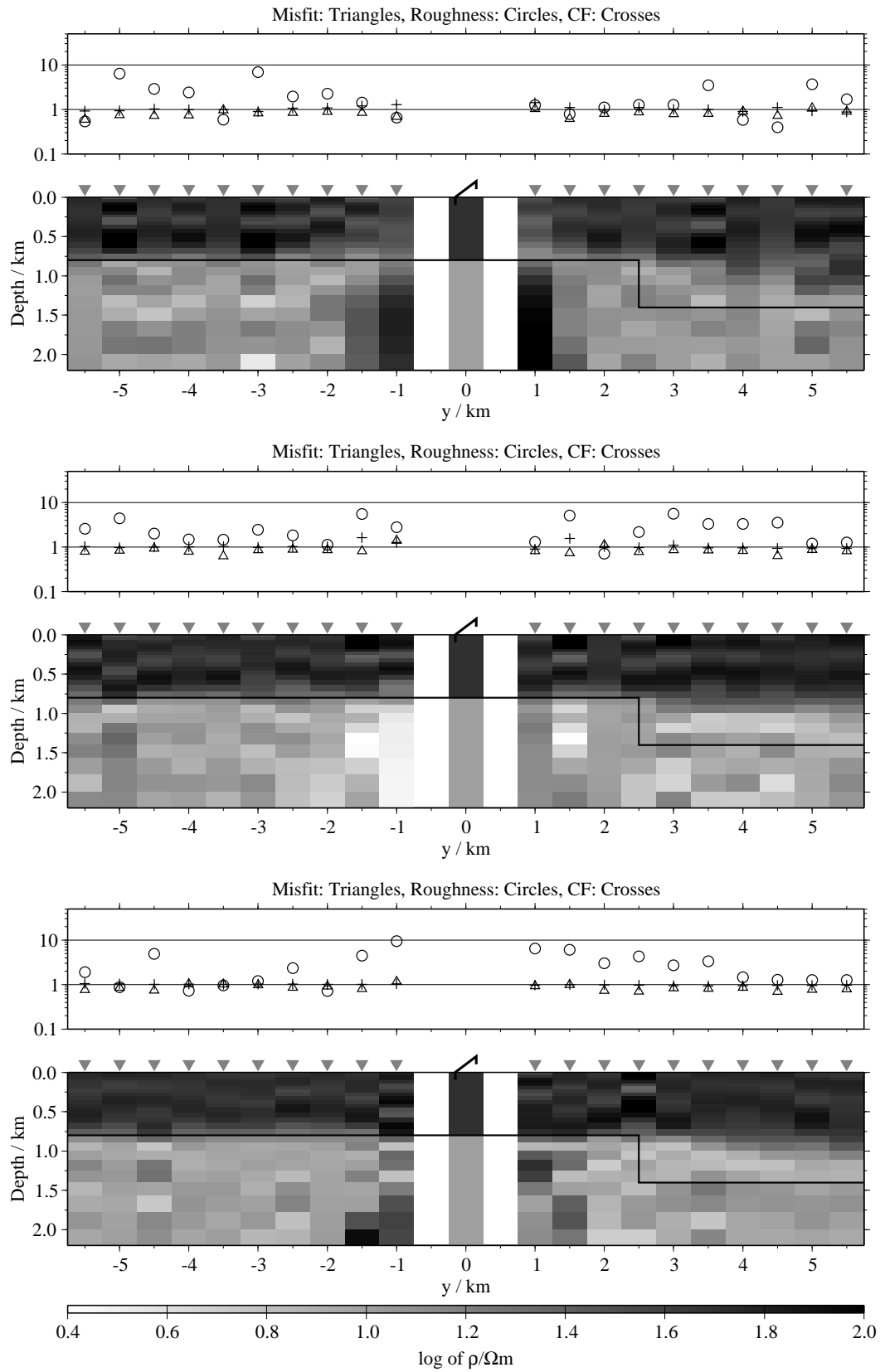


Figure B.231: Pseudo-sections of single 1-D inversion, model K3, regularisation scheme C4; from top to bottom E_x -, H_y - and H_z -component;

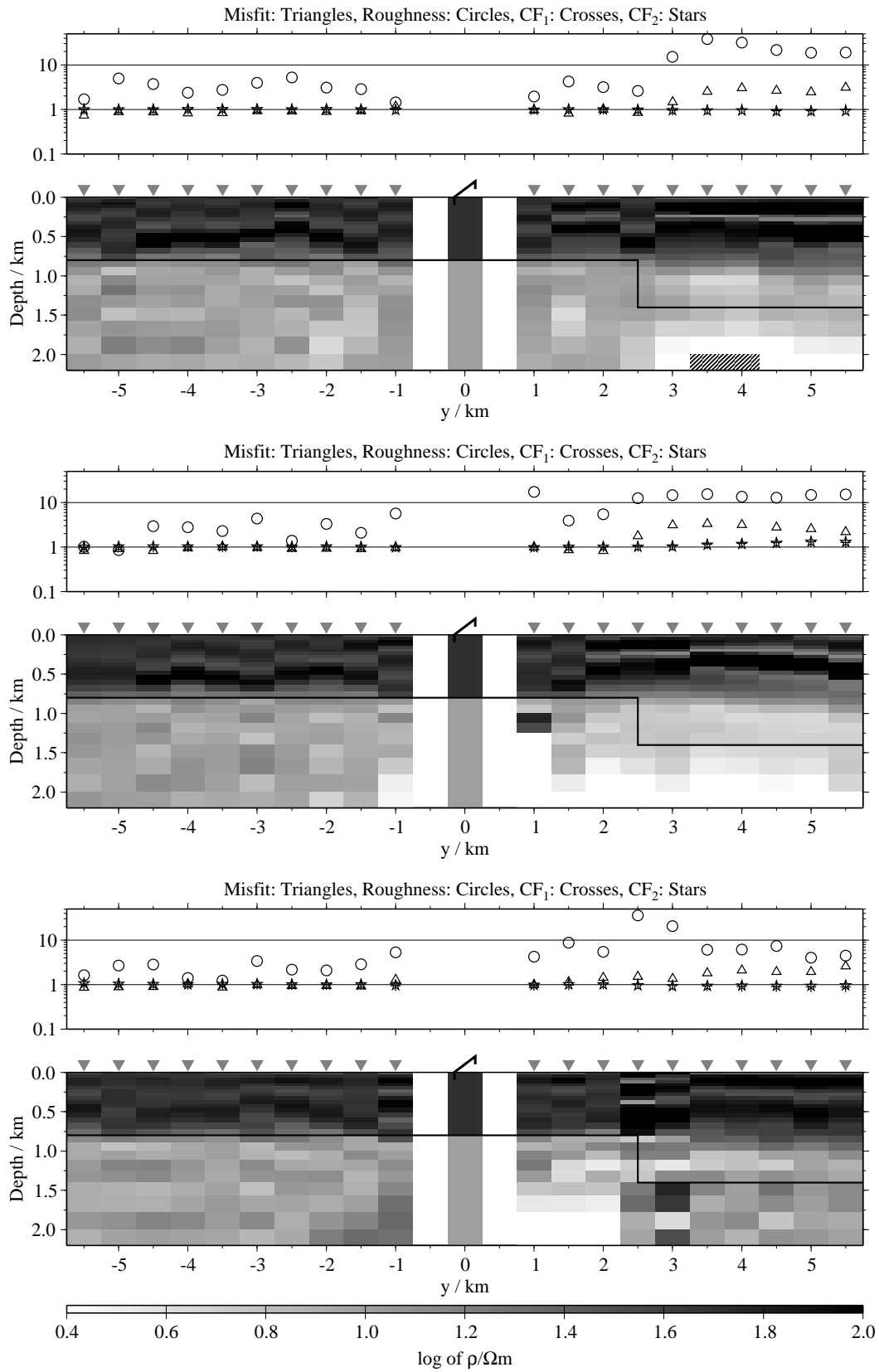


Figure B.232: Pseudo-sections of two component 1-D joint-inversions, model K3, regularisation scheme C1; from top to bottom $E_x-\dot{H}_y$, $E_x-\dot{H}_z$ and $\dot{H}_y-\dot{H}_z$;

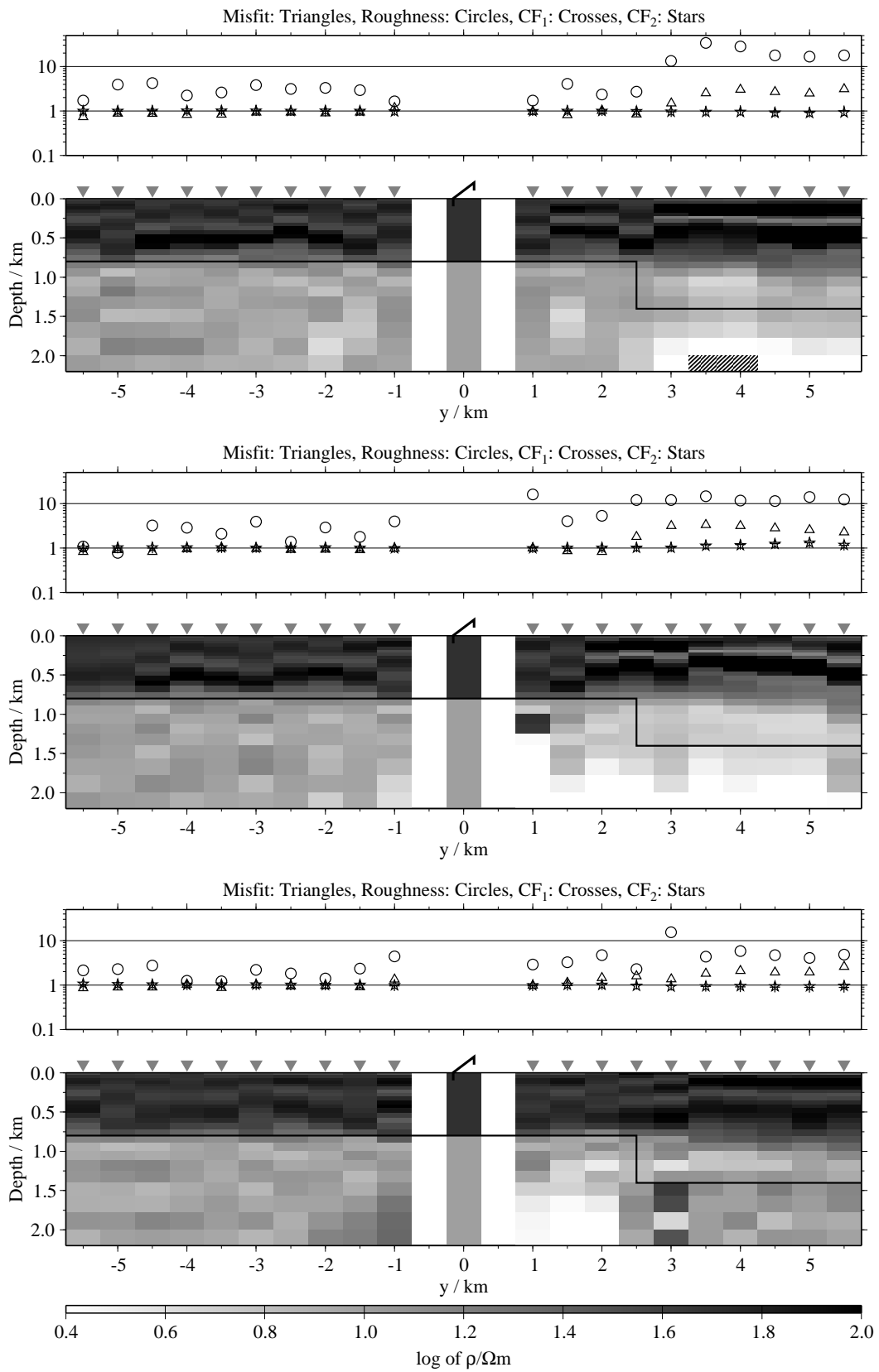


Figure B.233: Pseudo-sections of two component 1-D joint-inversions, model K3, regularisation scheme C4; from top to bottom $E_x-\dot{H}_y$, $E_x-\dot{H}_z$ and $\dot{H}_y-\dot{H}_z$;

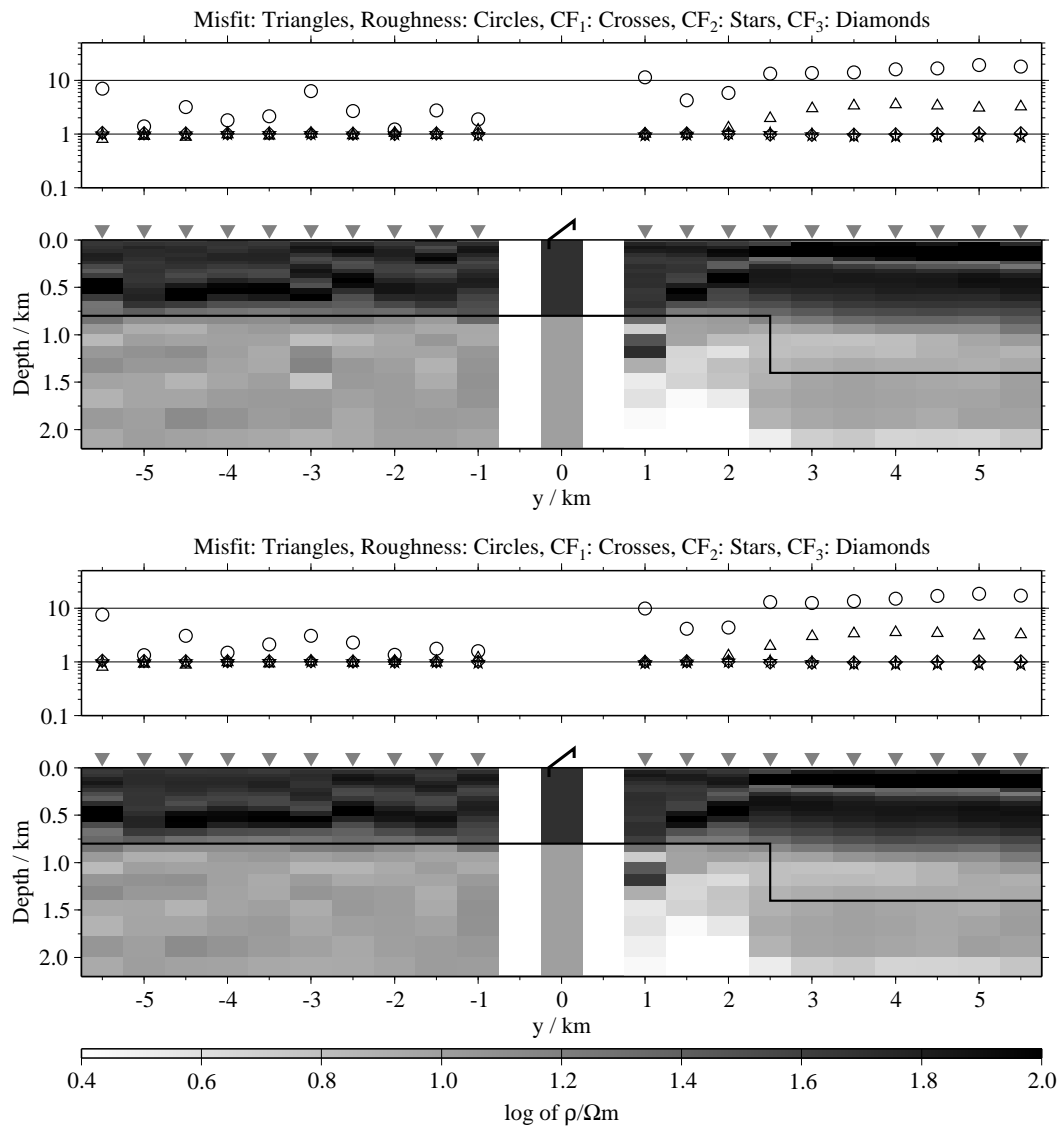


Figure B.234: Pseudo-sections of 1-D joint-inversions using all three components, model K3; top: Regularisation scheme C1; bottom: Regularisation scheme C4;

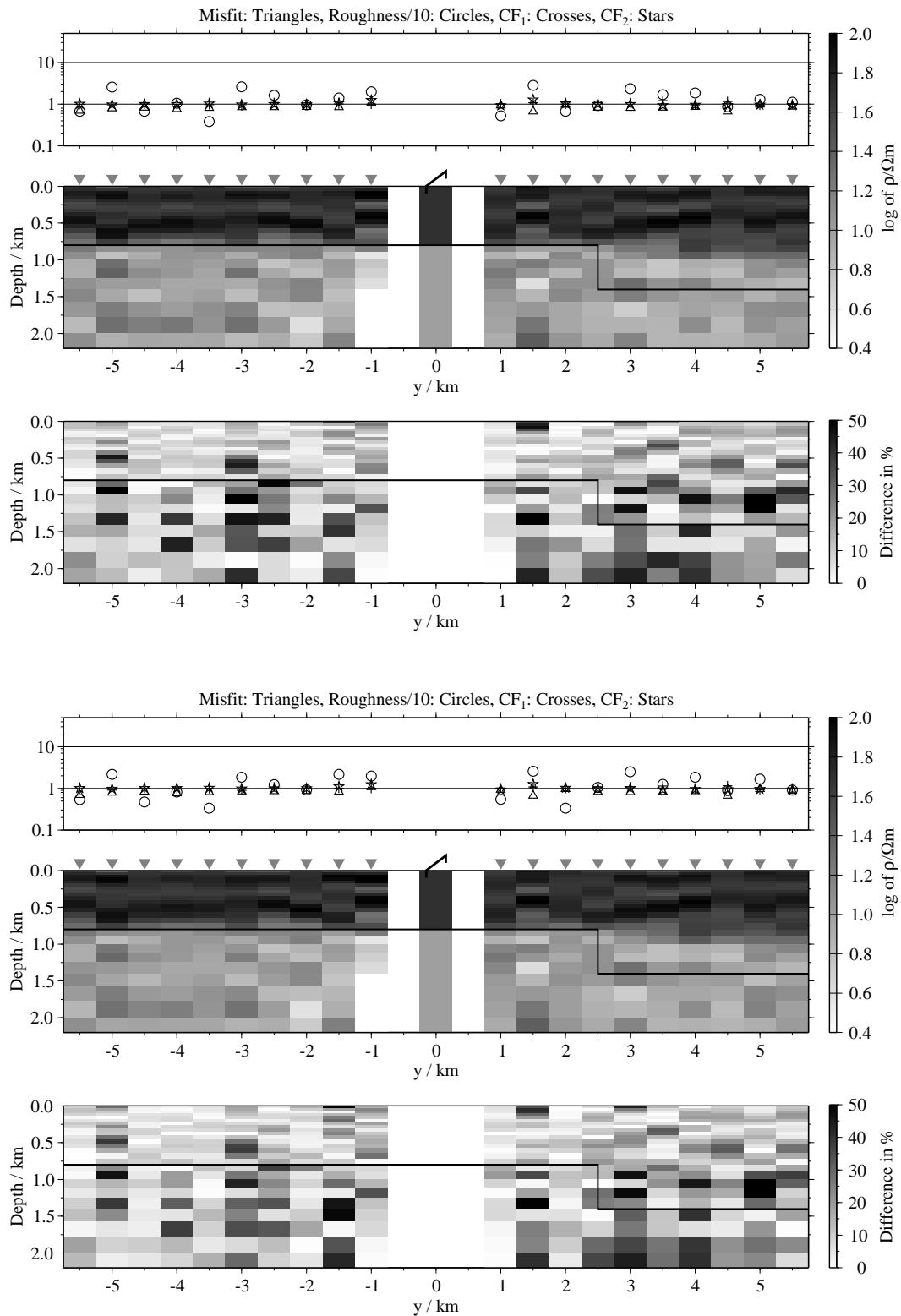


Figure B.235: Pseudo-sections of 1-D soft joint-inversions using the components E_x and H_y , model K3; Top panels: Average inversion results and relative differences (regularisation scheme C1); bottom: Average inversion results and relative differences (regularisation scheme C4);

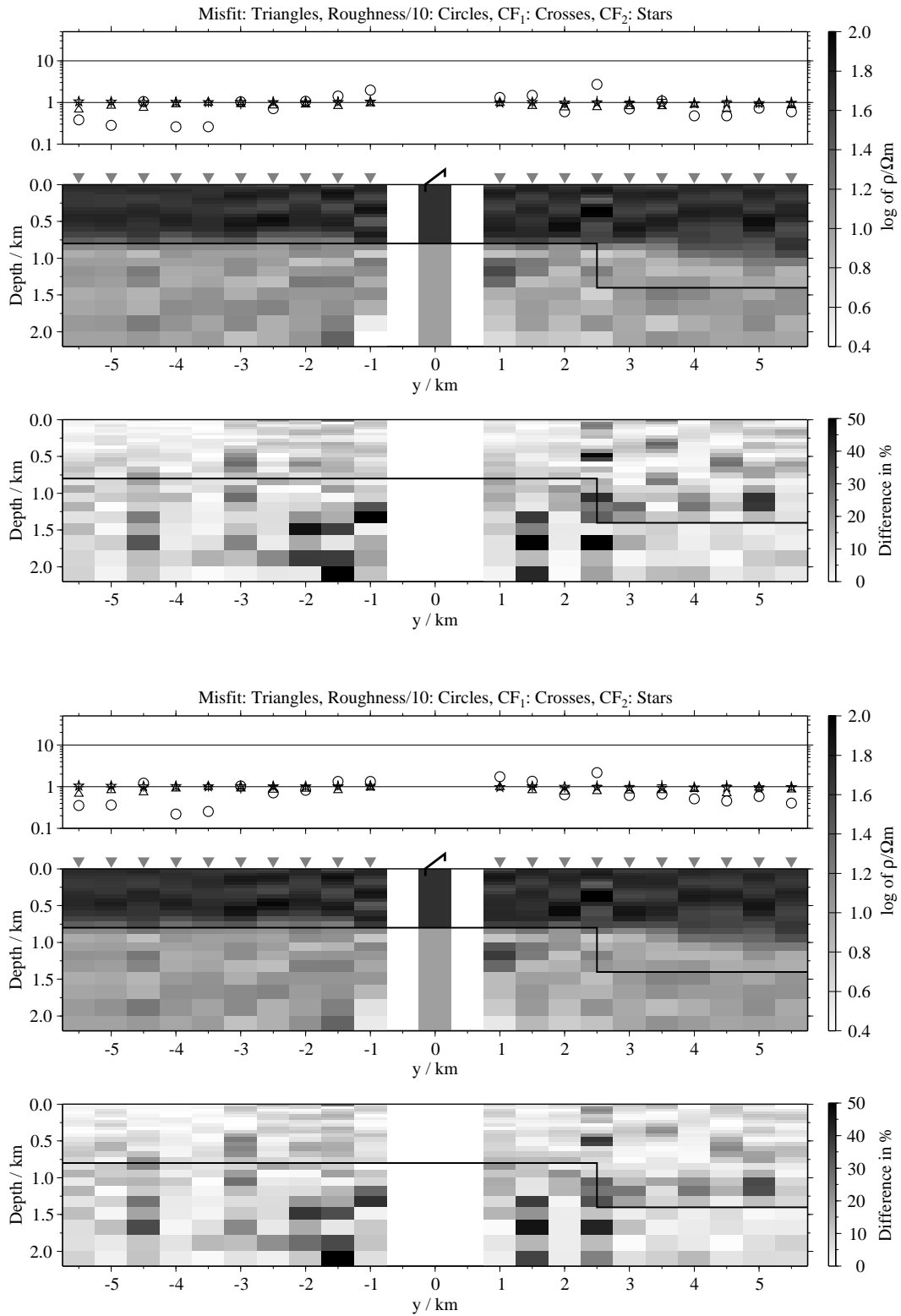


Figure B.236: Pseudo-sections 1-D of soft joint-inversions using the components E_x and H_z , model K3; Top panels: Average inversion results and relative differences (regularisation scheme C1); bottom: Average inversion results and relative differences (regularisation scheme C4);

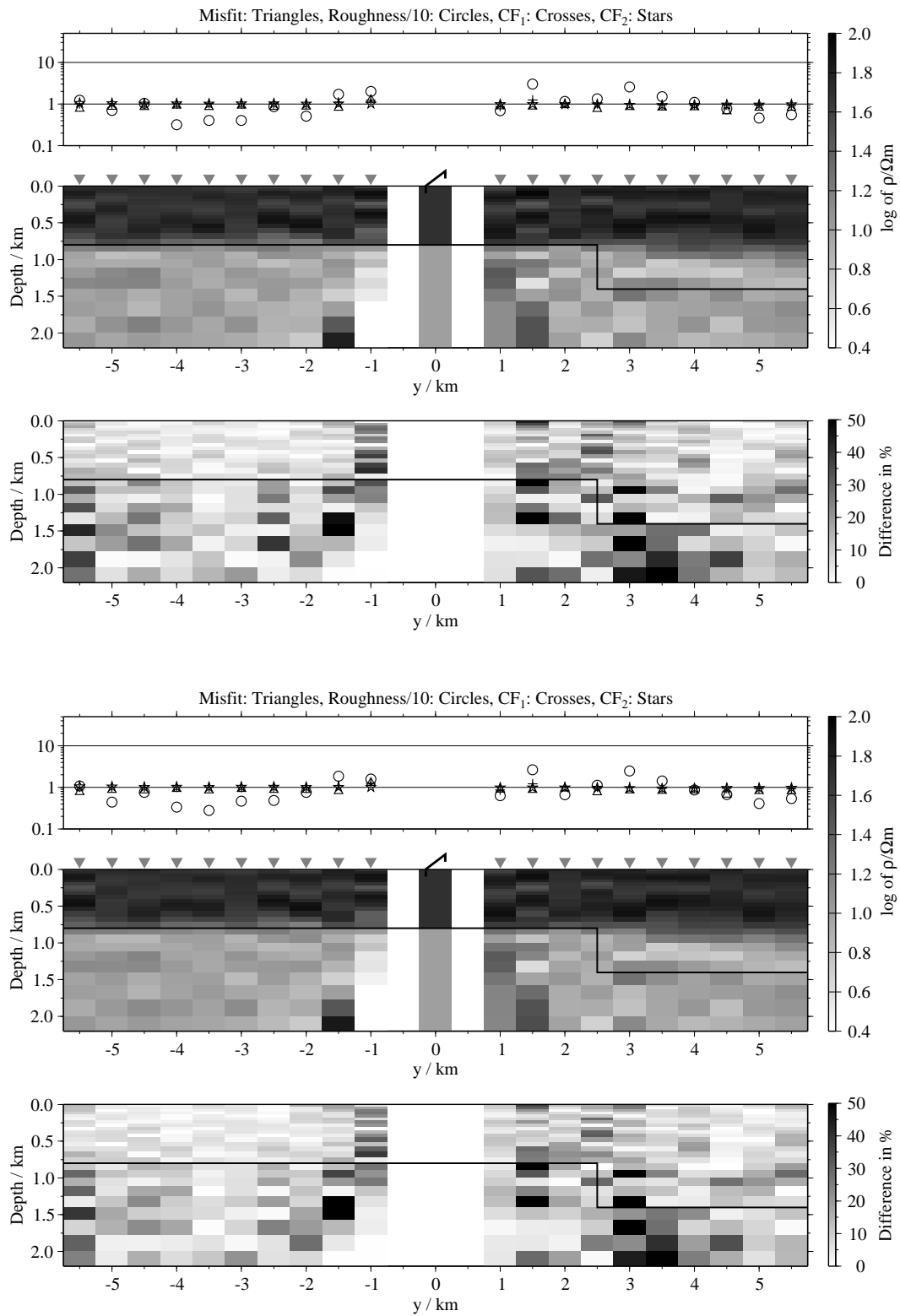


Figure B.237: Pseudo-sections of 1-D soft joint-inversions using the components \dot{H}_y and \dot{H}_{zi} , model K3; Top panels: Average inversion results and relative differences (regularisation scheme C1); bottom: Average inversion results and relative differences (regularisation scheme C4);

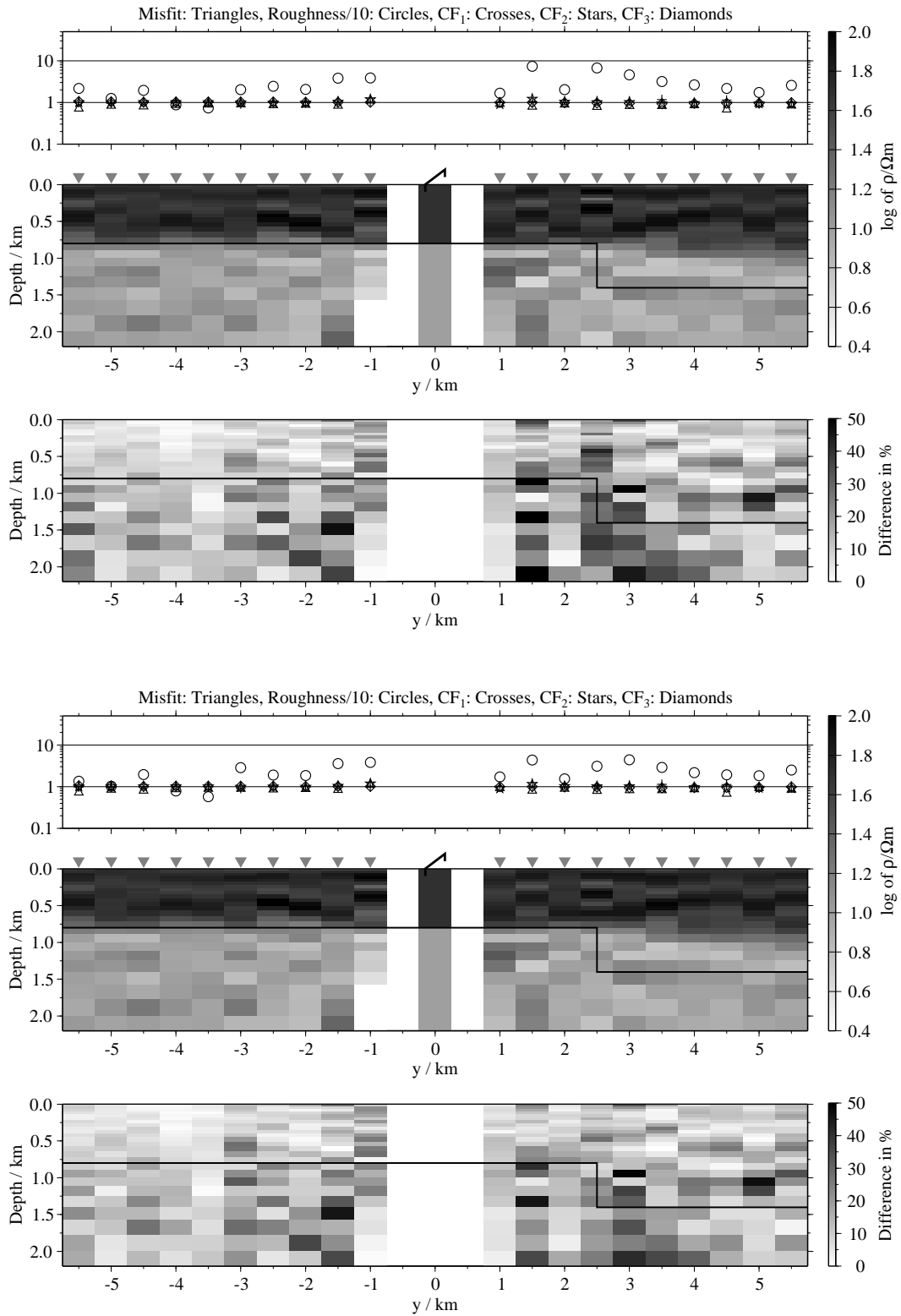
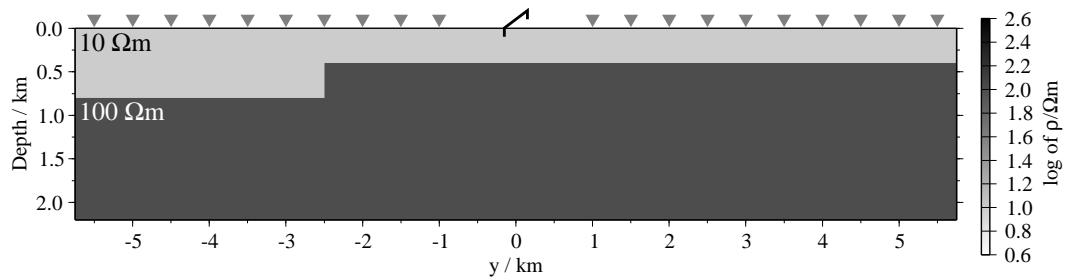


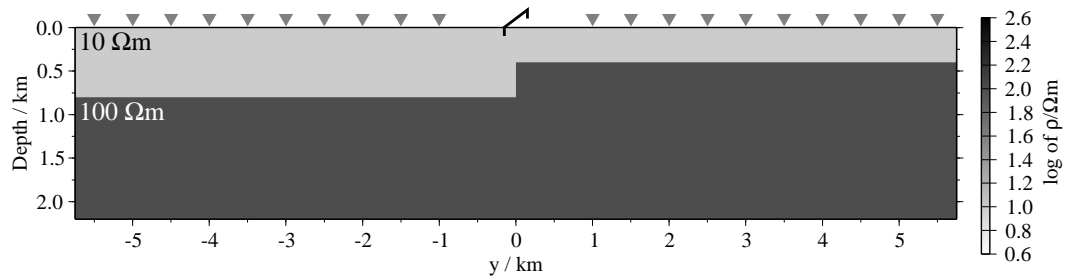
Figure B.238: Pseudo-sections of 1-D soft joint-inversions using all three components, model K3; Top panels: Average inversion results and relative differences (regularisation scheme C1); bottom: Average inversion results and relative differences (regularisation scheme C4);

B.2.10 Displacement in a conductive basement (models L1 to L3)

Model L1:



Model L2:



Model L3:

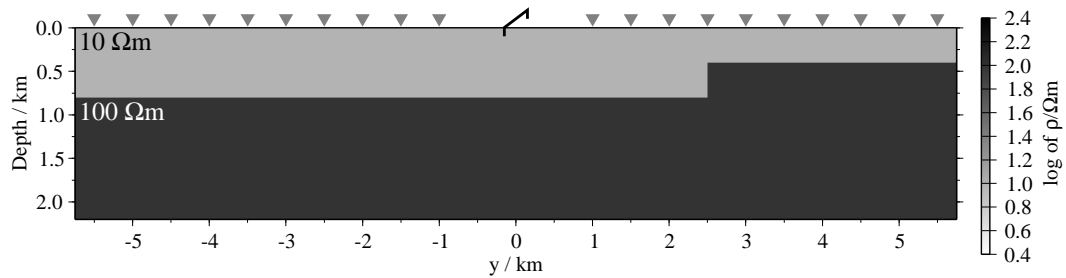


Figure B.239: Model for a fault with a resistive basement; the fault-line is at $y = -2.5 \text{ km}$ (model L1), $y = 0 \text{ km}$ (model L2) and $y = 2.5 \text{ km}$ (model L3).

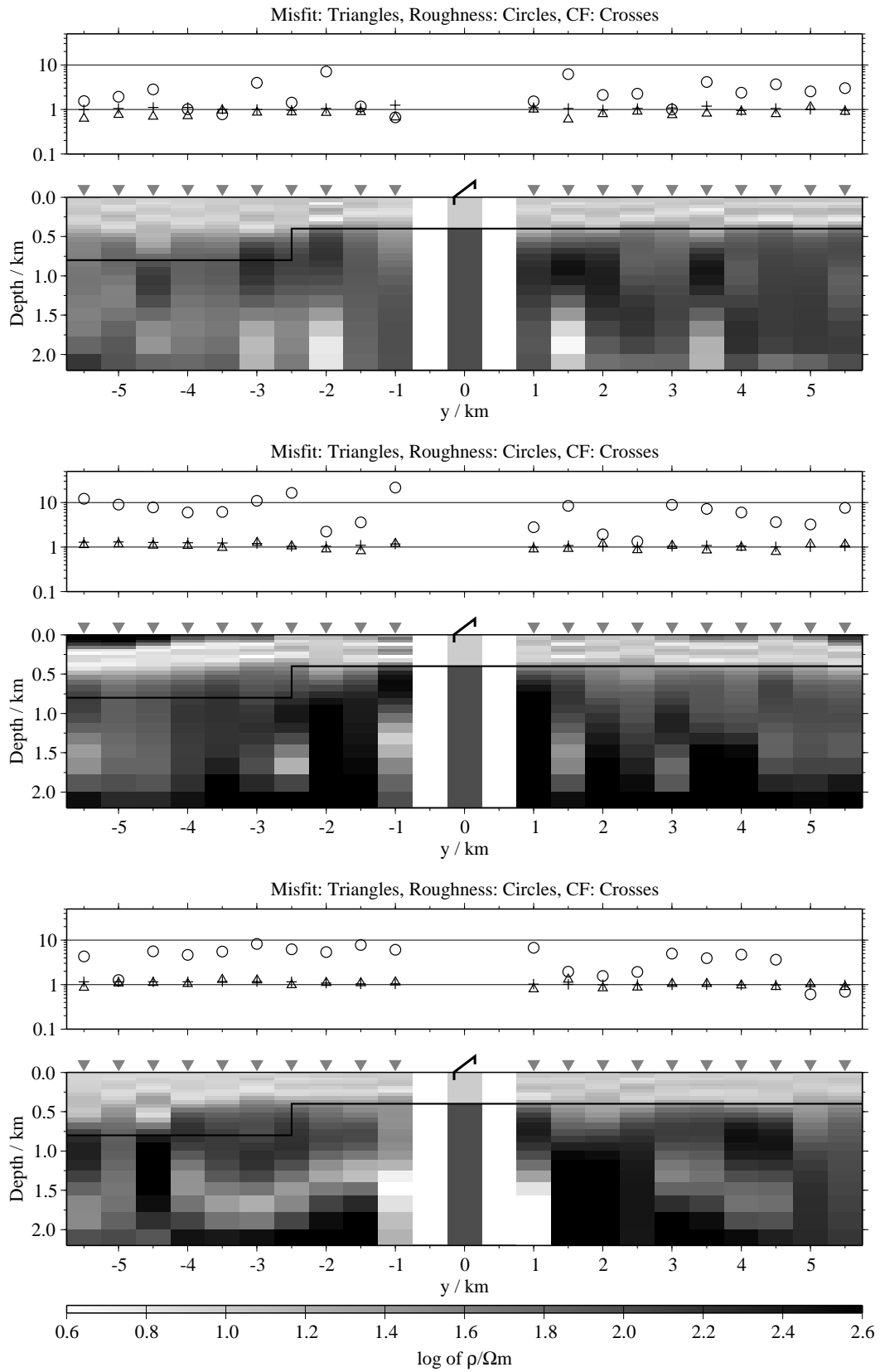


Figure B.240: Pseudo-sections of single 1-D inversion, model L1, regularisation scheme C1; from top to bottom E_x -, \dot{H}_y - and \dot{H}_z -component;

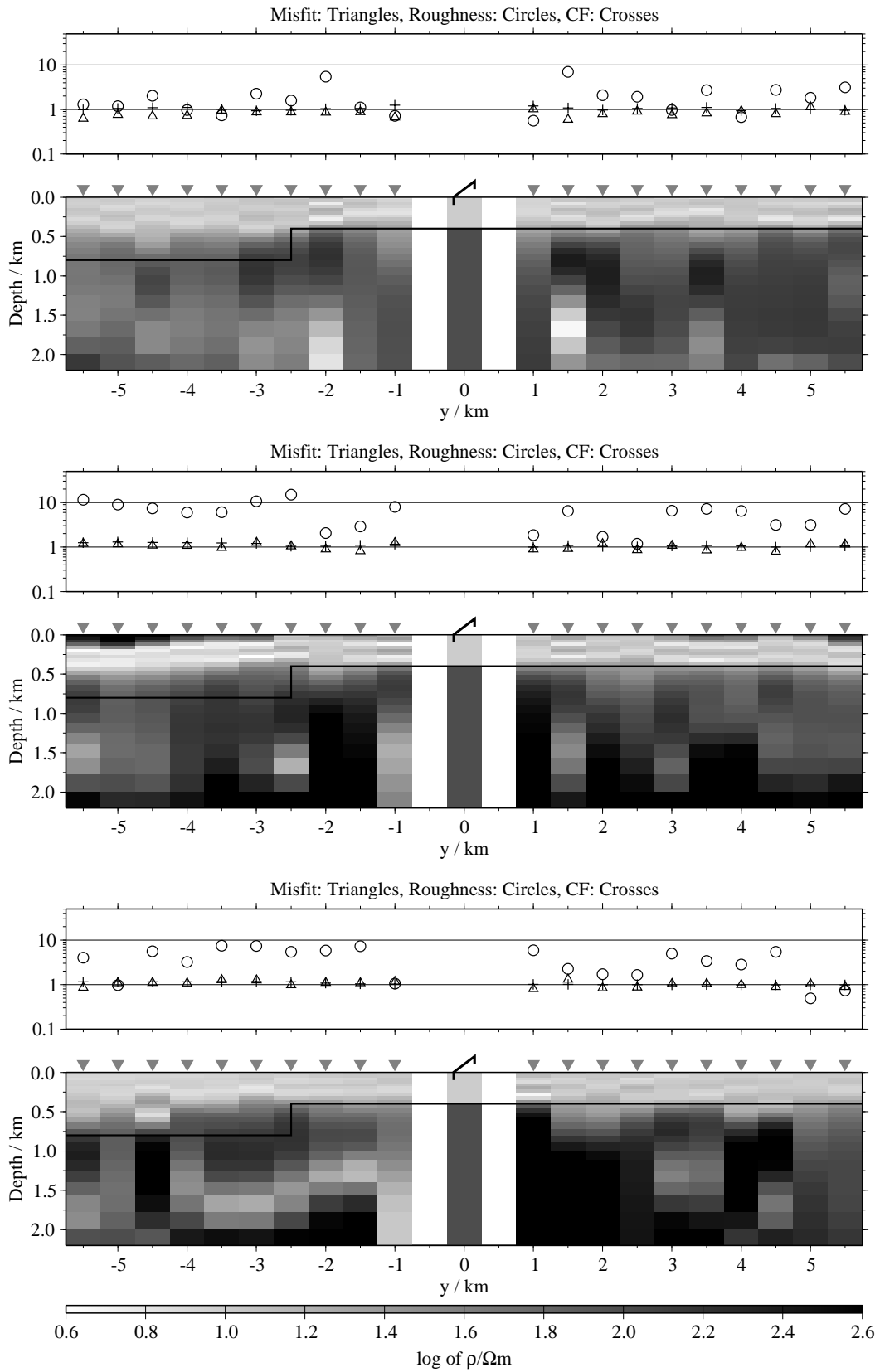


Figure B.241: Pseudo-sections of single 1-D inversion, model L1, regularisation scheme C4; from top to bottom E_x -, H_y - and H_z -component;

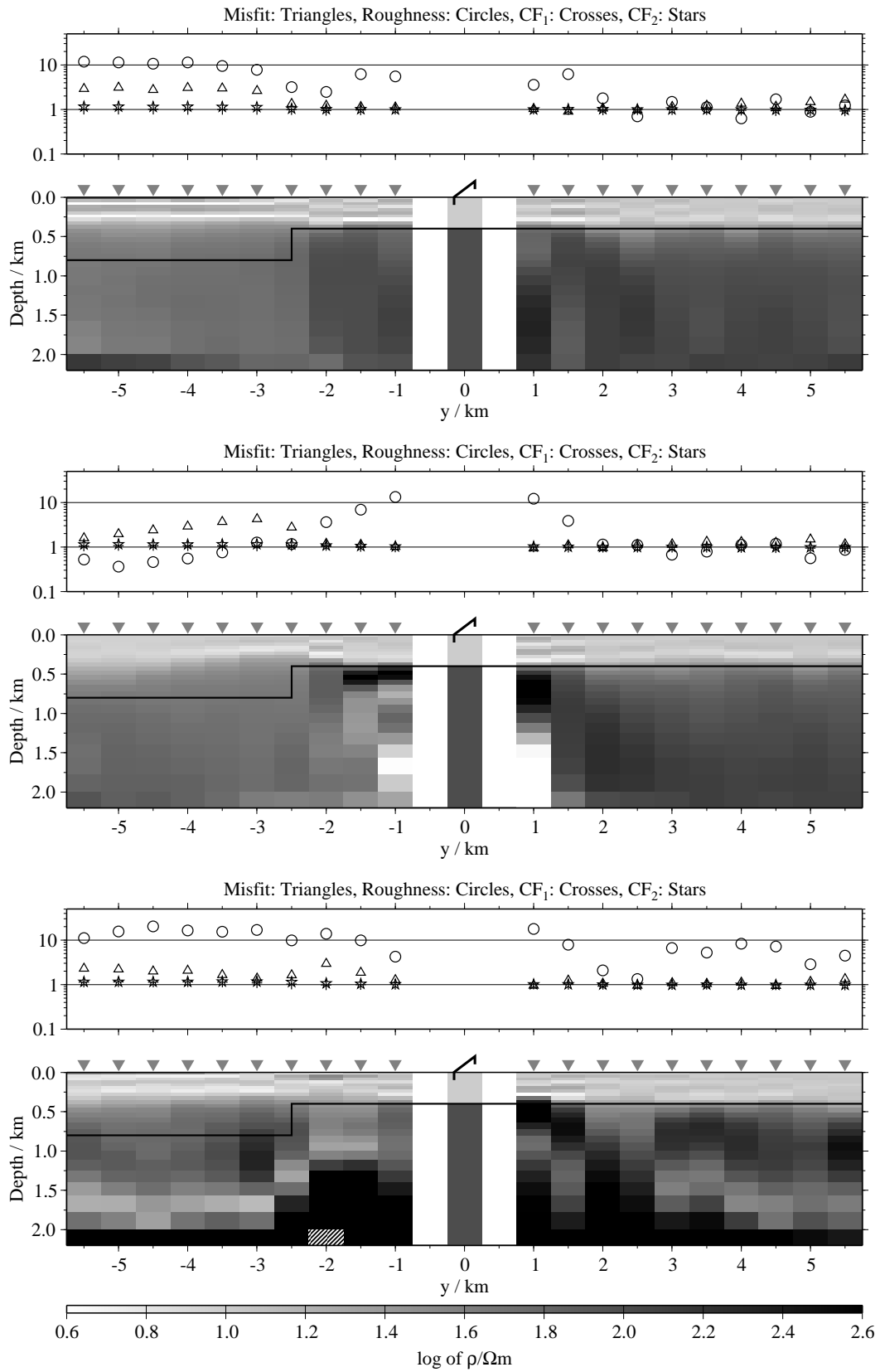


Figure B.242: Pseudo-sections of two component 1-D joint-inversions, model L1, regularisation scheme C1; from top to bottom $E_x-\dot{H}_y$, $E_x-\dot{H}_z$ and $\dot{H}_y-\dot{H}_z$;

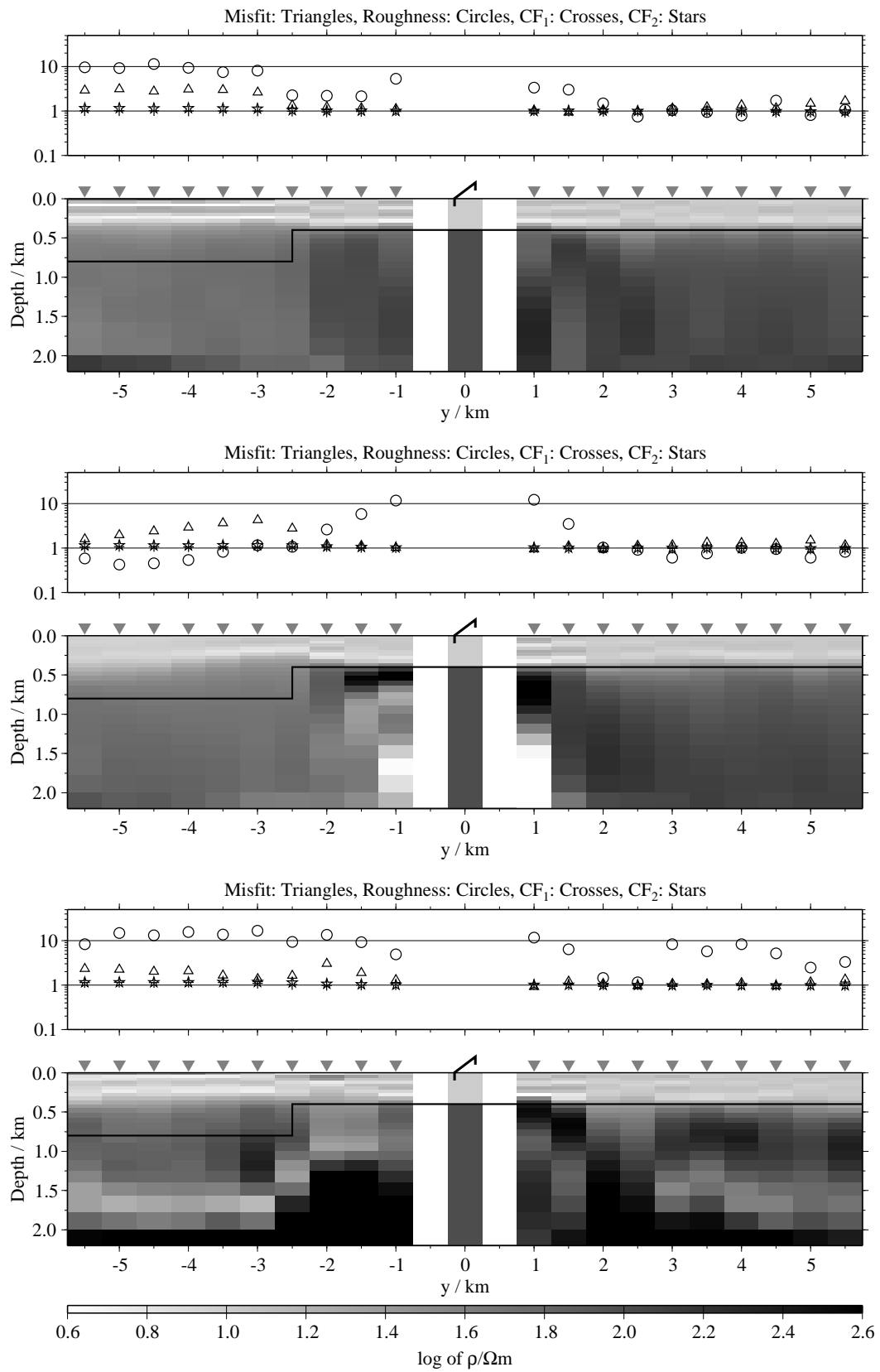


Figure B.243: Pseudo-sections of two component 1-D joint-inversions, model L1, regularisation scheme C4; from top to bottom $E_x-\dot{H}_y$, $E_x-\dot{H}_z$ and $\dot{H}_y-\dot{H}_z$;

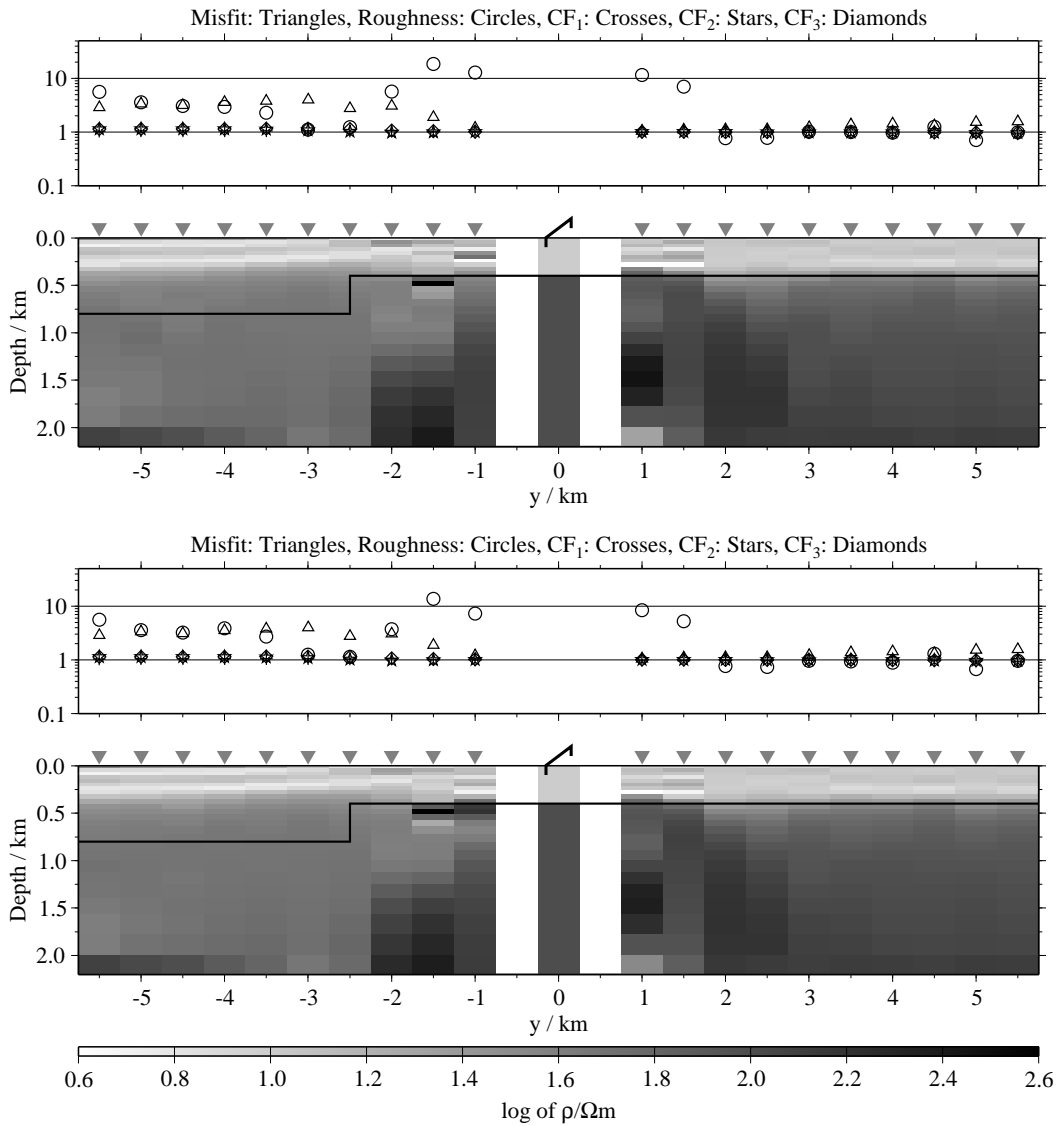


Figure B.244: Pseudo-sections of 1-D joint-inversions using all three components, model L1; top: Regularisation scheme C1; bottom: Regularisation scheme C4;

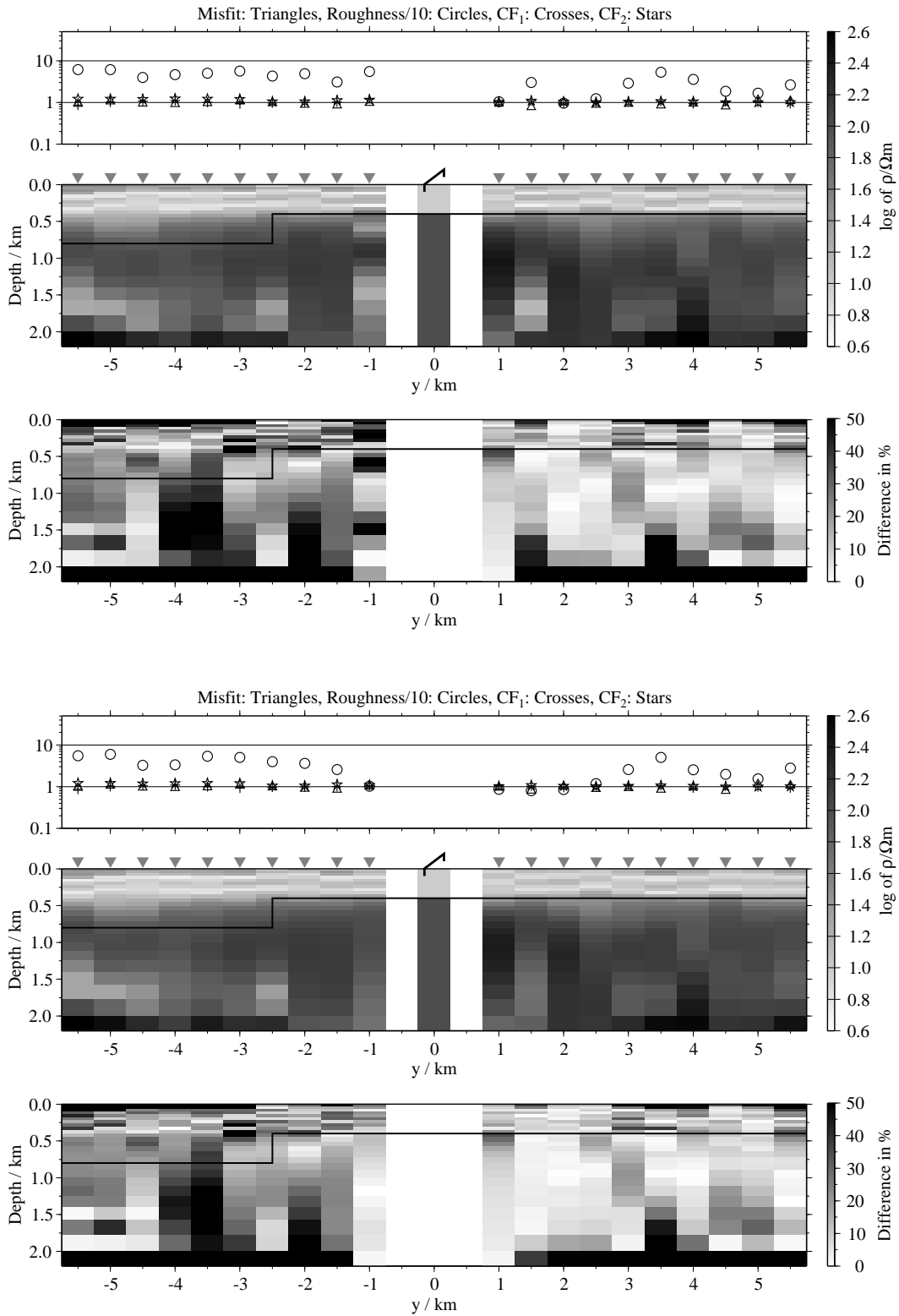


Figure B.245: Pseudo-sections of 1-D soft joint-inversions using the components E_x and H_y , model L1; Top panels: Average inversion results and relative differences (regularisation scheme C1); bottom: Average inversion results and relative differences (regularisation scheme C4);

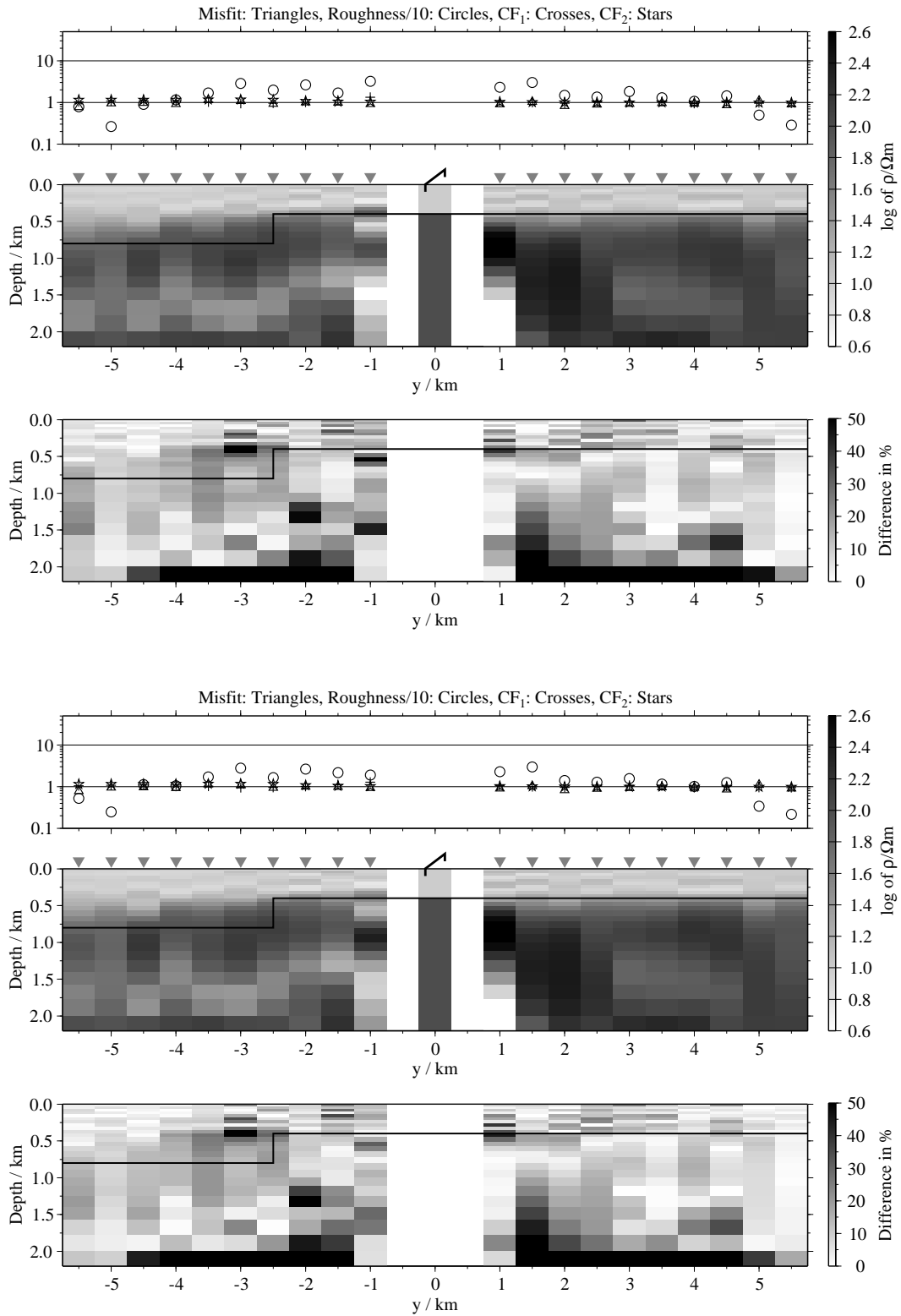


Figure B.246: Pseudo-sections 1-D of soft joint-inversions using the components E_x and H_z , model L1; Top panels: Average inversion results and relative differences (regularisation scheme C1); bottom: Average inversion results and relative differences (regularisation scheme C4);

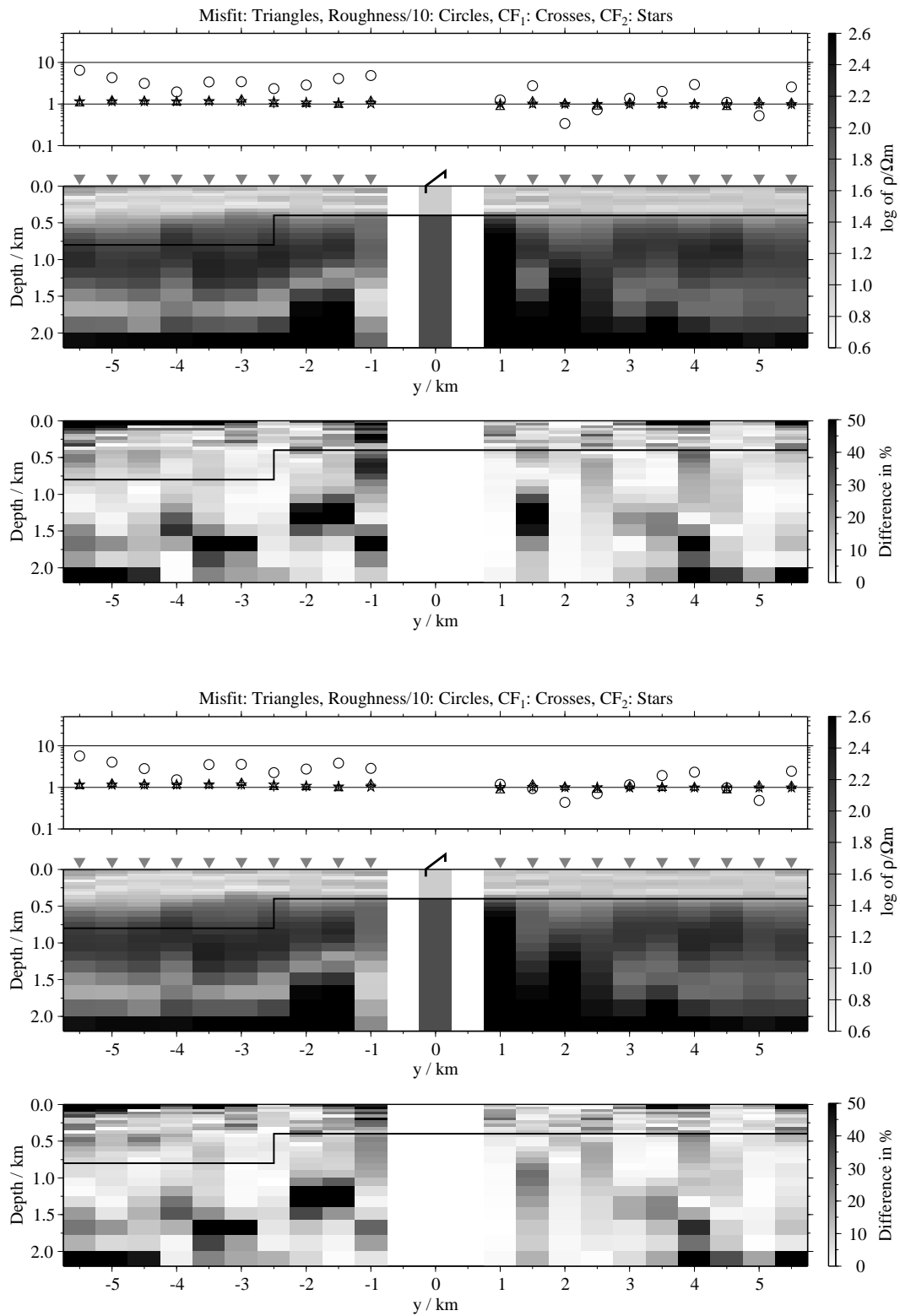


Figure B.247: Pseudo-sections of 1-D soft joint-inversions using the components \dot{H}_y and \dot{H}_{zi} , model L1; Top panels: Average inversion results and relative differences (regularisation scheme C1); bottom: Average inversion results and relative differences (regularisation scheme C4);

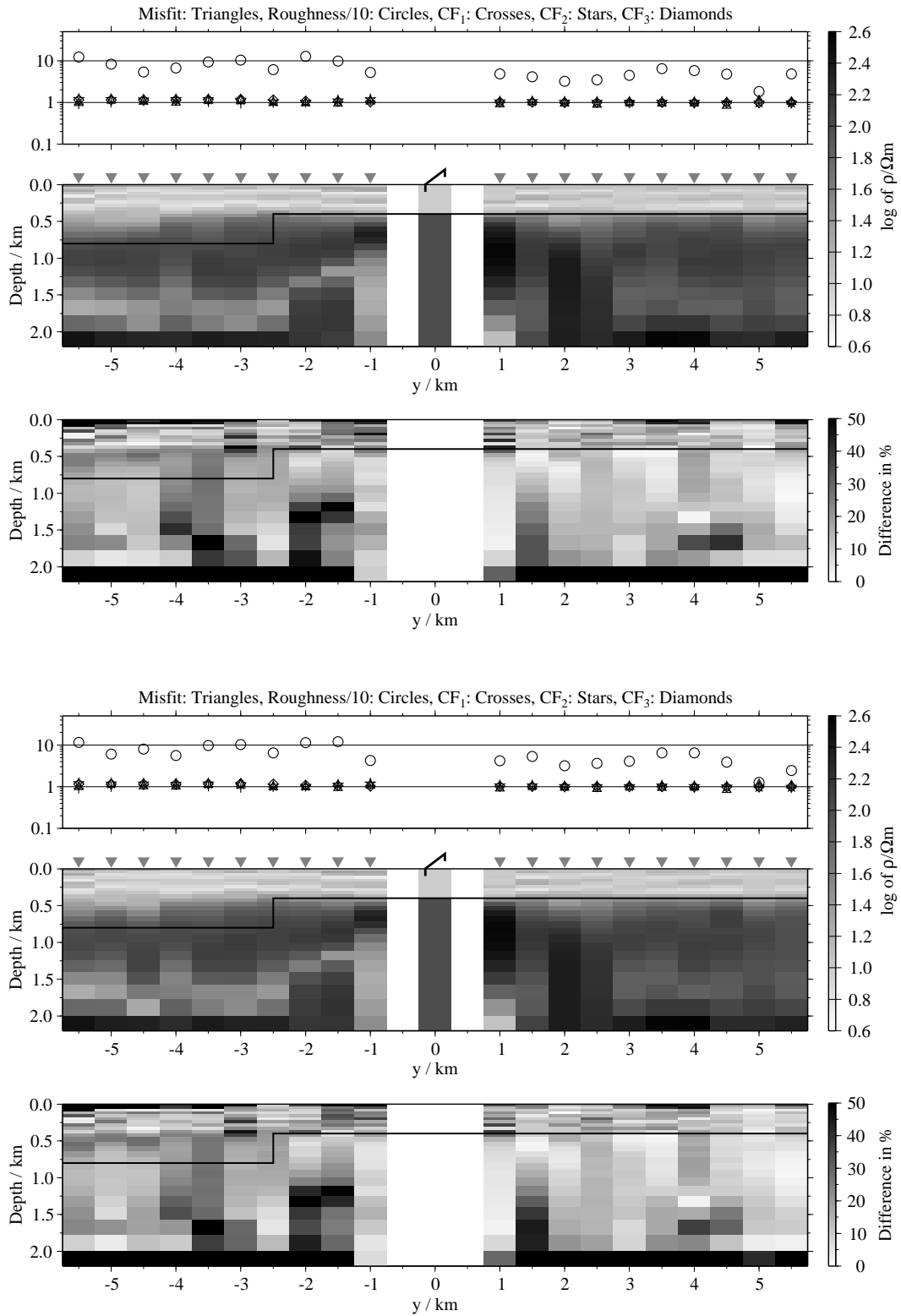


Figure B.248: Pseudo-sections of 1-D soft joint-inversions using all three components, model L1; Top panels: Average inversion results and relative differences (regularisation scheme C1); bottom: Average inversion results and relative differences (regularisation scheme C4);

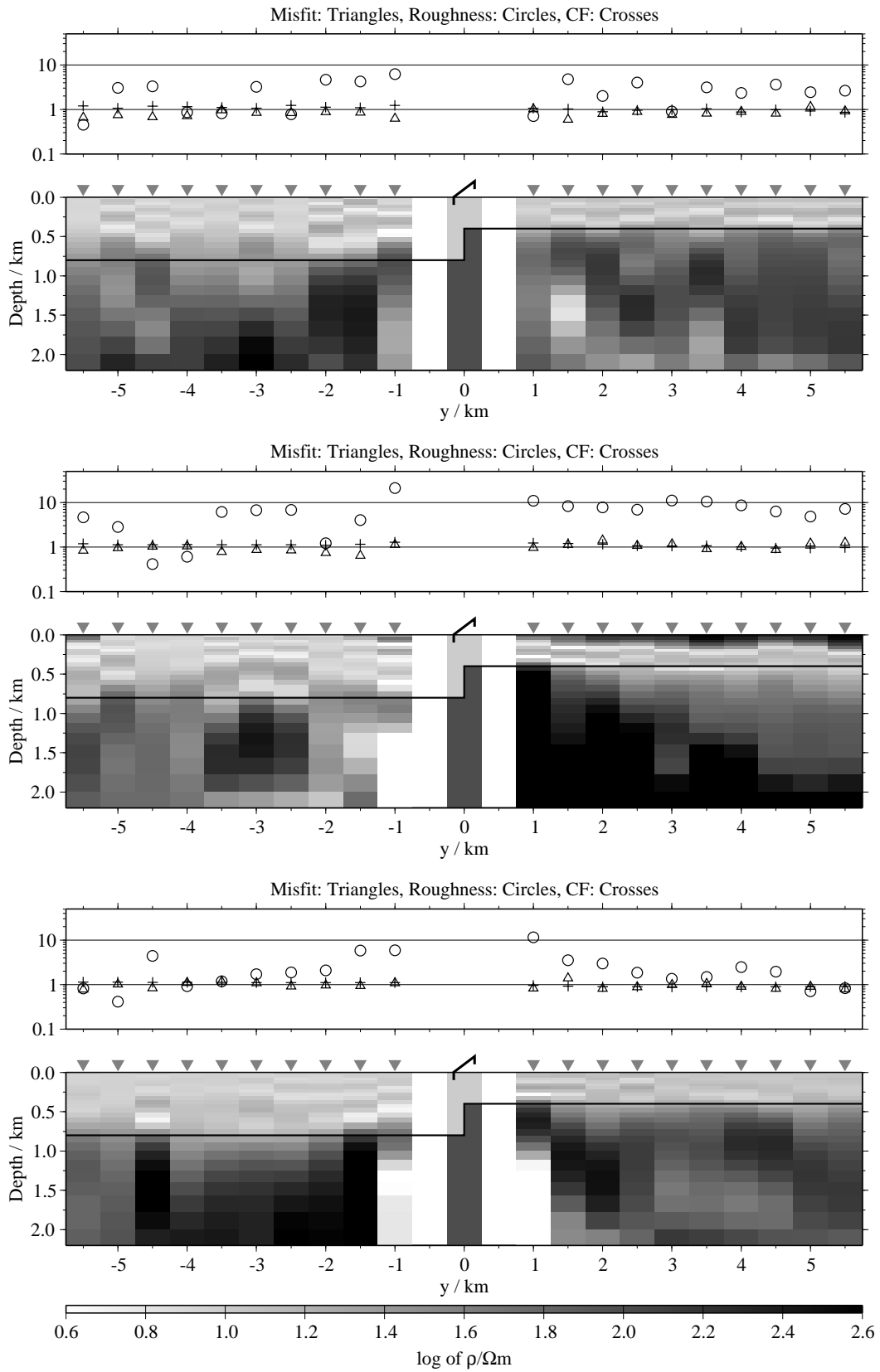


Figure B.249: Pseudo-sections of single 1-D inversion, model L2, regularisation scheme C1; from top to bottom E_x -, \dot{H}_y - and \dot{H}_z -component;

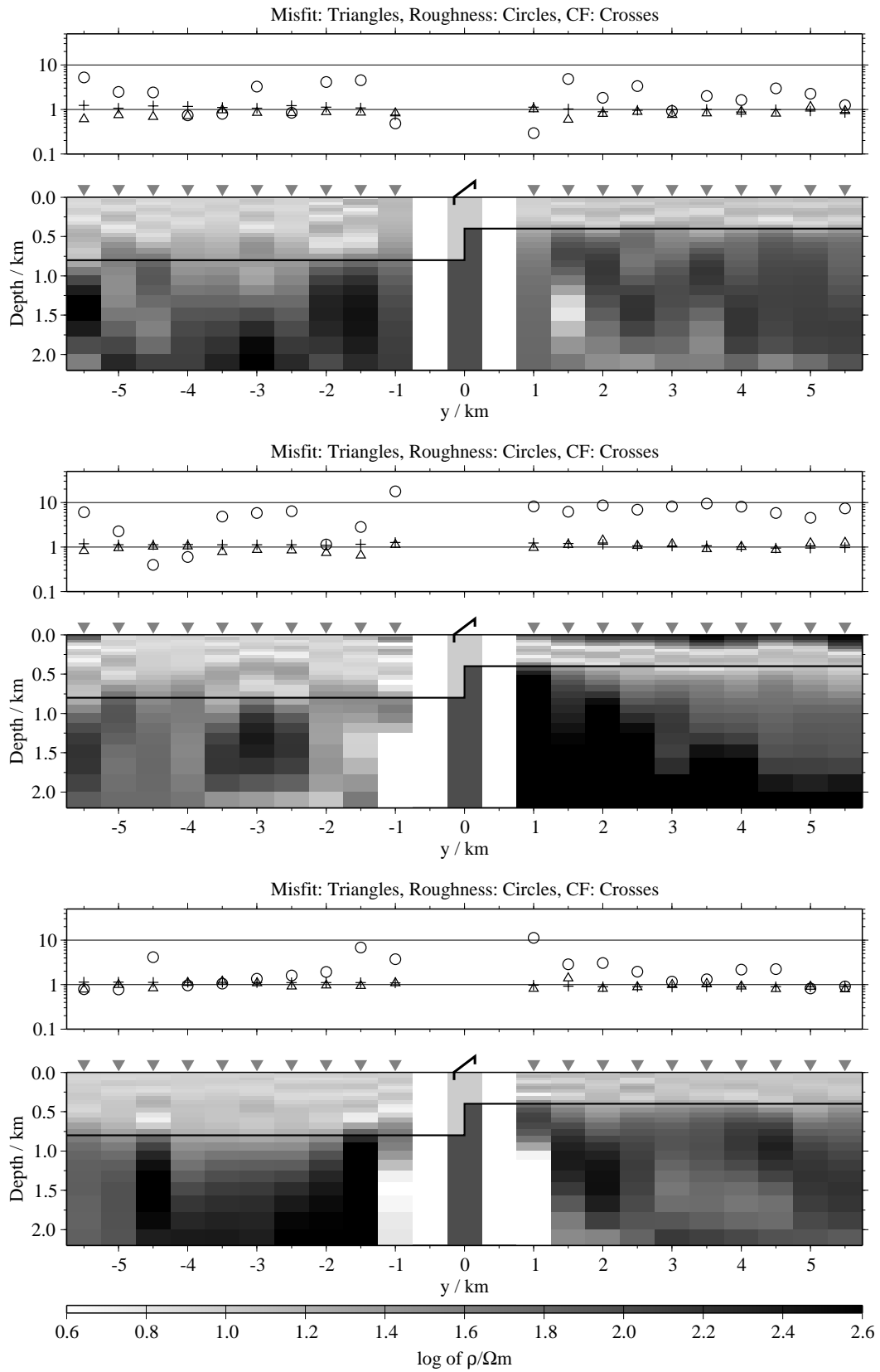


Figure B.250: Pseudo-sections of single 1-D inversion, model L2, regularisation scheme C4; from top to bottom E_x -, H_y - and H_z -component;

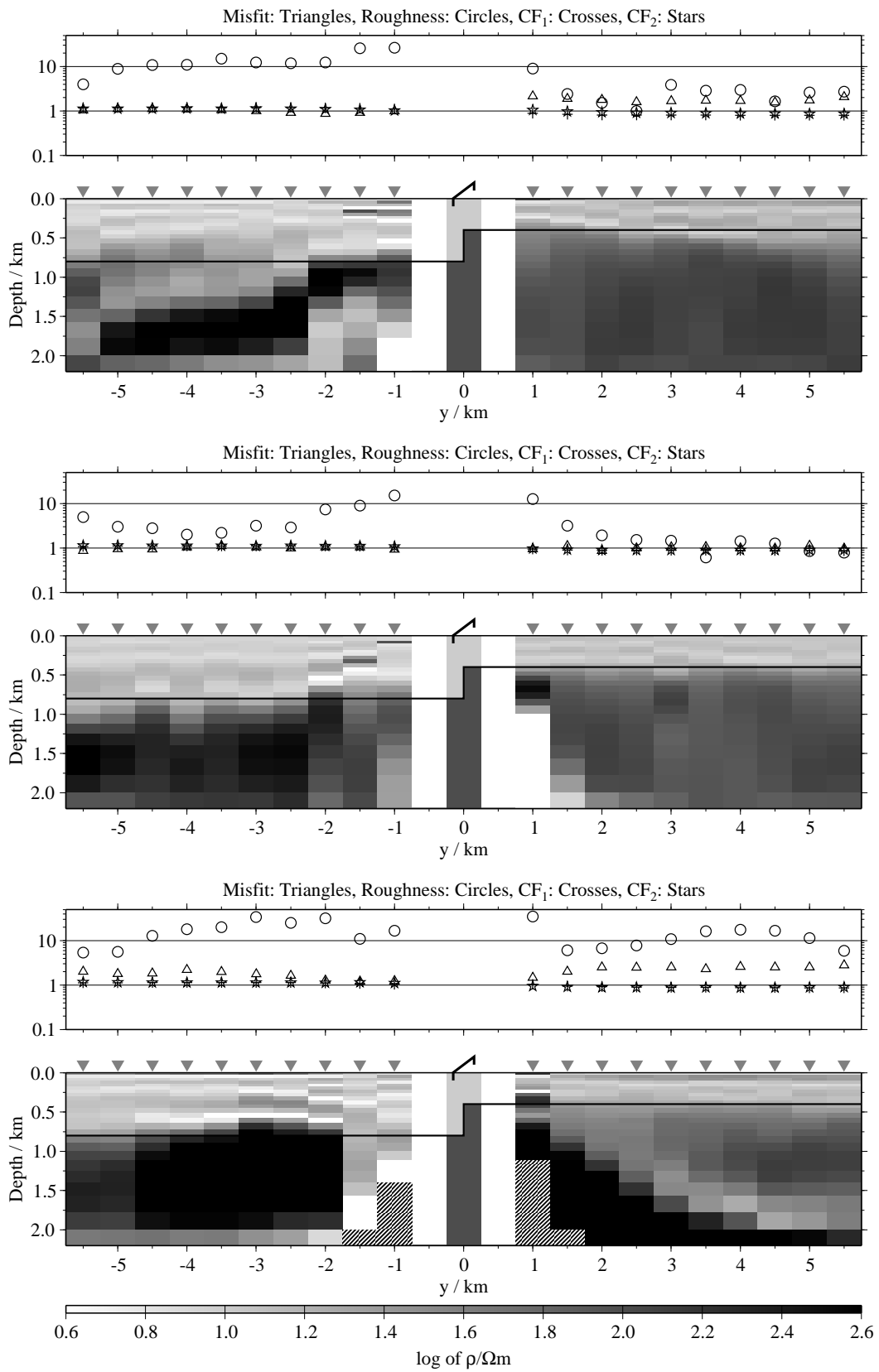


Figure B.251: Pseudo-sections of two component 1-D joint-inversions, model L2, regularisation scheme C1; from top to bottom $E_x - \dot{H}_y$, $E_x - \dot{H}_z$ and $\dot{H}_y - \dot{H}_z$;

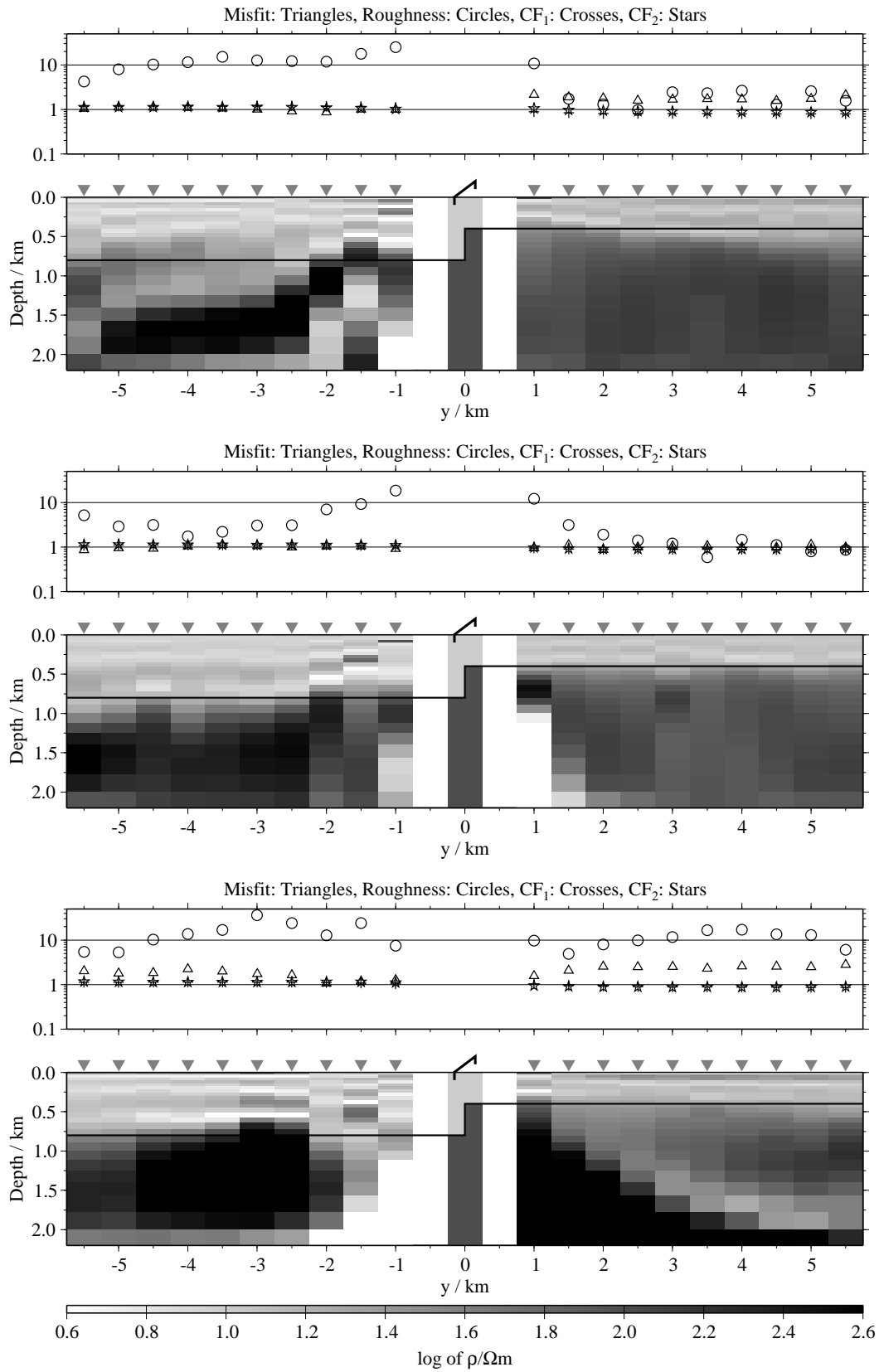


Figure B.252: Pseudo-sections of two component 1-D joint-inversions, model L2, regularisation scheme C4; from top to bottom E_x-H_y , E_x-H_z and H_y-H_z ;

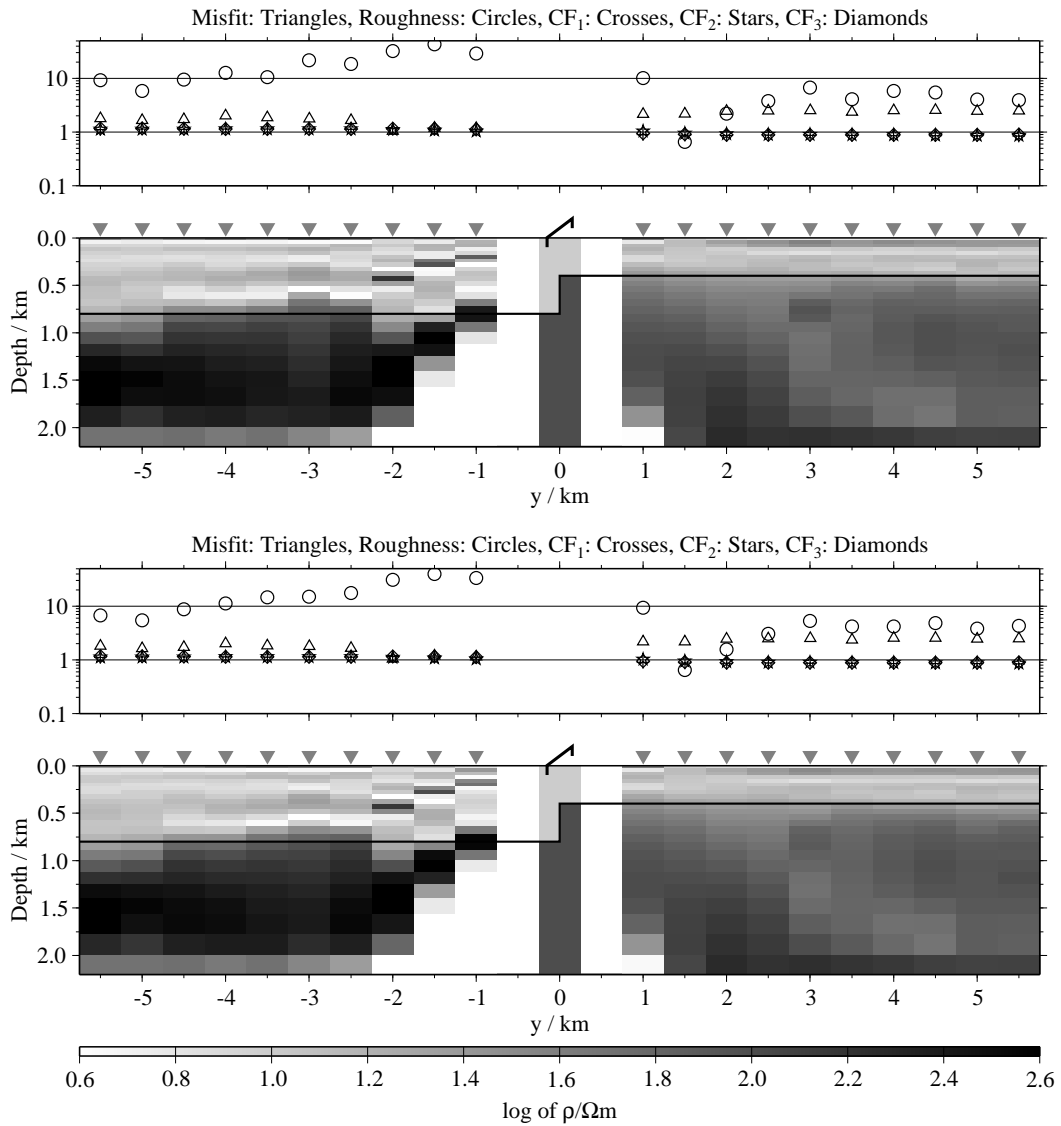


Figure B.253: Pseudo-sections of 1-D joint-inversions using all three components, model L2; top: Regularisation scheme C1; bottom: Regularisation scheme C4;

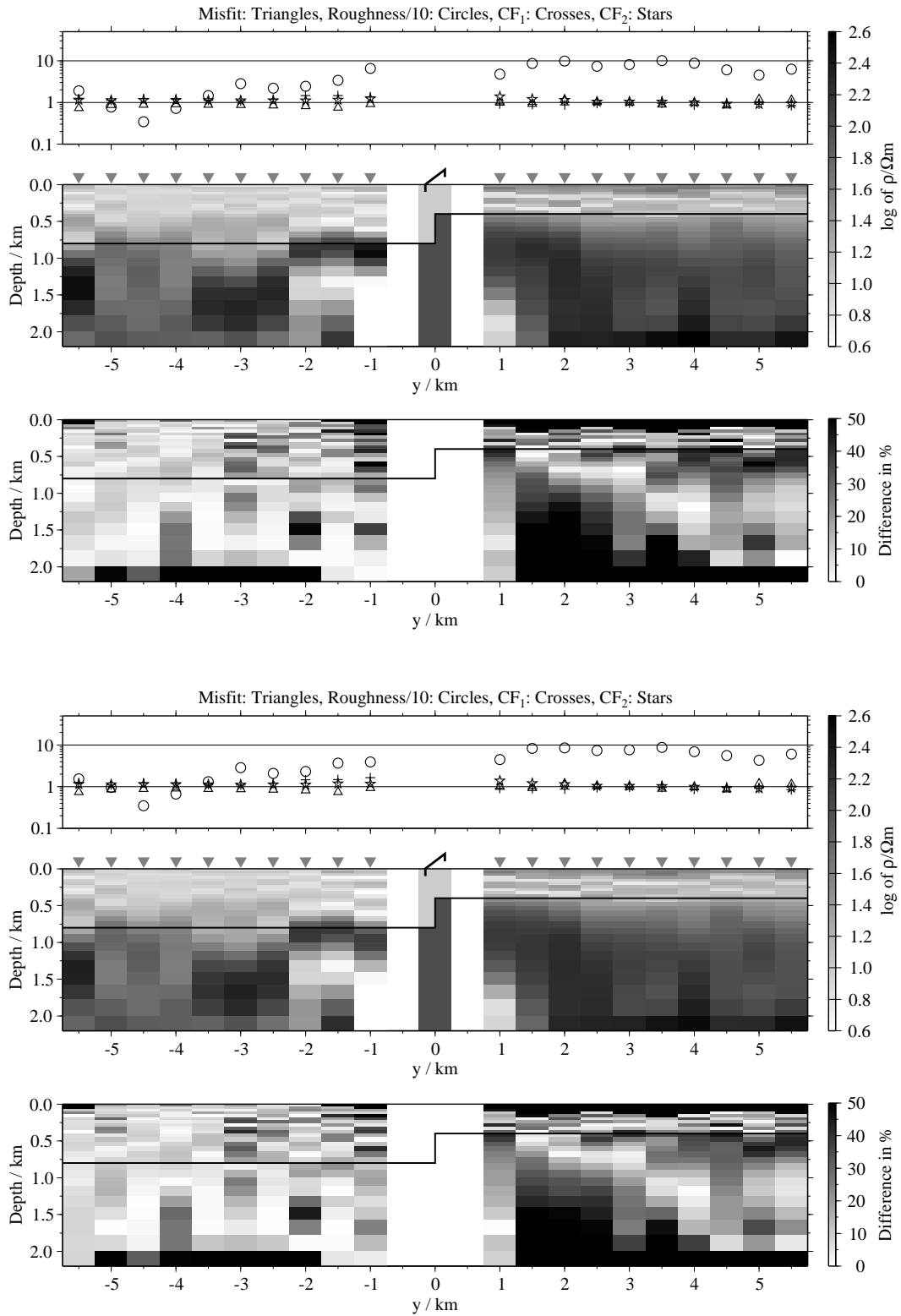


Figure B.254: Pseudo-sections of 1-D soft joint-inversions using the components E_x and H_y , model L2; Top panels: Average inversion results and relative differences (regularisation scheme C1); bottom: Average inversion results and relative differences (regularisation scheme C4);

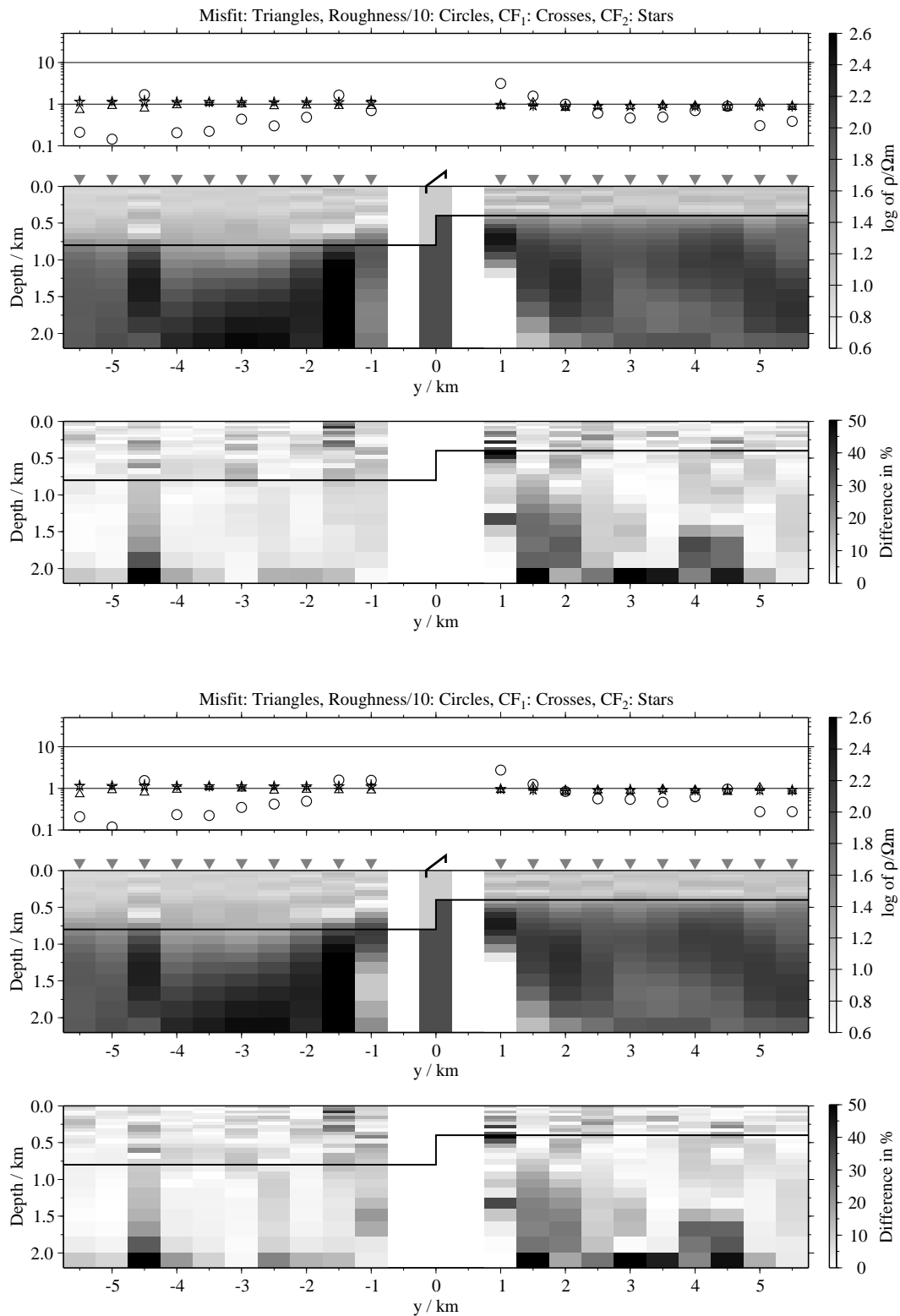


Figure B.255: Pseudo-sections 1-D of soft joint-inversions using the components E_x and H_{zi} , model L2; Top panels: Average inversion results and relative differences (regularisation scheme C1); bottom: Average inversion results and relative differences (regularisation scheme C4);

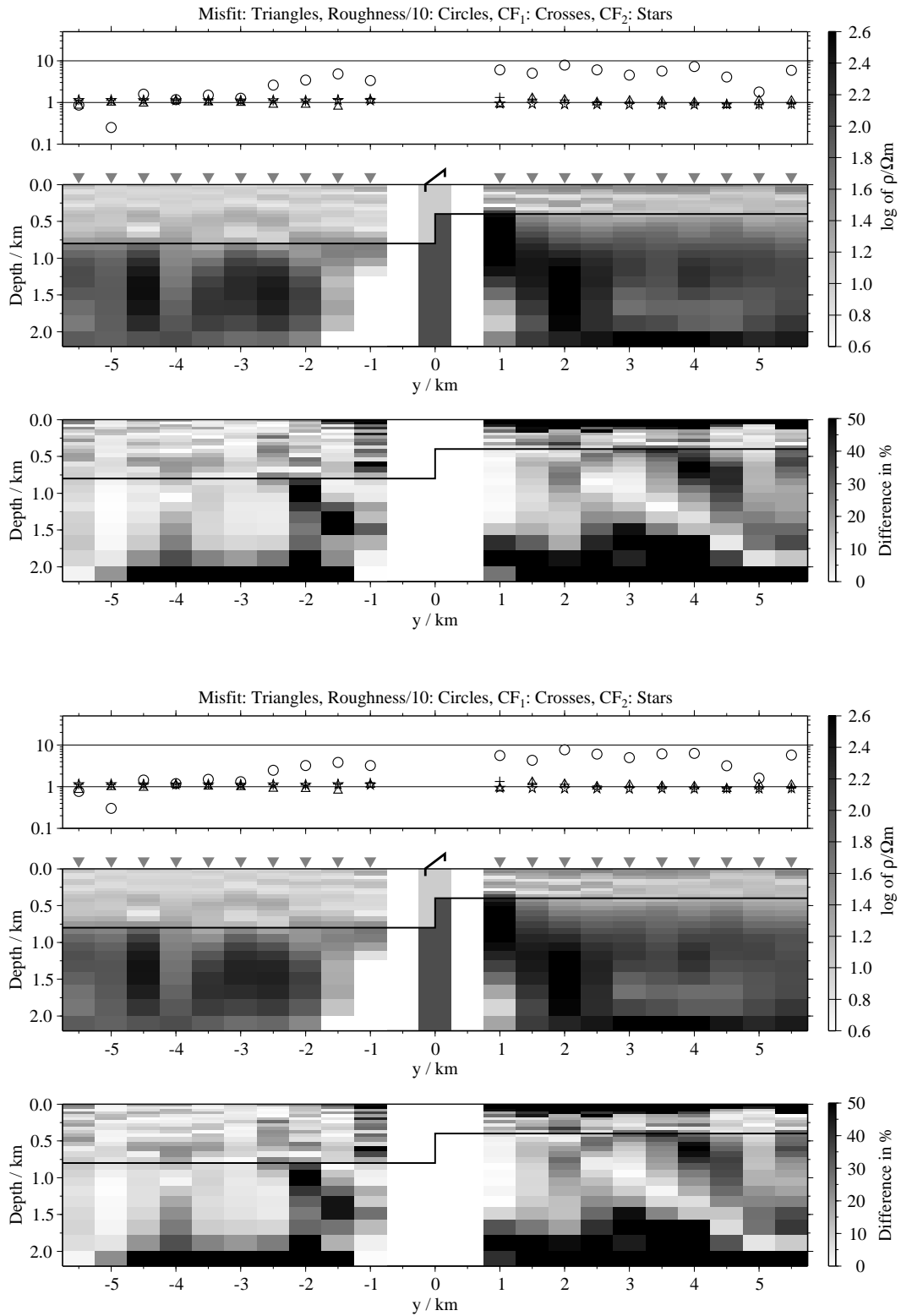


Figure B.256: Pseudo-sections of 1-D soft joint-inversions using the components \dot{H}_y and \dot{H}_z , model L2; Top panels: Average inversion results and relative differences (regularisation scheme C1); bottom: Average inversion results and relative differences (regularisation scheme C4);

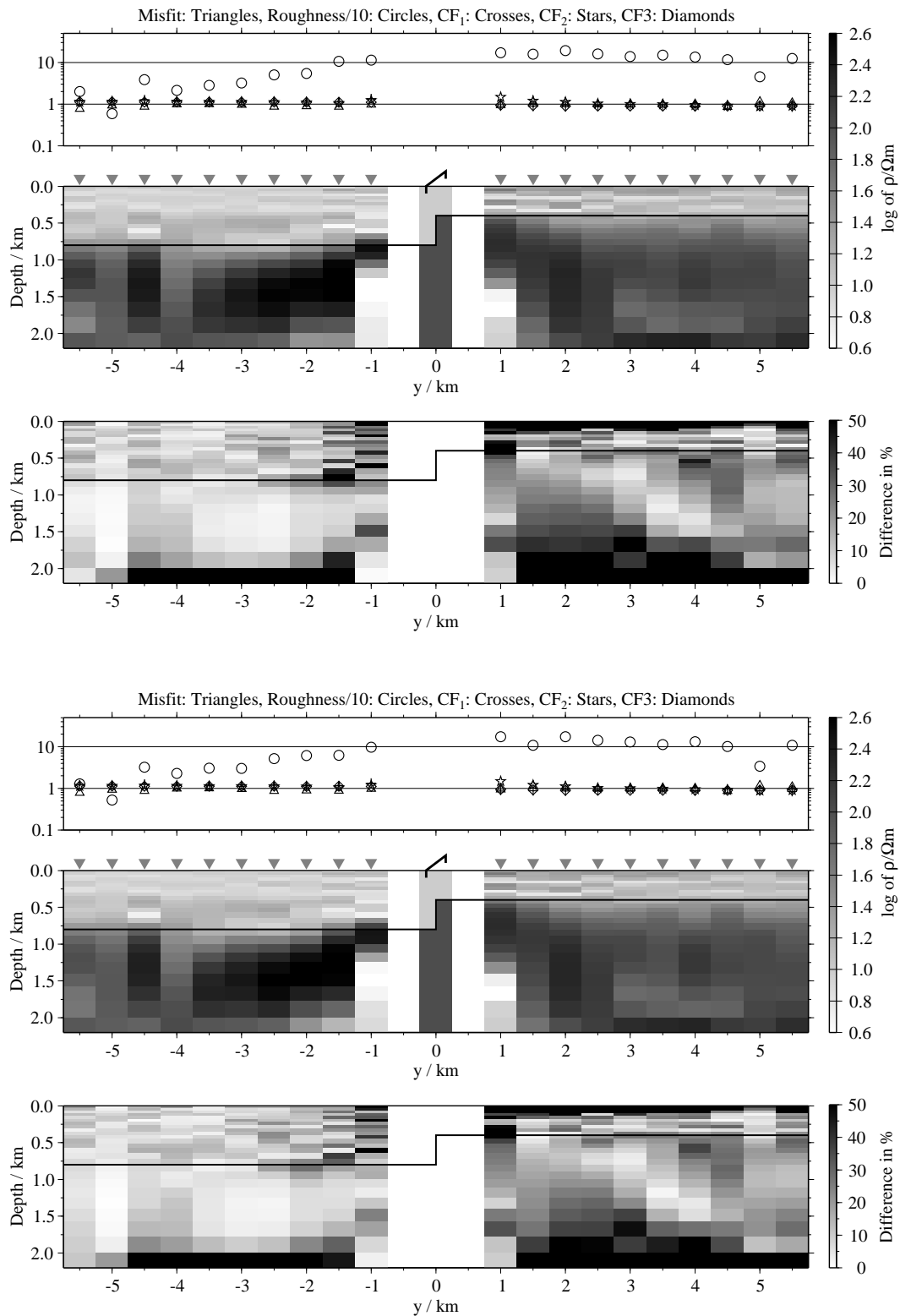


Figure B.257: Pseudo-sections of 1-D soft joint-inversions using all three components, model L2; Top panels: Average inversion results and relative differences (regularisation scheme C1); bottom: Average inversion results and relative differences (regularisation scheme C4);

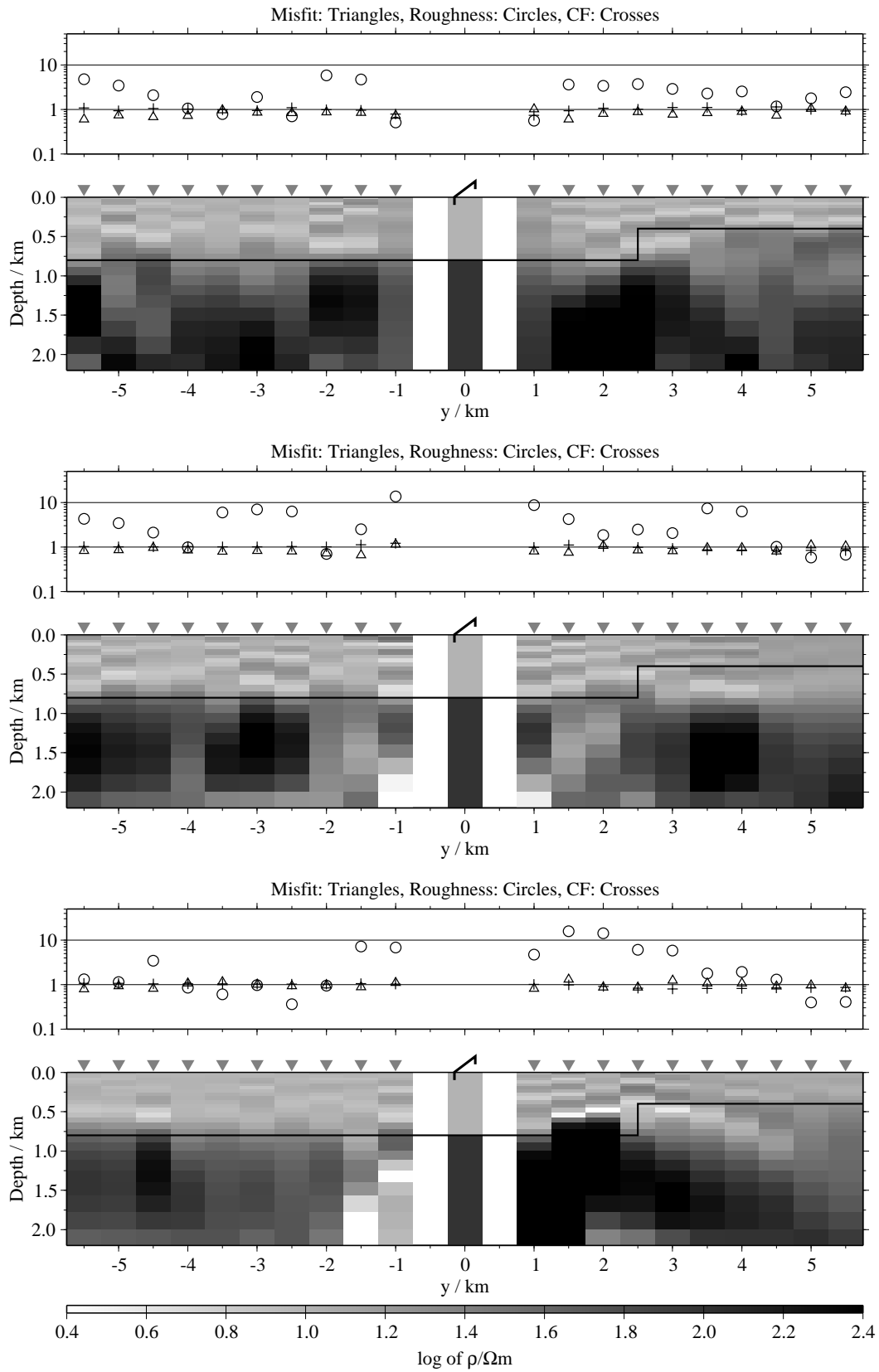


Figure B.258: Pseudo-sections of single 1-D inversion, model L3, regularisation scheme C1; from top to bottom E_x -, \dot{H}_y - and \dot{H}_z -component;

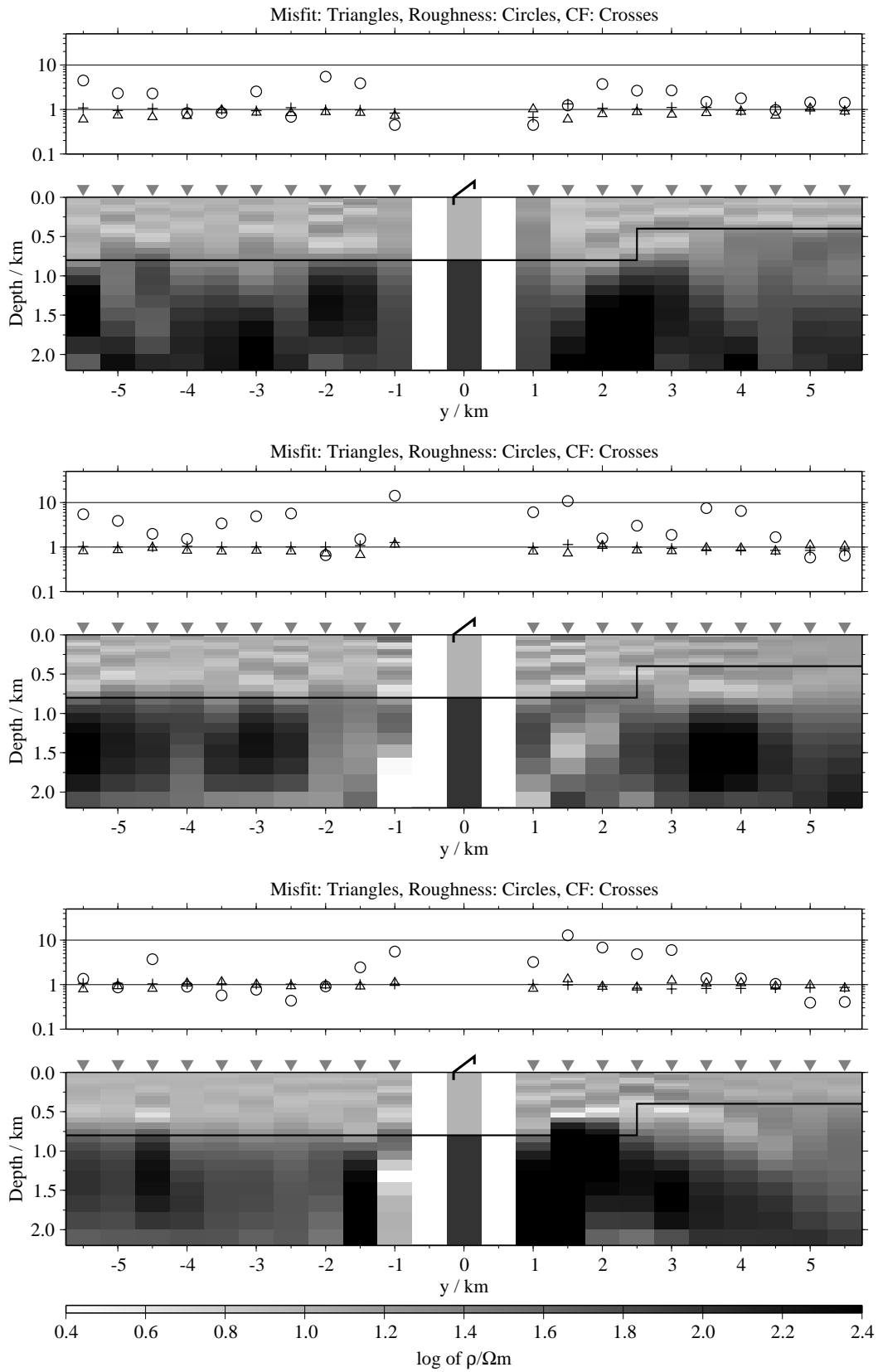


Figure B.259: Pseudo-sections of single 1-D inversion, model L3, regularisation scheme C4; from top to bottom E_x -, H_y - and H_z -component;

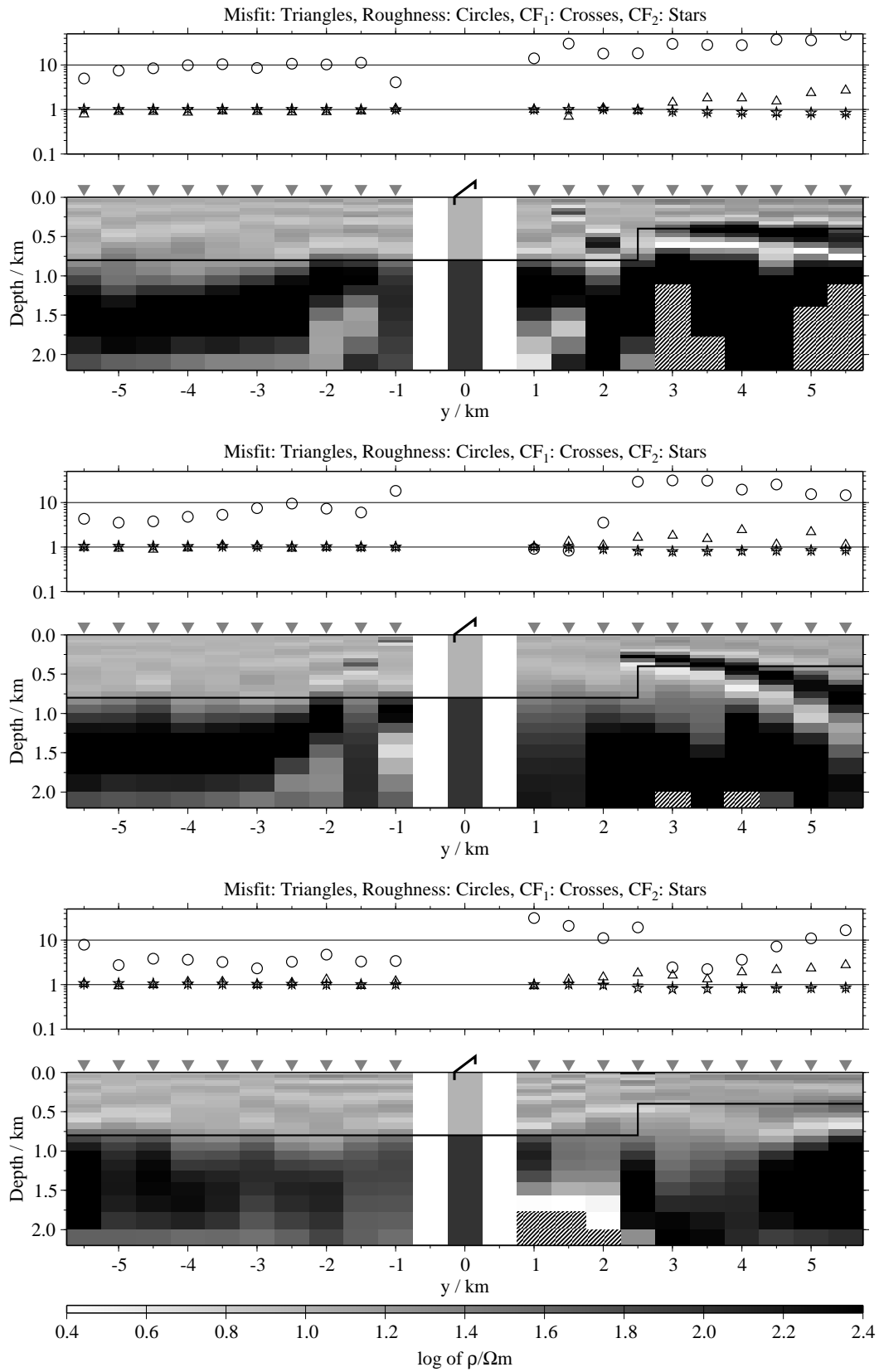


Figure B.260: Pseudo-sections of two component 1-D joint-inversions, model L3, regularisation scheme C1; from top to bottom E_x-H_y , E_x-H_z and H_y-H_z ;

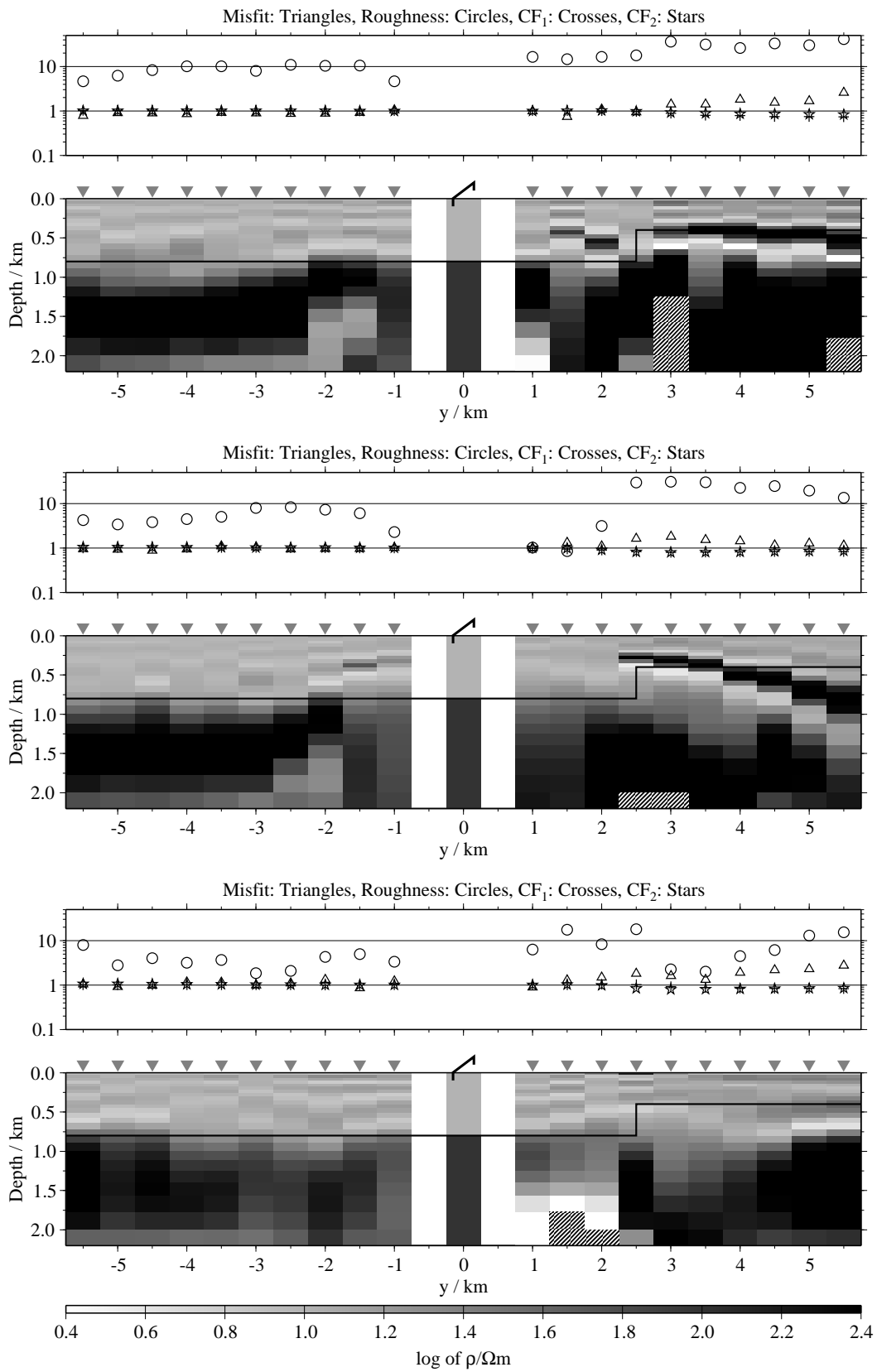


Figure B.261: Pseudo-sections of two component 1-D joint-inversions, model L3, regularisation scheme C4; from top to bottom $E_x-\dot{H}_y$, $E_x-\dot{H}_z$ and $\dot{H}_y-\dot{H}_z$;

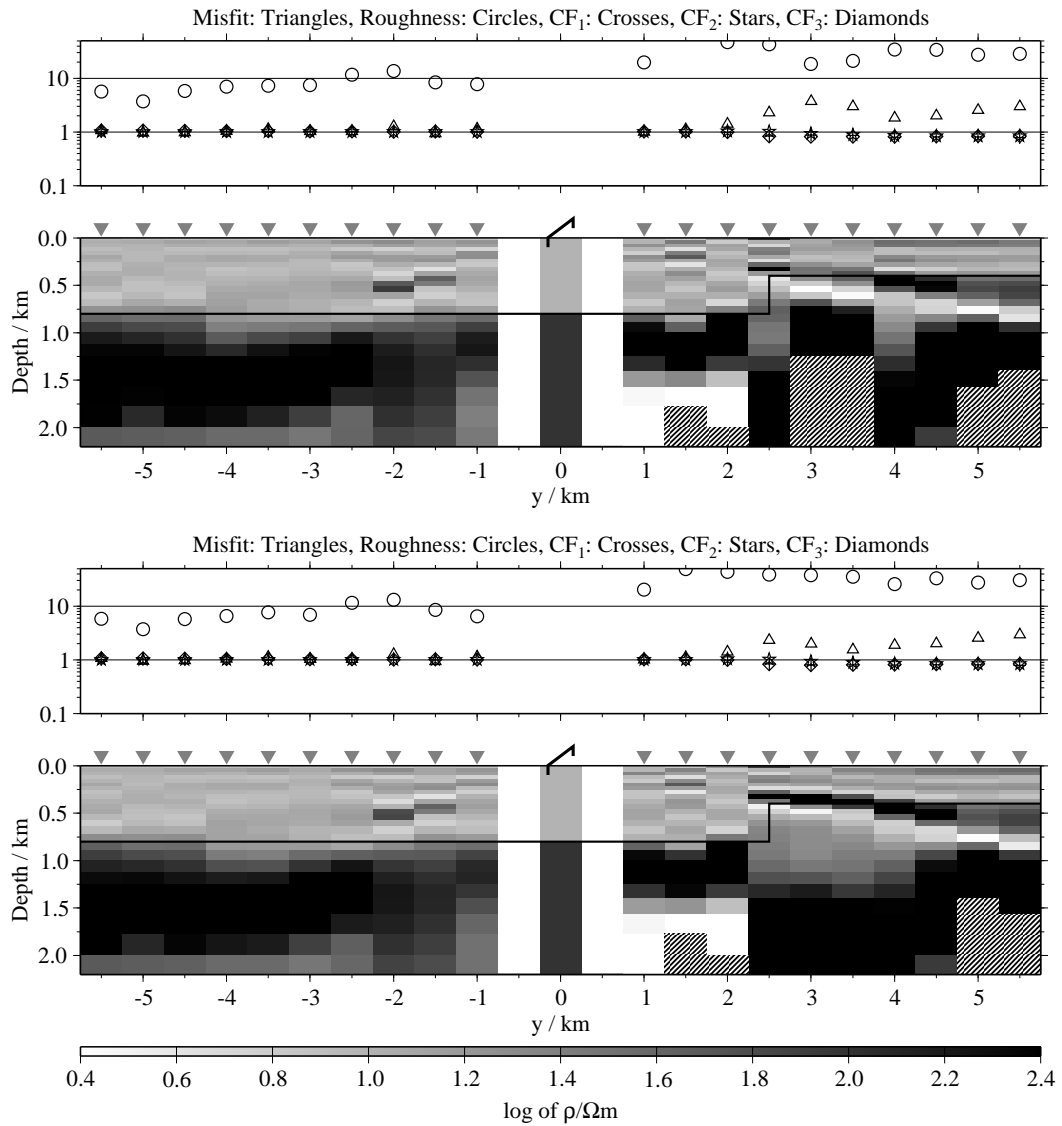


Figure B.262: Pseudo-sections of 1-D joint-inversions using all three components, model L3; top: Regularisation scheme C1; bottom: Regularisation scheme C4;

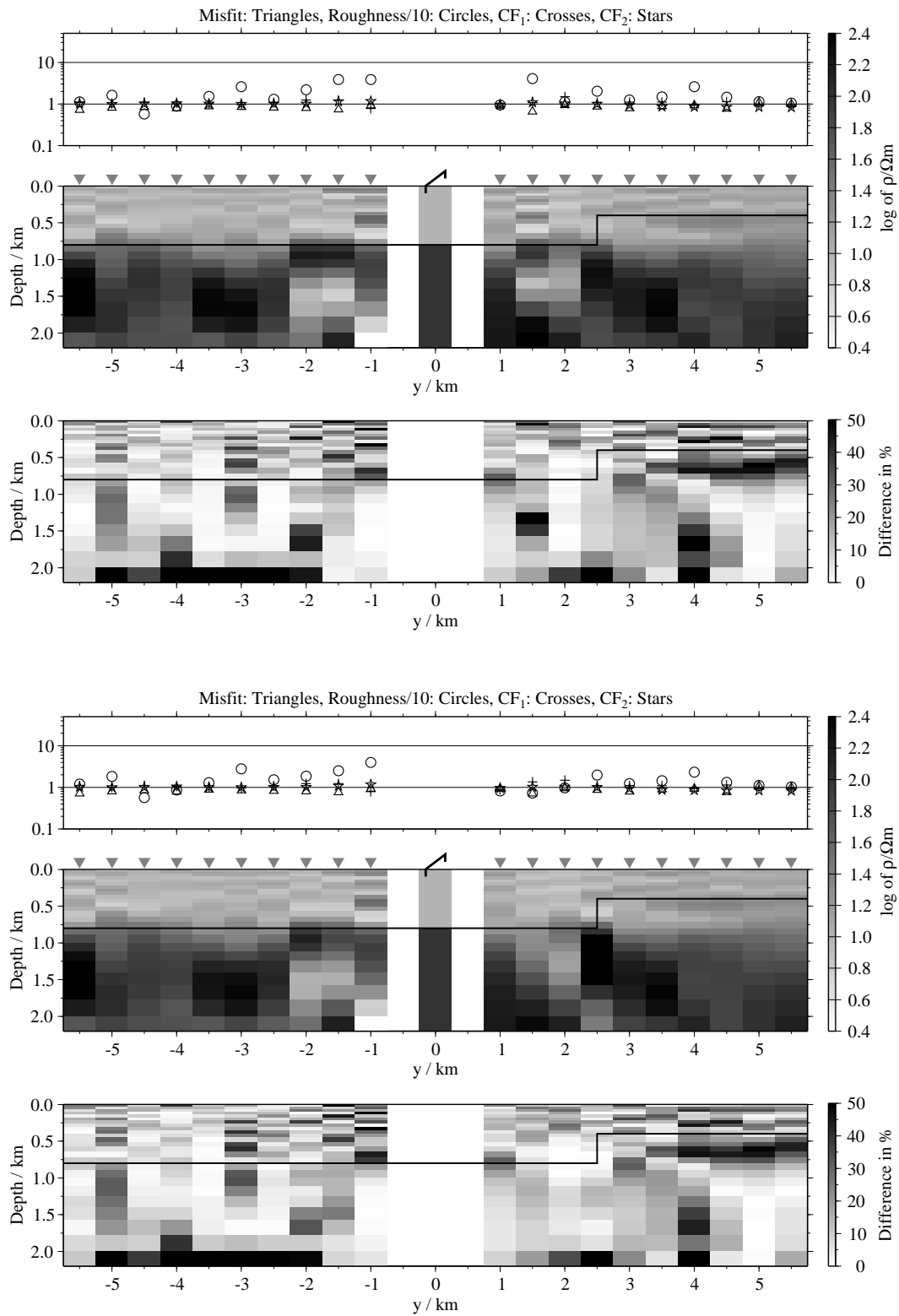


Figure B.263: Pseudo-sections of 1-D soft joint-inversions using the components E_x and \dot{H}_y , model L3; Top panels: Average inversion results and relative differences (regularisation scheme C1); bottom: Average inversion results and relative differences (regularisation scheme C4);

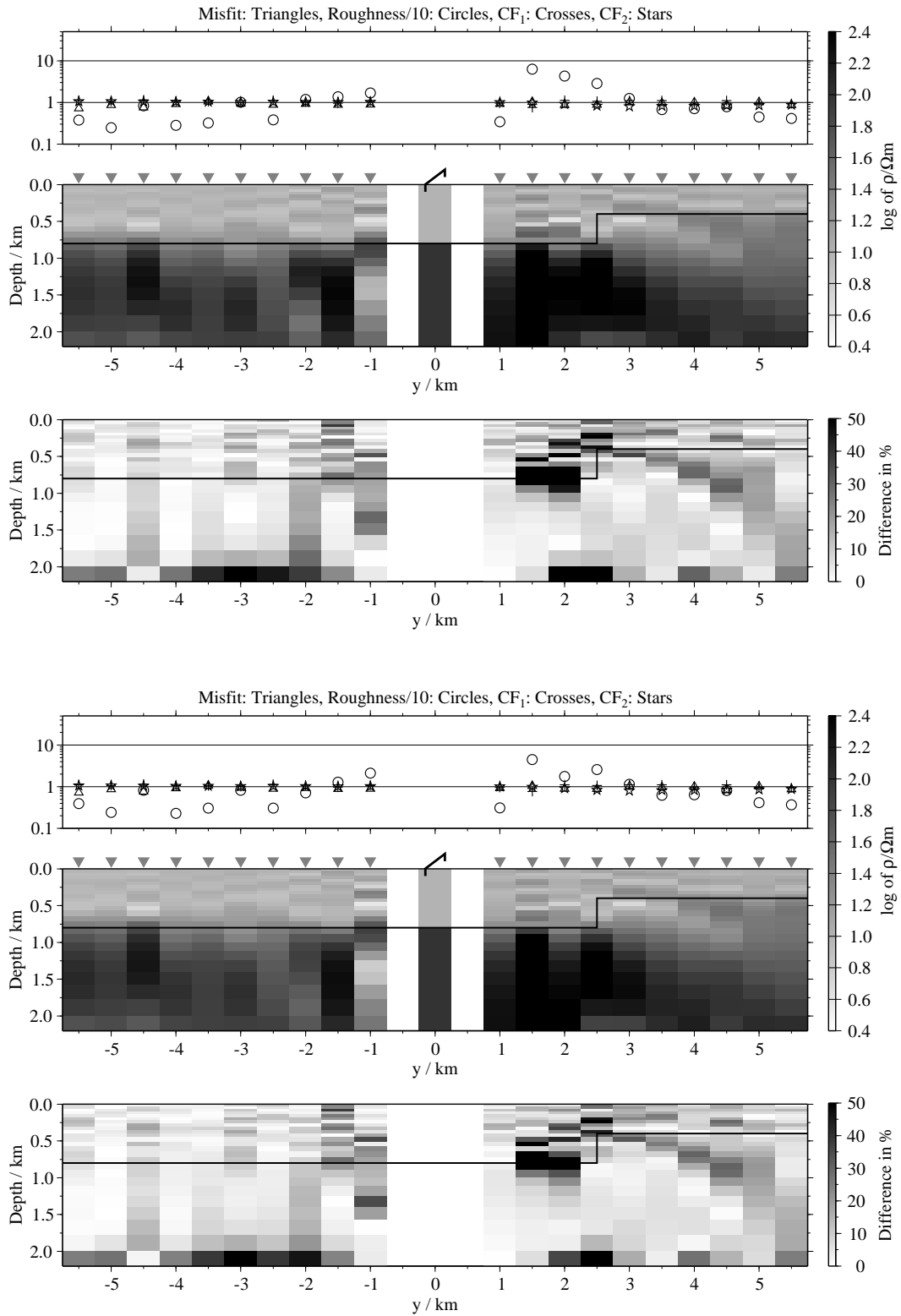


Figure B.264: Pseudo-sections 1-D of soft joint-inversions using the components E_x and H_z , model L3; Top panels: Average inversion results and relative differences (regularisation scheme C1); bottom: Average inversion results and relative differences (regularisation scheme C4);

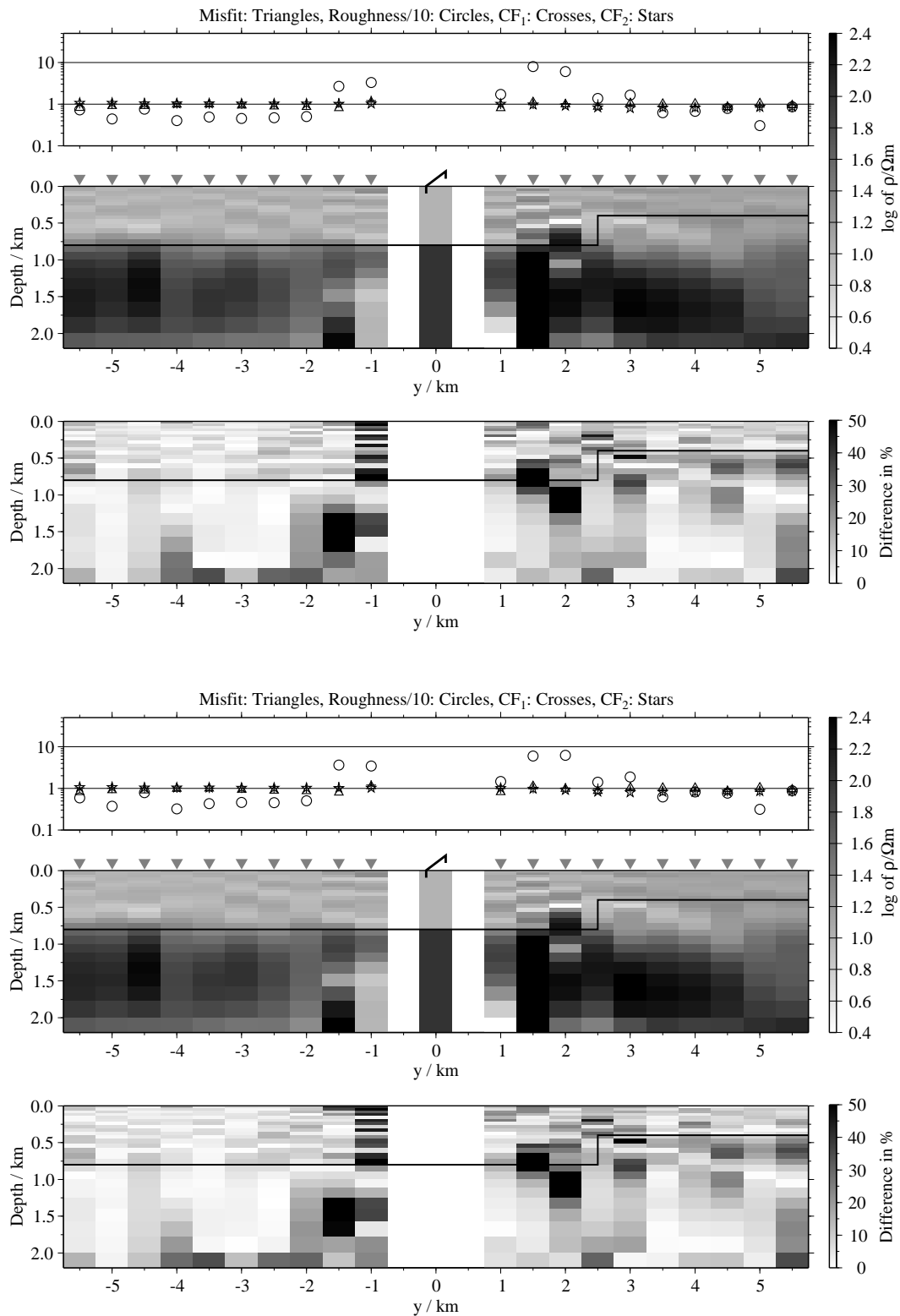


Figure B.265: Pseudo-sections of 1-D soft joint-inversions using the components \dot{H}_y and \dot{H}_{zi} , model L3; Top panels: Average inversion results and relative differences (regularisation scheme C1); bottom: Average inversion results and relative differences (regularisation scheme C4);

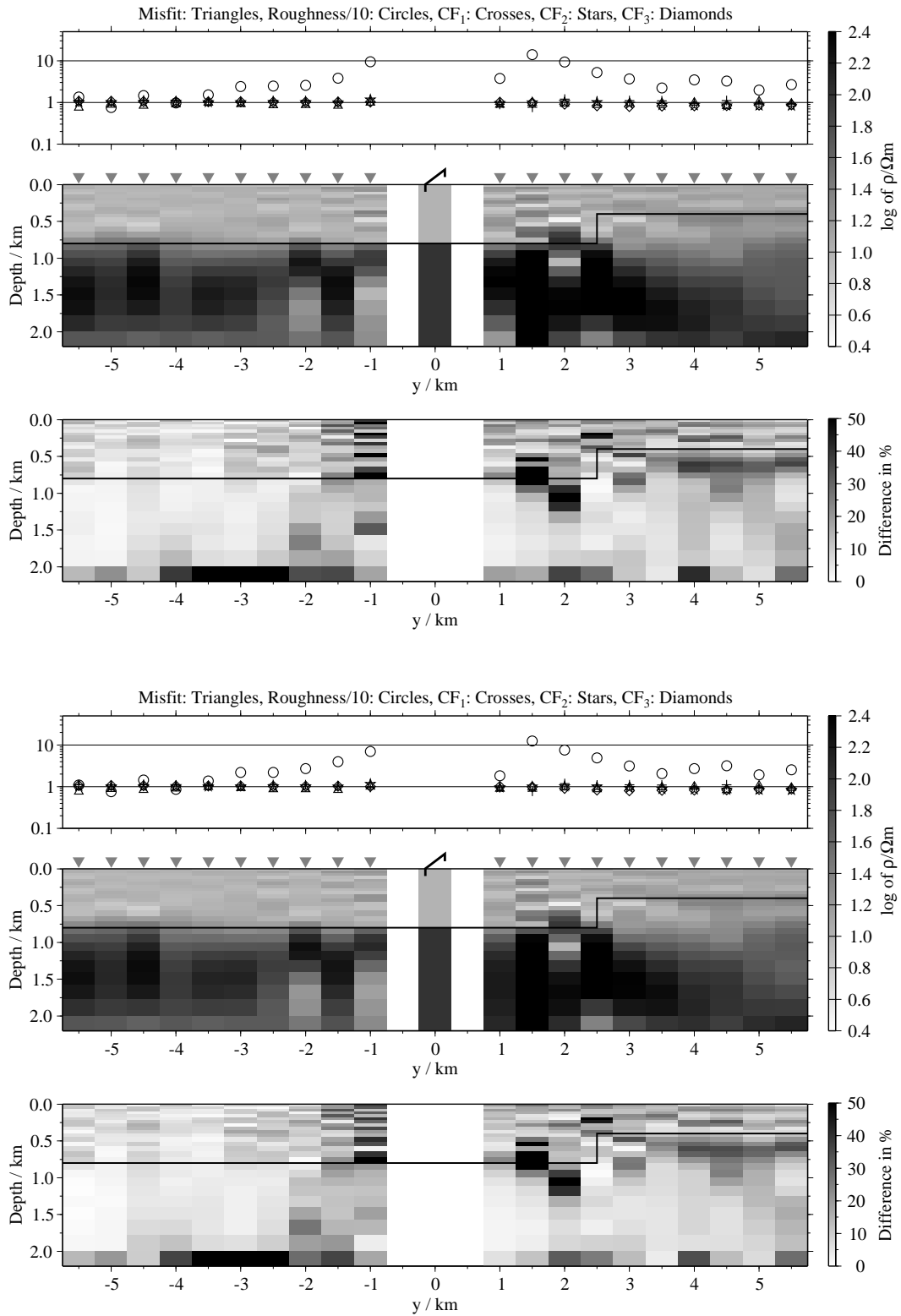
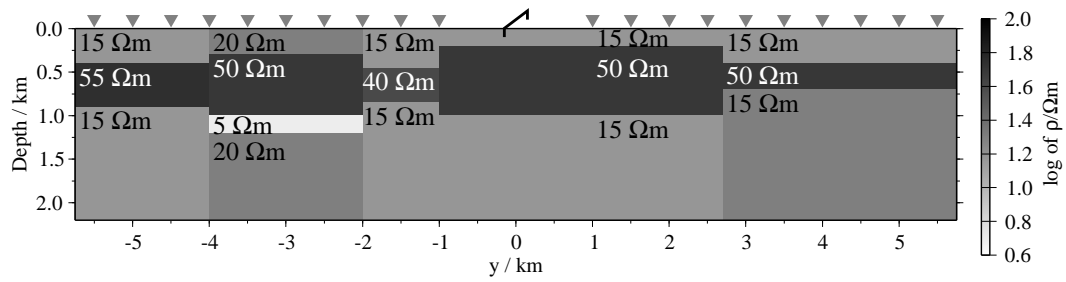


Figure B.266: Pseudo-sections of 1-D soft joint-inversions using all three components, model L3; Top panels: Average inversion results and relative differences (regularisation scheme C1); bottom: Average inversion results and relative differences (regularisation scheme C4);

B.2.11 Model with several lateral changes (model M)

Model M:

*Figure B.267: Model including various structures (model M);*

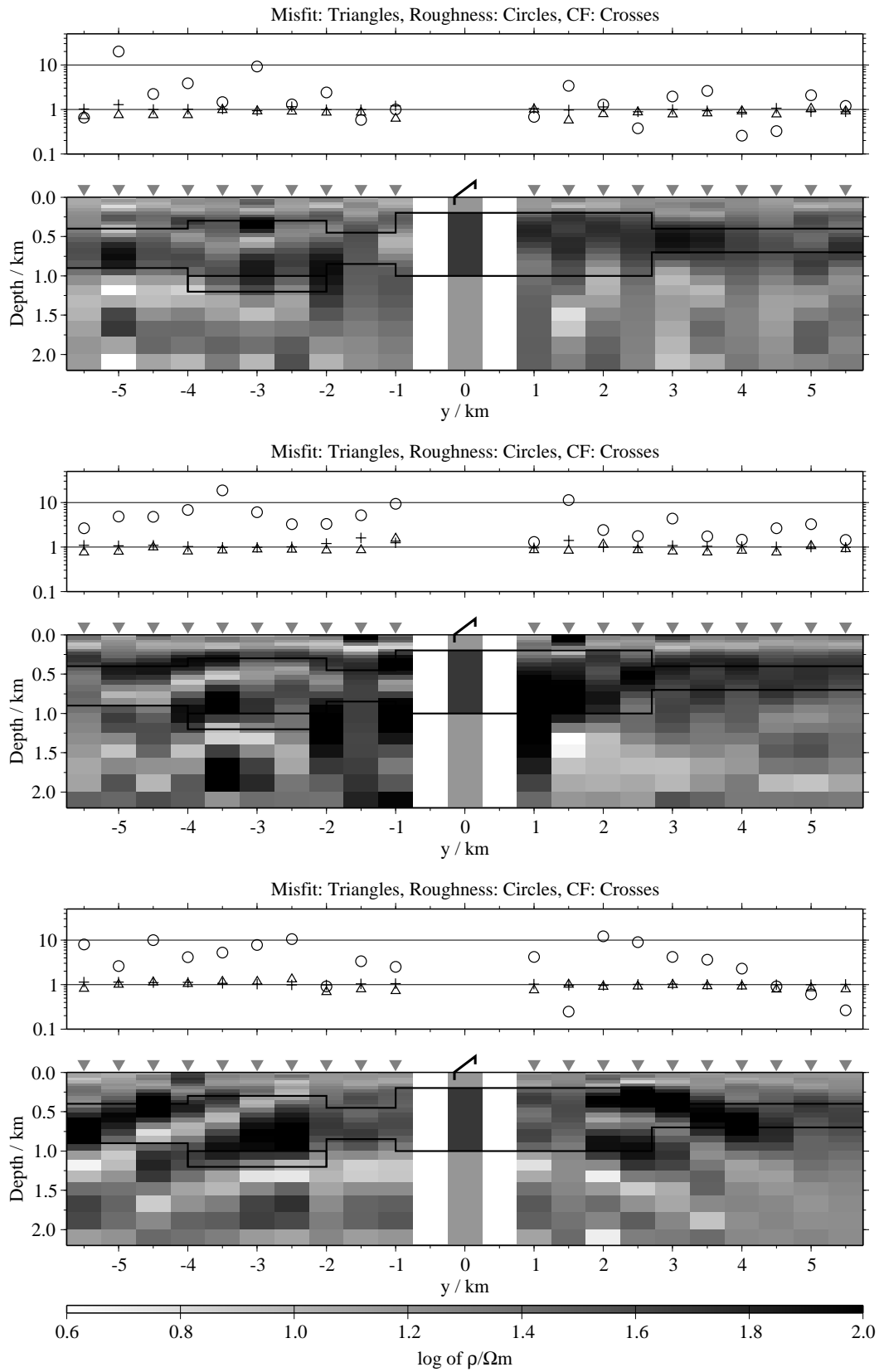


Figure B.268: Pseudo-sections of single 1-D inversion, model M, regularisation scheme C1; from top to bottom E_x -, H_y - and H_z -component;

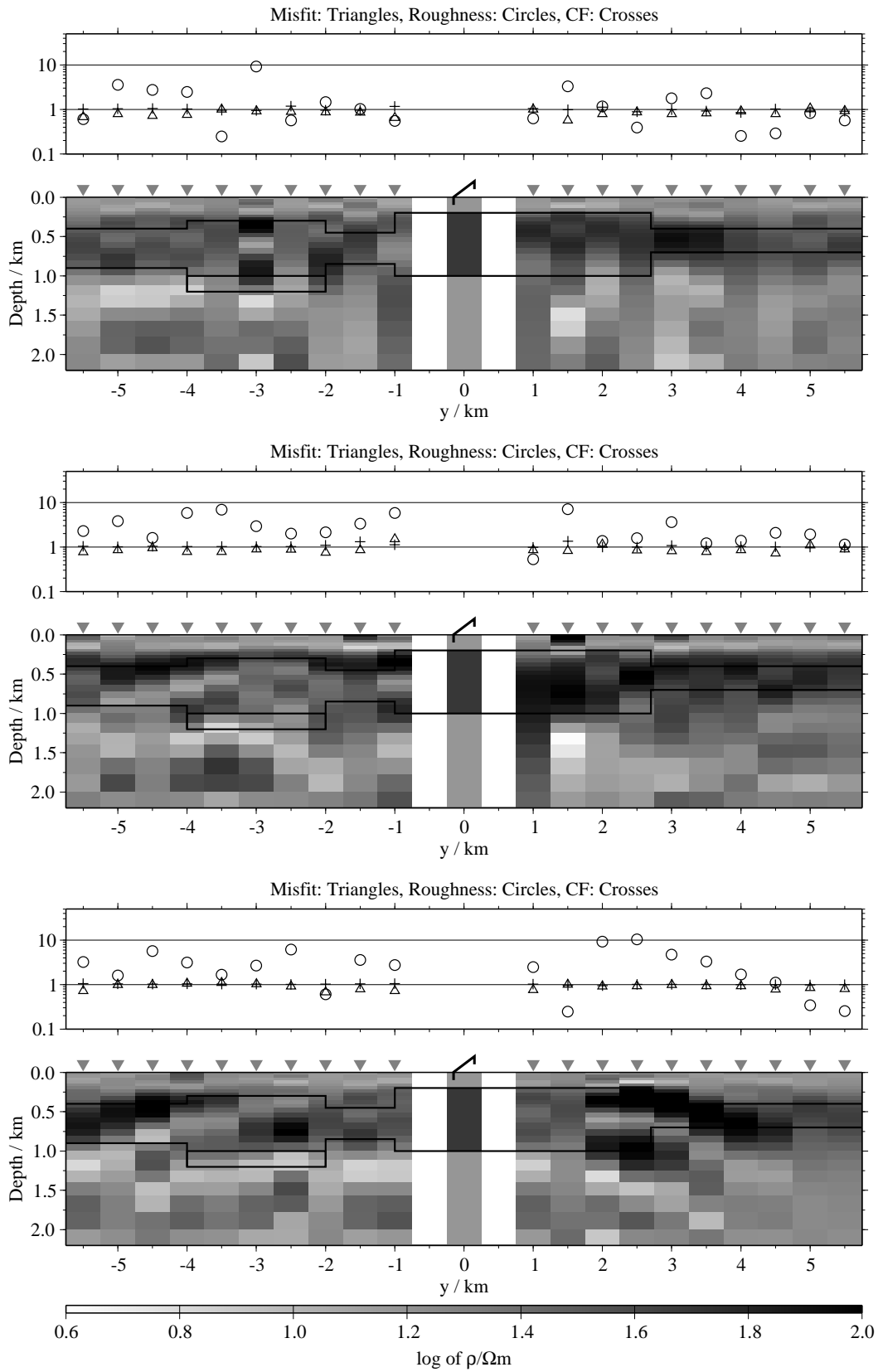


Figure B.269: Pseudo-sections of single 1-D inversion, model *M*, regularisation scheme *C4*; from top to bottom E_x -, H_y - and H_z -component;

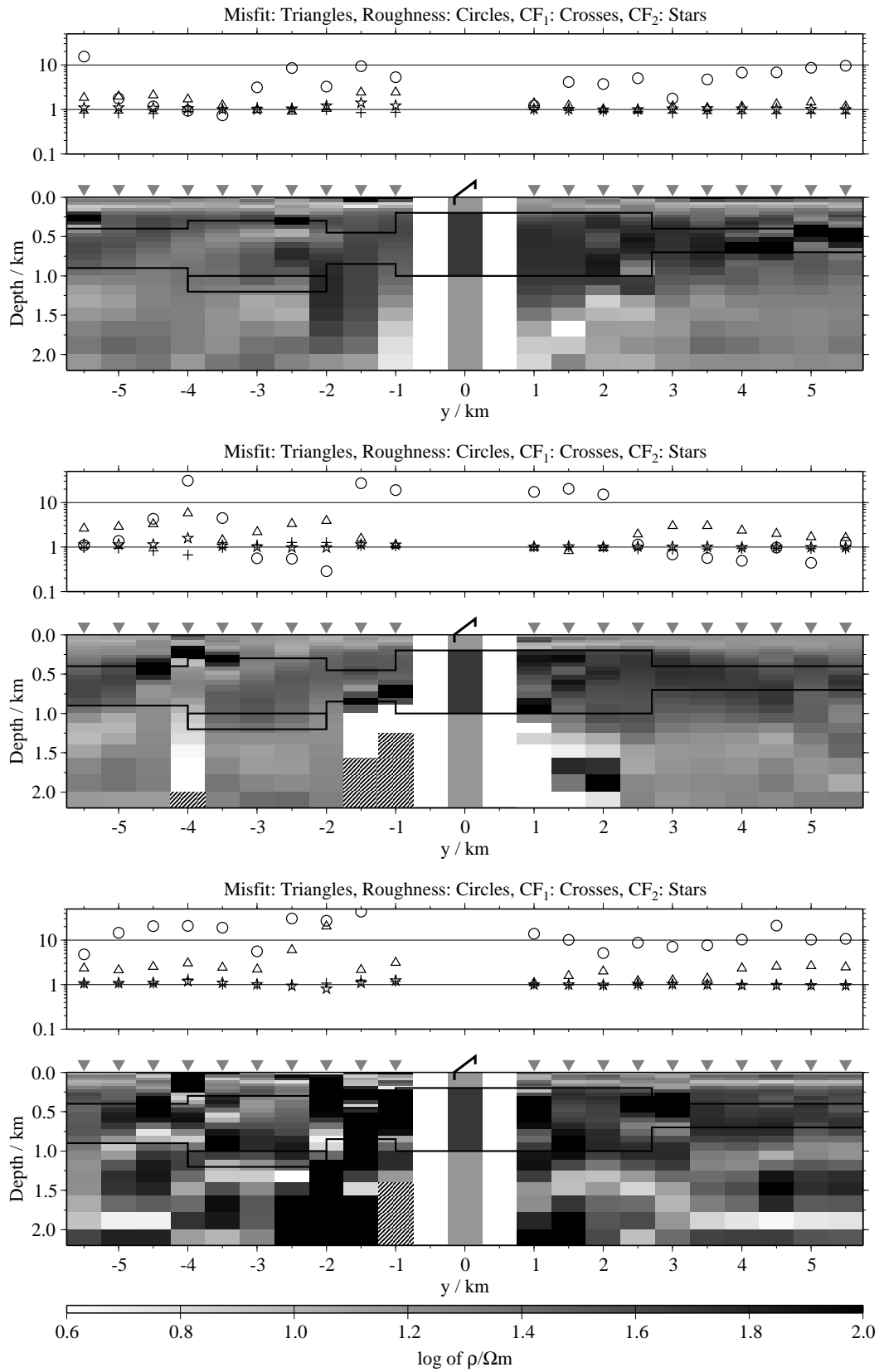


Figure B.270: Pseudo-sections of two component 1-D joint-inversions, model M, regularisation scheme C1; from top to bottom $E_x - \dot{H}_y$, $E_x - \dot{H}_z$ and $\dot{H}_y - \dot{H}_z$;

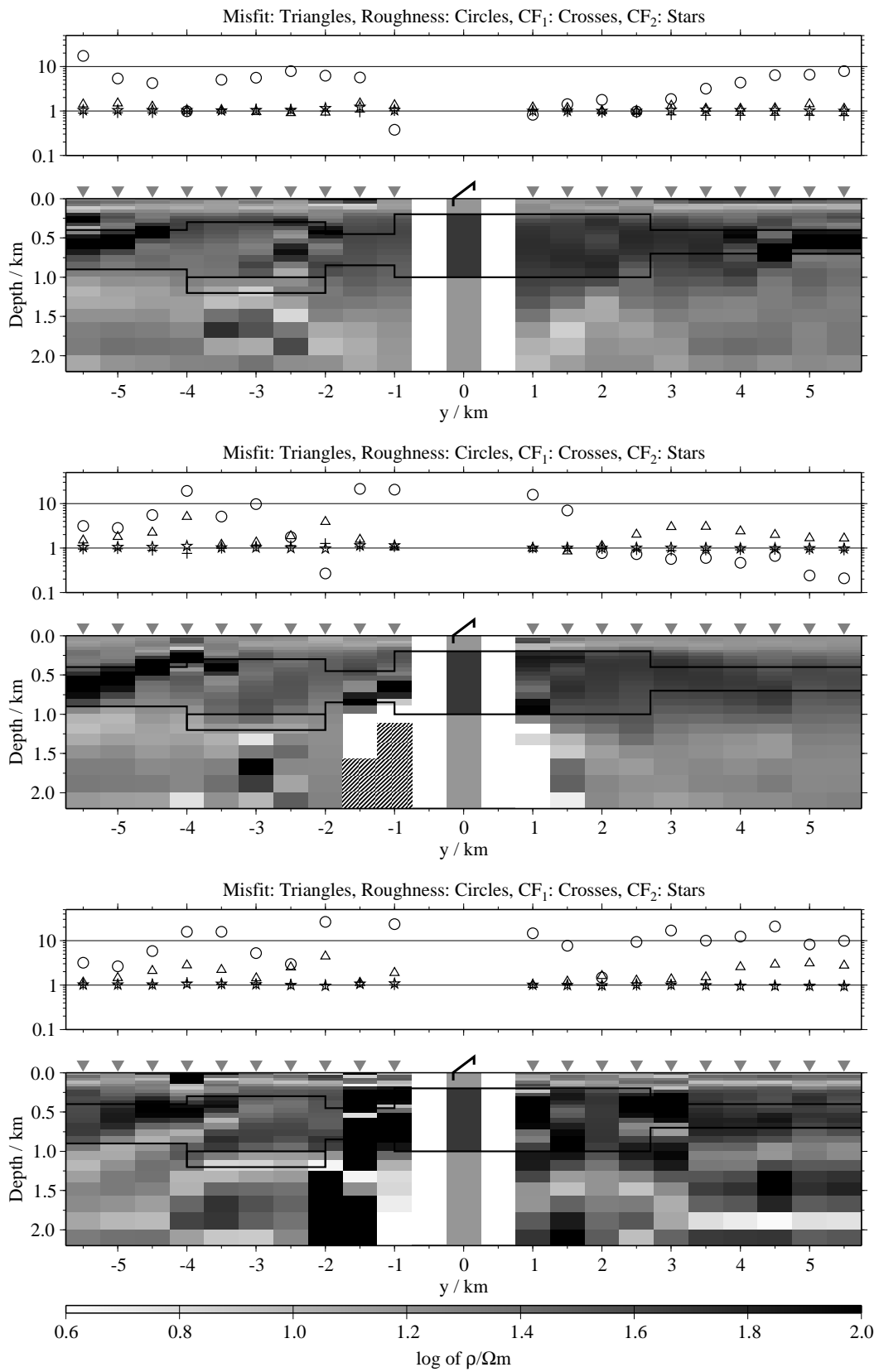


Figure B.271: Pseudo-sections of two component 1-D joint-inversions, model M, regularisation scheme C4; from top to bottom $E_x\text{-}\dot{H}_y$, $E_x\text{-}\dot{H}_z$ and $\dot{H}_y\text{-}\dot{H}_z$;

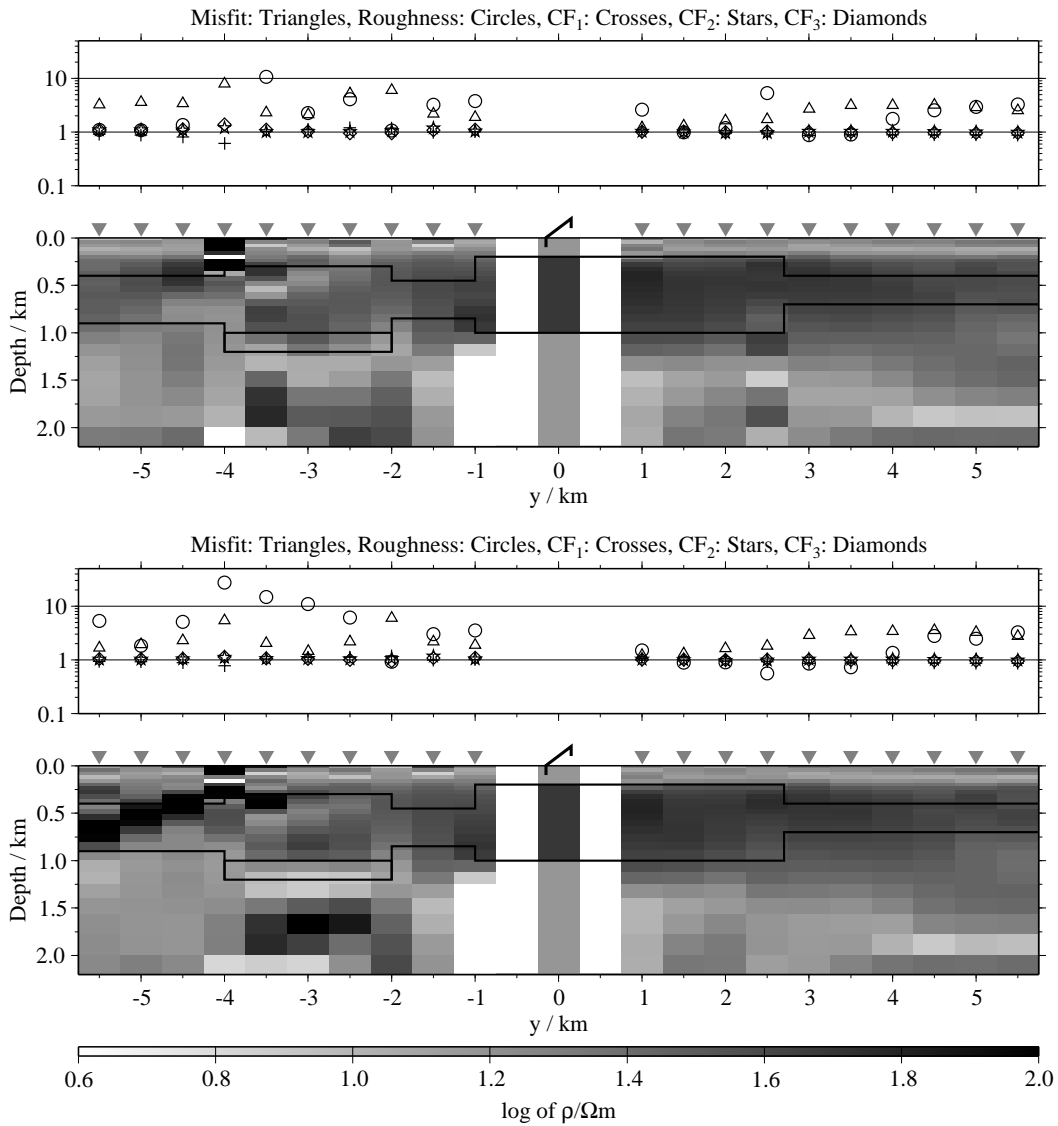


Figure B.272: Pseudo-sections of 1-D joint-inversions using all three components, model M; top: Regularisation scheme C1; bottom: Regularisation scheme C4;

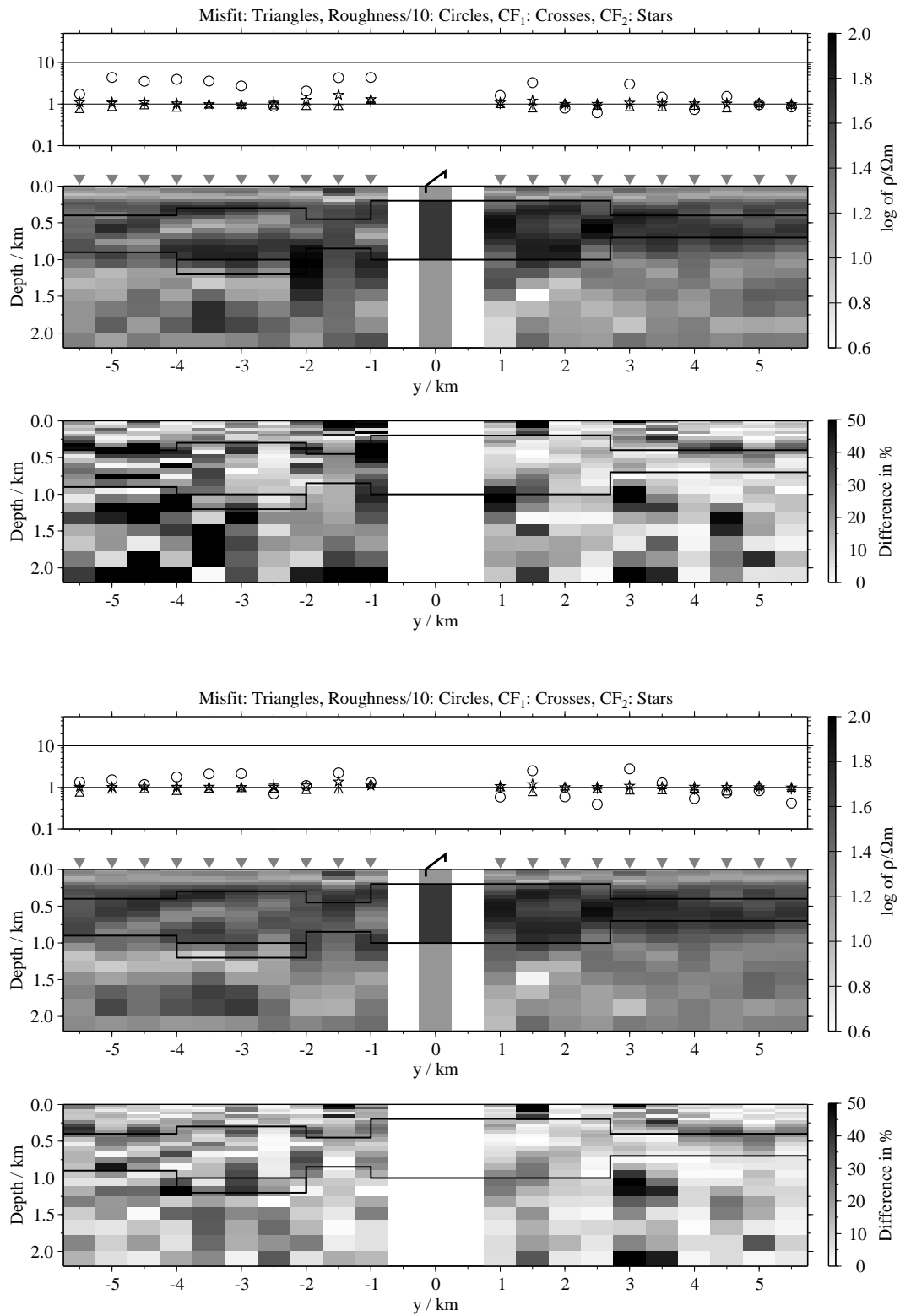


Figure B.273: Pseudo-sections of 1-D soft joint-inversions using the components E_x and \dot{H}_y , model M; Top panels: Average inversion results and relative differences (regularisation scheme C1); bottom: Average inversion results and relative differences (regularisation scheme C4);

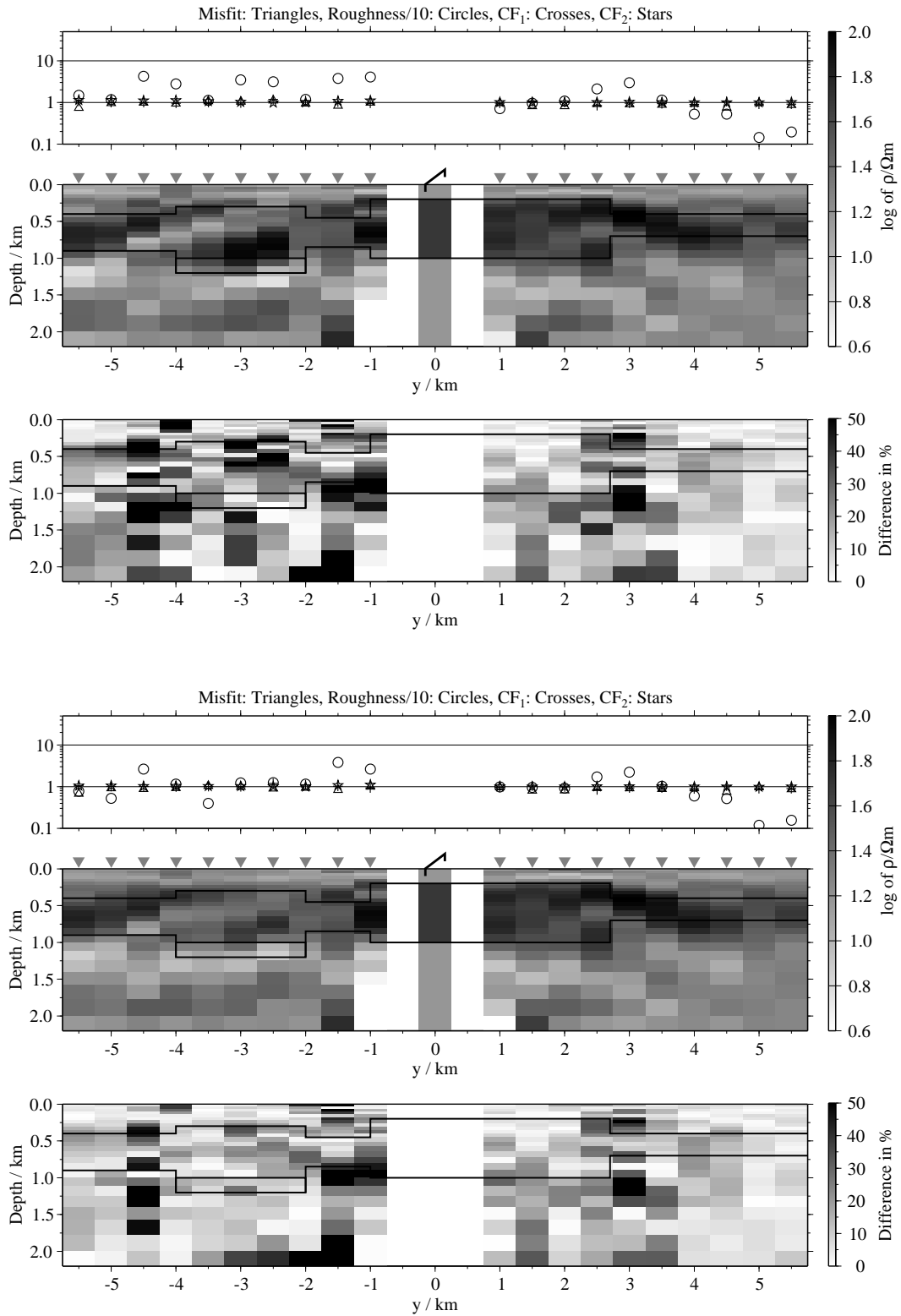


Figure B.274: Pseudo-sections 1-D of soft joint-inversions using the components E_x and H_z , model M; Top panels: Average inversion results and relative differences (regularisation scheme C1); bottom: Average inversion results and relative differences (regularisation scheme C4);

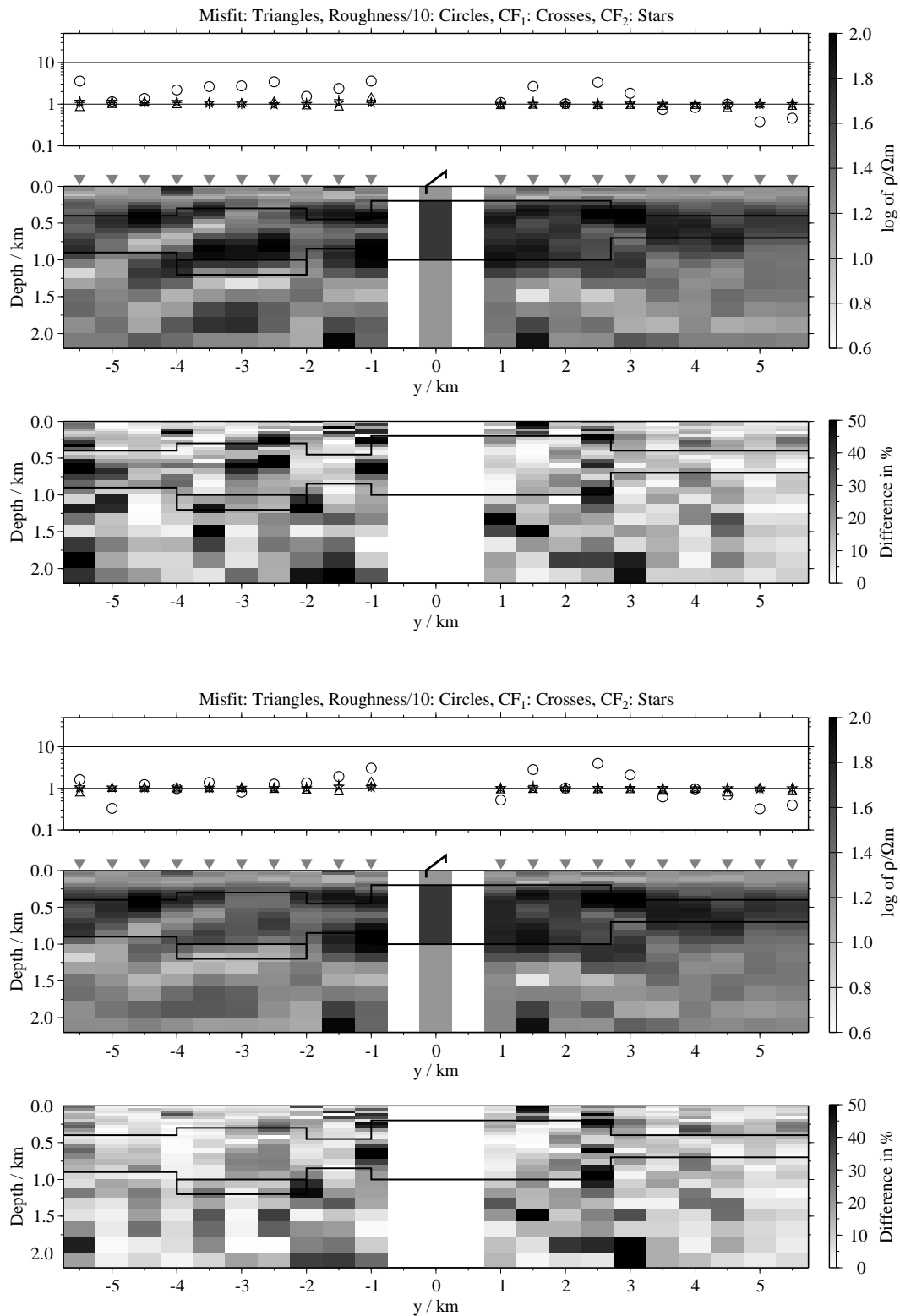


Figure B.275: Pseudo-sections of 1-D soft joint-inversions using the components \dot{H}_y and \dot{H}_{zi} , model M; Top panels: Average inversion results and relative differences (regularisation scheme C1); bottom: Average inversion results and relative differences (regularisation scheme C4);

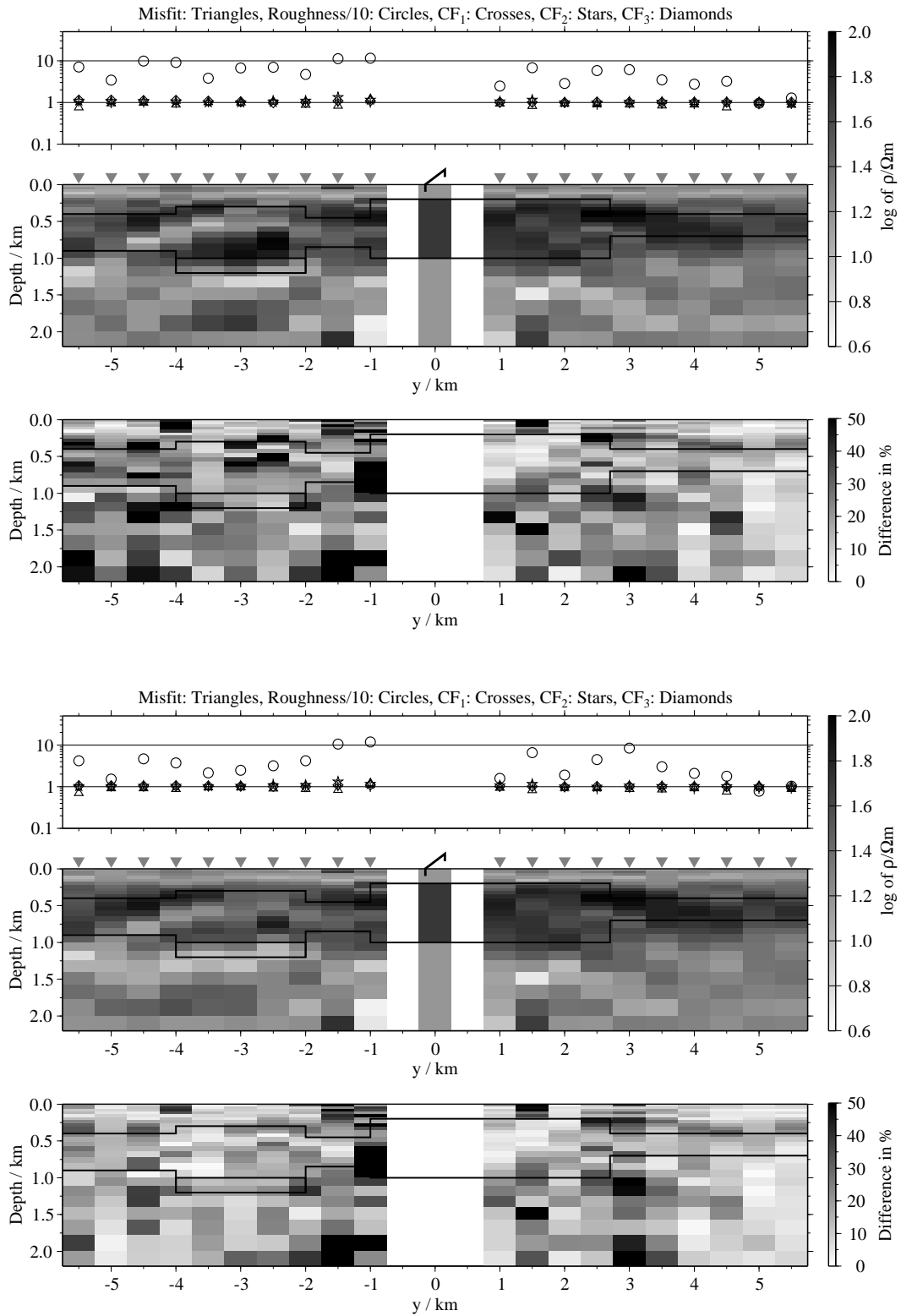


Figure B.276: Pseudo-sections of 1-D soft joint-inversions using all three components, model M; Top panels: Average inversion results and relative differences (regularisation scheme C1); bottom: Average inversion results and relative differences (regularisation scheme C4);

B.3 Inversions of synthetic SHOTEM data sets

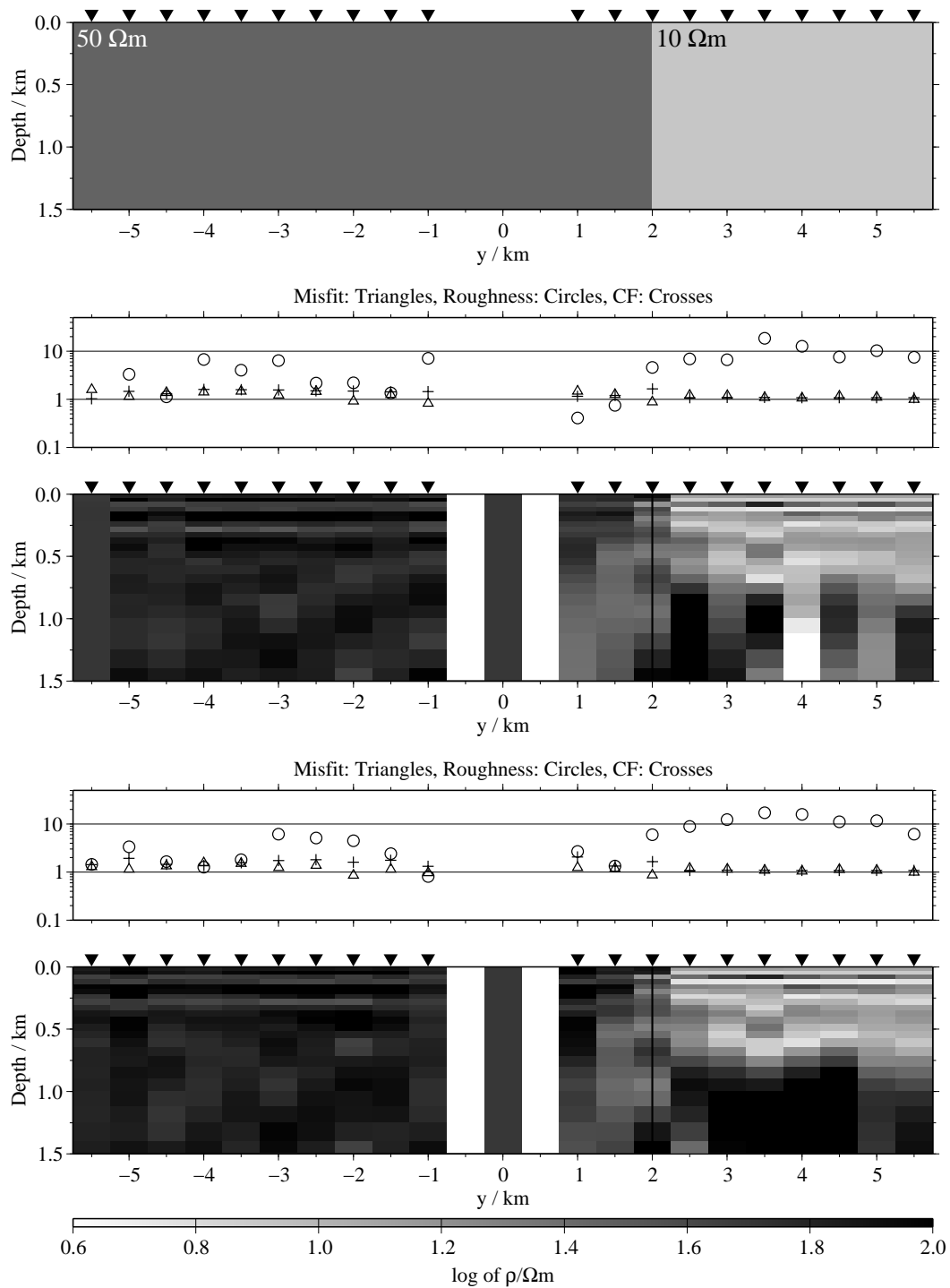


Figure B.277: Pseudo-sections of 1-D inversions of SHOTEM-transients simulated for model F3; from top to bottom: Original model, results using regularisation scheme C1, results using regularisation scheme C4;

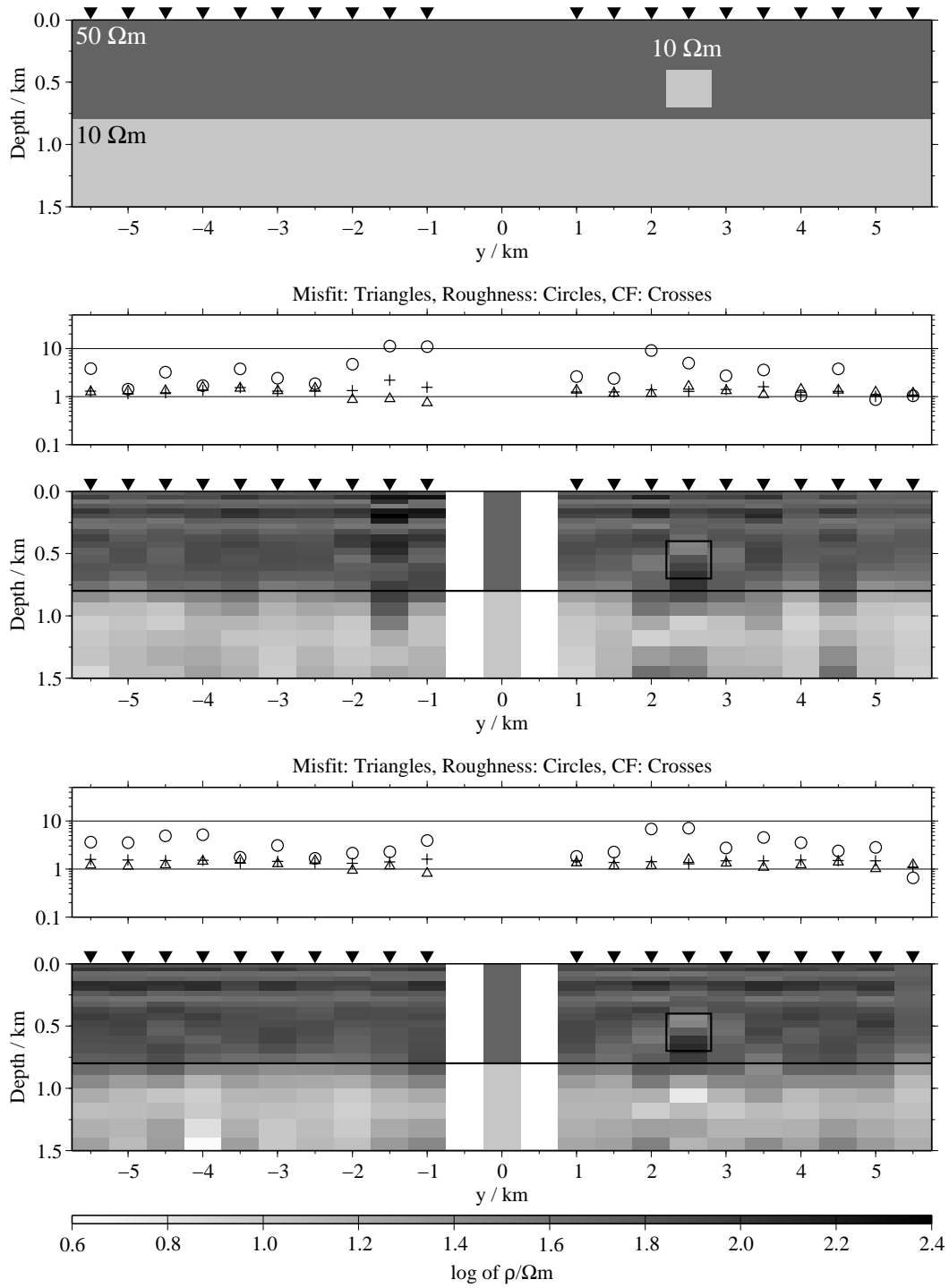


Figure B.278: Pseudo-sections of 1-D inversions of SHOTEM-transients simulated for model G2; from top to bottom: Original model, results using regularisation scheme C1, results using regularisation scheme C4;

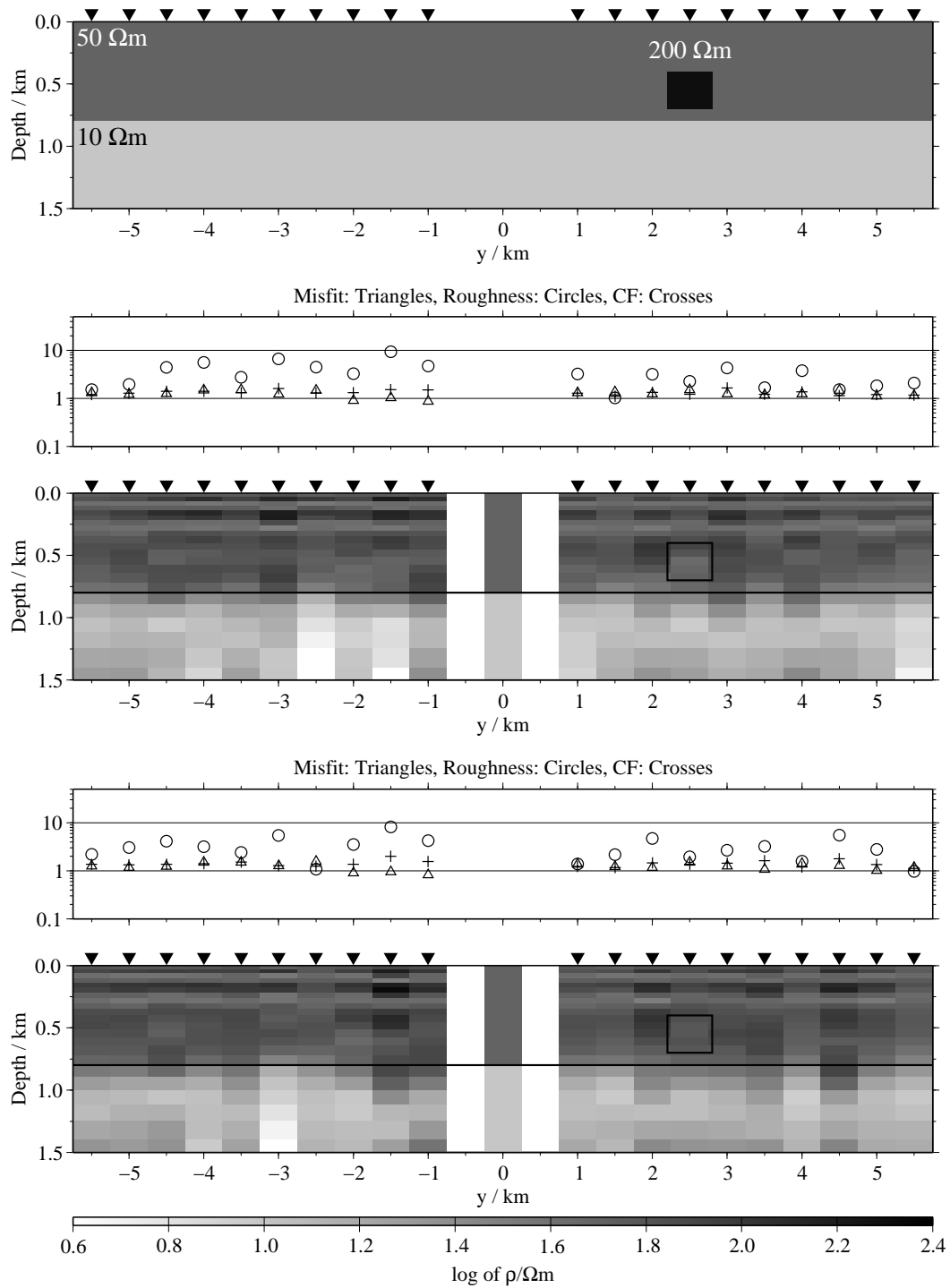


Figure B.279: Pseudo-sections of 1-D inversions of SHOTEM-transients simulated for model H2; from top to bottom: Original model, results using regularisation scheme C1, results using regularisation scheme C4;

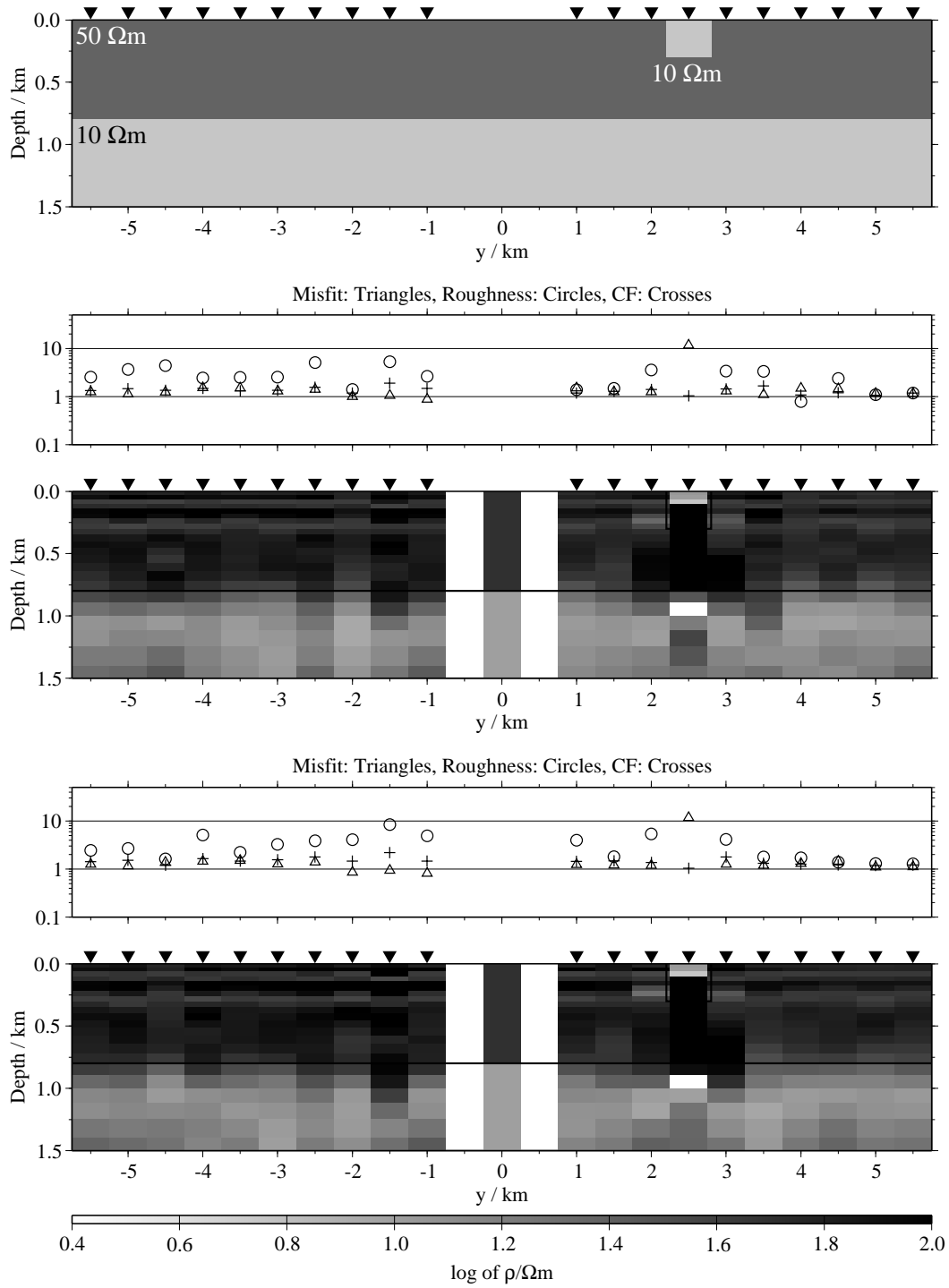


Figure B.280: Pseudo-sections of 1-D inversions of SHOTEM-transients simulated for model I2; from top to bottom: Original model, results using regularisation scheme C1, results using regularisation scheme C4;

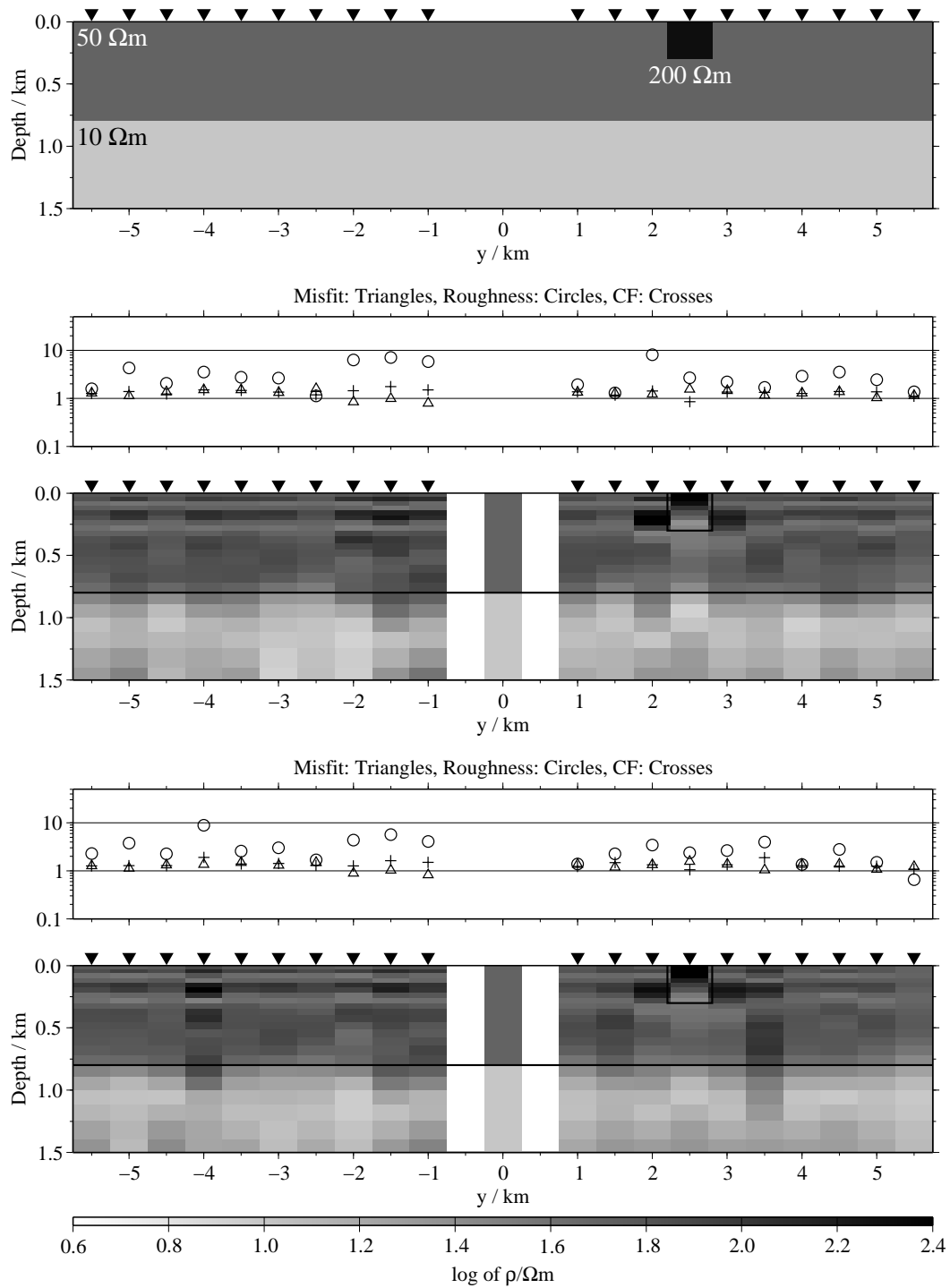


Figure B.281: Pseudo-sections of 1-D inversions of SHOTEM-transients simulated for model J2; from top to bottom: Original model, results using regularisation scheme C1, results using regularisation scheme C4;

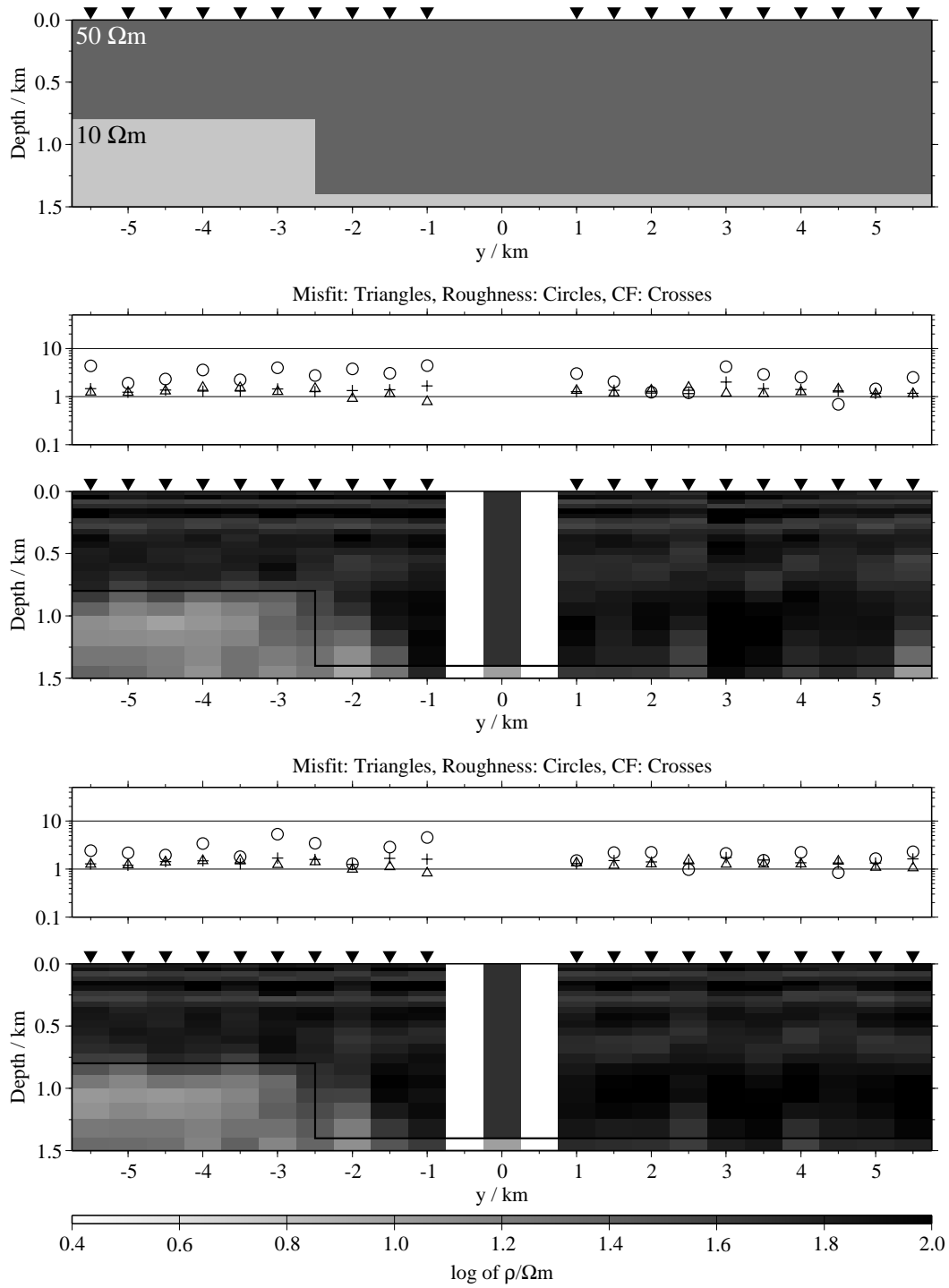


Figure B.282: Pseudo-sections of 1-D inversions of SHOTEM-transients simulated for model K1; from top to bottom: Original model, results using regularisation scheme C1, results using regularisation scheme C4;

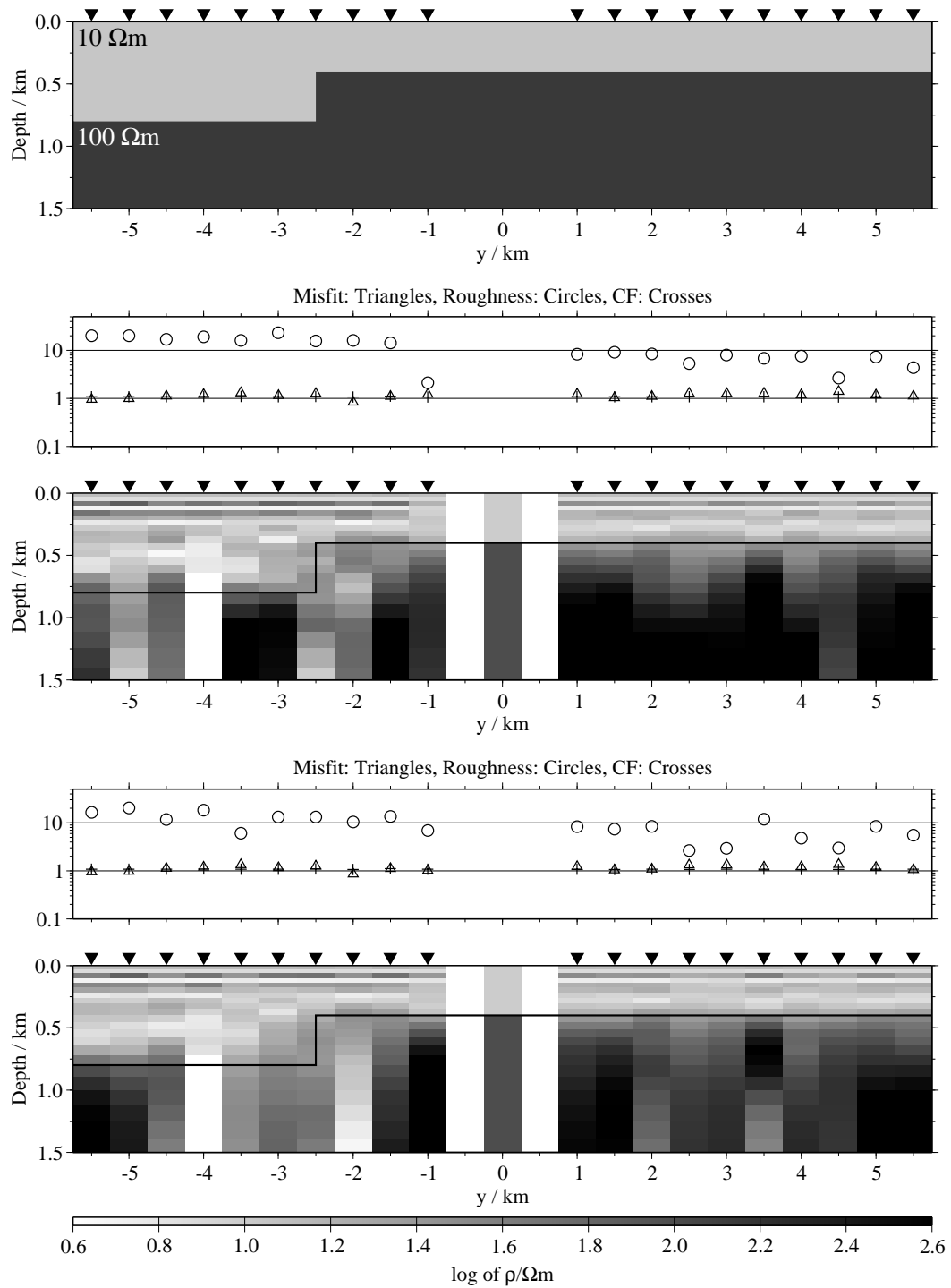


Figure B.283: Pseudo-sections of 1-D inversions of SHOTEM-transients simulated for model L1; from top to bottom: Original model, results using regularisation scheme C1, results using regularisation scheme C4;

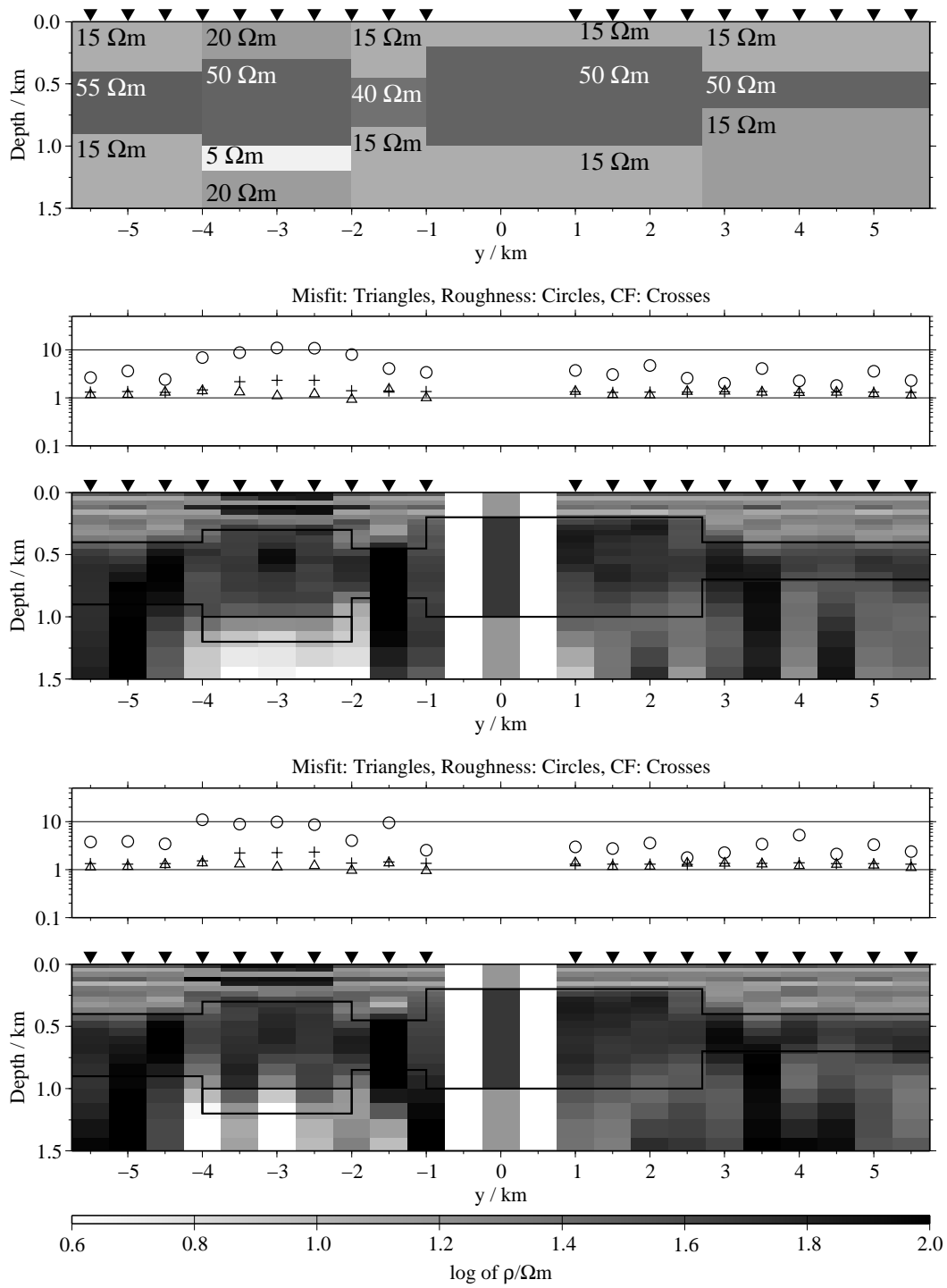


Figure B.284: Pseudo-sections of 1-D inversions of SHOTEM-transients simulated for model M_1 ; from top to bottom: Original model, results using regularisation scheme C1, results using regularisation scheme C4;

B.3.1 Joint-inversions of synthetic SHOTEM and LOTEM data sets

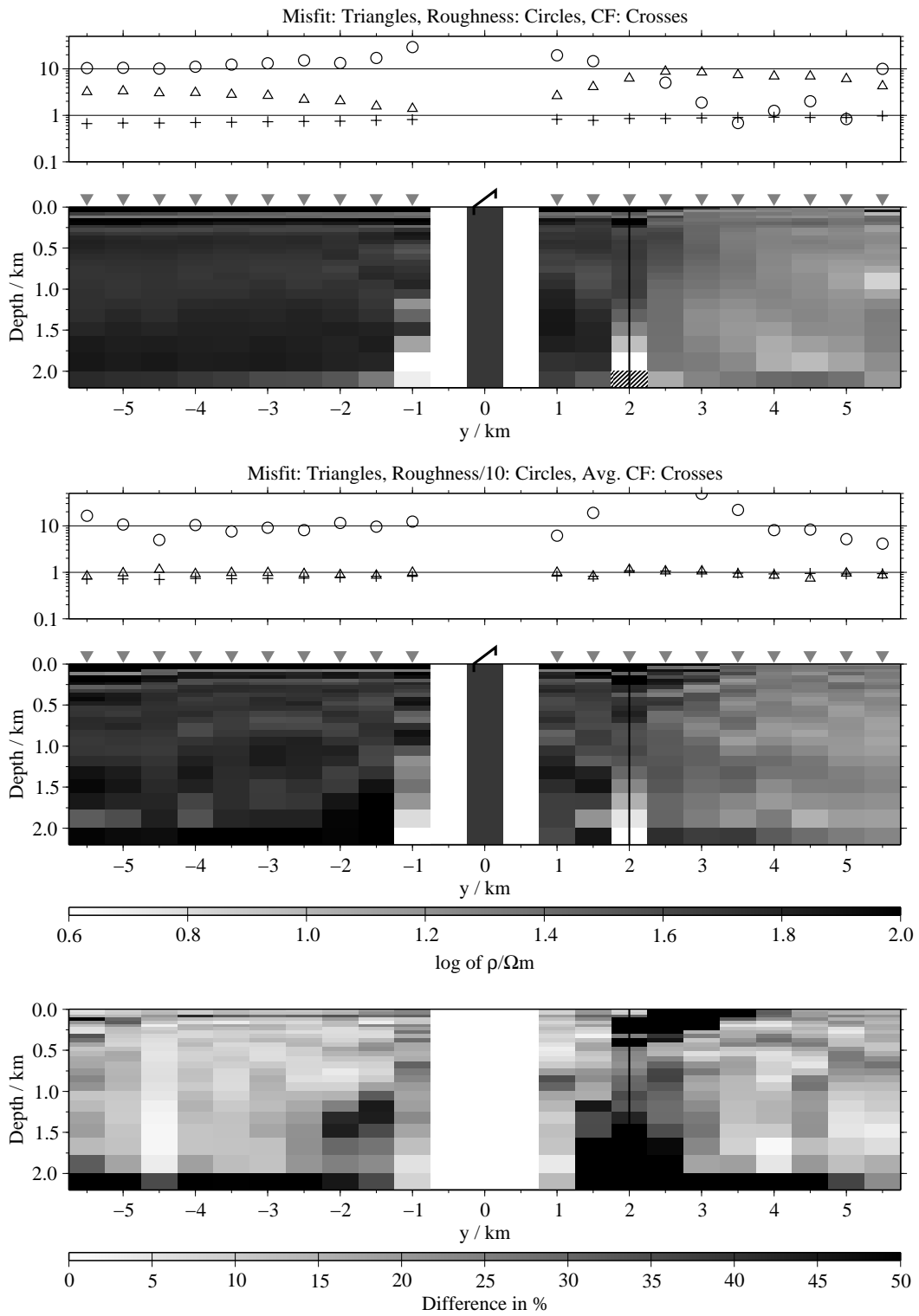


Figure B.285: Pseudo-sections of joint-inversion for the SHOTEM-transients and all three LOTEM data sets for regularisation scheme C1 and model F3; top panel: Results for the FJIs; bottom panels: Results for the SJs;

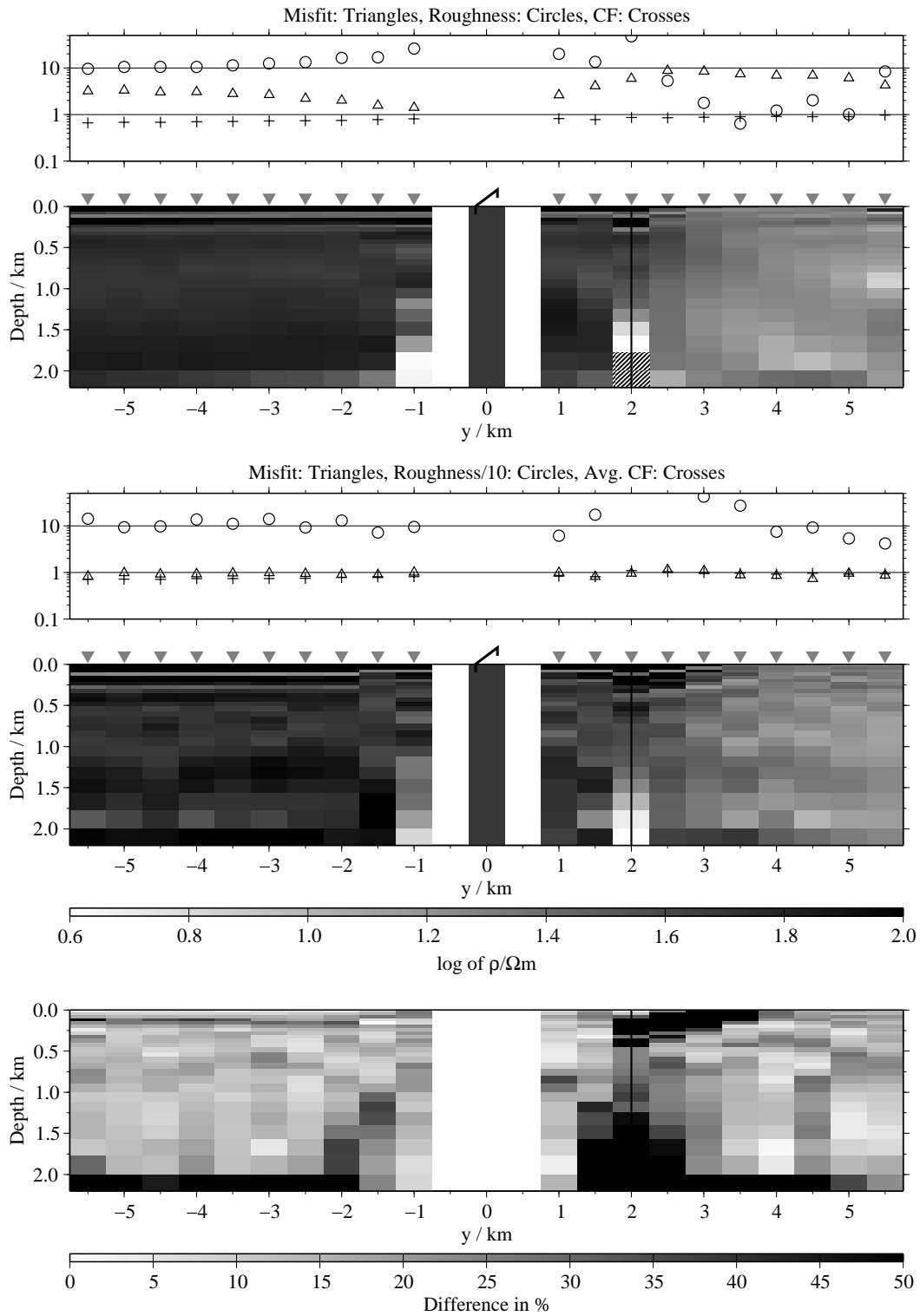


Figure B.286: Pseudo-sections of joint-inversion for the SHOTEM-transients and all three LOTEM data sets for regularisation scheme C4 and model F3; top panel: Results for the FJIs; bottom panels: Results for the SJIs;

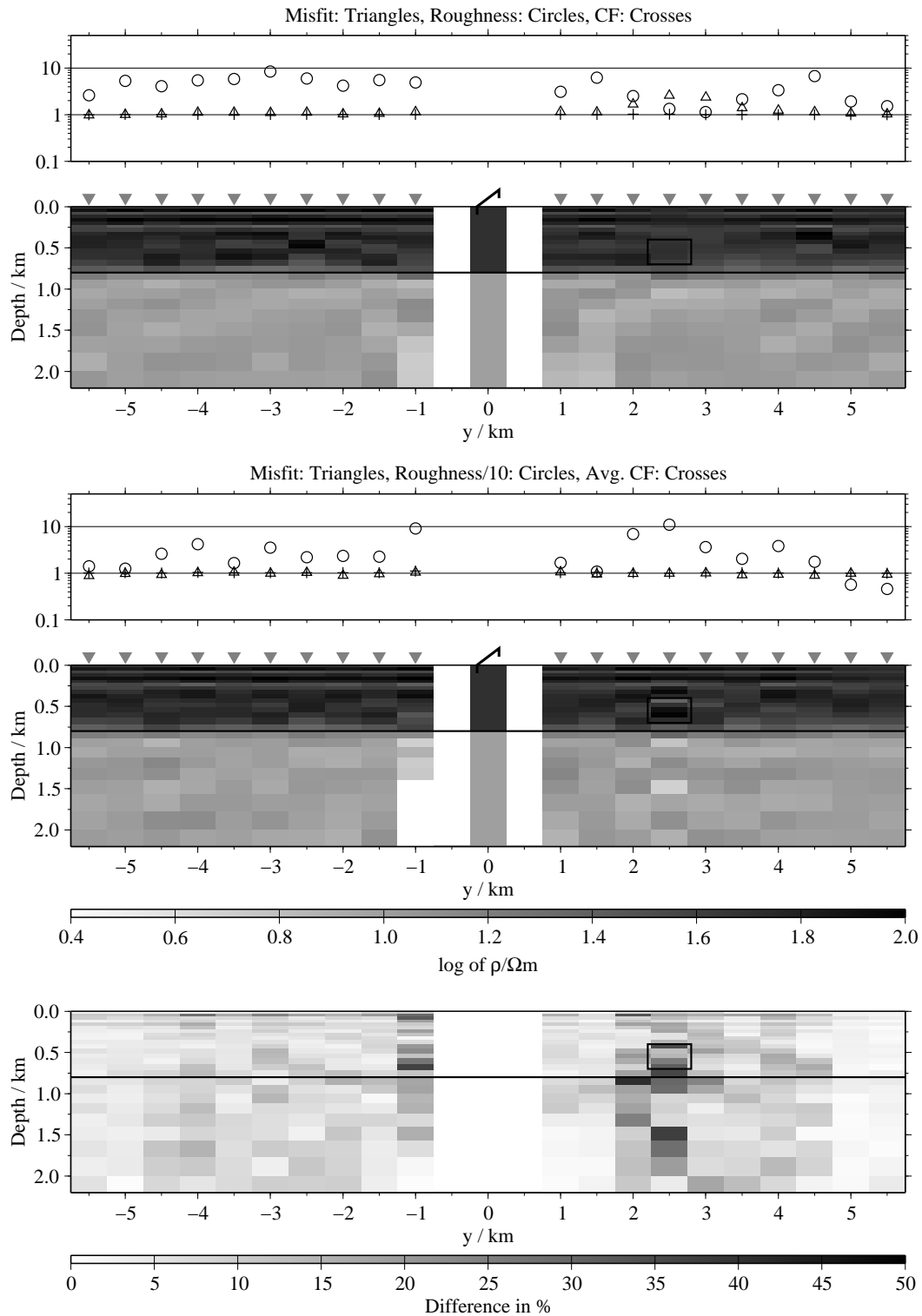


Figure B.287: Pseudo-sections of joint-inversion for the SHOTEM-transients and all three LOTEM data sets for regularisation scheme C1 and model G2; top panel: Results for the FJIs; bottom panels: Results for the SJI1s;

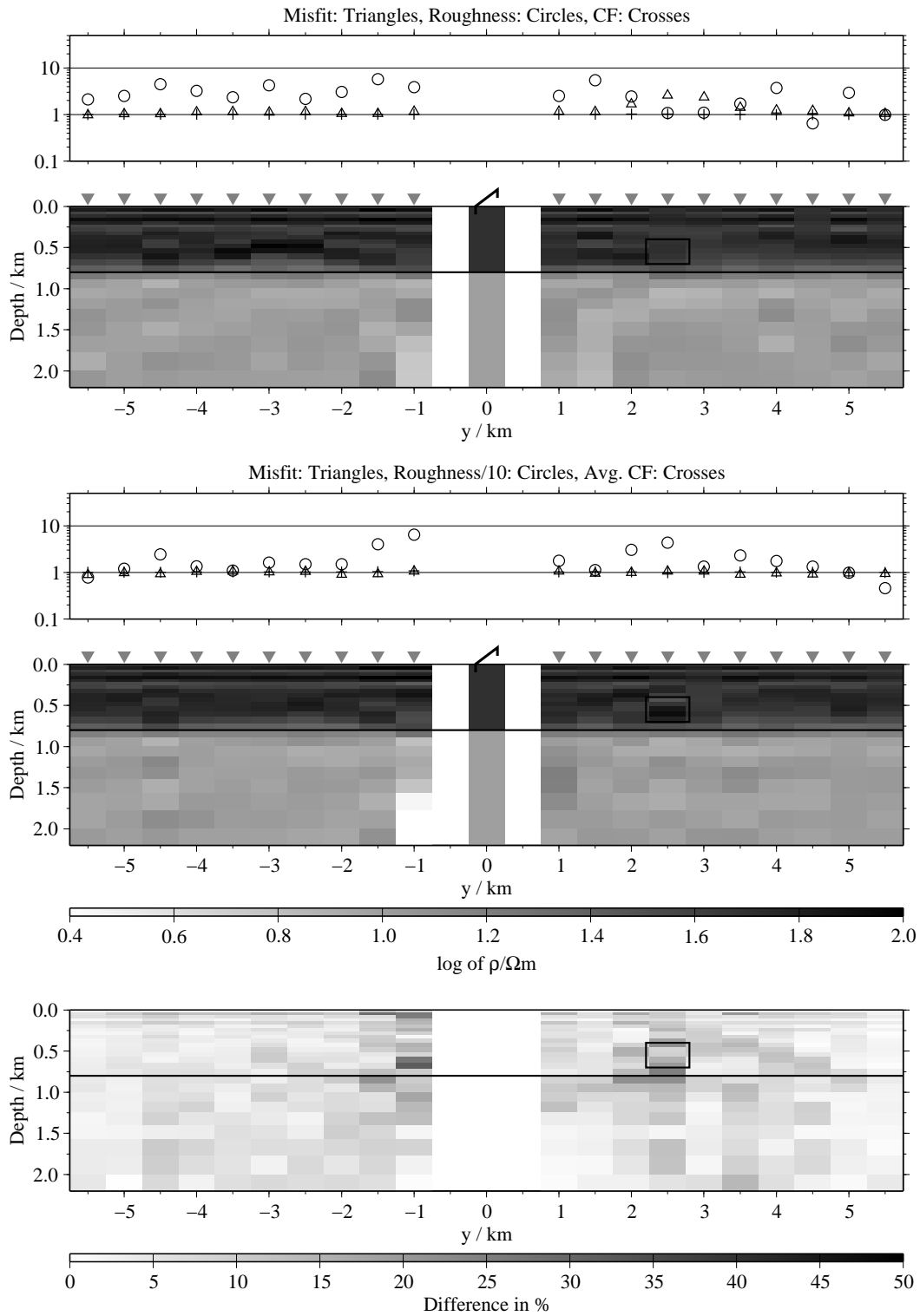


Figure B.288: Pseudo-sections of joint-inversion for the SHOTEM-transients and all three LOTEM data sets for regularisation scheme C4 and model G2; top panel: Results for the FJIs; bottom panels: Results for the SJIs;

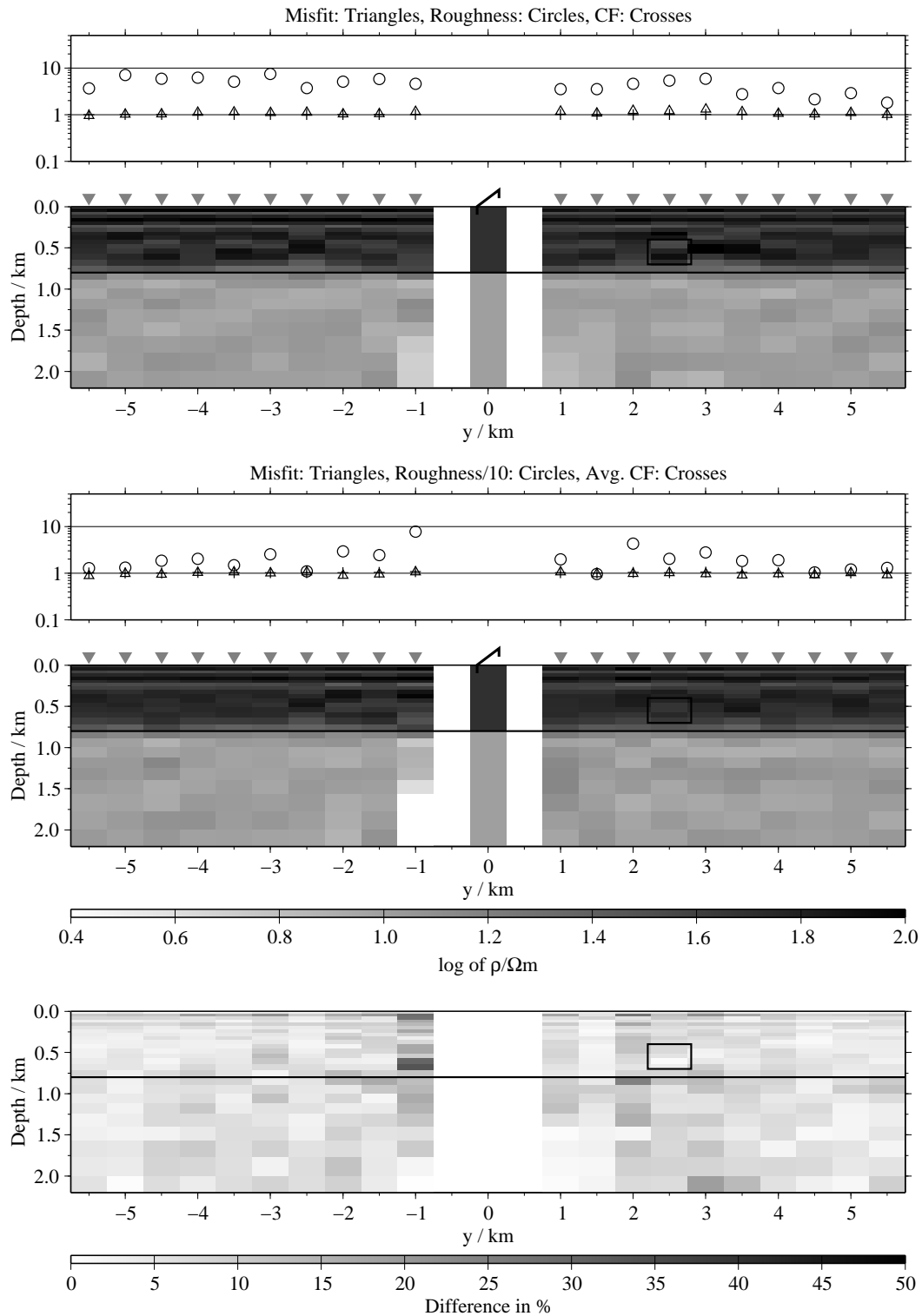


Figure B.289: Pseudo-sections of joint-inversion for the SHOTEM-transients and all three LOTEM data sets for regularisation scheme C1 and model H2; top panel: Results for the FJIs; bottom panels: Results for the SJIs;

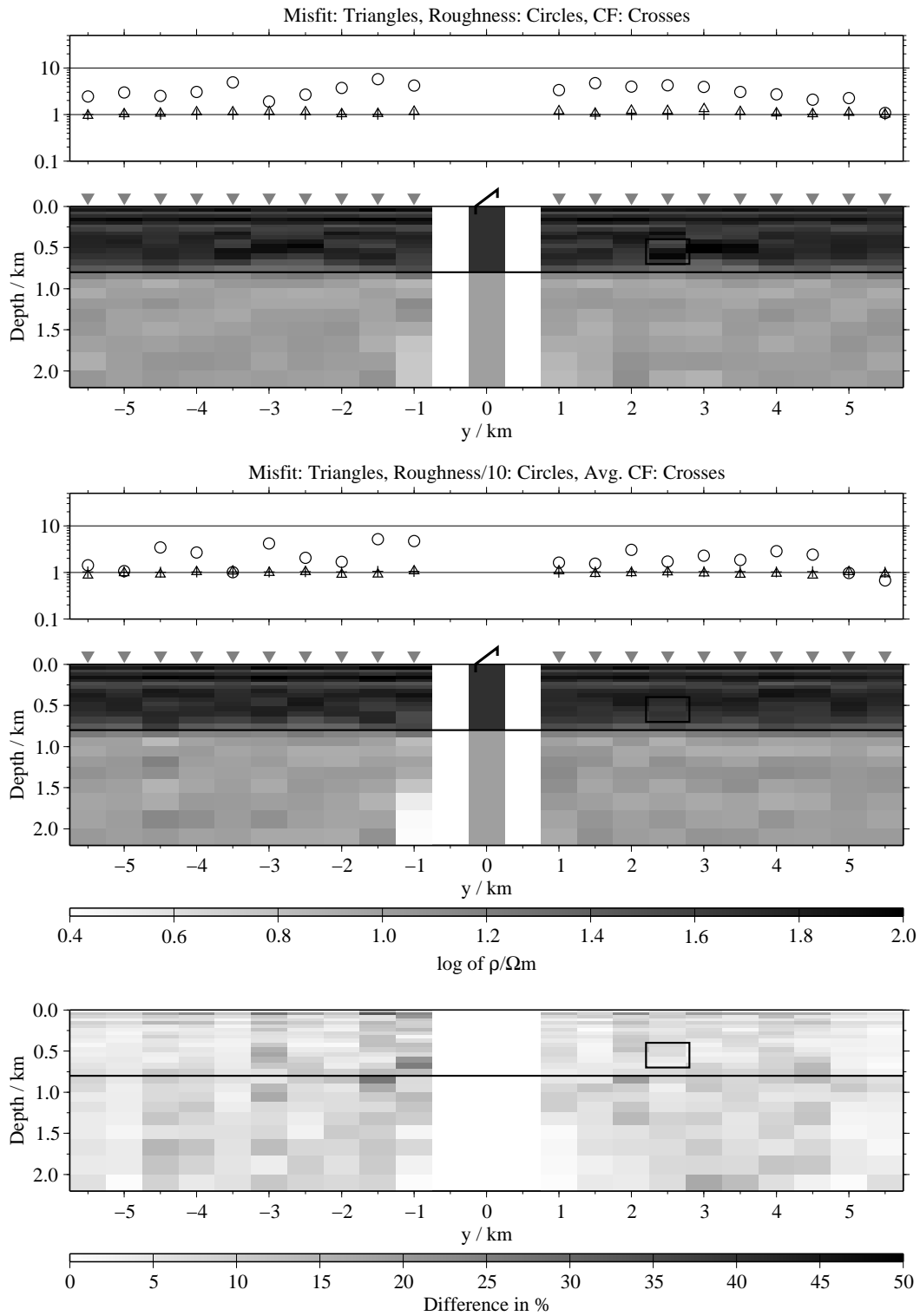


Figure B.290: Pseudo-sections of joint-inversion for the SHOTEM-transients and all three LOTEM data sets for regularisation scheme C4 and model H2; top panel: Results for the FJIs; bottom panels: Results for the SJI1s;

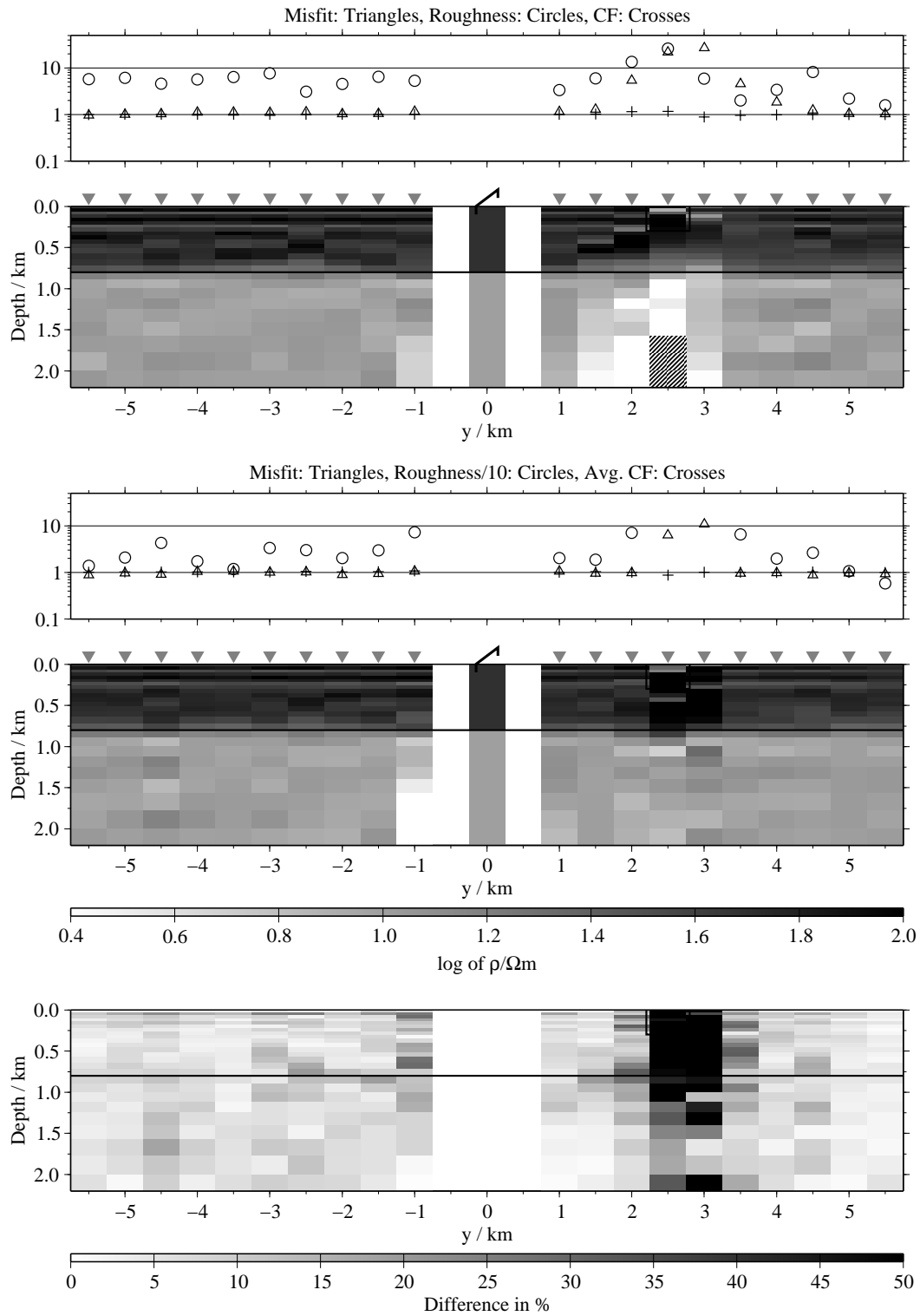


Figure B.291: Pseudo-sections of joint-inversion for the SHOTEM-transients and all three LOTEM data sets for regularisation scheme C1 and model I2; top panel: Results for the FJIs; bottom panels: Results for the SJIs;

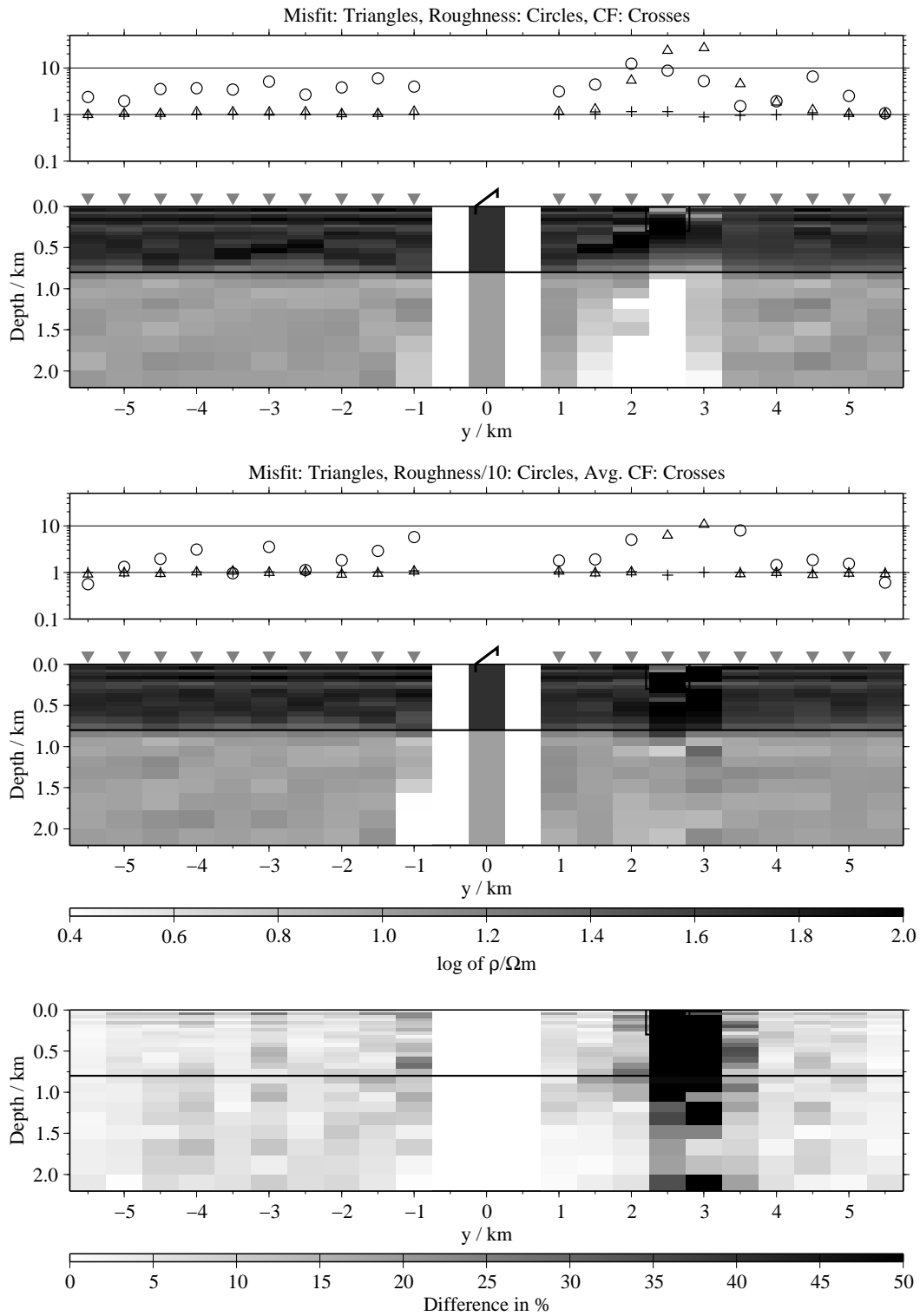


Figure B.292: Pseudo-sections of joint-inversion for the SHOTEM-transients and all three LOTEM data sets for regularisation scheme C4 and model I2; top panel: Results for the FJIs; bottom panels: Results for the SJI1s;

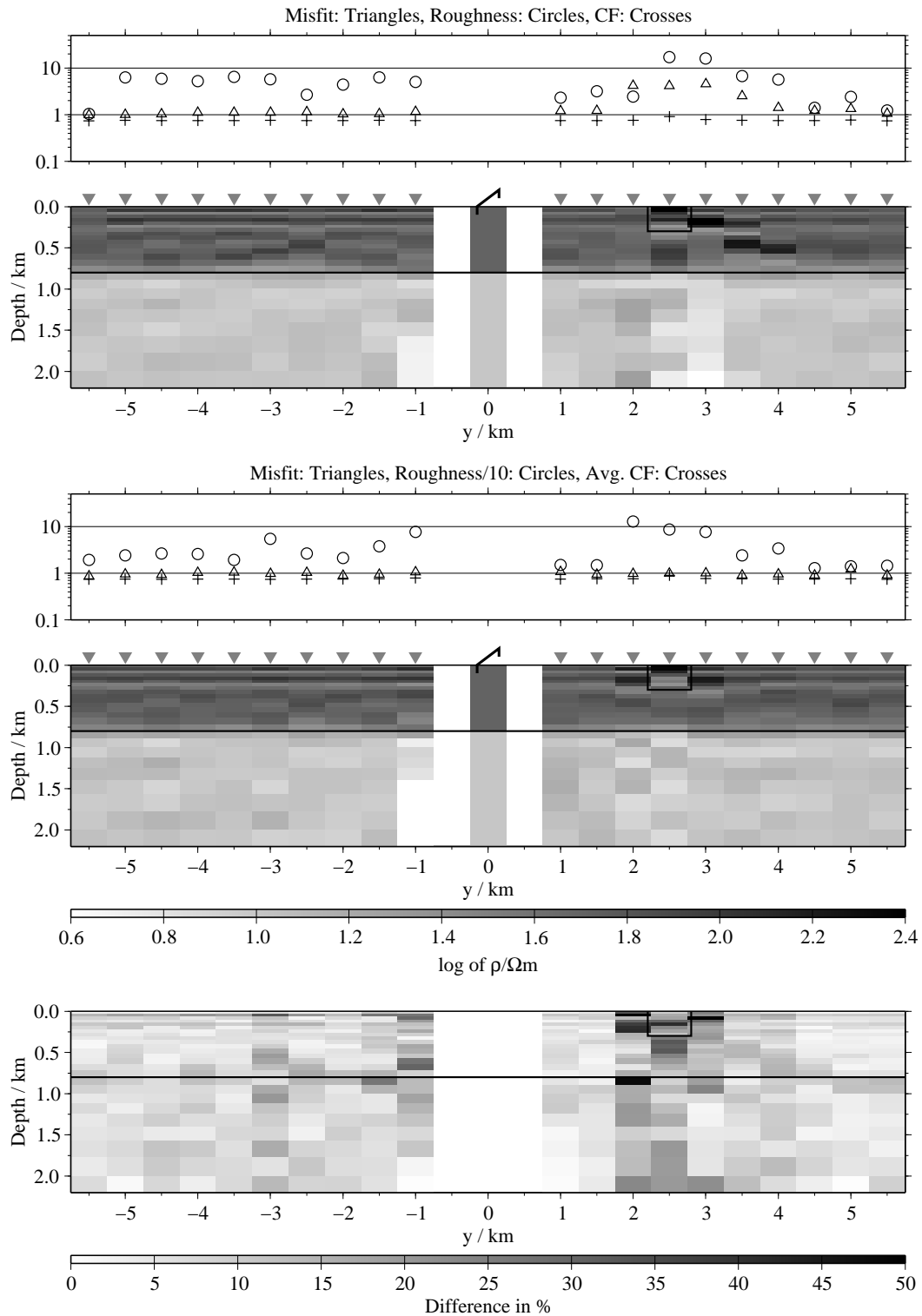


Figure B.293: Pseudo-sections of joint-inversion for the SHOTEM-transients and all three LOTEM data sets for regularisation scheme C1 and model J2; top panel: Results for the FJIs; bottom panels: Results for the SJIs;

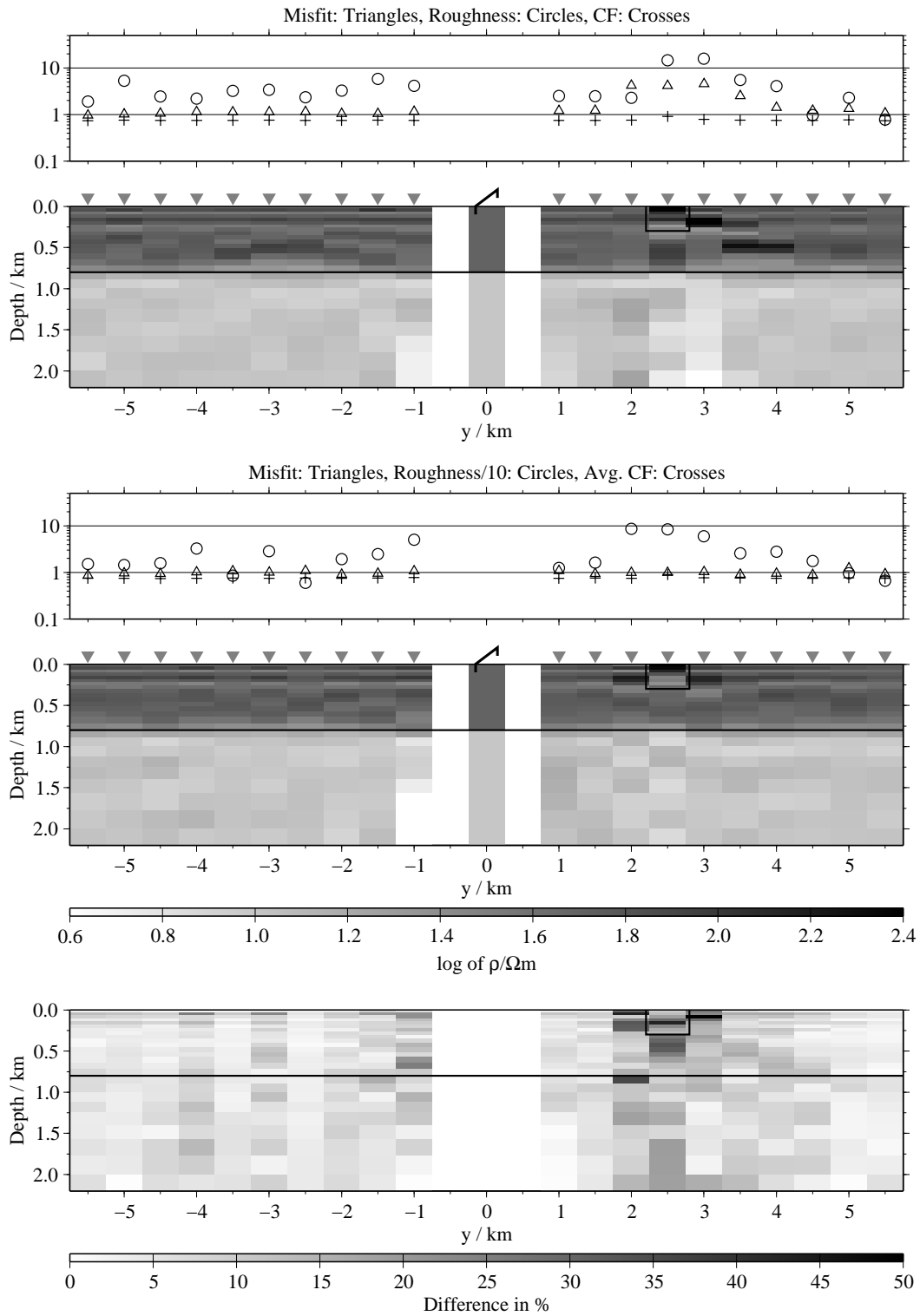


Figure B.294: Pseudo-sections of joint-inversion for the SHOTEM-transients and all three LOTEM data sets for regularisation scheme C4 and model J2; top panel: Results for the FJIs; bottom panels: Results for the SJI1s;

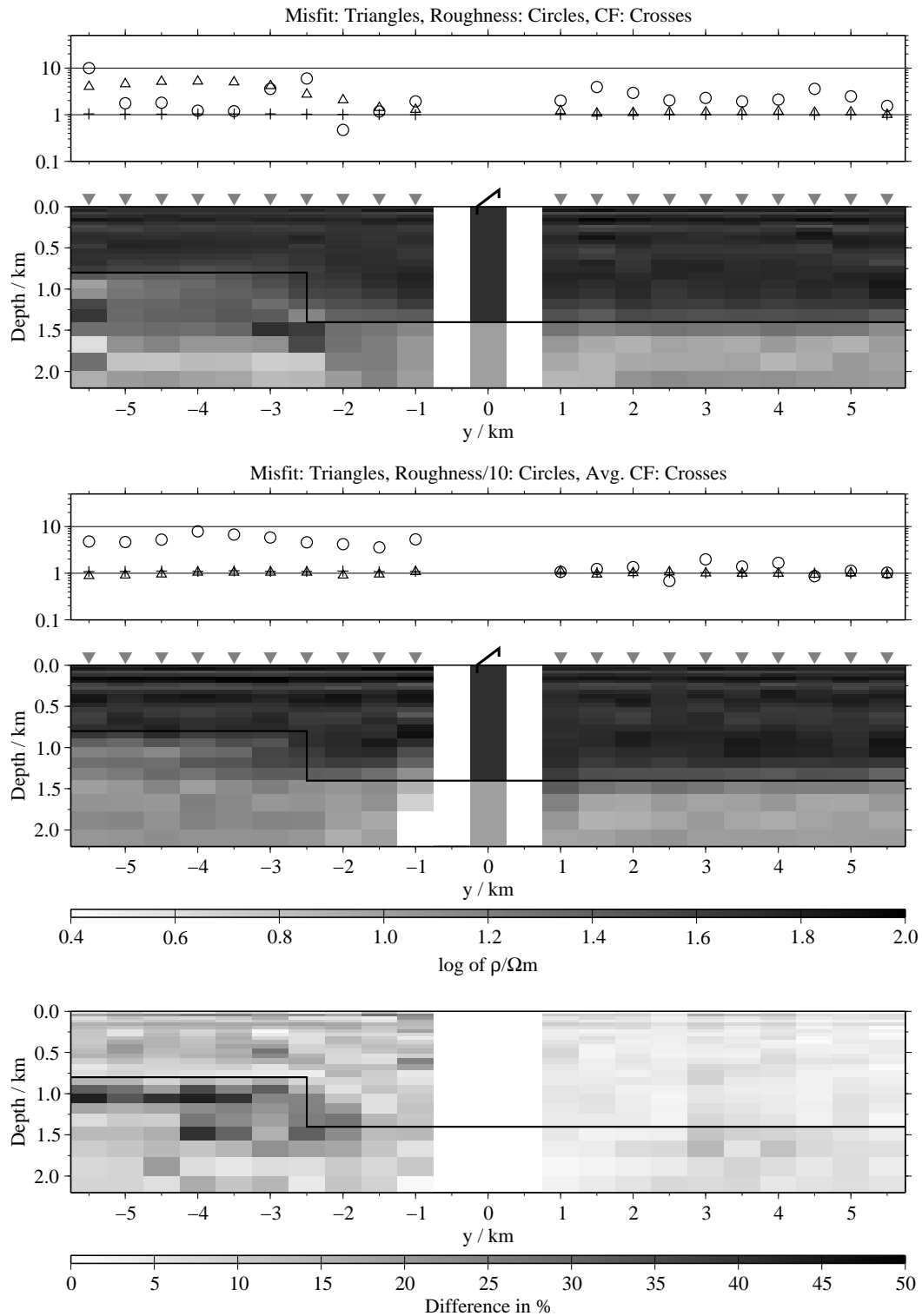


Figure B.295: Pseudo-sections of joint-inversion for the SHOTEM-transients and all three LOTEM data sets for regularisation scheme C1 and model K1; top panel: Results for the FJIs; bottom panels: Results for the SJI1s;

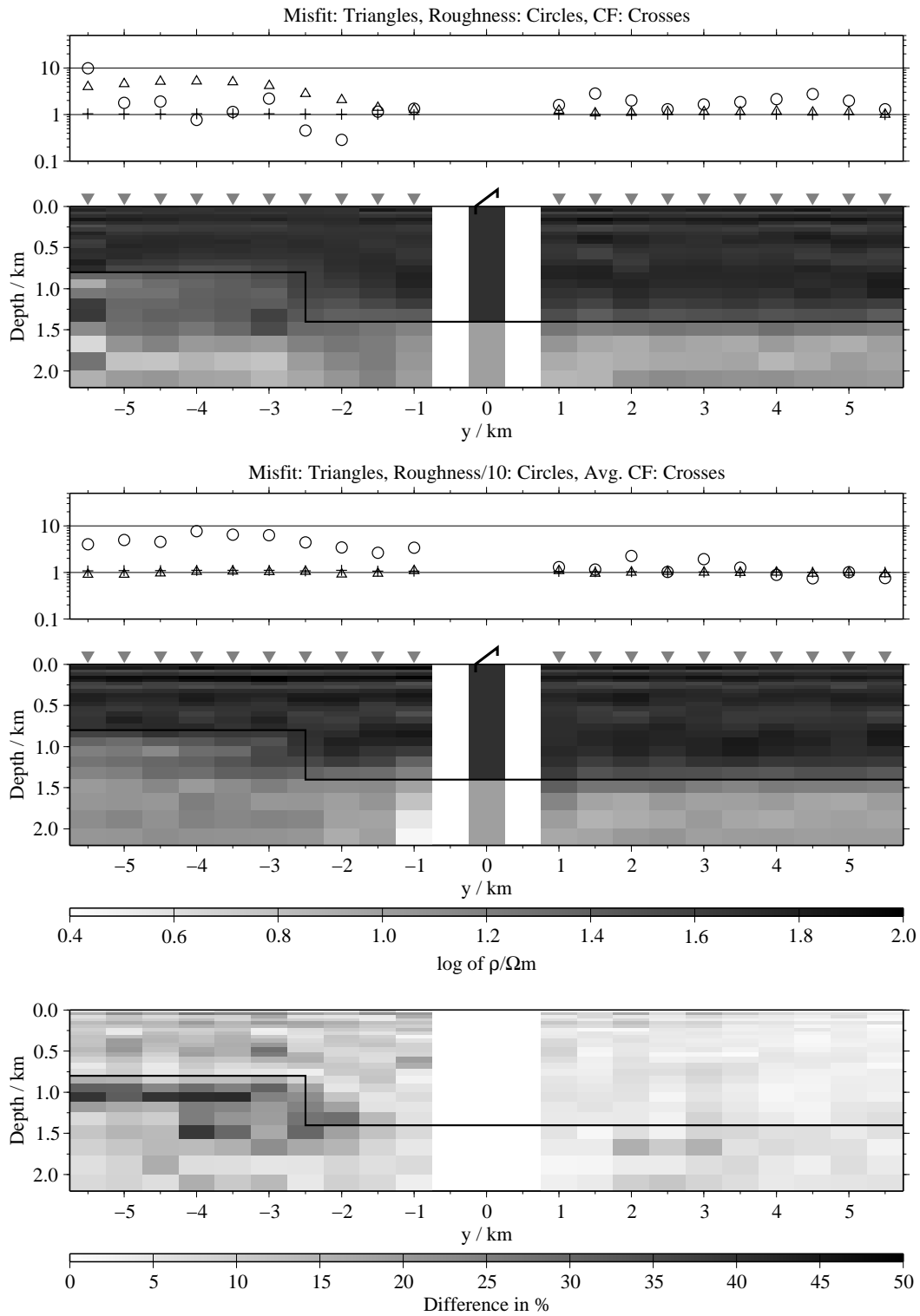


Figure B.296: Pseudo-sections of joint-inversion for the SHOTEM-transients and all three LOTEM data sets for regularisation scheme C4 and model K1; top panel: Results for the FJIs; bottom panels: Results for the SJI1s;

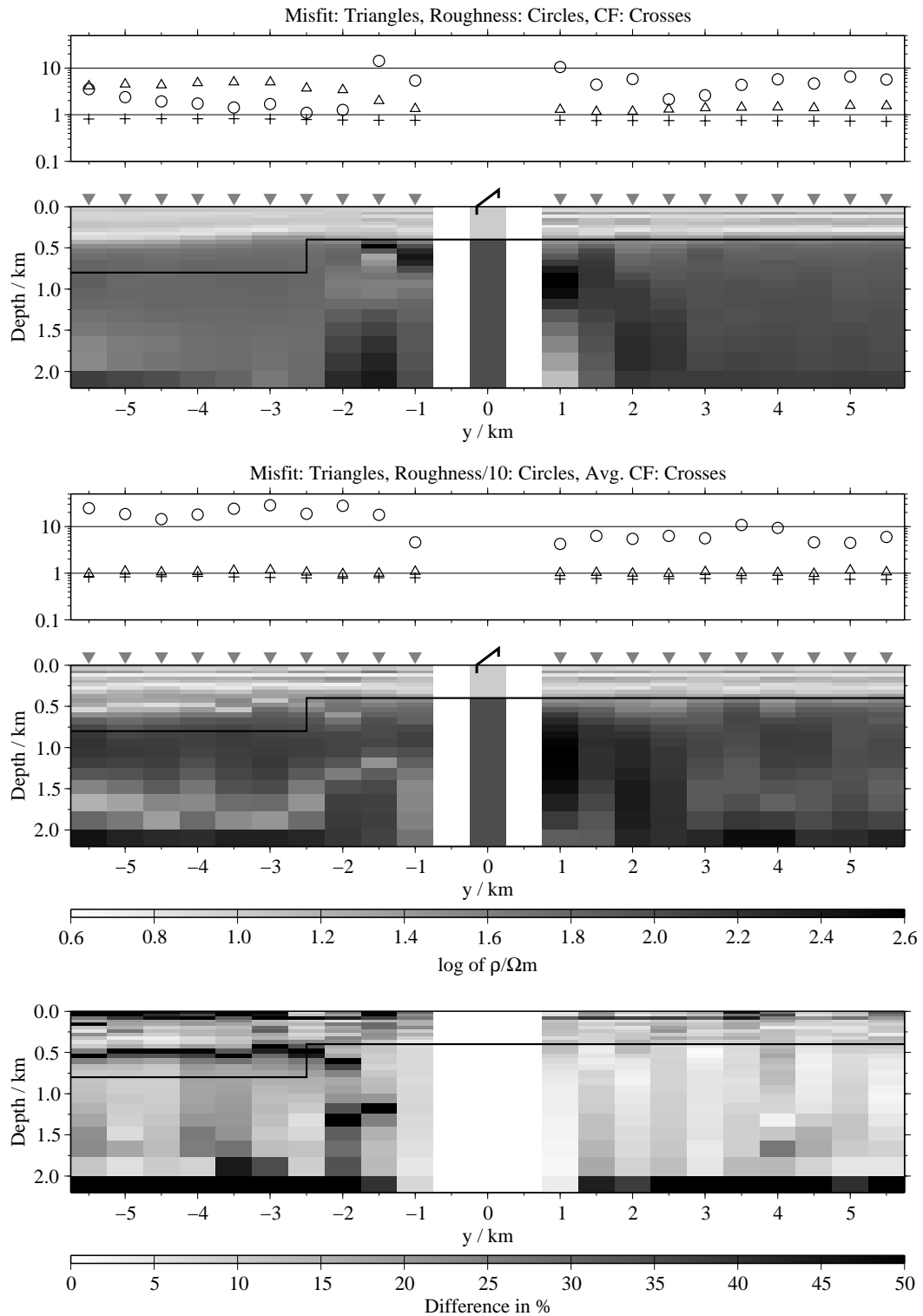


Figure B.297: Pseudo-sections of joint-inversion for the SHOTEM-transients and all three LOTEM data sets for regularisation scheme C1 and model L1; top panel: Results for the FJIs; bottom panels: Results for the SJIs;

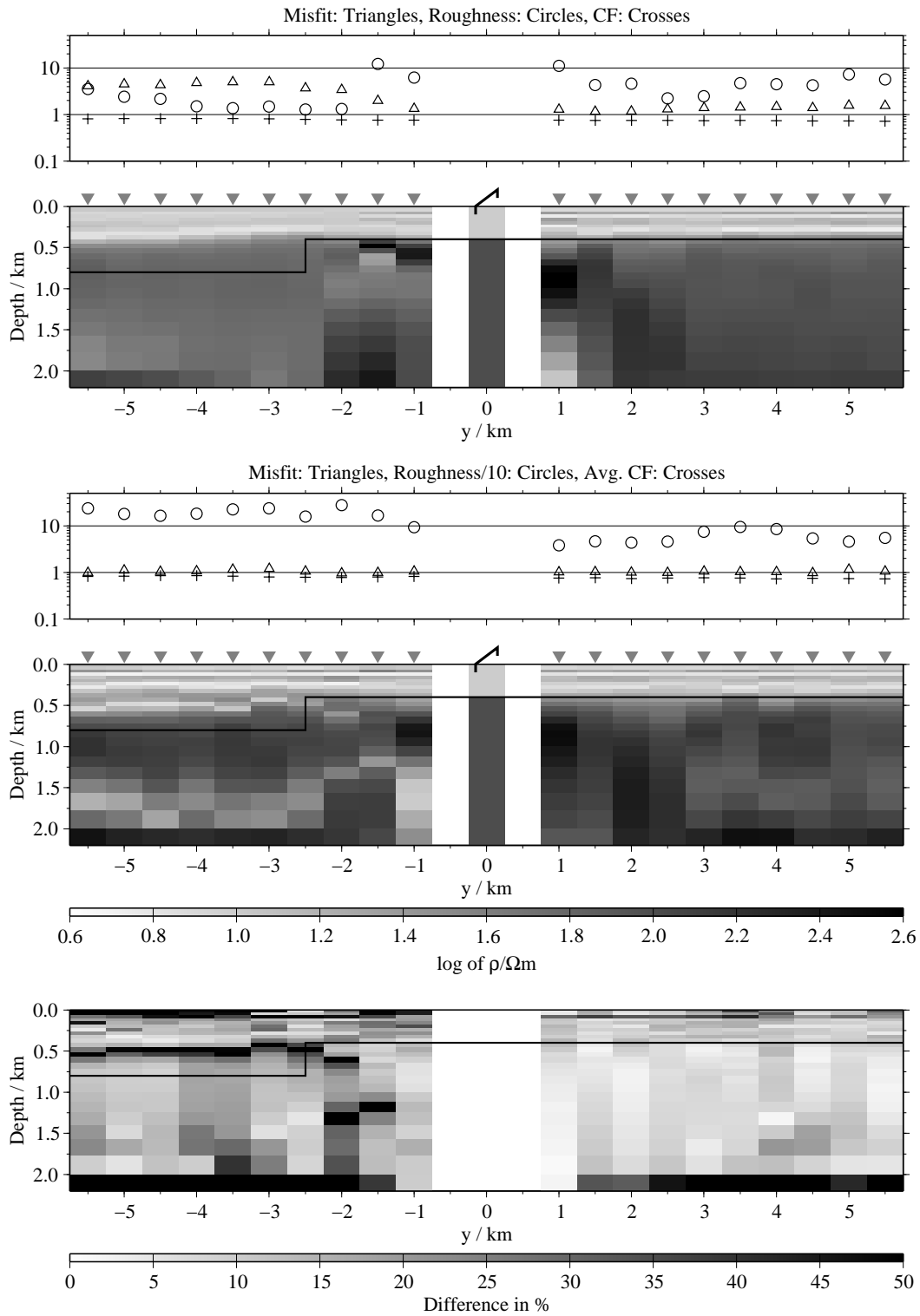


Figure B.298: Pseudo-sections of joint-inversion for the SHOTEM-transients and all three LOTEM data sets for regularisation scheme C4 and model L1; top panel: Results for the FJIs; bottom panels: Results for the SJI1s;

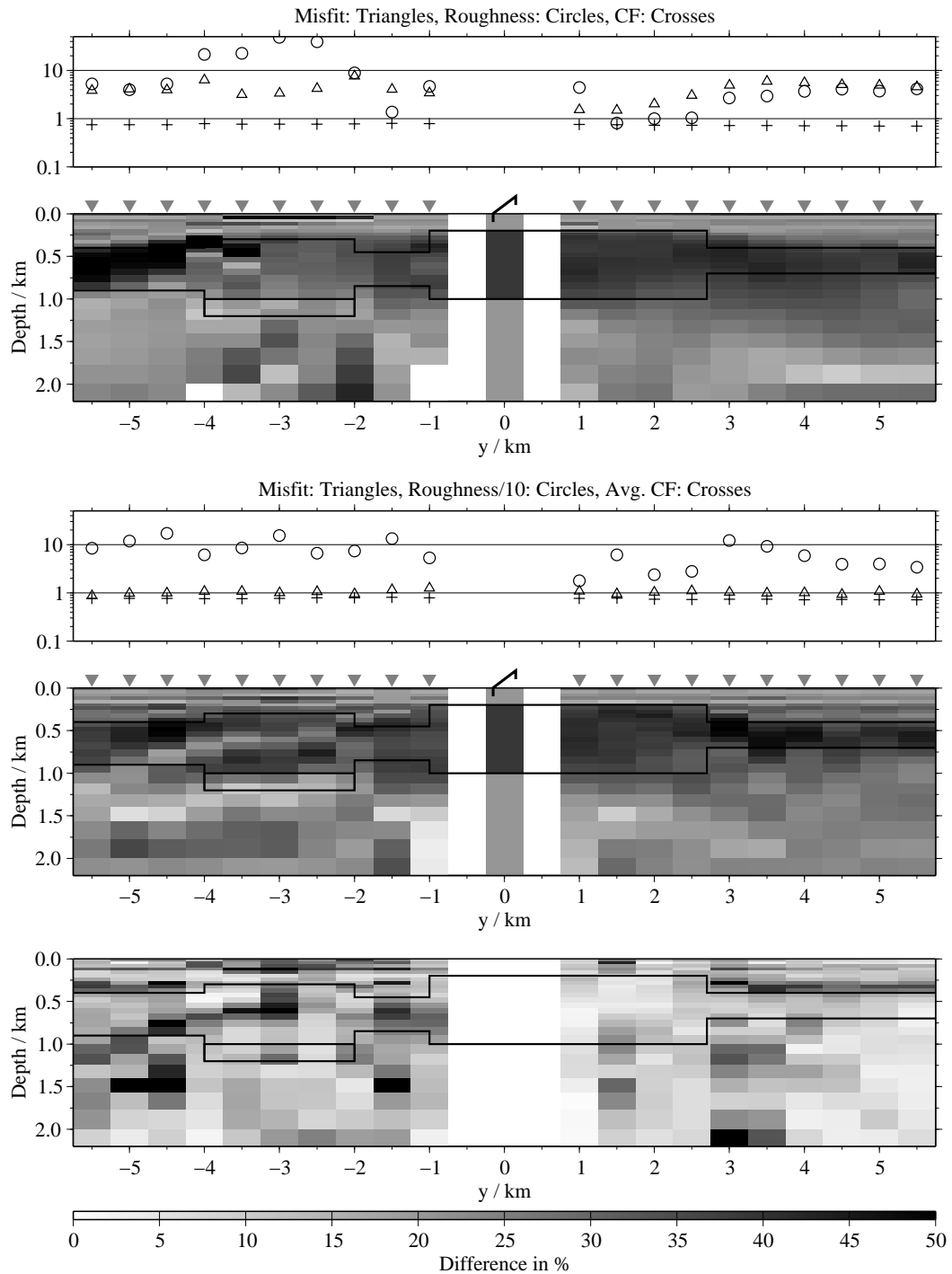


Figure B.299: Pseudo-sections of joint-inversion for the SHOTEM-transients and all three LOTEM data sets for regularisation scheme C1 and model M; top panel: Results for the FJIs; bottom panels: Results for the SJIs;

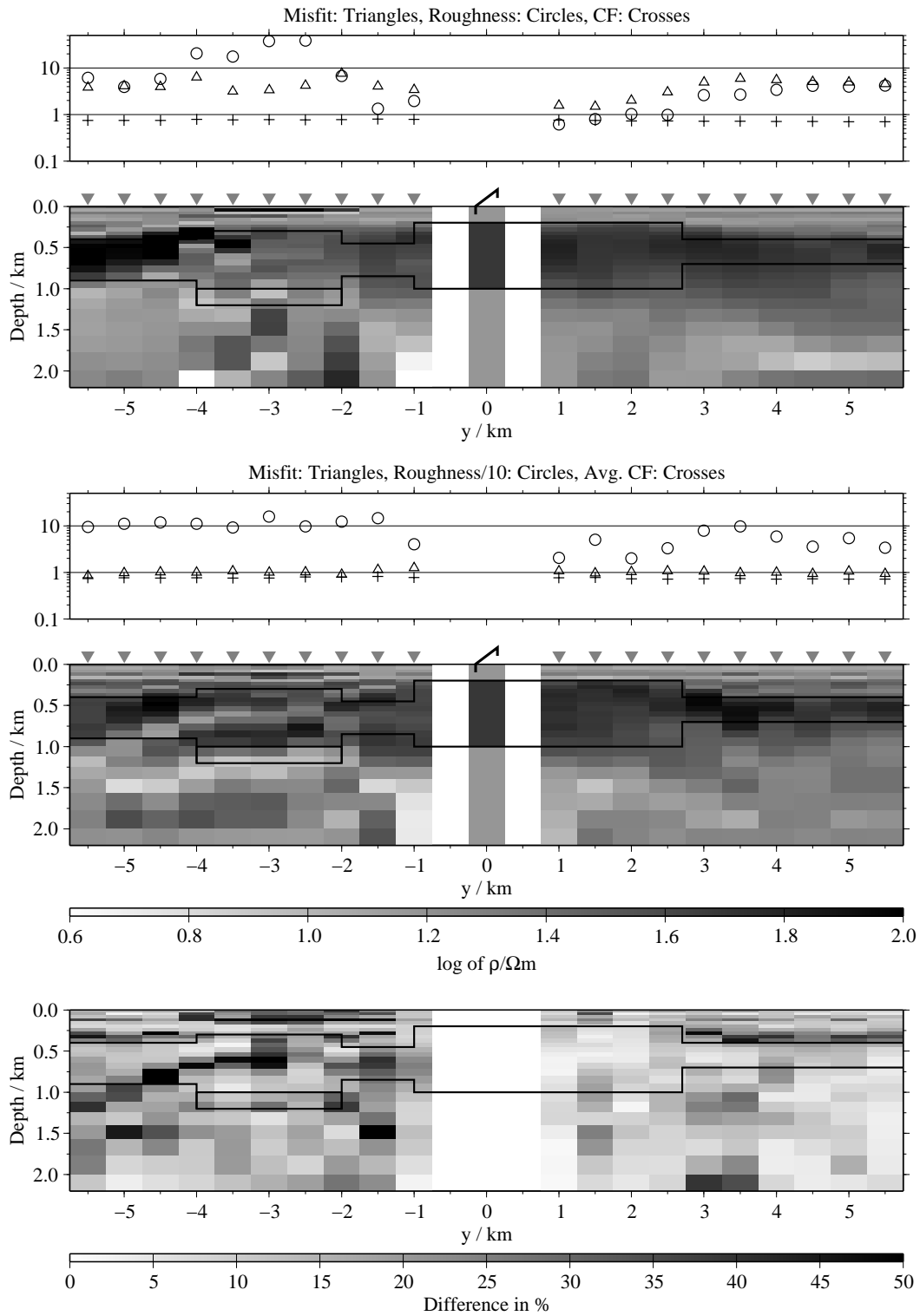
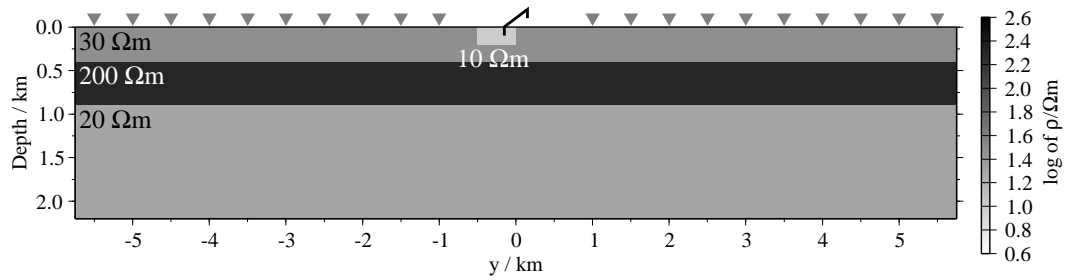


Figure B.300: Pseudo-sections of joint-inversion for the SHOTEM-transients and all three LOTEM data sets for regularisation scheme C4 and model M; top panel: Results for the FJIs; bottom panels: Results for the SJI1s;

B.4 Shallow patch close to the Tx (models N1 and N2)

Model N1:



Model N2:

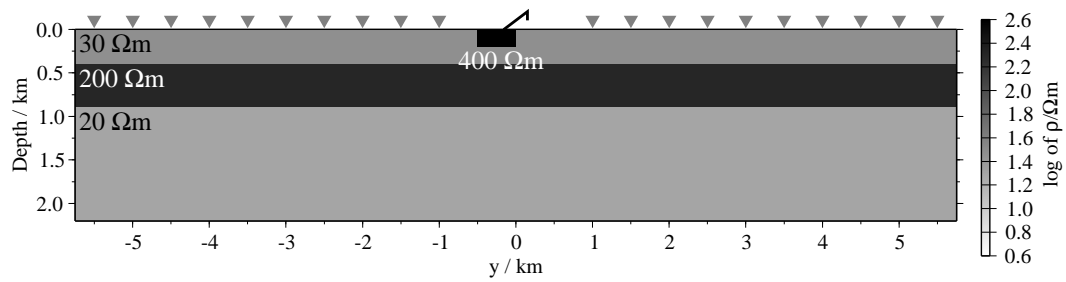


Figure B.301: Model with shallow conductive (model N1) or resistive (model N2) patch close to the Tx; the mid-point of the patches is in both cases at $x = y = -250$ m. The patches have the size $500 \times 500 \times 200$ m³.

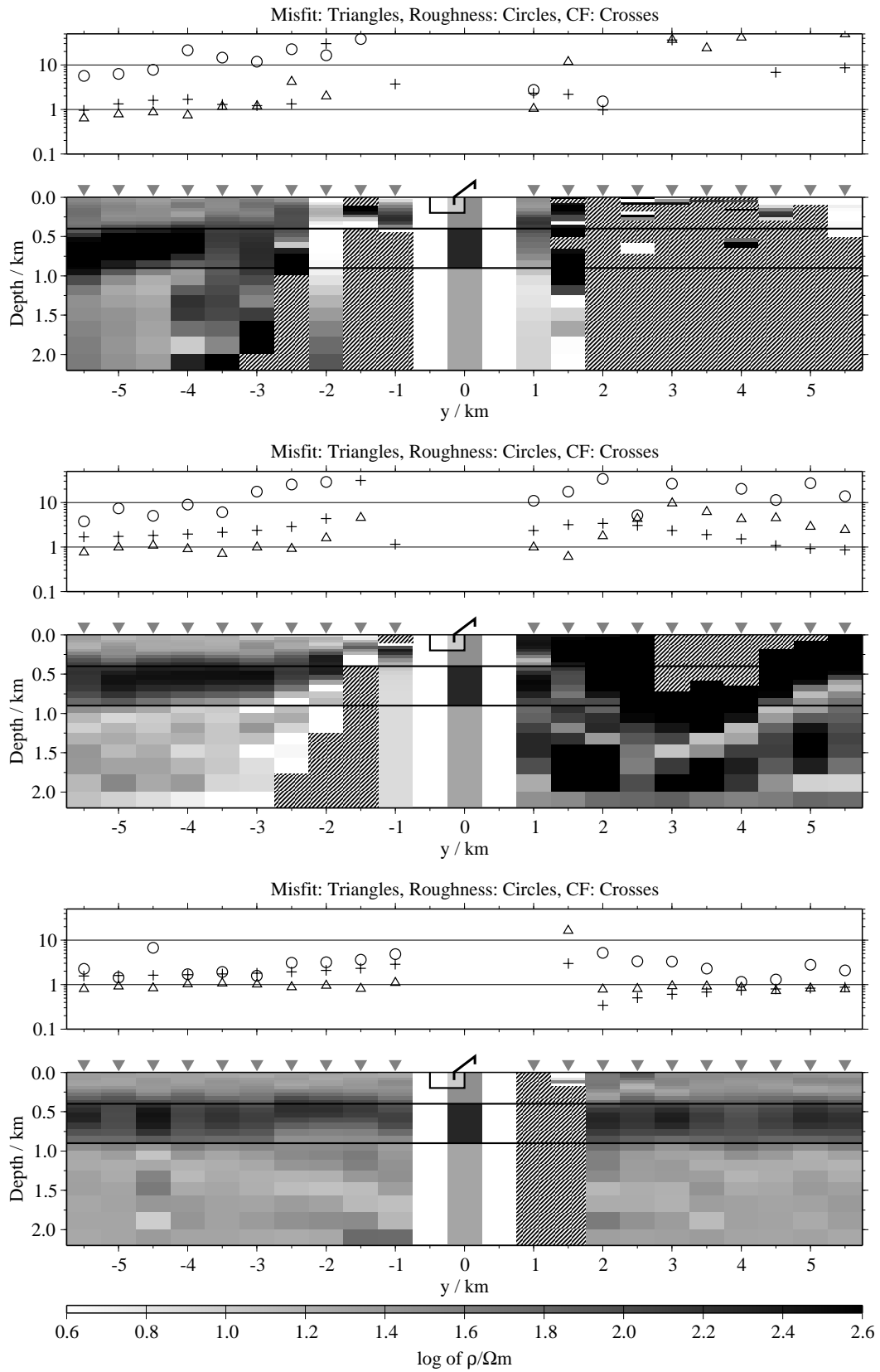


Figure B.302: Pseudo-sections of single 1-D inversion, model N1, regularisation scheme C1; from top to bottom E_x -, H_y - and H_z -component;

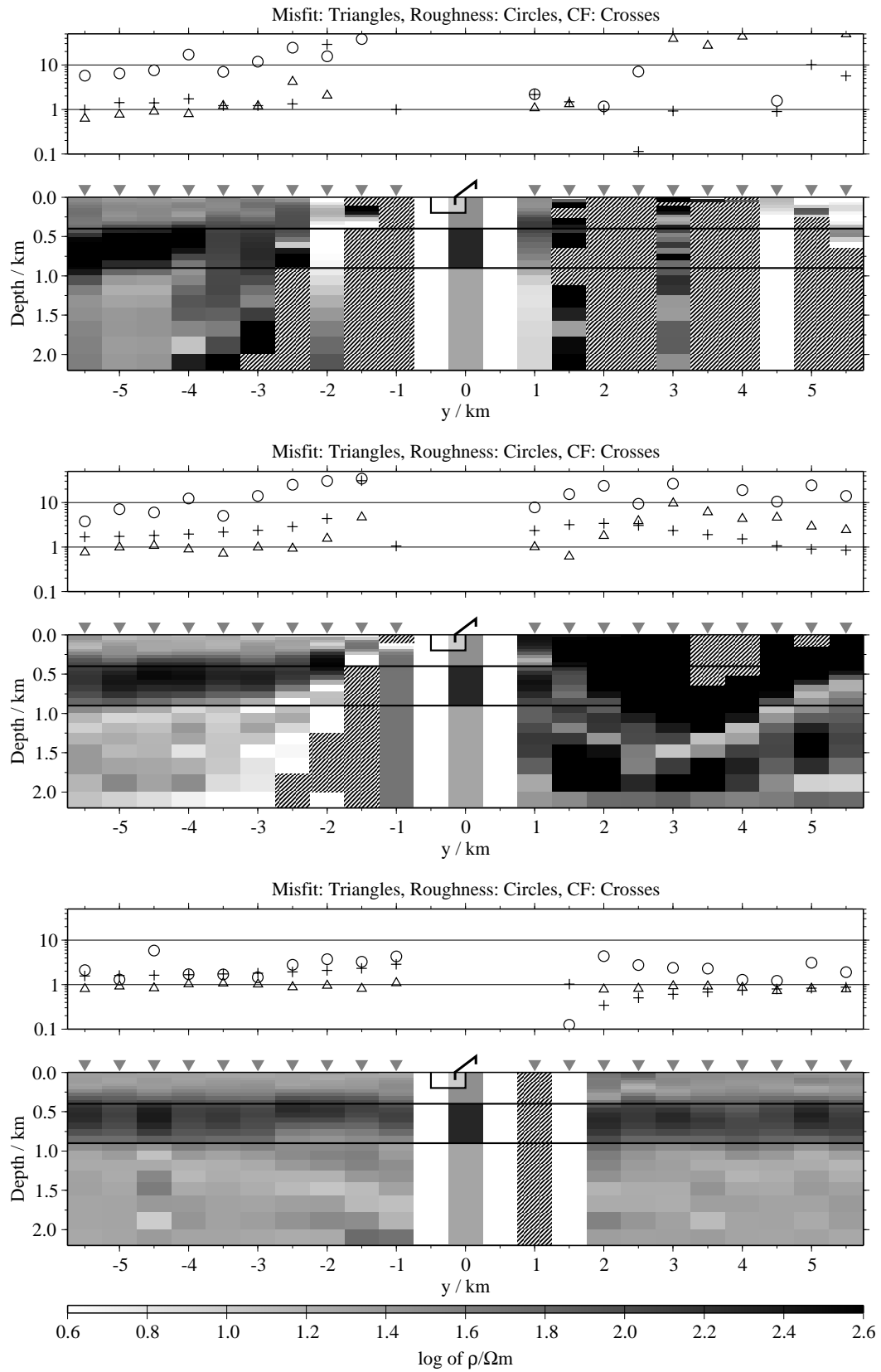


Figure B.303: Pseudo-sections of single 1-D inversion, model N1, regularisation scheme C4; from top to bottom E_x -, H_y - and H_z -component;

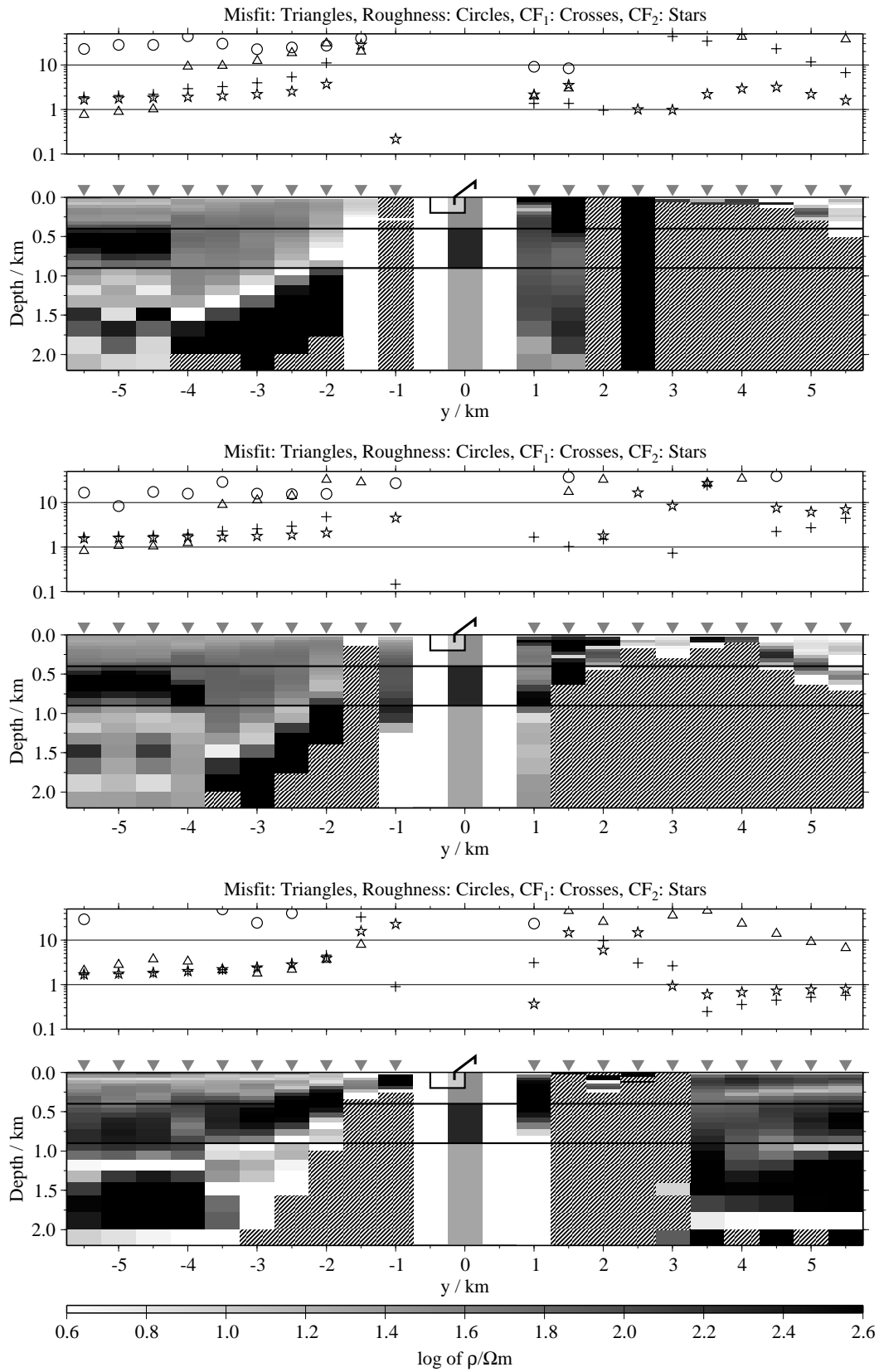


Figure B.304: Pseudo-sections of two component 1-D joint-inversions, model N1, regularisation scheme C1; from top to bottom E_x-H_y , E_x-H_z and H_y-H_z ;

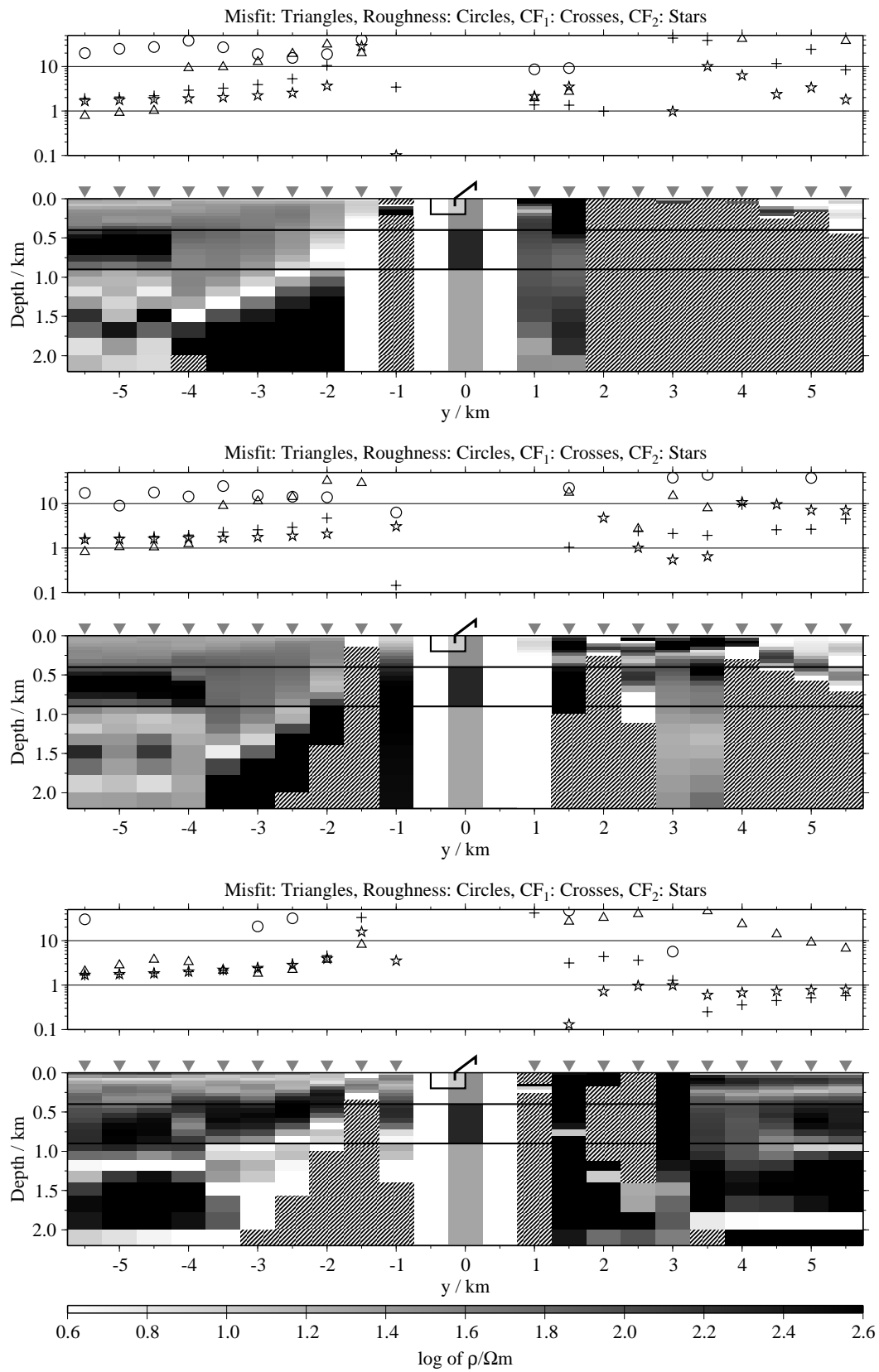


Figure B.305: Pseudo-sections of two component 1-D joint-inversions, model N1, regularisation scheme C4; from top to bottom $E_x-\dot{H}_y$, $E_x-\dot{H}_z$ and $\dot{H}_y-\dot{H}_z$;

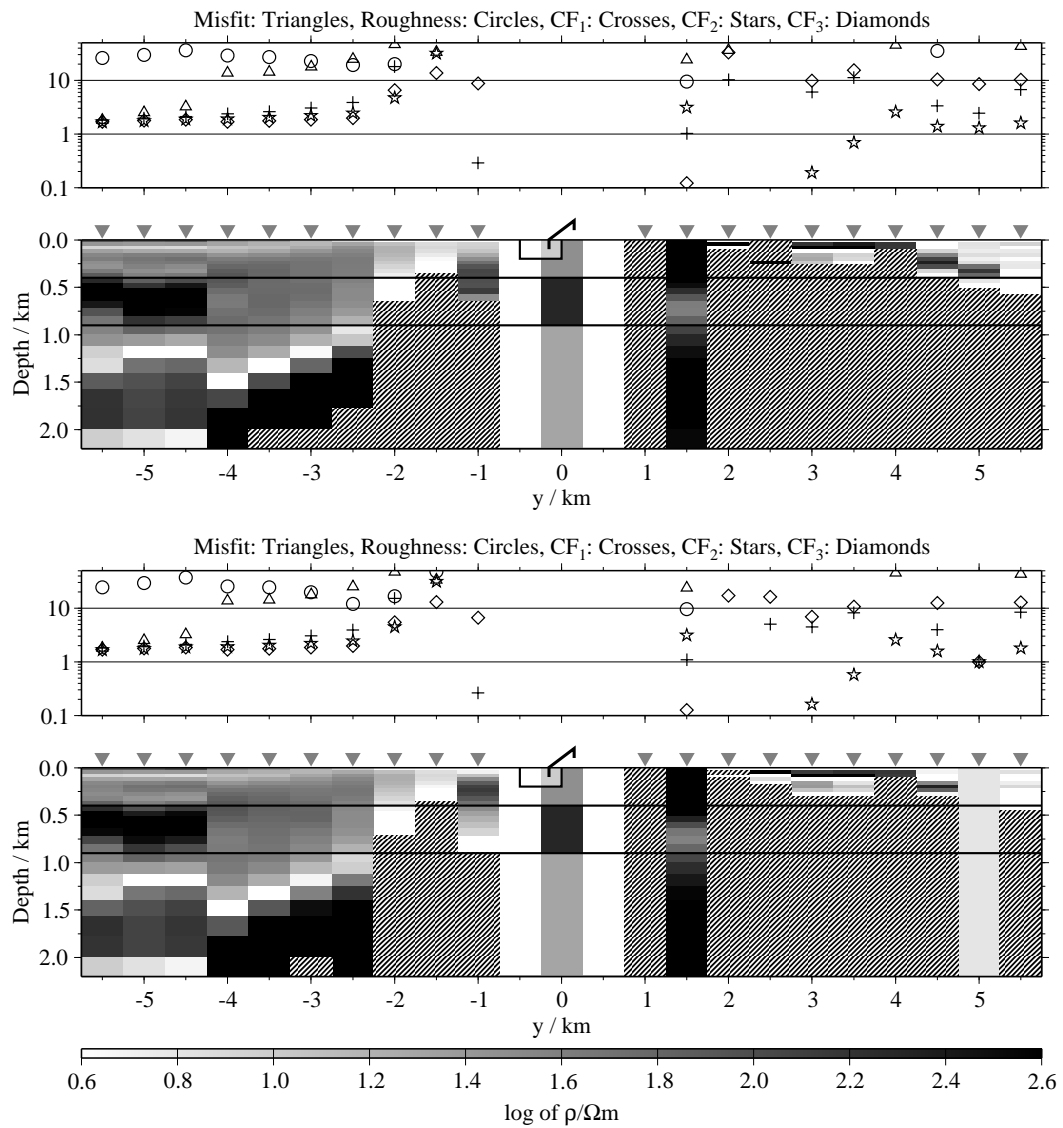


Figure B.306: Pseudo-sections of 1-D joint-inversions using all three components, model N1; top: Regularisation scheme C1; bottom: Regularisation scheme C4;

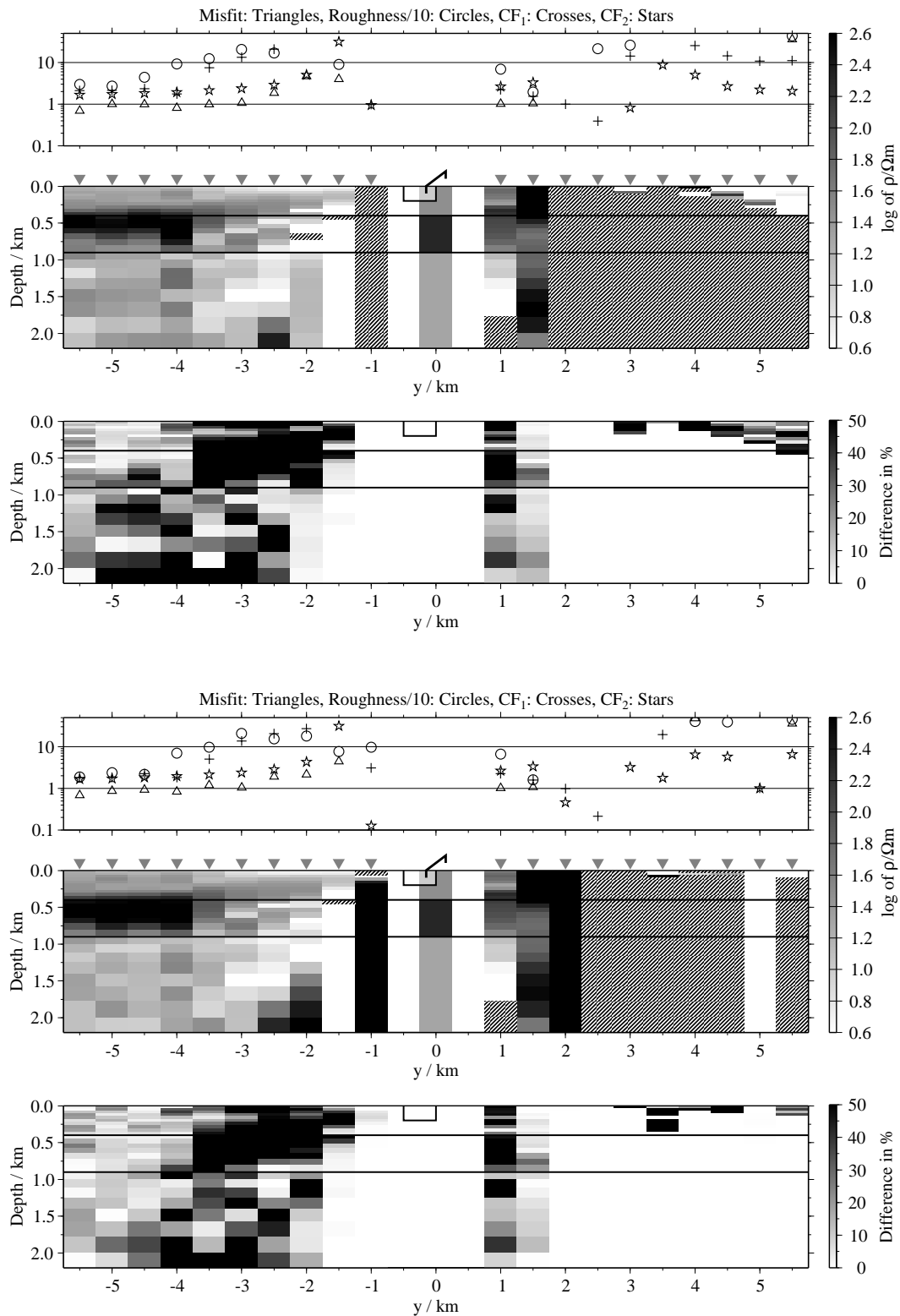


Figure B.307: Pseudo-sections of 1-D soft joint-inversions using the components E_x and H_y , model N1; Top panels: Average inversion results and relative differences (regularisation scheme C1); bottom: Average inversion results and relative differences (regularisation scheme C4);

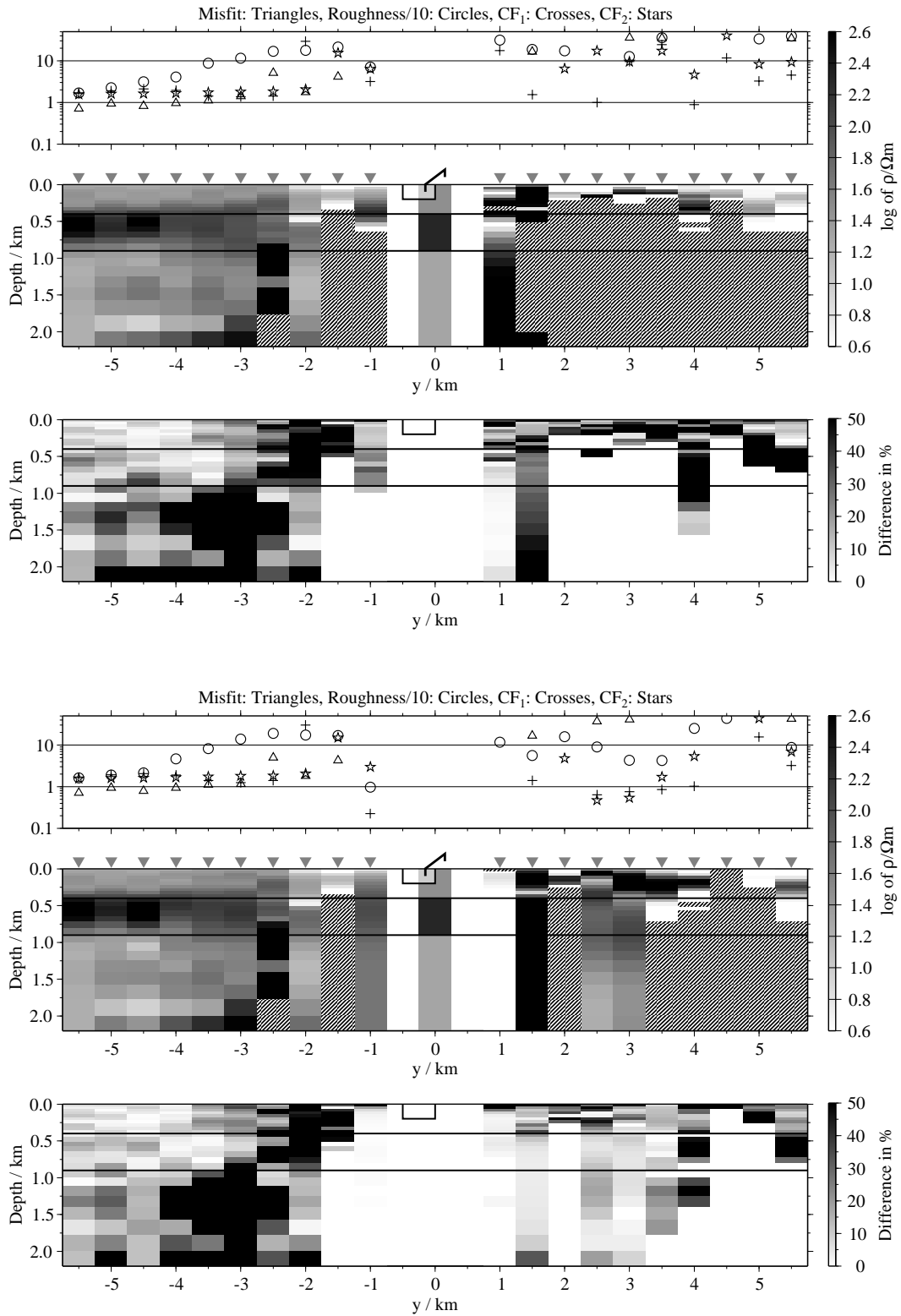


Figure B.308: Pseudo-sections 1-D of soft joint-inversions using the components E_x and H_z , model N1; Top panels: Average inversion results and relative differences (regularisation scheme C1); bottom: Average inversion results and relative differences (regularisation scheme C4);

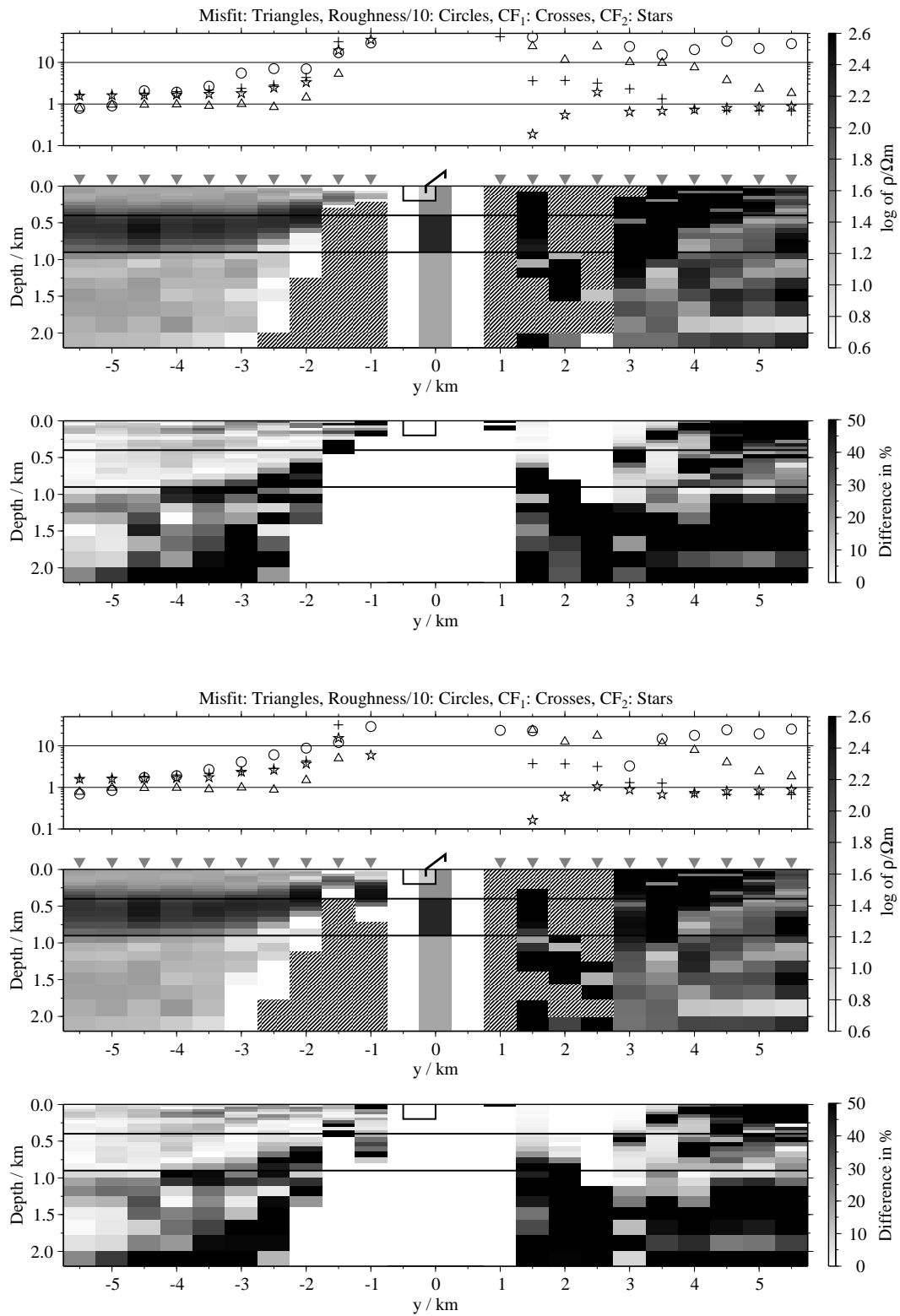


Figure B.309: Pseudo-sections of 1-D soft joint-inversions using the components \dot{H}_y and \dot{H}_z , model N1; Top panels: Average inversion results and relative differences (regularisation scheme C1); bottom: Average inversion results and relative differences (regularisation scheme C4);

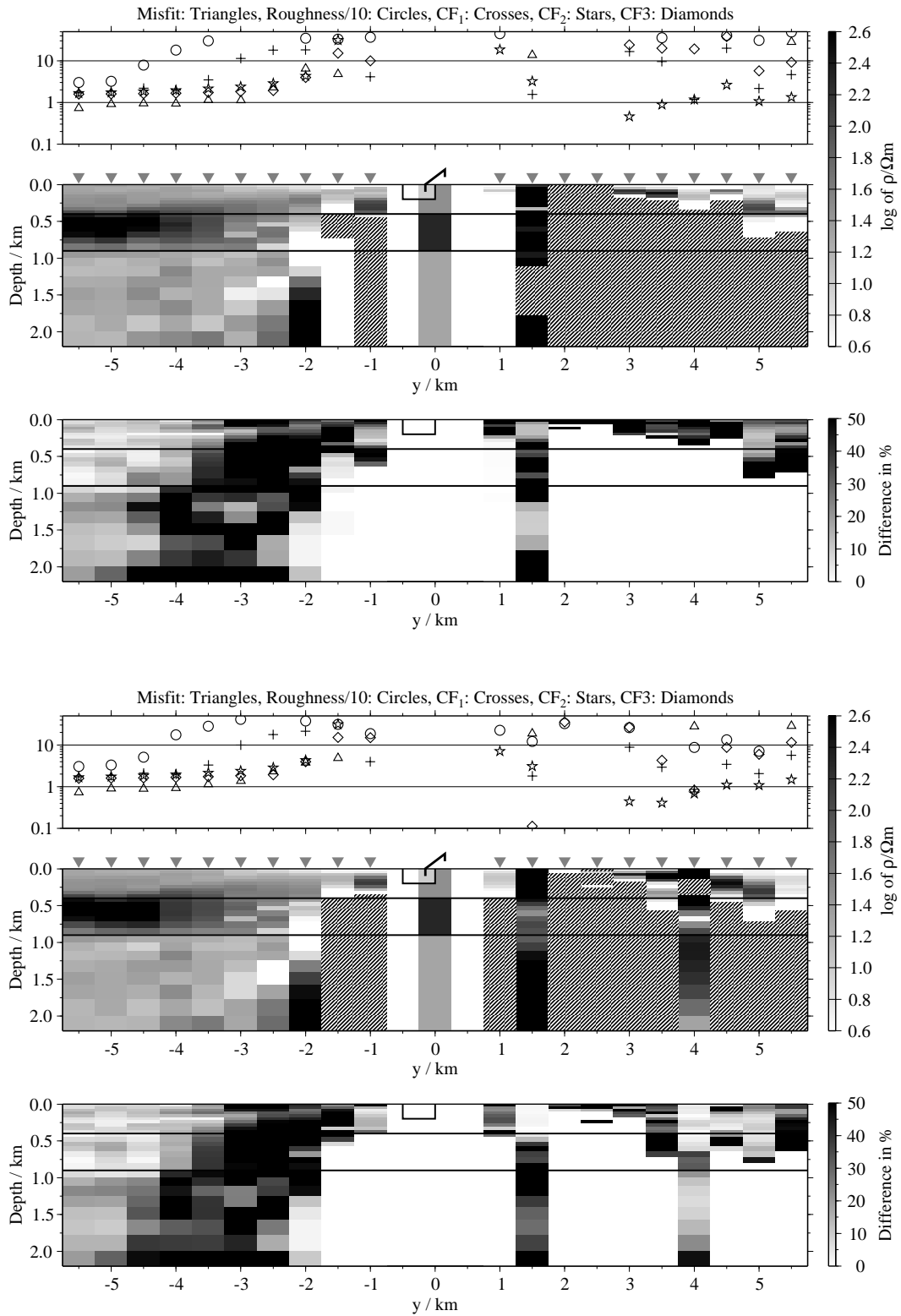


Figure B.310: Pseudo-sections of 1-D soft joint-inversions using all three components, model N1; Top panels: Average inversion results and relative differences (regularisation scheme C1); bottom: Average inversion results and relative differences (regularisation scheme C4);

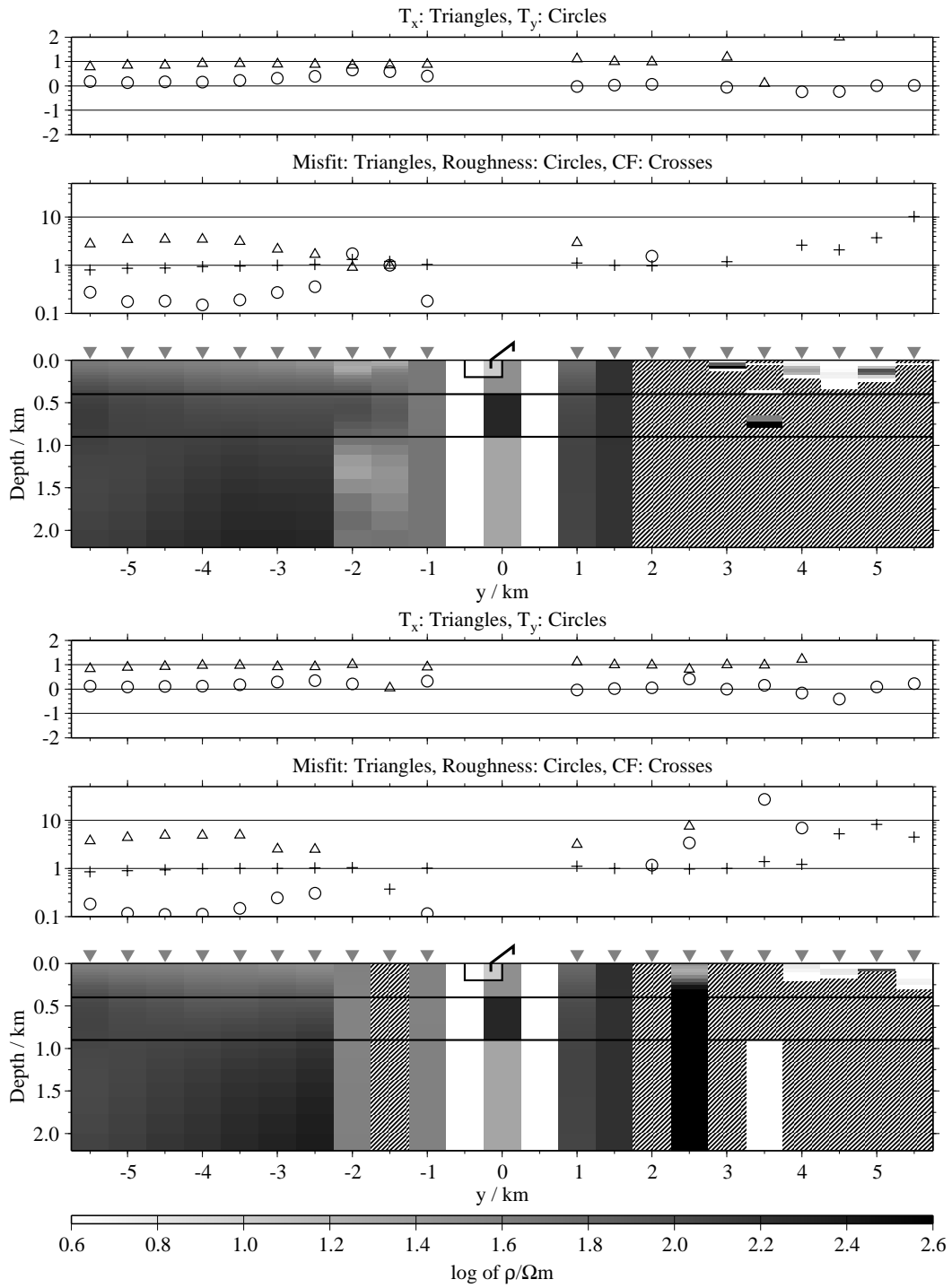


Figure B.311: The E_x inversion results for model N1; top: Regularisation scheme C1; bottom: Regularisation scheme C4; the inversions are done including the T_x -distortion parameters, which are displayed in the uppermost subpanels.

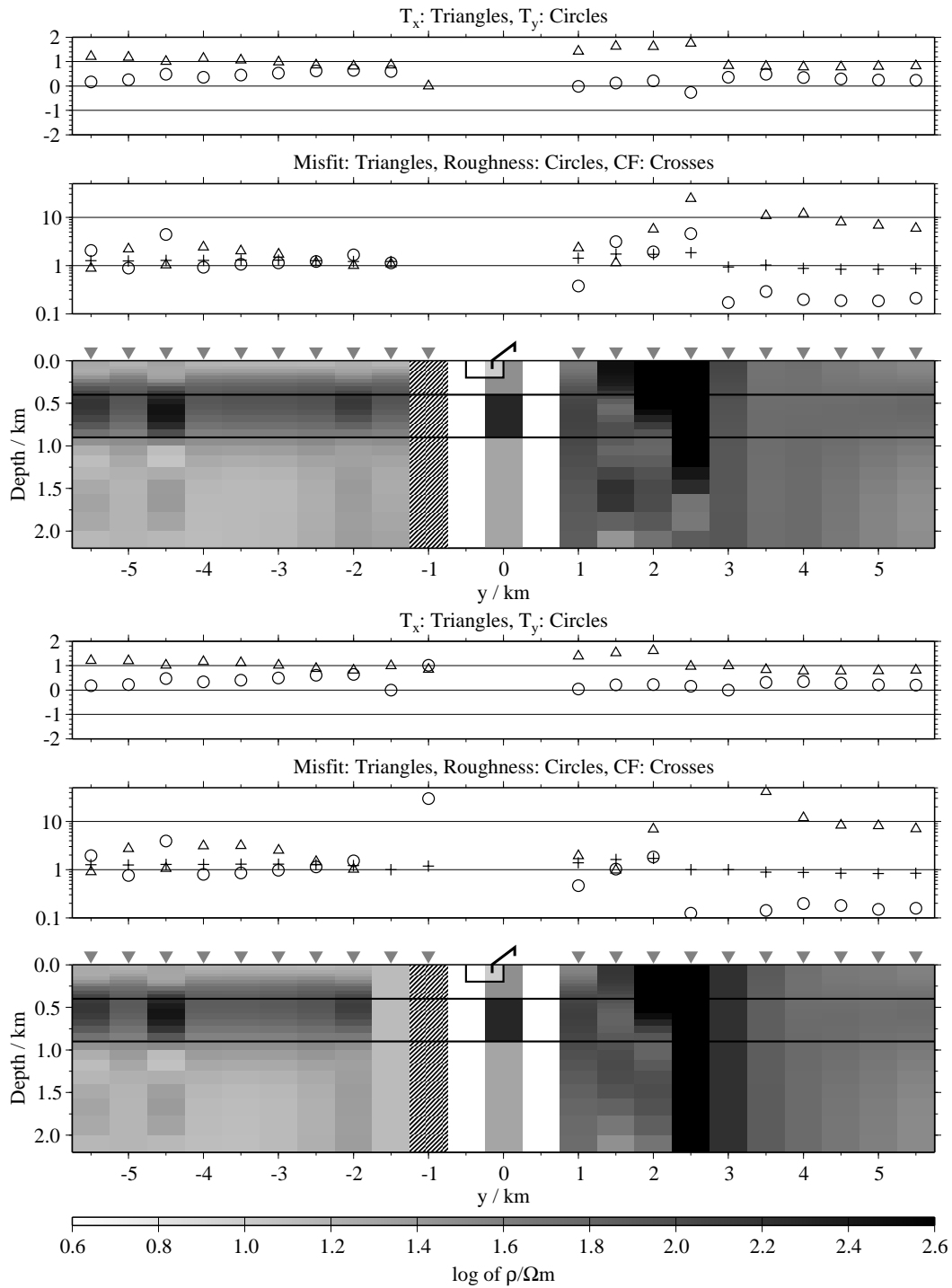


Figure B.312: The \dot{H}_y inversion results for model N1; top: Regularisation scheme C1; bottom: Regularisation scheme C4; the inversions are done including the T_x -distortion parameters, which are displayed in the uppermost subpanels.

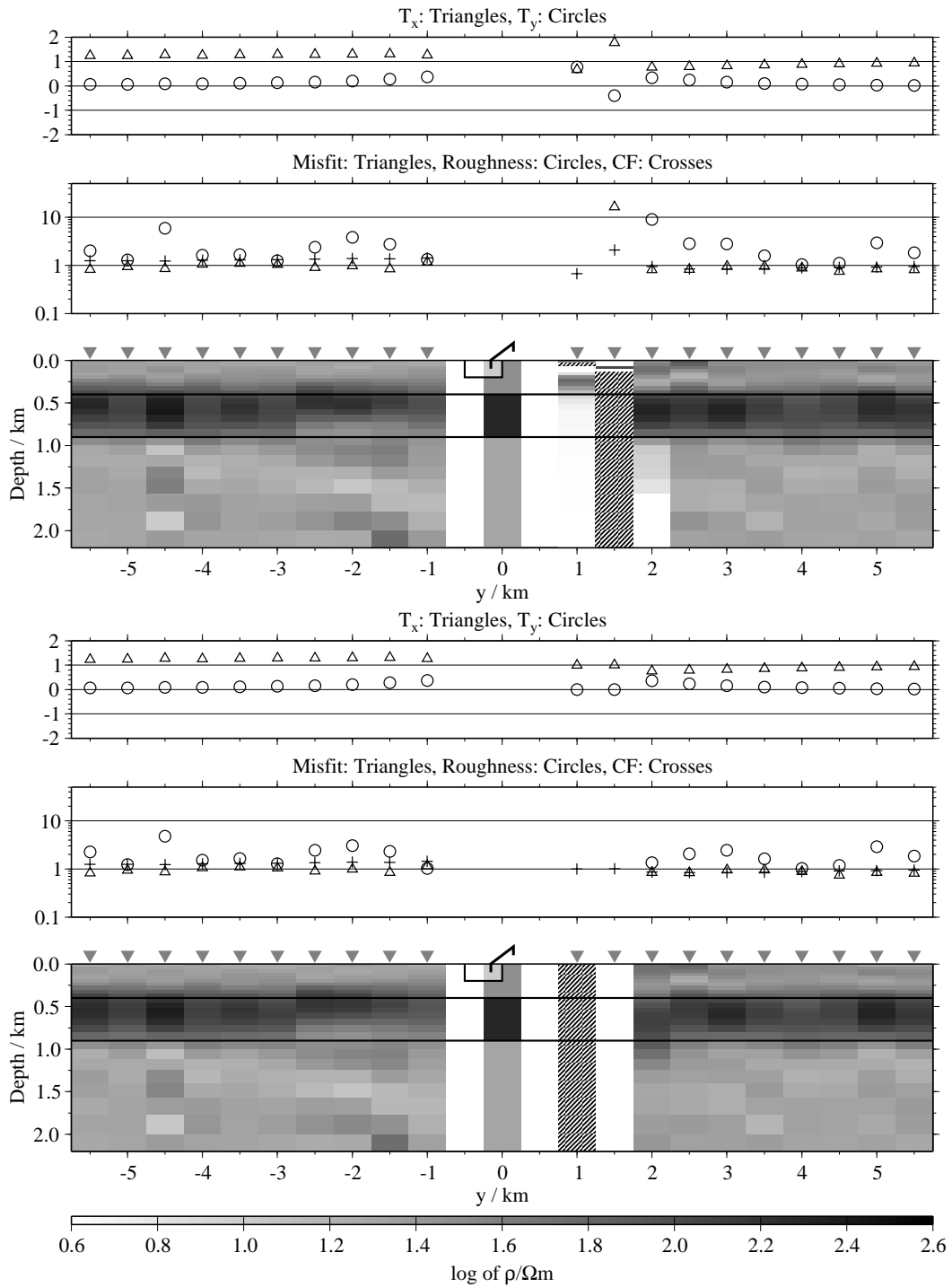


Figure B.313: The H_z inversion results for model N1; top: Regularisation scheme C1; bottom: Regularisation scheme C4; the inversions are done including the T_x -distortion parameters, which are displayed in the uppermost subpanels.

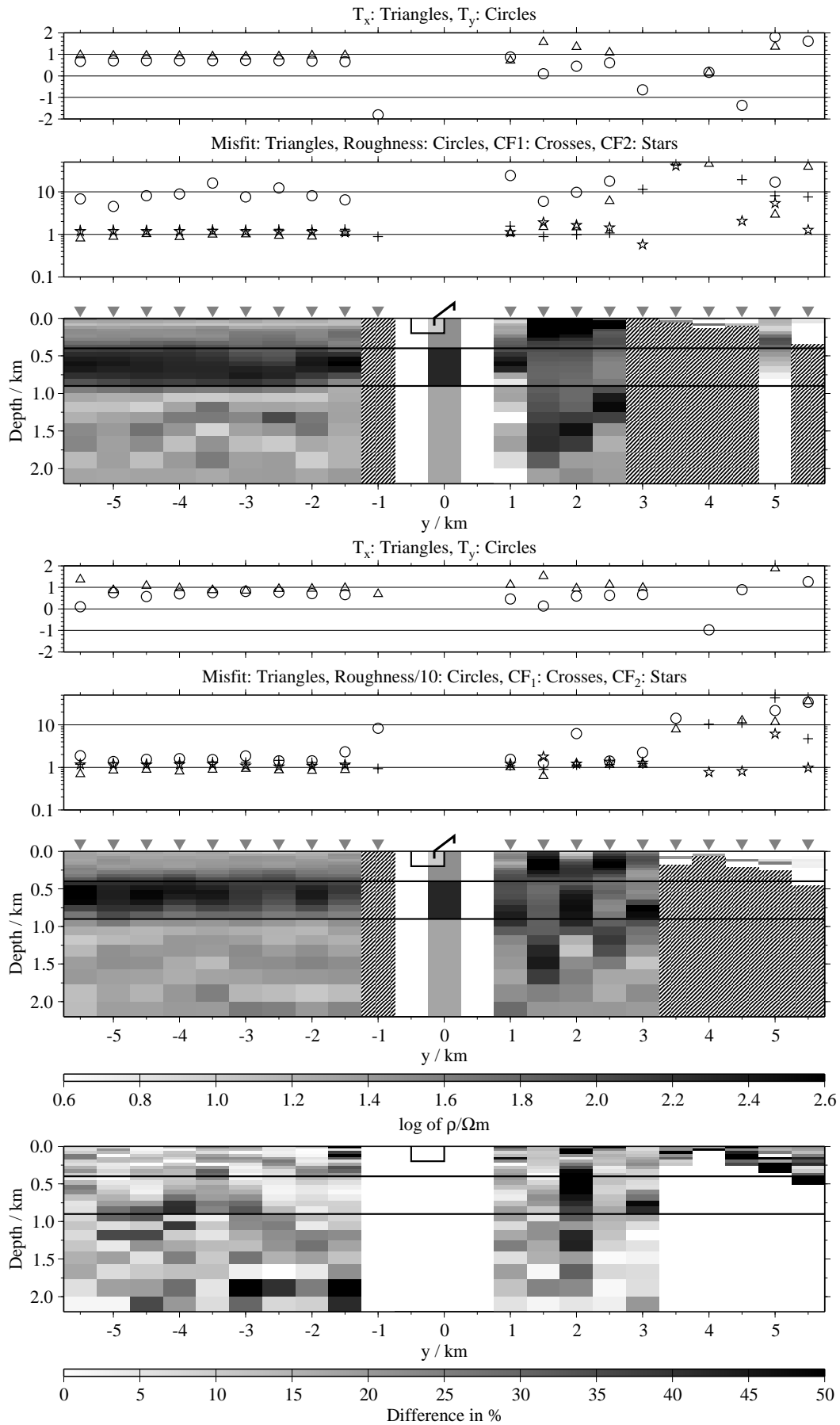


Figure B.314: Joint-inversion results for the components E_x and H_y , model N1, regularisation scheme C1; top: FJI; bottom: SJI; the inversions are done including the Tx-distortion parameters, which are displayed in the uppermost subpanels.

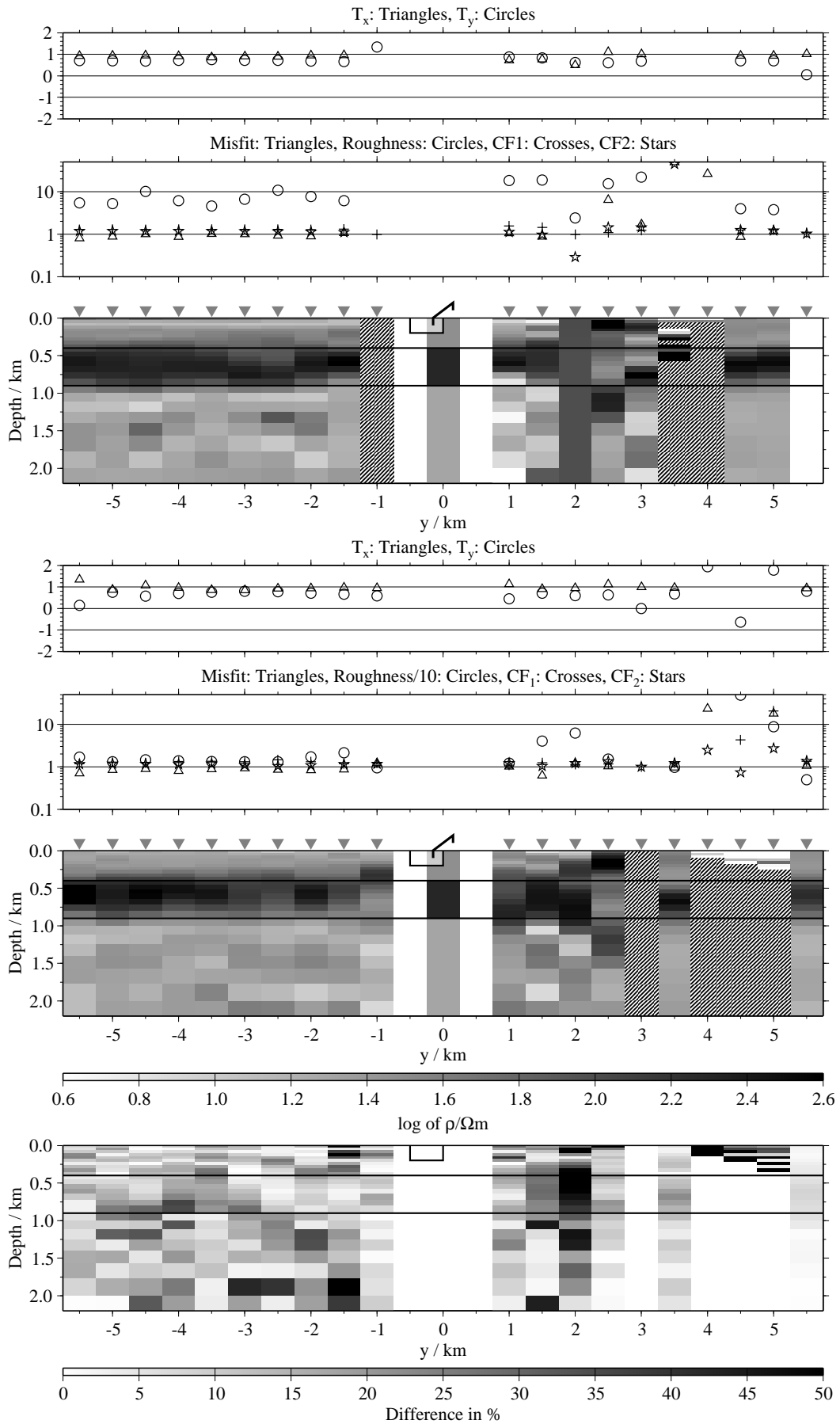


Figure B.315: Joint-inversion results for the components E_x and H_y , model N1, regularisation scheme C4; top: FJI; bottom: SJI; the inversions are done including the T_x -distortion parameters, which are displayed in the uppermost subpanels.

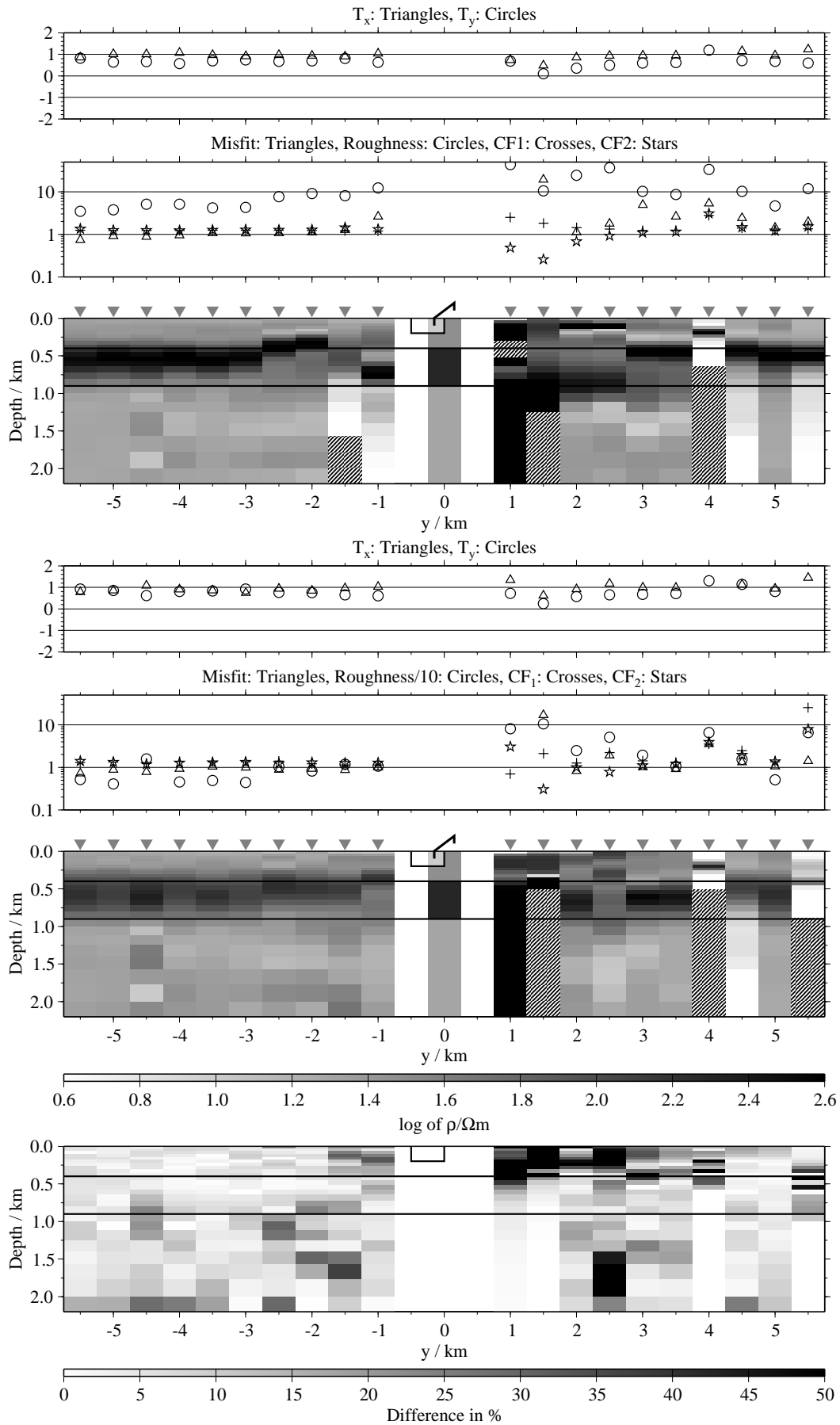


Figure B.316: Joint-inversion results for the components E_x and H_z , model N1, regularisation scheme C1; top: FJI; bottom: SJI; the inversions are done including the Tx-distortion parameters, which are displayed in the uppermost subpanels.

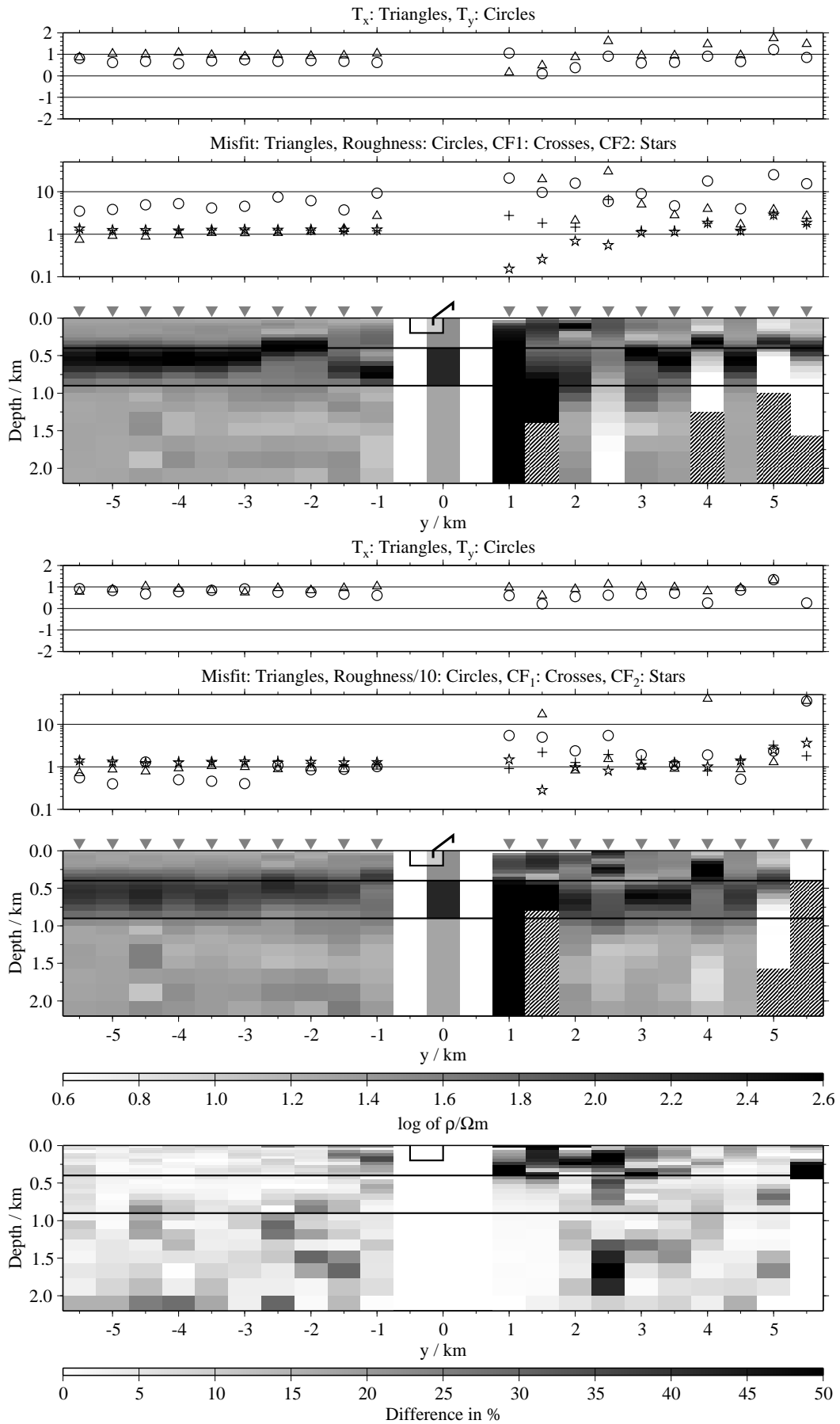


Figure B.317: Joint-inversion results for the components E_x and H_z , model N1, regularisation scheme C4; top: FJI; bottom: SJI; the inversions are done including the T_x -distortion parameters, which are displayed in the uppermost subpanels.

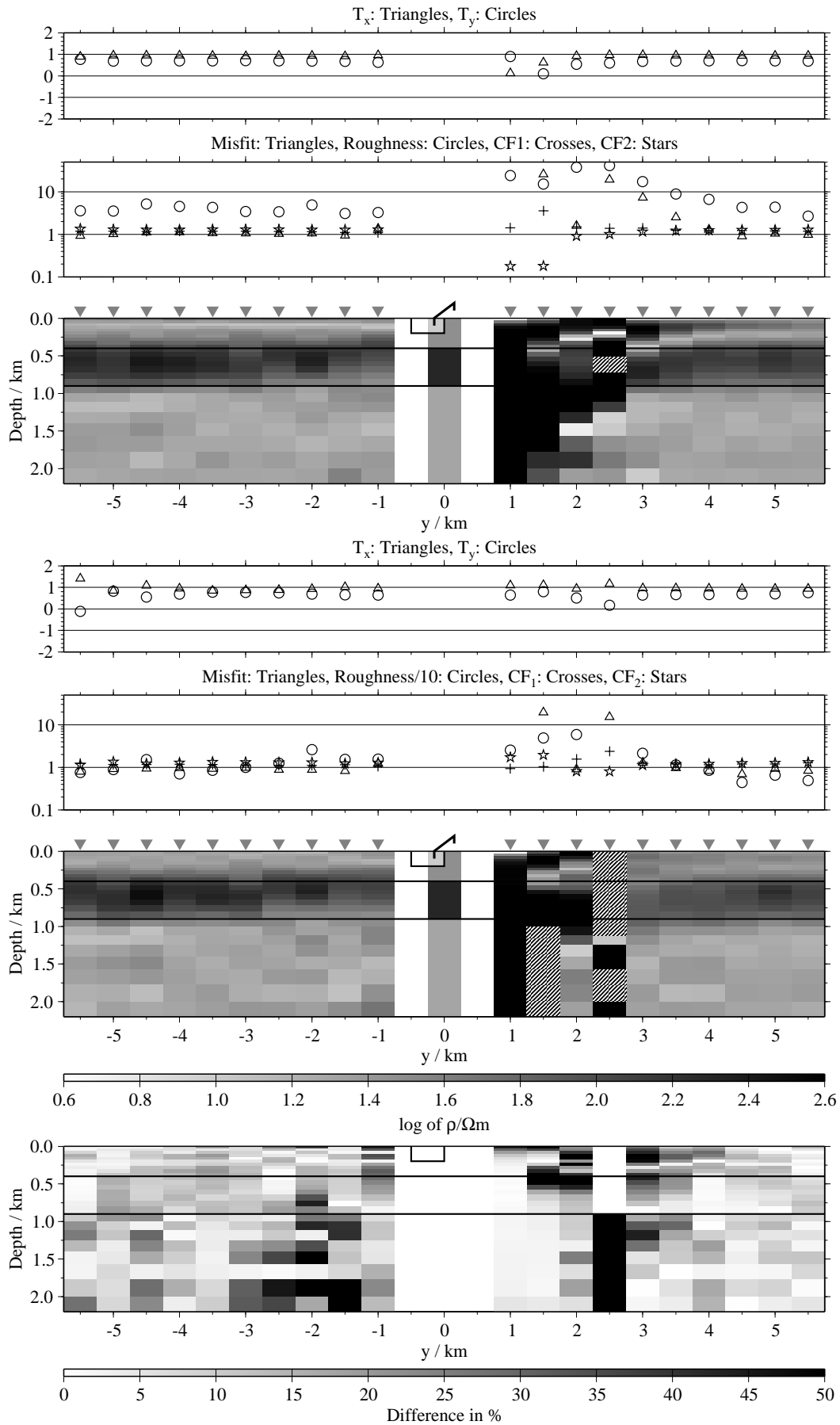


Figure B.318: Joint-inversion results for the components \dot{H}_y and \dot{H}_z , model N1, regularisation scheme C1; top: FJI; bottom: SJI; the inversions are done including the Tx-distortion parameters, which are displayed in the uppermost subpanels.

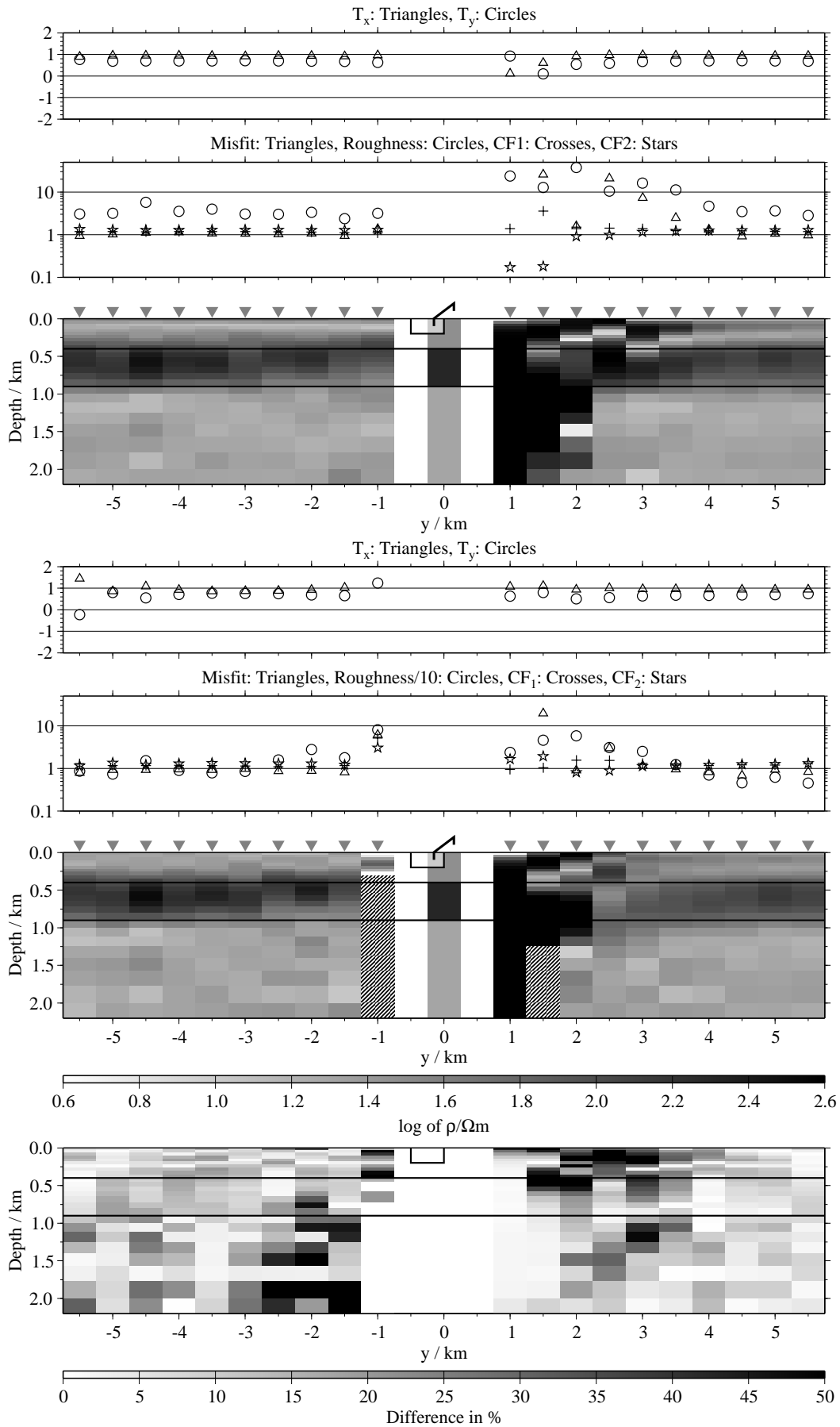


Figure B.319: Joint-inversion results for the components \dot{H}_y and \dot{H}_z , model N1, regularisation scheme C4; top: FJI; bottom: SJI; the inversions are done including the T_x -distortion parameters, which are displayed in the uppermost subpanels.

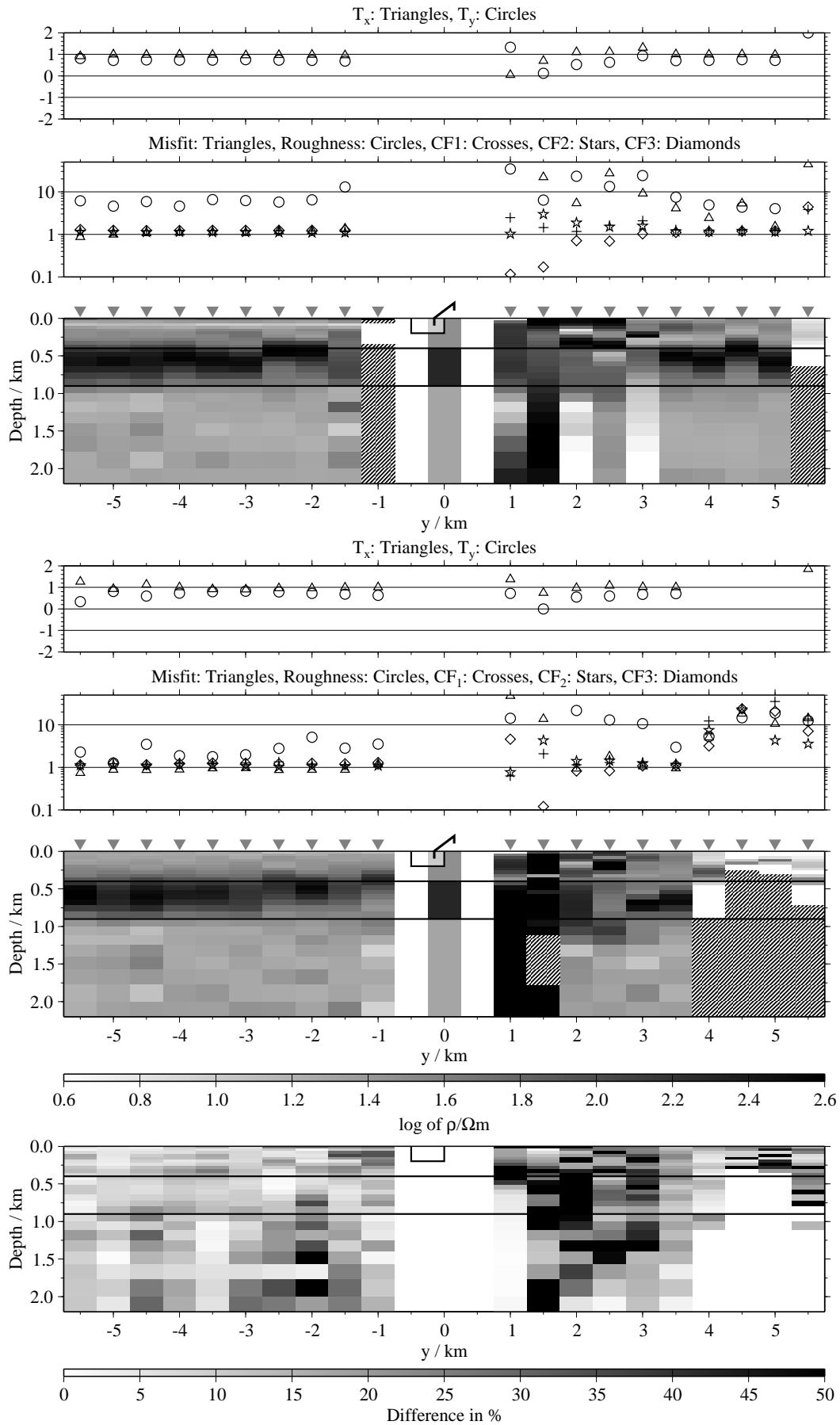


Figure B.320: Joint-inversion results for all three components, model N1, regularisation scheme C1; top: FJI; bottom: SJI; the inversions are done including the Tx-distortion parameters, which are displayed in the uppermost subpanels.

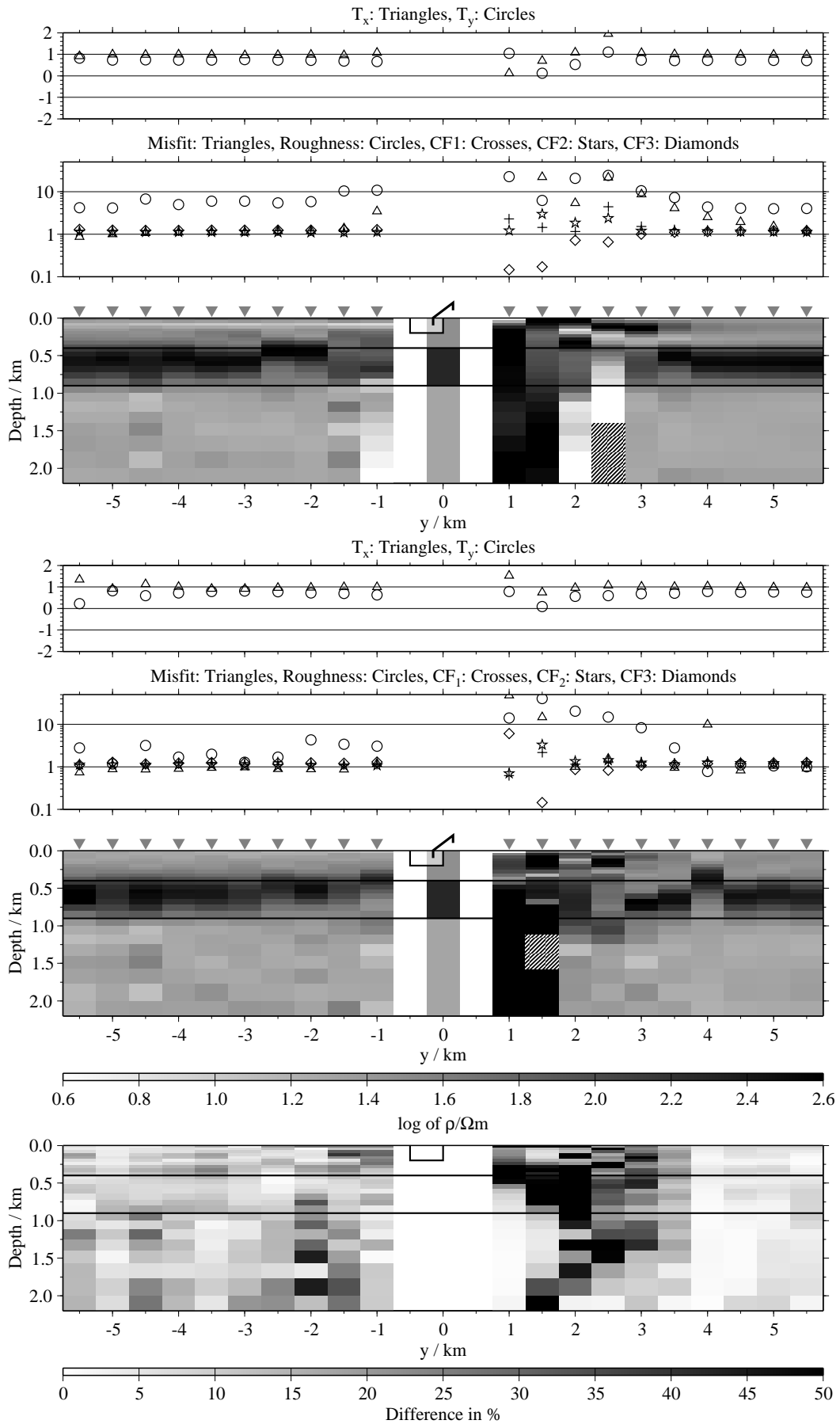


Figure B.321: Joint-inversion results for all three components, model N1, regularisation scheme C4; top: FJI; bottom: SJI; the inversions are done including the Tx-distortion parameters, which are displayed in the uppermost subpanels.

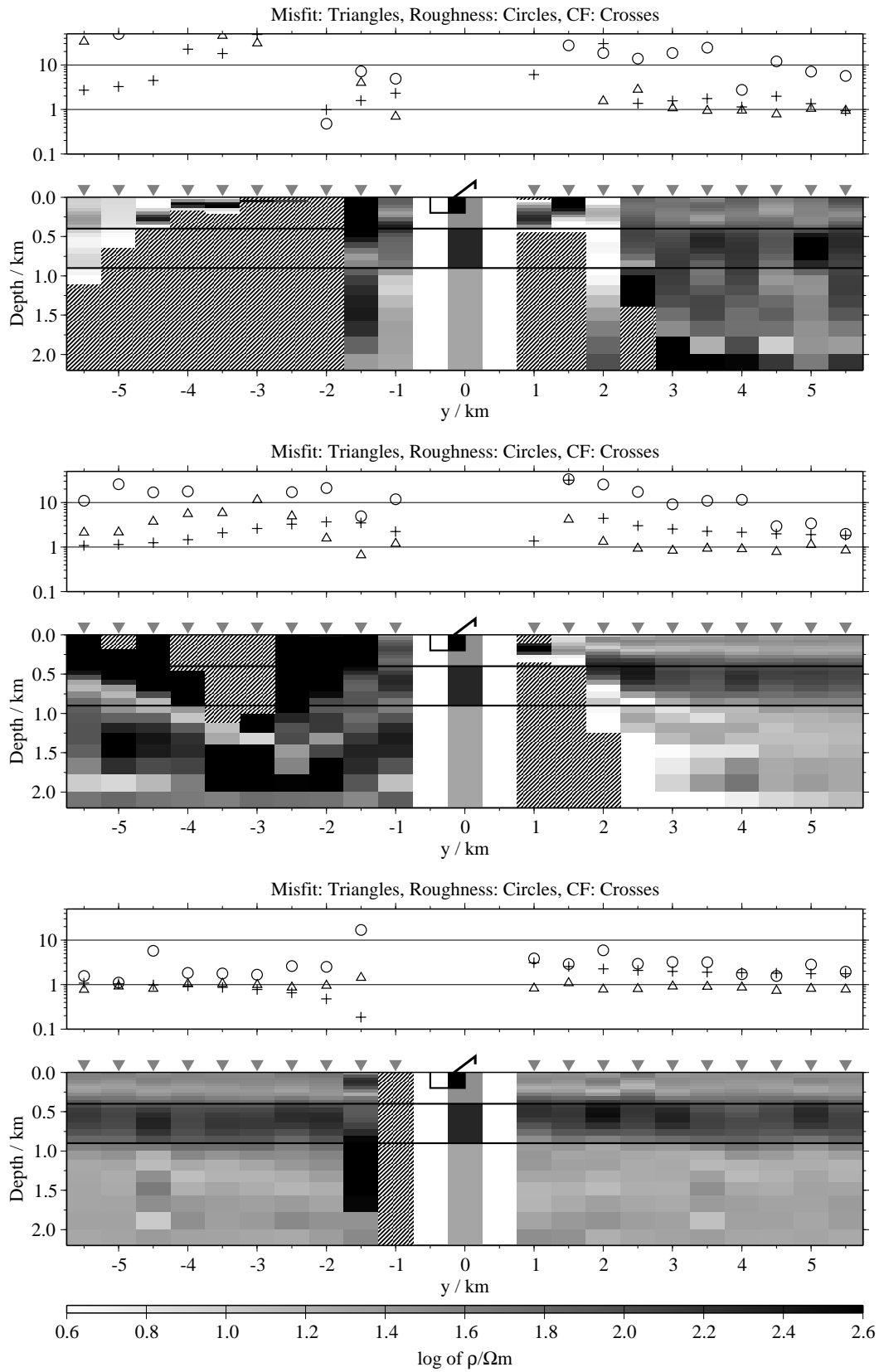


Figure B.322: Pseudo-sections of single 1-D inversion, model N2, regularisation scheme C1; from top to bottom E_x -, H_y - and H_z -component;

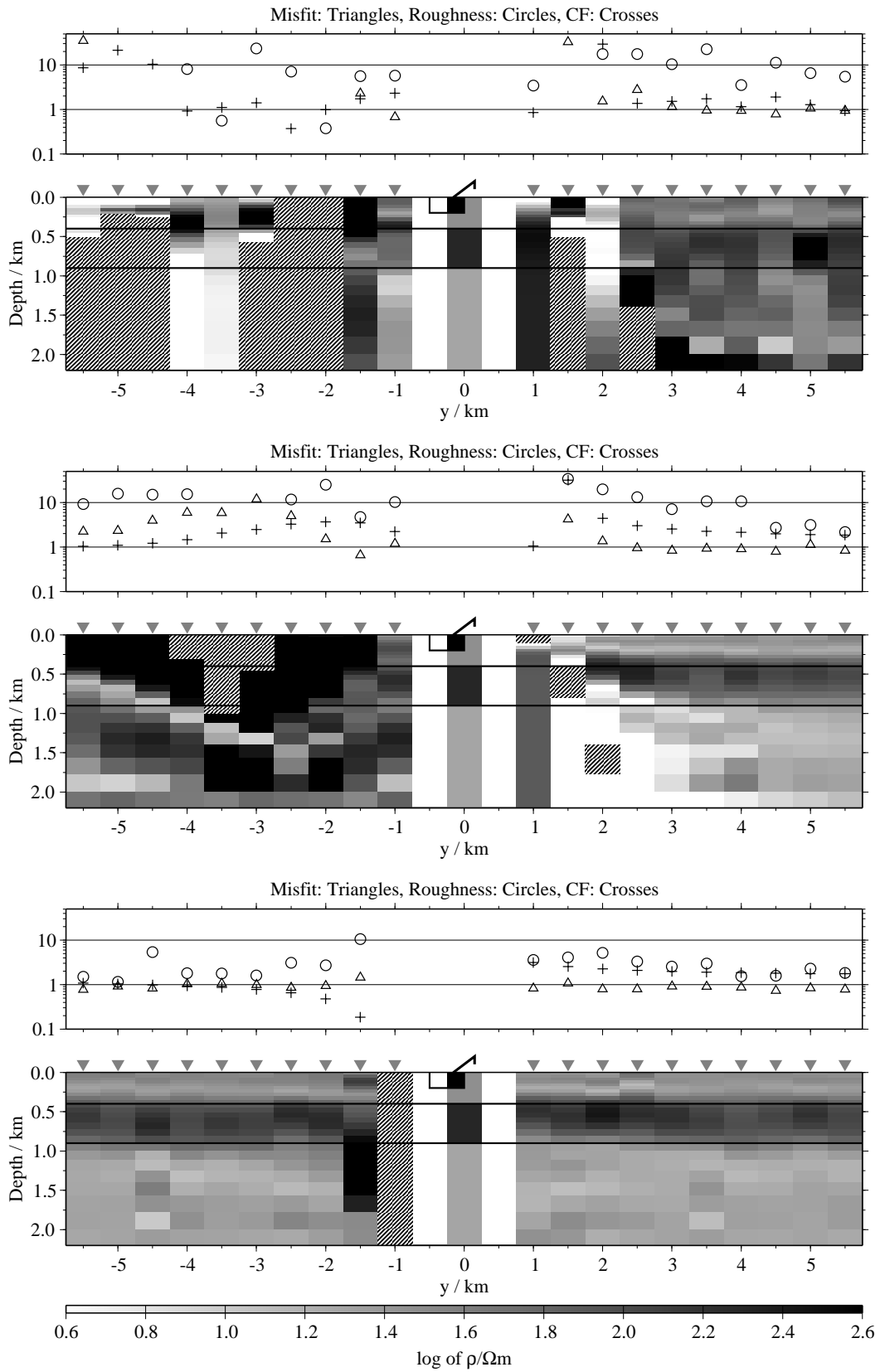


Figure B.323: Pseudo-sections of single 1-D inversion, model N2, regularisation scheme C4; from top to bottom E_x -, H_y - and H_z -component;

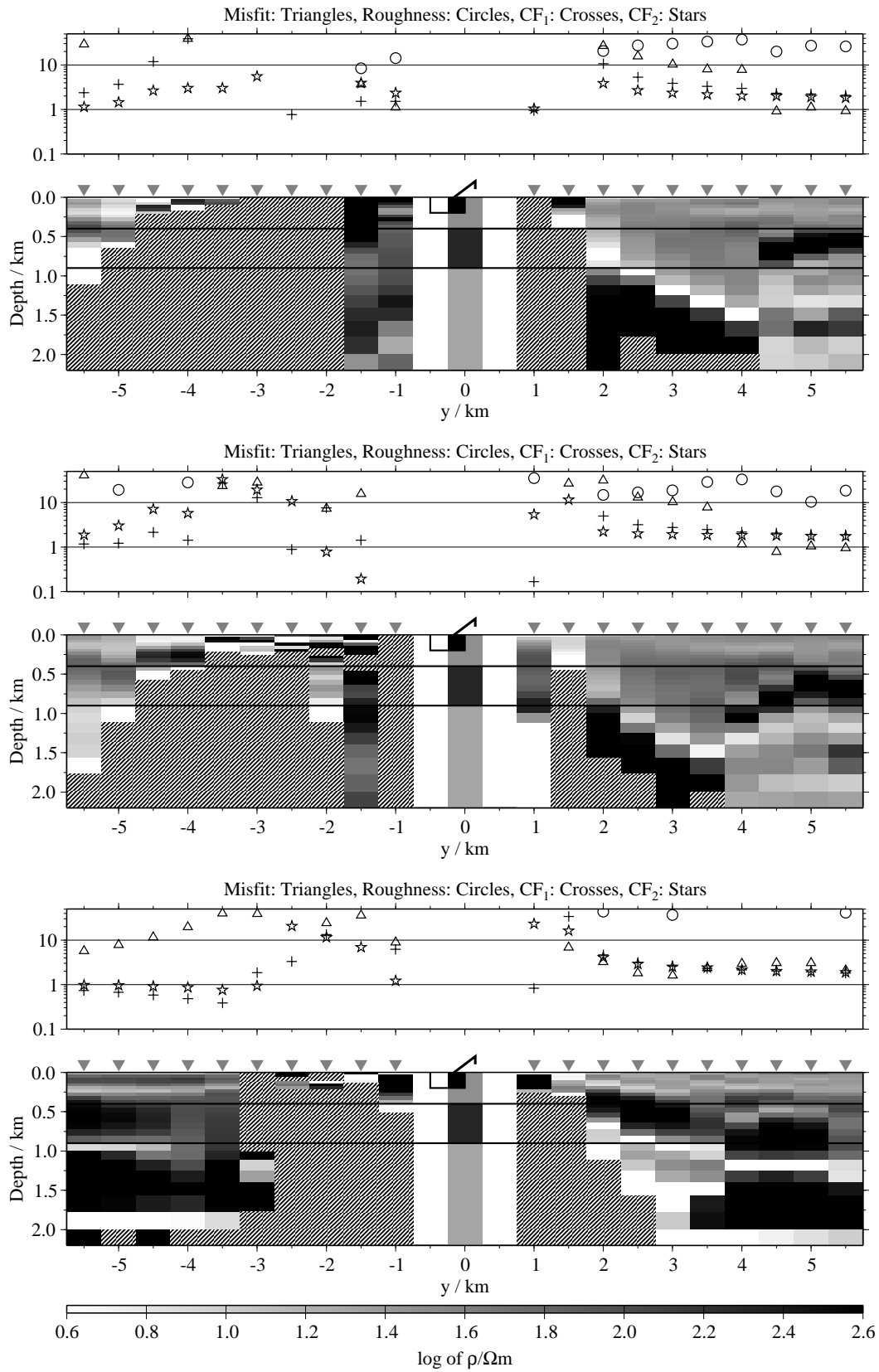


Figure B.324: Pseudo-sections of two component 1-D joint-inversions, model N2, regularisation scheme C1; from top to bottom $E_x-\dot{H}_y$, $E_x-\dot{H}_z$ and $\dot{H}_y-\dot{H}_z$;

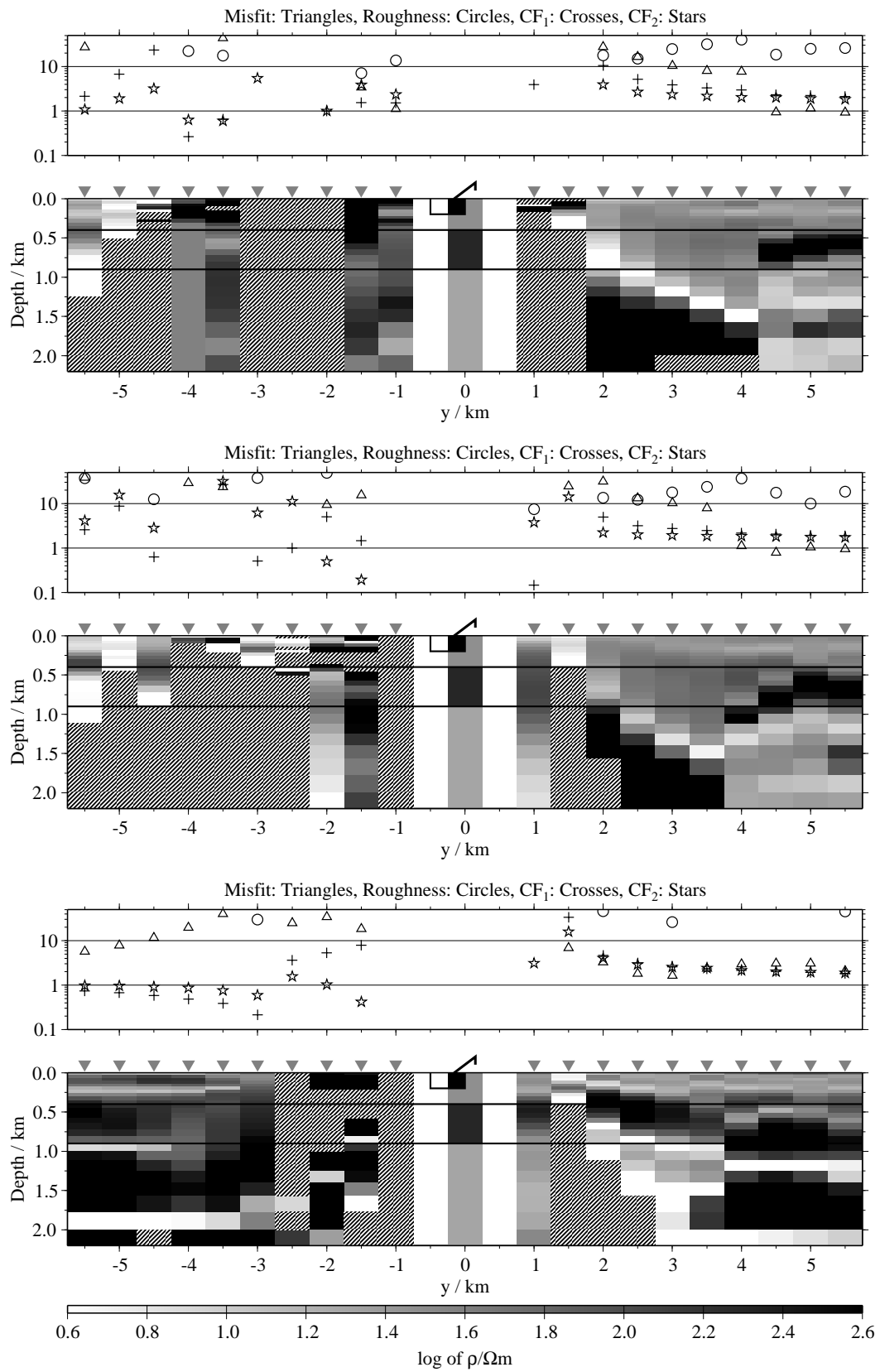


Figure B.325: Pseudo-sections of two component 1-D joint-inversions, model N2, regularisation scheme C4; from top to bottom $E_x - \dot{H}_y$, $E_x - \dot{H}_z$ and $\dot{H}_y - \dot{H}_z$;

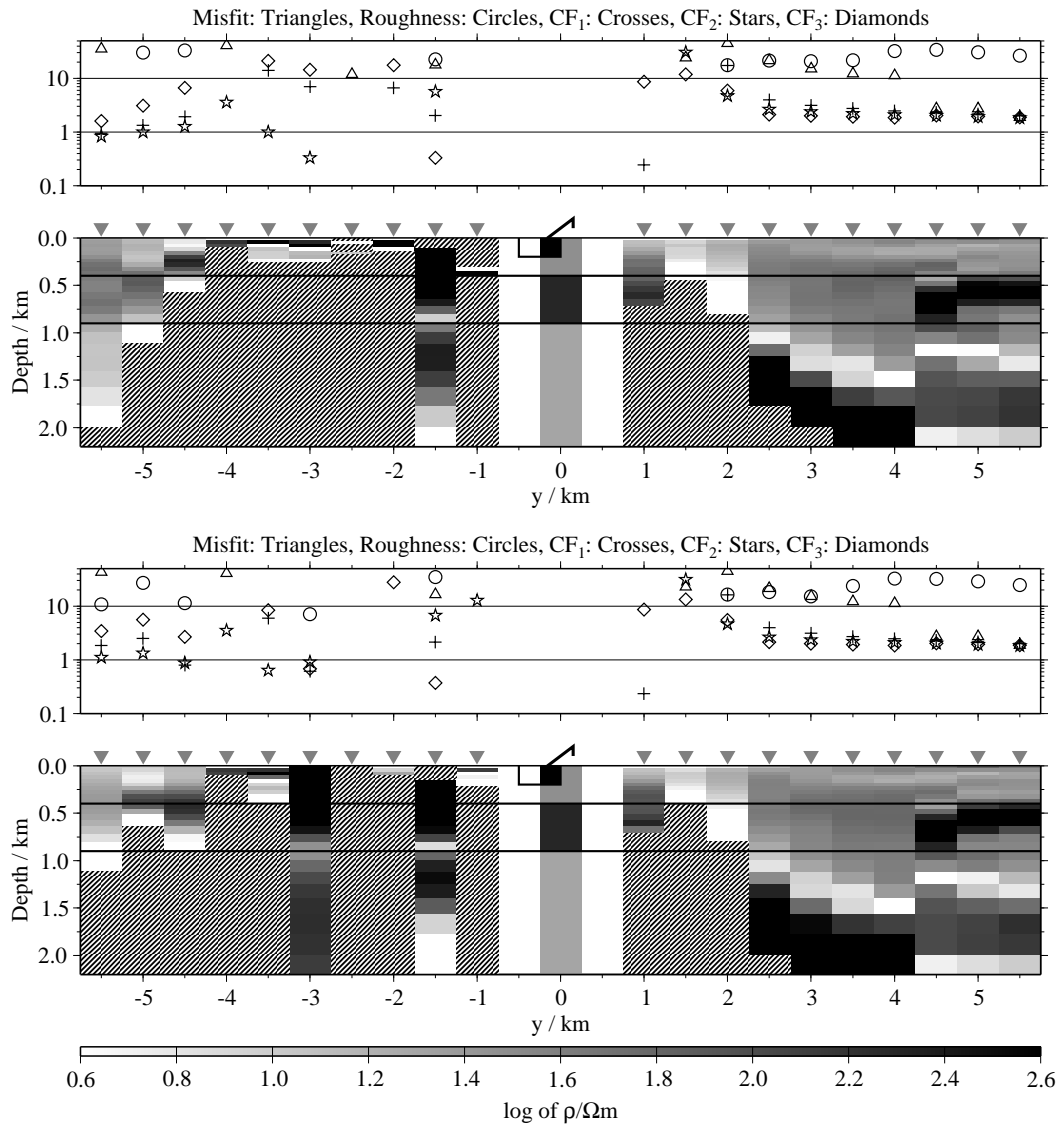


Figure B.326: Pseudo-sections of 1-D joint-inversions using all three components, model N2; top: Regularisation scheme C1; bottom: Regularisation scheme C4;

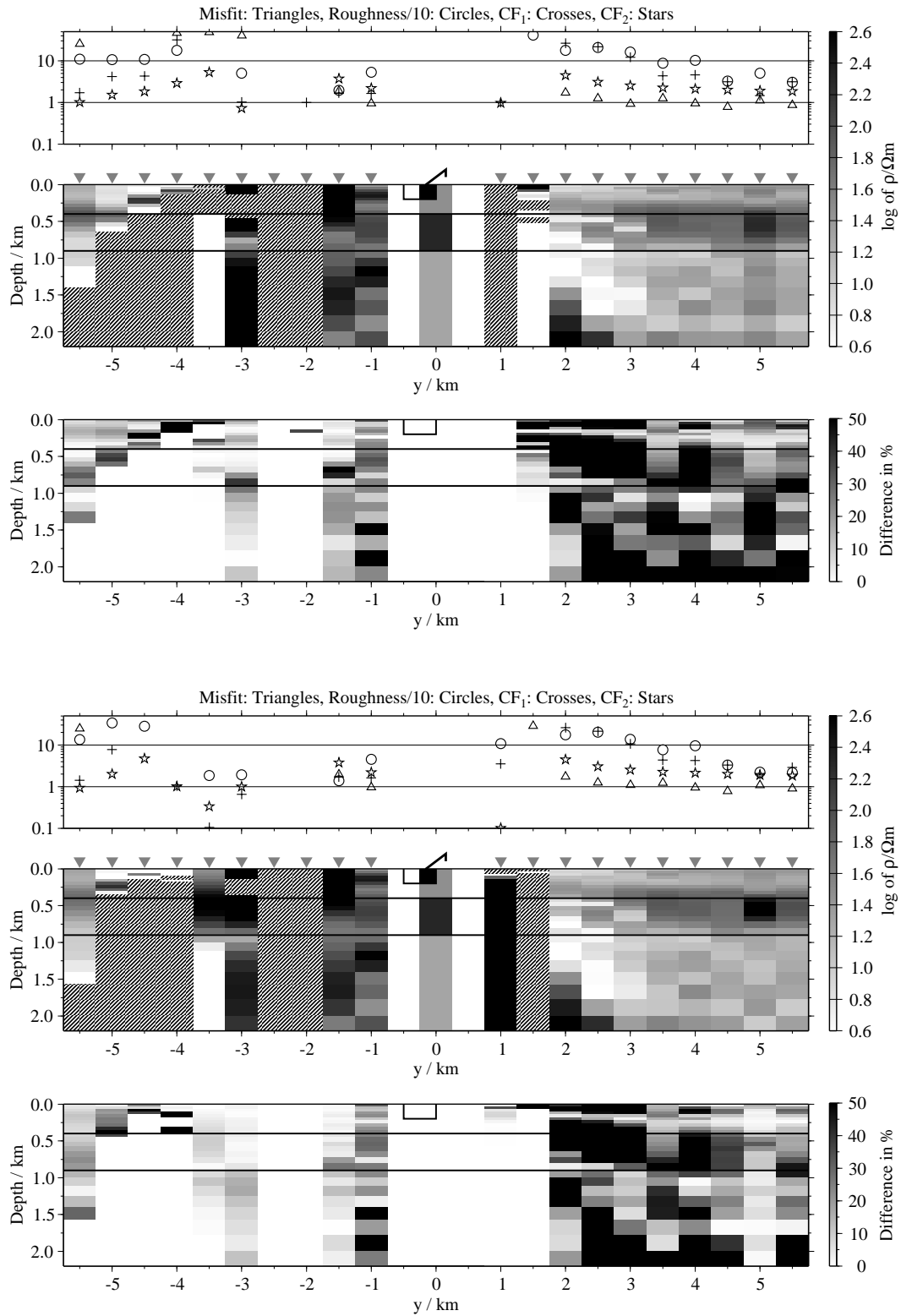


Figure B.327: Pseudo-sections of 1-D soft joint-inversions using the components E_x and H_y , model N2; Top panels: Average inversion results and relative differences (regularisation scheme C1); bottom: Average inversion results and relative differences (regularisation scheme C4);

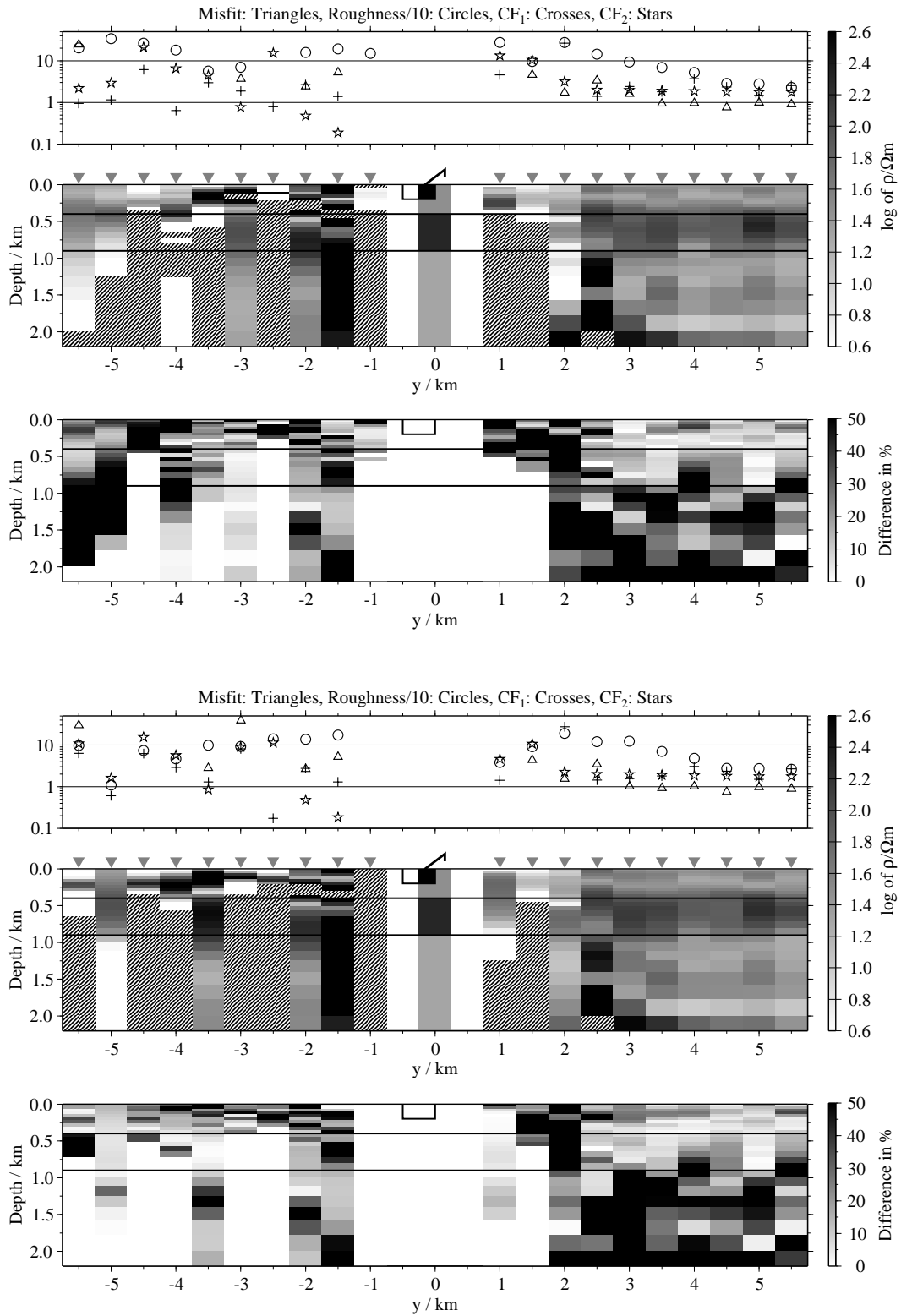


Figure B.328: Pseudo-sections 1-D of soft joint-inversions using the components E_x and H_z , model N2; Top panels: Average inversion results and relative differences (regularisation scheme C1); bottom: Average inversion results and relative differences (regularisation scheme C4);

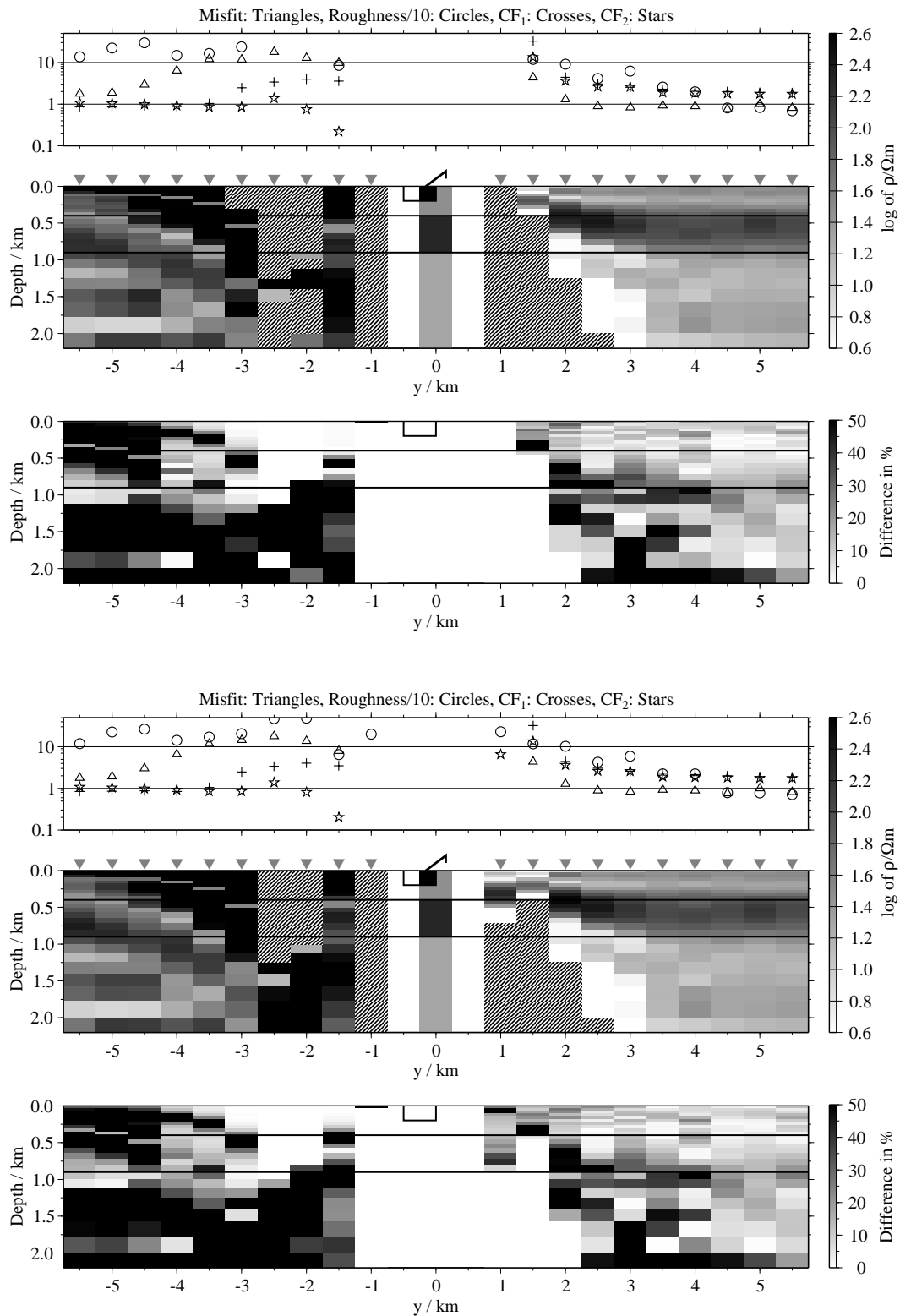


Figure B.329: Pseudo-sections of 1-D soft joint-inversions using the components \dot{H}_y and \dot{H}_z , model N2; Top panels: Average inversion results and relative differences (regularisation scheme C1); bottom: Average inversion results and relative differences (regularisation scheme C4);

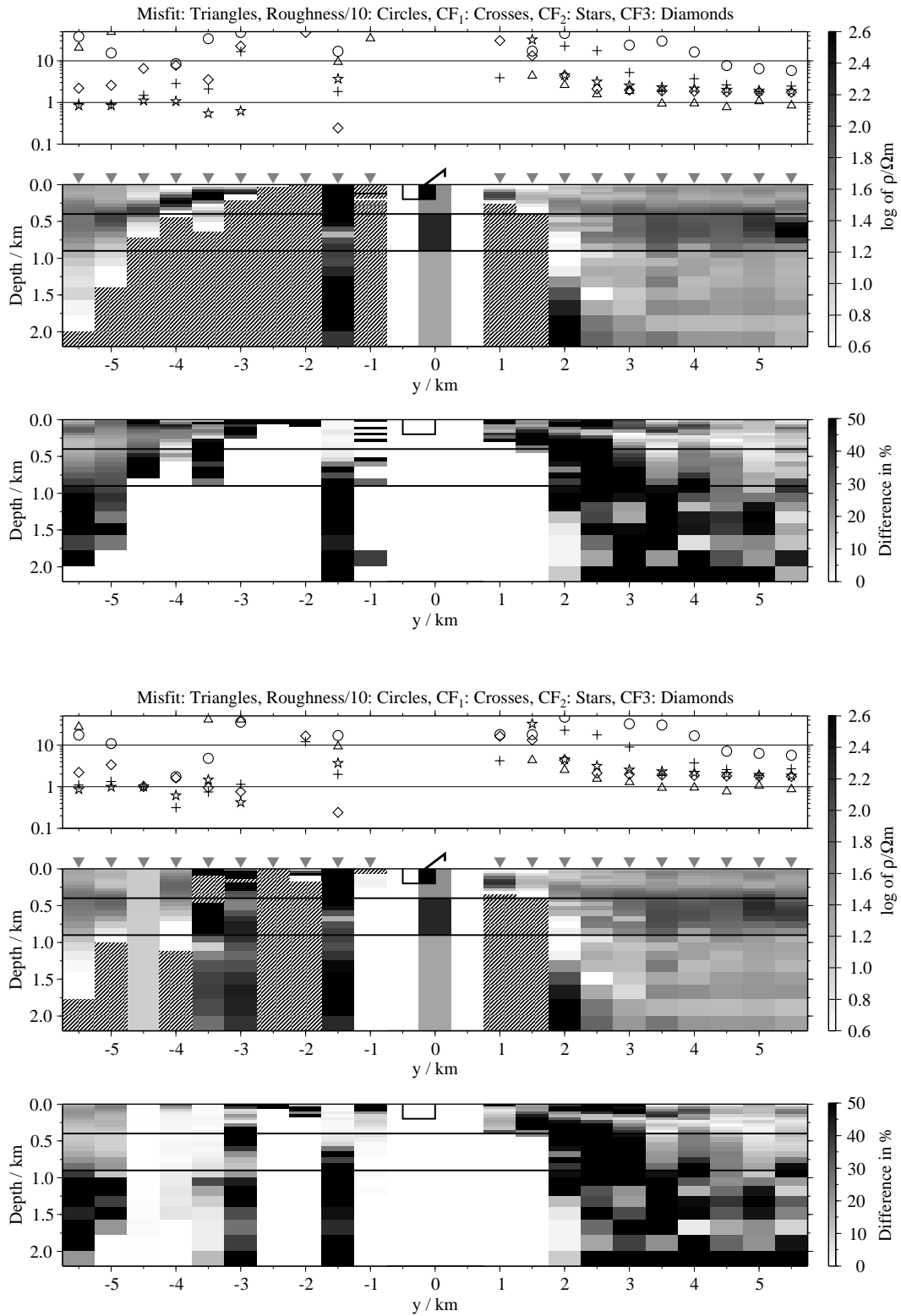


Figure B.330: Pseudo-sections of 1-D soft joint-inversions using all three components, model N2; Top panels: Average inversion results and relative differences (regularisation scheme C1); bottom: Average inversion results and relative differences (regularisation scheme C4);

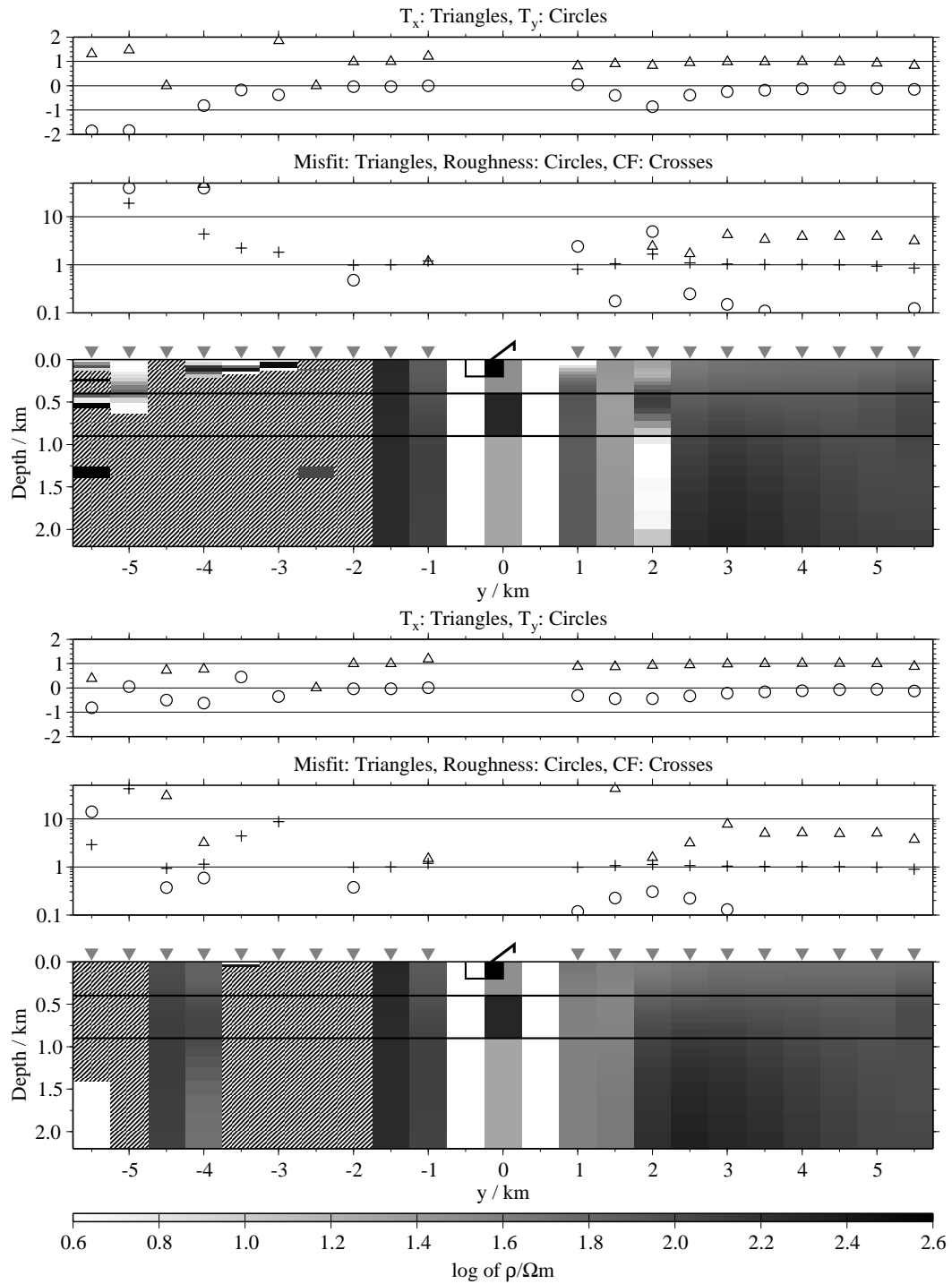


Figure B.331: The E_x inversion results for model N2; top: Regularisation scheme C1; bottom: Regularisation scheme C4; the inversions are done including the T_x -distortion parameters, which are displayed in the uppermost subpanels.

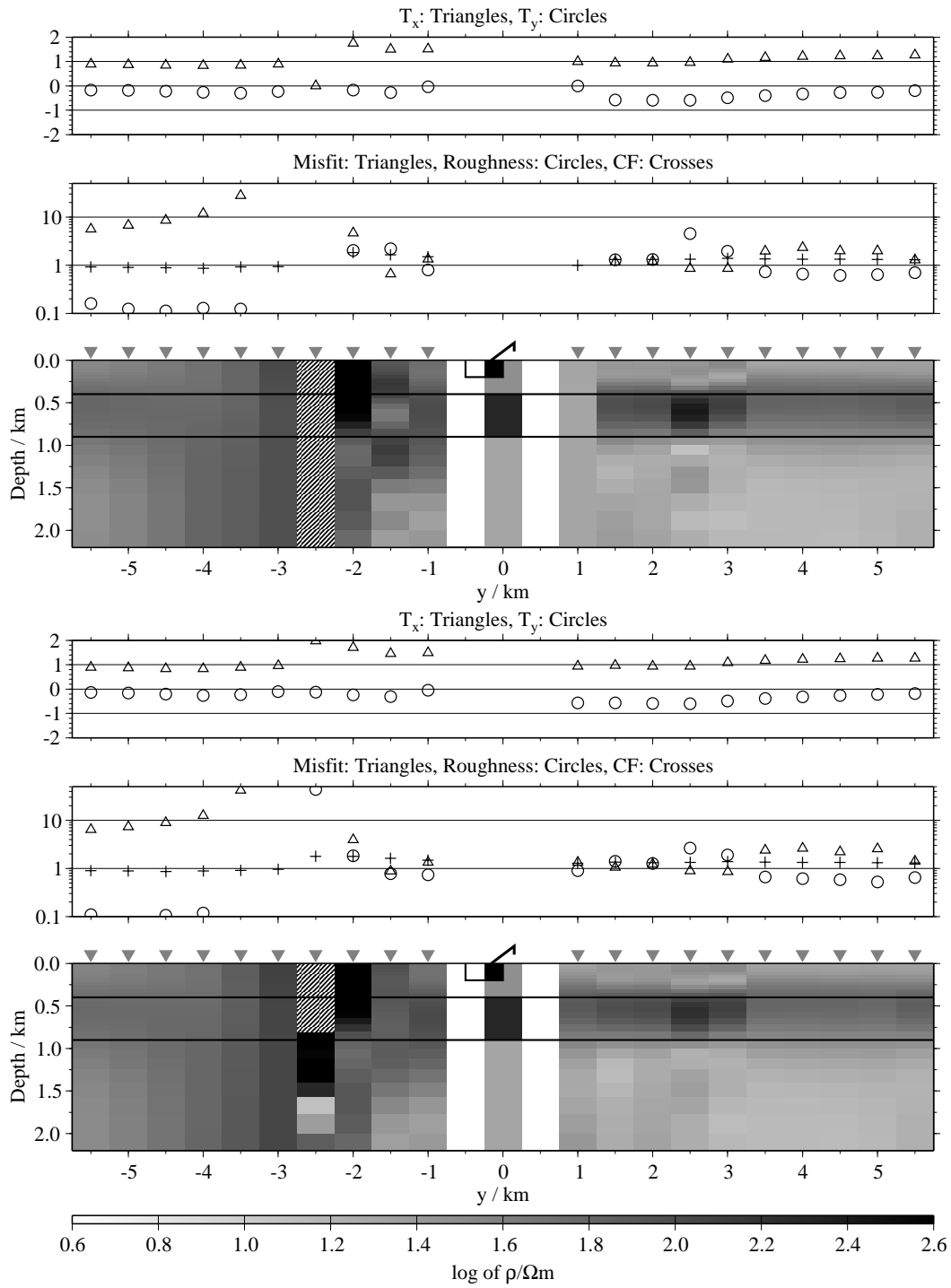


Figure B.332: The \dot{H}_y inversion results for model N2; top: Regularisation scheme C1; bottom: Regularisation scheme C4; the inversions are done including the T_x -distortion parameters, which are displayed in the uppermost subpanels.

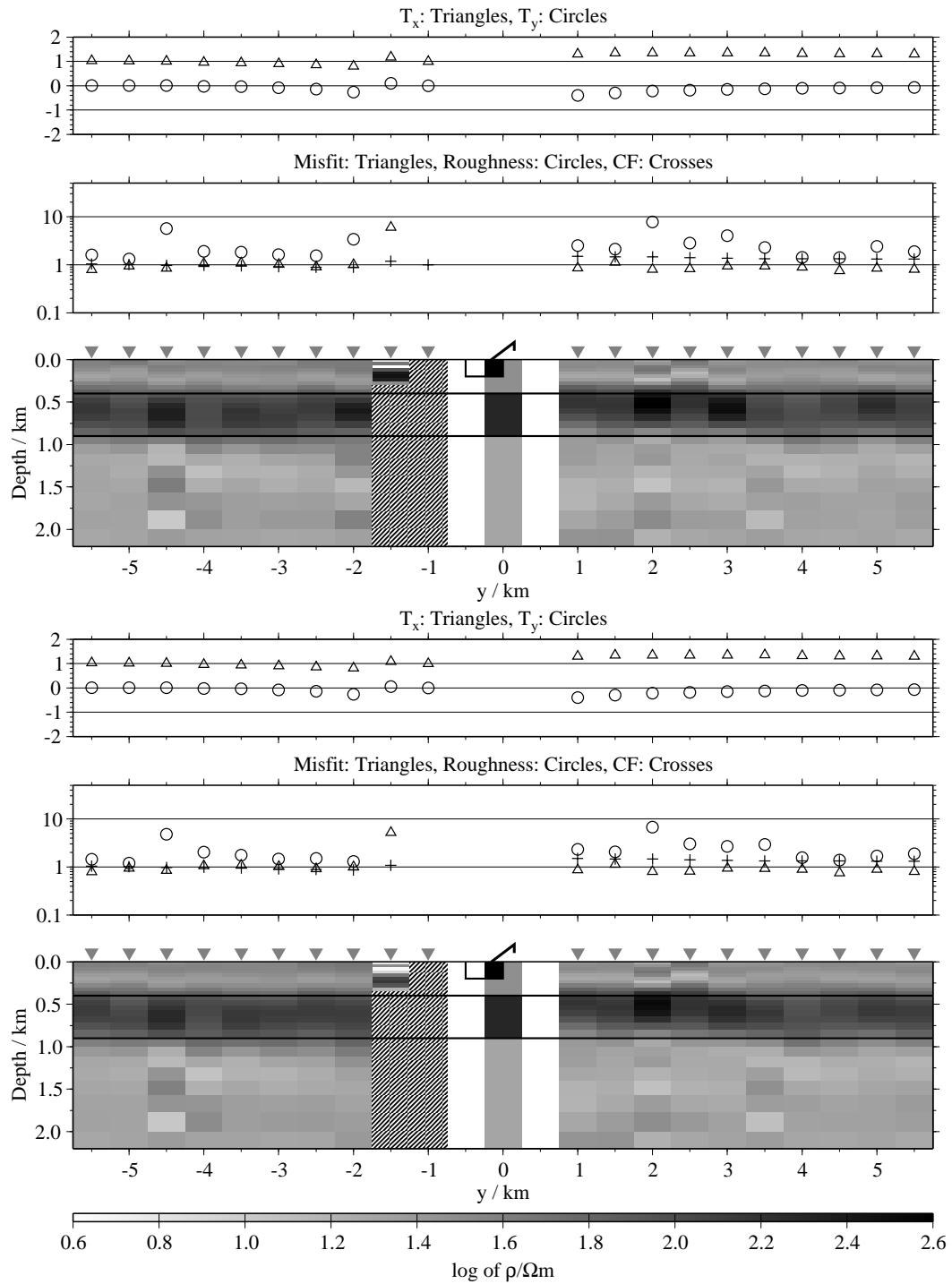


Figure B.333: The H_z inversion results for model N2; top: Regularisation scheme C1; bottom: Regularisation scheme C4; the inversions are done including the T_x -distortion parameters, which are displayed in the uppermost subpanels.

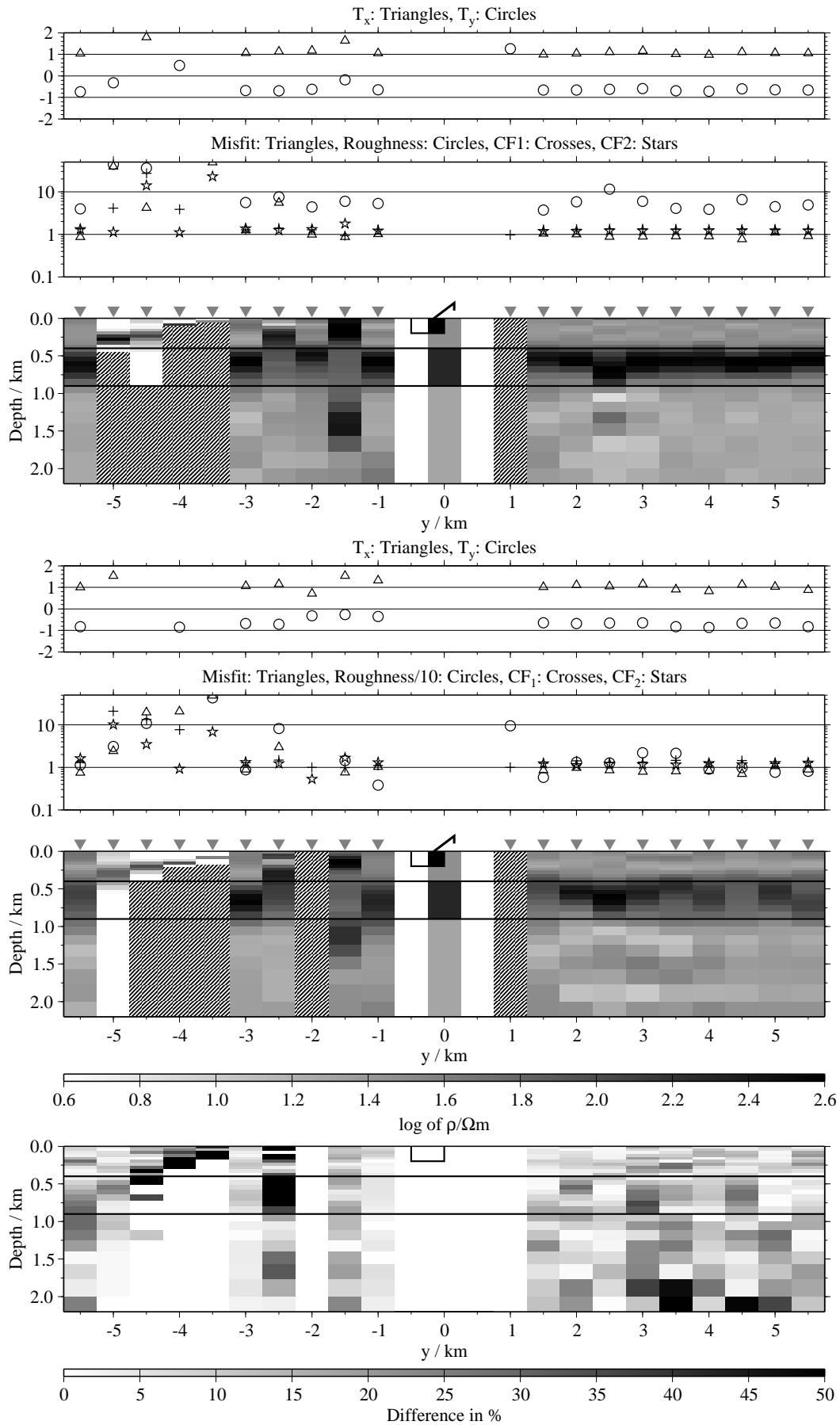


Figure B.334: Joint-inversion results for the components E_x and H_y , model N2, regularisation scheme C1; top: FJI; bottom: SJI; the inversions are done including the Tx-distortion parameters, which are displayed in the uppermost subpanels.

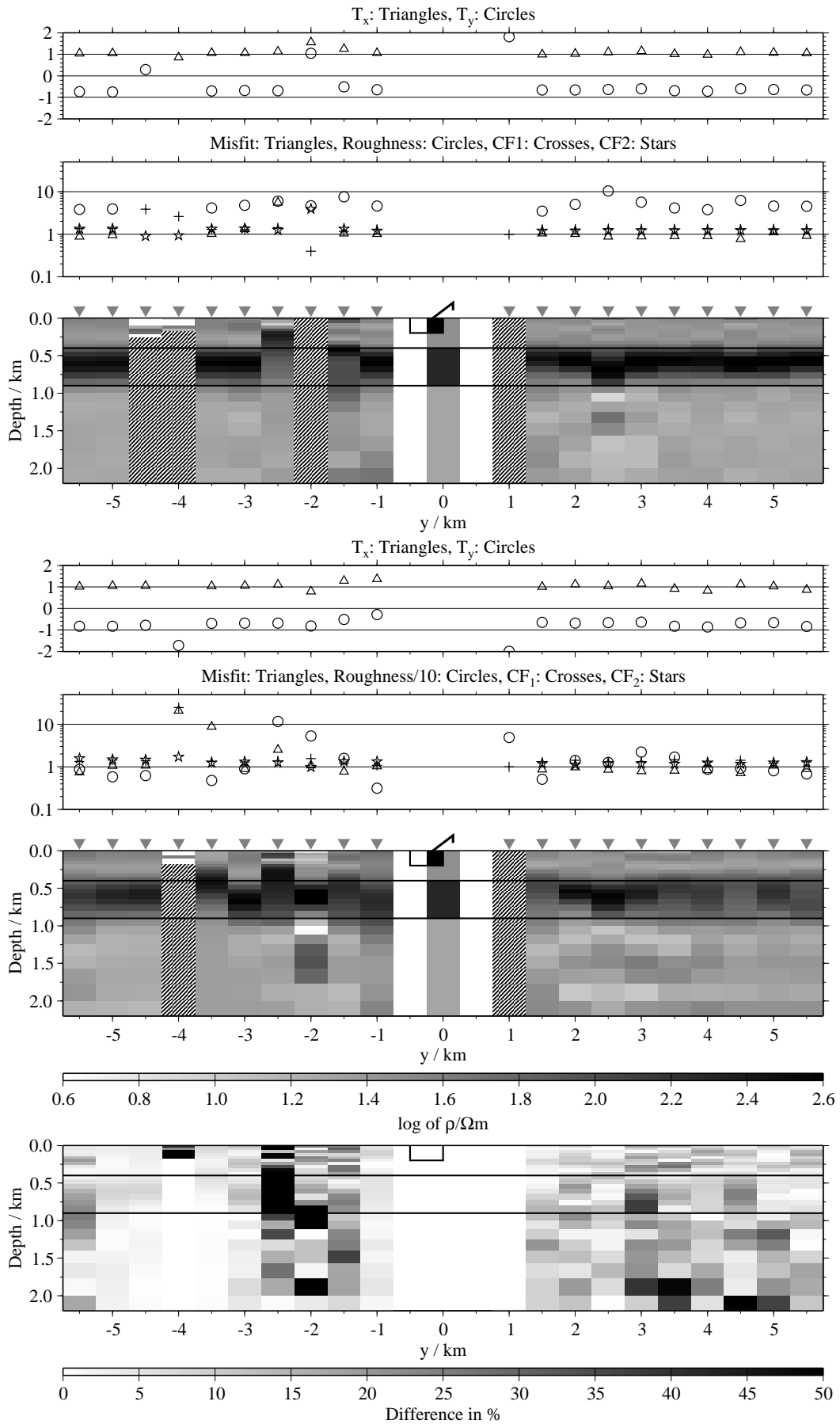


Figure B.335: Joint-inversion results for the components E_x and \dot{H}_y , model N2, regularisation scheme C4; top: FJI; bottom: SJI; the inversions are done including the T_x -distortion parameters, which are displayed in the uppermost subpanels.

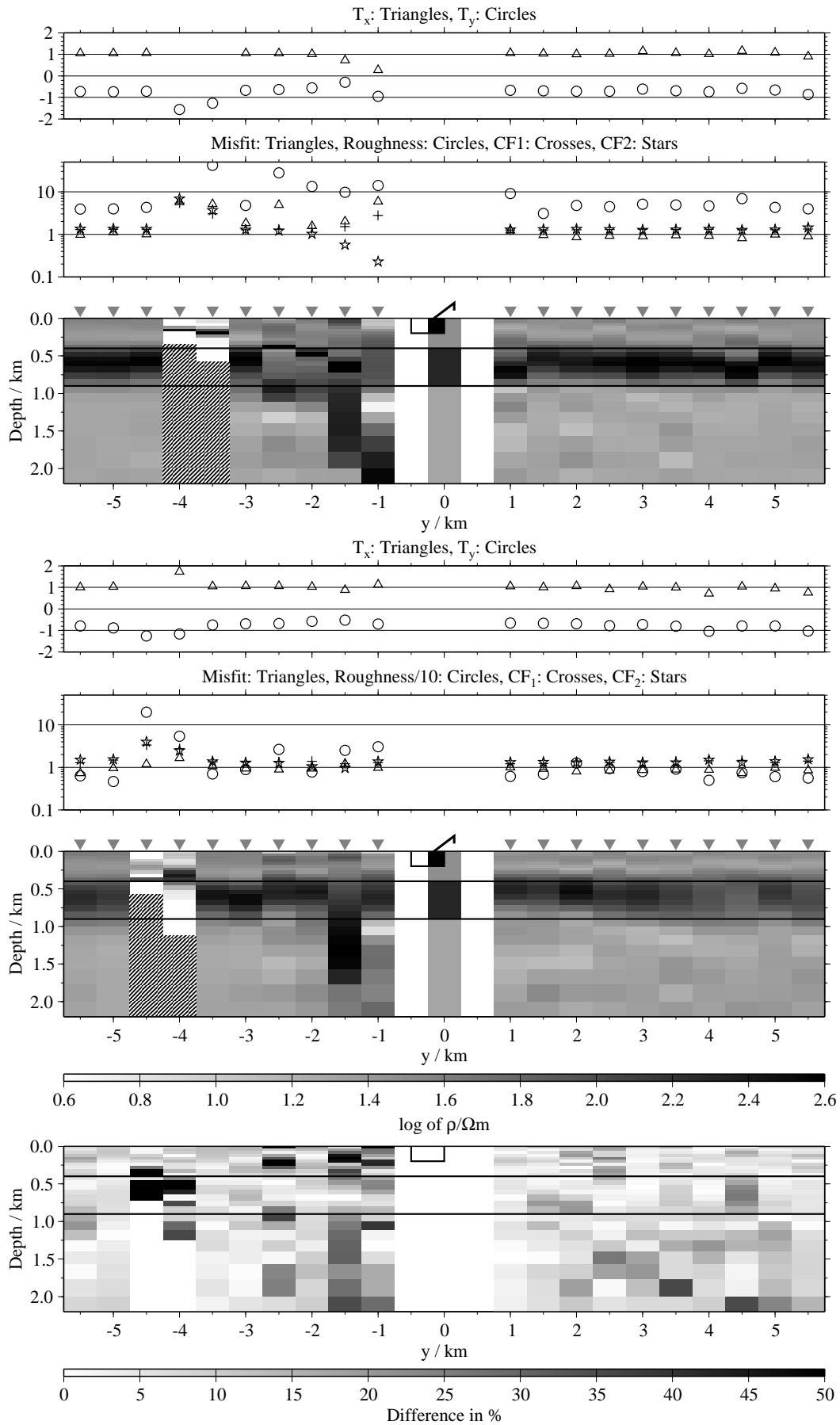


Figure B.336: Joint-inversion results for the components E_x and H_z , model N2, regularisation scheme C1; top: FJI; bottom: SJI; the inversions are done including the T_x -distortion parameters, which are displayed in the uppermost subpanels.

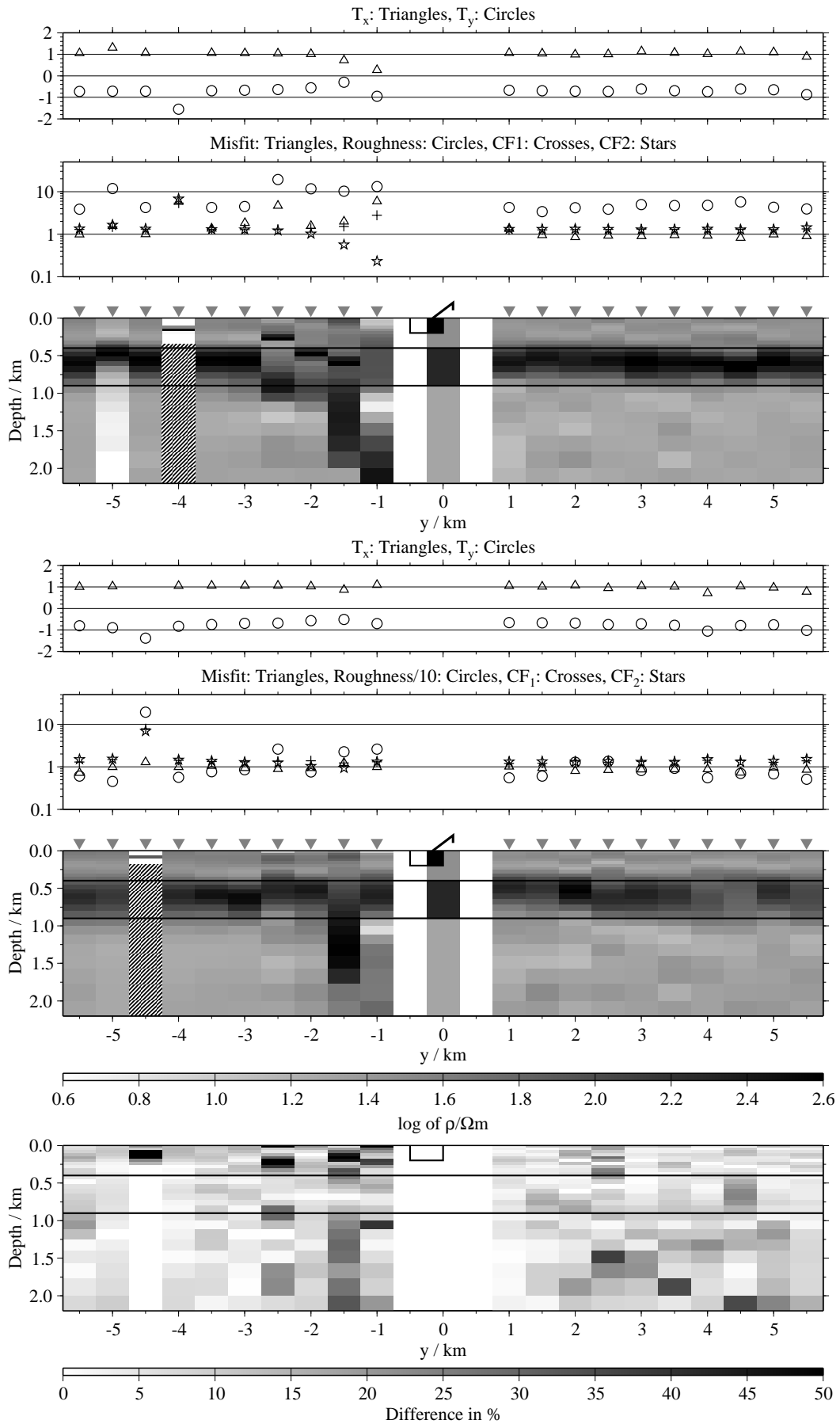


Figure B.337: Joint-inversion results for the components E_x and H_z , model N2, regularisation scheme C4; top: FJI; bottom: SJI; the inversions are done including the T_x -distortion parameters, which are displayed in the uppermost subpanels.

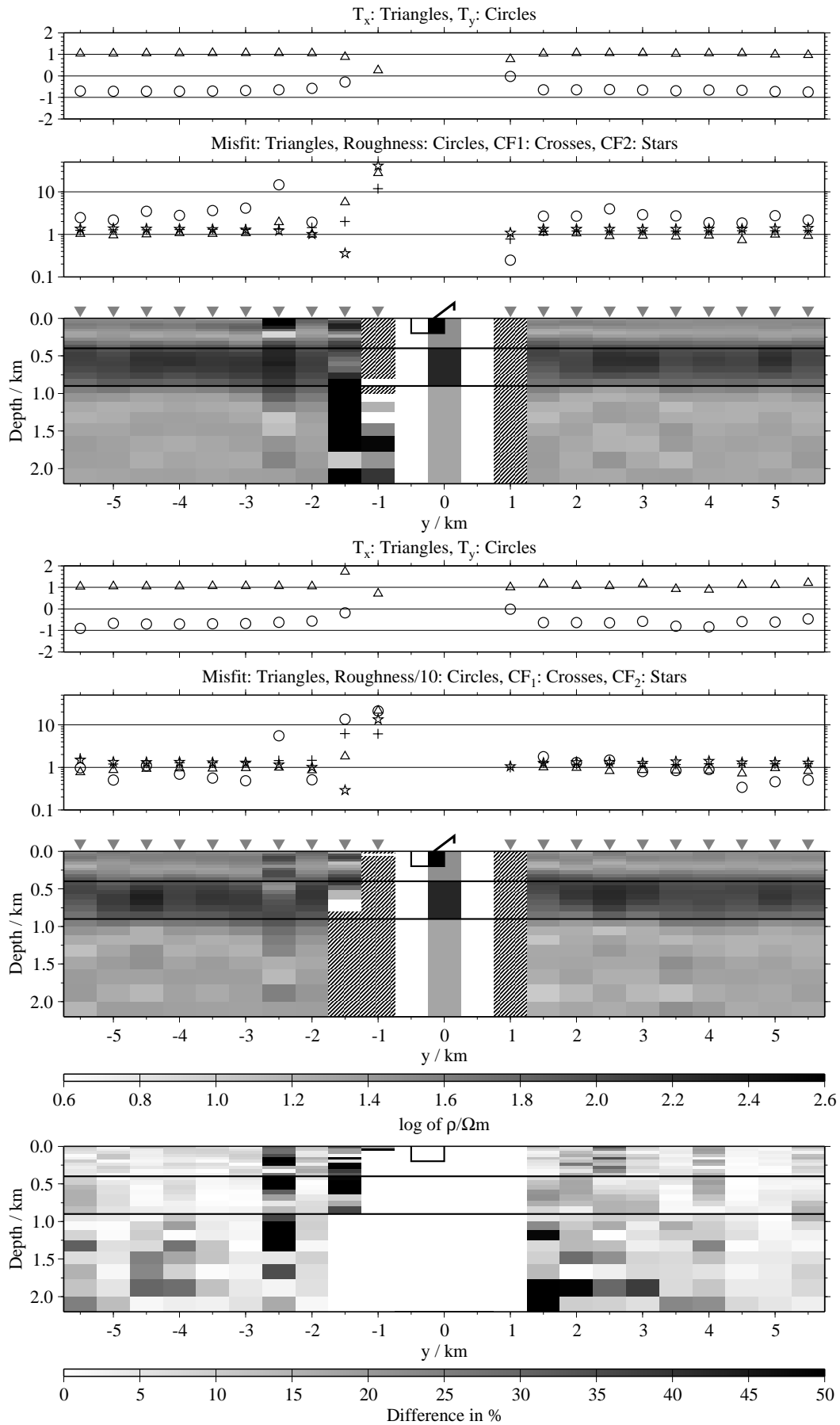


Figure B.338: Joint-inversion results for the components \dot{H}_y and \dot{H}_z , model N2, regularisation scheme C1; top: FJI; bottom: SJI; the inversions are done including the Tx-distortion parameters, which are displayed in the uppermost subpanels.

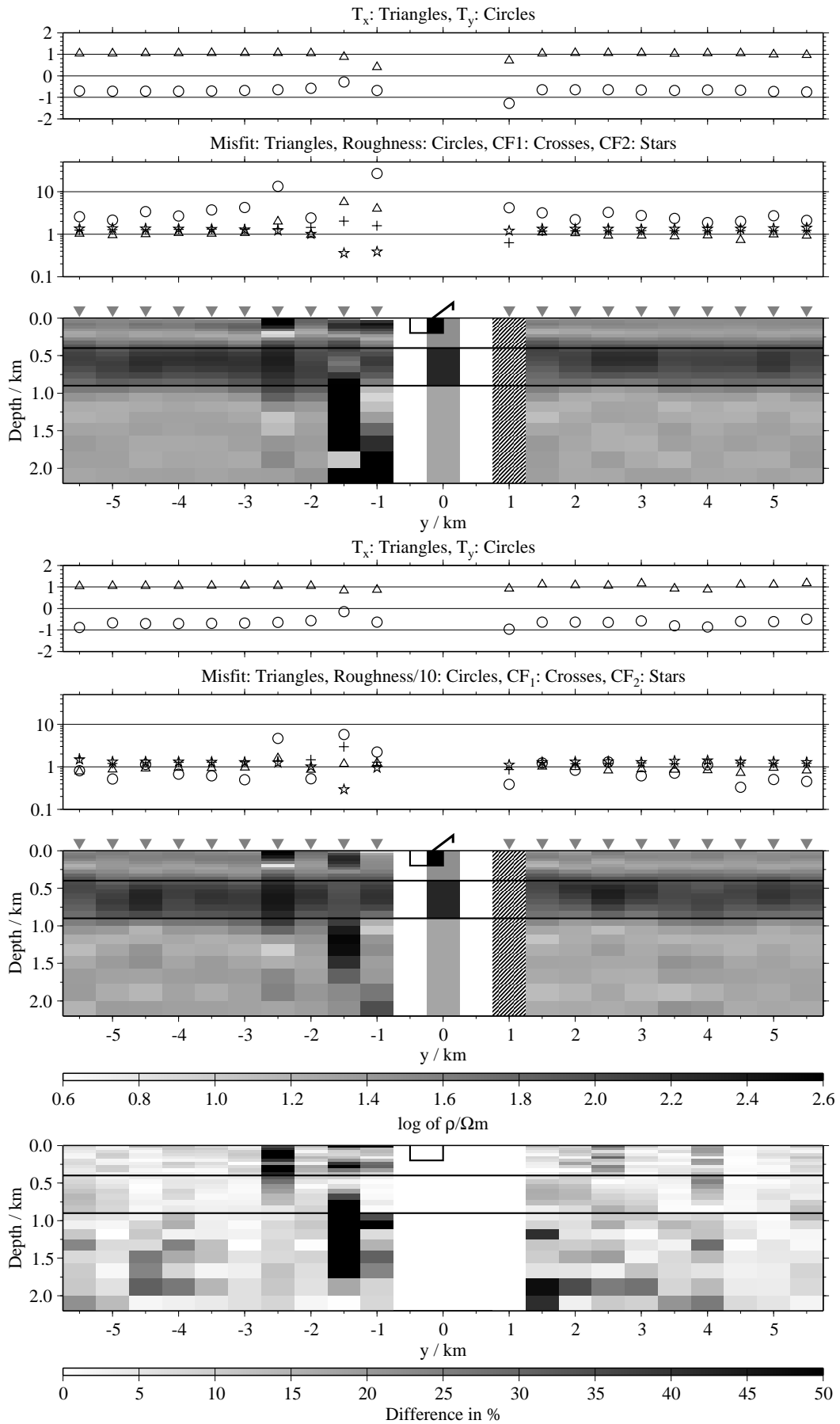


Figure B.339: Joint-inversion results for the components \dot{H}_y and \dot{H}_z , model N2, regularisation scheme C4; top: FJI; bottom: SJI; the inversions are done including the Tx-distortion parameters, which are displayed in the uppermost subpanels.

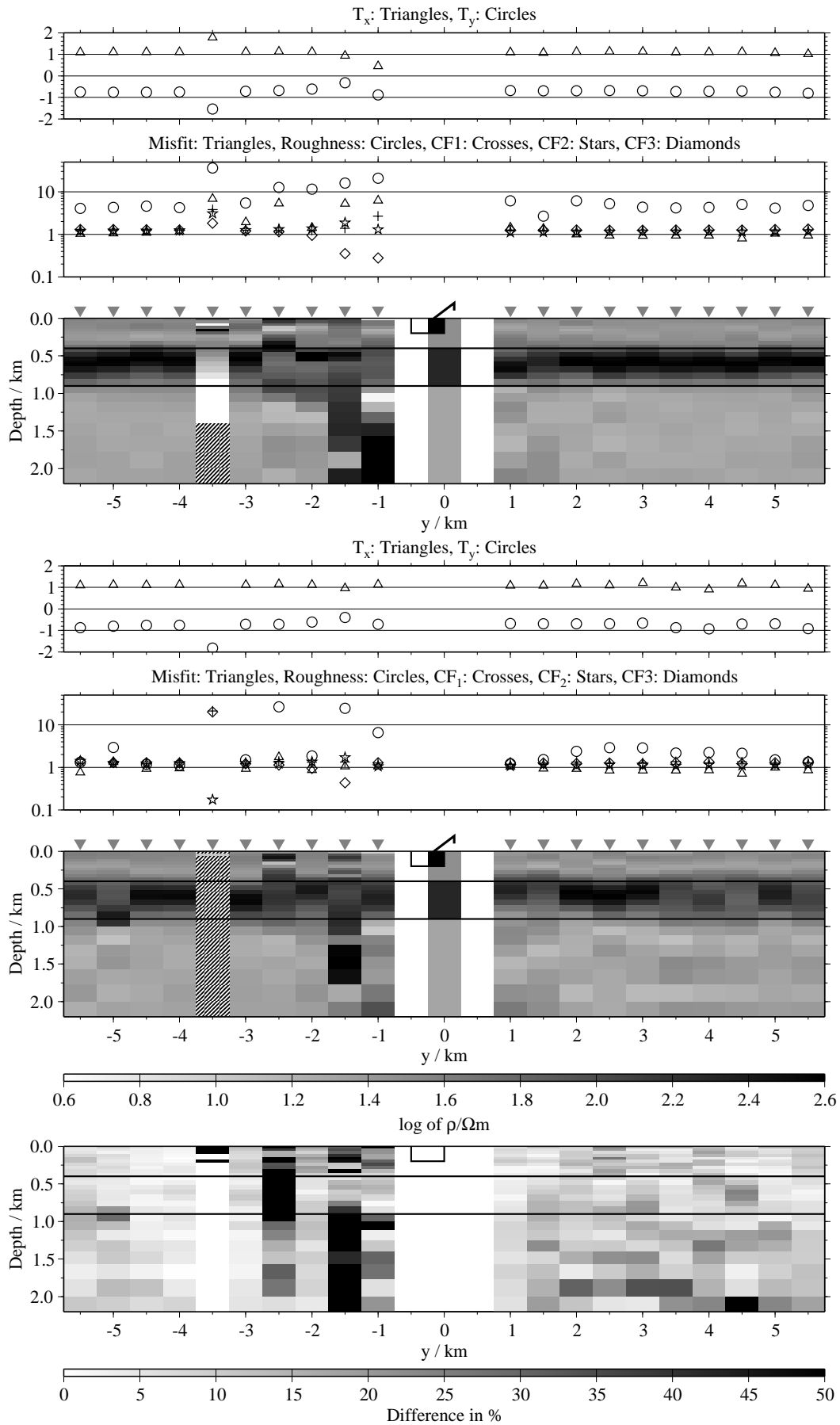


Figure B.340: Joint-inversion results for all three components, model N2, regularisation scheme C1; top: FJI; bottom: SJI; the inversions are done including the Tx-distortion parameters, which are displayed in the uppermost subpanels.

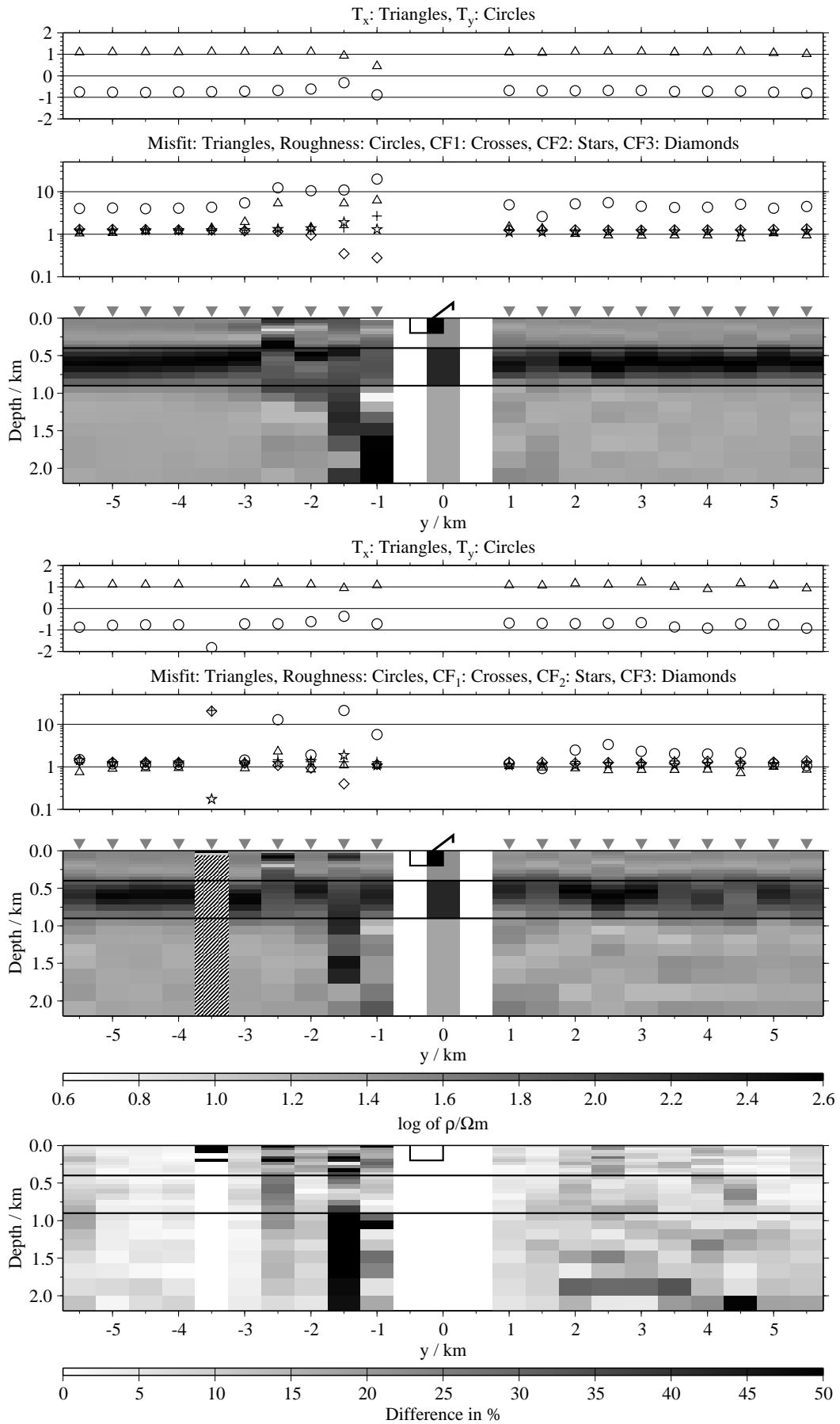


Figure B.341: Joint-inversion results for all three components, model N2, regularisation scheme C4; top: FJI; bottom: SJI; the inversions are done including the T_x -distortion parameters, which are displayed in the uppermost subpanels.

B.5 Inversions of edited transients of adjacent stations

In this section the results for the joint-inversions of the transients of adjacent stations are presented. The tables B.29 and B.30 show which data point are removed from the transients prior to inversion. In the tabs. and in the caption of figs. B.342, B.343, B.356, B.357, B.370 and B.371 station numbers are used. Station 1 is located at $y = -5.5$ km. Station 20 is located at $y = 5.5$ km. The other stations are numbered accordingly.

All magnetic transients not listed in the tables B.29 and B.30 are used without removing data points. The first four data points were removed uniformly from all E_x -transients. No data points had to be removed from the magnetic transients calculated for model K3.

St. #1	St. #2	Co.	cut/s	cut/e	y / km
4	5	\dot{H}_y	8	0	-3.75
5	6	\dot{H}_y	3	0	-3.25
6	7	\dot{H}_y	10	0	-2.75
7	8	\dot{H}_y	3	0	-2.25
8	9	\dot{H}_y	3	0	-1.75
9	10	\dot{H}_y	11	0	-1.75
11	12	\dot{H}_y	11	0	1.25
12	13	\dot{H}_y	8	0	1.75
13	14	\dot{H}_y	11	0	2.25
4	5	\dot{H}_z	8	0	-3.75
5	6	\dot{H}_z	19	0	-3.25
6	7	\dot{H}_z	18	0	-2.75
7	8	\dot{H}_z	19	0	-2.25
8	9	\dot{H}_z	19	0	-1.75

Table B.29: This table lists the number of data points removed from the transients for the inversions using the data sets from two adjacent stations (model F1). The rows "St. #1" and "St. #2" define the stations used. The result will be displayed at the position y . "Co." is the component used. The number printed in rows designated "cut/s" is the number of data points removed from the start whereas "cut/e" is the number of data points removed from the end of the transient.

St. #1	St. #2	Co.	cut/s	cut/e	y / km
9	10	\dot{H}_y	10	0	-1.75
11	12	\dot{H}_y	10	0	1.25
12	13	\dot{H}_y	5	0	1.75
13	14	\dot{H}_y	9	0	2.25
14	15	\dot{H}_y	7	0	2.75
3	4	\dot{H}_z	18	0	-4.25
4	5	\dot{H}_z	19	0	-3.75
5	6	\dot{H}_z	19	0	-3.25
7	8	\dot{H}_z	14	0	-2.25
8	9	\dot{H}_z	15	0	-1.75
9	10	\dot{H}_z	10	0	-1.75

Table B.30: This table lists the number of data points removed from the transients for the inversions using the data sets from two adjacent stations (model M). The rows "St. #1" and "St. #2" define the stations used. The result will be displayed at the position y . "Co." is the component used. The number printed in rows designated "cut/s" is the number of data points removed from the start whereas "cut/e" is the number of data points removed from the end of the transient.

B.5.1 Model F1

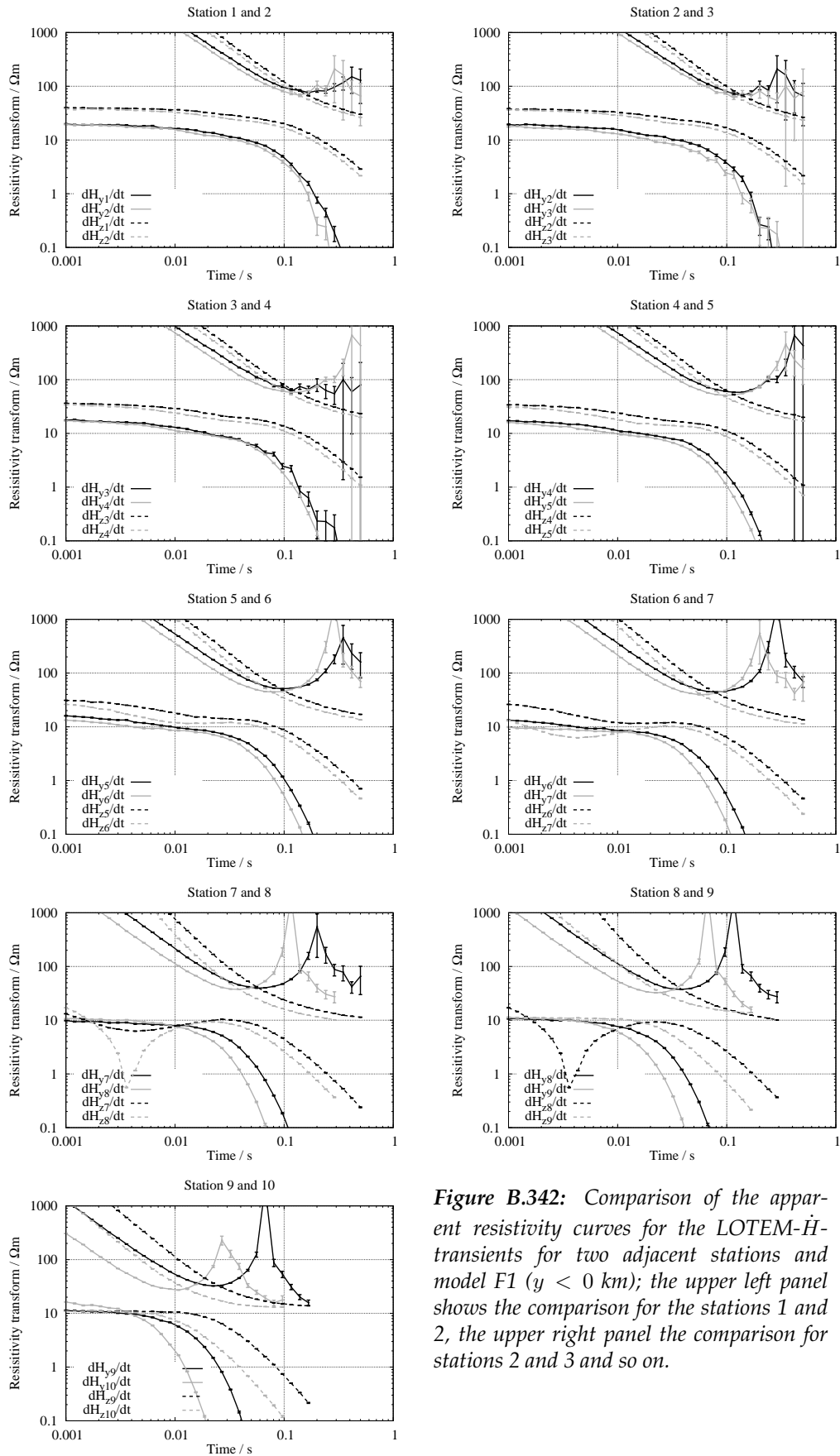


Figure B.342: Comparison of the apparent resistivity curves for the LOTEM-H-transients for two adjacent stations and model F1 ($y < 0$ km); the upper left panel shows the comparison for the stations 1 and 2, the upper right panel the comparison for stations 2 and 3 and so on.

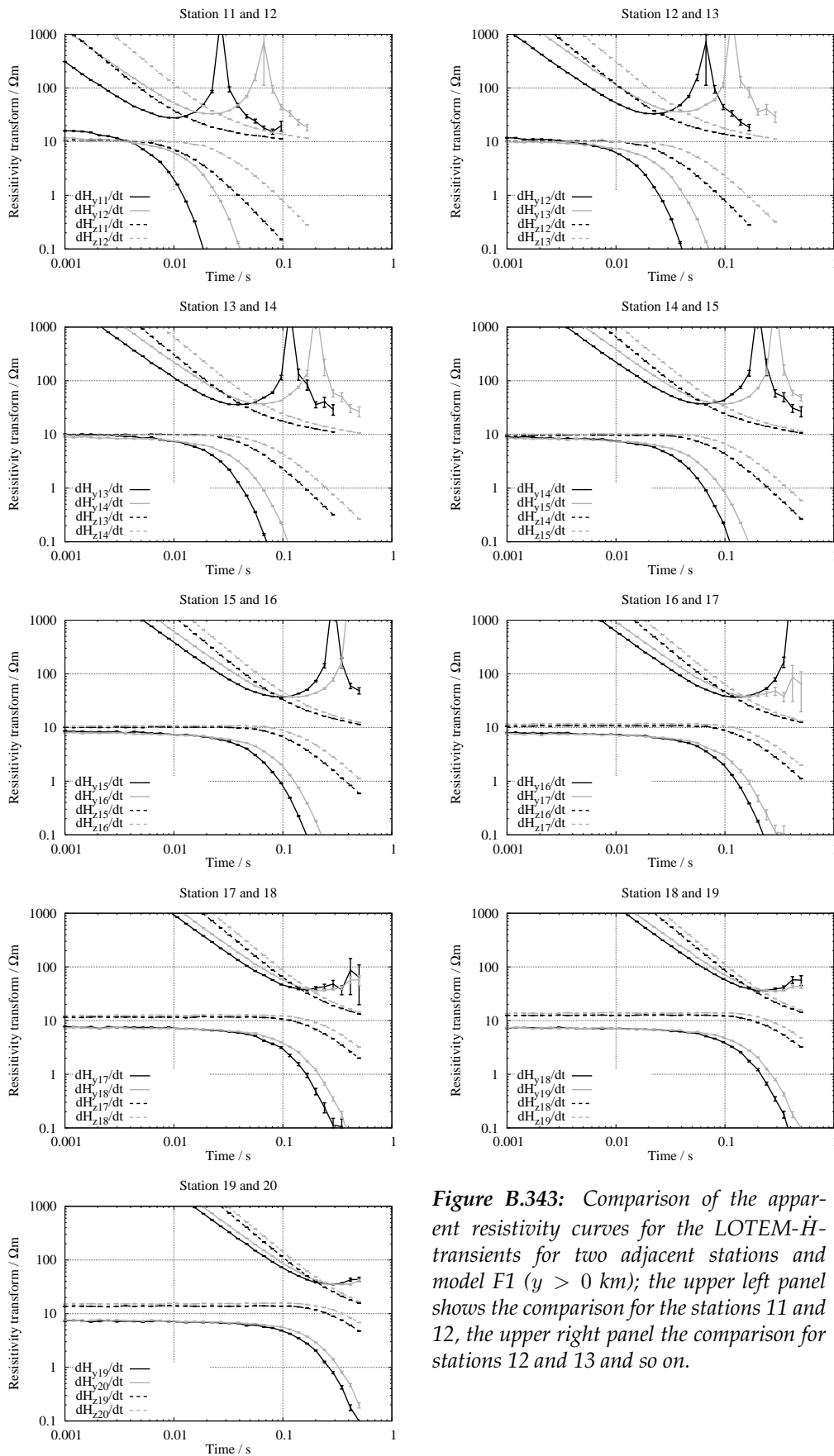


Figure B.343: Comparison of the apparent resistivity curves for the LOTEM- \dot{H} -transients for two adjacent stations and model F1 ($y > 0$ km); the upper left panel shows the comparison for the stations 11 and 12, the upper right panel the comparison for stations 12 and 13 and so on.

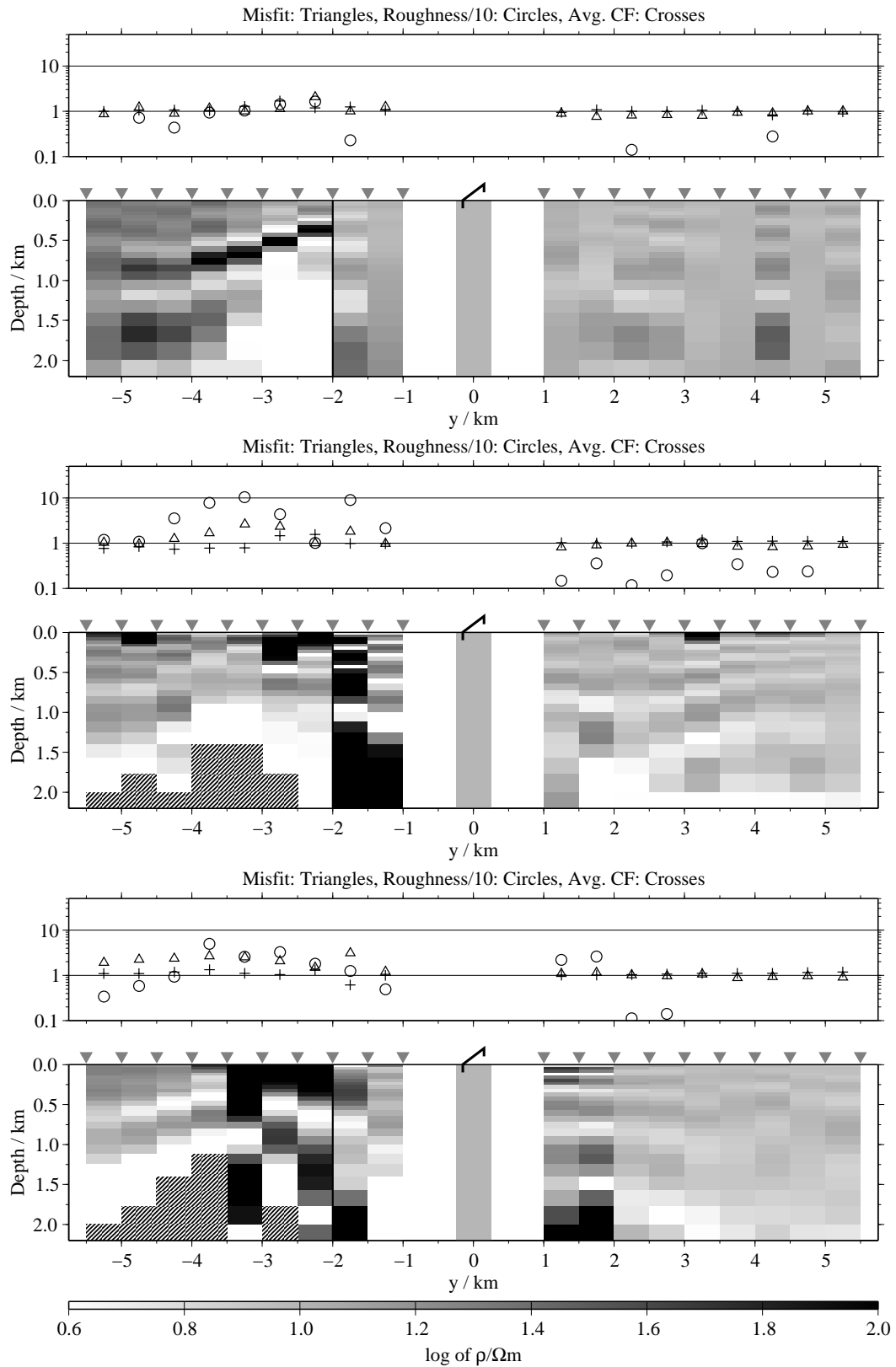


Figure B.344: FJI results for the transient of adjacent stations, model F1, regularisation scheme C1; from top to bottom E_x -, H_y - and H_z -components;

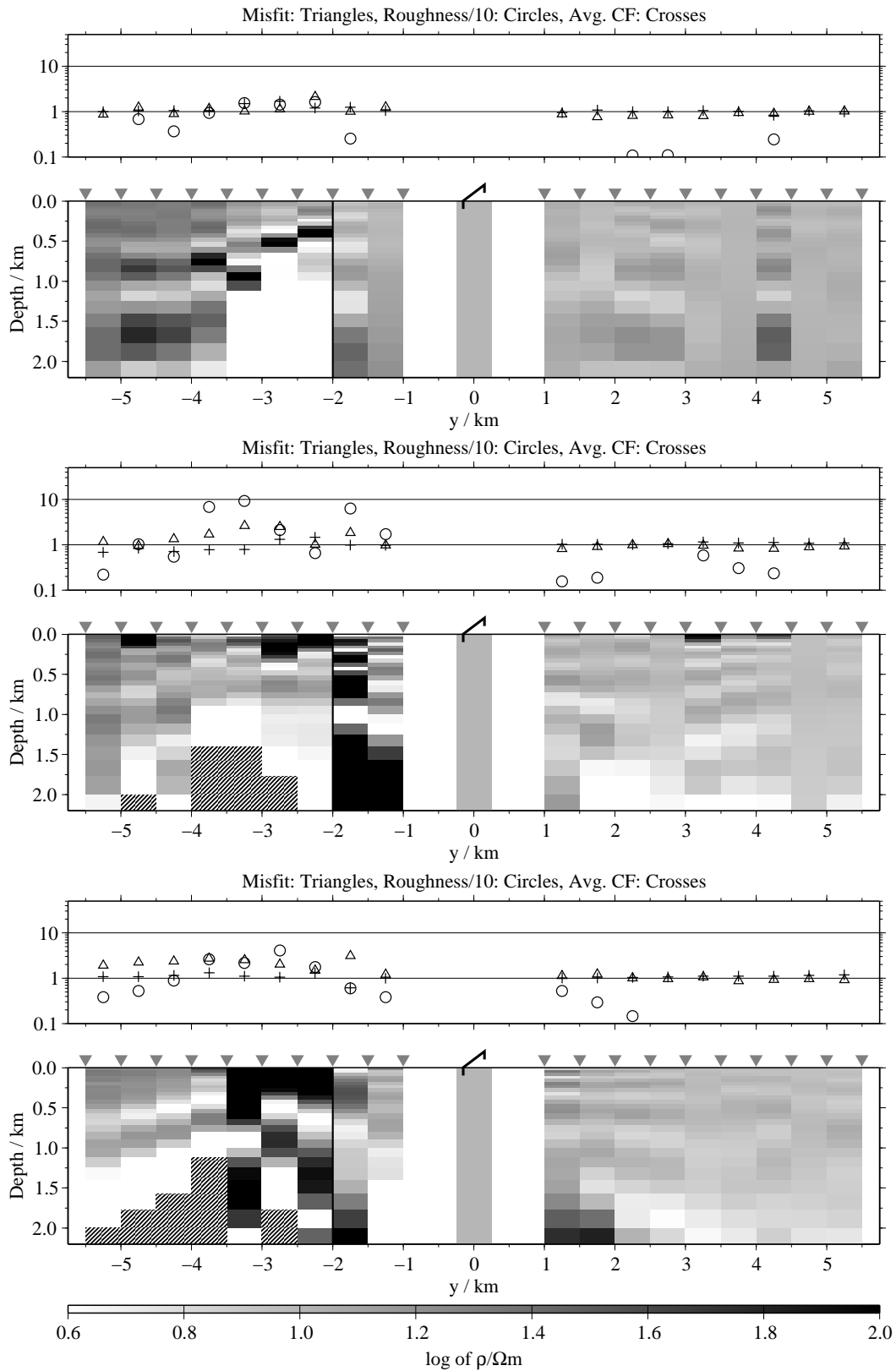


Figure B.345: FJI results for the transient of adjacent stations, model F1, regularisation scheme C4; from top to bottom E_x -, H_y - and H_z -components;

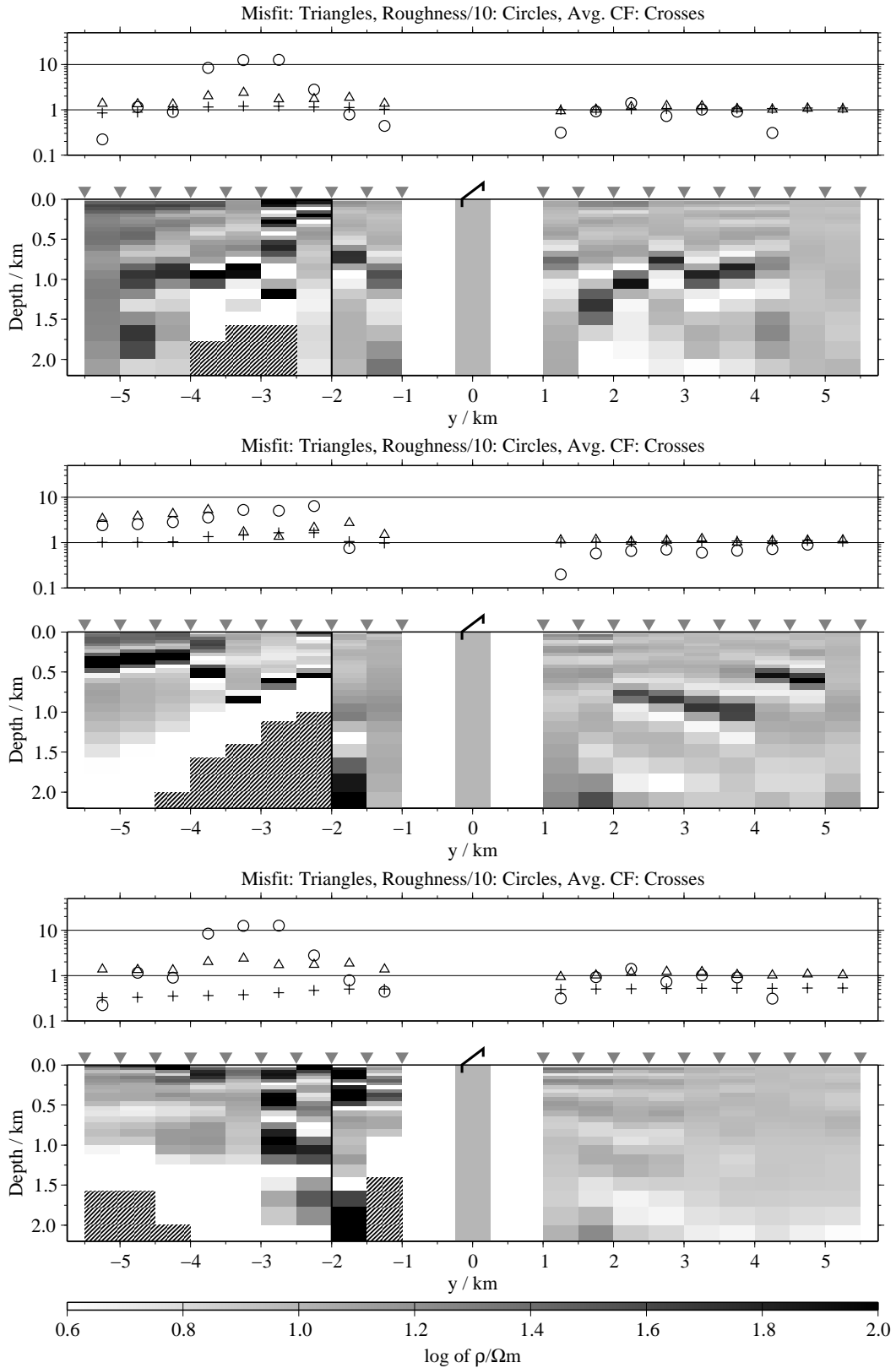


Figure B.346: FJI results for the transient of adjacent stations, model F1, regularisation scheme C1; from top to bottom $E_x-\dot{H}_y$, $E_x-\dot{H}_z$ and $\dot{H}_y-\dot{H}_z$;

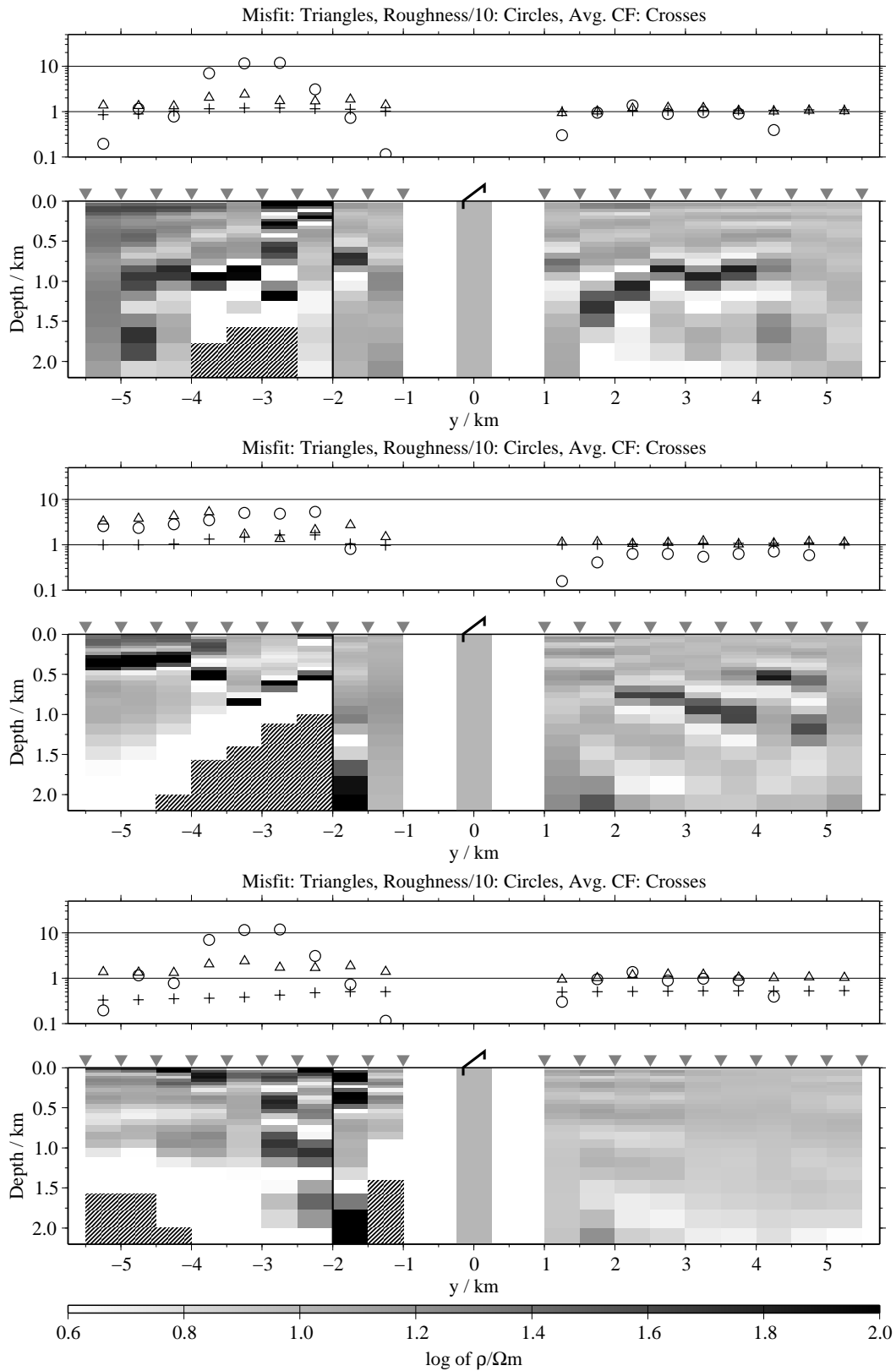


Figure B.347: FJI results for the transient of adjacent stations, model F1, regularisation scheme C4; from top to bottom $E_x - \dot{H}_y$, $E_x - \dot{H}_z$ and $\dot{H}_y - \dot{H}_z$;

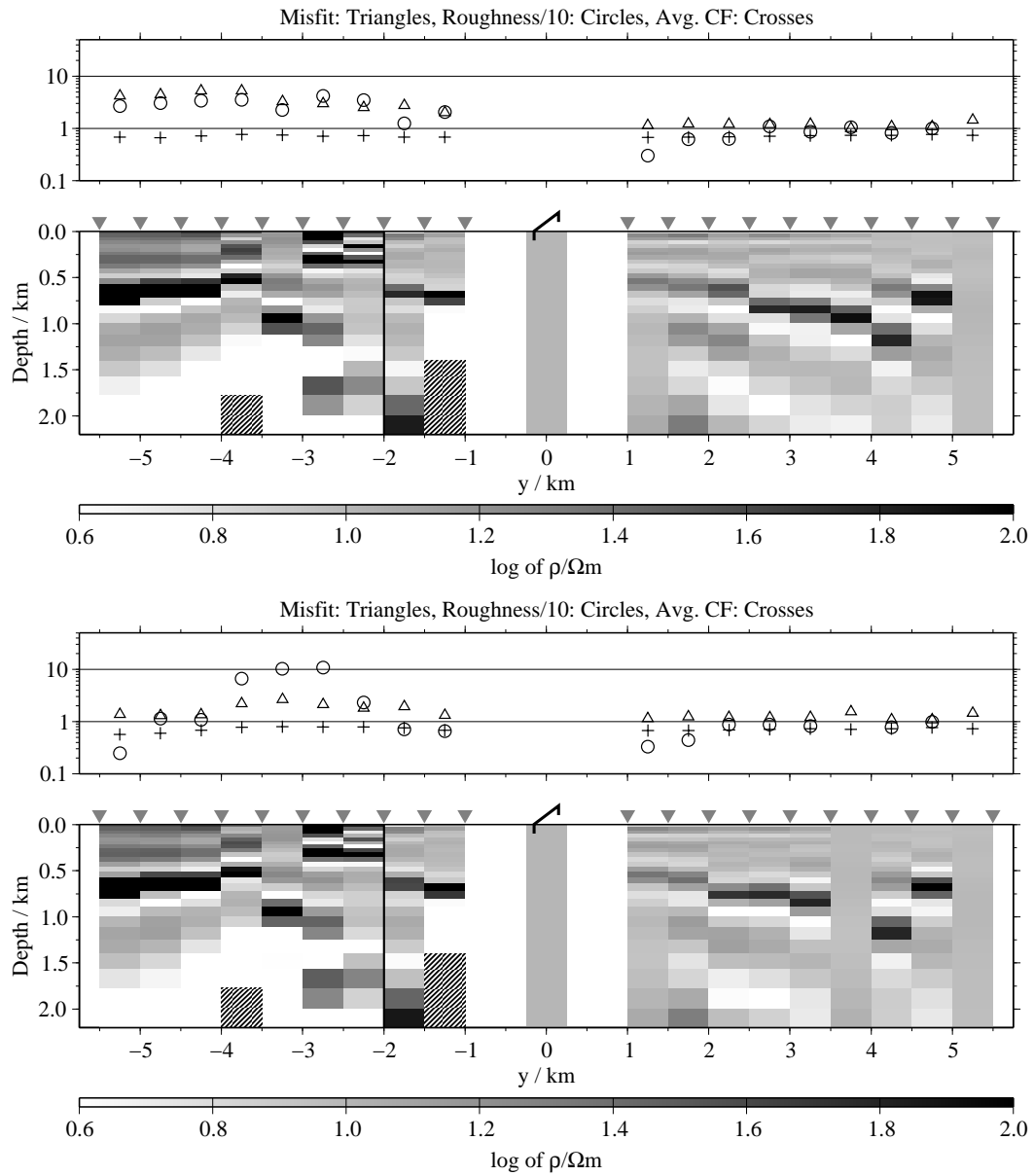


Figure B.348: FJI results for the transient of adjacent stations using all three components, model F1; top: Regularisation scheme C1; bottom: Regularisation scheme C4;

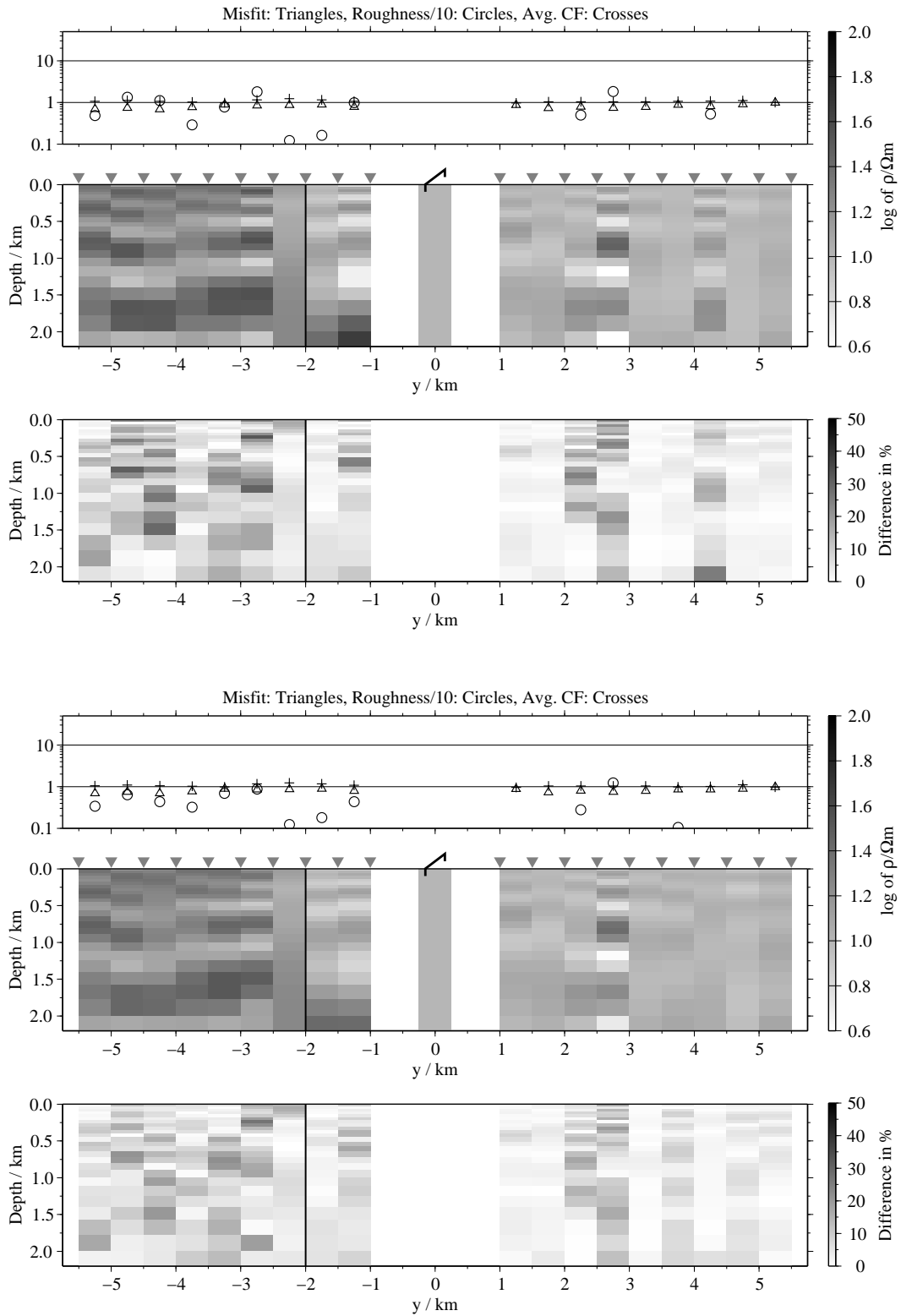


Figure B.349: SJI results for the E_x -transients from adjacent stations, model F1; Top panels: Average inversion results and relative differences (regularisation scheme C1); bottom: Average inversion results and relative differences (regularisation scheme C4);

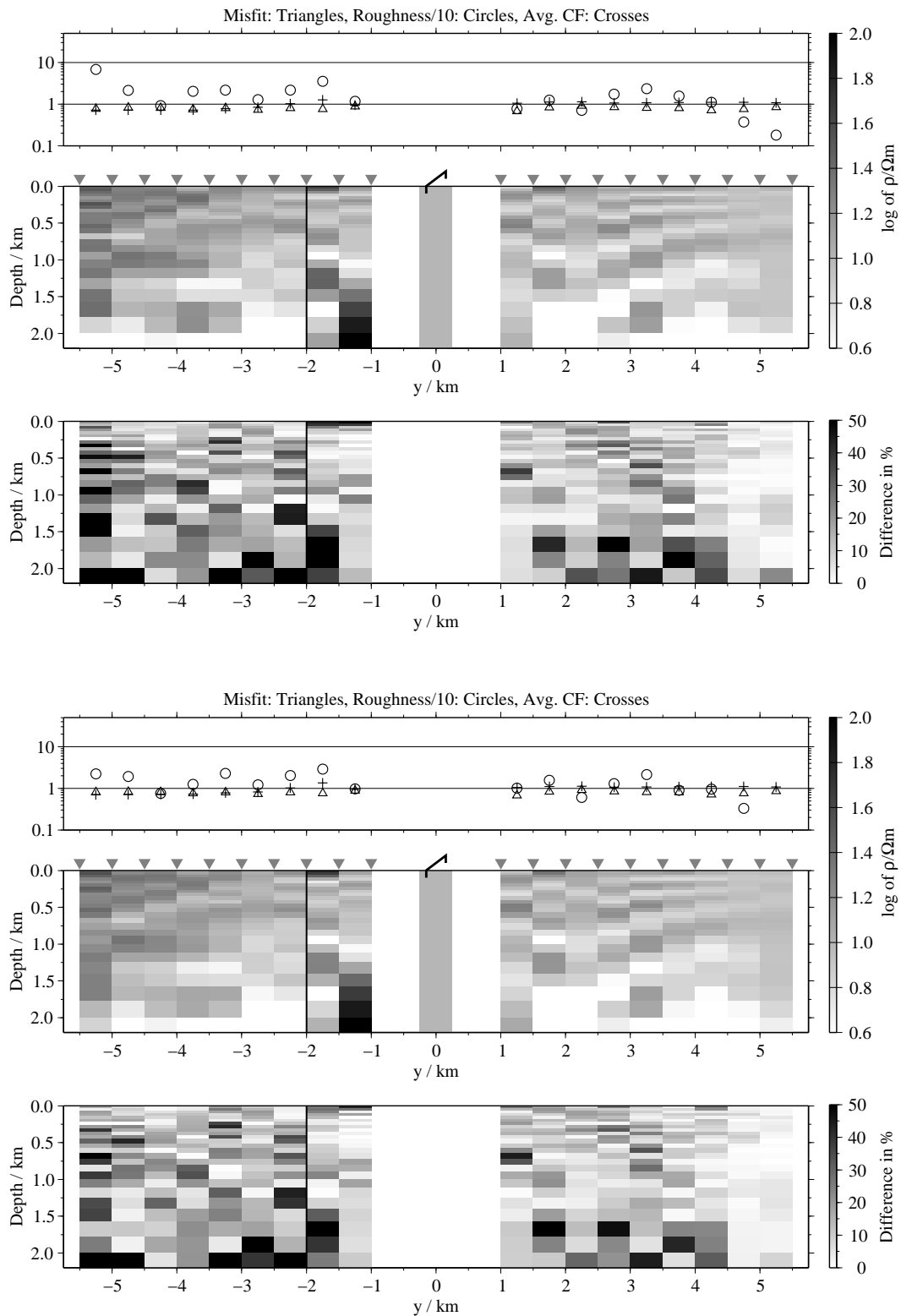


Figure B.350: SJI results for the \dot{H}_y -transients from adjacent stations, model F1; Top panels: Average inversion results and relative differences (regularisation scheme C1); bottom: Average inversion results and relative differences (regularisation scheme C4);

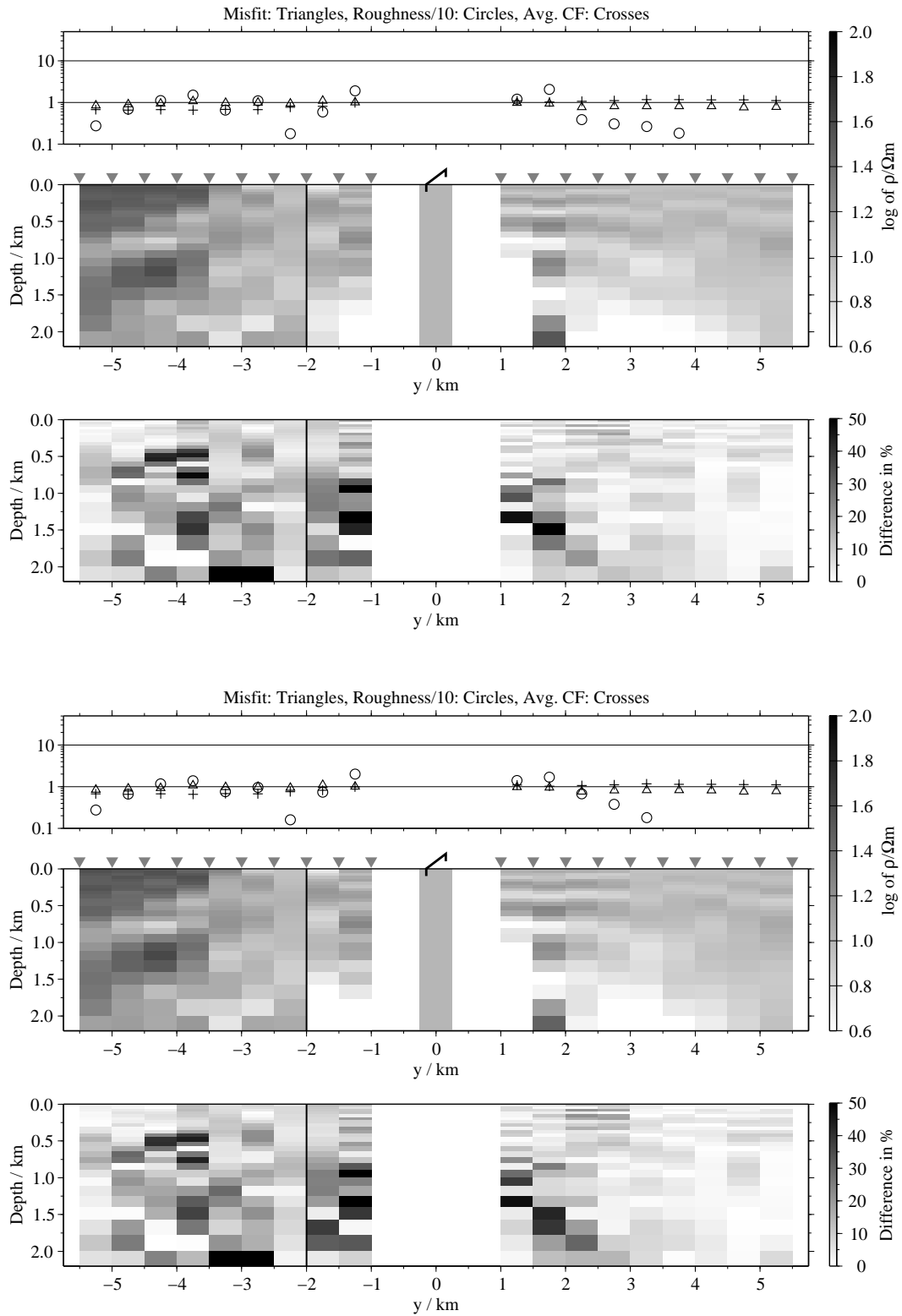


Figure B.351: SJI results for the \dot{H}_z -transients from adjacent stations, model F1; Top panels: Average inversion results and relative differences (regularisation scheme C1); bottom: Average inversion results and relative differences (regularisation scheme C4);

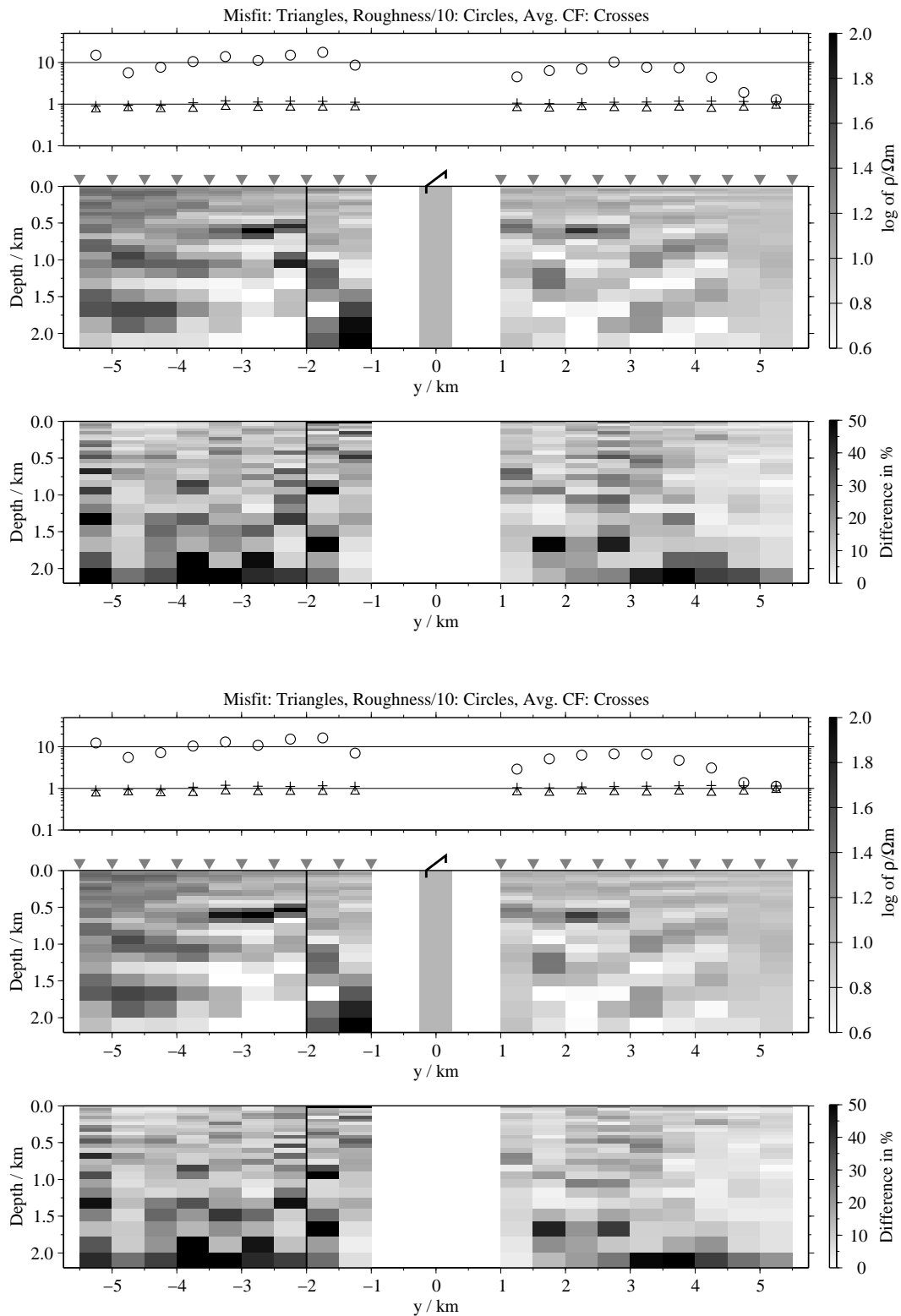


Figure B.352: SJI results for the E_x - and H_y -transients from adjacent stations, model F1; Top panels: Average inversion results and relative differences (regularisation scheme C1); bottom: Average inversion results and relative differences (regularisation scheme C4);

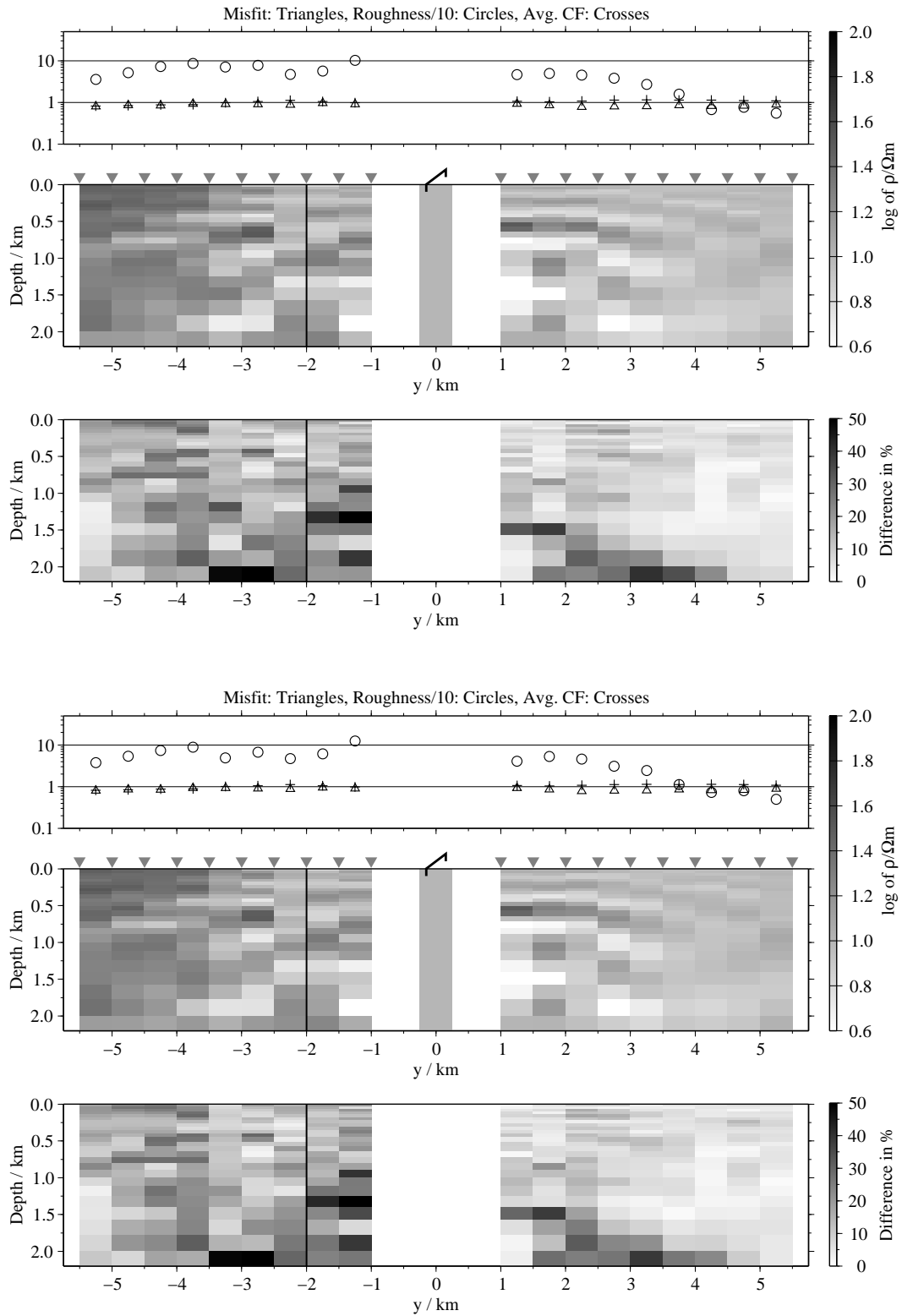


Figure B.353: SJI results for the E_x - and \dot{H}_z -transients from adjacent stations, model F1; Top panels: Average inversion results and relative differences (regularisation scheme C1); bottom: Average inversion results and relative differences (regularisation scheme C4);

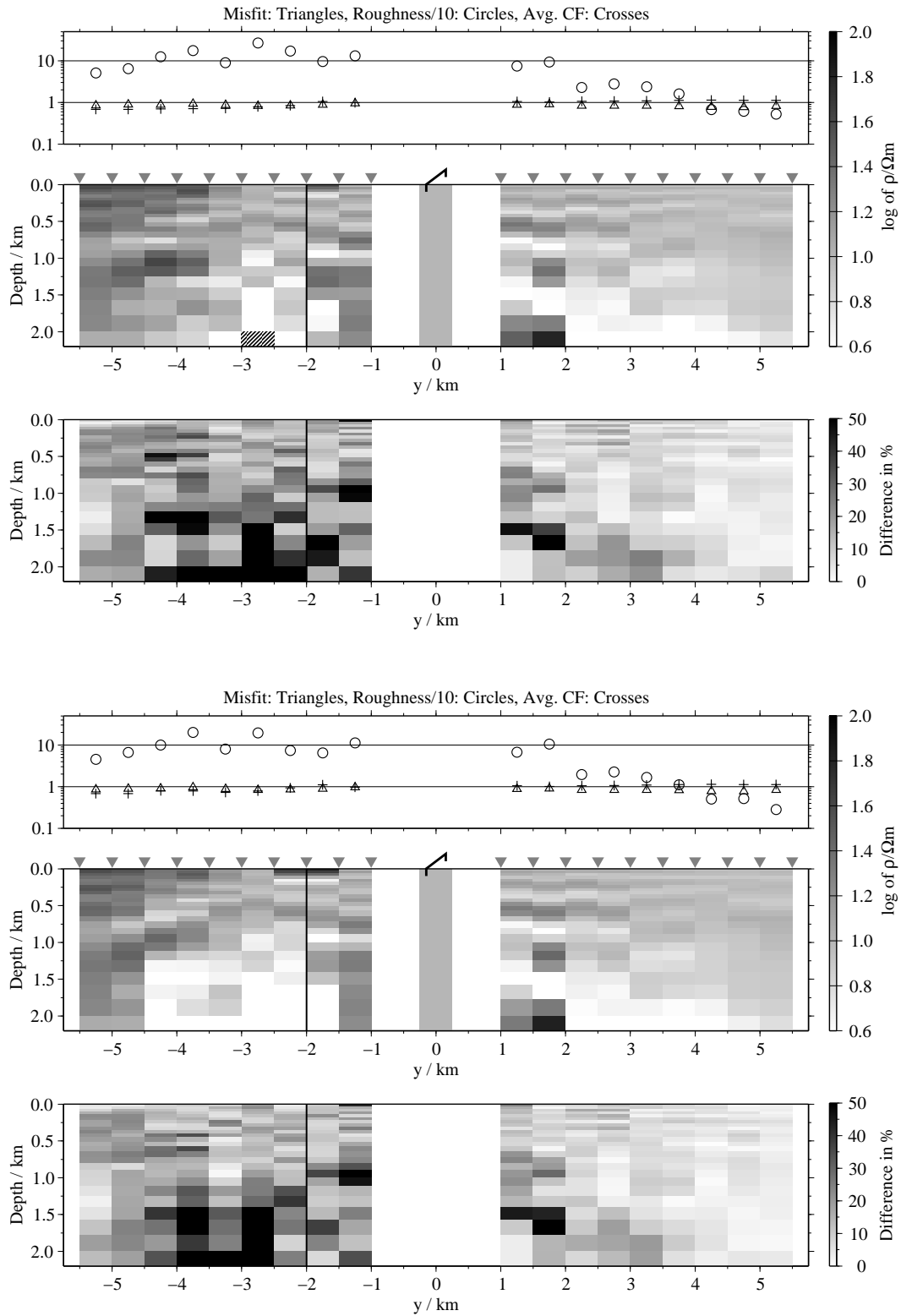


Figure B.354: SJI results for the \dot{H}_y - and \dot{H}_z -transients from adjacent stations, model F1; Top panels: Average inversion results and relative differences (regularisation scheme C1); bottom: Average inversion results and relative differences (regularisation scheme C4);

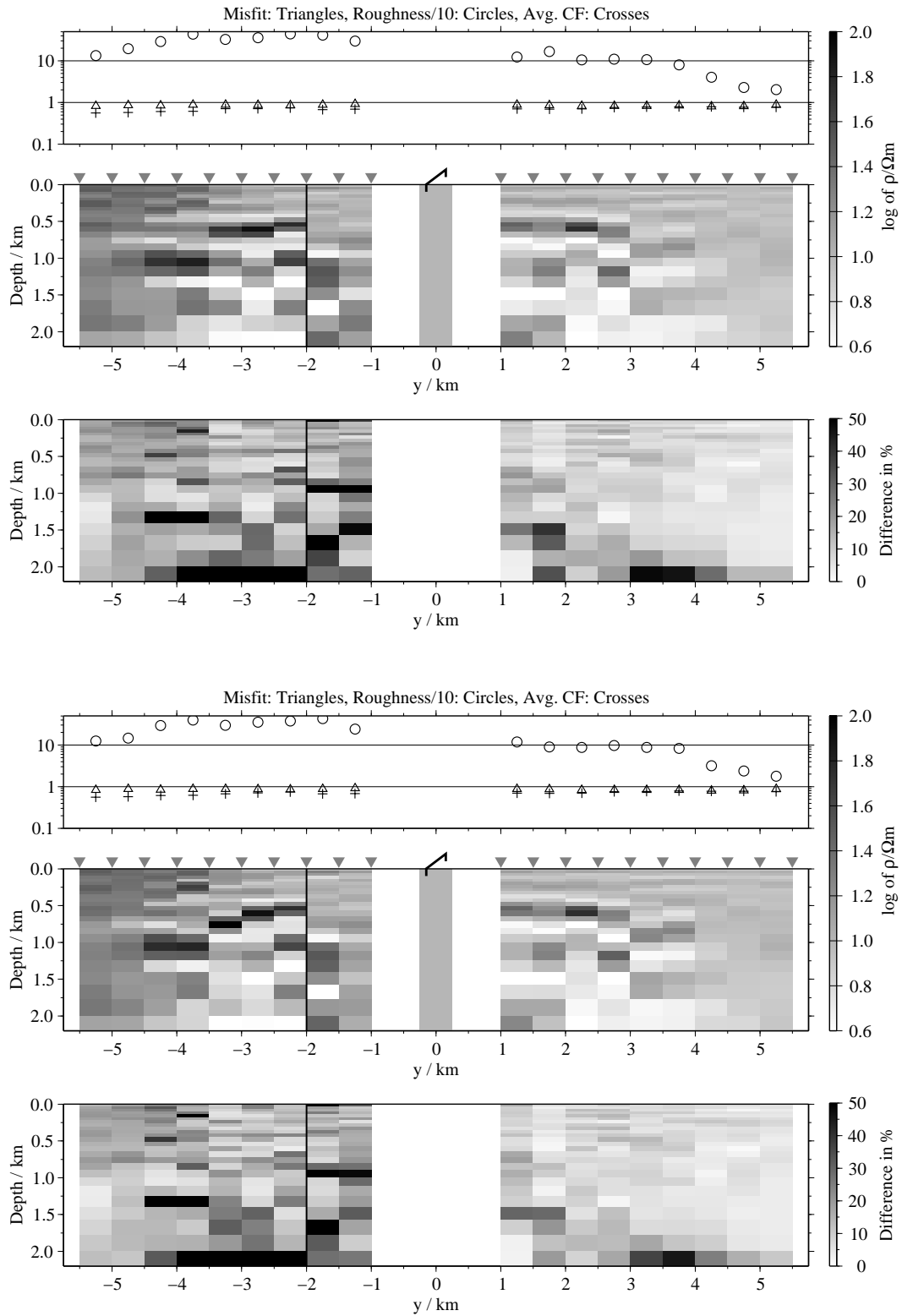


Figure B.355: SJI results for the E_x -, \dot{H}_y - and \dot{H}_z -transients from adjacent stations, model F1; Top panels: Average inversion results and relative differences (regularisation scheme C1); bottom: Average inversion results and relative differences (regularisation scheme C4);

B.5.2 Model K3

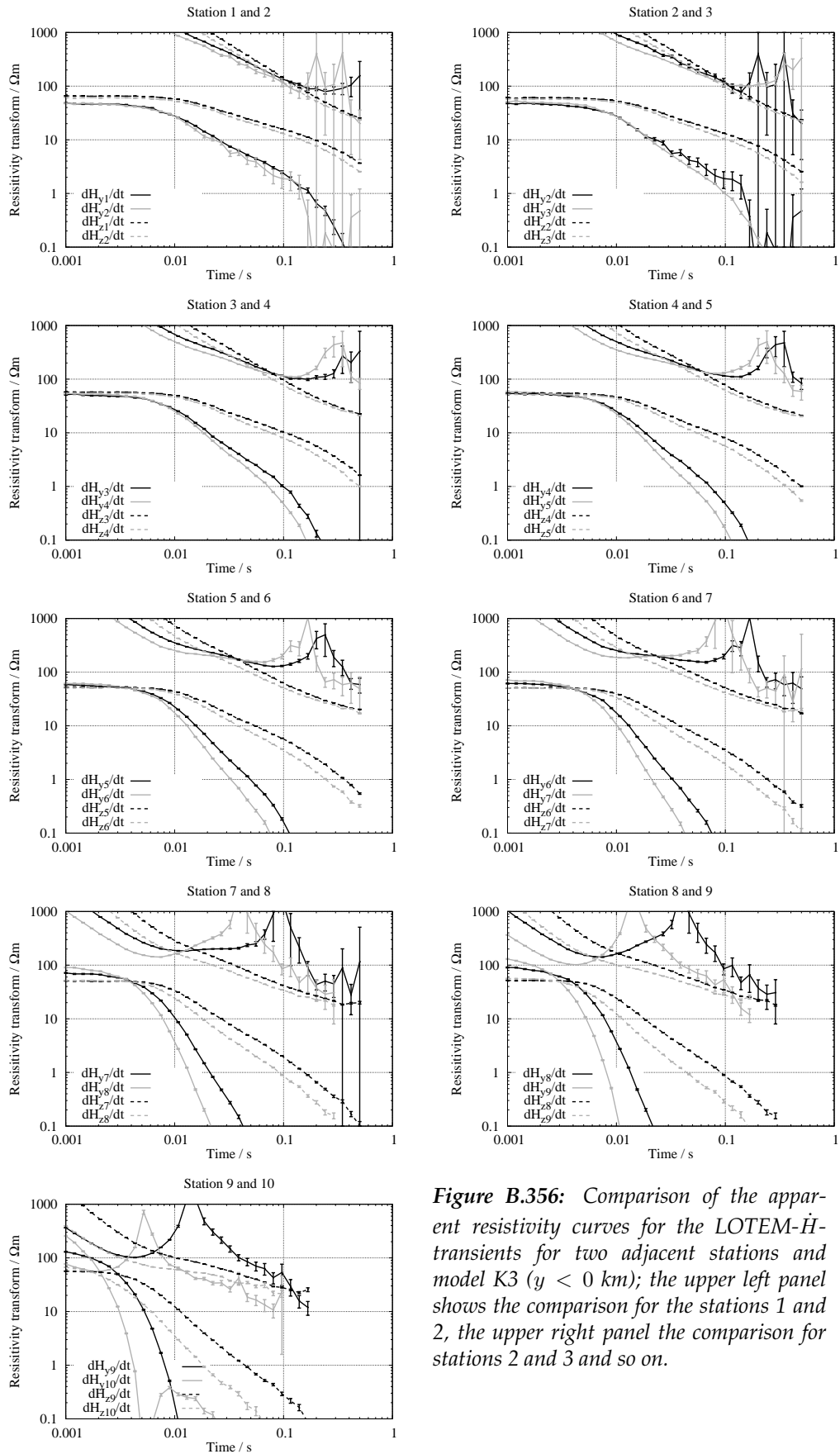


Figure B.356: Comparison of the apparent resistivity curves for the LOTEM- \dot{H} -transients for two adjacent stations and model K3 ($y < 0$ km); the upper left panel shows the comparison for the stations 1 and 2, the upper right panel the comparison for stations 2 and 3 and so on.

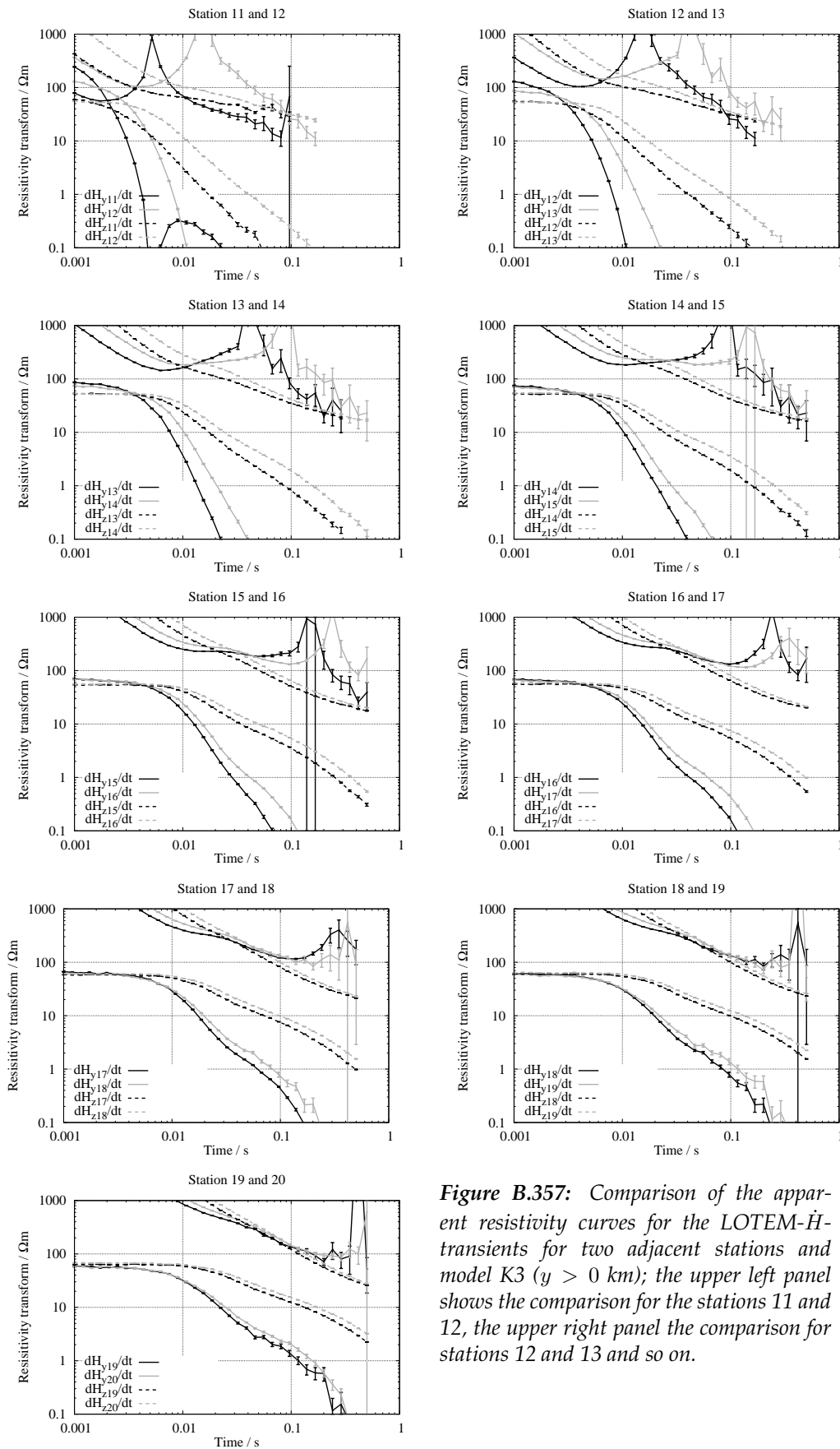


Figure B.357: Comparison of the apparent resistivity curves for the LOTEM- \dot{H} -transients for two adjacent stations and model K3 ($y > 0$ km); the upper left panel shows the comparison for the stations 11 and 12, the upper right panel the comparison for stations 12 and 13 and so on.

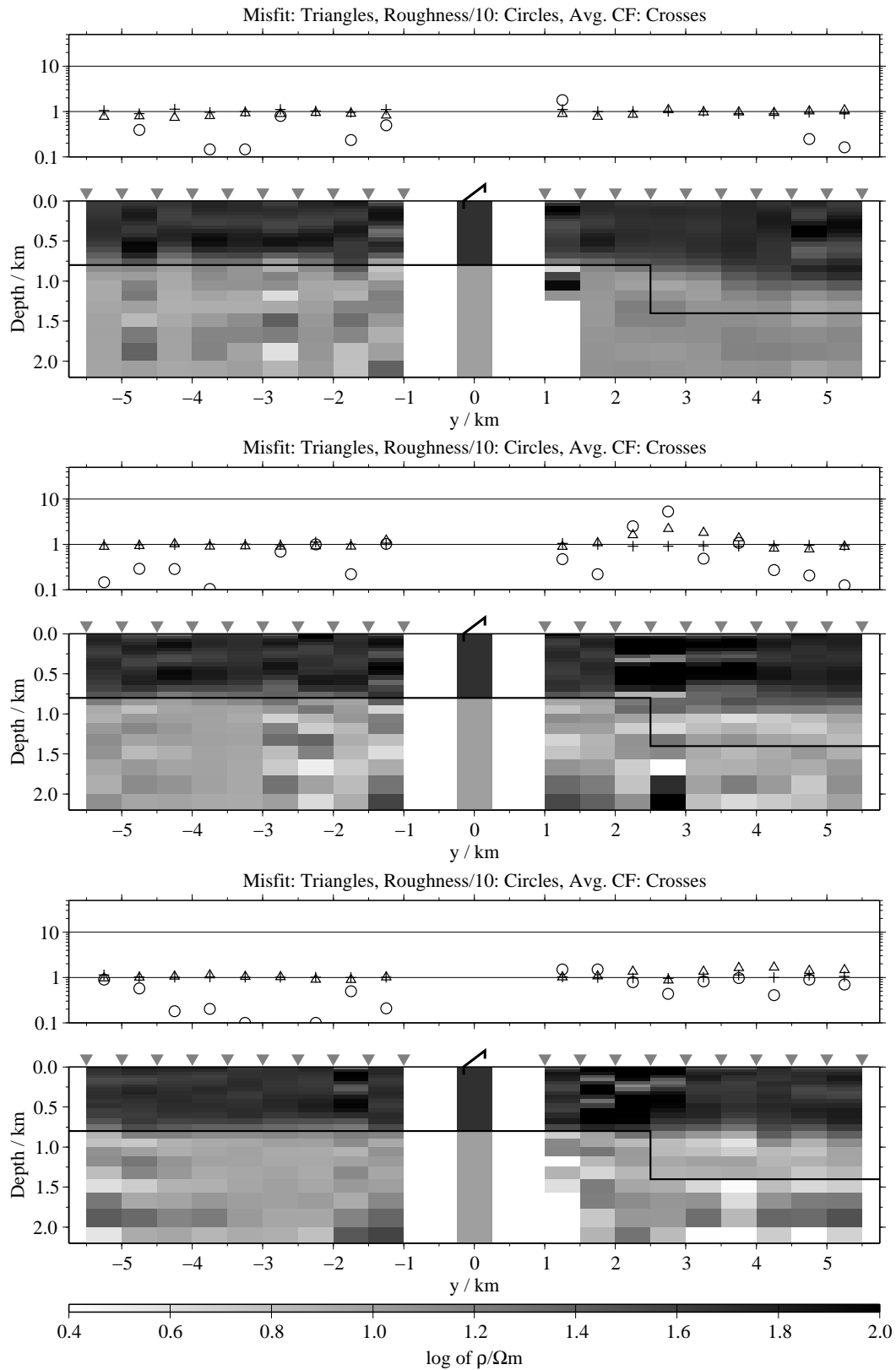


Figure B.358: FJI results for the transient of adjacent stations, model K3, regularisation scheme C1; from top to bottom E_x -, H_y - and H_z -components;

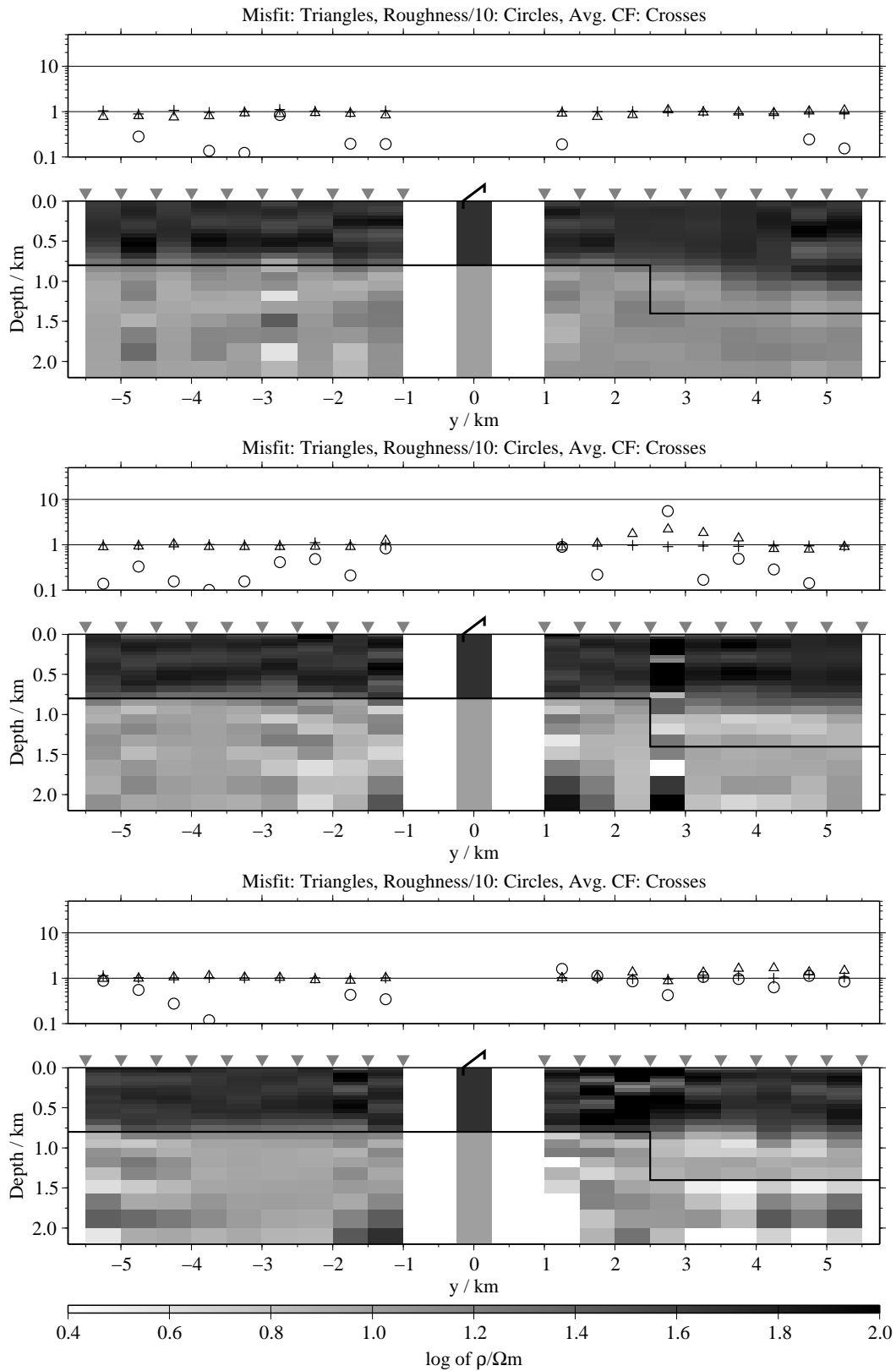


Figure B.359: FJI results for the transient of adjacent stations, model K3, regularisation scheme C4; from top to bottom E_x -, H_y - and H_z -components;

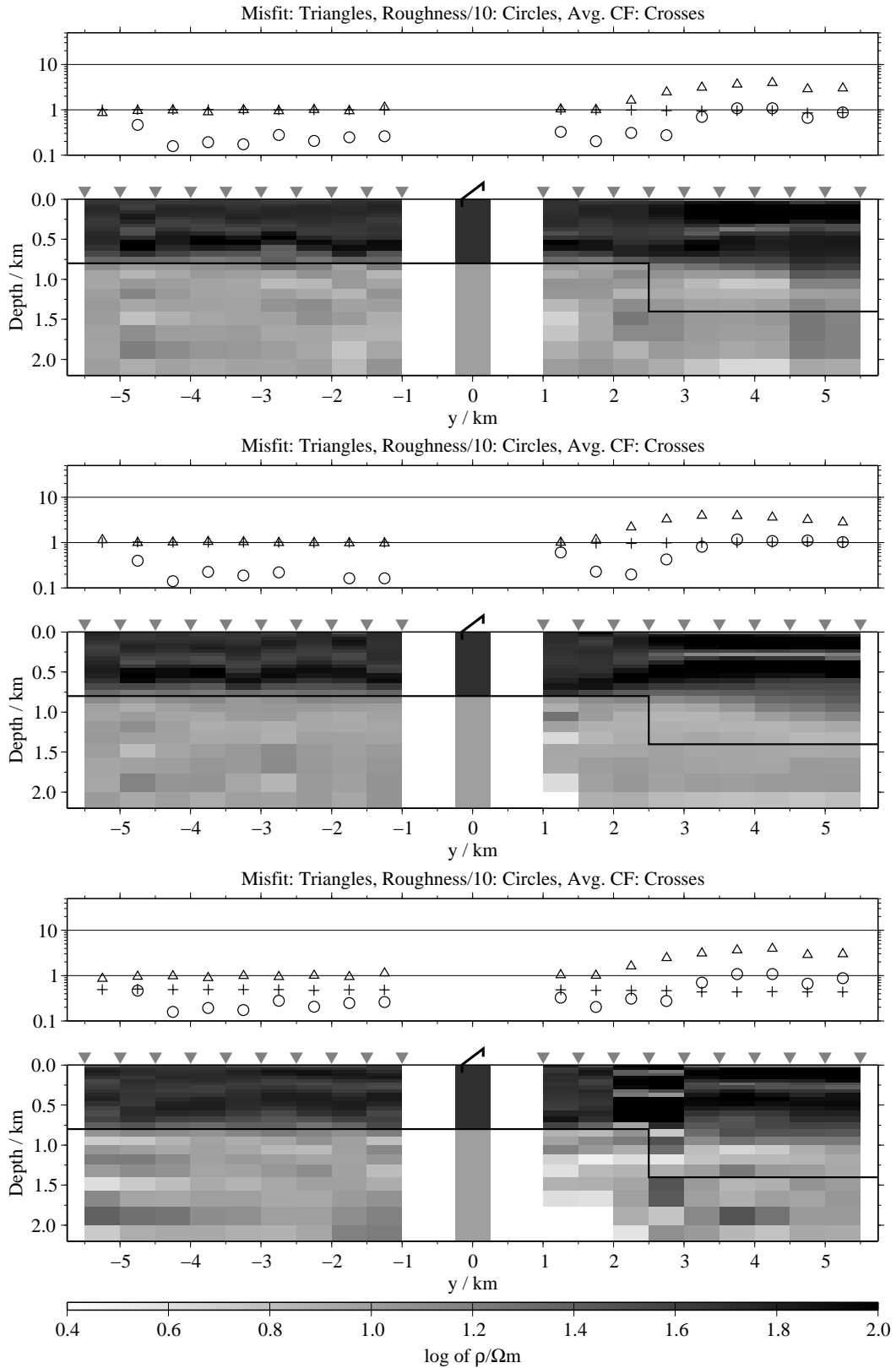


Figure B.360: FJI results for the transient of adjacent stations, model K3, regularisation scheme C1; from top to bottom $E_x-\dot{H}_y$, $E_x-\dot{H}_z$ and $\dot{H}_y-\dot{H}_z$;

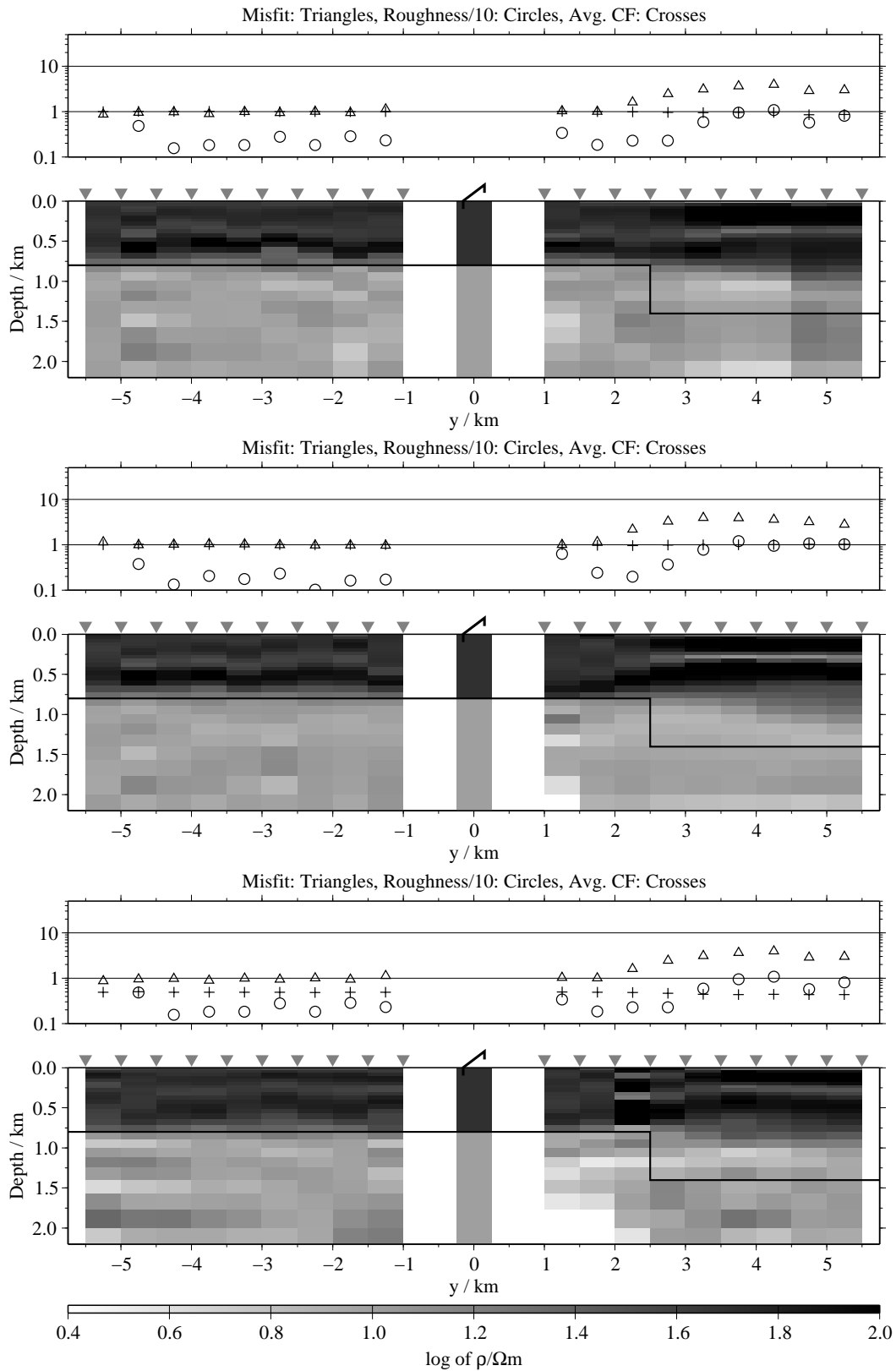


Figure B.361: FJI results for the transient of adjacent stations, model K3, regularisation scheme C4; from top to bottom $E_x - \dot{H}_y$, $E_x - \dot{H}_z$ and $\dot{H}_y - \dot{H}_z$;

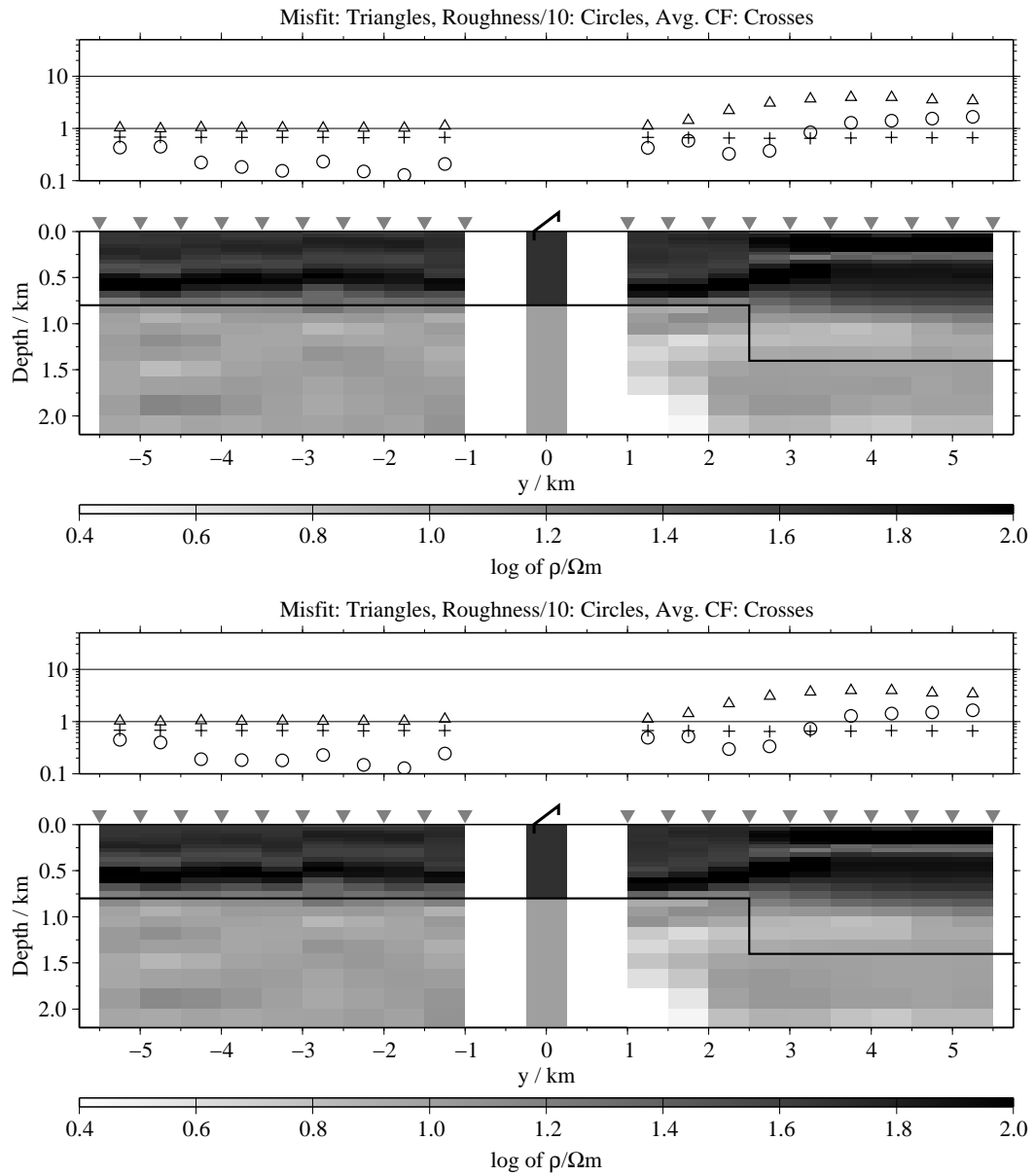


Figure B.362: FJI results for the transient of adjacent stations using all three components, model K3; top: Regularisation scheme C1; bottom: Regularisation scheme C4;

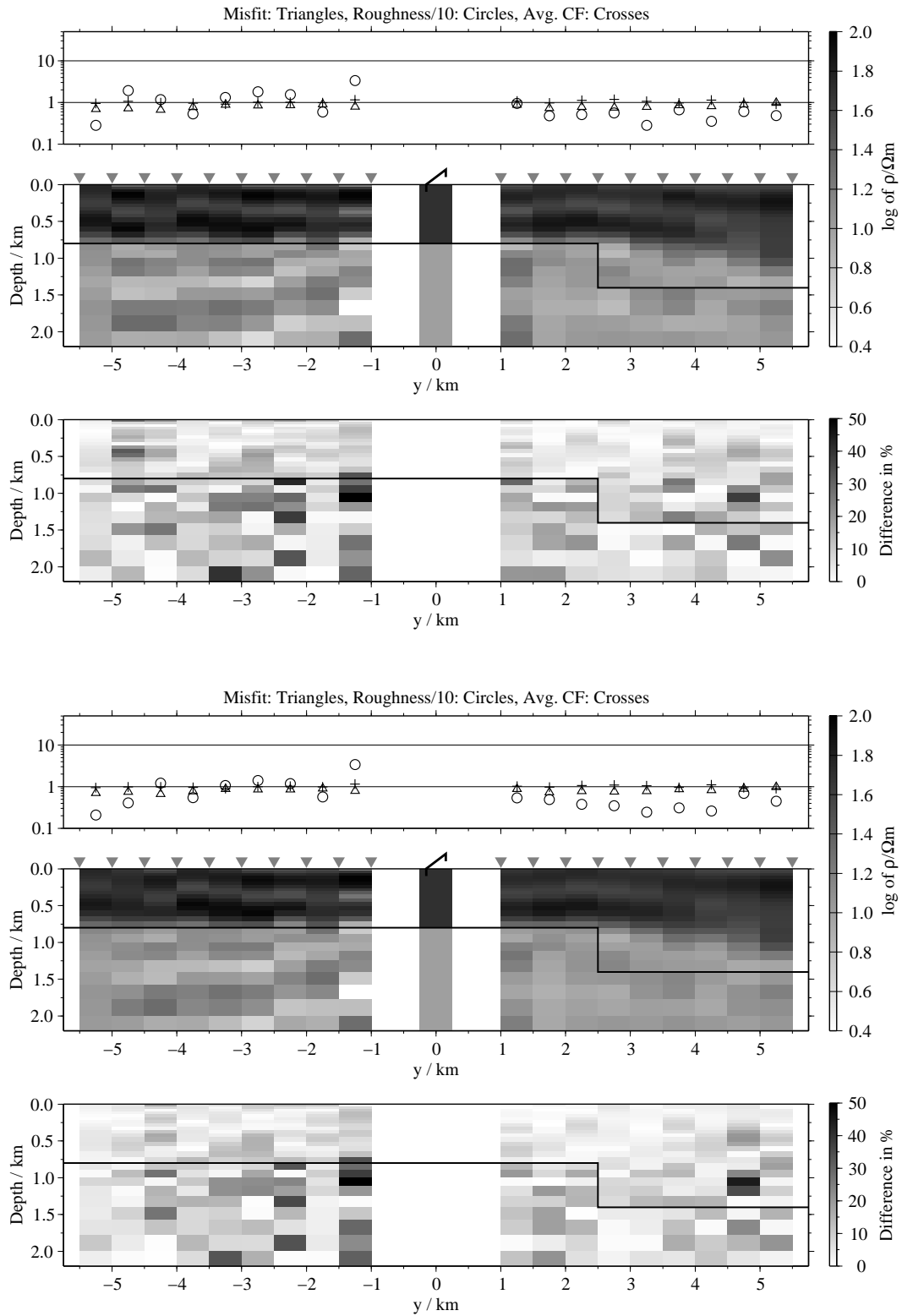


Figure B.363: SJI results for the E_x -transients from adjacent stations, model K3; Top panels: Average inversion results and relative differences (regularisation scheme C1); bottom: Average inversion results and relative differences (regularisation scheme C4);

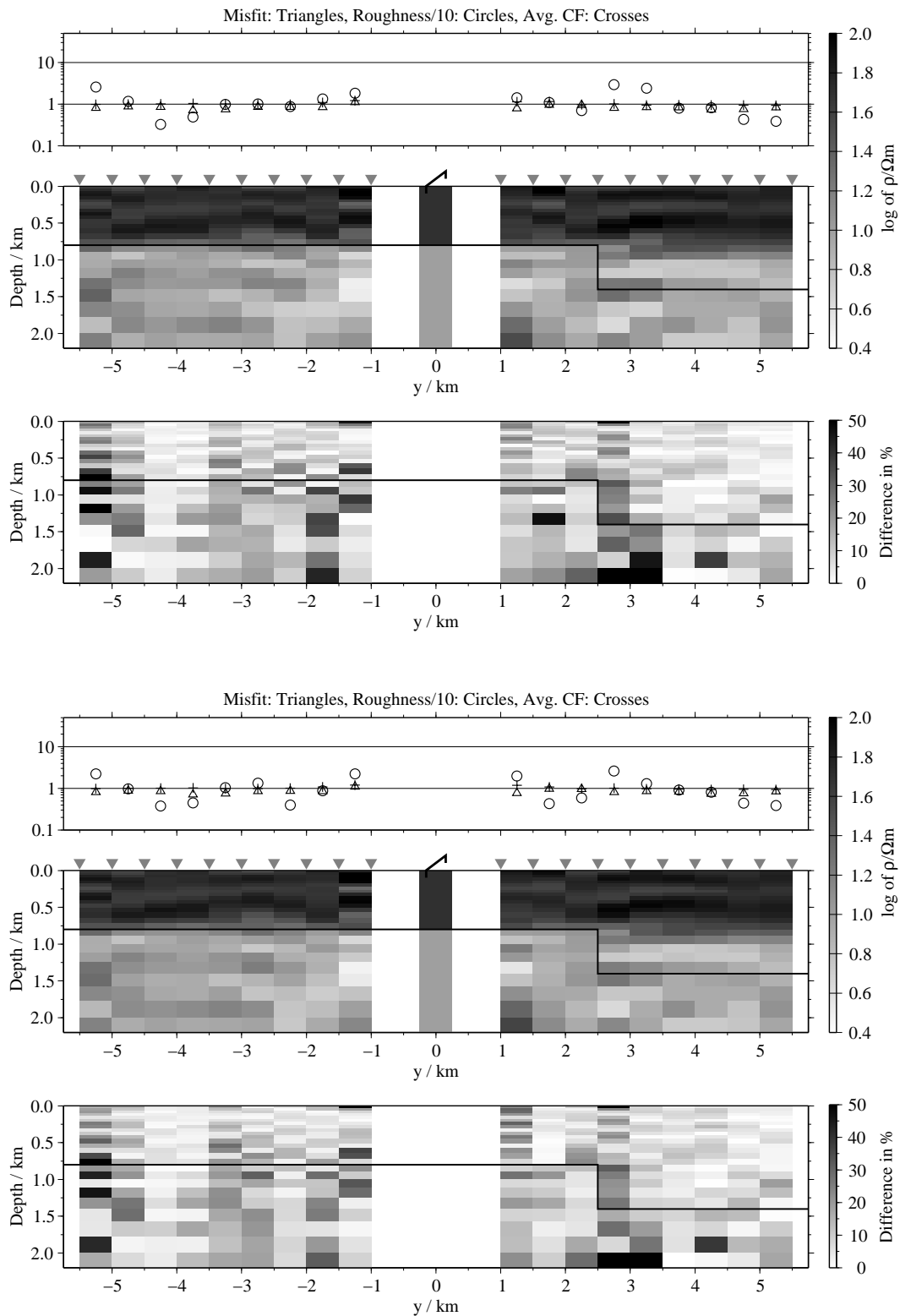


Figure B.364: SJI results for the \dot{H}_y -transients from adjacent stations, model K3; Top panels: Average inversion results and relative differences (regularisation scheme C1); bottom: Average inversion results and relative differences (regularisation scheme C4);

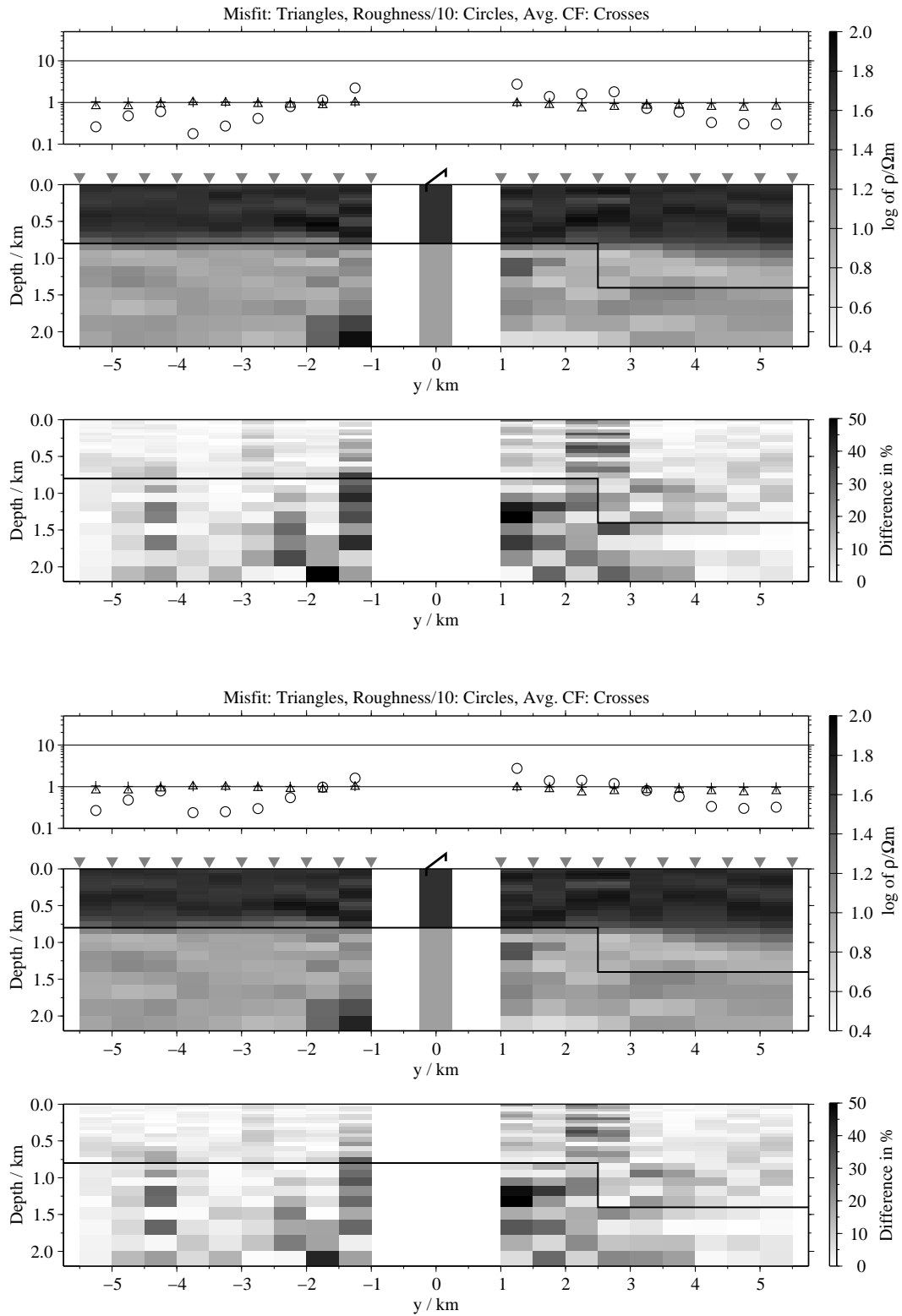


Figure B.365: SJI results for the \dot{H}_z -transients from adjacent stations, model K3; Top panels: Average inversion results and relative differences (regularisation scheme C1); bottom: Average inversion results and relative differences (regularisation scheme C4);

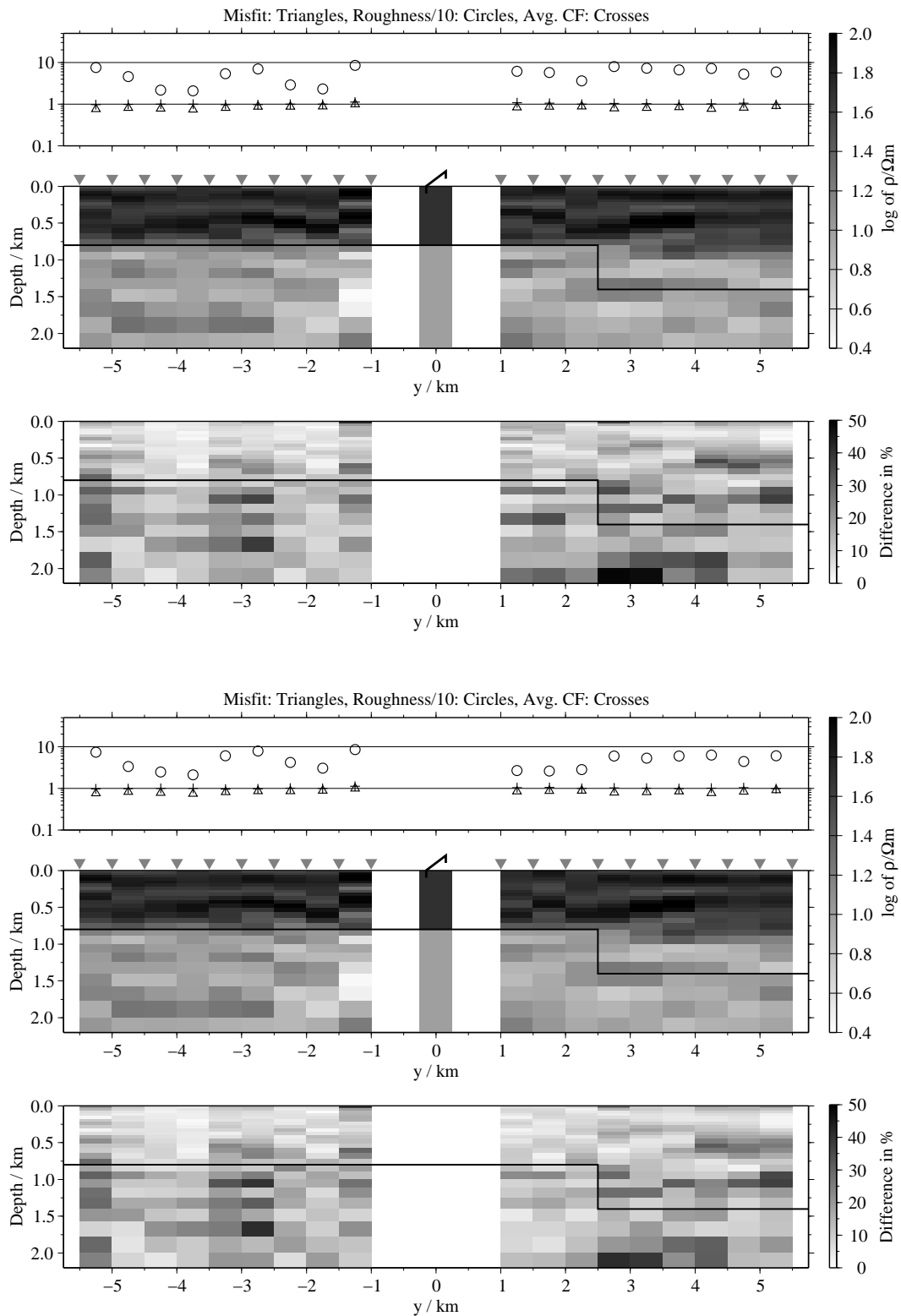


Figure B.366: SJI results for the E_x - and H_y -transients from adjacent stations, model K3; Top panels: Average inversion results and relative differences (regularisation scheme C1); bottom: Average inversion results and relative differences (regularisation scheme C4);

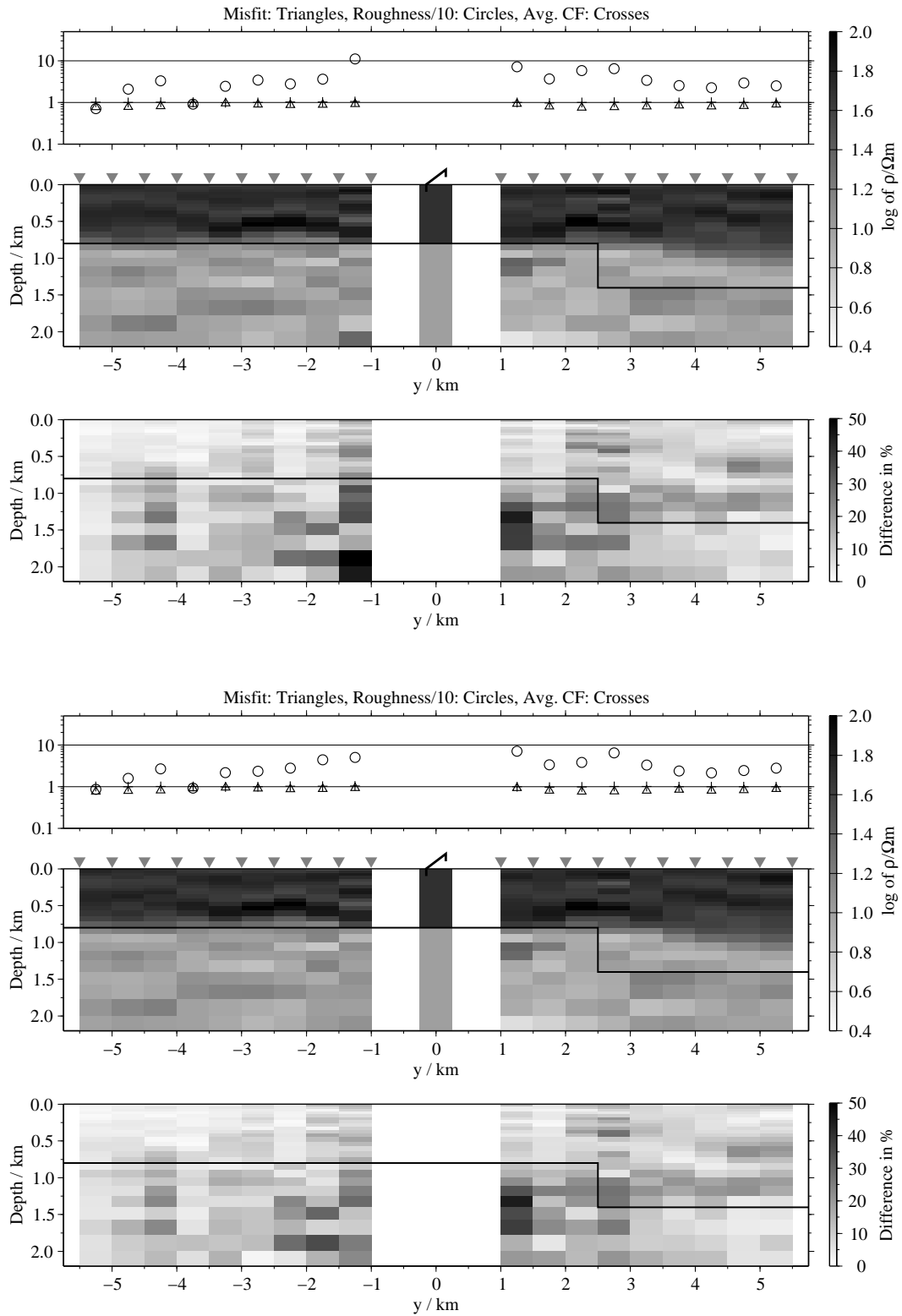


Figure B.367: SJI results for the E_x - and \dot{H}_z -transients from adjacent stations, model K3; Top panels: Average inversion results and relative differences (regularisation scheme C1); bottom: Average inversion results and relative differences (regularisation scheme C4);

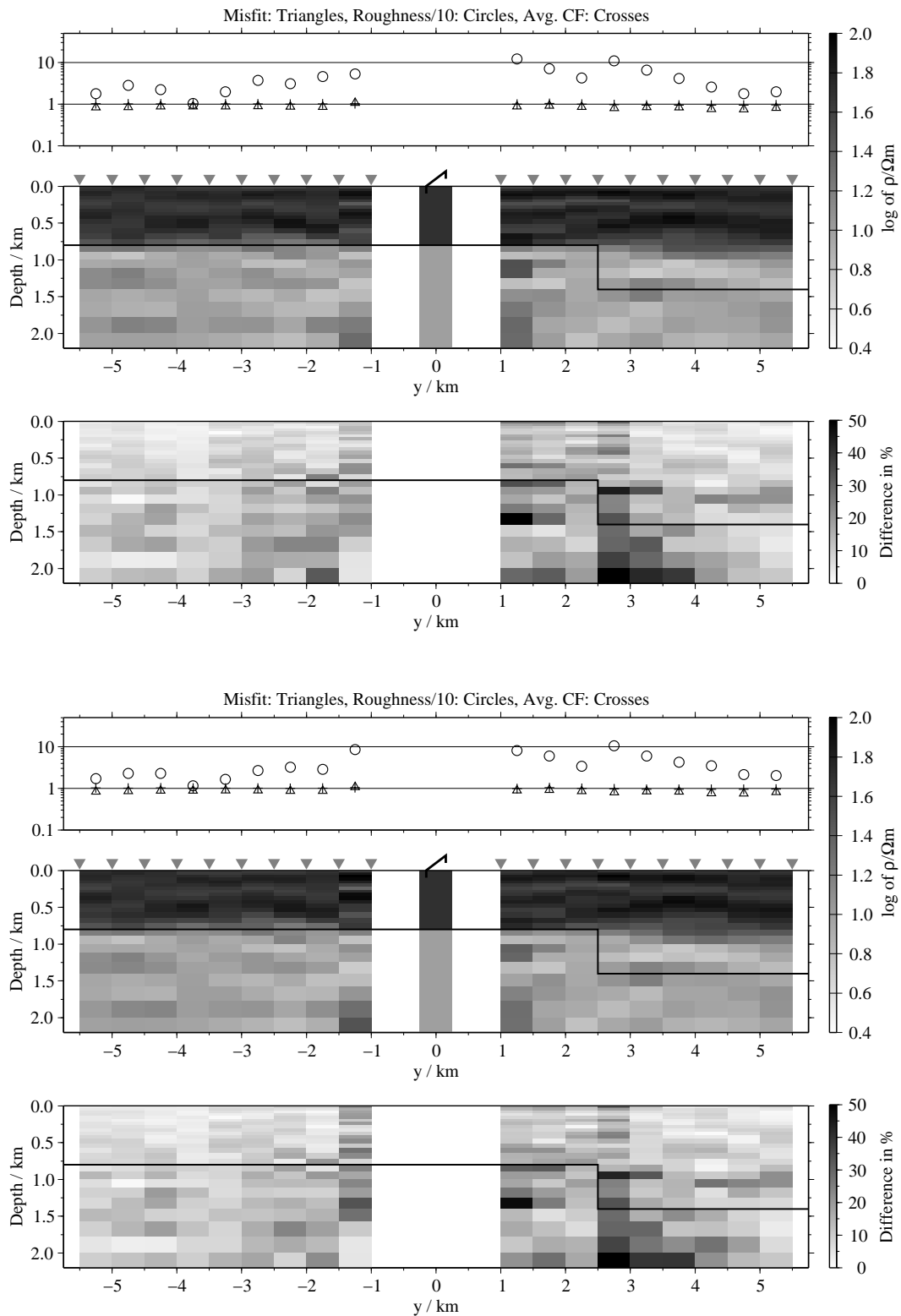


Figure B.368: SJI results for the \dot{H}_y - and \dot{H}_z -transients from adjacent stations, model K3; Top panels: Average inversion results and relative differences (regularisation scheme C1); bottom: Average inversion results and relative differences (regularisation scheme C4);

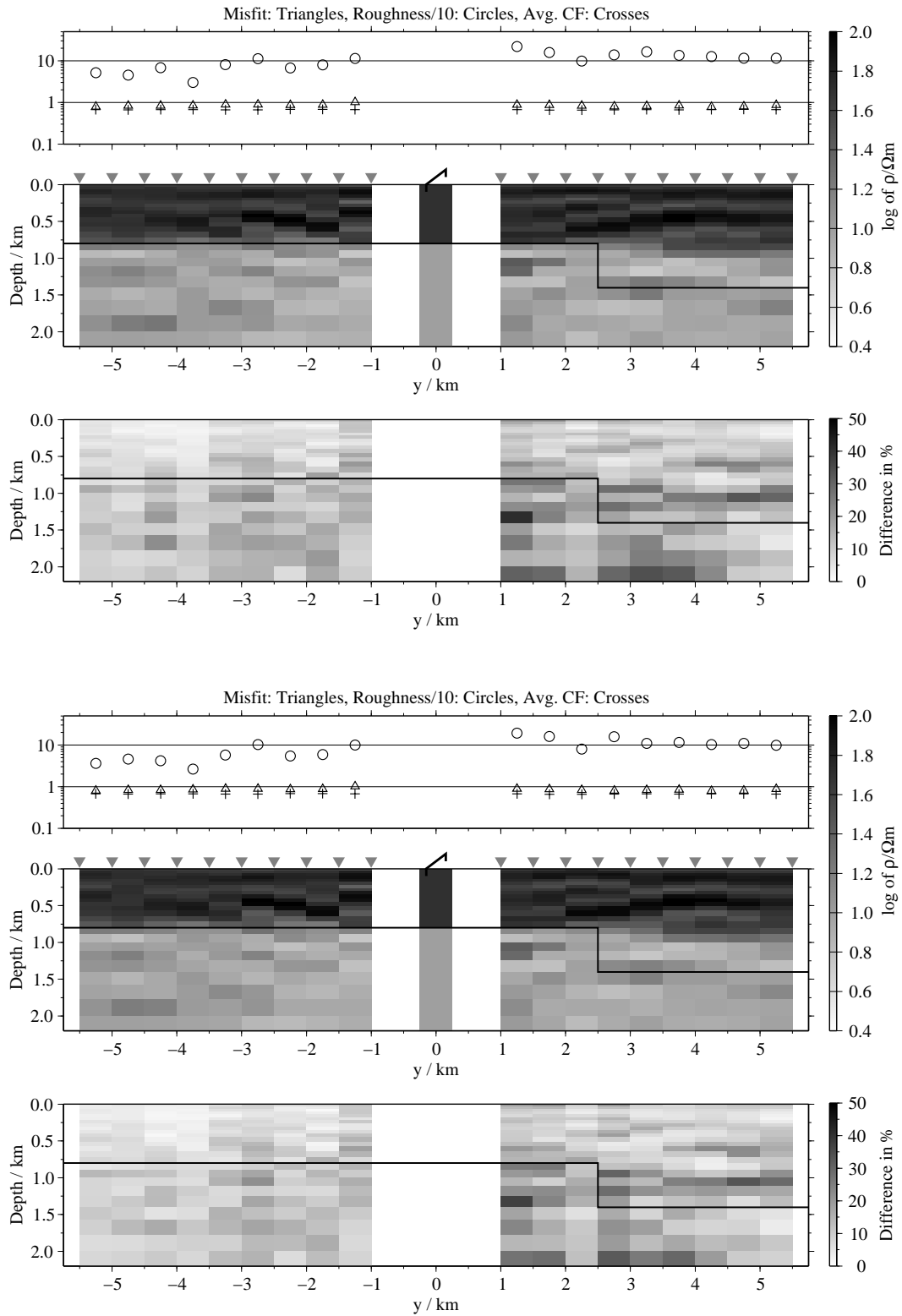


Figure B.369: SJI results for the E_x -, H_y - and H_z -transients from adjacent stations, model K3; Top panels: Average inversion results and relative differences (regularisation scheme C1); bottom: Average inversion results and relative differences (regularisation scheme C4);

B.5.3 Model M

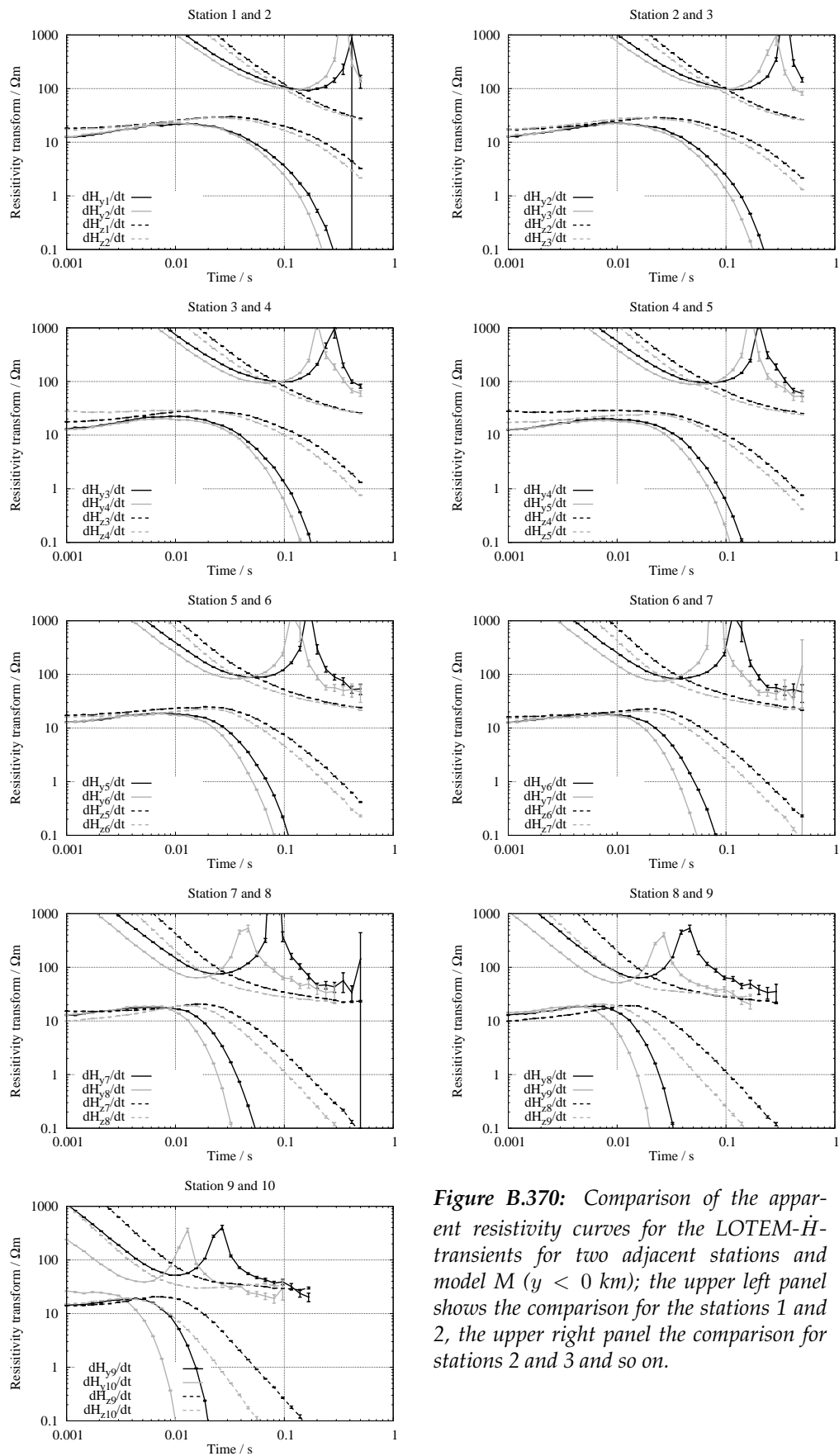


Figure B.370: Comparison of the apparent resistivity curves for the LOTEM-H-transients for two adjacent stations and model M ($y < 0$ km); the upper left panel shows the comparison for the stations 1 and 2, the upper right panel the comparison for stations 2 and 3 and so on.

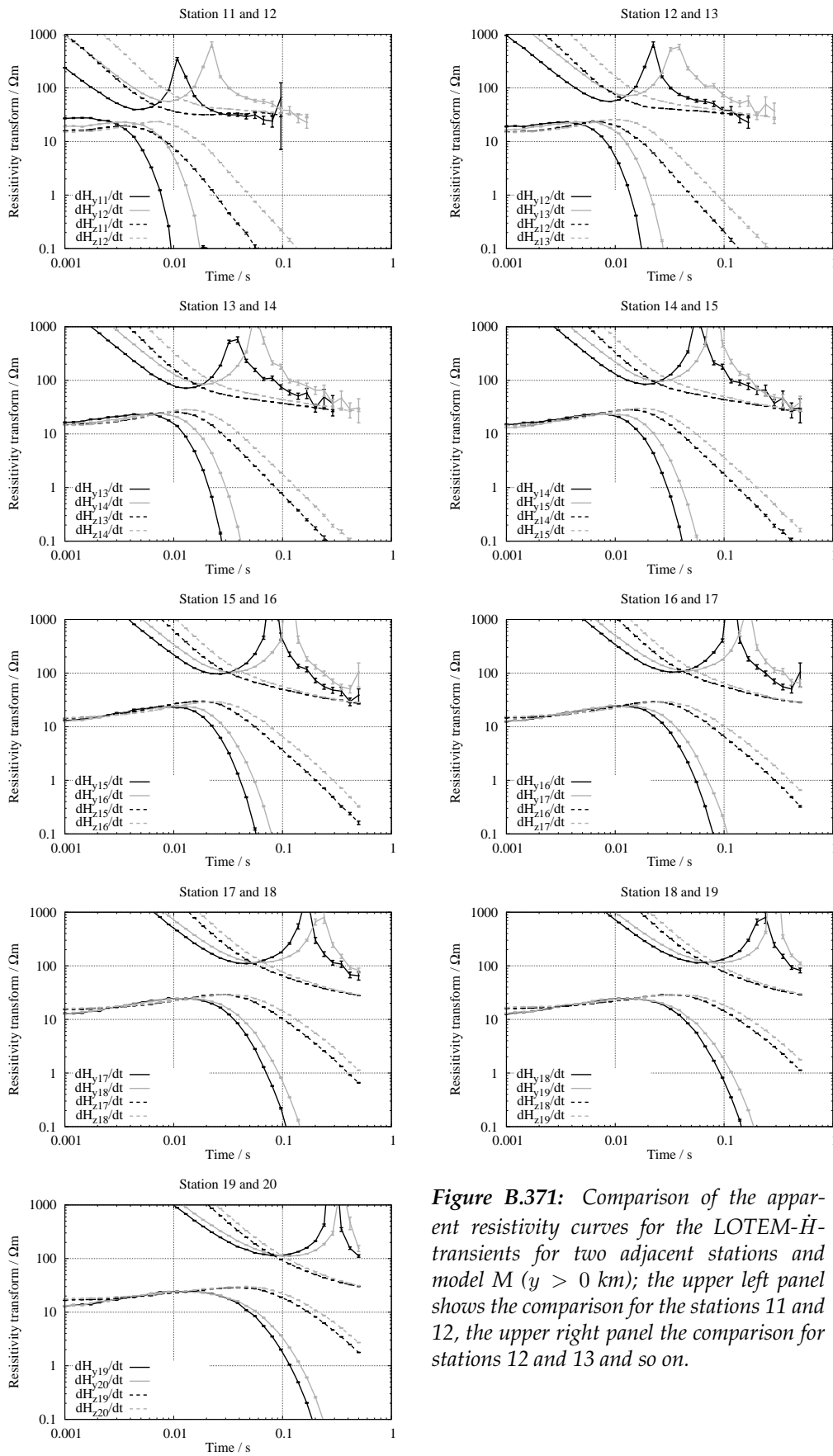


Figure B.371: Comparison of the apparent resistivity curves for the LOTEM- \dot{H} -transients for two adjacent stations and model M ($y > 0$ km); the upper left panel shows the comparison for the stations 11 and 12, the upper right panel the comparison for stations 12 and 13 and so on.

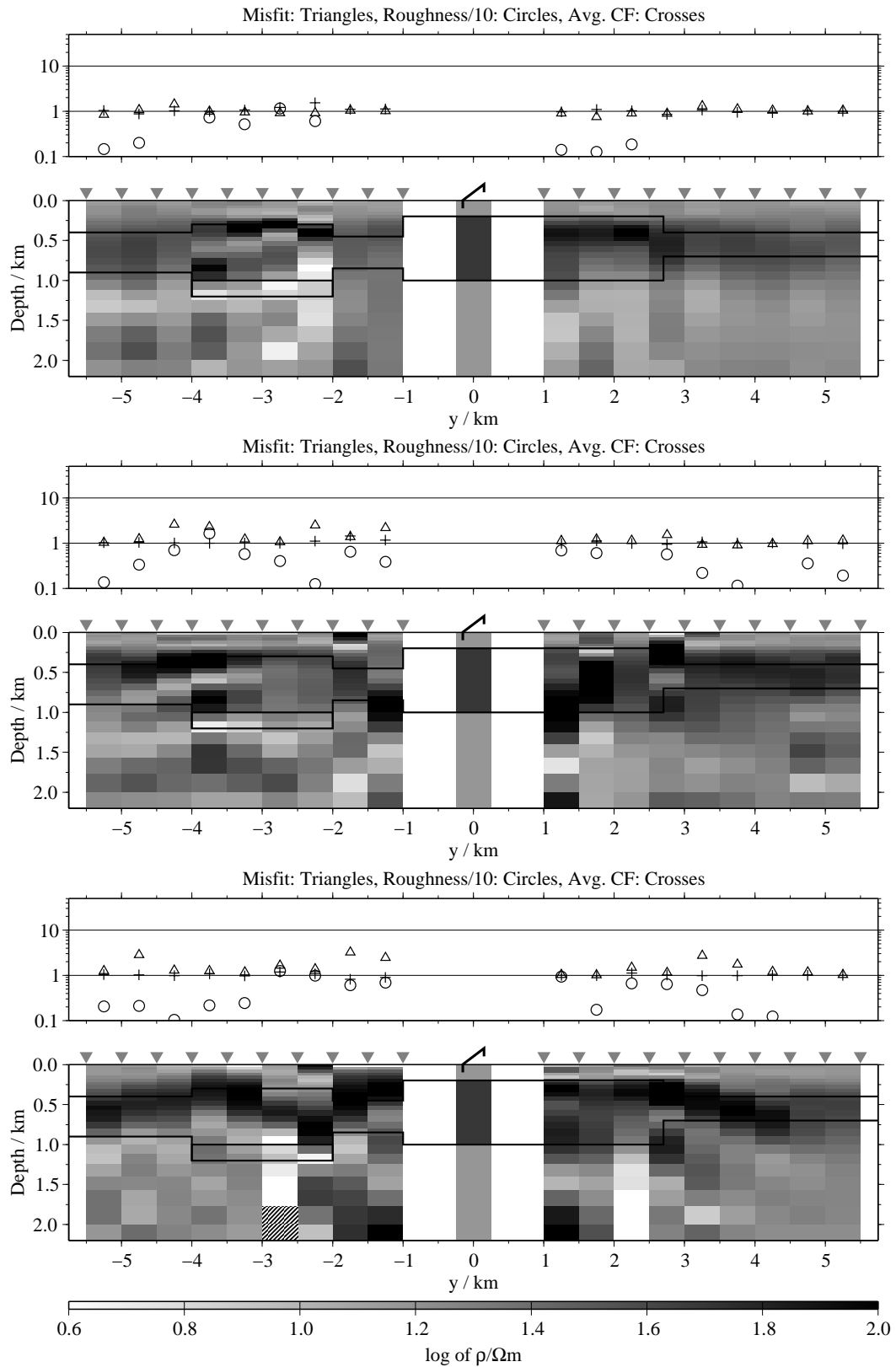


Figure B.372: FJI results for the transient of adjacent stations, model M, regularisation scheme C1; from top to bottom E_x -, H_y - and H_z -components;

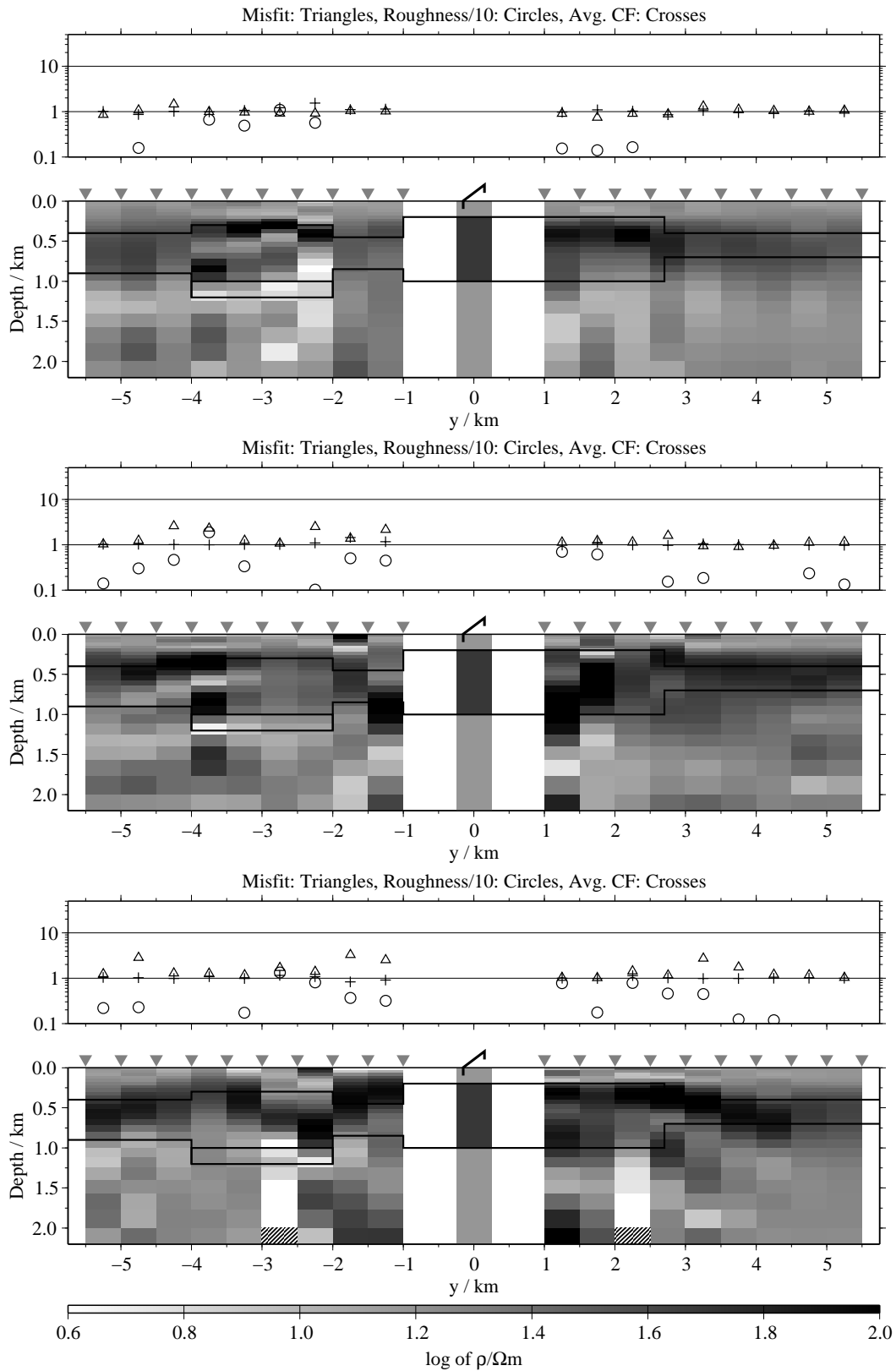


Figure B.373: FJI results for the transient of adjacent stations, model M, regularisation scheme C4; from top to bottom E_x -, H_y - and H_z -components;

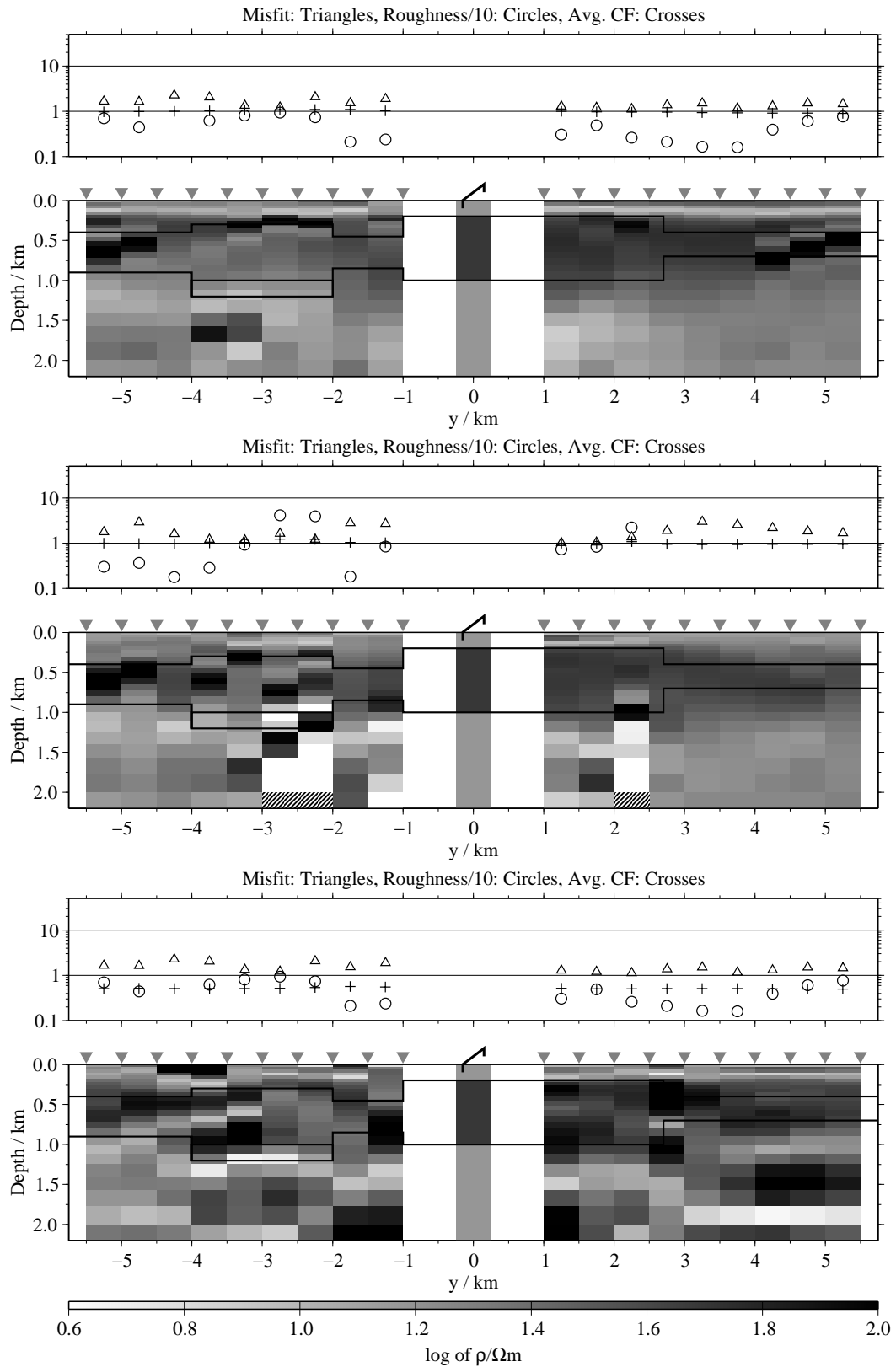


Figure B.374: FJI results for the transient of adjacent stations, model M, regularisation scheme C1; from top to bottom $E_x - \dot{H}_y$, $E_x - \dot{H}_z$ and $\dot{H}_y - \dot{H}_z$;

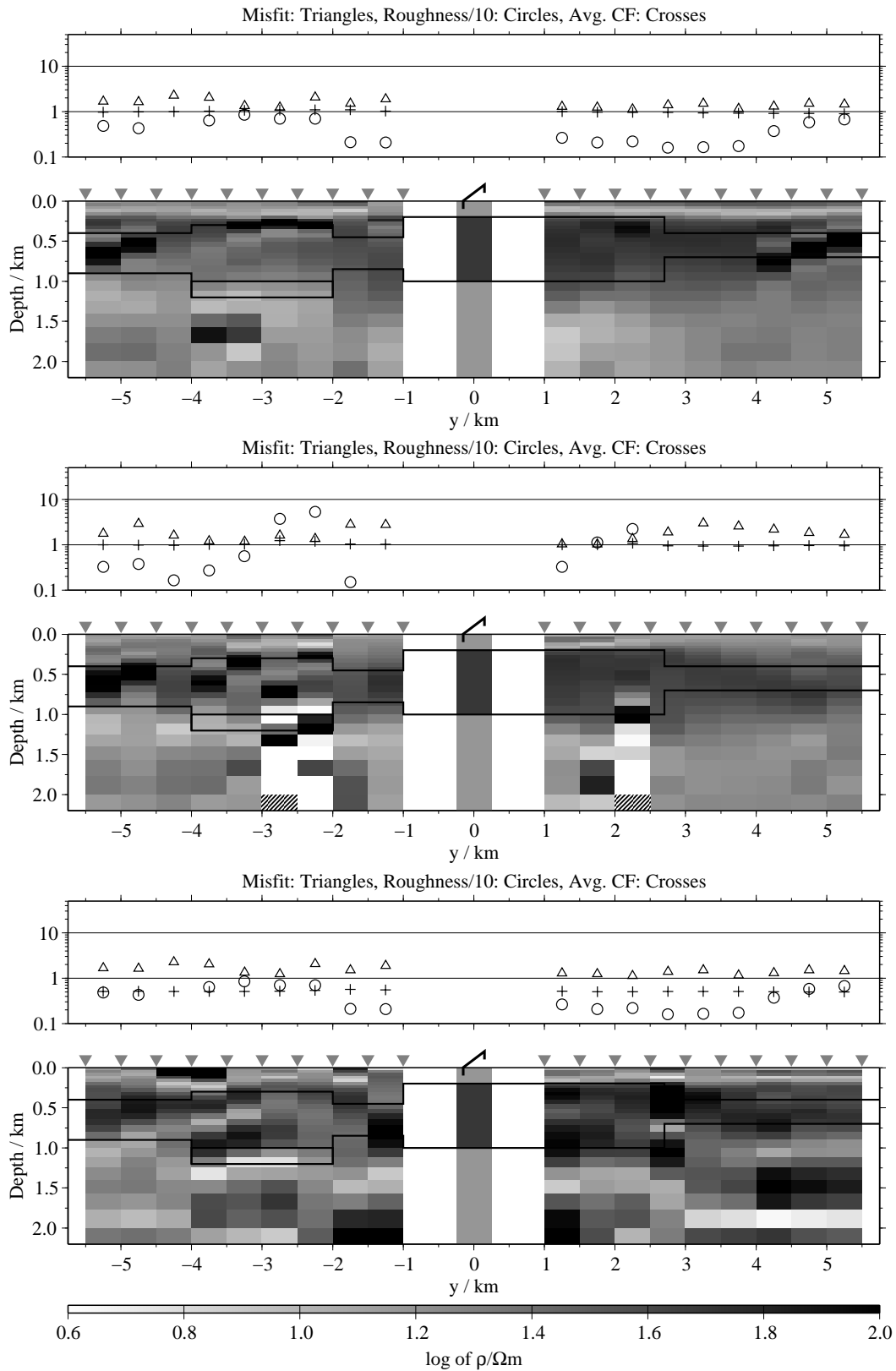


Figure B.375: FJI results for the transient of adjacent stations, model M, regularisation scheme C4; from top to bottom $E_x-\dot{H}_y$, $E_x-\dot{H}_z$ and $\dot{H}_y-\dot{H}_z$;

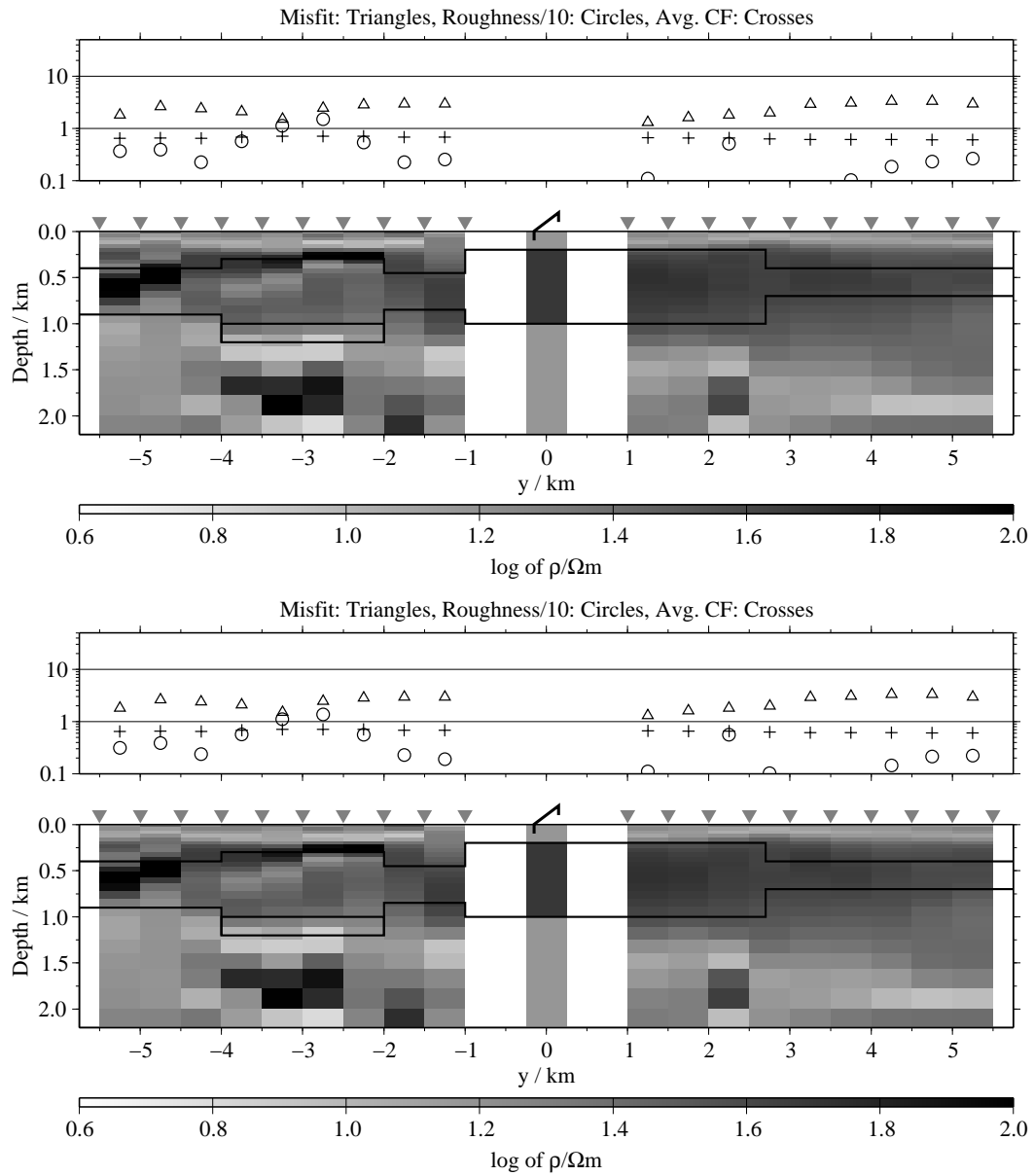


Figure B.376: FJI results for the transient of adjacent stations using all three components, model M; top: Regularisation scheme C1; bottom: Regularisation scheme C4;

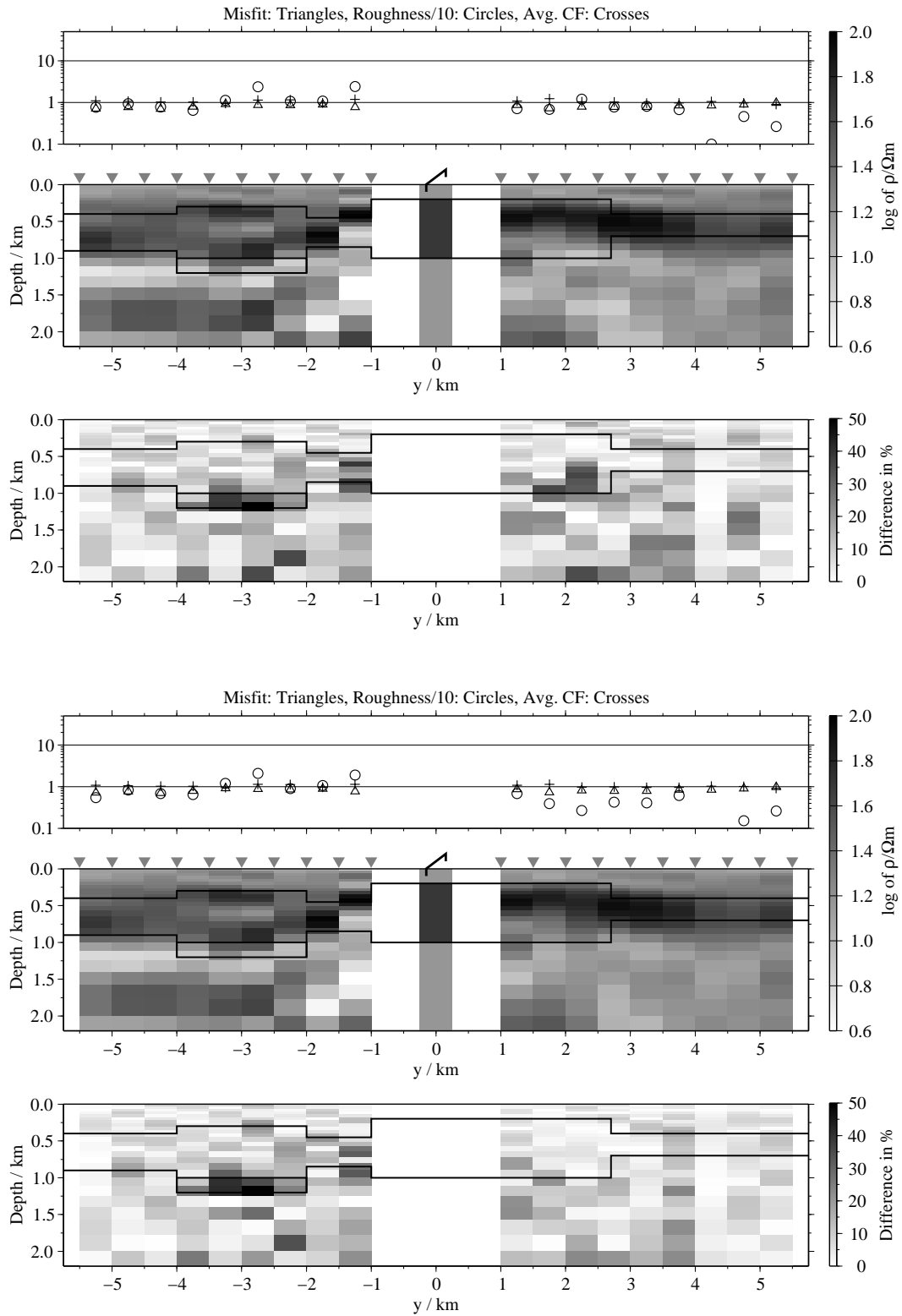


Figure B.377: SJI results for the E_x -transients from adjacent stations, model M; Top panels: Average inversion results and relative differences (regularisation scheme C1); bottom: Average inversion results and relative differences (regularisation scheme C4);

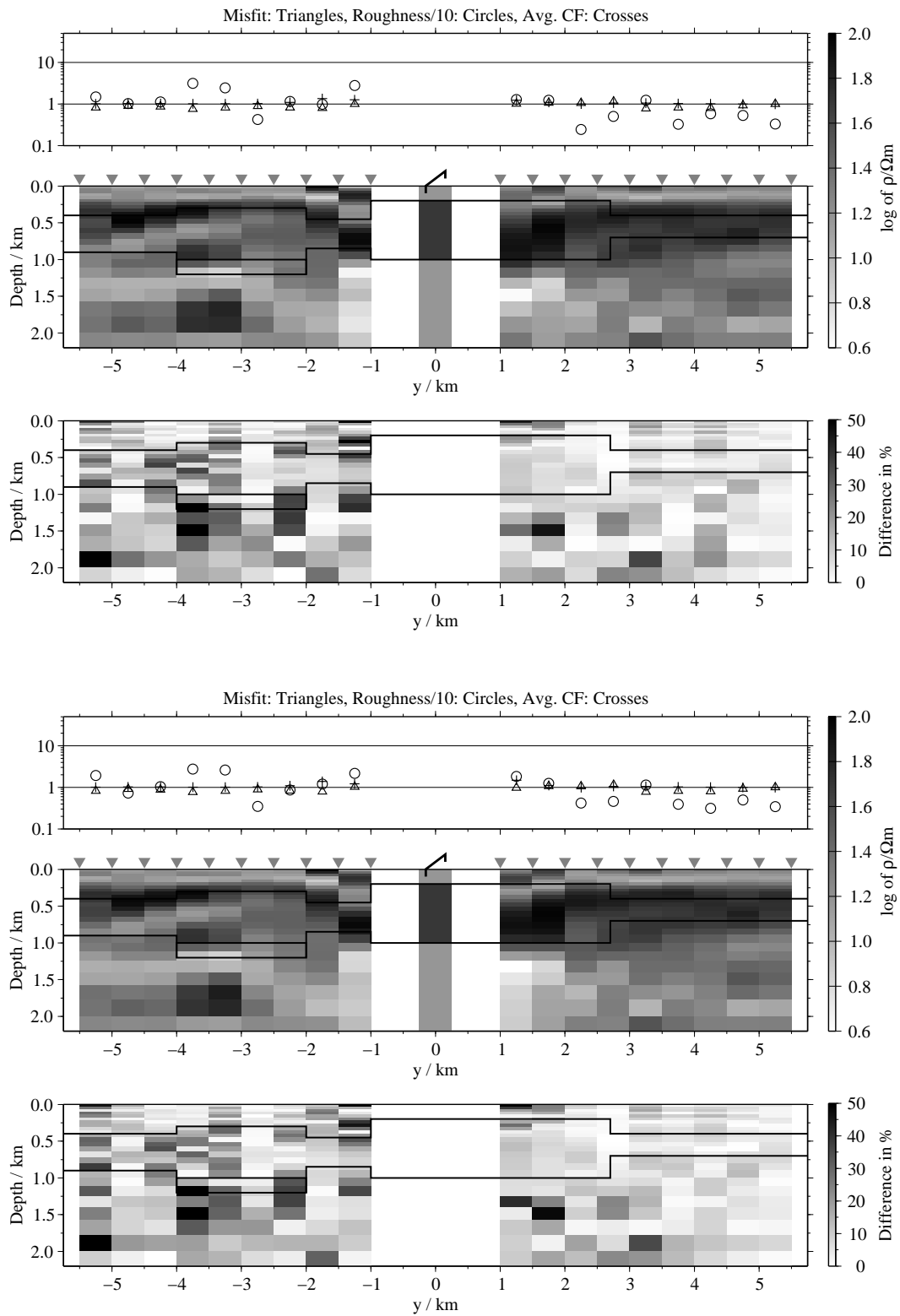


Figure B.378: SJI results for the \dot{H}_y -transients from adjacent stations, model M; Top panels: Average inversion results and relative differences (regularisation scheme C1); bottom: Average inversion results and relative differences (regularisation scheme C4);

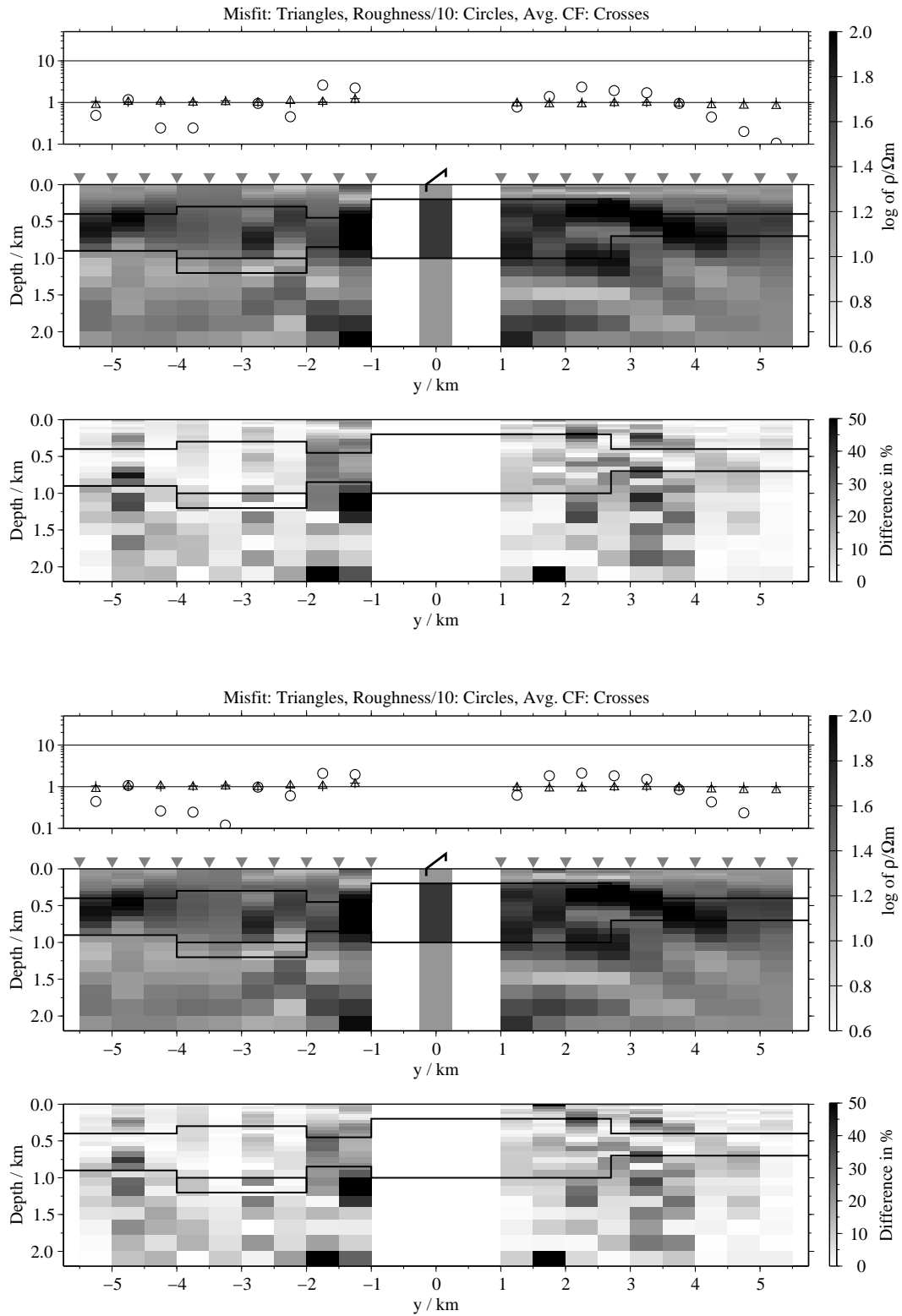


Figure B.379: SJI results for the \dot{H}_z -transients from adjacent stations, model M; Top panels: Average inversion results and relative differences (regularisation scheme C1); bottom: Average inversion results and relative differences (regularisation scheme C4);

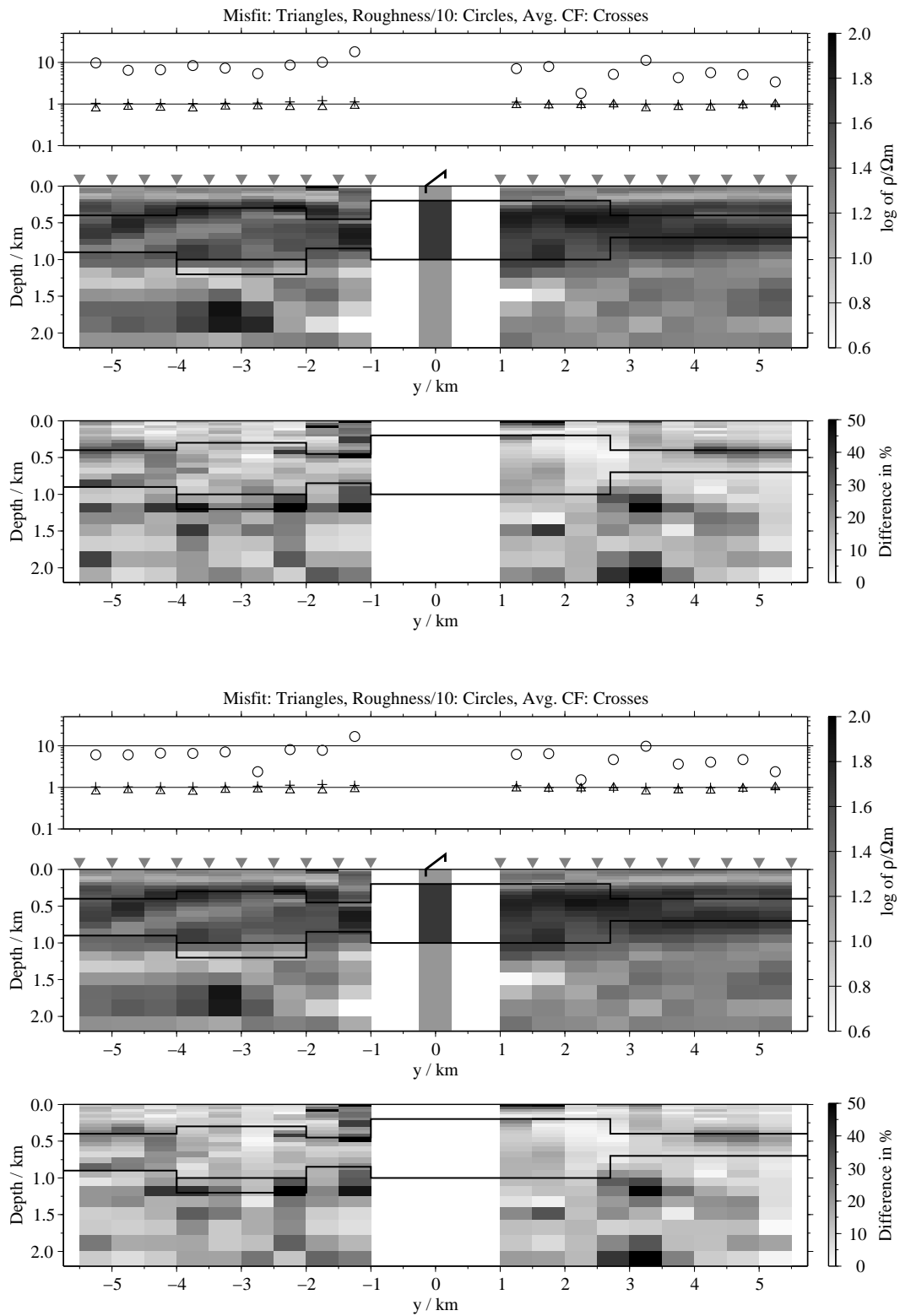


Figure B.380: SJI results for the E_x - and H_y -transients from adjacent stations, model M; Top panels: Average inversion results and relative differences (regularisation scheme C1); bottom: Average inversion results and relative differences (regularisation scheme C4);

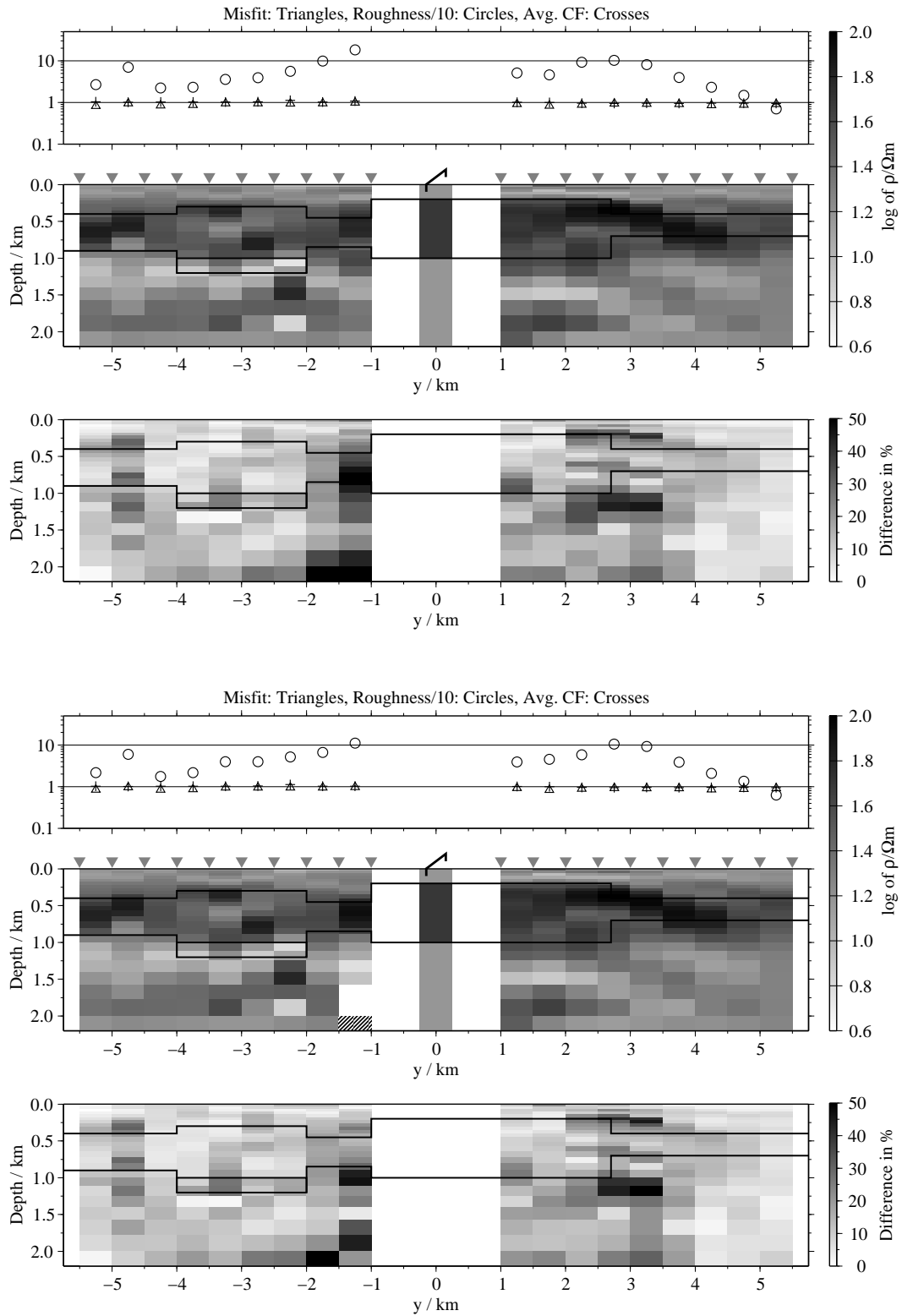


Figure B.381: SJI results for the E_x - and \dot{H}_z -transients from adjacent stations, model M; Top panels: Average inversion results and relative differences (regularisation scheme C1); bottom: Average inversion results and relative differences (regularisation scheme C4);

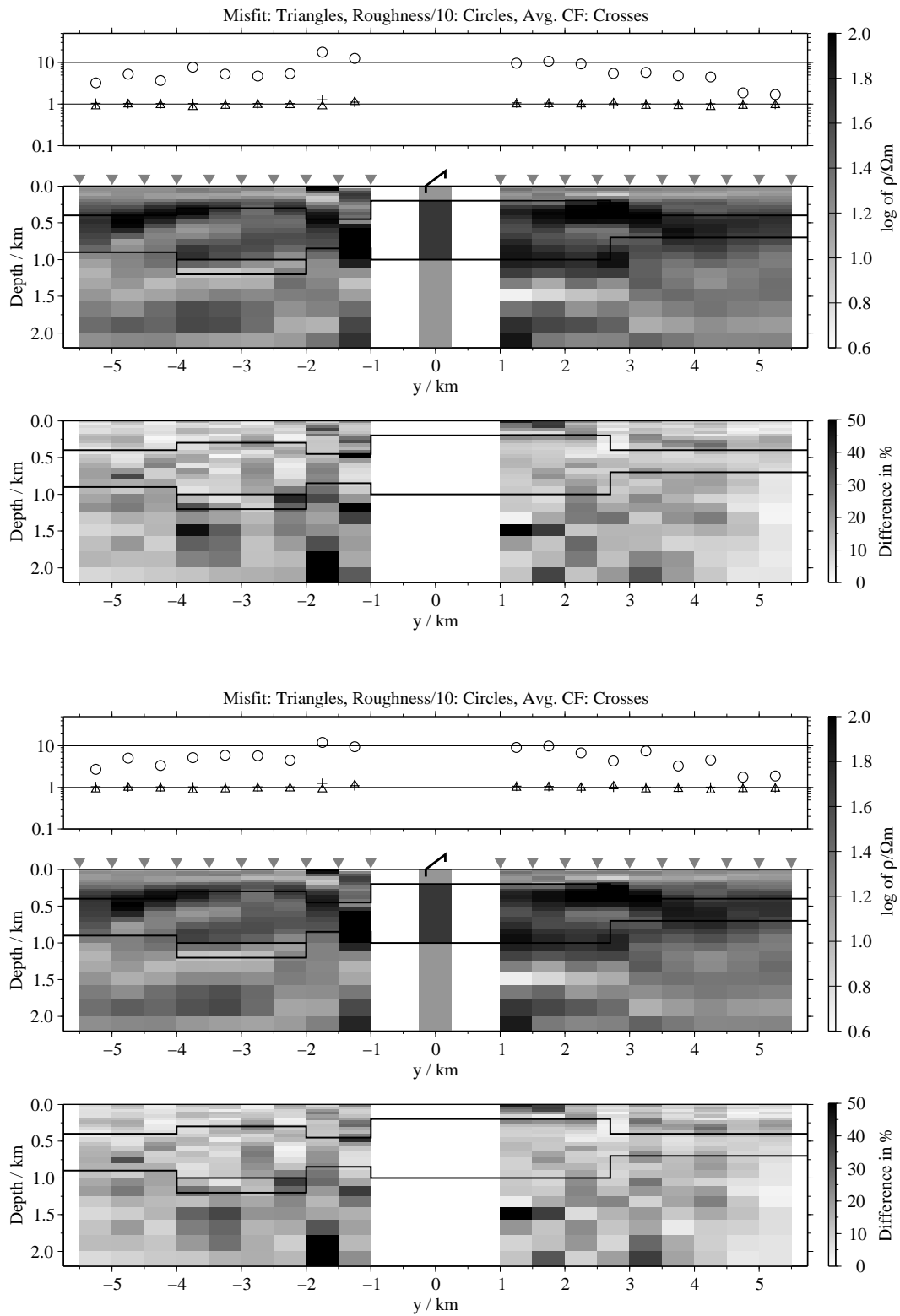


Figure B.382: SJI results for the \dot{H}_y - and \dot{H}_z -transients from adjacent stations, model M; Top panels: Average inversion results and relative differences (regularisation scheme C1); bottom: Average inversion results and relative differences (regularisation scheme C4);

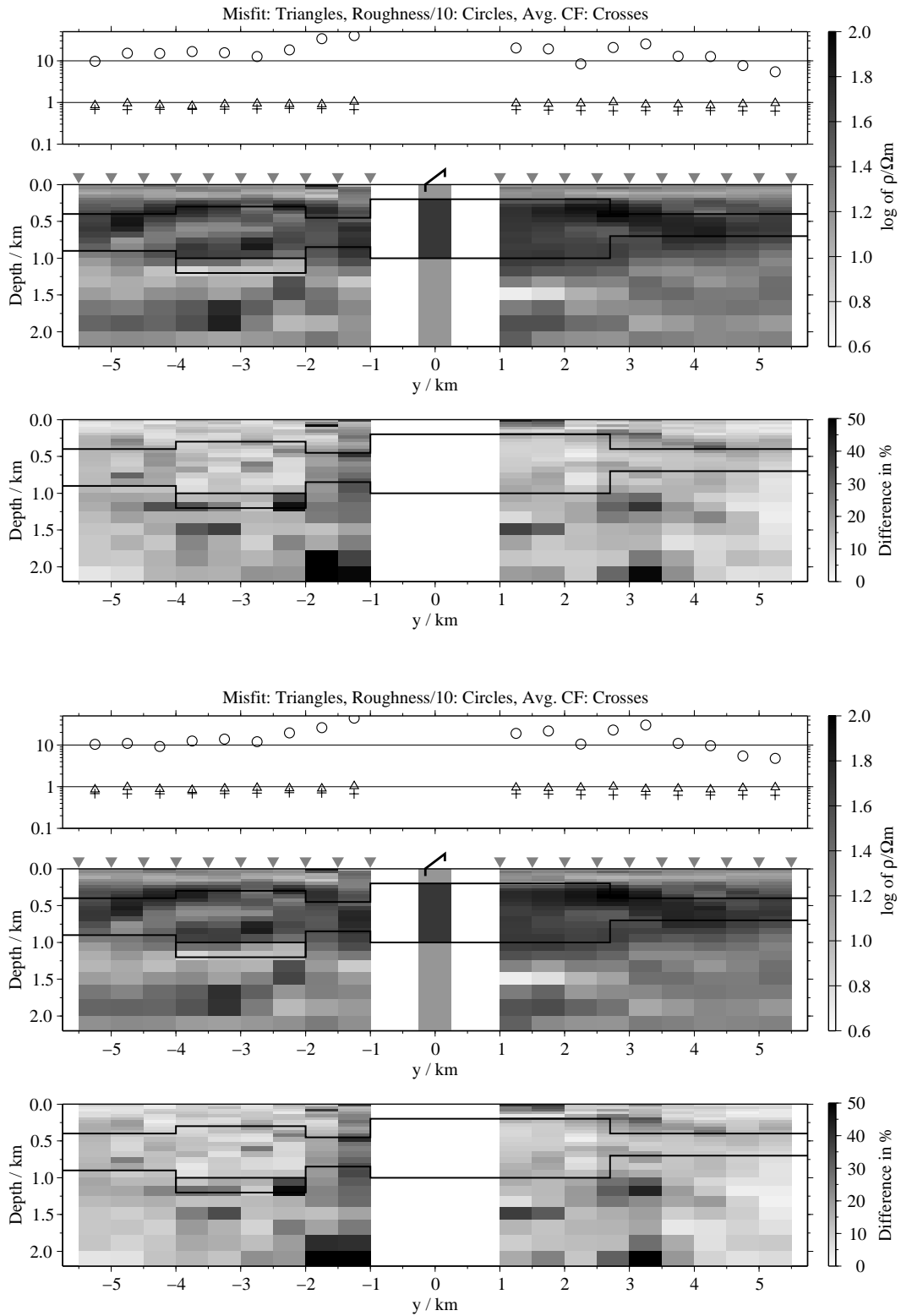


Figure B.383: SJI results for the E_x -, \dot{H}_y - and \dot{H}_z -transients from adjacent stations, model M; Top panels: Average inversion results and relative differences (regularisation scheme C1); bottom: Average inversion results and relative differences (regularisation scheme C4);

APPENDIX C

The field data sets

This section lists the coordinates, field parameters (sensor type, Tx-signal etc.) and the recorded LOTEM transients. In sec. C.1 the coordinates and parameters for all LOTEM-Tx and -Rx as well as the coordinates for the SHOTEM-sites can be found. Sec. C.2 shows all LOTEM transients. Additionally, the results for single Occam's inversions of these data sets are displayed.

C.1 Coordinates for transmitters and receivers in Israel

The LOTEM measurements in Israel took place between 14th and the 26th of March 2002 and between the 2nd and the 17th of December 2003 respectively. In the first campaign nine transmitters (plus one for the system response measurement) were set up. In the second campaign, 13 transmitters were set up. Table C.1 shows the designations and coordinates of all transmitters used (in chronological order).

C.1.1 Tx-coordinates

Tab. C.2 lists the parameters (angle with respect to north, Tx-signal, Tx-current and bipole length).

C.1.2 Rx-coordinates

The following tables show the parameters for all LOTEM-Rx-sites used. "St." designates the Rx-station, "Co." the measured component. A "CL" in the "Co." column indicates that no sensor was connected to this channel. The column entitled "RU" defines whether the TEAMEX ("T") or Summit-TEM ("S") recording units were used. The sampling interval for the Summit-TEM devices was set to 1 ms. On the TEAMEX remote units an interval of 2 ms was used.

Transmitters 2002					
Name	Sign	E1 / m	N1 / m	E2 / m	N2 / m
Sarid	sa	711831	3614036	712823	3613473
Devora	dv	720145	3615618	721516	3616042
Yoqneam	yo	700792	3615860	699506	3614723
Taninim	ta	680396	3604232	681235	3604006
Yagur	ya	695322	3627697	696078	3627075
Afek	af	697860	3633237	696774	3633490
Kerem Maharal	ke	685691	3614332	685673	3613209
Bet Alfa	be	728015	3601158	728579	3602551
Gan Shemuel	ga	681720	3595599	680689	3595354
Transmitters 2003					
Name	Sign	E1 / m	N1 / m	E2 / m	N2 / m
Pardes-Hanna	ph	684322	3597755	683576	3597551
Carmel	ca	693270	3617419	693929	3616586
Elyaqim	em	693427	3613917	692884	3613755
Afula	au	710102	3608085		
Kefar Kamar	kk	728002	3621421	728491	3622340
Ramat Zevi	rz	725595	3607238	726577	3607739
Beit Shean	bs	734794	3596104	734433	3594945
Hazoreim	ha	733815	3625601	732896	3625213
Ta'annakh	tk	720454	3606214	720122	3605478
Eliyakhin	en	686000	3588356	686182	3587318
Ra'ananna	ra	673382	3564554	673853	3565616
Kefar Kana	kn	718057	3627375	718140	3626300
Gan Shemuel B	gb	681051	3593315	680797	3592535

Table C.1: Eastings (E1 and E2) and northings (N1 and N2) for all transmitter electrode positions given in UTM coordinates (zone 36S); the transmitters are sorted in chronological order.

The next columns list the UTM-norting and easting (zone 36S). The column “Moment” indicates the length of the sensor (electric fields) in m or the area of the receiver coil (magnetic components) in m². “Angle” shows the horizontal angle to the Tx-direction.

The column “SNR” indicates the data quality of the transient in five grades.

++: The data quality is still good for $t > 500$ ms.

+: The last data point with a reasonable signal strength is found for $100 \ll t \leq 500$ ms.

0: The transient is usable up to ≈ 100 ms.

-: Only the first data point up to ≈ 50 ms show a signal.

–: The transient is too distorted to use it for the interpretation.

The columns entitled “Cut” indicate how many data points were removed at the beginning (first column) or the end (last column) of each transient prior to the single

Name	Sign	L / m	I / A	Angle / °	T_S / ms
Afek	AF	1115	50	103.1	1000
Afula	AU	940*	60		1000
Bet Alfa	BE	1503	60	22.0	1000
Beit Shean	BS	1214	49	17.3	1000
Carmel	CA	1062	34	141.7	1000
Devora	DV	1435	60	72.8	1500
Elyaqim	EM	916	36	143.7	1000
Eliyakhin	EN	1054	62	170.1	1000
Gan Shemuel	GA	1060	8	76.6	500
Gan Shemuel B	GB	820	60	18.0	500
Hazoreim	HA	998	57	67.1	1000
Kerem Maharal	KE	1123	46	0.9	1000
Kefar Kamar	KK	1041	57	95.5	1000
Kefar Kana	KN	1078	57	175.6	1000
Pardes-Hanna	PH	773	44	74.7	1000
Ra'ananna	RA	1162	62	23.9	1000
Ramat Zevi	RZ	1102	57	63.0	1000
Sarid	SA	1141	60	119.6	1000
Taninim	TA	869	68	105.1	1000
Ta'annakh	TK	807	57	24.3	1000
Yagur	YA	979	64	129.4	1000
Yoqneam	YO	1717	50	48.5	1500

Table C.2: Dipole lengths L , peak-to-peak amplitude of the current I , angle with respect to north and switching time T_S for each Tx. The transmitters are sorted in alphabetical order of their designations. The length of the AU-Tx was estimated using the recorded data sets (see sec. D.1.2)

Transmitter: Afek (AF)										
St.	Co.	RU	E / m	N / m	Moment	Angle	SNR	Cut		Rem.
								\	/	
A1	E_x	T	698566	3636075	130	13.1°	++	0	0	
A1	E_y	T	698566	3636075	130	13.1°	++	0	0	
A1	\dot{H}_x	T	698495	3635907	10000	-6.6°	--	0	0	
A1	\dot{H}_y	T	698495	3635907	10000	83.4°	+	0	0	
A1	\dot{H}_z	T	698487	3635932	86400	-	+	4	0	(N)

Table C.3: Parameters for each receiver component recorded using Tx Afek; for additional information refer to the text at the beginning of this section.

inversions shown in sec. C.2. In "Rem." the type of the used sensor is shown (for \dot{H}_z -components). An "SR" indicates that a \dot{H}_z -transient exhibits a sign reversal.

Transmitter: Afula (AU)										
St.	Co.	RU	E / m	N / m	Moment	Angle	SNR	Cut		Rem.
								\	/	
A1	\dot{H}_z	T	709157	3609562	10000	-	++	1	0	(K)
A1	CL	T	-	-	-	-	--	-	-	
A2	E_x	T	709248	3609880	135	-1.1°	++	0	0	
A2	E_y	T	709211	3609800	109	-93.1°	++	0	0	
A2	\dot{H}_y	T	709233	3609735	10000	90.0°	+	1	0	
A2	\dot{H}_z	T	709234	3609751	172800	-	++	0	0	(B)
A3	\dot{H}_z	T	709043	3607615	10000	-	+	2	4	(K) SR
A3	CL	T	-	-	-	-	--	-	-	
B1	E_x	S	712023	3604125	134	8.5°	++	4	0	
B1	\dot{H}_y	S	712078	3604163	10000	90.0°	-	0	0	
B1	\dot{H}_z	S	712059	3604184	86400	-	--	0	0	(N)
B2	E_x	S	712013	3604328	133	1.3°	+	4	0	
B2	\dot{H}_y	S	712075	3604362	10000	90.0°	-	0	0	
B2	\dot{H}_z	S	712065	3604364	250000	-	--	0	0	(R)

Table C.4: Parameters for each receiver component recorded using Tx Afula; for additional information refer to the text at the beginning of this section.

Transmitter: Bet Alfa (BE)										
St.	Co.	RU	E / m	N / m	Moment	Angle	SNR	Cut		Rem.
								\	/	
A1	E_x	T	725111	3602901	134	0.1°	++	0	0	
A1	E_y	T	725020	3602864	141	-88.7°	++	0	0	
A1	\dot{H}_y	T	725052	3602824	10000	87.3°	+	2	0	
A1	\dot{H}_z	T	725086	3602839	86400	-	++	3	0	(N)
A2	E_x	T	724783	3602931	131	-6.3°	++	0	0	
A2	E_y	T	724691	3602898	131	-89.4°	++	0	0	
A2	\dot{H}_y	T	724766	3602873	10000	87.3°	0	2	0	
A2	\dot{H}_z	T	724783	3602864	86400	-	+	3	0	(N)
B1	E_x	S	730903	3601337	131	-3.5°	++	3	0	
B1	\dot{H}_y	S	730655	3601194	10000	87.3°	+	2	0	
B1	\dot{H}_z	S	730655	3601194	250000	-	++	3	0	(R)
B2	E_x	S	730681	3601249	120	-5.7°	++	5	0	
B2	\dot{H}_y	S	730864	3601281	10000	87.3°	++	2	0	
B2	\dot{H}_z	S	730875	3601301	86400	-	++	4	0	(N)

Table C.5: Parameters for each receiver component recorded using Tx Bet Alfa; for additional information refer to the text at the beginning of this section.

Transmitter: Beit Shean (BS)										
St.	Co.	RU	E / m	N / m	Moment	Angle	SNR	Cut		Rem.
								\	/	
A1	E_x	T	732092	3595815	108	6.6°	++	0	0	
A1	E_y	T	732163	3595853	125	-87.1°	+	0	0	
A1	\dot{H}_y	T	732094	3595845	10000	93.3°	+	0	0	
A1	\dot{H}_z	T	732093	3595838	250000	-	++	0	0	(R)
A2	\dot{H}_y	T	732294	3595853	10000	93.3°	+	0	0	
A2	\dot{H}_z	T	732283	3595829	172800	-	++	0	0	(B, *)
B1	E_x	S	737192	3595157	134	4.8°	++	3	0	
B1	\dot{H}_y	S	737181	3595099	10000	93.3°	++	2	0	
B1	\dot{H}_z	S	737205	3595112	86400	-	++	9	0	(N)
B2	E_x	S	736993	3595143	133	4.7°	++	5	0	
B2	\dot{H}_y	S	736982	3595084	10000	93.3°	++	3	0	
B2	\dot{H}_z	S	736951	3595098	86400	-	++	4	0	(N)

Table C.6: Parameters for each receiver component recorded using Tx Beit Shean; the \dot{H}_z -sensor at station A2 was faulty (sec. 6.2.2). For additional information refer to the text at the beginning of this section.

Transmitter: Carmel (CA)										
St.	Co.	RU	E / m	N / m	Moment	Angle	SNR	Cut		Rem.
								\	/	
A1	E_x	T	695013	3619263	126	4.7°	+	1	0	
A1	\dot{H}_x	T	694970	3619313	10000	2.7°	0	0	25	
A1	\dot{H}_y	T	694970	3619309	10000	92.7°	0	0	0	
A1	\dot{H}_z	T	694951	3619306	172800	-	+	0	0	(B)
B1	\dot{H}_z	S	692171	3615451	86400	-	++	2	0	(N)

Table C.7: Parameters for each receiver component recorded using Tx Carmel; for additional information refer to the text at the beginning of this section.

Transmitter: Devora (DV)										
St.	Co.	RU	E / m	N / m	Moment	Angle	SNR	Cut		Rem.
								\	/	
A1	E_x	T	719450	3619146	131	-7.9°	++	2	0	(N)
A1	E_y	T	719524	3619089	136	-98.8°	+	3	0	
A1	\dot{H}_y	T	719514	3619157	10000	-79.1°	0	2	0	
A1	\dot{H}_z	T	719514	3619157	86400	-	+	3	0	
A2	E_x	T	719513	3618924	135	-9.9°	+	2	0	
A2	E_y	T	719590	3618870	128	-97.7°	-	2	0	
A2	\dot{H}_y	T	719579	3618933	10000	-79.1°	+	2	0	
A2	\dot{H}_z	T	719579	3618933	86400	-	+	3	0	
A2	\dot{H}_z	T	719579	3618933	250000	-	+	3	4	
A2	CL	T	-	-	-	-	--	-	-	
B1	E_x	S	721155	3612536	70	-10.7°	++	5	0	(N)
B1	\dot{H}_y	S	721141	3612564	10000	-79.1°	0	4	0	
B1	\dot{H}_z	S	721146	3612542	86400	-	+	15	0	
B2	E_x	S	720981	3612677	83	-0.6°	++	4	0	(N)
B2	\dot{H}_y	S	721022	3612681	10000	-79.1°	0	4	0	
B2	\dot{H}_z	S	721014	3612695	86400	-	+	15	0	

Table C.8: Parameters for each receiver component recorded using Tx Devora; for additional information refer to the text at the beginning of this section.

Transmitter: Elyaqim (EM)										
St.	Co.	RU	E / m	N / m	Moment	Angle	SNR	Cut		Rem.
								\	/	
A1	E_x	T	695476	3616093	124	5.7°	++	2	0	(B)
A1	E_y	T	695565	3616090	128	95.2°	++	0	0	
A1	\dot{H}_x	T	695512	3616041	10000	2.7°	0	2	15	
A1	\dot{H}_y	T	695517	3616053	10000	92.7°	0	2	0	
A1	\dot{H}_z	T	695499	3616084	172800	-	+	2	0	
A2	E_x	T	695469	3615914	133	4.4°	++	0	0	
A2	E_y	T	695463	3615818	134	94.7°	++	0	0	
A2	\dot{H}_x	T	695513	3615863	10000	2.7°	0	2	16	
A2	\dot{H}_y	T	695527	3615867	10000	92.7°	+	2	0	
A2	\dot{H}_z	T	695521	3615868	250000	-	+	2	0	

Table C.9: Parameters for each receiver component recorded using Tx Elyaqim; for additional information refer to the text at the beginning of this section.

Transmitter: Eliyakhin (EN)										
St.	Co.	RU	E / m	N / m	Moment	Angle	SNR	Cut		Rem.
								\	/	
A1	E_x	T	688683	3588352	124	3.5°	++	0	0	(B, *)
A1	E_y	T	688603	3588396	134	93.9°	++	0	0	
A1	\dot{H}_y	T	688667	3588418	10000	92.1°	0	0	10	
A1	\dot{H}_z	T	688653	3588387	172800	-	+	0	0	
A2	E_x	T	688410	3588339	132	1.9°	++	0	0	
A2	E_y	T	688332	3588390	131	91.5°	++	0	0	
A2	\dot{H}_y	T	688397	3588409	10000	92.1°	0	0	0	(R)
A2	\dot{H}_z	T	688392	3588403	250000	-	+	2	0	
B1	E_x	S	683390	3587601	132	-1.7°	++	4	0	(N)
B1	\dot{H}_y	S	683398	3587542	10000	92.1°	+	2	0	
B1	\dot{H}_z	S	683420	3587556	86400	-	++	4	0	
B2	\dot{H}_y	S	683202	3587514	10000	92.1°	+	2	0	(N)
B2	\dot{H}_z	S	683173	3587522	86400	-	++	4	0	

Table C.10: Parameters for each receiver component recorded using Tx Eliyakhin; the \dot{H}_z -sensor at station A1 was faulty (sec. 6.2.2). for additional information refer to the text at the beginning of this section.

Transmitter: Gan Shemuel (GA)										
St.	Co.	RU	E / m	N / m	Moment	Angle	SNR	Cut		Rem.
								\	/	
A1	E_x	S	682915	3592021	128	-6.2°	-	3	0	(N)
A1	\dot{H}_y	S	682852	3592013	10000	66.9°	-	3	0	
A1	\dot{H}_z	S	682876	3591998	86400	-	--	0	0	
A2	E_x	S	682826	3592221	128	-5.4°	-	3	0	
A2	\dot{H}_y	S	682762	3592212	10000	66.9°	-	3	0	
A2	\dot{H}_z	S	682788	3592203	86400	-	--	0	0	

Table C.11: Parameters for each receiver component recorded using Tx Gan Shemuel; for additional information refer to the text at the beginning of this section.

Transmitter: Gan Shemuel B (GB)										
St.	Co.	RU	E / m	N / m	Moment	Angle	SNR	Cut		Rem.
								\	/	
A1	E_x	T	682714	3592264	132	1.8°	++	0	0	(B)
A1	E_y	T	682633	3592212	126	-82.9°	++	0	0	
A1	\dot{H}_y	T	682691	3592205	10000	93.0°	+	1	0	
A1	\dot{H}_z	T	682702	3592231	172800	-	++	2	0	
A2	E_x	T	682857	3592118	128	5.4°	++	0	0	
A2	E_y	T	682902	3592040	123	-86.1°	++	0	0	
A2	\dot{H}_y	T	682842	3592061	10000	93.0°	+	1	0	(R)
A2	\dot{H}_z	T	682846	3592058	250000	-	+	1	0	
B1	\dot{H}_z	S	678730	3593503	86400	-	0	2	0	(O)
B1	\dot{H}_y	S	678752	3593499	10000	93.0°	+	4	0	(N)
B2	E_x	S	678865	3593367	133	4.1°	++	4	0	
B2	\dot{H}_y	S	678850	3593304	10000	93.0°	++	4	0	
B2	\dot{H}_z	S	678826	3593318	86400	-	+	4	0	

Table C.12: Parameters for each receiver component recorded using Tx Gan Shemuel B; for additional information refer to the text at the beginning of this section.

Transmitter: Hazoreim (HA)										
St.	Co.	RU	E / m	N / m	Moment	Angle	SNR	Cut		Rem.
								\	/	
A1	E_x	S	732457	3629063	134	4.3°	++	1	0	(N)
A1	\dot{H}_y	S	732504	3629092	10000	92.1°	+	1	0	
A1	\dot{H}_z	S	732519	3629067	86400	-	++	1	0	
A2	E_x	S	732295	3629162	127	2.3°	++	2	0	
A2	\dot{H}_y	S	732336	3629192	10000	92.1°	+	1	0	
A2	\dot{H}_z	S	732307	3629189	86400	-	++	1	0	
B1	E_x	T	735383	3622673	96	-3.3°	++	2	0	(R)
B1	E_y	T	735362	3622598	128	-91.3°	++	0	0	
B1	\dot{H}_y	T	735356	3622672	10000	92.1°	+	2	0	
B1	\dot{H}_z	T	735353	3622673	250000	-	+	3	0	
B2	E_x	T	735648	3622608	134	0.8°	++	2	0	
B2	E_y	T	735567	3622624	94	-89.1°	++	0	0	
B2	\dot{H}_y	T	735596	3622585	10000	92.1°	+	2	0	(B, *)
B2	\dot{H}_z	T	735598	3622605	172800	-	+	5	10	

Table C.13: Parameters for each receiver component recorded using Tx Hazoreim; the \dot{H}_z -sensor at station B2 was faulty (sec. 6.2.2). For additional information refer to the text at the beginning of this section.

Transmitter: Kerem Maharal (KE)										
St.	Co.	RU	E / m	N / m	Moment	Angle	SNR	Cut		Rem.
								\	/	
A1	E_x	S	687790	3614253	132.5	-10.4°	++	2	0	(N) SR
A1	\dot{H}_y	S	687776	3614188	10000	84.2°	--	0	0	
A1	\dot{H}_z	S	687753	3614206	86400	-	++	5	0	
A2	E_x	S	687636	3614271	133.7	-6.0°	++	3	0	(R) SR
A2	\dot{H}_y	S	687623	3614217	10000	84.2°	++	4	0	
A2	\dot{H}_z	S	687623	3614217	250000	-	++	5	0	
B1	E_x	T	682741	3613349	133	-5.6°	++	1	0	(N)
B1	E_y	T	682683	3613425	133	-97.8°	++	2	0	
B1	\dot{H}_y	T	681749	3613415	10000	84.2°	0	2	5	
B1	\dot{H}_z	T	682735	3613401	86400	-	-	4	0	
B2	E_x	T	681586	3613105	138	-8.3°	++	2	0	(N)
B2	E_y	T	682558	3613186	136	-93.3°	++	2	0	
B2	\dot{H}_y	T	682626	3613181	10000	84.2°	0	2	0	
B2	\dot{H}_z	T	682582	3613150	86400	-	0	2	0	

Table C.14: Parameters for each receiver component recorded using Tx Kerem Maharal; for additional information refer to the text at the beginning of this section.

Transmitter: Kefar Kamar (KK)										
St.	Co.	RU	E / m	N / m	Moment	Angle	SNR	Cut		Rem.
								\	/	
A1	E_x	T	725647	3623319	133	-4.1°	++	0	0	(B, *)
A1	E_y	T	725673	3623234	136	-86.8°	++	0	0	
A1	\dot{H}_y	T	725612	3623250	10000	94.0°	+	0	0	
A1	\dot{H}_z	T	715629	3623277	172800	-	++	6	10	
A2	E_x	T	725465	3623277	132	8.5°	++	0	0	(N) SR
A2	E_y	T	725504	3623199	126	-76.7°	++	0	0	
A2	\dot{H}_y	T	725445	3623221	10000	94.0°	+	0	0	
A2	\dot{H}_z	T	725469	3623605	86400	-	+	6	0	
B1	E_x	S	731408	3620909	138	6.8°	++	4	0	(R)
B1	\dot{H}_y	S	731440	3620968	10000	94.0°	++	4	0	
B1	\dot{H}_z	S	731430	3620978	250000	-	++	14	0	
B2	E_x	S	731581	3620987	134	5.1°	++	4	0	(N)
B2	\dot{H}_y	S	731612	3621044	10000	94.0°	+	4	0	
B2	\dot{H}_z	S	731639	3621045	86400	-	++	16	0	

Table C.15: Parameters for each receiver component recorded using Tx Kefar Kamar; for additional information regarding the type of information shown here, refer to the text at the beginning of this section. The \dot{H}_z -sensor at station B2 was faulty (sec. 6.2.2). For additional information refer to the text at the beginning of this section.

Transmitter: Kefar Kana (KN)										
St.	Co.	RU	E / m	N / m	Moment	Angle	SNR	Cut		Rem.
								\	/	
A1	E_x	T	714909	3627849	120	-2.5°	++	0	0	(B, *)
A1	E_y	T	714973	3627804	126	98.9°	++	2	0	
A1	\dot{H}_y	T	714918	3627795	10000	92.6°	0	3	0	
A1	\dot{H}_z	T	714912	3627830	172800	-	0	0	0	
A2	E_x	T	715100	3627765	99	1.4°	++	0	0	
A2	E_y	T	715170	3627726	131	94.4°	++	0	0	
A2	\dot{H}_y	T	715114	3627717	10000	92.6°	0	3	0	(R)
A2	\dot{H}_z	T	715111	3627720	250000	-	--	0	0	
B1	E_x	S	722327	3627251	141	2.9°	++	3	0	(N) SR
B1	\dot{H}_y	S	722346	3627189	10000	92.6°	+	4	0	
B1	\dot{H}_z	S	722354	3627214	86400	-	++	2	5	
B2	E_x	S	722128	3627272	137	2.7°	++	2	0	
B2	\dot{H}_y	S	722143	3627205	10000	92.6°	+	4	0	(N) SR
B2	\dot{H}_z	S	722119	3627221	86400	-	++	2	10	

Table C.16: Parameters for each receiver component recorded using Tx Kefar Kana; *: The \dot{H}_z -component at station A1 seemed to have a multidimensional feature at intermediate times. Therefore, data points 6 to 17 have been removed from the transient prior 1-D-inversion. For additional information refer to the text at the beginning of this section.

Transmitter: Pardes-Hanna (PH)										
St.	Co.	RU	E / m	N / m	Moment	Angle	SNR	Cut		Rem.
								\	/	
A1	E_x	T	683048	3601253	119	5.4°	0	0	0	(B)
A1	E_y	T	683080	3601329	118	-82.9°	-	0	0	
A1	\dot{H}_y	T	683105	3601270	10000	92.7°	0	0	0	
A1	\dot{H}_z	T	683096	3601306	172800	-	--	0	0	
B1	E_x	S	684118	3595561	126	9.3°	++	3	0	(N)
B1	\dot{H}_y	S	684159	3595581	10000	92.7°	+	1	0	
B1	\dot{H}_z	S	684171	3595564	86400	-	+	1	0	
B2	\dot{H}_y	S	684087	3595400	10000	92.7°	+	1	0	
B2	\dot{H}_z	S	684088	3595408	250000	-	+	1	0	(R)

Table C.17: Parameters for each receiver component recorded using Tx Pardes-Hanna; for additional information refer to the text at the beginning of this section.

Transmitter: Ra'ananna (RA)										
St.	Co.	RU	E / m	N / m	Moment	Angle	SNR	Cut		Rem.
								\	/	
A1	E_x	T	670995	3565007	126	6.3°	++	3	0	(B)
A1	E_y	T	671073	3565043	127	-88.8°	++	3	0	
A1	\dot{H}_y	T	671014	3565070	10000	92.9°	++	3	0	
A1	\dot{H}_z	T	671031	3565044	172800	-	++	3	0	
A2	\dot{H}_y	T	670823	3565062	10000	92.9°	++	3	0	
A2	\dot{H}_z	T	670817	3565063	250000	-	++	3	0	(R)
B1	E_x	S	675703	3564586	125	4.3°	++	2	0	(N)
B1	\dot{H}_y	S	675690	3564528	10000	92.9°	++	2	0	
B1	\dot{H}_z	S	675702	3564506	86400	-	++	2	0	
B2	E_x	S	675563	3564612	123	4.0°	++	2	0	
B2	\dot{H}_y	S	675545	3564582	10000	92.9°	++	2	0	
B2	\dot{H}_z	S	675543	3564612	86400	-	++	2	0	(N)

Table C.18: Parameters for each receiver component recorded using Tx Ra'ananna; for additional information refer to the text at the beginning of this section.

Transmitter: Ramat Zevi (RZ)											
St.	Co.	RU	E / m	N / m	Moment	Angle	SNR	Cut		Rem.	
								\	/		
A1	\dot{H}_y	T	724537	3610247	10000	92.0°	+	0	0	(R)	
A1	\dot{H}_z	T	724542	3610250	250000	-	+	6	0		
A2	\dot{H}_z	T	724615	3610113	10000	-	+	5	0		(K)
A2	CL	T	-	-	-	-	--	-	-		
B1	E_x	S	728373	3604869	104	3.5°	++	0	0		
B1	\dot{H}_y	S	728331	3604848	10000	92.0°	+	1	0	(N) SR	
B1	\dot{H}_z	S	728332	3604814	86400	-	++	4	0		
B2	E_x	S	728471	3605064	125	2.8°	++	0	0		
B2	\dot{H}_y	S	728415	3606014	10000	92.0°	++	1	0		
B2	\dot{H}_z	S	728444	3605029	86400	-	++	6	0		(N) SR

Table C.19: Parameters for each receiver component recorded using Tx Ramat Zevi; for additional information refer to the text at the beginning of this section.

Transmitter: Sarid (SA)										
St.	Co.	RU	E / m	N / m	Moment	Angle	SNR	Cut		Rem.
								\	/	
A1	E_x	T	711009	3611880	119	-28.5°	++	0	0	(N) SR
A1	E_y	T	711034	3611966	134	61.5°	++	0	0	
A1	\dot{H}_y	T	710977	3611931	10000	60.8°	+	2	0	
A1	\dot{H}_z	T	710977	3611931	86400	-	++	3	0	
A2	E_x	T	710646	3612032	132	-21.6°	++	0	0	
A2	E_y	T	710662	3612119	134	61.1°	++	3	0	
A2	\dot{H}_y	T	710605	3612084	10000	60.8°	+	2	0	(N) SR
A2	\dot{H}_z	T	710630	3612092	86400	-	+	4	0	
A3	E_y	S	710891	3611630	112	56.7°	++	3	0	
A3	\dot{H}_x	S	710859	3611680	10000	-29.2°	0	2	0	(N) SR
A3	\dot{H}_y	S	710859	3611680	10000	60.8°	+	2	0	
A3	\dot{H}_z	S	710889	3611693	86400	-	++	4	0	

Table C.20: Parameters for each receiver component recorded using Tx Sarid; for additional information refer to the text at the beginning of this section.

Transmitter: Taninim (TA)										
St.	Co.	RU	E / m	N / m	Moment	Angle	SNR	Cut		Rem.
								\	/	
A1	E_x	T	680437	3602356	129	0.3°	+	0	0	(N)
A1	E_y	T	680392	3602438	136	90.2°	+	0	0	
A1	\dot{H}_x	T	680385	3602383	10000	-0.7°	-	0	0	
A1	\dot{H}_y	T	680385	3602383	10000	89.3°	0	1	0	
A1	\dot{H}_z	T	680385	3602283	86400	-	+	3	0	
A1	CL	T	-	-	-	-	--	-	-	
B1	E_x	S	680311	3600733	132	1.6°	++	2	0	(R)
B1	\dot{H}_y	S	680368	3600720	10000	89.3°	+	4	0	
B1	\dot{H}_z	S	680353	3600732	250000	-	++	5	0	
B2	\dot{H}_y	S	680252	3600859	10000	89.3°	+	4	0	
B2	\dot{H}_z	S	680245	3600813	101610	-	++	5	0	

Table C.21: Parameters for each receiver component recorded using Tx Taninim; for additional information refer to the text at the beginning of this section.

Transmitter: Ta'annakh (TK)										
St.	Co.	RU	E / m	N / m	Moment	Angle	SNR	Cut		Rem.
								\	/	
A1	E_x	S	718149	3606724	132	4.3°	+	2	0	(N) SR
A1	\dot{H}_y	S	718125	3606675	10000	93.3°	0	3	0	
A1	\dot{H}_z	S	718118	3606707	86400	-	+	11	0	
A2	E_x	S	718246	3606559	136	3.2°	+	3	0	
A2	\dot{H}_y	S	718228	3606499	10000	93.3°	0	4	0	
A2	\dot{H}_z	S	718252	3606482	86400	-	+	8	0	
B1	CL	T	-	-	-	-	--	-	-	(R)
B1	\dot{H}_z	T	722523	3604274	250000	-	0	1	4	
B2	\dot{H}_y	T	722706	3604145	10000	93.3°	0	0	0	(K)
B2	\dot{H}_z	T	722706	3604145	10000	-	0	0	0	

Table C.22: Parameters for each receiver component recorded using Tx Ta'annakh; for additional information refer to the text at the beginning of this section.

Transmitter: Yagur (YA)										
St.	Co.	RU	E / m	N / m	Moment	Angle	SNR	Cut		Rem.
								\	/	
A1	E_x	T	698316	3628689	130	-10.9°	+	1	0	(N) SR
A1	\dot{H}_z	T	698256	3628710	86400	-	+	9	0	
A2	E_x	T	697961	3628433	139	-8.5°	0	0	0	
A2	E_y	T	697970	3628523	136	74.9°	+	0	0	
A2	\dot{H}_y	T	697952	3628479	10000	80.7°	0	0	0	
A2	\dot{H}_z	T	697952	3628479	86400	-	0	8	0	
B1	E_x	S	693383	3625565	124	-8.5°	++	3	0	(R) SR
B1	\dot{H}_y	S	693377	3625562	10000	80.7°	++	4	0	
B1	\dot{H}_z	S	693377	3625562	250000	-	+	2	19	
B2	E_x	S	693483	3625587	132	-8.0°	++	2	0	(N) SR
B2	\dot{H}_y	S	693528	3625538	10000	80.7°	++	4	0	
B2	\dot{H}_z	S	693528	3625538	86400	-	++	4	10	

Table C.23: Parameters for each receiver component recorded using Tx Yagur; for additional information refer to the text at the beginning of this section.

Transmitter: Yoqneam (YO)										
St.	Co.	RU	E / m	N / m	Moment	Angle	SNR	Cut		Rem.
								\	/	
A1	E_x	T	697344	3617298	134	-3.8°	++	4	0	
A1	E_y	T	697426	3617239	133	-93.2°	++	0	0	
A1	\dot{H}_x	T	697412	3617288	10,000	-5.2°	0	2	0	
A1	\dot{H}_y	T	697412	3617288	10,000	84.8°	+	2	0	
A1	\dot{H}_z	T	697384	3617291	86,400	-	-	15	0	(N) SR
A1	\dot{H}_z	T	697412	3617288	250,000	-	0	15	0	(R) SR
A1	CL	T	-	-	-	-	--	-	-	
B1	E_x	S	701922	3612644	134	-3.4°	++	4	0	
B1	\dot{H}_y	S	701981	3612678	10,000	84.8°	+	4	0	
B1	\dot{H}_z	S	701948	3612673	86,400	-	0	13	0	(N) SR
B2	E_x	S	702145	3612553	135	-4.6°	++	4	0	
B2	\dot{H}_y	S	702189	3612587	10,000	84.8°	+	4	0	
B2	\dot{H}_z	S	702207	3612569	86,400	-	++	10	0	(N) SR

Table C.24: Parameters for each receiver component recorded using Tx Yoqneam; for additional information refer to the text at the beginning of this section.

C.1.3 Coordinates of the SHOTEM sites

Site	E / m	N / m	Sys.	Close to
BSH7	732095	3596161	G	BSA
BSH19	737242	3595407	G	BS (Tx)
BSH20	737260	3593606	G	BSB
N1	680411	3600660	C	TAB
N2	719474	3618913	C	DVA
N3	697109	3635517	C	AF (Tx)
N4	695183	3618310	C	CAA
N5	712022	3613728	G	SA (Tx)
N6	711020	3612029	G	SAA
N7	720871	3615815	G	DV (Tx)
N8	697514	3633942	G	AFA
N9	687780	3614305	G	KEA
N10	682632	3613168	G	KEB
N11	724643	3603288	G	BEA
N12	730875	3601493	G	BEB
N13	680880	3603988	G	TAA
N14	680479	3602231	G	PHA
N15	731486	3620839	G	KKB
N16	725309	3623493	G	KKA
N17	698173	3628554	G	YAA
N18	701861	3612595	G	YOB
N19	682780	3592228	G	GAA/GBA
N20	678948	3593155	G	GBB
N21	711603	3604113	G	AUB
N22	708873	3609534	G	AUA
N23	737487	3594900	G	BSB
N24	731648	3597115	G	BSA
N25	728405	3604495	G	RZB
N26	724469	3610329	G	RZA
N27	732500	3628836	G	HAA
N28	718341	3606545	G	TKA
N29	695510	3615943	G	EMA
N30	694964	3619327	G	CAA
N31	735449	3622719	G	HAB
N32	722390	3627332	G	KNB
N33	715129	3627543	G	KNA
NRU1	681488	3595717	C	GA (Tx)
NRU2	683459	3587673	C	ENB
NRU3	687015	3597455	C	-
NRU4	684112	3596125	C	PHB
NRU5	676021	3565304	C	RAB
NRU6	687234	3588752	C	ENA
NRU7	686135	3590656	C	-
NRU8	692174	3600292	C	-

Table C.25: Designations and coordinates of all SHOTEM sites; the column "Site" shows the designation of the data sets used in this work. The next two columns give the UTM coordinates ("E" is easting, "N" northing, zone 36S). The column named "Sys." contains the information which of the two SHOTEM-systems was used at that site. "G" stands for Geonics EM-67, "C" for Cycle-5M. The last column assigns the SHOTEM sites to LOTEM positions.

C.2 Single inversion results

In the section the single Occam's inversion results of all LOTEM data sets recorded in Israel are presented. The coordinates and Tx-parameter can be found in sec. C.1. The points denote the measured data set. The error bars indicate the error estimates. The solid lines denote the resulting forward curve for the final model. Negative values are displayed in gray, positive values in black. The Occam's inversions are done with R_1 (eqn. 3.16) and R_2 (eqn. 3.17) roughness definitions. Both models are displayed left of the data sets. The black models represent the results for the inversions with the R_1 -constraint. The gray line denotes the R_2 -model. The forward curve is calculated for the R_1 model.

The title of each panel quotes the station name and the measured component (e.g. the figure "AFA1HZ" shows the result for the Tx AF, Rx-site A, Rx-station 1, component \dot{H}_z). The misfit and the CF is also given in the title. The subscript 1 refers to the R_1 -model, whereas 2 refers to the R_2 -model.

If the data sets are too noisy or no acceptable misfit was achieved, no inversion result is displayed. Some of the time series which contained only noise (see sec. C.1.2) were omitted completely. If early or late time data points could not be fitted during the inversion (because of obvious multidimensional distortions or inaccurate system responses), they were removed prior to inversion. The tables in C.1 indicate which data points were removed.

The inversion with both smoothness constraints allows to estimate the exploration depth of the individual transient. At depths where both models show significant differences the models are not well constrained by the data. However, the models are only comparable, if the misfit is similar.

First, all LOTEM-transients will be displayed in alphabetical order. After this all SHOTEM-transients are shown.

Figure C.1: Single inversion results for the transients measured at AEA;

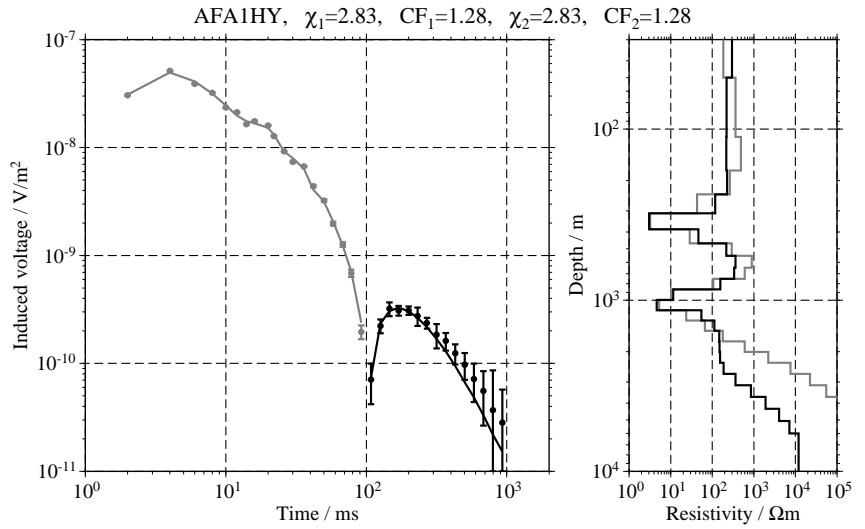
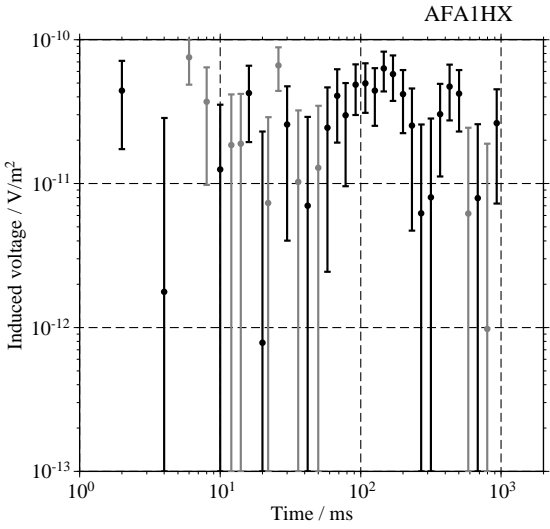
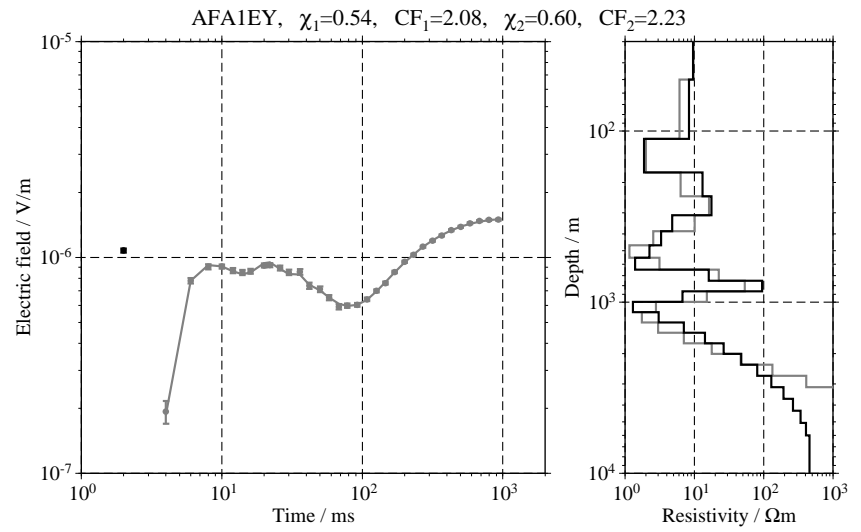
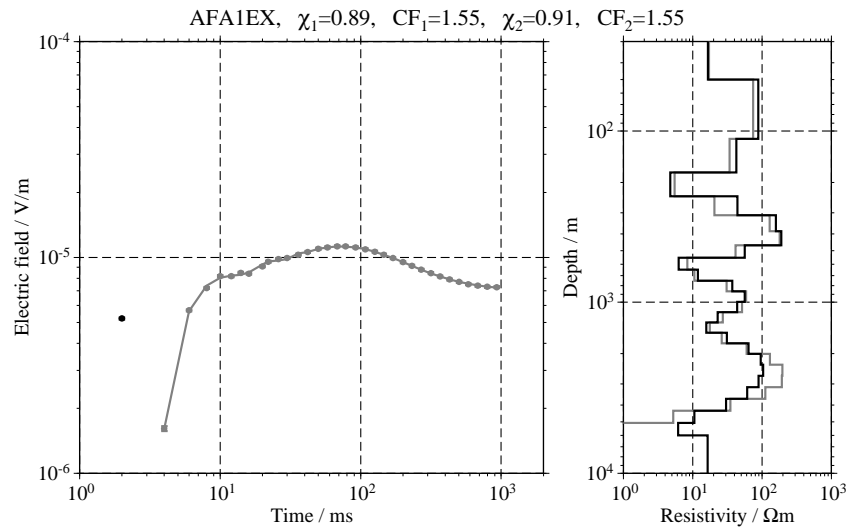


Figure C.2: Single inversion results for the transients measured at AFA and AUA;

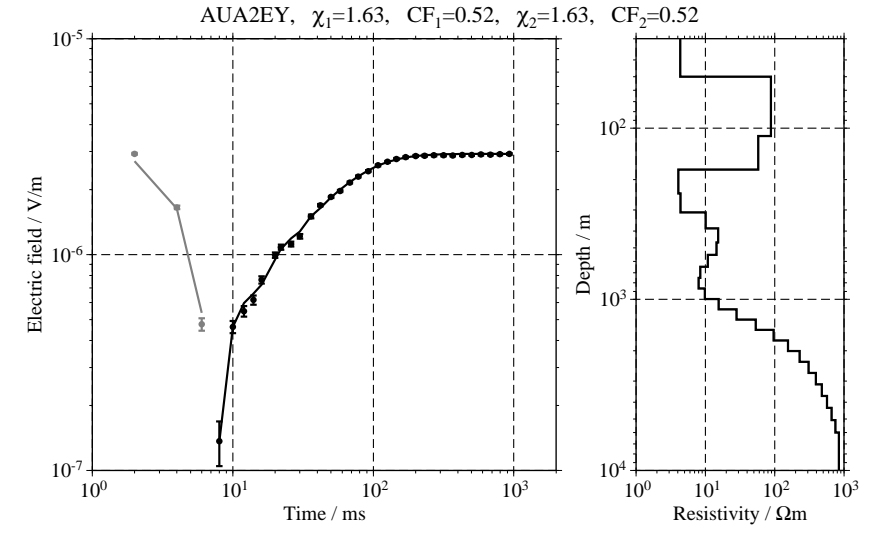
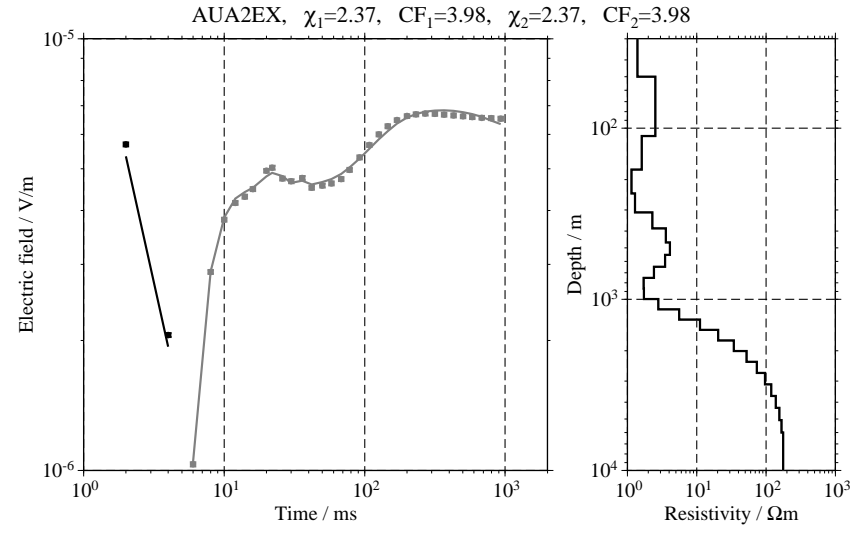
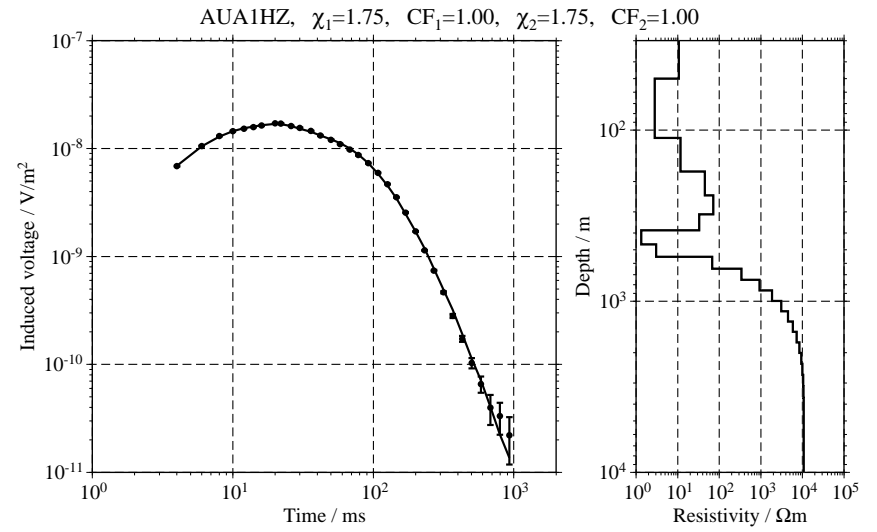
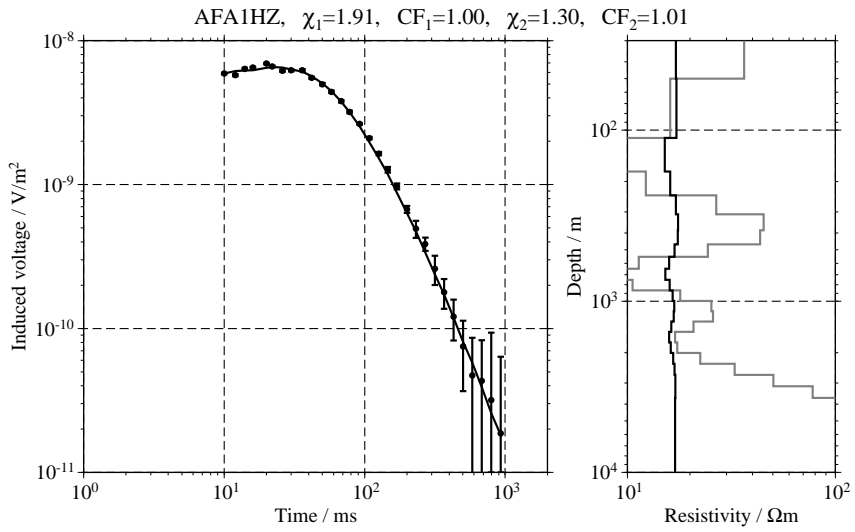


Figure C.3: Single inversion results for the transients measured at AUA and AUB;

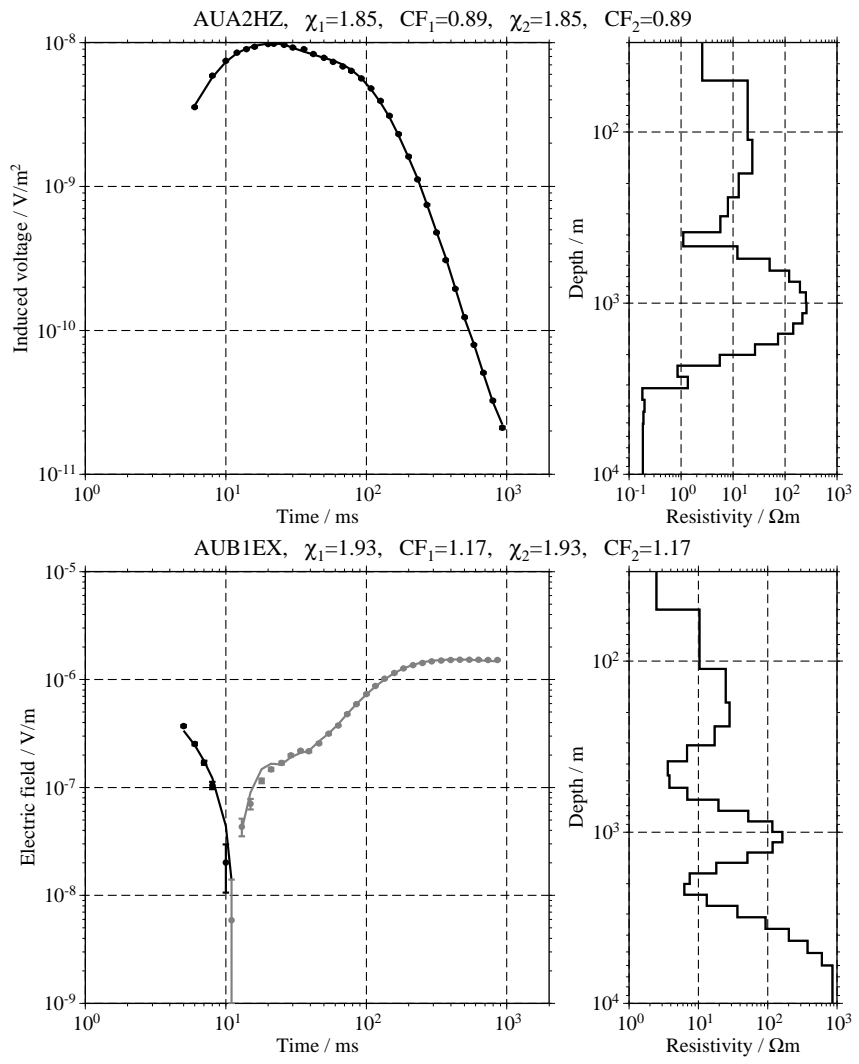
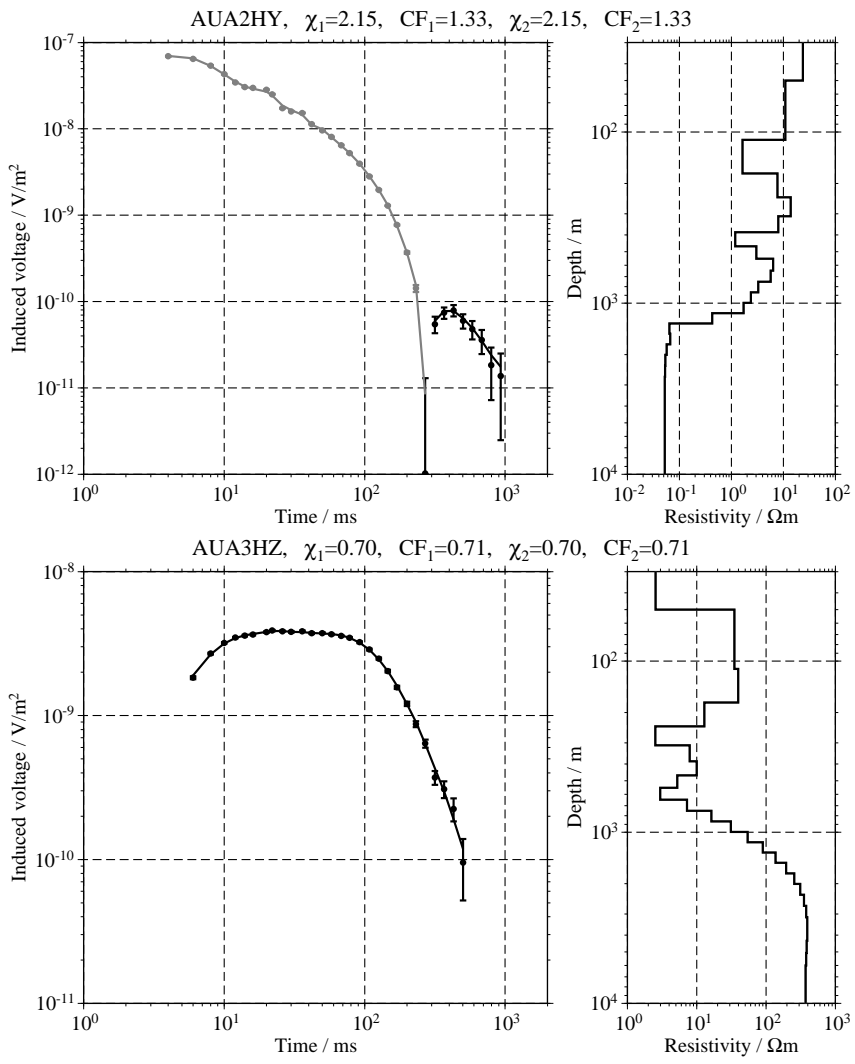


Figure C.4: Single inversion results for the transients measured at AUB;

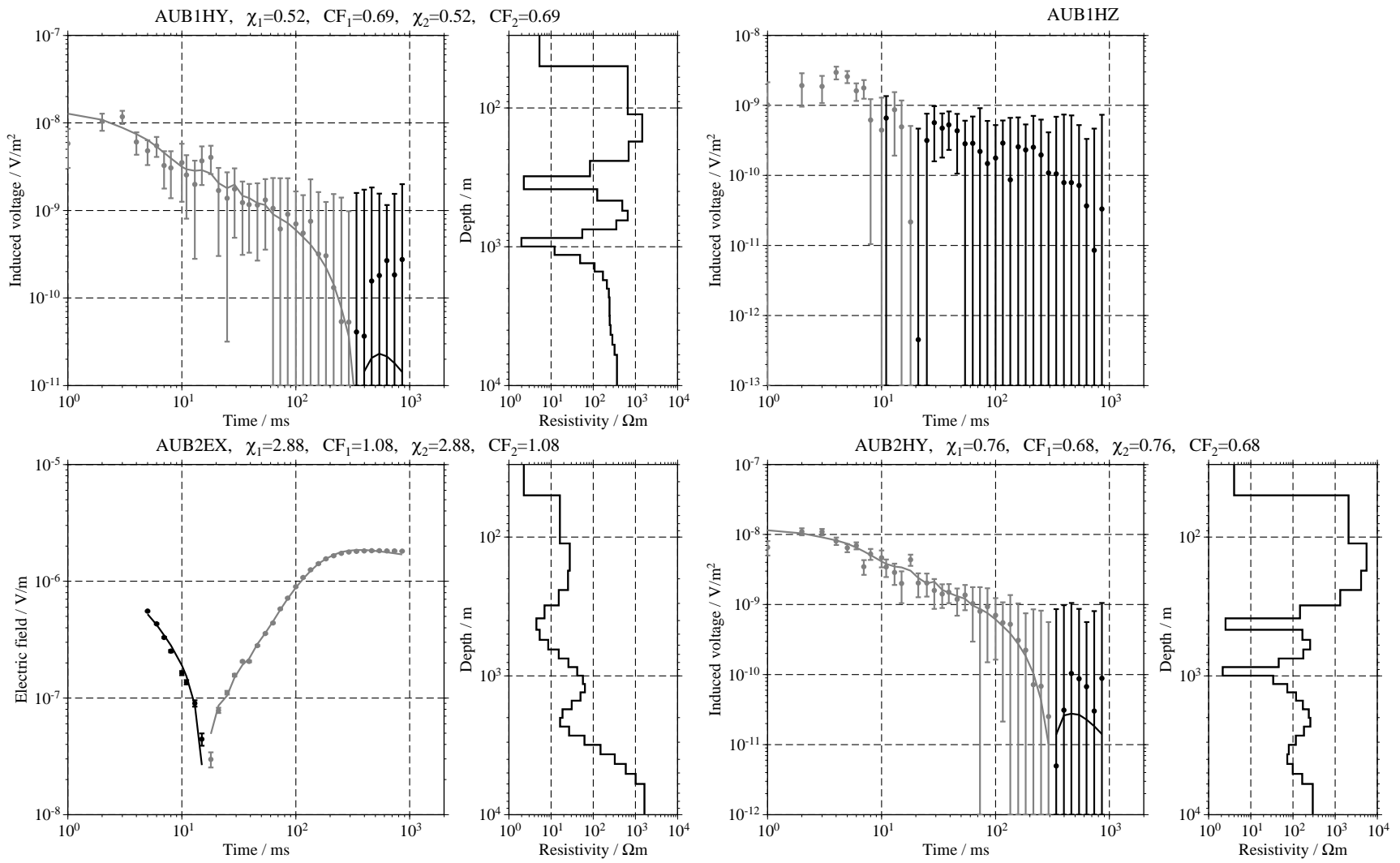


Figure C.5: Single inversion results for the transients measured at AUB and BEA.

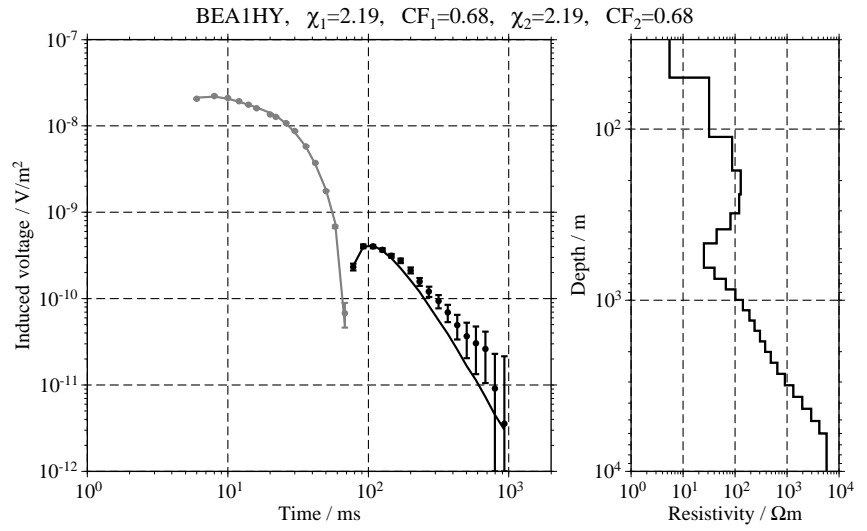
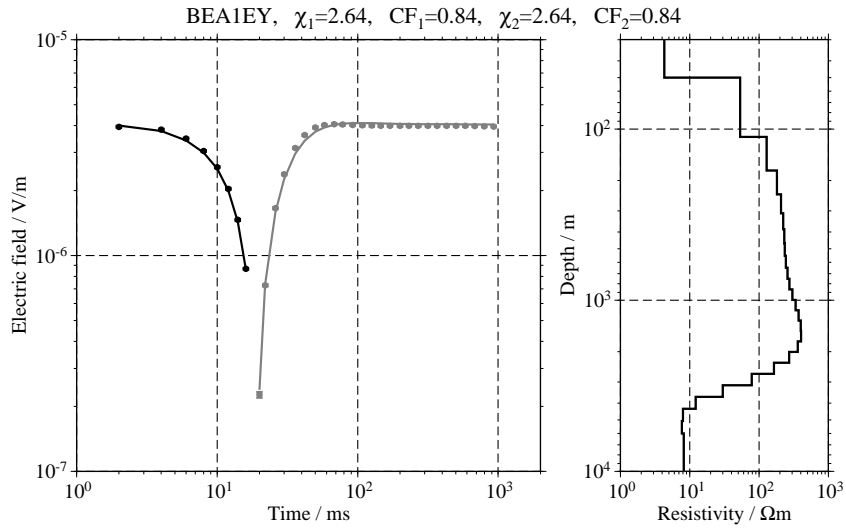
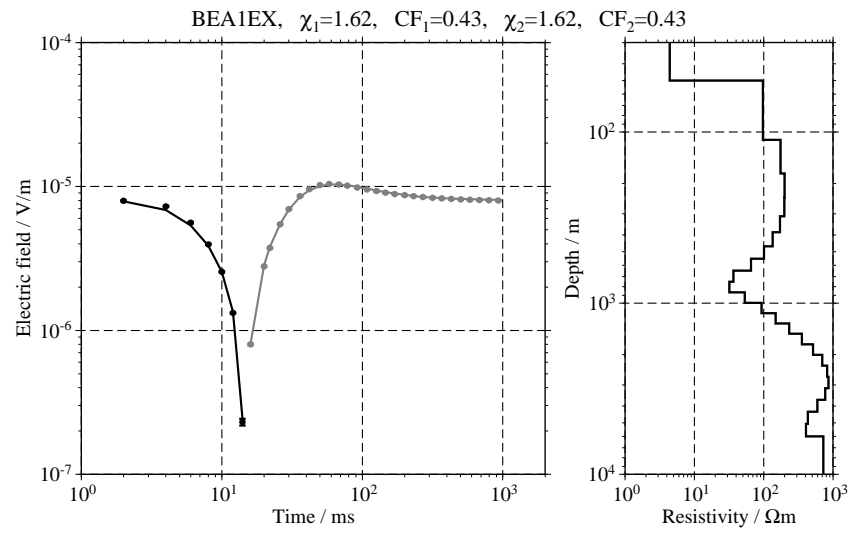
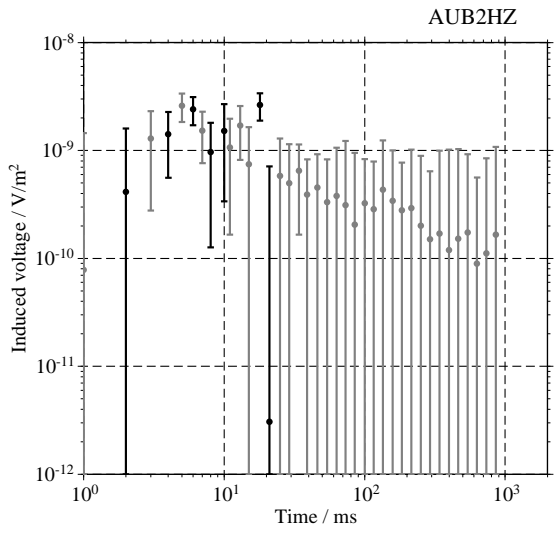


Figure C.6: Single inversion results for the transients measured at BEA.

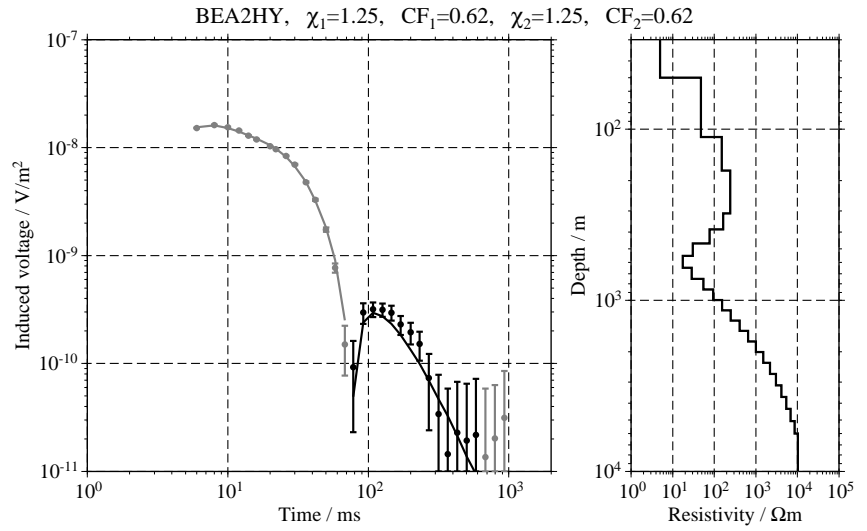
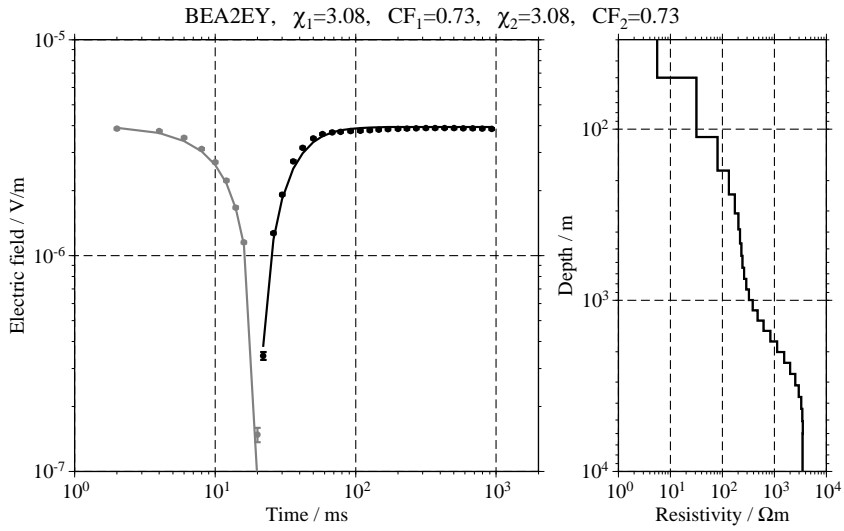
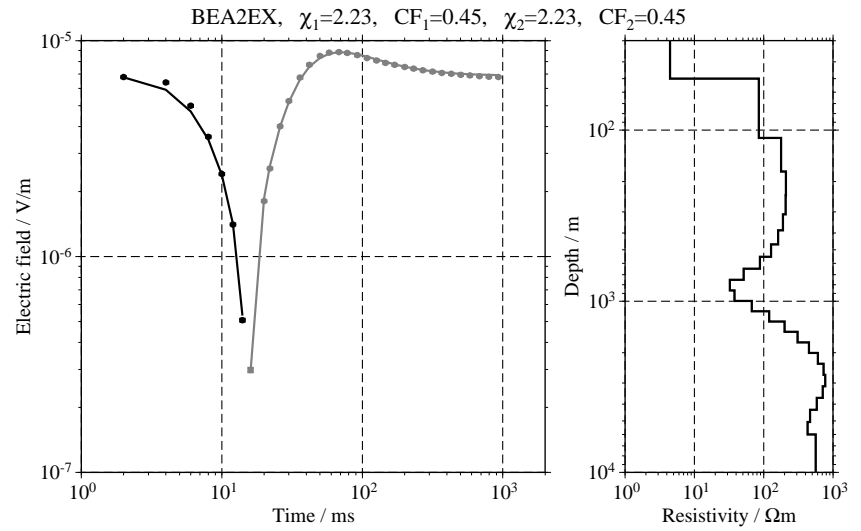
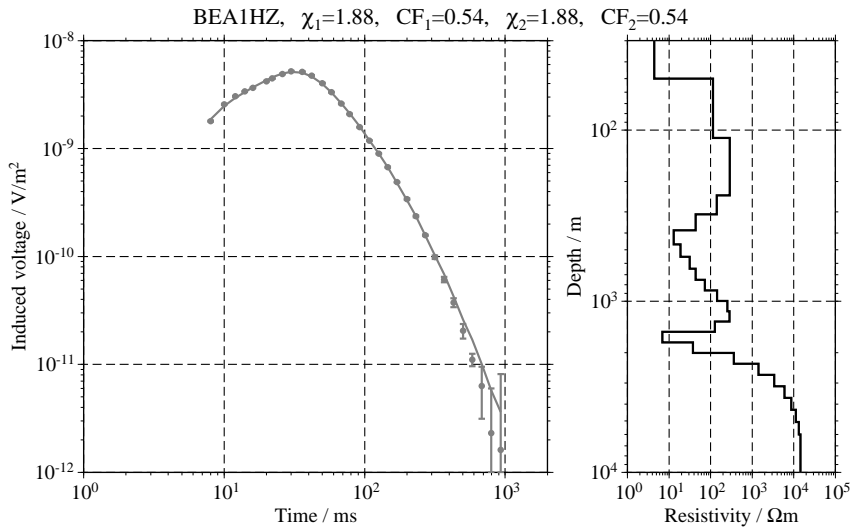


Figure C.7: Single inversion results for the transients measured at BEA and BEB;

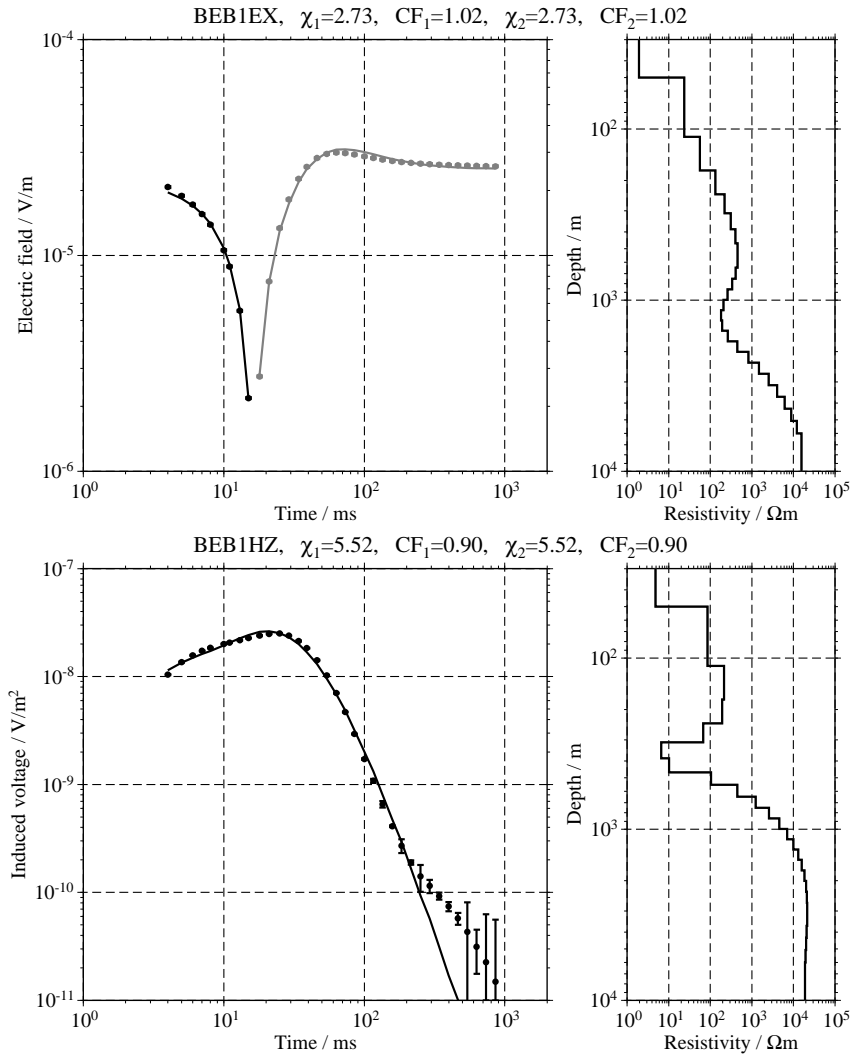
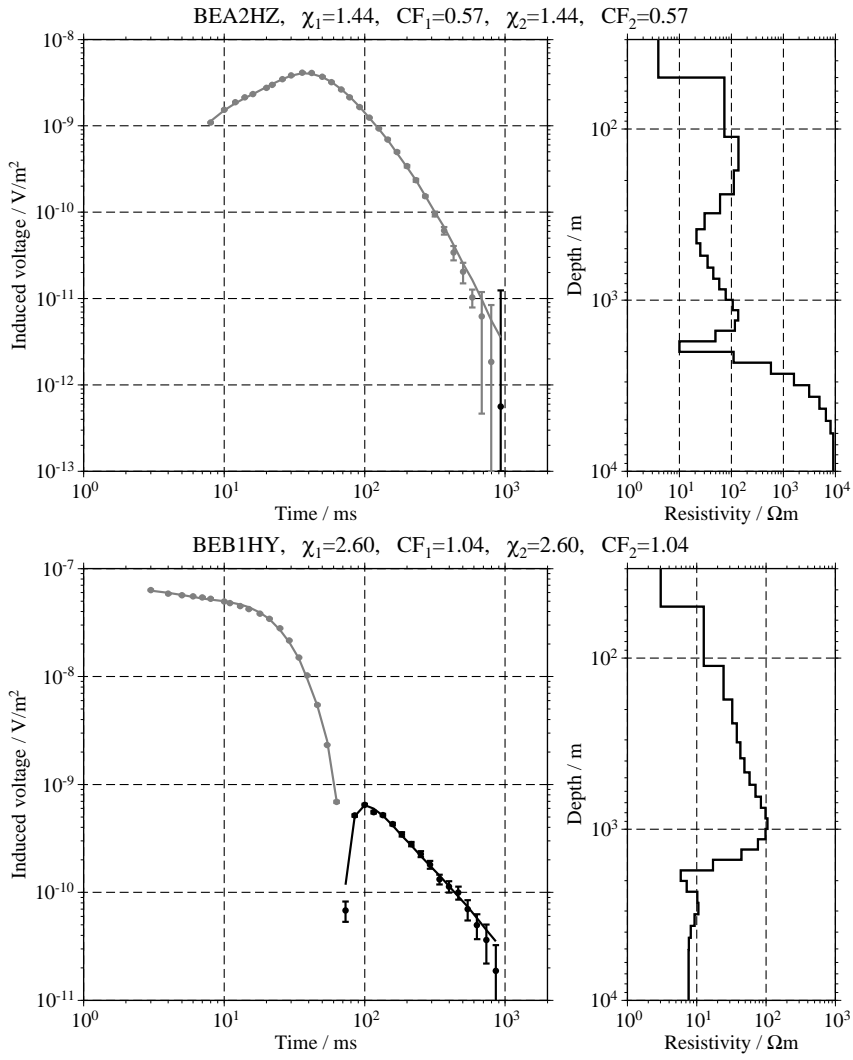


Figure C.8: Single inversion results for the transients measured at BEB and BSA.

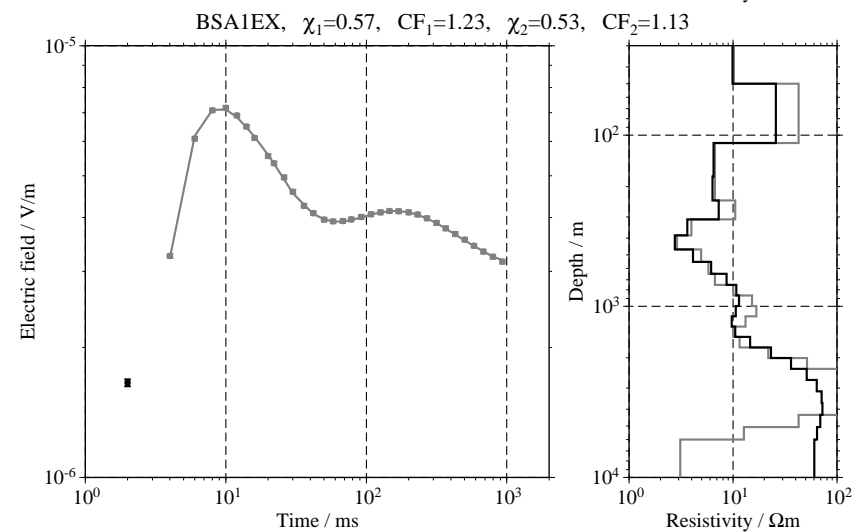
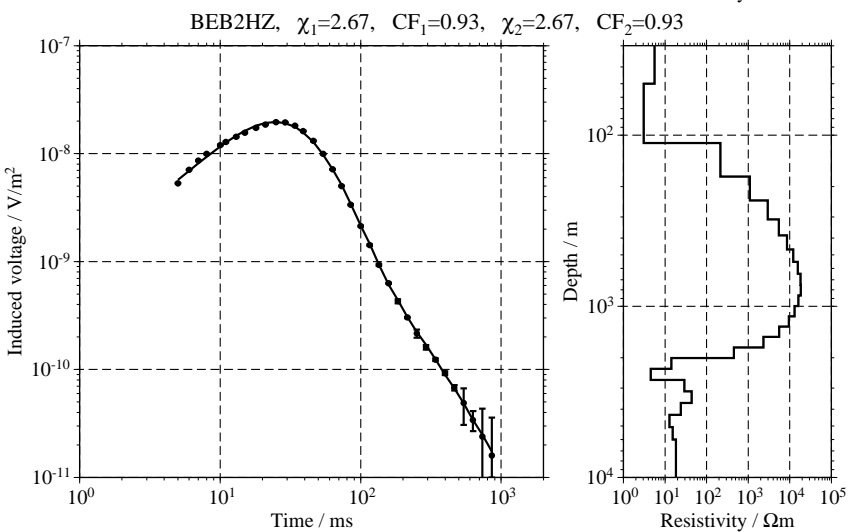
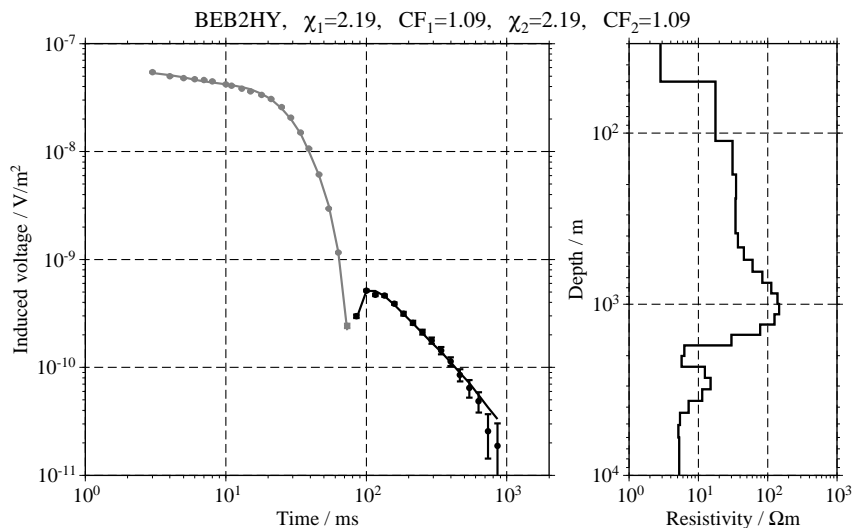
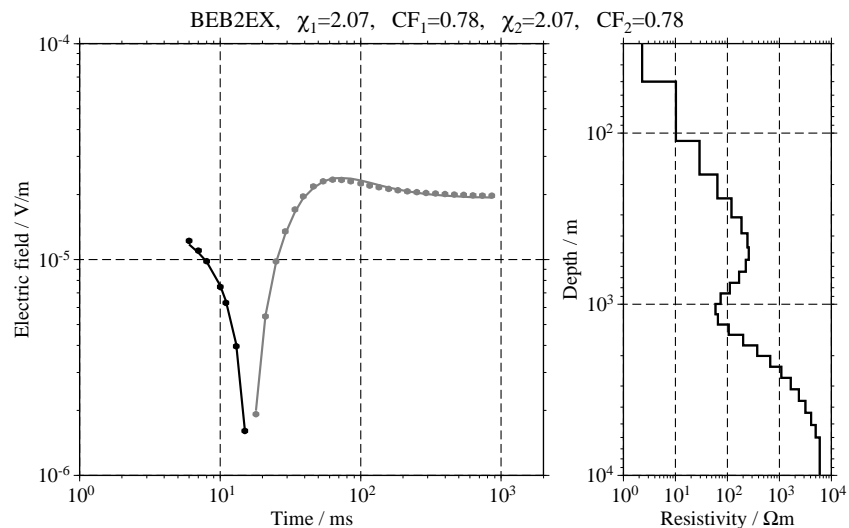


Figure C.9: Single inversion results for the transients measured at BSA;

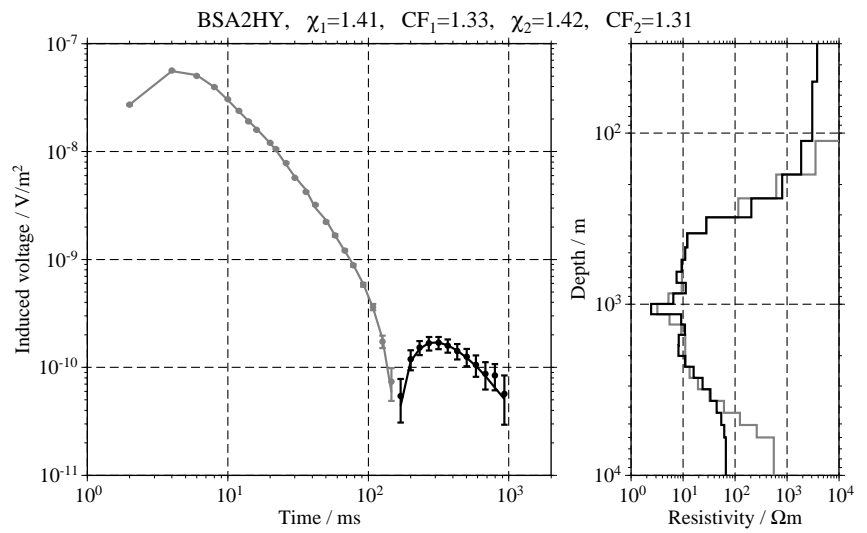
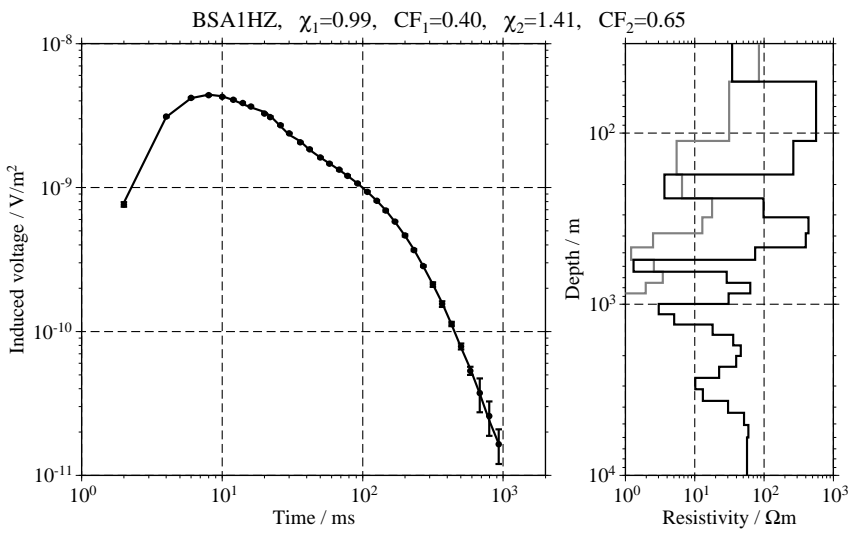
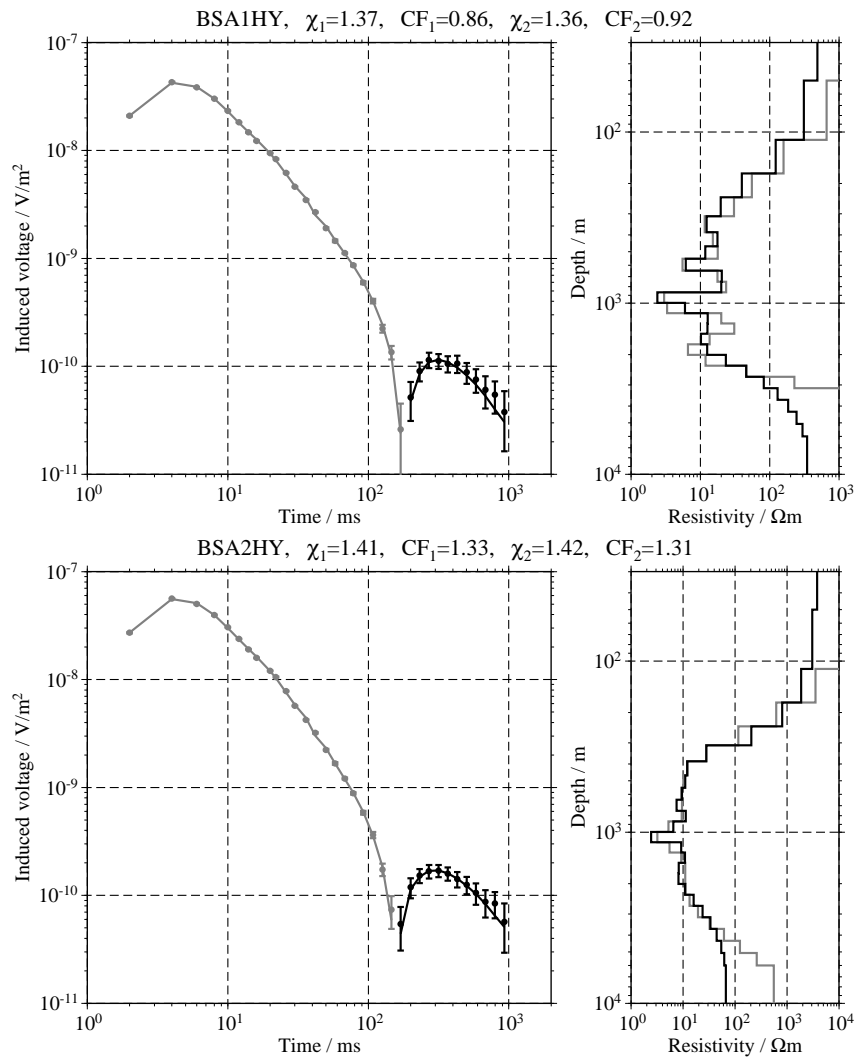
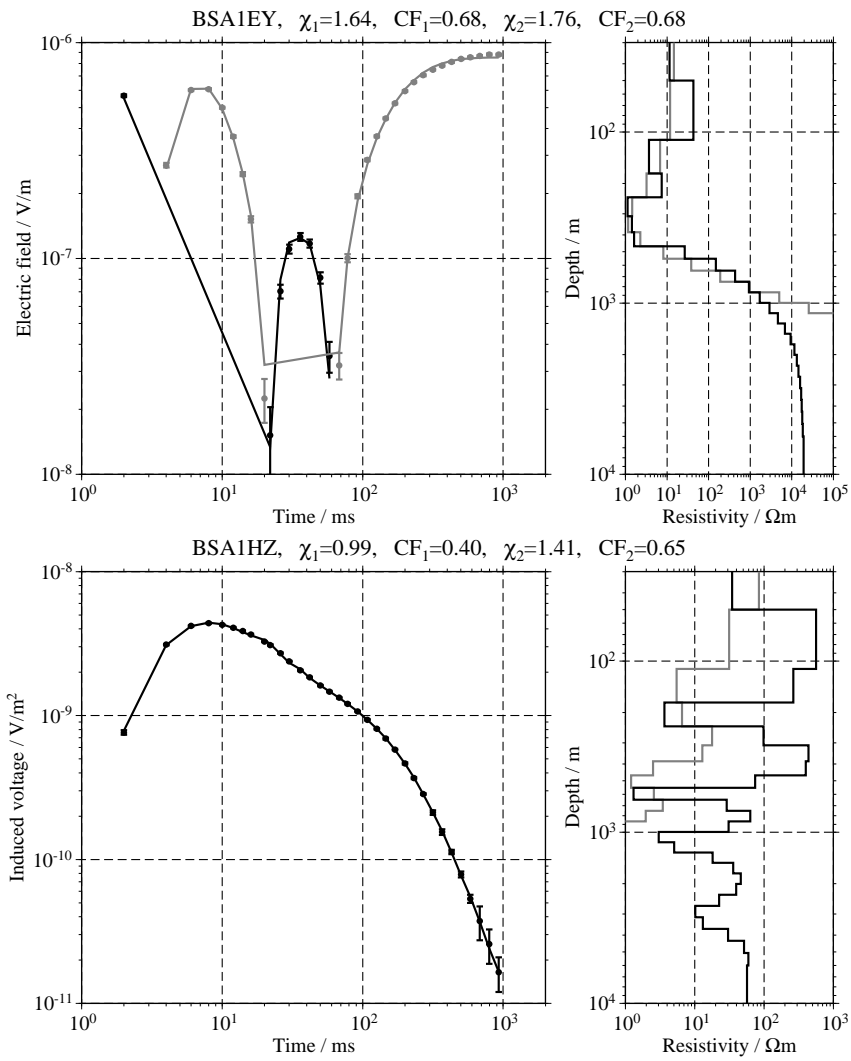


Figure C.10: Single inversion results for the transients measured at BSB;

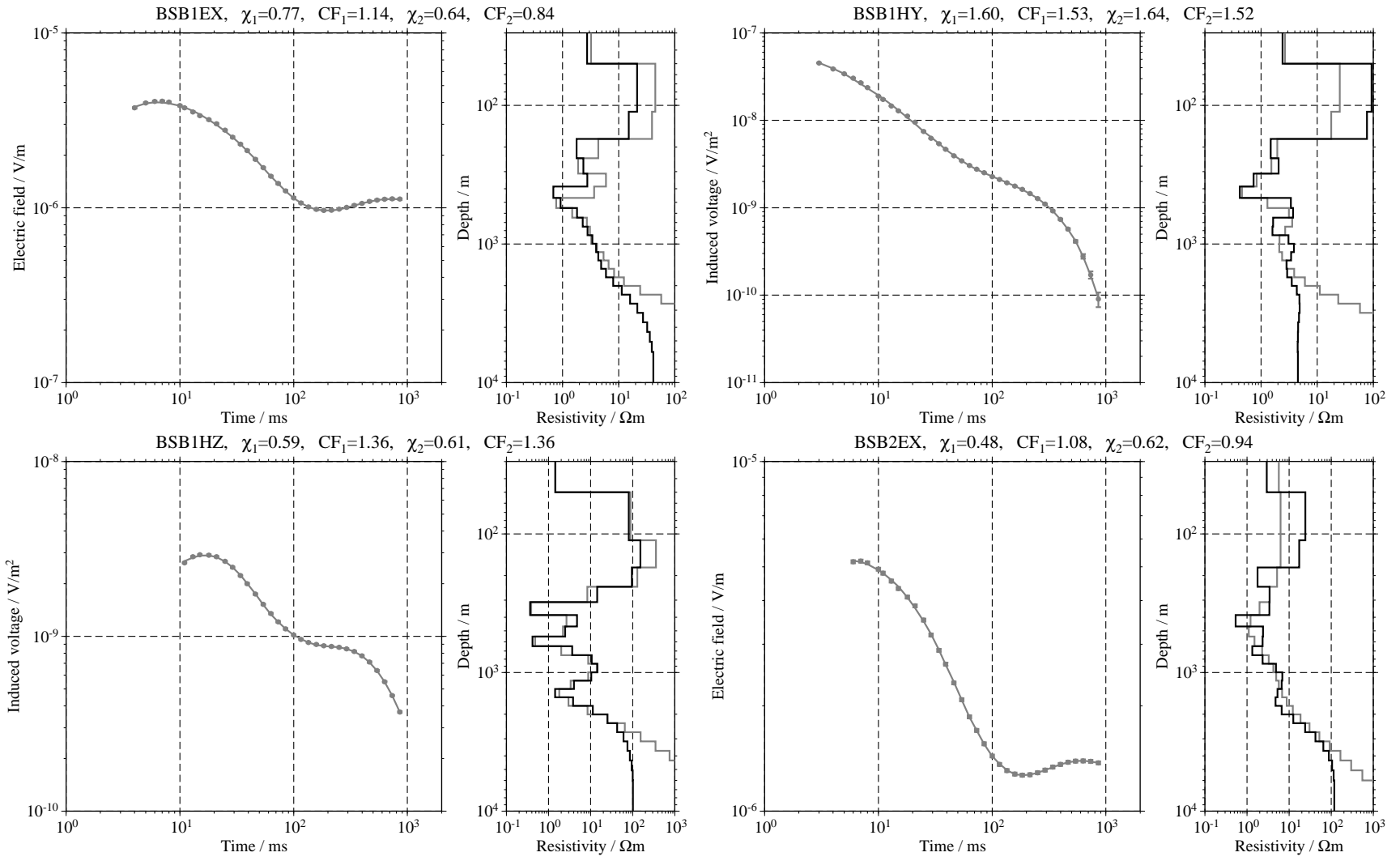


Figure C.11: Single inversion results for the transients measured at BSB and CAA;

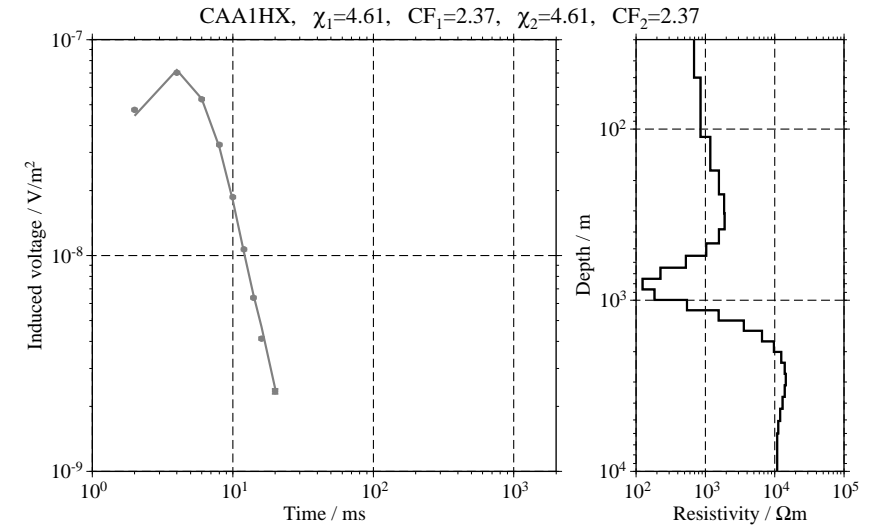
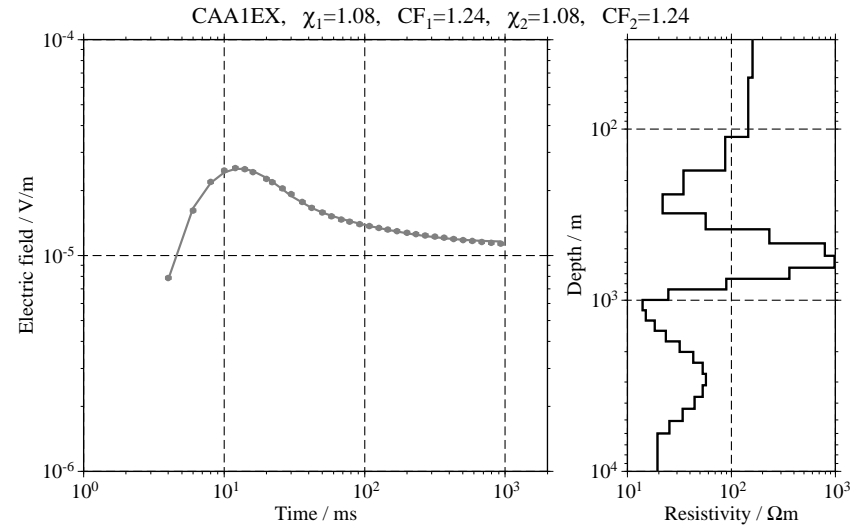
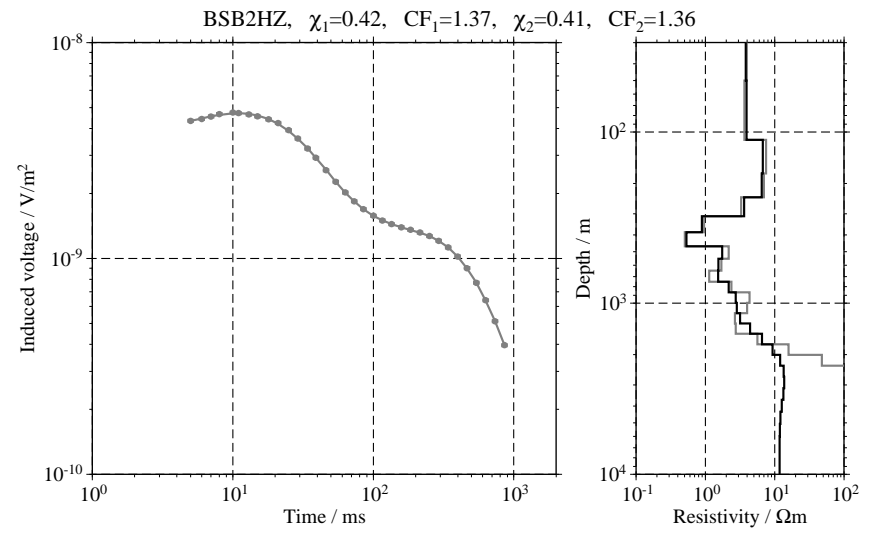
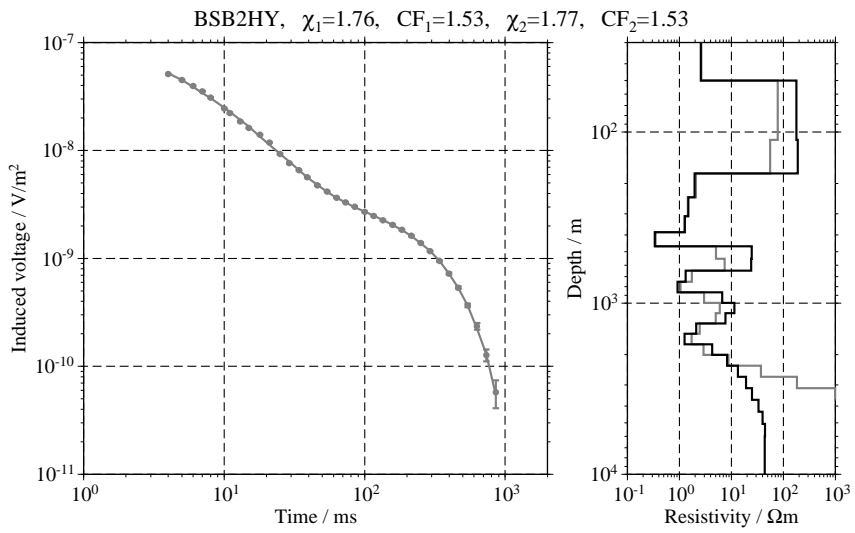


Figure C.12: Single inversion results for the transients measured at CAA, CAB and DVA.

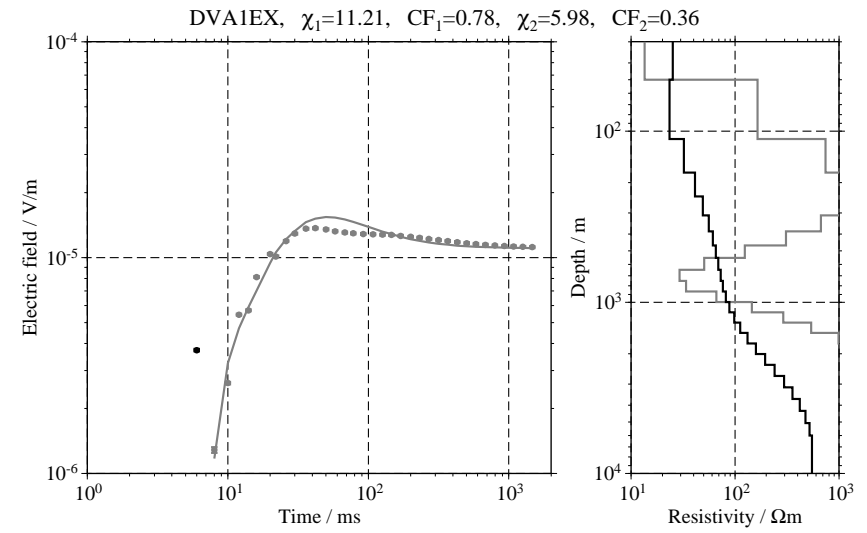
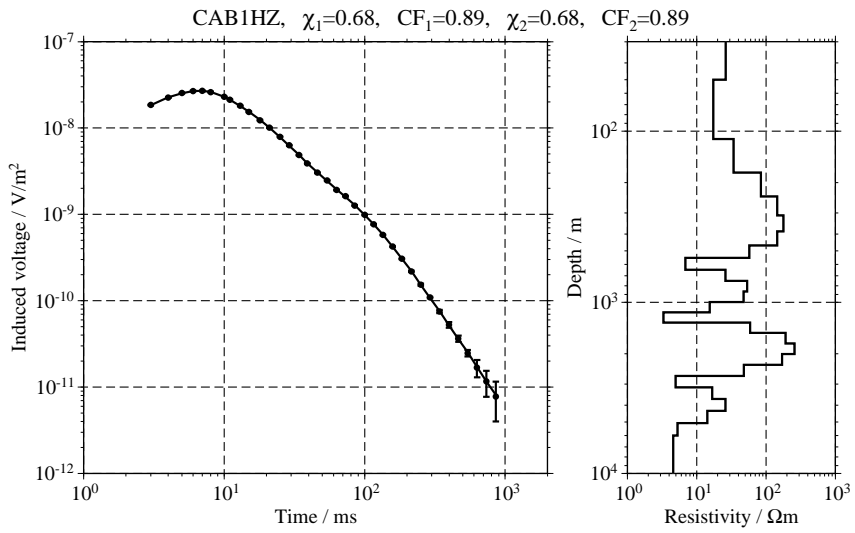
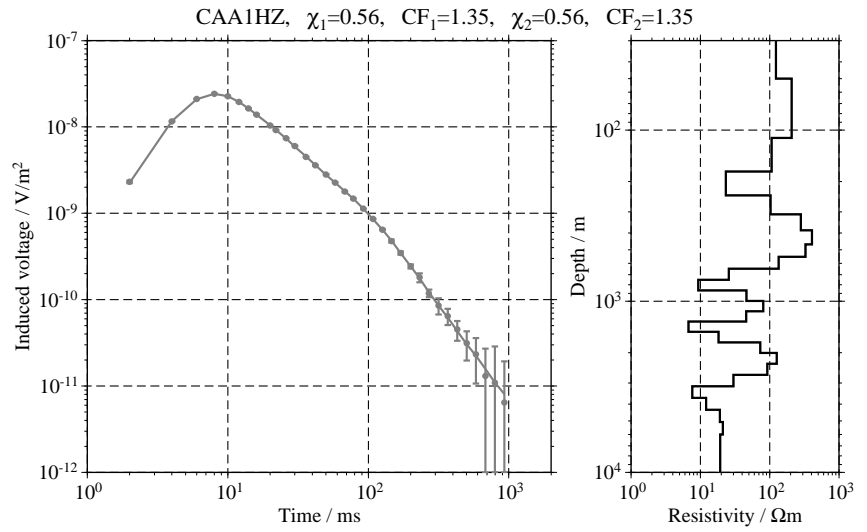
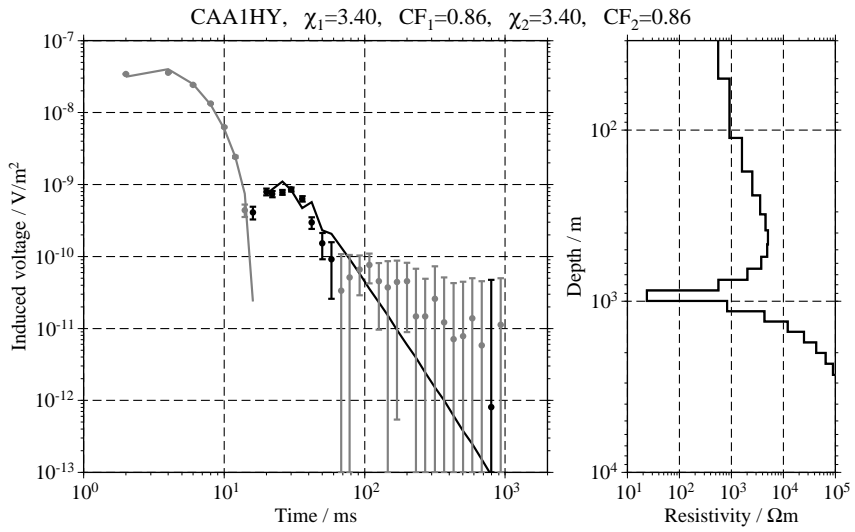


Figure C.13: Single inversion results for the transients measured at DVA.

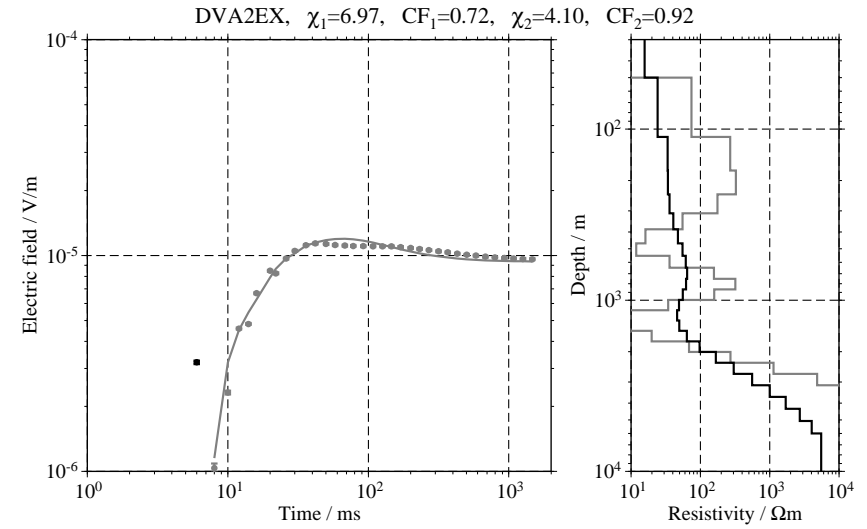
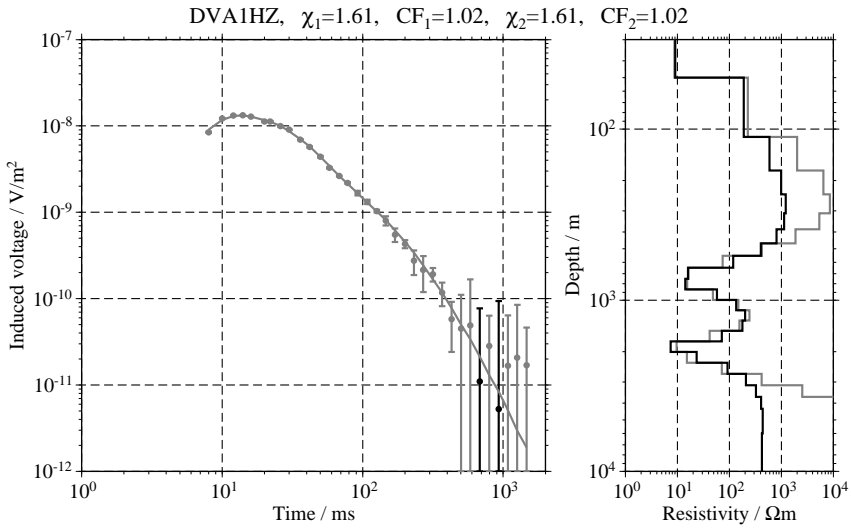
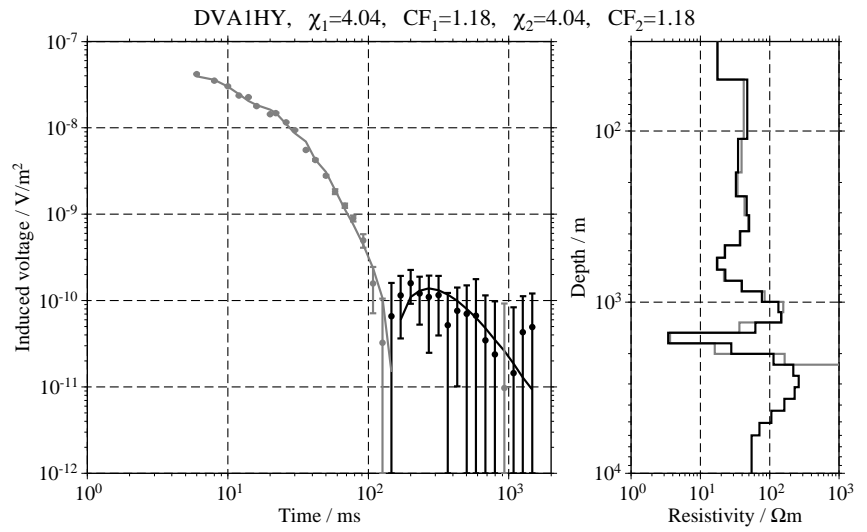
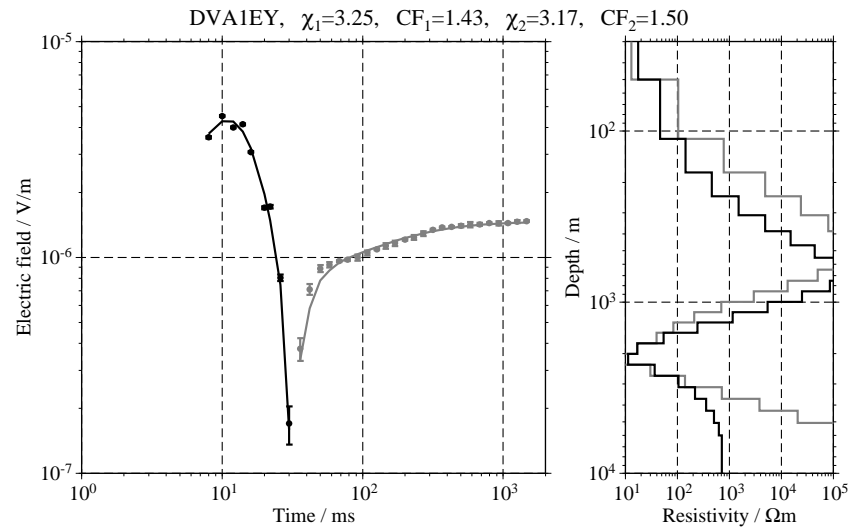
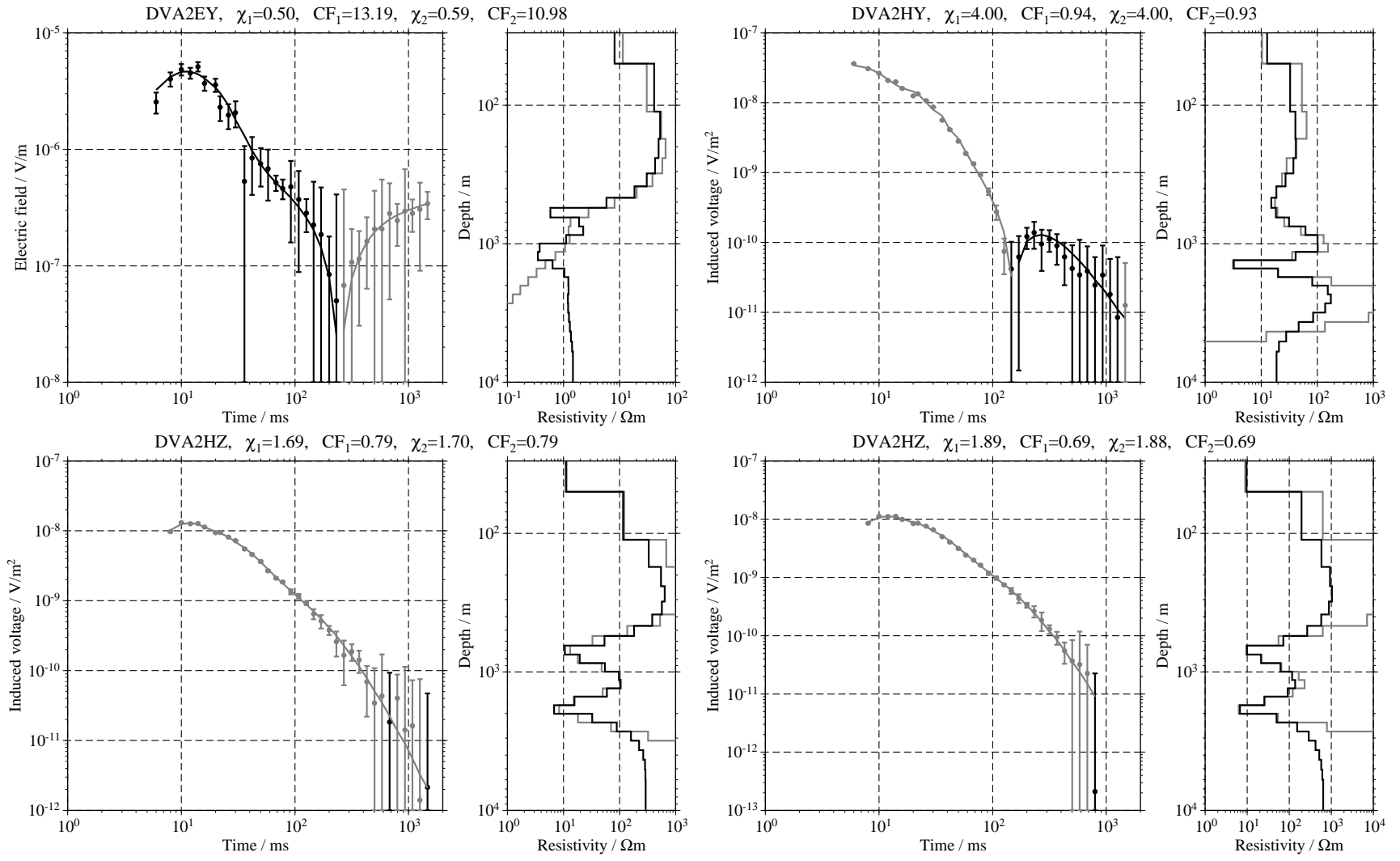


Figure C.14: Single inversion results for the transients measured at DVA;



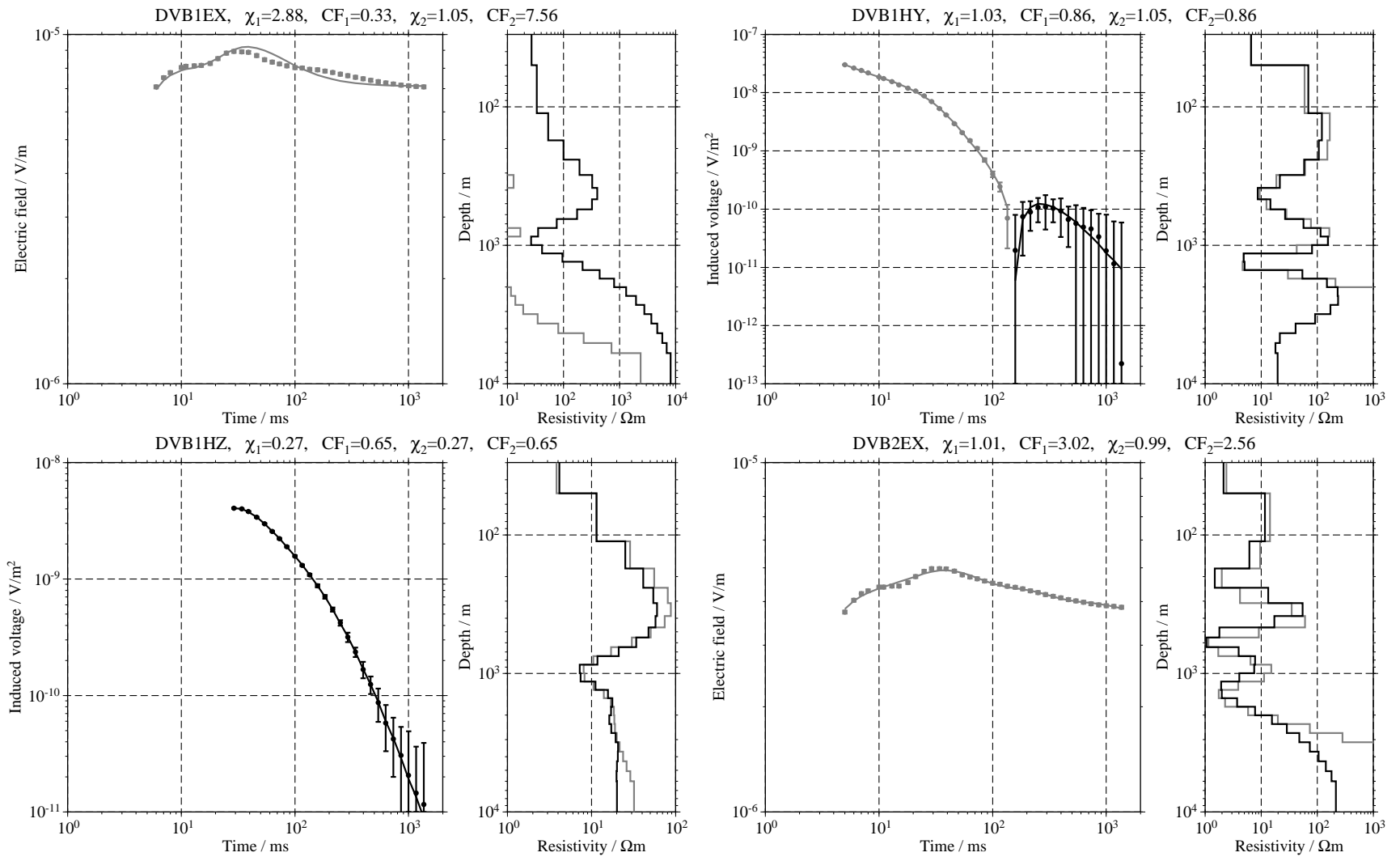
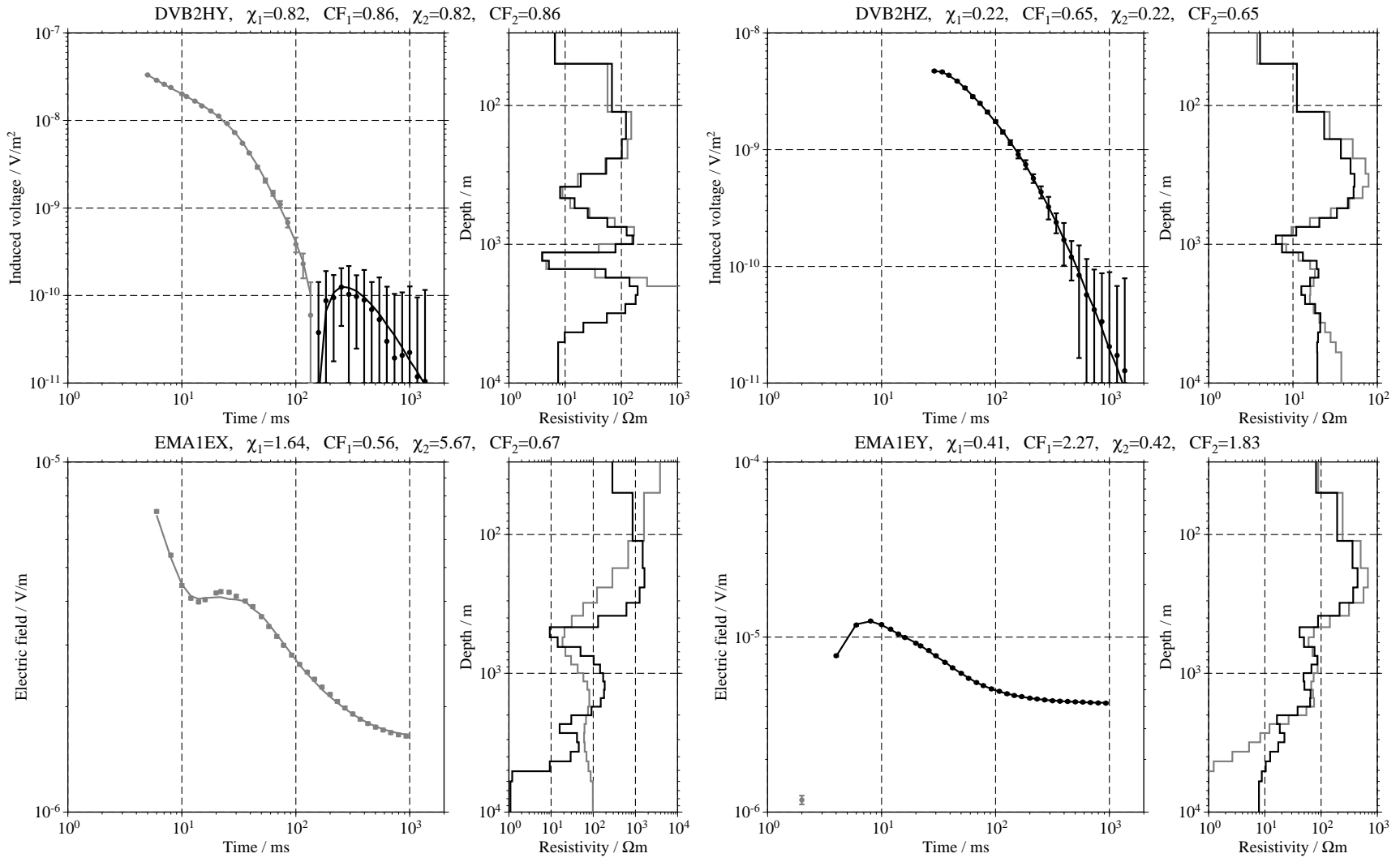


Figure C.15: Single inversion results for the transients measured at DVB;

Figure C.16: Single inversion results for the transients measured at DVB and EMA.



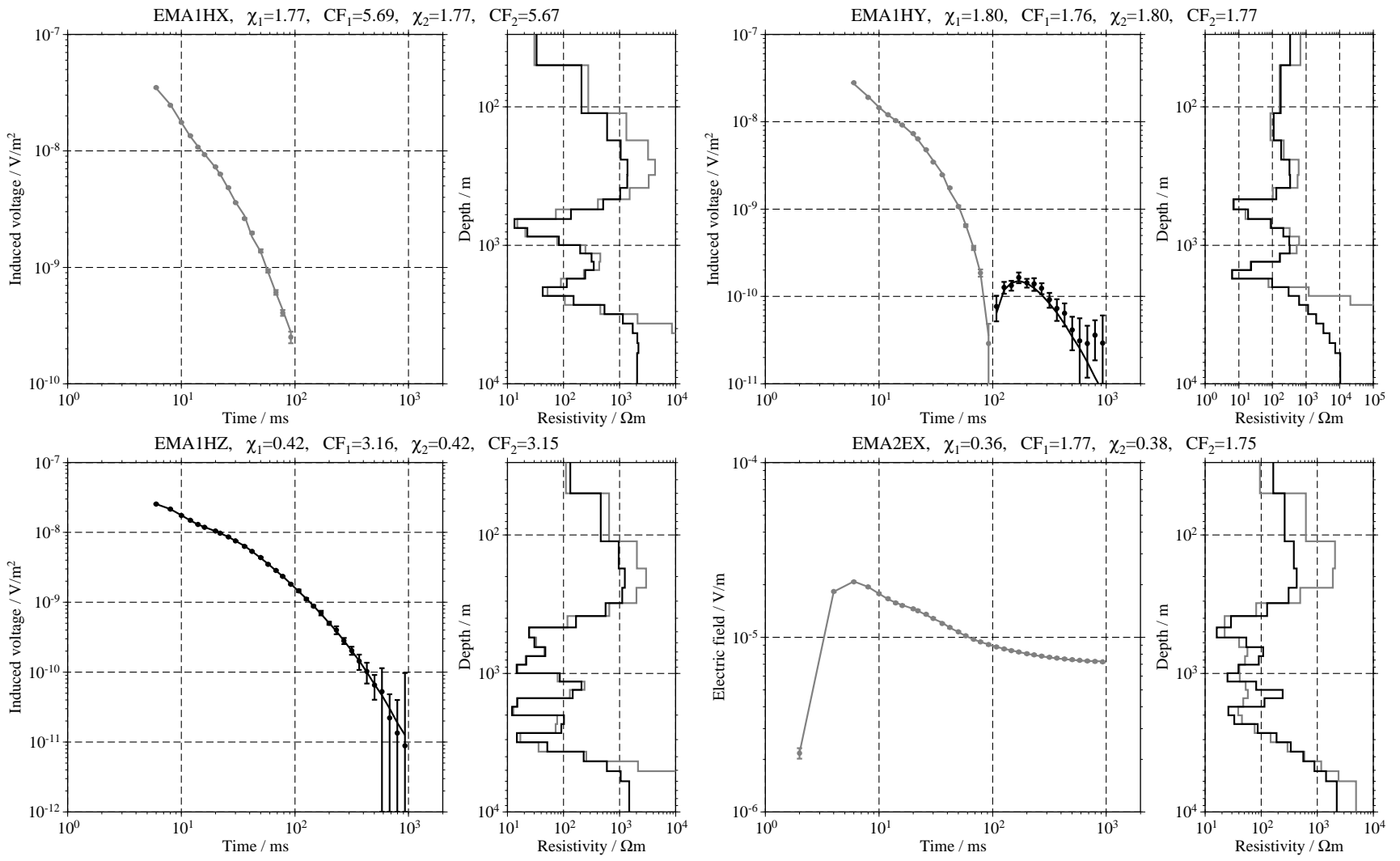


Figure C.17: Single inversion results for the transients measured at EMA;

Figure C.18: Single inversion results for the transients measured at EMA;

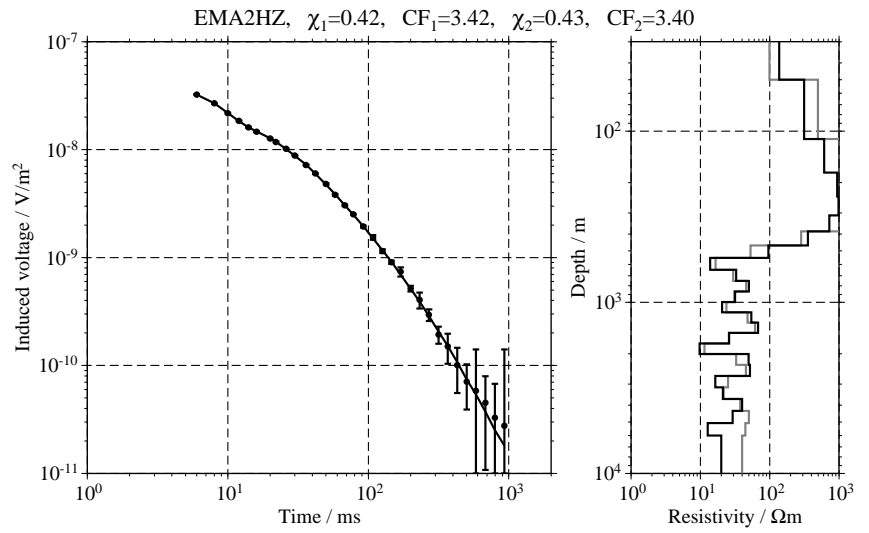
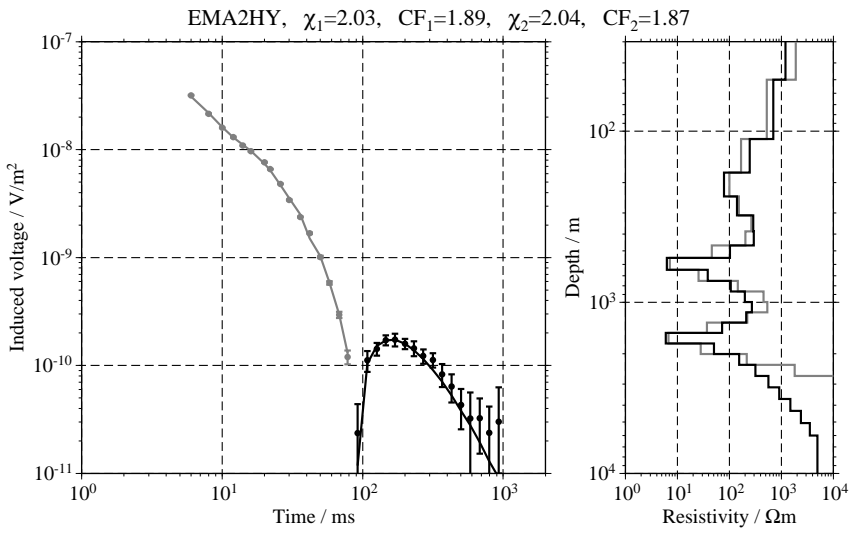
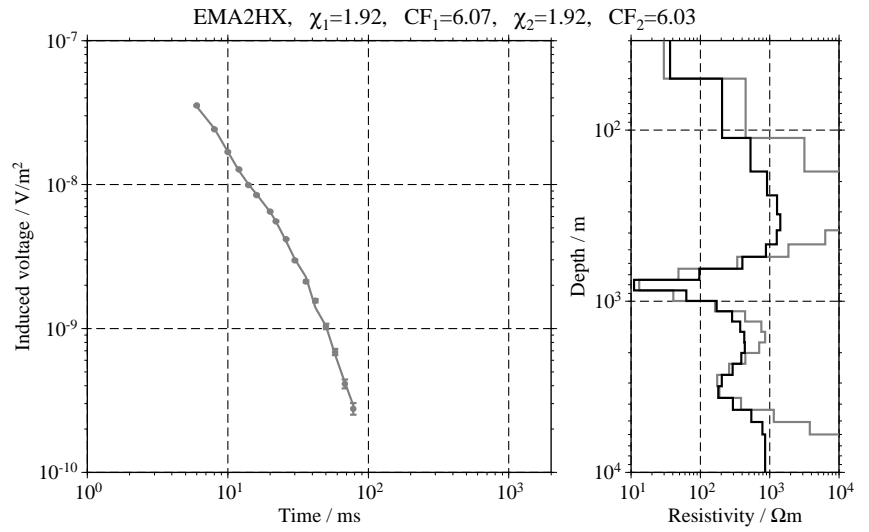
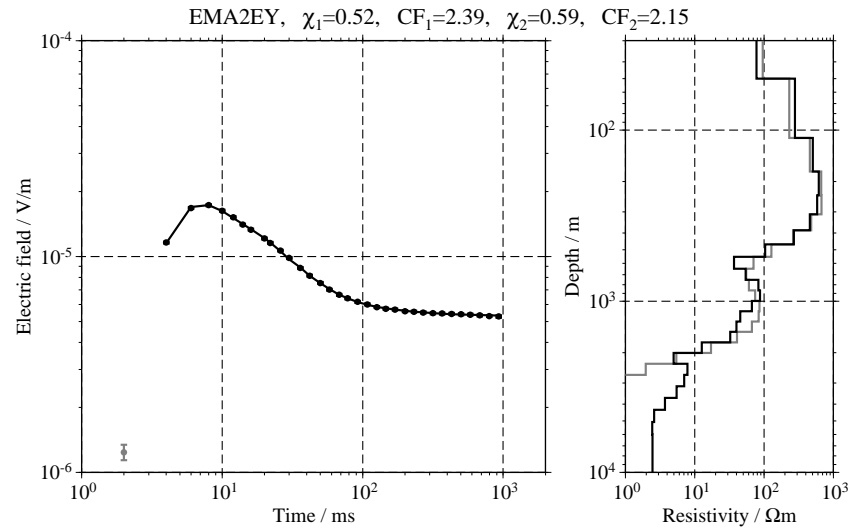


Figure C.19: Single inversion results for the transients measured at ENA;

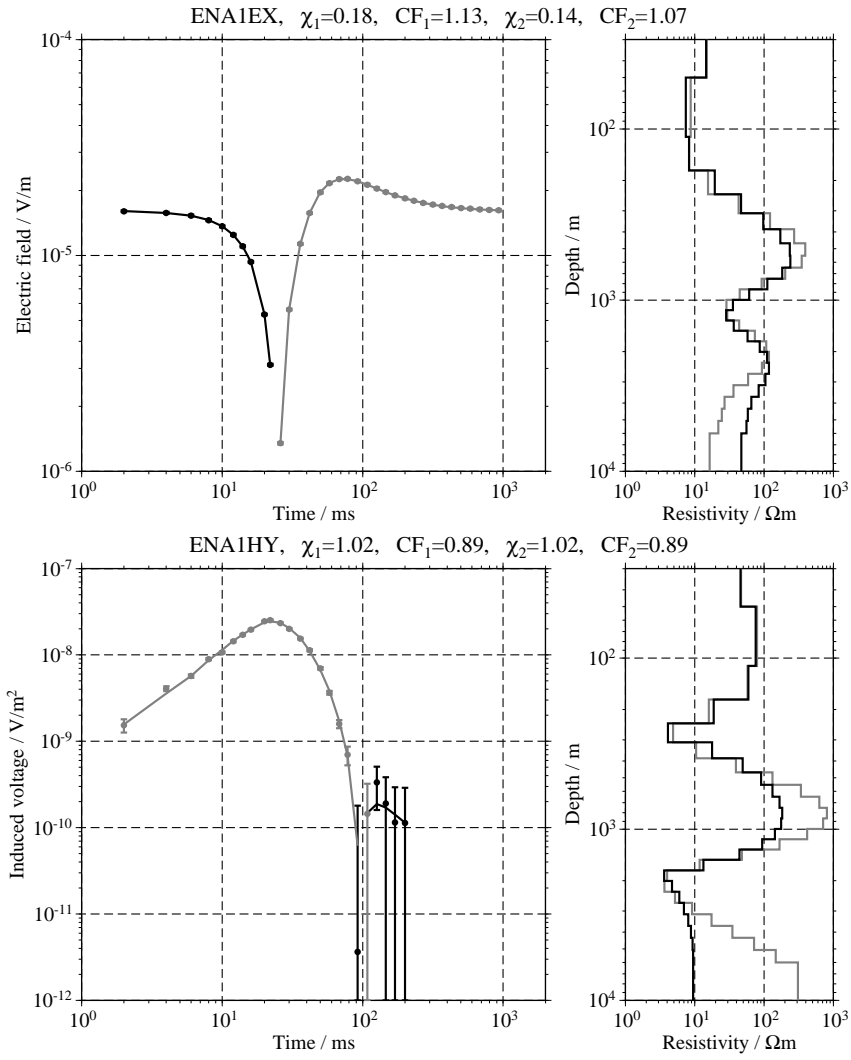


Figure C.20: Single inversion results for the transients measured at ENA and ENB;

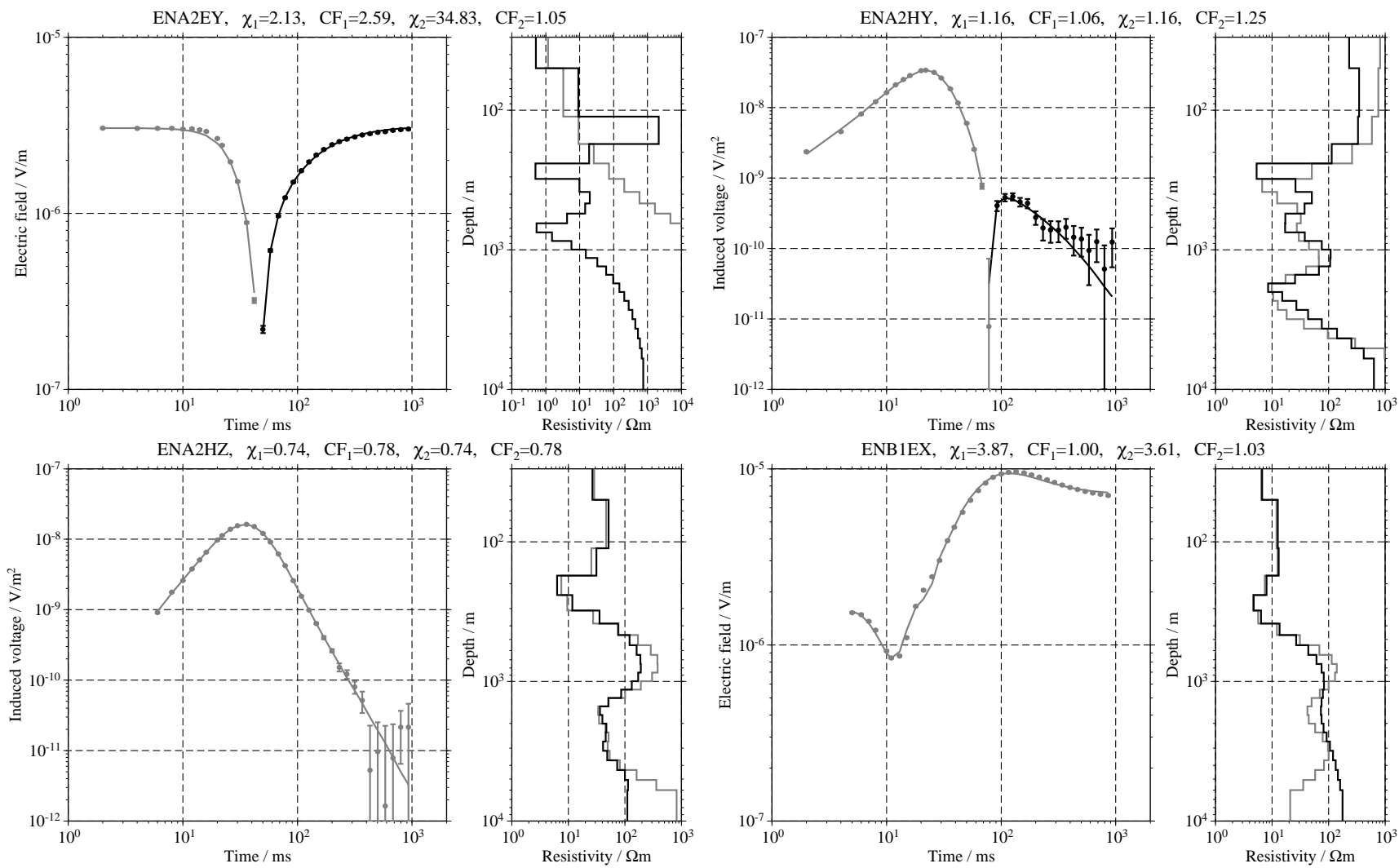


Figure C.21: Single inversion results for the transients measured at ENB;

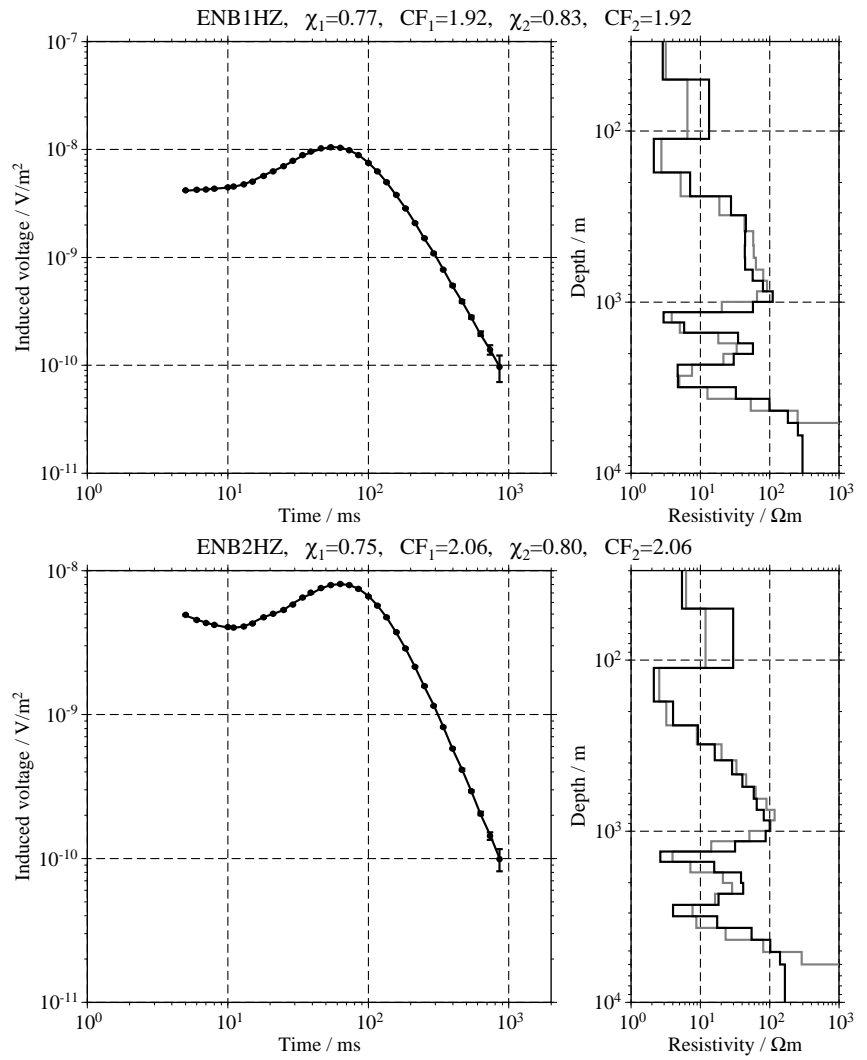
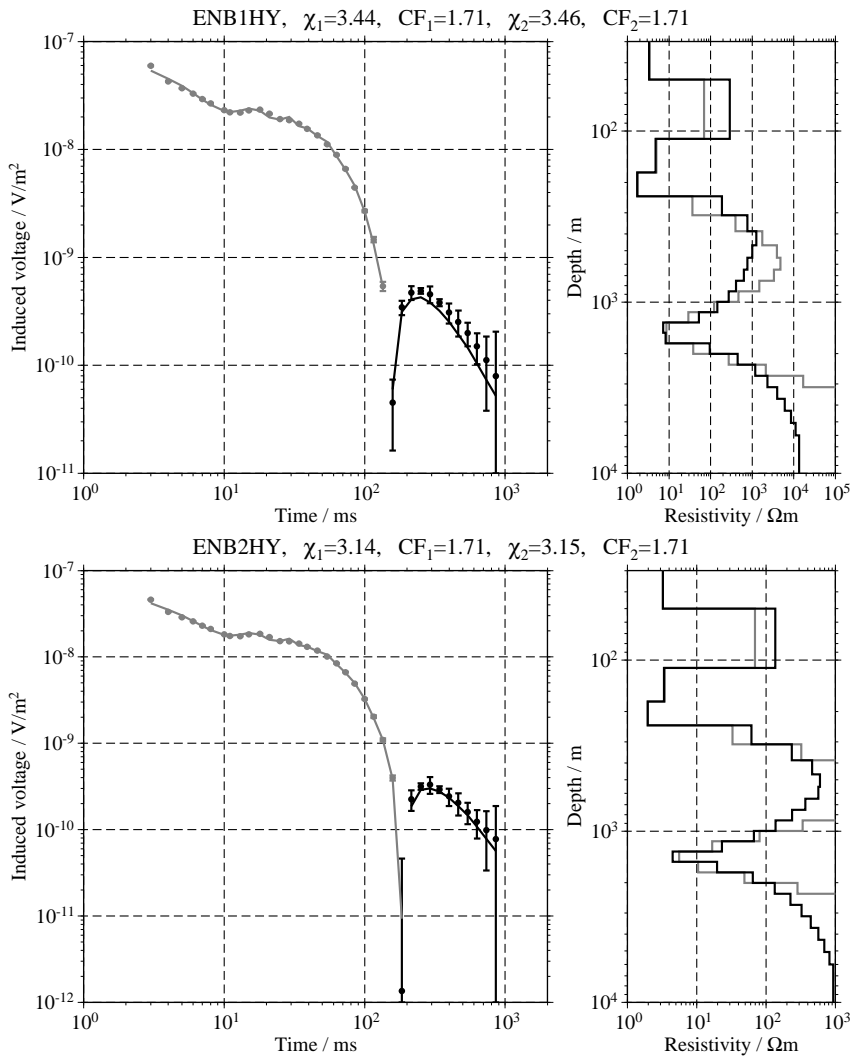
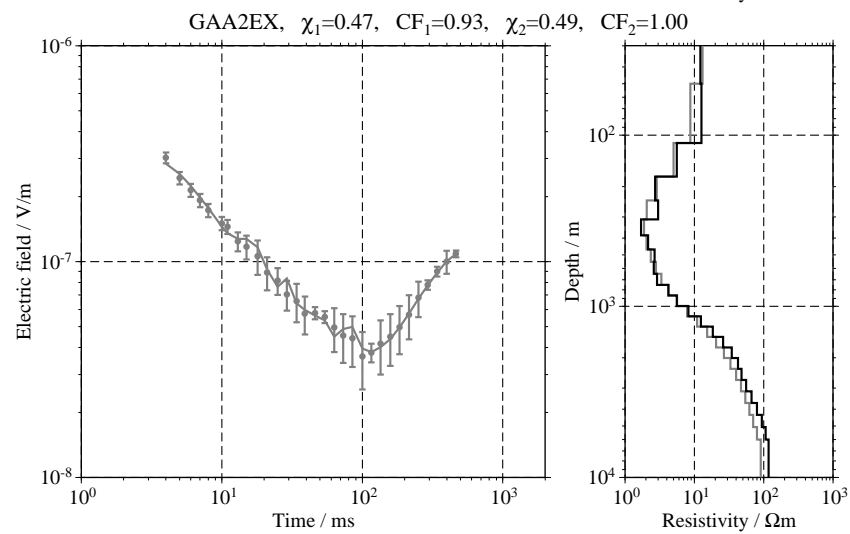
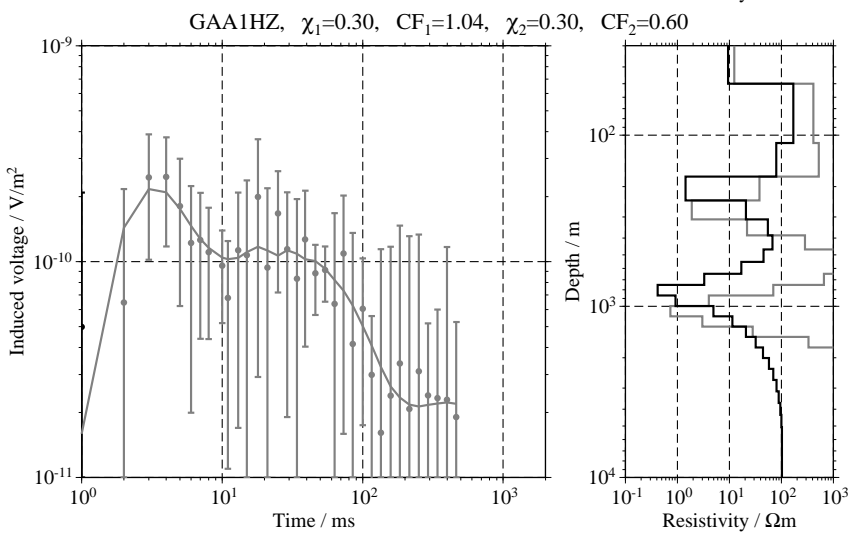
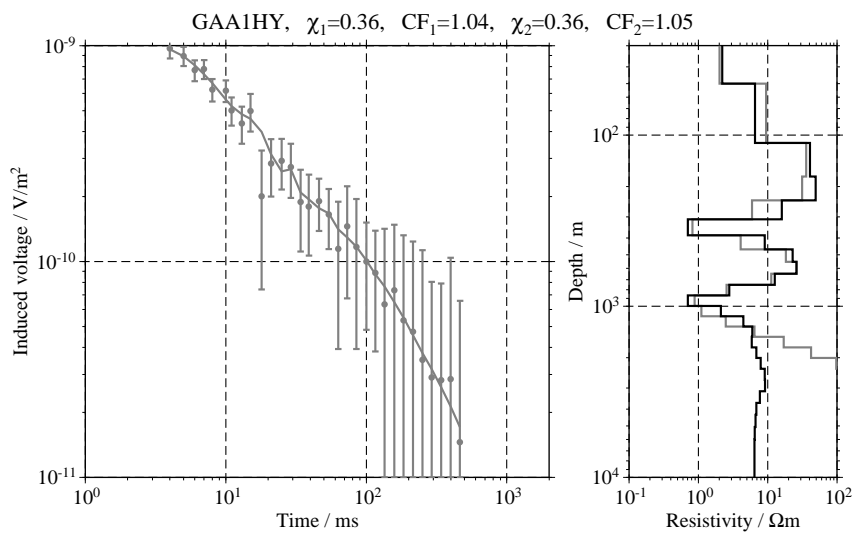
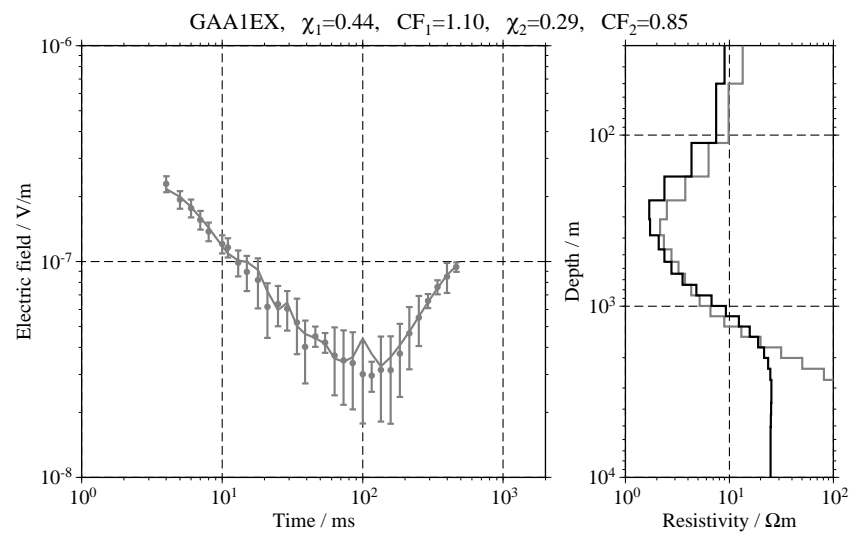


Figure C.22: Single inversion results for the transients measured at GAA;



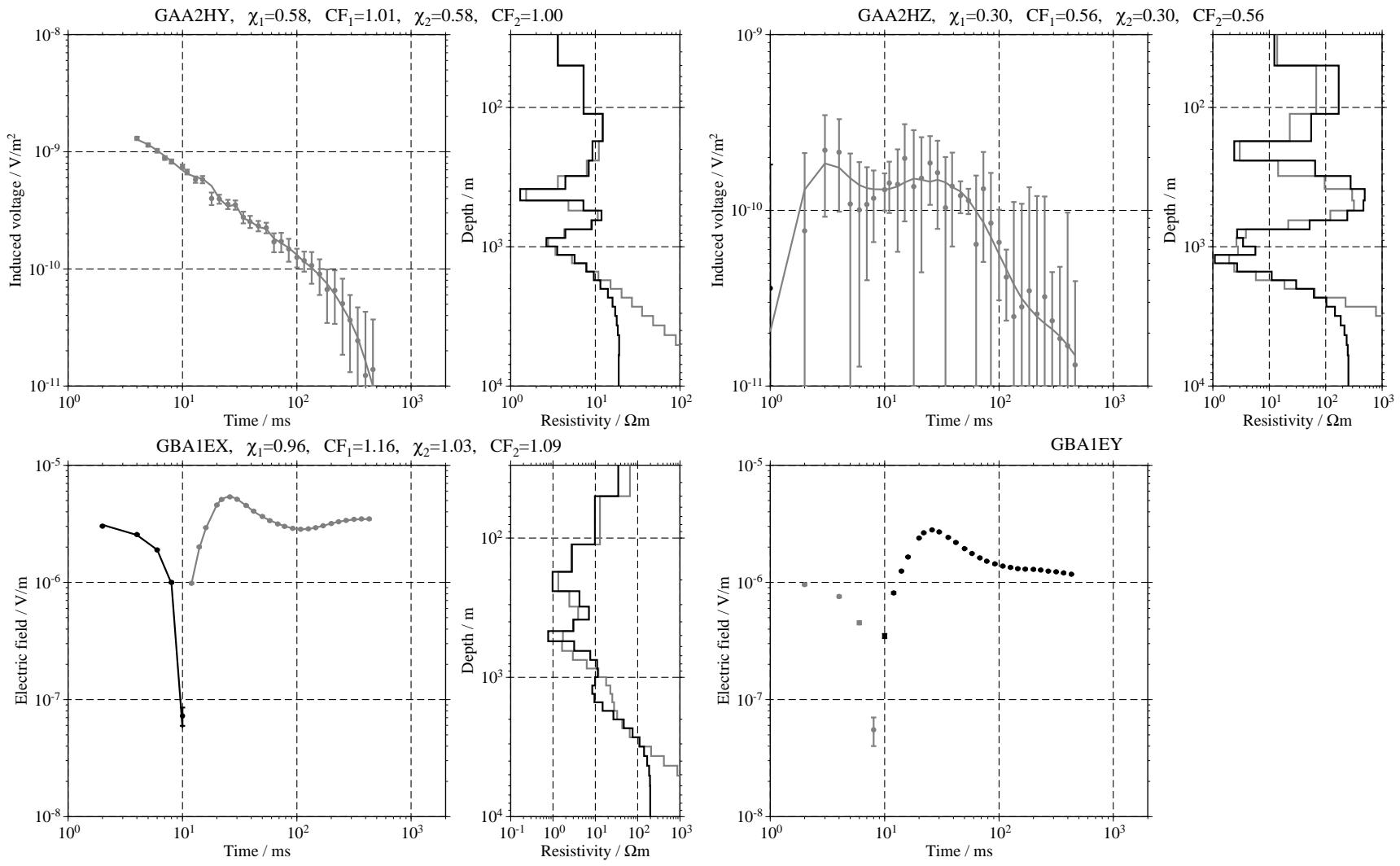
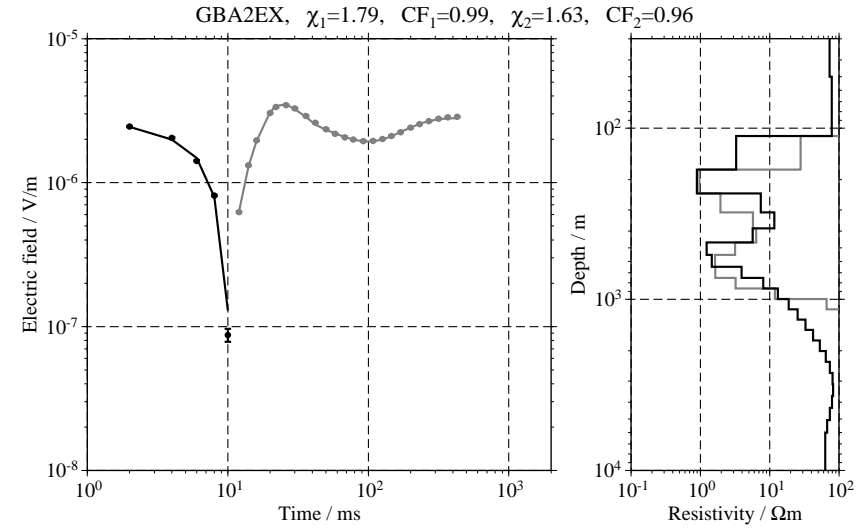
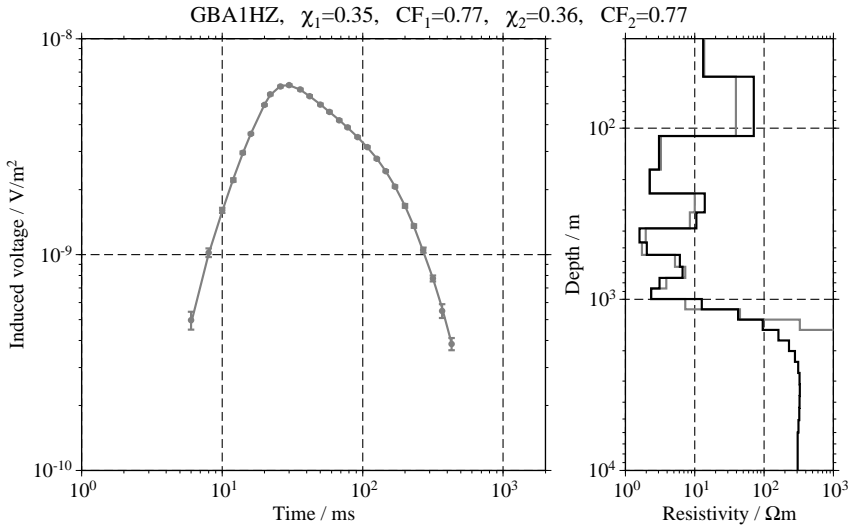
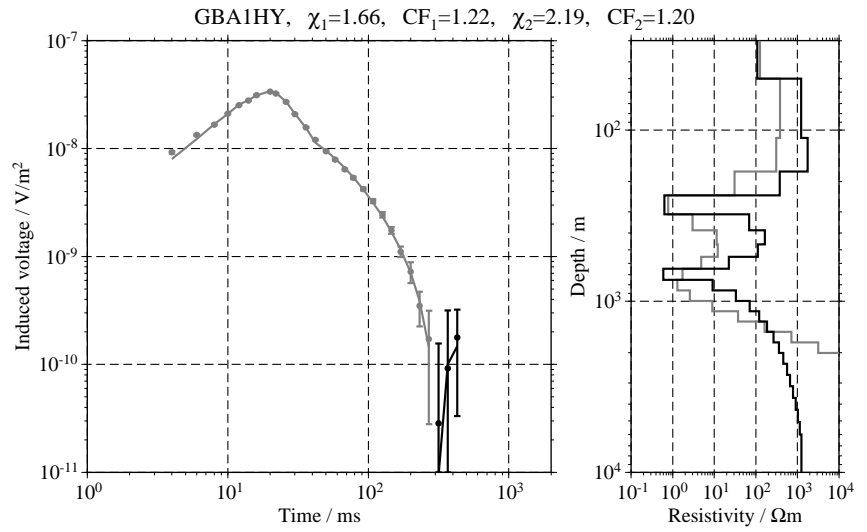
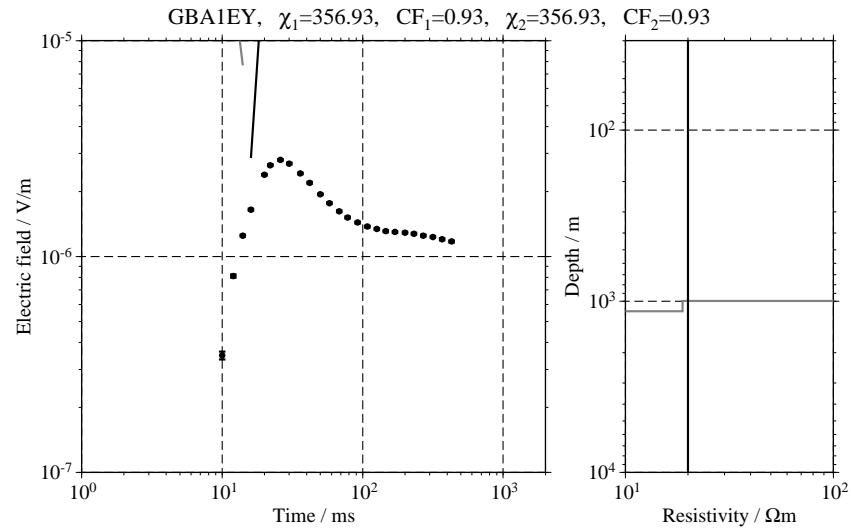


Figure C.23: Single inversion results for the transients measured at GAA and GBA;

Figure C.24: Single inversion results for the transients measured at GBA;



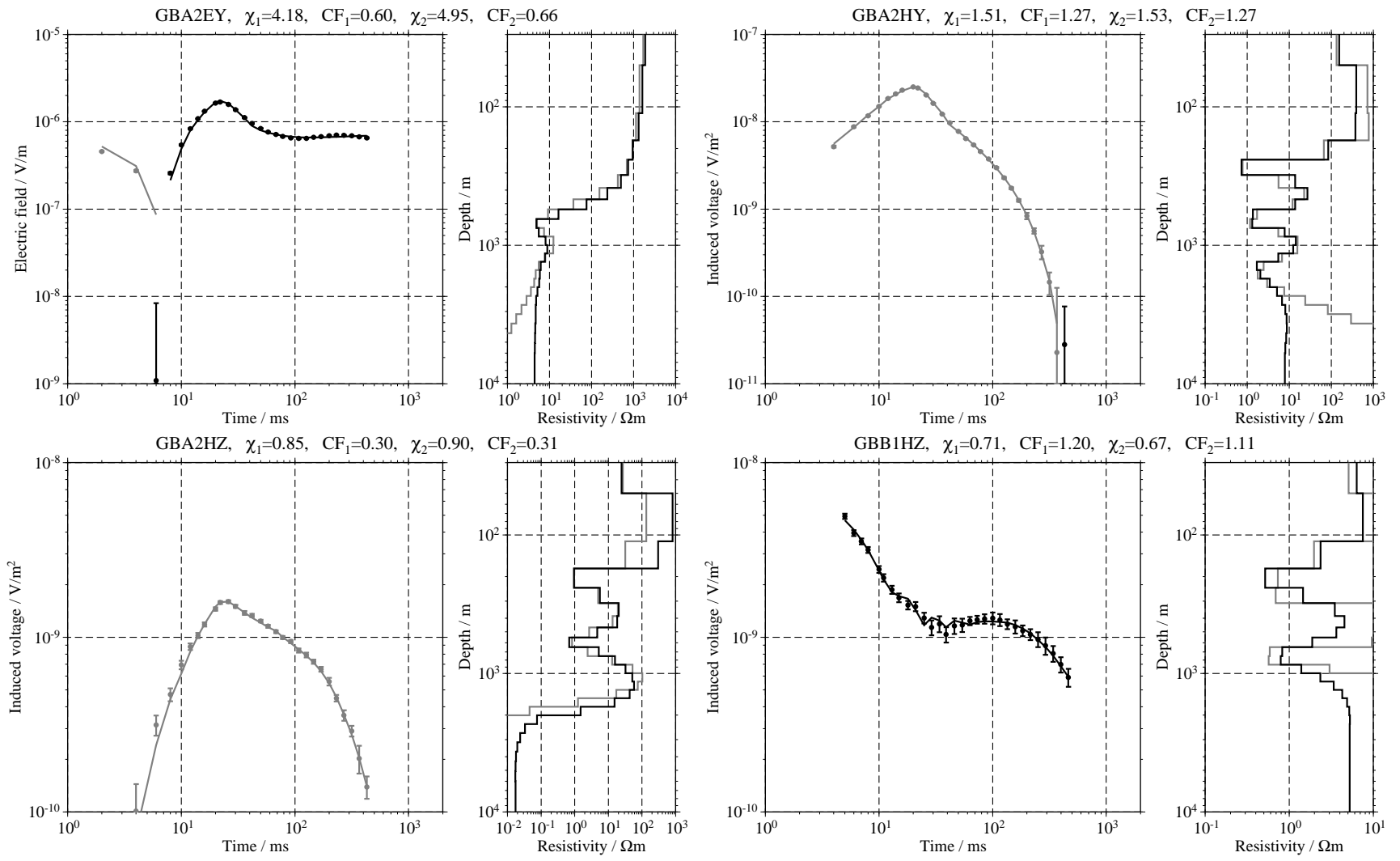
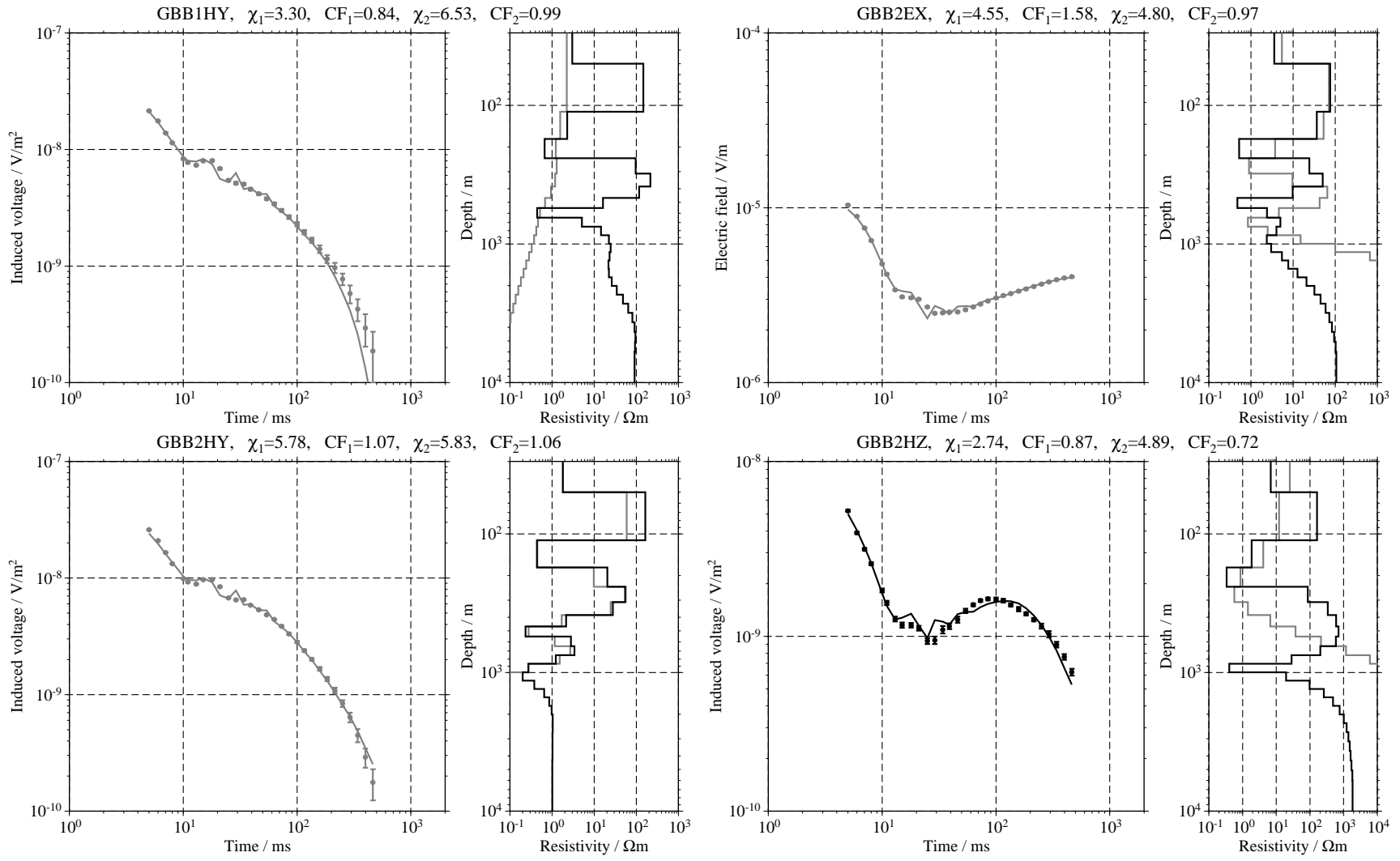


Figure C.25: Single inversion results for the transients measured at GBA and GBB;

Figure C.26: Single inversion results for the transients measured at GBB;



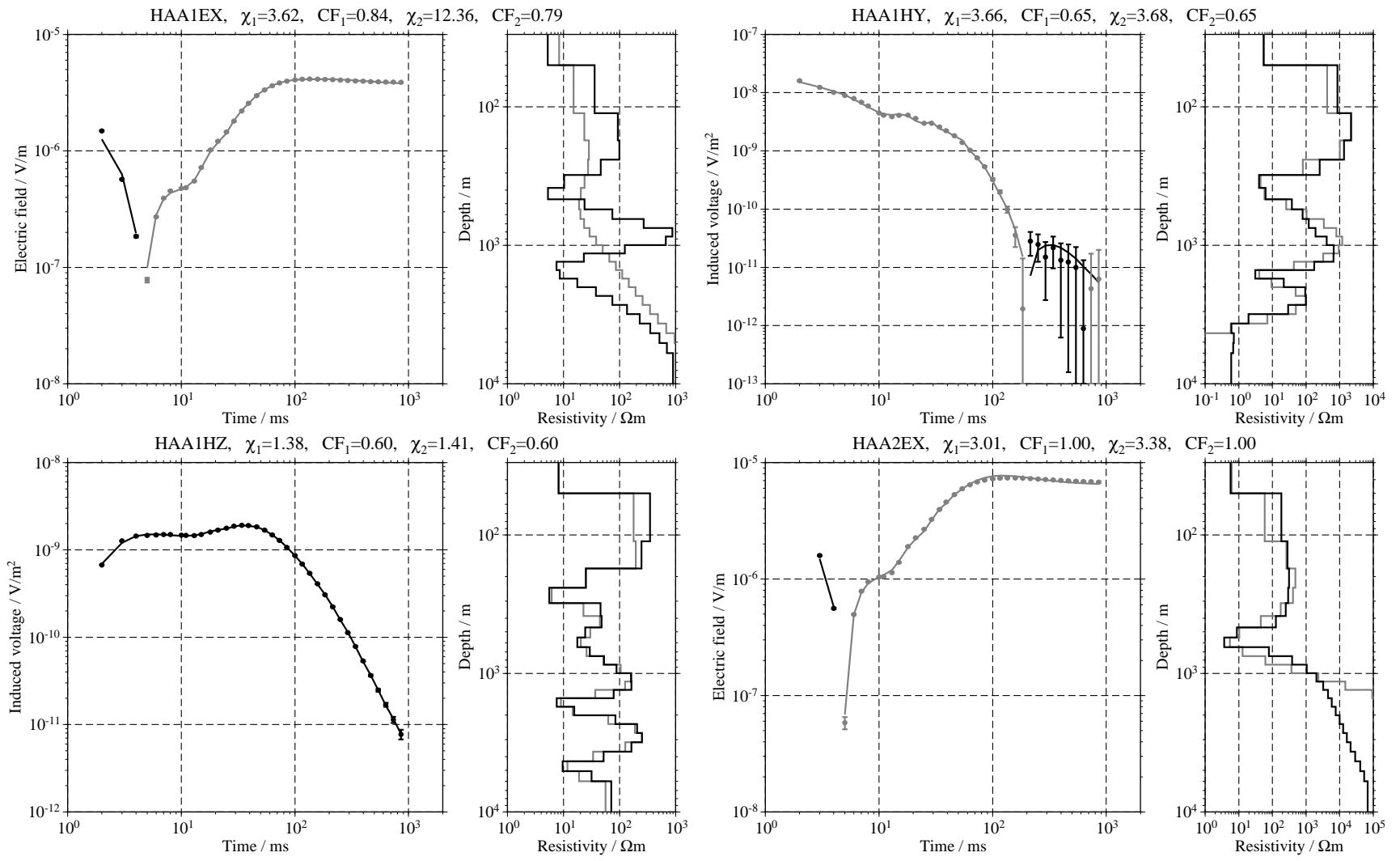


Figure C.27: Single inversion results for the transients measured at HAA;

Figure C.28: Single inversion results for the transients measured at HAA and HAB;

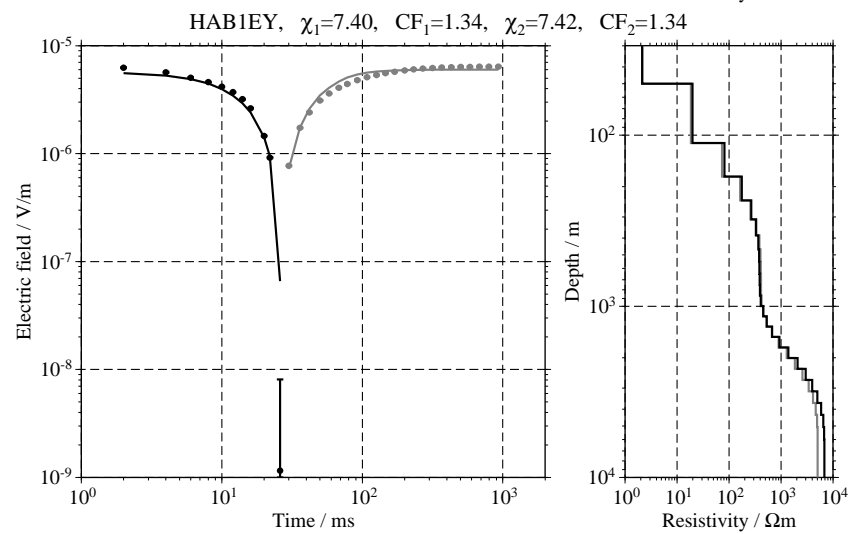
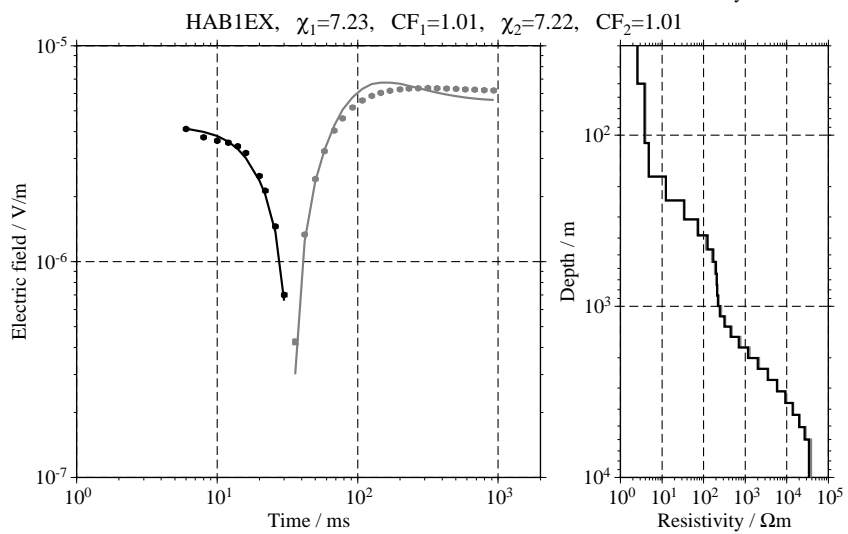
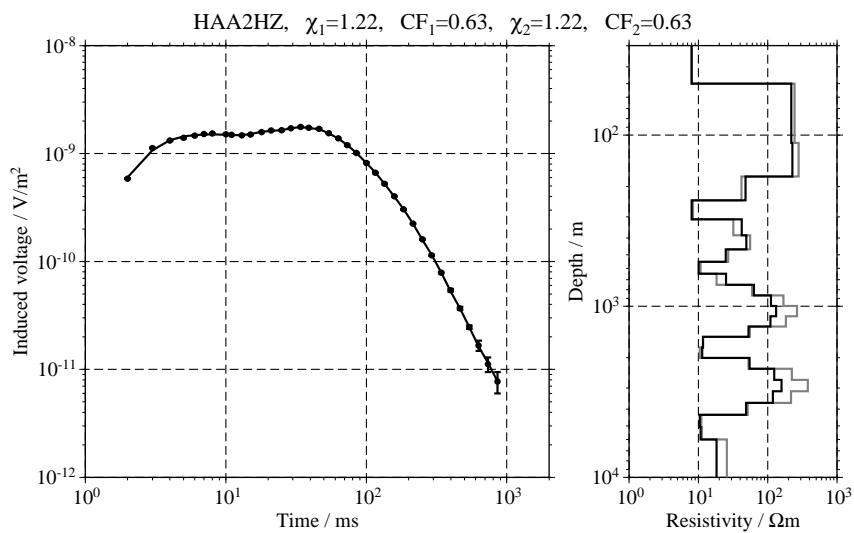
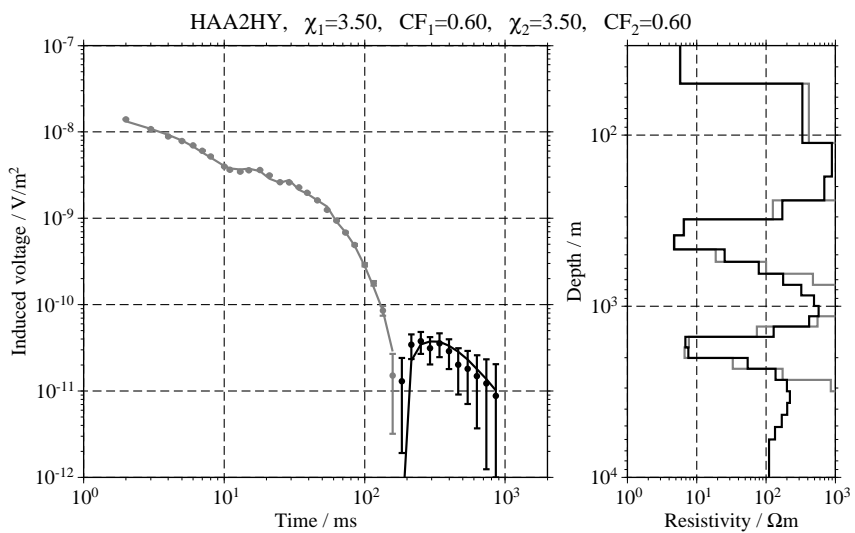
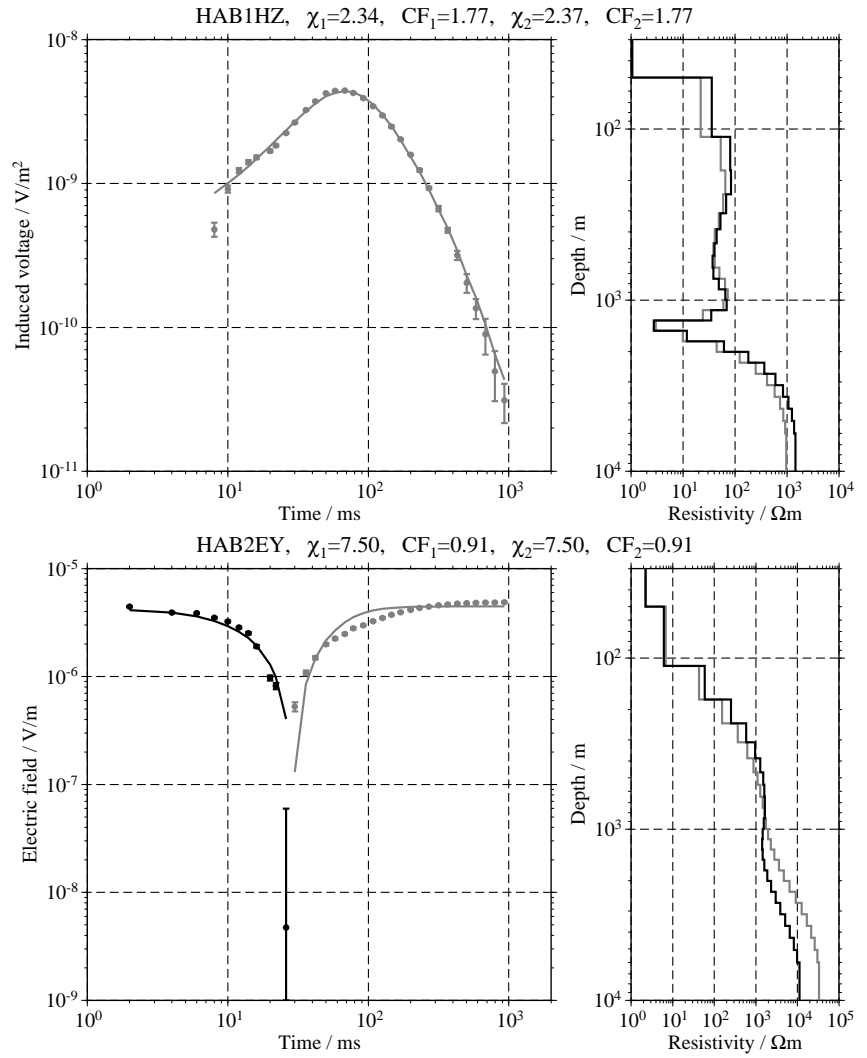
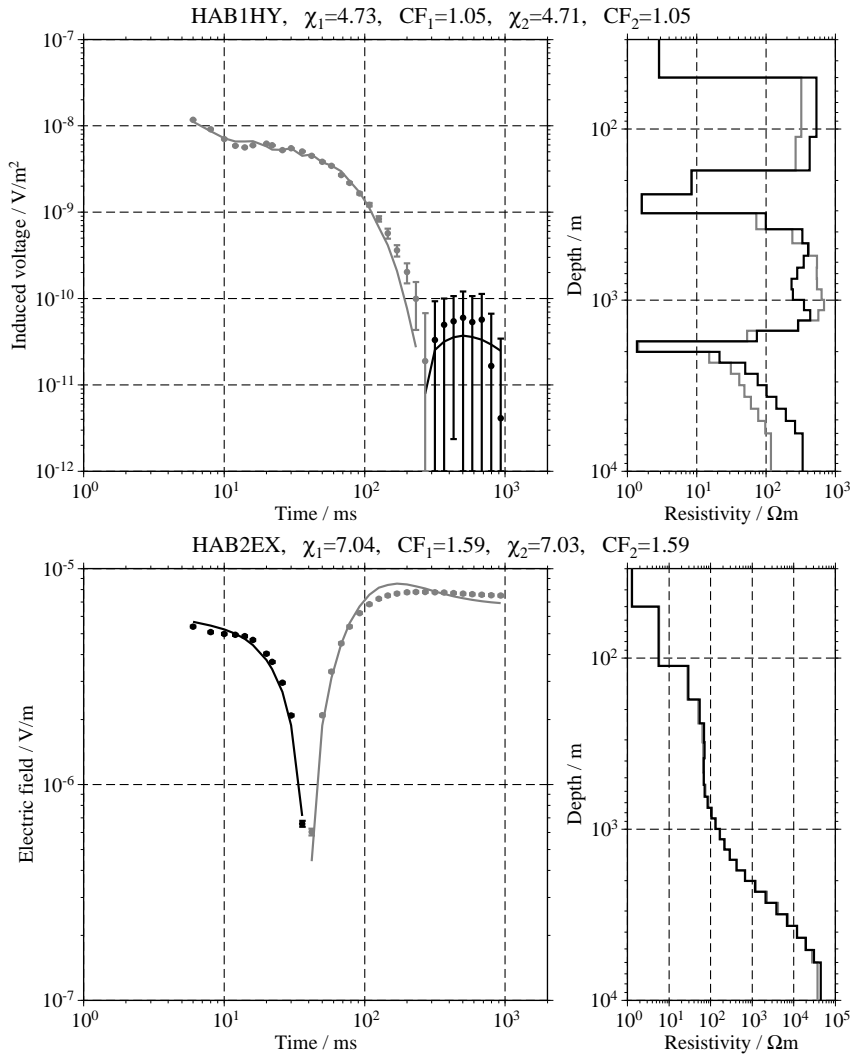


Figure C.29: Single inversion results for the transients measured at HAB;



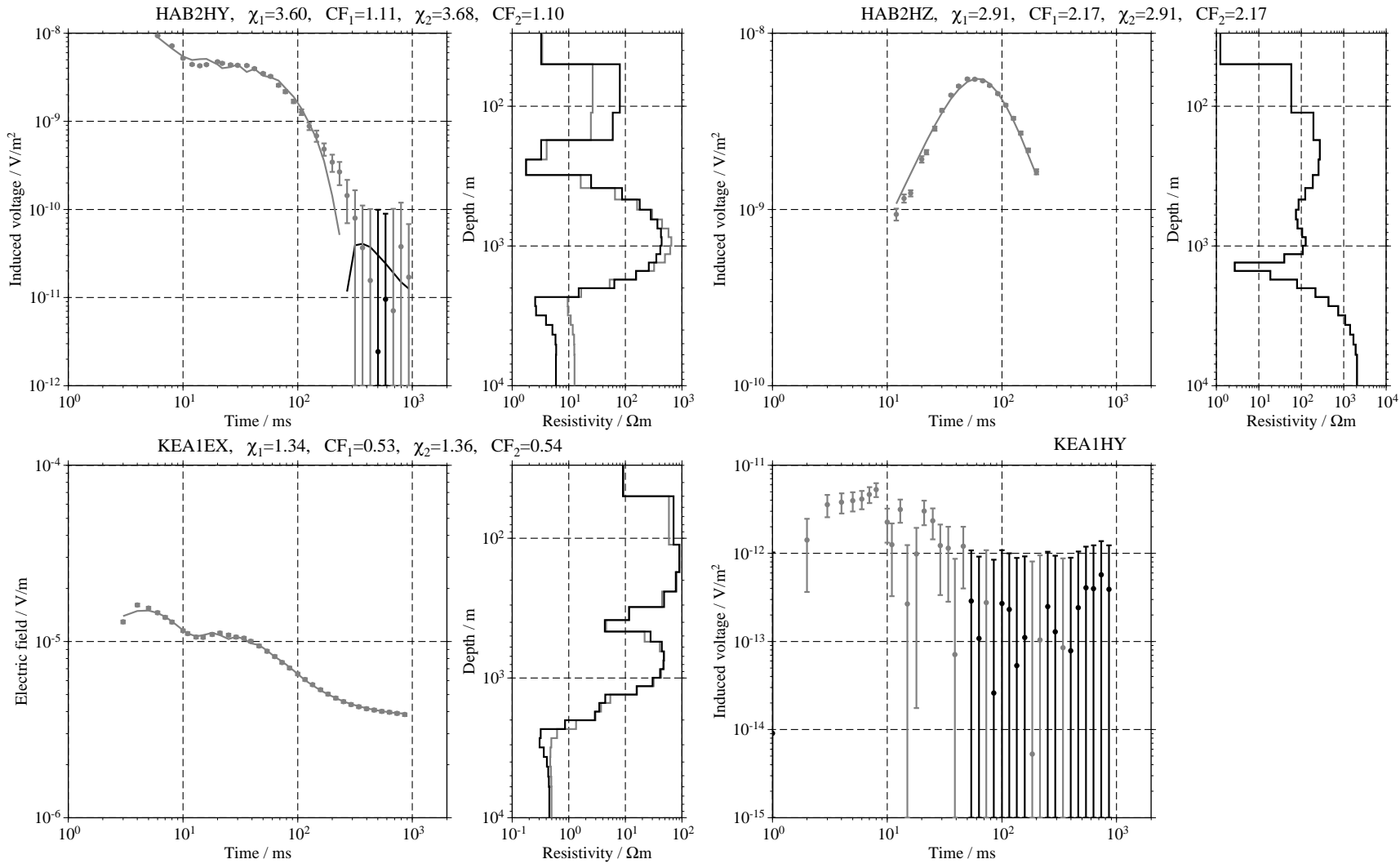
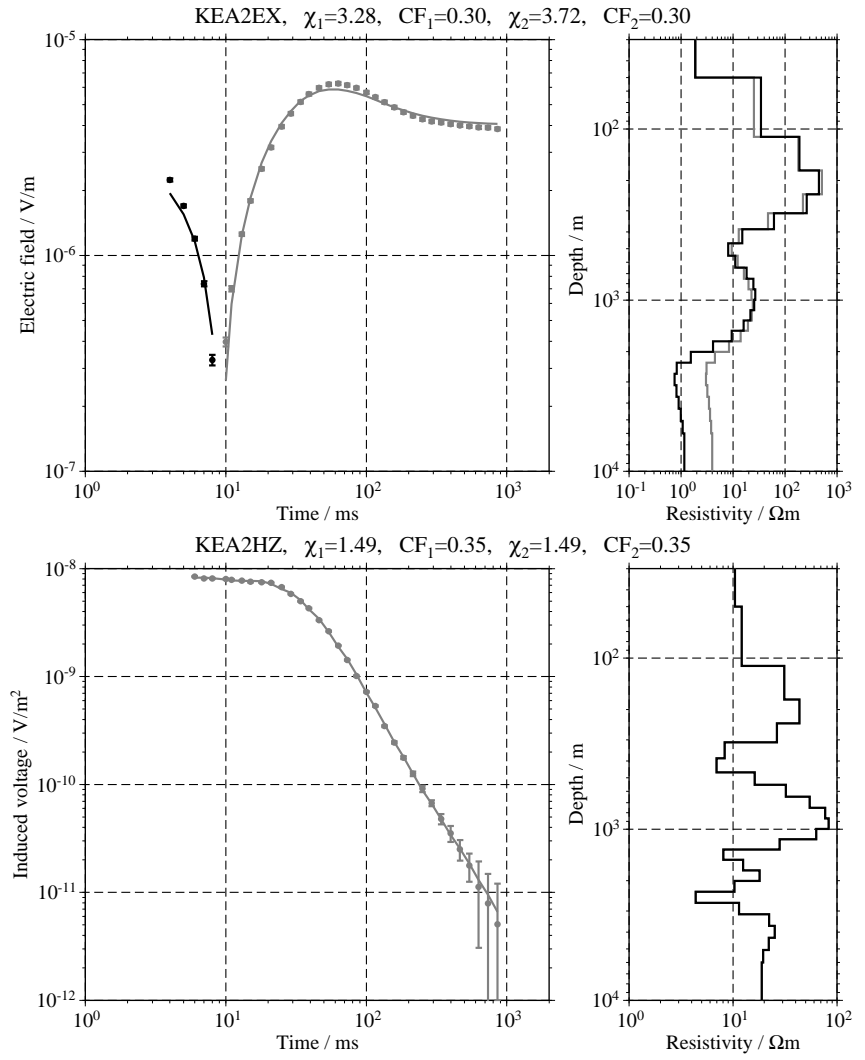
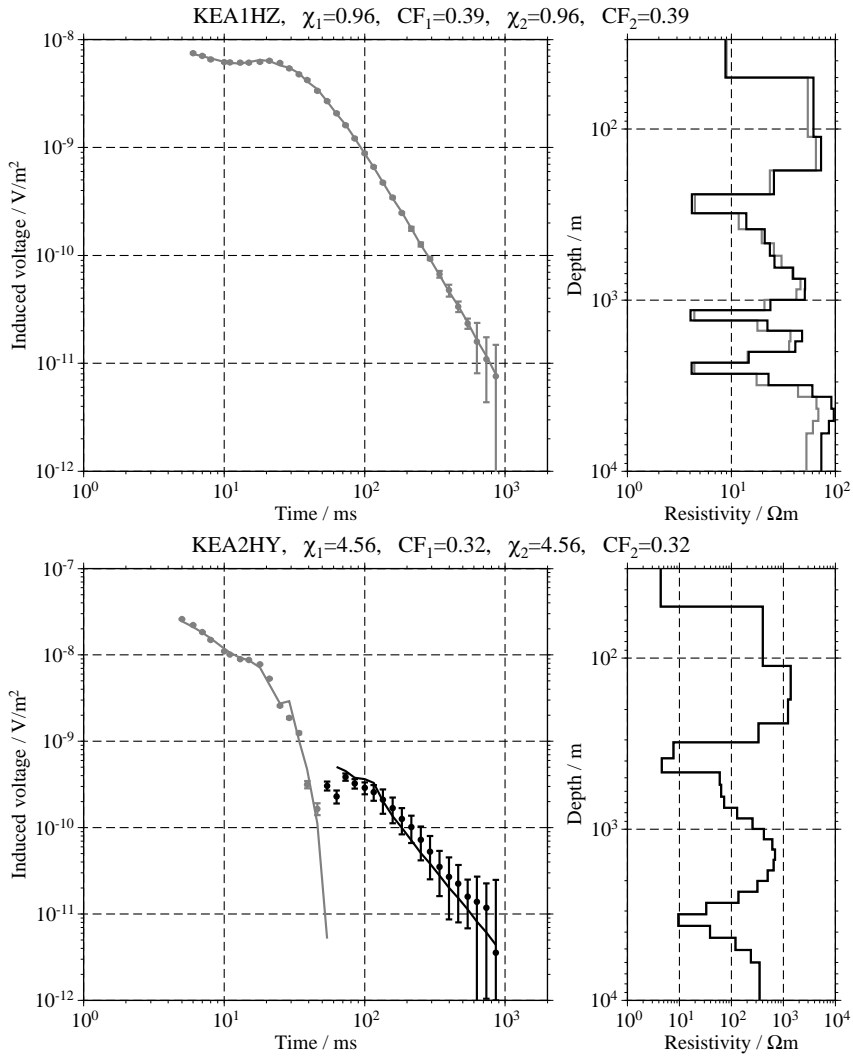


Figure C.30: Single inversion results for the transients measured at HAB and KEA;

Figure C.31: Single inversion results for the transients measured at KEA.



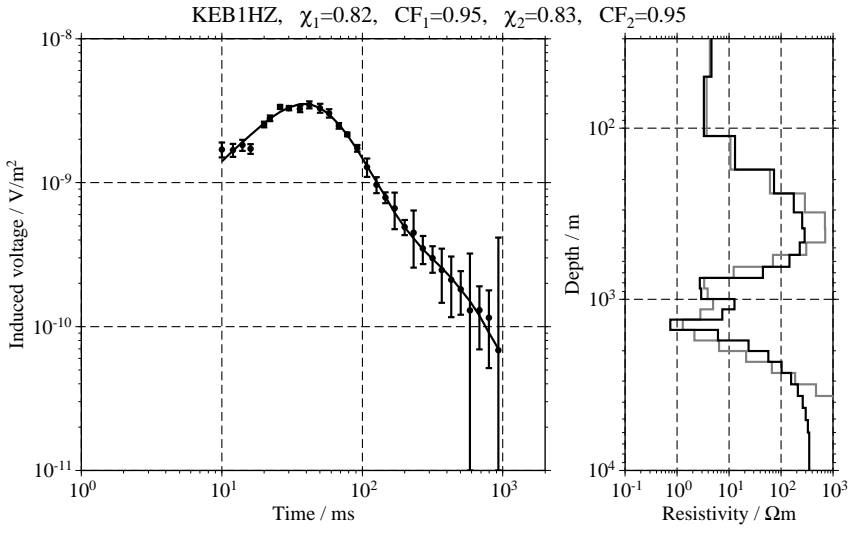
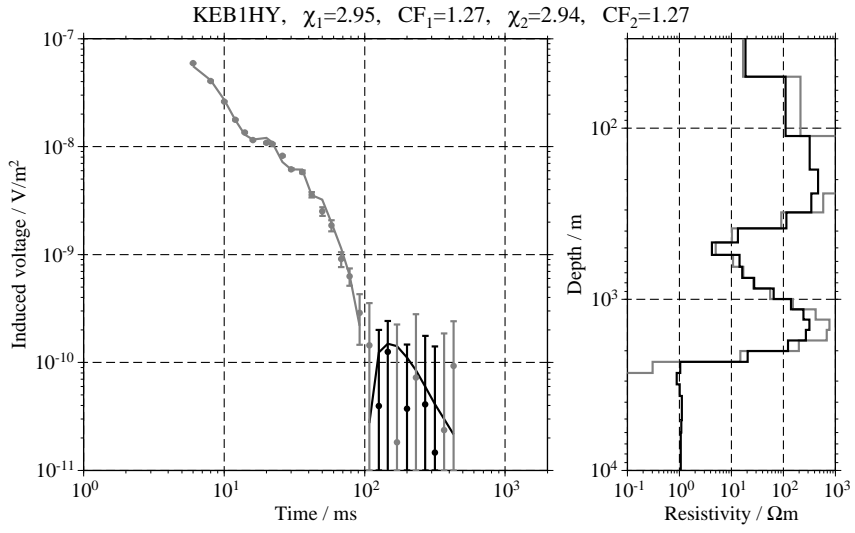
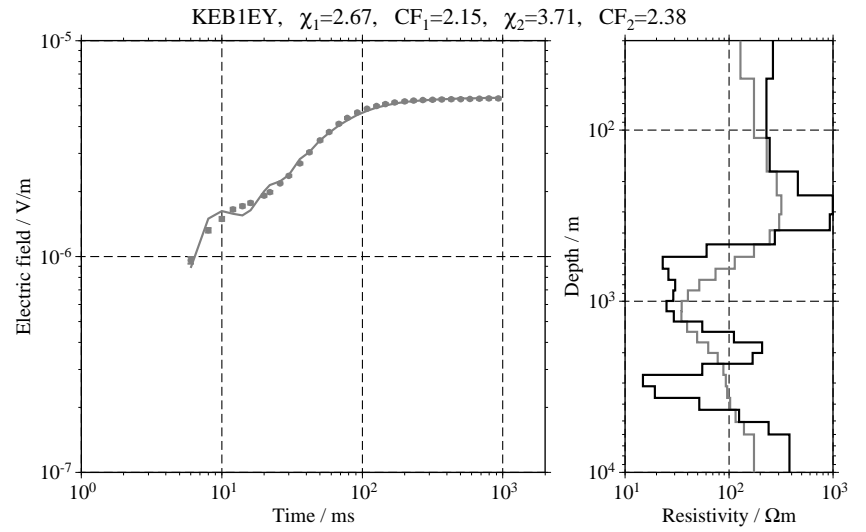
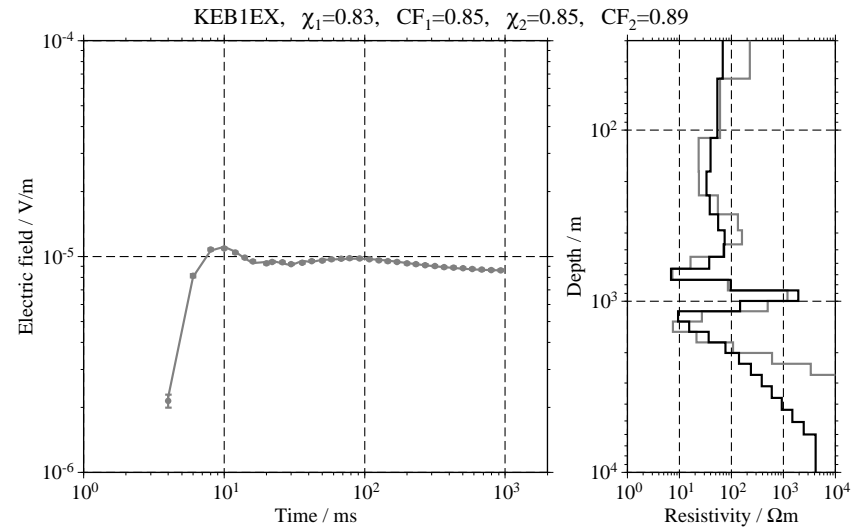


Figure C.32: Single inversion results for the transients measured at KEB;

Figure C.33: Single inversion results for the transients measured at KEB;

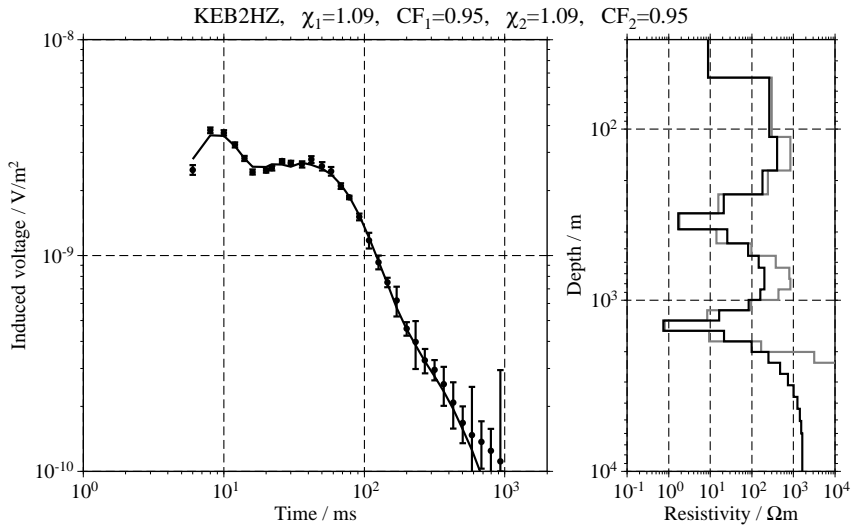
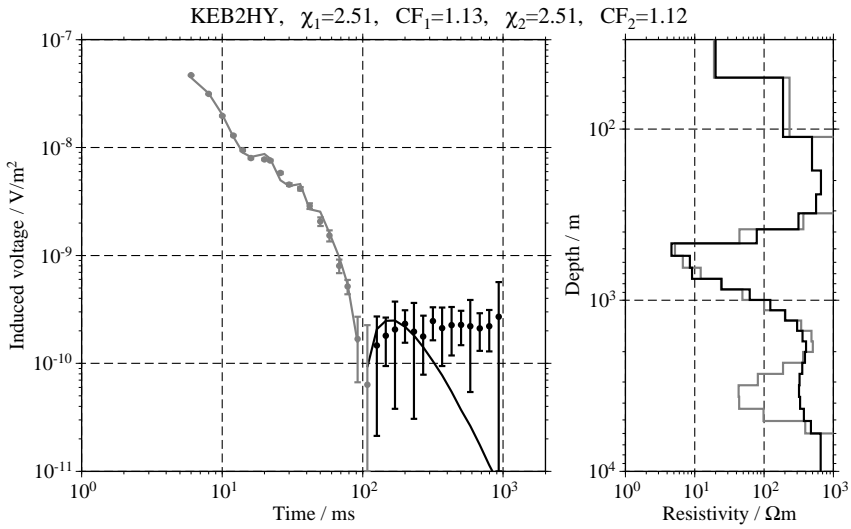
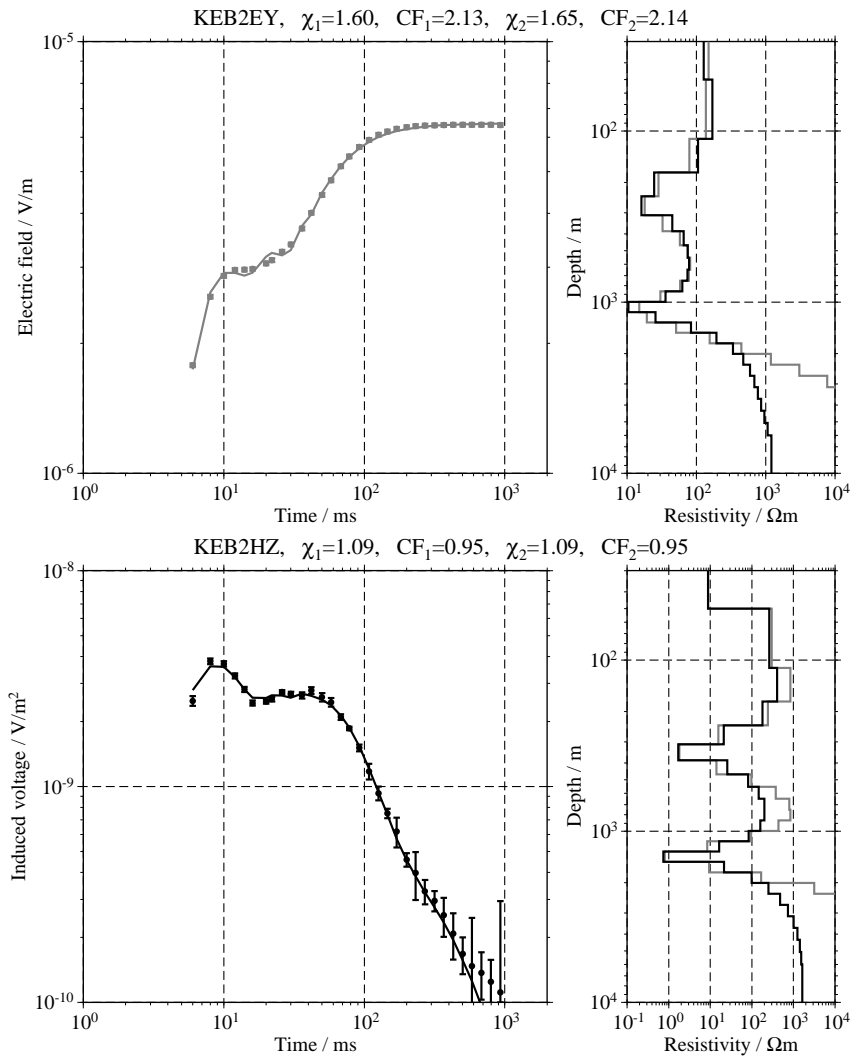
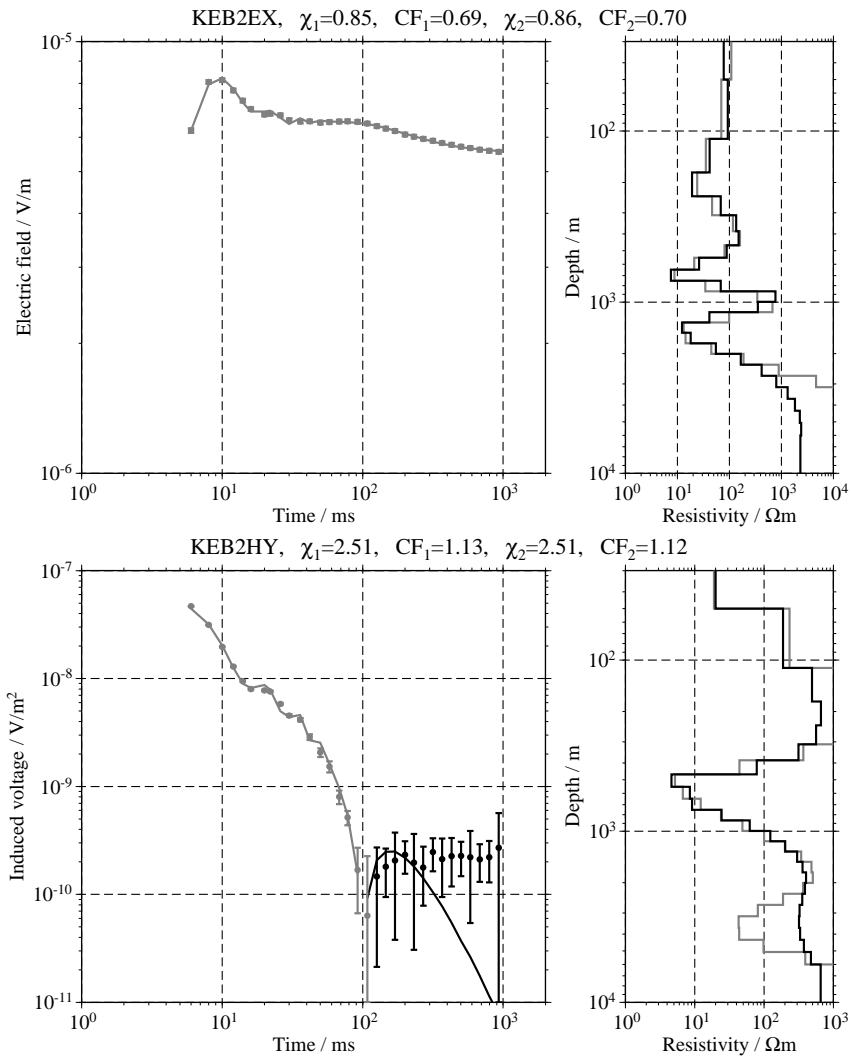


Figure C.34: Single inversion results for the transients measured at KKA;

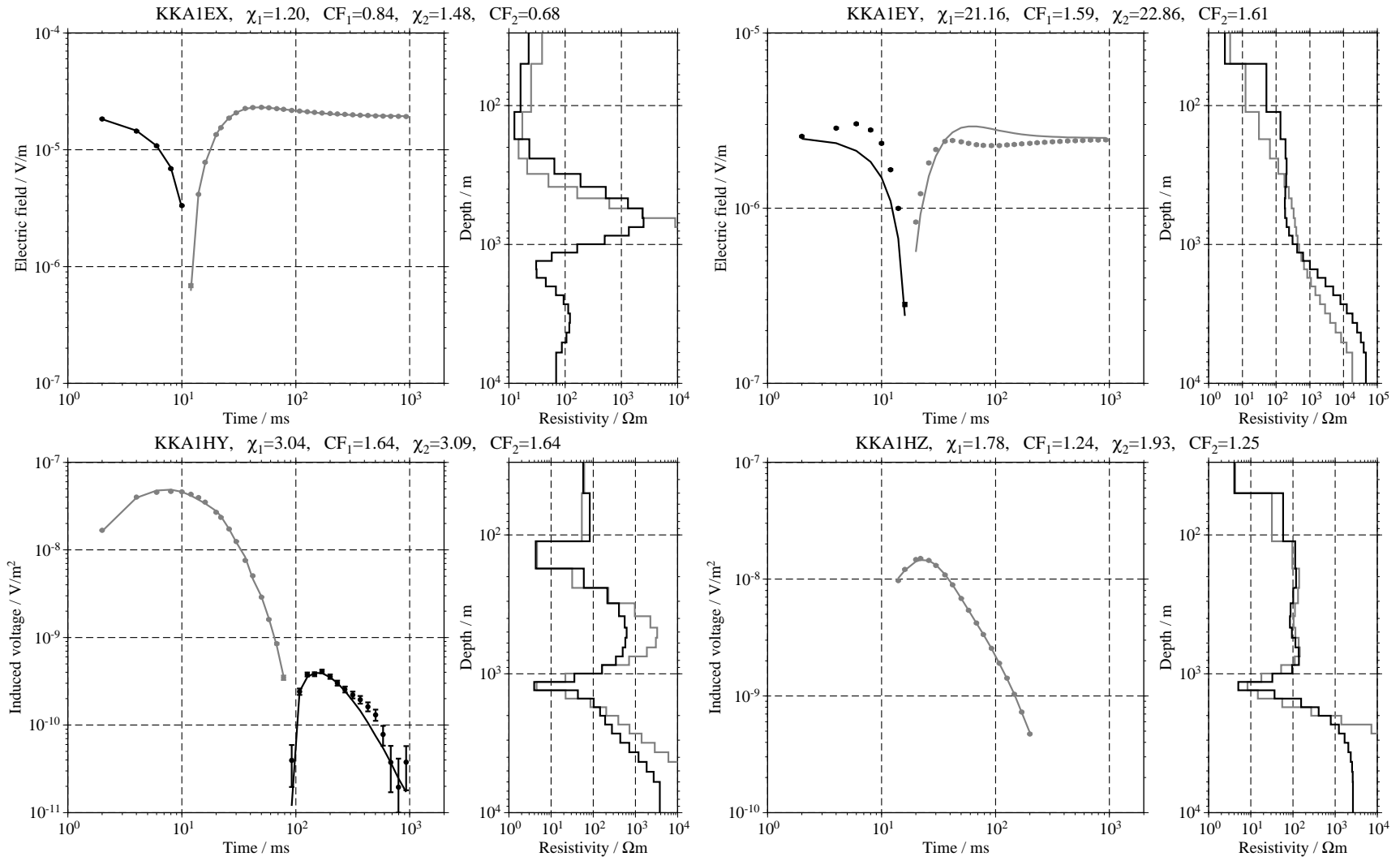


Figure C.35: Single inversion results for the transients measured at KKA.

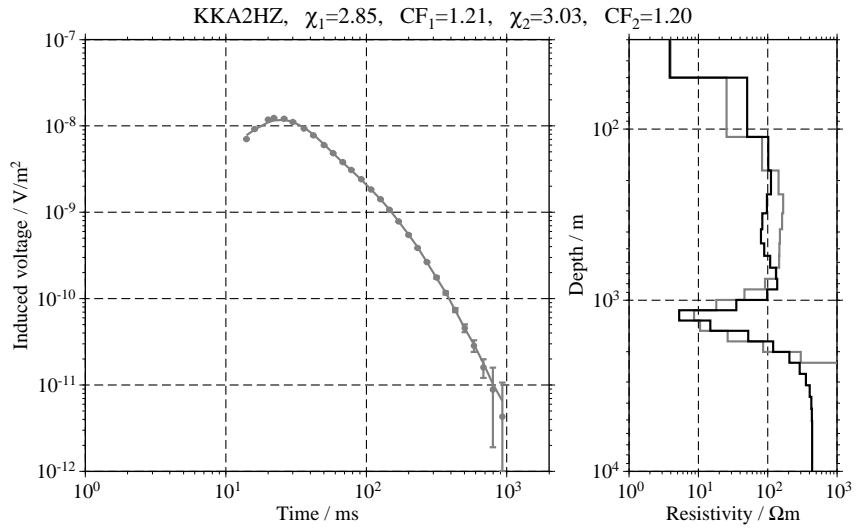
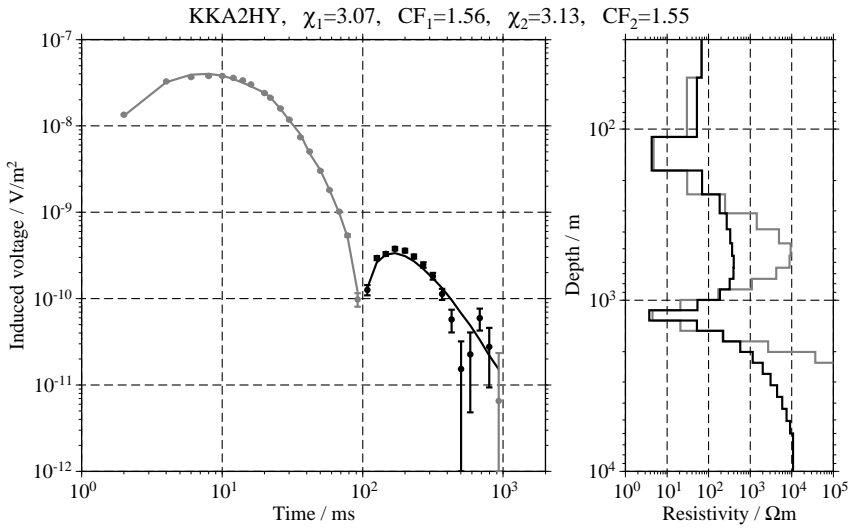
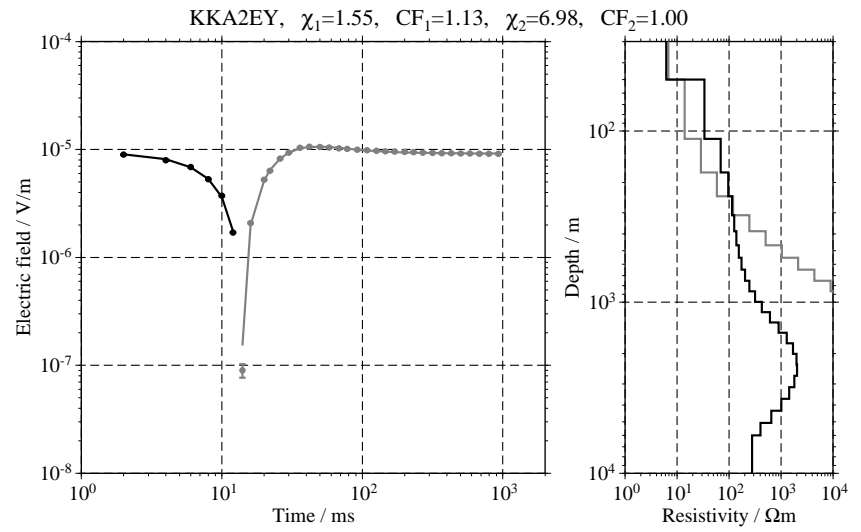
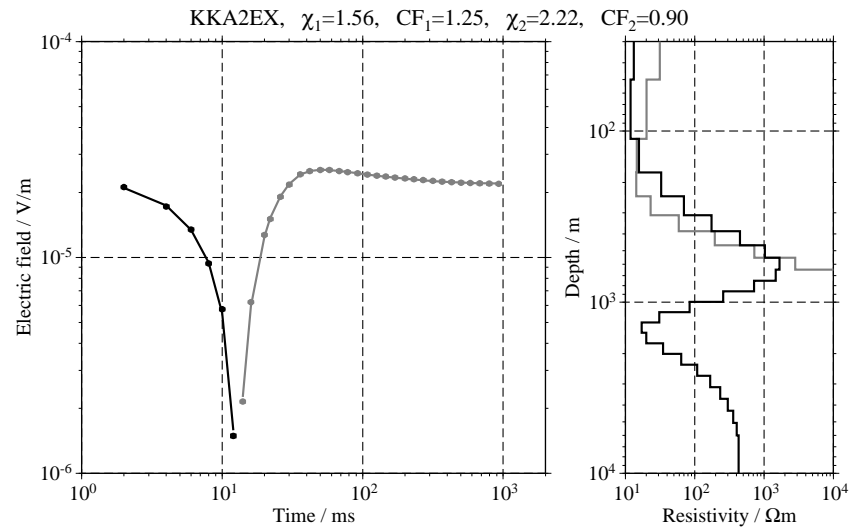
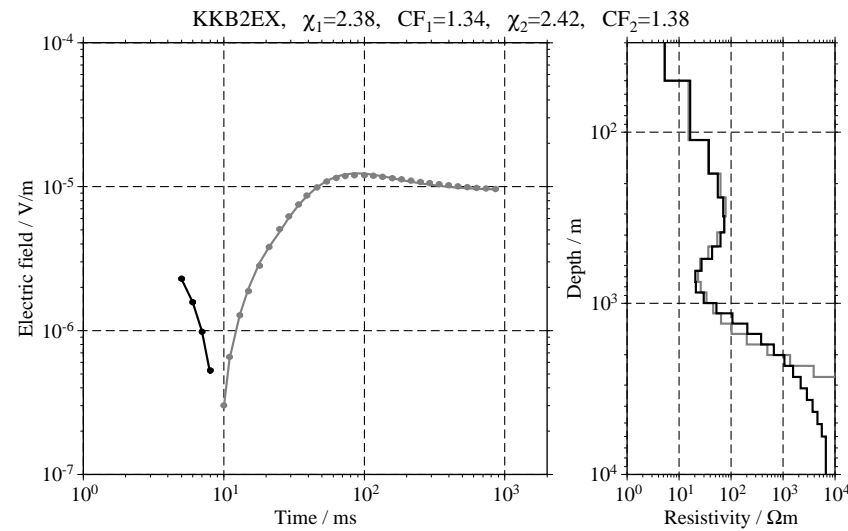
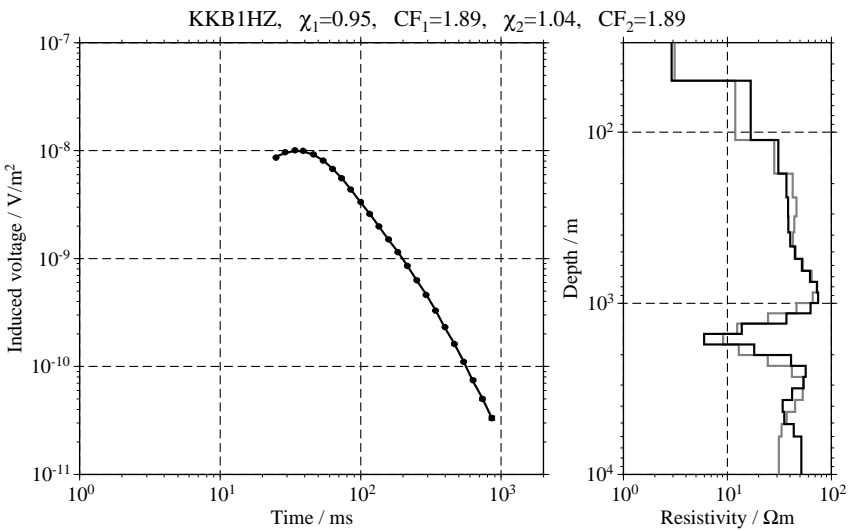
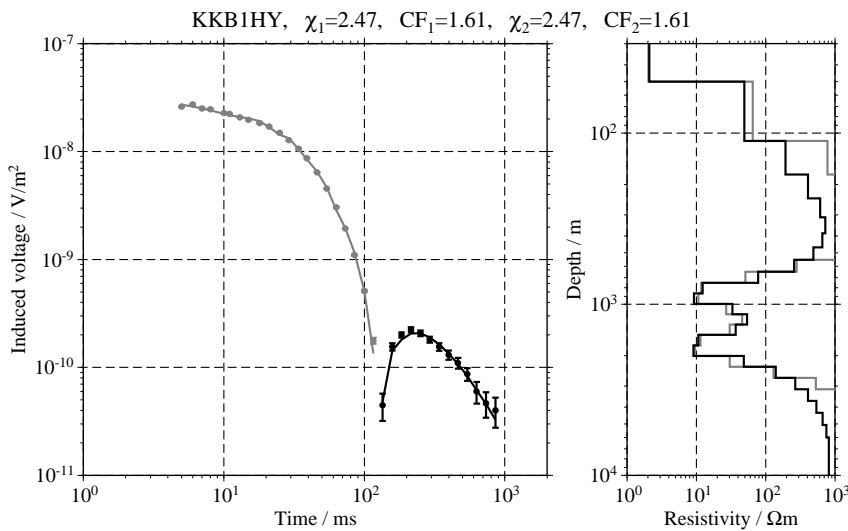
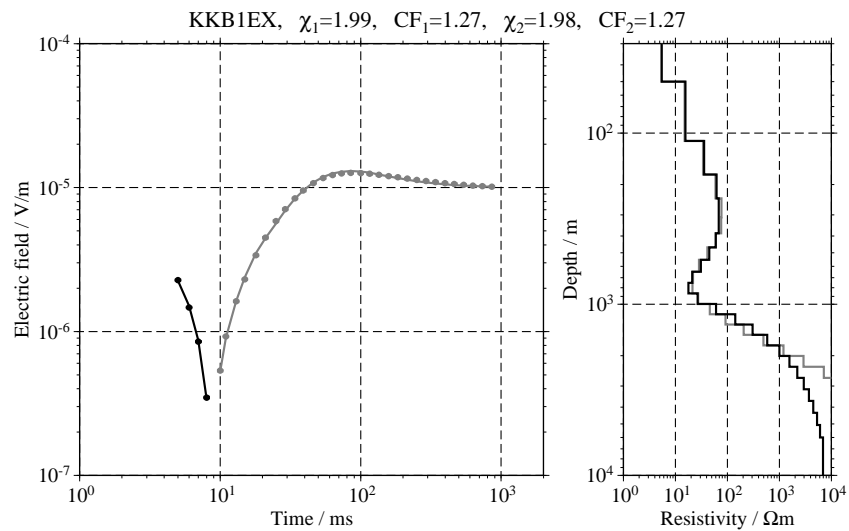


Figure C.36: Single inversion results for the transients measured at KKB;



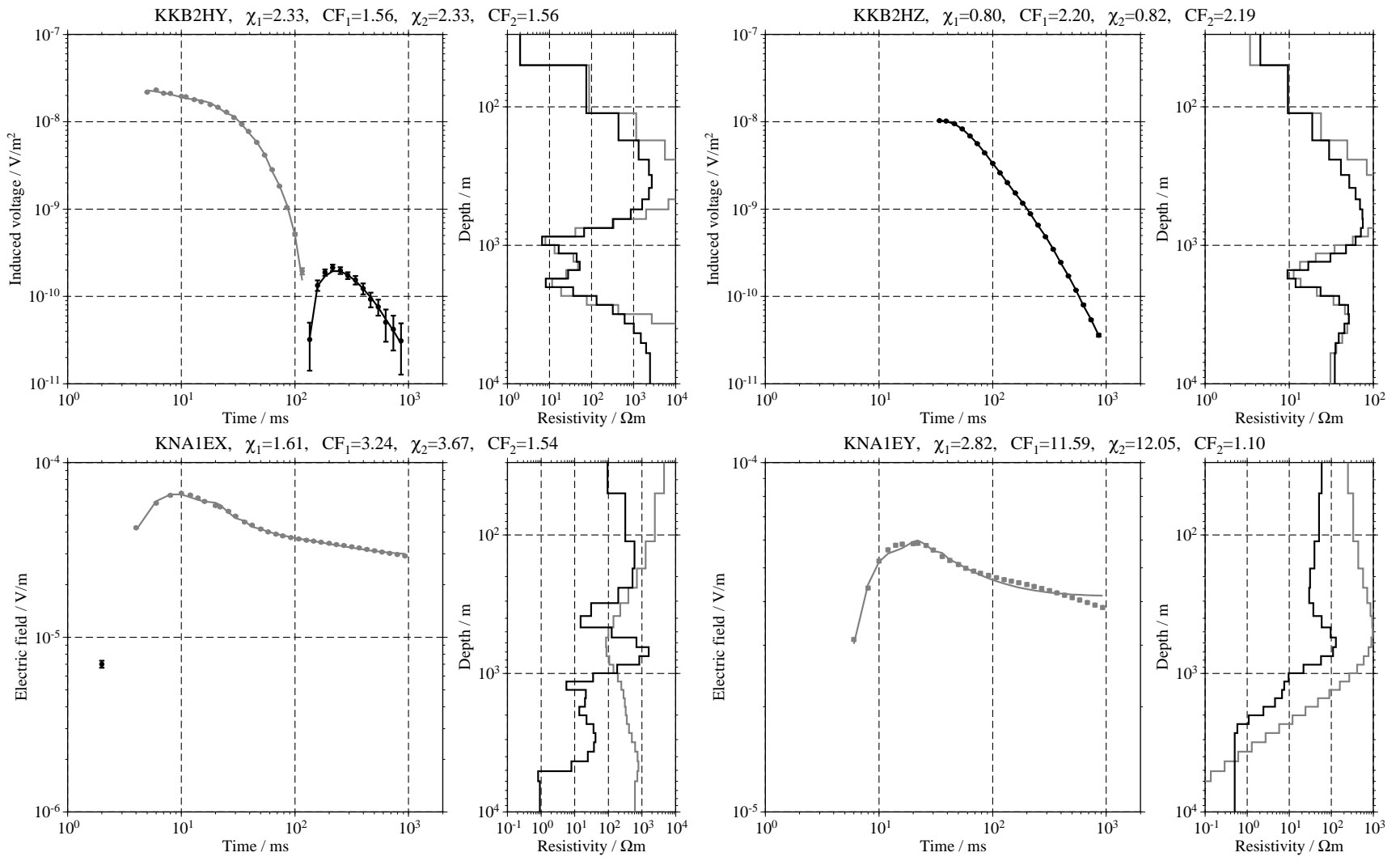


Figure C.37: Single inversion results for the transients measured at KNA;

Figure C.38: Single inversion results for the transients measured at KNA;

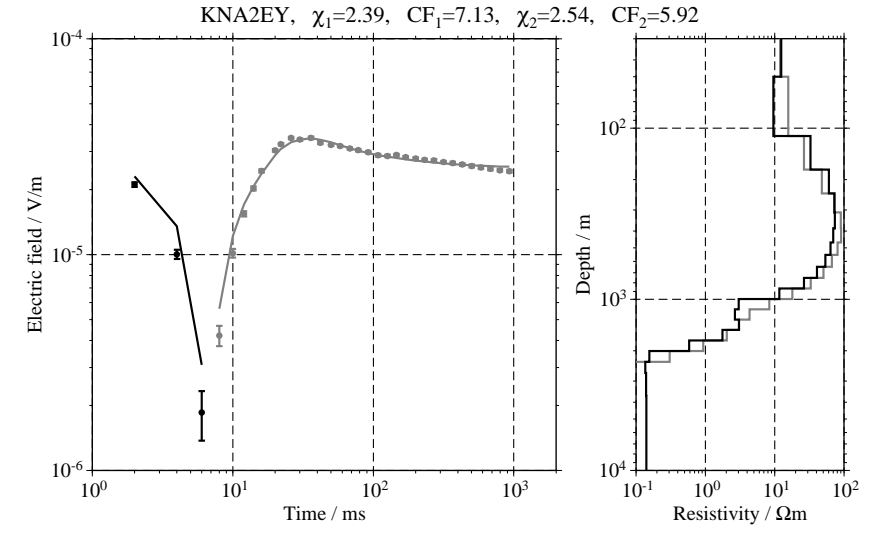
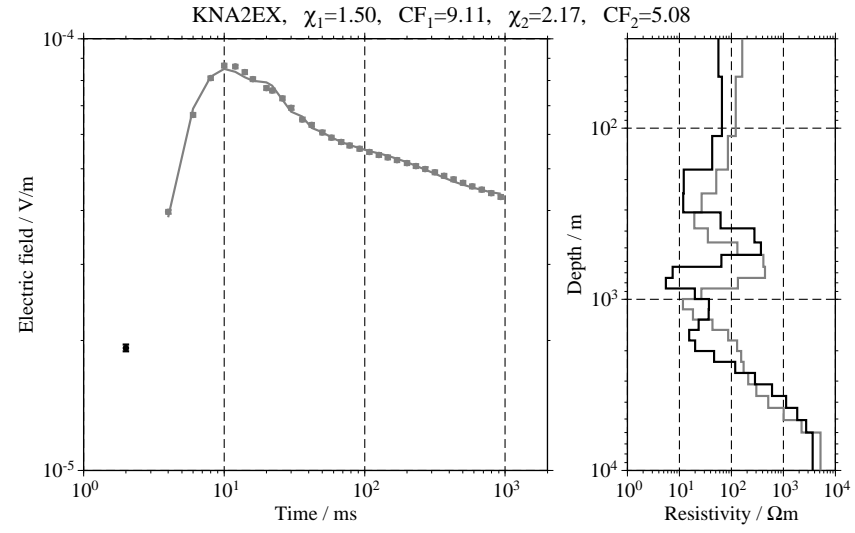
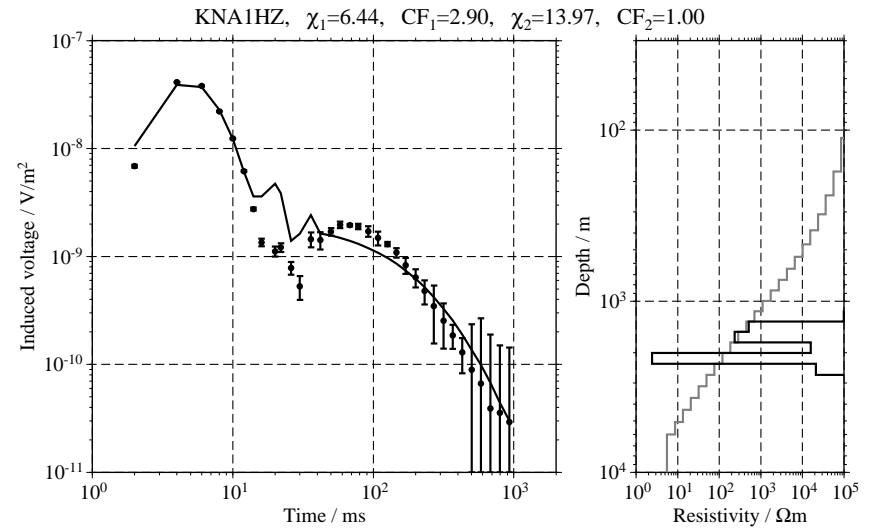
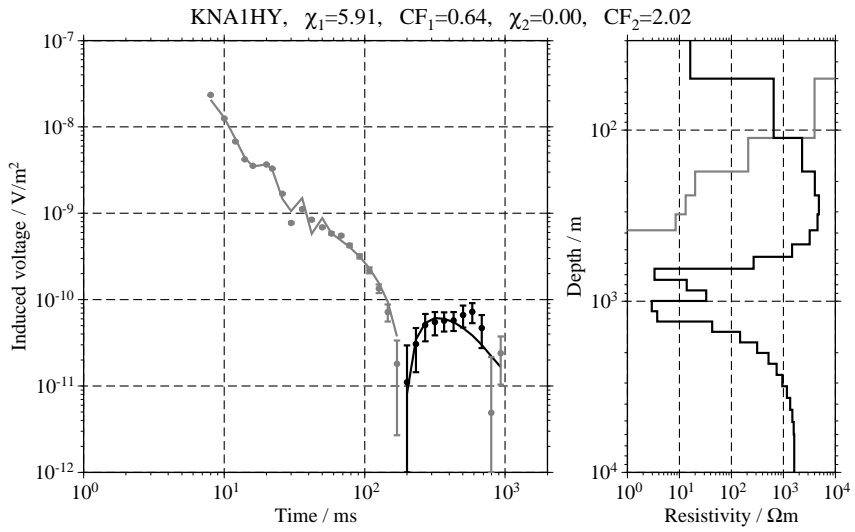


Figure C.39: Single inversion results for the transients measured at KNA and KNB;

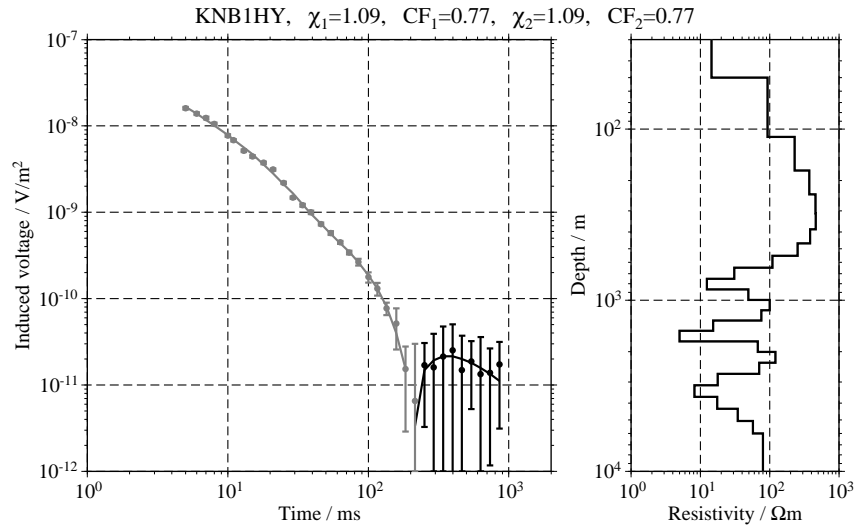
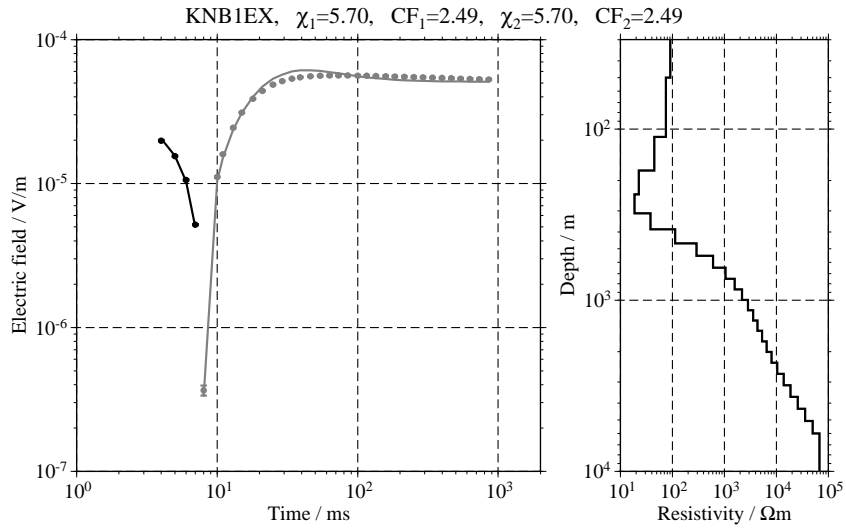
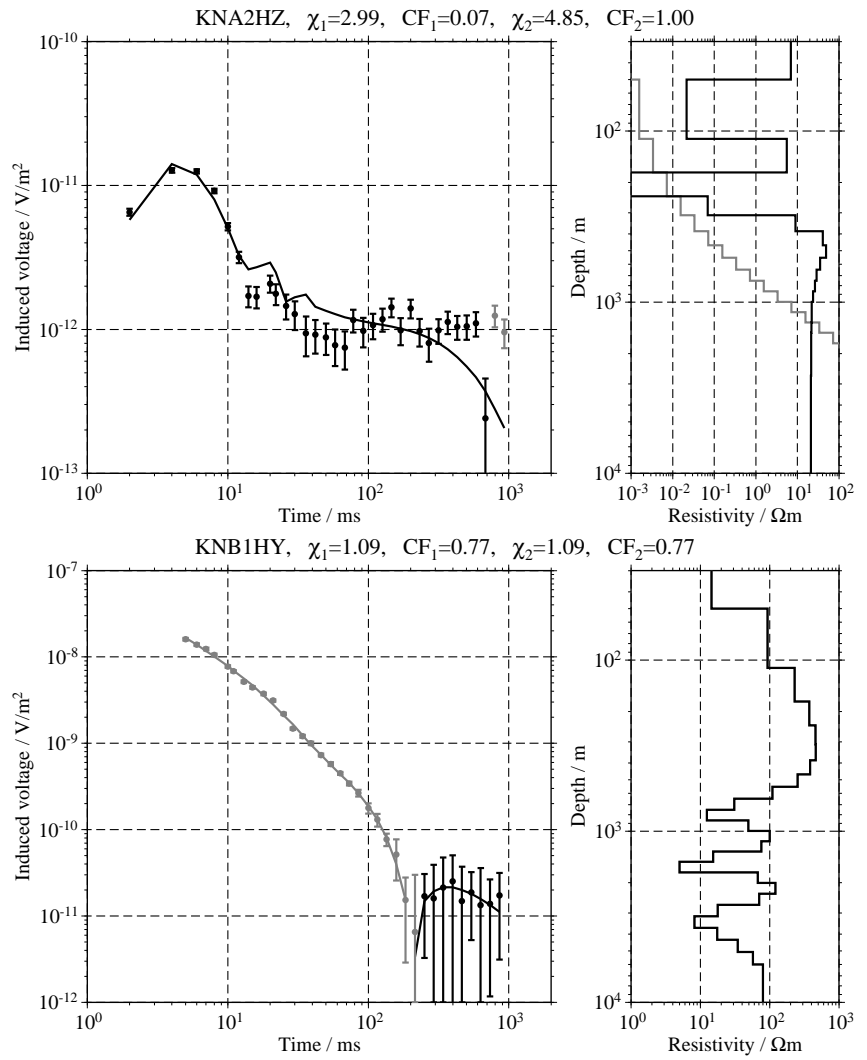
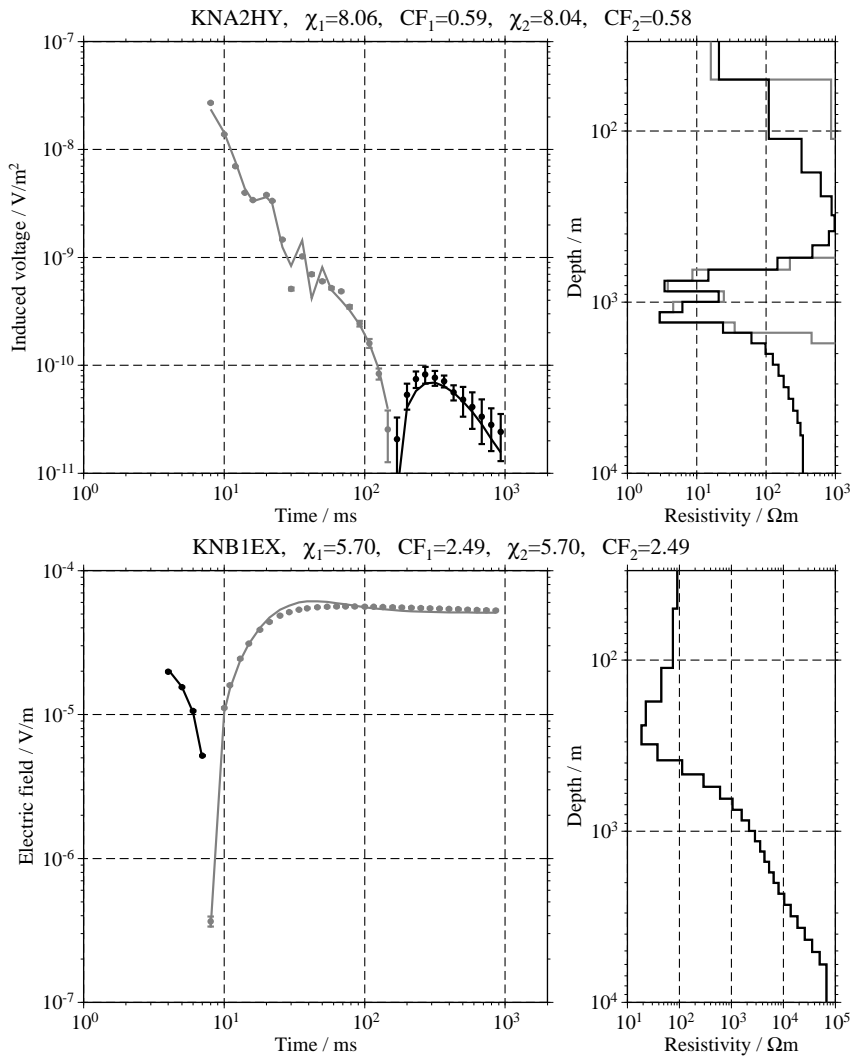
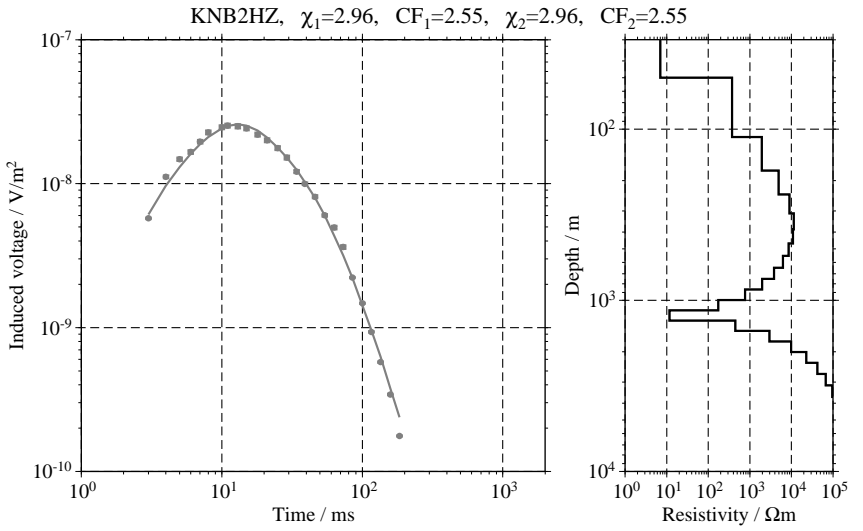
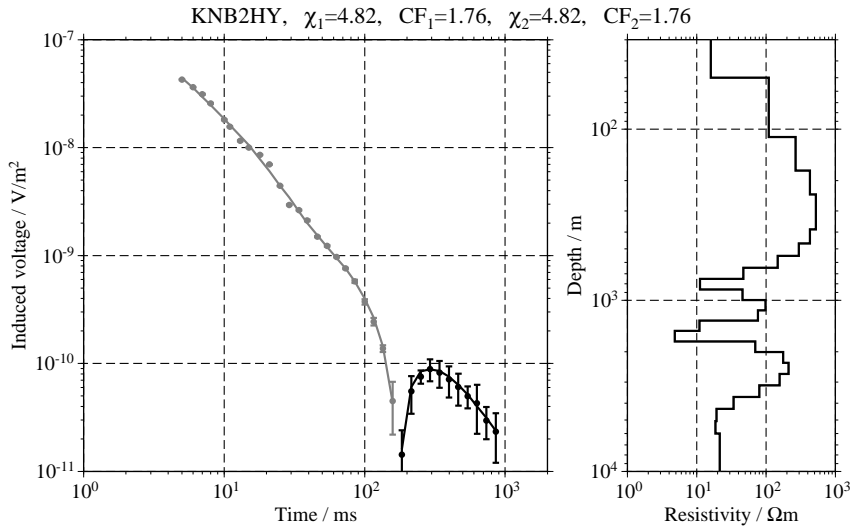
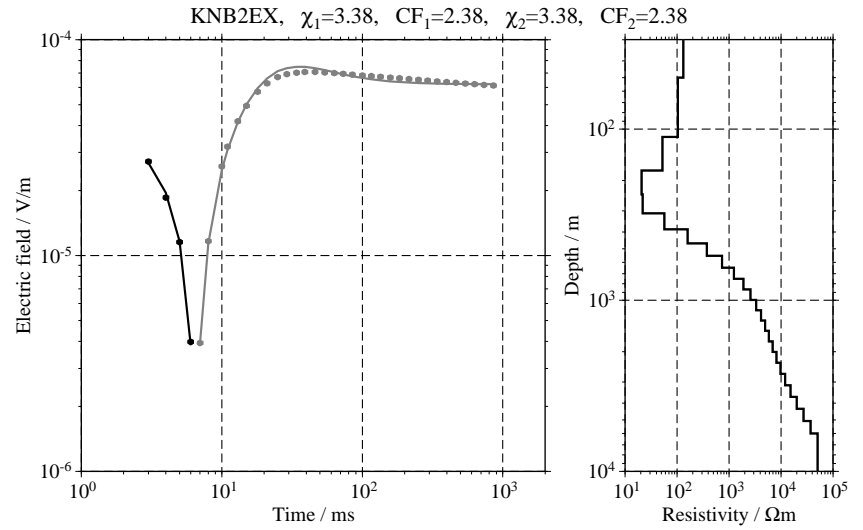
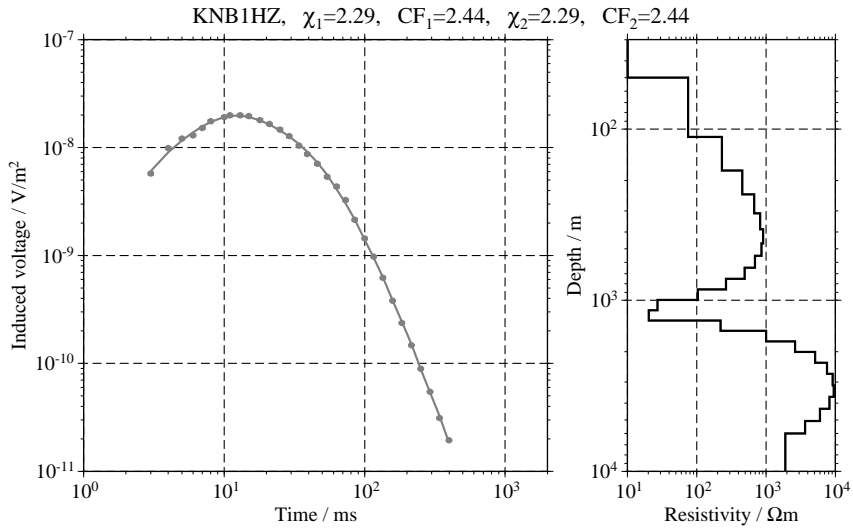


Figure C.40: Single inversion results for the transients measured at KNB;



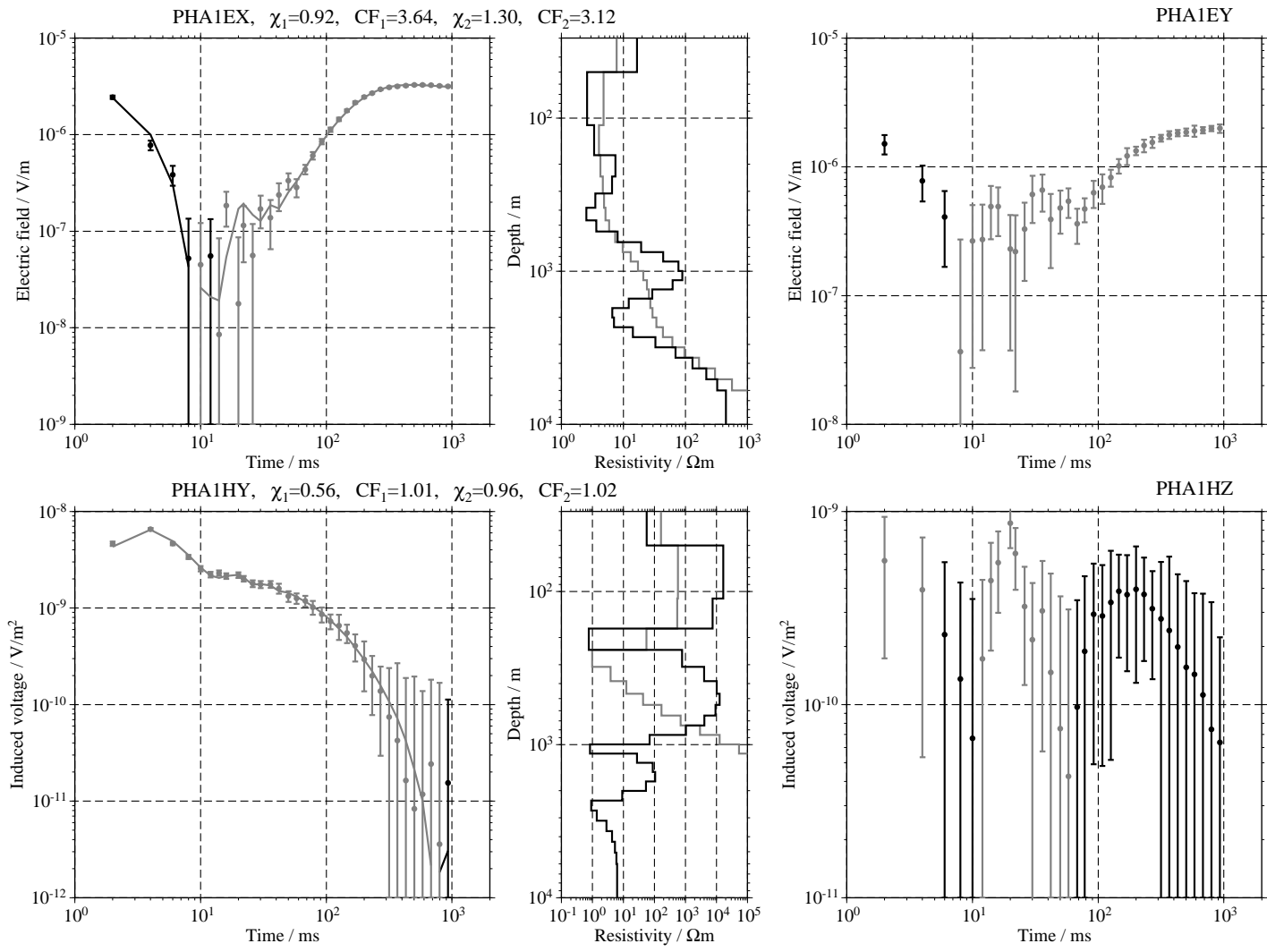
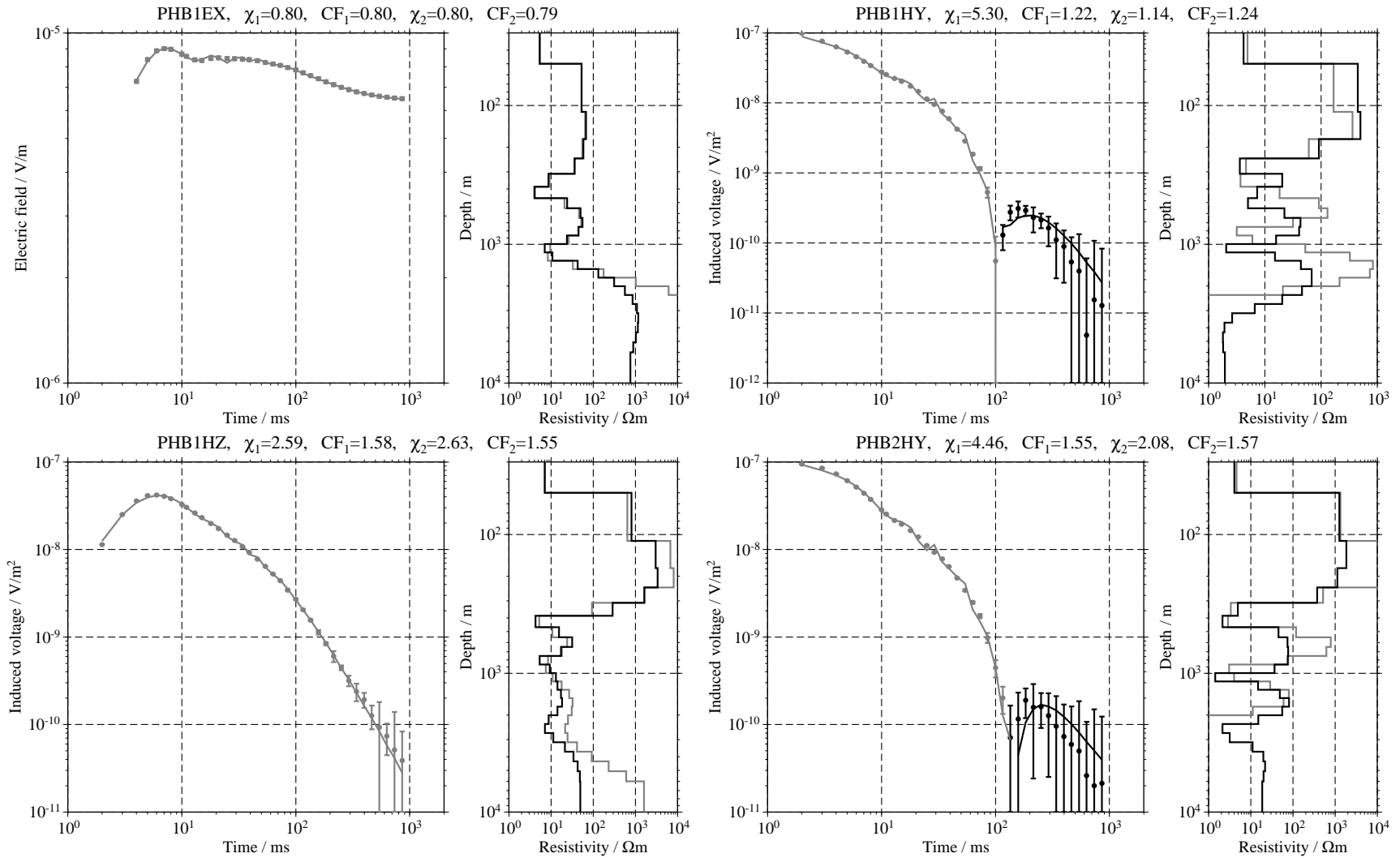


Figure C.41: Single inversion results for the transients measured at PHA;

Figure C.42: Single inversion results for the transients measured at PHB;



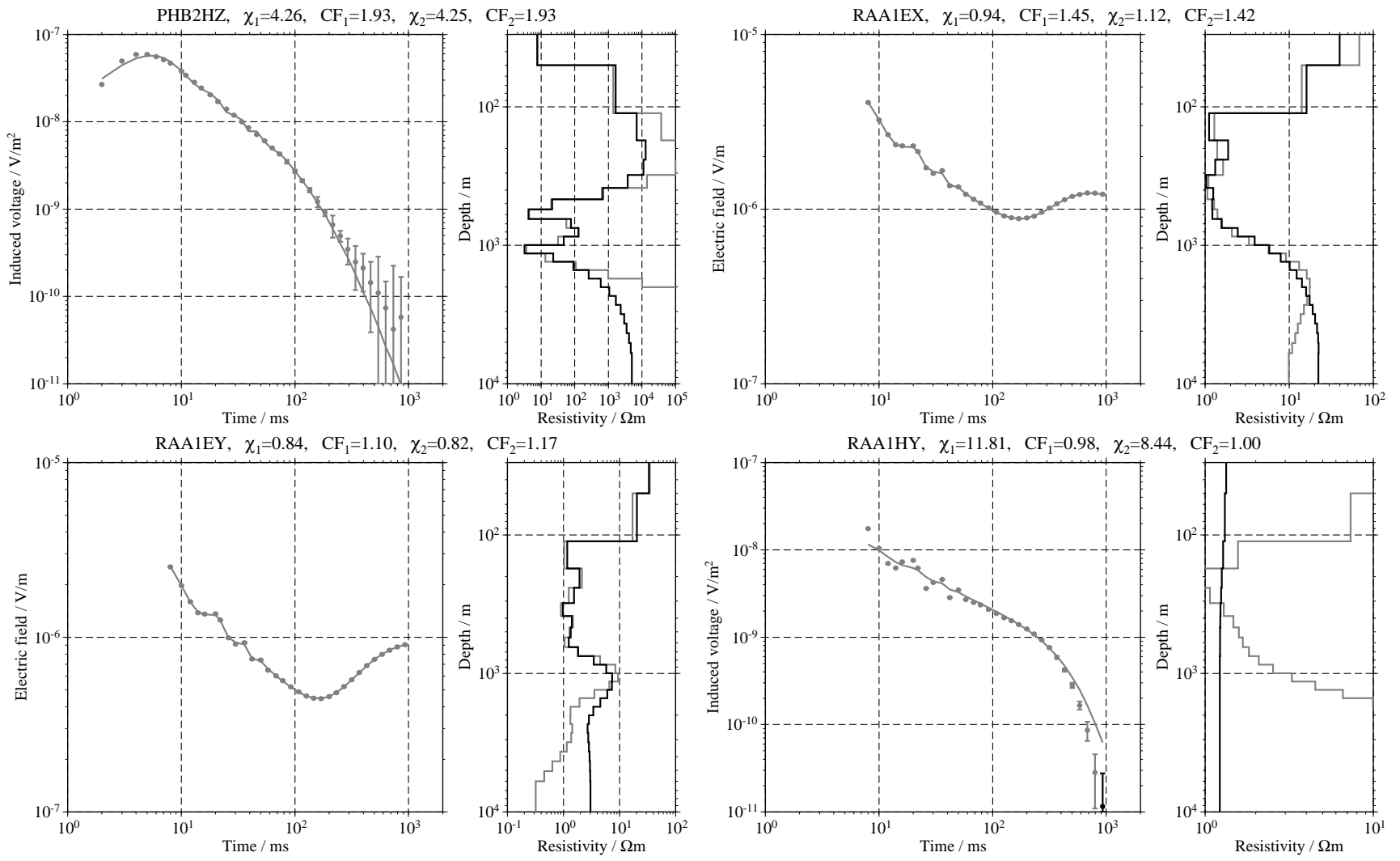


Figure C.43: Single inversion results for the transients measured at PHB and RAA;

Figure C44: Single inversion results for the transients measured at RAA and RAB;

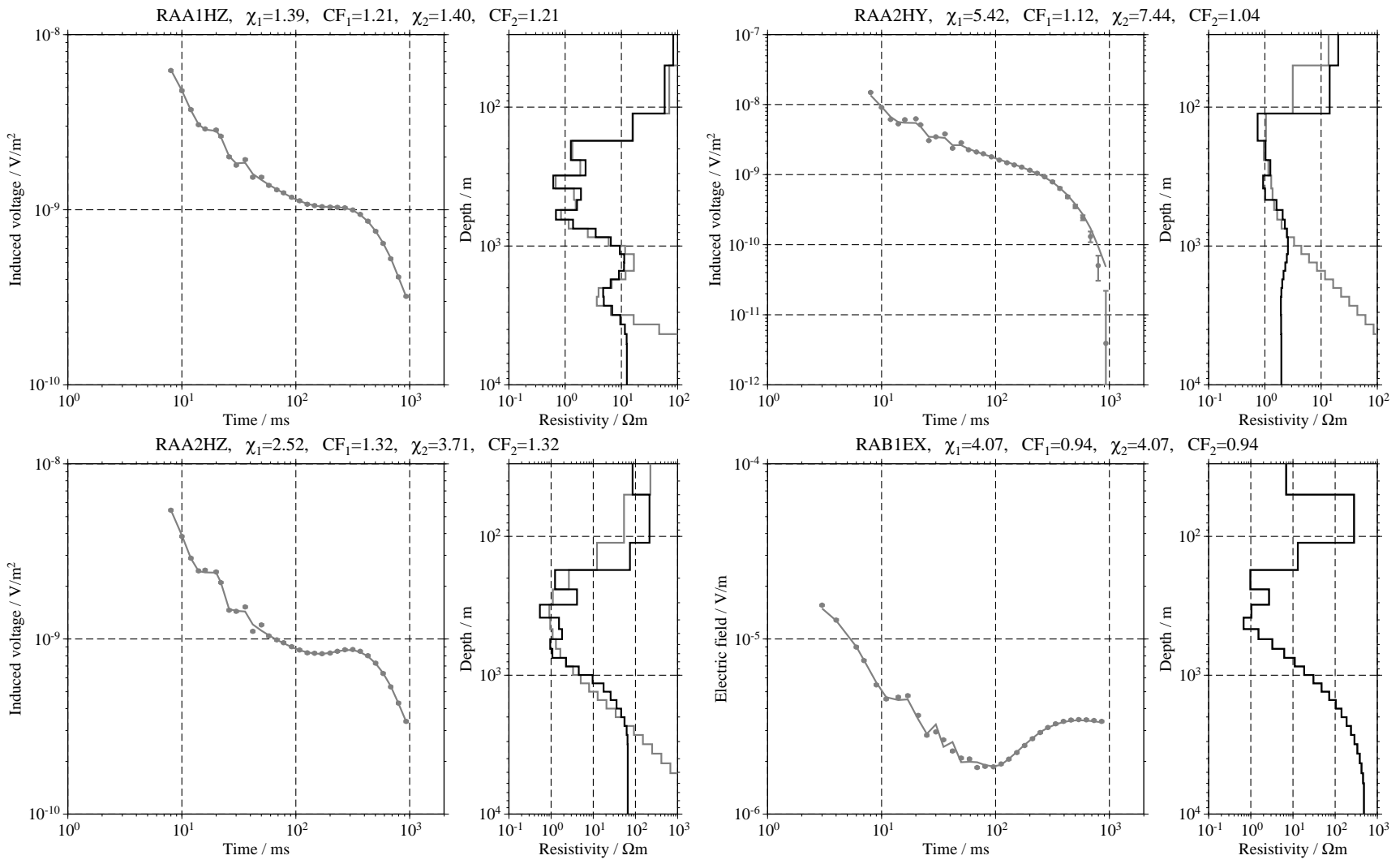


Figure C.45: Single inversion results for the transients measured at RAB;

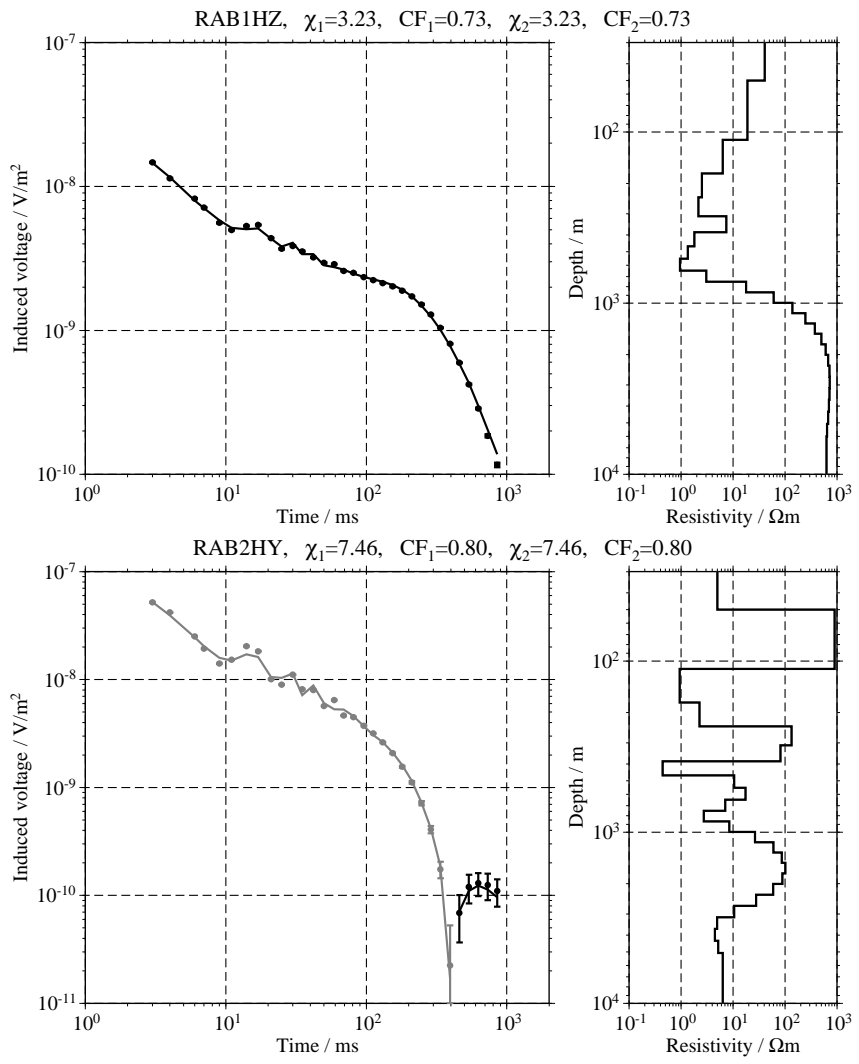
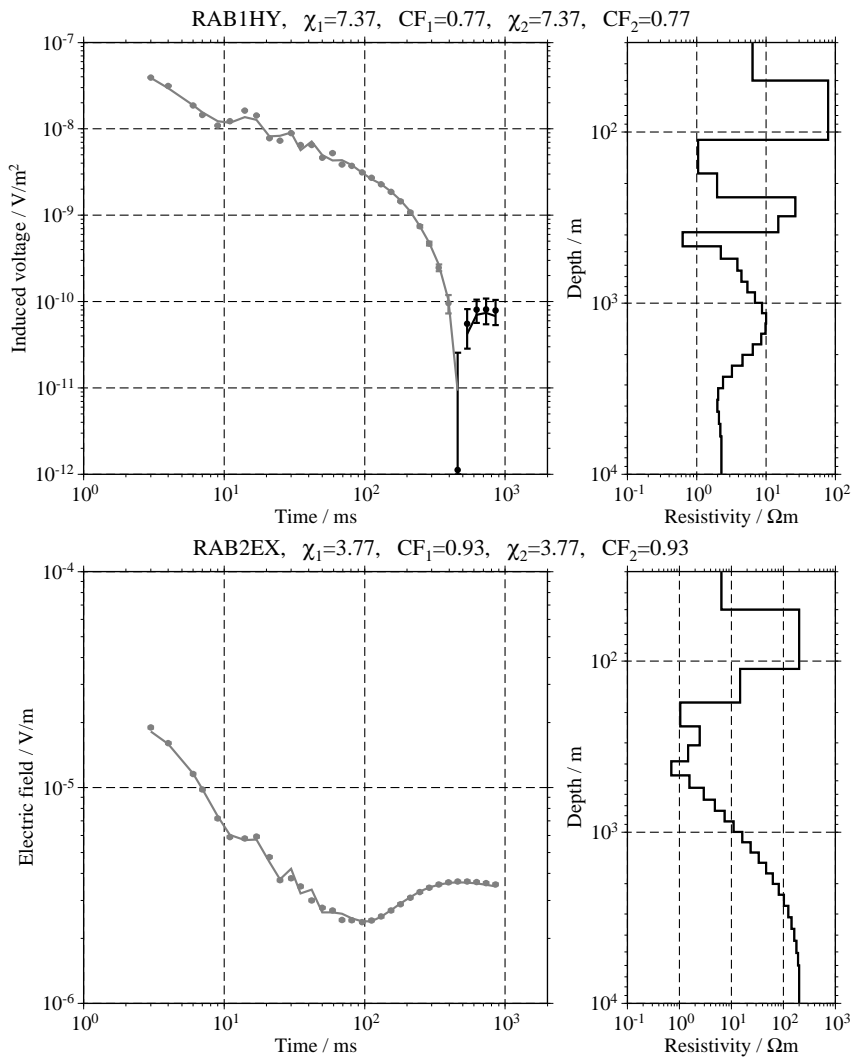


Figure C.46: Single inversion results for the transients measured at RAB and RZA;

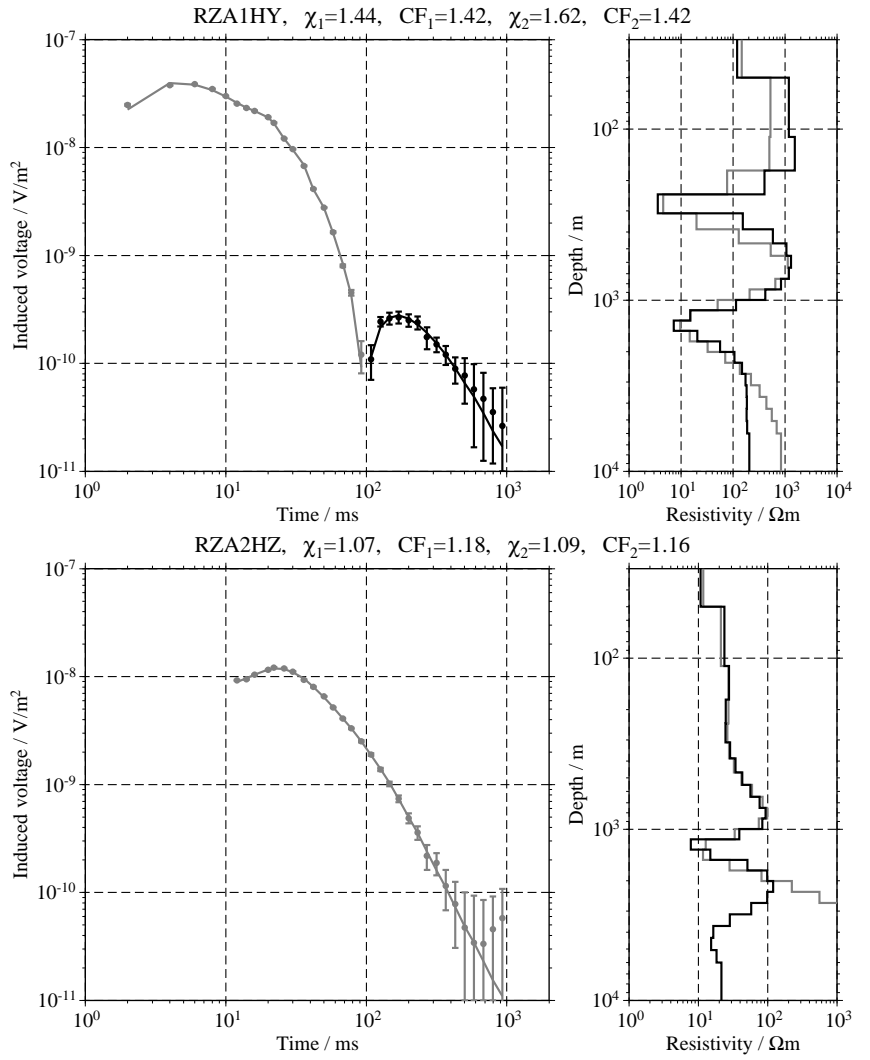
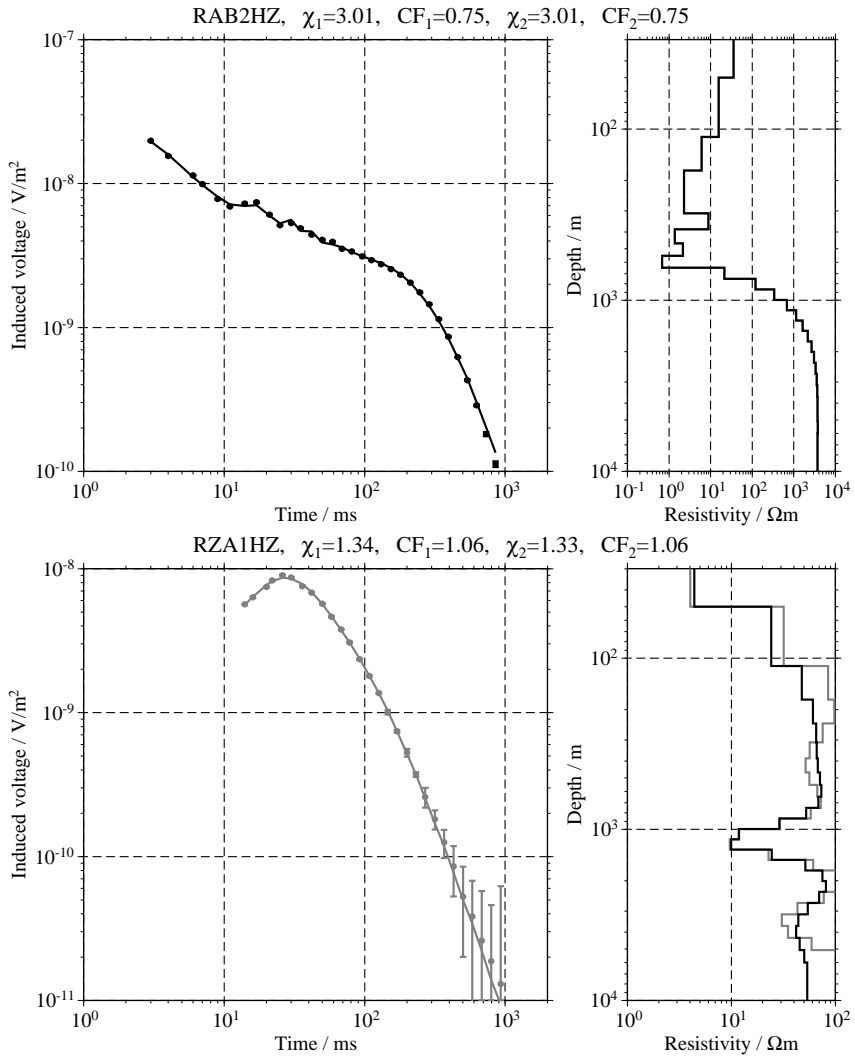


Figure C.47: Single inversion results for the transients measured at RZB.

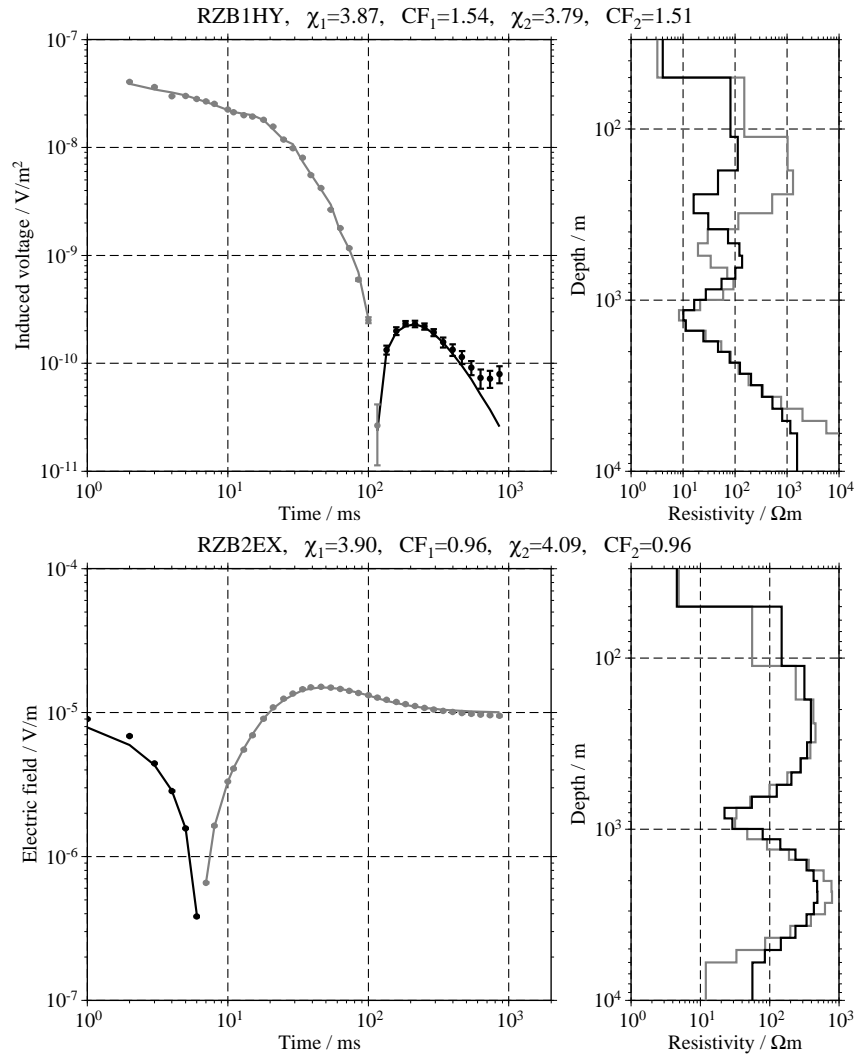
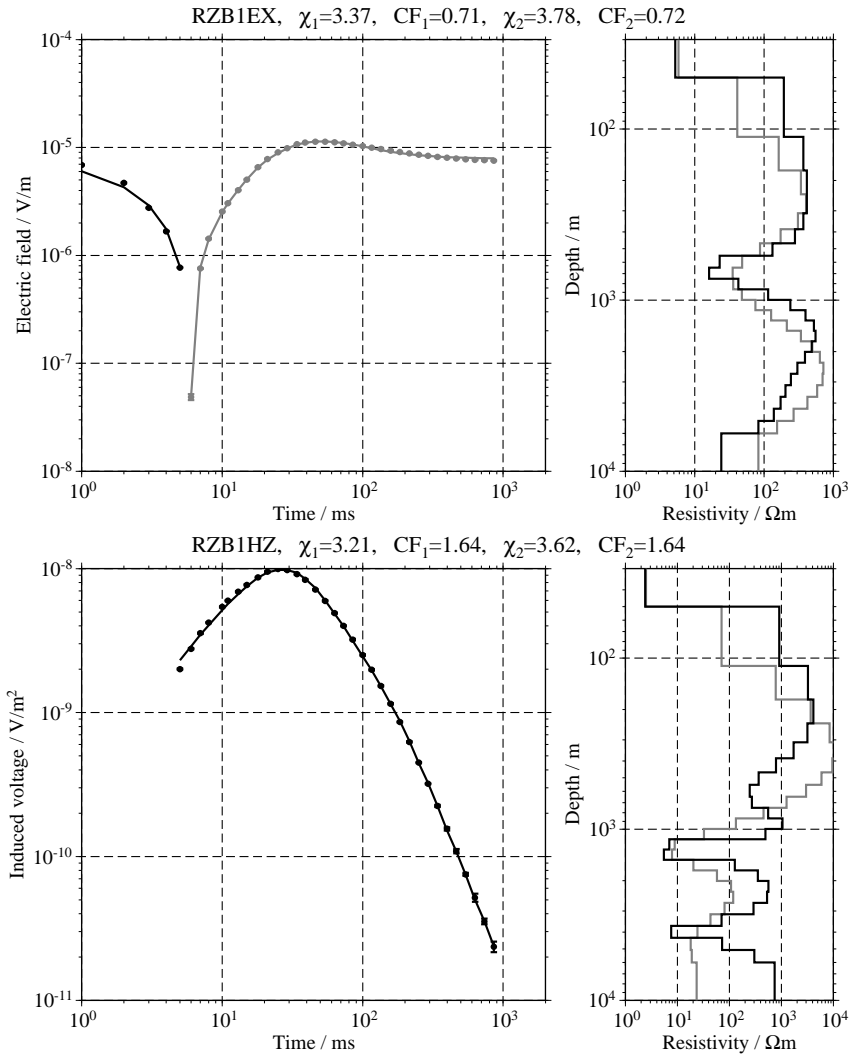


Figure C.48: Single inversion results for the transients measured at RZB and SAA;

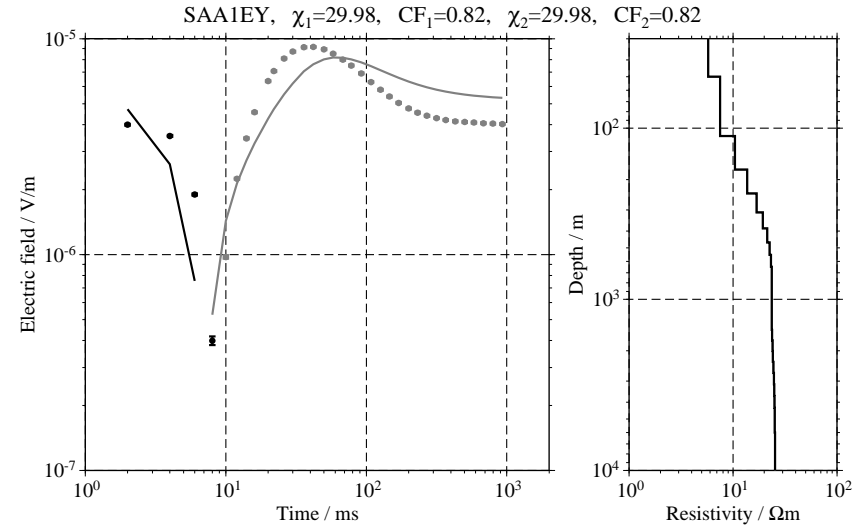
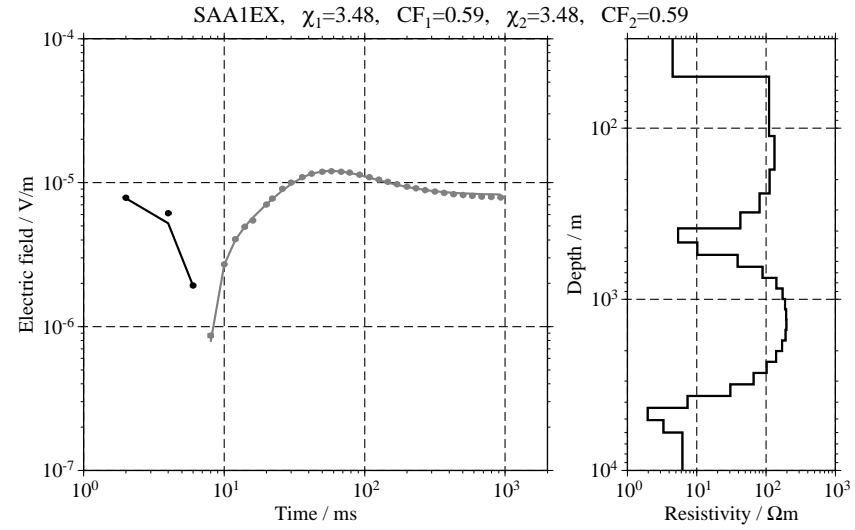
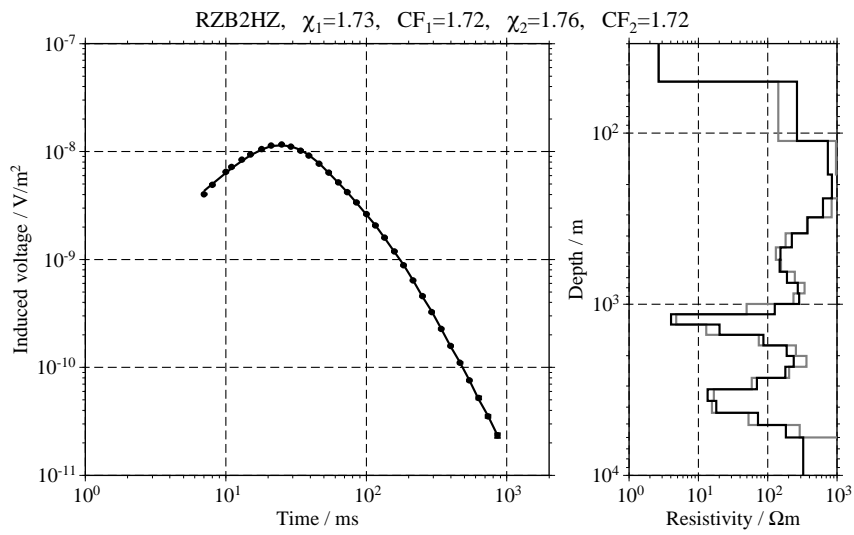
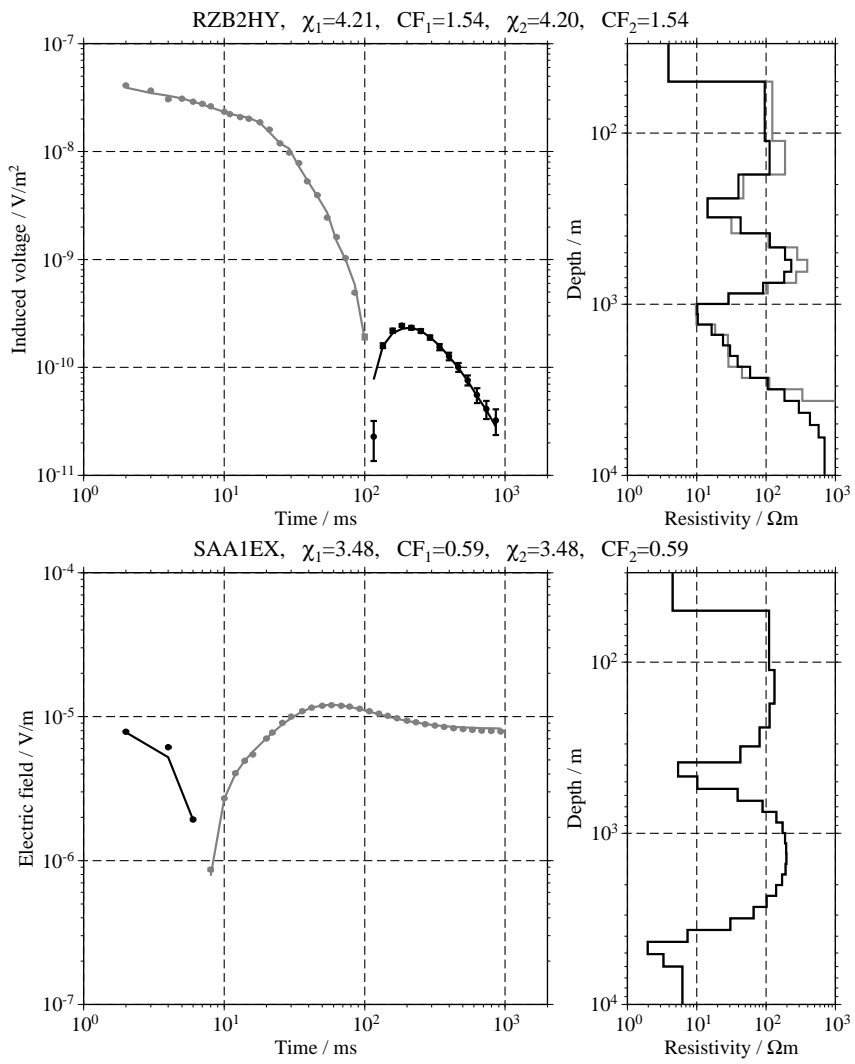


Figure C.49: Single inversion results for the transients measured at SAA.

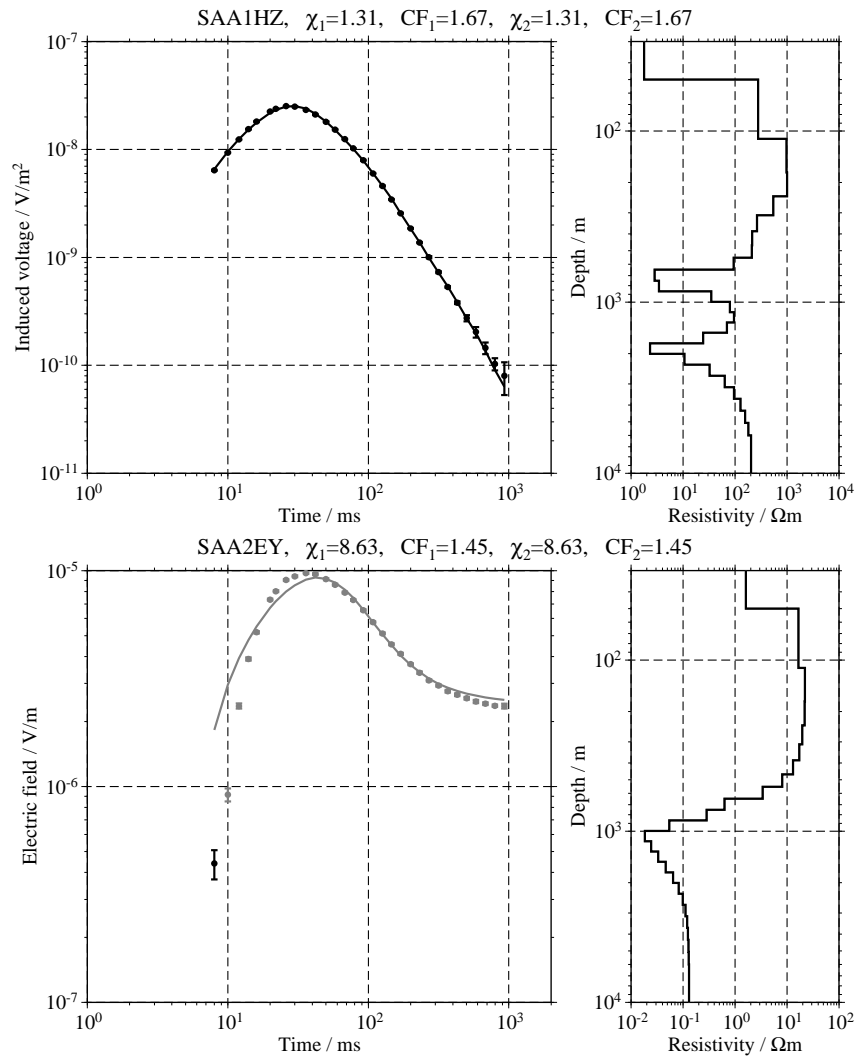
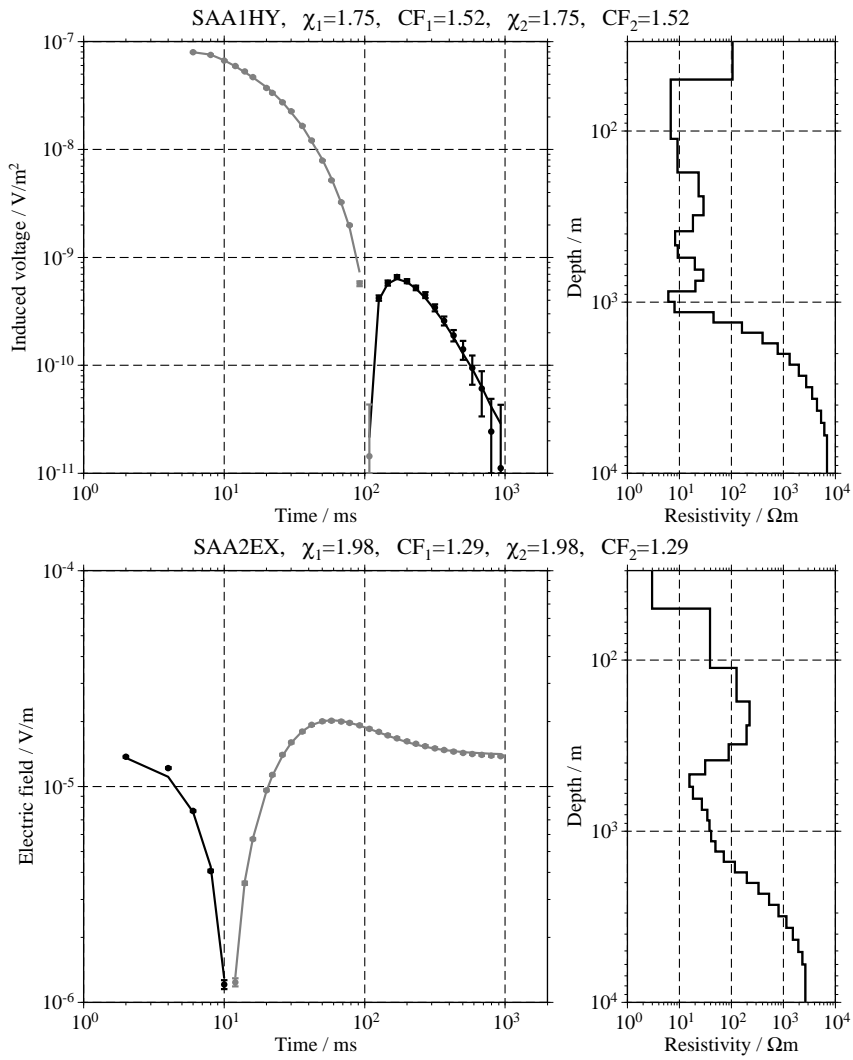
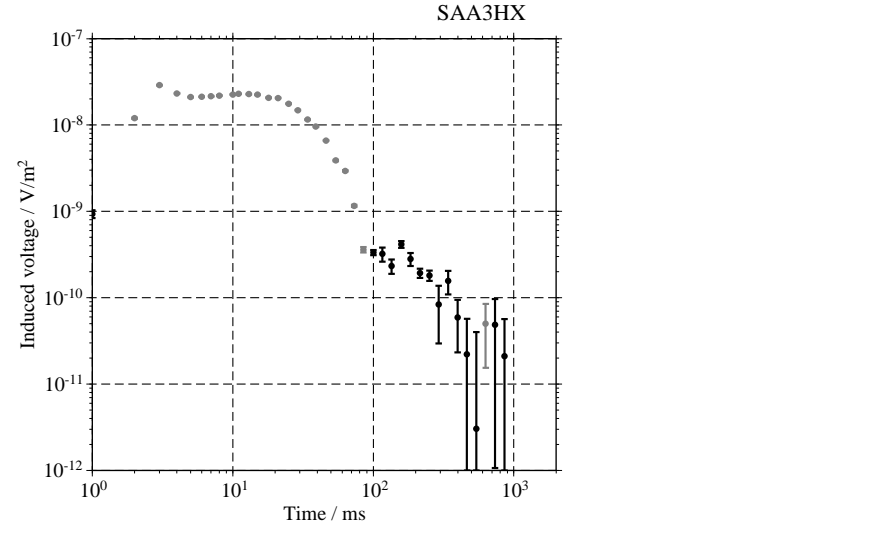
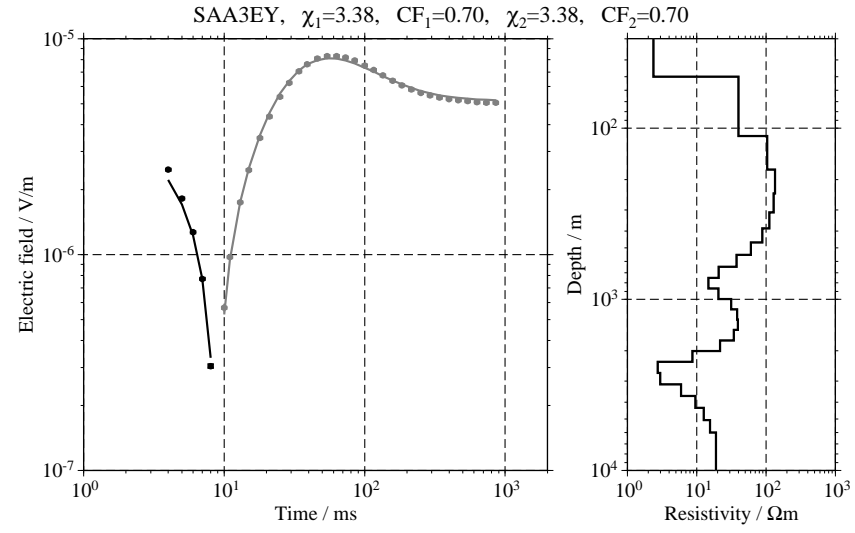
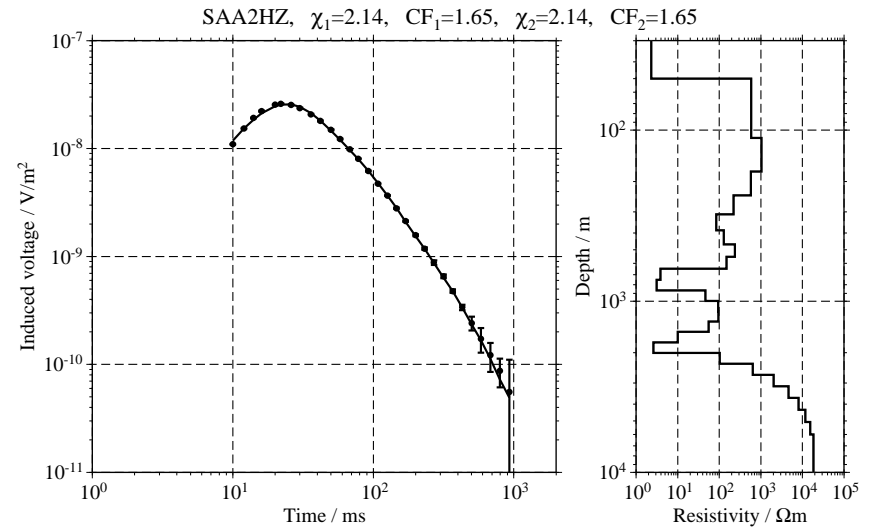
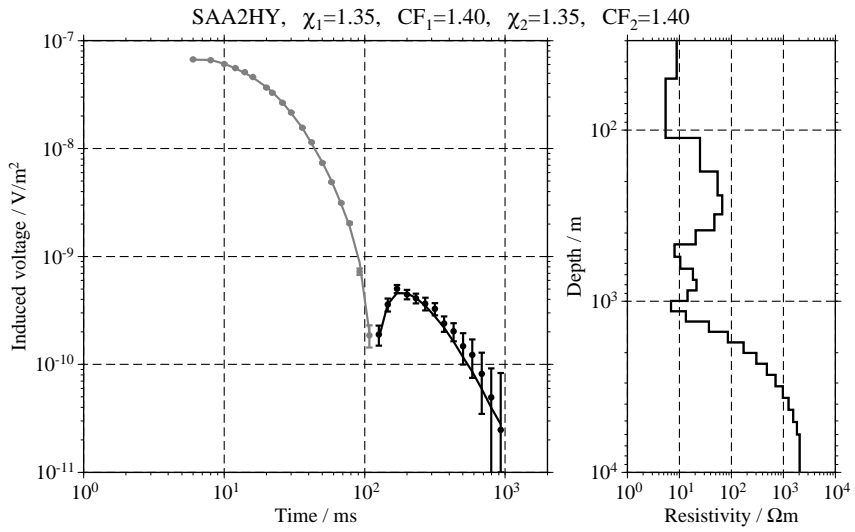


Figure C.50: Single inversion results for the transients measured at SAA;



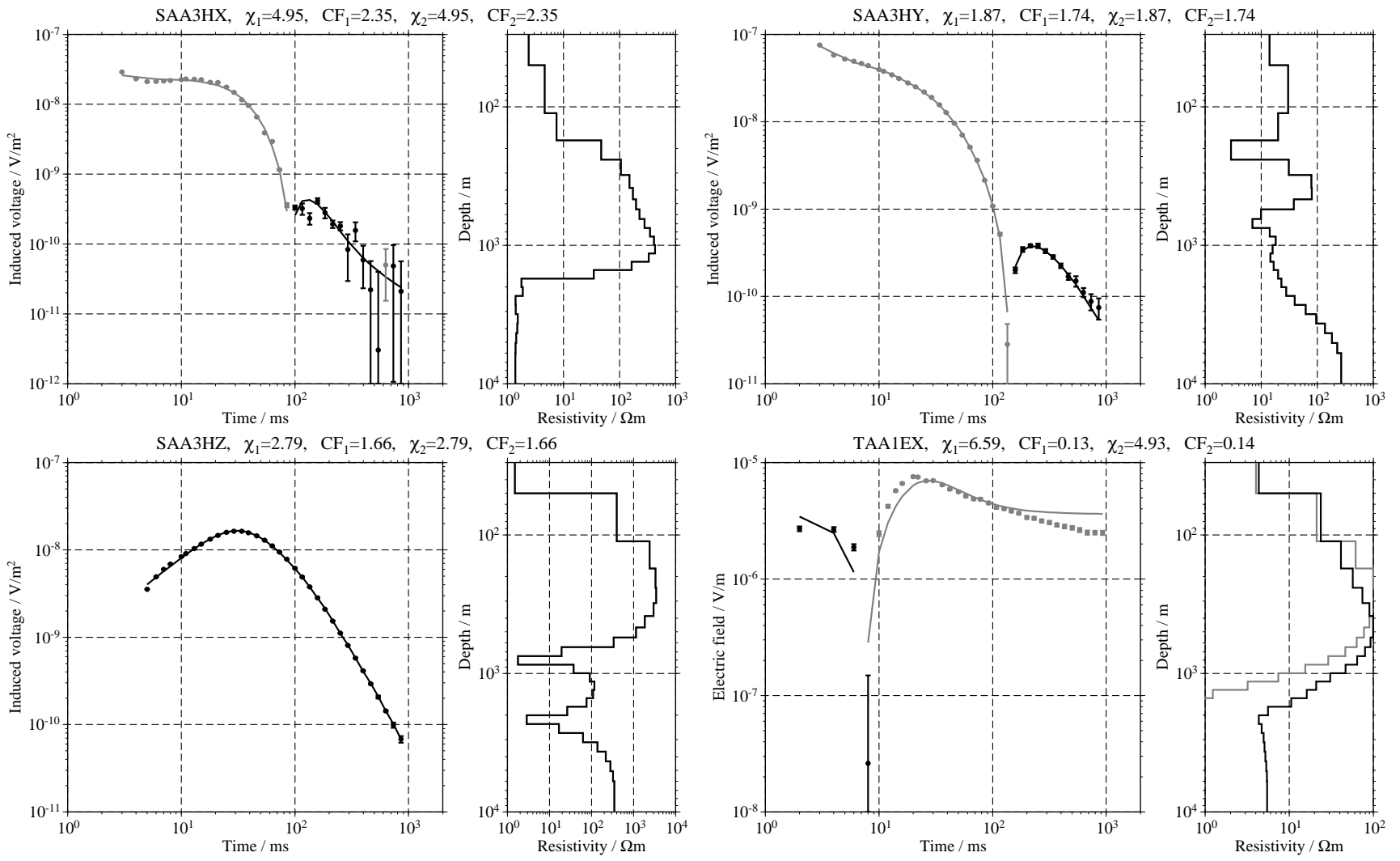


Figure C.51: Single inversion results for the transients measured at SAA and TAA;

Figure C.52: Single inversion results for the transients measured at TAA;

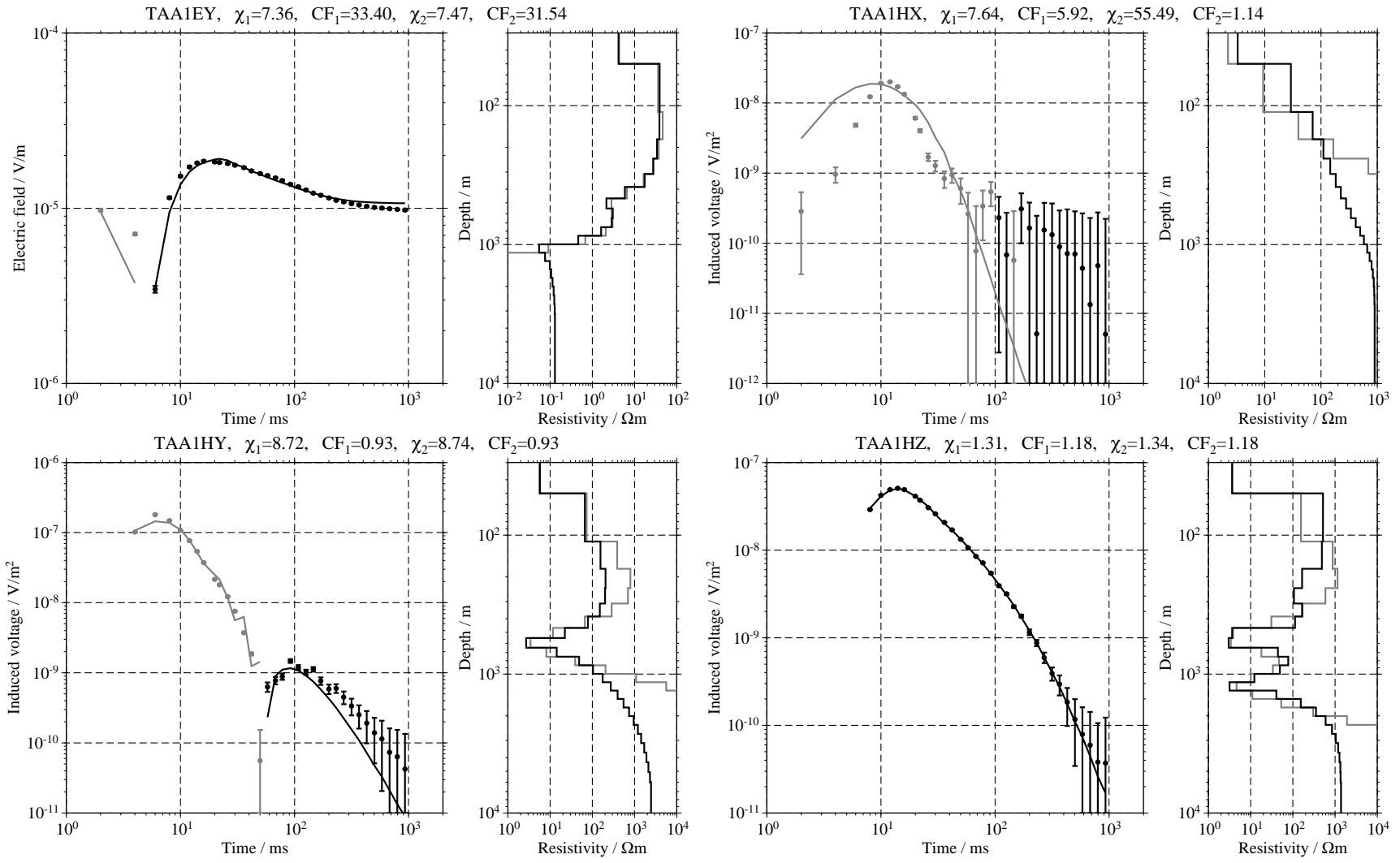


Figure C.53: Single inversion results for the transients measured at TAB;

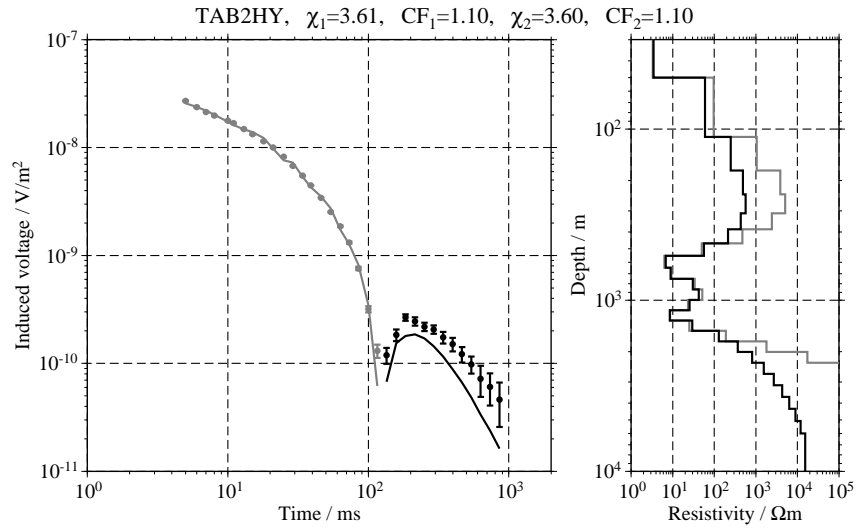
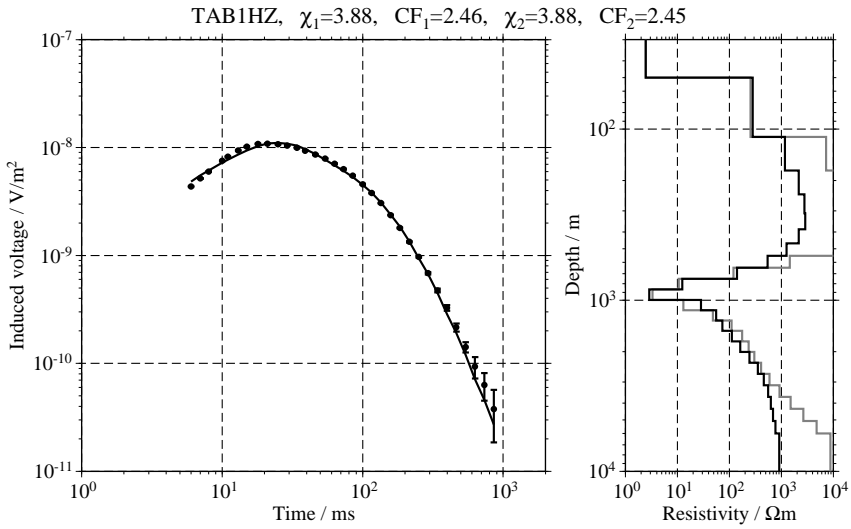
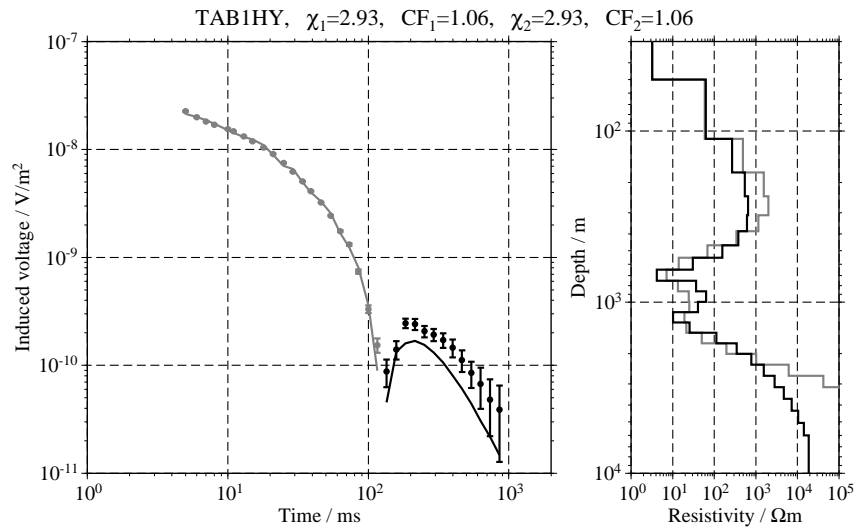
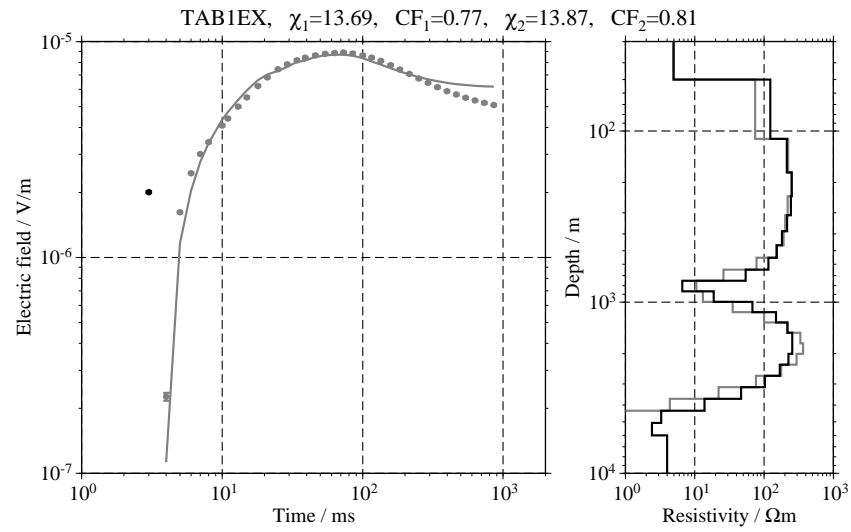


Figure C.54: Single inversion results for the transients measured at TAB and TKA;

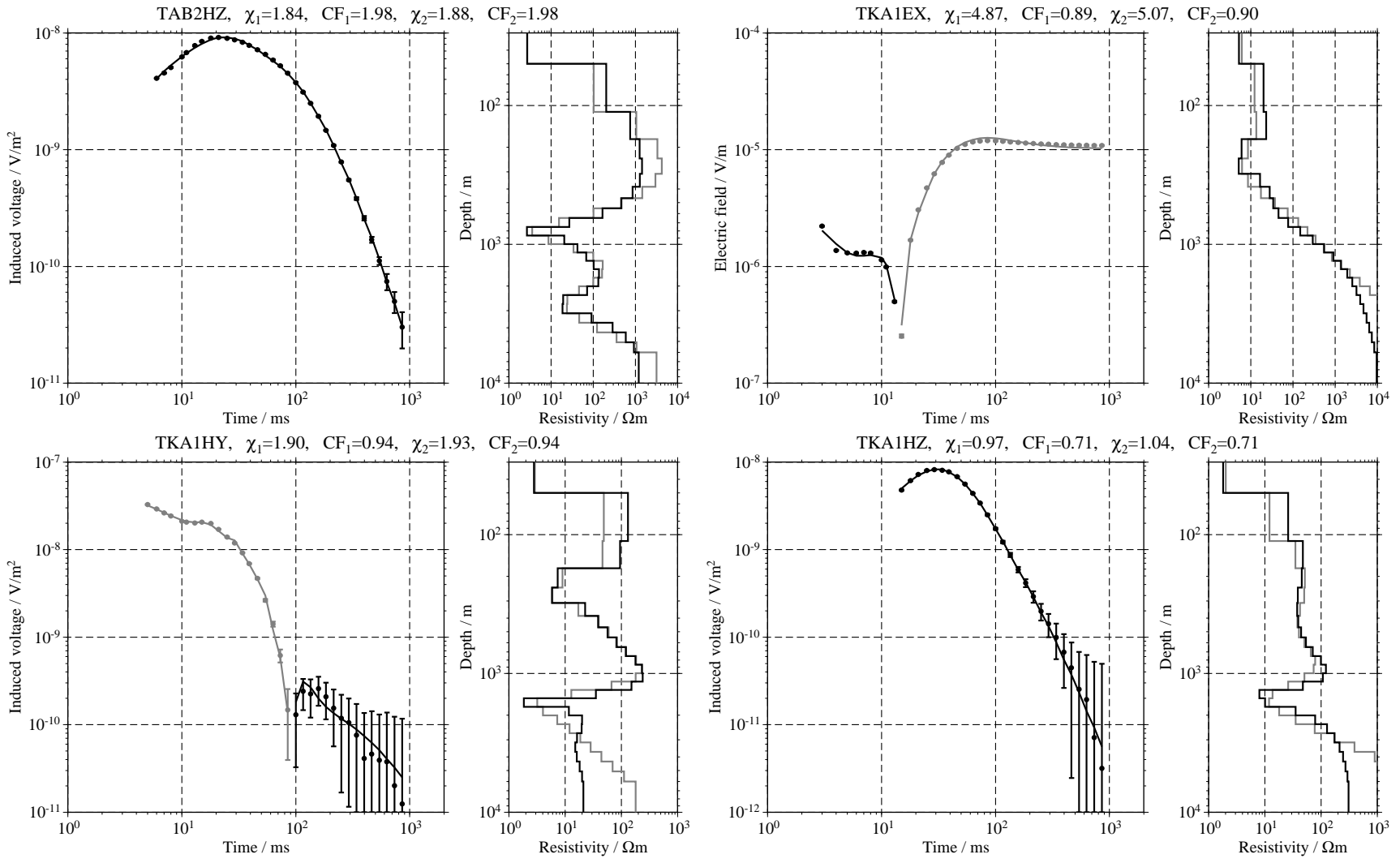


Figure C.55: Single inversion results for the transients measured at TKA and TKB;

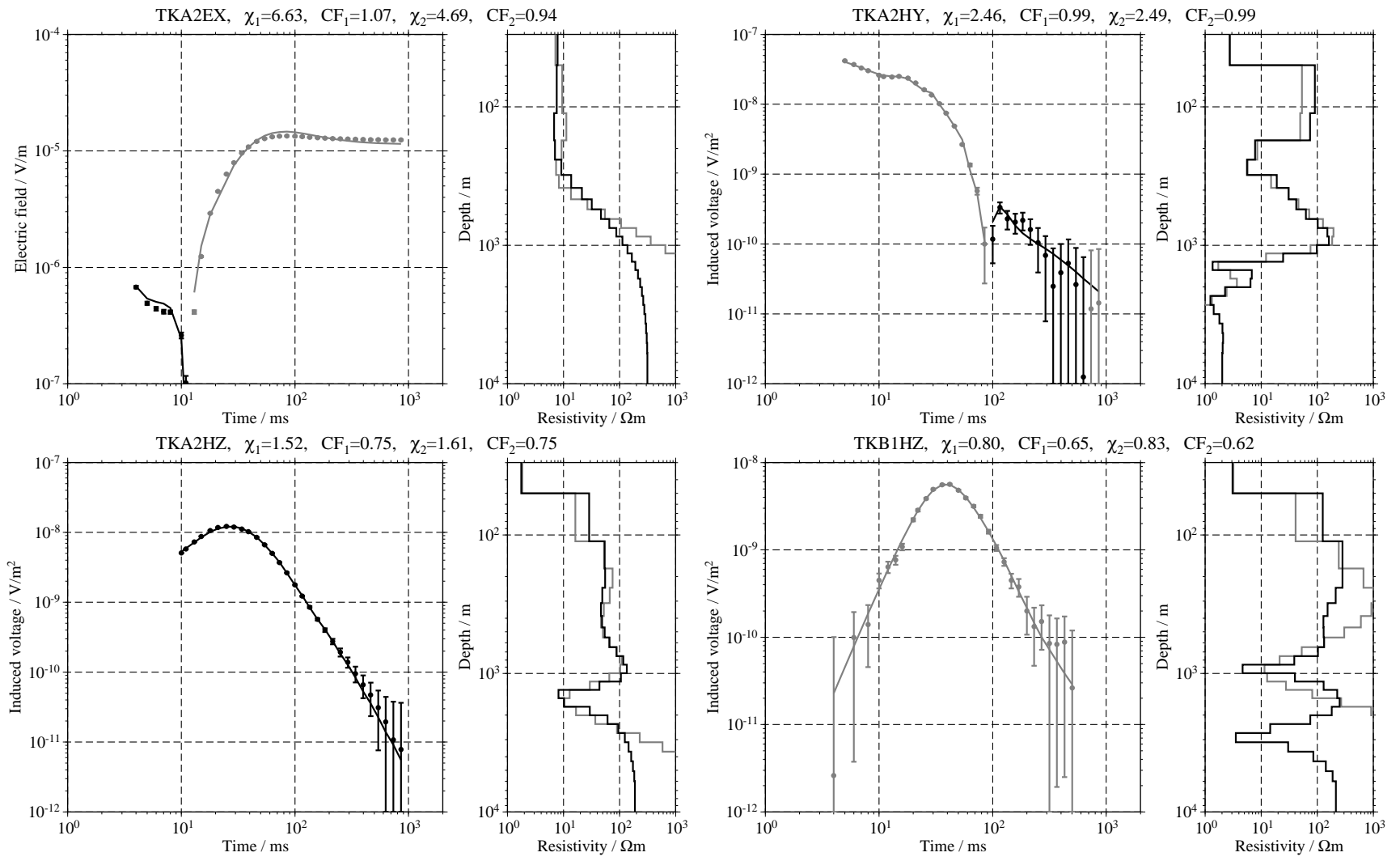


Figure C.56: Single inversion results for the transients measured at TKB and YAA;

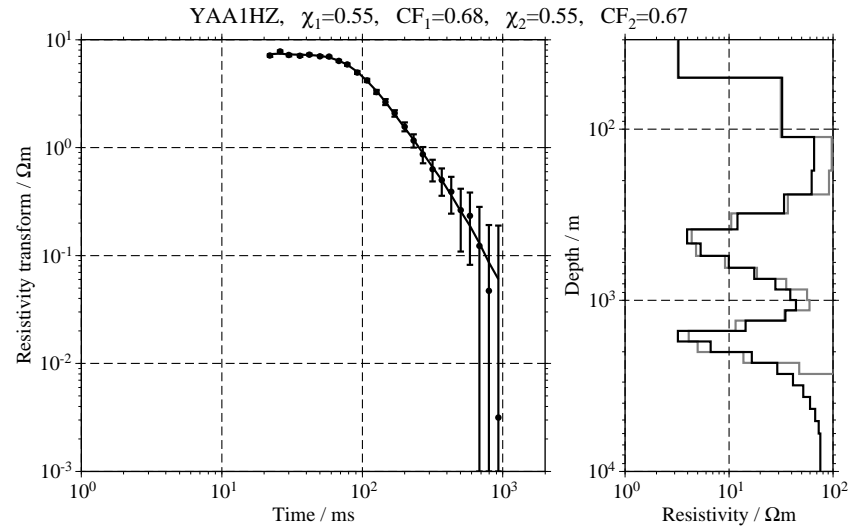
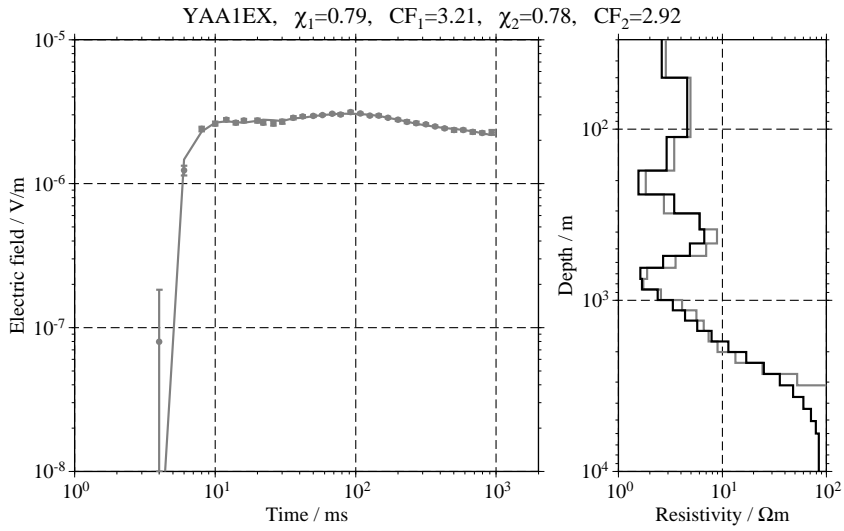
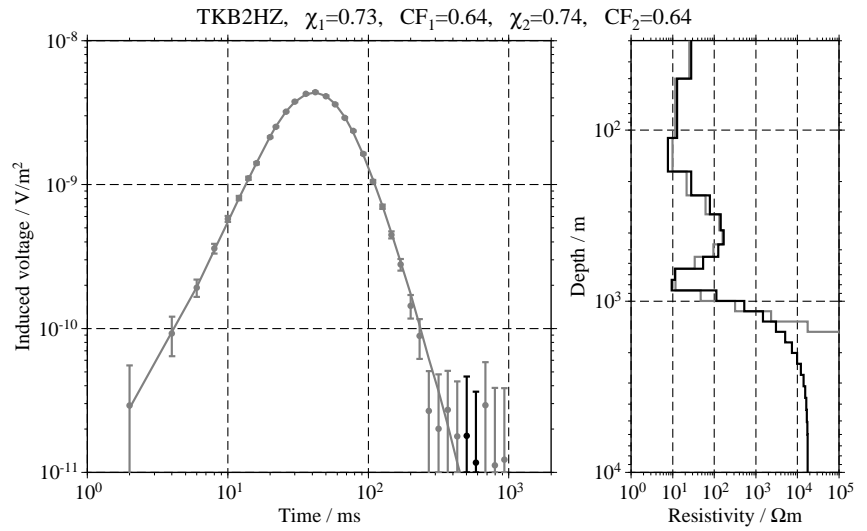
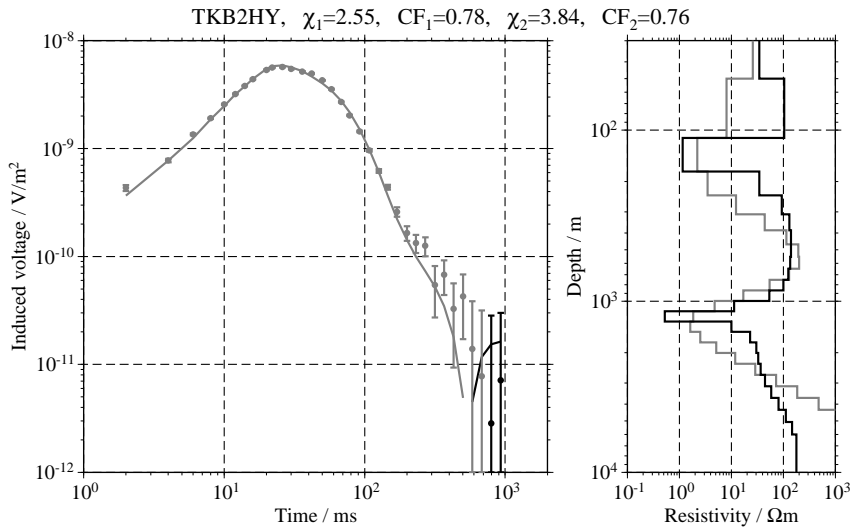


Figure C.57: Single inversion results for the transients measured at YAA.

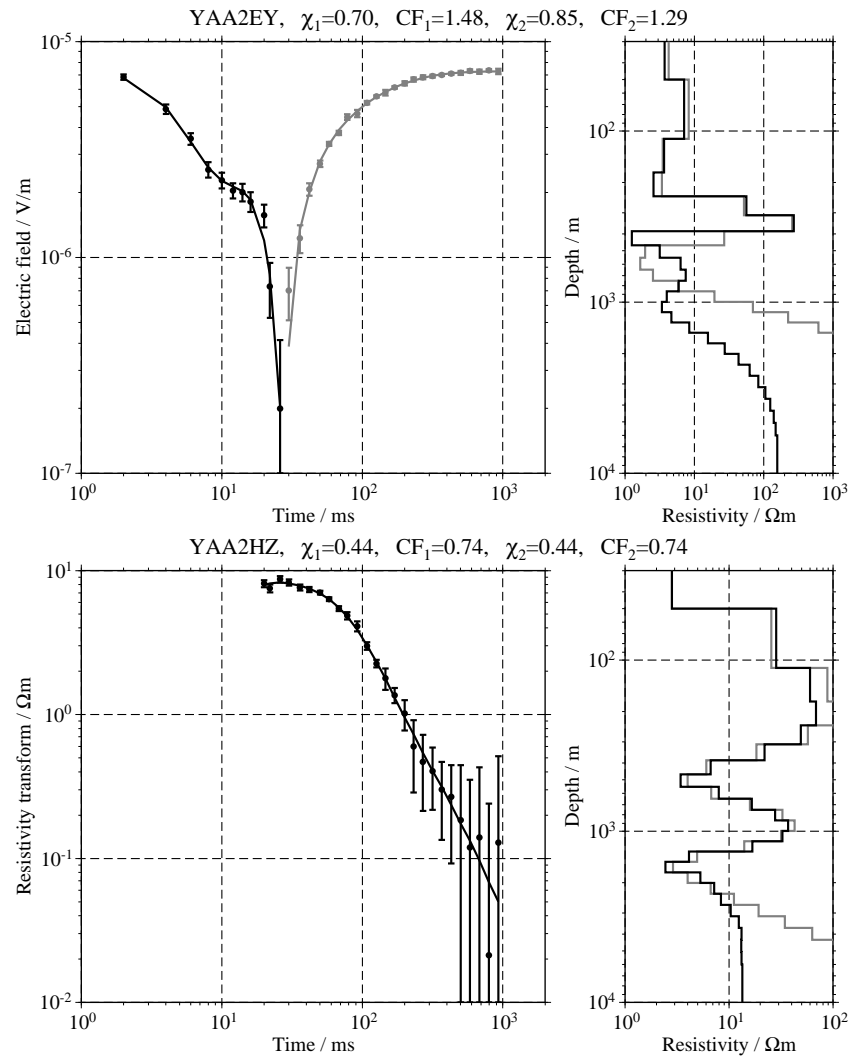
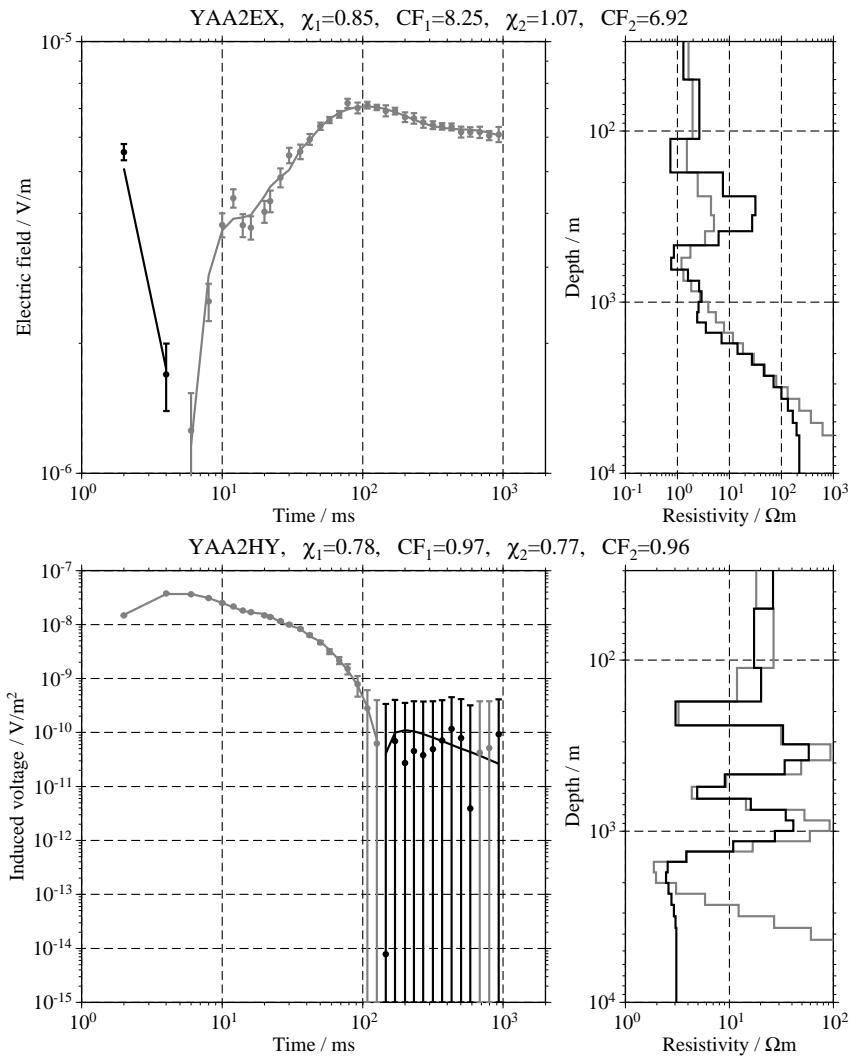


Figure C.58: Single inversion results for the transients measured at YAB;

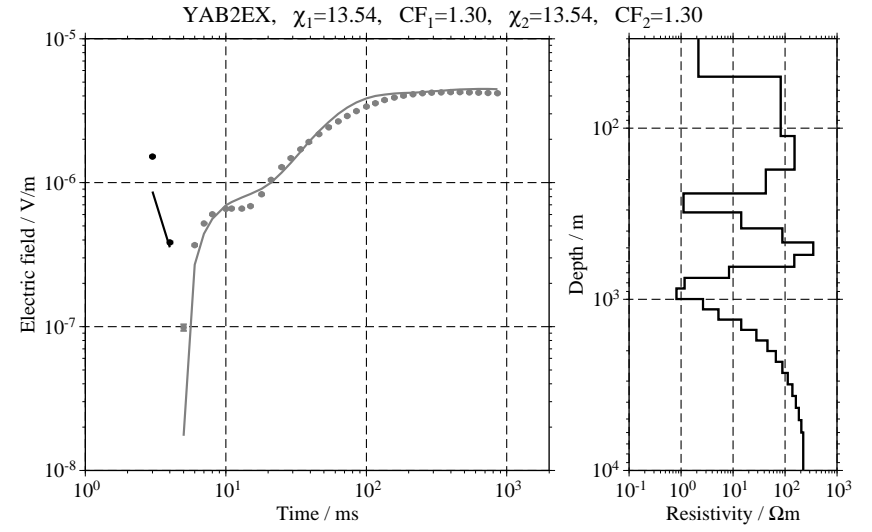
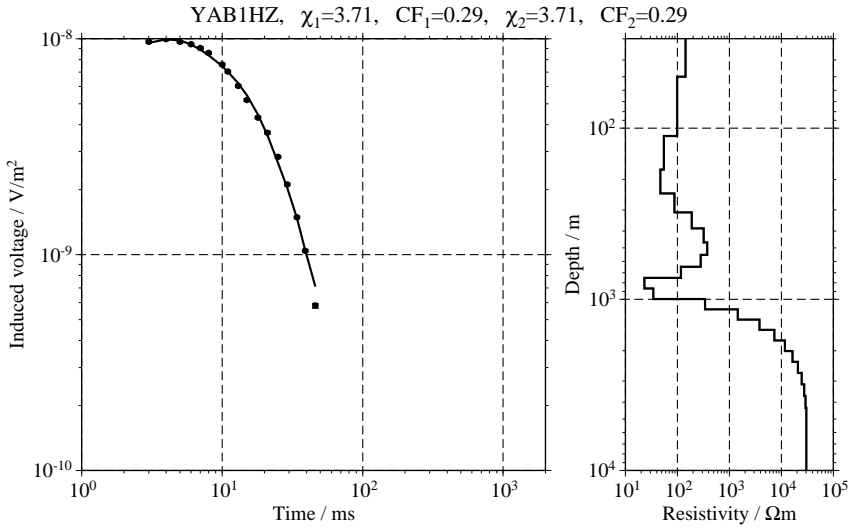
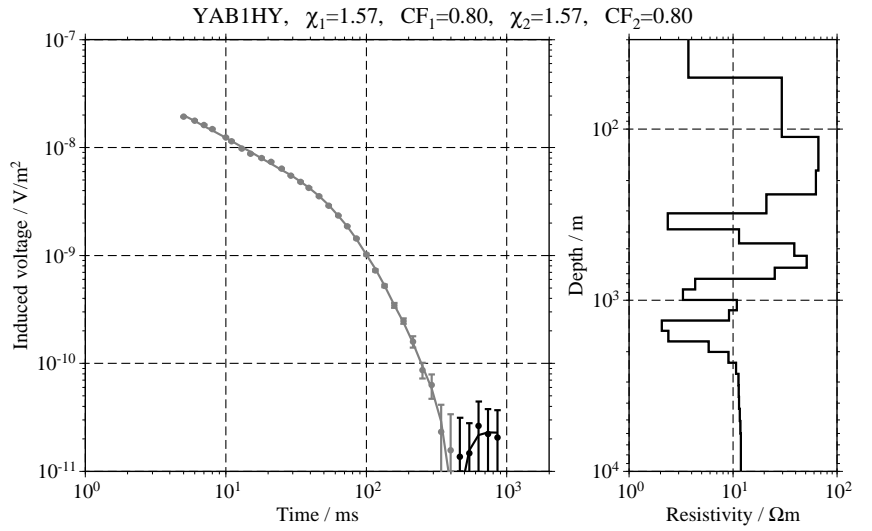
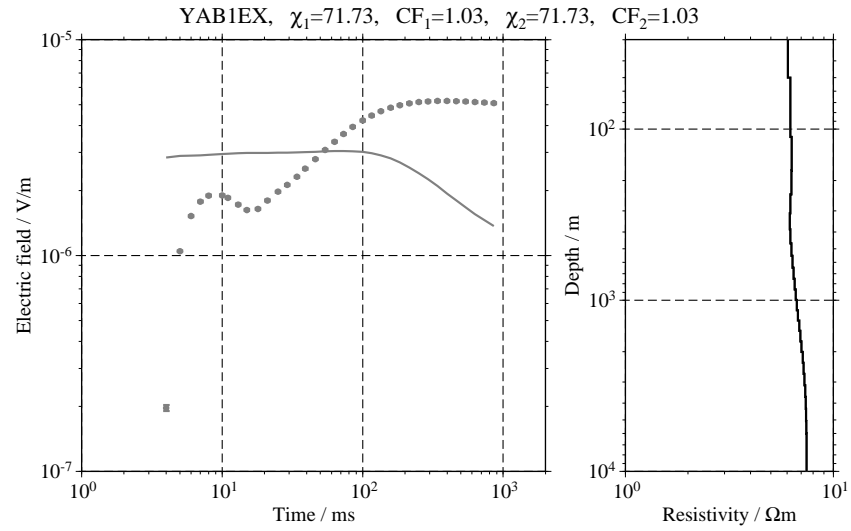
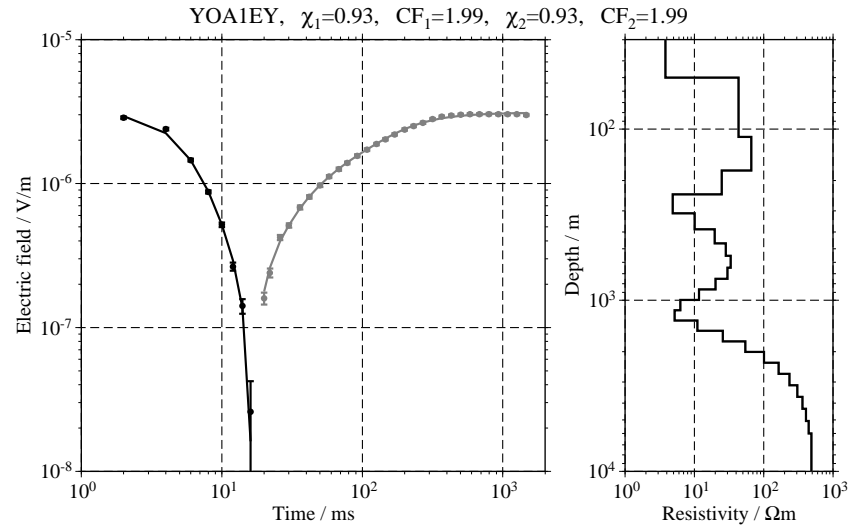
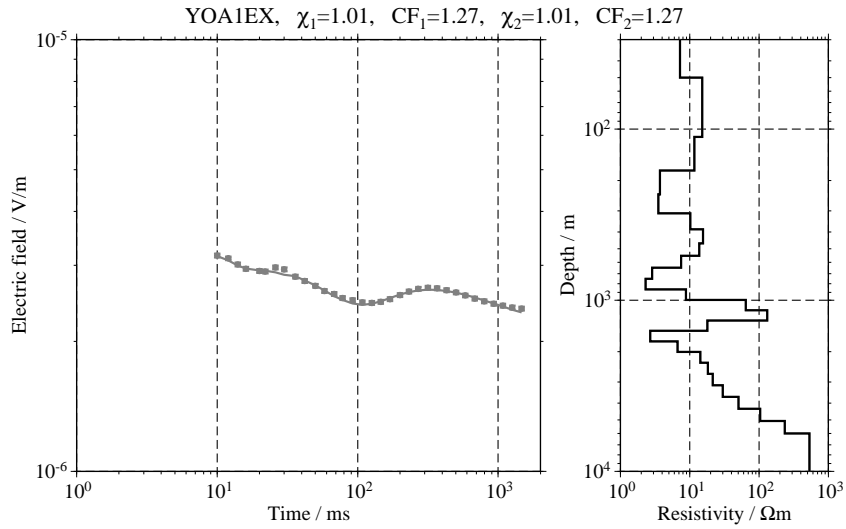
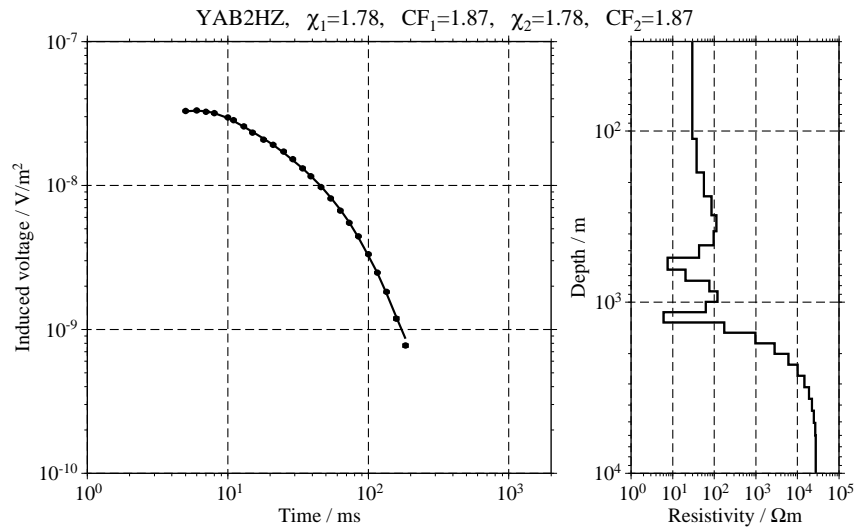
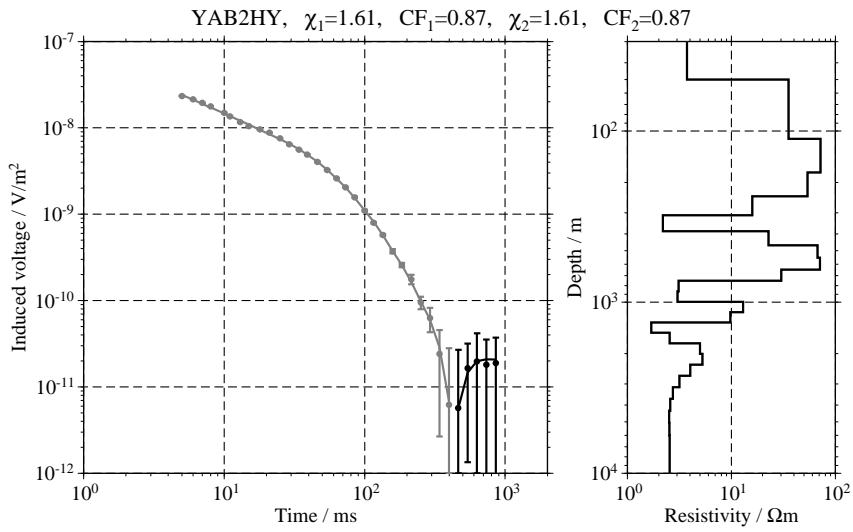


Figure C.59: Single inversion results for the transients measured at YAB and YOA;



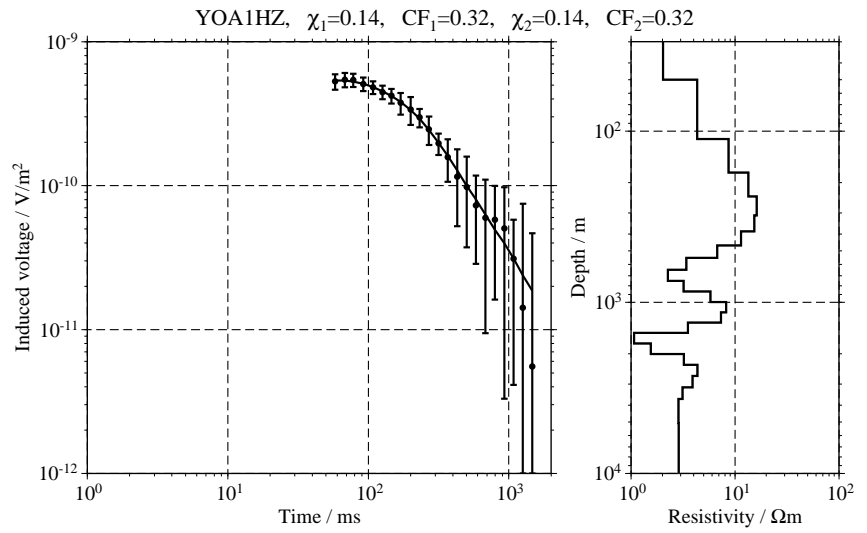
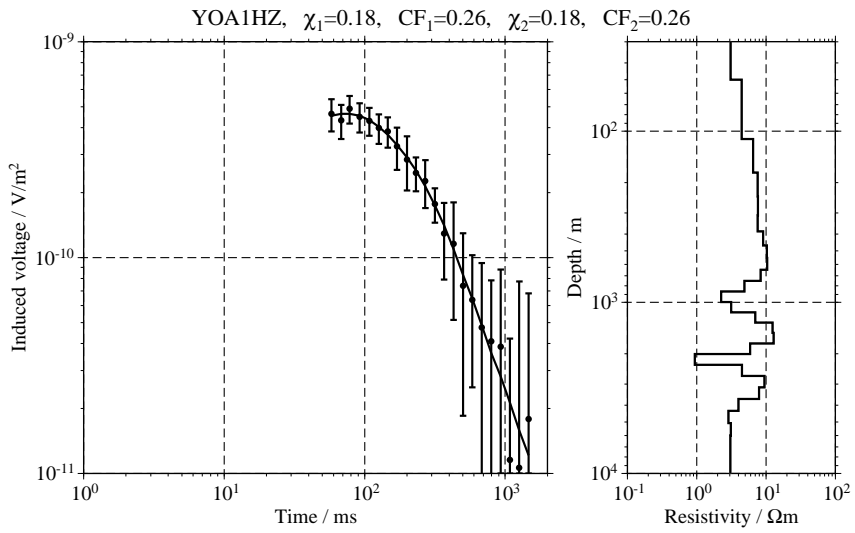
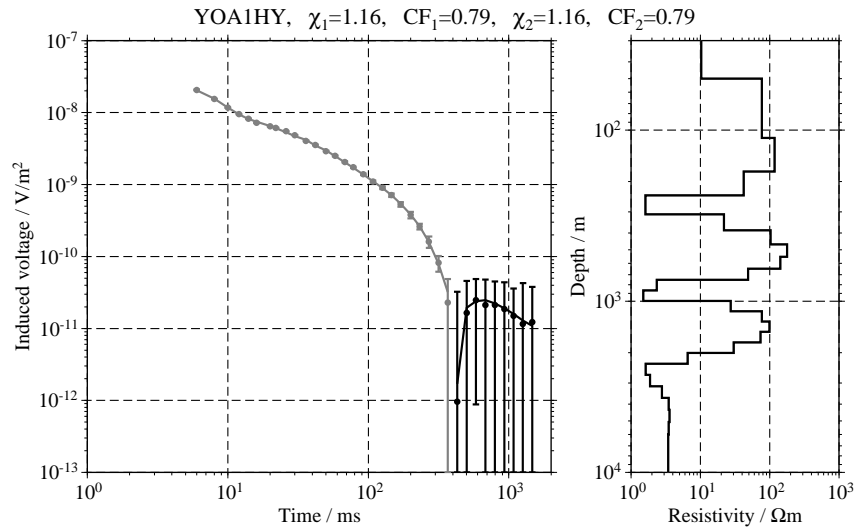
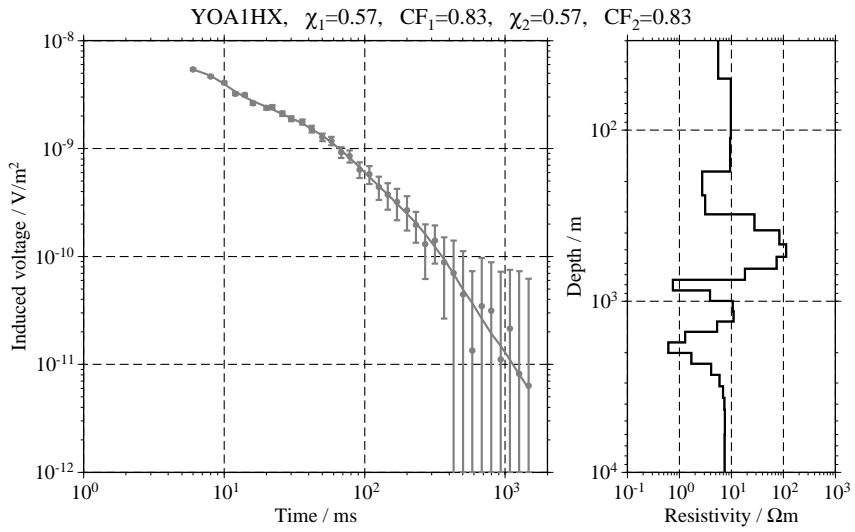
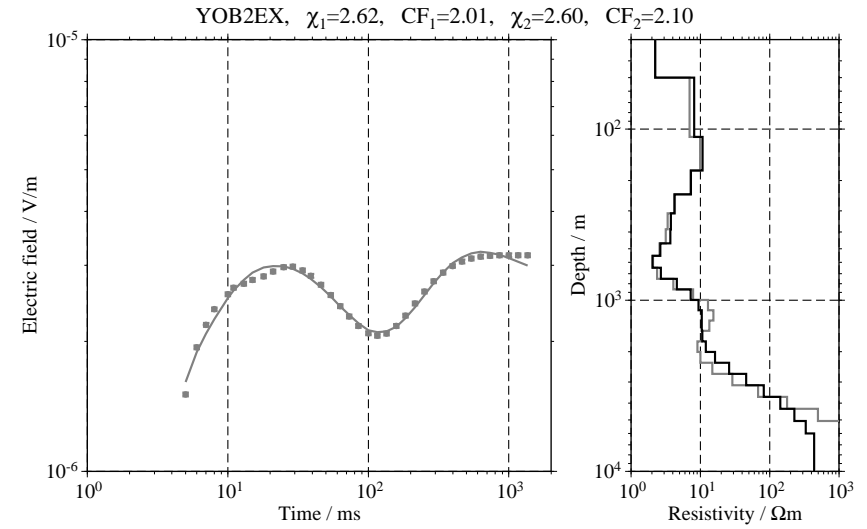
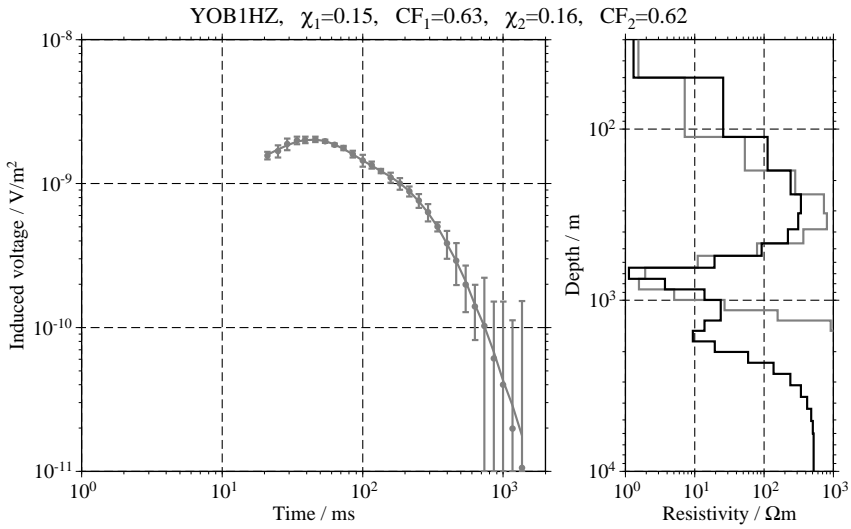
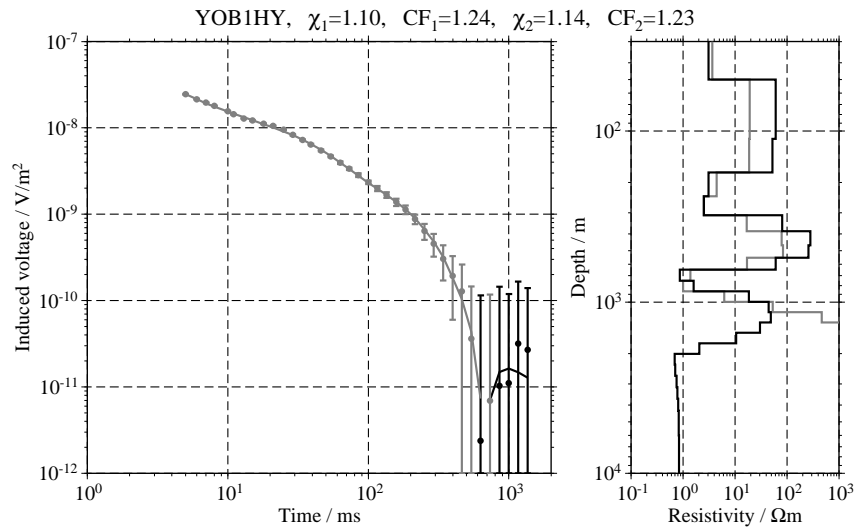
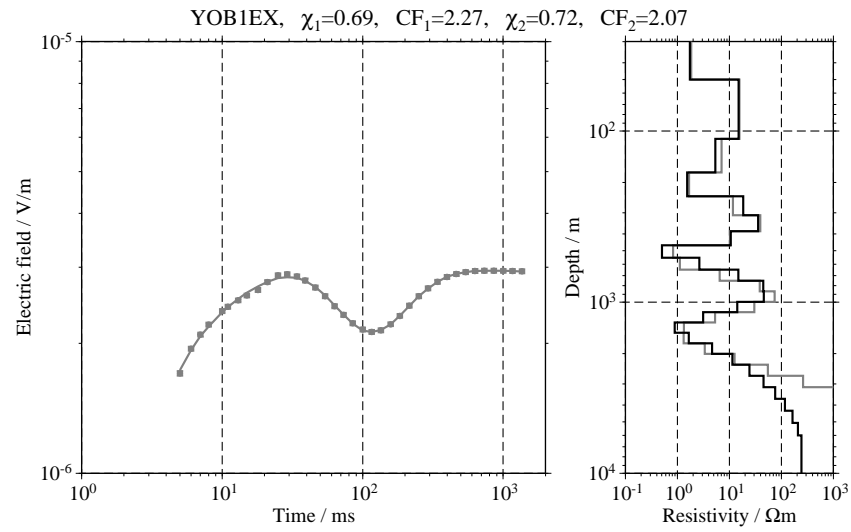


Figure C.60: Single inversion results for the transients measured at YOA;

Figure C.61: Single inversion results for the transients measured at YOB;



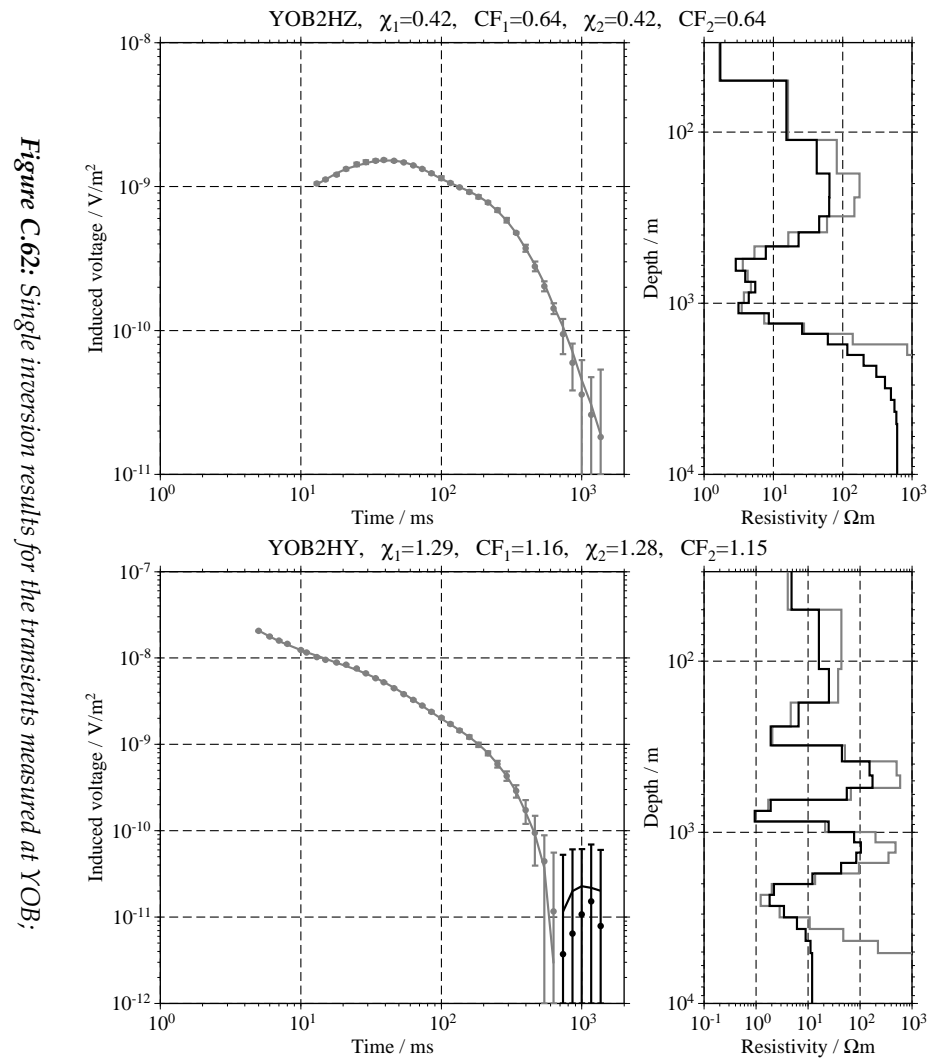


Figure C.62: Single inversion results for the transients measured at YOB;

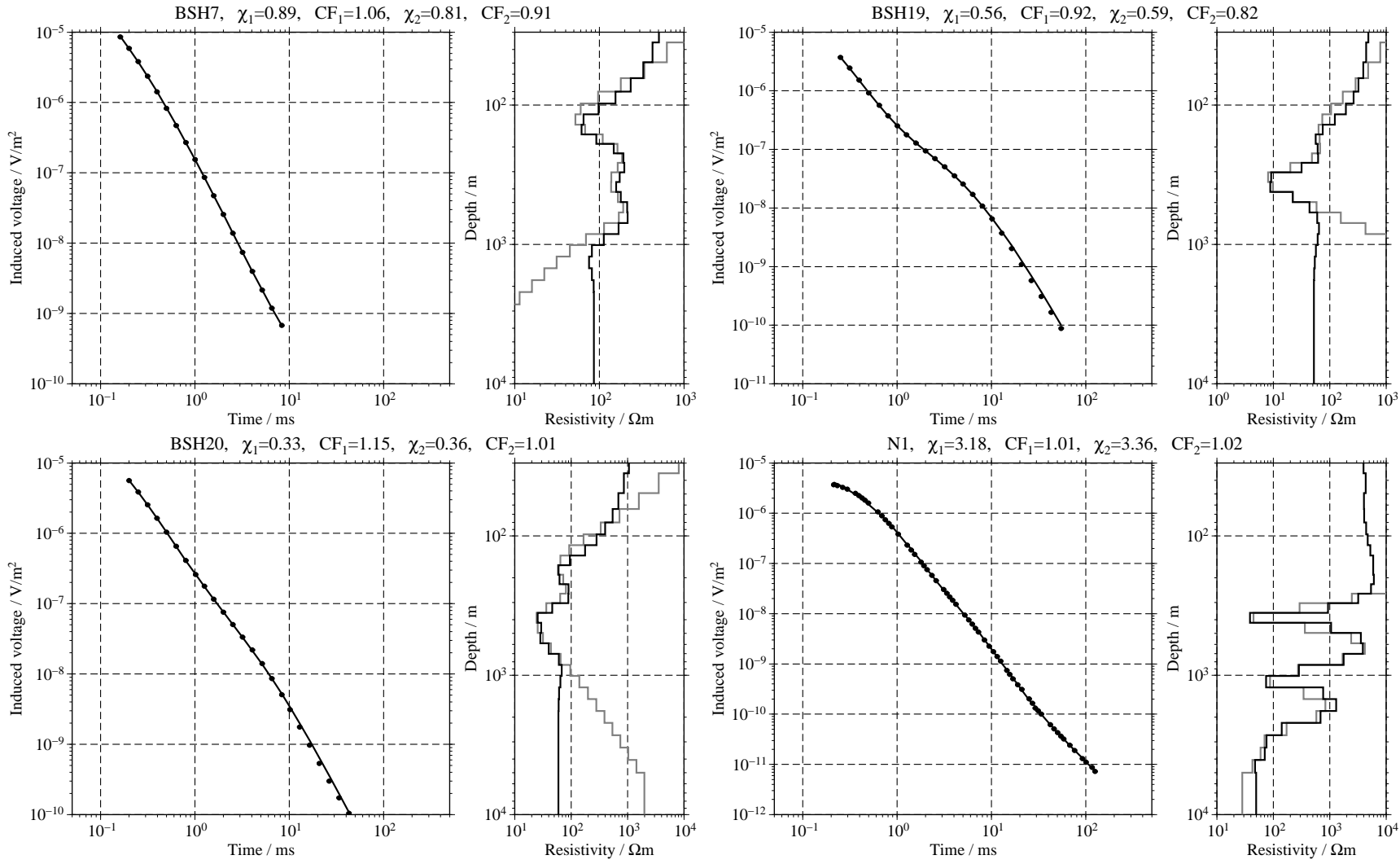


Figure C.63: Single inversion results for the SHOTEM-transients BSH7, BSH19, BSH20 and N1.

Figure C.64: Single inversion results for the SHOTEM-transients N2 to N5;

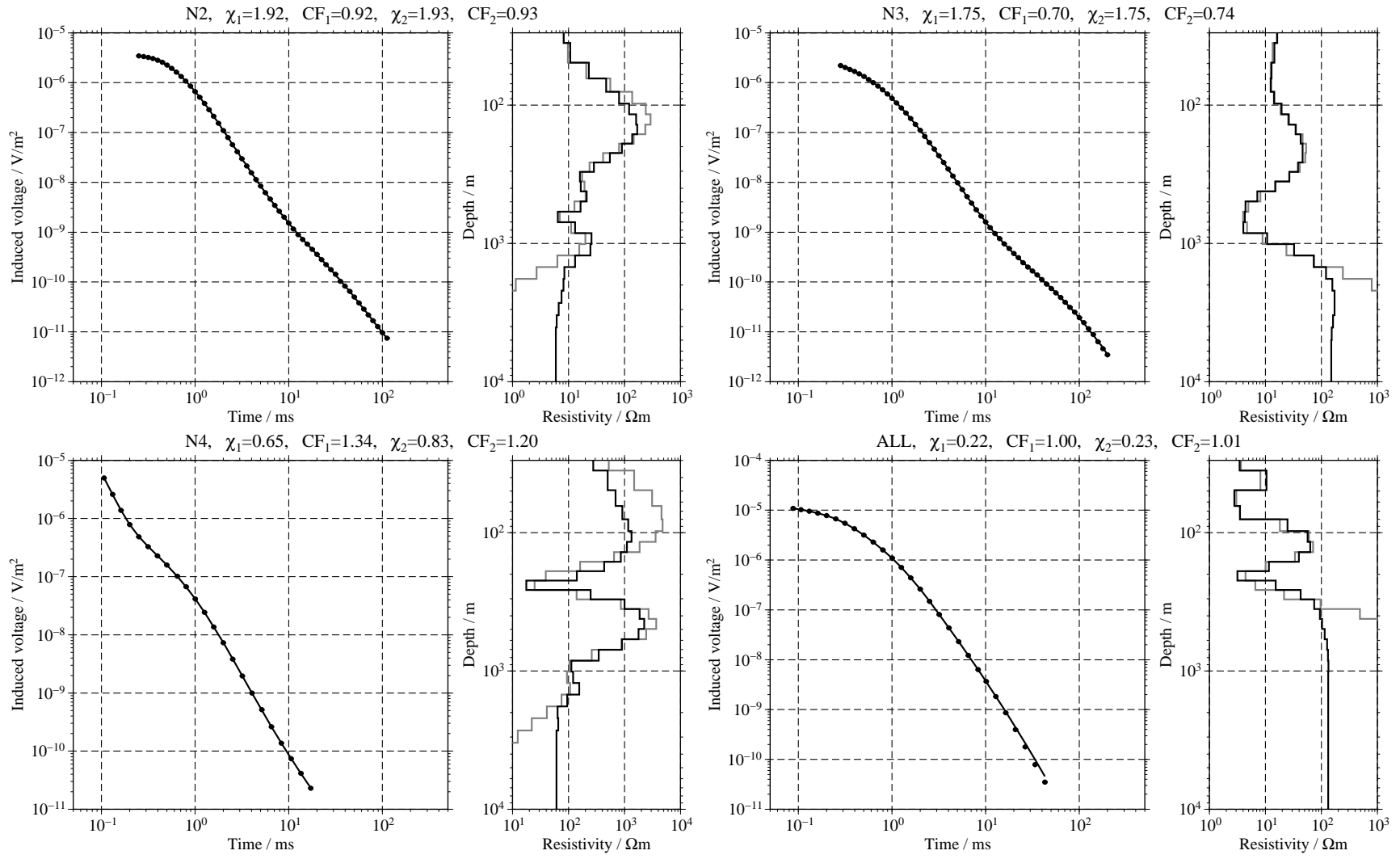


Figure C.65: Single inversion results for the SHOTEM-transients N6 to N9;

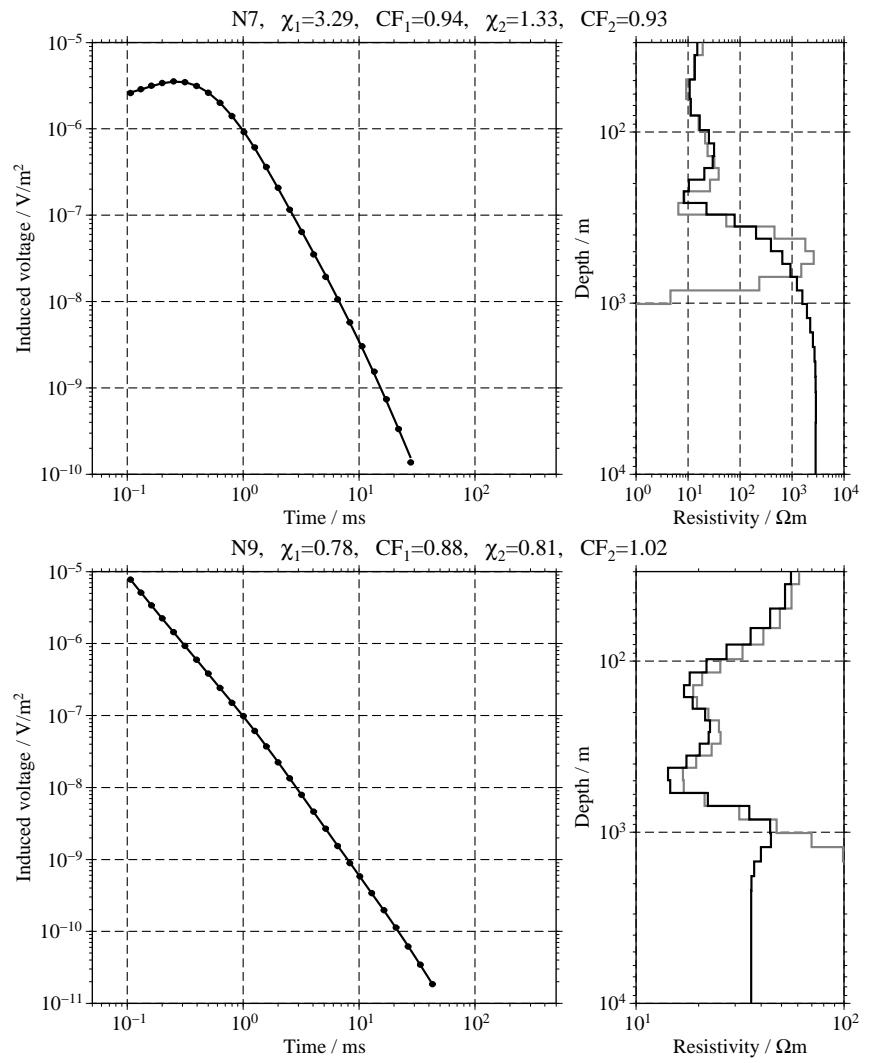
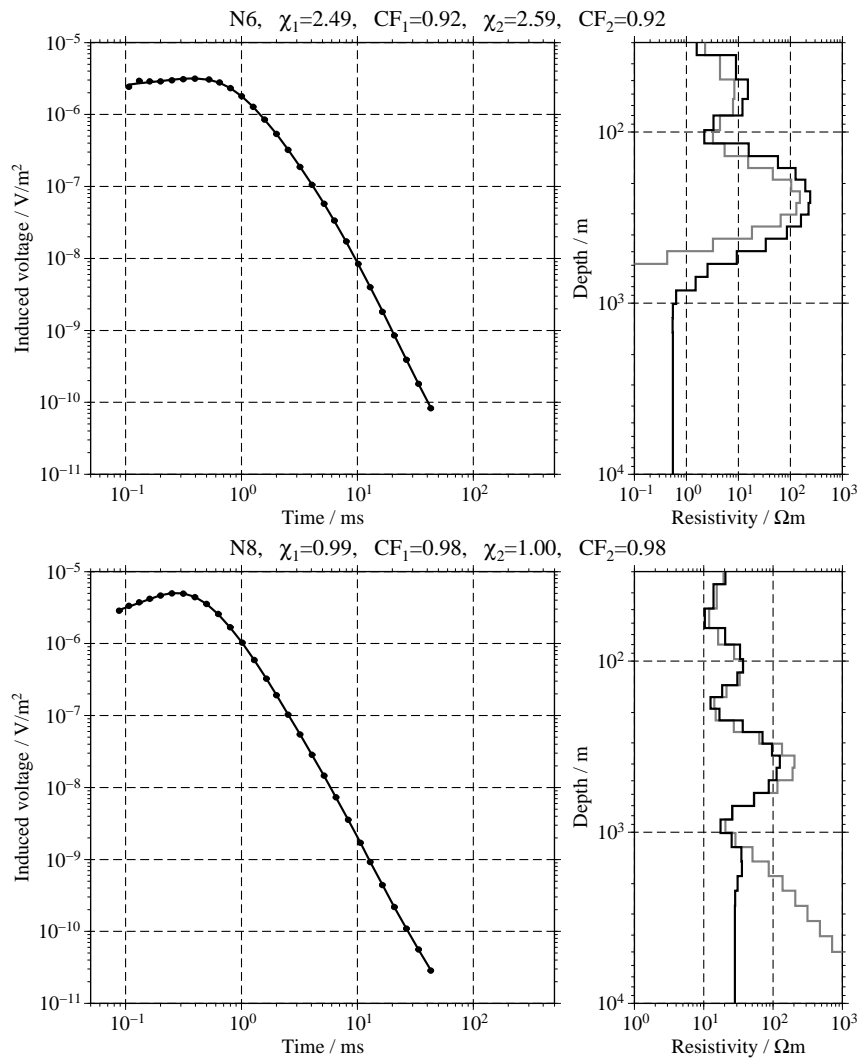
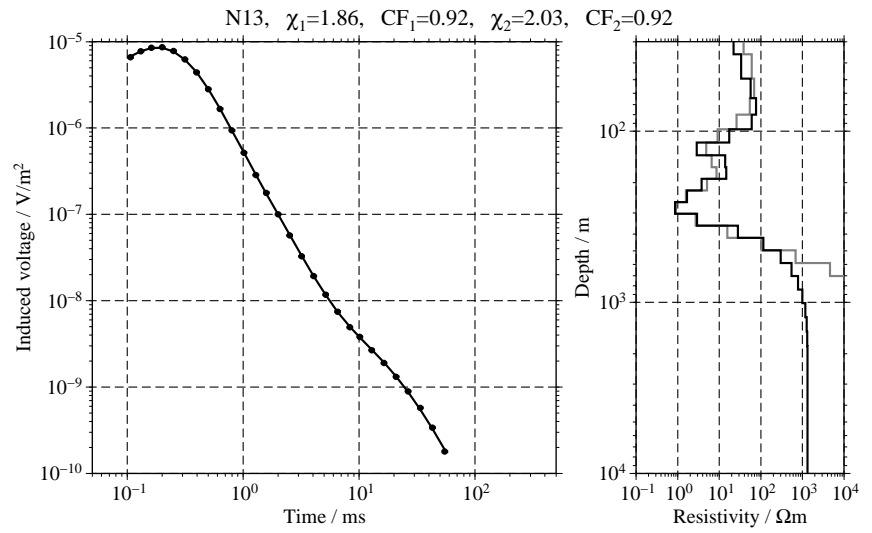
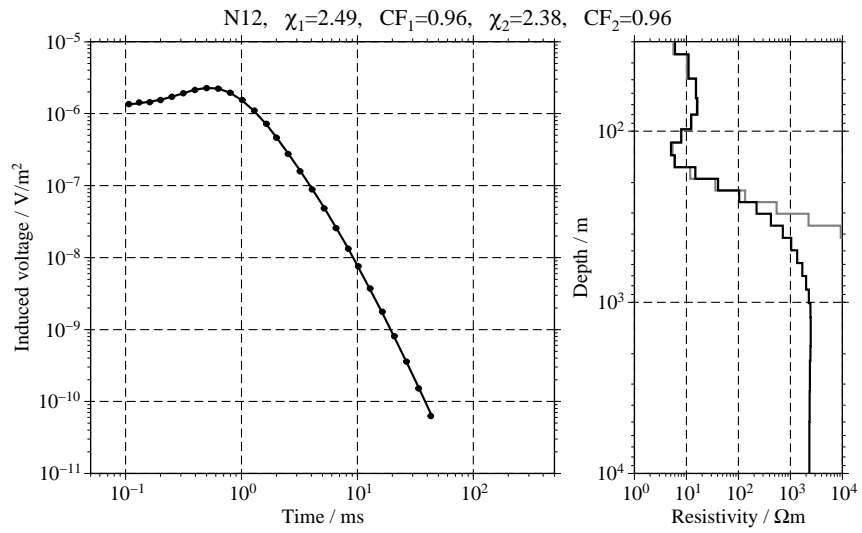
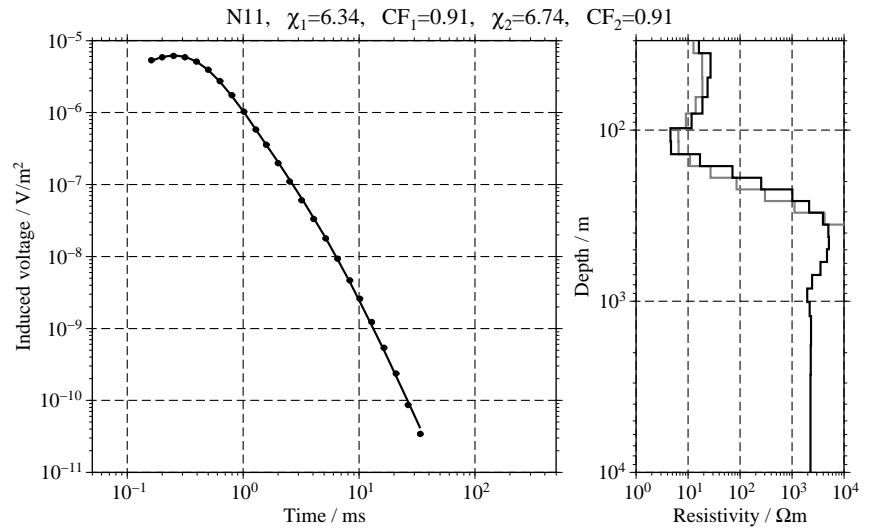
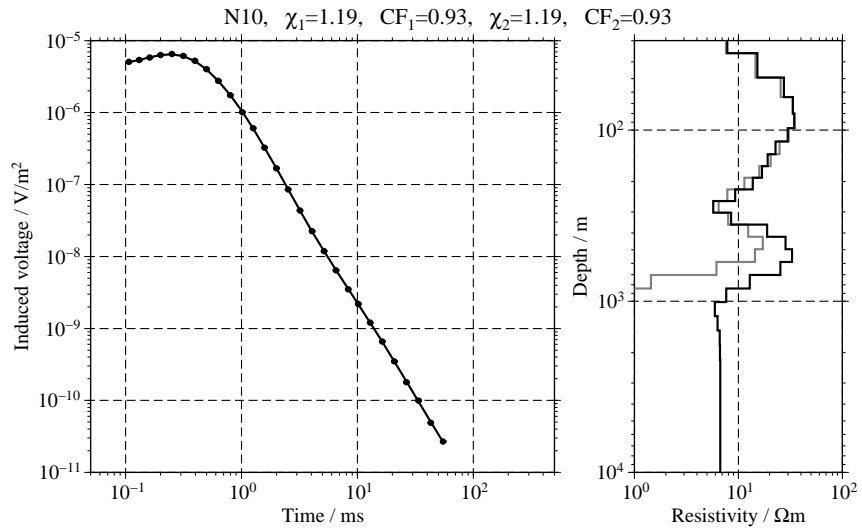


Figure C.66: Single inversion results for the SHOTEM-transients N10 to N13;



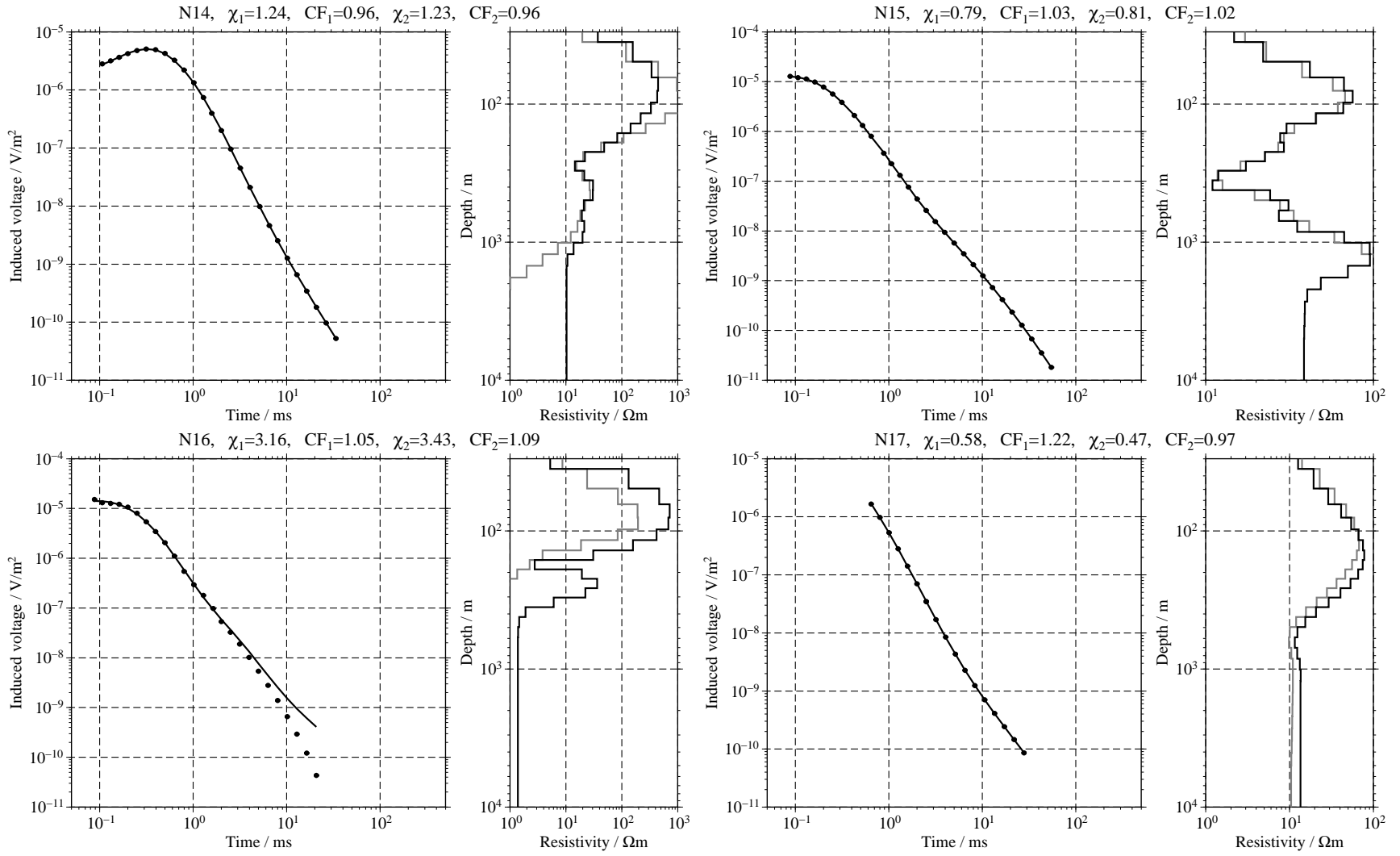


Figure C.67: Single inversion results for the SHOTEM-transients N14 to N17;

Figure C.68: Single inversion results for the SHOTEM-transients N18 to N21;

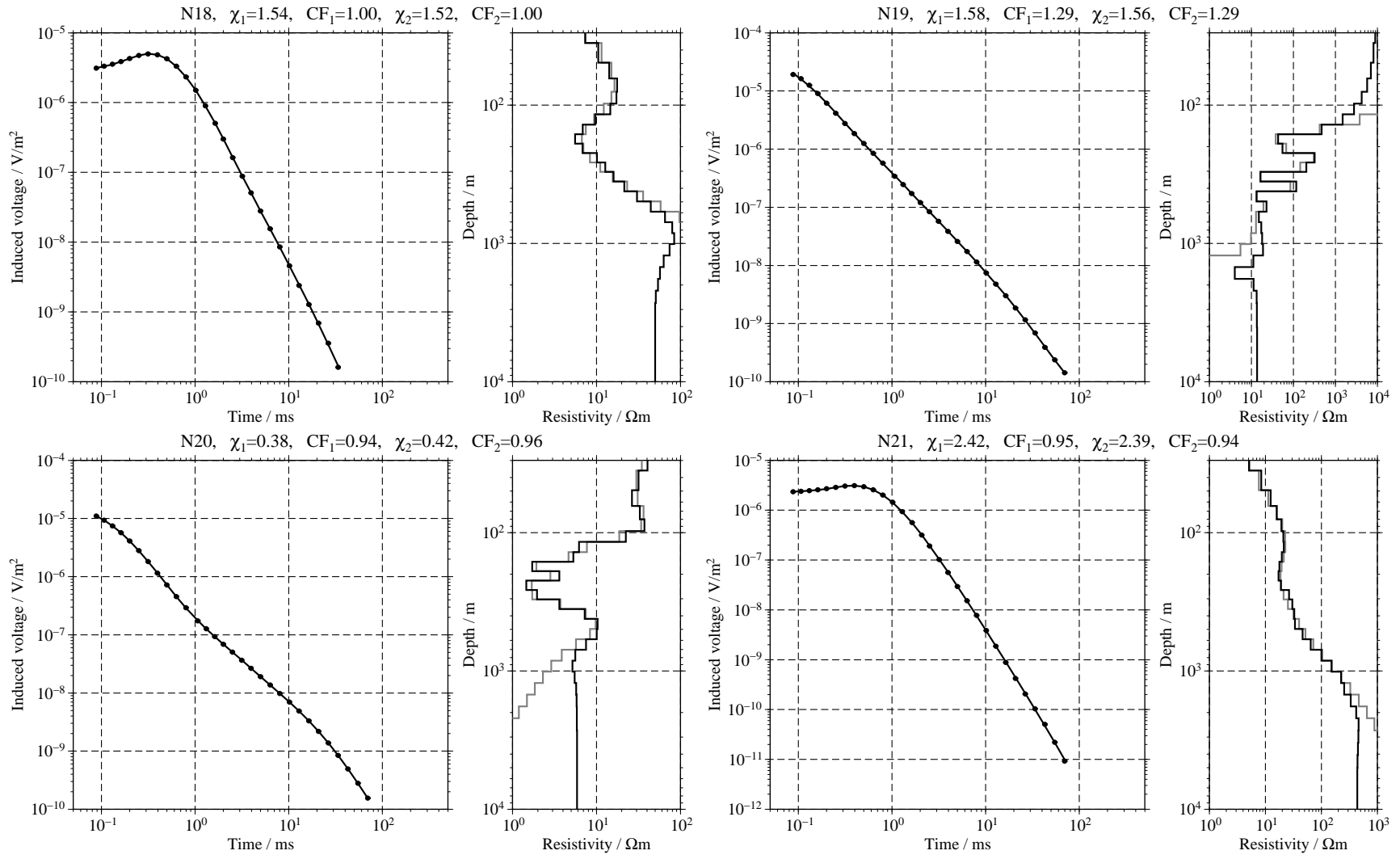


Figure C.69: Single inversion results for the SHOTEM-transients N22 to N25;

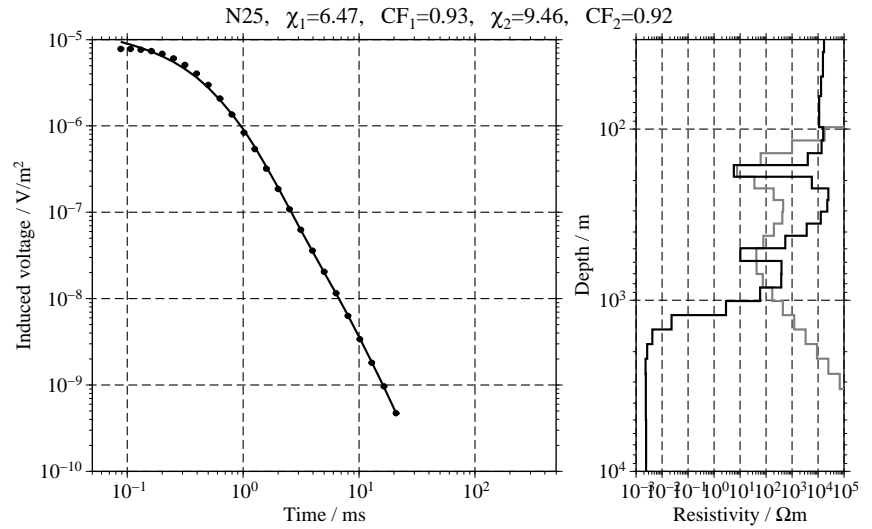
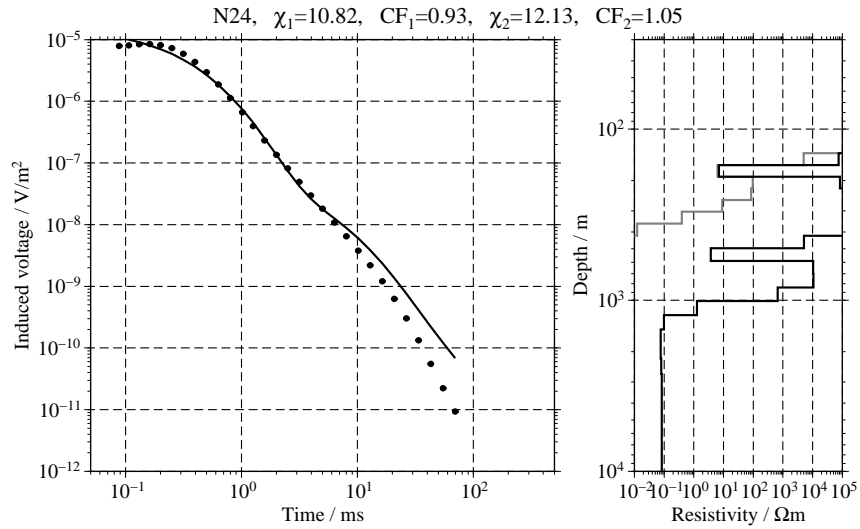
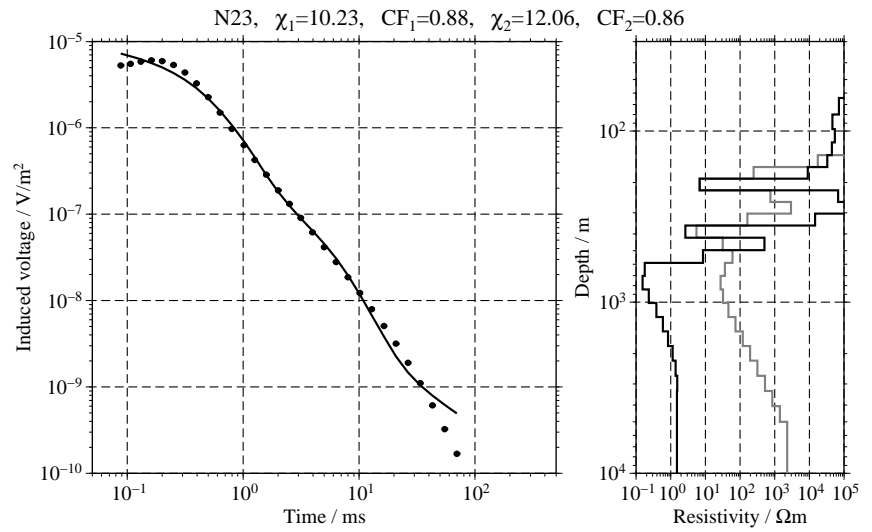
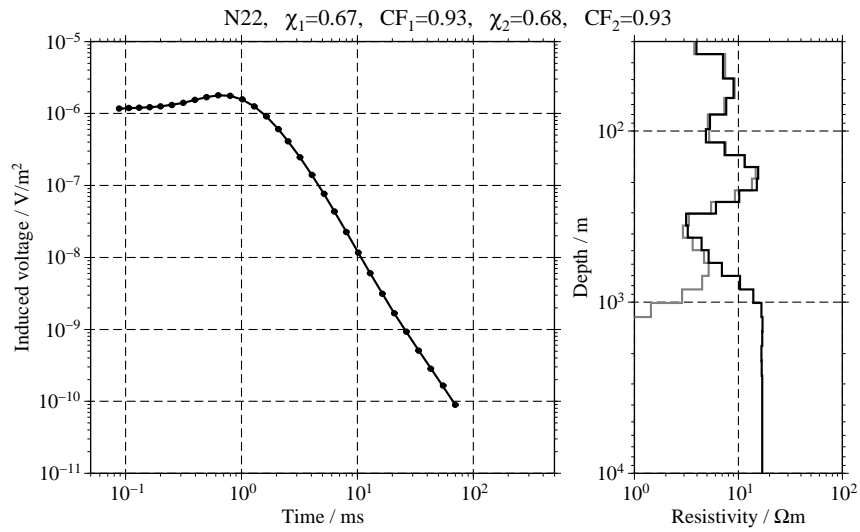


Figure C.70: Single inversion results for the SHOTEM-transients N26 to N29;

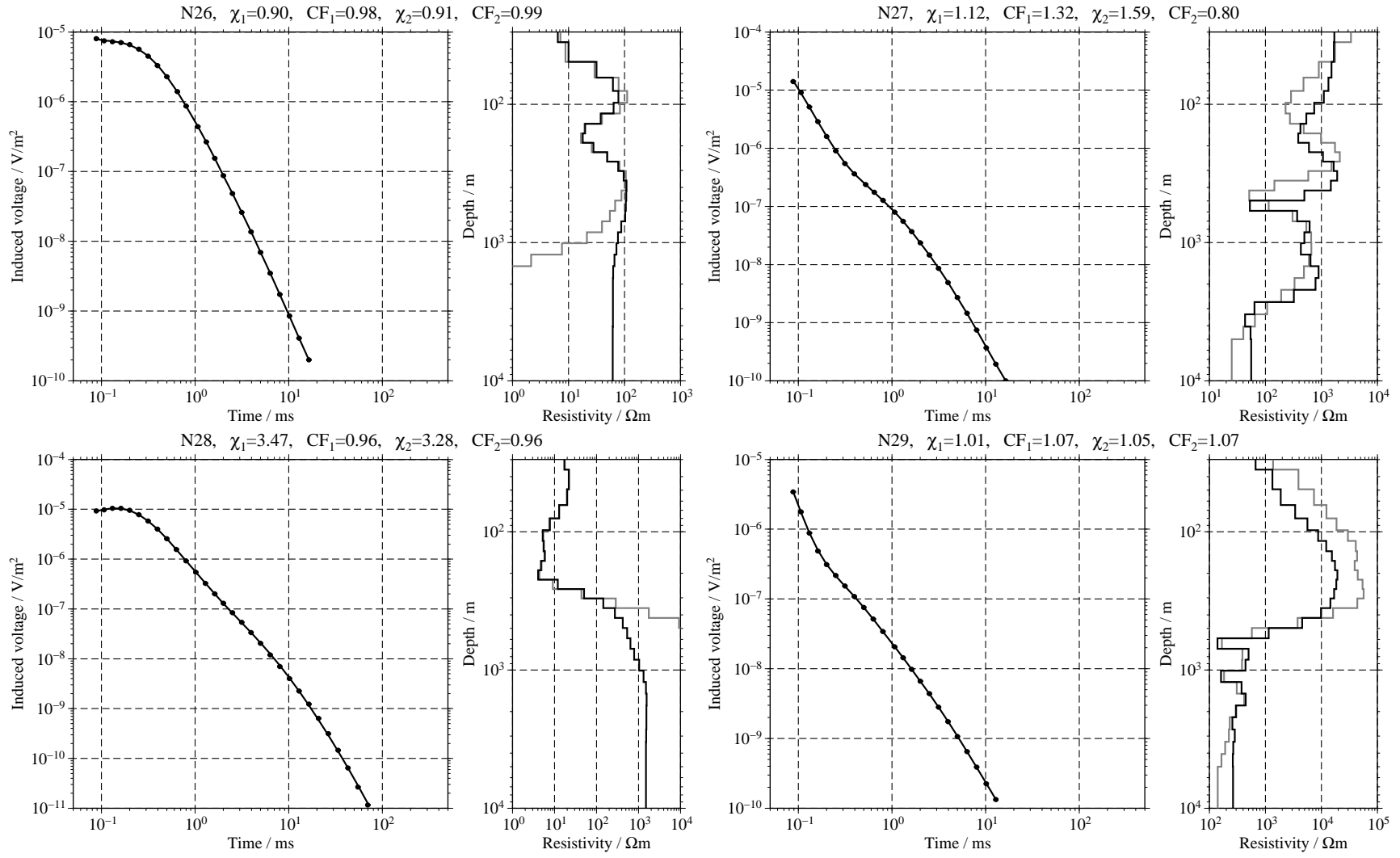
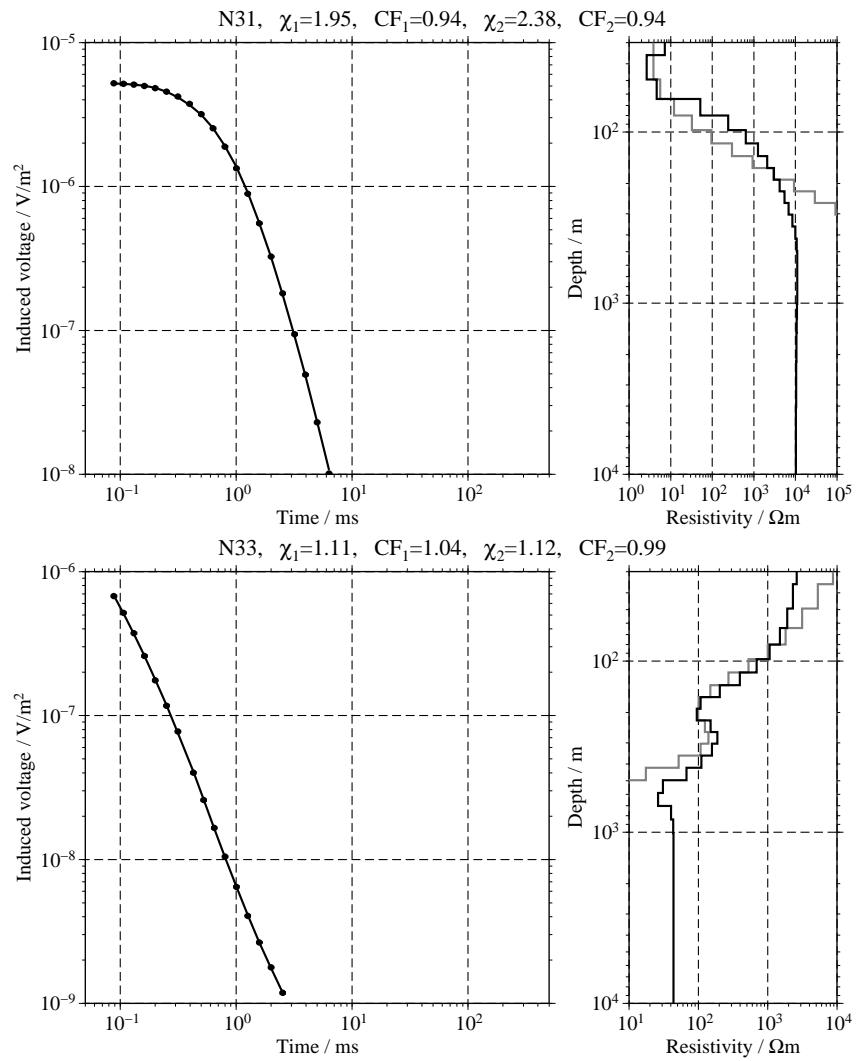
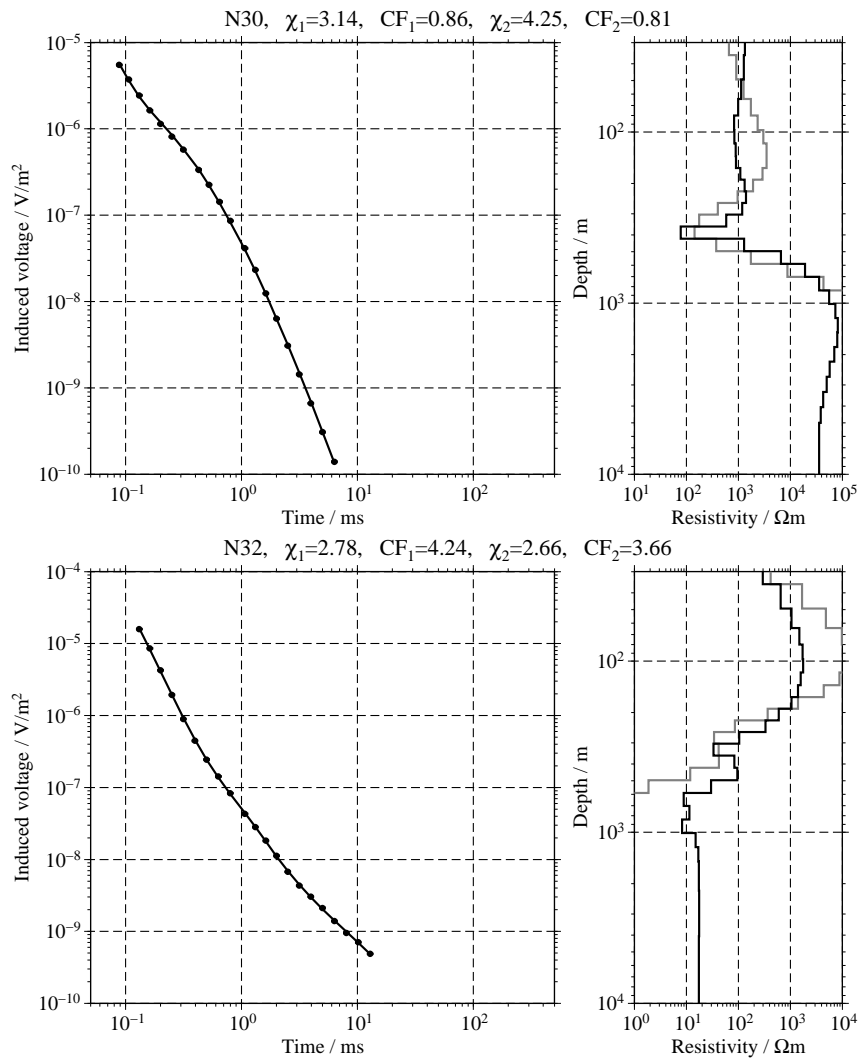


Figure C.71: Single inversion results for the SHOTEM-transients N30 to N33;



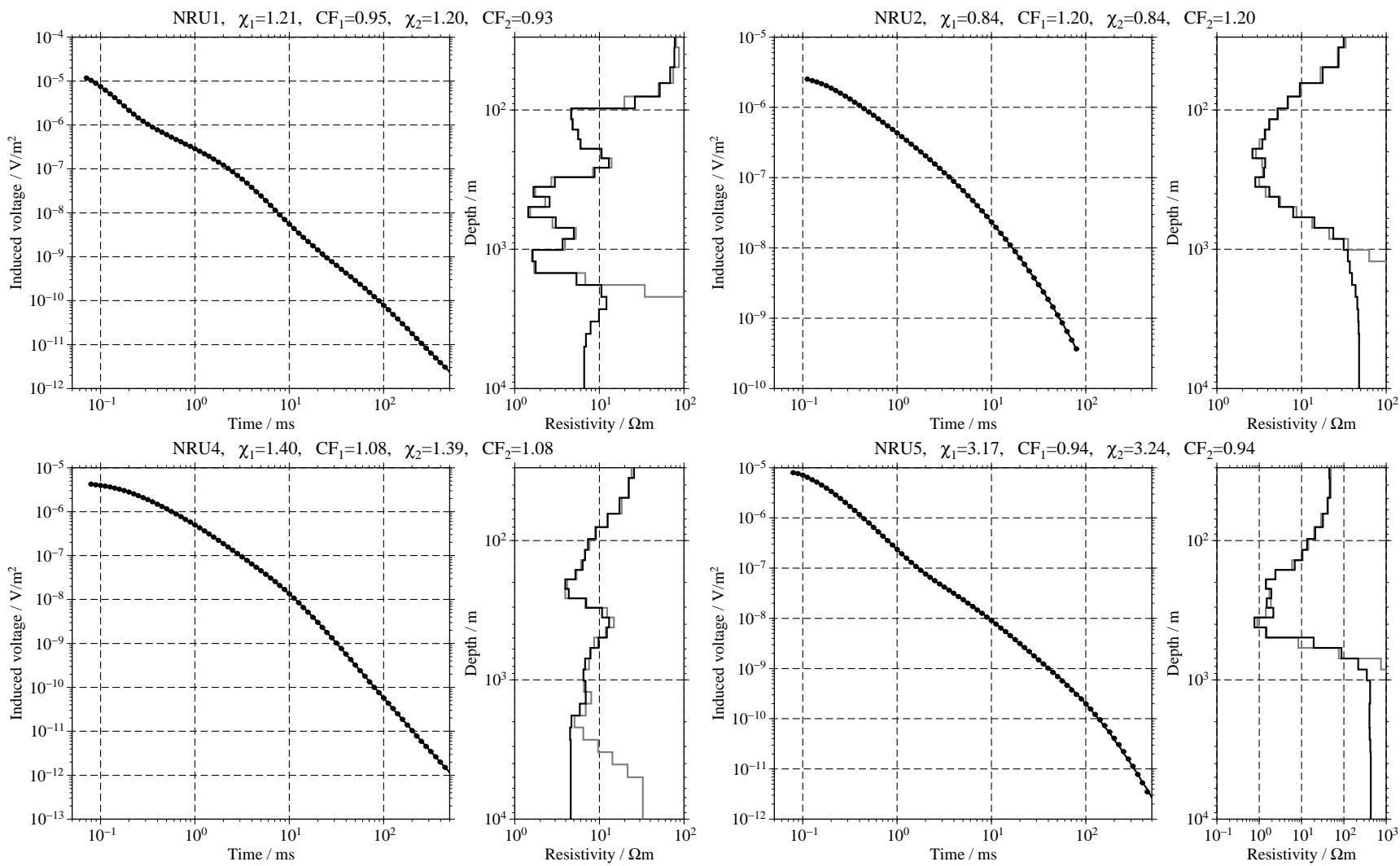


Figure C.72: Single inversion results for the SHOTEM-transients NRU1, NRU2, NRU4 and NRU5;

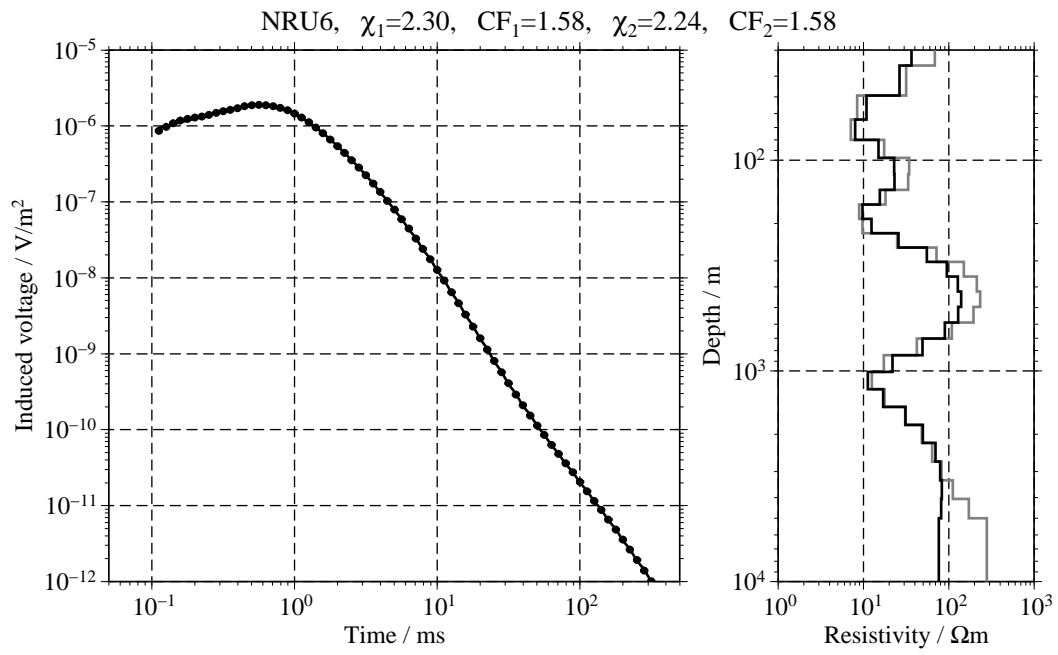


Figure C.73: Single inversion results for the SHOTEM-transient NRU6;

Geophysical interpretation of the field data sets

This appendix discusses the results at all Rx-sites. In sec. D.1 the interpretations for all sites measured during the campaign are presented, except for those which are already shown in chapter 6. Sec. D.2 shows the statistics for all SJIs and FJIs made for the interpretation. Tables in this section lists how many data point were removed from each data set prior to inversion. The section is only included in the CD-version.

D.1 Geophysical interpretation of the Rx-sites

In this section the geophysical interpretation for all sites are presented. Excluded are the calibration sites (see sec. 6.3.1) and the sites BSA and BSB (see sec. 6.3.3).

D.1.1 Site AFA

The site AFA is located in the Zevulun plain, in the northern part of the area under investigation. There is only one LOTEM-Rx-station close to a borehole "Afeq". Two SHOTEM measurements were done close to the spread: N3, a Cycle-5M data set NW of the spread and N8, a Geonics data set closer to the Tx. The borehole and the LOTEM-Rx are located on a dome structure (see fig. 6.8). Left panel of fig. D.1 shows a schematical plot.

From the synthetic data modelling (cp. sec. 5.3.3), it is expected that the resistive dome structure will not resolved by the LOTEM data. The resulting model thus should resemble the model below the Tx.

At AFA all five components were measured. E_y and \dot{H}_x are far smaller than their perpendicular counterparts, indicating that the (relevant) resistivity structure is nearly symmetric to a line perpendicular to the Tx. The right panel of fig. D.1 shows the resistivity transforms for the two magnetic components \dot{H}_y and \dot{H}_z .

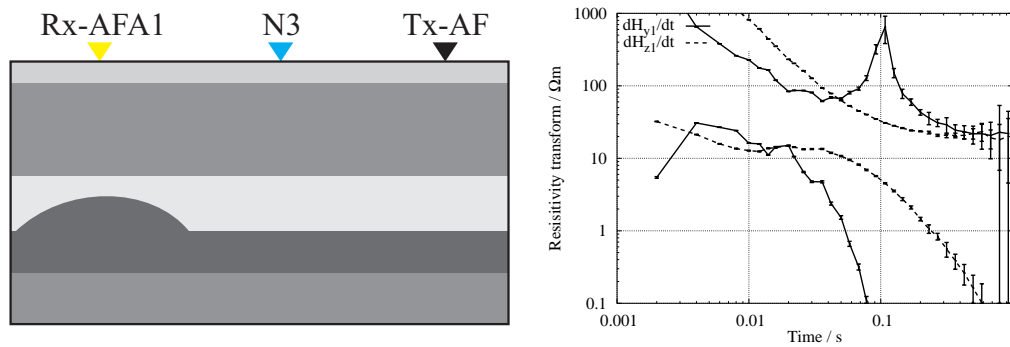


Figure D.1: Left: Sketch of the dome structure at the AF-spread; the position of the LOTEM-Rx coincides with the borehole location. The gray-scale indicate the resistivity structure from black (resistive) to white (conductive). The light area above the dome structure displays an aquifer filled with saline water. Right: Resistivity transform curves for the Rx-site AFA;

The SJI of the two SHOTEM data sets shows moderately consistent results (fig. D.2a), especially at depth. I decided to choose N8 for joint-inversions with the LOTEM data set, as N3 is off the spread. N8 is thus supposed to reflect better the situation at the LOTEM-spread. Fig. D.2b shows the result of a SJI without Tx-distortion. Two conductors are found, one around 200 m depth, the other at around 800-1100 m depth. This fits the inversion results for N8. Similar results are found for different combinations of components. However, the exact depth to the top of deeper conductor changes. Often, the top is found shallower.

Fig. D.2c shows the results of FJIs of the three LOTEM-components with the N8 transient in comparison with one typical SJI-result of these components. They basically show the same behaviour, although the top of the conductor is slightly deeper in the models derived by the FJIs. The final analysis (fig. D.2c) was done using these four components. The deep conductive feature is well resolved. However, comparing the result to the SJI-result shown in fig. D.2c and single inversion result for the Cycle-5M data set N3, models with a shallower top of the conductor are more likely. This conductor is interpreted as aquifer bearing saline water.

The result from the equivalence analysis (fig. D.2d) fits the SHOTEM result at N3 comparatively well (fig. D.2a). The lithological information from the borehole is not useful for the interpretation as it shows mainly carbonatic formations, besides a thin layer of volcanics between 2000 and 2070 m depth. A resistive feature is detected below the supposed saline water interface. As pointed out in the discussion of site TAB, at first this seemed unreasonable, as the salinity in general is expected to increase with depth. In fact, water samples taken from the borehole at a depth of around 2250 m exhibit high salinities (19,000 mg Cl^-/l). However, a resistivity log, which is unfortunately not available, showed medium resistivities above 670 m and below 900 m depth and a conductive zone in between [U. Kafri, pers. comm.]. This fits the TEM results very well. The increase in resistivity thus is caused by a change of the physical parameters of the geological formations, perhaps a change in porosities.

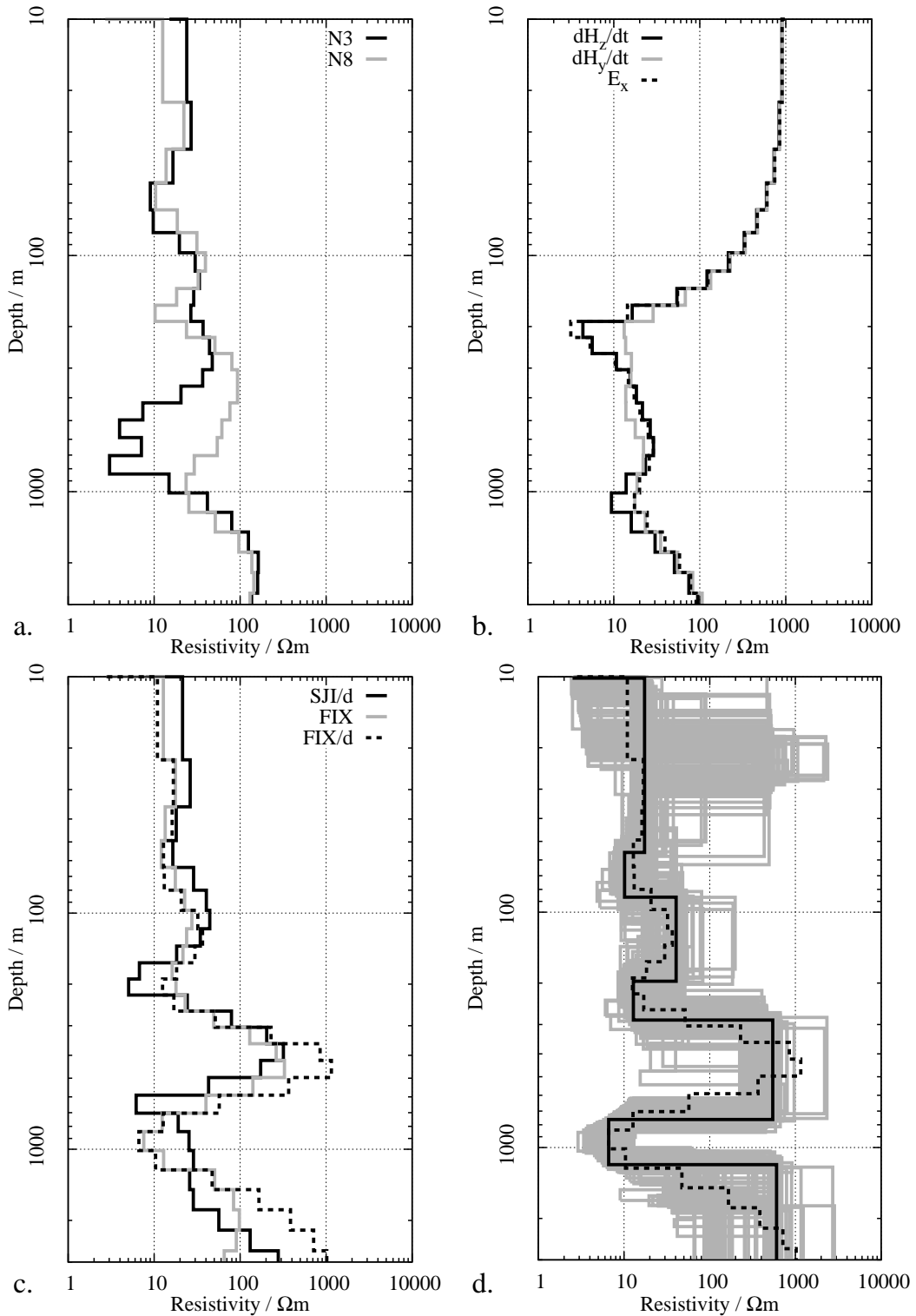


Figure D.2: Inversion results for the transients recorded at AEA; a: Comparison of the SJI-results for the SHOTEM data sets N8 and N3; b: SJI result for all LOTEM-components excluding Tx-distortion; c: SJI and FJI results for the LOTEM-components and the SHOTEM-transient N8 with Tx-distortion (“FJI/d” and “SJI/d”) and without (“FJI”); d: Equivalence analysis using the LOTEM-transients and the SHOTEM data set N8; the black lines shows the best model ($\chi = 3.83$), the dashed line the Occam’s-inversion result ($\chi = 3.89$) and the gray lines models with $\chi < 4.21$.

D.1.2 Sites AUA and AUB

The three stations at AUA approach a SW-NE trending fault visible as a displacement of ≈ 500 of the Judea Group in fig. 6.8. This fault intersects Tx and Rx-sites of the SA setup. Because distortions are expected at SAA, the AUA-site was set up in the second survey as a backup.

Unfortunately, the GPS-record for the ESE electrode of the Tx AU got lost. The approximate length (≈ 1000 m) and direction is known from the field logs. To interpret the transients, I calculated the calibration factors of the AUA- \dot{H}_z -components for different electrode positions (and thus different Rx-positions relative to the Tx). They were closest to 1.0 for a dipole length of 940 m. The positions of the Rx-components were chosen accordingly.

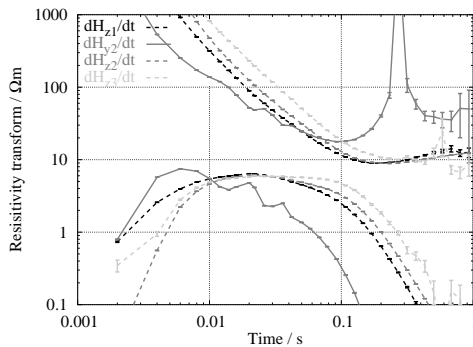


Figure D.3: Resistivity transform curves for the Rx-site AUA; The SHOTEM site N22 is located close to the Rx-stations.

SJIs of the \dot{H}_z -transients resulted in quite similar models showing conductive features at a depth of around 100 m and between 300-500 m. These conductors are also resolved by the SHOTEM-transient (fig. D.4a). The models obtained by SJIs of different components are similar with respect to these features (fig. D.4b). However, the thickness of the deeper conductor and anything below it is not stable. The SJIs of all six TEM-components show a similar behaviour (fig. D.4c), as well as the equivalence analysis (fig. D.4d).

The resolved features in the equivalence analysis are similar to the results of the SJIs. The shallow conductor is not well resolved, nor is the top of the lower conductor. The thickness of this lower conductor, as well as anything deeper are not reliably obtained from SJIs. In this case, the LOTEM data set could not provide additional information to the SHOTEM data set. The probably slightly distorted LOTEM-transients however, fit the model of the SHOTEM data set, but they degrade the misfit. For a final interpretation, only the SHOTEM data set should be used.

The second Rx-site AUB was set up SE of the Tx. SSW of the Rx-site AUB, the SHOTEM-transient N21 was recorded. Unfortunately, all LOTEM- \dot{H}_y and $-\dot{H}_z$ are too distorted by ambient noise, leaving only two E_x - and the SHOTEM-transient for the interpretation.

Only one \dot{H}_y - and one E_x -sensor was set up at AUA. The resistivity transform curves for the \dot{H}_z -components show a similar behaviour until late times (fig. D.3). There, all \dot{H}_z s in general show an increase in the resistivity transform curves but the shape is different. This increase is produced by an unusually fast decay at late times in the transients. The \dot{H}_z at the station AUA3 closest to the fault even exhibits a sign reversal at late times. To counteract this distortion, the last 12 data points were removed from the transient.

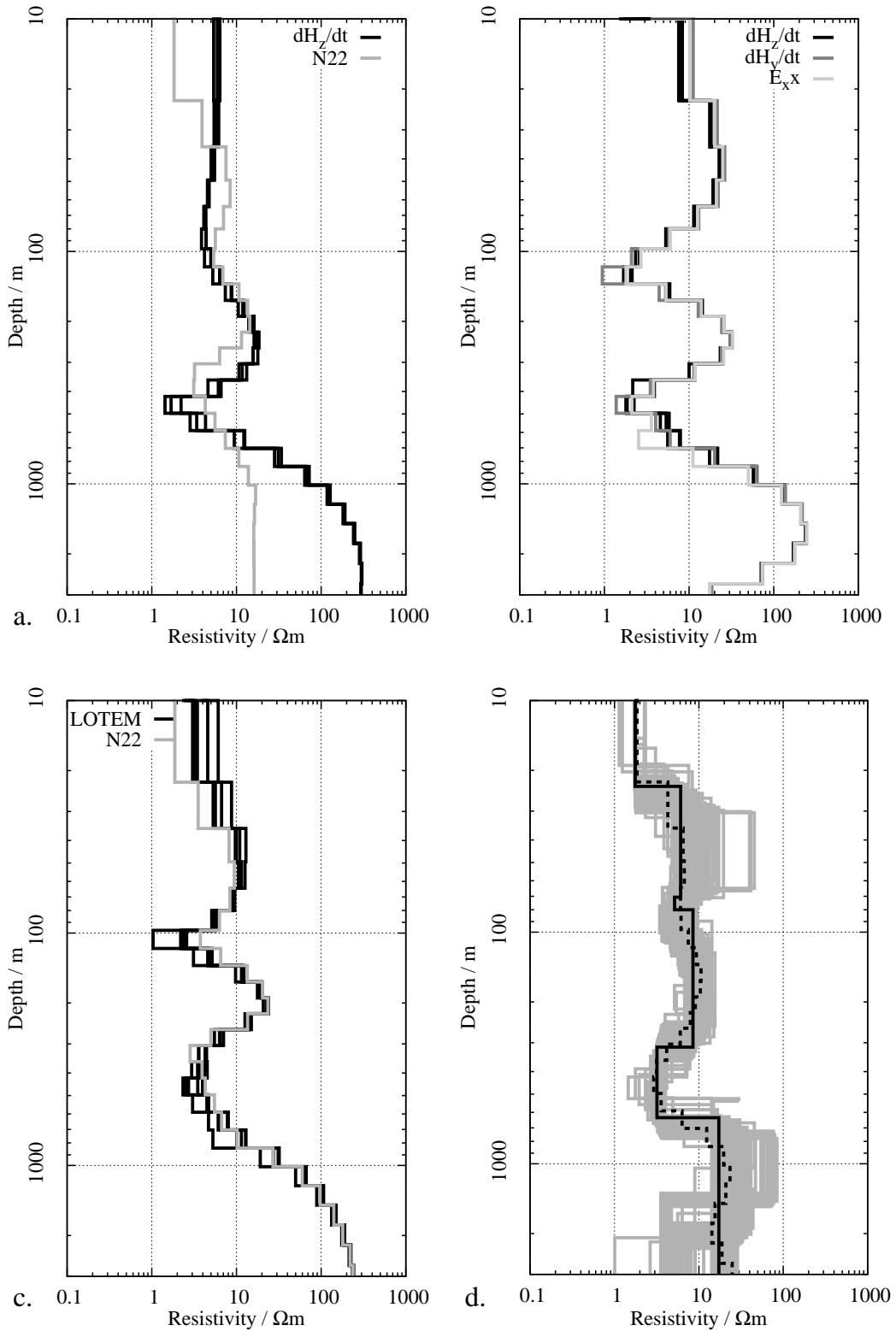


Figure D.4: Inversion results for the transients recorded at AUA; all inversion shown involving horizontal components are done with free Tx-distortion parameters. a: Comparison of the SJI-results for the \dot{H}_z s and the inversion of the SHOTEM data set N22; b: SJI result for all LOTEM-components; c: SJI results for all TEM-components; d: Equivalence analysis using all six TEM-components; the black lines shows the best model ($\chi = 2.30$), the dashed line the Occam's-inversion result ($\chi = 2.29$) and the gray lines models with $\chi < 2.52$.

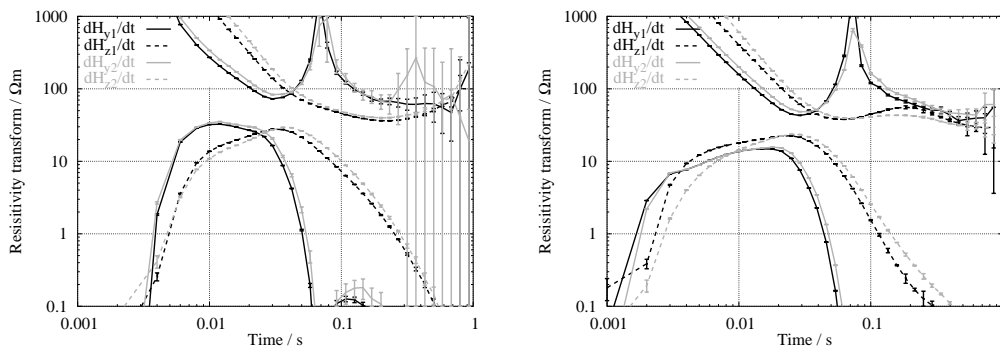


Figure D.5: Resistivity transform curves for the Rx-sites BEA (left) and BEB (right);

Using free Tx-distortion parameters, the misfit is improved in the SJI of the two E_x -transients. Both E_x s see a conductive feature in intermediate depths. However, the depth and resistivity for both transients is not consistent. Also, they are not consistent to the SHOTEM-transient. Thus, no reliable resistivity models could be expected from the LOTEM data sets. The site was discarded.

D.1.3 Sites BEA and BEB

The BE-spread is placed in the Harod Valley. A fault with a displacement of ≈ 1 km runs parallel to the spread. Fig. D.5 shows the resistivity transform curves for the two sites BEA and BEB. Although the \dot{H}_y -components seem to be consistent along the spread, the \dot{H}_z -transients show a opposite behaviour. The rapid decay of the \dot{H}_z -transients at late times at Rx-site BEA suggest an extremely resistive basement. At BEB, the slow decay in the late time part of the \dot{H}_z -transients produces very low late time apparent resistivities. The \dot{H}_z -transients are also not very consistent in the early time part.

The cause for the inconsistent behaviour of the \dot{H}_z -transients at BEA and BEB is unknown. The most prominent multidimensional feature, the fault parallel to the spread, may effect the data. However, since the distance to the fault is similar at both sites, it would be expected that the distortion would be the same at both sites and not the opposite. It is more likely that the distortions are caused by lateral changes along the directions of the spread.

The model calculations in sec. 5.3 show that if the Tx is placed on a model boundary, sites on particular sides of the Tx will almost exclusively represent the subsurface between their location and the Tx-position. If different transients on both sides of the Tx are measured, it thus is reasonable that they reflect the subsurface below each Rx-site.

However, no indication for a geological boundary at the position of the Tx is found at BE. The shape of the distorting structure remains unknown. Regardless of what the analysis below will show, the results at these sites can not be considered to be very reliable.

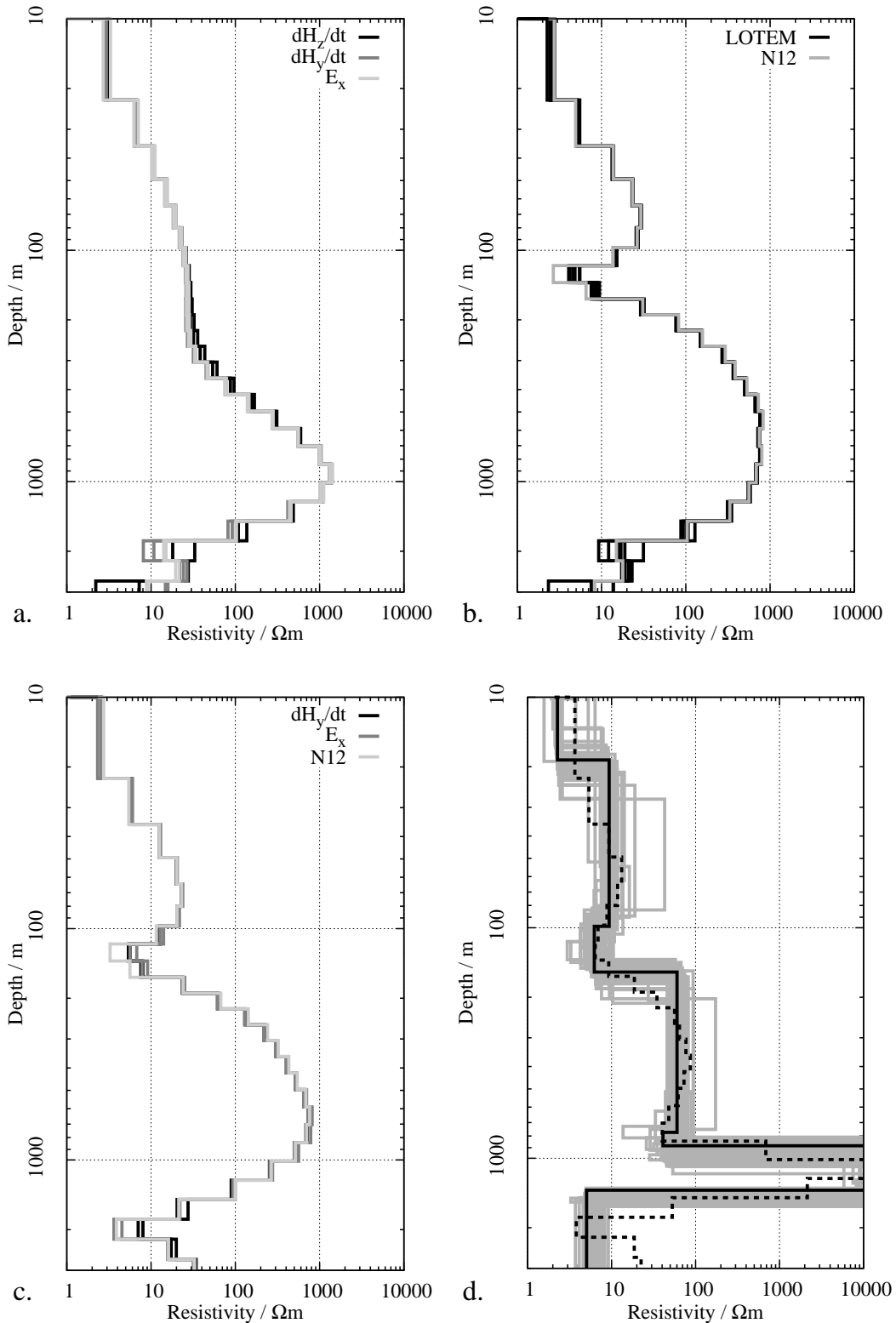


Figure D.6: Inversion results for the transients recorded at BEB; a: SJI results for all LOTEM-components including Tx-distortion inversion; b: SJI result for all seven TEM including Tx-distortion; c: SJI results for all TEM-components, excluding the two LOTEM- \dot{H}_z s with Tx-distortion; d: Equivalence analysis for all transients, except for the LOTEM- \dot{H}_z s; the black lines shows the best model ($\chi = 2.64$), the dashed line the Occam's-inversion result ($\chi = 3.00$) and the gray lines models with $\chi < 2.90$.

Close to the Rx-stations the SHOTEM data sets N11 (BEA) and N12 (BEB) were recorded. N11 and N12 are possibly distorted by multidimensional structures [M. Goldman, pers. comm.]. However, inverting the data sets in an SJI, all models show a similar behaviour. They exhibit a conductive feature between 100 and 200 m depth. This is also in accordance with the results for the nearby SHOTEM site N25. The misfits, however, are not good, especially at N11.

The results for site BEB are comparatively stable. Including the Tx-distortion parameters in general did not change the resulting models much. However, in most cases a lower misfit was achieved with Tx-distortion. Fig. D.6a shows the results of a SJI using all LOTEM-components with Tx-distortion. The models are quite consistent. Nevertheless, the models for the two \dot{H}_z -transients differ slightly from the ones for the other four data sets. Even a seven component joint-inversion is possible (fig. D.6b). The SHOTEM-transient introduces a shallow conductor between 100 and 200 m depth.

Comparison of the different inversion results showed that using the \dot{H}_z -transients causes the deep conductor to move downward. Its top is then around 2000 m deep, compared with ≈ 1400 m required by the other components. Fig. D.6c) shows a SJI of all TEM-components except the LOTEM- \dot{H}_z s. The model is very similar to the model from fig. D.6b, but the deep conductor has moved upwards.

As mentioned above, the \dot{H}_z -transients at the BE-sites are questionable, as they differ from one site to the other over the whole time range. I thus decided to skip the LOTEM- \dot{H}_z -transients for the final inversion. The result of the final equivalence analysis is shown in fig. D.6d. Here, the LOTEM- \dot{H}_y s and $-E_x$ s were used in addition to the SHOTEM-transient. The FJI result displayed is the one without Tx-distortion parameters, as the other FJI failed to converge on a low misfit level. The resulting models are similar to the ones from the different SJIs. However, the shape of the deep resistive feature changed, compared with the SJIs.

The inversion of the data from BEA is more problematic. All TEM-components show a similar behaviour with an increased resistivity at depths > 200 m. However, the depth to this increase is very different. The \dot{H}_z -components show a very sharp conductive zone between 1000 and 2000 m depth (fig. D.7a). Depending on the choice of components, mainly two different models can be obtained. If only the horizontal components E_x and \dot{H}_y are used, the model shown in fig. D.7b is obtained, exhibiting conductive zones at 400-900 m and below 2000 m depth. If either the SHOTEM data set or the LOTEM- \dot{H}_z s are used, the model looks very different (fig. D.7c), although the misfit of the horizontal components is only a little higher, unless the SHOTEM-transient is included. The SHOTEM data set mainly introduces the shallow conductor including the rapid increase in resistivity at a depth of 200 m. The deeper part is not changed.

The models obtained using also the \dot{H}_z -components are more consistent with the ones obtained at BEB (and RZB, sec. D.1.15), but these data sets are supposed to be distorted. From the data set, it can not be decided which model is more likely. For the horizontal components, the FJI-inversions gave models, which are somewhere in between the two choices. Thus, for the equivalence analysis all seven TEM-components are used (fig. D.7d). The features are similar to the ones found in the SJIs including the vertical magnetic field derivatives.

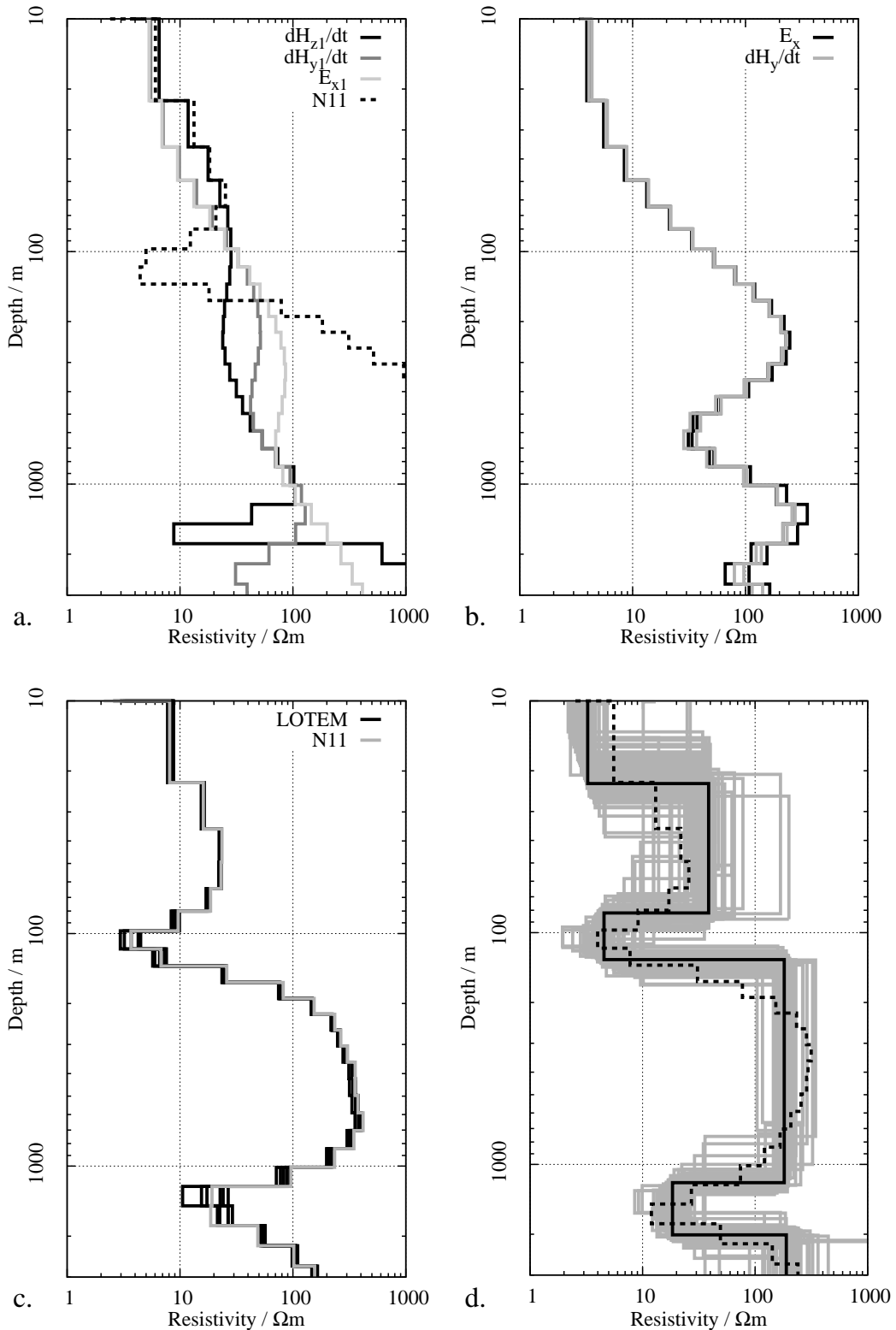


Figure D.7: Inversion results for the transients recorded at BEA; All inversions shown including horizontal components are done with Tx-distortion; a: SJI results for the individual LOTEM-components and the single inversion result for N11; b: SJI result for the LOTEM-components E_x and dH_y ; c: SJI results for all TEM-components; d: Equivalence analysis for all transients; the black lines shows the best model ($\chi = 5.37$), the dashed line the Occam's-inversion result ($\chi = 5.37$) and the gray lines models with $\chi < 5.90$.

The deeper conductors found in the equivalence analyses at BEA and BEB are interpreted as aquiferous formations bearing saline water. Neglecting the two equivalent models found at BEA, these conductors in general are well resolved. Because of unclear origin of the different late time behaviour of the transients at BEA and BEB, the results are considered only medium reliable.

D.1.4 Sites CAA and CAB

The Tx CA is located in the Carmel mountains. The Rx-site CAA was placed on a small anticline. Here, only one station could be set up. For the interpretation, the E_x -, \dot{H}_y - and \dot{H}_z -transients are used. Nearby two SHOTEM data sets – N4 and N30 – were recorded. The latter is located exactly at the Rx-position. At N4 the Geonics and Cycle-5M equipment was used. In this particular case, the Cycle-5M data is worse than the Geonics data set. Thus, the latter was used for the inversions.

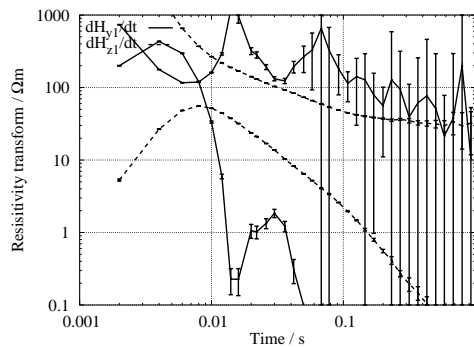


Figure D.8: Resistivity transforms curves for site CAA;

As fig. D.8 shows, the \dot{H}_y decays to noise level at very early times. Besides the information that the shallow part of the earth is resistive, nothing can be derived from this transient. The SHOTEM data set N30 is skipped, because it shows signs of multidimensional distortions [M. Goldman, pers. comm.]. The inversions shown here were done using only N4 and the LOTEM- E_x and $-\dot{H}_z$. Using the SHOTEM data set N30 gave qualitatively the same results as N4.

SJIs of the usable LOTEM-components results in much better misfits if Tx-distortion is included in the inversion. However, the resulting models show the opposite behaviour to the single inversion of N4 in the upper part (fig. D.9a). An SJI of the three TEM-components worked well and gave roughly the same misfits as inverting the N4 or the two LOTEM-components. As could be expected, the result is dominated by the N4-transient (fig. D.9b). The models show a conductive feature between 100 and 200 m depth and a drop in resistivity at ≈ 550 m to values of around 20 Ωm . Between 1000 and 2000 m depth indications for an additional conductive feature are found. The same features are found using a FJI.

Fig. D.9c shows the equivalence analysis for the three TEM-components. The models resemble the SJI-results. It is not clear from this plot, if there is a deep conductive feature in every model. In fig. D.10 (left) the minimal resistivity of each model shown in fig. D.9c in the depth range between 1000 and 1600 m is plotted versus the model's misfit relative to the best misfit. It shows that all models show a conductive zone with less than 12 Ωm in this depth range.

In a nearby borehole, water with a salinity of only 262 mg Cl^-/l is found at a depth of 395 m. This rapidly increases to values of 5,500 to 6,100 below 510 m depth. This correlates very well to the drop in resistivities found in fig. D.9c. The deep conductive feature may reflect water of higher salinities.

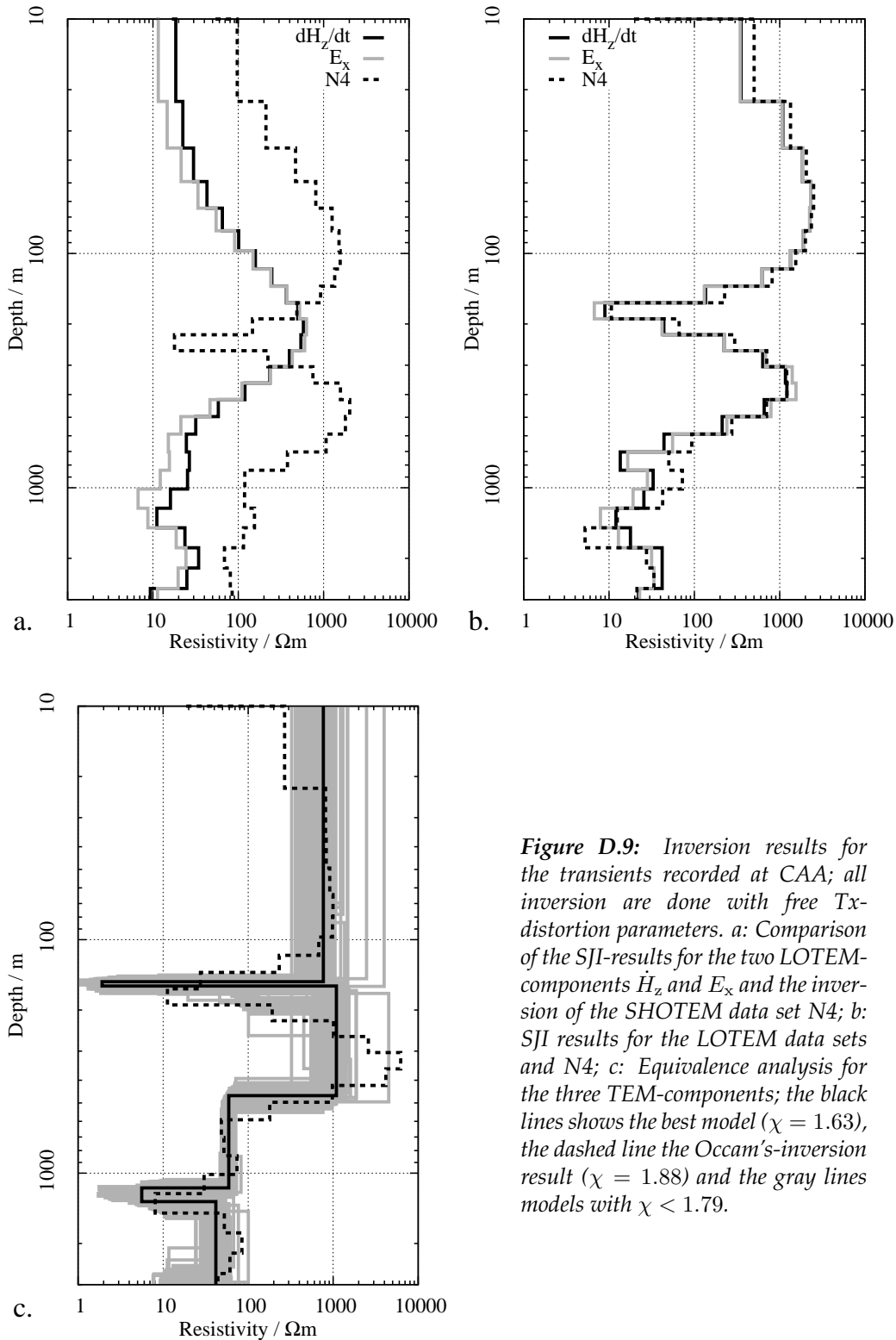


Figure D.9: Inversion results for the transients recorded at CAA; all inversion are done with free Tx-distortion parameters. a: Comparison of the SJI-results for the two LOTEM-components \dot{H}_z and E_x and the inversion of the SHOTEM data set N4; b: SJI results for the LOTEM data sets and N4; c: Equivalence analysis for the three TEM-components; the black lines shows the best model ($\chi = 1.63$), the dashed line the Occam's-inversion result ($\chi = 1.88$) and the gray lines models with $\chi < 1.79$.

At site CAB only one single \dot{H}_z was recorded. There are no signs of distortion (fig. D.10, right). Fig. D.11 shows the inversion results. In the depth range roughly between 1000 and 1500 the models show an indication for a conductive layer with $\rho < 10 \Omega\text{m}$. Again, the smaller the resistivity the deeper and thinner the layer is. Below, resistivity increases to values higher than $50 \Omega\text{m}$, to drop again to values

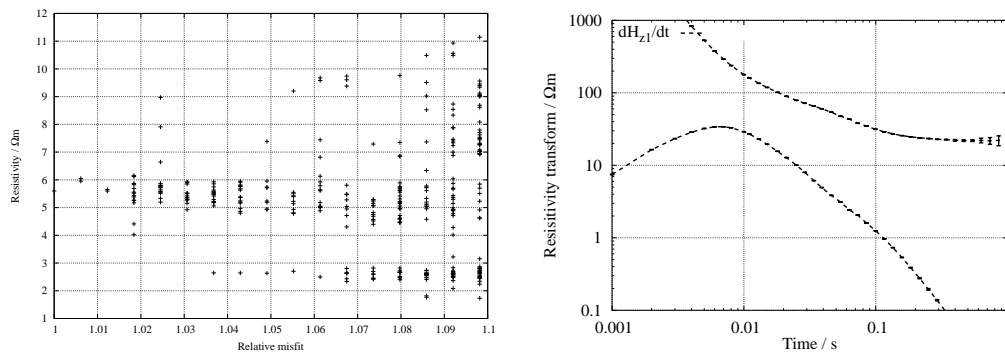


Figure D.10: Left: The minimal resistivities for every model from the equivalence analysis shown in fig. D.9c in a depth range from 1000 and 1600 m (site CAA); the resistivity is plotted against the misfit of the individual model relative to the misfit of the best model found. Right: Resistivity transforms for the H_z -component recorded at CAB (right);

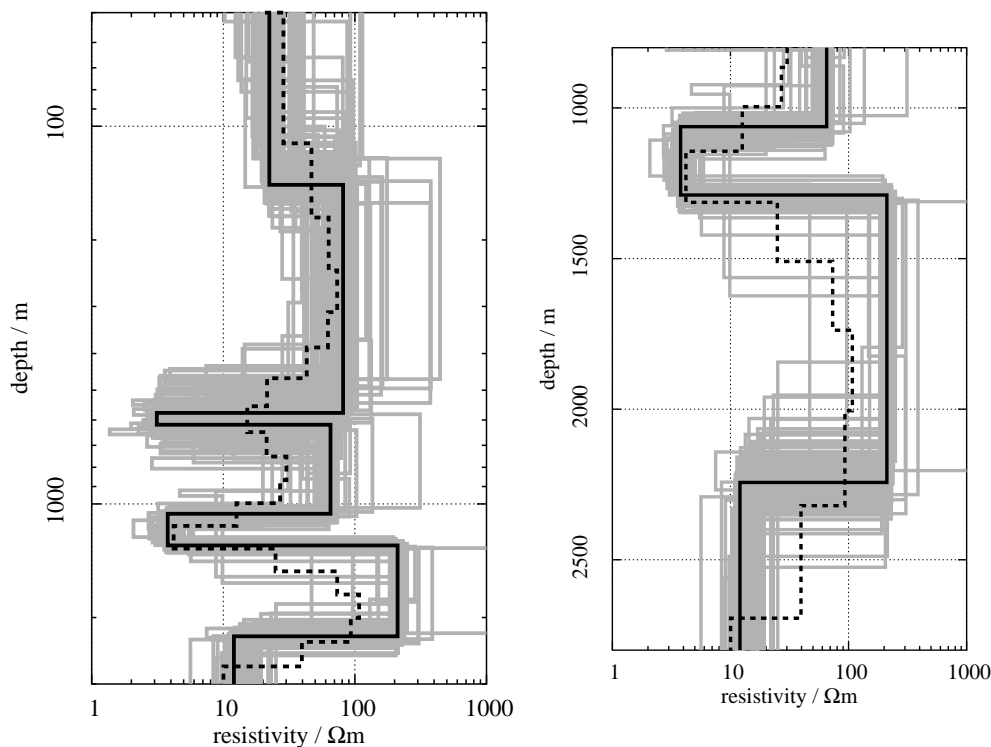


Figure D.11: Equivalence analysis for Rx-site CAB for the depth range between 50 and 3000 m (left) and 800 and 2800 m (right); the best model (black line) has a misfit of $\chi = 0.70$, the average misfit is 0.74. The plots show all models with $\chi \leq 0.77$ (light gray) and the Occam's inversion result (dark gray) with $\chi = 0.70$.

around 10 Ωm at depths greater than 2 km.

The conductive feature between 1000 and 1500 m depth at CAB may reflect the aquiferous formation which is the target of the survey. However, as the interpretation at CAA and CAB is based on a few transients only, these results are only semi-reliable.

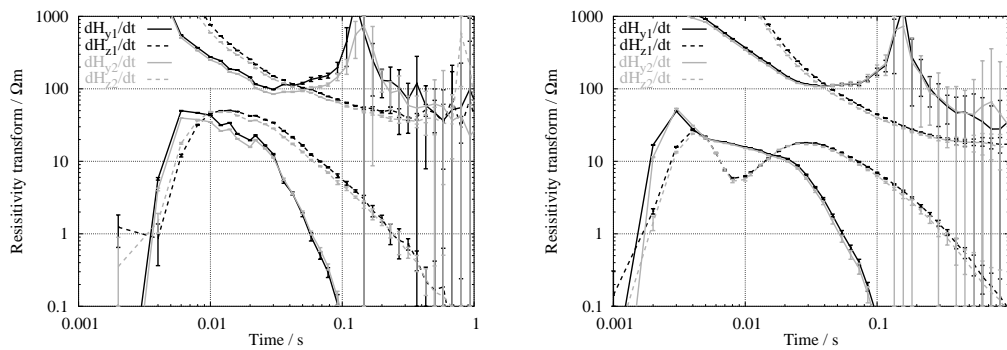


Figure D.12: Resistivity transform curves for the Rx-site DVA (left) and DVB (right);

D.1.5 Sites DVA and DVB

The Tx DV was placed in the valley branching off the Yizre'el Valley to the Sea of Galilee. The site DVA is placed on the foot of a hill rising behind the stations. The hill is divided from the valley by a fault line with a huge displacement of several hundred meters. DVA was originally planned as calibration site, as a deep borehole is drilled close to the fault structure. It was possible to place the Rx-sites a few hundred meters away from the fault to avoid the expected distortions.

At one of the two Rx-stations at DVA the (R)-coil was set up in addition to a (N)-coil to compare the signals from both coils. The transients look the same. For interpretation only the data from the (R)-coil was used, because the SNR is slightly better. The resistivity transform curves are shown in the left panel of fig. D.12. They show no obvious signs of distortions.

DVB is located on a basaltic hillside south of the Tx DV. Two stations were set up with two E_x -, \dot{H}_y - and \dot{H}_z -sensors each. As can be seen in the left panel of fig. D.12, the \dot{H}_z -components show strange depressions around 9 ms. Therefore, the first 14 data points were removed from these transients. For logistical reasons, no SHOTEM-transient could be recorded there. The data N7 was recorded at the Tx-site. However, as the Rx-site is elevated a few hundred meters above the Tx, the depths are not comparable. I regarded joint-inversions of SHOTEM and LOTEM data sets therefore as unreasonable.

Two SHOTEM-measurements were made in the vicinity of DVA. The Cycle-5M transient N2 was recorded at the Rx-site DVA and the Geonics data set N7 was recorded at the position of the Tx. A SJI of these two transients result in quite different models (fig. D.13a). This indicates lateral changes between the Tx- and Rx-positions as would be expected because of the fault.

The hill behind the Rx-site acts as a shallow conductor behind the spread [Hördt and Müller, 2000]. The model calculations in sec. 5.3 showed that the \dot{H}_z -component close a lateral boundary tend to introduce artificial structure. Skipping the \dot{H}_z -transients thus is reasonable. The fault, however, will be suppressed in the inversions. The model will reflect mainly on the subsurface towards the Tx (see the model calculations for the models K1 to L3 and the left part of model M in chapter 5).

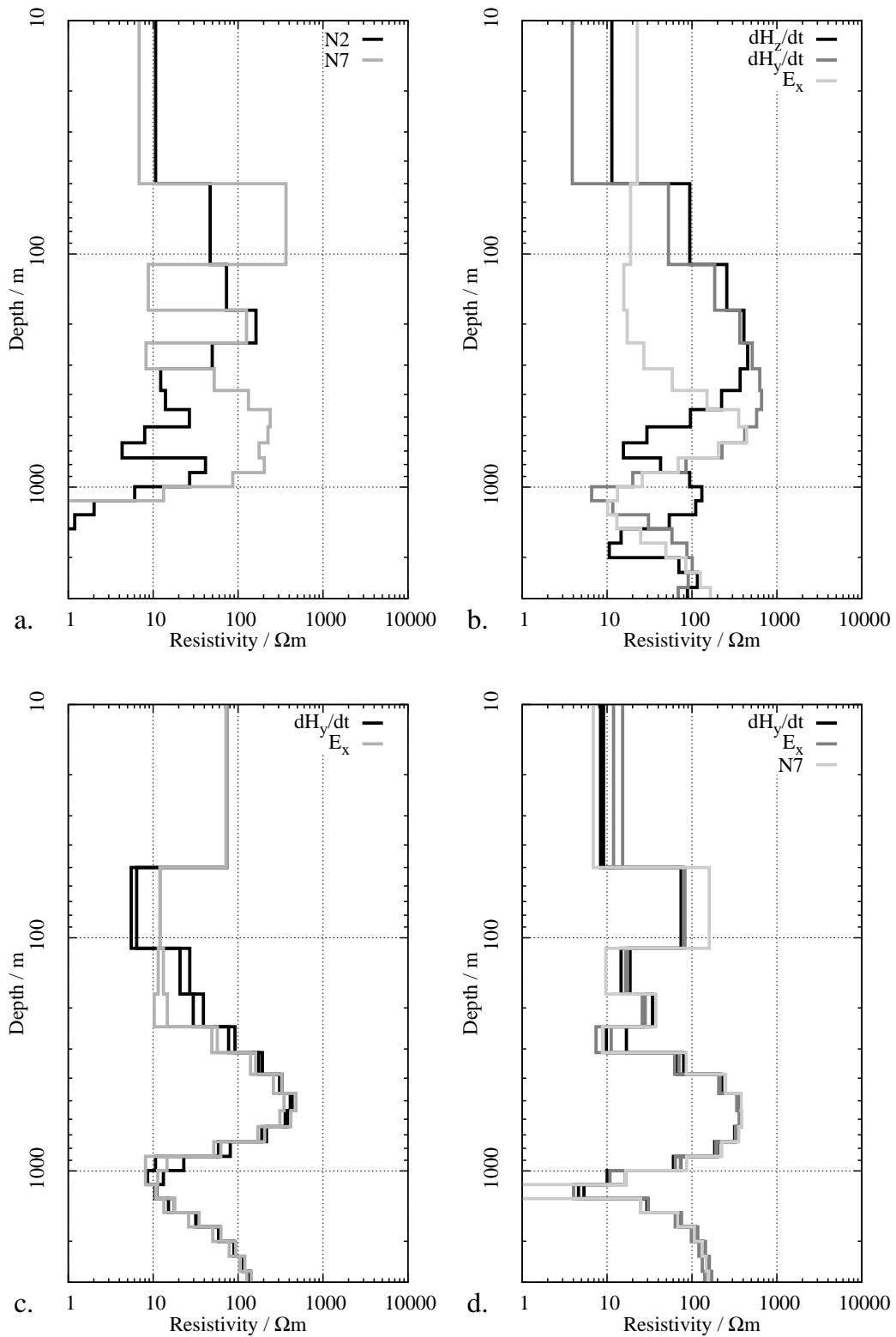


Figure D.13: Inversion results for the transients recorded at DVA; all inversions shown including horizontal field components are done with Tx-distortion. a: Results for the SJI of the SHOTEM data sets N2 and N7; b: Results for the SJI of the individual LOTEM-components; c: Results of the SJI for the LOTEM-components E_x and \dot{H}_y ; d: Results of the SJI for the LOTEM-components E_x and \dot{H}_y and the SHOTEM data set N7;

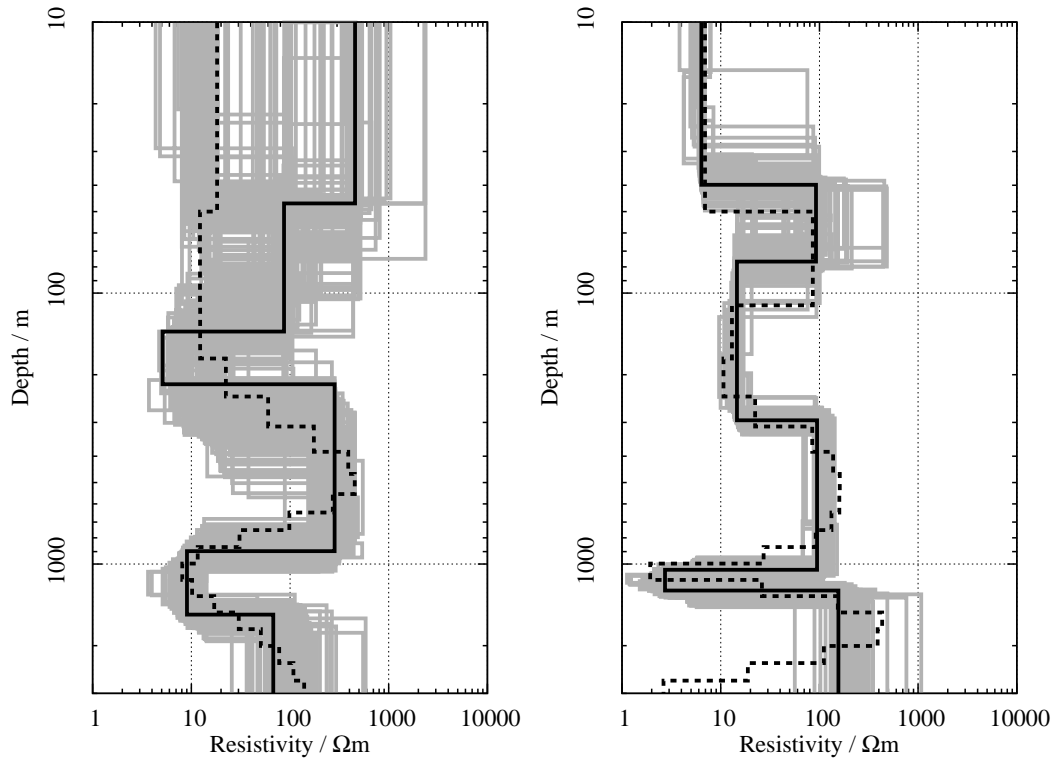


Figure D.14: Equivalence analyses for data sets recorded at DVA; left: Equivalence analysis for the LOTEM- E_x s and $-\dot{H}_y$ s; the black lines shows the best model ($\chi = 1.55$), the dashed line the Occam's-inversion result ($\chi = 1.55$) and the gray lines models with $\chi < 1.71$. Right: Equivalence analysis for the LOTEM- E_x s and $-\dot{H}_y$ s and the SHOTEM data set N7; the black lines shows the best model ($\chi = 2.61$), the dashed line the Occam's-inversion result ($\chi = 2.56$) and the gray lines models with $\chi < 2.87$.

Inversions including the electric fields result in high misfits and inconsistent models if no Tx-distortion is allowed. The horizontal components give similar results, whereas the LOTEM- \dot{H}_z s suggest models which show a completely contrary behaviour in deeper parts (fig. D.13b). Where E_x and \dot{H}_y see a conductive zone around 1000 m depth, the \dot{H}_z indicates two distinct zones significantly above and below this depth. The upper one is in accordance to the SHOTEM data set N2. This inconsistency is not resolved by SJIs including the other components, unless all LOTEM-components are used. Here, the information from the \dot{H}_z -transients is suppressed. The resulting models are similar to the results obtained by using \dot{H}_y or E_x only.

SJIs of the \dot{H}_y - and E_x -transients give stable results, which are similar to the ones obtained by inverting either the E_x s or the \dot{H}_y s (fig. D.13c). Adding the SHOTEM-transient N7 mainly changes the depth to the shallow conductor, but the depth to the deep conductive feature also increases slightly (fig. D.13d). FJIs of the components give roughly the same results, but the structures below the deep conductor are not stable and thus considered unreliable.

Fig. D.14 shows the results of the equivalence analysis using the LOTEM- \dot{H}_y s and $-E_x$ s (left) and the SHOTEM-transient N7 (right) in addition to the LOTEM-transients. Both ensembles resemble their FJI results. The SHOTEM result is far better constrained. However, the conductive feature still has to be deeper than

without the SHOTEM data set. Although this might indicate a deeper top of the conductor, this seems not very reliable.

At DVB including the Tx-distortion parameters in inversions results in far better misfits. The SJIs of the individual components of both stations are quite consistent for the \dot{H}_y s and E_x s, showing two conductive features around 400 and 1100 m depth, respectively. The \dot{H}_z s show a different picture with only one deep conductor at 1000 m (fig. D.15a). Due to the removal of the first time points shallow structures can not be resolved with these transients.

The discrepancy between the \dot{H}_z -transients' results and the ones for the other components are not severe. Even SJIs of all six LOTEM-components were successful and give about the same model as the SJIs of the \dot{H}_y s and E_x s, respectively (fig. D.15b). FJIs including all LOTEM-components however, produced different models (fig. D.15c).

The situation here is similar to DVA and YAB, with respect to the Rx-position relative to the Tx and the hill. Also, as the stations were set up on the slope of the hill, the \dot{H}_z -sensors could be tilted. This means, it is reasonable to discard the \dot{H}_z -transients from the inversions. FJI of the two \dot{H}_y - and E_x -transients resulted in models similar to the ones produced by the SJI of all components. Fig. D.15d shows the result of the equivalence analysis using all but the \dot{H}_z -transients. The most prominent feature is a conductive zone $\leq 10 \Omega\text{m}$ between 1 and 2 km depth.

Overall, I obtain slightly different models along the spread. At the Rx-site DVA, inversions of the SHOTEM data set N2 found a conductive feature at depths of around 600 m. This is in very good accordance to the results of the shallow borehole "Devora-1", to the north of this site, where salinities of 780 and 18,000 mg Cl^-/l were found at depths of 317 and 645 m, respectively. The LOTEM-inversions using the \dot{H}_y - and E_x -transients at DVA found a different minimal depth of 800 m. This result is supposed to reflect also the subsurface closer to the Tx. The depth increases, if the SHOTEM-transient N7 located at the Tx is included in the inversion. At DVB the top of the conductor is found at around 1000. As this site is elevated ≈ 120 m above the Tx, this depth have to be reduced by, say, 60 m, locating the result roughly between Tx and Rx-site. In a shallow borehole in the vicinity of DVB water with a salinity of $\approx 1,000$ mg Cl^-/l at a depth of 360 m was found in pumping tests. As a source of salinity a saline layer at a depth of 1000 m is likely [U. Kafri, pers. comm.]. Overall, the DV-spread shows a consistent picture of a NW-SE sloping saline water interface.

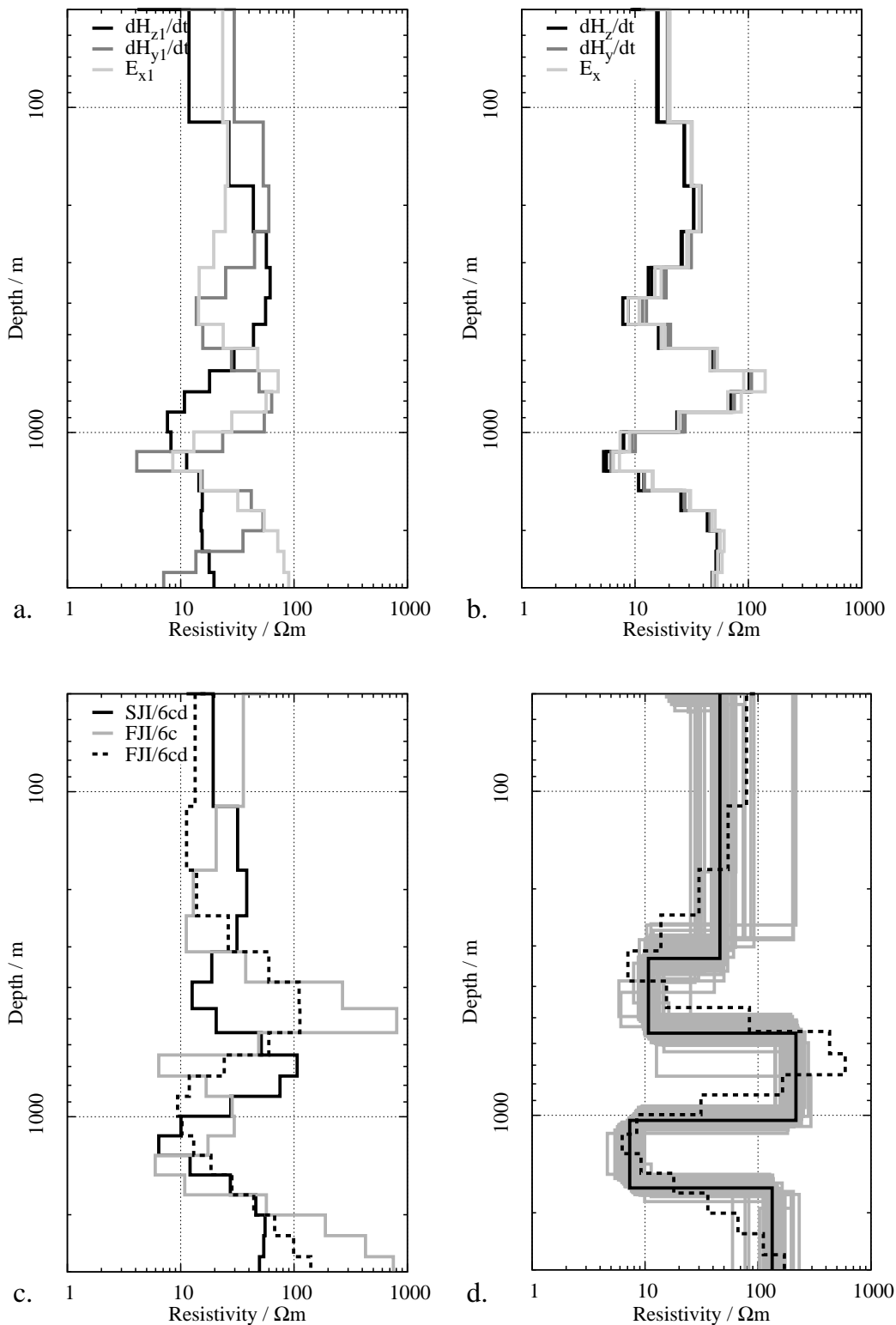


Figure D.15: Inversion results for the transients recorded at DVB; unless otherwise stated, all inversions shown are done with Tx-distortion. *a:* Comparison of the SJI results for the individual LOTEM-components; *b:* Results for the SJI of all LOTEM-components; *c:* Results of the FJI of all six LOTEM-components with (“FJI/6cd”) and without Tx-distortion (“FJI/6c”) compared to one SJI-result of these components (“SJI/6cd”); *d:* Equivalence analysis for the LOTEM- E_x s and $-\dot{H}_y$ s; the black lines shows the best model ($\chi = 0.52$), the dashed line the Occam’s-inversion result ($\chi = 0.82$) and the gray lines models with $\chi < 0.57$.

D.1.6 Site EMA

The EM spread is located in the Carmel mountains, parallel to the CA spread. Only one site is used with Tx EM, because there is a military base located ESE of the Tx. EMA consists of two stations on an anticline between two hills. All five measurable components were recorded, from which two E_x , \dot{H}_y and \dot{H}_z will be used for 1-D interpretation. Additionally, the SHOTEM data set N29 was recorded here. The resistivity transforms for the LOTEM-components show only slight deviations at the first view data points.

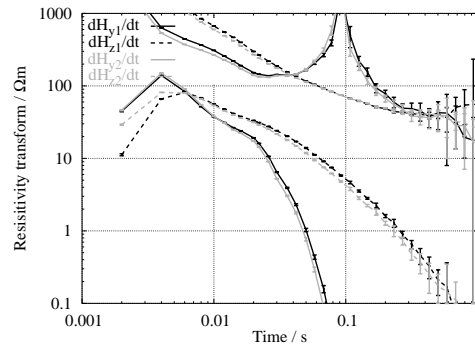


Figure D.16: Resistivity transform curves for the Rx-site EMA;

SJIs of the different components show a rather inconsistent picture. The magnetic components' SJIs work well but the \dot{H}_y -results look significantly different if Tx-distortion is introduced. However, if this is done, the models are similar to the \dot{H}_z -SJI-results. Also, the misfit is lower. The E_x -SJI fails to converge on to low misfit, when the Tx-distortion is included. Without distortion, the models for both stations' electric fields differ and contradict the results for the magnetic components. Common to all models is the highly resistive upper part (possibly below a thin conductive overburden) and a drop in conductivity in deeper parts. They differ, however, in the depth to this drop (≈ 600 m for the magnetic components, see fig. D.17a).

SJI-results for all LOTEM- \dot{H} s show a similar behaviour, but there is an additional conductive layer between 300 and 400 m depth. Similar models are found using the E_x -transients as well. The resistive zone at 500 to 800 m depth becomes more resistive. If the SHOTEM data set is included, the model changes slightly: The drop in resistivity occurs at shallower depths and the underlying earth shows no obvious features. It is more or less a homogenous half-space with $\approx 30 \Omega\text{m}$. However, the misfit in this case is significantly worse than for SJIs without the SHOTEM-transient.

FJIs of all TEM-components gave models roughly similar to the ones from the SJIs. However, from the previous results showed that if the model changes at depth when including SHOTEM data sets, the model is less reliable. Also, the misfit was degraded, when including N29. FJIs of the LOTEM-components only resulted in models different to the ones from the SJIs.

fig. D.17 shows also the outcome of the equivalence analysis for the six LOTEM-(c) and the all TEM-components (d). Both are quite ambiguous. Well resolved is only the existence of a drop in resistivity, but the depth to this decrease is questionable. The existence of this increase, however, fits the results of CAA. The deeper part is not resolved, as the different inversions showed no consistent features.

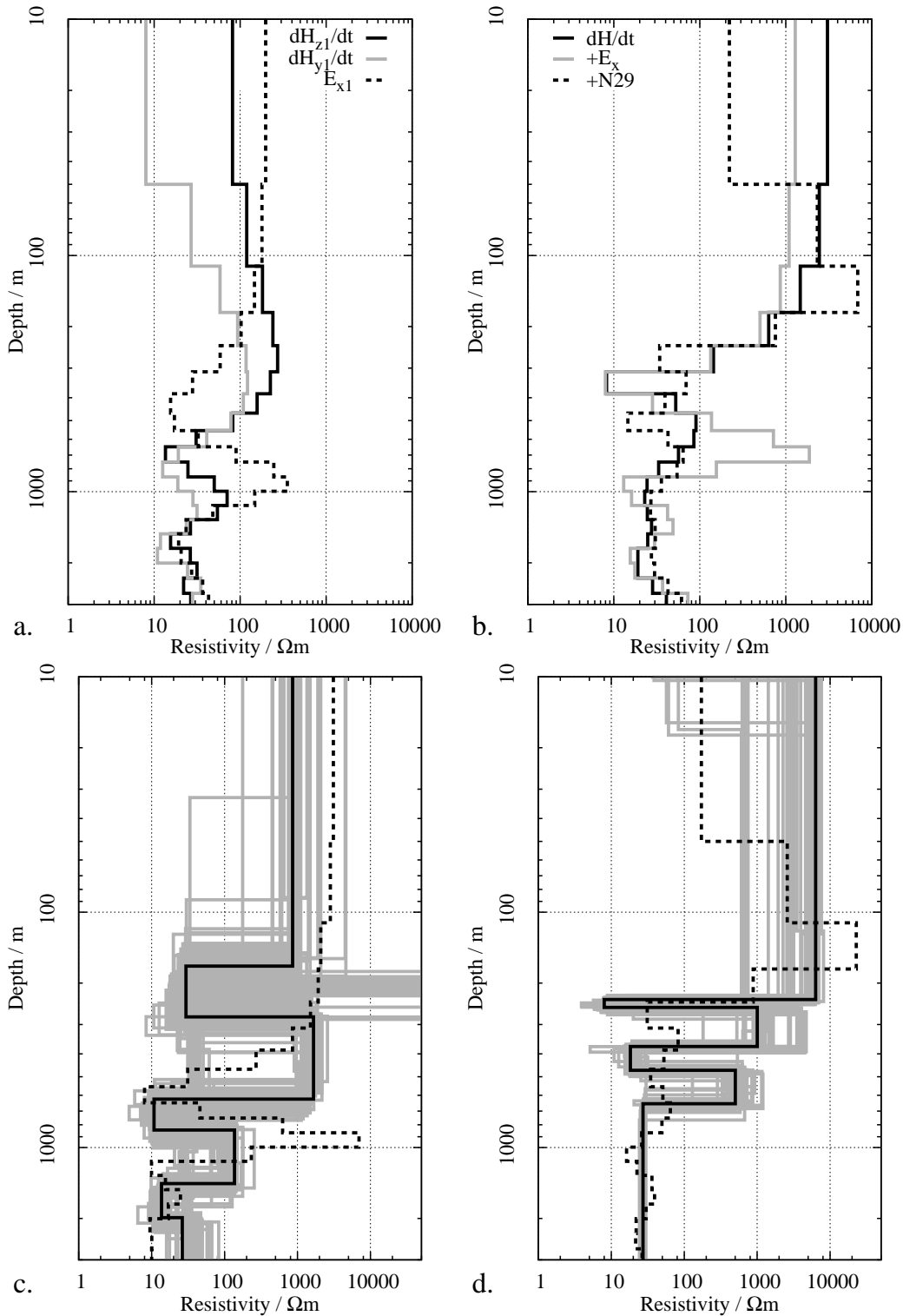


Figure D.17: Inversion results for the transients recorded at EMA; unless otherwise stated, all inversions shown are done with Tx-distortion. *a:* Comparison of the SJI results for the individual LOTEM-components; *b:* Comparison of the results of SJIs using different combinations of components: With all LOTEM- \dot{H} s (“dH/dt”), with all LOTEM-components (“+E_x”) and with all TEM-components (“+N29”); The displayed models are representative for all other models obtained by these SJIs; *c:* Equivalence analysis for all LOTEM-components; *d:* Equivalence analysis for all TEM-components; the black lines shows the best model ($\chi = 1.57$), the dashed line the Occam’s-inversion result ($\chi = 1.89$) and the gray lines models with $\chi < 1.73$.

D.1.7 Site ENA

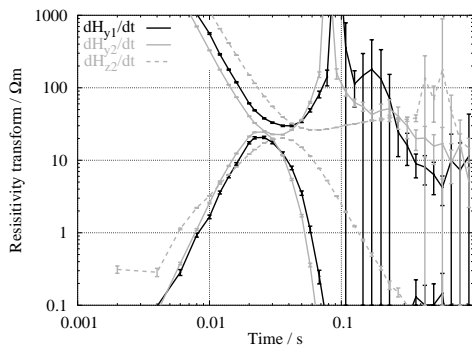


Figure D.18: Resistivity transform curves for the Rx-site ENA;

Rx-position. Instead, the data set NRU6 was recorded between Tx and Rx, using the Cycle-5M equipment.

Most stable are the SJIs of both E_x -transients. Including Tx-distortion does not change the resulting models. The models for the SJIs of the \dot{H}_y -transients differ for both stations, especially at depths > 1000 m. Although the misfit is similar when Tx-distortion parameters are included in the inversion, the model changes. The E_x -results also fit the SHOTEM results very well and are comparable to the SJI of the \dot{H}_y s with Tx-distortion (fig. D.19a). All models show a shallow conductor around 200 m depth. Additionally, a deep conductive feature is found. The depth to this second conductor differs however, depending on the component used.

SJIs of different TEM-components show different results. They can be divided into two classes. The first one exhibits a resistive zone at depths of 600 to 1300 m (fig. D.19b). This class of models is mainly created from SJIs dominated by the LOTEM- \dot{H}_y s. In the larger second class the resistive feature is shallower (between 300 and 900 m, see fig. D.19c). With the additional information from the borehole at ENB, the second class seems more likely. Thus, the LOTEM- \dot{H}_y s seem to be distorted. The equivalence analysis was made using all both LOTEM- E_x s, the LOTEM- \dot{H}_z and the SHOTEM data set NRU6 (fig. D.19d).

The model here is similar to the result as ENB (sec. 6.3.1), especially with respect to the deep conductive feature, which correlate well with the saline water interface.

D.1.8 Site GBB

GBB is the site east of the Tx GB. The resistivity transforms for the magnetic components show a behaviour similar to the transients recorded at BSB indicating a very conductive earth (fig. D.20). At intermediate times (6-60 ms) the \dot{H}_z -transients show some inconsistencies. If these data points are removed, too few time-points remain for inversion. However, the discrepancies are not very big, thus only the first five time points were cut off. The SJIs should show, whether the \dot{H}_z -data sets have to be discarded completely. In addition to the four LOTEM- \dot{H} -components, one E_x -transient and the SHOTEM data set N20 was recorded at this site.

The site at ENA is located in the coastal plain, 5 km east of the borehole “Beit-Eliezer”. The Rx-site had to be set up close to several power-lines. The analog notch-filter at 50 Hz was used, to suppress the noise. This results in long system responses (fig. D.18).

On this day, the damaged (B)-sensor was used at one station. The transient is not included in the interpretation, leaving two E_x s and \dot{H}_y s and one \dot{H}_z . For logistical reasons, no SHOTEM measurement was made at the exact

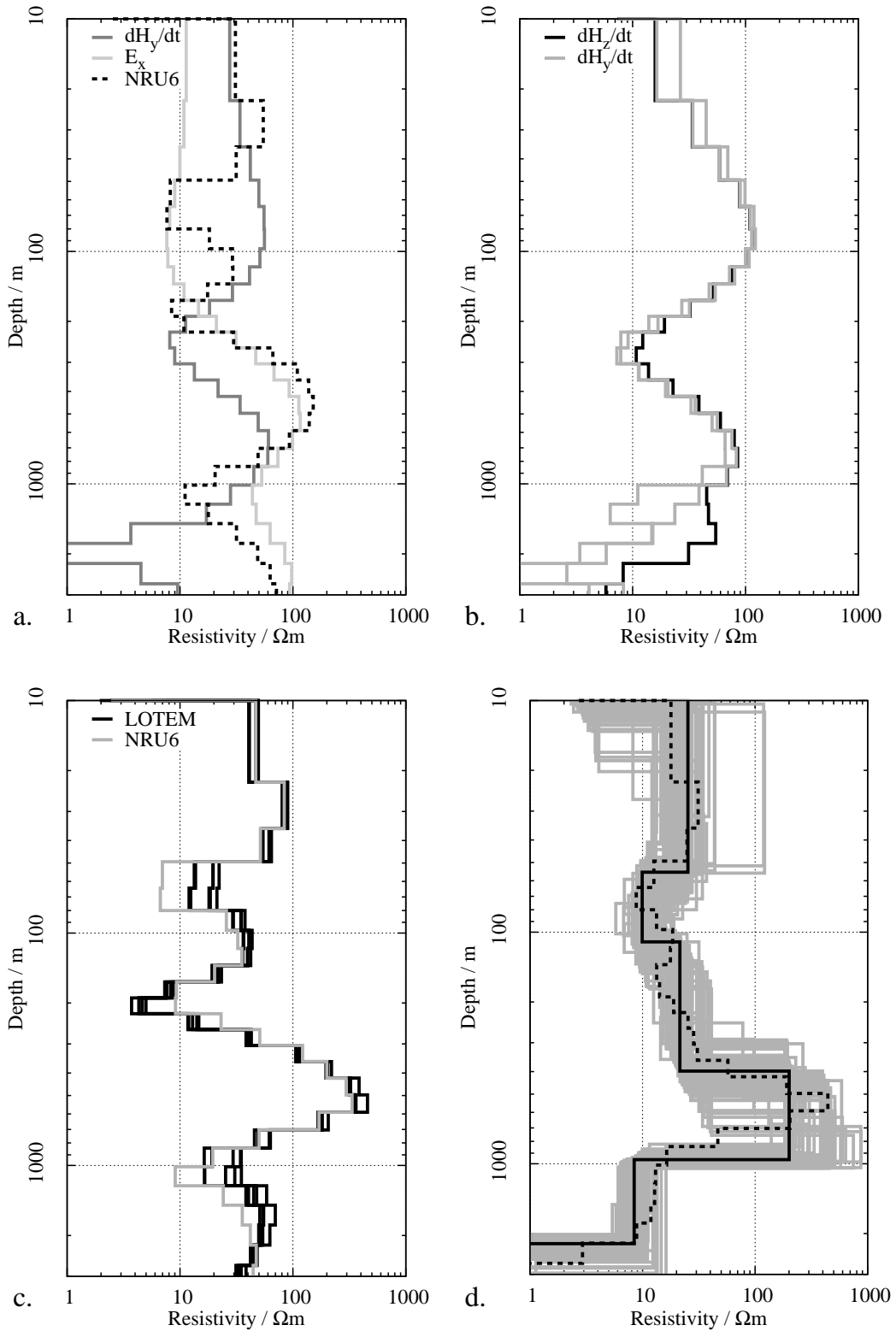


Figure D.19: Inversion results for the transients recorded at ENA; all inversions shown are done with Tx-distortion. a: Comparison of the SJI results for the individual LOTEM-components and the SHOTEM data set NRU6; b: Results for the SJI of all LOTEM- \dot{H} -components; c: SJI-results for all TEM-components; d: Equivalence analysis for all but the LOTEM- \dot{H}_y -components; the black lines shows the best model ($\chi = 3.73$), the dashed line the Occam's-inversion result ($\chi = 3.71$) and the gray lines models with $\chi < 4.10$.

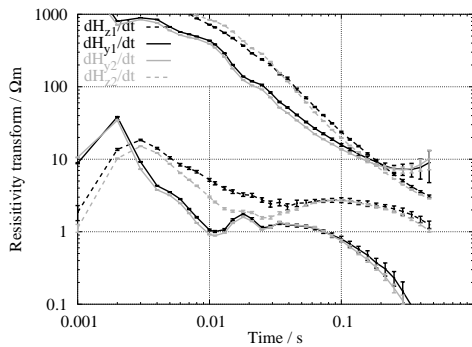


Figure D.20: Resistivity transform curves for the Rx-site GBB;

SJI of the single components show similar features, namely a drop in resistivities below 100 m depth followed by a resistive zone in a depth range of 250 to 500 m. The next conductive zone is located at depths between 600 and 900 m. In the upper part these models are similar to the SHOTEM model (fig. D.21a) and also to the result at GBA. The model do not change significantly, when Tx-distortion is included into the inversion process.

SJIs of different LOTEM-components also do not change the resulting models. In particular omitting the distorted \dot{H}_z -transients does not change the result. The biggest difference in the models are found in the resistivity of the resistive feature and the base of the deep conducting feature. All in all, using all five LOTEM-components seems reasonable (fig. D.21b).

Including the N20 data set, the shallow part of the model changes. Interestingly, a thin layer with an extremely low resistivity $< 1 \Omega\text{m}$ is introduced by the LOTEM-components. This layer did not even show up in the single SHOTEM inversion. The conductive feature between 100 and 250 m depth moves downward. The deeper part does not change (fig. D.21c).

FJIs of all LOTEM-components reproduced the models from the SJIs. FJIs including the SHOTEM data set in general converged at high misfit levels. Also, the models differed from the SJI with and without the N20 data set. For the equivalence analysis (fig. D.21d) only the LOTEM-transients were used.

The model is very similar to the one found at GBA and PHB. The upper part is less resistive, which might be related to the fact that this site is closer to the sea. As discussed in the sections for GBA and PHB the conductive features are believed to be caused by the geology, although how is unknown. As discussed for site GBA, the saline water interface can not be detected here, due to the shorter transients and the low resistivities of the overlying formations.

D.1.9 Sites HAA and HAB

These two sites are located in the NE of the survey-area, close to the Sea of Galilee. Fig. D.22 shows the apparent resistivity curves for HAA (left) and HAB (right). At HAA, the \dot{H}_z -transients show only slight differences around 10 ms. All in all, the agreement between the two Rx-stations' data sets is good. Two of each E_x -, \dot{H}_y - and \dot{H}_z -transients were used. At HAB, the faulty (B)-coil was used. The data recorded with this sensor was not used for interpretation. The early times of all magnetic components indicate that the subsurface exhibits a conductive upper part. However, both \dot{H}_y -transients differ slightly at early times. Also, the early time depression in the \dot{H}_z -component is suspicious. Additionally to the LOTEM data sets, the SHOTEM data sets N27 (at HAA) and N31 (at HAB) are available.

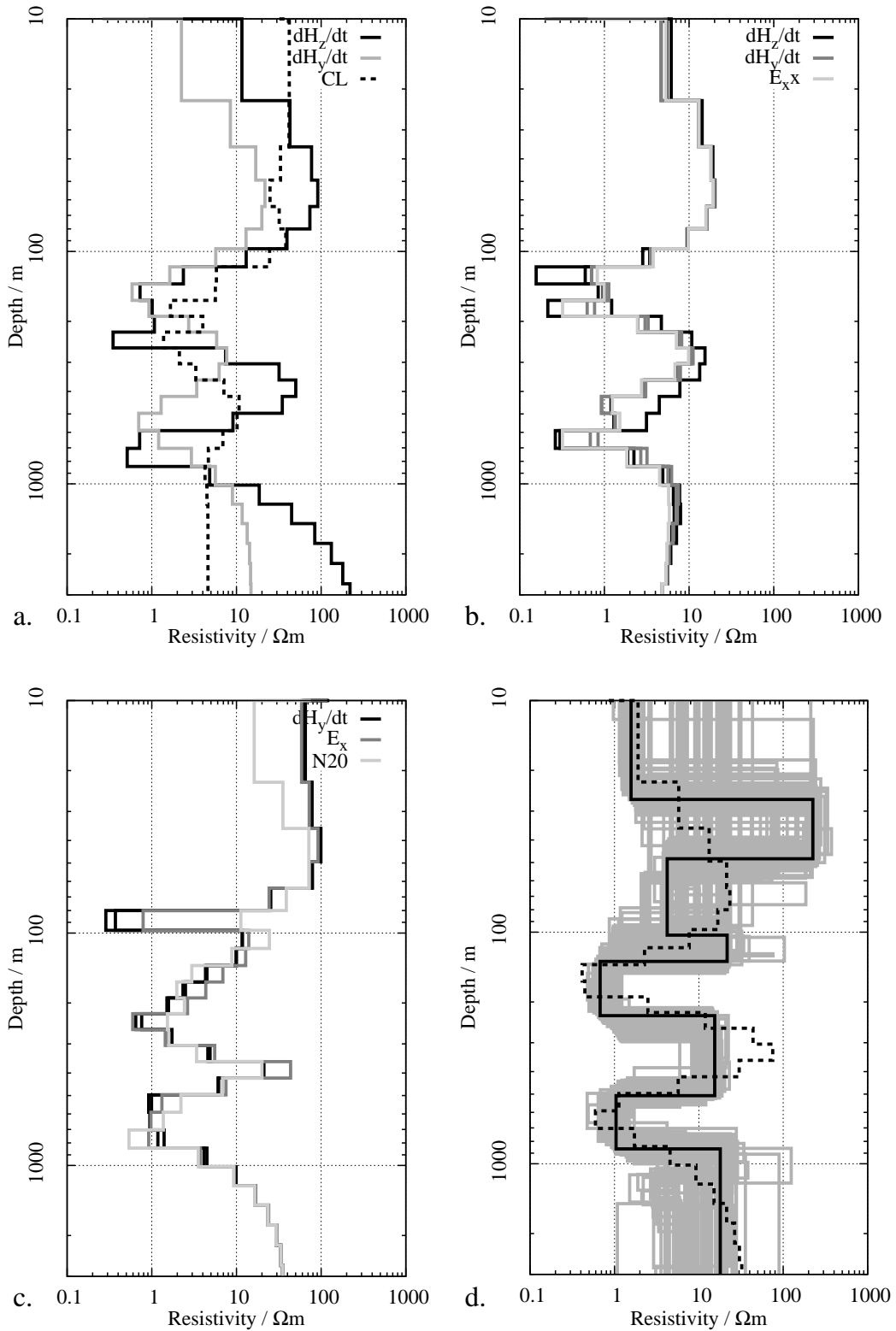


Figure D.21: Inversion results for the transients recorded at GBB; a: Comparison of the SJI results for the individual LOTEM-components without Tx-distortion and the SHOTEM data set N20; b: Results for the SJI of all LOTEM-components including Tx-distortion; c: SJI-results for the two \dot{H}_y -, the E_x - and the SHOTEM-transient including Tx-distortion; d: Equivalence analysis for all LOTEM-components; the black lines shows the best model ($\chi = 2.56$), the dashed line the Occam's-inversion result ($\chi = 2.45$) and the gray lines models with $\chi < 2.82$.

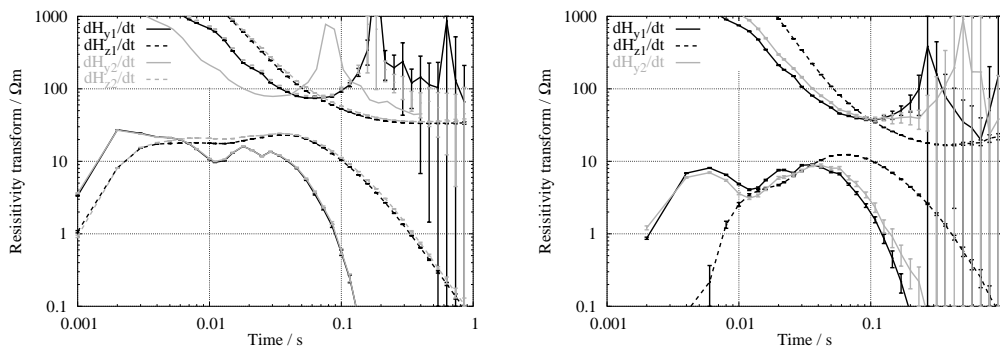


Figure D.22: Resistivity transform curves for the Rx-sites HAA (left) and HAB (right);

At HAA, SJIs of the individual LOTEM-components worked well. For all components similar models were obtained, showing conductive zones between 200 to 500 and 1000 to 2000 m depth. The depth to these features varies, depending on the component. SJIs of the LOTEM- \dot{H}_y s result in models where the shallow conductor is deeper, and the deeper is shallower than for the \dot{H}_z -components (fig. D.23a). The results of for the electric fields are in agreement with the \dot{H}_z s for the shallow feature and with the \dot{H}_y s at depths greater than 1000 m. Inverting the Tx-distortion parameter in general does not change the results. All SJIs including the LOTEM- E_x s fail to converge at lower misfits, thus showing very smooth models. SJIs with the SHOTEM data set fail.

The slight discrepancy between the magnetic components remains even in SJIs of all LOTEM- \dot{H} s (fig. D.23b). FJIs of either the magnetic transients only or all LOTEM-components give similar results (fig. D.23c). The equivalence analysis was done using all six LOTEM data sets (fig. D.23d). The lower part of the model is well constrained. However, the exact depth to the deep conductive feature varies, as well as the exact conductivity. The reason for this could be the slightly inconsistent parameters for this feature found in the different components. Nevertheless, the existence of this conductive feature is very likely as it was resolved by any inversion which reached a sufficient misfit.

At HAB, the results are similar. The inversions including the electric fields only converge at low misfit levels if Tx-distortions are included. SJIs of the different components work well and give similar results. Fig. D.24a and fig. D.24b show the results for SJIs of the three LOTEM- \dot{H} -components and all five LOTEM-components, respectively. They are similar, except for the resistive feature in 500-950 m depth, which is more pronounced if the electric fields are included. Inversions including the SHOTEM-transient do not reach a sufficiently low misfit and their results differ significantly from the other inversions (fig. D.24c). For the equivalence analysis, either the LOTEM- \dot{H} s or all LOTEM-components could be used. FJIs using all five LOTEM data sets showed a different behaviour in the upper part. For the equivalence analysis shown in fig. D.24d, only the magnetic LOTEM-components were used. The deep conductive feature is considered reliable, as it was found in any inversion excluding the SHOTEM data set, even when all five LOTEM-components were used for the equivalence analysis.

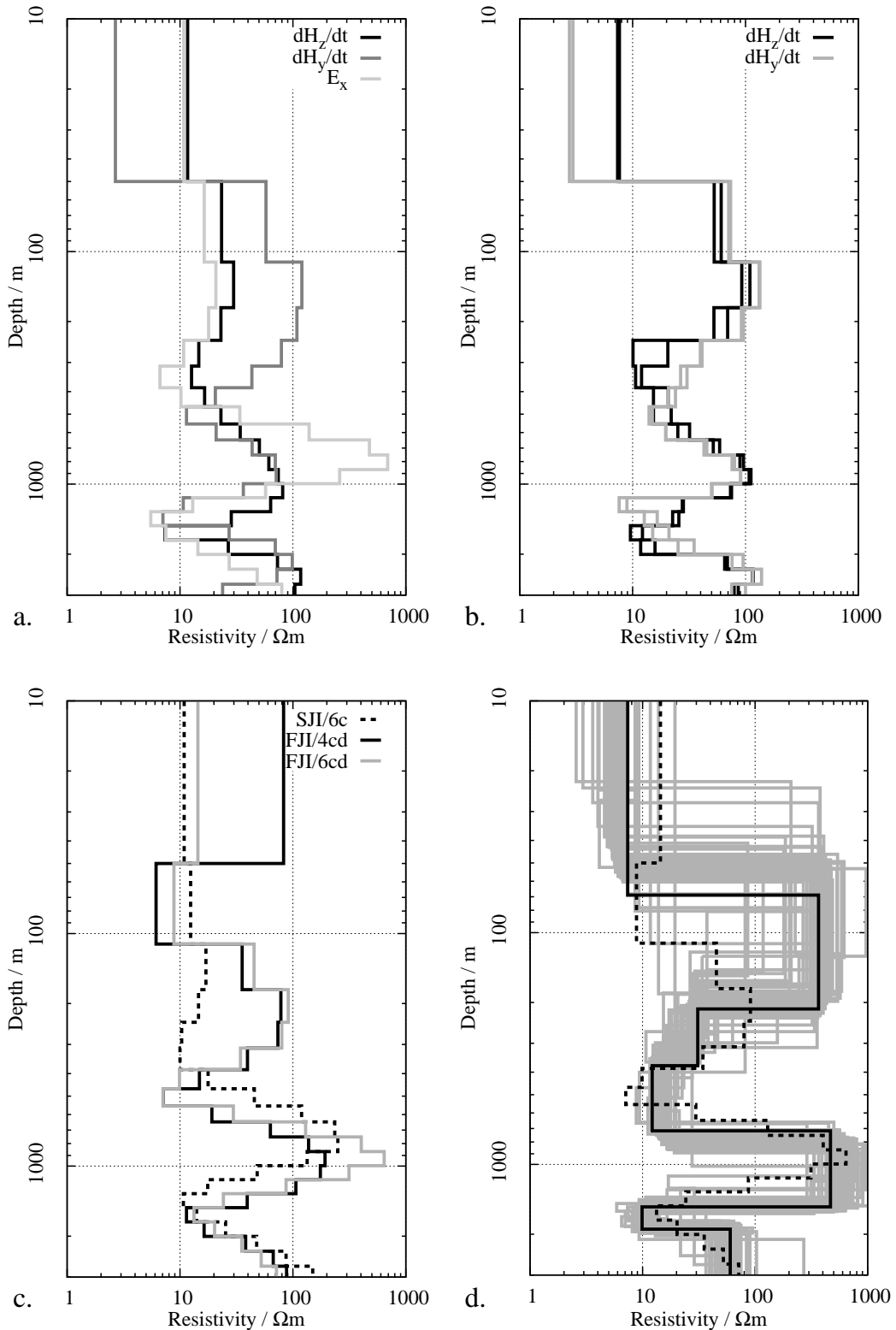


Figure D.23: Inversion results for the transients recorded at HAA; a: Comparison of the SJI results for the individual LOTEM-components without Tx-distortion; b: Results for the SJI of the LOTEM- \vec{H} -components without Tx-distortion; c: Comparison between one representative SJI-result for the SJI of all LOTEM-components without Tx-distortion ("SJI/6c") and the FJIs with Tx-distortion either for all LOTEM-Hs ("FJI/4cd") or all LOTEM-components ("FJI/6cd"); d: Equivalence analysis for all LOTEM-components; the black lines shows the best model ($\chi = 1.78$), the dashed line the Occam's-inversion result ($\chi = 1.76$) and the gray lines models with $\chi < 1.95$.

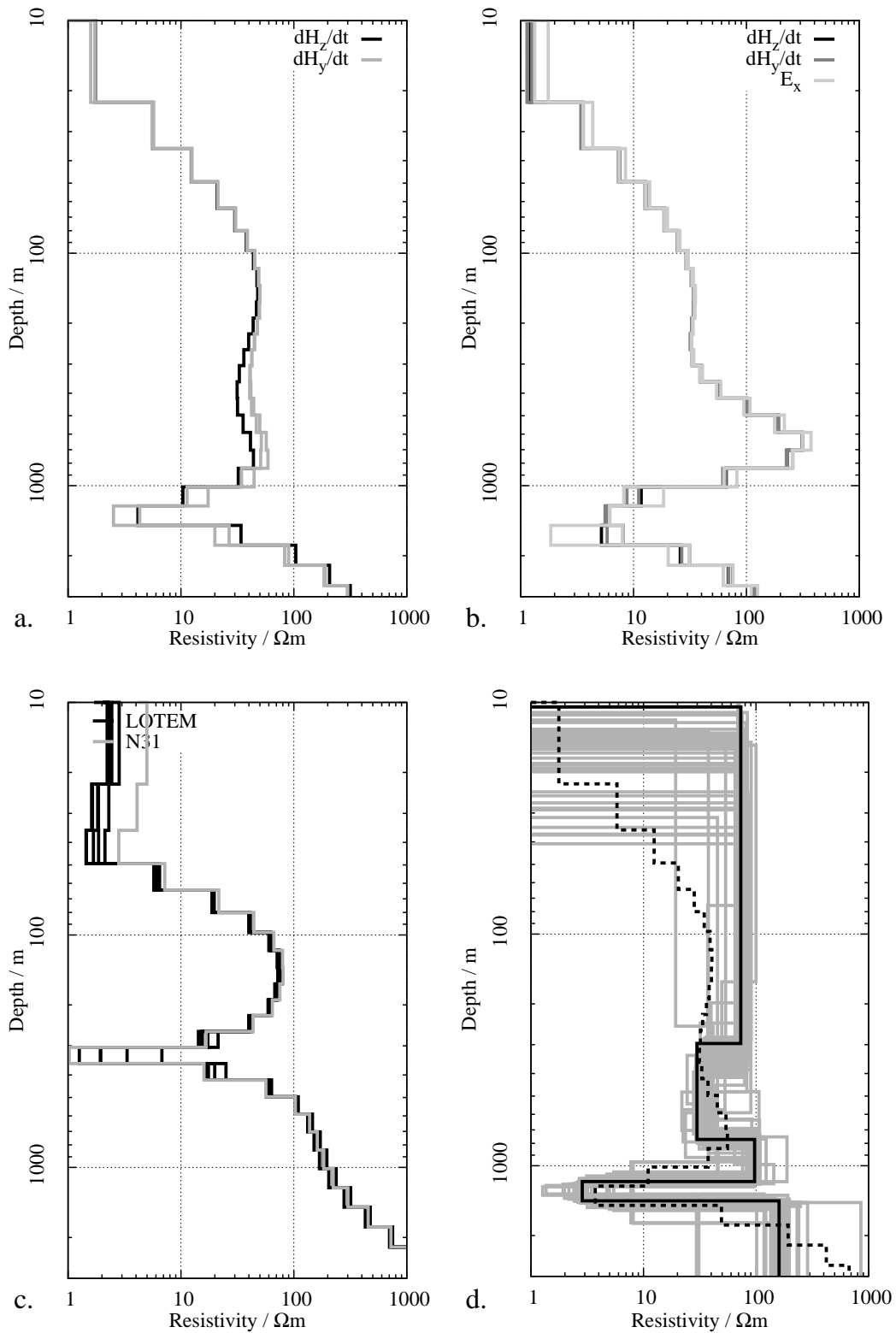


Figure D.24: Inversion results for the transients recorded at HAB; all results are obtained including Tx-distortion. *a:* Results for the SJI of the LOTEM- \dot{H} -components; *b:* Results for the SJI of all LOTEM-components; *c:* Results for the SJI using all six TEM-components; *d:* Equivalence analysis for all LOTEM- \dot{H} -components; the black lines shows the best model ($\chi = 1.28$), the dashed line the Occam's-inversion result ($\chi = 1.27$) and the gray lines models with $\chi < 1.38$.

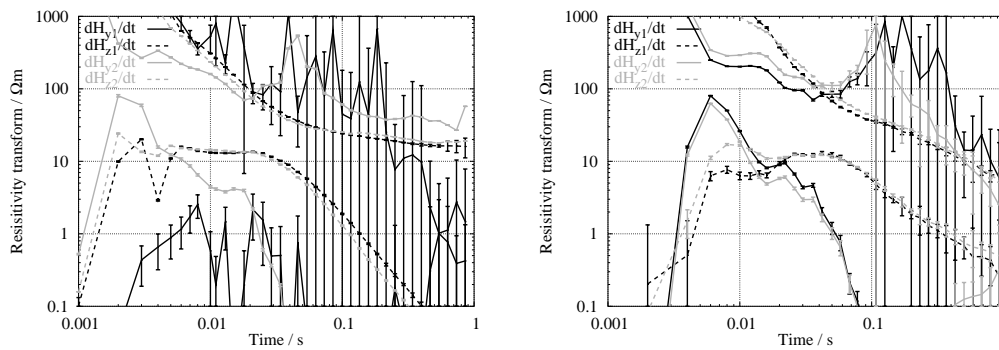


Figure D.25: Resistivity transform curves for the Rx-site KEA (left) and KEB (right);

D.1.10 Sites KEA and KEB

The Tx KE is located on a foothill of the Carmel. The Rx-site KEB is situated on the coastal plain, whereas KEA is further eastward in Carmel. The data quality at both sites is not very good.

At KEA, two stations were set up, each with an E_x -, \dot{H}_y - and \dot{H}_z -sensor. At the same location the SHOTEM-transient N9 was recorded. One \dot{H}_y -transient does not contain any signal (fig. D.25, left). Possibly, the (K)-sensor was not switched on. The log sheet also records that the protection cap was not removed from one of the electrodes of the second E_x -sensor. The E-field sensor thus was coupled half-capacitively to the ground which changes the system response significantly. The transient therefore was not used for the inversion. The \dot{H}_z -transients exhibit a strange behaviour at early times. At KEA1 the \dot{H}_z -curve even shows a sign reversal within a few ms. For $t > 10$ ms both \dot{H}_z -curves are similar. The cause for this strong but rapid sign change is not clear.

At KEB two stations were set up with E_x -, E_y -, \dot{H}_y - and \dot{H}_z -sensors. The SHOTEM data set N10 was also recorded there. The data sets here are even noisier than at KEA, especially at late times. The \dot{H}_z -transients differ at early times and are similar only after 30 ms. All resistivity transform curves indicate a conductive basement (fig. D.25, right).

The remaining \dot{H}_y -transient at KEA does not fit the other four data sets. In SJI the associated models differ very much from the other components' models. Fig. D.26a shows an example for the SJI including Tx-distortion using all LOTEM- \dot{H}_z s. The other components, two LOTEM- \dot{H}_z s, one E_x and the SHOTEM data set fit well (fig. D.26b). Tx-distortion changes neither the misfit nor the structure of the models. Similar results are obtained by the FJIs.

In general, the models are resistive for depths up to 100 m and again exhibit a resistive zone between 650 and 1000 m depth. Below the behaviour is erratic and thus not reliable. As this position is quite close to the coast, the supposed seawater intrusion should appear at shallow depths. The conductive feature at depths of around 400-500 m is a likely candidate. It is not well resolved. Still, all models within the equivalence range show resistivities $< 14 \Omega\text{m}$ in this depth range.

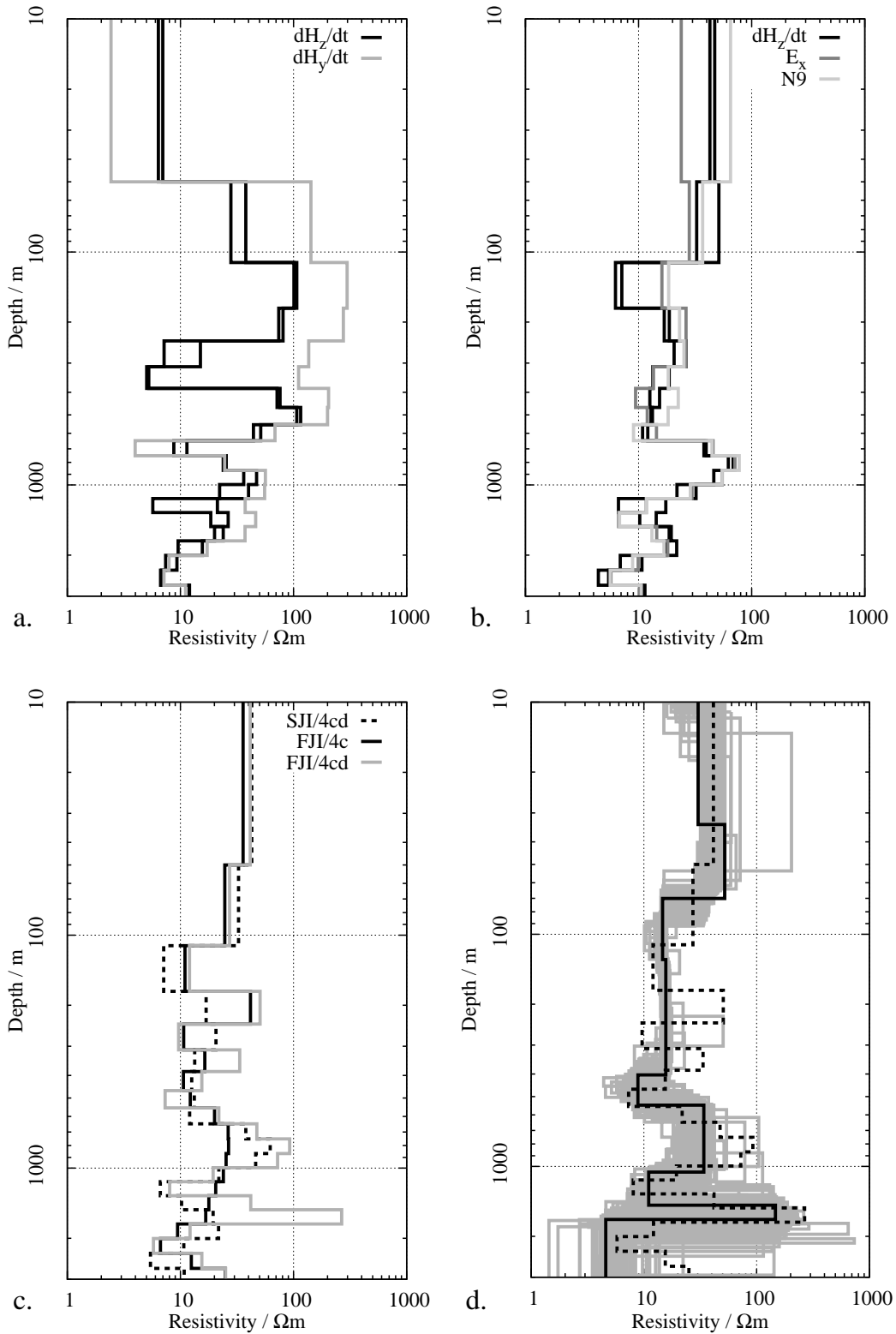


Figure D.26: Inversion results for the transients recorded at KEA; a: Results for the SJI of the LOTEM- \dot{H} -components with Tx-distortion; b: Results for the SJI including Tx-distortion of all TEM-components except the LOTEM- \dot{H}_y ; c: Comparison between one representative SJI-result from panel b (“SJI/4cd”) and the FJIs for the same components without (“FJI/4c”) or with Tx-distortion (“FJI/4cd”); d: Equivalence analysis for all but the LOTEM- \dot{H}_y data set; the black lines shows the best model ($\chi = 1.55$), the dashed line the Occam’s-inversion result ($\chi = 1.59$) and the gray lines models with $\chi < 1.85$.

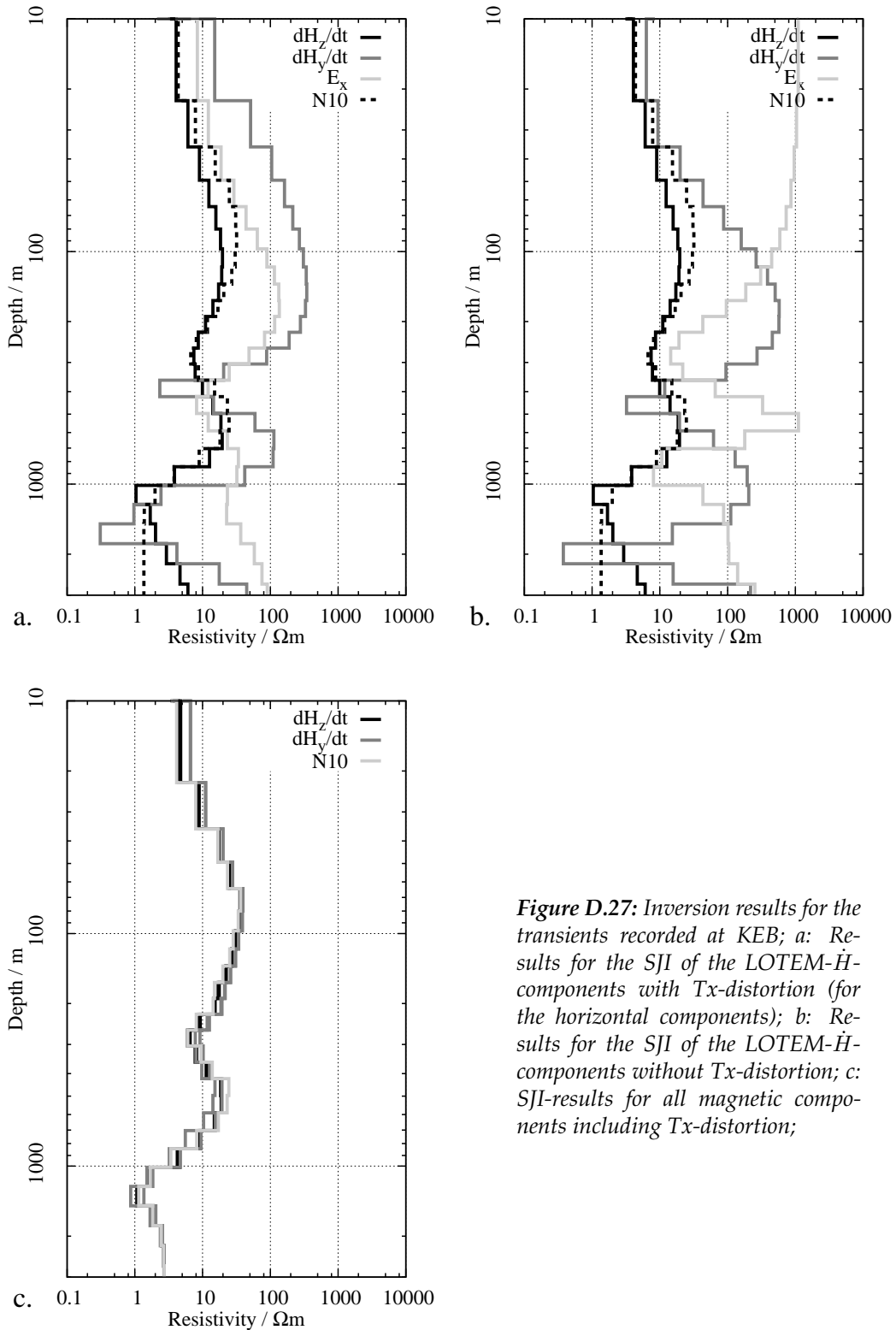


Figure D.27: Inversion results for the transients recorded at KEB; a: Results for the SJI of the LOTEM- \dot{H} -components with Tx-distortion (for the horizontal components); b: Results for the SJI of the LOTEM- \dot{H} -components without Tx-distortion; c: SJI-results for all magnetic components including Tx-distortion;

At KEB, the SJIs of the individual LOTEM-components show similar features, if the Tx-distortion is included (fig. D.27a). Two conductive features are found at depth, one around 300 m, the other below 1000 m. Especially the LOTEM- \dot{H}_z s fit the SHOTEM inversion results extraordinarily well. If no Tx-distortion is allowed, the misfit of the horizontal components is increased by 50 %. The resulting models

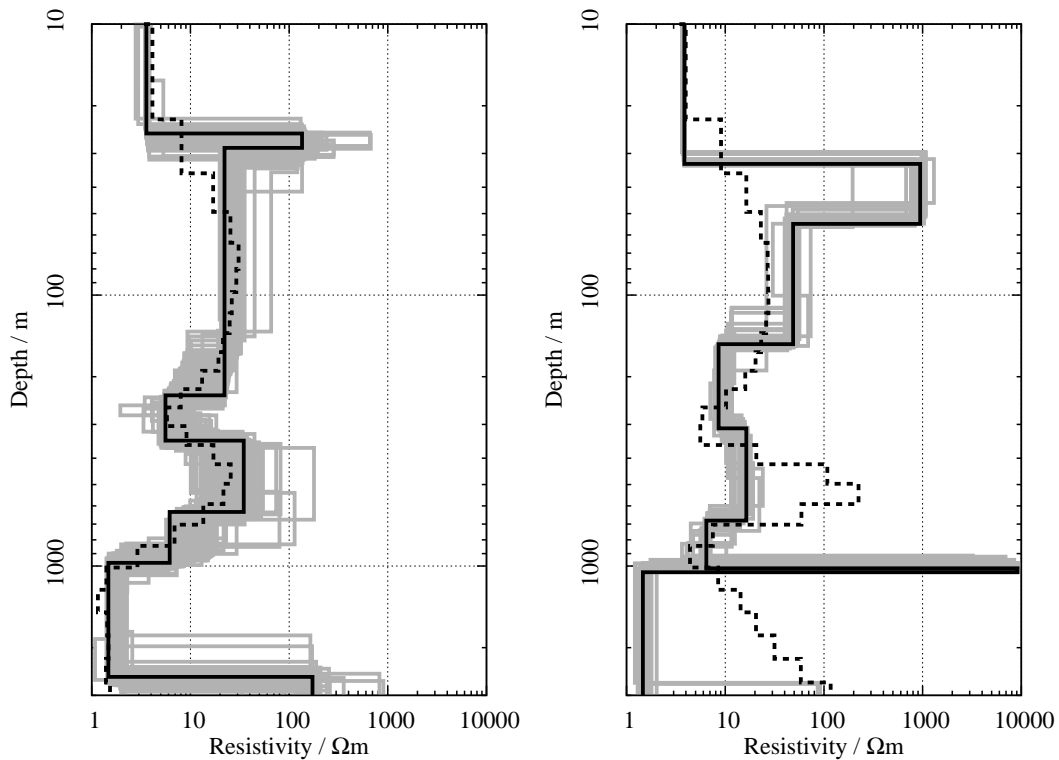


Figure D.28: Results of the equivalence analysis at KEB; left: Equivalence analysis for the five magnetic components; the black lines shows the best model ($\chi = 1.37$), the dashed line the Occam's-inversion result ($\chi = 1.37$) and the gray lines models with $\chi < 1.50$. Right: Equivalence analysis for all TEM-components; the black lines shows the best model ($\chi = 1.79$), the dashed line the Occam's-inversion result ($\chi = 2.59$) and the gray lines models with $\chi < 1.96$.

differ significantly from the ones for the other components (fig. D.27b).

Unless the two E_x s are included, the models of the SJIs give a consistent picture. Fig. D.27c) shows the SJI results for all magnetic components including the SHOTEM data set. The results resembles the SJI results for the individual TEM-components.

The equivalence analysis for all magnetic components is shown in the left panel of fig. D.28. The results are similar to the SJI results, showing two conductive features – the first between 200 and 400 m depth and the second below 800-1000 m.

The inversions seem to be more complicated when the electric fields are included. Although the main features are similar, some differences show up. The right panel of fig. D.28 shows the equivalence analysis for the inversion of all seven TEM-components. The dotted smooth model shows similar behaviour to the inversion of the magnetic components only. The biggest difference is the very resistive layer at a depth of around 1000 m. This layer, which shows up in every equivalence analysis including the electric fields, is most likely the reason for the bad performance in the smooth model inversions of E_x -transients.

This Rx-site is even closer to the coast than KEA. The seawater interface thus is supposed to be shallower. The conductive zone around 200 m depth is a likely candidate. These shallow depths are only well resolved by the SHOTEM-transient, the LOTEM-transients thus are not pertinent to the target of the survey.

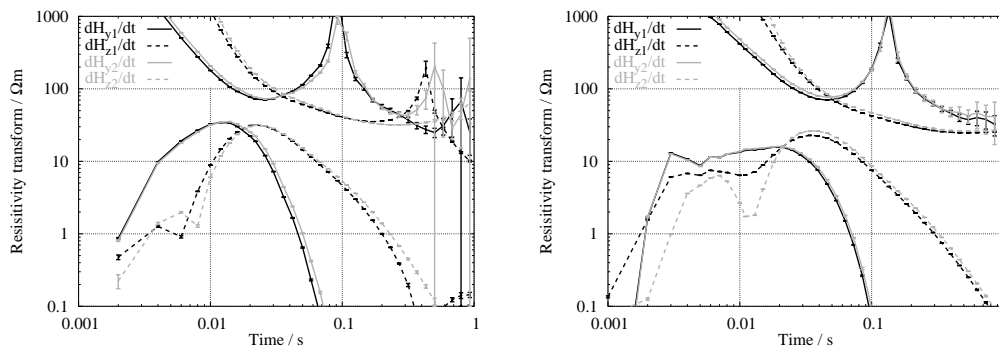


Figure D.29: Resistivity transform curves for the Rx-sites KKA (left) and KKB (right);

D.1.11 Sites KKA and KKB

The Tx KK is located in the north-eastern part of the area under investigation between the DV Tx and the HA-stations. Both sites provide two E_x -, \dot{H}_y - and \dot{H}_z -transients apiece. Close to the Rx-sites the SHOTEM data sets N16 (KKA) and N15 (KKB) were recorded.

At KKA (fig. D.29, left), the resistivity transforms for the magnetic transients show an early time depression even in the \dot{H}_y s. The \dot{H}_z exhibit early and late time sign reversals. The time range where both transients are parallel is small (≈ 20 -150 ms), which makes them almost useless.

Fig. D.29 (right) shows the resistivity transform curves for KKB. The \dot{H}_z s show mid-size distortions at early times. The late times seem to be undistorted. Also, the \dot{H}_y s show a normal behaviour at early times.

The SJIs of the different TEM-components from KKA – even the shortened \dot{H}_z -transients – give consistent models. The E_x s alone resolve only a shallow conductor around 200 m depth, which is in accordance to the SHOTEM results (fig. D.30a), whereas the magnetic LOTEM-components resolve a deep conductive feature. The results do not change if Tx-distortion is included, though the misfit is slightly better.

The same results can be obtained by different combinations of TEM-components. Even SJIs with all seven components converge on a low misfit level, giving consistent results (fig. D.30b). Thus, the equivalence analysis was made using all seven TEM-transients (fig. D.30c). All in all, the model is well constrained showing a conductive feature around 200 m and a second around 1000 m depth. From this plot it is not clear whether all models show this conductive feature or not. In fig. D.31 the minimal resistivity of each model shown in fig. D.30c in the depth range between 900 and 1200 m is plotted versus the model's misfit relative to the best misfit. It shows that all models exhibit a conductive zone with less than 15 Ωm in this depth range.

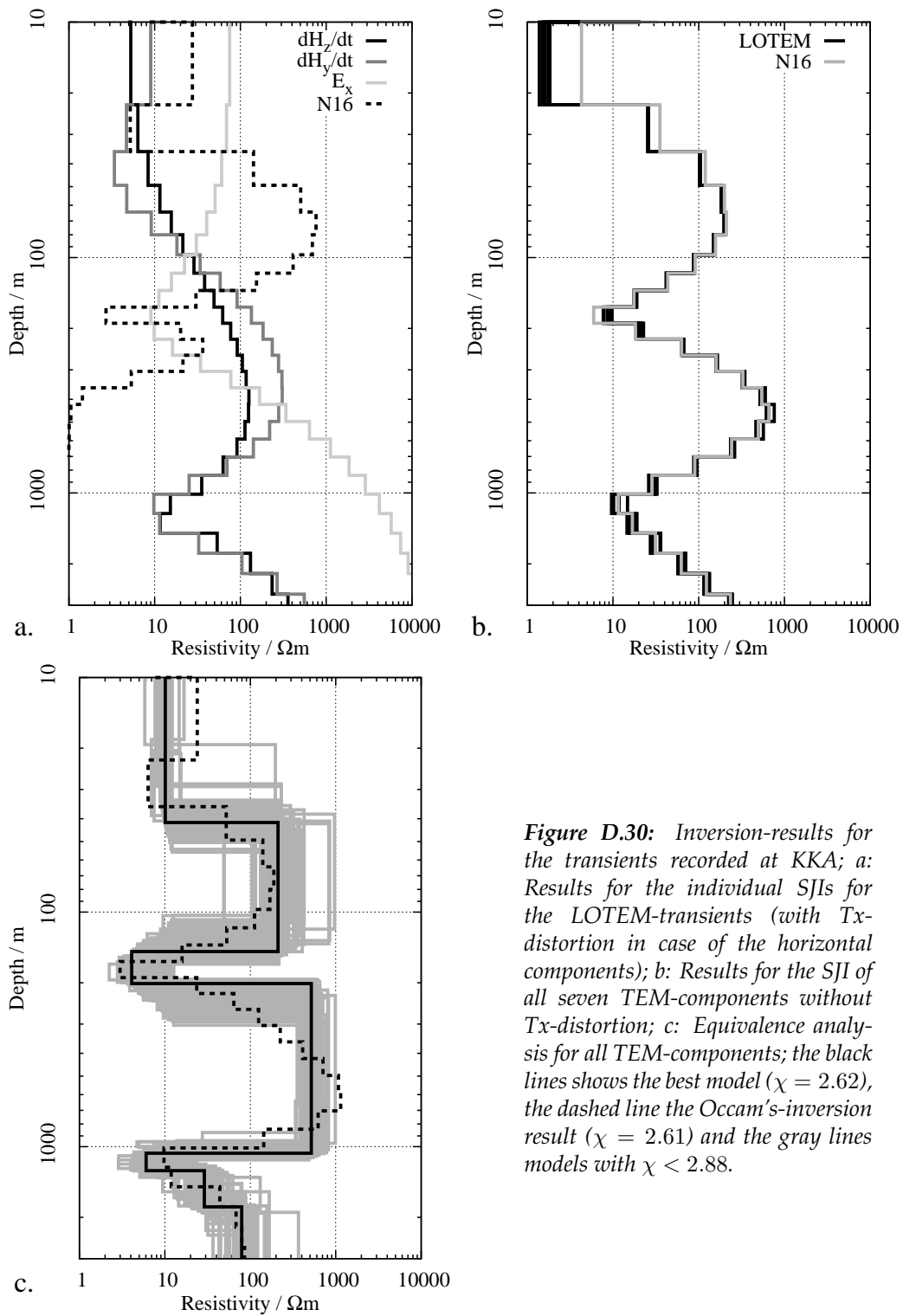


Figure D.30: Inversion-results for the transients recorded at KKA; a: Results for the individual SJIs for the LOTEM-transients (with Tx-distortion in case of the horizontal components); b: Results for the SJI of all seven TEM-components without Tx-distortion; c: Equivalence analysis for all TEM-components; the black lines shows the best model ($\chi = 2.62$), the dashed line the Occam's-inversion result ($\chi = 2.61$) and the gray lines models with $\chi < 2.88$.

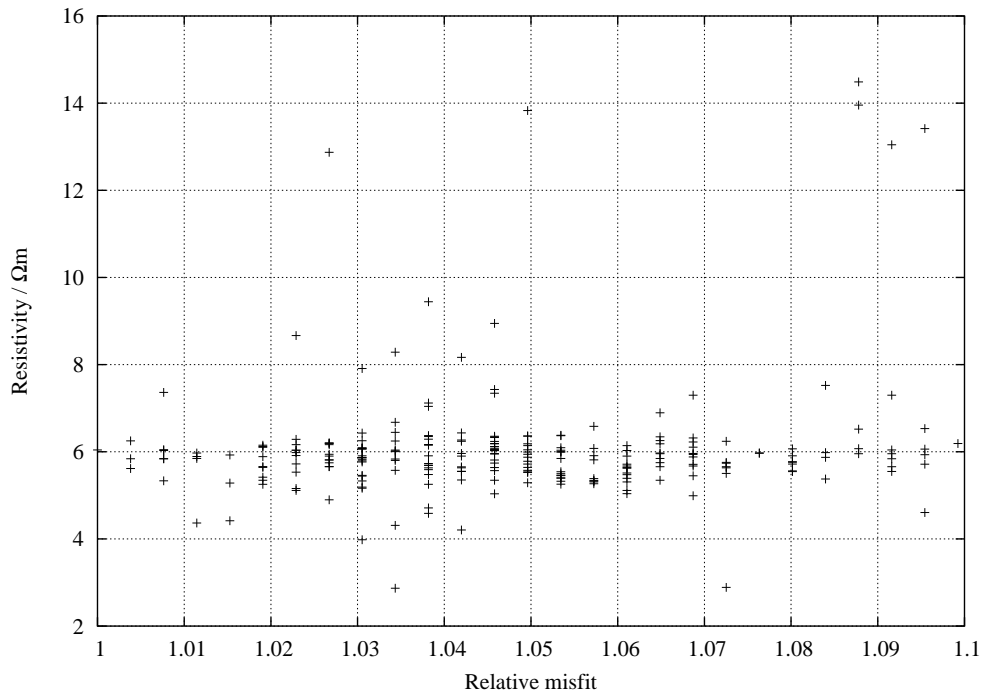


Figure D.31: The minimal resistivities for every model from the equivalence analysis shown in fig. D.30c in a depth range from 900 and 1200 m; the resistivity is plotted against the misfit of the individual model relative to the misfit of the best model found.

At KKB, the results in general are also quite consistent. In all SJIs of the individual LOTEM-components a conductive zone is found between 1000 and 2000 m depth. The top of this zone varies depending on the used component (fig. D.32a). It is deeper (≈ 1500 m) for the LOTEM- \dot{H}_z s and $-E_x$ s and around 1000 m for the \dot{H}_y s. This discrepancy remains even when the \dot{H}_z s and \dot{H}_y s are used in one SJI (fig. D.32b). Testing inversions with different components, the general features of the model are quite stable. The depth to the conductor changes slightly depending on the choice of components. In the lower panels of fig. D.32 the equivalence analyses for either all six LOTEM-components (panel c) or all seven TEM-components (panel d) is shown. The upper part of the model of course is better constrained if the SHOTEM-transient is included in the inversion. The lower part is similar in both models but seems to be less crisp than in the LOTEM-only inversions. The misfit for the FJIs including the SHOTEM-transient is much worse than either the SJIs of all seven components or the FJIs of the LOTEM-components only. For interpreting the deeper part of the model, the LOTEM-only analysis (fig. D.32c) is preferable.

From the inversion results it is clear that there is a conductor at depths greater than 1000 m. Because of the discrepancies with respect to the top of the conductor, this top is not well resolved. Both \dot{H}_z and E_x data lead to a deeper upper bound whereas \dot{H}_y s model calculations (5.3) suggest the conductive feature is deeper the Rx than below the Tx.

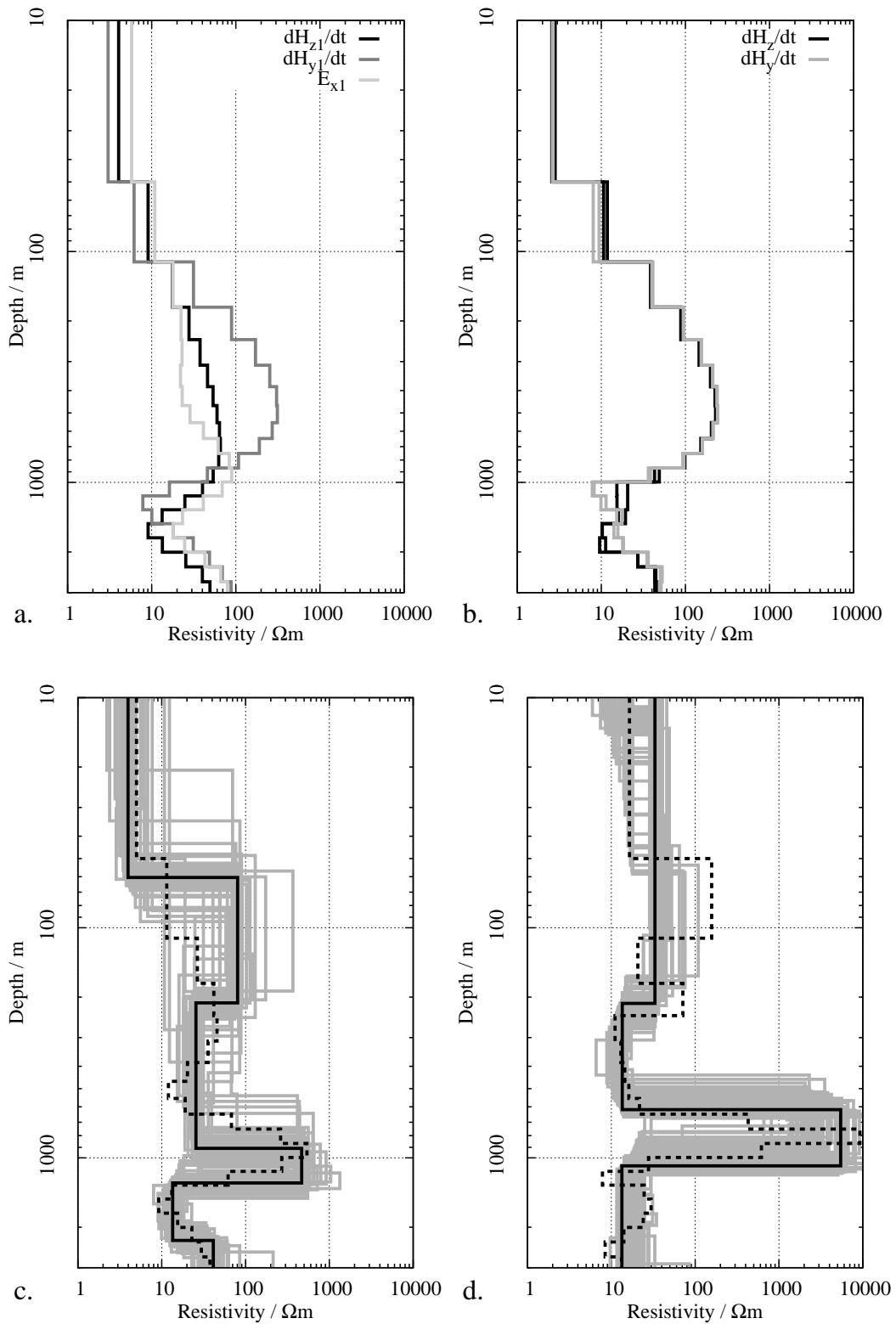


Figure D.32: Inversion results for the transients recorded at KKB; a: Comparison of the SJI results for the individual LOTEM-components with Tx-distortion; b: Results for the SJI of the LOTEM- \tilde{H} -components without Tx-distortion; c: Equivalence analysis for all LOTEM-components; the black lines shows the best model ($\chi = 2.50$), the dashed line the Occam's-inversion result ($\chi = 2.51$) and the gray lines models with $\chi < 2.74$. d: Equivalence analysis for all TEM-components; the black lines shows the best model ($\chi = 4.37$), the dashed line the Occam's-inversion result ($\chi = 4.49$) and the gray lines models with $\chi < 4.80$.

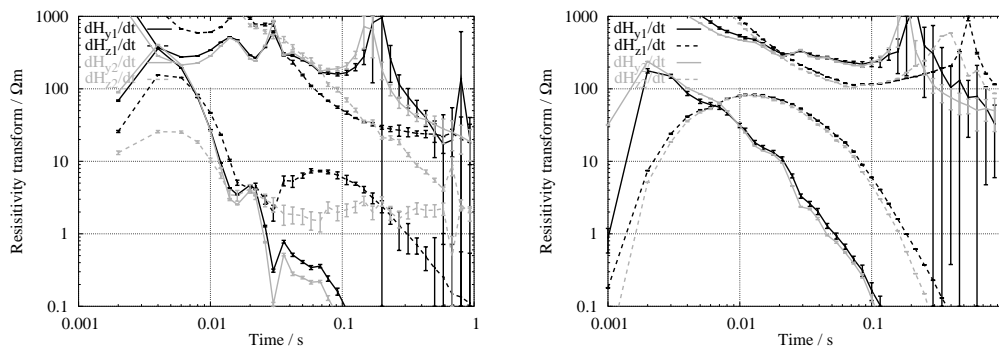


Figure D.33: Resistivity transform curves for the Rx-sites KNA (left) and KNB (right);

D.1.12 Sites KNA and KNB

The spread KN is located north of the Yizre'el Valley in the Galilee mountains. For the \dot{H}_z -component of Rx-station KNA2 the (R)-coil was used. At this day the problems regarding the battery pack occurred which are described in sec. 6.2.2. Therefore, the second \dot{H}_z -transient is not usable as can be seen in fig. D.33 (left). The \dot{H}_z -transient at station KNA1 shows a depression [Strack, 1992] in the time range between 10 and 50 ms, which is unique within the data sets of this campaign.

Especially since we are lacking the second \dot{H}_z , it is impossible to determine which data points have to be removed. Regardless, it is most likely that only the last few data points with huge error estimates would remain. For this reasons no \dot{H}_z -transient was used for interpretation.

At KNB, the \dot{H}_z s exhibit sign reversals at late times. The last data points are thus removed. These distortion are likely to be produced by the same structure, which is observed in the \dot{H}_z -transient at KNA. At early times, the data points are fairly consistent, although the curves are quite steep.

SJIs of the E_x - and \dot{H}_y -transients, respectively, show the consistency of the data sets of both stations. The resulting models show quantitatively similar features, especially the pronounced conductor at depths of 900-1100 m. The upper part differs, as it also does from the SHOTEM result (fig. D.34, left).

The inversions of the electric fields benefit greatly from the introduction of the Tx-distortion parameters to the inversion. The data fit is clearly superior (without distortion $\chi = 0.90$, with distortion: $\chi = 0.53$). However, the resistive feature at medium depths disappears (fig. D.34, right).

SJIs of all LOTEM-components are inconsistent with respect to the depth of the deep conductor (fig. D.35, upper left). This time, inversions including Tx-distortion fail completely, i.e. the algorithm fails to find a model with an acceptable misfit. If the SHOTEM-transient is also used for the inversion, the results are stabilised. Including the Tx-distortion, the misfit is even slightly better than for the SJIs of the single components. In this case the model is much rougher than without the Tx-distortion. Still, the main features are the same as for inversions without Tx-distortion (fig. D.35, upper right and lower left). The final result for the LOTEM-components only or all TEM data sets are similar except for the shallow part (lower right of fig. D.35). Pertinent to the hydrogeological question is the conductor be-

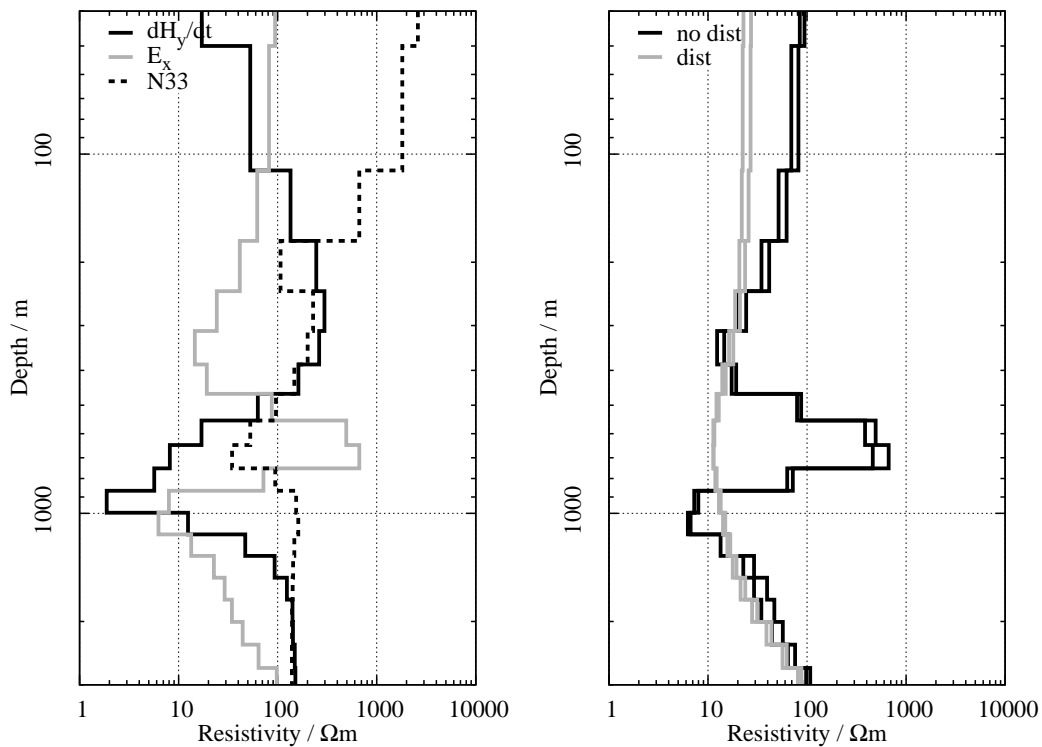


Figure D.34: SJI-results for the transients recorded at KNA; left: Comparison of the SJI-results for E_x and \dot{H}_y and the single inversion of the SHOTEM-transient N33; left: SJI-results for the E_x -transients with and without free T_x -distortion parameters.

tween ≈ 850 and 1000 m depth. However, the results are considered less reliable because of the strong distortion in the \dot{H}_z , due to an unknown structure.

At KNB, the SJIs of the E_x -transients fail to converge on a low misfit level. The resulting models are unrealistic, showing resistivities higher than 10 k Ω m throughout the hole depth range. SJI results of for the magnetic components show a similar behaviour with a resistive body in intermediate depths and a drop in resistivity roughly below 500 m (fig. D.36a). Unfortunately, SJIs of different components do not give a consistent picture. The figs. D.36b-d show the results of different inversions. Although the qualitative structure (a very shallow conductor, followed by a resistor below 100 m depth, followed by a conductor) is similar, the depths and resistivities vary strongly.

If the electric fields are included in inversions with other components, in most cases an acceptable misfit was reached. The algorithm achieves this by introducing high calibration factors around 5.0 for both transients.

No further interpretation steps were taken, because of the inconsistent inversion results and the unknown structure which causes the distortions. This site had to be discarded.

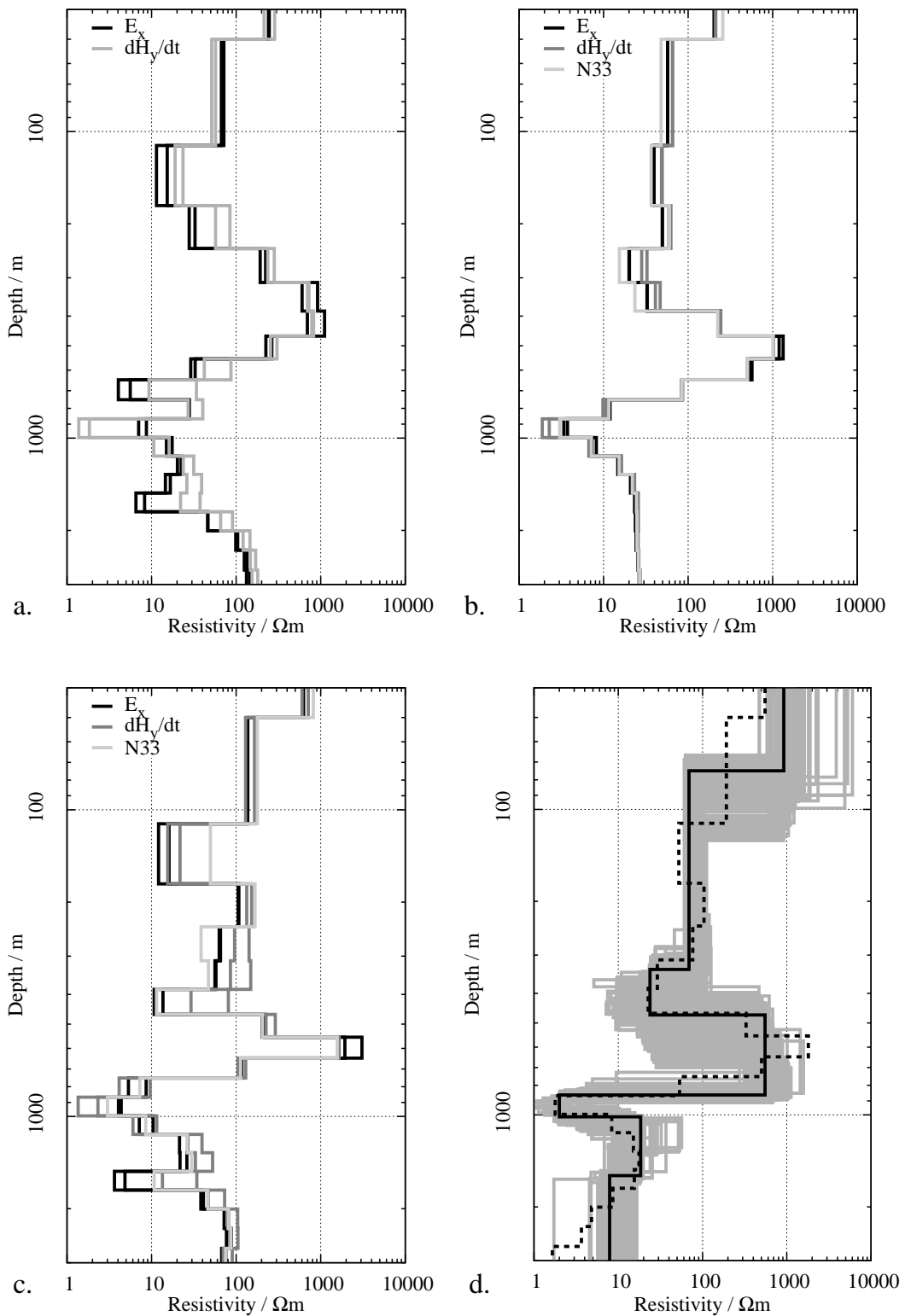


Figure D.35: Inversion-results for the transients recorded at KNA; a: Results for the SJI of all four LOTEM-components without Tx-distortion; b: Results for the SJI of all five TEM data sets without Tx-distortion; c: Results for the SJI of all five TEM data sets with Tx-distortion; d: Equivalence analysis for all TEM-components; the black lines shows the best model ($\chi = 3.99$), the dashed line the Occam's-inversion result ($\chi = 3.92$) and the gray lines models with $\chi < 4.39$.

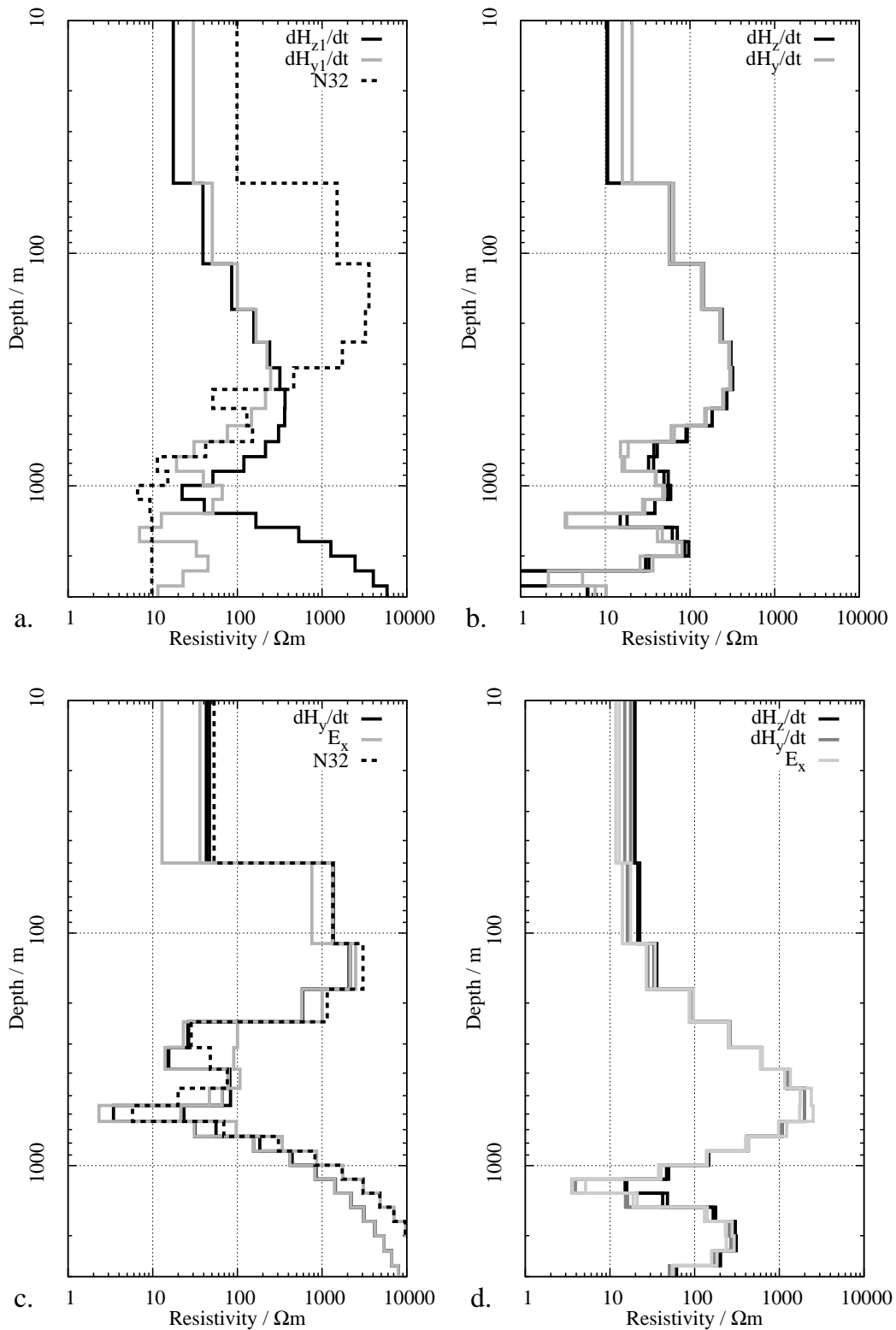


Figure D.36: Inversion-results for the transients recorded at KNB; all inversions shown including horizontal field components are done with free T_x -distortion parameters. *a:* Results for the SJIs of the individual LOTEM-components; results for the E_x -transients show resistivities > 10 k Ω m. *b:* Results for the SJI of all LOTEM- H_s ; *c:* Results for the SJI of the SHOTEM-transient and the LOTEM- H_{ys} and $-E_{xs}$; *d:* Results for the SJI of all LOTEM-components;

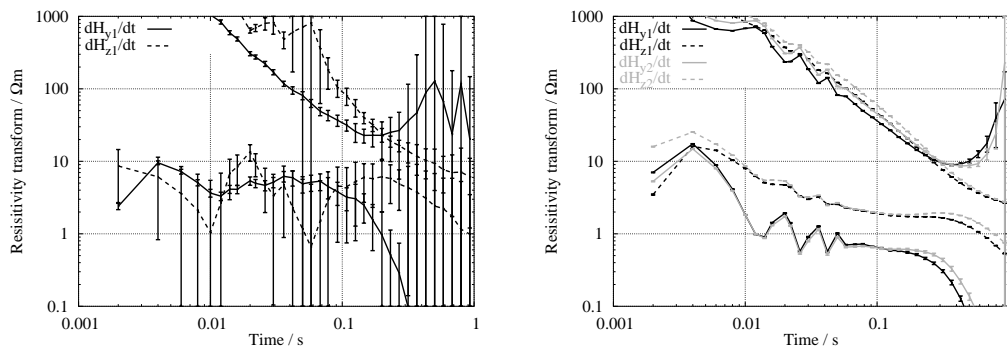


Figure D.37: Resistivity transform curves for the Rx-site PHA (left) and RAA (right);

D.1.13 Site PHA

The site PHA is located in the coastal area SE of the Carmel. After some minutes of recording with one Rx-station, the equipment failed due to heavy rainfall. Only a few stacks could be recorded. The SNR is very low (fig. D.37, left), leaving the E_x - and \dot{H}_y -transient as only usable components. Unfortunately, the models derived for both components by SJIs show no consistent features. The data from this site is thus discarded.

D.1.14 Site RAA

The Rx-site RAA is located in the coastal plain, ≈ 30 km south of the area shown in fig. 6.7 (fig. 6.21, left). Two stations were build up. In total, one E_x - and two \dot{H}_y - and \dot{H}_z -transients are recorded. Like the transients at RAB, the recorded data sets show strong oscillations (fig. D.37, right). However, these are well fit using the oscillating system-response. Similar to the transients at BSB and GBB, the magnetic field derivatives decay very slowly at late times, indicating a highly conductive subsurface. No SHOTEM data set was recorded here.

Inversions including the Tx-distortion parameters achieve about the same misfit as inversion excluding these parameters. SJIs of the \dot{H}_z - or \dot{H}_y -components show few differences (fig. D.38a). The main feature is a massive conductive zone between 200 and 800 m depth. The differences relate to the depth to the top of the conductor and the part deeper than 900 m.

SJIs of the different LOTEM-components lead to similar results. Fig. D.38b shows the results for the SJI of all five LOTEM-components without Tx-distortion as an example. Fig. D.38c displays the final results for RAA. In general, only the massive conductor is resolved, which is formed by the Saqiye Group clays (see RAB, sec. 6.3.1). There are indications of a deeper conductor, which is not resolved. In addition, there are indications of a shallow conductor atop of the Saqiye Group which can be related to sea-water intrusion to the clastic coastal aquifer.

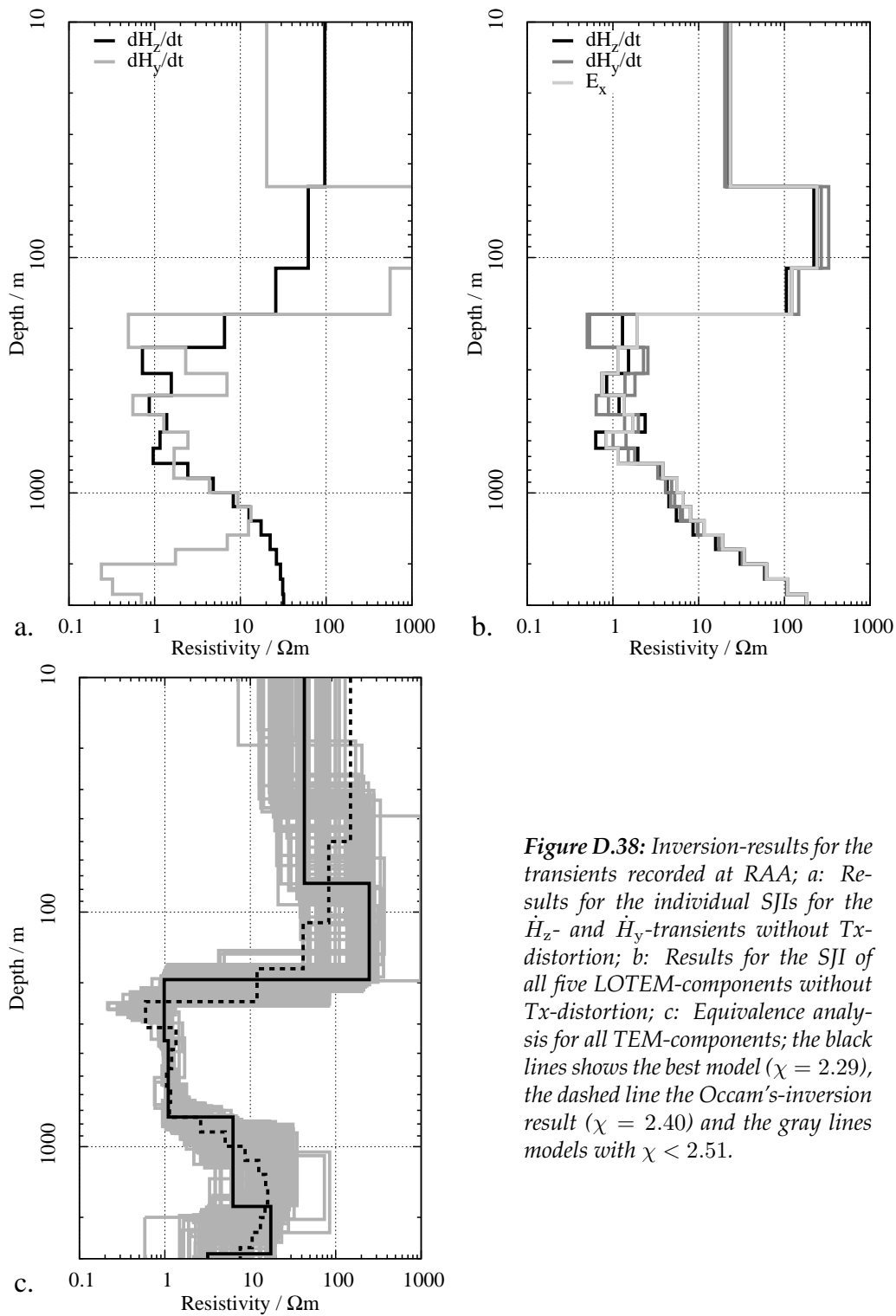


Figure D.38: Inversion-results for the transients recorded at RAA; a: Results for the individual SJIs for the \dot{H}_z - and \dot{H}_y -transients without Tx-distortion; b: Results for the SJI of all five LOTEM-components without Tx-distortion; c: Equivalence analysis for all TEM-components; the black lines shows the best model ($\chi = 2.29$), the dashed line the Occam's-inversion result ($\chi = 2.40$) and the gray lines models with $\chi < 2.51$.

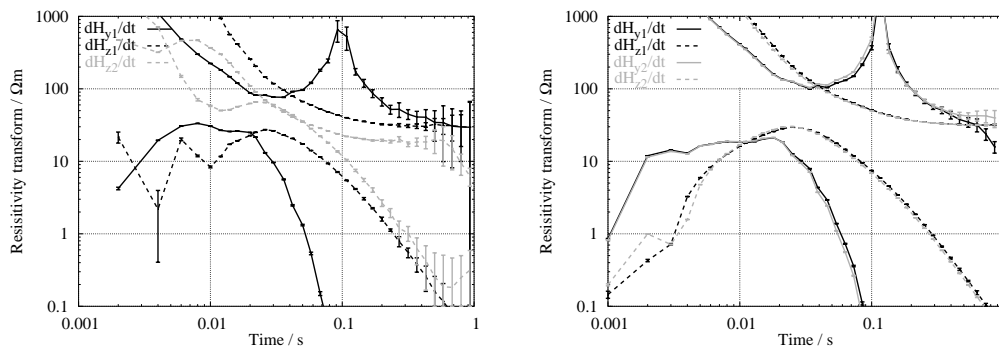


Figure D.39: Resistivity transform curves for the Rx-sites RZA (left) and RZB (right);

D.1.15 Sites RZA and RZB

The Tx RZ is located in the hilly area between the Sea of Galilee and Harod Valley. At RZA only three LOTEM-components, two \dot{H}_z s and one \dot{H}_y , were recorded in addition to the SHOTEM data set N26. The \dot{H}_z -transients show big deviations at up to 30 ms (fig. D.39, left).

At RZB, two stations with one E_x -, \dot{H}_y - and \dot{H}_z -sensor were build up. The SHOTEM data set at this location is named N25. The apparent resistivity curves show no obvious distortions. The \dot{H}_z -transients differ at times < 10 ms, where the voltage increases very slow. These early time points are discarded (fig. D.39, right).

The few data sets available at RZA are moderately consistent after the early time points of the LOTEM- \dot{H}_z s are removed. Fig. D.40a shows the results of an SJI with all four TEM-components, including Tx-distortion. Fixing the distortion parameters does not change the resulting models, but decreases the misfit by a few percent. There are two conductive features, one around 200 m depth, which is resolved only by the SHOTEM-transient, and the other at around 1000 m depth. The latter is also found using only LOTEM-components.

Finding a combination of components which reproduces these results in FJIs is difficult. FJIs of both sets (all LOTEM / all TEM) produce additional structures at depth, which are not very trustworthy, according to the model calculation from sec. 5.4 (e.g. fig. D.40b). Both the position of the top of the conductive feature and underlying structure are not reliably determined by the data. Fig. D.40c shows the results of a equivalence analysis using all four TEM data sets. Unfortunately, no Marquardt model was found which achieved the same misfit as the Occam's inversion result. Nevertheless, the equivalent models resemble the trend of the smooth model. There are indications for a conductive zone between 800 and 1000 m depth, which might have a resistivity $< 10 \Omega\text{m}$. However, this layer is not well resolved.

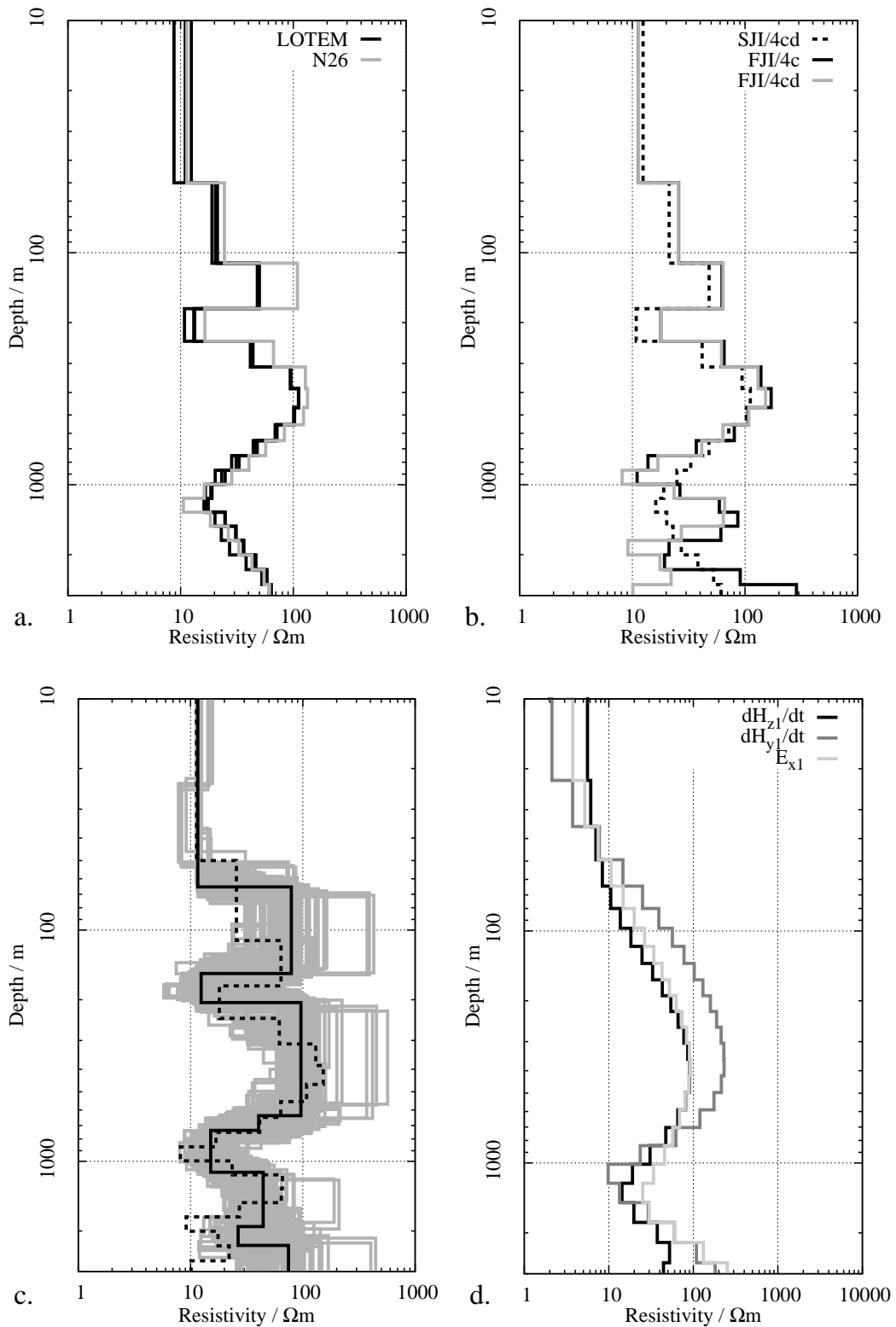


Figure D.40: Inversion-results for the transients recorded at RZA and RZB; a: Results for the SJI of all four TEM-components recorded at RZA with Tx-distortion; b: Comparison of the results of the SJI of the four transients with Tx-distortion ("SJI/4cd"), and the FJIs of these data sets with ("FJI/4c") and without Tx-distortion ("FJI/4cd"); all data sets are from RZA; c: Equivalence analysis for all TEM-components from RZA; the black lines shows the best model ($\chi = 1.81$), the dashed line the Occam's-inversion result ($\chi = 1.60$) and the gray lines models with $\chi < 1.99$. d: Results for the individual SJIs for the LOTEM-transients recorded at RZB without Tx-distortion;

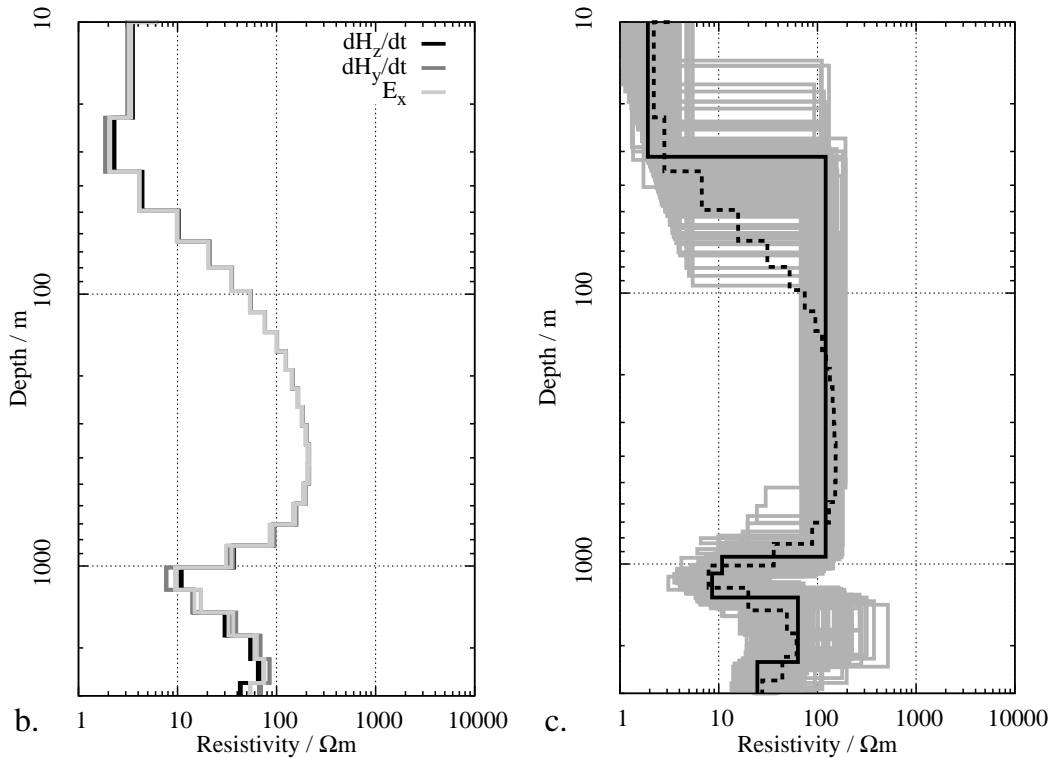


Figure D.41: Inversion-results for the transients recorded at RZB; left: Results for the SJI of all six LOTEM-components without Tx-distortion; right: Equivalence analysis for all TEM-components; the black lines shows the best model ($\chi = 2.41$), the dashed line the Occam's-inversion result ($\chi = 2.38$) and the gray lines models with $\chi < 2.65$.

At RZB the SJIs of the individual LOTEM-components give about the same results (fig. D.41d). Including the Tx-distortion does not change anything. SJIs of different components give similar results. Fig. D.41 (left) shows the results of the SJI of all six LOTEM-components. The most obvious feature is the conductive feature at depths > 1000 m. If the SHOTEM data set is included, the misfit is significantly degraded. Although the deeper structure does not change, the upper part is more structured. These structures are not stable. Also, FJIs with the SHOTEM-component fail. For the interpretation an equivalence analysis using all LOTEM-components is used (fig. D.41, right).

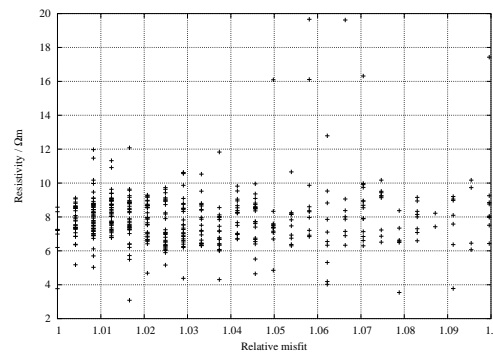


Figure D.42: The minimal resistivities for every model from the equivalence analysis shown in fig. D.41c in a depth range from 900 and 1300 m; the resistivity is plotted against the misfit of the individual model relative to the misfit of the best model found.

From this plot it is not clear whether all models show a conductive feature around 1000 m depth. In fig. D.42 the minimal resistivity of each model shown in fig. D.41 (right) in the depth range between 900 and 1200 m is plotted versus the model's misfit relative to the best misfit. It shows that all models show a conductive zone

with less than 20 Ωm in this depth range. All models providing a misfit of within 104.8 % of the best model's misfit show resistivities below 13 Ωm .

D.1.16 Site SAA

SAA was the first LOTEM site to be measured. Although the topography is almost flat except for some ponds, a fault with a displacement > 500 m is found in the subsurface (cp. fig. 6.8). Unfortunately, this was not known at the time when this site was planned. The setup places the Tx north of the fault, whereas the Rx-stations are south of it. The fault cuts the spread in an angle of almost 45° .

Additionally, the Tx-direction was miscalculated by $\approx 30^\circ$. All horizontal components thus are rotated. Three stations were measured with a total of three \dot{H}_z s and \dot{H}_y s, two E_x s and one \dot{H}_x and E_y . The resistivity transforms are shown in fig. D.43. The big differences at early times between the data sets from station 3 compared to the other two stations are due to the fact, that the latter is recorded with the Summit-TEM system, whereas the others are recorded using the TEAMEX-units. However, the H_z -transients show smaller deviations over the whole time-range. Also the \dot{H}_y -s differ.

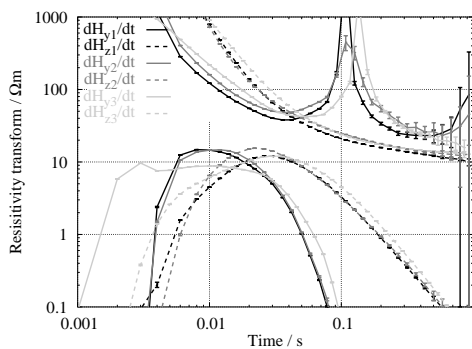


Figure D.43: Resistivity transform curves for the Rx-site SAA;

including Tx-distortion parameters in the inversion reduces the misfit slightly. It changes mainly the shallow part of the models. Similar results are obtained using all six magnetic components (fig. D.44c).

Fig. D.44d shows the results of the SJI using all eight LOTEM-components. They are similar to the results of the magnetic data sets only, apart from the conductor around a depth of 300 m, which seems to be required by the electric field components. The most interesting feature is deeper conductor starting at a depth of ≈ 600 m. As already mentioned, this conductor is also found in the other SJIs, although its depth extension varied slightly.

Due to the fault between the Tx and the Rx and the different results for SHOTEM data sets, the reliability of the inversion is very questionable. Because of the 45° angle of the model geometry to the spread, the set-up can not be compared to one of the model studies in chapter 5.

Two SHOTEM measurements were carried out. At the Tx- and Rx-position the data sets N5 and N6 were recorded. The models derived from these transient show contrary behaviour (fig. D.44a). The SJIs of the LOTEM-components work well, although the results for the two E_x -transients are only qualitatively similar. Fig. D.44b shows results from the SJIs of individual TEM-components. They show a similar behaviour, exhibiting a conductor above a depth of 1 km. Including Tx-distortion parameters in the inversion reduces the misfit slightly. It changes mainly the shallow part of the models. Similar results are obtained using all six magnetic components (fig. D.44c).

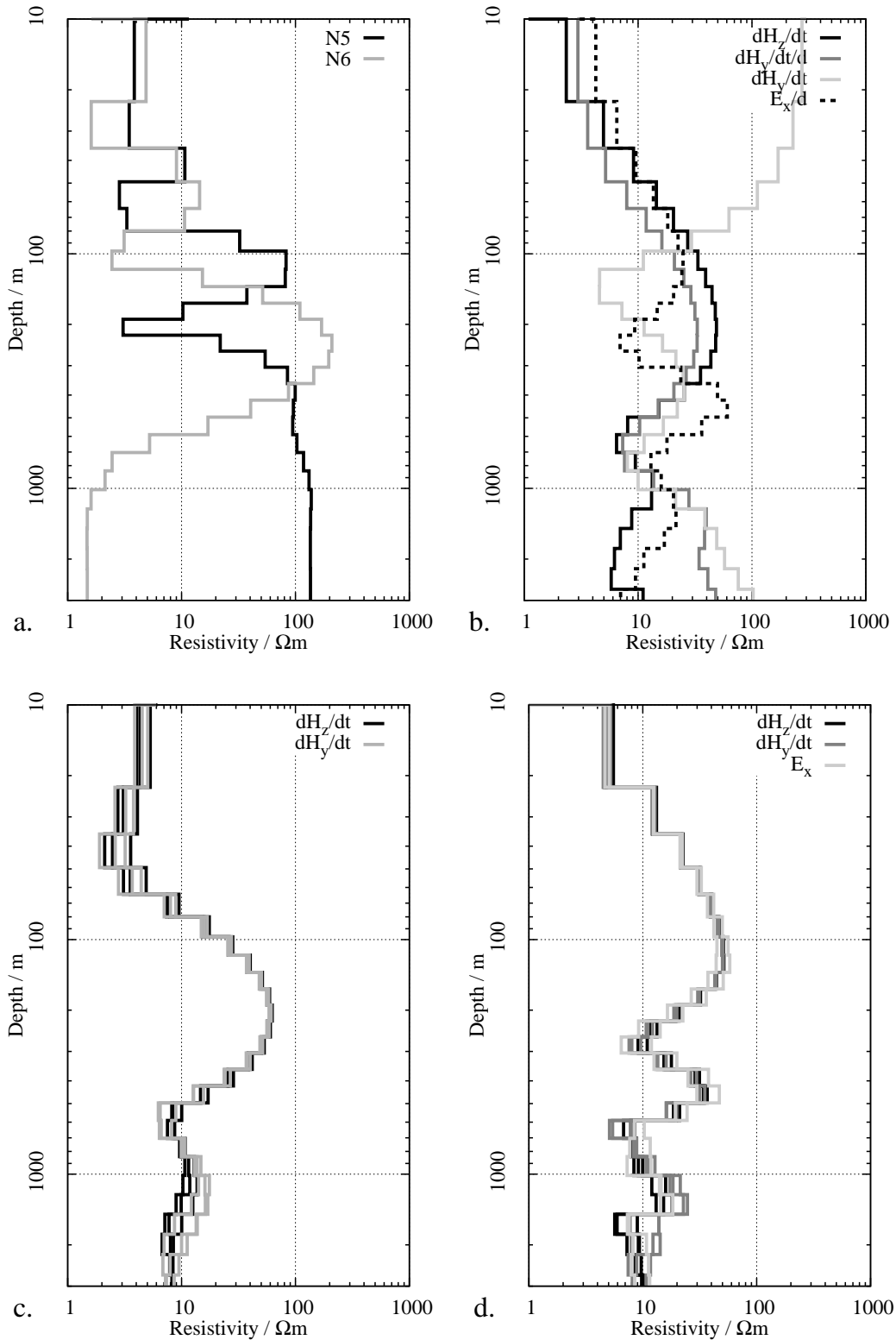


Figure D.44: Inversion-results for the transients recorded at SAA; unless otherwise stated, all inversions shown including horizontal field components are done with free T_x -distortion parameters. *a:* Results for the single inversions of the two SHOTEM data sets N5 and N6; *b:* Results for the SJI of the individual LOTEM-components; the “/d” in the legend marks the inversion results with free T_x -distortion parameters. *c:* Results for the SJI of all LOTEM- \dot{H} s; *d:* Results for the SJI of all LOTEM-components.

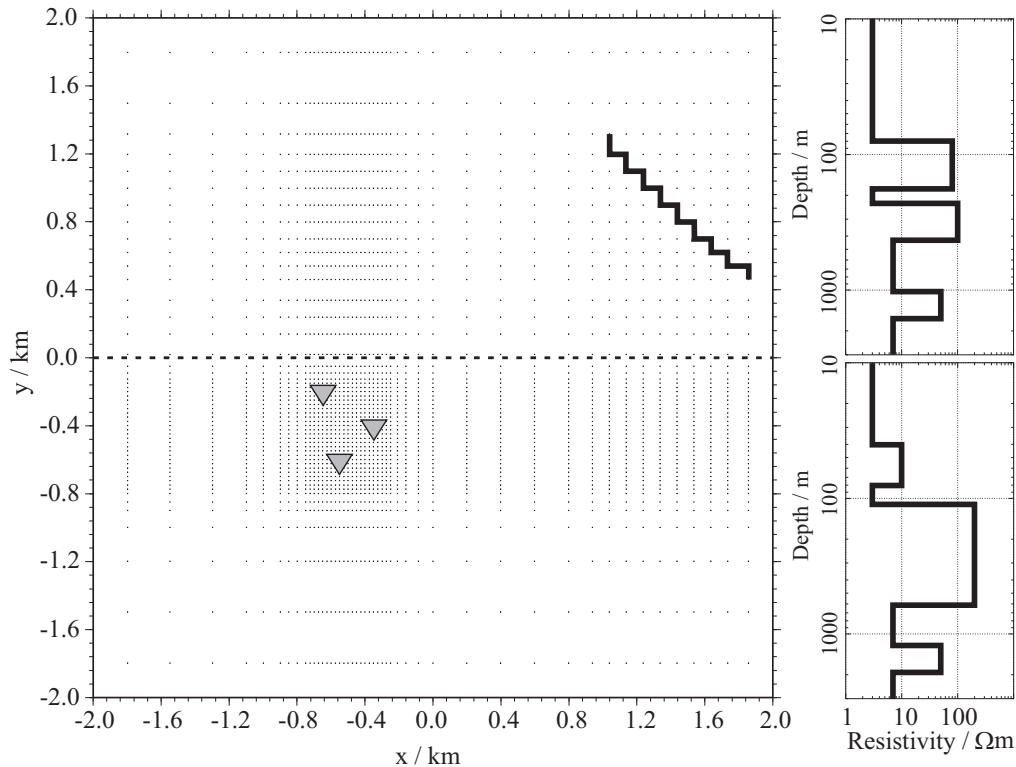


Figure D.45: Model and Tx-Rx-geometry used for modelling the situation at the SA-spread. The points indicate the inner part of the horizontal discretisation of the grid used with SLDMEM3T. The triangles denote the position of the three Rx-stations. The step-like black line shows the Tx-dipoles. The positive y -direction approximately points northward. The earth model consist of two layered quarter-spaces. The dashed line at $y = 0$ km denotes the parting line between the two models. In the left part, the two models are displayed. The upper panel shows the model for $y \geq 0$ km, the lower panel the other model.

Besides the different SHOTEM results, it is not clear whether the lithological complexity also constitutes an important electric inhomogeneity. If all formations are of comparable porosity, the resistivity structure will be solely defined by the distribution of saline water. The saline water interface is expected to cross permeable lithologic boundaries, and thus might form a layered structure electrically.

The borehole is located in the vicinity of the Rx. However, little can be derived from the borehole data, since it is placed in the most inhomogeneous part. The lithology from the borehole thus might reflect only a small part of the subsurface. Most pronounced is a basaltic layer between 502 to 712 m depth. If this consists of solid basalts, it is expected to be very resistive. However, the SHOTEM result at N6 show a conductive layer starting around 500 m depth (which is not supposed to be very well resolved). Also, in the LOTEM SJI's the top of the deep conductor is at depths < 700 m.

To check the effect of the supposed resistivity structure, 1-D inversions were tested on synthetic data sets with the original geometry. Fig. D.45 shows the model and the Tx-Rx-geometry. A fault structure is modelled with two layered quarter-spaces on each side of the model. The position of the fault line is estimated using the data set show in fig. 6.8. The shallow parts of the model is taken from the SHOTEM results.

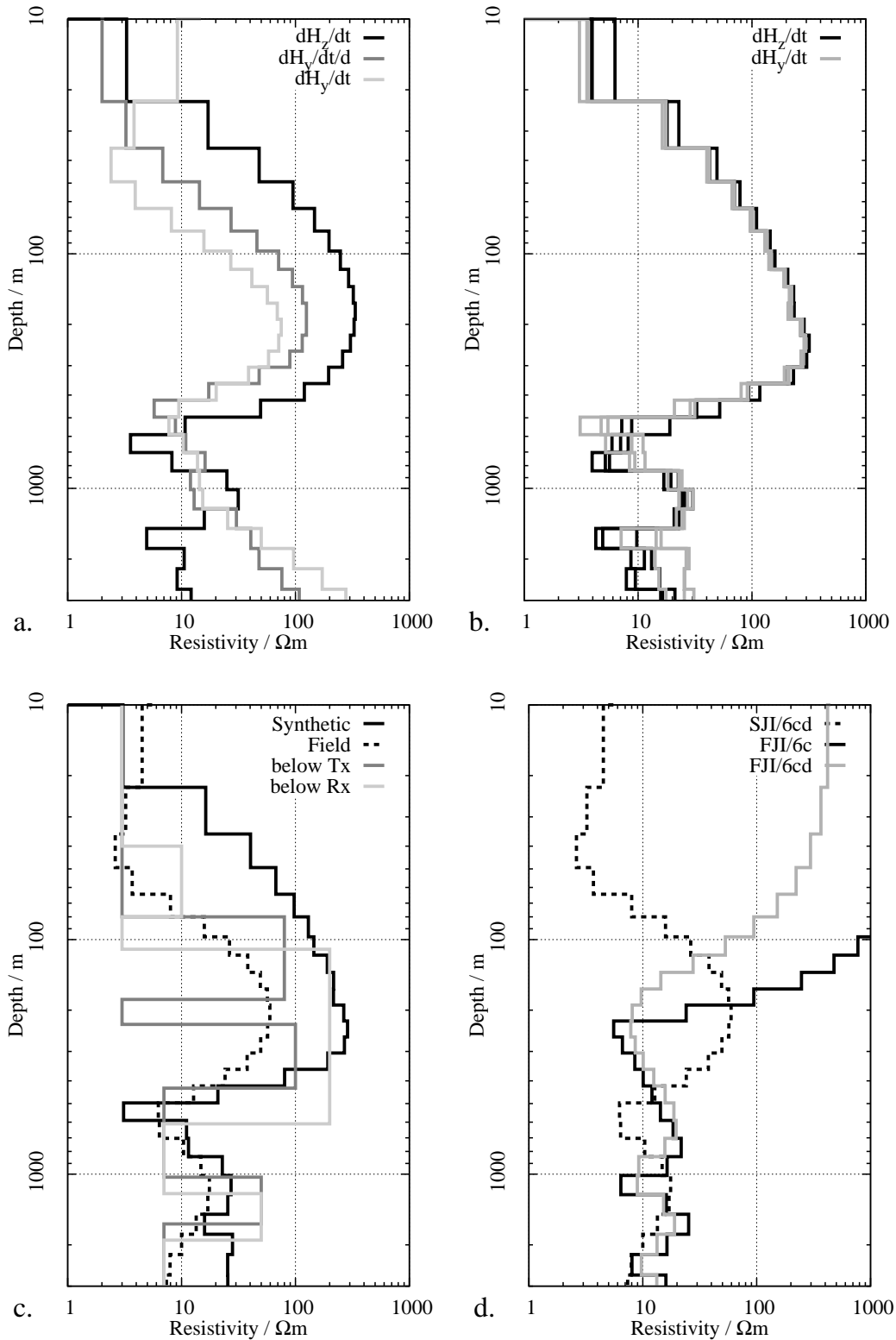


Figure D.46: a: Results for the SJIs of the individual LOTEM-components of the simulated data; the “/d” in the key marks the inversion results with free Tx-distortion parameters. b: Results for the SJI of all six simulated LOTEM- \dot{H} s; c: Comparison of the inversion results for all six \dot{H} s for the measured transients (Field) and the simulated data (Synthetic) with the models below Tx and Rx used for the modelling; d: Comparison of one SJI result for all measured LOTEM- \dot{H} s including the distortion parameters (“SJI/6cd”) and of FJIs of the same data sets with (“FJI/6c”) and without Tx-distortion (“FJI/6cd”).

A conductor with $7 \Omega\text{m}$ was placed in a depth range between 430 and 1030 m (Tx-side) or 610 to 1210 m (Rx-side), respectively. The selection of the top on the Tx-side is motivated by the depth to a conductor found at the near-by Rx-site YOB, which is placed on the same side of the fault as the Tx. Similar results were obtained at DVA, which again is close to the Tx. Because of the basaltic layer observed in the borehole, the top of the resistive layer is placed lower beneath the Rx-site. Additionally, the Rx-site AUA, south of SAA found a conductor in even greater depths, but this is considered unreliable.

The synthetic data sets were used in the same inversions as the measured data. The results are very similar except for the electric components (fig. D.46a)¹. Also the SJI of all simulated LOTEM- \dot{H} s gives results similar to the ones for the measured data sets (fig. D.46b).

A comparison of the inversion results for the measured and simulated magnetic components and the models below the Tx and Rx used in the modelling is shown in fig. D.46c. It shows the similarity between the model derived from the synthetic data set and the measured data set. The result for the synthetic data set seems to resemble the model below the Tx more than the one below the Rx. It thus also seems likely that the inversion results for the measured data sets are more representative of the structure below the Tx.

Unfortunately, FJIs of the measured data sets result in models which are contrary to the SJI results (fig. D.46d). Further interpretation steps thus were not taken. This phenomenon is not found for the simulated data sets.

All in all, it seems to be likely that the deeper conductor found in the SJI results can be found at least closer to the Tx. The resulting model fits the one found at YOB to the west and at DVA to the north-east. What happens in term of resistivity across the fault is not clear. The modelling could not explain all aspects of the measured data sets. The inconsistent FJIs and the distortions found at Rx-site AUA close to the same fault indicate that this fault also imposes a lateral change in resistivity. However, to quantify this further more stations would be needed.

D.1.17 Site TAA

The Rx-site is located between TAB and the Tx-position TA on the coastal plain close to the Carmel. At the sole Rx-station all five LOTEM-Rx-components were measured. Fig. D.47 shows the resistivity transform curves for all magnetic components.

The electric fields show a strange behaviour. The measured E_y -transient is about 20 times stronger than the E_x , resulting in CFs much different from 1.0. This could be caused by strong distortions. Another possibility is that the electric field sensors are not assembled correctly, e.g. the wrong electrodes were connected for form the electric field sensors. Therefore, the two electric fields are discarded from the interpretation.

Two SHOTEM data sets are available: N14 at the Rx-position and N13 at the

¹The resistivities for the resistors at around 300 m depth are derived from the SHOTEM-transients, which do not resolve resistive targets very well. The discrepancy with the electric components, which are more sensitive to resistors, might be caused by inaccurate estimations for these layers.

position of the Tx only ≈ 1700 m north of TAA. The models obtained by a SJI of the two SHOTEM-transients show significant differences, indicating strong lateral changes in the subsoil between the Tx and Rx (fig. D.48, left). The LOTEM data sets are also inconsistent with N13.

Including Tx-distortion the misfit of joint-inversions including the \dot{H}_y -transient is decreased significantly. The models also show bigger differences to models obtained without distortion parameters. However, the distortion obtained is extremely large ($T_y/T_x \approx 13.2$). The distortion found at TAB is far smaller ($T_y/T_x \approx 1.37$). This makes it likely that in fact the distorting feature is close to the Rx-site. The lack of an additional station does not allow a better analysis.

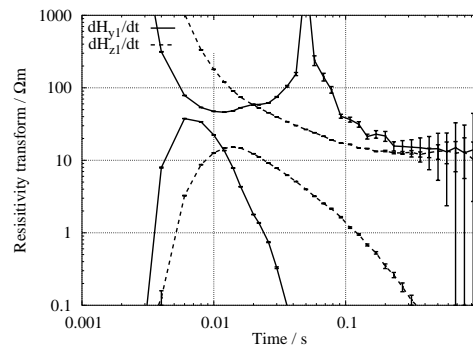


Figure D.47: Resistivity transform curves for the Rx-site TAA;

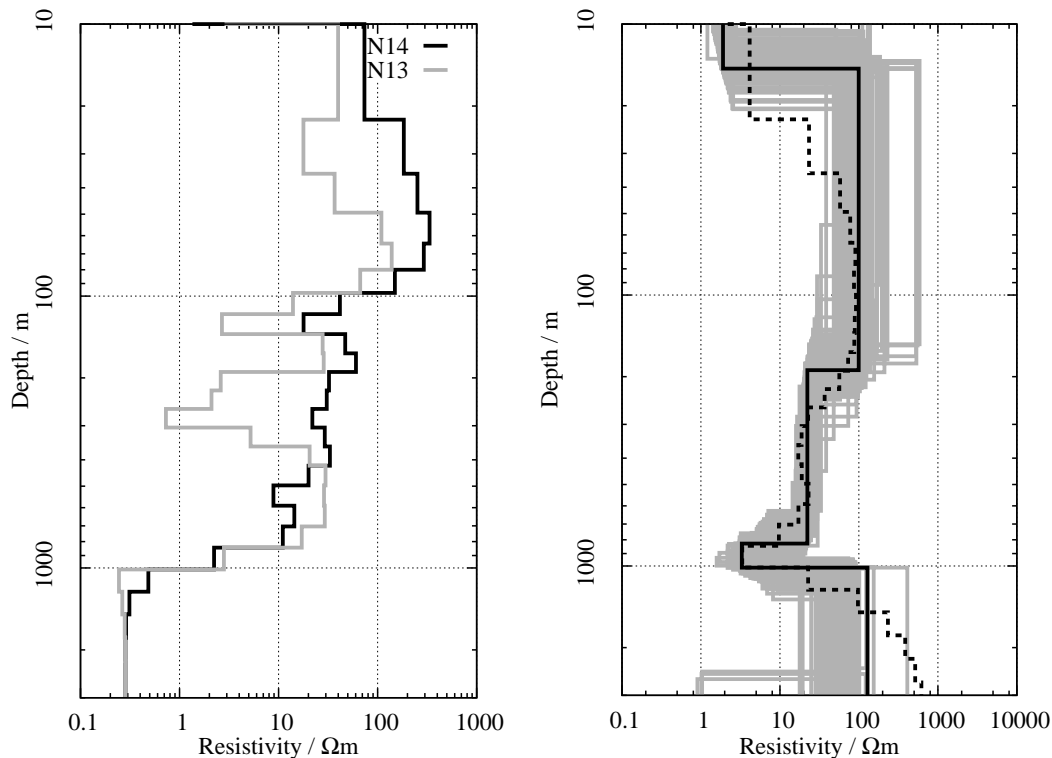


Figure D.48: Inversion-results for the transients recorded at TAA; Left: Results for the SJI of the two SHOTEM-transients; Right: Equivalence analysis for the LOTEM- \dot{H}_s -components and the SHOTEM data set N14; the black lines shows the best model ($\chi = 4.24$), the dashed line the Occam's-inversion result ($\chi = 3.63$) and the gray lines models with $\chi < 4.66$.

The right panel of fig. D.48 shows the result of the equivalence analysis using both LOTEM- \dot{H}_s and the SHOTEM-transient N14. Marquardt inversions with Tx-distortion are biased towards the undistorted solutions, because of the choice of the initial values for T_x and T_y . They fail to find models with misfits equal to the Occam's-inversion-results. However, the models resemble the main trend of the

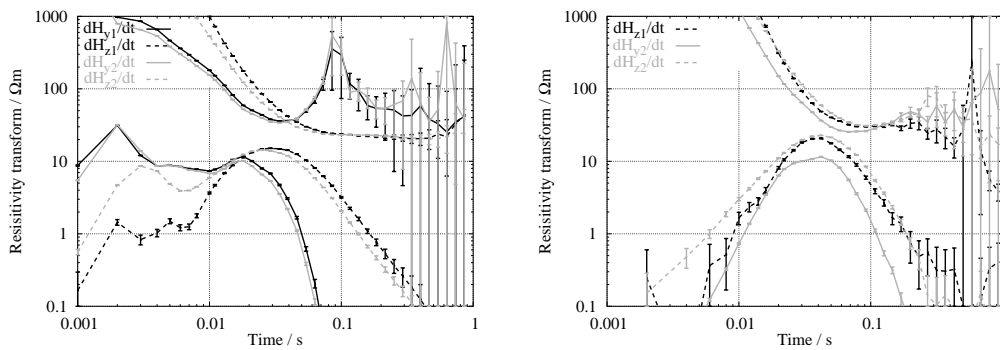


Figure D.49: Resistivity transform curves for the Rx-sites TKA (left) and TKB (right);

smooth model. The model is also similar to the one found at TAB. For the reasons given above, these results are considered to be very unreliable.

D.1.18 Sites TKA and TKB

The site TKA and TKB are located in the central part of the survey area. At TKA, two stations with two E_x -, \dot{H}_y - and \dot{H}_z -sensors each were deployed. The SHOTEM-transient N28 was recorded at the Rx-position. The resistivity transform curves are displayed in the left panel of fig. D.49. The \dot{H}_z -components show significant deviations at early times. Therefore, every data point before 20 ms was removed.

The Rx-site TKB is located close to the entrance of Harod Valley. As fig. 6.8 shows, there are several faults close to the Rx-site. From a hydrological point of view this position is very interesting. Geophysically, distortions could be expected here due to the known faults. It was decided, to set up a small site here when (for logistical reasons) the other possibility had been to measure only TKA.

Only two \dot{H}_z - and one \dot{H}_y -transient were recorded here. The area is contaminated by power-lines. Therefore, the analogue 50 Hz notch-filters of the TEAMEX-units were used. This is clearly visible in the slow increase in the resistivity transforms at early times (fig. D.49, right).

The SJI of the individual components at TKA show similar features for the magnetic LOTEM-components, mainly a resistive feature at intermediate depth followed by a drop in resistivity around 1000 m depth. Inversions including the electric fields converge at an acceptable misfit-level only if the Tx-distortion is included in the inversion. Even then, there is no similarity to the magnetic components' inversion. The model derived from the SHOTEM data set exhibits a conductive zone between 100 and 200 m depth (fig. D.50a).

SJIs including all LOTEM- \dot{H} s work well and result in models similar to the SJI of the individual components (fig. D.50b). Similar models can be obtained by including the electric field components. If the SHOTEM-transient is included, the models change. A shallow conductor is introduced, and the deep conductor moves downward (fig. D.50c). The misfit of the LOTEM-components is degraded by 50%. Similar models are found for SJIs of all seven TEM-components.

Unfortunately, the FJIs of the components fail to find models similar to the SJI

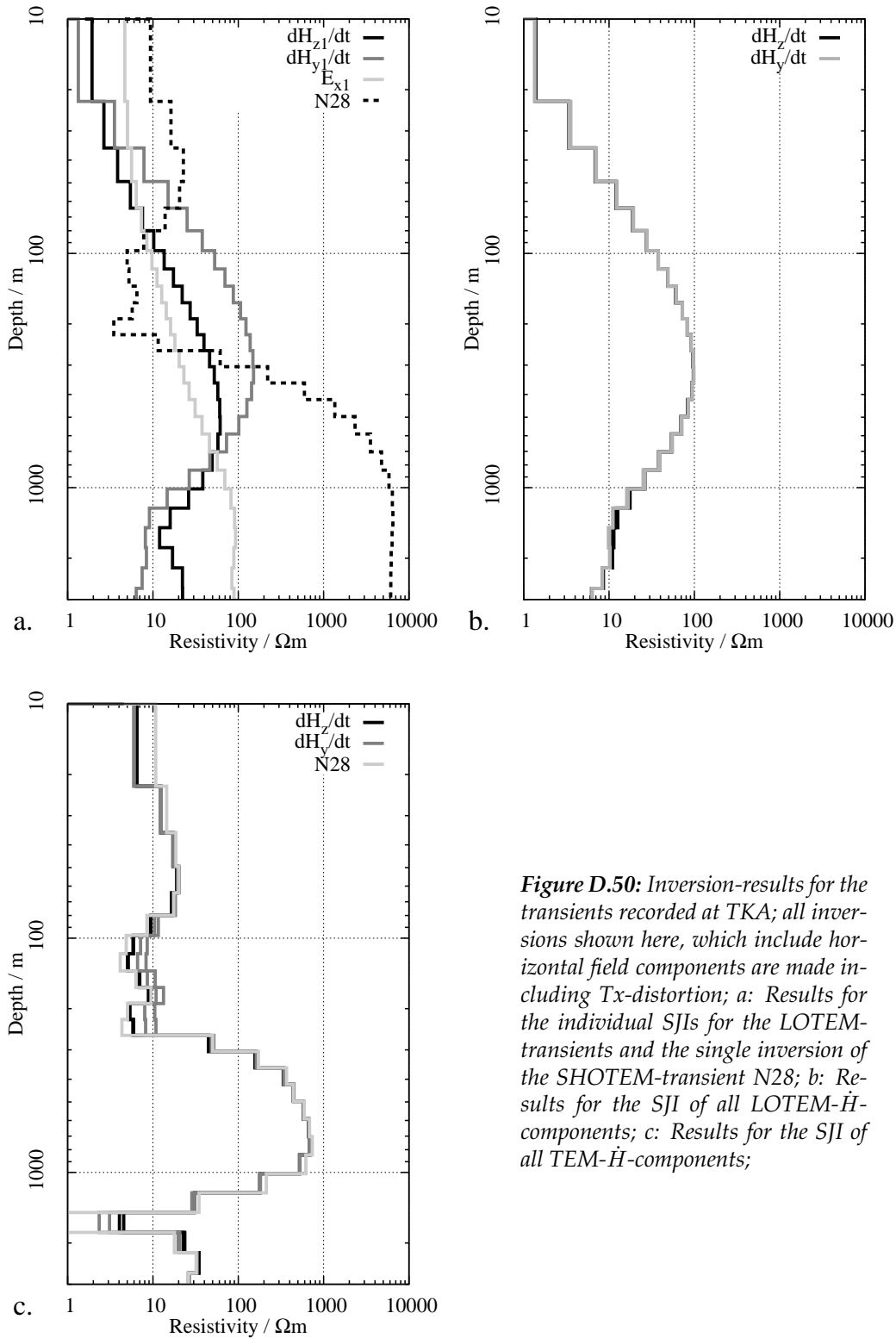


Figure D.50: Inversion-results for the transients recorded at TKA; all inversions shown here, which include horizontal field components are made including Tx-distortion; a: Results for the individual SJIs for the LOTEM-transients and the single inversion of the SHOTEM-transient N28; b: Results for the SJI of all LOTEM- \dot{H} -components; c: Results for the SJI of all TEM- \dot{H} -components;

results, especially when the LOTEM- E_x s are included in the inversion (as can be seen in fig. D.51). Fig. D.51 displays the results of the equivalence analysis using the LOTEM- \dot{H} s only (left) and all TEM-components (right). The models in the left panel show a behaviour similar to the SJI-results, with a conductive feature around 10 Ωm at depths greater 900 m. However, the upper part is not resolved. The model

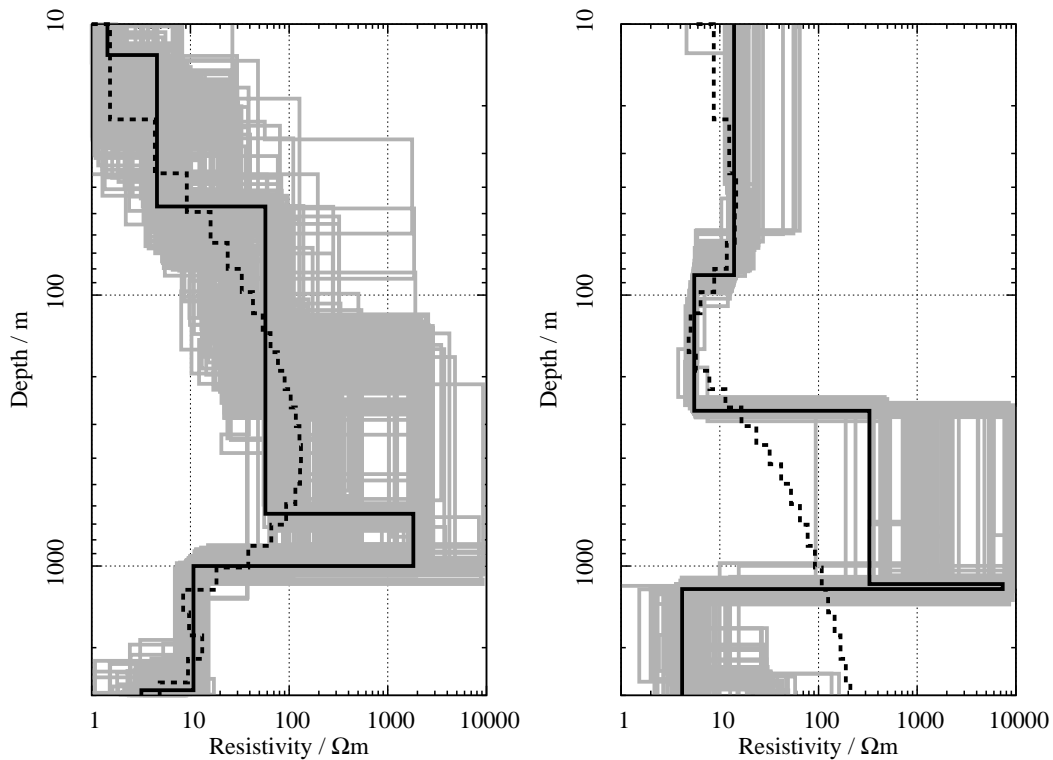


Figure D.51: Equivalence analysis for the Rx-site TKA; left: Equivalence analysis for the LOTEM- \dot{H}_s -components; the black lines shows the best model ($\chi = 0.66$), the dashed line the Occam's-inversion result ($\chi = 0.66$) and the gray lines models with $\chi < 0.73$. Right: Equivalence analysis for all TEM-components; the black lines shows the best model ($\chi = 3.10$), the dashed line the Occam's-inversion result ($\chi = 4.65$) and the gray lines models with $\chi < 3.41$.

in the right panel is far better constrained. It shows a shallow conductive feature up to 300 m, which is resolved by the SHOTEM data set and a deeper conductor similar to the one found using only the LOTEM- \dot{H}_s . Like at KEB, a thin resistive layer shows up atop of the deep conductor. This feature is responsible for the poor convergence in the Occam's inversion when the electric fields are included.

Most pertinent for the project is the deep conductor below 1 km depth with resistivities around 7 Ωm .

At TKB even SJIs of the two \dot{H}_z -transients result in two different models (fig. D.52, left). This gets worse, if the \dot{H}_y -transient is also included (fig. D.52, right). As a result all FJIs of the different components are very unstable. What seems to be quite common is the resistive feature from 300 to 500 depth. Even this is not very reliable, due to the long system responses. No other information can be derived from this data set, as was expected.

D.1.19 Sites YAA and YAB

The Tx YA is located in the Zevulun plain north of the Carmel. The noise level is high in this area.

YAA is located NE of the Tx in the Zevulun-plain. Two Rx-stations were set up here, where in total two \dot{H}_z -transients and one E_x - and \dot{H}_y -transient were recorded.

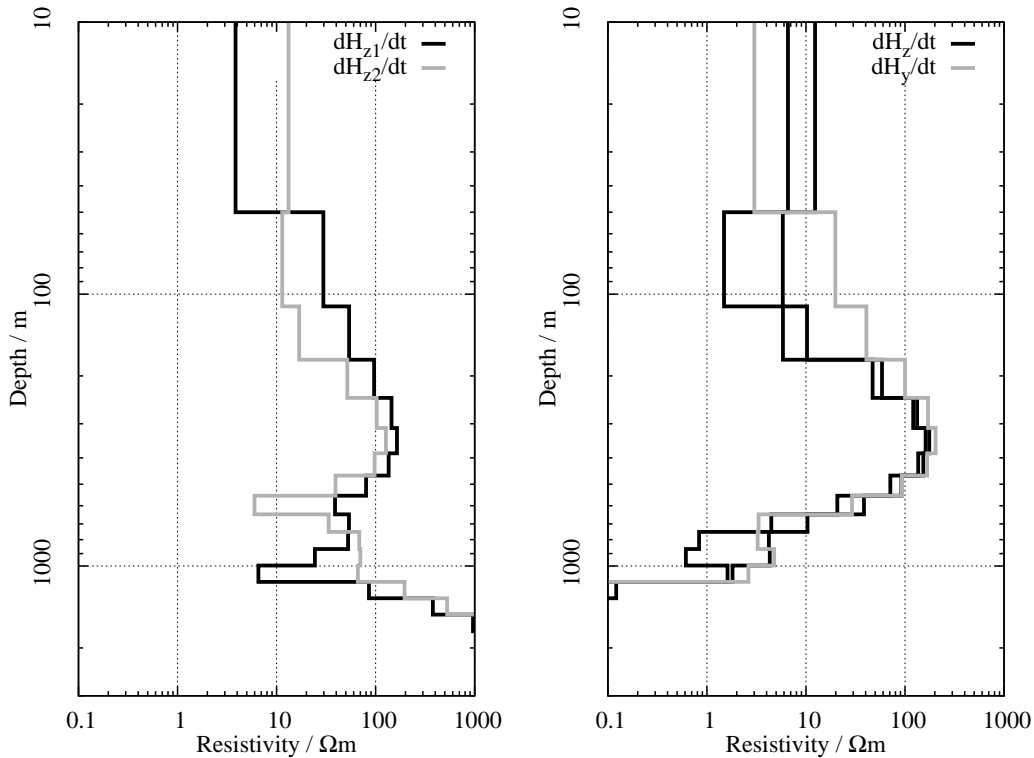


Figure D.52: Inversion-results for the transients recorded at TKB; left: SJI results for the two LOTEM- \dot{H}_z s; right: SJI results for all three LOTEM-components excluding Tx-distortion;

In addition, one SHOTEM data set (N17) was recorded at the Rx-site. The resistivity transform curves are shown in the left panel of fig. D.53.

The site YAB is located close to a borehole drilled in a fault zone (figs. 6.3). The situation here is similar to that at DVA. Directly SW of the Rx-site, the topography rises to a NW-SE striking mountain parallel to the Tx-direction. In fig. 6.8 the fault is indicated by the huge displacement of the top of the Judea Group. It was not possible to set up a LOTEM spread further away from the fault because of the dense infrastructure in the area. For the same reasons no SHOTEM data set could be recorded here.

Two stations with two E_x -, \dot{H}_y - and \dot{H}_z -sensors were built up. The two \dot{H}_z -transients differ throughout the whole time range and show late time sign reversals (fig. D.53, right). The \dot{H}_y s on the other hand show a similar behaviour after a few ms.

At YAA, SJI of the different data sets show a consistent picture. Fig. D.54a displays a comparison between the SJI of the two LOTEM- \dot{H}_z s and the single inversion of the SHOTEM-transients. Similar results are obtained by using all five data sets, although there are slight differences between the models associated with the different transients (fig. D.54b). Mainly, two conductors are found at 400 m and 1500 m depth. Inversions including the E_x -transient work well only after freeing the Tx-distortion parameters.

Unfortunately, all FJIs fail to produce models similar to the SJI-results. In most cases they introduce an additional shallow conductor but fail to reconstruct the deep one (e.g. fig. D.54c). The models found by the equivalence analysis thus only

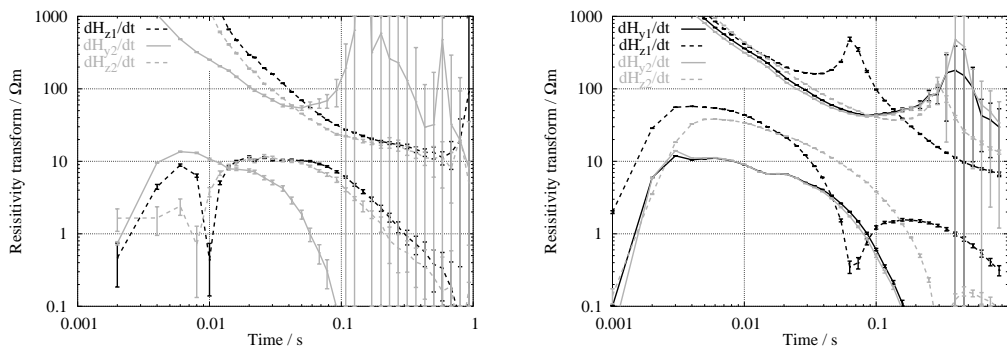


Figure D.53: Resistivity transform curves for the Rx-site YAA (left) and YAB (right);

reproduce the conductor at intermediate depths (fig. D.54d). The depth and thickness of this conductor changes, depending on the choice of components. The result is thus considered to be not reliable.

At YAB, SJIs of the \dot{H}_z -transients failed. The resulting models differed significantly even after removal of 20 to 30 data points. They were excluded from the further inversions. SJIs for the other components found similar models. The resulting misfit depended on the Tx-distortion. However, SJIs of the electric fields with distortions produced models, which are more similar to the ones for the \dot{H}_y -components (fig. D.55a). In any case, the models show two conductors, one around a depth of 200 m, and a deep one at ≈ 1000 m.

The SJI results for E_x - and \dot{H}_y -transients show different resistivities. The depth to the conductive layers are similar (fig. D.55b). The misfit of the inversions including the Tx-distortion is ≈ 2.5 times smaller than without. Still, the conductors remain at similar depths, which are also reproducible with fixed joint-inversions including Tx-distortions (fig. D.55c). Inconsistencies show up at depths greater than 900 m.

Fig. D.55d shows the results of the equivalence analysis. Obviously, the data set is quite ambiguous. General trends from the analysis show a resistive zone between ≈ 350 and 600 m depth followed by a conductive region with resistivities up to 10 Ωm . In the depth range from 900 to 1000 m indications for a second resistive zone are found, followed by a conductor with resistivity $< 8 \Omega\text{m}$.

The comparison to the information from the borehole is difficult, as the LOTEM results are supposed to mainly reflect the part between the Tx and Rx. The borehole on the other hand is drilled in the Yagur-block behind the Rx-site and thus reflects a different lithology.

The ambiguity of this data set is too high to extract useful information from the inversions.

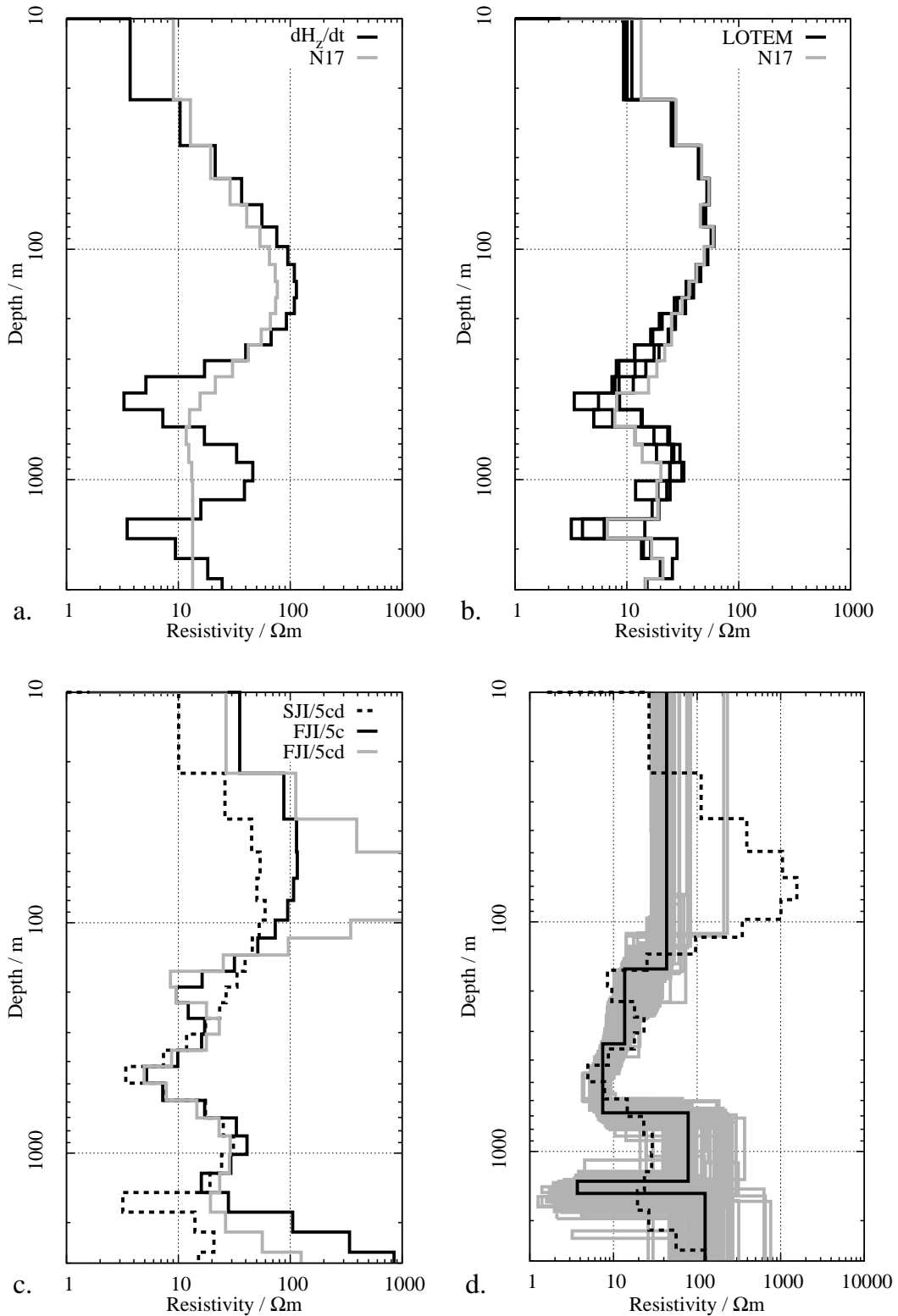


Figure D.54: Inversion-results for the transients recorded at YAA; a: Results for the SJIs of the LOTEM- \dot{H}_z s and the single inversion of the SHOTEM-transient N17; b: Results for the SJI of all TEM-components with Tx-distortion; c: Comparison of inversions using all five TEM-components in a SJI and FJI with Tx-distortion ("SJI/5cd" and "FJI/5cd", respectively) and a FJI without Tx-distortion ("FJI/5c"); d: Equivalence analysis for all TEM-components; the black lines shows the best model ($\chi = 1.61$), the dashed line the Occam's-inversion result ($\chi = 1.60$) and the gray lines models with $\chi < 1.77$.

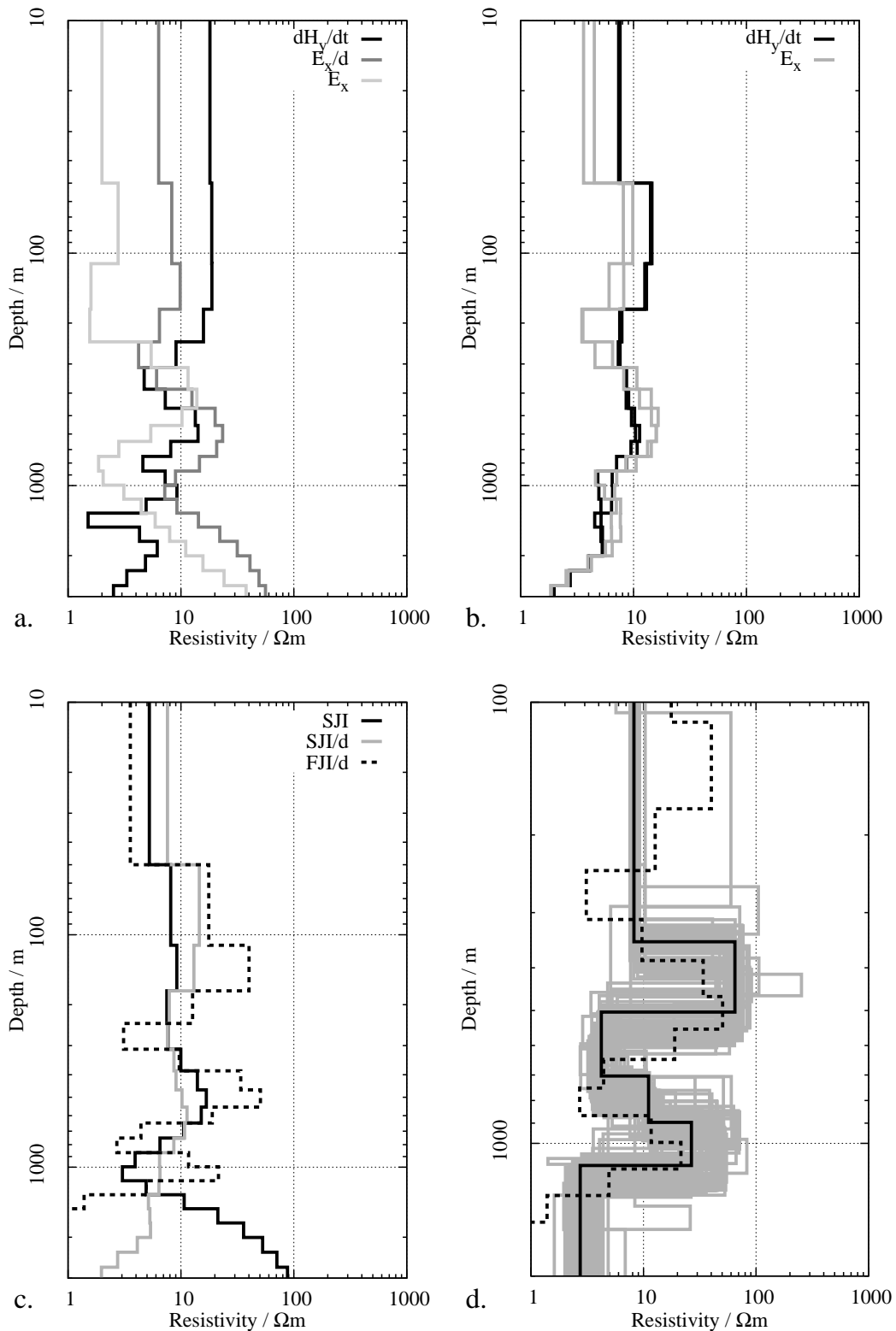


Figure D.55: Inversion results for the transients recorded at YAB; a: Comparison of the SJI-results for \dot{H}_y s and E_x s without Tx-distortion and E_x s with distortion (E_x/d); b: SJI result for the LOTEM-components \dot{H}_y and E_x including Tx-distortion; c: SJI and FJI results for the four components with Tx-distortion (“FJI/d” and “SJI/d”) and without (“SJI”); d: Equivalence analysis using the E_x - and \dot{H}_y -transients; the black lines shows the best model ($\chi = 2.25$), the dashed line the Occam’s-inversion result ($\chi = 2.13$) and the gray lines models with $\chi < 2.47$.

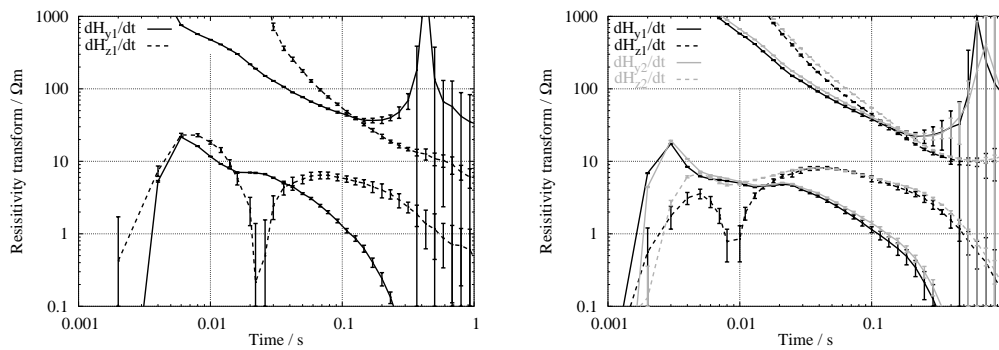


Figure D.56: Resistivity transform curves for the Rx-site YOA (left) and YOB (right);

D.1.20 Sites YOA and YOB

The Tx YO is located in the central position of the survey area. The first site, YOA is positioned at the foothill of the Carmel. Only one Rx-station was deployed here. Like at DVA, two \dot{H}_z -transients were recorded with the (N)-coil and the (R)-coil for comparison. Both sensors give similar results. The transient obtained by using the (N)-coil was discarded for it contains a slightly higher noise level. The resistivity transforms for the magnetic components are displayed in the left panel of fig. D.56. The (very noisy) \dot{H}_z -transient has a sign reversal at intermediate times. For the inversion the first 19 data points were removed, leaving only 15 data points with high error estimates.

The situation here is similar to the one at YAB and DVA, with a steep hill and a fault with a huge displacement right behind the site. Unlike the other two places, the fault line in this case is not parallel to the Tx-direction. Distortions caused by this structure are expected to be different from the ones at YAB and DVA.

The three transients measured at YOA give similar results. SJIs result in models with similar features, namely two conductors around 300 and 800 m depth (fig. D.57, left). These features also are found in FJI-results and the equivalence analysis (fig. D.57, right). The deeper conductor is pertinent to the aim of the project. Only few data sets were used to derive it, and its top, thickness and resistivity is not well resolved.

At YOB two stations with one E_x -, \dot{H}_y - and \dot{H}_z -sensor each were set up. The resistivity transforms for the magnetic components are shown in the right panel of fig. D.56. The \dot{H}_z -transients differ significantly at early times. The transient closer to the Tx (“ dH_{z1}/dt ”) even features a sign reversal. Only slight deviations at early times are found in the two \dot{H}_y -transients. At the Rx-site, the SHOTEM data set N18 was recorded.

The SJIs of the individual components are consistent within each SJI. Fig. D.58a shows a comparison of representative models. The electric field components do not converge on a sufficiently low misfit-level. The models are thus not comparable to the others. The SHOTEM data set resolves a conductor around 200 m depth, which is also seen by the LOTEM- \dot{H}_y s. The magnetic LOTEM-components show a conductor around 800 m depth. At 1000 m depth the resistivity increases again. Below, no stable features are resolved, although there are indications for a conductive basement.

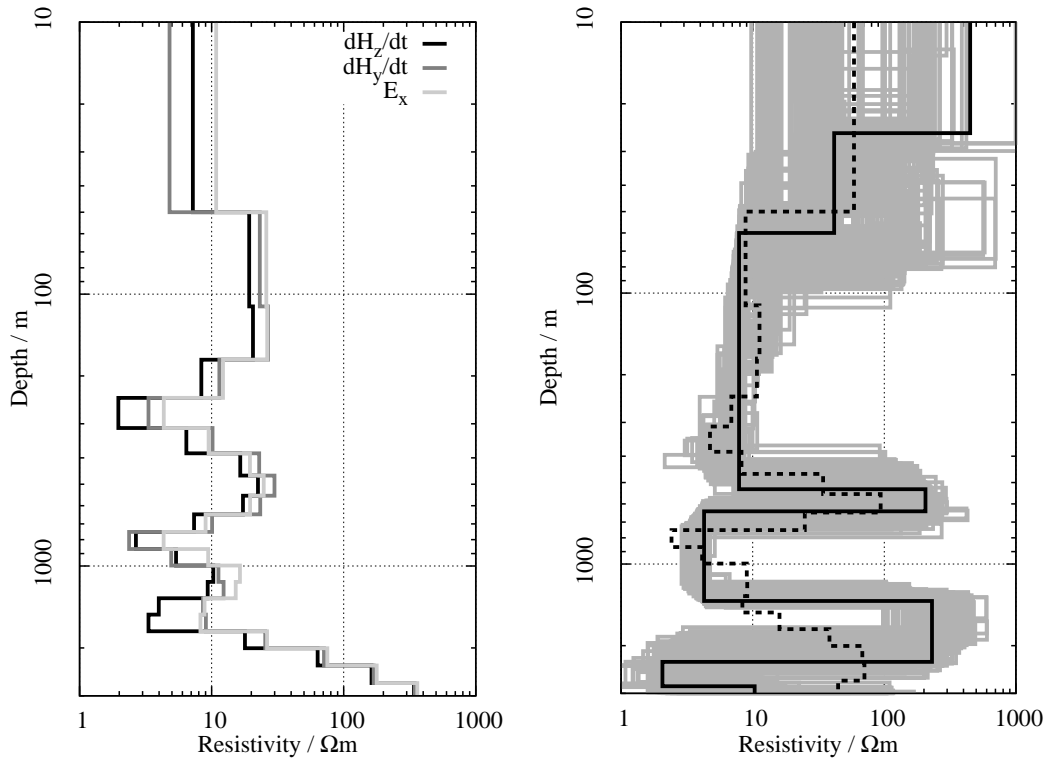


Figure D.57: Inversion-results for the transients recorded at YOA; left: SJI results for the three LOTEM-components including Tx-distortion; right: Equivalence analysis for the three LOTEM-components; the black lines shows the best model ($\chi = 0.42$), the dashed line the Occam's-inversion result ($\chi = 0.67$) and the gray lines models with $\chi < 0.46$.

The deep conductor is found in any SJI including LOTEM-components. Inversions of the electric fields show convergence problems, especially when the Tx-distortion parameters are fixed. Some inversions without the SHOTEM-transient show indications for the shallow conductor (e.g. fig. D.58b).

Similar results can be obtained by FJIs of the different components. In some cases the inversion failed to find models producing a sufficient misfit. The lower panels of fig. D.58 show equivalence analyses for all components but the LOTEM- \dot{H}_z s (c) and all LOTEM-components (d). Here the shallow conductor is only resolved, when the SHOTEM-transient is included. The deep conductor is found regardless of the choice of components. It starts between 450 and 550 m depth and has a maximum thickness of 850 m and a resistivity $< 4 \Omega\text{m}$. This fits the results of site YOA very well, which makes this feature far more believable.

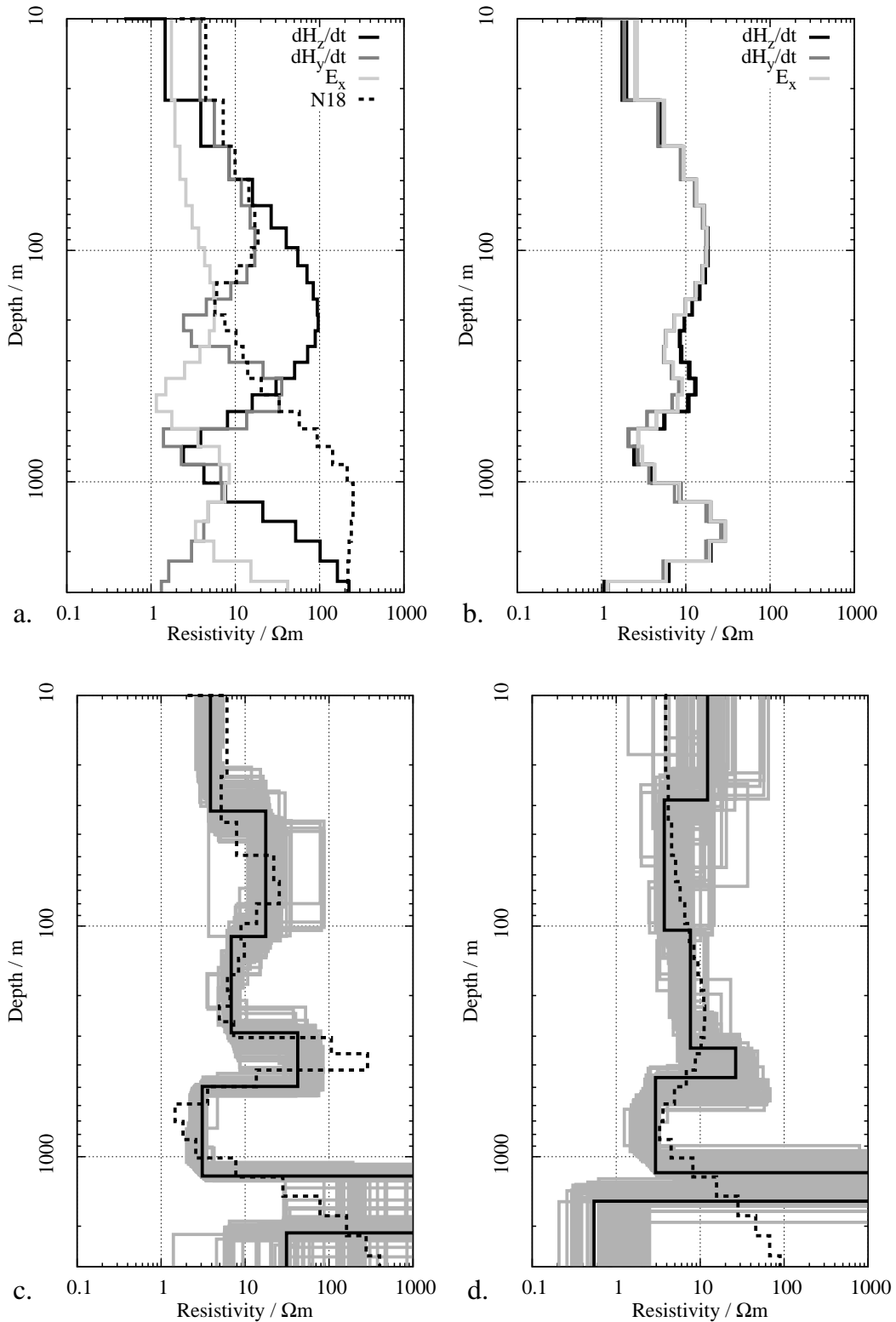


Figure D.58: Inversion-results for the transients recorded at YOB; a: Results for the individual SJIs for the LOTEM-transients without Tx-distortion and the single inversion of the SHOTEM-transient N18; b: Results for the SJI of all LOTEM-components with Tx-distortion; c: Equivalence analysis for all TEM-components, except the LOTEM- \dot{H}_z s; the black lines shows the best model ($\chi = 1.81$), the dashed line the Occam's-inversion result ($\chi = 2.77$) and the gray lines models with $\chi < 1.99$. d: Equivalence analysis for all LOTEM-components; the black lines shows the best model ($\chi = 1.00$), the dashed line the Occam's-inversion result ($\chi = 2.14$) and the gray lines models with $\chi < 1.10$.

D.2 The statistics for field data set inversions

This section presents the statistics for all joint-inversions of field data sets used for the interpretation. In addition, the statistics for the SHOTEM single inversion results are shown. The data is displayed in tabular form. The lines “cut/s” and “cut/e” denote how many data points were removed from start and the end of the individual transients prior to inversion. The next lines show the results for single inversions (sgl.), SJIs or FJIs. If a “/d” is appended to the inversion type the inversion was carried out including the T_x -distortion parameters. The other rows show the individual misfits (χ) the misfit for all data sets (χ_{tot}) and the roughness of the final model (R.). Instead of denoting the distortion parameters T_x and T_y , the quantity T_y/T_x is displayed which should be stable if different CFs are found.

Station AFA

	A1HZ	A1HY	A1EX	N8	N3			
cut/s	4	4	4	0	0			
cut/e	0	0	0	0	0			
Inv.	χ	χ	χ	χ	χ	T_y/T_x	χ_{tot}	R.
sgl.				7.84		0.00	7.84	127
sgl.					1.69	0.00	1.69	9.35
SJI				1.05	1.74	0.00	1.55	80.4
SJI	0.56	0.87				0.00	0.73	50.4
SJI/d	0.52	0.87				-1.15	0.70	27.2
SJI		1.45			1.76	0.00	1.66	15.7
SJI/d		1.11			1.80	-1.05	1.66	19.7
SJI	0.53		0.25			0.00	0.41	25.1
SJI/d	0.56		0.23			1.02	0.42	10.2
SJI	0.58	1.04	0.34			0.00	0.72	46.4
SJI/d	0.92	0.58	0.30			-0.38	0.63	85.0
SJI	0.60	1.35		1.06		0.00	1.05	91.4
SJI/d	2.31	1.90		26.2		-0.00	14.5	3.28
SJI	0.70	1.40			1.79	0.00	1.48	52.8
SJI/d	0.80	1.45			2.03	0.02	1.63	51.4
SJI	0.61	1.42	0.43	1.11		0.00	0.97	160
SJI/d	0.65	1.20	0.33	1.05		-0.40	0.85	154
SJI	0.71	1.42	0.46		1.77	0.00	1.33	108
SJI/d	0.74	1.26	0.43		1.81	-0.33	1.30	107
SJI	0.66	1.45	0.44	1.20	1.82	0.00	1.34	432
SJI/d	0.66	1.24	0.43	1.30	1.85	-0.36	1.30	431

Table D.1: Inversion statistics for all components measured at Rx-position AFA;

Station AUA

	A1HZ	A2HZ	A3HZ	A2HY	A2EX	N22			
cut/s	5	5	5	1	5	0			
cut/e	12	12	12	0	0	0			
Inv.	χ	χ	χ	χ	χ	χ	T_y/T_x	χ_{tot}	R.
sgl.						0.67	0.00	0.93	2.78
SJI	0.53	0.55	0.31				0.00	0.48	25.1
SJI	0.35	0.40	0.26	0.95			0.00	0.65	157
SJI/d	0.60	0.67	0.33	1.08			2.29	0.78	70.3
SJI	0.43	0.47	0.30	1.03		0.71	0.00	0.72	178
SJI/d	0.62	0.65	0.35	1.15		0.70	2.24	0.78	128
SJI	1.28	1.02	0.66	1.97	1.21		0.00	1.41	208
SJI/d	0.60	0.64	0.30	1.04	0.36		2.06	0.67	186
SJI	0.68	0.69	0.38	1.47	1.13	0.72	0.00	1.00	421
SJI/d	0.66	0.67	0.34	1.16	0.35	0.71	2.21	1.29	345
FJI	4.86	2.87	4.19	4.24		3.32	0.00	3.93	6.33
FJI/d	5.12	2.61	3.84	4.32		4.90	-0.00	4.19	2.48
FJI	7.87	4.05	2.29	6.07	6.22		0.00	5.77	26.7
FJI/d	3.03	1.32	1.78	2.80	0.78		3.29	2.06	8.31
FJI	5.16	3.23	4.05	6.65	6.10	5.89	0.00	5.60	56.5
FJI/d	2.91	1.65	1.81	3.47	1.42	1.81	3.31	2.28	5.37

Table D.2: Inversion statistics for all components measured at Rx-position AUA;

Station AUB

	B1EX	B2EX	N21			
cut/s	5	5	0			
cut/e	0	0	0			
Inv.	χ	χ	χ	T_y/T_x	χ_{tot}	R.
sgl.			0.95	0.00	0.95	1.69
SJI	3.29	3.15		0.00	3.22	3.92
SJI/d	1.20	1.41		-3.98	1.29	11.3
SJI	1.63	1.72	2.62	0.00	2.02	134
SJI/d	1.46	1.43	3.00	-4.41	2.01	105
FJI	7.49	5.02		0.00	6.38	11.4
FJI/d	3.31	3.25		0.49	3.23	14.9

Table D.3: Inversion statistics for all components measured at Rx-position AUB;

Station BEA

	A1HZ	A2HZ	A1HY	A2HY	A1EX	A2EX	N11			
cut/s	4	4	3	3	4	4	0			
cut/e	0	0	0	0	0	0	0			
Inv.	χ	χ	χ	χ	χ	χ	χ	T_y/T_x	χ_{tot}	R.
sgl.							6.46	0.00	6.46	9.79
SJI					0.44	0.54		0.00	0.49	4.87
SJI/d					0.44	0.54		-0.19	0.49	3.71
SJI			1.32	0.66				0.00	1.05	10.7
SJI/d			1.00	0.59				0.83	0.80	5.48
SJI	1.10	0.72						0.00	0.93	59.3
SJI			1.44	0.72	0.41	0.45		0.00	0.87	45.9
SJI/d			1.23	0.64	0.54	0.45		0.27	0.76	40.0
SJI	1.12	0.75	1.48	0.67				0.00	1.06	140
SJI/d	1.17	0.75	1.35	0.59				0.34	0.99	113
SJI			1.76	1.09	1.40	1.42	7.38	0.00	3.27	53.9
SJI/d			1.28	0.94	1.49	1.46	7.56	0.43	3.18	62.0
SJI	1.59	1.15	2.03	1.24			6.02	0.00	2.82	273
SJI/d	2.10	1.40	2.11	1.22			6.85	0.72	3.10	145
SJI	1.41	1.12	1.55	1.00	0.66	0.64		0.00	1.12	178
SJI/d	1.49	1.11	1.22	0.83	0.77	0.59		0.45	1.02	158
SJI	1.74	1.20	2.18	1.58	1.57	1.59	1.58	0.00	3.03	186
SJI/d	2.04	1.31	1.70	1.24	1.65	1.85	7.73	0.75	2.96	152
FJI			1.61	1.05	1.02	1.32		0.00	1.27	7.26
FJI/d			1.78	1.06	0.66	0.87		-0.12	1.15	4.87
FJI	4.44	3.97	9.10	3.16				0.00	5.69	17.6
FJI/d	1.87	2.44	4.01	1.81				2.05	2.62	30.7
FJI			5.10	2.18	2.76	2.63	9.59	0.00	4.96	14.7
FJI/d			4.67	2.07	3.10	4.33	9.75	0.39	5.03	9.42
FJI	4.90	3.72	9.61	3.42	1.73	2.39		0.00	5.04	10.9
FJI/d	3.61	3.15	4.41	1.89	2.77	6.11		1.59	3.78	14.9
FJI	4.53	3.52	10.42	3.81	1.18	1.90	7.85	0.00	5.59	15.9
FJI/d	4.20	3.66	9.15	3.37	2.20	4.73	8.23	0.53	5.37	12.7

Table D.4: Inversion statistics for all components measured at Rx-position BEA;

Station BEB

	B1HZ	B2HZ	B1HY	B2HY	B1EX	B2EX	N12			
cut/s	8	8	4	4	8	8	0			
cut/e	0	0	0	0	0	0	0			
Inv.	χ	χ	χ	χ	χ	χ	χ	T_y/T_x	χ_{tot}	R.
sgl.							2.64	0.00	2.64	5.47
SJI					2.18	1.49		0.00	1.86	6.75
SJI/d					1.04	1.00		-1.01	1.00	8.52
SJI			1.16	1.10				0.00	1.13	8.21
SJI/d			1.17	1.14				0.18	1.14	6.32
SJI	1.08	0.89						0.00	0.99	30.7
SJI			7.42	8.44	27.22	27.14		0.00	19.49	1.22
SJI/d			1.28	1.19	1.37	1.02		-0.36	1.19	40.1
SJI	1.59	1.11	1.37	1.28				0.00	1.35	107
SJI/d	1.43	1.06	1.47	1.38				-0.35	1.32	109
SJI			1.29	1.19	1.26	0.97	2.12	0.00	1.40	133
SJI/d			1.36	1.22	1.25	0.96	2.25	-0.25	1.41	126
SJI	1.63	1.14	1.32	1.29			2.15	0.00	1.52	225
SJI/d	1.56	1.12	1.57	1.45			2.34	-0.42	1.59	177
SJI	15.38	13.52	8.05	8.08	24.39	28.42		0.00	17.73	1.66
SJI/d	1.53	1.14	1.38	1.24	1.05	0.95		-0.43	1.20	190.3
SJI	1.78	1.16	1.95	1.63	1.58	1.25	2.16	0.00	1.67	358
SJI/d	1.47	1.04	1.55	1.36	1.53	1.19	2.26	-0.43	1.47	381
FJI			2.21	2.45	1.98	2.89		0.00	2.40	15.9
FJI/d			3.17	3.59	3.53	3.61		-0.68	3.39	8.60
FJI	6.28	2.45	3.81	3.93				0.00	4.31	21.6
FJI/d	5.25	1.85	2.68	3.14				-0.74	3.35	20.5
FJI			1.75	1.76	2.10	3.66	4.91	0.00	3.00	52.4
FJI/d			3.72	3.79	3.48	4.93	4.81	-1.03	4.04	6.68
FJI	6.50	2.51	4.42	4.56			3.01	0.00	4.45	18.2
FJI/d	3.12	1.78	3.17	3.42			2.46	-0.91	3.31	29.5
FJI	7.25	3.84	3.76	3.85	1.26	3.63		0.00	4.28	28.0
FJI/d	17.26	14.78	9.31	8.06	31.67	28.97		-0.20	19.52	0.35
FJI	7.03	3.55	4.18	4.45	1.41	4.33	4.38	0.00	4.45	64.3
FJI/d	7.03	8.72	3.67	3.83	2.69	6.26	4.24	-1.19	5.38	7.00

Table D.5: Inversion statistics for all components measured at Rx-position BEB;

Station BSA

	A1HZ	A1HY	A2HY	A1EX	A2EX	BSH7			
cut/s	1	1	1	1	2	0			
cut/e	0	0	0	0	0	0			
Inv.	χ	χ	χ	χ	χ	χ	T_y/T_x	χ_{tot}	R.
sgl.						0.59	0.00	0.59	24.0
SJI			0.87	0.86			0.00	0.87	20.6
SJI/d			0.88	0.86			1.72	0.86	12.6
SJI	0.43	0.87	0.88				0.00	0.75	121
SJI/d	0.40	0.89	0.87				1.16	0.74	108
SJI	0.43	0.92	1.01	0.37			0.00	0.74	300
SJI/d	0.45	0.91	0.98	0.30			0.26	0.71	240
SJI	0.44	0.91	1.01			0.63	0.00	0.80	275
SJI/d	0.45	0.88	0.87			0.64	1.49	0.72	245
SJI	0.43	0.92	1.03	0.34		0.62	0.00	0.73	748
SJI/d	0.47	0.92	1.00	0.35		0.66	0.27	0.71	481
FJI	2.46	1.96	1.70				0.00	2.07	55.9
FJI/d	1.79	1.56	1.36				1.20	1.55	33.8
FJI	2.89	2.43	2.19	2.69			0.00	2.56	33.4
FJI/d	4.16	2.89	2.62	4.23			0.22	3.47	41.7
FJI	2.79	2.56	2.30	2.57		1.82	0.00	2.48	43.0
FJI/d	2.43	1.78	1.60	1.05		2.08	0.59	1.77	67.0

Table D.6: Inversion statistics for all components measured at Rx-position BSA;

Station BSB

	B1HZ	B2HZ	B1HY	B2HY	B1EX	B2EX	BSH19	BSH20	N23			
cut/s	12	12	3	3	8	8	0	0	0			
cut/e	0	0	0	0	0	0	0	0	0			
Inv.	χ	χ	χ	χ	χ	χ	χ	χ	χ	T_y/T_x	χ_{tot}	R.
sgl.									0.24	0.00	0.24	8.41
sgl.								0.33		0.00	0.33	0.58
sgl.							0.53			0.00	0.53	3.01
SJI					0.17	0.16				0.00	0.17	5.51
SJI/d					0.21	0.24				-0.55	0.22	3.28
SJI			0.41	0.42						0.00	0.42	6.04
SJI/d			0.42	0.42						0.26	0.41	12.3
SJI	0.19	0.16								0.00	0.18	8.95
SJI							0.51	0.32	0.29	0.00	0.38	36.0
SJI	0.24	0.19	0.42	0.43						0.00	0.35	28.6
SJI/d	0.23	0.20	0.44	0.44						-0.80	0.35	29.0
SJI	0.36	0.26	0.46	0.46			0.54			0.00	0.43	70.4
SJI/d	0.37	0.26	0.46	0.48			0.57			-1.14	0.43	69.0
SJI	0.26	0.21	0.42	0.44	0.23	0.19				0.00	0.32	113
SJI/d	0.21	0.19	0.42	0.43	0.17	0.16				-1.26	0.29	106
SJI	0.37	0.26	0.48	0.51	0.23	0.23	0.55			0.00	0.40	179
SJI/d	0.34	0.24	0.45	0.47	0.17	0.17	0.52			-1.54	0.35	204
FJI	2.09	1.78	1.05	0.97						0.00	1.48	8.51
FJI/d	2.15	1.75	1.09	0.99						-1.21	1.46	6.16
FJI	3.67	2.32	1.78	1.63	2.53	3.30	0.74			0.00	2.44	22.6
FJI/d	2.12	1.54	2.13	1.90	2.18	1.38	0.86			-1.27	1.77	14.7

Table D.7: Inversion statistics for all components measured at Rx-position BSB;

Station CAA

	A1HZ	A1EX	N30	N4			
cut/s	4	4	0	0			
cut/e	0	0	0	0			
Inv.	χ	χ	χ	χ	T_y/T_x	χ_{tot}	R.
sgl.			0.25		0.00	0.25	61.6
sgl.				0.84	0.00	0.84	101
SJI			3.02	1.10	0.00	2.21	80.8
SJI	0.66	1.41			0.00	1.10	27.0
SJI	0.36	0.28			-0.30	0.32	20.6
SJI	1.18	0.99	3.32		0.00	1.91	54.3
SJI/d	1.51	1.44	2.01		0.49	1.58	126
SJI	0.47	0.44		0.68	0.00	0.53	148
SJI/d	0.39	0.37		0.97	0.08	0.59	148
SJI	1.57	1.60	2.81	1.30	0.00	1.84	343
SJI/d	2.12	1.67	2.72	1.31	0.34	1.92	273
FJI	0.53	0.67			0.00	0.60	14.5
FJI/d	0.46	0.69			-0.45	0.57	5.46
FJI	2.26	1.25		2.56	0.00	2.06	31.6
FJI/d	2.21	1.09		2.35	0.33	1.88	41.9
FJI	1.79	1.42	3.99		0.00	2.44	27.5
FJI/d	3.86	2.66	2.52		0.59	3.06	37.4

*Table D.8: Inversion statistics for all components measured at Rx-position CAA;***Station CAB**

Only one transient was recorded at CAB. The result of the single Occam's inversion can be found in fig. C.12.

Station DVA

	A1HZ	A2HZ	A1HY	A2HY	A1EX	A2EX	N7	N2			
cut/s	5	5	4	4	5	5	0	0			
cut/e	0	0	0	0	0	0	0	0			
Inv.	χ	χ	χ	χ	χ	χ	χ	χ	T_y/T_x	χ_{tot}	R.
sgl.								1.92	0.00	1.92	10.5
sgl.							4.32		0.00	4.32	16.1
SJI							1.94	3.25	0.00	2.43	274
SJI					2.33	2.72			0.00	2.53	24.5
SJI/d					0.57	0.55			1.07	0.55	19.5
SJI			1.35	1.08					0.00	1.22	40.3
SJI/d			1.39	1.12					-0.08	1.24	28.4
SJI	0.55	0.61							0.00	0.58	45.0
SJI			1.52	1.21	0.76	0.73			0.00	1.11	38.4
SJI/d			1.44	1.15	0.59	0.56			-0.30	0.99	119
SJI	0.58	0.66	1.37	1.10					0.00	0.99	250
SJI/d	0.59	0.67	1.41	1.13					-0.12	0.99	278
SJI			1.45	1.27	0.68	0.62		3.43	0.00	1.69	475
SJI/d			1.52	1.34	0.75	0.66		3.83	-0.35	1.80	306
SJI	0.59	0.67	1.67	1.61				1.93	0.00	1.48	590
SJI/d	0.64	0.76	1.52	1.14				1.95	2.40	1.36	343
SJI	0.67	0.76	1.43	1.15	0.63	0.58			0.00	0.93	326
SJI/d	0.93	0.93	1.52	1.27	0.75	1.14			-0.86	1.09	172
SJI	0.63	0.72	1.47	1.19	0.70	0.72		1.90	0.00	1.23	742
SJI/d	0.62	0.73	1.48	1.19	0.65	0.64		1.93	-0.31	1.21	815
FJI			2.00	1.48					0.00	1.76	28.6
FJI/d			1.93	1.49					-0.49	1.70	24.1
FJI	0.84	0.86							0.00	0.85	50.0
FJI			2.07	1.61	1.13	1.21			0.00	1.55	16.3
FJI/d			2.11	1.65	1.08	1.33			0.13	1.56	8.47
FJI			3.13	1.52	2.10	2.08			0.00	2.84	28.5
FJI/d			2.82	1.64	1.12	1.44			1.02	2.56	43.0
FJI	2.45	1.69	2.20	3.33	1.67	2.16			0.00	2.32	26.5
FJI/d	2.25	3.08	2.00	1.50	1.55	2.13			-2.08	2.10	22.4
FJI	2.76	2.01	3.46	3.60	3.47	3.87		4.23	0.00	3.49	89.2
FJI/d	2.88	2.19	3.31	3.70	3.59	3.96		4.31	0.79	3.48	77.0

Table D.9: Inversion statistics for all components measured at Rx-position DVA; sah f jsf fkjs fj fjlks jfka dkfj ssjf as flsyf

Station DVB

	B1HZ	B2HZ	B1HY	B2HY	B1EX	B2EX	N7			
cut/s	14	14	5	5	8	8	0			
cut/e	0	0	0	0	0	0	0			
Inv.	χ	χ	χ	χ	χ	χ	χ	T_y/T_x	χ_{tot}	R.
sgl.							4.32	0.00	4.32	16.1
SJI					0.60	0.62		0.00	0.61	42.3
SJI/d					0.22	0.24		0.79	0.23	12.9
SJI			0.40	0.31				0.00	0.36	14.7
SJI/d			0.37	0.28				-1.30	0.32	32.6
SJI	0.21	0.23						0.00	0.22	6.89
SJI	0.25	0.25	0.39	0.31				0.00	0.31	105
SJI/d	0.26	0.26	0.38	0.31				-1.17	0.30	81.4
SJI	0.36	0.33	0.58	0.52			3.14	0.00	1.35	599
SJI/d	0.40	0.35	0.59	0.53			3.21	-0.22	1.34	646
SJI	0.44	0.39	0.57	0.51	0.41	0.32		0.00	0.45	156
SJI/d	0.42	0.34	0.44	0.35	0.26	0.27		1.03	0.34	38.5
SJI	0.34	0.31	0.57	0.51	0.42	0.42	3.03	0.00	1.11	1448
SJI/d	0.57	0.36	0.65	0.59	0.69	0.81	4.14	0.75	1.47	364
FJI			0.73	0.61	0.70			0.00	0.68	17.0
FJI/d			0.43	0.36	0.22			1.19	0.34	10.7
FJI	0.63	0.65				0.87		0.00	0.74	17.5
FJI/d	0.53	0.47				0.29		8.64	0.42	15.3
FJI	1.02	1.15	1.27	1.15				0.00	1.05	42.0
FJI/d	0.92	0.69	1.15	0.90				-1.44	0.92	34.0
FJI			0.72	0.62	0.87	0.65		0.00	0.72	17.1
FJI/d			0.82	0.67	0.95	0.89		0.36	0.82	8.28
FJI	1.24	1.34	1.44	0.83	1.00	0.65		0.00	1.11	29.1
FJI/d	1.75	1.36	1.43	0.85	1.40	1.41		0.50	1.33	5.27

Table D.10: Inversion statistics for all components measured at Rx-position DVB;

Station EMA

	A1HZ	A2HZ	A1HY	A2HY	A1EX	A2EX	N29			
cut/s	4	4	4	4	4	4	0			
cut/e	0	0	0	0	0	0	0			
Inv.	χ	χ	χ	χ	χ	χ	χ	T_y/T_x	χ_{tot}	R.
sgl.							1.31	0.00	1.31	91.6
SJI					0.36	0.39		0.00	0.37	34.3
SJI/d					1.03	3.04		0.42	2.23	24.8
SJI			0.78	0.86				0.00	0.82	24.5
SJI/d			0.65	0.70				1.37	0.66	24.2
SJI	0.30	0.29						0.00	0.30	18.4
SJI	0.35	0.35	0.68	0.75				0.00	0.56	113
SJI/d	0.38	0.35	0.69	0.73				0.60	0.55	80.1
SJI	0.36	0.37	0.84	0.95			1.31	0.00	0.82	529
SJI/d	0.38	0.36	0.69	0.75			1.49	0.71	0.77	375
SJI	0.62	0.56	0.94	1.06	0.78	0.36		0.00	0.76	213
SJI/d	0.51	0.46	0.69	0.75	0.48	0.21		0.50	0.53	287
SJI	0.77	0.73	1.27	1.37	1.65	0.73	2.20	0.00	1.31	252
SJI/d	0.76	0.70	1.18	1.32	1.24	0.46	2.10	-0.05	1.14	280
FJI	0.50	0.78	0.87	0.93				0.00	0.79	27.1
FJI/d	0.48	0.78	0.90	0.88				-0.52	0.76	23.3
FJI	0.60	0.82	1.64	1.68			1.89	0.00	1.93	107
FJI/d	1.59	1.82	1.58	1.74			7.72	-0.00	3.34	30.4
FJI	1.33	1.41	1.43	1.63	4.91	5.22		0.00	3.16	17.2
FJI/d	1.07	1.32	1.41	1.56	1.75	2.67		0.83	1.66	51.8
FJI	1.11	1.11	1.93	1.98	5.05	4.80	2.95	0.00	3.10	46.7
FJI/d	0.93	1.08	2.00	1.97	1.70	1.28	3.00	0.16	1.89	45.5

Table D.11: Inversion statistics for all components measured at Rx-position EMA;

Station ENA

	A2HZ	A1HY	A2HY	A1EX	A2EX	NRU6			
cut/s	4	4	4	4	4	0			
cut/e	0	0	0	0	0	0			
Inv.	χ	χ	χ	χ	χ	χ	T_y/T_x	χ_{tot}	R.
sgl.						2.26	0.00	2.26	15.3
SJI				0.24	0.14		0.00	0.20	6.80
SJI/d				0.18	0.10		-0.79	0.14	7.20
SJI		1.37	0.75				0.00	1.11	56.8
SJI/d		1.40	0.71				5.30	1.09	40.0
SJI	0.51	1.41	0.79				0.00	0.97	191
SJI/d	0.54	1.41	0.66				4.41	0.93	206
SJI	0.67	1.62	1.19			2.26	0.00	1.75	175
SJI/d	0.66	1.65	1.13			2.30	1.31	1.75	202
SJI	0.89			0.26	0.19	2.27	0.00	1.55	137
SJI/d	1.07			0.37	0.42	2.34	-2.09	1.62	112
SJI	0.59	1.59	1.21	0.69	0.55		0.00	1.01	88.0
SJI/d	2.37	2.40	2.77	1.66	0.60		-2.26	2.05	12.8
SJI	0.88	1.75	1.32	0.43	0.43	2.29	0.00	1.58	324
SJI/d	0.78	1.75	1.29	0.42	0.40	2.31	-0.44	1.55	394
FJI	0.80	1.73	1.61				0.00	1.44	26.4
FJI/d	0.77	2.03	1.51				-1.84	1.49	24.2
FJI	6.35	2.04	3.19			2.67	0.00	3.66	26.1
FJI/d	5.46	2.06	4.81			2.66	-20.94	3.63	31.9
FJI	6.77			3.42	3.22	2.91	0.00	4.05	29.5
FJI/d	5.90			4.00	2.44	2.93	-3.37	3.71	28.8
FJI	2.54	2.16	2.68	1.81	0.80		0.00	2.11	9.54
FJI/d	2.48	2.26	2.69	1.98	0.72		-1.45	2.08	10.6
FJI	7.05	2.10	2.91	3.45	2.93	2.97	0.00	3.76	21.6
FJI/d	6.61	3.95	2.49	3.95	2.49	3.10	-2.67	3.70	26.7

Table D.12: Inversion statistics for all components measured at Rx-position ENA;

Station ENB

	B1HZ	B2HZ	B1HY	B2HY	B1EX	NRU2			
cut/s	9	9	5	5	8	0			
cut/e	0	0	0	0	0	0			
Inv.	χ	χ	χ	χ	χ	χ	T_y/T_x	χ_{tot}	$R.$
sgl.						1.95	0.00	1.95	21.9
SJI			1.25	0.80			0.00	1.05	23.5
SJI/d			0.98	0.78			-0.85	0.87	17.4
SJI	0.50	0.54					0.00	0.52	13.0
SJI	0.52	0.64	1.28	0.84			0.00	0.88	213
SJI/d	0.56	0.63	1.00	0.81			-1.38	0.76	71.2
SJI	1.14	0.97	1.42	1.08		2.06	0.00	1.56	496
SJI/d	1.22	0.95	1.40	1.15		2.10	-0.34	1.56	540
SJI	0.71	0.64	1.55	1.10	0.81		0.00	1.04	206
SJI/d	0.67	0.61	1.10	0.88	0.71		-1.18	0.80	129
SJI	1.20	0.93	1.54	1.17	1.25	2.10	0.00	1.57	622
SJI/d	1.34	0.97	1.50	1.25	0.90	2.13	-0.48	1.54	509
FJI	1.56	1.59	2.87	1.85			0.00	2.07	26.1
FJI/d	1.16	0.83	1.64	1.84			-0.88	1.41	14.5
FJI	5.47	4.12	8.41	6.23		6.96	0.00	6.58	175
FJI/d	7.33	4.77	5.93	4.05		6.40	-1.89	5.80	112
FJI	1.88	1.56	3.25	1.97	1.59		0.00	2.17	6.52
FJI/d	1.60	0.77	1.87	1.76	1.02		-0.861	1.45	31.8
FJI	5.42	4.25	8.36	6.26	7.02	8.11	0.00	7.04	41.6
FJI/d	7.21	4.75	5.78	4.12	6.03	6.88	-1.79	5.94	99.1

Table D.13: Inversion statistics for all components measured at Rx-position ENB;

Station GBA

	A1HZ	A2HZ	A1HY	A2HY	A1EX	A2EX	N19			
cut/s	11	11	4	4	5	5	0			
cut/e	0	0	0	0	0	0	0			
Inv.	χ	χ	χ	χ	χ	χ	χ	T_y/T_x	χ_{tot}	R.
sgl.							2.12	0.00	2.52	8.89
SJI					0.32	0.62		0.00	0.49	17.9
SJI/d					0.34	0.67		0.04	0.52	17.3
SJI			0.64	0.86				0.00	0.76	86.2
SJI/d			0.72	0.94				-0.43	0.82	56.5
SJI	0.19	0.43						0.00	0.34	30.5
SJI	0.29	0.46	0.65	0.88				0.00	0.64	202
SJI/d	0.38	0.51	0.71	0.95				0.89	0.68	146
SJI	0.29	0.45	0.67	0.88			2.53	0.00	1.40	510
SJI/d	0.33	0.47	0.68	0.92			2.62	0.36	1.41	620
SJI	0.35	0.49	0.93	1.11	0.46	0.78		0.00	0.77	174
SJI/d	0.36	0.53	0.92	1.07	0.42	0.76		0.90	0.72	237
SJI	0.34	0.48	0.79	1.09	0.37	0.58	2.53	0.00	1.25	584
SJI/d	0.34	0.50	0.81	1.03	0.36	0.60	2.62	1.28	1.24	682
FJI	1.23	1.21	0.91	1.10				0.00	1.10	51.1
FJI/d	1.18	1.18	0.97	1.12				2.50	1.06	44.8
FJI	1.10	0.89	2.39	2.45			2.92	0.00	2.24	10.8
FJI/d	1.34	1.11	2.35	2.35			3.64	0.33	2.43	4.62
FJI	3.11	1.07	1.71	2.24	1.81	2.84		0.00	2.23	22.9
FJI/d	2.60	0.79	1.55	1.78	2.15	3.35		2.36	2.12	24.0
FJI	2.59	0.94	2.49	2.84	2.21	3.77	3.07	0.00	2.74	36.3
FJI/d	2.02	0.79	2.45	2.46	2.40	4.38	3.07	2.34	2.12	30.8

Table D.14: Inversion statistics for all components measured at Rx-position GBA;

Station GBB

	B1HZ	B2HZ	B1HY	B2HY	B2EX	N20			
cut/s	5	5	5	5	5	0			
cut/e	0	0	0	0	0	0			
Inv.	χ	χ	χ	χ	χ	χ	T_y/T_x	χ_{tot}	R.
sgl.						0.37	0.00	0.37	7.46
SJI	0.47	1.78					0.00	1.30	150
SJI			1.15	1.36			0.00	1.26	35.2
SJI/d			1.19	1.42			-0.76	1.28	45.2
SJI			1.16	1.38	1.42		0.00	1.32	84.5
SJI/d			1.24	1.50	1.53		-0.77	1.39	48.5
SJI			1.17	1.40		0.44	0.00	1.08	384
SJI/d			1.33	1.61		2.49	-0.03	1.84	166
SJI			1.23	1.46	1.67	0.66	0.00	1.31	420
SJI/d			1.27	1.52	1.61	0.67	-3.76	1.28	390
SJI	0.57	2.02	1.19	1.41			0.00	1.40	252
SJI/d	0.57	1.74	1.21	1.42			-32.19	1.27	360
SJI	0.58	1.99	1.17	1.39	1.53		0.00	1.41	452
SJI/d	0.56	1.86	1.21	1.45	1.56		-12.10	1.36	420
SJI	0.66	2.60	1.25	1.50		0.70	0.00	1.51	916
SJI/d	0.86	2.84	1.53	1.81		0.97	-2.66	1.70	519
SJI	0.69	2.66	1.34	1.62	1.73	1.11	0.00	1.64	933
SJI/d	0.74	2.77	1.45	1.71	1.76	1.22	-4.00	1.67	807
FJI			1.63	2.18	1.70		0.00	1.86	23.0
FJI/d			1.61	2.17	1.74		-2.36	1.27	20.9
FJI			5.11	7.74		3.21	0.00	5.65	24.3
FJI/d			5.32	7.90		3.25	-0.04	5.65	20.4
FJI	2.74	3.16	2.02	2.46			0.00	2.63	56.0
FJI/d	2.49	3.07	1.92	2.74			2.56	2.52	50.1
FJI			5.10	7.69	3.49	3.40	0.00	5.21	48.5
FJI/d			5.30	7.80	3.57	3.39	0.86	5.17	53.08
FJI	2.37	3.57	2.08	2.66	1.76		0.00	2.56	19.1
FJI/d	2.67	3.31	2.08	2.67	1.56		0.92	2.45	27.1
FJI	2.55	8.49	5.10	7.71	4.99	5.09	0.00	5.98	35.4
FJI/d	2.48	7.36	5.27	8.14	6.12	4.80	1.65	5.80	31.9

Table D.15: Inversion statistics for all components measured at Rx-position GBB;

Station HAA

	A1HZ	A2HZ	A1HY	A2HY	A1EX	A2EX	N27			
cut/s	4	4	5	5	8	8	0			
cut/e	0	0	0	0	0	0	0			
Inv.	χ	χ	χ	χ	χ	χ	χ	T_y/T_x	χ_{tot}	R.
sgl.							0.85	0.00	0.85	29.0
SJI					0.71	0.68		0.00	0.69	28.0
SJI/d					0.82	0.67		8.29	0.73	9.68
SJI			1.06	1.06				0.00	1.06	56.7
SJI/d			1.11	1.11				0.86	1.09	41.7
SJI	0.57	0.45						0.00	0.51	24.9
SJI	0.59	0.45	1.08	1.08				0.00	0.84	241
SJI/d	0.61	0.47	1.12	1.12				0.35	0.86	188
SJI	0.88	0.83	1.31	1.23			5.61	0.00	2.40	382
SJI/d	0.79	0.74	1.34	1.30			1.30	0.50	1.08	435
SJI	1.58	1.60	2.36	1.90	2.38	2.01		0.00	1.99	71.4
SJI/d	4.10	4.41	2.37	3.12	3.16	1.91		5.14	3.24	12.2
SJI	1.03	1.01	1.45	1.32	1.01	0.89	5.60	0.00	2.15	1167
SJI/d	1.17	0.98	1.29	1.35	0.82	1.16	5.65	1.05	2.09	1401
FJI	0.89	1.69	2.10	2.18				0.00	1.79	35.7
FJI/d	1.08	1.74	1.89	1.97				2.09	1.66	21.6
FJI	1.67	3.28	4.44	2.74	2.51	2.32		0.00	2.97	23.4
FJI/d	1.21	1.82	2.09	2.06	1.76	1.79		2.22	1.76	19.6

Table D.16: Inversion statistics for all components measured at Rx-position HAA;

Station HAB

	B1HZ	B1HY	B2HY	B1EX	B2EX	N31			
cut/s	5	5	5	4	4	0			
cut/e	0	0	0	0	0	0			
Inv.	χ	χ	χ	χ	χ	χ	T_y/T_x	χ_{tot}	R.
sgl.						2.10	0.00	2.10	6.33
SJI				6.47	6.00		0.00	6.24	7.60
SJI/d				2.25	2.14		-6.80	2.15	19.0
SJI		0.92	1.09				0.00	1.01	67.5
SJI/d		1.03	1.00				-10.43	1.00	64.1
SJI	1.29	0.95	1.12				0.00	1.13	70.8
SJI/d	1.32	1.02	1.13				3.74	1.13	58.3
SJI	1.62	1.06	1.24			2.06	0.00	1.49	189
SJI/d	1.65	1.08	1.25			2.19	-4.40	1.49	167
SJI	5.87	2.93	2.42	6.41	6.18		0.00	5.08	27.1
SJI/d	1.83	1.14	1.14	1.61	3.00		-2.81	1.83	140
SJI	5.25	3.05	2.65	6.82	6.02	1.96	0.00	4.79	400
SJI/d	5.13	1.65	1.68	2.07	3.18	3.16	0.42	11.61	275
FJI	1.58	1.10	1.66				0.00	1.47	22.9
FJI/d	1.32	1.20	1.38				-9.46	1.27	20.9
FJI	7.10	3.12	3.13	9.55	10.03		0.00	7.28	6.08
FJI/d	3.27	1.12	1.72	3.88	5.53		-1.77	3.40	8.66

Table D.17: Inversion statistics for all components measured at Rx-position HAB;

Station KEA

	A1HZ	A2HZ	A2HY	A1EX	A2EX	N9			
cut/s	5	5	6	5	5	0			
cut/e	0	0	0	0	0	0			
Inv.	χ	χ	χ	χ	χ	χ	T_y/T_x	χ_{tot}	R.
sgl.						0.69	0.00	0.69	5.00
SJI				0.47	0.77		0.00	0.64	58.2
SJI/d				0.51	0.88		0.17	0.71	49.0
SJI	0.60	0.86					0.00	0.74	27.1
SJI/d	0.63	0.90					-0.13	0.77	17.4
SJI	0.65	1.09	2.38				0.00	1.55	355
SJI/d	0.68	1.10	2.38				0.39	1.52	260
SJI	0.60	0.86		0.45			0.00	0.66	76.0
SJI/d	0.61	0.89		0.44			0.29	0.66	89.5
SJI	0.61	0.87				0.67	0.00	0.73	67.2
SJI	0.66	1.10	2.40	0.49			0.00	1.37	812
SJI/d	0.74	1.11	2.46	0.51			0.42	1.38	222
SJI	0.74	1.08		0.49	0.80		0.00	0.80	168
SJI/d	0.79	1.12		0.50	0.84		0.90	0.82	136
SJI	0.62	0.91	2.48			0.73	0.00	1.42	927
SJI/d	0.66	0.96	2.56			0.74	0.33	1.43	610
SJI	0.61	0.86		0.50		0.70	0.00	0.68	132
SJI/d	0.63	0.90		0.53		0.72	0.29	0.49	106
FJI	1.73	2.11		1.19			0.00	1.72	8.91
FJI/d	1.88	2.17		0.82			0.82	1.69	13.4
FJI	4.75	4.02		14.03	6.67		0.00	8.37	15.9
FJI/d	4.22	3.67		10.13	5.59		-0.85	6.27	18.3
FJI	1.98	2.13		1.04		1.69	0.00	1.76	9.13
FJI/d	1.97	2.16		0.65		1.16	1.11	1.59	32.0

Table D.18: Inversion statistics for all components measured at Rx-position KEA;

Station KEB

	B1HZ	B2HZ	B1HY	B2HY	B1EX	B2EX	N10			
cut/s	10	10	4	4	4	4	0			
cut/e	0	0	0	0	0	0	0			
Inv.	χ	χ	χ	χ	χ	χ	χ	T_y/T_x	χ_{tot}	R.
sgl.							1.21	0.00	1.21	4.03
SJI					0.54	0.56		0.00	0.55	46.5
SJI/d					0.31	0.36		-10.72	0.33	17.3
SJI			0.63	1.10				0.00	0.89	124
SJI/d			0.68	0.58				1.74	0.62	101
SJI	0.31	0.37						0.00	0.34	10.5
SJI	0.35	0.40					1.20	0.00	0.79	17.1
SJI	0.40	0.52	0.65	1.11				0.00	0.74	656
SJI/d	0.32	0.38	0.68	0.59				1.88	0.51	206
SJI	0.66	0.95	1.19	1.75			1.39	0.00	1.27	91.0
SJI/d	0.39	0.38	1.08	1.92			1.32	1.95	0.90	83.0
SJI	1.21	1.73	1.08	1.48	1.02	1.00		0.00	1.26	132
SJI/d	0.93	1.11	0.95	1.00	0.45	0.90		0.77	0.88	216
SJI	0.65	0.92	1.20	1.70	0.53	0.55	1.35	0.00	1.08	437
SJI/d	0.82	1.17	1.25	1.78	1.03	0.90	1.59	-0.09	1.23	320
FJI	0.56	0.71					1.26	0.00	0.92	4.44
FJI/d	0.49	0.52					1.28	0.10	0.85	6.07
FJI	1.24	1.67	1.57	2.02				0.00	1.67	29.2
FJI/d	0.90	0.71	1.49	0.95				1.67	1.04	23.7
FJI	0.70	0.83	2.41	3.02			1.24	0.00	1.95	4.89
FJI/d	0.79	0.48	2.04	1.64			1.25	1.92	1.37	12.9
FJI	1.63	2.39	1.60	1.83	1.17	1.09		0.00	1.65	10.6
FJI/d	1.50	2.16	1.63	1.40	0.81	0.97		0.72	1.40	23.0
FJI	1.09	1.64	2.54	3.12	2.59	2.84	1.64	0.00	2.36	51.06
FJI/d	1.67	2.71	2.68	3.00	3.08	3.29	1.52	0.50	2.60	17.7

Table D.19: Inversion statistics for all components measured at Rx-position KEB;

Station KKA

	A1HZ	A2HZ	A1HY	A2HY	A1EX	A2EX	N16			
cut/s	8	8	4	4	5	5	0			
cut/e	11	4	0	0	0	0	0			
Inv.	χ	χ	χ	χ	χ	χ	χ	T_y/T_x	χ_{tot}	R.
sgl.							3.15	0.00	3.15	35.0
SJI					1.00	1.49		0.00	1.27	9.81
SJI/d					1.17	1.06		-0.29	1.10	9.64
SJI			2.02	1.94				0.00	1.98	16.5
SJI/d			1.77	2.08				0.64	1.90	21.6
SJI	0.37	0.43						0.00	0.41	14.4
SJI	0.44	0.52	1.99	1.92				0.00	1.57	35.0
SJI/d	0.46	0.53	1.77	2.12				0.64	1.53	36.7
SJI	0.41	0.52	2.07	1.97			3.22	0.00	2.05	226
SJI/d	0.47	0.53	1.83	2.19			3.36	0.69	2.04	220
SJI	0.44	0.47	1.99	1.93	0.34	0.49		0.00	1.27	78.8
SJI/d	0.48	0.49	1.96	2.02	0.32	0.56		0.15	1.25	93.1
SJI	0.47	0.47	2.11	2.04	0.42	0.55	3.23	0.00	1.73	309
SJI/d	0.53	0.47	2.15	2.15	0.40	0.64	3.41	-0.06	1.76	288
FJI	2.27	1.34	2.07	2.15	1.94	2.72		0.00	2.14	9.46
FJI/d	2.51	1.59	2.43	2.24	0.59	0.98		-0.68	1.76	11.3
FJI	2.17	1.52	2.55	2.58	2.70	3.09	3.44	0.00	2.69	35.1
FJI/d	2.39	1.74	2.82	2.72	2.20	2.76	3.65	-0.22	2.60	32.4

Table D.20: Inversion statistics for all components measured at Rx-position KKA;

Station KKB

	B1HZ	B2HZ	B1HY	B2HY	B1EX	B2EX	N15			
cut/s	14	14	7	7	8	8	0			
cut/e	0	0	0	0	0	0	0			
Inv.	χ	χ	χ	χ	χ	χ	χ	T_y/T_x	χ_{tot}	R.
sgl.							0.78	0.00	0.78	8.04
SJI					1.34	1.48		0.00	1.41	9.22
SJI/d					0.38	0.47		-1.09	0.42	8.31
SJI			1.61	1.34				0.00	1.48	21.5
SJI/d			1.68	1.40				0.15	1.52	17.6
SJI	0.78	0.91						0.00	0.85	8.46
SJI	0.81	0.94	1.66	1.39				0.00	1.29	103
SJI/d	0.84	0.96	1.69	1.40				0.45	1.28	68.3
SJI	0.83	0.97			0.52	0.56		0.00	0.72	74.4
SJI/d	0.90	1.15			0.59	0.66		-1.32	0.80	19.3
SJI	0.77	0.87	1.76	1.47			0.83	0.00	1.24	382
SJI/d	0.81	0.89	1.79	1.49			0.87	0.35	1.24	361
SJI	0.77	0.86			0.30	0.31	0.82	0.00	0.65	250
SJI/d	0.82	0.93			0.32	0.38	0.86	-1.04	0.67	164
SJI	0.89	1.06	1.82	1.55	0.36	0.44		0.00	1.17	210
SJI/d	0.91	1.07	1.86	1.58	0.36	0.47		0.06	1.16	223
SJI	0.82	0.94	1.84	1.56	0.29	0.36	0.87	0.00	1.11	570
SJI/d	0.83	0.94	1.91	1.63	0.34	0.38	0.93	0.11	1.12	524
FJI	1.46	4.16	3.29	2.28				0.00	2.96	22.1
FJI/d	1.68	3.70	3.10	2.48				-0.33	2.75	20.0
FJI	27.4	27.2			16.02	13.91		0.00	21.35	1.59
FJI/d	2.75	1.99			1.23	1.28		-0.56	1.79	11.4
FJI	2.62	4.82	6.23	5.01			2.90	0.00	4.60	33.8
FJI/d	2.42	3.77	5.81	5.08			2.36	-1.23	4.12	26.2
FJI	2.29	3.45			3.80	3.65	1.83	0.00	3.13	69.1
FJI/d	2.34	3.18			3.72	3.48	2.33	0.14	3.00	78.6
FJI	1.42	4.72	3.70	2.55	1.04	0.79		0.00	2.72	21.6
FJI/d	1.64	3.99	3.47	2.84	1.22	1.00		-0.40	2.51	12.8
FJI	2.79	4.74	6.29	4.93	4.10	4.30	3.70	0.00	4.57	98.1
FJI/d	2.75	4.37	6.27	5.10	4.48	4.71	3.34	-0.35	4.49	61.1

Table D.21: Inversion statistics for all components measured at Rx-position KKB;

Station KNA

	A1HY	A2HY	A1EX	A2EX	N33			
cut/s	1	1	2	2	0			
cut/e	0	0	0	0	0			
Inv.	χ	χ	χ	χ	χ	T_y/T_x	χ_{tot}	R.
sgl.					1.06	0.00	1.06	7.25
SJI			0.81	0.99		0.00	0.90	43.3
SJI/d			0.51	0.57		0.62	0.53	7.98
SJI	3.88	4.88				0.00	4.41	21.8
SJI/d	4.00	4.83				-0.18	4.37	39.4
SJI	3.87	4.78	0.64	0.74		0.00	3.14	314
SJI/d	22.12	23.03	7.41	8.49		-0.18	16.64	15.2
SJI	4.02	5.22	1.44	1.39	3.05	0.00	3.42	148
SJI/d	4.02	4.85	0.46	0.51	1.19	-0.20	2.96	582
FJI	4.08	5.47	2.24	2.52		0.00	3.82	20.7
FJI/d	28.24	28.66	10.73	8.94		-0.31	20.92	0.22
FJI	4.12	5.86	2.54	2.68	2.22	0.00	3.89	49.1
FJI/d	4.26	6.03	2.59	2.86	2.38	-0.04	3.92	44.5

Table D.22: Inversion statistics for all components measured at Rx-position KNA;

Station KNB

	B1HZ	B2HZ	B1HY	B2HY	B1EX	B2EX	N32			
cut/s	4	4	3	3	5	5	0			
cut/e	13	13	0	0	0	0	0			
Inv.	χ	χ	χ	χ	χ	χ	χ	T_y/T_x	χ_{tot}	R.
sgl.							2.83	0.00	2.83	25.2
SJI					22.11	6.61		0.00	16.32	66.8
SJI/d					22.95	6.96		2.95	16.69	4.71
SJI			0.33	0.42				0.00	0.38	25.7
SJI/d			0.34	0.44				0.67	0.39	28.5
SJI	0.64	1.10						0.00	0.90	20.6
SJI			0.44	0.52	0.20	0.21		0.00	0.38	71.1
SJI/d			13.23	15.16	22.78	6.81		-59.1	15.18	22.8
SJI	0.49	0.85	0.38	0.48				0.00	0.54	340
SJI/d	0.52	0.87	0.36	0.44				-5.95	0.52	327
SJI			3.32	3.80	1.88	1.44	4.62	0.00	3.12	479
SJI/d			4.09	4.71	2.61	1.87	6.31	-1.00	3.90	372
SJI	1.17	1.37	0.44	0.56			2.78	0.00	1.37	633
SJI/d	1.40	1.58	0.44	0.63			2.89	-5.23	1.42	546
SJI	1.17	1.49	0.62	0.95	0.88	0.50		0.00	0.93	432
SJI/d	0.64	1.04	0.77	0.87	0.73	0.53		0.03	0.75	512
SJI	1.83	1.57	3.49	3.95	2.69	1.92	5.87	0.00	3.31	682
SJI/d	2.14	1.82	4.12	4.69	2.69	2.48	7.06	-1.29	3.77	457

Table D.23: Inversion statistics for all components measured at Rx-position KNB;

Station PHA

	A1HY	A1EX			
cut/s	2	2			
cut/e	0	0			
Inv.	χ	χ	T_y/T_x	χ_{tot}	R.
SJI	0.67	1.02	0.00	0.86	18.9
SJI/d	0.49	0.80	-3.80	0.65	40.0
SJI	1.02	0.79	0.00	0.91	26.2
SJI/d	1.03	0.81	2.22	0.91	34.5

Table D.24: Inversion statistics for all components measured at Rx-position PHA;

Station PHB

	B1HZ	B2HZ	B1HY	B2HY	B1EX	NRU4			
cut/s	12	12	8	8	8	0			
cut/e	0	0	0	0	0	0			
Inv.	χ	χ	χ	χ	χ	χ	T_y/T_x	χ_{tot}	R.
sgl.						1.60	0.00	1.60	11.3
SJI			0.35	0.43			0.00	0.40	37.3
SJI/d			0.37	0.46			0.06	0.41	32.7
SJI	0.39	0.19					0.00	0.33	27.3
SJI	0.42	0.21	0.39	0.45			0.00	0.40	184
SJI/d	0.44	0.23	0.38	0.45			-0.60	0.39	155
SJI	0.74	0.68	0.51	0.62	0.51		0.00	0.61	98.5
SJI/d	0.68	0.64	0.54	0.51	0.45		0.50	0.54	142
SJI	0.52	0.26	0.48	0.48		1.59	0.00	1.11	183
SJI/d	0.53	0.26	0.43	0.26		1.61	-0.46	1.11	166
SJI	0.67	0.27	0.56	0.56	0.55	1.60	0.00	1.08	278
SJI/d	0.66	0.29	0.57	0.60	0.63	1.64	-0.08	1.10	303
FJI	2.16	0.27	1.13	0.87			0.00	1.36	29.0
FJI/d	2.17	0.46	1.16	0.91			0.00	1.34	22.4
FJI	5.61	0.55	4.24	2.67		2.29	0.00	3.33	39.3
FJI/d	7.32	0.75	2.37	1.79		2.54	-1.00	3.39	85.1
FJI	1.76	2.49	1.64	1.33	0.96		0.00	1.69	58.1
FJI/d	1.74	2.60	1.98	1.51	0.75		1.62	1.74	20.0
FJI	6.18	0.61	3.95	2.56	1.17	2.54	0.00	3.26	99.3
FJI/d	7.35	0.74	2.54	1.75	1.69	2.69	-0.87	3.27	87.3

Table D.25: Inversion statistics for all components measured at Rx-position PHB;

Station RAA

	A1HZ	A2HZ	A1HY	A2HY	A1EX			
cut/s	2	2	4	4	4			
cut/e	0	0	0	0	0			
Inv.	χ	χ	χ	χ	χ	T_y/T_x	χ_{tot}	R.
SJI			2.01	1.58		0.00	1.81	178
SJI/d			1.99	1.61		0.81	1.78	112
SJI	1.10	2.07				0.00	1.66	26.1
SJI	1.10	2.12	2.06	2.12		0.00	1.77	190
SJI/d	1.14	2.25	2.15	1.69		-0.04	1.82	141
SJI	1.14	2.17	2.06	1.60	0.75	0.00	1.64	321
SJI/d	1.17	2.23	2.14	1.67	0.74	-0.11	1.65	239
FJI	1.75	2.41	2.18	2.15		0.00	2.14	23.9
FJI/d	1.62	2.46	2.33	2.18		-0.26	2.12	13.9
FJI	2.26	2.52	2.47	2.18	2.87	0.00	2.41	14.0
FJI/d	2.22	2.66	2.25	2.07	3.03	-0.16	2.40	14.6

Table D.26: Inversion statistics for all components measured at Rx-position RAA;

Station RAB

	B1HZ	B2HZ	B1HY	B2HY	B1EX	B1EX	NRU5			
cut/s	7	7	7	7	7	7	0			
cut/e	0	0	0	0	0	0	0			
Inv.	χ	χ	χ	χ	χ	χ	χ	T_y/T_x	χ_{tot}	R.
sgl.							3.32	0.00	3.32	10.6
SJI	1.65	1.54						0.00	1.60	21.5
SJI			0.98	1.02				0.00	1.00	28.8
SJI/d			1.01	1.03				0.99	1.00	26.7
SJI					0.52	0.48		0.00	0.50	16.1
SJI/d					0.54	0.51		-0.78	0.52	4.58
SJI	1.63	1.51	1.10	1.10				0.00	1.36	95.0
SJI/d	1.59	1.46	1.09	1.11				-0.22	1.30	139
SJI	2.01	1.97	1.41	1.37			2.41	0.00	2.01	349
SJI/d	2.12	1.87	1.67	1.80			3.12	-3.01	2.39	178
SJI	1.83	1.78	1.14	1.14	0.94	0.94		0.00	1.35	158
SJI/d	1.79	1.71	1.13	1.21	0.74	0.69		-0.67	1.25	205
SJI	0.98	0.88	1.17	1.24	1.36	1.38	2.26	0.00	1.58	1111
SJI/d	0.67	0.63	1.24	1.38	0.96	0.92	2.12	-0.64	1.40	1218
FJI	0.94	1.04	1.49	1.71				0.00	1.33	99.36
FJI/d	1.84	1.58	1.47	1.75				-1.41	1.63	60.4
FJI	3.76	3.60	2.41	2.53			4.88	0.00	3.90	39.3
FJI/d	3.81	3.52	2.53	2.62			4.54	0.68	3.69	47.7
FJI	3.17	2.85	2.03	2.29	3.23	2.85		0.00	2.77	10.7
FJI/d	2.10	1.90	1.44	1.76	1.06	1.07		-1.62	1.56	20.8
FJI	3.32	3.21	3.27	3.31	4.80	4.38	5.68	0.00	4.45	14.3
FJI/d	3.33	3.40	2.51	2.56	2.89	2.97	5.89	-1.20	3.98	10.9

Table D.27: Inversion statistics for all components measured at Rx-position RAB;

Station RZA

	A1HZ	A2HZ	A1HY	N26			
cut/s	9	9	3	0			
cut/e	0	0	0	0			
Inv.	χ	χ	χ	χ	T_y/T_x	χ_{tot}	R.
sgl.				1.47	0.00	1.47	14.4
SJI	0.51	0.49			0.00	0.51	13.7
SJI	0.59	0.54	0.58		0.00	0.57	25.6
SJI/d	0.57	0.55	0.57		5.73	0.55	20.7
SJI	0.57	0.54	0.63	1.48	0.00	0.87	84.4
SJI/d	0.57	0.56	0.58	1.56	5.27	0.87	74.0
FJI	1.16	0.63	0.94		0.00	0.93	18.5
FJI/d	0.97	0.89	0.74		4.84	0.84	12.8
FJI	1.78	1.08	1.84	2.25	0.00	1.79	14.7
FJI/d	1.53	1.35	1.47	2.18	9.21	1.60	36.0

Table D.28: Inversion statistics for all components measured at Rx-position RZA;

Station RZB

	B1HZ	B2HZ	B1HY	B2HY	B1EX	B2EX	N25			
cut/s	13	13	6	6	8	8	0			
cut/e	0	0	0	0	0	0	0			
Inv.	χ	χ	χ	χ	χ	χ	χ	T_y/T_x	χ_{tot}	R.
sgl.							6.52	0.00	6.25	116
SJI					0.15	0.15		0.00	0.15	8.12
SJI/d					0.15	0.15		-0.29	0.15	8.29
SJI			2.60	3.01				0.00	2.85	14.1
SJI/d			2.52	3.07				0.27	2.76	17.5
SJI	0.60	0.75						0.00	0.68	6.23
SJI	0.68	0.79	2.56	3.07				0.00	2.17	124
SJI/d	0.66	0.80	2.52	3.09				0.40	2.12	38.4
SJI	0.82	.091	2.69	3.79			5.34	0.00	3.07	394
SJI/d	0.75	0.89	2.62	3.21			5.48	0.32	3.00	393
SJI	0.76	0.86	2.64	3.16	0.41	0.21		0.00	1.83	121
SJI/d	0.82	1.02	2.66	3.15	0.77	0.64		0.22	1.83	59.2
SJI	0.82	0.92	2.80	3.28	0.39	0.60	2.73	0.00	2.05	530
SJI/d	0.67	0.80	2.59	3.16	0.26	0.39	4.91	0.30	2.35	638
FJI	2.20	2.01	3.10	3.97				0.00	3.01	8.72
FJI/d	1.73	1.80	3.23	4.03				-0.13	2.90	12.1
FJI	2.93	2.21	4.92	5.96			5.54	0.00	4.60	54.0
FJI/d	2.96	3.09	4.77	5.92			8.19	-0.00	5.19	23.1
FJI	2.32	2.12	2.99	3.92	0.83	0.58		0.00	2.46	17.8
FJI/d	1.74	1.81	3.27	4.08	0.58	0.45		-0.15	2.39	9.67
FJI	2.11	1.97	4.96	6.02	2.96	3.40	5.94	0.00	4.28	60.1
FJI/d	1.98	1.96	5.81	6.95	4.62	5.05	7.52	-0.28	5.16	52.5

Table D.29: Inversion statistics for all components measured at Rx-position RZB;

Station SAA

	A1HZ	A2HZ	A3HZ	A1HY	A2HY	A3HY	A1EX	A2EX	N6			
cut/s	5	6	7	7	7	12	4	4	0			
cut/e	0	0	0	0	0	0	0	0	0			
Inv.	χ	χ	χ	χ	χ	χ	χ	χ	χ	T_y/T_x	χ_{tot}	R.
sgl.									2.50	0.00	2.50	16.7
SJI								0.24	0.23	0.00	0.24	40.6
SJI/d								0.24	0.19	0.41	0.21	23.8
SJI				1.68	1.26	1.02				0.00	1.34	33.4
SJI/d				1.70	1.33	0.99				0.24	1.33	27.6
SJI	0.42	0.28	0.65							0.00	0.47	23.2
SJI	1.35	0.73	1.32	1.90	1.42	1.03				0.00	1.34	191
SJI/d	0.64	0.45	0.83	1.84	1.62	1.09				0.51	1.17	111
SJI	0.64	0.47	1.08	1.97	1.38	1.17			2.54	0.00	1.49	724
SJI/d	0.51	0.36	0.75	1.69	1.42	1.02			2.65	0.52	1.36	445
SJI	0.64	0.53	1.03	1.92	1.38	1.14	0.58	0.35		0.00	1.07	845
SJI/d	0.56	0.39	0.75	1.81	1.52	1.06	0.67	0.56		0.50	1.00	363
SJI	0.62	0.50	1.06	1.95	1.36	1.14	0.51	0.40		0.00	1.31	1517
SJI/d	0.57	0.39	0.80	1.77	1.51	1.06	0.79	0.53		0.46	1.28	848
FJI	3.15	3.37	3.46	3.09	3.71	2.74				0.00	3.26	12.7
FJI/d	3.03	3.73	3.35	3.62	4.03	3.34				0.06	3.42	3.64
FJI	3.80	6.09	3.73	6.69	4.63	4.31				0.00	4.89	42.3
FJI/d	2.72	6.73	1.90	4.87	5.33	4.32				0.47	4.38	37.4

Table D.30: Inversion statistics for all components measured at Rx-position SAA;

Station TAA

	A1HZ	A1HY	N13	N14			
cut/s	5	4	0	0			
cut/e	0	0	0	0			
Inv.	χ	χ	χ	χ	T_y/T_x	χ_{tot}	R.
sgl.			1.25		0.00	1.25	10.0
sgl.				1.90	0.00	1.90	19.8
SJI			1.38	1.79	0.00	1.61	169
SJI	0.75	3.60			0.00	2.62	37.1
SJI/d	0.63	2.72			11.52	1.96	45.2
SJI		3.46	1.90		0.00	2.82	201
SJI/d		4.53	2.22		0.05	3.54	60.0
SJI	0.59			1.25	0.00	0.96	32.0
SJI	0.63	3.69		1.27	0.00	2.33	175
SJI/d	0.63	2.74		1.30	11.72	1.77	116
SJI	0.72	3.76	1.53	2.12	0.00	2.35	596
SJI/d	0.66	2.81	1.64	2.11	11.55	1.93	548
FJI	2.09	3.73			0.00	3.03	34.7
FJI/d	1.15	2.87			13.17	2.16	27.8
FJI		13.69	2.09		0.00	9.96	163
FJI/d		17.11	17.10		0.19	16.80	67.3
FJI	3.36			2.76	0.00	3.09	15.0
FJI	3.77	5.31		2.78	0.00	4.14	16.7
FJI/d	2.89	4.54		3.47	6.27	3.63	22.9

Table D.31: Inversion statistics for all components measured at Rx-position TAA;

Station TAB

	B1HZ	B2HZ	B1HY	B2HY	B1EX	N1			
cut/s	10	10	7	7	10	0			
cut/e	0	0	0	0	0	0			
Inv.	χ	χ	χ	χ	χ	χ	T_y/T_x	χ_{tot}	R.
sgl.						0.61	0.00	1.68	3.64
SJI			1.76	2.41			0.00	2.11	30.5
SJI/d			1.20	1.66			1.86	1.42	52.7
SJI	0.42	0.51					0.00	0.47	12.3
SJI	0.44	0.52	1.77	2.41			0.00	1.57	202
SJI/d	0.45	0.56	1.23	1.69			1.61	1.10	113
SJI	0.52	0.64	1.98	2.64	0.83		0.00	1.60	285
SJI/d	0.45	0.57	1.22	1.72	0.24		1.50	1.00	131
SJI	0.53	0.59	1.75	2.37		2.44	0.00	1.90	656
SJI/d	0.49	0.60	1.28	1.75		2.49	1.45	1.70	554
SJI	0.50	0.61	1.88	2.50	0.74	2.49	0.00	1.85	1005
SJI/d	0.55	0.63	1.44	2.11	1.01	2.66	1.11	1.77	328
FJI	0.84	1.51	2.52	3.00			0.00	2.18	20.8
FJI/d	0.88	0.67	1.34	2.00			1.18	1.31	22.3
FJI	0.98	1.95	3.30	3.93	2.46		0.00	2.77	13.8
FJI/d	0.94	0.86	1.41	1.99	0.51		1.37	1.24	23.1

Table D.32: Inversion statistics for all components measured at Rx-position TAB;

Station TKA

	A1HZ	A2HZ	A1HY	A2HY	A1EX	A2EX	N28			
² cut/s	15	15	6	6	13	13	0			
³ cut/e	0	0	0	0	0	0	0			
⁴ Inv.	χ	χ	χ	χ	χ	χ	χ	T_y/T_x	χ_{tot}	R.
⁵ sgl							3.32	0.00	3.32	10.0
⁶ SJI					2.94	3.69		0.00	3.34	12.1
⁷ SJI/d					0.26	0.28		-3.44	0.27	4.48
⁸ SJI			0.59	0.88				0.00	0.75	13.8
⁹ SJI/d			0.60	0.90				-1.29	0.76	11.0
¹⁰ SJI	0.28	0.38						0.00	0.33	3.75
¹¹ SJI	0.32	0.40	0.60	0.89				0.00	0.62	31.0
¹² SJI/d	0.32	0.41	0.62	0.93				-1.95	0.63	17.0
¹³ SJI	0.44	0.52	0.81	1.25			2.31	0.00	1.31	517
¹⁴ SJI/d	0.43	0.54	0.85	1.11			2.41	-3.08	1.30	460
¹⁵ SJI	1.22	1.73	0.89	1.75	2.12	2.85		0.00	1.84	58.1
¹⁶ SJI/d	0.34	0.46	0.68	1.02	0.60	0.49		-3.93	0.64	29.4
¹⁷ SJI	1.96	3.19	1.93	3.12	3.08	3.86	3.35	0.00	2.99	169
¹⁸ SJI/d	0.47	0.61	0.91	1.25	0.47	0.54	2.54	-1.60	1.21	676
¹⁹ FJI	0.43	0.70	0.86	0.99				0.00	0.80	12.8
²⁰ FJI/d	0.41	0.59	0.62	0.91				-2.60	0.66	8.32
²¹ FJI	1.75	1.40	2.05	3.80			5.07	0.00	3.25	13.8
²² FJI/d	1.87	1.23	2.09	3.64			5.42	-0.02	3.25	13.7
²³ FJI	2.61	4.12	1.59	2.65	3.01	3.89		0.00	3.02	8.00
²⁴ FJI/d	0.39	0.87	1.04	1.36	0.64	0.84		-5.11	0.92	10.2
²⁵ FJI	1.88	2.54	2.48	6.25	5.80	6.93	10.94	0.00	6.20	1.38
²⁶ FJI/d	1.44	2.26	3.02	5.72	3.44	3.62	8.61	-0.91	4.65	2.28

Table D.33: Inversion statistics for all components measured at Rx-position TKA;

Station TKB

	B1HZ	B2HZ	B2HY			
cut/s	4	4	4			
cut/e	0	0	0			
Inv.	χ	χ	χ	T_y/T_x	χ_{tot}	R.
SJI	0.86	0.73		0.00	0.80	64.9
SJI	1.00	0.66	1.52	0.00	1.12	234
SJI/d	1.01	1.03	1.44	20.67	1.15	139
FJI	1.58	1.12		0.00	1.37	7.14
FJI/d	1.66	1.16		-1.53	1.41	11.65
FJI	4.72	6.88	5.97	0.00	5.92	62.1
FJI/d	3.87	5.20	5.82	521.67	4.91	86.0

Table D.34: Inversion statistics for all components measured at Rx-position TKB;

Station YAA

	A1HZ	A2HZ	A2HY	A1EX	N17			
cut/s	6	6	4	4	0			
cut/e	0	0	0	0	0			
Inv.	χ	χ	χ	χ	χ	T_y/T_x	χ_{tot}	Roughn.
sgl.					0.84	0.00	0.84	2.85
SJI	0.65	0.44				0.00	0.56	46.3
SJI	0.66	0.44	0.27			0.00	0.48	130
SJI/d	0.68	0.45	0.26			1.21	0.48	105
SJI	0.91	0.65	0.37	0.94		0.00	0.75	118
SJI/d	0.71	0.50	0.28	0.54		1.15	0.51	103
SJI	0.67	0.46	0.31		0.33	0.00	0.47	141
SJI/d	0.69	0.46	0.28		0.35	0.56	0.47	176
SJI	0.77	0.52	0.39	0.70	0.53	0.00	0.60	264
SJI/d	0.70	0.48	0.28	0.53	0.34	0.85	0.48	288
FJI	0.79	0.63	0.50			0.00	0.65	23.3
FJI/d	0.82	0.65	0.51			-0.01	0.65	22.6
FJI	0.98	0.86	0.46	1.35		0.00	0.97	34.7
FJI/d	0.87	0.82	0.49	0.66		0.13	0.70	35.9
FJI	2.53	2.38	2.33		4.04	0.00	2.77	69.7
FJI/d	3.88	3.22	2.43		19.25	0.00	8.14	3.14
FJI	2.99	2.42	2.22	2.61	4.77	0.00	2.96	33.4
FJI/d	2.88	2.61	2.33	0.99	4.27	0.01	2.56	50.6

Table D.35: Inversion statistics for all components measured at Rx-position YAA;

Station YAB

	B1HZ	B2HZ	B1HY	B2HY	B1EX	B2EX			
cut/s	6	6	5	5	5	5			
cut/e	23	12	0	0	0	0			
Inv.	χ	χ	χ	χ	χ	χ	T_y/T_x	χ_{tot}	$R.$
SJI					0.58	0.93	0.00	0.78	16.4
SJI/d					0.60	1.03	1.97	0.83	10.5
SJI			0.44	0.41			0.00	0.42	14.1
SJI/d			0.45	0.43			-0.23	0.43	11.3
SJI	0.28	0.64					0.00	0.55	28.0
SJI			2.11	2.04	2.84	2.83	0.00	2.49	73.5
SJI/d			0.84	0.75	0.79	1.28	10.75	0.92	66.2
SJI	0.29	0.57	0.48	0.46			0.00	0.48	187
SJI/d	0.29	0.58	0.46	0.42			-1.30	0.45	194
SJI	1.21	1.90	0.88	0.91	1.27	1.17	0.00	1.21	550
SJI/d	6.34	8.08	2.55	3.60	1.62	2.55	40.75	3.84	124
FJI	2.24	1.49	1.63	1.34			0.00	1.58	75.5
FJI/d	2.39	2.08	1.89	1.57			0.84	1.81	50.3
FJI			4.24	3.88	3.88	4.30	0.00	4.08	34.0
FJI/d			1.42	1.19	3.13	2.41	40.42	2.13	34.2
FJI	5.57	15.33	4.34	4.26	9.03	10.47	0.00	8.82	52.0
FJI/d	5.04	8.08	3.83	4.26	3.18	3.53	124.32	4.39	52.0

Table D.36: Inversion statistics for all components measured at Rx-position YAB;

Station YOA

	A1HZ	A1HY	A1EX			
cut/s	16	4	4			
cut/e	0	0	0			
Inv.	χ	χ	χ	T_y/T_x	χ_{tot}	<i>Roughn.</i>
SJI		0.76	0.88	0.00	0.83	42.1
SJI/d		0.73	0.40	-0.77	0.58	49.4
SJI	0.40		0.71	0.00	0.61	12.5
SJI/d	0.22		0.43	-3.82	0.36	10.0
SJI	0.15	0.70		0.00	0.56	60.2
SJI/d	0.15	0.73		0.65	0.57	41.9
SJI	0.19	0.77	0.50	0.00	0.57	72.4
SJI/d	0.21	0.73	0.40	-0.73	0.51	115
FJI		1.05	0.68	0.00	0.88	22.2
FJI/d		0.88	0.51	-0.85	0.71	32.9
FJI	0.25		0.50	0.00	0.42	27.3
FJI/d	0.27		0.38	-4.00	0.34	14.8
FJI	0.35	0.71		0.00	0.60	28.0
FJI/d	0.29	0.74		0.84	0.60	22.5
FJI	0.34	1.04	0.67	0.00	0.78	24.2
FJI/d	0.50	0.88	0.55	-0.62	0.67	30.2

Table D.37: Inversion statistics for all components measured at Rx-position YOA;

Station YOB

	B1HZ	B2HZ	B1HY	B2HY	B1EX	B2EX	N18			
cut/s	12	12	7	7	8	8	0			
cut/e	0	0	0	0	0	0	0			
Inv.	χ	χ	χ	χ	χ	χ	χ	T_y/T_x	χ_{tot}	R.
sgl.							1.00	0.00	1.51	3.02
SJI					1.08	1.01		0.00	1.05	14.2
SJI/d					1.52	1.59		1.12	1.53	3.58
SJI			0.29	0.31				0.00	0.30	25.4
SJI/d			0.29	0.33				1.99	0.31	23.3
SJI	0.23	0.33						0.00	0.29	24.7
SJI			0.59	0.61	1.54	1.48		0.00	1.14	83.3
SJI/d			0.32	0.39	0.24	0.23		7.77	0.29	30.6
SJI	0.32	0.25	0.35	0.38				0.00	0.33	92.3
SJI/d	0.29	0.26	0.35	0.40				4.30	0.33	87.9
SJI			0.46	0.77	0.82	0.81	2.13	0.00	1.09	157.7
SJI/d			1.33	2.09	3.67	3.90	7.95	2.84	4.10	10.0
SJI	0.47	0.48	0.37	0.41			1.47	0.00	0.73	262
SJI/d	0.67	0.66	0.45	0.47			1.86	-1.30	0.91	153
SJI	0.41	0.38	0.42	0.58	0.83	0.85		0.00	0.62	350
SJI/d	0.40	0.44	0.34	0.43	0.41	0.38		9.00	0.39	156
SJI	1.00	0.66	0.56	0.68	1.12	1.05	2.20	0.00	1.12	287
SJI/d	2.21	3.05	1.40	2.28	3.35	4.04	7.63	4.28	3.67	13.3
FJI			0.71	1.53	1.70	1.75		0.00	1.48	11.9
FJI/d			0.35	0.44	0.39	0.39		6.99	0.39	17.2
FJI	0.78	0.52	0.41	0.59				0.00	0.58	14.0
FJI/d	0.81	0.51	0.41	0.58				0.27	0.58	15.0
FJI	1.91	2.04	1.49	1.99			2.70	0.00	2.03	10.5
FJI/d	1.50	1.44	0.89	1.44			2.18	-2.73	1.47	14.5
FJI			2.09	2.88	2.47	2.53	3.81	0.00	2.77	28.8
FJI/d			1.53	2.40	5.95	5.85	9.30	0.42	5.37	2.07
FJI	1.87	4.27	0.78	1.11	2.38	2.26		0.00	2.34	20.0
FJI/d	1.89	4.02	0.89	1.40	1.99	2.02		1.55	2.14	3.74
FJI	2.37	4.18	1.58	2.04	3.17	3.14	3.51	0.00	2.93	35.1
FJI/d	2.18	3.21	1.37	2.06	3.24	3.11	5.06	1.58	2.94	4.55

Table D.38: Inversion statistics for all components measured at Rx-position YOB;

On the inversion of geophysical data

Two and two is not always four. It depends...
Massimo "Mr. Bombastic" Petrucci, 1999

Inversion is a very important tool for geophysical interpretation of measured data sets. Although the inversion theory as laid out in chapter 3 appears to be straightforward, many mistakes can be done by misinterpreting inversion results.

At several places I pointed out critical or dangerous points within the inversion process. In this section I would like to compile these points and elaborate on how to do inversions and to interpret their results. I worked mainly with TEM inversion. Some of the issues addressed here will be the same for other geophysical methods, others will not.

WARNING: This represents the personal point of view I developed after five years of programming and using different inversion algorithms. I included it in this work, because I hope that the reader might find this useful. Some of the issues addressed here are debatable.

Most importantly, inversions are subjective. They are based on several assumptions which are not necessarily right (and in general they are not). Unfortunately, often solutions appearing to avoid any assumptions just represent different assumptions.

E.1 Assumptions included in inversions

The central characteristic of any inversion is the misfit. The better the misfit, the more likely the model. In most cases a least-squares misfit is used in inversions. However, the model providing the lowest least-squares misfit is the most likely only in case of normal distributed measurement errors. In most cases, this requirement is not fulfilled. Other residual norms might be as reasonable, and probably

will give different results.

In this work I used a weighted misfit under the assumption that the error estimates are standard deviations of normally distributed noise. As I pointed out in sec. 2.2.3, in several cases I found that this is incorrect. The other possibility would be to discard the error estimates and use an unweighted misfit. However, this assumes that all data points have the same error. Obviously distorted data points should be removed in this case. Of course, defining “obvious distortions” is again subjective and based on the experience of the interpreter.

Often a diagonal weighting matrix \mathbf{W} is used. This includes the assumption that the data errors are not correlated. In any other case \mathbf{W} has non-zero off-diagonal entries. In general, the data point values are correlated, either by the measurement system or by applying, for instance, digital filters in the preprocessing stage. Again, these dependencies are unknown or ignored for simplicity¹.

Often constraints (mostly smoothness constraints) are used in inversions. These of course are also approximations. Constable et al. [1987] in their famous paper defined two different roughness-measures. Smoothness constraints are based on the principle often used in sciences of favouring the simplest theory possible, if more than one explains the observation. Beside the fact that “simple” is an subjective term, the complex explanation might be right.

If more than one constraint is used, the weighting between these constraints is not defined. As pointed out in sec. 5.4.1, the weight between smoothness of the models and the likeness of other models in the SJI algorithm is set to 1.0, which is also artificial. Other weights are as justified and will give other results. The same is true for the damping of the calibration factors.

In multidimensional inversions a choice for the weight between, for instance, horizontal and vertical smoothness has to be set. The choice again is arbitrary and will change the result². Using an isotropic smoothness does not mean avoiding an assumption. It is just making a different one.

The biggest problem in using constraints is the weighting against the data misfit, i.e. setting the regularisation parameter. In the case of well-defined error estimates this is easy, as a proper target misfit which has to be reached is defined. The regularisation parameter has to be set to the highest value with which the target misfit can be reached. However, error estimates in general are not correct. If one fixed regularisation can be used, the L-curve criterion is a good candidate to set this parameter. As shown in sec. 5.2.1, fixed regularisation parameters do not provide good results when inverting TEM data sets.

¹In many inversion papers, the authors start with an arbitrarily-shaped data covariance matrix. In almost all cases, they assume a diagonal matrix at a certain step.

²This question is related to correlation lengths of the geology, e.g. how many features one will cross in 1 km laterally and vertically. In sedimentary environments the weight for the horizontal smoothness should be much higher than for the vertical.

E.2 Linearisation error

The linear approximation of $\mathbf{f}(\mathbf{m})$ by the Jacobian \mathbf{J} seems not to be very accurate in the TEM case, as pointed out at several places in this thesis (see e.g. secs. 3.5 and 5.2.1). It is based on small perturbations (typically around some percent) of the actual model parameters. Changing a parameter several tens of percent might change the dependencies significantly. Also, the matrix reflects only first order terms. Changing m_1 and m_2 simultaneously might result in a different $\mathbf{f}(\mathbf{m})$ than predicted by \mathbf{J} . Finally, the Jacobian is defined locally for $\mathbf{m} \rightarrow \mathbf{m}_0$. It will look different when calculated elsewhere in parameter space.

Any analysis based on the Jacobian thus has to be treated with care. They might be useful to understand and analyse the inversion result but are subject to the restrictions listed above. Moreover, importances [Hördt et al., 1992] or parameter resolution matrices [Menke, 1984] depend on the final regularisation parameter. All of these analyses depend on the resulting model, the latter also on the course of the inversion. Another inversion run with other parameters might lead to a different result.

Non-linear model appraisal schemes as used in this thesis or presented e.g. in [Oldenburg and Li, 1999] are superior in that way, but their results are often not easy to quantify. Often they include several inversion runs, which makes them computationally expensive.

Global inversion schemes (sec. 3.2.3) in general do not rely on any problem linearisation, but are computationally extremely expensive. Their convergence depends greatly on the way to sample the model space. To improve this step, most authors use some assumptions about the structure of the model space or the forward function \mathbf{f} , which again will bias the results.

E.2.1 Few layers with variable thicknesses vs. many layers with fixed thicknesses

Although I described the typical parameterisation of the model for either Marquardt or Occam's inversion in chapter 3, they do not have to be chosen like this. A Marquardt inversion may alternatively be used to invert a model with many layers of fixed thicknesses (see Constable et al. [1987] for an example), although this will probably result in very rough models because the algorithm will try to fit even the noise in the transients. Also, Occam's inversion might even be thinkable with a few layer model (here, an appropriate roughness matrix has to be constructed to somehow regularise the thickness parameters).

The main drawback of models with many layers of fixed thicknesses (hereafter referred to as "MLFT-models") is the computation time. The computation time required for an evaluation of $\mathbf{f}(\mathbf{m})$ increases with every layer added. To discretise every feature in the – unknown – subsurface, many layers are needed.

There is also a big drawback of models with few layers and variable thickness ("FLVT-models"). In general, the misfit function of a FLVT-model will have more local minima than the misfit function of MLFT-models. The reason is that the different layers of an earth model have impacts of varying strengths on \mathbf{f} in the LOTEM

	Original	\mathbf{m}_0	Result 1	Result 2
$\rho_1 / \Omega\text{m}$	100.00	10.00	10.33	15.33
$\rho_2 / \Omega\text{m}$	5.00	100.00	41.26	3.66
h_1 / m	200.00	500.00	15640.18	500.00
<i>RMS</i> / %	0.00	81.64	44.98	26.37

Table E.1: Synthetic inversion example; The column “Original” shows the synthetic earth model used to produce the data to invert. \mathbf{m}_0 is the initial model used in both inversions. The next two columns show the inversion results of Marquardt inversions with variable thickness of the first layer (“Result 1”) and with fixed layer thickness (“Result 2”).

case. Effects are bigger if the layers are shallower, thicker and conductive (for magnetic) or resistive (for electric Rx-components), respectively. To lower the misfit, it may be most important to have a conductive layer in a certain depth. An inversion algorithm fed with an MLFT-model has no other choice than to decrease the resistivity of the model for layers at this depth.

If there are already some structures in the model, an algorithm confronted with a FLVT-models may instead also move an existing conductive layer to this depth by in- or decreasing the thicknesses of the shallower layers. Choosing one of the two solutions will mean to fix which of the layers will represent a certain feature, e.g. a conductive feature will be represented by layer two. In general, both solutions will lead to distinct minima.

Table E.1 shows an example. Here, a synthetic data set was produced using a two layered case. The transient was simulated for an \dot{H}_z -Rx in broadside configuration with an offset of 5 km in a time range of 1 ms to 1 s. The dominant feature of the original model is the conductive 5 Ωm -half-space initial in a depth of 200 m. The initial model used for the Marquardt inversion is shown in the column named “ \mathbf{m}_0 ”. Misleadingly, the resistivity trend of the original model was reversed. To reconstruct the original model, the algorithm has to increase the resistivity of first layer and decrease both depth to and resistivity of the half-space.

Leaving the thickness of the first layer variable, the inversion result is quite unsatisfying. The thick, conductive first layer seems to represent the two layers of the original model fairly. The layer boundary is moved downwards, so the resistive layer, which contradicts the transient, does not influence the shape of the transient. Actually, a homogenous half-space with 10.33 Ωm produces the same misfit.

This problem is caused by the insufficient approximation of $\mathbf{f}(\mathbf{m}_0 + \hat{\mathbf{m}})$ by $\mathbf{f}(\mathbf{m}_0) + \mathbf{J}\hat{\mathbf{m}}$. \mathbf{J} is calculated by small perturbances of one parameter per column around the initial model. In the example, a small change of the parameters will roughly result in the following responses:

Resistivity ρ_1 : This layer represents the conductive part of the model, which obviously is most important for the misfit. To increase the ρ_1 thus will result in larger misfits, as the model will lack the conductive part then.

Resistivity ρ_2 : With the conductive first layer, there is no need for an additional conductor, although it seems to be favourable to decrease ρ_2 . The influence of ρ_2 is not very big.

	Original	\mathbf{m}_0	Result
$\rho_1 / \Omega\text{m}$	100.00	50.00	28.56
$\rho_2 / \Omega\text{m}$	10.00	50.00	33.85
$\rho_3 / \Omega\text{m}$	100.00	50.00	104.83
h_1 / m	200.00	600.00	623.38
h_2 / m	200.00	600.00	211.37
<i>RMS</i> / %	0.00	43.78	10.21

Table E.2: Synthetic inversion example; The column “Original” shows the synthetic earth model used to produce the data to invert. \mathbf{m}_0 is the initial model used in the inversion. The column “Result” shows the result of a Marquardt inversion.

Thickness h_1 : Decreasing the thickness will move the (wrong) resistive layer to shallower depths. The model part which has influence on the transient will thus become more resistive, which is not desirable. Obviously, h_1 has to be increased. As “Result 1” indicates, this solution seems to be more effective.

Especially the information about the thickness h_1 will lead in a wrong direction, unless ρ_{h_2} will somehow get smaller than ρ_{h_1} . As the increasing h_1 will decrease the relevance of ρ_2 , which thus will be strongly damped. This might be avoided using second order terms. The inversion would reach the original model, if the approximation of $\mathbf{f}(\mathbf{m})$ would indicate that a better misfit can be reached by decreasing ρ_2 and h_1 . Still, both parameter would have to be changed largely, although the Taylor-expansion is only valid near \mathbf{m}_0 .

The possible solutions for the inversion algorithm change, if h_1 is kept fixed at 500 m. In this case the only real improvement in fit can be reached by decreasing ρ_2 . The resulting model (“Result 2” in tab. E.1) much better reflects the characteristics of the original model. Of course, the misfit stays high in this case, for the first layer can not be changed to its original values. The first layer in “Result 2” has to represent the upper 500 m of the original model and therefore the resistivity is changed to a value between 100 and 5 Ωm . Anyhow, the original model is far better represented by “Result 2” than by “Result 1”.

The example here is comprised of only one layer and a half-space. If more layers are included, the problem gets much bigger. One might claim that it is possible to circumvent this problem by using a homogenous initial model. In this case columns of \mathbf{J} representing the layer thicknesses are $\equiv 0$ in the first iteration and the algorithm can only change the layer resistivities. Therefore, the model after the first iteration will reveal a rough image of the resistivity trend.

The inversion result displayed in tab. E.2 however shows that this does not work in general. Here, a transient was calculated for a three layer case. The other parameters are the same as for the previous example. Again, the inversion algorithm fails to find the original model. The reason here is that at first, decreasing the resistivity ρ_1 will improve the misfit most. After the first iteration step, the algorithm is caught in the same trap as in the previous example.

In this case, fixing the layer thicknesses will not improve the result. However, the comparison can not be made directly. First, the number of free parameters is smaller in the MLFT-case. Increasing the number of layers to five will result in a

better picture of the subsurface. In addition there is a fundamental difference. The discretisation of the MLFT-model is not sufficient. MLFT-models have to consist of many more layers than FLVT. That is what makes them computationally expensive. With this discretisation the MLFT inversion has no chance of achieving a better misfit.

The used discretisation of the FLVT-model in the example however is sufficient with respect to the number and the type of the parameters. It simply does not reach the global minimum. However, the inversion will reach the global if the thickness discretisation of the initial model is close enough to the the one of the “true” model.

Using a FLVT-model provides much more local minima in which the linearised inversion can get stuck than a MLFT-model. On the other hand the computational effort is lower.

E.3 Inversion results

The inversion result does not only depend on the measured data. Although most inversions (except Monte-Carlo-algorithms) are deterministic, the dependencies between the multiple aspects of an inversion are very complex. Beside the obvious influence of the initial model, changing any of these aspects (model discretisation, data weighting, regularisation strategy, definition of misfit) will result in unforseeably different models. Fortunately, the geological interpretation of these different models may be the same. However, it is very important to check which feature of the model is constrained by the measured data and which is a side effect of any parameter. Never mistake an inversion result as the unique and true solution (see also sec. 3.5).

E.3.1 Model discretisation

As pointed out in the preface of chapter 4, any model discretisation is insufficient. Nevertheless, the model discretisation can be good enough to lead to a reasonable and meaningful geological model. In this case the model discretisation is appropriate to describe the geology under investigation.

However, the choice of the model discretisation will influence the inversion result (see sec. E.2.1). Even adding new parameters (i.e. new degrees of freedom) may degrade the misfit of the final model. In the sec. 5.6 or the field inversion results in chapter 6 many examples can be found, where adding the distortion parameters degrades the misfit of the inversion outcome.

Even adding additional layers to a MLFT-model might result in an opposite model when the CF is included (fig. E.1).

There are at least two reasons for this behaviour. First, the structure of the Jacobian changes, especially its condition number. To dampen the inversion of the matrix other regularisation parameters have to be chosen. This affects the composition of the model update vector. Second, if an additional constraint is used in the inversion, as in Occam’s inversion, the additional parameter has to be reflected in the regularisation matrix. This means, adding additional parameters might change

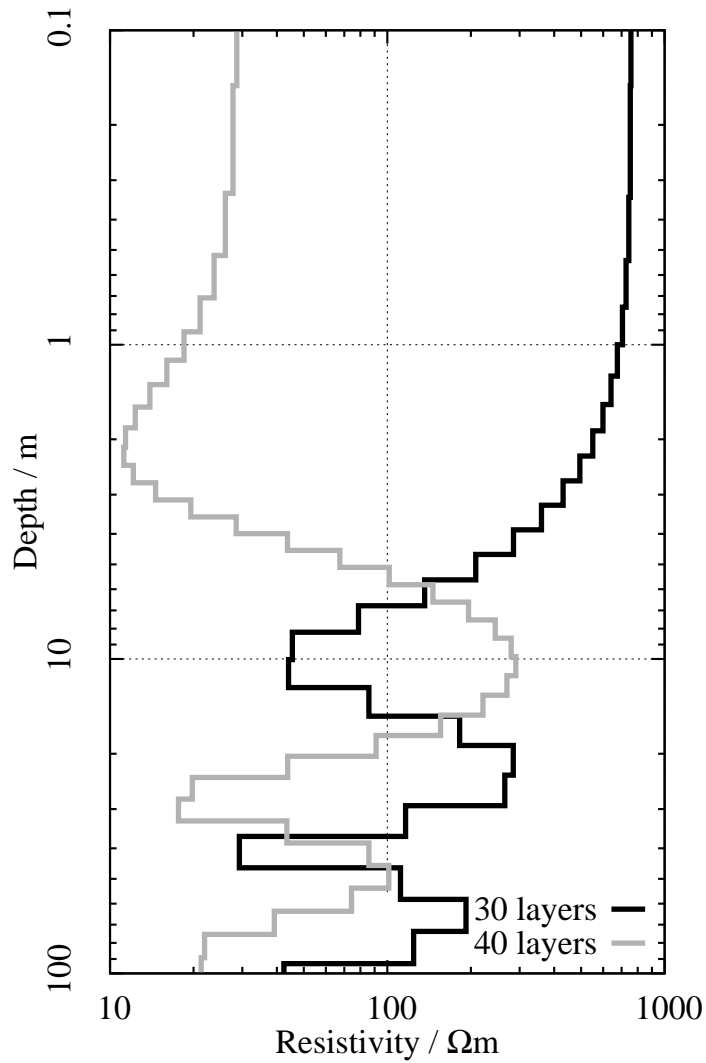


Figure E.1: Inversion results for the same SHOTEM data set using a 30 layer (black line) and a 40 layer model (gray line); the data set was recorded above a waste site close to Düren, Germany [Raimundo, 2005]. The misfit is comparable ($\chi_{30} = 1.03$, $\chi_{40} = 1.59$), but the CFs differ ($CF_{30} = 2.10$, $CF_{40} = 0.95$).

the definition of “smooth” or the relations between different parts of the smoothness.

APPENDIX F

Manual for EMUPLUS

This section describes the basic functions and commands of EMUPLUS. The manual is written for version 6.0. For scientific purposes, the source code can be obtained by writing an e-mail to `helwig@geo.uni-koeln.de`.

The program code itself is very old (the oldest files date back to the eighties) and was adopted by a lot of students. Some of the older features are not supported anymore, although the commands might still work. I will focus only on commands, which work to my knowledge.

For applications of the program in special cases, refer to Commer [1999] (on including *a priori* knowledge to Occam's inversion) and Lange [2003] (on joint-inversion of SHOTEM and LOTEM data sets).

F.1 General remarks

The program can be compiled using the g77 Fortran compiler. Typing `make` in the path of the source codes will produce the binary `emuplus`. To start the program, simply enter `emuplus`. The program will print

```
*****
*      EMUPLUS  -  (E)lectro(M)agnetic (U)niversal      *
*                               Inversion package        *
*                               Version 6.0              *
*****
```

```
<E> Error during open of .def file, creating new one
Emuplus>
```

and wait for commands. The error message (the line starting with <E>) simply says, that no default file named `EMUPLUS.def` is found. The program will create a new one. Every change in the setup, made with the command `SETU` will be saved in this file.

Alternatively, a text file containing all commands to be carried out can be piped to the program. E.g.

```
emuplus < test_script.emu
```

will execute all commands in `test_script.emu` and exit. This is most useful, if a lot of inversions need to be done automatically by a script.

All EMUPLUS-commands consist of four characters. All characters entered after the fourth will be ignored (e.g. typing `LOADI` will execute the command `LOAD`). However, the execution of most commands requires additional input, which may be longer than four characters. EMUPLUS is not case sensitive. Case sensitivity of entries related to file system operations (i.e. data file names) is determined by the file system in use.

It is possible to call other commands from the EMUPLUS prompt by prepending a '!'. For instance, entering

```
Emuplus> !mv OCCAM.log hallo.log
Emuplus> !gnuplot
```

will first move the file `OCCAM.log` to `hallo.log` and invoke `GNUPLOT` afterwards. The possible length of the line is restricted to 50 characters.

When asked for the name of a file to load or save, the extension can be omitted. In this case, EMUPLUS will add its standard extension. If the user enters only `*`, EMUPLUS will list all files with this extension in the actual directory.

In many cases EMUPLUS suggests a default value given in brackets after request. The user can accept this value by pressing `RETURN`.

Some routines, which require random numbers ask for an initial number. The default is a random number which is derived from the system clock¹. If the same initial number is entered, the pseudo random sequence will be the same. This can be interesting for model studies and comparisons.

To use the plotting routines of EMUPLUS, `GNUPLOT` in version 3 or 4 and a `GHOSTVIEW(gv)` are needed.

To exit EMUPLUS, type `EXIT`.

F.2 The data set concept

EMUPLUS allows one to invert several data sets jointly. For several operations it is important to know, how EMUPLUS handles these data sets. Besides some additional information (data type, signal type, offset and so on) each data set consists of

¹Probably, this does not work on every machine.

five arrays: The measured times after shut-off (TEM) or the measured frequencies (MT and CSAMT), the measured data (“MD-array”), the measurement error, the data weights and the synthetic model response (“SMR-array”). The first three have to be provided by the user, the latter are calculated by the program upon execution.

The data from the synthetic model response array can be copied to the measured data array with the command `XFER`

If the user wants to use several data sets simultaneously, he has to shift the data from the active arrays to storage-arrays (in the program they are referred to as “storages”). When in joint-inversion mode, EMUPLUS will overwrite the active arrays with data from the storage-arrays during certain steps. There are several commands regarding these storage-arrays:

`DISP` Displays the contents of all storages, especially the data type, the data set title and to which model the data set is associated with (see `SHMO`).

`SHIF` Shifts a data set from the active arrays to a storage-array.

`RESH` Retrieves a data set from a storage-array to the active array. If a different model is associated with this data set, the model in the active storage-array also overwrites the actual model (see `SHMO`).

`KIBU` A data set is removed from a storage.

`SHMO` Associate an already shifted data set with a certain earth model parameter set. This affects only the Occam’s inversion. If two data sets are inverted jointly with different model parameter sets, EMUPLUS will do a soft joint-inversion (see section 5.4.1).

F.3 The setup

The setup menu can be entered by typing `SETU`. All settings are saved in the file `EMUPLUS.def` every time the menu is exited. The `RESE`-command resets all values from the setup to the default value. The setup menu looks like:

```
Emuplus> setu
Setups available:
INVM  change inversion method
INVP  inversion parameters
OUTP  output
TXPA  transmitter parameters/distortion
CFHD  calibration factor handling
ERRO  data error/weight settings
EXIT  leave setup

Emuplus.Setup> (EXIT)
```

The options are:

INVM Change between Marquardt and Occam's inversion;

INVP Here, all inversion parameters are set; the entries depend on the inversion type set. For Marquardt:

Required tolerance for fit: The inversion stops, if the misfit is below this value.

Minimum relative misfit decrease: The inversion stops, if the relative decrease in misfit between two iterations is below this value.

Maximum number of iterations: The inversion stops after this iteration step.

Minimum for relative singular value threshold: The minimal damping value.

Enter transformation type: Choose the data transformation type [Scholl, 2001]. If 2 is chosen, next line is:

Scale-factor-type: Choose a scale factor for the area sine hyperbolicus ($\operatorname{asinh}x = \ln|x + \sqrt{x^2 + 1}|$). If "fixed" is chosen, the setup will ask for a scale factor.

For Occam's inversion, few different entries will show up. These are:

Roughness 1,2: Choose roughness criterion (either first or second derivative);

Criterion for choosing Lagrange multiplier: If this is set to zero, the inversion will look for the Lagrange multiplier, which provides the lowest misfit. If the entry is one, an L-curve criterion is used. If it is two, the algorithm will still look for the smallest misfit, but will accept the model update only if the cost functional (misfit+roughness) is decreased.

Minimal Lagrange multiplier decrease: If not zero, the Lagrange multiplier may only decrease this much from one iteration to the next, unless it is required to achieve a better model.

Enable OCCAM-anisotropy: In addition to freeing the fixes for the anisotropy parameters, this has to be set to YES in order to also invert anisotropies.

OUTP Set the verbose mode for Marquardt-inversion;

TXPA Here parameters regarding the Tx are set:

Normalized source moment: If on, the source moment is normalised²;

Source current: Enter the source current; Normally, this is set by the input-file.

Dipole length: Here, the dipole length may be changed. Normally, this is set by the input-file. In case of a loop source, this value actually is the loop area.

Include periodicity: If on, the forward calculations for TEM will include previous switching signals. In this case, EMUPLUS will ask for some signal parameters:

²The program uses the american spelling.

Vibrotem(0), 50%(50) or 100%(100) duty cycle: The signal form: Either Vibrotem, or two different duty cycles. "50%" means that the transmitter is switched off, then changes polarity and again is switched off. "100%" means that simply the polarity of the transmitting current is changed. SHOTEM will normally use 50% duty cycle, LOTEM 100%.

Switching time/Frequency: Here, the time between two switching signals (Vibrotem or 100%) or the signal frequency has to be entered.

Extended bipole: If switched off, the forward calculation will assume only a transmitting dipole (infinitesimally short). If switched on, several dipoles will be superpositioned for a bipole.

Invert Tx-Distortion: If switched on, the Tx-distortion Parameters T_{xx} and T_{xy} will be inverted /em in a joint-inversion. The next two items set the starting values for these parameters for every inversion.

CFHD Here, parameters regarding the calibration factor handling can be set:

Preset for CF: Each inversion will start with this value for the CFs. This information will be shifted to the storage-arrays to allow different presets for each data set.

Weigh CF as much as all layers: This sets the entry in the smoothness matrix for the CFs either to one or equal to the number of layers in an Occam's inversion.

Free CF-fixes in iteration: If this is not zero, the (formerly fixed) CFs will in this iteration step be freed in a Marquardt inversion. This forces the inversion code to find a model without changing the CFs. If this is set to -1, the inversion will free the CFs after an inversion with fixed CFs converged.

Never free CF-fixes in storages over: The storage-arrays higher than this value will be excluded, if the CFs are automatically freed.

ERRO Set all parameters regarding the definition of the misfit and the data error estimates:

χ or RMS: If set to YES, the misfit will be a misfit weighted on the data errors (eqn. 3.6). If not, the misfit is an unweighted, relative error in percent (eqn. 3.4).

Take number of free parameter into account: If switched on, the misfit is not normalised on the number of data points but on the number of data points minus the number of free parameters (the misfit thus will be higher). This can be useful, if the misfit of two models with a different number of layers must be compared. Depending on these two entries, EMUPLUS will call the misfit on output either χ_i , $\chi_i - P$, RMS or $RMS - P$.

Lowest accepted error in %: Data errors below this value are set to this value.

Enter error-estimate in %: If the error estimates are zero, they are set to this value.

Relative to each individual data point: In this case, the percentage from the previous item is applied to each datum, which means, that each data

point will have the same relative error estimate (only if no error estimates are found). Otherwise, each datum will have the same absolute error estimate. Then, an additional entries shows up next:

Relative to which data point: If no error estimates are found, and the previous entry was set to NO, all data points get an percentage of this data point as absolute error estimate.

Normalize weights: If switched on, the weights of each data set are normalised. This means for a joint-inversion that all data sets have the same importance.

EXIT Leave the setup menu;

F.4 Commands related to earth models

MODL Enter a new earth model; if the user wants to enter a model with more than ten layers, EMUPLUS offers to automatically produce a model with logarithmical spaced thicknesses. After entering all parameters, it is possible to save the model. Neither any distortion parameters nor calibration factors can be entered.

LMOD List current model; after 20 layers the program will say Hit key and return to continue.... Then, enter q to resume.

SAVM Save model; unless otherwise stated by the user the file will have the extension mod.

GETM Load model saved with SAVM; if the extension of the model file is mod, it may be omitted.

GNUM Save model to a file which can be plotted, e.g. using GNUPLOT; unless otherwise stated by the user the file will have the extension plt.

DIST Change Tx-distortion parameters for the model (see sec. 5.6);

CHPA Change parameters of model; the following sub-menu pops up:

```
Emuplus> chpa
Change Parameter:
  R - Resistivity      T - Thickness
  A - Anisotropy      C - Calibration
  L - List model      E - EXIT
```

```
Change parameter> (          )
```

Use E to exit this menu and L to list the actual parameter values (except the calibration factor). Use R, A or T followed by a number to change a specific parameter or C to change the calibration factor.

FIX Fix model parameter; the following sub-menu pops up:

```

Emuplus> fix
Available commands for Parameter fixing:
  L - List           R - Resistivity
  C - Calibration   T - Thickness
  Z - Zero          A - Anisotropy
  H - Help         E - EXIT
COMMANDS: L P T A C Z H E ( H = HELP)

```

```
Emuplus.Fix> ( )
```

After entering or loading a model, all anisotropies are fixed and all other parameters are not fixed. Use R, A or T followed by a number to fix a specific parameter during the inversion. Enter C to fix the calibration factor. Once fixed, it is not possible to free a certain parameter. Instead, use Z to free ALL parameters. H displays a help page. Use E to return to the standard EMUPLUS command line. IMPORTANT: The fixing information for the calibration factor will also be stored in the storage-array. If you want to fix calibration factors in a joint-inversion, do this prior to the SHIF command. Otherwise the calibration remains unfixed.

MODP A sub-menu pops up, which allows one to incorporate *a priori* information to Occam's inversion. This is done by allowing resistivity jumps in the model [Commer, 1999].

BAMO Take actual model as reference model for a soft joint-inversion;

AVMO Average all models from the storages;

MAMA Produce a starting model for a Marquardt inversion from a Occam's inversion result; the algorithm puts layer boundaries in depths where the model is roughest. This normally does not work very well.

F.5 Commands related to the data sets

EMUPLUS has its own data file format with the extension `dat` (unless the user specifies a different extension). This format contains all information needed to make inversions with the data set (besides the system response, see below). After a header with additional information about the measurement (data type, geometry, signal type and so on) five columns of numbers are written. The first contains only increasing integers, which are of no interest. The second to fourth contain the time/frequency array, the MD- and the SMR-array. The fifth column contain the data errors in percent. As all header lines start with #, the `dat`-files can be plotted using e.g. GNUPLOT³. To save and load data sets in the `dat`-file-format, use the commands `SAVD` and `GETD`, respectively. `SAVD` will also produce a model file with the same name but the extension `mod`. The program will not give an overwrite warning!

³The 3-D-TEM modelling and inversion program SINValso writes out files named `sinrx???.dat`, which are compatible with the EMUPLUS file format.

```

Commands available for data editing
      EDIT:                                DELETE:
"D"  data value                            "\"  first i data points
"W"  weights                               "-"  ith data point
      (enter error in percent)            "/"  last i data points
"A"  time/frequency in s/Hz              ">"  big percentual errors

"E"  exit                                  "H"  print this list
Usage: command <data#> <value>
Emuplus.Edit>

```

Figure F.1: The edit sub-menu in EMUPLUS;

In addition to this proprietary EMUPLUS-dat-format, EMUPLUS can read additional formats for TEM data using the command LOAD. For LOTEM EMUPLUS tries to read rek files produced by the processing package Segy_Pro and maxproc. However, as these files do not contain all information relevant for the forward calculations, the user has to enter the additional information manually. Especially, the signal type has to be defined in the TXPA entry of the SETU sub-menu (see sec. F.3). For SHOTEM-data, EMUPLUS can read also the clt-file-format described in Lange [2003].

For measured TEM-data typically a system response file with the extension syt has to be provided [Scholl, 2001]. Using the LOAD-command EMUPLUS asks if a system response file should be used and its name. Saving the data set afterwards with SAVD will save this information in the dat file BUT NOT THE SYSTEM RESPONSE ITSELF. If the system response file is not available when the user tries to read a dat-file with GETD, EMUPLUS will report an error.

GENE Calculate a synthetic data set; after entering all relevant parameters, the synthetic data is copied to the MD- and SMR-arrays.

FUDG EMUPLUS calculates the shift factor between the data in the MD- and the SMR-array. Then it asks, which factor should be applied. The proposed value is the calculated shift factor. The factor entered by the user then is applied to the data in the MD-array.

SIGN EMUPLUS checks, whether both curves in the MD- and the SMR-array have the same polarity. If not, it changes the sign of the data in the MD-array.

ADD Add a certain value to the data in the MD-array;

EDIT Edit the data; the menu shown in fig. F.1 pops up. Use E to return to the standard EMUPLUS prompt and H to redisplay this menu. The data arrays can be edited by typing D, W or A DIRECTLY followed by the number of the data point and the new value. To e.g. change the third datum of the MD-array to a value of 15, enter D3 15. Enter e.g. \10 to remove the first ten data points, or /5 to remove the last five. -5 will remove only the fifth. Typing > will prompt for a certain percentual error. Any data point with a higher percentual error will be removed from the data set.

DELA Shift TEM data sets along the time-axis. A certain time interval will be added to the time array. This may require the removal of data points which would otherwise have negative times. The program will print the delay already applied to this transient.

SYST Load a system response file;

RENA Enter the data set title;

TYPE Enter the data type; This can be MT for MT data, or CT for CSAMT data. For TEM data sets, the type designation consists of four characters starting with a T. The second character defines the source type, which can be either L for a loop source (SHOTEM) or D for a grounded dipole (LOTEM). The last two characters specify the receiver component, which could one of EX, EY, HX, HY or HZ. Additionally, a rotated electric field (XY) or a tilted and rotated magnetic component (HN) can be used. In this case, one or two angles defining the tilt and rotation have to be provided. The angles are defined in Müller [2000]⁴. If the receiver component HN or HZ are used, EMUPLUS asks whether the data should be calculated as induced voltages or as apparent resistivities.

CUSR Remove the data points around sign reversals;

CUTS Remove the data point with the smallest value;

NOIS Add noise to the data set; normally distributed noise with a standard deviation relative to each datum is added (e.g. 10 %).

NOIA Add noise to the data set; here, normally distributed noise with a fixed standard deviation is added to each data point. The default value is calculated from the last data points of the transient and should give a realistic amount of noise for a mediocre distorted data set (eqn. 5.1. Additionally, a lower relative limit for the standard deviation can be chosen.

DOWE Downweighting of early time data points of TEM transients; early times are dominated by the system response or ramp time. If the system response is not well known, the error estimates for early times can be increased. It asks, where to start and end with what percentages. In between, the percentage will be linear interpolated on log times.

LDAT Shows information about the data set; the commands SHOR and LONG toggle between two modes. The first one only displays the data type, title and information about the source, the latter displays the whole data set.

F.6 Plotting, forward calculation and inversion

With the command `MODE` the user can switch between the single mode, in which all calculations are done for the data set in the actual array and the joint mode, where all calculations are done for the data sets in the storage-arrays. Which type of data is stored is not important.

⁴This is very tricky! Be sure that you use the right angles with the right sign!

In joint mode, most commands described in this section ask, how many data sets should be used. EMUPLUS will use the data sets from the first storage-array, which contain data. An example: If the storage-arrays 1, 2, 4 and 6 contain data and the user says the program should use three data sets, the data from the storages 1, 2 and 4 will be used.

The command `CALC` calculates synthetic data for the model(s). The model response is stored in the SMR-array. If the program is in the joint mode, the synthetic data is shifted back to the storage-arrays. EMUPLUS will write out the misfit, either of one or of all data sets.

The command `AUTO` starts an inversion. Depending on the settings in the `SETU` sub-menu `INVM`, an Occam's or Marquardt inversion is started. Depending on the inversion type, differently named log-files will be written out (see tab. F.1).

The Tx-distortion parameters effect only LOTEM data sets. These parameters are only inverted if a joint-inversion is chosen. Soft joint-inversions will only work for joint Occam's inversions. Most inversions will reset the calibration factors and distortion parameters to the presets defined in the `SETU` sub-menus.

`STEP` Perform one step of a Marquardt single inversion;

`PLAN` Calculates model ((TEM-) responses for different geometries/earth models; this command thus can be used to plan a measurement or to do sensitivity analyses. After some input made by the user the program will create a file `plan.dat` and (if `GNUPLOT` is installed) a plot named `plan.ps`

`EQUI` Check for equivalence models; this is done by changing every model parameter systematically and doing a Marquardt inversion. All other parameters may be changed randomly a few percent to smear out less resolved parameters. If a model with a better misfit is found, it can be used as new reference model. If this happens, the equivalence check is started anew. The models, which are considered equivalent (with a misfit which is less then e.g. 15 % worse then the reference model) are written to the file `EQ_MODELS.DAT`.

`PLOT` Plots actual model and actual data set; two postscript plots are generated via `GNUPLOT` and displayed with `GHOSTVIEW`. Obviously this only works, if compatible versions of `GNUPLOT` and `GHOSTVIEW` are installed.

`XYPL` Produce and save model and data set plot; the same plots as for `PLOT` are produced. Instead of displaying them, EMUPLUS asks for two filenames under which the two postscript files are saved. Alternatively, all files needed to produce the postscript files are saved to a certain subdirectory (`GNUPLOT-script` and `data` files). This is useful, if the computer has no `GNUPLOT` installed or another program is used to plot the data.

inversion/calculation type	log-file name	contains
Occam's, single	\$title.olo	inversion progress
Occam's, joint	OCCAM.log	inversion progress
Marquardt, single	\$title.log	inversion progress
Marquardt, single	\$title.sta	inversion statistics
Marquardt, joint	\$title.jlo	inversion progress
Marquardt, joint	\$title.jst	inversion statistics
PLAN	plan.dat	forward curves for the different cases
PLAN	plan.gnu	GNUPLOT-script for plotting plan.dat
PLAN	plan.ps	plot of different forward curves (*)
equivalence check	EQ_MODELS.DAT	all models found

Table F.1: List of files generated during different types of inversion/calculation; \$title stands for the title of the (last) data set. The lines marked with (*) designate files which will be produced only if a compatible GNUPLOT is installed.

Acknowledgments

I would like to thank Prof. Dr. Bülent Tezkan and Dr. Stefan L. Helwig for being the doctoral thesis supervisor and providing advice and support during the whole time of this work. Also many thanks to Prof. Dr. Andreas Junge for appraising this thesis.

I want to thank Dr. Mark Goldman, Dr. Stefan L. Helwig, Priv.-Doz. Dr. Andreas Hördt, Jörn O. Lange and Prof. Dr. Bülent Tezkan for fruitful discussions which helped to set me back on track and to see things from a different point of view.

Thanks also to Inga Löhken and Lukas Mollidor who helped significantly by creating several scripts and tables for this work. I hope they know now what they worked for.

I gratefully acknowledge funding of the surveys in Israel by the German Bundesministerium für Bildung und Forschung (BMBF) through the research project “Integrated electromagnetic geophysical technology applied to the detection of deep/saline groundwater interfaces in northern and central Israel” (project 02 WT 0248). The measurement would not have been possible without the help of Andreas Gaidetzka, Dr. Mark Goldman, Gaby Haim, Tilman Hanstein, Dr. Stefan L. Helwig, Stefan Hendricks, Sven Jacobsen, Dr. Uri Kafri, Jörn Lange, Jan Neumann, Thilo Schmalz and Martin Thiemer. Logistical support and additional information was provided by the Geophysical Institute of Israel (GII). Thanks also to Dr. Stefan L. Helwig, Priv.-Doz. Dr. Andreas Hördt and Prof. Dr. Bülent Tezkan who managed to employ me for more than four years.

I am especially thankful to Ele Willoughby who fought her way through an early version of the manuscript. Her critical comments on my English makes it (hopefully) possible for native speakers to understand at least the crucial parts of this work. Unfortunately, I had to write several sections after her revision... I also want to thank Stefan L. Helwig, Olaf Koch, Barbara Nix, Jörg Schwinger and Regina Stille for their reviews which improved the manuscript significantly.

The Regional Computing Centre of the University of Cologne (RRZK) provided much computation time. Without clio.rrz.uni-koeln.de, the synthetic model calculations would have taken years. All field data inversions were carried out on

the computers markus, lukas, johannes and matthaeus.geo.uni-koeln.de from the Institute of Geophysics and Meteorology.

My roommates Roland Martin, Olaf Koch and Naser Meqbel provided a great and inspiring working atmosphere. Thanks also to the other “applied geophysics” group members at the institute and especially the folks from the former Außenstelle.

I like to express my gratitude to Regina Stille. Her support in the (sometimes very frustrating) times while completing this work was invaluable. And finally, thanks to Franz and Hanny Scholl for their support through my years of study.

Ich versichere, daß ich die von mir vorgelegte Dissertation selbständig angefertigt, die benutzten Quellen und Hilfsmittel vollständig angegeben und die Stellen der Arbeit - einschließlich Tabellen, Karten und Abbildungen -, die anderen Werken im Wortlaut oder dem Sinn nach entnommen sind, in jedem Einzelfall als Entlehnung kenntlich gemacht habe; daß diese Dissertation noch keiner anderen Fakultät oder Universität zur Prüfung vorgelegen hat; daß sie - abgesehen von unten angegebenen Teilpublikationen - noch nicht veröffentlicht worden ist sowie, daß ich eine solche Veröffentlichung vor Abschluß des Promotionsverfahrens nicht vornehmen werde. Die Bestimmungen dieser Promotionsordnung sind mir bekannt. Die von mir vorgelegte Dissertation ist von Prof. Dr. B. Tezkan betreut worden.

Carsten Scholl

Adresse: Gutenbergstr. 37-39
50823 Köln

Telefon: 0221/426240

E-Mail: scholl@geo.uni-koeln.de

Geburtsdatum: 24.09.1972

Geburtsort: Kevelaer

Staatsangehörigkeit: Deutsch

Schullaufbahn: 1979-1983: Overberg-Grundschule, Winnekendonk
1983-1992: Kardinal-von-Galen-Gymnasium, Kevelaer
01.06.1992: Abitur

Wehrdienst: Juli 1992 bis Juni 1993

Studium: Immatrikulation: 01.10.1993 an der Universität zu Köln,
Fachrichtung Geophysik
Zum SS 96 Wechsel zur Fachrichtung Physik
15.05.2001: Vordiplom Physik
Zum SS 98 Wechsel zur Fachrichtung Geophysik
12.07.2001: Abschluss des Studiums als "Diplom-Geophysiker"

Berufserfahrung: 1997-2001: Studentische Hilfskraft am
Institut für Geophysik und Meteorologie der Universität zu Köln
Seit 2001: Wissenschaftlicher Mitarbeiter am
Institut für Geophysik und Meteorologie der Universität zu Köln